

M. Campanelli
A. Clark
X. Wu
(Eds.)

Hadron Collider Physics 2005

Proceedings of the
1st Hadron Collider Physics
Symposium,
Les Diablerets, Switzerland,
July 4–9, 2005



Springer

SPRINGER PROCEEDINGS IN PHYSICS

- 87 **Proceedings
of the 25th International Conference
on the Physics of Semiconductors**
Editors: N. Miura and T. Ando
- 88 **Starburst Galaxies**
Near and Far
Editors: L. Tacconi and D. Lutz
- 89 **Computer Simulation Studies
in Condensed-Matter Physics XIV**
Editors: D.P. Landau, S.P. Lewis,
and H.-B. Schüttler
- 90 **Computer Simulation Studies
in Condensed-Matter Physics XV**
Editors: D.P. Landau, S.P. Lewis,
and H.-B. Schüttler
- 91 **The Dense Interstellar Medium
in Galaxies**
Editors: S. Pflanzner, C. Kramer,
C. Straubmeier, and A. Heithausen
- 92 **Beyond the Standard Model 2003**
Editor: H.V. Klapdor-Kleingrothaus
- 93 **ISSMGE**
Experimental Studies
Editor: T. Schanz
- 94 **ISSMGE**
Numerical and Theoretical Approaches
Editor: T. Schanz
- 95 **Computer Simulation Studies
in Condensed-Matter Physics XVI**
Editors: D.P. Landau, S.P. Lewis,
and H.-B. Schüttler
- 96 **Electromagnetics in a Complex World**
Editors: I.M. Pinto, V. Galdi,
and L.B. Felsen
- 97 **Fields, Networks,
Computational Methods and Systems
in Modern Electrodynamics**
A Tribute to Leopold B. Felsen
Editors: P. Russer and M. Mongiardo
- 98 **Particle Physics and the Universe**
Proceedings of the 9th Adriatic Meeting,
Sept. 2003, Dubrovnik
Editors: J. Trampetić and J. Wess
- 99 **Cosmic Explosions**
On the 10th Anniversary of SN1993J
(IAU Colloquium 192)
Editors: J. M. Marcaide and K. W. Weiler
- 100 **Lasers in the Conservation of Artworks**
LACONA V Proceedings,
Osnabrück, Germany, Sept. 15–18, 2003
Editors: K. Dickmann, C. Fotakis,
and J.F. Asmus
- 101 **Progress in Turbulence**
Editors: J. Peinke, A. Kittel, S. Barth,
and M. Oberlack
- 102 **Adaptive Optics
for Industry and Medicine**
Proceedings
of the 4th International Workshop
Editor: U. Wittrock
- 103 **Computer Simulation Studies
in Condensed-Matter Physics XVII**
Editors: D.P. Landau, S.P. Lewis,
and H.-B. Schüttler
- 104 **Complex Computing-Networks**
Brain-like and Wave-oriented
Electrodynamic Algorithms
Editors: I.C. Gökner and L. Sevgi
- 105 **Computer Simulation Studies
in Condensed-Matter Physics XVIII**
Editors: D.P. Landau, S.P. Lewis,
and H.-B. Schüttler
- 106 **Modern Trends in Geomechanics**
Editors: W. Wu and H.S. Yu
- 107 **Microscopy of Semiconducting Materials**
Proceedings of the 14th Conference,
April 11–14, 2005, Oxford, UK
Editors: A.G. Cullis and J.L. Hutchison
- 108 **Hadron Collider Physics 2005**
Proceedings of the 1st Hadron
Collider Physics Symposium,
Les Diablerets, Switzerland, July 4–9, 2005
Editors: M. Campanelli, A. Clark,
and X. Wu

M. Campanelli A. Clark X. Wu (Eds.)

Hadron Collider Physics 2005

Proceedings of the 1st Hadron Collider Physics Symposium,
Les Diablerets, Switzerland,
July 4–9, 2005

With 441 Figures

Mario Campanelli
Allan Clark
Xin Wu
Université de Genève
24, qai Ernest-Ansermet
CH-1211 Genève 4, Switzerland

ISSN 0930-8989

ISBN-10 3-540-32840-8 Springer Berlin Heidelberg New York

ISBN-13 978-3-540-32840-7 Springer Berlin Heidelberg New York

Library of Congress Control Number: 2006925168

This work is subject to copyright. All rights are reserved, whether the whole or part of the material is concerned, specifically the rights of translation, reprinting, reuse of illustrations, recitation, broadcasting, reproduction on microfilm or in any other way, and storage in data banks. Duplication of this publication or parts thereof is permitted only under the provisions of the German Copyright Law of September 9, 1965, in its current version, and permission for use must always be obtained from Springer-Verlag. Violations are liable to prosecution under the German Copyright Law.

Springer is a part of Springer Science+Business Media.

springer.com

© Springer-Verlag Berlin Heidelberg 2006
Printed in Germany

The use of general descriptive names, registered names, trademarks, etc. in this publication does not imply, even in the absence of a specific statement, that such names are exempt from the relevant protective laws and regulations and therefore free for general use.

Production: LE-TeX Jelonek, Schmidt & Vöckler GbR, Leipzig
Cover concept: Frido Steinen, eStudio Calamar, Spain
Cover production: *design & production* GmbH, Heidelberg

Printed on acid-free paper SPIN: 11681991 54/3100/LeTeX 5 4 3 2 1 0

Preface

The first Hadron Collider Physics Symposium (HCP2005) was held in Les Diablerets, Switzerland from 4-9 July 2005. With data samples exceeding 1 fb^{-1} collected by the CDF and D0 experiments at the Fermilab Tevatron, and with the projected commissioning of CERN's Large Hadron Collider (LHC) in 2007, the Hadron Collider Conference (HCP) series was merged with the LHC Symposium series and renamed the Hadron Collider Physics Symposium.

The Symposium was attended by more than 150 physicists and was jointly organized by the Swiss Institute for Particle Physics (CHIPP) and CERN. Previously, the 15th HCP Conference (HCP2004) had been held at Michigan State University in June, 2004, and the 4th. LHC Symposium was held at Fermilab in May 2003.

Following an introductory theoretical overview focusing on the Higgs sector of the Standard Model and the role of hadron colliders in its study, the first major session was devoted to the machine and detector status at the Tevatron and LHC. Historically, a major function of hadron colliders has been to probe physics at the high-energy frontier. At the Tevatron, the CDF and D0 experiments are operating well and an integrated luminosity exceeding 1 fb^{-1} has already been delivered to each experiment. Prior to LHC turn-on, one can expect to probe the Standard Model at the TeV (atto-metre) scale. At the same time, there has been impressive construction progress on the LHC and the associated experiments (ATLAS, CMS, LHCb and TOTEM). Indeed, the new phase of detector integration and commissioning at the LHC has started.

With the goal of maximizing the shared experience of the Tevatron and LHC communities, sessions were then organized around the key physics directions of experimental hadron collider research:

- QCD physics;
- Precision electroweak physics;
- Results on c-quark, b-quark, and t-quark physics;
- Probing for physics beyond the Standard Model; and
- Heavy Ion physics (RHIC and LHC).

Each session was introduced with a theoretical overview of the subject and followed by experimental talks from

the Tevatron and LHC experiments. Summary talks from the RHIC, HERA and b-factory experiments (BELLE and BABAR) complemented the relevant sessions. In addition, specific sessions were devoted to experimental issues such as particle identification or tracking and b-tagging, where experts from both communities could present their solutions and exchange ideas.

A special guest at the symposium, 10 years after the discovery of the top quark by the CDF and D0 experiments, was Alvin Tollestrup (Fermilab) who played a crucial role in the machine, detector and analysis activities leading to its discovery.

The local organizing committee from CERN and CHIPP, together with the ATLAS and CMS secretaries (Jodie Hallman and Nadejda Bogolioubova) and the local hotel staff made this Symposium a real success. Only the unpredictable factor, weather, played foul. Those fortunate participants who remained an extra day discovered the beauty of Les Diablerets in brilliant sunshine.

The next meeting of the series will be hosted by Duke University in May 2006, and in Summer 2007 the meeting will be hosted by INFN Pisa in or near Pisa.

Allan Clark,
University of Geneva,
December 2005.

Committee

Scientific Program Committee

J.Blazey	(NIU)
A.Clark (chair)	(Geneva)
M.Della Degra	(CERN)
D.Green	(FNAL)
R.K.Ellis	(FNAL)
J.Engelen	(CERN)
L.Foa'	(Pisa)
R.Fleischer	(CERN)
H.Frisch	(Chicago)
F.Gianotti	(CERN)
A.Goshaw	(Duke)
H.A.Gustafsson	(Lund)
J.Hobbs	(Stony Brook)
D.Jacobs	(CERN)
P.Jenni	(CERN)
Y.K. Kim	(Chicago)
T.Kobayashi	(Tokyo)
A.Kotwal	(Duke)
K.Maeshima	(FNAL)
M.Mangano	(CERN)
H.Montgomery	(FNAL)
T.Nakada	(CERN/EPFL)
J.Schukraft	(CERN)
A.Seiden	(Santa Cruz)
P.Sphicas	(CERN/Athens)
M.Spira	(PSI)
S.Stone	(Syracuse)
U.Straumann	(Zurich)
I.Tikhonov	(Novosibirsk)
J.Virdee	(CERN/IC)
H.Weerts	(MSU)
X.Wu	(Geneva)
T.Wyatt	(Manchester)

Organizing Committee

H.P. Beck	(Bern)
M.Campanelli	(Geneva)
G.Dissertori	(ETH Zurich)
W.Erdmann	(PSI)
D.Jacobs (co-chair)	(CERN)
F.Lehner	(Zurich)
T.Schietinger	(EPF Lausanne)
X.Wu (co-chair)	(Geneva)

Summary of the Program Committee meeting for future HCP Symposia

On Thursday 7 July, 2005, those members of the HCP Symposium Scientific Program Committee who attended the meeting met to discuss future meetings of the series. (Present: A. Clark, R. Ellis, J. Engelen, H. Frisch, A. Goshaw, H.-A. Gustafsson, P. Jenni, M. Mangano, H. Montgomery, A. Seiden, U. Straumann, X. Wu. Invited: R. Castaldi, D. Rousseau, M. Lancaster, N. Russakovich)

It was confirmed that the HCP2006 Symposium would be hosted by Duke University in the period May 22-26, 2006. A. Kotwal (Duke) will coordinate the Symposium.

Following a call for possible venues of the HCP2007 Symposium, the following proposals were received.

1. University of Oklahoma, USA, 10-15 December, 2007, contact: P. Gutierrez, C. Kao
2. Dubna, Russia, late in 2007, contact: N. Rusakovich
3. Paris, France, late in 2007, contact: D. Fournier, D. Rousseau (LAL)
4. UK (location to be decided), Oct 2007- February 2008, contact: N. Mc.Cubbin (RAL)
5. Pisa, Italy, Elba (June 2007) or Pisa (late 2007), contact: G. Tonelli, R. Castaldi
6. Rio de Janeiro (Brazil), late in 2007, contact: H. da Motta Fihó, G. Alves

In addition, P. Jenni suggested a venue near CERN to present the first LHC physics results. In particular, Evian was suggested as a possibility, in view of the previous meeting there to present LHC proposals.

There was a discussion on the timing of the HCP2007 Symposium, in view of the LHC turn-on and it was concluded by unanimous consensus that:

- the HCP2007 Symposium should be held prior to LHC turn-on and should concentrate on Tevatron results and the preparations for LHC;
- the HCP2008 Symposium should be timed to present initial LHC data.

In the discussion it became clear that all proposals except for that of Pisa had been intended for the presentation of initial LHC data, and would need to be reconsidered.

The meeting agreed that:

- The HCP2007 Symposium would be hosted by INFN (Pisa), in the period May-June 2007. R. Castaldi (INFN Pisa) agreed to submit a detailed planning at the HCP2006 Symposium at Duke University.
- The HCP2008 Symposium would be organized by CERN and the LHC experiments at a location near CERN. The symposium would be timed to present initial LHC results. CERN and the LHC experiments were invited to present a definite proposal at the HCP2006 Symposium at Duke University.
- The other submitted proposals should be reconsidered for future Symposia at the HCP2006 meeting, and that in future regional rotations of the venue should be attempted.

Allan Clark,
Chair,
HCP2005 Scientific Program Committee,
University of Geneva,
December 2005.

List of Participants

Name	Institution
Clemens Adler	Physikalisches Institut Heidelberg
Lorenzo Agostino	CERN
Manuel Aguilar-Benitez	CIEMAT
Ijaz Ahmed	Quaid-i-Azam Univ. (Pakistan)
Frederik Akesson	CERN
Benjamin Allanach	University of Cambridge
Nicola Amapane	CERN
Silvia Arcelli	INFN Bologna
Kurmar Ashok	Panjab University (India)
Giuseppe Avolio	Universita della Calabria
Pierre Barrillon	Imperial College London
Ulrich Baur	SUNY
Hans-Peter Beck	LHEP, University of Bern
Birkan Belin	TUBITAK – Istanbul Technical University
Anwar Bhatti	Rockefeller University
Anju Bhasin	University of Jammu
Jean-Jacques Blaising	CERN
Norm Buchanan	Florida State University
Emmanuel Busato	LPNHE Paris
Orhan Cakir	Ankara University
Mario Campanelli	University of Geneva
Joao Carvalho	LIP – Coimbra
Brendan Casey	Brown Univ.
Heriberto Castilla-Valdez	Cinvestav-IPN
Paoti Chang	National Taiwan University
Allan Clark	Univ. Geneva
Gustavo Conesa Balbastre	IFIC – Universidad de Valencia
Marie-Claude Cousinou	C.P.P.M. Universite de la Mediterranee
Timothy Cox	University of California at Davis
Andrea Dainese	University of Padova & INFN
Evelyne Daubie	Universite de Mons-Hainaut
Giovanna Davatz	ETH Zurich
Mario Deile	CERN
Bilge Demirkoz	Oxford University
Frederic Derue	LPNHE
Michael Diesburg	Fermilab
Mauro Dinardo	Universita degli Studi di Milano
Günther Dissertori	ETH Zurich

Name	Institution
Mauro Donega	University of Geneva
Shashikant Dugad	Tata Institute of Fundamental Research
Jan Ehlers	ETH Zurich
Keith Ellis	Fermilab
Jos Engelen	CERN
Wolfram Erdmann	Paul Scherrer Institut
Lyndon Evans	CERN
Peter Fauland	LPHE-IPEP, EPFL
Roger Forty	CERN
Henry Frisch	University of Chicago
Szymon Gadomski	Univ. Bern
Ludovic Gaudichet	Universita di Torino&INFN
Simone Gennai	Scuola Normale Superiore & INFN Pisa
Cecilia Gerber	University of Illinois
Heather Gerberich	University of Illinois
Andrea Giammanco	SNS and INFN Pisa
Fabiola Gianotti	CERN
Agostinho Gomes	LIP-Lisbon
Guillermo Gomez-Ceballos	Instituto de Fisica de Cantabria
Al Goshaw	Duke University
Anna Goussiou	University of Notre Dame
Hans-Ake Gustafsson	CERN/Lund University
Kazu Hanagaki	Fermilab
Luc Hinz	LPHE – EPFL
John Hobbs	SUNY Stony Brook
Sadiq Hussain	National Institute of Sciences and Technology
Hiroyuki Iwasaki	KEK
David Jacobs	CERN
Christian Jacoby	LPHE, EPF Lausanne
Karl Jakobs	Freiburg University
Daniel Jeans	CNAF
Peter Jenni	CERN
Max Klein	DESY
Olga Kodolova	SINP MSU
Otto Kong	National Central University
Zoltan Kunszt	ETH Zurich
Didier Lacour	LPHNE Paris – IN2P3/CNRS
Mark Lancaster	University College London
Federica Legger	EPFL
Frank Lehner	Univ. Zurich
Jessica Leveque	University of Arizona
Stephen Levy	University of Chicago
Alison Lister	ETH Zurich
Arnaud Lucotte	LPSC / IN2P3
Tariq Mahmoud	Universite Libre Bruxelles
Amélia Teixeira	Maio LIP
Fabio Maltoni	CERN
José Maneira	LIP
Michelangelo Mangano	CERN
David McGinnis	Fermilab
Emilio Meschi	CERN
Hugh Montgomery	Fermilab
Usman Muhammad	Quaid-i-Azam University
Thomas Muller	Universitat Karlsruhe
Korkut Ozansoy	Ankara University
Cigdem Ozkan	Middle East Tach. Univ. Ankara
Mitesh Patel	CERN
Thomas Peitzmann	Utrecht University / NIKHEF

Name	Institution
Davide Perego	Universita' degli Studi di Milano Bicocca & INFN
Pascal Perret	Laboratoire de Physique Corpusculaire CNRS/IN2P3
Chariclia Petridou	Aristotle University of Thessaloniki
Marco Pieri	University of California San Diego
Davide Pinci	Unisversita "La Sapienza" INFN Roma 1
Serban Protopopescu	Brookhaven National Laboratory
Arnulf Quadt	University of Bonn
Kenneth Read	Oak Ridge National Laboratory
Laurent Rosselet	Geneva University
Giuseppe Salamanna	INFN Roma 1
João Saraiva	LIP
Alessio Sarti	LNF Frascati
Vladimir Savinov	University of Pittsburgh
Stephane Savoff	CERN
Thomas Schietinger	EPF Lausanne
Michael Schmelling	Max Planck Institute for Nuclear Physics
Abraham Seiden	UC Santa Cruz
Anna Sfyrla	University of Geneva
Luca Silvestrini	INFN Roma 1
Tomasz Skwarnicki	Syracuse University
Frederick Snider	Fermilab
Steinar Stapnes	University of Oslo
Norbert Straumann	Univ. Zurich
Ueli Straumann	Univ. Zurich
Anyes Tafford	University of Illinois
Fabien Tarrade	IN2P3/CNRS
Jeff Temple	University of Arizona
Yury Tikhonov	Budker Institute of Nuclear Physics
Alvin Tollestrup	Fermilab
Tomonobu Tomura	University of Tsukuba
Salma Umme	PCSIR
Pascal Vanlaer	IIHE – ULB
Ann Van Lysebetten	CERN
Gregory Veramendi	University of Illinois
Stefano Villa	EPF Lausanne
Tejinder Virdee	CERN/Imperial College
Iacopo Vivarelli	INFN Pisa
Georg Weiglein	IPPP Durham
Christian Weiser	University of Karlsruhe
Urs Achim Wiedemann	CERN/University of Bielefeld
John Womersley	US Department of Energy
Xin Wu	Univ. Geneva
Boleslaw Wyslouch	MIT
Yuehong Xie	University of Edinburgh
Nicolas Zwahlen	LPHE – EPFL





Contents

Preface	V
Committee	VI
Summary of the Program Committee meeting for future HCP Symposia	VII
List of Participants	VIII

Section 1 Introduction and Experimental Status

Status of the ALICE Detector at LHC	
<i>Hans-Ake Gustafsson, For the ALICE Collaboration</i>	
1 Introduction	3
2 Status of the detector subsystems.	3
3 Status of control systems and computing	6
4 Conclusion	7
ATLAS status	
<i>Steinar Stapnes - For the ATLAS collaboration</i>	
1 Introduction	8
2 Magnet Systems	8
3 Inner Detector	9
4 Calorimeters	10
5 Muon Spectrometer	10
6 Trigger and DAQ System	12
7 Computing, Software and Physics Preparation	12
8 Summary	12
9 Acknowledgement	12
Status of CMS	
<i>Tejinder S. Virdee</i>	
1 Introduction	13
2 CMS: The Compact Muon Solenoid	13
3 The Status of CMS	14
4 Conclusions	18
5 Acknowledgements	18
Status of the LHCb experiment	
<i>Roger Forty</i>	
1 Introduction	19
2 Detector status	20
3 Expected performance	22
4 Conclusion	23

Section 2 QCD Physics at the Tevatron and LHC

Theoretical Perspectives in QCD:	
<i>R. Keith Ellis</i>	
1 Introduction	27
2 The role of tree graphs	27
3 Spinor techniques and MHV amplitudes	27
4 Next-to-leading order	29
5 Next-to-next-leading order	30
6 Conclusion	32

Physics at HERA	
<i>Max Klein</i>	
1 Introduction	33
2 Low x Physics	34
3 Physics at the Rapidity Plateau	36
4 Recent Developments in HERA Physics	38
5 Concluding Remarks	39
Diffraction and Total Cross-Section at the Tevatron and the LHC	
<i>M. Deile, G. Anelli, A. Aurola, V. Avati, V. Berardi, U. Bottigli, M. Bozzo, E. Brücken, A. Buzzo, M. Calicchio, F. Capurro, M.G. Catanesi, M.A. Ciocci, S. Cuneo, C. Da Vià, E. Dimovasili, K. Eggert, M. Eräluoto, F. Ferro, A. Giachero, J.P. Guillaud, J. Hasi, F. Haug, J. Heino, T. Hilden, P. Jarron, J. Kalliopuska, J. Kaspar, J. Kempa, C. Kenney, A. Kok, V. Kundra, K. Kurvinen, S. Lami, J. Lämsä, G. Latino, R. Lauhakangas, J. Lippmaa, M. Lokajicek, M. Lo Vetere, D. Macina, M. Macrì, M. Meucci, S. Minutoli, A. Morelli, P. Musico, M. Negri, H. Niewiadomski, E. Noschis, J. Ojala, F. Oljemark, R. Orava, M. Oriunno, K. Österberg, R. Paoletti, S. Parker, A.-L. Perrot, E. Radermacher, E. Radicioni, E. Robutti, L. Ropelewski, G. Ruggiero, H. Saarikko, G. Sanguinetti, A. Santroni, S. Saramad, F. Sauli, A. Scribano, G. Sette, J. Smotlacha, W. Snoeys, C. Taylor, A. Toppinen, N. Turini, N. Van Remortel, L. Verardo, A. Verdier, S. Watts, J. Whitmore</i>	
1 Introduction	40
2 Elastic pp and $p\bar{p}$ Scattering	41
3 Total pp and $p\bar{p}$ Cross-Section	42
4 Diffraction	43
The Jet Energy Scale and Inclusive Jet Cross Section at DØ	
<i>Norm J. Buchanan</i>	
1 Introduction	46
2 The DØ Calorimeter	46
3 Jet Energy Scale	46
4 Inclusive Jet Cross Section	48
5 Conclusion	49
6 Acknowledgments	49
Determination of Jet Energy Scale and Measurement of Inclusive Jet Production at CDF-II	
<i>Anwar A Bhatti</i>	
1 Jet Energy Scale Determination	50
2 Inclusive Jet Cross Section	52
Fragmentation, Underlying Event and Jet Shapes at the Tevatron (CDF)	
<i>Alison Lister for the CDF Collaboration</i>	
1 Introduction	54
2 Fragmentation	54
3 Underlying event	55
4 Jet Shapes	56
5 Conclusions	57
6 Acknowledgements	57

High p_T Jets and Photons at the Tevatron

<i>Cecilia E. Gerber</i>	58
1 Introduction	58
2 Dijet Azimuthal Decorrelations	58
3 b Jet Cross Sections	58
4 Photon Studies	60
5 Conclusions	62
6 Acknowledgments	62

Jet Measurements in ATLAS

<i>I. Vivarelli</i>	63
1 Introduction	63
2 The ATLAS calorimeter	63
3 Cell Clustering	63
4 Jet Reconstruction	64
5 Jet Calibration	65
6 In Situ Calibration	65
7 Conclusions	66

Jet energy measurements in CMS

<i>Olga Kodolova (CMS Collaboration)</i>	67
1 Introduction	67
2 CMS detector	67
3 Jet reconstruction	67
4 Jet calibration	68

Section 3

Electroweak Physics at the Tevatron and LHC

Electroweak Physics at the Tevatron and LHC:
Theoretical Status and Perspectives

<i>Ulrich Baur</i>	73
1 Introduction	73
2 Weak Boson Physics	73
3 Di-boson Production	76
4 Higgs Boson Physics	77
5 Summary	77

 W/Z Production Cross Sections and Asymmetries at
 $\sqrt{s} = 1.96$ TeV

<i>Serban Protopopescu</i>	79
1 Introduction	79
2 $W/Z \rightarrow \mu$'s or e 's	79
3 $W/Z \rightarrow \tau$'s	80
4 $Z/\gamma^* \rightarrow ee$ Forward Backward Asymmetry	81
5 $W \rightarrow e\nu$ Charge Asymmetry	82
6 Conclusion	82
7 Acknowledgements	82

W Mass and Properties

<i>Mark Lancaster (on behalf of the CDF and DØ collaborations)</i>	83
1 Introduction	83
2 CDF W Mass Measurement	83
3 W Width measurement	84
4 Future measurements	85
5 Acknowledgements	85

Di-Boson Physics at the Tevatron

<i>A. T. Goshaw (for the CDF and DØ Collaborations)</i>	86
1 Introduction	86
2 W boson production with a photon	86
3 W^+W^- and $W^\pm Z$ boson pair production	87
4 Z boson production with a photon	87
5 Summary and conclusions	88
6 Acknowledgements	88

Precision Electroweak Measurements at ATLAS and CMS

<i>Nicola Amapane</i>	91
1 Introduction	91
2 Measurement of the W boson and top quark mass	91
3 Drell-Yan production of lepton pairs	93
4 Parton Distribution Functions	93
5 Production of Vector Boson Pairs	94
6 Conclusions	94

Section 4

Preparing for LHC I

Muon Identification at the Tevatron

<i>Jeff Temple, for the CDF and DØ Collaborations</i>	99
1 Introduction	99
2 Muon Detection	99
3 Muon Triggering	100
4 Muon Reconstruction	100
5 Conclusion	101

Tau Identification at the Tevatron

<i>Stephen Levy (on behalf of the CDF and DØ collaborations)</i>	102
1 Introduction	102
2 Hadronic Tau Reconstruction	102
3 Tau Triggers	104
4 Electroweak Tau Results	104
5 Searches for New Physics	105
6 Conclusion	105

Electron and photon identification in ATLAS

<i>F. Derve - For the ATLAS collaboration</i>	107
1 Introduction	107
2 The electron and photon selection goals	107
3 Beam test performance	107
4 Combined ID/EM calorimeter performance	109
5 Conclusion	111

Muon identification at CMS, and confrontation with Monte Carlo and test beam data

<i>Tim Cox</i>	112
1 Introduction	112
2 Simulation confrontation with test beam data	113
3 Muon identification: the level 1 trigger	114
4 Muon identification: the higher-level trigger	114
5 Muon identification: offline reconstruction	115
6 Conclusions	116

Muon Identification at Atlas and Comparison with Simulation and Test Beam Data		Searches for BSM (non-SUSY) physics at the Tevatron	
<i>G. Avolio, on behalf of the ATLAS muon community</i> . . .	117	<i>Heather K Gerberich (for the CDF and DØ Collaborations)</i>	149
1 Muon System Overview	117	1 Introduction	149
2 Muon Spectrometer Sub-Detectors	118	2 High Mass Dilepton Searches	149
3 The Alignment System	118	3 Charged Heavy Vector Boson (W')	151
4 The Muon Trigger System	118	4 Leptoquarks	152
5 Muon Momentum Measurement	119	5 Excited Electrons	152
6 Muon System Test at CERN H8 Area	119	6 Summary	153
7 Conclusions	121	Higgs Searches at the Tevatron	
8 Acknowledgements	121	<i>Anna Goussiou</i>	154
Tau identification at ATLAS : importance, method and confrontation with Monte Carlo and test beam		1 Introduction	154
<i>F. Tarrade, on behalf of the ATLAS Collaboration</i> . . .	122	2 Standard Model Higgs	154
1 Introduction	122	3 Higgs in the MSSM	157
2 ATLAS detector	122	Searches for Higgs Bosons at LHC	
3 Physics processes with τ leptons and their decays . .	123	<i>Marco Pieri</i>	159
4 Hadronic tau reconstruction	123	1 Introduction	159
5 Tau trigger	125	2 Standard Model Higgs Boson	159
6 Experimental results from test beam	125	3 MSSM Higgs searches	161
7 Conclusion	126	4 Measurement of Higgs bosons parameters	164
Tau identification in CMS		5 Conclusions	164
<i>Simone Gennai</i>	127	Sensitivity to New Physics in the B -Sector	
1 Introduction	127	<i>Michael Schmelling</i>	165
2 Tau Trigger	127	1 Introduction	165
3 Level 1 Trigger	127	2 CP-Violation Measurements	165
4 Off Line Selection	129	3 CKM-Matrix and Unitarity Triangle	166
5 Conclusions	130	4 Probing New Physics	166
6 Acknowledgement	130	5 Experimental Constraints on New Physics	168
Particle identification of the LHCb experiment		6 B -Physics at LHC	169
<i>A. Van Lysebetten</i>	131	7 Summary	170
1 Introduction	131	Section 6	
2 Hadron identification with the RICH detectors . . .	131	Heavy Ions	
3 Lepton identification	133	Nucleus-nucleus and proton-nucleus collisions at the LHC	
4 Conclusions	134	<i>Urs Achim Wiedemann</i>	173
Section 5		1 Introduction	173
Beyond the Standard Model		2 Collective phenomena at RHIC and open questions .	174
Theoretical Developments Beyond the Standard Model		3 Probes of the produced dense matter	175
<i>B.C. Allanach</i>	137	Direct Photons, Vector Mesons and Heavy Flavor Production at RHIC	
1 The Technical Hierarchy Problem and Supersymmetry	137	<i>K.F. Read</i>	179
2 Higgsless Models	141	1 Introduction	179
3 Little Higgs and T-Parity	142	2 Direct Photons	180
4 Conclusions	142	3 Vector Mesons	181
Searches for Supersymmetry at the Tevatron		4 Heavy Flavor Production	181
<i>Marie-Claude Cousinou</i>	144	5 Summary and Conclusions	183
1 Introduction	144	Jet production and high p_T hadrons at RHIC	
2 Searches for Charginos, Neutralinos and Sleptons. .	144	<i>Thomas Peitzmann</i>	184
3 Searches for squarks and gluinos.	146	1 Introduction	184
4 Searches for $B_s^0 \rightarrow \mu^+ \mu^-$ decays	148	2 Single Hadron Suppression	184
5 Conclusion	148	3 Jet-Like Correlations	186
		4 Summary	189

Open heavy-flavour production in ALICE		B_s Properties at the Tevatron	
<i>A. Dainese for the ALICE Collaboration</i>	190	<i>Guillermo Gómez-Ceballos</i>	228
1 Introduction	190	1 Introduction	228
2 Heavy-flavour production from pp to AA	190	2 $B_{s(d)} \rightarrow h^+ h'^-$ Decays	228
3 Heavy-flavour detection in ALICE	191	3 $\Delta\Gamma_s/\Gamma_s$ Measurement in $B_s \rightarrow J/\Psi\phi$ Decays	229
4 Measurement of charm production and in-medium quenching	191	4 B_s Mixing	230
5 Measurement of beauty production in the semi-electronic decay channel	193	5 Conclusions	232
6 Measurement of beauty production in the semi-muonic decay channel	194	Searches for Rare B meson decay at Tevatron	
7 Conclusions	194	<i>Shashikant R. Dugad</i>	233
Identification of high energy direct photons and photon-jet events at LHC with ALICE		1 Introduction	233
<i>G. Conesa, H. Delagrangé, J. Díaz, Y.V. Kharlov, Y. Schutz</i>	195	2 Methodology	233
1 Introduction	195	3 Data Processing	234
2 Event simulation and main reconstruction features	195	4 Analysis of D0 Data	235
3 Prompt photon identification: Isolation Cut Method	196	5 Analysis of CDF Data	236
4 Photon-tagged jets identification	198	6 Results	236
5 Conclusions	200	Trigger Strategy and Performance of the LHCb Detector	
Electron Identification with the ALICE TRD		<i>Mitesh Patel</i>	237
<i>Clemens Adler (for the ALICE TRD Collaboration)</i>	201	1 Introduction	237
1 Introduction	201	2 Trigger Strategy	237
2 The ALICE TRD	201	3 The three levels of the LHCb trigger	238
3 Electron Identification	202	4 Using RICH information in the trigger	239
4 Recent Test Beam Results	203	5 Conclusion	240
5 Conclusions	205	Event reconstruction and physics performance of the LHCb experiment	
Heavy Ions in ATLAS		<i>Yuehong Xie (on behalf of the LHCb Collaboration)</i>	242
<i>L. Rosselet for the ATLAS Collaboration</i>	206	1 Introduction	242
1 Introduction	206	2 Event reconstruction performance	242
2 Simulations	206	3 Physics sensitivity	243
3 Global observables	207	4 Conclusion	244
4 Heavy-quarkonia suppression	207	B-Physics expectations at ATLAS and CMS	
5 Jet quenching	208	<i>Petridou Charichia</i>	248
6 Proton-nucleus physics	208	1 Introduction	248
7 Conclusion	209	2 The strategy of ATLAS and CMS on B-Physics	248
		3 Detector performance	249
		4 Measurement of the B_s mixing parameters	250
		5 Rare Decays, prospects for ATLAS and CMS	250
		6 Conclusions	251
		7 Acknowledgments	252
		Section 8	
		Preparing for LHC II	
		b-tagging at DØ	
		<i>K. Hanagaki for the DØ Collaboration</i>	255
		1 Introduction	255
		2 The DØ Detector	255
		3 Methods	255
		4 Performance & Issues	256
		5 Conclusions	258
		B tagging at CDF	
		<i>Daniel Jeans for the CDF collaboration</i>	259
		1 Introduction	259
		2 Tevatron and CDF	259
		3 Tracking and Primary Vertex finding	259
		4 Lifetime tagging algorithms	260
		5 Soft Muon tagger	262
		6 Conclusions and plans for improvements	262
Section 7			
Heavy Quark Physics			
Beauty Physics: Theoretical Status and Future Perspectives			
<i>Luca Silvestrini</i>	213		
1 Introduction	213		
2 The SM UT analysis	213		
3 The UT analysis beyond the SM	214		
4 MFV models	216		
5 New Physics in $\mathbf{b} \rightarrow \mathbf{s}$ transitions	217		
6 Outlook	219		
Results from Belle and BaBar			
<i>Paoti Chang</i>	221		
1 Introduction	221		
2 ϕ_1/β Extraction	221		
3 CP violation in $b \rightarrow s\bar{q}q$	222		
4 $\phi_2(\alpha)$ and $\phi_3(\gamma)$	223		
5 Rare Decays with Leptons or Photons	224		
6 Other CPV Results and More Observations	226		
7 Summary	227		

Pixel detector in BTeV		Single Top At The Tevatron	
<i>Mauro Dinardo for the BTeV collaboration</i>	263	<i>Anyes Taffard (on behalf of the CDF & DØ collaborations)</i>	296
1 Introduction	263	1 Introduction	296
2 The physics basis of the trigger	263	2 CDF Search For Single Top Quark Production	296
3 Pixel detector	264	3 DØ Search for Single Top Quark Production	297
4 The BTeV front end electronics and data acquisition system	265	4 Conclusions And Projections	298
5 First level trigger implementation	265	Top Properties and Rare Decays from the Tevatron	
6 Level 1 trigger performancies	266	<i>Arnulf Quadt</i>	300
7 Conclusions	267	1 Introduction	300
Track and Vertex Reconstruction in CMS for Key Physics Processes		2 Top Quark Interactions to Gauge Bosons	300
<i>P. Vanlaer, for the CMS collaboration</i>	268	3 Fundamental Properties of the Top Quark	302
1 Introduction	268	4 Anomalous Top Quark Production	303
2 Track reconstruction	269	5 Anomalous Top Quark Decays	303
3 Gaussian-Sum track reconstruction for electrons	270	6 New Physics in Events with $t\bar{t}$ Topology	304
4 Vertex Finding	271	7 Summary	304
5 Vertex Fitting	272	Top physics prospects in ATLAS	
6 Conclusions	273	<i>Arnaud Lucotte</i>	305
CDF computing and event data models		1 Introduction	305
<i>F.D. Snider for the CDF Collaboration</i>	274	2 Top quark mass measurement	305
1 Introduction ¹	274	3 W and top quark polarization in $t\bar{t}$ events	307
2 Computing model and data flow	274	4 Single-top cross-section measurement	309
3 Computing systems	275	5 Conclusion	310
4 Grid migration plans	276	Top quark studies and perspectives with CMS	
5 Event data model	277	<i>Andrea Giammanco</i>	311
6 Successes	278	1 Introduction	311
7 Summary	278	2 Top quark mass measurement at LHC	311
8 Acknowledgments	278	3 Spin correlations	312
Preparation for Analysis at CMS		4 W polarization in top decay	312
<i>Christian Weiser</i>	279	5 Single top production	313
1 Introduction	279	6 Conclusions	314
2 Tools for Analysis	279	Section 10	
3 Conditions	280	Conclusion	
4 Algorithm Calibration in Data	282	Experimental Summary and Perspectives	
5 Example Analysis: Associated Higgs Boson Production	282	<i>John Womersley</i>	317
6 Summary	283	1 Outline	317
Section 9		2 What is the universe made of?	317
Top Quark Physics		3 Describing the Universe	318
Top Mass at the Tevatron		4 A Few Closing Comments	321
<i>Tomonobu Tomura for the CDF and DØ Collaborations</i>	287	5 Conclusions	321
1 Introduction	287	Einstein's Contributions to Quantum Theory	
2 Measurements of Top Mass	287	<i>Norbert Straumann</i>	322
3 Summary	291	1 Introduction	322
$t\bar{t}$ cross section at the Tevatron		2 Einstein's first paper from 1905	322
<i>Emmanuel Busato</i>	292	3 Energy and momentum fluctuations of the radiation field	324
1 Introduction	292	4 Reactions	325
2 Di-lepton channels	292	5 Derivation of the Planck distribution	325
3 Lepton+jets channels	293	6 Bose-Einstein statistics for degenerate material gases	326
4 All-jets channel	294	7 Einstein and the interpretation of quantum mechanics	326
5 Summary	295	References	327

¹ Work supported by the U.S. Department of Energy under contract No. DE-AC02-76CH03000.

Section 11 Posters

The construction of the ALICE hmpid rich detector

<i>B. Belin* on behalf of the ALICE-HMPID group</i>	331
1 Introduction	331
2 Detector	331
3 Quality Control	332
4 CsI Photocathode	332
5 Test Beam	333
6 Conclusion	333

CDF spectroscopy results

<i>Mario Campanelli</i>	334
1 Introduction	334
2 $D_s^+ D^+$ mass difference	334
3 Masses of B hadrons	334
4 Mass and width of orbitally-excited charm states	334
5 Observation of the X(3872)	334
6 Study of the helicity of the X(3872)	335
7 Conclusions	335

Effective K-factors: a method to include higher order QCD corrections in parton shower Monte Carlos: the example of $H \rightarrow WW^* \rightarrow 2\ell 2\nu$

<i>Giovanna Davatz</i>	336
----------------------------------	-----

Construction and Performance of the ATLAS Semi-Conductor Tracker Barrels

<i>Bilge M. Demirköz</i>	338
1 Introduction	338
2 SCT modules and readout	338
3 SCT Barrel Construction and testing	338
4 Conclusions	339

Charmless B decays at CDF

<i>Mauro Donegà for the CDF collaboration</i>	340
1 Introduction	340
2 $B_{d/s}^0 \rightarrow h^\pm h^\mp$	340
3 $B_s \rightarrow VV$ decays	341
4 Conclusion	341

Standard Model Higgs Searches at ATLAS

<i>Luis Roberto Flores Castillo, on behalf of the Higgs Working Group of the ATLAS collaboration</i>	342
1 Introduction	342
2 Inclusive final states	342
3 Vector Boson Fusion	342
4 References	343

The LHCb trigger and readout

<i>Federica Legger, Thomas Schietinger</i>	344
1 Introduction	344
2 Readout system and trigger architecture	344
3 The trigger strategies	345
4 Conclusions	345

Anomalous single top production with ATLAS

<i>Orhan Çakır</i>	346
1 Introduction	346
2 Anomalous Production	347
3 Conclusion	347

LHCb RICH Detectors

<i>D. L. Perego on behalf of the LHCb RICH Collaboration</i>	348
1 LHCb RICH Detectors	348
2 Silica Aerogel	348
3 Hybrid Photon Detectors	349
4 RICH Particle ID Performance	349
5 Status RICH Detectors	349

Production and test of the LHCb Muon Wire Chambers

<i>D. Pinci and A. Sarti on behalf of the LHCb collaboration</i>	350
1 Introduction	350
2 Quality tests	350
3 Production status	352
4 Conclusion	352

Techniques for B_s mixing at CDF

<i>Giuseppe Salamanna on behalf of the CDF Collaboration</i>	353
1 Introduction	353
2 Flavour Tagging	353
3 Decay length	354
4 Final state reconstruction	354
5 Significance and results	354

Heavy flavour production at CDF

<i>Mario Campanelli Monica D'Onofrio Sofia Vallecorsa, Anant Gajjar A. Metha Tara Shears</i>	355
1 Introduction	355
2 Heavy flavour jets identification at CDF	355
3 Inclusive b-jet production cross section	355
4 $b\bar{b}$	356
5 Photon + heavy flavour	356
6 Conclusions	356

Introduction and Experimental Status

Status of the ALICE Detector at LHC

Hans-Ake Gustafsson, For the ALICE Collaboration¹

CERN, Geneva and Lund University, e-mail: hans-ake.gustafsson@cern.ch

Abstract. The status of the ALICE experiment is presented and discussed. Details on the progress of the major detector systems together with results on performance tests are given.

1 Introduction

ALICE (A large Ion Collider Experiment) is the experiment mainly focussing on heavy-ion physics at the LHC. The main goal in the field of relativistic heavy-ion collisions is to create and study an extremely dense and hot subatomic system named the Quark-Gluon Plasma (QGP). QCD, the theory of strong interaction, provides quantitative estimates of the critical temperature and density at which the phase transition from hadronic to quark matter should occur. Once established, the QGP provides a unique laboratory to study bulk properties of quark matter as well as the fundamental interaction of coloured objects in a coloured medium. In addition to the heavy-ion program, ALICE will make use of the p-p running at LHC to collect reference data but also to pursue a p-p physics program complementary to the studies by the ATLAS and CMS experiments. ALICE, during the initial phase of the LHC, will, collect p-p data and plans for an early short low luminosity pilot run with heavy ions. A few days of running will give enough data to study global properties of the heavy-ion collisions and to measure large cross-section phenomena. The 2008 LHC running will, besides p-p collisions, include a long heavy-ion run although not yet at full luminosity. Plans for the years after including p-A, light ions and different energies have been developed.

The ALICE collaboration has about 1000 collaborators from 80 institutes in 30 countries worldwide. 6 new institutes have joined the collaboration during 2004 and there are ongoing discussions with institutes from Brazil, Japan, Pakistan, Spain, Turkey and US on joining the collaboration.

The ALICE detector has been designed to measure at midrapidity most of the particles emitted in heavy-ion collisions. These measurements include identification and momentum determination with high precision. Hadrons with long lifetime will be identified by use of energy-loss and time-of-flight measurements while hadrons with short lifetime will be identified through their decay products. The identification of photons will be performed through electromagnetic calorimetry, and measurements

of transition radiation will be used to identify electrons. The momentum of the emitted charged particles are determined through tracking in a magnetic field ranging from 0.2-0.5 T. The full suit of detectors in the mid-rapidity region is used to achieve this. These detector systems are designed to cover a wide range in momentum, from very low values (100 MeV/c) to rather high values (100 GeV/c). This broad range makes ALICE unique in studying both soft and hard phenomena in heavy-ion as well as p-p collisions. The central tracking systems are complemented by a few systems for measurements of specific signals such as o'nium (J/ψ , Υ) states, photons, high momentum identified particles and global aspects of the collisions. The big challenge ALICE has to meet is to perform high precision measurements in an environment of extremely high particle densities which could go up to 8 000 particles per unit of rapidity. This corresponds to about 15 000 particles in the acceptance ($|\eta| < 0.9$) of the ALICE detectors. The ALICE detector performance has been optimized for 4 000 particles per unit of rapidity and checked still with good performance up to 8 000 particles per unit of rapidity. A general discussion of the physics aspects of high-energy heavy-ion collisions can be found in [1]

In the following paragraphs the status of the different detector systems of the ALICE detector will be discussed.

2 Status of the detector subsystems.

The ALICE experiment is in the process of being assembled in the P2 cavern of the LHC inside the LEP L3 magnet. A schematic view of the detector is shown in figure 1.

2.1 The tracking system

The central tracking system covers the pseudo-rapidity range $|\eta| < 0.9$ and full azimuth. The Inner Tracking System (ITS) placed closest to the interaction point

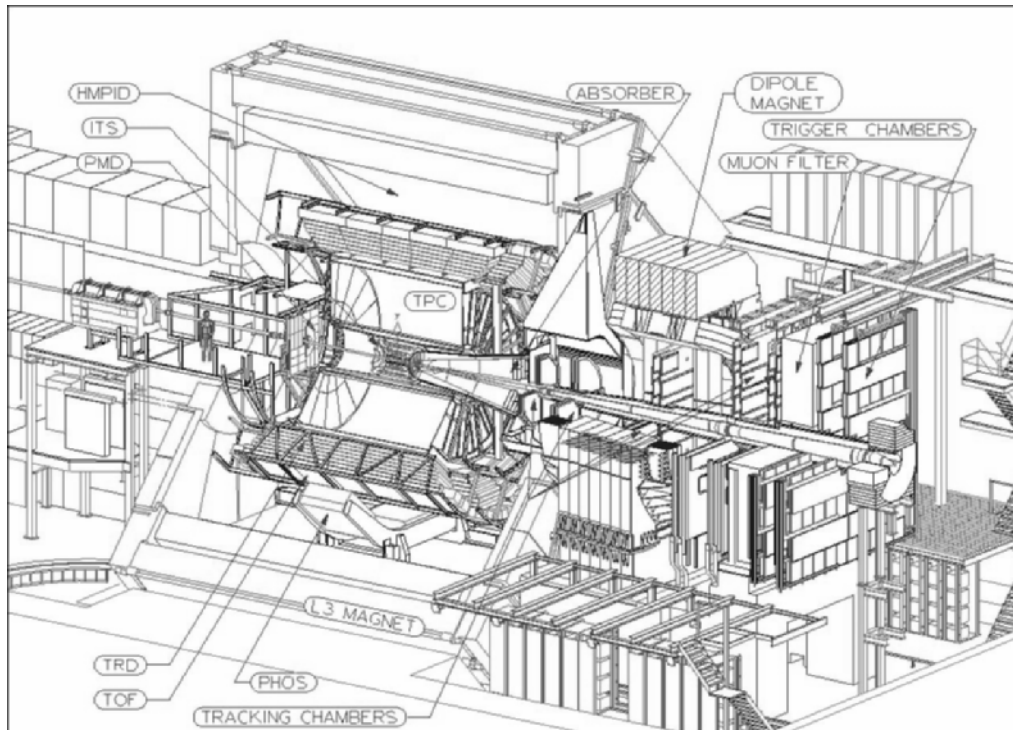


Fig. 1. A schematic view of the ALICE experiment

($4 \text{ cm} < R < 44 \text{ cm}$) is composed of 6 layers of Si detectors of 3 different technologies. Outside the ITS at a distance $0.9 \text{ m} < R < 2.5 \text{ m}$ is the Time Projection Chamber (TPC) which is the main tracking device of ALICE. The Transition Radiation Detector (TRD) and the Time-Of-Flight detector (TOF) placed at $2.9 \text{ m} < R < 3.7 \text{ m}$ and $3.7 \text{ m} < R < 4.0 \text{ m}$ is completing the ALICE central tracking system.

2.2 Inner Tracking System, ITS.

The ITS has multiple purposes, one being an integrated part of the central tracking system to provide high resolution ($< 100 \mu\text{m}$) measurements of the primary vertex position as well as secondary vertexes for identification of short-lived particles. Another being a standalone system for measurements of low momentum particles ($< 100 \text{ MeV}/c$). To cope with the extremely high particle density anticipated in heavy-ion collisions, a special ITS design is required.

The two innermost layers of the ITS are made of Si Pixel Detectors (SPD). They will provide good spatial and two-track resolution in the bending plane which is required in the high-multiplicity environment of heavy-ion collisions. The basic unit of the SPD is called a ladder which contains one Si sensor and bonded to 5 pixel chips. The chips are produced in radiation tolerant $0.25 \mu\text{m}$ CMOS technology. A detector chain was evaluated in a test beam and the resulting position resolution was measured to be better than the design value of $12 \mu\text{m}$ in $r\phi$ and $100 \mu\text{m}$ in z .

The two next layers of the ITS system consisting of Si Drift Detectors (SDD) is mounted on a ladder structure holding 6 respectively 8 modules. The sensors contain the high-voltage divider which shapes the drift and collection fields. A readout unit was successfully tested in beam. After corrections for non-linearities in the high-voltage divider, diffusion and drift velocity variations, a resolution of $30 \mu\text{m}$ was achieved.

The two outer layers of the ITS are composed of double sided Si Strip Detectors (SSD). They are mounted in a ladder structure similar to the SDD. The ladder frames are made of extremely thin and complex carbon-fiber structures to minimize the amount of material. These frames support the SDD ladders, the services for the SDD and SSD and the silicon rings of the FMD.

All components for the three ITS systems are in the production stage and they are expected to be ready for installation according to the global installation schedule.

2.3 Time Projection Chamber, TPC

The TPC is the main tracking device of the ALICE detector. It is capable of measuring with high precision the momentum of all charged particles below $10 \text{ GeV}/c$, and together with the other tracking detectors, provide good resolution up to $100 \text{ GeV}/c$. Particle identification in the TPC require good energy loss measurements which will depend on the track multiplicity inside the TPC. The resolution in the energy loss measurements is predicted to be about 5-6% at a particle density below 2000 per unit of

rapidity increasing to about 7% at 4000 particles per unit of rapidity.

The TPC is constructed of 4 cylindrical vessels 5 m long. The active drift volume of the TPC is defined by the two field cage vessels which have the radii 0.9 m and 2.5 m, respectively. The two containment vessels provide isolation of the TPC high voltage. The readout of the TPC is done using conventional multiwire proportional chambers with cathode pads. The signals from the cathode planes are processed in custom designed Front End Card (FEC). The production of all components for the TPC is finished and the installation work of the different components is in progress. The very delicate readout chamber mounting was recently completed on one of the two end caps and the mounting on the second end cap is in the process of being started. The installation of the readout electronics on the chambers will start before the end of the year and finish in early 2006. This will then allow for about 6 months of commissioning at the surface before the TPC goes down in the cavern to be installed in the L3 magnet.

2.4 Particle identification systems

Particle identification over a broad range of momenta is very important for most of the observables anticipated in ALICE. The central tracking system of ALICE provides through energy loss measurements in the TPC and ITS discrimination of $\pi/K/p$ in the non-relativistic regime. The vertex finding capability of the central tracking detectors gives identification of short-lived particles through their hadronic decays. Complementary to the central tracking system, ALICE has several other particle identifying detector systems like, TOF, TRD, HMPID and PHOS. The TOF systems provides separation for $\pi/K/p$ and electrons with $p_t > 1 \text{ GeV}/c$ are identified and discriminated against charged pions in the TRD system. The Ring Imaging Cerenkov detector (HMPID) extends in a limited solid angle the PID capability of ALICE towards higher particle momenta, π/K up to 3 GeV/c and K/p up to 5 GeV/c . The PHOS detector system identifies photons in a limited solid angle by a combination of electromagnetic calorimetry and charged particle vetoing. A dedicated spectrometer in the forward direction identifies muons. A detailed description of the global tracking in ALICE can be found in [2].

2.5 Transition Radiation Detector, TRD

Combining the information from the TPC, ITS and TRD will provide identification of high momentum electrons as well as discrimination against pions. The TRD will also operate as an electron spectrometer to measure charm and beauty through their semi-leptonic decays and o^{onium} states in their e^+e^- decay channels. The fast tracking capability of the TRD will be used to trigger on high momentum electrons- and hadron events which will be of interest for the jet-physics program. The proof of principle was achieved in beam tests using a full size prototype. These

tests resulted in an overall electron detection efficiency of 90% and with a pion rejection factor of 100. The production of the different components is in progress and more than 50% of the chambers will be produced by the end of the year. The electronics production is well under control and the first supermodule will be ready in the spring of 2006 and four more in the spring of 2007. The electron identification with the ALICE TRD is discussed in more detail in [3]

2.6 Time-Of-Flight system, TOF

The outer most part of the ALICE central barrel is the TOF system which is built on Multi-gap Resistive-Plate Chambers (MRPC) technique. This system will together with the information from the ITS and TPC significantly improve the identification of pions, kaons and protons in the momentum range 200 MeV/c to 2.5 GeV/c . To achieve this, a time resolution of about 100 ps is required. Beam tests of a full prototype chamber and prototype electronics gave an impressive time resolution of 60 ps. The strip mass production is ongoing and the assembly has started. It is anticipated that 50% of the supermodules will be ready by the summer of 2006 and the rest in the first half of 2007.

2.7 High Momentum Particle Identification Detector, HMPID

The HMPID based on ring-imaging Cerenkov technique has a liquid radiator and a multi-wire proportional chamber with pad readout. A thin layer of CsI is evaporated on the pad plane. The HMPID, with a limited coverage in rapidity ($-0.6 < \eta < 0.6$) and azimuth (57.6°) is located 5 m from the interaction point. The purpose of this detector system is to extend the range of identifying and separating charged hadrons towards higher p_t , 3 GeV/c for π/K and 5 GeV/c for K/p . A prototype module was successfully operated in the STAR experiment during the first heavy-ion run at RHIC. All 7 modules have been produced and they will be ready for installation in the second half of 2006. A detailed discussion of the HMPID construction can be found in [4].

2.8 Photon Spectrometer, PHOS

The PHOS detector placed 5 m from the interaction point covers a limited part in rapidity ($-0.12 < \eta < 0.12$) and azimuth (100°). PHOS is a highly segmented PbWO_4 calorimeter with the purpose of performing high resolution photon measurements and to discriminate against leptons and charged hadrons. The readout of PHOS is using low-noise APDs. A detector system based on multi-wire proportional chambers is placed in front of the PHOS spectrometer acting as a veto detector for charged particles. The high segmentation of the PHOS spectrometer makes it possible to identify neutral mesons through their

two-photon decay channel. Using time-of-flight, shower-topology and isolation technique will provide additional particle identification especially to discriminate neutrons and anti-neutrons and identification of direct protons. Measurements of neutral pions and direct photons will be made over a broad range in momentum from about 1 GeV/c to about 80 GeV/c. North Crystal Company in Russia has delivered about 10 000 crystal which is about half of what is needed to complete the PHOS spectrometer. The first PHOS module is planned to be complete in the end of 2005 and the electronics for this module is in production. A presentation of γ and jet physics in ALICE is given in [5].

2.9 Muon spectrometer

ALICE has in the forward direction a complex spectrometer for identification of muons. The main goal with this detector system is to perform high quality measurements of o'nium states with a resolution of 100 MeV/c² at the Υ mass. The spectrometer consists of a complex hadron absorber, a 3 Tm dipole magnet, 5 planes of tracking chambers and 2 planes of trigger chambers. The dipole magnet was successfully installed and commissioned this summer and the complete field mapping is in progress. About 50% of the chambers are produced and will be completed at the end of 2005 and the production of the front end electronics is in progress.

2.10 Forward detectors

ALICE will have various detector systems at large rapidities on both sides of the interaction point. These detector systems will provide information for triggering, event selection and global properties.

The Zero Degree Calorimeters (ZDC), located 110 m from the interaction point, are constructed of tantalum or brass with embedded quartz fibers. The neutron spectators will be measured by the tantalum systems while the proton spectators, deflected by the LHC dipole magnets, by the brass systems. The ZDCs will provide information for triggering and impact parameter determination. All calorimeter modules are produced and ready for installation in the LHC tunnel. The trigger and readout electronics, based on commercial modules, is already procured.

The Photon Multiplicity Detector, PMD, is located 3.6 m from the interaction point on the side opposite to the muon spectrometer. It is composed of proportional chambers sandwiching a passive Pb converter. The purpose of this detector system is to measure photons and charged particles at large rapidities to search for non-statistical event-by-event fluctuations and flow. A prototype module of the PMD was successfully tested in the STAR experiment. All components of the system are in the production stage and the full system will be ready for installation in the beginning of 2007.

The Forward Multiplicity Detector, FMD, is composed of 5 discs of Si pad detectors, 2 of them are located on the

muon spectrometer side and 3 on the opposite side. The FMD together with the ITS cover from -5.1 to 3.4 in rapidity for charged particle measurements. The Technical Design Report including the V0 and T0 detector systems was approved by the LHCC this spring. Successful tests of the first prototype have been performed and the production order for the silicon was placed this summer. Most of the components for the readout are produced and the module assembly is planned to start in the beginning of next year to be ready for installation in the end of 2006. The T0 detector system, based on Cerenkov radiator + PMTs, consists of 2 arrays each having 12 elements. The arrays are placed one on each side of the interaction point, at 70 cm on the muon side and 350 cm on the opposite side. The purpose of the T0 detector system is to provide the start signal for the time-of-flight measurements as well as a signal for the L0 trigger with a time resolution better than 50 ps. The electronics design review and the detector production readiness review were passed this spring together with the V0 detector system. The production of the detector components has started and the electronics production readiness review is scheduled for late this year. The V0 detector system consists of 2 arrays of scintillators embedded with wavelength shifting fibres + PMTs. The arrays are placed on each side of the interaction point, at 90 cm on the muon side and at 355 cm on the opposite side. The purpose of the V0 systems is to provide the main interaction trigger but also to determine the vertex position online. It will also, through coincidence between the two arrays, be able to identify beam-gas interactions. The detector components are in production and the electronics production readiness review is scheduled for late this year together with the T0 detector system.

3 Status of control systems and computing

3.1 Detector and Experiment Control Systems, DCS and ECS

The DCS system will provide tools for an ALICE operator to have full control over all modes of operations of the experiment. It will allow the detector and service groups to have full control of their specific equipment in the experiment. It will also allow running the systems in a standalone mode during installation and commissioning. The DCS group has together with each detector systems written a user requirement document in which all requirements for the control of the systems have been defined. Most of the hardware and software for the DCS systems have been defined and several systems have, during test beam activities, run with full scale prototypes of the DCS system. All essential DCS components are available. The DCS systems for all services and infrastructure will be installed and ready for the first LHC p-p collisions.

The ECS system is developed to coordinate all the activities in the DCS, DAQ, TRG and HLT systems. The architecture has been defined and the first prototype was successfully used during the beam test of the HMPID and ITS systems.

3.2 Trigger, DAQ and HLT

The ALICE trigger system delivers one pre-trigger and three trigger levels (L0, L1, L2). The T0 and V0 detector systems provide in less than 100 ns a pre-trigger with the purpose of sending a wake-up signal to the FEE of the TRD system. The L0 ($1.2\mu\text{s}$) and L1 ($6.5\mu\text{s}$) triggers are sent to the fast detectors while the L2 ($100\mu\text{s}$) triggers the readout of the slow TPC detector. The Central Trigger Processor (CTP) and the Local Trigger Unit (LTU), used to distribute the triggers, are in production.

The data are transferred in parallel to the Data Acquisition System (DAQ) over the Detector Data Link (DDL) via the Read Out Receiver Card (RORC) to a farm of individual computers called the Local Data Concentrators (LDC). The LDCs are building the sub-event that are sent to the final eventbuilder, the Global Data Collector (GDC) which has the capacity of processing in parallel 40 different events. The software framework of the ALICE DAQ, DATE (Data Acquisition and Test Environment), provides all the controls for the data flow. The DAQ system has been tested in Data Challenges with increasing complexity. DATE demonstrated in one of the recent challenges a throughput to mass storage with a sustained rate of 450 Mbyte/s over a week. The commissioning of both hardware and software is in progress and integration tests have been successfully performed in test beam activities of several detector system.

The High Level Trigger (HLT) is a software trigger system which will be used for extracting rare event. Another very important task of the HLT system is to perform data compression. It will also perform fast partial or full reconstruction of the events which will be sent to the DAQ data flow at the LDC level. All these tasks will be done on a dedicated computer farm. The HLT system is fully defined and prototype tests have been performed during tests beam activities of several detector systems.

3.3 Offline

AliRoot is the ALICE offline-software framework based on the ROOT package. Tasks for reconstruction, event simulation and data analysis are all performed within AliRoot. This framework is constantly evolving to extend its functionalities. Interfaces to different external packages are developed to allow the users to switch between different packages. Interfaces for GEANT3, FLUKA and a selection of event-generators are in operation. Several physics data challenges have been performed using about 10-20% of the final offline capacity. The main goals of the data challenges have been to produce and analyse about 10% of the data taken in a standard data taking year, use the complete offline chain and to test the software and physics analysis of data for the Physics Performance Report (PPR). This was all entirely done on the GRID with the AliEn/LCG GRID services. The ALICE computing model was presented to the LHCC and the Computing Technical Design Report (TDR) [7] has been delivered to LHCC.

4 Conclusion

All major detector systems in ALICE are in the production phase. A detailed installation and commissioning plan has been developed to have the ALICE baseline detector ready for the first p-p collisions in the summer of 2007 and to take data in an early pilot run with heavy-ions. ALICE has developed a framework for producing the large number of simulated event needed for the preparation of the Physics Performance Report in which the details of the physics program will be defined. The ALICE collaboration is looking forward to an exciting future of high energy heavy-ion physics in a new regime of physics as well as a dedicated p-p scientific program complementary to the ATLAS and CMS experiments.

References

1. U. Wiedemann, these proceedings
2. S. Arce, these proceedings
3. C. Adler, these proceedings
4. B. Belin, these proceedings
5. G. Conesa Balbastre, these proceedings
6. ALICE Forward Detectors Technical Design Report, CERN-LHCC-2004-025
7. ALICE Computing Technical Design Report, CERN-LHC-2005-018

ATLAS status

Steinar Stapnes - For the ATLAS collaboration

University of Oslo, Dep. of Physics, P.O.Box 1048, 0316 Blindern, Oslo, Norway

Abstract. The emphasis of the ATLAS project has shifted from distributed construction of the detector components to their integration at CERN on the surface, and most importantly, to their final installation and commissioning in the underground cavern. The detector construction is today (September 2005) more than 85% complete. The barrel calorimeter systems are installed in the underground cavern, the central solenoid and barrel toroid system the same, and the muon chamber installation has started. Off-detector parts, both for the ATLAS Data Acquisition and Detector Control Systems, and for the readout of the various detector parts, and services installation are ongoing. As the detector parts are being installed, their electronics are mounted, tested and commissioned. The first cosmic rays events have been observed in the barrel hadronic calorimeter system. Completion and preparation of the remaining parts of ATLAS, as for example Inner Detector parts, Muon chambers, End-cap/Forward calorimeter systems, and the Endcap Toroid System, are ongoing in the institutes or at CERN. In parallel distributed computing and physics analysis are being set up and exercised with large simulated data samples, embedded in the LHC Computing Grid Project framework.

1 Introduction

The ATLAS detector uses a superconducting magnet system with a central solenoid around the inner detector and large air-core toroid magnets for the muon spectrometer. Between the two are the liquid Argon (LAr) and tile calorimeters. A hierarchical trigger and data acquisition system provides the data for the collaboration-wide computing and physics analysis activities. The ATLAS Collaboration consists today of 152 Institutions from 34 countries with roughly 1850 scientific authors (including PhD students). The ATLAS detector is shown in fig.1.

2 Magnet Systems

The ATLAS superconducting magnet system consists of a central solenoid, a barrel and two end-cap toroids, and their common services.

2.1 Central Solenoid

The LAr barrel cryostat, housing also the solenoid previously tested at the surface, was installed in the cavern at the end of October 2004, in a temporary position. The services connection after movement into the final position (November 2005), will be followed by an operational test and field mapping in Spring 2006.

2.2 Barrel Toroid (BT)

The BT integration and testing at the surface are completed. The toroids were tested individually cold and at

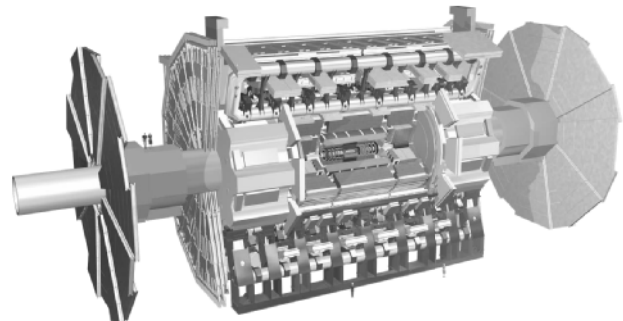


Fig. 1. The ATLAS detector. The diameter is 25m, the barrel toroid length 26m and the overall length 46m.

full current before installation in the underground cavern. One coil, BT3, underwent three thermal cycles in order to investigate a non-conform resistance to ground. With the lowest measured value of 30 k Ω it stayed always well above the acceptance value of 10 k Ω . After a thorough risk analysis (only two real shorts would be harmful) it was decided to accept the coil, and as a precaution to install it closest to the current input where the internal voltage is minimal. All eight coils are now mechanically installed in their final position in the cavern as shown in fig.2, and their cryogenic connections are being completed, in view

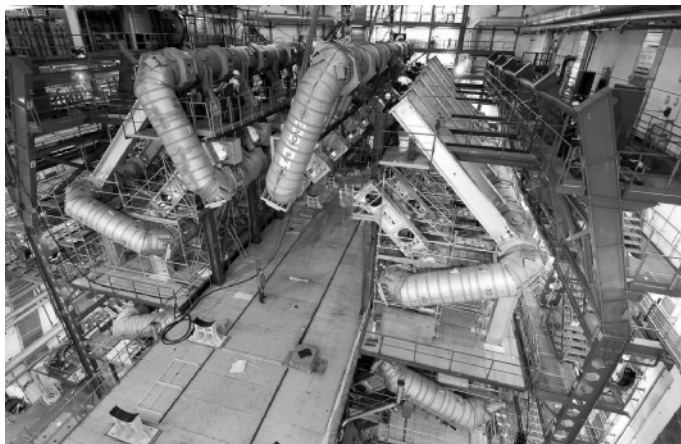


Fig. 2. The Barrel Toroid System installed in the underground cavern.

of a first cool-down in-situ, followed by an excitation test early 2006. The work is now ongoing to complete cryogenic and electrical connections of the eight coils.

2.3 Endcap Toroids (ECT)

All components for the final assembly of the End Cap Toroids (ECTs) are at CERN, and integration of the first ECT is ongoing. The first ECT integration is scheduled for completion by May 2006, the second one for October 2006.

3 Inner Detector

The Inner Detector (ID) combines three concentric sub-system layers, from inside out the Pixel detectors, the Silicon Strip detectors (SCT) and the Transition Radiation Straw Tracker (TRT). The module series production is finished for SCT and TRT, and the emphasis has shifted to the assembly of modules onto the support structures ('macro-assembly') and to the integration of the overall ID including the services. An important milestone will be the integration of the barrel SCT and TRT sub-systems towards the end of 2005.

3.1 The PIXEL Detector

The PIXEL system consists of 3 barrel layers and 3+3 disks in the forward directions, and contains 1744 modules. The Pixel sensor series fabrication is nearing completion for the full system, all front-end electronics chips are delivered and tested, and 2/3 of the module production is done (fig.3). Currently the main technical worry in the PIXEL project is related to corrosion leaks in some barrel cooling tubes. A repair strategy is currently being followed with the aim of minimizing cost and schedule impacts. The end-cap Pixel disk macro-assembly is proceeding on schedule, and the overall mechanics supports and the installation tooling are ready.

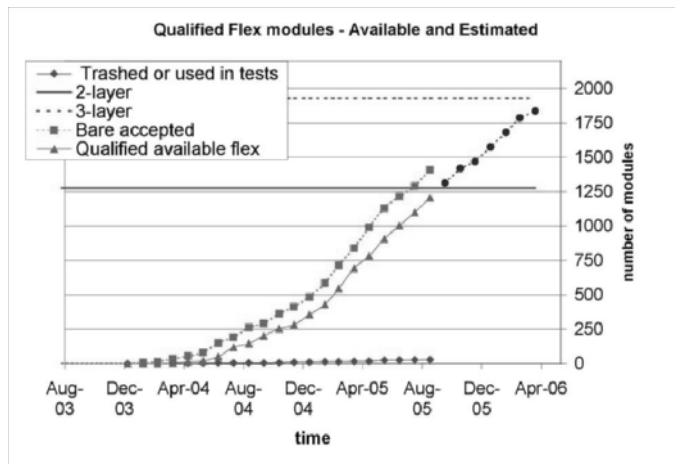


Fig. 3. The status of the PIXEL module production - the horizontal lines show the number of modules needed for 2 or 3 layers, including spares.



Fig. 4. The completed outer SCT barrel cylinder being installed in the thermal enclosure.

3.2 The Silicon Strip Detector (SCT)

The SCT system consists of 4 barrels and 9 disks in each end-cap region, altogether containing 4088 individual silicon strip modules. The SCT module construction is finished and the module mounting on all four barrel cylinders has been completed, and they have been shipped to CERN. The first three are already integrated inside the thermal enclosure (insertion of the first is shown in fig.4) and are being prepared for system tests. The end-cap module assembly on the support disks is well advanced, and for one side already completed. The work to install the completed disks in the end-cap support structures with the final services remains on the critical path because of previously accumulated delays. However the first disks have now been connected to final services and tested. The production of the off-detector read-out electronics and of the power supplies is largely completed. The next steps include completing the macro-assembly of modules for the end-cap disks, and integration into the end-cap support structures.

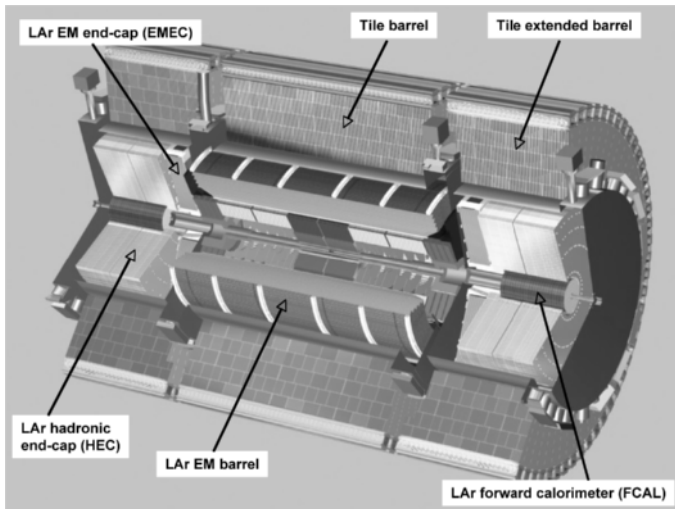


Fig. 5. The ATLAS calorimeter system.

3.3 The Transition Radiation Tracker (TRT)

The straw tracker consists of around 400000 individual straws of 4 mm diameter. The active gas contains 70% Xe, allowing detection of TR photons as well as minimum ionizing particles. The module production for the initial TRT configuration has been completed, and the last EC wheels are expected to arrive at CERN end of October 2005. The barrel cylinder is fully integrated, and first cosmic ray events have been recorded with it on the surface. The integration work for the two end-caps is proceeding well. Tests of the cooling distribution, gas distribution and final electronics are ongoing.

4 Calorimeters

The ATLAS calorimeter system showing the 3 cryostats for the barrel and the two endcap/forward LAr systems, and outside the Tile hadronic calorimeters, with the barrel part and the two extended barrels, is shown in fig.5.

4.1 LAr Calorimeters

The barrel cryostat, containing the central solenoid and the LAr EM barrel calorimeter, was lowered into the cavern end of October 2004. It is installed and positioned inside the barrel Tile calorimeter, in the temporary position below the smaller installation shaft as shown in fig.6. The calorimeter barrel is ready for displacement into the final central position at the end of October 2005, after completion of the BT. In the meantime the installation of services and of the FE electronics crates is ongoing. The surface cold tests of the first end-cap cryostat containing the end-cap EM system, the hadronic and forward LAr systems have been completed successfully this spring. It is ready for installation in the cavern before the end of this year. The second LAr end-cap calorimeter is cold and



Fig. 6. The barrel calorimeter system in the underground cavern, with the cryostat containing the central solenoid and the barrel EM calorimeter, surrounded by the Tile Barrel Hadronic Calorimeter.

tests are ongoing. Its installation in the cavern is scheduled for March 2006. The critical path items are the Front End Board (FEB) production, for which two components (timing circuit, and optical transmitters) needed corrective actions before series fabrication could resume, and also the power supply systems. A special effort is being made to recover part of the accumulated delay (the FEB production stopped for 6 months). The installation and commissioning of the FEB crates on the barrel cryostat is ongoing. The series production of the other components and the back-end electronics proceeds on schedule.

4.2 Tile Calorimeter

The barrel hadronic Tile Calorimeter cylinder was completed in the cavern in the temporary location below the shaft on side C at the end of 2004. Since then commissioning of its electronics has been proceeding, and first cosmic ray events were recorded this summer. An example is shown in fig.7. The complete barrel calorimeter is ready for transfer to the final position after the BT completion end of October 2005. The extended barrel Tile Calorimeters for both sides are ready for installation in the pit after surface pre-assemblies. The installations will start in November 2005 and February 2006, for the C and A ends respectively. The fabrication and insertion of the 'drawer' system, housing all on-detector electronics circuits, were finished in May 2005. There is also good progress for the off-detector electronics and the power supplies, albeit with a tight schedule for the latter.

5 Muon Spectrometer

The Muon Spectrometer is instrumented with precision chambers - Monitoring Drift Tubes (MDT) everywhere except in the high rate forward region where Cathode Strip

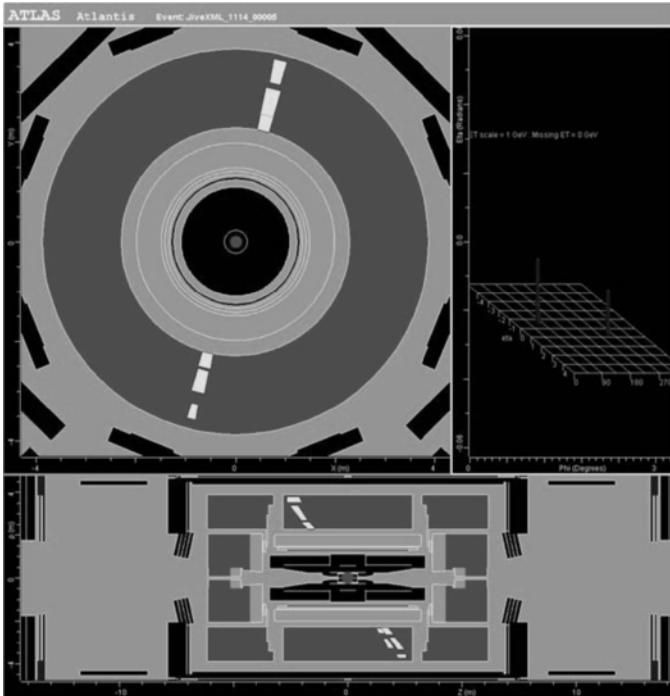


Fig. 7. A cosmic ray event in the Tile Calorimeter system.

Chambers (CSC) are used - for the momentum measurement, and with fast chambers - Resistive Plate Chambers (RPC) in the barrel and Thin Gap Chambers (TGC) in the end-caps - for triggering. All chamber sub-systems have reached (or are close to) completion of the series construction. A major effort is spent in assembling of complete stations and sectors. Installation and commissioning in the cavern have also started.

5.1 Precision Chambers

The series construction of bare chambers is essentially complete, except for very few special chambers. About 80% of the MDTs for the initial detector are fully integrated with their services and electronics. All the 32 CSCs, which are used in the innermost end-cap region because of the high radiation fluxes, are produced.

5.2 Trigger Chambers

About 75% of the barrel RPC modules are assembled. The fabrication was significantly slowed down earlier in the year because of a delamination problem for support panels, and completion is now scheduled for the end of 2005. This is critical for the overall muon chamber integration and installation schedule. Furthermore, a small batch of early-construction RPCs will have to be re-worked because they have high leakage currents. The end-cap regions are instrumented with TGCs that are able to cope with high rates. The TGC series fabrication is finished. The on-chamber trigger electronics ASICs required a new



Fig. 8. An MDT EC sector being integrated.



Fig. 9. Barrel muon chambers being installed.

iteration for both chamber types. The results are positive, however both ASICs remain on the critical path and are available just-in-time.

5.3 Muon Spectrometer Integration

The pre-assembly and testing of the combined trigger and precision chamber stations for the barrel are a major focus of this activity. The fabrication for the large end-cap chamber support structures ('Small and Big Wheels' - see fig.1) is well underway. The first complete end-cap MDT (fig.8) and TGC sectors have been assembled, and this activity is now ramping up rapidly, for the total of 72 TGC and 32 MDT sectors. The installation and commissioning of barrel chamber stations in critical positions in the lower parts of the BT have proceeded according to schedule (fig.9). The installation and commissioning of the alignment system have also started in-situ for the barrel region as well as on the end-cap sectors.

6 Trigger and DAQ System

The Level-1 Trigger, the High Level Trigger (HLT), the Data Acquisition (DAQ) and the Detector Control System (DCS) have all been field-proven in the combined test beam running during 2004. First components of the final system are now installed and are being operated in the experimental area. The level-1 trigger system (with the sub-systems calorimeter, muon and central trigger logic, CTP) is in the production phase for both hardware and software. The High Level Trigger, DAQ and Detector Control System work proceeds according to the plans. There has been further progress on system performance and scalability studies. Major activities concentrate on all aspects of HLT and DAQ software developments. For the HLT and DAQ hardware pre-series are being installed now at Point-1 (the ATLAS experimental area) for starting-up significant system tests. An important element in the planning is the setting up of local DAQ capability for initial detector system commissioning, using the so-called Read Out Driver (ROD) crate DAQ. Also the operational infrastructure at Point-1 has started to become active (system administration, networking). The DCS is already widely used and is one of the first systems being operational, at least in part, in the underground installations at Point-1.

7 Computing, Software and Physics Preparation

The running of Data Challenges (DCs) has been the major computing focus for several years. After completion of DC2 earlier in 2005 giving input to the resources estimates for the Computing Model, a first very broad computing campaign involving mainly non-expert users was launched to simulate events for the 5th ATLAS Physics Workshop which took place in Rome in early June 2005. About 10 Million events were simulated with GEANT4, and the operation was based entirely on POOL persistency and GRID infrastructure. The data were used for large-scale physics studies, with an emphasis on commissioning the detector and early physics for the first years of LHC. This large-scale distributed computing activity was fully embedded into the framework of the CERN LHC Computing Grid Project (LCG) of which ATLAS is a very active partner. The operation was largely successful and revealed in a constructive manner several areas where improvements need to be achieved, and which are now being followed up, in order to reach the planned efficient and smooth running of the collaboration-wide computing for LHC turn-on. A further large effort for the computing was the simulation and analysis for the data from the combined test beam 2004 with as many as possible real components of the software and computing framework deployed as a real-life test.

8 Summary

The ATLAS detector system is now being installed in the underground cavern at CERN. The progress is good and as the parts are being installed commissioning and combined tests are becoming an increasingly central activity. The construction of parts for ATLAS is approaching its completion and many parts are in the process of final assembly and integration on the surface. Even though there are daily problems to solve and several technical issues to deal with in the integration process, the overall progress is fully compatible with being ready for beam in the middle of 2007.

9 Acknowledgement

This summary, both text and pictures, is a compilation from reports and talks prepared by many of my ATLAS colleagues. I therefore want to acknowledge the entire ATLAS collaboration for their contributions to the project and progress described here, and apologizes for all the work I had to leave out in this summary report.

Status of CMS

Tejinder S. Virdee^{1a}

CERN and Imperial College, London

Abstract. After a description of CMS the progress in its construction, installation and commissioning is outlined. Good progress is being made and CMS should be ready for recording data from collisions in the late summer of 2007.

1 Introduction

Although the Standard Model (SM) of particle physics has so far been tested to exquisite precision, it is considered to be an effective theory up to some scale $\Lambda \sim \text{TeV}$. The prime motivation of the Large Hadron Collider (LHC) is to elucidate the nature of electroweak symmetry breaking for which the Higgs mechanism is presumed to be responsible. The experimental study of the Higgs mechanism will also shed light on the issue of the mathematical consistency of the SM at energy scales above 1 TeV. However, there are alternatives that invoke more symmetry such as supersymmetry or invoke new forces or constituents such as strongly-broken electroweak symmetry, technicolour, etc. An as yet unknown mechanism is also possible. Furthermore there are high hopes for discoveries that could pave the way towards a unified theory. These discoveries could take the form of supersymmetry or extra dimensions, the latter requiring modification of gravity at the TeV scale. The Compact Muon Solenoid (CMS) is a general purpose detector at the LHC capable of discovering, and studying, any of this wide range of phenomena.

The availability of high energy heavy-ion beams at energies over 30 times higher than at the present day accelerators will also allow CMS to further extend the range of the heavy-ion physics programme to include studies of hot nuclear matter.

2 CMS: The Compact Muon Solenoid

The overall layout of CMS is shown in Figure 1. At the heart of CMS [12] sits a 13 m-long, 5.9 m diameter, 4 T superconducting solenoid. In order to achieve good momentum resolution within a compact spectrometer without making stringent demands on muon-chamber resolution and alignment, a high magnetic field was chosen. The return field is large enough to saturate 1.5 m of iron, allowing four muons stations to be integrated to ensure

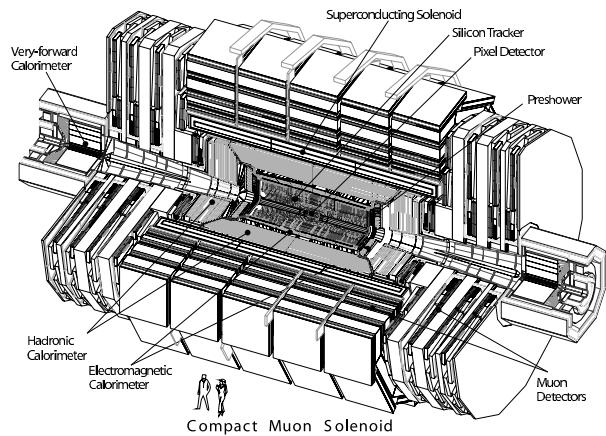


Fig. 1. A view of the CMS detector.

robustness and full geometric coverage. In the barrel region ($|\eta| < 1.2$), where the neutron induced background is small, the muon rate is low and the residual magnetic field in the chambers is low, drift tube (DT) chambers are used. In the two endcaps, where the muon rate as well as the neutron induced background rate is high, and the magnetic field is also high, cathode strip chambers (CSC) are deployed and cover the region up to $|\eta| < 2.4$. In addition to this, resistive plate chambers (RPC) are used in both the barrel and the endcap regions. RPCs provide a fast response with good time resolution but with a coarser position resolution than the DTs or CSCs.

The bore of the magnet coil is also large enough to accommodate the inner tracker and the calorimetry inside.

The tracking volume is given by a cylinder of length 5.8 m and diameter 2.6 m. In order to deal with high track multiplicities, CMS employs ten layers of silicon microstrip detectors, which provide the required granularity and precision. In addition, three layers of silicon pixel detectors are placed close to the interaction region to improve the measurement of the impact parameter of charged-particle tracks, as well as the position of secondary vertices.

The EM calorimeter (ECAL) uses lead tungstate (PbWO_4) crystals. These crystals have short radiation

^a Present address: PH Dept., CERN, CH-1211 Geneva 23

($X_0 = 0.89$ cm) and Moliere (2.2 cm) lengths, are fast (80% of the light is emitted within 25 ns) and radiation hard (up to 10 Mrad). The scintillation light is detected by Si avalanche photodiodes in the barrel region and vacuum phototriodes in the endcap region. The sensitivity of both the crystals and the APD response to temperature changes requires a temperature stability at the level of about 0.1°C . The use of PbWO_4 crystals has thus allowed the design of a compact calorimeter that is fast with fine granularity. A preshower system is installed in front of the endcap ECAL for π^0 rejection.

Most of the CMS HCAL is located inside the magnet coil and surrounds the ECAL system. In order to minimize the non-Gaussian tails of the energy resolution function an additional layer of scintillators, referred to as the hadron outer (HO) detector, line the outside of the coil. Brass has been chosen as absorber material. The active elements consist of plastic scintillator tiles read out with embedded wavelength-shifting (WLS) fibers. The WLS fibres are spliced to high-attenuation-length clear fibres outside the scintillator that carry the light to Hybrid Photo-Diodes that can provide gain and operate in high axial magnetic fields. The overall assembly concept enables the HCAL to be built with essentially no un-instrumented cracks or dead areas in ϕ . Each hadron endcap (HE) covers the pseudorapidity region $1.3 < |\eta| < 3.0$. Coverage between pseudorapidities of 3.0 and 5.0 is provided by the iron/quartz fibre Hadron Forward (HF) calorimeter. This design leads to narrower and shorter hadronic showers and hence is ideally suited to the congested environment in the forward region. The Cerenkov light emitted in the quartz fibres is detected by photomultipliers. The forward calorimeters ensure full geometric coverage for the measurement of the transverse energy in the event.

The overall dimensions of the CMS detector are a length of 21.6 m, a diameter of 14.6 m and a total weight of 12500 tons.

The performance of CMS can be summarized as follows:

- Good muon identification and momentum resolution over a wide range of momenta in the region $|\eta| < 2.5$ (about 1% at $100 \text{ GeV}/c^2$).
- Good charged particle momentum resolution (about 1% at $100 \text{ GeV}/c^2$) and reconstruction efficiency in the inner tracker. Efficient b/τ -jet tagging and triggering on τ 's.
- Good electromagnetic energy resolution, good diphoton and dielectron mass resolution ($< 1\%$ at $100 \text{ GeV}/c^2$), wide geometric coverage ($|\eta| < 2.5$), measurement of the direction of photons and/or correct localization of the primary interaction vertex, π^0 rejection.
- Good missing E_T and dijet mass resolution with fine lateral segmentation ($\Delta\eta \times \Delta\phi < 0.1 \times 0.1$) in HCAL.



Fig. 2. Assembly of the yoke of the CMS magnet. The outer vacuum tank and the coil can be seen.

3 The Status of CMS

The construction, installation and commissioning of CMS is progressing well in the surface assembly hall (SX5) at Point 5, though not without challenges, towards the goal of being ready for collisions in the second half of 2007.

For ease of assembly, installation and maintenance, the Barrel yoke is sectioned into 5 ring-sections and each Endcap yoke into 3 disk-sections. The Hadronic Forward (HF) calorimeters have been pushed outside of the yoke to allow easy sliding of the Endcaps along the beam-pipe. This modularity lends itself to assembly on the surface where constraints of space are not as restrictive as they are underground.

The modular parts, containing installed and commissioned detector elements, will then be lowered into the experiment cavern (UX5) in 15 large-lift operations using a gantry crane that can carry loads up to 2500 tons. All the CMS sub-detectors will be essentially commissioned as large systems, including electronics, power and control systems, on the surface before they are lowered into the experimental cavern.

The CMS assembly started several years ago in SX5. The barrel and endcap yoke were assembled first, the barrel and endcap hadron calorimeters next, followed by the installation of muon chambers on the endcap yoke and inside the barrel wheels. The solenoid coil has been assembled and, at the time of writing, is in position between the outer and inner vacuum tank (Figure 2). The solenoid will be taken up to full current in the second quarter of 2006.

Civil Engineering (CE) work at Point 5 (located at Cessy, France) has finished. Installation of the counting room and service infrastructure in underground cavern USC is advancing well. The counting room is expected to be ready for sub-detector readout crate installation by the end of Q1-2006. The experiment cavern (UXC) will be ready to receive detector elements in Q2-2006.

3.1 The Inner Tracker

Close to the interaction vertex, in the barrel region, are 3 layers of hybrid pixel detectors at a radii of 4, 7, and



Fig. 3. A TIB shell with silicon strip modules mounted

11 cm. The size of the pixels is $100 \times 150 \mu\text{m}^2$. In the barrel part, ten layers of Si microstrip detectors are placed at r between 20 and 115 cm. The forward region has two pixel and nine micro-strip layers in each of the two Endcaps. The total area of the pixel detector is $\approx 1 \text{ m}^2$, whilst that of the silicon strip detectors is 220 m^2 , providing coverage up to $|\eta| < 2.4$. The inner tracker comprises 66 million pixels and 9.6 million silicon strips.

There are three main phases in the assembly of the Tracker: module production, assembly of modules into TOB-rods, TIB-shells, and TEC-petals, and finally the integration of TOB rods, complete TIB and complete TEC structures into the Tracker Support Tube. The first phase is almost complete, the second is progressing and the third is expected to be completed by the summer of 2006.

All 21000 sensors for the 15000 modules are now in hand. The last delivery of the hybrids is expected by the end of 2005. Module production is now progressing well. All 3450 TIB modules should have been produced by the end of 2005, the 5200 TOB modules by the end of February 2006 and the 6400 TEC modules by the end of March 2006. The quality of the production is good.

The assembly of modules on TOB-rods, TEC-petals and TIB-shells is now proceeding. One of the TIB half-shells is shown in Figure 3. These elements will be mounted on carbon-fibre structures and housed inside a temperature controlled outer support tube. This is expected to finish in mid-2006. The commissioning of the full tracker, 25% at a time, is foreseen in the autumn of 2006, before transport to Point 5 at the end of 2006.

3.2 The Electromagnetic Calorimeter

The barrel section (EB) has an inner radius of 129 cm. It is structured as 36 identical super-modules, illustrated in Figure 4, each covering half the barrel length and corresponding to a pseudorapidity interval of $0 < |\eta| < 1.479$. The crystals are quasi-projective and have a front face cross-section of $\approx 22 \times 22 \text{ mm}^2$ and a length of 230 mm, corresponding to $25.8 X_0$.

The endcaps (EE) cover a pseudorapidity range of $1.479 < |\eta| < 3.0$. The endcap crystals also off-point from

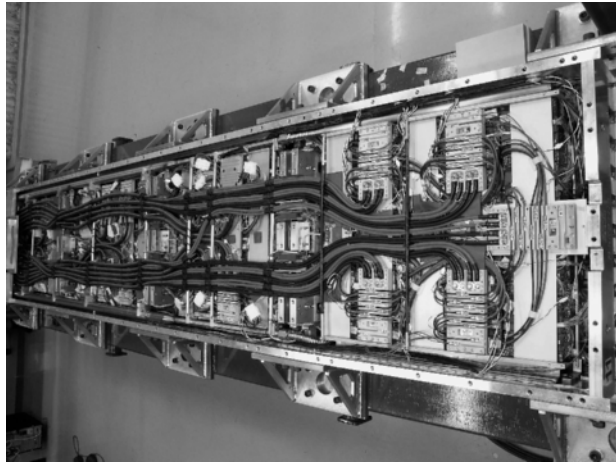


Fig. 4. Assembled ECAL module.

the nominal vertex position, but are arranged in an $x-y$ grid (i.e. not an $\eta-\phi$ grid). They have a front face cross section of $28.6 \times 28.6 \text{ mm}^2$ and a length of 220 mm ($24.7 X_0$).

The delivery of crystals defines the critical path for the ECAL. At the time of writing, some 44000 out of 61200 barrel crystals have been delivered. The serial integration of electronics into bare supermodules (SMs) has started. These SMs comprise 1700 crystals, which are tested after assembly in the laboratory for a period of 1 week and inter-calibrated with cosmic rays for another one week. The first half-barrel should be lowered into UXC by mid-2006. The whole barrel ECAL should be ready for the pilot physics run in 2007.

After amplification by a multi-gain preamplifier, the signal, shaped to peak after about 50 ns, is sampled and digitized at 40 MHz in one of three selected 12-bit ADCs used for each channel. A dynamic range of over 15 bits is attained. For each trigger, consecutive digitizations within a defined time frame (10 crossings) are read out. In order to obtain the amplitude of a digitized pulse, the samples within the time frame are weighted and summed. The noise performance has been measured in several super-modules and found to be close to the original specification of approximately 40 MeV/channel.

The performance of a supermodule was measured in a test beam. The energy resolution has been parameterized as a function of energy:

$$\left(\frac{\sigma}{E}\right)^2 = \left(\frac{3\%}{\sqrt{E}}\right)^2 + \left(\frac{0.16}{E}\right)^2 + (0.3\%)^2, \quad (1)$$

where E is in GeV.

3.3 The Hadronic Calorimeter

All HCAL module types [HB (barrel), HE (endcap), HO (outer) and HF (forward)], including absorber and optics, are completed. Photodetectors and electronics have been installed and a comprehensive calibration of HCAL using Co-60 sources is being carried out. HF will be the first sub-detector to be lowered in the 2nd quarter of 2006.

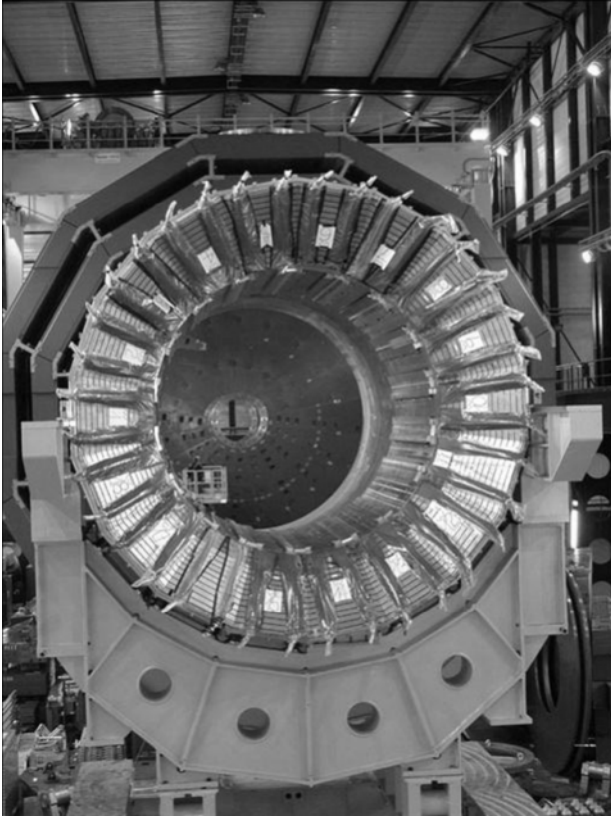


Fig. 5. Assembled HB in the surface hall at SX5.

The barrel and endcap hadron calorimeter can be seen in UX5 in Figure 5 and Figure 6.

3.4 The Muon System

The Muon Endcap (ME) system comprises 468 CSCs in the two endcaps. All these chambers and spares are at CERN. At the time of writing, some 342 (75%) have been installed on the magnet yoke disks; all of the installed chambers have been fully commissioned using cosmic rays. The completed installation of chambers on one disk can be seen in Figure 7.

Each CSC is trapezoidal in shape and consists of six gas gaps, each gap having a plane of radial cathode strips and a plane of anode wires running almost perpendicularly to the strips. The spatial resolution provided by each chamber ranges from $100\mu\text{m}$ in Station 1 and about $100\mu\text{m}$ in Stations 2, 3 and 4. The signal on the wires is fast and is used in the Level-1 Trigger. However, it leads to a coarser position resolution.

The manufacture of Barrel DT chambers should be completed by the beginning of 2006, except for the MB4 chambers which will be finished by April 2006. The installation of DT chambers in two out of the five yoke wheels, YB+2 and YB+1 (84 DT and RPC packages), is complete. The chambers installed into the YB1 yoke can be seen in Figure 8, organized in 4 stations. Each DT chamber has one or two RPCs coupled to it before

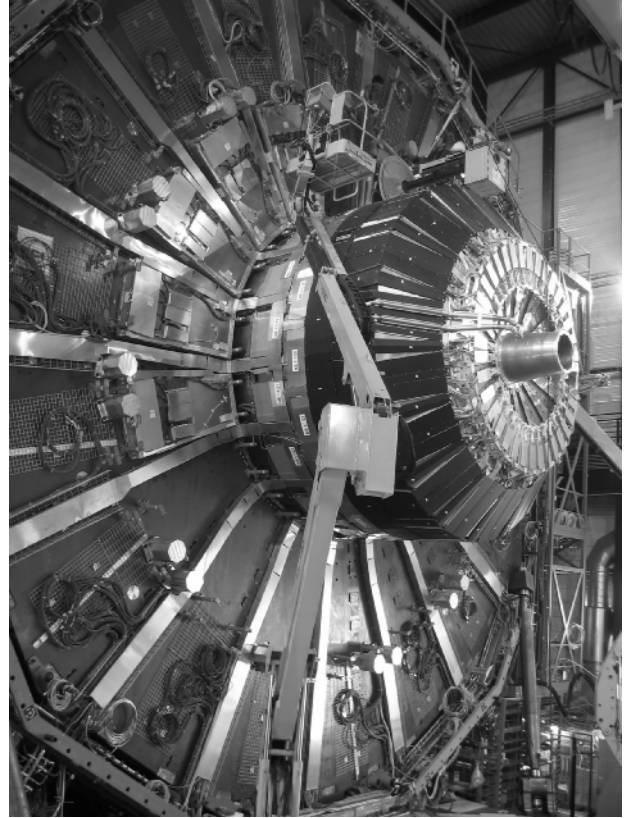


Fig. 6. The 'nose' on one YE1 yoke disk with HE and ME1/1 chambers mounted. Some ME1/2 and RE1/2 chamber packages can also be seen.

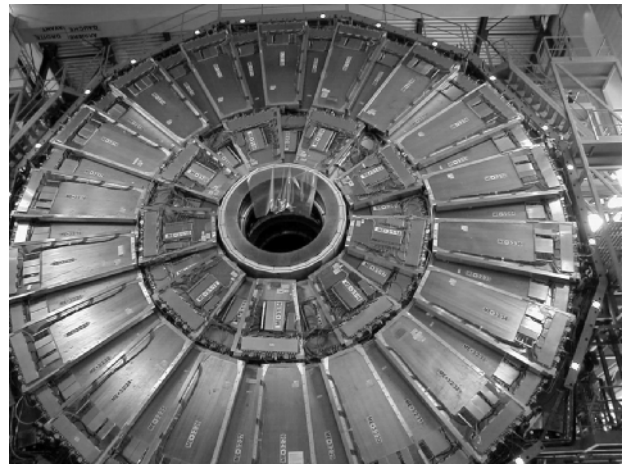


Fig. 7. Installation of CSC chambers onto one YE2 disk.

installation. Chambers in different stations are staggered so that a high- p_T muon produced near a sector boundary crosses at least three out of the four stations. The installation will be completed in the other wheels before they are lowered. The commissioning of YB+2 chambers using cosmic rays has been finished and the cabling operation has just started. The chambers consist of twelve planes of aluminium drift tubes; four r - ϕ measuring planes in each of the two outermost "superlayers," separated by about

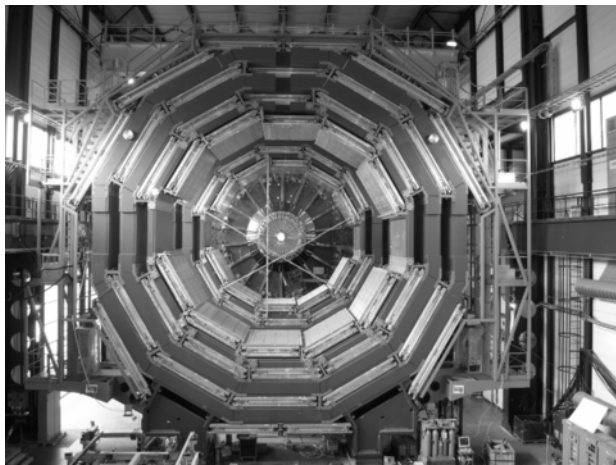


Fig. 8. Installation of DT chambers into one YB1 wheel.

20 cm and sandwiching a z -superlayer comprising four z -measuring planes. Each station is designed to give a muon vector in space, with a precision better than $100\mu\text{m}$ in position and better than 1 mrad in direction.

The forward RPC system covers the pseudorapidity region up to $|\eta| < 2.1$ but chambers sitting beyond $|\eta| > 1.6$ have been staged. The installation of RPC chambers on the first endcap yoke disk chambers should be completed by the end of 2005.

The muon-alignment hardware for the magnet test is in production. All MABs (carbon fibre position reference structures) are at CERN. Installation and cabling of components has started on YE+.

3.5 The Level-1 Trigger System

The trigger system is mostly in production. Production of some trigger components has already finished. There is much work underway on software and firmware. Integration tests of detector primitive generators, trigger system and DAQ are underway. Components of the trigger system are being thoroughly exercised and integrated with other trigger and detector electronics systems in the Electronics Integration Centre (Building 904 on the CERN-Preveessin site) in preparation for installation in USC. Some components of the final system will be used in data taking during the magnet test at SX5 in early 2006.

3.6 The Data Acquisition System

As far as the DAQ system is concerned, the production of the Data-to-Surface (D2S) custom components has been completed and the electrical and functional tests have been passed. The final system tests have started in CERN. The D2S FED builder system, including the switches, has been delivered, and part of the modules have been installed in the pre-series system at Point 5. All D2S components (except PC and fibers) will be available in December 2005, ready for the installation and the start of the read-out commissioning in USC. A 16×16 readout builder with

16 FRL-FED columns is permanently running in Point 5 and used to test the integration of the central DAQ with the detector systems participating in the Magnet Test.

3.7 CPT

In CMS, the project comprising Computing, Software, Physics Reconstruction and Selection is labeled CPT.

The software for the experiment is advancing well, and has been used to perform detailed simulations of the detector response and to implement sophisticated reconstruction algorithms already reported in, for example, the Data Acquisition and High-Level Trigger Technical Design Report as well as for most of the results reported here. Recently, however, the need was identified to restructure the software framework in preparation for CMS data-taking in order to implement calibration and alignment strategies, ensure tractable reconstruction results, simplify and standardize the reconstruction modules, and facilitate interactive analyses.

Within the computing area, the recent emphasis was placed on the preparation of the Computing TDR, which was submitted in June 2005. In Spring 2004 the DC04 Computing Data Challenge was completed. DC04 used 70M generated pp events as input. These were simulated, mostly with GEANT4, in a large pre-production exercise using more than 30 computing centres worldwide. DC04 was an end-to-end exercise.

The computing sub-project also provides production and analysis services to enable the work of the physics groups for the Physics TDR, due to be submitted at the end of 2005. The DST that was created in the context of DC04 is now used extensively in numerous analyses. A total of almost 100 million events have now been reconstructed and are fully utilized for all the studies of the Physics TDR (Volume I). This Volume will document the full procedures and code that will be used to commission and operate the CMS detector. Broadly speaking, the basic aim of the Physics TDR is to document the way in which CMS will carry out its physics program. A second volume of the Physics TDR is planned for completion in late Spring 2006. This work will document the actual startup of the experiment in 2007, along with the very early physics reach with 0.1 fb⁻¹ and 1fb⁻¹. The last part of Volume II will document the physics reach with 10 and 30 fb⁻¹. In the autumn of 2006 a combined Computing, Software and Analysis Challenge (CSA2006) is scheduled. This will be an integrated test of the full end-to-end chain of the complete system, from (simulated) raw data to analysis at Tier-1 and Tier-2 centers.

3.8 The Magnet Test and 'Cosmic Challenge' (MTCC).

The MTCC has been scheduled in the first half of 2006 to check the functionality of the magnet, including cooling, power and control systems. The magnetic field will

be mapped. The closure tolerances, the movements under field, and the muon alignment system will be checked. The field tolerance of the yoke mounted components will be checked. Finally a combined test of all sub-detectors will be carried out using cosmic rays.

3.9 The CMS Schedule

In the current CMS Master Schedule, v34.2, the initial detector is foreseen to be installed and closed for beam on 30 June 2007 and be ready for first collisions in late summer of 2007. Installation of the pixel tracker, although ready in summer 2007, and the ECAL endcaps is foreseen during the 2007/2008 winter shutdown, in time for the first long physics run in spring 2008. The staged items include part of the fourth endcap muon station ME4/2, RPC chambers at low angles ($|\eta| > 1.6$), 60% of the DAQ online farm and the third pair of forward pixel disks.

4 Conclusions

Much effort has been expended in R and D, prototyping and construction of CMS detectors in the last 10 years. The construction of these detectors is on a truly massive scale and production of individual sub-detectors is on an industrial scale. Much hardware has already been built and assembled. The installation and commissioning of these detectors is making good progress in order to be ready for beam in the late summer of 2007. The CMS detector should be capable of discovering whatever Nature has in store at the TeV energy scale and are likely to provide answers to some of the biggest questions in physics. Data taking is eagerly anticipated and phenomena such as supersymmetry should be revealed fairly quickly if relevant at the TeV energy scale.

5 Acknowledgements

We would like to thank the organisers for the invitation and holding the symposium in such magnificent surroundings. The construction of CMS cannot be carried without the effort and the dedication of thousands of scientists, engineers and technicians worldwide. We very humbly acknowledge this effort.

References

1. <http://cmsinfo.cern.ch/> and references to Technical Design Reports therein.

Status of the LHCb experiment

Roger Forty ^a

CERN, Geneva

Abstract. LHCb is a dedicated B-physics experiment at the LHC. The experiment is currently under construction, to be ready for first collisions in 2007. The motivation for a future B-physics experiment is touched upon, followed by a discussion of the current status of the detector components, and an overview of the expected performance.

1 Introduction

The LHCb experiment is designed for the precision study of CP violation and rare decays in the B system at the LHC. Following the cancellation of BTeV and the foreseen closure of BaBar, LHCb may become the *only* running B-physics experiment after the B-factories (unless the continuation of Belle is approved). The Syracuse University group from BTeV recently joined LHCb, taking the number of institutes involved to 47, with over 600 authors, from 16 countries. Why we are preparing a B-physics experiment, following the success of the B-factories?

1.1 Motivation

There has been spectacular progress from the B-factory experiments. The precision result of their baseline measurement, the CP asymmetry of $B^0 \rightarrow J/\psi K_S$ decays, is in striking agreement with the Standard Model CKM picture, as illustrated in Fig. 1 (a). They have also performed an impressive range of additional measurements, providing the first constraints on the other angles of the Unitarity Triangle. However, their measurements have also thrown up some puzzles.

For example, the values of $\sin 2\beta$ measured via the $b \rightarrow c$ transition (as in $B^0 \rightarrow J/\psi K_S$ decays) and in $b \rightarrow s$ penguin decays such as $B^0 \rightarrow \phi K_S$ are expected to agree, to a good approximation, in the Standard Model. There is some indication from the B-factory results that the value from $b \rightarrow s$ penguins is lower (although admittedly the discrepancy is reduced when the latest results from Belle are included [2]). If the $b \rightarrow s$ transition has a contribution from new physics, then we should see the effect in other modes, such as $B_s^0 \rightarrow \phi\phi$; it may give rise to an increased branching ratio for $B_s^0 \rightarrow \mu^+\mu^-$; $B_s^0-\bar{B}_s^0$ oscillation may be affected, leading to a higher frequency Δm_s ; or larger CP violation might result in $B_s^0 \rightarrow J/\psi\phi$ than that expected from the Standard Model. Each of these signatures of new

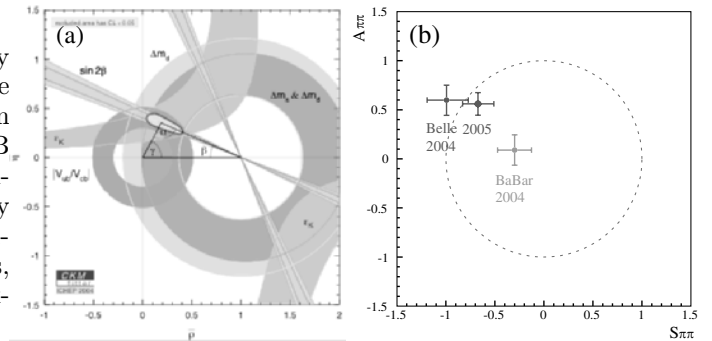


Fig. 1. (a) Current constraints on the apex of the CKM Unitarity Triangle [1]. (b) Results from the B-factory experiments for the CP asymmetry in $B^0 \rightarrow \pi^+\pi^-$ decays: $A_{\pi\pi}$ and $S_{\pi\pi}$ are coefficients of the $\cos \Delta m_d$ and $\sin \Delta m_d$ terms of the asymmetry [16].

physics can be studied in detail by LHCb, which will have a copious supply of B_s^0 mesons. Concerning $B_s^0-\bar{B}_s^0$ oscillations, the expected value of the frequency within the Standard Model is $< 30 \text{ ps}^{-1}$, as extracted from the CKM fits. If the value is as expected in the Standard Model, CDF or D0 might measure it first. But if the value is *beyond* the Standard Model expectation, LHCb should be the first to see it (or to rule out the entire Standard Model range).

A second example is the situation concerning the CP asymmetry of $B^0 \rightarrow \pi^+\pi^-$, where interesting (and not very consistent) results have come from the B-factory experiments, as seen in Fig. 1 (b). Here, the enormous statistics available at the LHC are relevant: for this decay mode, LHCb expects to reconstruct 26,000 events in the first year of data-taking (before tagging), a substantial increase compared to the currently available samples of about 500 events per experiment. We will also be able to investigate the various two-body modes, including $B^0 \rightarrow \pi^+\pi^-$, $K^+\pi^-$ and $B_s^0 \rightarrow K^+K^-$, $K^-\pi^+$, giving more handles with which to pin down any contribution from new physics.

^a On behalf of the LHCb Collaboration

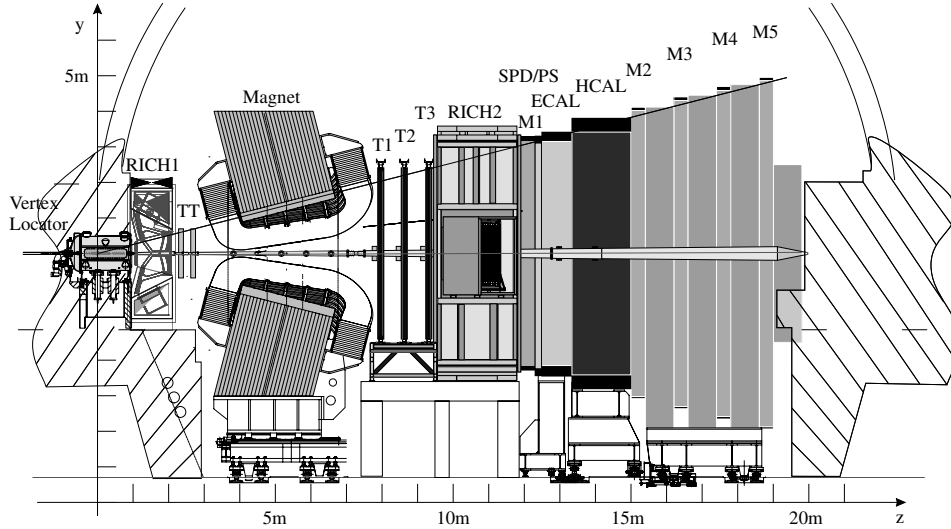


Fig. 3. The LHCb spectrometer (side view).

1.2 B production at the LHC

There is a large cross section for $b\bar{b}$ production at the LHC, of about $500\mu\text{b}$. However, this is only $\sim 0.5\%$ of the total cross section, and in addition the B decays of interest typically have low branching ratios of order 10^{-5} or less, so selection of the events of interest from the large background is a key issue.

Pile-up of pp interactions per bunch crossing is a problem at high luminosity, particularly for B events where we wish to identify the b-hadron decays by their vertex structure. However, the luminosity is tunable by defocussing the beams locally at our interaction point, so we choose to run at $2 \times 10^{32} \text{ cm}^{-2} \text{ s}^{-1}$, at which most events have a single pp interaction, as shown in Fig. 2(a). In addition, by running at relatively low luminosity the radiation dose that the detector needs to cope with is reduced.

A nominal “year” of data taking is taken as 10^7 seconds, which corresponds to an integrated luminosity of 2 fb^{-1} . Given the $b\bar{b}$ production cross section, this cor-

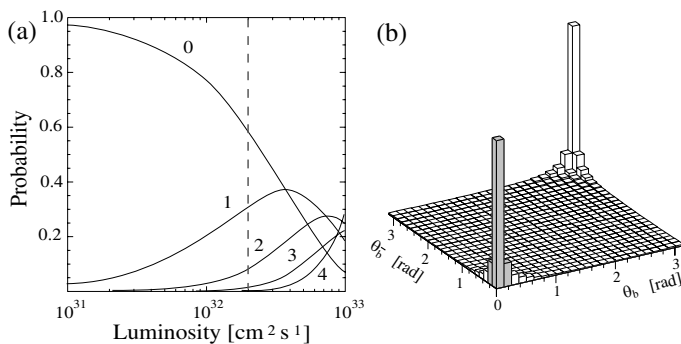


Fig. 2. (a) Probability of different numbers of pp interactions per bunch crossing, as a function of luminosity: the nominal luminosity of LHCb is indicated by the dashed line. (b) Polar angle distribution of the b and \bar{b} hadrons produced at the LHC: the region selected by LHCb is shaded.

responds to 10^{12} produced $b\bar{b}$ pairs per year, illustrating the enormous statistics that should be accessible at the LHC. The b hadrons are produced predominantly in the forward direction, as shown in Fig. 2(b), so LHCb has been designed as a forward spectrometer, covering polar angles between 10 and 300 mrad. The arrangement of the spectrometer within the experimental area (Point 8 of the LHC) is such that the interaction point is offset from the centre of the cavern, to allow the detectors to fit into the available space. A concrete shielding wall divides the cavern into two zones, with much of the read-out electronics and the event filtering CPU farm situated on the other side of the wall from the detector, so that they will be in a low radiation region.

2 Detector status

The components of the spectrometer are illustrated in Fig. 3, and the current status of installation in the pit can be seen in Fig. 4. The beam pipe, which defines the inner acceptance of the experiment, has two conical sections made of beryllium, the first with an opening angle of 25 mrad, which has been completed, and the second with an opening angle of 10 mrad that is nearing completion. The large dipole magnet of the spectrometer has an integrated field of 4 Tm, and regular field reversal is planned to help in the systematic control for CP studies. The magnet has been completed, visible on the left-hand side of Fig. 4, and field mapping is in progress. First results are in good agreement with the simulation, as illustrated in Fig. 5. The other sub-systems will be briefly described and their current status discussed in the following paragraphs; details can be found in Ref. [4].

2.1 Vertex locator

The Vertex Locator (VELO) is a silicon microstrip detector that surrounds the interaction region. The silicon

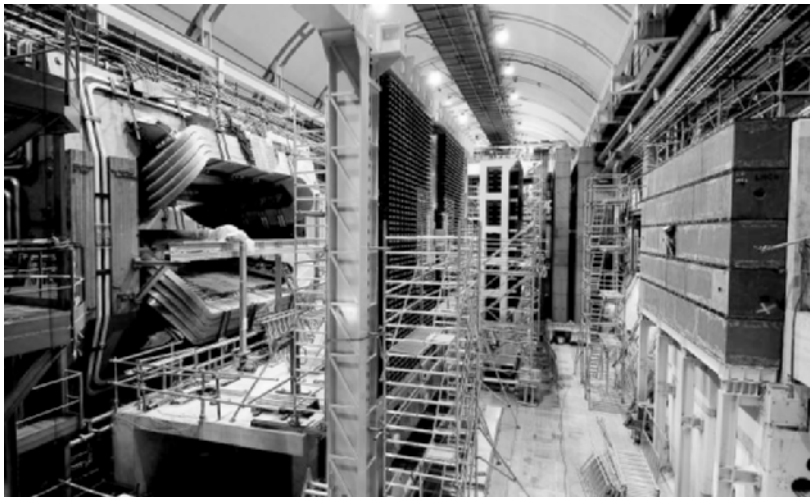


Fig. 4. Photograph of the LHCb cavern, from June 2005.

wafers are $300\ \mu\text{m}$ thick, and the strips have $r\phi$ geometry, with variable pitch between 40 and $100\ \mu\text{m}$ depending on radius. In total there are 21 stations measuring r and ϕ , distributed along the beam axis as shown in Fig. 6. Each silicon disk is about $8\ \text{cm}$ in diameter, and approaches to $8\ \text{mm}$ from the beam axis, to give precise reconstruction of the impact parameter of tracks. To achieve this close approach, a secondary vacuum system is employed, like a large Roman Pot. This system, which allows the silicon to be retracted during injection of the beams, is close to completion. The silicon module production is just starting.

2.2 Tracking system

The Trigger Tracker (TT) is a silicon strip detector covering the full acceptance upstream of the magnet, with an area of about $8\ \text{m}^2$ of silicon. Together with the VELO it measures the p_T of tracks for use in the trigger. It is made using $500\ \mu\text{m}$ thick silicon, of the type used by CMS. These give sufficient signal for the long ladders (of up to three wafers length) that are read out using low-mass Kapton

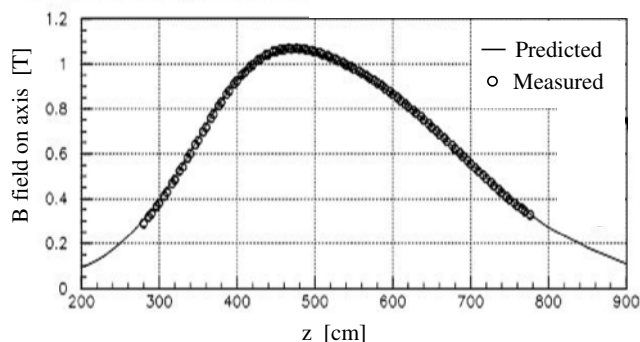


Fig. 5. Measurement of the magnetic field along the beam axis (points) compared to the simulation (line).

cables to the front-end electronics situated outside the acceptance. The final prototypes of the ladders have been successfully tested, and production is now starting.

The three tracking stations after the magnet (T1–T3 in Fig. 3) are made up of Outer Tracker that covers most of the area, and an Inner Tracker around the beam pipe, where the track density is highest. The Outer tracker stations each have four double-layers of Kapton/aluminium straws glued together to form modules. About 60% of the modules have already been produced. Although the Inner Tracker only covers 2% of the area, compared to the Outer Tracker, about 20% of the tracks pass through it. Its silicon strip detectors have $198\ \mu\text{m}$ pitch, and are arranged in boxes around the beam pipe. Production of the ladders is under way.

2.3 RICH system

The ring-imaging Cherenkov system uses three radiators: silica aerogel, C_4F_{10} gas and CF_4 gas, to give π -K separation between about 2 and $100\ \text{GeV}/c$. The first two

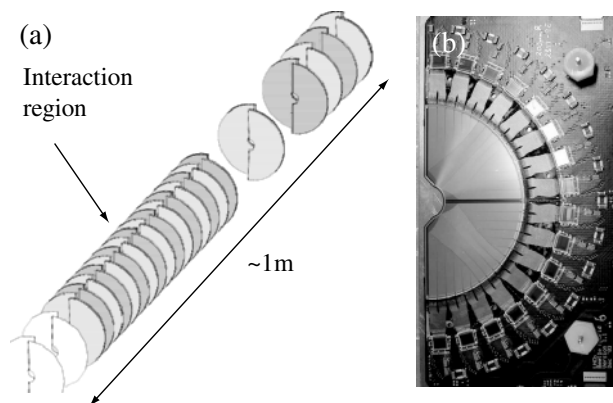


Fig. 6. (a) Layout of the silicon detectors of the VELO, along the beam axis. (b) Photograph of one of the silicon detectors.

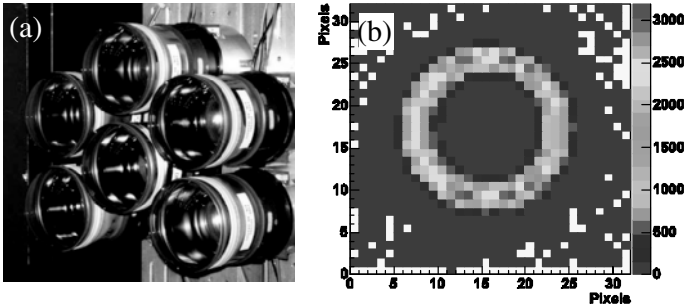


Fig. 7. (a) Photograph of a cluster of the final prototype HPDs, as installed in the beam test. (b) Cherenkov ring image recorded within a single HPD.

radiators are both incorporated in the RICH1 detector (before the magnet), for the identification of low and intermediate momentum tracks over the full acceptance. The RICH1 vessel is under construction, and high clarity aerogel has been developed for use in the detector. A second RICH detector is situated after the magnet, and covers the high-momentum particle identification at polar angle below 120 mrad. The RICH2 vessel has now been completed, and the mirrors installed and aligned. Both RICH detectors use a novel photon detector, the HPD, in which over 1000 pixels sensitive to single photoelectrons are combined within each 8 cm diameter tube. The final prototypes of these tubes gave exceptional performance in test beam studies, as illustrated in Fig. 7. Production of the ~ 500 tubes required is under way.

2.4 Calorimeter and muon systems

The calorimeter system consists of a pre-shower (SPD/PS), with scintillating pad detectors either side of a $2X_0$ sheet of lead, followed by a $25X_0$ electromagnetic calorimeter (ECAL), of lead-scintillator Shashlik construction, and finally a $5.6\lambda_I$ hadronic calorimeter (HCAL) of iron-scintillator tile construction. The ECAL consists of 3300 modules, that have been stacked to form a wall ~ 6 m high, with dimensions that agree with the specification to better than 1 mm. The ECAL is visible in the middle of Fig. 4. The HCAL modules have also now all been installed, and connection of the readout is in progress.

The muon system is made up of 5 stations, separated by iron filters that can be seen on the right-hand side of Fig. 4. MWPCs are used for all except the highest rate region, the inner part of the first station, for which triple-GEM detectors are used. Wiring of the MWPCs is progressing steadily: so far, about 30% of the chambers have been produced.

2.5 Trigger

The trigger has to reduce the 40 MHz bunch crossing rate down to a rate of interesting events that can be written to storage. This is achieved in three steps. The first, known

Table 1. Composition of the output rate from the High Level Trigger, of events that will be written to storage, and their role for detector calibration.

Rate	Event type	Calibration
200 Hz	Exclusive B candidates	Tagging
600 Hz	High mass di-muons	Tracking
300 Hz	D* candidates	Particle ID
900 Hz	Inclusive (eg $b \rightarrow \mu$)	Trigger

as Level-0, is a hardware-based trigger, that searches for high p_T particles in the calorimeter and muon systems. It has a latency of $4\mu\text{s}$ and an output rate of 1 MHz. The remaining two steps are software triggers, that will be run in the filter farm of about 2000 CPU nodes, sited in the pit. The first, Level-1, searches for tracks with large impact parameter, using the VELO information, and also with high p_T , either from correlation with the Level-0 results, or by use of the TT information. It has a latency of about 1 ms and an output rate of 40 kHz. Finally, the High Level Trigger (HLT) performs a full reconstruction of the event, allowing events of interest to be selected in a similar fashion to the offline selection. The HLT output rate has recently been increased to 2 kHz, a relatively high rate that can be afforded since the event size is small, ~ 25 kB. This large output rate allows us to include calibration samples that will be used to understand the performance of the detector, as listed in Table 1, in addition to extending the physics reach of the experiment. For details of the current status, see Ref. [3].

3 Expected performance

The expected performance of the experiment has been studied using fully-simulated events, that were generated using PYTHIA [2] and GEANT4 [10], and using full pattern recognition [4]. Tracks passing through the full spectrometer are reconstructed with an efficiency of about 95%, with a few percent of ghost tracks, as shown in Fig. 8.

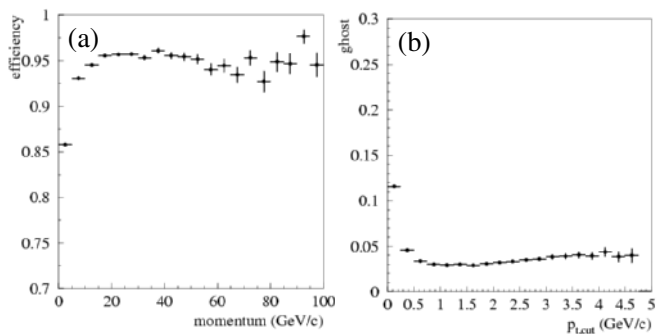


Fig. 8. (a) Reconstruction efficiency versus momentum, and (b) ghost rate versus p_T cut, for tracks that pass through the full spectrometer.

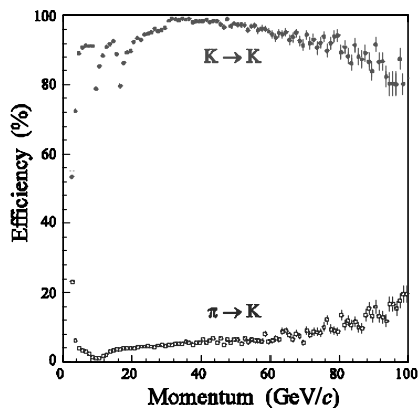


Fig. 9. Efficiency for kaon identification in the RICH, and misidentification rate of pions as kaons, as a function of momentum.

The RICH system provides excellent hadron identification, illustrated in Fig. 9. This allows the use of kaon tagging as a contribution to the flavour tagging, where the K^- that results from the decay $b \rightarrow c \rightarrow s$ is identified, and its charge reflects that of the initial b quark. It also permits a clean separation of the two-body B decays, as shown in Fig. 10. The calorimeter and muon systems provide excellent lepton identification, with an efficiency for electron and muon identification of about 90% for pion misidentification rates below 1% [8].

The B physics sensitivity can be illustrated with the analysis of $B_s^0 - \bar{B}_s^0$ oscillation. The mode $B_s^0 \rightarrow D_s^- \pi^+$ is used, for which we expect 80,000 fully-reconstructed events per year of data-taking. The signature of the oscillations is shown in Fig. 11 before and after the reconstruction. The dilution due to flavour tagging corresponds to an effective tagging efficiency of about 6% for B_s^0 decays. The proper-time resolution is about 40 fs for this mode, and the signal/background ratio is expected to be about 3 (from the study of 10^7 inclusive $b\bar{b}$ events). Finally, after including the effect of the acceptance, which removes events at short proper-time, the oscillation signal is still clearly visible. When studied as a function of the oscillation frequency Δm_s , we find a 5σ significance of the oscillation signal up to $\Delta m_s < 68 \text{ ps}^{-1}$.

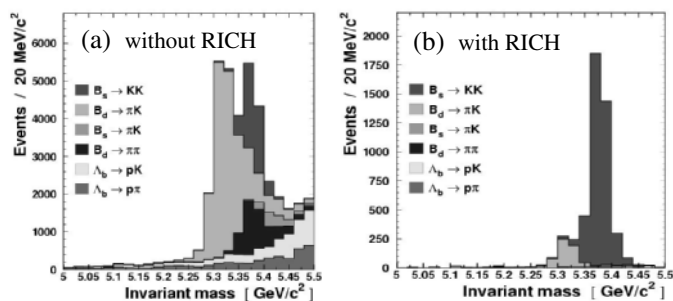


Fig. 10. Invariant mass plot of two-body B decays, in the selection of $B_s^0 \rightarrow K^+ K^-$ (a) without using the RICH, and (b) after RICH selection has been applied.

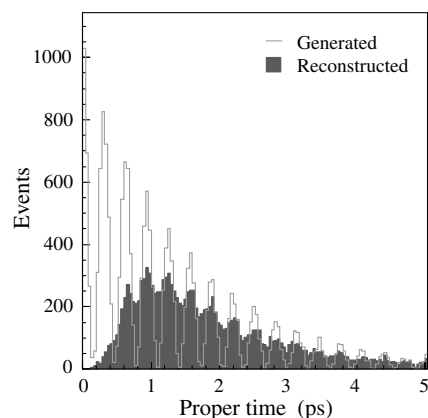


Fig. 11. Annual yield of $B_s^0 \rightarrow D_s^- \pi^+$ decays tagged as not having mixed, as a function of proper time, generated (line) and reconstructed (histogram), for $\Delta m_s = 20 \text{ ps}^{-1}$.

For a review of the other physics goals and sensitivity of LHCb, both for CP measurements and rare decays, see Refs. [9,10].

4 Conclusion

LHCb will extend the B physics results from the B factories, due to the high statistics expected at the LHC, plus access to the B_s^0 system (as well as b-baryons and the B_c^+ , that I have not covered here). The experiment will look for new physics in a complementary way to ATLAS and CMS: instead of searching for the direct production of new heavy particles, we should see their contribution to loop diagrams, influencing CP phases.

The LHCb spectrometer combines precision vertexing with excellent particle identification and a flexible trigger. Construction of the detector components is progressing well, on target to be ready for overall commissioning by end-2006. LHCb has a real capability to produce physics from day one, due to the modest luminosity required, and the open geometry which facilitates installation and commissioning of the detectors. We are eagerly looking forward to the first collisions in 2007.

References

1. See for example, <http://ckmfitter.in2p3.fr>.
2. P. Chang, these proceedings.
3. BaBar collab., [hep-ex/0501071](http://arxiv.org/abs/hep-ex/0501071);
Belle collab., [hep-ex/0502035](http://arxiv.org/abs/hep-ex/0502035).
4. LHCb collab., TDR 9, CERN/LHCC 2003-030.
5. M. Patel, these proceedings.
6. T. Sjöstrand *et al.*, *Comp. Phys. Commun.* **135** (2001) 238.
7. <http://wwwasd.web.cern.ch/wwwasd/geant4>.
8. A. van Lysebetten, these proceedings.
9. M. Schmelling, these proceedings.
10. Y. Xie, these proceedings.

QCD Physics at the Tevatron and LHC

Theoretical Perspectives in QCD:

Key issues, now and towards LHC

R. Keith Ellis¹

Fermilab
PO Box 500
Batavia, IL 60510, USA

Abstract. A review of the current status of perturbative QCD as applied to high energy collisions is presented.

1 Introduction

This article provides a review of processes which have been recently calculated in perturbative QCD. The feasibility of these calculations is a direct consequence of the property of asymptotic freedom, which was recognized by the Nobel prize committee last year. So it seems particularly appropriate to take stock of where we are, and where we need to be, in order to interpret the data which will come from the Tevatron and the LHC. The challenge is to provide the most accurate information possible to experimenters. Proton (anti)proton collisions give rise to a rich event structure which will become more complex as we pass from the Tevatron to the LHC.

QCD has many aspects, for example, non-perturbative QCD, lattice QCD, and the quark-gluon plasma. For the purposes of this talk I shall limit the discussion to the calculation of the short distance cross section in perturbative QCD, and to the evolution of the parton distribution functions. These features of QCD rely directly on the discovery of asymptotic freedom and are also of most interest for high mass scale physics at hadronic colliders.

The value of the strong coupling constant can be derived from recent results on α_S [7]

$$\alpha_S(M_Z) = 0.1182 \pm 0.0027 \quad (1)$$

where α_S is given in the $\overline{\text{MS}}$ scheme in NNLO. The value of α_S has been quite stable for the last few years. At currently accessible scales, α_S is quite large and certainly much larger than fine structure constant α . Radiative corrections in QCD are therefore correspondingly more important than in QED.

Taking a pragmatic approach, the aim is to use perturbation theory to provide physics software tools which are both flexible and give the most accurate representations of the underlying theories. A second aim is to discover more about the structure of perturbative QCD and hence learn new efficient ways of calculating in QCD.

2 The role of tree graphs

The simplest approach to calculating a short distance cross section is to evaluate the contribution at tree graph level. This approach has a number of problems. First, the overall normalization is uncertain. For example, the process $W+4$ jets occurs at tree graph level in $O(\alpha_S^4)$. Hence if the scale uncertainty changes α_S by 10%, this leads to a 40% uncertainty in cross section. Second, if we wish to calculate the rates for hadron production, (rather than parton production) we must apply fragmentation. To use universal fragmentation, we must evolve to a fixed scale. In this case tree graphs require a procedure to combine with parton showers. A third problem occurs when a new parton process appears at NLO, leading to large change in shapes, (e.g., the appearance in NLO of gluon induced processes at the LHC).

Nevertheless, the technology of the automatic generation of tree graph rates is well developed and of great use to the experimenters. For example, if we specialize to vector boson + jet processes, Madgraph II [23, 30] can generate processes with ≤ 9 external particles. Vecbos [5], can provide results for a W -boson plus up to 4 jets or a Z -boson plus up to 3 jets and Alpgen [24], can calculate W (or Z) + up to 6 jets. CompHEP [29] is a program which is simple to use which generates a matrix element squared for a tree graph and evaluates it numerically after folding with parton distributions.

The combination of tree level matrix elements with parton showers has been addressed by a number of authors. For example, the procedure of CKKW [14] separates the matrix element and parton shower regimes by a parameter y and performs a veto on the parton shower, so that the leading dependence on y cancels.

3 Spinor techniques and MHV amplitudes

The last two years have seen a remarkable advance in methods for the calculation of gluonic amplitudes primar-

ily using maximum helicity violating (MHV) amplitudes as effective vertices. In order to motivate these ideas, I shall give a brief introduction to spinor techniques. I denote the right-handed and left-handed spinors for a quark of momentum k as follows:-

$$\begin{aligned} |k+\rangle &= \text{right-handed spinor for massless vector } k \\ |k-\rangle &= \text{left-handed spinor for massless vector } k \end{aligned} \quad (2)$$

In terms of these spinors we may write the gluon polarization vectors

$$\varepsilon_{\mu}^{+}(k) = \frac{\langle q^{-} | \gamma_{\mu} | k^{-} \rangle}{\sqrt{2} \langle qk \rangle}, \quad \varepsilon_{\mu}^{-}(k) = \frac{\langle q^{+} | \gamma_{\mu} | k^{+} \rangle}{\sqrt{2} [kq]} \quad (3)$$

where the choice of the auxiliary momentum q is equivalent to a gauge choice. As a consequence of the Dirac equation the choices in Eq. (3) obey all the requirements for a polarization vector, namely

$$\varepsilon_i^2 = 0, \quad k \cdot \varepsilon(k) = 0, \quad q \cdot \varepsilon(k) = 0, \quad \varepsilon^{+} \cdot \varepsilon^{-} = -1. \quad (4)$$

Several equivalent notations for the spinor products are extant in the literature, (I shall adopt the first)

$$\langle jl \rangle \equiv \langle k_j^{-} | k_l^{+} \rangle \equiv \epsilon^{ab} \lambda_{ja} \lambda_{lb} = +\sqrt{2k_j \cdot k_l} e^{i\phi} \quad (5)$$

$$[jl] \equiv \langle k_j^{+} | k_l^{-} \rangle \equiv \epsilon^{ab} \tilde{\lambda}_{ja} \tilde{\lambda}_{lb} = -\sqrt{2k_j \cdot k_l} e^{-i\phi} \quad (6)$$

but for what follows the important point is that the inner product of two spinors goes like the square root of the normal dot product.

3.0.1 MHV 5 and n gluon amplitudes

To introduce the concept of the Maximally Helicity Violating (MHV) amplitudes we consider the amplitude for five gluon scattering. A considerable simplification is achieved by the decomposition into color-ordered sub-amplitudes

$$A = \text{Tr}\{t^{a_1} t^{a_2} t^{a_3} t^{a_4} t^{a_5}\} m(1, 2, 3, 4, 5) + 23 \text{ permutations} \quad (7)$$

Two of the color stripped amplitudes (with all momenta taken to be outgoing) vanish

$$m(g_1^{+}, g_2^{+}, g_3^{+}, g_4^{+}, g_5^{+}) = 0 \quad (8)$$

$$m(g_1^{-}, g_2^{-}, g_3^{-}, g_4^{-}, g_5^{-}) = 0 \quad (9)$$

and the maximal helicity violating five gluon amplitude is given by the simple formula

$$m(g_1^{-}, g_2^{-}, g_3^{+}, g_4^{+}, g_5^{+}) = \frac{\langle 12 \rangle^4}{\langle 12 \rangle \langle 23 \rangle \langle 34 \rangle \langle 45 \rangle \langle 51 \rangle} \quad (10)$$

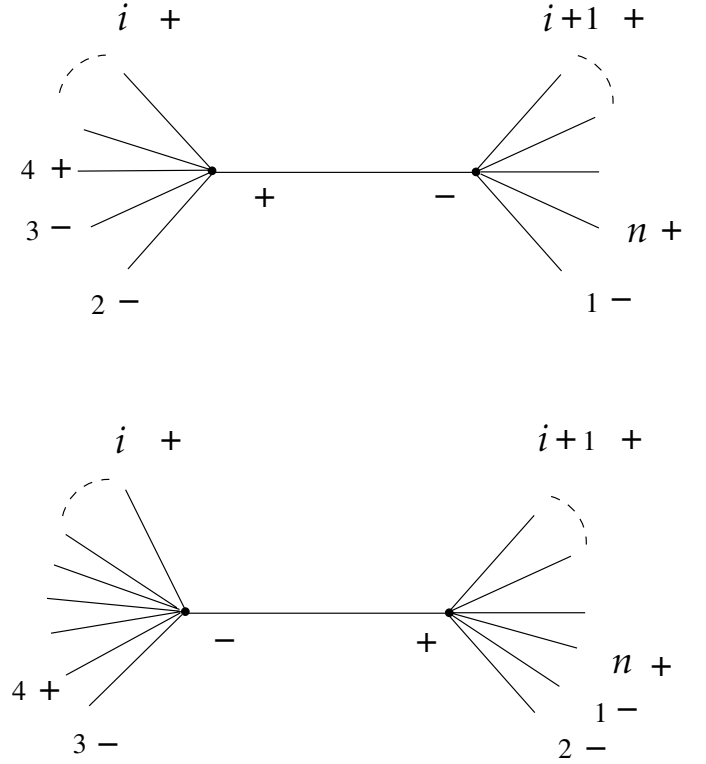
The spinor products $\langle ij \rangle$, $[ij]$ are useful because QCD amplitudes have square root singularities.

The generalization to the case with two contiguous positive helicity gluons and $n-2$ negative gluons is [4, 28]

$$m(g_1^{-}, g_2^{-}, g_3^{+}, \dots, g_n^{+}) = \frac{\langle 12 \rangle^4}{\langle 12 \rangle \langle 23 \rangle \dots \langle n1 \rangle} \quad (11)$$

Because QCD amplitudes contain singularities in the square root of the dot product, the expression in terms of spinor products leads to compact expressions.

Fig. 1. Class of diagrams which can be calculated using MHV effective theory



3.0.2 MHV calculus

In a series of beautiful papers Cachazo et al. [10,11], have shown that one can use MHV amplitudes as effective vertices to build more complicated amplitudes. They obtain simple expressions for tree amplitudes in terms of spinor products. Individual terms in the expressions for tree amplitudes contain spurious poles which cancel in the sum. These poles may compromise the utility of the expressions for numerical evaluation.

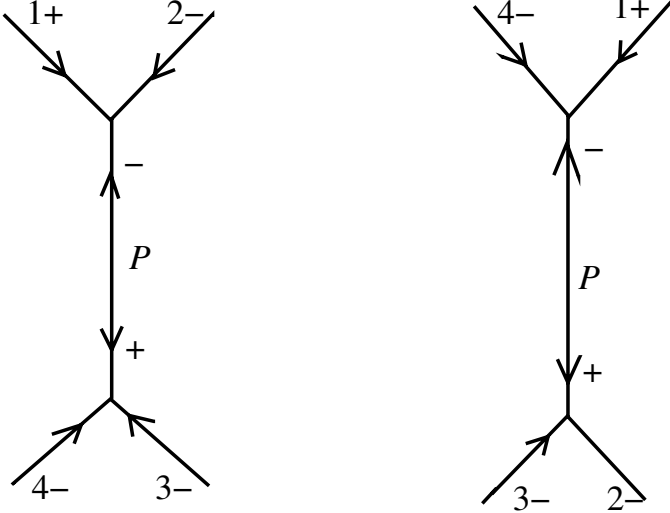
Define an offshell MHV vertex using the QCD Parke-Taylor amplitude.

$$V(1^{-}, 2^{-}, 3^{+}, \dots, n^{+}, P^{+}) = \frac{\langle 12 \rangle^4}{\langle 12 \rangle \dots \langle n-1, n \rangle \langle n, P \rangle \langle P1 \rangle} \quad (12)$$

The continuation of the spinor P off-shell is taken to be $\langle iP \rangle = \eta \sum_{j=1}^n \langle i^{-} | k_j | q^{-} \rangle$ where $P = k_1 + k_2 + \dots + k_n$, with lightlike auxiliary q . The final results are independent of η and q . It is easy to sew MHV vertices together to obtain more complicated amplitudes. For example, the n gluon $---+++\dots++$ amplitude is the sum of $2(n-3)$ MHV diagrams.

3.0.3 MHV example, ($n=4$)

Consider the two MHV vertex diagrams which give $----$ gluon amplitude (it vanishes in Yang-Mills theory)

Fig. 2. MHV amplitude diagrams for $+- --$ amplitude.

The first diagram in Fig. 2 gives

$$m_1(1, 2, 3, 4) = \frac{\langle 2P \rangle^4}{\langle 12 \rangle \langle 2P \rangle \langle P1 \rangle} \frac{1}{P^2} \frac{\langle 34 \rangle^4}{\langle 34 \rangle \langle 4P \rangle \langle P3 \rangle} \quad (13)$$

According to our continuation this is ($\not{Y} = \gamma_\mu k_1^\mu$)

$$\begin{aligned} & \frac{\langle 2 | (\not{Y} + \not{q})^3 | 1 \rangle \langle 12 \rangle \langle 21 \rangle \langle 4 | \not{q} | 3 \rangle \langle 3 | \not{q} | 4 \rangle}{\langle 12 \rangle \langle 1 | (\not{Y} + \not{q}) | 2 \rangle \langle 12 \rangle \langle 21 \rangle \langle 4 | \not{q} | 3 \rangle \langle 3 | \not{q} | 4 \rangle} \\ &= \frac{[1q] \langle 34 \rangle}{[2q][3q][4q] [21]} \end{aligned} \quad (14)$$

The second diagram is equivalent to the exchange ($2 \leftrightarrow 4$) in diagram 1. Note that $\langle ij \rangle [jk] = \langle i | j | k \rangle$

$$m_1(1, 2, 3, 4) + m_1(1, 4, 3, 2) = \frac{[1q]}{[2q][3q][4q][21][41]} (\langle 34 \rangle [41] + \langle 32 \rangle [21]) = 0 \quad (15)$$

which is zero as consequence of momentum conservation.

3.1 MHV outlook

The techniques using maximum helicity violating amplitudes lead to beautiful results for gauge theory amplitudes; however the evaluation of pure gluon tree graphs is a numerically solved problem, using Berends-Giele recursion [4]. So far the impact of these results on real phenomenology is limited, although simple tree graph results have been obtained for Higgs+5 parton amplitudes [3, 15].

The extension to loops is the next frontier. These new techniques solve the problem of computing one-loop amplitudes of gluons in super Yang-Mills theories [8, 9]. There are even indications that these techniques may lead to a comparable simplification of standard model one loop amplitudes [6].

Table 1. MCFM overview

$p\bar{p} \rightarrow W^\pm/Z$	$p\bar{p} \rightarrow W^+ + W^-$
$p\bar{p} \rightarrow W^\pm + Z$	$p\bar{p} \rightarrow Z + Z$
$p\bar{p} \rightarrow W^\pm + \gamma$	$p\bar{p} \rightarrow W^\pm/Z + H$
$p\bar{p} \rightarrow W^\pm + g^* (\rightarrow b\bar{b})$	$p\bar{p} \rightarrow Zb\bar{b}$
$p\bar{p} \rightarrow W^\pm/Z + 1 \text{ jet}$	$p\bar{p} \rightarrow W^\pm/Z + 2 \text{ jets}$
$p\bar{p}(gg) \rightarrow H$	$p\bar{p}(gg) \rightarrow H + 1 \text{ jet}$
$p\bar{p}(VV) \rightarrow H + 2 \text{ jets}$	$p\bar{p} \rightarrow t + X$
$pp \rightarrow t + W$	

4 Next-to-leading order

The benefits of next-to-leading order calculations are well known. First, they lead to less sensitivity to unphysical input scales, such as renormalization and factorization scales. They therefore give the first prediction of normalization of observables at NLO. This yields both more accurate estimates of backgrounds for new physics searches, and confidence that cross-sections are under control for precision measurements. Second, NLO calculations are a closer approximation to the real world. In a NLO calculation the partons are merged to form jets, so there is, for the first time, a dependence on the jet cone size. Third, for some processes, new species of incoming partons enter at NLO. This is particularly important at the LHC, where calculations performed at LO without large fluxes of gluons can give a misleading estimate of the cross section. Fourth, it is a necessary first step for more sophisticated procedures such as the matching with parton showers which will be described in Sect. 4.4.

The ingredients in a NLO calculation are the Born level amplitude, a real emission contribution, (i.e. the addition of one extra parton to Born level process), and the virtual contribution (i.e. the interference of one-loop amplitude with the Born amplitude). The real and virtual contributions separately contain singularities from the soft and collinear regions which cancel in the sum. The calculation of one loop amplitude rapidly becomes complicated as number of partons increases. This is especially true as we go beyond the most symmetric cases with all gluons.

4.1 MCFM overview

The MCFM program aims to provide a unified approach to the calculation of NLO processes in hadron-hadron collisions. Similar approaches to individual processes have been given by many authors, for example, ref. [25]

In Table. 1 we give a succinct list of the processes already included in MCFM and calculated to NLO in α_S . The new result this year is the completion of the discussion of single top within MCFM [12, 13]

Reliable estimates for many processes are still needed. A partial list of the processes to which one would like to know the NLO corrections is given in Table 2. This list is partial because one needs to add single top production

Table 2. A wishlist of processes which one would like to know at NLO for LHC [22]

Single Boson	Diboson	Triboson	Heavy Flavour
$W + \leq 5j$	$WW + \leq 5j$	$WWW + \leq 3j$	$t\bar{t} + \leq 3j$
$W + b\bar{b} + \leq 3j$	$W + b\bar{b} + \leq 3j$	$WWW + b\bar{b} + \leq 3j$	$t\bar{t} + \gamma + \leq 2j$
$W + c\bar{c} + \leq 3j$	$W + c\bar{c} + \leq 3j$	$WWW + \gamma\gamma + \leq 3j$	$t\bar{t} + W + \leq 2j$
$Z + \leq 5j$	$ZZ + \leq 5j$	$Z\gamma\gamma + \leq 3j$	$t\bar{t} + Z + \leq 2j$
$Z + b\bar{b} + \leq 3j$	$Z + b\bar{b} + \leq 3j$	$ZZZ + \leq 3j$	$t\bar{t} + H + \leq 2j$
$Z + c\bar{c} + \leq 3j$	$ZZ + c\bar{c} + \leq 3j$	$WZZ + \leq 3j$	$t\bar{b} + \leq 2j$
$\gamma + \leq 5j$	$\gamma\gamma + \leq 5j$	$ZZZ + \leq 3j$	$b\bar{b} + \leq 3j$
$\gamma + b\bar{b} + \leq 3j$	$\gamma\gamma + b\bar{b} + \leq 3j$		
$\gamma + c\bar{c} + \leq 3j$	$\gamma\gamma + c\bar{c} + \leq 3j$		
	$WZ + \leq 5j$		
	$WZ + b\bar{b} + \leq 3j$		
	$WZ + c\bar{c} + \leq 3j$		
	$W\gamma + \leq 3j$		
	$Z\gamma + \leq 3j$		

and other combinations of top production and vector boson production. Such processes all give rise to leptons, missing energy and heavy quarks. Only the simplest of these processes have been calculated, so much remains to be done.

4.2 Automatic NLO corrections

What is needed is an automatic procedure to calculate NLO corrections. The current stumbling block is the calculation of virtual corrections. The virtual corrections contain singularities from the regions of collinear and soft gluon emission, (and in general also UV divergences). A completely numerical procedure using, say, a gluon mass could cause problems with gauge invariance and is hence deprecated. Divergences are normally controlled by dimensional regularization.

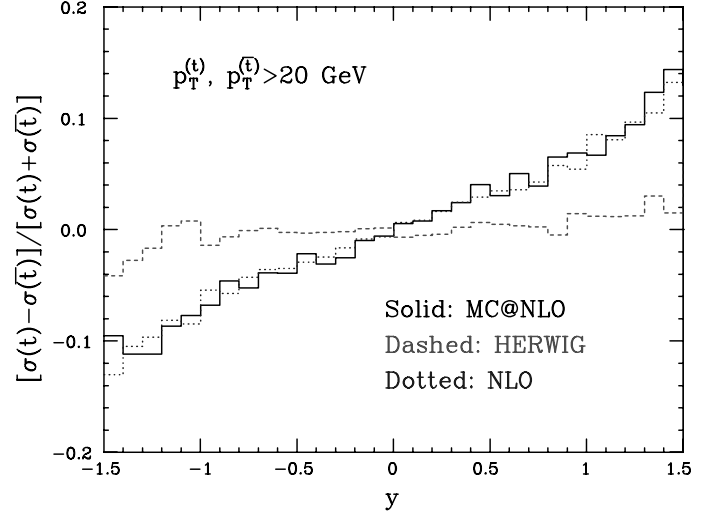
4.3 Semi-numerical approach

A seminumerical approach has been adopted in ref. [16,17,21,32]. This approach reduces tensor integrals numerically to a simple basis set for which analytic expressions as a Laurent series in ϵ are known.

There now exists a proof of principle that this method is viable. In ref. [17] the analytic result for the process $H \rightarrow q\bar{q}q'\bar{q}'$, calculated with the Lagrangian $HG^{\mu\nu}G_{\mu\nu}$, is compared with the semi-numerical result. The comparison of the two results indicates that the semi-numerical method is accurate to better than 1 part in 10^{13} .

4.4 Can one improve on NLO?

There has been considerable progress in techniques to combine NLO calculations with parton showers. The most developed if these is the MC@NLO program [18,19], but there are number of other proposals at various stages of development [26,27]. Clearly this procedure relies on the appropriate NLO process having been calculated.

Fig. 3. Top asymmetry calculated using various theoretical approaches

In the case of MC@NLO the total rates are accurate to NLO and NLO results for all observables are recovered upon expansion in α_S . Currently in this program there are a limited number of available processes, namely Higgs boson production, W/Z production, vector boson pair production WW , and heavy quark pair production $Q\bar{Q}$. The output is a set of events, which are fully exclusive.

As an example of the utility of MC@NLO, in Fig. 3 I show the expected asymmetry in $t\bar{t}$ -production at $\sqrt{S} = 2.0$ TeV. using various theoretical approaches. The MC@NLO curve follows the NLO curve (in blue, dotted) [18].

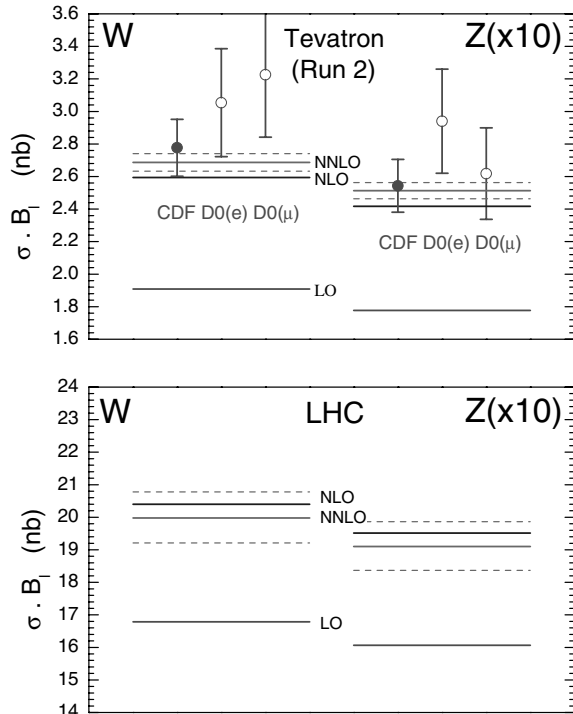
5 Next-to-next-leading order

By now a number of calculations have appeared at next-to-next-leading order, (NNLO). The advantages cited above for NLO calculations continue to hold for NNLO calculations. Thus the dependence on unphysical scales such as the renormalization and factorization scales is expected to be further reduced. The event also has more partons in the final state and hence closer to the real world. Just as NLO was the first estimate of the normalization, NNLO is the the first serious estimate of error. But, perhaps the most important reason for performing NNLO calculations is that they are a potent theoretical tool for investigating the structure of perturbation theory.

However the number of processes known at NNLO is rather small. An up-to-date list is given in ref. [31]. The processes calculated tend to be the most inclusive. For more exclusive processes, with greater numbers of external legs the calculations are more challenging. Furthermore, for more exclusive processes there may be other theoretical uncertainties of the same order as the NNLO contributions.

The most often cited application requiring an NNLO calculation is the 3-jet structure in e^+e^- annihilation. The

Fig. 4. Predictions for W and Z cross sections at the Tevatron and LHC compared with data [31] where available



full NNLO calculation, when completed, will lead to a reduction of uncertainty in the measurement of α_s at e^+e^- colliders. Currently, only a partial calculation is available [20]. The error on current measurement of α_s is dominated by the theoretical error, $\alpha_s = 0.121 \pm 0.001(\text{exp}) \pm 0.006(\text{theory})$.

5.1 W and Z production at NNLO

As an example I cite the case of W and Z production at the Tevatron and the LHC. The results are shown in Fig. 4, taken from ref. [31]. The large correction at NLO, indicates that we need the NNLO result to inspire confidence in stability of prediction. The small change from NLO to NNLO indicates that we can be confident in the estimates, and that the agreement with Tevatron data is not fortuitous. The 4% theoretical uncertainty at LHC is comparable with estimate of error on luminosity measurement from elastic scattering. Measurement of the W and Z cross sections is therefore competitive with other methods of monitoring the luminosity at the LHC.

Since measurement of the luminosity using vector boson production will be performed in a limited region of ac-

Fig. 5. The dilepton rapidity distribution for (Z, γ^*) production at run I of the Tevatron [1], compared with data from CDF. The LO and NLO curves are for the MRST PDF set. The thin NNLO bands are for the MRST lower and Alekhin upper parametrizations.

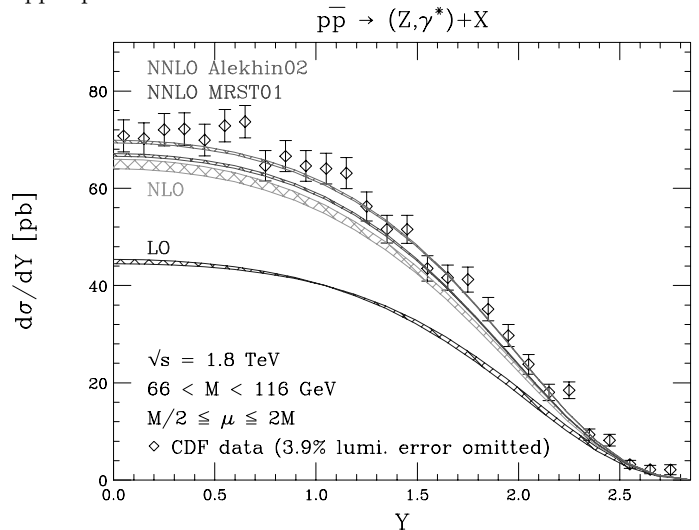
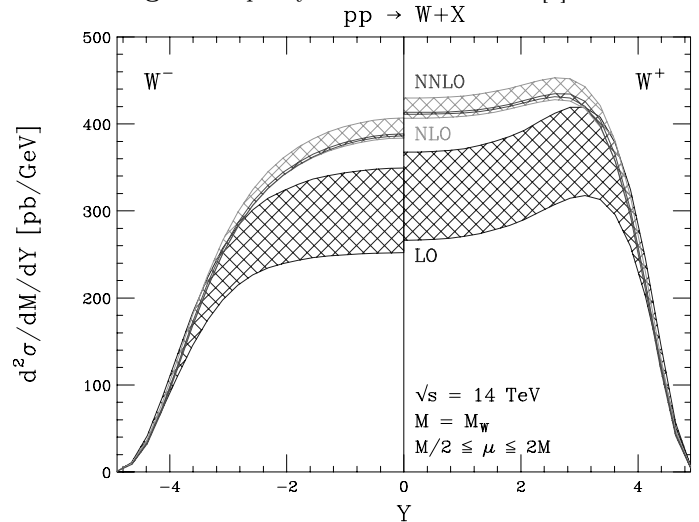


Fig. 6. Rapidity distribution at LHC [1]



ceptance, it is important to establish whether the shape of kinematic distributions is changed by higher order corrections. This concern is laid to rest by the work of ref. [47]. Fig. 5 shows the change of the rapidity distribution as the order of perturbation theory is increased. The shape of the CDF data agrees well with theoretical prediction. Furthermore, the prediction for the W -rapidity distribution at the LHC is stable as shown in Fig. 6. In Fig. 6 the bands correspond to scale variation only, but it is found that reweighting NLO results by $\sigma_{NNLO}/\sigma_{NLO}$ is good to $\leq 1\%$.

6 Conclusion

Further study of ideas regarding combining parton showers and tree graph matrix elements is the easiest and most promising in the short term; the application to many more processes is needed. As indicated in the main text, the extension of jet cross-sections to NLO is clearly desirable. The stumbling block, especially for higher leg processes, has been the evaluation of virtual corrections. New methods are needed technology needed and the semi-numerical method shows a lot of promise. The NLO calculations have now been merged with a parton showers for a limited number of processes. The strategic question to be answered is whether it is more efficient to merge NLO calculations with existing Monte Carlos, or whether it is more efficient to redesign the Monte Carlo showers to facilitate the inclusion of NLO corrections. Last, but never least, comparisons of all the approaches amongst themselves and with data is crucial both for the Tevatron and the LHC.

References

1. Charalampos Anastasiou, Lance J. Dixon, Kirill Melnikov, and Frank Petriello. High-precision qcd at hadron colliders: Electroweak gauge boson rapidity distributions at nnlo. *Phys. Rev.*, D69:094008, 2004.
2. Charalampos Anastasiou, Kirill Melnikov, and Frank Petriello. Fully differential higgs boson production and the di-photon signal through next-to-next-to-leading order. 2005.
3. S. D. Badger, E. W. N. Glover, and Valentin V. Khoze. Mhv rules for higgs plus multi-parton amplitudes. *JHEP*, 03:023, 2005.
4. Frits A. Berends and W. T. Giele. Recursive calculations for processes with n gluons. *Nucl. Phys.*, B306:759, 1988.
5. Frits A. Berends, H. Kuijff, B. Tausk, and W. T. Giele. On the production of a w and jets at hadron colliders. *Nucl. Phys.*, B357:32–64, 1991.
6. Zvi Bern, Lance J. Dixon, and David A. Kosower. Bootstrapping multi-parton loop amplitudes in qcd. 2005.
7. Siegfried Bethke. α_s at zinnowitz 2004. *Nucl. Phys. Proc. Suppl.*, 135:345–352, 2004.
8. Ruth Britto, Evgeny Buchbinder, Freddy Cachazo, and Bo Feng. One-loop amplitudes of gluons in sqcd. 2005.
9. Ruth Britto, Freddy Cachazo, and Bo Feng. Generalized unitarity and one-loop amplitudes in $n = 4$ super-yang-mills. *Nucl. Phys.*, B725:275–305, 2005.
10. Freddy Cachazo and Peter Svrcek. Lectures on twistor strings and perturbative yang-mills theory. 2005.
11. Freddy Cachazo, Peter Svrcek, and Edward Witten. Mhv vertices and tree amplitudes in gauge theory. *JHEP*, 09:006, 2004.
12. John Campbell, R. K. Ellis, and Francesco Tramontano. Single top production and decay at next-to-leading order. *Phys. Rev.*, D70:094012, 2004.
13. John Campbell and Francesco Tramontano. Next-to-leading order corrections to wt production and decay. 2005.
14. S. Catani, F. Krauss, R. Kuhn, and B. R. Webber. Qcd matrix elements + parton showers. *JHEP*, 11:063, 2001.
15. Lance J. Dixon, E. W. N. Glover, and Valentin V. Khoze. Mhv rules for higgs plus multi-gluon amplitudes. *JHEP*, 12:015, 2004.
16. R. K. Ellis, W. T. Giele, and G. Zanderighi. Semi-numerical evaluation of one-loop corrections. 2005.
17. R. K. Ellis, W. T. Giele, and G. Zanderighi. Virtual qcd corrections to higgs boson plus four parton processes. 2005.
18. Stefano Frixione, Paolo Nason, and Bryan R. Webber. Matching nlo qcd and parton showers in heavy flavour production. *JHEP*, 08:007, 2003.
19. Stefano Frixione and Bryan R. Webber. The mc@nlo 3.1 event generator. 2005.
20. A. Gehrmann-De Ridder, T. Gehrmann, and E. W. N. Glover. Infrared structure of $e^+ e^- \rightarrow 3$ jets at nnlo: The $c(f)^{**2}$ contribution. *Nucl. Phys. Proc. Suppl.*, 135:97–101, 2004.
21. W. T. Giele and E. W. N. Glover. A calculational formalism for one-loop integrals. *JHEP*, 04:029, 2004.
22. Bruce Knuteson. Run ii monte carlo workshop. 2004.
23. Fabio Maltoni and Tim Stelzer. Madevent: Automatic event generation with madgraph. *JHEP*, 02:027, 2003.
24. Michelangelo L. Mangano, Mauro Moretti, Fulvio Piccinini, Roberto Pittau, and Antonio D. Polosa. Alpgen, a generator for hard multiparton processes in hadronic collisions. *JHEP*, 07:001, 2003.
25. Zoltan Nagy. Next-to-leading order calculation of three-jet observables in hadron hadron collision. *Phys. Rev.*, D68:094002, 2003.
26. Zoltan Nagy and Davison E. Soper. Matching parton showers to nlo computations. 2005.
27. Paolo Nason. A new method for combining nlo qcd with shower monte carlo algorithms. *JHEP*, 11:040, 2004.
28. Stephen J. Parke and T. R. Taylor. An amplitude for n gluon scattering. *Phys. Rev. Lett.*, 56:2459, 1986.
29. A. Pukhov et al. Comphep: A package for evaluation of feynman diagrams and integration over multi-particle phase space. user’s manual for version 33. 1999.
30. T. Stelzer and W. F. Long. Automatic generation of tree level helicity amplitudes. *Comput. Phys. Commun.*, 81:357–371, 1994.
31. W. J. Stirling. Qcd theory. 2004.
32. Andre van Hameren, Jens Vollinga, and Stefan Weinzierl. Automated computation of one-loop integrals in massless theories. *Eur. Phys. J.*, C41:361–375, 2005.

Physics at HERA

Max Klein

DESY D - 15 738 Zeuthen Platanenallee 6 klein@ifh.de

Abstract. A brief review is given of the physics at HERA with emphasis on what it means for the LHC.

1 Introduction

Kinematics and Reconstruction

HERA is the world's only lepton-proton collider. It operates at beam energies of 27.6 GeV for polarised electrons or positrons and of 920 GeV for protons. The centre-of-mass energy \sqrt{s} is 319 GeV, as determined from $s = 4E_e E_p$. HERA thus is equivalent to a 54 TeV fixed target lepton scattering machine. Therefore it reaches very high negative momentum transfers squared, $Q^2 < 10^5 \text{ GeV}^2$, i.e. it resolves spatial distances as small as 10^{-18} m . From the neutral current inclusive cross section measurements, $\sigma_{NC}(ep \rightarrow eX)$, quark substructure limits have been set to 1/1000 of the proton radius by the two collider experiments H1 [1] and ZEUS [2]. Compared to previous fixed target lepton scattering experiments, the Q^2 range of deep inelastic scattering (DIS) has been extended with HERA by more than two orders of magnitude, see Fig.1. Due to the very high energy a new kinematic region of very low Bjorken x has been explored, down to $x \simeq 10^{-5}$, for $Q^2 \simeq 1 \text{ GeV}^2$.

HERA physics is precision physics. The scattering kinematics is reconstructed from the angles (θ_e, θ_h) and energies (E'_e, E_h) of both the scattered electron (e) and the hadronic (h) final state. The uncertainties currently reached are: 0.3 – 1% for the electron energy scale, 0.2 – 1 mrad for the electron scattering angle, 1% for the hadronic energy scale and 1 – 2 mrad for the scattering angle of the struck quark as reconstructed from the final state particles. The electron energy calibration uses the "double angle method" by reconstructing E'_e from θ_e and θ_h and the fact that in a large part of the kinematic region, at larger x and medium Q^2 , the scattered electron energy has to agree with the known electron beam energy ("kinematic peak method"). The hadronic energy scale can be determined accurately from the transverse momentum balance of the neutral current (NC) events. The polar angle measurement profits from redundant tracking based on Silicon detectors, drift and proportional chambers. The luminosity is measured from the Bethe-Heitler scattering process,

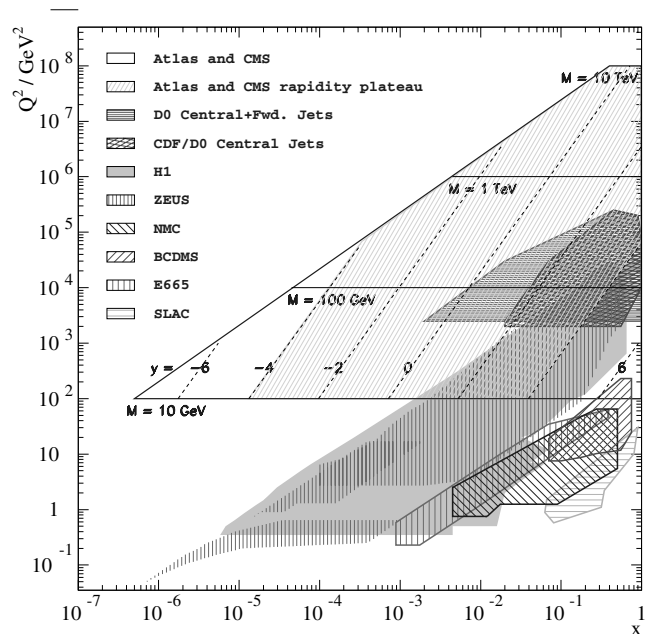


Fig. 1. Kinematic range of momentum transfers squared Q^2 and Bjorken x covered by deep inelastic fixed target experiments and by HERA and the equivalent kinematic ranges of the Tevatron and the LHC pp collider experiments.

$ep \rightarrow e\gamma$, to within an accuracy of about 1%. Therefore the accuracy of inclusive cross section measurements reaches a few % extending with increased luminosity to larger Q^2 . Both H1 and ZEUS are highly efficient apparatus of nearly 4π acceptance. This allows the complete final state to be reconstructed, apart from losses close to the beam pipe, in p and in e beam direction. Calorimeters and fibre detectors placed in forward direction, upstream the proton beam, allow charge exchange processes with forward going neutrons and colourless ("pomeron") exchange processes with forward going protons to be tagged, respectively. HERA physics thus extends much beyond the classic inclusive NC measurements: by including inverse charged current processes ($ep \rightarrow \nu X$), heavy flavour pro-

duction, often lifetime tagged, final state physics to study parton radiation and diffractive physics. Operating at the current energy frontier, H1 and ZEUS have been searching for new physics beyond the standard model.

1.1 Low x , high x and the LHC - Outline

The observation of the rise of the quark distributions, as determined from the proton structure function $F_2(x, Q^2) = x \sum_q (q + \bar{q})$, towards low x at fixed Q^2 came unexpected. Soon after, the derivative $\partial F_2 / \partial \ln Q^2$ was observed to rise as well towards low x . This implies a rise of the gluon distribution $xg(x, Q^2)$ which dynamically causes a large sea quark density. Low x physics thus is devoted to the exploration of a high density, gluon dominated dynamic system of partons. The low x region, as can be seen in Figure 1, corresponds to the forward acceptance region at the LHC with a rapidity range of η between -1 and -5 depending on the mass of the produced system. Low x physics is an exciting field as it regards a new state in which the density of partons is high but the strong coupling constant small [3]. At very high density, saturation effects are predicted to set in, when gluon recombination $gg \rightarrow g$ becomes dominant [4], which restores unitarity. Signs for saturation may have been seen at HERA [5]. Low x physics is intimately related also to neutrino astrophysics at very high energies [6]. Ongoing developments of low x physics are presented in Section 1.

The region of larger x corresponds to the central, the rapidity plateau region at the LHC. In this region of x , the parton densities are not large at HERA. The Q^2 evolution from the DIS fixed target experiment region to HERA has been proven to follow the DGLAP approximation of perturbative QCD, in which partons are radiated collinearly and strongly ordered in transverse momentum. One thus expects that the parton distribution functions (*pdf*'s) measured at HERA can be evolved to the kinematic region of the LHC experiments¹. The second part of this talk comprises the results and prospects of determining the possibly full set of parton distributions, of up, down and heavy quarks, from the H1 and ZEUS data. Besides perhaps determining the parton luminosity at the LHC, this programme, performed at higher order pQCD, would be a most reliable basis for discriminating new phenomena from ordinary parton radiation background.

While forward physics and the physics in the rapidity plateau region at the LHC have clear relations to the low and medium x regions at HERA, respectively, there are many more subjects being investigated at HERA which possibly are relevant for the LHC and for developing a consistent view on high energy deep inelastic scattering. The third section thus briefly describes some recent developments and directions of HERA physics.

¹ The extrapolation from HERA to the LHC is yet over nearly three orders of magnitude. New physics, however, as due to new strongly interacting particles [7] may alter the parton distributions at large Q^2 .

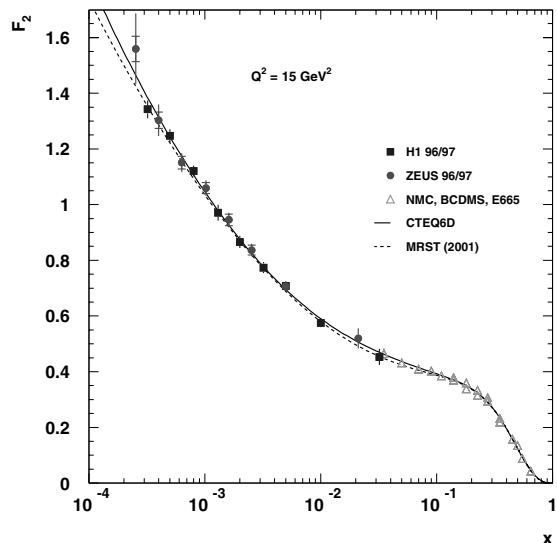


Fig. 2. Accurate data have been obtained at HERA in the measurement of the proton structure function $F_2(x, Q^2)$ which is observed to rise towards low x . The range covered by the F_2 data is from $10^{-6} - 0.5$ in x and from $0.1 - 30000 \text{ GeV}^2$ in Q^2 .

Within the framework of a still ongoing workshop [9] the relations of the physics and experimentation at HERA and at the LHC are being intensively studied in working groups on parton density functions, multi-jet final states, heavy quarks, diffraction and issues and tools for simulation. Naturally, these relations are wider and deeper than can possibly be demonstrated in this brief summary.

2 Low x Physics

The rise of the sea quarks towards low x

Already from the first small data set, the proton structure function $F_2(x, Q^2)$ was observed to rise towards low x . This observation has subsequently been verified with much improved precision, see Figure 2. Currently F_2 is measured to an accuracy of up to 2% in the bulk region of the data, for x approximately between 10^{-4} and 10^{-2} , and for Q^2 between 5 and 50 GeV^2 . The data of H1 and ZEUS agree rather well and they match also well to the fixed target data. At low x the structure function F_2 rises approximately like $x^{-\lambda}$. The Q^2 dependence of λ is logarithmic, $\lambda \simeq 0.05 \ln Q^2 / \Lambda^2$ ($\Lambda \simeq 0.3 \text{ GeV}$) [1] but flattens at Q^2 near to 1 GeV^2 . In this region, corresponding to dimensions of 0.3 fm, the transition from a partonic to soft behaviour seems to occur: here λ approaches the value, of about 0.08, determined in soft hadron reactions using Regge theory.

The proton structure function measures at low x only one specific combination of up and down quarks, $F_2 \simeq 2x(4\bar{u} + \bar{d})/9$, neglecting for illustration the strange s and

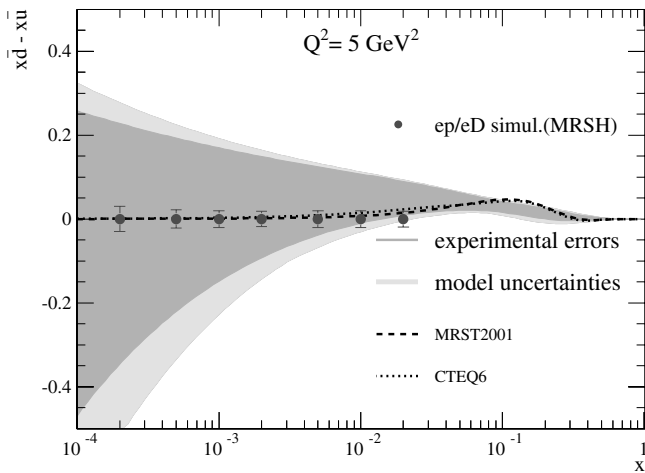


Fig. 3. Simulation of the difference of sea quarks, here assumed to be zero at low x based on additional 20 pb^{-1} of electron-deuteron data at HERA. The error band represents the uncertainty of the H1 NLO QCD fit to the H1 ep and the BCDMS μp and μd data without the constraint $\bar{d} = \bar{u}$ at low x . The dashed curves represent calculations by MRST and CTEQ which for $x \simeq 0.1$ account for the sea asymmetry measured in Drell Yan fixed target scattering

the heavy c, b quark contributions. Any QCD analysis directed to a determination of the parton distributions inside the proton assumes that $\bar{u} = \bar{d}$ at low x . This, however, is a very strong assumption, as is illustrated in Figure 3, which can be verified in electron-deuteron scattering at HERA. Measurements of ed would also disentangle the singlet and non-singlet evolution in pQCD at low x , where it is a particular issue [10], and improve the accuracy of the measurement of the strong coupling constant α_s by about a factor of two. Deuteron scattering at HERA would be much more accurate than at fixed target experiments because, by tagging the spectator proton with high resolution, one could reconstruct the electron-neutron scattering kinematics essentially free of nuclear corrections. Furthermore, shadowing effects could be related to and likely controlled [2] with diffractive scattering data. Unfortunately there has been no time allocated to pursue such an experimental programme at HERA [12] although this means a significant loss of insight to nucleon structure and a substantial reduction of the predictive power of the HERA data for the LHC.

The Gluon Distribution

A central role for predicting physics at the LHC plays the gluon momentum distribution in the proton. High transverse momentum jets at the LHC, the rate of which is predicted to be 6 orders of magnitude higher than the pair production of squarks, are predominantly due to gluon-gluon interactions, i.e. $gg \rightarrow qq$. The production of the Higgs decaying into two photons or into a bottom quark pair is as well due to gluon-gluon interactions. An accurate determination of $xg(x, Q^2)$ is of crucial importance for the LHC, as are hadronisation effects and simulations, see

e.g. [13]. The current accuracy of the gluon distribution achieved at HERA is illustrated in Figure 4. Improvements on the gluon distribution are still expected [14] from a variety of measures: in the whole x range by an improved measurement accuracy, from typically 3% to 1% in the bulk region ($x \sim 10^{-3}$ and $Q^2 \sim 30 \text{ GeV}^2$) and from 10% to a few % at large x ; from HERA jet data at $x \sim 0.05$, mostly di-jets in photoproduction; and at small $x \sim 5 \cdot 10^{-4}$ from a measurement ² of $F_L(x, Q^2)$. The Q^2 evolution of valence quarks is a non-singlet evolution and thus not sensitive to the gluon distribution. Therefore, in the region of $x > 0.3$, where xg becomes very small, DIS constrains the gluon distribution essentially only via the momentum sum rule. This may explain the large differences observed at large x of otherwise rather compatible parton distribution fits. Further work is needed and improvements are expected to come with averaging the HERA data, see below, and critically assessing the fit assumptions regarding the error treatment and parameter choices.

Parton Radiation

HERA provides phase space in x and transverse parton momentum k_t which allows the mechanism of gluon radiation at low x to be studied in detail. In the low x DIS region, the gluon density is high. Also, $\alpha_s \cdot \ln(1/x)$ is large and DGLAP evolution should not be applicable without resummation of the large $\ln(1/x)$ terms. Nevertheless, DGLAP seems to describe the bulk of the inclusive DIS, heavy flavour and diffractive data, with the x shapes of the pdf 's determined from the low x data. PYTHIA and HERWIG simulation programs are successfully used which are based on the DGLAP radiation mechanism. Alternative (BFKL) and complementary (CCFM) prescriptions have been worked out to describe gluon emission. Monte Carlo programs have been written which model k_t ordered (as DISENT/NLOJET), angular ordered (CASCADE) and emission random in k_t (ARIADNE), corresponding to the DGLAP, CCFM and BFKL equations to some extent. A dedicated working group within the HERA-LHC workshop deals with simulation programs and techniques [15].

A wealth of data has been investigated in order to find deviations from the DGLAP prescription and contribute to the development of low x theory. Recent analyses of H1 and ZEUS suggest that DGLAP theory in NLO may fail in the description of the emission of jets in the forward, the proton beam direction at low x and Q^2 , for $x_{jet} < x$ (to enhance BFKL effects) and $E_T(jet) \simeq Q^2$ (to suppress DGLAP evolution). Hints for a breakdown of the conventional theory come also from the study of azimuthal correlations between dijets, which at low x and Q^2 seem to be weaker than predicted in NLO DGLAP theory. Firm

² This requires to run HERA at lowered proton beam energy. Such a measurement is of crucial importance for testing the whole consistency of QCD to high orders perturbation theory in the region of large parton densities. As this is written, detector and machine studies are being done to prepare a possible low energy run of a few months duration in 2007.

interpretations of these observations are subject to the uncertainties connected with yet higher order pQCD contributions and with effects of the resolved photon structure. "Unintegrated", k_t dependent parton distributions are being introduced [16] which may allow a more accurate description of the final state as they incorporate transverse momentum kinematic effects in their definition.

Hard Diffraction

The observation of hard diffraction at HERA, characterised by a gap of activity in forward region, along the proton beam direction, came unexpected. Since then a wealth of measurements has been performed by both H1 and ZEUS, in which this process is tagged by the rapidity gap or the leading proton in Roman pot detectors. Much of the discussion in the HERA-LHC workshop has been devoted to both to the interpretation of the results and the measurement techniques, having in mind the Roman pot installations from 17 m to perhaps 420 m at the LHC, and the TOTEM experiment in particular. For diffractive ep scattering, a factorization theorem has been proven which allows diffractive structure functions and parton distributions to be introduced, which quantify the density of partons in the exchanged particle, the "Pomeron".

At the LHC the key interest is perhaps the double diffractive production of the Higgs particle which supposedly occurs in a clean environment. The reaction $pp \rightarrow pHp$ is proportional to the product of unintegrated gluon distributions which are related to the gluon distribution as $\int^{\mu^2} d^2 k_t^2 / k_t^2 f(x, k_t^2) = xg(x, \mu^2)$. A possibility used, e.g. in the description of J/Ψ production, to determine the unintegrated distribution consists in a differentiation of xg . This requires to measure the (integrated) gluon distribution much more accurately than hitherto, see above. Strictly speaking, the cross section is described by an unintegrated gluon distribution, a function $f(x, x', k_t^2, t)$ which is skewed since $x \simeq M_H^2/s \sim 10^{-2}$ and $x' \simeq k_t^2/s \ll x$, see [17]. Such generalised parton distributions could be accessed with deeply virtual Compton scattering (DVCS, $ep \rightarrow ep\gamma$) and vector meson measurements at HERA. The t dependence is characterised by the shrinkage effect $f \propto x^{-\alpha'(t)}$. Exclusive Higgs production at the LHC is related to the gap survival probability which is being studied at HERA by comparing resolved virtual photon-Pomeron scattering to theory with unsuppressed gap probability, with actually a surprising result: suppression is not only observed for the resolved part but as well for the direct part of the γ^*IP interaction, by a factor of two in the whole accessible range of x_γ .

Diffraction is a basic phenomenon possibly related to confinement. Diffraction, saturation and multiple parton interactions, i.e. remnant-remnant interactions which lead to the "underlying event", are intimately connected [19]. The development of the QCD of hard diffraction is a fundamental task in its own. At HERA many processes are studied, more and more relating diffraction to charm and jet production, but as well improving the accuracy and

consistency of the inclusive data, mostly in NC but recently also in CC reactions. In view of the LHC, HERA has the challenging tasks to measure precisely the gluon distribution, to determine the diffractive parton distributions, study the gap suppression and constrain the models for unintegrated and generalised parton distributions. Regarding DVCS, first cross section data have been published. With the availability of polarised positron and electron data of high luminosity, beam charge and beam spin asymmetries become measurable, not only at HERMES³ but as well at low x at H1 and ZEUS. Further progress is expected from tagged and thus 4 fold differential diffractive data and from a measurement of the longitudinal diffractive structure function F_L^D when HERA will be operated at low proton beam energies. At the LHC diffraction will not be easy to measure. Rapidity gap detection may require dedicated data taking at reduced luminosities of $\sim 4 \cdot 10^{32} \text{ cm}^{-2} \text{ s}^{-1}$, and the installation of Roman pots in the cold will be a challenge. Techniques acquired at HERA are for sure of help, from theory to cold bypass and Roman pot technology.

3 Physics at the Rapidity Plateau

Parton Distributions

The measurement of the parton distributions in DIS enables a prediction of the cross sections of the production of the weak bosons, W and Z , from the fusion of two quarks, at the LHC. The weak boson production has been proposed to be used to determine the pp luminosity [8], assuming the rate measurements and the cross section prediction could be accurate to the level of a few per cent. An accurate determination of the different quark and anti-quark momentum distributions at HERA will thus be very important for such a precision to be reliably achieved.

The HERA collider experiments have measured the full set of NC and CC double differential $e^\pm p$ inclusive scattering cross sections which are determined by structure functions and quark momentum distributions in the proton as follows:

$$\sigma_{NC}^\pm \sim Y_+ F_2 \mp Y_- x F_3, \quad (1)$$

$$F_2 \simeq e_u^2 x(U + \bar{U}) + e_d^2 x(D + \bar{D}), \quad (2)$$

$$x F_3 \simeq 2x[a_u e_u(U - \bar{U}) + a_d e_d(D - \bar{D})], \quad (3)$$

$$\sigma_{CC}^+ \sim x\bar{U} + (1-y)^2 xD, \quad (4)$$

$$\sigma_{CC}^- \sim xU + (1-y)^2 x\bar{D}. \quad (5)$$

Here $y = Q^2/sx$ is the inelasticity, $Y_\pm = 1 \pm (1-y)^2$, $U = u+c+b$ is the sum of the momentum distributions of the up-type quarks with charge $e_u = 2/3$ and axial vector

³ HERMES is the fixed target eN experiment at HERA. Measurements are focused on the longitudinal and transverse spin structure of the proton. For measurements in the coming years, a detector will be installed to tag the recoiling proton in DVCS interactions, and the physics will be focused to investigate generalised parton distributions at larger x [20].

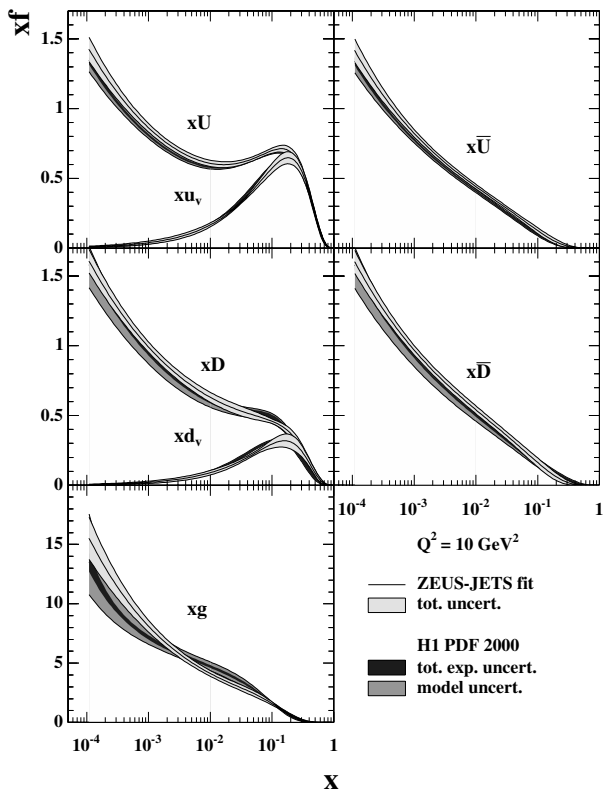


Fig. 4. Determinations of the quark and gluon distributions from NLO QCD fits to NC, CC, and to jet data (ZEUS), at $Q^2 = 10 \text{ GeV}^2$ as a function of Bjorken x . The differences $U - \bar{U}$ and $D - \bar{D}$ are used to determine the valence quark distributions u_v and d_v , which dominate at large x .

coupling $a_u = 1/2$ while $D = d + s$ is the sum of the momentum distributions of the down type quarks with charge $e_d = -1/3$, $a_d = -1/2$. Similar relationships hold for the anti-quark distributions \bar{U} and \bar{D} . In the kinematic range of HERA, the NC structure function F_2 is dominated by its electromagnetic part, Eq.(2), while xF_3 is dominated by its γZ interference part, Eq.(3). The structure function xF_3 is a direct measure of the sum $2u_v + d_v$ of the valence up and down quark distributions, unless there is an asymmetry between anti-quarks and sea quarks⁴. The exchange of W^\pm bosons in CC $e^\pm p$ scattering allows different quark flavour distributions to be accessed and the valence quark distributions to be directly determined, for large $x > 0.3$. NC and CC scattering data, as measured by H1 and ZEUS, therefore allow the complete set of parton distributions to be unfolded in a single experiment. Results for the determinations of the quark and the gluon distributions [2] are consistent, see Fig.4. Residual differences between the parton distribution functions and their uncertainties reflect different conventions regarding the parameterisations and error treatments and hint to subtle effects in the data. The *pdfs* presented here rely only on

⁴ Indications for such an asymmetry have been discussed in the strange sea, in connection with the NuTeV $\sin^2 \theta$ anomaly [18].

H1 or ZEUS data. They are in agreement with recent fits from the MRST and CTEQ Collaborations, which include fixed target DIS, jet and Drell-Yan data. Analyses based on HERA data only have the advantage of being systematically coherent: global fits often use *ad hoc* χ^2 definitions in order to compensate for apparent inconsistencies in the world's data sets. With increased luminosity and range the *pdf* determinations at HERA, including charm and beauty, will become rather precise. This is expected to reduce the spread of the extrapolated cross sections, which, for example, for $pp \rightarrow HW$ is as large as 20% [21]. Thus predictions for the LHC require still much more data and analysis work to become reliable at the few per cent level. Theoretical questions regard for example the validity of the DGLAP approximation used towards low x (do partons have to be “conservative”? [22]) and the effect of soft gluon resummation [23]. QCD is a subtle theory and requires extreme care and high knowledge to be fully developed and practically useful.

Strong Coupling Constant and Jets

The strong coupling constant is the least well-measured of the fundamental coupling constants. It thus dominates the uncertainty of extrapolations of the electromagnetic, weak and strong coupling constants to a unification scale near the Planck mass [24]. The average $\alpha_s(M_Z^2)$ value to NLO from ZEUS and H1 as determined in inclusive DIS and in jet production currently is

$$\alpha_s = 0.1186 \pm 0.0011 (exp) \pm 0.005 (thy). \quad (6)$$

Here the first uncertainty comprising all experimental and model dependent effects is already smaller than the current world average error. A striking peculiarity of this result is the so-called theoretical error. Its size reflects the *ad hoc* convention that the renormalisation (and factorisation) scale should be varied by factors of 2 and 1/2. This convention is not supported by the data: in both the H1 and the ZEUS inclusive NLO QCD analyses, fits are very poor at the extremes of these scale variations and thus the variation prescription is questionable. With forthcoming exact NNLO analyses the scale dependence will be further reduced but the arbitrariness of the scale choice remains to be resolved.

Jets at HERA are measured at scales of the order of 10 GeV, while ATLAS and CMS will focus on much higher energies. Jets at lower scales at the LHC will be measured in the forward region by the LHCb experiment [19]. At HERA jets are studied in DIS and photoproduction, used not only to measure α_s , as from the three-to-two jet ratio, but as well to study parton correlations, event shapes and alike.

Beauty and Charm Quark Distributions

Heavy flavour physics is an important, still much developing part of HERA physics. Initial measurements of the

charm structure function $F_2^{c\bar{c}}(x, Q^2)$ have measured the charm quark contribution to the sea quark density at low x to be about 20%. This and further measurements of charm and beauty production at HERA are stimulating much theoretical activity in describing heavy flavour production near and above threshold within QCD. While near threshold one thinks of heavy quarks being produced in the fusion of the interacting photon with a gluon from a proton made of u , d and s quarks, much above threshold, $Q^2 > m_Q^2$, the heavy quarks $Q = c, b$ appear light and behave as ordinary constituent partons with momentum distributions, $c(x, Q^2)$ and $b(x, Q^2)$, inside the proton.

Charm production at HERA is usually tagged using the reaction $D^* \rightarrow D^0 \pi_{slow} \rightarrow K \pi \pi_s$ and the $\Delta M = M(K\pi\pi) - M(K\pi)$ technique. Beauty production mostly has been observed in events with enlarged transverse momentum of muons with respect to jets. Both H1 and ZEUS have observed an excess of beauty production in the reaction $ep \rightarrow ejet\mu X$ with respect to NLO QCD predictions for large muon rapidities $\eta \sim 1$. Measurements of vector mesons and of quark-antiquark correlations involving charm and beauty quarks are being performed to constrain theory and understand parton dynamics, e.g. the fusion $\gamma^* g \rightarrow Q\bar{Q}$, which provides independent information on the gluon distribution.

Recently, the first measurements of $F_2^{b\bar{b}}$ and of $F_2^{c\bar{c}}$ became available based on the characteristic signature of the long lifetime of D and B particles, as measured in H1's central Silicon strip detector. Both H1 and ZEUS have extended their Silicon detector systems and upgraded the forward tracking. The inclusive, lifetime based measurements of heavy flavour production promise the charm and beauty densities in the proton to be accurately measured. In the kinematic range of the LHC, both charm and beauty quarks acquire a flavour democratic share of proton's momentum. The beauty contribution to the total Z production at the LHC amounts to about 5%. It thus needs to be measured at HERA with an accuracy of 10-20% in order not to dominate the Z cross section prediction which one hopes to determine at the per cent level of accuracy. The b quarks will play an extensive role at the LHC, in the investigations of parton dynamics as in the searches for new physics, as for example in the gluon-gluon Higgs production, $gg \rightarrow bH\bar{b}$ or $gb \rightarrow Hb$. Some information on the strange quark distribution can be obtained from strange (Φ) particle production and charm production in charged current scattering (e.g. $W^{+s} \rightarrow c$) and be confronted with the common assumption $xs = 2x(\bar{U} + \bar{D})$ at the initial Q^2 .

HERA is the ideal place to measure the heavy quark densities accurately. Since beauty at HERA contributes only about a per cent of F_2 , this requires high luminosity, which is being collected.

4 Recent Developments in HERA Physics

Beyond the developments which are briefly presented below, there are further very interesting results and ideas, for

example i) deeply virtual Compton scattering, a process which allows parton correlations to be measured for the first time, ii) detailed studies of correlations, e.g. between heavy quarks, or between diffraction and heavy quark production, iii) the puzzling observations of pentaquark states involving strange but also charm quarks, and many others. It is difficult to ascribe to all these developments a definite or even practical value for better understanding physics at the LHC. However, surely only a consistent picture of the standard model and parton dynamics in particular may allow firm extrapolations to be made to the LHC.

Electroweak Physics

With the proton structure becoming better determined and the luminosity increasing, $e^\pm p$ NC and CC scattering data from HERA can be used to perform interesting tests of the standard electroweak theory in the spacelike region. A recent first analysis [25], which treated the parton distribution and the electroweak parameters in a common NLO QCD and $SU(2)_L \times U(1)$ fit, has determined the light quark axial and vector couplings to the Z_0 . Using data in the region of high Q^2 , this analysis resolves sign ambiguities inherent in LEP data at resonance. Results have also been obtained for the measurement of the propagator mass in CC scattering, for the top mass from radiative corrections and of $\sin^2 \theta$. All results are consistent with the standard model. The accuracy will be much enhanced when the full set of polarised electron and positron data will become available and analysed.

Combination of Cross Sections

Within the framework of the HERA LHC workshop a method has been put forward to average the cross section data prior to analyzing them in QCD fits [26]. This procedure has the attractive feature of cross calibrating the H1 and ZEUS measurements and of reducing the limiting effects of both statistical and systematic nature. Thus new data sets will become available, which may be used in subsequent analyses and in predicting cross sections for the LHC. This method requires the input of large and analysed data sets, and it will require to return to the individual analyses with the aim of averaging results. By exploiting the systematics correlations, the approach goes beyond a simple statistical average and beyond fitting the data prior to averaging them. The benefit of this method has been investigated [14], but quite some studies on the data and the method are still ahead.

Searches for Physics Beyond the Standard Model

HERA, as the TeVatron, is a machine operating at the energy frontier. Thus a strong effort is made to search for physics beyond the Standard Model [27]. Competitive limits have been set, for example in searches for contact

interactions, leptoquarks, extra dimensions or supersymmetric particles, which in ep may be singly produced as is allowed in R parity violating SUSY theories. An intriguing peculiarity are events in which the final state contains an isolated lepton, large missing transverse momentum and a hadronic system with a large transverse energy, which by the H1 Collaboration are regularly observed in e^+p scattering, at an excess rate of 3.4 standard deviations from 158 pb^{-1} of integrated luminosity. The data still to be taken are expected to shed further light on this observation, which currently is the largest deviation from the standard model observed at large scales at HERA.

5 Concluding Remarks

The HERA collider experiments are still taking data of high luminosity and with polarised lepton beams. From these data new insight is expected on the dynamics of parton interactions. Many results which are being obtained can be predicted to become more accurate. For example, the gluon distribution at low x will be reexamined at NNLO QCD with more accurate data and with new data on jet production and on the longitudinal structure function. Refined analyses of heavy quark production, jet production and diffraction, and of data combining these characteristics are still being performed. New concepts as DVCS and unintegrated parton distributions are at their infancy and will develop further. It thus will take time to explore ep HERA physics fully. While the accuracy of the HERA data will still be increased, the first LHC data are expected to become available. This will much strengthen the fruitful interaction of the communities. One would wish HERA a longer lifetime than is currently foreseen for its physics is fundamental and complementary to the LHC.

Acknowledgment It has been a good tradition that HERA physics is being presented at the HCP conference as are TeVatron results at DIS Workshops. I would like to thank the organisers for the invitation and the realisation of such a stimulating meeting.

References

1. For results of the H1 experiment at HERA see: <http://www.h1-desy.de>
2. For results of the ZEUS experiment at HERA see: <http://www.zeus-desy.de>
3. sometimes called Colour Glass Condensate, for a review see E. Iancu, A. Leonidov and L. McLerran, hep-ph/0202270.
4. L. Gribov, E. Levin and M. Ryskin Phys. Rep. **100**, (1983) 1.
5. J. Bartels, Eur. Phys. J. **C 43** (2005), 3.
6. see for example M. Glück, S. Kretzer and E. Reya, Astropart. Phys. **11** (1999), 327 [astro-ph/9809273].
7. E. Berger et al., Phys. Rev. **D71** (2005), 014007 [hep-ph/0406143]
8. M. Dittmar, F. Pauss and D. Zuercher, Phys. Rev. **D56** (1997), 7284 [hep-ex/9705004].
9. HERA and the LHC, "A workshop on the implications of HERA for LHC physics", <http://www.desy.de/heralhc>, A first round of meetings has been finished and Proceedings will appear in 2006. The workshop participants have agreed to meet annually to discuss the progress and exchange information between the HERA and the LHC communities.
10. S. Forte, private communication.
11. M. Strikhman, private communication.
12. T. Alexopoulos *et al.*, eD Scattering with H1, A Letter of Intent, DESY 03-194; H. Abramowicz *et al.*, A New Experiment for HERA, MPI-2003-62; F. Willeke and G. Hoffstaetter, Talks at the Workshop on the Future of DIS, Durham 2001, unpublished; <http://hep.ph.liv.ac.uk/~green/HERA3/>.
13. G. Corcella and S. Moretti, Phys. Lett. B **590** (2004), 249 [hep-ph/0402146] and in [9].
14. M. Cooper Sarkar, in [9].
15. V. Lenderman, Summary Talk March 2005, in [9].
16. G. Watt, A. Martin and M. Ryskin, Eur. Phys. J. **C 31** (2003), 73 [hep-ph/0306169]; J. Collins and X. Zu, JHEP **03** (2005), 059 [hep-ph/0411332].
17. M. Diehl, Summary Talk March 2005, in [9].
18. F. Olness *et al.*, Eur. Phys. J. **C 40** (2005), 145 [hep-ph/0312323].
19. L. Loennblad, Summary Talk March 2005, in [9].
20. For results of the HERMES experiment at HERA see: <http://www.hermes-desy.de>
21. S. Forte, Summary Talk March 2005, in [9].
22. R. Thorne, in [9].
23. L. Magnea, in [9].
24. B.C. Allanach *et al.*, Nucl. Phys. Proc. Suppl. **135** (2004) 107 [hep-ph/0407067].
25. H1 Collaboration, A. Aktas et al., Phys. Lett. **B** in print [hep-ex/0507080].
26. A. Glazov, Summary Talk March 2005, in [9].
27. M. Kuze and Y. Sirois, Prog. Part. Nucl. Phys. **50** (2003), 1 [Erratum-ibid. **53** (2004), 583] [hep-ex/0211048].

Diffraction and Total Cross-Section at the Tevatron and the LHC

M. Deile¹, G. Anelli¹, A. Aurola², V. Avati¹, V. Berardi³, U.Bottigli⁴, M. Bozzo⁵, E. Brücken², A. Buzzo⁵, M. Calicchio³, F. Capurro⁵, M.G. Catanesi³, M.A.Ciocci⁴, S. Cuneo⁵, C. Da Vià⁶, E. Dimovasili¹, K. Eggert¹, M. Eräluoto², F. Ferro⁵, A. Giachero⁵, J.P. Guillaud⁷, J. Hasi⁶, F. Haug¹, J. Heino², T. Hilden², P. Jarron¹, J. Kalliopuska², J. Kaspar⁸, J. Kempa⁹, C. Kenney¹⁰, A. Kok⁶, V. Kundrat⁸, K. Kurvinen², S. Lami⁴, J. Lämsä², G. Latino⁴, R. Lauhakangas², J. Lippmaa², M. Lokajicek⁸, M. LoVetere⁵, D. Macina¹, M. Macri⁵, M. Meucci⁴, S. Minutoli⁵, A. Morelli⁵, P. Musico⁵, M. Negri⁵, H. Niewiadomski¹, E. Noschis¹, J. Ojala², F. Oljemark², R. Orava², M. Oriunno¹, K. Österberg², R.Paoletti⁴, S. Parker¹¹, A.-L. Perrot¹, E. Radermacher¹, E. Radicioni³, E. Robutti⁵, L. Ropelewski¹, G. Ruggiero¹, H. Saarikko², G.Sanguinetti⁴, A. Santroni⁵, S. Saramad¹, F. Sauli¹, A.Scribano⁴, G. Sette⁵, J. Smotlacha⁸, W. Snoeys¹, C. Taylor¹², A. Toppinen², N.Turini⁴, N. Van Remortel², L. Verardo⁵, A. Verdier¹, S. Watts⁶, and J. Whitmore¹³

¹ CERN, Genève, Switzerland

² Helsinki Institute of Physics and University of Helsinki, Finland

³ INFN Sezione di Bari and Politecnico di Bari, Bari, Italy

⁴ Università di Siena and Sezione INFN-Pisa, Italy

⁵ Università di Genova and Sezione INFN, Genova, Italy

⁶ Brunel University, Uxbridge, UK

⁷ LAPP Annecy, France

⁸ Academy of Sciences of the Czech Republic and Institute of Physics, Praha, Czech Republic

⁹ Warsaw University of Technology, Plock, Poland

¹⁰ Molecular Biology Consortium, SLAC, USA

¹¹ University of Hawaii, USA

¹² Case Western Reserve University, Dept. of Physics, Cleveland, OH, USA

¹³ Penn State University, Dept. of Physics, University Park, PA, USA

Abstract. At the Tevatron, the total $p\bar{p}$ cross-section has been measured by CDF at 546 GeV and 1.8 TeV, and by E710/E811 at 1.8 TeV. The two results at 1.8 TeV disagree by 2.6 standard deviations, introducing big uncertainties into extrapolations to higher energies. At the LHC, the TOTEM collaboration is preparing to resolve the ambiguity by measuring the total pp cross-section with a precision of about 1%. Like at the Tevatron experiments, the luminosity-independent method based on the Optical Theorem will be used. The Tevatron experiments have also performed a vast range of studies about soft and hard diffractive events, partly with antiproton tagging by Roman Pots, partly with rapidity gap tagging. At the LHC, the combined CMS/TOTEM experiments will carry out their diffractive programme with an unprecedented rapidity coverage and Roman Pot spectrometers on both sides of the interaction point. The physics menu comprises detailed studies of soft diffractive differential cross-sections, diffractive structure functions, rapidity gap survival and exclusive central production by Double Pomeron Exchange.

1 Introduction

Elastic and diffractive scattering (see Fig. 1, left) represent a significant fraction (44% at both $\sqrt{s} = 1.8$ TeV and 14 TeV) of the total pp or $p\bar{p}$ cross-section. Many details of these processes with close ties to proton structure and low-energy QCD are still not understood. The main signature – large gaps in the scattering products’ rapidity distribution due to exchange of colour singlets between the interacting protons – leads to the requirement of a good rapidity coverage up to the very forward region. This is also needed for the detection of high- p_T particles and jets from hard diffractive events – i.e. those with hard par-

tonic subprocesses – which convey information about the partonic structure of the colour singlet (a.k.a. “Pomeron”) exchanged. A big fraction of diffractive events exhibits surviving (“leading”) protons at very small scattering angles which can be detected in Roman Pot detectors far away from the interaction point.

Another purpose of high-coverage detector systems is the luminosity-independent determination of the total cross-section based on the Optical Theorem which requires the measurement of the total elastic and inelastic rates and the extrapolation of the nuclear elastic scattering cross-

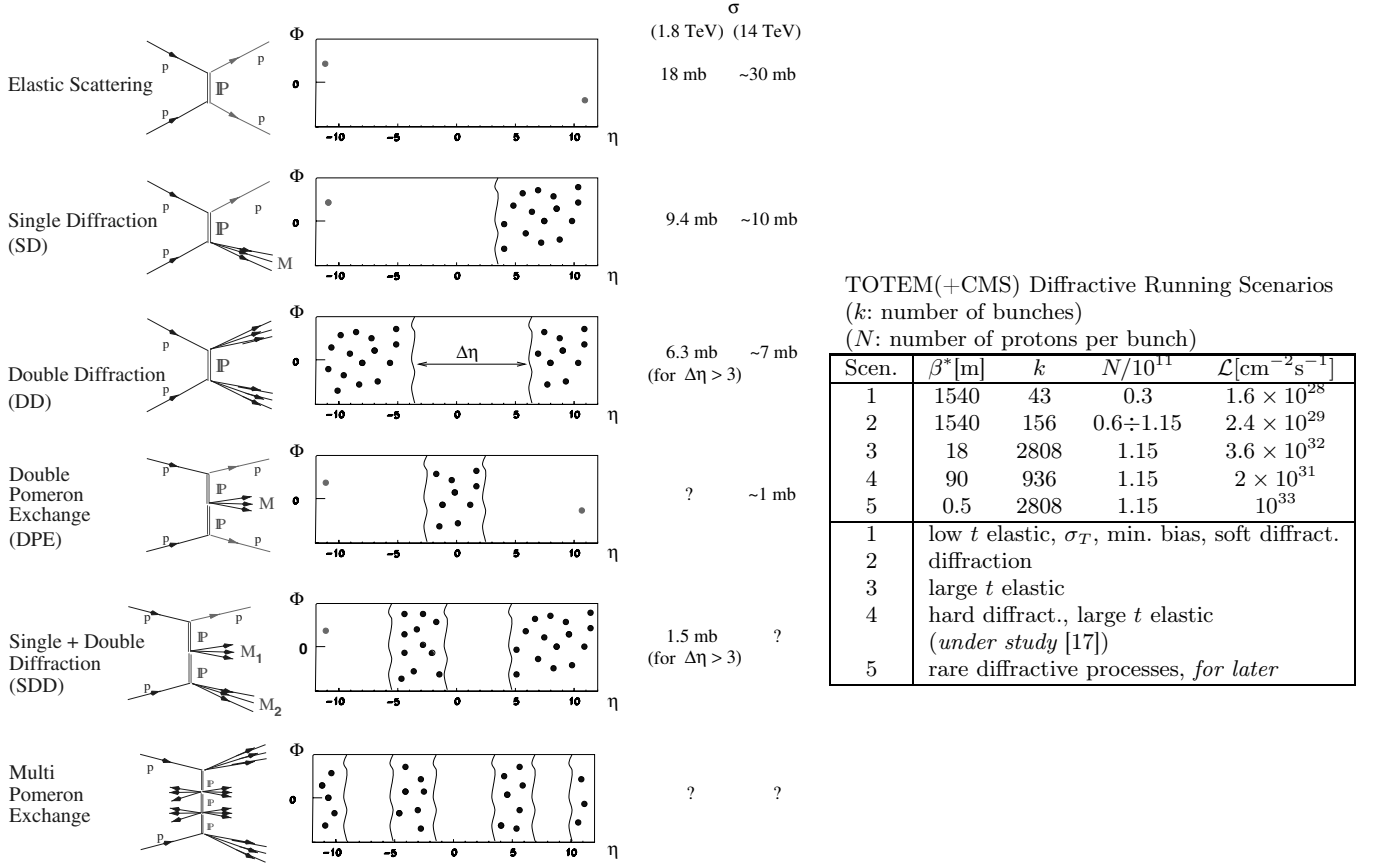


Fig. 1. Left: diffractive process classes and their cross-sections at Tevatron and LHC. Right: running scenarios for diffractive physics at LHC; for more details see [8].

section $d\sigma/dt$ to zero momentum transfer, $t = 0$, as explained in Section 3.

The Tevatron experiments CDF [2], E710 [3] and its very similar successor E811 [4] had Roman Pots on both sides of the interaction points for detecting elastically scattered protons. For diffractive physics, only the antiproton side had enough dispersion for measuring leading particle momenta with Roman Pot spectrometers. The rapidity coverage for measuring the inelastic rate ranged from 5.2 to 6.5 at E710/811 and from 3.2 to 6.7 at CDF. For tagging diffractive events by their rapidity gaps, additional central detectors were available extending the coverage to $\pm(3.8 \div 6.5)$ for E710 and $0 \div \pm 5.9$ (7.5) for CDF in Run I (Run II).

At DØ, a double-arm Roman Pot spectrometer (FPD) was installed for Run II [5], allowing to measure elastic and diffractive processes with (anti-) proton acceptance on both sides of the interaction point. In Run I, rapidity gap tagging was possible for $|\eta| < 5.9$.

The TOTEM experiment [1] at the LHC will have Roman Pot stations at 147 m and at 220 m from the interaction point, on both sides. The inelastic event rate will be measured in a rapidity interval from 3.1 to 6.5. For diffractive physics, TOTEM will collaborate with CMS, resulting in a rapidity coverage from 0 to ± 6.5 .

2 Elastic pp and p \bar{p} Scattering

The elastic scattering cross-section $d\sigma/dt$ is characterised by several t -regions with different behaviour (see Fig. 2):

- The Coulomb region where elastic scattering is dominated by photon exchange; this region lies at $|t| < 1.2 \times 10^{-3} \text{ GeV}^2$ for $\sqrt{s}=546 \text{ GeV}$, $|t| < 0.9 \times 10^{-3} \text{ GeV}^2$ for $\sqrt{s}=1.8 \text{ TeV}$, and $|t| < 6.5 \times 10^{-4} \text{ GeV}^2$ for $\sqrt{s}=14 \text{ TeV}$.
- The nuclear/Coulomb interference region, where the cross-section is given by

$$\frac{d\sigma_{el}}{dt} = \pi |f_C e^{-i\alpha\phi(t)} + f_N|^2 = \pi \left| -\frac{2\alpha G^2(t)}{|t|} e^{-i\alpha\phi(t)} + \frac{\sigma_{tot}}{4\pi} |i + \rho| e^{-B|t|/2} \right|^2. \quad (1)$$

Here, $G(t)$ is the electromagnetic form factor of the proton, ρ the ratio between real and imaginary part of the forward nuclear elastic amplitude,

$$\rho = \frac{\mathcal{R}[f_{el}(0)]}{\mathcal{I}[f_{el}(0)]}, \quad (2)$$

and ϕ is the relative phase between the nuclear and Coulomb amplitudes. E710 and E811 [3,4] have measured ρ and B in this region (see Table 1), using the

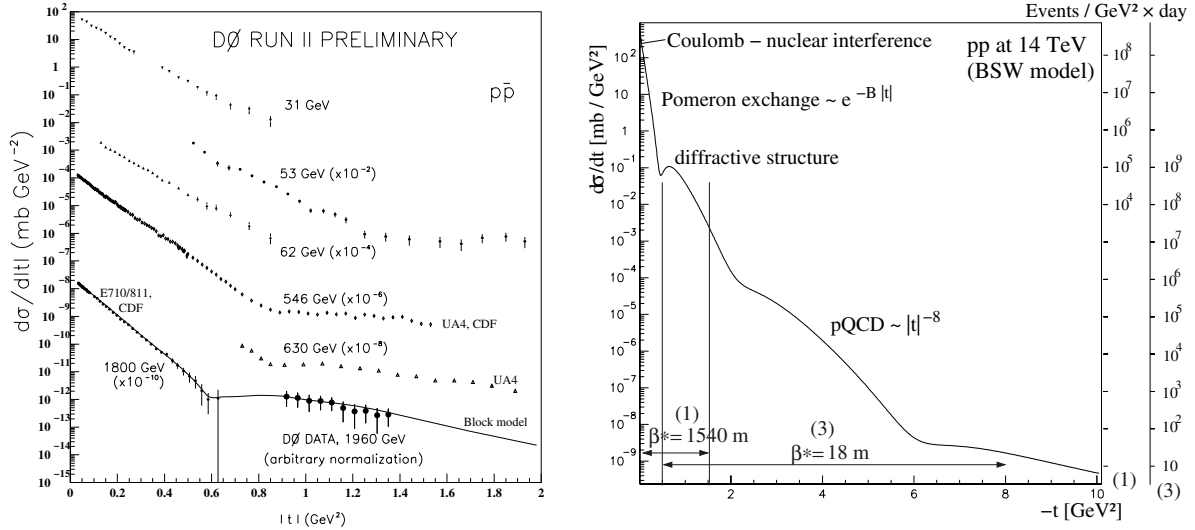


Fig. 2. Left: elastic $p\bar{p}$ scattering from ISR to Tevatron (taken from [7]); right: prediction for elastic pp scattering at LHC; the one-day statistics on the right-hand scales correspond to the running scenarios 1 and 3 (defined in Fig. 1).

West-Yennie parameterisation for $\phi(t)$ [6]. The interest of ρ lies in its predictive power for σ_{tot} at higher energies via the dispersion relation

$$\rho(s) = \frac{\pi}{2\sigma_{tot}(s)} \frac{d\sigma_{tot}}{d \ln s} \quad (3)$$

- The “single-Pomeron exchange” region with a cross-section $d\sigma/dt \propto e^{-B|t|}$. The parameter B was measured by several Tevatron experiments (Table 1).
- A region with diffractive minima which move to lower $|t|$ as the energy increases (Fig. 2, left).
- The triple-gluon exchange region at high $|t|$ described by perturbative QCD and showing a cross-section proportional to $|t|^{-8}$.

Table 1. Elastic scattering at the Tevatron [2–4, 7]

\sqrt{s}	Exp.	t -range [GeV ²]	B [GeV ⁻²], ρ
546 GeV	CDF	0.025 \div 0.08	$B = 15.28 \pm 0.58$
1.8 TeV	CDF	0.04 \div 0.29	$B = 16.98 \pm 0.25$
		0.034 \div 0.65	$B = 16.3 \pm 0.3$
	E710	0.001 \div 0.14	$B = 16.99 \pm 0.25$ $\rho = 0.140 \pm 0.069$
	E811	0.002 \div 0.035	using $\langle B \rangle_{CDF, E710}$ $\rho = 0.132 \pm 0.056$
1.96 TeV	DØ	0.9 \div 1.35	–

The TOTEM experiment at LHC will cover the $|t|$ -range from $2 \times 10^{-3} \text{ GeV}^2$ to 8 GeV^2 (Fig. 2, right) with two running scenarios with special beam optics and different luminosities (scenarios 1 and 3 (or 4) in Fig. 1, right). For details of the t -acceptances of the scenarios see Ref. [8]. The minimum $|t|$ -value corresponds to a distance of $1.3 \text{ mm} = 10 \sigma_{beam} + 0.5 \text{ mm}$ between the Roman Pot at 220 m and the beam centre. Reaching the Coulomb-nuclear interference region to measure ρ will be attempted

either by approaching the beam closer with the Roman Pot or by operating the LHC at $\sqrt{s} \leq 6 \text{ TeV}$ (see Fig. 4 in [8]).

3 Total pp and $p\bar{p}$ Cross-Section

The total pp or $p\bar{p}$ cross-section is related to nuclear elastic forward scattering via the Optical Theorem which can be expressed as

$$\mathcal{L}\sigma_{tot}^2 = \frac{16\pi}{1 + \rho^2} \cdot \frac{dN_{el}}{dt} \Big|_{t=0}. \quad (4)$$

With the additional relation

$$\mathcal{L}\sigma_{tot} = N_{el} + N_{inel} \quad (5)$$

one obtains a system of 2 equations which can be resolved for σ_{tot} or \mathcal{L} independently of each other:

$$\sigma_{tot} = \frac{16\pi}{1 + \rho^2} \cdot \frac{dN_{el}/dt|_{t=0}}{N_{el} + N_{inel}}, \quad (6)$$

$$\mathcal{L} = \frac{1 + \rho^2}{16\pi} \cdot \frac{(N_{el} + N_{inel})^2}{dN_{el}/dt|_{t=0}} \quad (7)$$

Hence the quantities to be measured are:

- the nuclear part of the elastic cross-section extrapolated to $t = 0$;
- the total elastic and inelastic rate, the latter consisting of diffractive (18 mb at LHC) and minimum bias (65 mb at LHC) events.

The ρ parameter has to be taken from external knowledge unless it can be measured from elastic scattering in the interference region between nuclear and Coulomb scattering. CDF have measured σ_{tot} at 546 GeV and 1.8 TeV

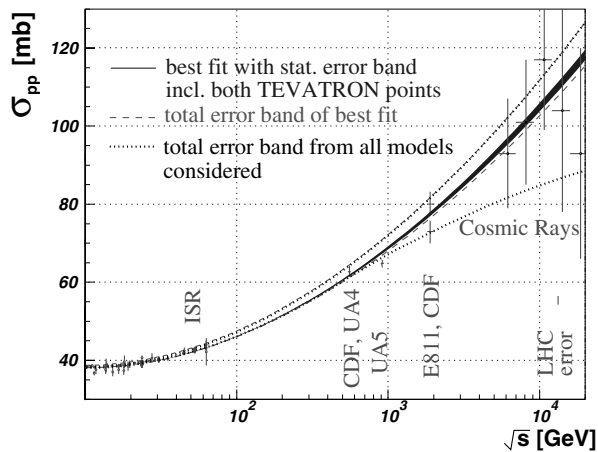


Fig. 3. COMPETE fits [10] to all available pp and $p\bar{p}$ scattering data with statistical (blue solid) and total (green dashed) error bands, the latter taking into account the Tevatron ambiguity. The outermost curves (dotted) give the total error band from all parameterisations considered.

using Eqn. 6 with $\rho = 0.15$ [2] (see Table 2). Their measurement at 546 GeV agrees with the value from UA4 [9]. E710 and E811 have determined ρ and σ_{tot} simultaneously at 1.8 TeV [3, 4] by combining Eqns. (4) and (5) with (1). Their result for σ_{tot} differs from CDF’s number by 2.6 standard deviations. The origin of the discrepancy is unknown.

Table 2. Measurements of the total pp or $p\bar{p}$ cross-section for $\sqrt{s} \geq 546$ GeV and expectations for the LHC.

\sqrt{s}	Experiment	σ_{tot} [mb]
546 GeV	UA4	61.9 ± 1.5
	CDF	61.26 ± 0.93
1.8 TeV	CDF	80.03 ± 2.24
	E710	72.8 ± 3.1
	E811	71.42 ± 2.41
14 TeV	(extrapolation [10] to LHC)	$111.5 \pm 1.2^{+4.1}_{-2.1}$
	TOTEM	$? \pm 1$

TOTEM will follow the same method as CDF. The total expected uncertainty of 1% after 1 day of taking data at $\mathcal{L} = 1.6 \times 10^{28} \text{ cm}^{-2} \text{ s}^{-1}$ will have the following contributions (combined in quadrature):

- The statistical errors of $N_{el} + N_{inel}$ and $dN_{el}/dt|_{t=0}$ are negligible: 0.01% and 0.07% respectively.
- The systematic error of the total rate stems primarily from trigger losses and amounts to 0.8%.
- The systematic error of the extrapolation of the elastic cross-section to $t = 0$ is dominated by the theoretical uncertainty of the functional form (0.5%). The next-to-leading contributions come from beam energy, alignment and crossing-angle uncertainties (each typically 0.1%).
- If ρ cannot be measured, the uncertainty in its prediction (e.g. $\rho = 0.1361 \pm 0.0015^{+0.0058}_{-0.0025}$ [10]) will contribute another 0.2%.

The ATLAS collaboration proposes [11] to extract the four parameters σ_{tot} , ρ , B and \mathcal{L} from a fit to (1) and using $dN/dt = \mathcal{L}d\sigma/dt$. The main difficulties of this approach lie in reaching low enough t -values ($-t < 6 \times 10^{-4} \text{ GeV}^2$) and in the uncertainty of the phase ϕ .

4 Diffraction

At Tevatron, a vast number of studies on soft and hard diffraction has been carried out (see Table 3 for a brief overview).

Table 3. The diffractive programmes of the Tevatron experiments, the methods for tagging diffractive events, and the coverage in kinematic variables (t is given in units of GeV^2) The abbreviations for the diffractive event classes are defined in Fig. 1 (left).

Exp., Run	Tagging	Coverage	Physics
E710 [3]	rap. gap	$3.8 < \eta < 6.5$	} soft SD
	leading \bar{p}	$0.05 < -t < 0.11$ $\xi < 0.01$	
CDF I,0 [2]	rap. gap	$ \eta < 6.7$	} soft SD
	leading \bar{p}	$-t < 0.4$ $\xi < 0.2$	
CDF IA,B [12]	rap. gap no RP	$ \eta < 5.9$	soft SD, DD, DPE, SDD
CDF IC [13]	rap. gap	$ \eta < 5.9$	} hard diffract.: dijets, W, $b\bar{b}$, J/Ψ
	leading \bar{p}	$-t < 1$ $0.03 < \xi < 0.1$	
CDF II [14]	rap. gap	$ \eta < 7.5$	} diffr. struct. funct., search for excl. DPE
	leading \bar{p}	$-t < 2$ $0.02 < \xi < 0.1$	
DØ I [15]	rap. gap no RP	$ \eta < 5.9$	} hard diffr.: dijets, W, Z
DØ II [7]	rap. gap	$ \eta < 5.9$	} all above with p, \bar{p} tagging
	lead. p, \bar{p}	$0.8 < -t < 2$ any ξ	

In Run I, diffractive events were tagged by their rapidity gaps and – in some cases – by a leading antiproton. Leading diffractive protons were not detected. For the ongoing Run II on the other hand, DØ has installed a double-arm proton- and antiproton spectrometer.

At TOTEM/CMS, for all diffractive processes (except DD) leading proton tagging is foreseen with the possibility of using rapidity gaps for redundancy. With scenarios 1 and 2, used for soft and semi-hard diffraction, protons of all ξ will be detected; the total acceptance integrated over t and ξ is 95%; the resolution in ξ is about 5×10^{-3} . Hard diffraction with its much smaller cross-sections (e.g. $1 \mu\text{b}$ for SD dijets at $\sqrt{s} = 14 \text{ TeV}$) will be studied with scenario 4 where the total proton acceptance is about 65%, and the ξ resolution is about 4×10^{-4} .

4.1 Soft Diffraction

At Tevatron, the total and differential soft diffractive cross-sections have been measured for the processes of SD

(E710, CDF), DD and SDD (CDF), see Fig. 1. A central result of these cross-section studies is that the t and ξ dependences of the differential cross-sections conform to the predictions of Regge Theory, but that the total normalisations measured are suppressed, as also observed in hard diffraction (see below). With increasing \sqrt{s} this suppression becomes more pronounced. The behaviour of the diffractive cross-sections at energies above 1.8 TeV is controversial between different models predicting it either to increase further or to remain constant [16]. From the ratios between σ_{diff} , σ_{elast} and σ_{tot} , information about opacity and size of the proton can be deduced.

In DPE, CDF's one-armed antiproton spectrometer tagged the slightly wider "inclusive" event class $\bar{p}p \rightarrow \bar{p} + X + Y$ where the proton is allowed to dissociate into a low-mass system Y with $m_Y^2 \leq 8 \text{ GeV}^2$. In the central diffractive system, masses up to a few 10^2 GeV were seen. At LHC, diffractive masses up to about 1.4 TeV will be observable with sufficient statistics. Surviving protons will be detected on both sides of the IP.

4.2 Hard Diffraction

A central result in diffraction at Tevatron is the breaking of QCD factorisation, i.e. of the hypothesis that the cross-sections of hard diffractive processes can be written as a convolution

$$\sigma = \int d\beta dQ^2 d\xi dt \hat{\sigma}(\beta, Q^2, \xi, t) F_2^D(\beta, Q^2, \xi, t) \quad (8)$$

of a parton-level cross-section $\hat{\sigma}$ and a process-independent diffractive structure function F_2^D . Comparing F_2^D from dijet production in diffractive deep inelastic scattering (DDIS) at HERA with the result from single diffractive dijet production at Tevatron yields a suppression of the latter by roughly a factor 10 (Fig. 4).

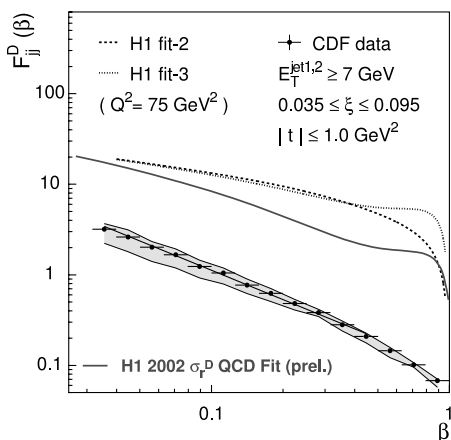


Fig. 4. Diffractive structure function for dijet production in DDIS at H1 and in SD at CDF. The mean $(E_T^{jet})^2$ at CDF corresponds approximately to Q^2 at H1.

This suppression of the diffractive cross-section is independent of the hard subprocess, as can be seen by

comparing for different partonic subprocesses the fractions of events showing rapidity gaps (Table 4). They are all of the order 1%. The variations are due to different sensitivities to the gluon and quark components of the Pomeron and led to the determination of the gluon fraction $f_g = 0.59 \pm 0.14 \pm 0.06$ in agreement with HERA's $f_g = 0.75 \pm 0.15$.

Table 4. Ratio R between the diffractive subsample (with rapidity gap) and all events for a given hard subprocess (j = jet, G = gap). $\sqrt{s} = 1.8 \text{ TeV}$.

Process	Cuts	R [%]	Exp.
SD: j + j + G	$E_T > 20 \text{ GeV},$ $\eta_j > 1.8$	0.75 ± 0.10	CDF
	$E_T > 12 \text{ GeV},$ $ \eta_j > 1.6$	0.65 ± 0.04	DØ
DD: j + G + j	$E_T > 20 \text{ GeV},$ $ \eta_j > 1.8$	1.13 ± 0.16	CDF
	$E_T > 30 \text{ GeV},$ $ \eta_j > 1.6, \Delta\eta_j > 4$	0.94 ± 0.13	DØ
SD: W + G $\rightarrow e\nu + G$	$\cancel{E}_T, E_{Te} > 20 \text{ GeV}$	1.15 ± 0.55	CDF
	$\cancel{E}_T, E_{Te} > 25 \text{ GeV}$	$0.89^{+0.20}_{-0.19}$	DØ
SD: Z + G $\rightarrow ee + G$	$E_{Te} > 25 \text{ GeV}$	$1.44^{+0.62}_{-0.54}$	DØ
	$p_{Te} > 9.5 \text{ GeV},$ $\rightarrow eX + G$ $ \eta_e < 1.1$	0.62 ± 0.25	CDF
SD: J/ψ + G $\rightarrow \mu^+ \mu^- + G$	$p_{T\mu} > 2 \text{ GeV},$ $ \eta_\mu < 0.6$	1.45 ± 0.25	CDF

A possible explanation lies in the different initial states in DDIS and in proton-antiproton diffraction. In the latter case, additional soft scattering between the two initial hadrons can fill the rapidity gap and thus destroy the signature used for identifying diffractive events. Hence the cross-section in Eqn. (8) needs the "gap survival probability" $|S|^2$ as another convolution factor. $|S|^2$ was observed by CDF to decrease by a factor 1.3÷2.4 from 630 GeV to 1.8 TeV and is expected to be further reduced at LHC energies. The measurement of gap probabilities at the LHC will be an important input for the study of exclusive production processes discussed in the next section.

At LHC, additional hard phenomena offering insight into proton structure are being explored, like exclusive SD into three jets, $pp \rightarrow p + jjj$, which would indicate a *minimal Fock space* parton configuration $|qqq\rangle$ in the proton [18]. For a jet threshold of 10 GeV, a cross-section between 0.04 and 0.4 nb is predicted, yielding 80 to 800 events per day at $\mathcal{L} = 2 \times 10^{31} \text{ cm}^{-2}\text{s}^{-1}$ (scenario 4).

4.3 Exclusive Production by DPE

A particularly interesting subclass of DPE events is exclusive central production, characterised by only one single particle or a dijet in the diffractive system. The vacuum quantum numbers of the two colliding colour singlets lead to selection rules on spin J , parity P and charge conjugation C [19]:

$$J^P = 0^+, 2^+, 4^+; J_z = 0; C = +1 \quad (9)$$

(in the limit of $t = 0$). The $J_z = 0$ rule strongly suppresses $g\bar{g} \rightarrow q\bar{q}$ background because of helicity conservation (this background would totally vanish for massless quarks). The rules can also be used for determining the quantum numbers of a new state observed. Table 5 lists some examples for exclusive production. For exclusive dijet and χ_{c0} production, CDF has seen event candidates and set upper limits on the cross-section. At LHC, these processes should be well within reach using scenario 4. The observability of the χ_{b0} is doubtful because the branching ratio for its muonic decay is unknown (upper limit: 10^{-3}).

Table 5. Examples of exclusive DPE processes ($p + p \rightarrow p + X + p$). For cross-sections see e.g. [20]. The numbers in square brackets are experimental upper limits from CDF, Run II [14].

Diffraction system	Decay channel	$\sigma(Tev.) \times BR$	$\sigma(LHC) \times BR$
dijet ($E_T > 10$ GeV)	jj	0.97 nb [≤ 1.1 nb]	7 nb
χ_{c0} (3.4 GeV)	$\gamma J/\psi \rightarrow \gamma \mu^+ \mu^-$	390 pb [≤ 204 pb] ¹	1.8 nb
	$\pi^+ \pi^- K^+ K^-$	12 nb	54 nb
χ_{b0} (9.9 GeV)	$\gamma Y \rightarrow \gamma \mu^+ \mu^-$	≤ 0.5 pb	≤ 4 pb

¹scaled from CDF's rapidity range ± 0.6 to ± 2.5 used by KMRS [20].

Table 6. Cross-sections for exclusive Higgs production in the SM and the MSSM (examples) [21]. A mass resolution $\sigma(M) = 3$ GeV from the Roman Pot spectrometer is assumed.

SM, $m_H = 120$ GeV		
$\sigma \times BR(H \rightarrow b\bar{b})$	2 fb (S/B @ $30 \text{ fb}^{-1} = 11/10$)	
$\sigma \times BR(H \rightarrow WW^*)$	0.4 fb (S/B @ $30 \text{ fb}^{-1} = 8/3$)	
MSSM, $m_A = 130$ GeV		
	$\tan \beta = 30$	$\tan \beta = 50$
	$m_h = 122.7$ GeV	$m_h = 124.4$ GeV
	$m_H = 134.2$ GeV	$m_H = 133.5$ GeV
$\sigma \times BR(A \rightarrow b\bar{b})$	0.07 fb	0.2 fb
$\sigma \times BR(h \rightarrow b\bar{b})$	5.6 fb	13 fb
$\sigma \times BR(H \rightarrow b\bar{b})$	8.7 fb	23 fb
MSSM, $m_A = 100$ GeV		
	$\tan \beta = 30$	$\tan \beta = 50$
	$m_h = 98$ GeV	$m_h = 99$ GeV
	$m_H = 133$ GeV	$m_H = 131$ GeV
$\sigma \times BR(A \rightarrow b\bar{b})$	0.4 fb	1.1 fb
$\sigma \times BR(h \rightarrow b\bar{b})$	70 fb	200 fb
$\sigma \times BR(H \rightarrow b\bar{b})$	8 fb	15 fb

At a later stage it might even be possible for TOTEM + CMS to observe exclusive production of the Higgs boson. However, the low cross-section requires running at $\mathcal{L} \sim 10^{33} \text{ cm}^{-2} \text{ s}^{-1}$, i.e. with scenario 5 whose optics are such that additional Roman Pots in the cryogenic LHC region at 420 m from the IP would be needed for sufficient leading proton acceptance. Still, the diffractive production rate of a Standard Model Higgs is very low, as is the signal-to-background ratio for the dominant decay channel $H \rightarrow b\bar{b}$ (see Table 6, top block). More favourable is the MSSM case, particularly for large $\tan \beta$ and low m_A (Table 6, middle and bottom blocks). Due to the selection rules (9), exclusive production of the CP-odd A is suppressed, giving the opportunity to separate it from the CP-even h and H, which is difficult for conventional inclusive production,

particularly in the region of $m_A \approx 130$ GeV where all three neutral Higgs bosons have very similar masses.

References

1. TOTEM: Technical Design Report, CERN-LHCC-2004-002; addendum CERN-LHCC-2004-020.
2. CDF Collaboration (F. Abe et al.), Phys. Rev. **D 50**, (1994) 5518; Phys. Rev. **D 50**, (1994) 5535; Phys. Rev. **D 50**, (1994) 5550;
3. E710 Collaboration (N.A. Amos et al.), PRL **61**, (1988) 525; PRL **63**, (1989) 2784; Phys. Lett. **B 243**, (1990) 158; Phys. Lett. **B 247**, (1990) 127; PRL **68**, (1992) 2433; Phys. Lett. **B 301**, (1993) 313.
4. E811 Collaboration (C. Avila et al.), Phys. Lett. **B 445**, (1999) 419; Phys. Lett. **B 537**, (2002) 41.
5. D0 Collaboration (A. Brandt et al.), A Forward Proton Detector at D0, FERMILAB-PUB-97-377, 1997.
6. G.B. West and D.R. Yennie, Phys. Rev. **172**, (1968) 1413.
7. T. Edwards et al., Elastic and Diffractive Scattering at D0, Proc. of the XII International Workshop on Deep Inelastic Scattering, IEP SAS Košice 2004, pp. 466-471.
8. M. Deile et al., The First Year at LHC: Diffractive Physics; hep-ex/0503042; submitted to Czech.J.Phys.
9. UA4 Collaboration (M. Bozzo et al.), Phys. Lett. **147B** (1984) 392.
10. J.R. Cudell et al.; Benchmarks for the Forward Observables at RHIC, the Tevatron-Run II, and the LHC; PRL **89**, (2002) 201801.
11. ATLAS Forward Detectors for Luminosity Measurement and Monitoring, Letter of Intent, CERN/LHCC/2004-010.
12. CDF Collaboration (F. Abe et al.), PRL **74**, (1995) 855; PRL **78**, (1997) 2698; PRL **79**, (1997) 2636; PRL **80**, (1998) 1156; PRL **81**, (1998) 5278; (T. Affolder et al.), PRL **84**, (2000) 232; PRL **87**, (2001) 241802;
13. CDF Collaboration (T. Affolder et al.), PRL **84**, (2000) 5043; PRL **85**, (2000) 4215; PRL **87**, (2001) 141802; PRL **88**, (2002) 151802; PRL **91**, (2003) 011802; PRL **93**, (2004) 141601.
14. For Run II see e.g. K. Terashi on behalf of the CDF Collaboration, Diffractive Measurements at CDF, Proc. of the XII International Workshop on Deep Inelastic Scattering, IEP SAS Košice 2004, pp. 546-553.
15. D0 Collaboration (S. Abachi et al.), PRL **72**, (1994) 2332; PRL **76**, (1996) 734; Phys. Lett. **B 440**, (1998) 189; Phys. Lett. **B 531**, (2002) 52; Phys. Lett. **B 574**, (2003) 169;
16. K. Goulianos, Phys. Lett. **B 358**, (1995) 379; S. Sapeta and K. Golec-Biernat, Phys. Lett. **B 613**, (2005) 154.
17. K. Eggert, proceedings from the XIth International Conference on Elastic and Diffractive Scattering, Blois 2005.
18. L. Frankfurt, M. Strikman, Surveys High Energ.Phys. **14** (1999) 9-27; A. Ageev et al. (FELIX Collaboration), J. Phys. G **28**, (2002) R117.
19. V.A. Khoze, A.D. Martin, M.G. Ryskin, Eur. Phys. J. C19 (2001) 477.
20. V.A. Khoze et al., Eur. Phys. J. **C23** (2002) 311.; Eur. Phys. J. C35 (2004) 211-220. V.A. Petrov, R.A. Ryutin, JHEP 0408 (2004) 013.
21. A.B. Kaidalov et al., Eur. Phys. J. **C33**, (2004) 261.

The Jet Energy Scale and Inclusive Jet Cross Section at DØ

Norm J. Buchanan^{1 a}

Florida State University

Abstract. The determination of the jet energy scale correction for the central calorimeter of the DØ experiment is presented. The correction ranges between 15% and 50% of the uncorrected jet transverse energy. The jet inclusive cross section has also been measured for the central region, out to a rapidity of 0.8. This cross section is consistent with theoretical calculations.

1 Introduction

The vast majority of events collected by the DØ detector at the Tevatron contain one or more jets coming from quarks or gluons scattering from the primary proton-antiproton collisions, or from initial or final state radiation. It is thus crucial that the properties of jets be carefully measured and understood.

Jets consist of a collimated collection of particles including, but not limited to, photons, pions, kaons, neutrons, protons and antiprotons. These particles will travel in a path that closely approximates that of the initial parton-level quark or gluon. Measured jets are described by the properties of the energy deposits the associated particles leave in the calorimeter. Once the measured jet has been reconstructed a conversion must be made to obtain the properties of the parton-level jet.

The jets described in this note are reconstructed using the DØ Run II cone algorithm [1], which is a seed-based algorithm. All towers above a given threshold energy become seeds and the energy weighted centroid is calculated for a cone of $R=0.7$, where $R=\sqrt{(\Delta\phi)^2+(\Delta y)^2}$, where ϕ is the azimuthal angle and y is the rapidity given by $y = \frac{1}{2} \ln \left(\frac{E+p_z}{E-p_z} \right)$. To prevent infrared divergence the midpoint between each of the resulting “pseudo-jets” is then used as a new seed and the same procedure repeated. Only jets with a transverse energy greater 8 GeV are kept.

2 The DØ Calorimeter

The DØ calorimeter is a liquid argon-based sampling calorimeter that resides in a central and two forward cryostats, which is illustrated in figure 1 (a description of the Run 2 upgraded DØ detector can be found in reference [2]). Depleted uranium is used as an absorber between the active layers. For $|\eta| < 3.2$, where the pseudorapidity η is given by $\eta = -\ln \left(\tan \left(\frac{\theta}{2} \right) \right)$, the calorimeter is divided

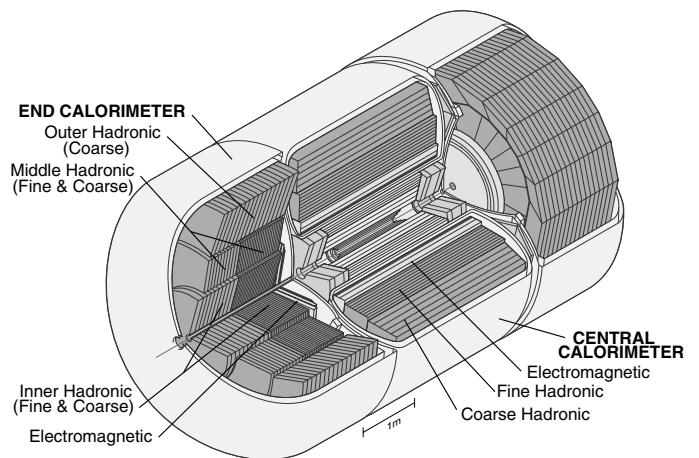


Fig. 1. DØ calorimeter with Run 2 upgrades.

into electromagnetic and hadronic components and is segmented into $\Delta\eta = 0.1$ and $\Delta\phi = 0.1$ with the exception of the 3rd layer of the electromagnetic calorimeter which is twice as fine in granularity to allow precise sampling of the electromagnetic shower maximum. Coverage is hermetic out to $|\eta| < 4.2$. The inter-cryostat region, covering $1.1 < |\eta| < 1.4$, contains a scintillator-based detector that is used to recover some lost resolution in the space between the central and forward calorimeters.

The calorimeter samples every 132 ns and stores the data in analog pipelines until a level 1 trigger decision has been made. A second set of analog pipelines stores the level 1 accepted signals for the level 2 latency time. Baseline subtraction is performed on signals between the two sets of analog storage.

3 Jet Energy Scale

The conversion from measured jet energy E_{jet}^{meas} to particle level jet energy E_{jet}^{ptcl} is performed using the

^a On behalf of the DØ Collaboration

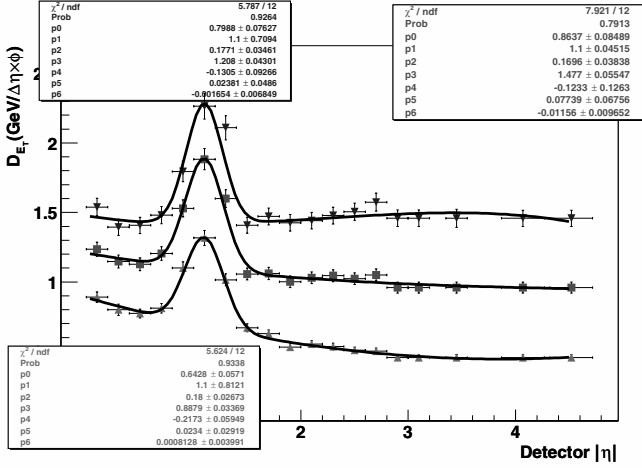


Fig. 2. Offset energy as a function of detector η for one, two, and three primary vertices. The error bars account for statistical, ϕ , and luminosity dependence uncertainties.

following correction:

$$E_{jet}^{ptcl} = \frac{E_{jet}^{meas} - E_0(\mathcal{R}\eta\mathcal{L})}{R_{jet}(\mathcal{R}\eta\mathcal{L})R_{cone}(\mathcal{R}\eta\mathcal{L})}$$

where $E_0(\mathcal{R}\eta\mathcal{L})$ is the offset energy, which includes multiple interactions, underlying event energy, electronic noise, uranium noise, and pile-up from previous bunch crossings, $R_{jet}(\mathcal{R}\eta\mathcal{L})$ is the calorimeter response to the hadronic jet, and $R_{cone}(\mathcal{R}\eta\mathcal{L})$ the the fraction of particle jet energy contained within the algorithm cone.

3.1 Offset Factor

Any energy that is not associated with the hard interaction must be accounted for. Contributions to this correction are electronics noise, pileup, uranium noise, the energy that can be attributed to the underlying event and additional minimum bias interactions. The uranium and electronics noise can be determined using zero bias events, which have the single requirement of a bunch crossing. Minimum bias events are those where the luminosity counters on each side of the detector are hit. These events are used with the information obtained using zero bias events to determine the contribution of the underlying event, and thus the offset energy distribution.

Figure 2 shows the offset energy density, summed over 0.1 η rings for one, two, and three primary vertices. The offset energy density has been parameterized by the number of primary vertices, which largely removes the dependence on instantaneous luminosity. The bump in the offset energy density data comes from large weighting factors used for the inter-cryostat detector and coarse hadronic layers.

3.2 Jet Response

The energy deposited in the calorimeter is not equal to the measured energy. This is due to the fact that the calorime-

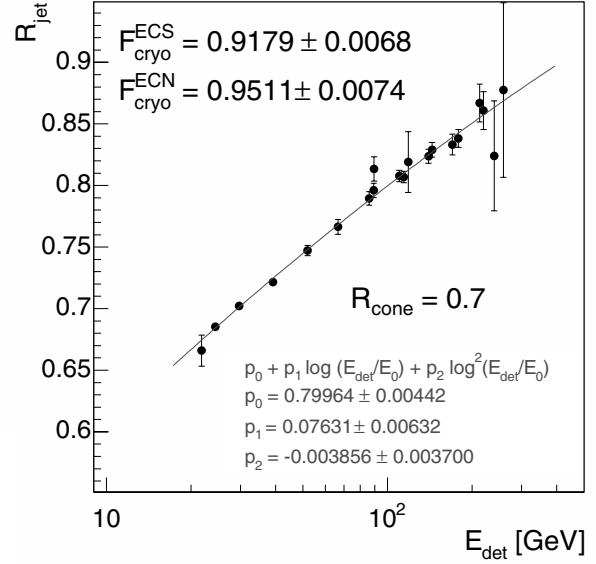


Fig. 3. The jet response plotted as a function of detector η for a cone size of 0.7.

ter is not completely compensating, there is dead material in front of, and within the calorimeter, there are response fluctuations between calorimeter modules, etcetera.

The balance of transverse energy in γ +jet events is used to obtain the response of the calorimeter to jets. For an ideal calorimeter the energy of the photon would exactly balance that of the recoiling jet. In reality, the following balance results:

$$R_{em}p_{T\gamma} + R_{had}p_{T_{had}} = -\cancel{E}_T.$$

where $R_{em}p_{T\gamma}$ is the electromagnetic response of the calorimeter and $R_{had}p_{T_{had}}$ is the hadronic response of the calorimeter. The Z mass is used to determine the electromagnetic calorimeter response and the hadronic response can then be obtained using back-to-back γ +jet events.

The jet response is plotted for a jet cone size of 0.7 in figure 3. The response values for the end-caps are scaled to account for the corresponding cryostat walls. The dominant error in the jet response comes from the differences in photon response for the forward and central calorimeters.

3.3 Out of Cone Showering

A correction must be made for particles that scatter into, or out of, the jet cone. Particles that have trajectories taking them outside of the algorithm cone, will only have a fraction of their energy accounted for and particles that travel into the cone, under the influence of a magnetic field for example, will artificially increase the measured jet energy. In addition to the instrumental effects of out of cone scattering, physics processes can also legitimately contribute. The physics out of cone processes are determined using Monte Carlo studies.

Table 1. Out of cone showering corrections for cone sizes of 0.5 and 0.7. The systematic error for the measurements is approximately 5%.

Detector	$R_{\text{cone}}=0.7$	$R_{\text{cone}}=0.5$
central	0.99	0.92
ICD	0.96	0.89
forward	0.94	0.85

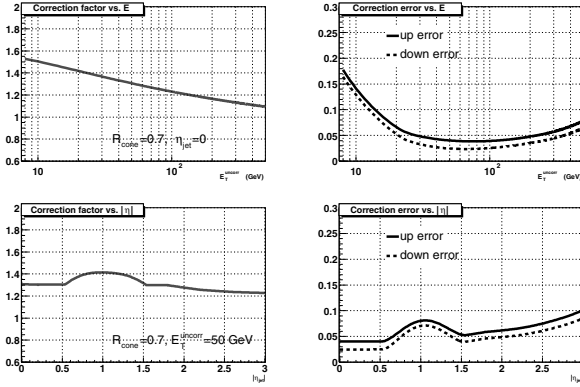


Fig. 4. Data JES correction factor (left) and its absolute error (right) as a function jet uncorrected energy (top) and pseudorapidity (bottom). Results are shown for $R=0.7$ cone jet in events with 1 reconstructed primary vertex. Jet physics and detector η are set to the same value. Up and down errors are shown separately.

The shower corrections are given in table 1 for cone sizes of 0.5 and 0.7. Dijet and γ +jet events are used to determine the shower correction factor. The energy density is measured outward from the cone center in a radial direction (in η - ϕ space). The offset energy density, by η -ring, was subtracted off of the energy densities used to calculate this correction. The final correction comes from the ratio to the energy density inside the algorithm cone to the total summed energy. The uncertainty in the corrections is approximately 5% and primarily attributed to statistics and model dependence.

3.4 Total Jet Energy Scale Correction

Combining the corrections for the offset energy, jet response, and out of cone showering gives the final jet energy scale correction factors plotted in figure 4. The correction values are plotted as a function of detector η and transverse, uncorrected, jet energy, a cone size is 0.7, and for events with only one primary vertex. The T42 algorithm [3] has been applied during jet reconstruction.

4 Inclusive Jet Cross Section

The inclusive jet cross section at high jet energies provides a good probe for examining perturbative QCD. Deviations

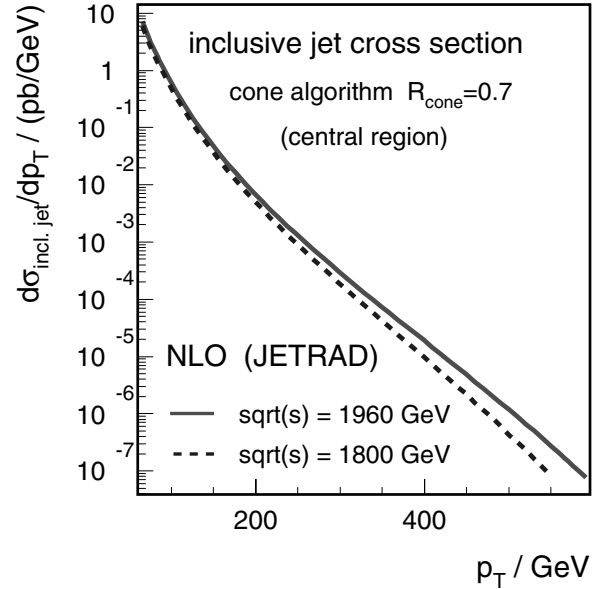


Fig. 5. Comparison of the next-to-leading order predictions for the jet inclusive cross-section for center-of-mass energies of 1.8 TeV and 1.96 TeV.

from the predicted cross section could signify physics beyond the Standard Model.

For Run 2 of the Fermilab Tevatron the center of mass energy was increased from 1.8 TeV to 1.96 TeV. The corresponding change in theoretical prediction for the next-to-leading order inclusive jet cross section is shown in figure 5. At 500 GeV the increase is predicted to be almost 300% larger.

The jet inclusive cross section, using 378 pb^{-1} of integrated luminosity, is presented for 2 rapidity regions ($|y| < 0.4$ and $0.4 < |y| < 0.8$). A combination of single jet triggers, based on energy deposition in the calorimeter, was used in the selection of the data used for this analysis. The data have been corrected for the jet energy scale, selection efficiencies, and migrations due to the transverse momentum resolution. The dominant error in the cross section measurement comes from the uncertainty in the jet energy scale. Theoretical next-to-leading order perturbative QCD predictions are made using the NLOJET++ code [3] and the CTEQ6.1M [5] and MRST2004 [6] parton distribution functions. Factorization and normalization scales are set equal to the jet transverse momentum and a factor of 2 for variation in the scale factors is folded into the theoretical uncertainty.

Figure 6 shows the preliminary measurement of the inclusive jet cross section with full experimental uncertainty. The results for the rapidity region $|y| < 0.4$ have been scaled by a factor of 10 to aid the viewer. The results agree well with the next-to-leading order predictions through 8 orders of magnitude.

The ratios of measured cross section values to next-to-leading order PDF predictions are shown in figure 7. The total experimental uncertainties are the overlaid shaded band and the dashed and dotted lines illustrate

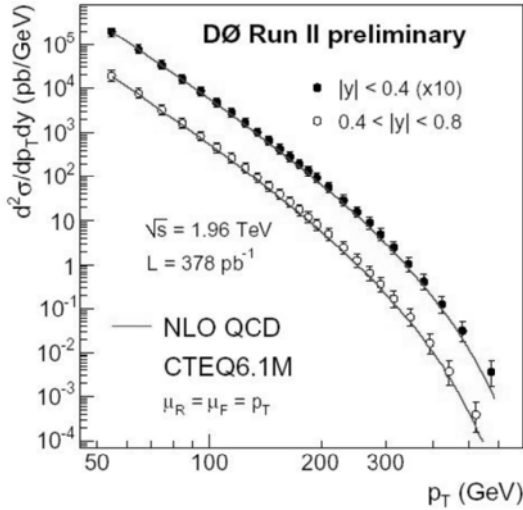


Fig. 6. Inclusive jet cross section measured for two rapidity regions ($|y| < 0.4$ and $0.4 < |y| < 0.8$) and an integrated luminosity of 378 pb^{-1} . The error bars correspond to the total experimental uncertainty.

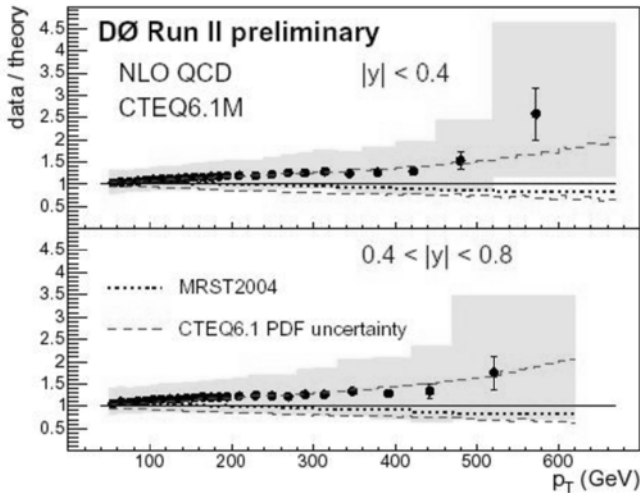


Fig. 7. The ratio of inclusive jet cross section measured in data to next-to-leading order PDF predictions in 2 rapidity regions. The shaded band corresponds to the total experimental uncertainty, while the dashed and dotted lines correspond to the uncertainties in the CTEQ6.1M and MRST2004 uncertainties, respectively.

the CTEQ6.1M and MRST2004 PDF uncertainties, respectively. The experimental uncertainties are too large to constrain the PDFs beyond their current precision.

5 Conclusion

The jet energy scale has been measured for the DØ experiment and varies in value between 1.5 at low jet transverse energies, to 1.1 at large transverse jet energies. The un-

certainty in the jet energy scale is largest, approximately 18% at low jet transverse energy to about 6% at 500 MeV uncorrected jet energy.

A preliminary measurement of the inclusive jet cross section for the central rapidity region $|y| < 0.8$ shows good agreement with CTEQ6.1M and MRST2004 PDF next-to-leading order predictions over 8 orders of magnitude, corresponding to jet transverse energies of 50 MeV to almost 600 MeV. The dominant error in the cross section measurement comes from the uncertainty in the jet energy scale and is too large to allow further constraints on the PDFs.

6 Acknowledgments

We thank the staffs at Fermilab and collaborating institutions, and acknowledge support from the DOE and NSF (USA); CEA and CNRS/IN2P3 (France); FASI, Rosatom and RFBR (Russia); CAPES, CNPq, FAPERJ, FAPESP and FUNDUNESP (Brazil); DAE and DST (India); Colciencias (Colombia); CONACyT (Mexico); KRF (Korea); CONICET and UBACyT (Argentina); FOM (The Netherlands); PPARC (United Kingdom); MSMT (Czech Republic); CRC Program, CFI, NSERC and WestGrid Project (Canada); BMBF and DFG (Germany); SFI (Ireland); Research Corporation, Alexander von Humboldt Foundation, and the Marie Curie Program.

References

1. G.C. Blazey *et al*, *Proceedings of "QCD and Weak Boson Physics in Run II" Workshop*, ed. U. Bauer
2. DØCollaboration, *Nucl. Inst. and Meth. A* **123**, 456 (2004)
3. J-R Vlimant *et al*, *DØ Note* **4146**, (2003)
4. Z. Nagy, *Phys. Rev. Lett.* **88**, (2002)
5. D. Stump *et al*, *JHEP* **0310**, (2003)
6. A.D. Martin *et al*, *Phys. Lett. B* **604**, (2004)

Determination of Jet Energy Scale and Measurement of Inclusive Jet Production at CDF-II

Anwar A Bhatti ^a

The Rockefeller University, 1230 York Ave, New York NY 10021

Abstract. The procedure used by CDF Collaboration to determine the jet energy scale and associated uncertainties is described. The CDF detector simulation has been tuned to reproduce the calorimeter response to single particles measured in $p\bar{p}$ collisions and test beam data. The response to jets is determined by passing the individual particles, generated using PYTHIA fragmentation model, through CDF detector simulations. The accuracy of the jet energy scale depends on the location and energy of the jet. For jets with transverse energy above 50 GeV, accuracy of 3% is achieved. The measurement of inclusive jet cross section in $p\bar{p}$ collisions at $\sqrt{s} = 1.96$ TeV based on integrated luminosity of 385 pb^{-1} is also reported.

1 Jet Energy Scale Determination

Precision and validity of many results at hadron colliders depends on the accurate determination of energy of the jets. In particular, the top quark mass determination, and inclusive jet cross section measurement, two flagship analyses at the Fermilab Tevatron $p\bar{p}$ collider, are limited by uncertainty on the jet energy scale. The determination of jet energy scale is difficult because a) the calorimeter has non-linear response to charge hadrons b) the calorimeters have different response to charged and neutral pions and c) calorimeter has un-instrumented regions and non-uniform response in η . In addition large fluctuation in both jet fragmentation and calorimeter showers results in large fluctuations in jet energy, making the determination of corrections difficult. Situation is further complicated by the fact that the jet clustering cone does not contain all the energy of parent parton. Thus the mass of hadronic resonances or transverse momenta (P_T) of the jet balancing a photon or Z boson can not be constrained independently of Monte Carlo predictions.

In addition to a hard interaction, a $p\bar{p}$ interaction contains many soft interactions between spectator partons which may deposit energy in the jet cone. Any additional $p\bar{p}$ interaction occurring in the same bunch crossing also contributes energy to the jet cone. These soft contributions play a larger role at low P_T and higher luminosities.

At CDF, determination of the calorimeter jet energy scale relies on a detector simulation and a jet fragmentation model. The calorimeter simulation has been tuned to reproduce the response measured in the $p\bar{p}$ collision data at low momenta and test beam data at high momenta. The PYTHIA fragmentation model is used to simulate the jets. The jet energy corrections and associated uncertainties are derived from a combination of measurements in

dijet, γ -jet, minimum bias events, and simulated dijet and γ -jet events. The energy scale is validated by comparing the γ -jet P_T balance observed in collision data with the simulated events.

1.1 CDF Detector

The CDF II detector is a magnetic spectrometer [1]. The tracking system consists of a silicon vertex detector inside a cylindrical drift chamber. Surrounding the tracking detectors is a superconducting solenoid which provides a 1.4 T magnetic field. The CDF calorimeters are sampling calorimeters where lead and iron are used as absorbers for electromagnetic and hadronic sections respectively. The central calorimeter, $|\eta| < 1.1$, consists of 18 radiation lengths of electromagnetic section and 4.7 interaction lengths of hadronic section. This calorimeter was built in 1985 and calibrated using the test beam data in 1985 and 1990. In the plug calorimeter, upgraded for Run II, covering $1.1 < |\eta| < 3.6$, the electromagnetic (hadronic) section is 21 radiation lengths (7 interaction lengths) deep. It was tested in electron and pion beams in 1997. The region between central and plug calorimeters is covered by a hadron calorimeter which has similar segmentation and technology as the central hadron calorimeter. The calorimeters are divided into projective towers. The tower size in the central region is $\Delta\eta \times \Delta\phi = 0.11 \times 2\pi/24$. The plug calorimeter is divided in 24 or 48 towers in azimuth and the η segmentation changes as the physical size of towers becomes small. A jet of $R_{cons} = 0.7$ covers ~ 53 towers in the central region. Most of the energy from a hadronic shower is contained in 3×3 towers in the hadronic section. The electromagnetic sections are very linear and are calibrated using electrons from Z boson decays. The hadronic sections are non-linear and are calibrated such that the energy deposited by a 50 GeV pion, that did not

^a Representing CDF Collaboration

interact in the electromagnetic section, is 50 GeV. These calorimeters are essentially noise free, having ~ 1 noise tower with $E_T > 50$ MeV per event. For all physics studies only the towers with $E_T > 100$ MeV are used. The calibration is monitored by a laser system and periodic radioactive source runs. In addition the time dependence of electromagnetic calorimeter calibration is derived using electrons from the data. The hadronic calibration is maintained using muon MIP peak and tower occupancy in the minimum bias data. This procedure keeps the time variation of jet scale within 0.5%.

1.2 Energy Corrections Procedure

At CDF, the jet energy corrections are applied in steps as given in

$$P_T = \left[P_T^{Cal} \times f_{rel} - P_T^{Pile-up} \right] \times f_{abs} - P_T^{UE} + P_T^{OOC}.$$

The calorimeter jet energy is scaled by $f_{rel}(R, P_T, \eta)$ to make the effective calorimeter response uniform over η . The correction factor f_{rel} is determined by requiring the transverse momenta of two jets in dijet events to balance (Section 1.4). The energy from additional interactions in the same bunch crossing, $P_T^{Pile-up}$ is measured from the minimum bias data and is subtracted based on the number of vertices in an event. After these two corrections, jet energy needs to be corrected for calorimeter response. The scaling factor, $f_{abs}(R, P_T)$, is determined by matching particle jets with calorimeter jets (Sect. 1.6). At this stage, the jet energy is independent of any detector effects and can be compared with theory predictions. An observed jet normally contains particles from multiple parton interactions and beam remnants. This transverse energy, P_T^{UE} , is measured from minimum bias data. In some analyses e.g. top quark mass measurement, it is essential to determine the energy of the parent parton. For this, a correction, P_T^{OOC} , determined from PYTHIA is provided (Sect. 1.7). This multi step approach allows CDF to compare the data with Monte Carlo simulation at each level and isolate different physics contributions and detector effects.

1.3 Calorimeter Simulation

The CDF calorimeter response to single particles is tuned to reproduce the measured response in collision and test beam data. The simulation is based on a parameterized shower generation procedure [2]. Shower longitudinal and lateral profile parameterizations are used to deposit energy in (x, y, z) space, assuming a homogeneous calorimeter. The energy in a tower is a sum of all the energy spots within the tower. Some of these shower parameters are adjusted to reproduce E/p and lateral profiles measured in the CDF collision and test beam data. The simulated response agrees with the measured response within 2% for $p < 12$ GeV and 3% at $12 < p < 20$ GeV. At higher momenta, the uncertainty is 3.5% due to the test beam

momentum measurement uncertainty, the smaller ADC gate used in Run II and ability to carry over the test beam calibration over time. We are working on improving the lateral profile simulation and extend the P_T range of in-situ calibration. About 20% of the 100 GeV jet energy is carried by charged hadrons with $P_T > 20$ GeV.

1.4 Relative Corrections

The CDF calorimeter response is not uniform in η because differences in response in various sections of the calorimeter, un-instrumented regions at the boundaries and varying amount of material in front. The calorimeter jet energy scale is made uniform by scaling jet energies outside $0.2 < |\eta| < 0.6$ to those within this η region. The energy scale at $0.2 < |\eta| < 0.6$ is best understood. The scaling factor is determined using dijet events where, to leading order, two jets should have the same transverse momenta and any imbalance is due to detector effects. The QCD radiation effects are minimized by requiring a) the two leading jets are at least 2.7 radians apart b) any additional jets in the event have small P_T . As the P_T balance is strictly true only at production, this procedure, implicitly, corrects for any differences in parton showering, calorimeter shower leakage outside the jet cone, hadronization, underlying event and pile-up energy in two regions. The corrections for the real and simulated data are determined separately as the current simulation of plug calorimeter due to limited precision in the tuning. The two corrections differ by a 1-2% except for $|\eta| > 2.4$ where shower transverse size becomes important as the jet clustering cone size in (x, y) space is small.

1.5 Pile Up Corrections

The pile-up contribution to a jet cone from the additional $p\bar{p}$ interactions in the same bunch crossings is measured from minimum bias events in $0.2 < |\eta| < 0.6$ region. For each additional primary vertex in an event, a very good indicator of additional $p\bar{p}$ interactions, $P_T = 0.93 \pm 0.14$ GeV is subtracted from the jet P_T .

1.6 Absolute Energy Corrections

The calorimeter jet to particle jet correction is determined from PYTHIA dijet events generated with P_T^{min} from 0 to 700 GeV and passed through CDF detector simulation. The particle jet momenta is determined by clustering the final state stable particles using the same clustering algorithm. The corrections are determined by matching two leading particle jets to corresponding calorimeter jets. Only the calorimeter jets with $0.2 < \eta < 0.6$ are used. We use the most probably value of two dimensional histogram between calorimeter and particle jet energies as the correction. In this procedure the effect of smearing from falling QCD spectrum is taken out. After these corrections, the jet is independent of all detector effects, e.g. non-linearity

of calorimeter, energy loss in un-instrumented regions, interactions in material in front of calorimeter and bending of particles due to magnetic field.

1.7 Underlying Event Corrections and Out-of-Cone Corrections

The energy contribution to a jet from multi parton-parton interactions and beam remnants, UE, is estimated from PYTHIA Tune A dijet events [3]. In this version, the parameters controlling the multiple partons and initial state radiation have been adjusted to reproduce the energy density transverse to the leading jet observed in the CDF data. To obtain the parton energy, any energy radiated outside the jet clustering, either during parton showering or during hadronization must be added to the particle jet. The combined UE and Out-of-Cone (OOC) corrections are determined by matching the particle jet to parent parton. For analyses not doing the OOC corrections, $P_T^{UE}(R)$ measured from minimum bias data is provided.

After these generic corrections, some analyses at CDF apply additional corrections to account for other physics effects specific to the analysis. For example jets containing a b -quark require additional corrections.

1.8 Systematic Uncertainties

The systematic uncertainty on the jet energy scale is measured at each step of jet correction. The uncertainty on the relative corrections is determined from the accuracy of the procedure. The uncertainty on the absolute corrections arises from accuracy of the calorimeter simulation, time-variation of calorimeter response and jet fragmentation model. The charged particle spectrum in PYTHIA describes the collision data quite well. The remaining difference results in 1% change in jet energy scale over the available unbiased data, 20-300 GeV, jet P_T range. The HERWIG fragmentation model gives the consistent results. The combined uncertainty from calorimeter simulation, fragmentation model and time dependence of calorimeter response, increases from $\sim 2\%$ at 20 GeV to $\sim 3\%$ at 500 GeV. The pile-up (15%) and underlying event (30%) correction uncertainties are estimated from the energy observed in the minimum bias data taking into account the calorimeter corrections to soft particles and luminosity dependence, and comparison of energy density transverse to the jet and that in minimum bias events, and Pythia studies. The uncertainty on the OOC corrections is determined by comparing the energy observed outside the cone in $p\bar{p}$ data with simulated γ -jet events.

The P_T balance ($P_T^{Jet}/P_T^\gamma - 1$) in γ -jet samples is shown in Fig. 1. Events with any additional jet with $P_T > 3$ GeV or where $|\phi^\gamma - \phi^{jet}| < 3.0$ radians are not used. The γ -jet P_T balance in these highly restricted samples is +1.0% (data), +1.1% (PYTHIA) and -1.8% (HERWIG). Two Monte Carlo samples disagree at generator level also.

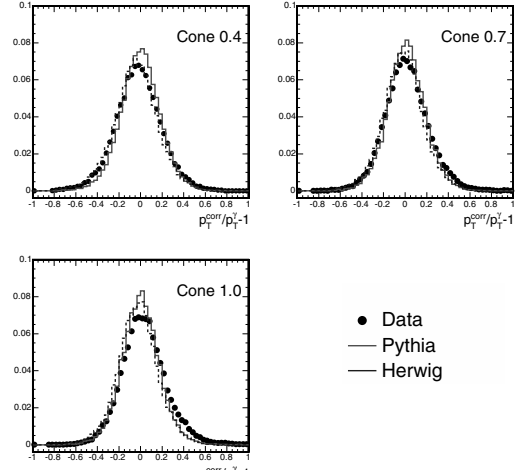


Fig. 1. The P_T balance between the photon and leading in γ -jet events. The jets have been corrected to parton-level.

Analysis of the W boson mass from two jets in top quark events shows that jet energy scale in the data is $(-0.25 \pm 1.22)\sigma$ relative to the expected Monte Carlo scale. σ is the uncertainty on the jet energy scale [10].

1.9 Conclusion

CDF has determined the jet energy scale from first principles i.e. by convolving the single particle response with the particle momenta and multiplicity in the jet. The current uncertainty on the jet scale is 6.5% at 20 GeV, dominated by the OOC uncertainty, 3% at 100 GeV and 3.5% at 500 GeV where it is dominated by calorimeter simulation uncertainty. The uncertainty on the jet energy scale can be further reduced by improving the detector simulation and better understanding of QCD radiation and hadronization in photon-jet events. Details of the CDF jet scale determination procedure can be found in [4].

2 Inclusive Jet Cross Section

Parton-parton interactions producing high energy jets at the Tevatron probe the smallest distance and are potentially sensitive to a wide variety of new physics, such as quark oppositeness. The previous measurement of differential jet production cross section by the CDF Collaboration at $\sqrt{s} = 1.8$ TeV [5] exhibited an excess in the high transverse energy E_T region when compared to next-to-leading order (NLO) QCD predictions obtained using then-current parton distribution functions (PDF) leading to many speculations. However, that excess was easily accommodated by new parton distribution functions which have enhanced gluon distribution at high x , while still consistent with the other data. In fact, at high x , the gluon distributions are mainly constrained by the Tevatron jet data. In Run II, we have measured the inclusive jet cross

section at higher center of mass energy $\sqrt{s} = 1.96$ TeV using 385 pb^{-1} of data collected between February 2002 and August 2004.

The Run II measurement is based on an improved iterative cone, Midpoint, algorithm. The iterative cone algorithms used in previous measurements showed a singular behavior when used in next-to-next-to-leading order perturbative QCD calculations [7]. To avoid these singularities, additional seeds are added at the middle of the two previously reconstructed clusters less than $2R_{cone}$ apart and clustering is repeated. In experimental data, the old and improved algorithms give very similar results. In Midpoint algorithm a jet is described by P_T and the rapidity $y = -1/2 \ln((E + p_Z)/(E - p_Z))$.

The Level 1 trigger requires a calorimeter trigger tower, consisting of two calorimeter towers adjacent in η , to have either $E_T > 5$ or 10 GeV. At Level 2, the calorimeter towers are clustered using a nearest neighbor algorithm. Four trigger paths with cluster $E_T > 15, 40, 60,$ and 90 GeV are used. Events in these paths are required to pass jet $E_T > 20$ (J20), 50 (J50), 70 (J70) and 100 (J100) GeV thresholds at Level 3, where the clustering is performed using a cone algorithm with a cone radius $R_{cone} = 0.7$. Jets are corrected for energy from additional interaction in the same bunch crossing by subtracting 0.93 GeV from jet P_T each extra vertex in the event. The energy for each jet is corrected, on average, for the energy loss due to non-linearity in the calorimeter and lower response at tower and calorimeter boundaries. After these P_T corrections, a binned raw spectrum is formed by combining data from four trigger paths such that each bin $> 99.5\%$ efficient and consists of data from only one trigger path. This spectrum is corrected for smearing from finite energy resolution of the calorimeter. Both of these corrections are determined from PYTHIA dijet events after re-weighting the spectrum to match the CDF spectrum. After the smearing corrections the jets are independent of any detector effects. To compare with parton level predictions, the P_T contribution from multiple parton interaction and beam remnant to the jet should be subtracted. In addition, the energy of the particles outside the jet cone originating from partons that lie within the jet cone has to be taken into account. These corrections are determined from PYTHIA Tune A, where the parameters governing the multiple parton interaction and initial state radiation have been tuned to describe the energy flow transverse to the jet. The corrections are determined by clustering the partons just before hadronization in a PYTHIA sample where multiple parton interactions have been turned off and comparing the resulting cross section with particle level cross section. These non-perturbative UE and hadronization corrections range from $+12\%$ at 60 GeV to $< 1\%$ at $P_T > 250$ GeV. The comparison of corrected data with NLO QCD predictions [8] is shown in Fig 2. The NLO QCD predictions are calculated with $\mu_R = \mu_F = P_T/2$, and an additional parameter $R_{sep} = 1.3$. In NLO QCD, where final state can have at most three partons, two partons are clustered into a single jet if they are with $R_{cone} \times R_{sep}$ of each other. The data are in good agree-

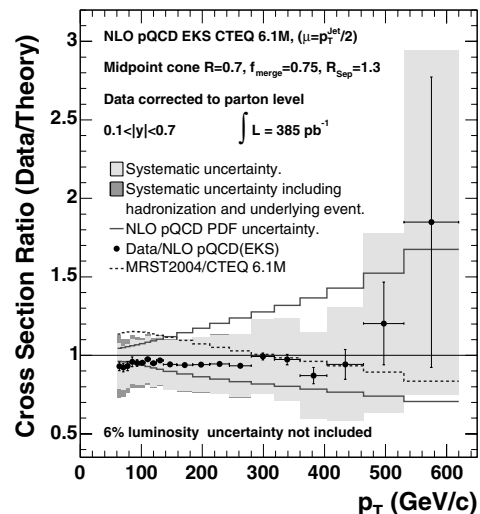


Fig. 2. The ratio of the data corrected to the parton level over the NLO pQCD prediction of the EKS calculation using CTEQ6.1M. Also shown are the experimental systematic errors, dominated by the energy scale error, and the theoretical errors from the PDF uncertainty. The ratio of MRST2004/CTEQ6.1M is shown as the dashed line. An additional 6% uncertainty on the determination of the luminosity is not shown.

ment with NLO QCD calculations based on CTEQ6.1M PDF set. In this set, the gluon distributions are primarily constrained by the Tevatron inclusive jet data from Run I. Thus new data are consistent with Run I data.

CDF has also measured the jet cross section using a K_T based algorithm where the particles are clustered into a jet based on their relative momenta [9]. The analysis procedure is similar to the one used for measurement based on cone-based jet clustering. The corrected data are compared with NLO QCD predictions calculated JETRAD and show a good agreement.

References

1. CDF Collaboration, D. Acosta *et al.*, Phys. Rev. D **71**, 032001 (2005), hep-ex/0412071.
2. G. Grindhammer, M. Rudowicz, S. Petersen, Nucl. Instrum. Meth. A **290**, 469 (1990).
3. R. Field, “Herwig, Jimmy and PYTHIA Tune A”, talk given at TeV4LHC at Fermilab (2004).
4. A. Bhatti *et al.*, *Jet Energy Scale Determination at CDF*, to be submitted to Nucl. Instrum. Meth. A.
5. CDF Collaboration, F. Abe *et al.*, Phys. Rev. Lett. **77**, 438 (1996). CDF Collaboration, T. Affolder *et al.*, Phys. Rev. D **64**, 032001 (2001), hep-ph/0102024.
6. H.L. Lai *et al.*, Phys. Rev. D **55**, 1280 (1997).
7. W. Kilgore and W. Giele, Phys. Rev. D **55**, 7183 (1997)
8. S.D. Ellis, Z. Kunszt and D.E. Soper, Phys. Rev. Lett. **64**, 2121 (1990).
9. S. Catani *et al.* Nucl. Phys. **B406** 187(1993), S.D. Ellis and D.E. Soper, Phys. Rev. **DD48**, 3160(1993).
10. T. Tomura, *Top mass at Tevatron*, this proceedings.

Fragmentation, Underlying Event and Jet Shapes at the Tevatron (CDF)

Alison Lister¹ for the CDF Collaboration
¹ETH Zürich, Switzerland

Abstract. Experimental tests of QCD processes, in particular fragmentation, underlying event and jet shape studies, are not only essential in their own right to allow an improved understanding of the theoretical models and their limitations but they are also important in searches for new physics. Recent results of such tests are presented here. All the results show good agreement between the latest theoretical models or Monte Carlo predictions.

1 Introduction

In a hadron-hadron collision there is much more going on than simply the hard scattering processes between the partons. Soft QCD processes give rise to initial- and final-state radiation, beam - beam remnant interactions as well as possible multiple parton interactions. These are all processes which are not yet thoroughly understood.

There are many models which describe the hadronisation process and these need to be thoroughly tested in order to understand better the mechanism linking what we see in our detector, the hadrons, to what we can calculate from a theoretical point of view, the partons.

The study of fragmentation effects deals with final-state radiation along with hadronisation processes. Some recent studies will be shown in the next section. Initial- and final-state radiation along with beam - beam remnants and multiple parton interactions are what are collectively referred to as the underlying event. Some CDF Run II results will be presented in section 3. Finally, in section 4, the fractional transverse momentum distribution inside jets, known as the jet shape, is investigated in inclusive jet production.

2 Fragmentation

The reasons for studying fragmentation are numerous. Fragmentation processes are driven by soft QCD ($k_T < 1$ GeV) which are a theoretical challenge to describe as it pushes the limits of perturbative QCD theory down to $k_T \sim \Lambda_{\text{QCD}}$. Moreover the hadronisation stage is not well understood from a theoretical point of view although several phenomenological models exist which can be tuned to describe the data reasonably well.

The Tevatron in particular and hadron-hadron colliders in general are particularly difficult environments in which to study fragmentation because there are many underlying processes which occur that are not directly related to the primary hard interactions. It is nevertheless interesting to study hadronisation processes at the Tevatron because the energy scale probed is higher than any previous studies and more processes become available than at lepton colliders.

The results shown in this section are for CDF Run I data. These analyses as well as some additional measurements are currently being carried out using Run II data.

One measurement of interest is the study of the particle momentum spectra of charged particles. The analysis is performed in the dijet centre of mass frame and looks at charged particles inside angular cones around the jet axis of $\sim 0.3 - 0.5$ radians. Central dijet events with a dijet mass in the range $M_{\text{jj}} \sim 80 - 600$ GeV are considered.

The results for different dijet mass bins as a function of the momentum transfer are shown in figure 1. A fit to the data using both the shape and the normalisation is performed and also shown on these plots [1]. The agreement between the data and the fit is very good. The shape of the distributions is driven by a single parameter, the Next to Next to Leading Log Approximation (NNLA) effective cutoff scale, Q_{eff} . The fit for all distributions consistently gives $Q_{\text{eff}} = 240 \pm 40$ MeV which tells us that the k_T cut-off can be set as low as Λ_{QCD} . The normalisation constant of the distribution is related to the ratio between the number of charged hadrons and partons, which is found to be 0.56 ± 0.10 .

An interesting ratio to look at when studying fragmentation is the ratio of the average number of charged particles in gluon-jets to that in quark-jets. From basic

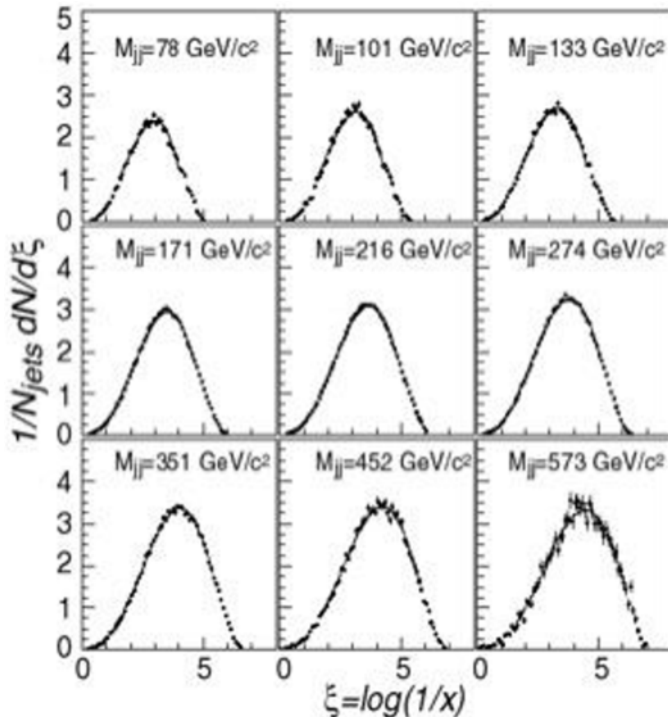


Fig. 1. Average distribution of charged particles as a function of the momentum transfer for different dijet mass bins using CDF Run I data (points). A fit to the data is also shown (smooth curve).

considerations, as well as when using Next to Leading Log Approximation (NLLA), one expects this ratio to be $\frac{9}{4}$. Extensions of this approximation show that this ratio should be slightly lower. This measurement is difficult to carry out without biasing the result and historically the measurements have not been in very good agreement with the different theoretical models.

The CDF analysis looks at two distinct data samples; the first is a dijet sample with dijet mass, M_{jj} , around 100 GeV and the second is a photon + jet sample with dijet mass, $M_{\gamma j}$, also around 100 GeV. From Monte Carlo studies, the fraction of gluon and quark jets can be extracted for each sample. The gluon fraction is found to be $\sim 60\%$ for the first sample and $\sim 20\%$ in the latter. The number of charged particles inside a cone of $\sim 0.3 - 0.5$ radians around the jet axis is computed for both samples and from this the average number of charged particles for gluon and quark jets as well as their ratio is extracted. The results for this analysis are shown in figure 2 for two different jet energies (41 and 53 GeV) and are compared to the latest results from other experiments and different theoretical predictions. The CDF Run I results are found to be in good agreement with the latest NNLA extensions. The final result, combining the two jet energies, is found to be 1.6 ± 0.2 .

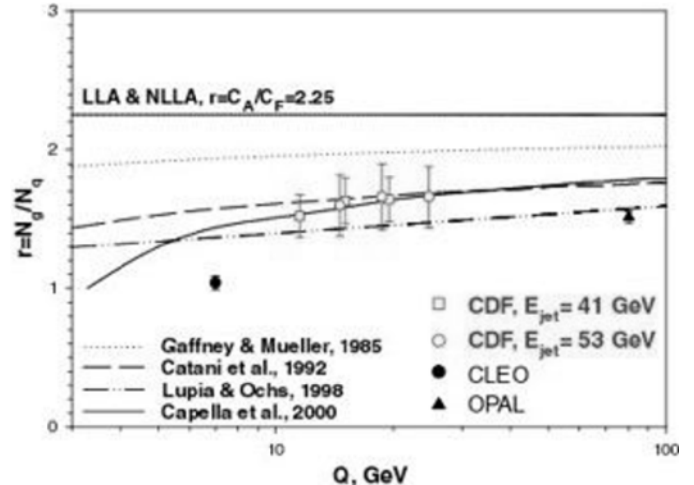


Fig. 2. Ratio of the charged particle multiplicity between gluon and quark jets for different values of jet energies at CDF, along with other recent measurements and theoretical predictions.

3 Underlying event

Charged particle correlations are important quantities to study when looking at the underlying event. There are many variables which can be studied but the charged particle density per unit (η, ϕ) , $dN_{\text{chg}}/d\eta d\phi$, where η is the pseudo-rapidity, as a function of the leading jet transverse energy, E_T , or the angle away from the leading jet, $\Delta\phi$, is representative of what is observed. This study uses CDF Run II data [2]. Jets are reconstructed using the JetClu cone algorithm with a cone size of 0.7. The results shown here are detector level quantities.

Event topologies are defined as follows. Leading jet events are events where the highest transverse energy, E_T , jet in the event is central ($|\eta| \leq 0.7$). A subset of these events, called back to back events, have the second highest E_T jet almost opposite in ϕ to the leading jet ($\Delta\phi \geq 5\pi/6$), they must also have a similar transverse energy ($\frac{E_{T,2}}{E_{T,1}} \geq 0.8$) and any potential third jet must have a low transverse energy ($E_{T,3} \leq 15$ GeV).

Having defined these two event topologies one can plot, as done in figure 3, the charged particle density as a function of the angle ϕ away from the leading jet. Figure 3 shows this distribution in a polar plot, where the charged particle multiplicity is shown in the radial direction, for a particular range of E_T of the leading jet ($30 \leq E_T \leq 70$ GeV). The distance between each concentric circle represents a charged particle density interval of 0.5.

One can see that for back to back events the charged particles are strongly aligned with the leading jet direction with a more or less constant charged particle density of about 0.5 in the rest of the ϕ -space. For leading jet events this distribution is slightly less one-dimensional, with a

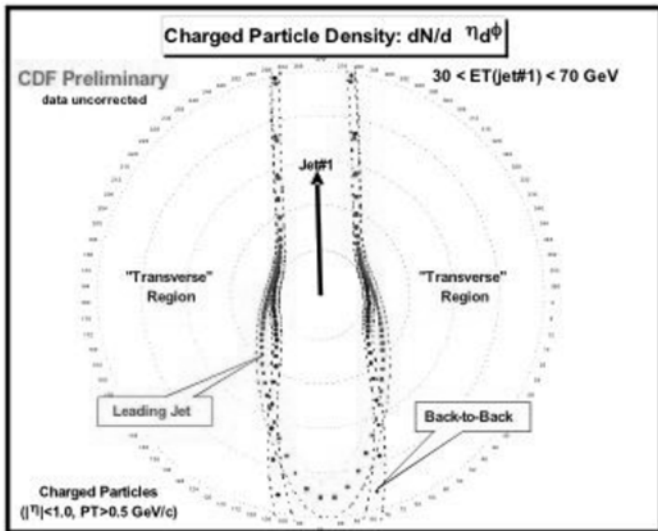


Fig. 3. Polar plot of the charged particle density for leading jet and back to back events. The concentric markers are $\frac{dN_{\text{chg}}}{d\eta d\phi} = 0.5$ apart.

larger spread of charged particles. This is probably due to the formation of three or more jet events.

One can define two spatial regions which are transverse to the leading jet direction ($\frac{1}{3}\pi \leq |\Delta\phi| \leq \frac{2}{3}\pi$) and look at correlations in the charged particle densities in these regions (called here transverse charged particle densities). Figure 4 shows the difference between the transverse charged particle densities in these two regions for both the leading jet and the back to back samples as a function of the transverse energy of the leading jet. This quantity is sensitive to the initial- and final-state radiation components for the underlying event. The data obtained is compared to Pythia Tune A and Herwig. Pythia Tune A was tuned to the underlying event using CDF Run I data and it is interesting to see that this tune still seems to describe Run II data very well. The agreement is not as good with the Herwig Monte Carlo; Herwig does not have multiple parton interactions and has not been tuned to CDF data. This shows how important the underlying event and other soft QCD processes are in the description of the data.

Other similar quantities have also been studied such as the distribution of the smallest of the two transverse charged particle densities, which is very sensitive to the beam-beam remnant component of the underlying event, or the average value of the transverse charged particle densities. In all cases the agreement between the data and Pythia Tune A is very good.

4 Jet Shapes

The fractional transverse momentum distribution inside jets as a function of the distance from the jet axis

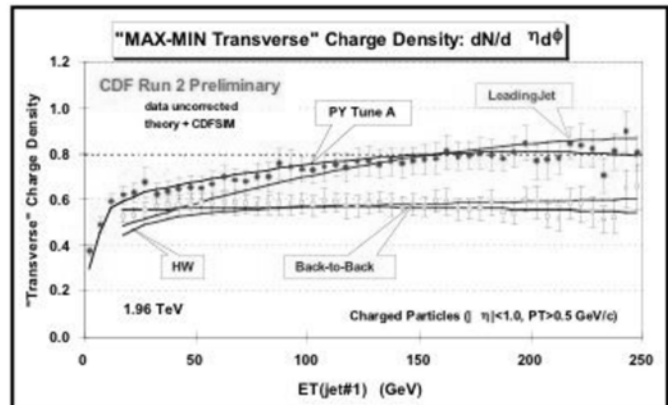


Fig. 4. Difference in the transverse charged particle multiplicity between the two transverse regions as a function of E_T of the leading jet.

is known as the jet shape. This distance is measured in (ϕ, Y) -space where Y , the rapidity, is defined as $Y = 0.5 \ln\left(\frac{E+p_T}{E-p_T}\right)$.

The integrated jet shape is defined as:

$$\Psi(r) = \frac{\int_0^r p_T(r') dr'}{\int_0^R p_T(r') dr'}$$

where by definition $\Psi(r=R) = 1$.

In this analysis, the shapes are computed at calorimeter level and corrected back to hadron level [3]. The MidPoint cone algorithm with a cone size of 0.7 is used to reconstruct the jets. The jets are central, with $0.1 \leq Y \leq 0.7$. The results shown in figure 5 use 170 pb^{-1} of CDF Run II data and are binned in jet p_T regions which span the whole spectrum from 37 to 380 GeV.

As expected, it is found that the shapes get narrower as the jet's transverse momentum increases. This is due to perturbative QCD effects related to the running of the strong coupling as well as the fact that the mixture of quark- and gluon-jets in the final state changes with p_T . This second effect can be seen when comparing the shapes with those obtained using Pythia Tune A for gluon- and quark-jets separately. Figure 5 (top) shows the fractional p_T outside a cone of $0.3/R$ as a function of p_T of the jet. It shows that jets originate mainly from gluons (dashed line) at low p_T and from quarks (dotted line) at high p_T .

The same evolution of the shape with jet p_T is compared to different Monte Carlo models in figure 5 (bottom). The best agreement is found with Pythia Tune A. It is very encouraging to see that the tune which describes so well the underlying event also describes well other quantities described by QCD, such as the jet shapes. Herwig, despite not having multiple parton interactions, still describes the data reasonably well (dashed line). The importance of the tuning of Pythia can be seen by comparing the data to the default Pythia (dotted-dashed line). Moreover, the inclusion of multiple

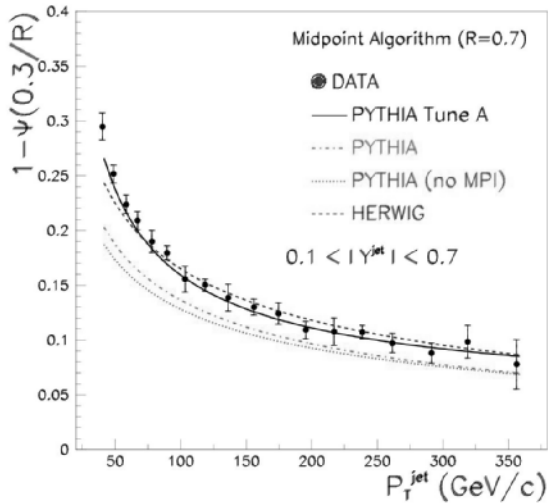
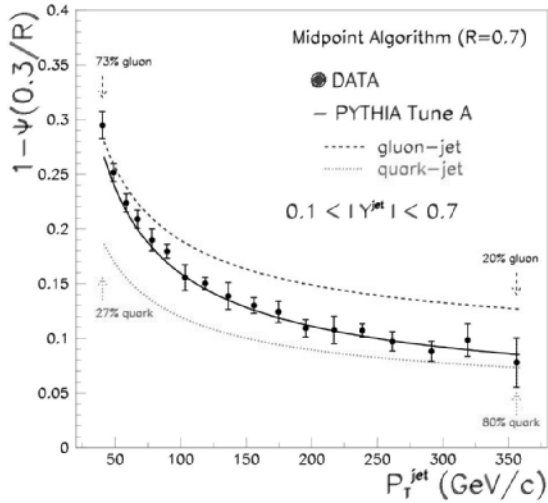


Fig. 5. Fractional p_T outside a cone of $0.3/R$ as a function of the jet p_T . The data is compared to Pythia Tune A Monte Carlo as well as the shapes expected for quark and gluon jets (top) and the shapes obtained from different theoretical models (bottom)

parton interactions in the models is also important, as shown by the difference between the default Pythia with no multiple parton interactions (dotted line) and the data.

5 Conclusions

A number of different measurements of QCD processes at the Tevatron have been presented here. All have shown that the theory and models behind processes such as soft radiation, hadronisation, fragmentation, to name but a few, describe the data very well. In particular the use of the Pythia Tune A Monte Carlo was found to be very important in the understanding of some processes such as the jet shapes and the underlying event.

6 Acknowledgements

I would like to thank all the people who work so hard to run the CDF experiment as well as all the collaborators who participate in QCD analyses. In particular I would like to thank, R. Field, A. Korytov and M. Martinez for their work which I presented here. I would also like to thank the organising committee of HCP2005 for an extremely diverse and interesting conference.

References

1. D. Acosta *et al.*, Phys. Rev. D **68**, (2003) 012003
2. R. Field, <http://www-cdf.fnal.gov/physics/new/qcd/run2/ue/chgjet/index.html>
3. D. Acosta *et al.*, Phys. Rev. D **71**, (2005) 112002

High p_T Jets and Photons at the Tevatron

Cecilia E. Gerber^a

University of Illinois at Chicago, e-mail: gerber@uic.edu

Abstract. I present recent results on high p_T jets and photon production in $\bar{p}p$ collisions at a center of mass energy of 1.96 TeV. The measurements were performed by the CDF and DØ collaborations using between 150 and 300 pb^{-1} of data taken during Run II at the Tevatron.

1 Introduction

Quantum Chromodynamics (QCD) emerged as a mathematically consistent theory in the 1970s, and nowadays is regarded as one of the cornerstones of the Standard Model. One of the triumphs of modern particle physics has been the extent to which QCD has successfully accounted for the strong interaction processes observed experimentally at hadron colliders. Recent measurements of multi-parton processes, heavy flavor production, and direct photon production are pushing the comparisons with available theoretical models to a new era of precision QCD studies. This confrontation between measurements and predictions is important in itself as a test of QCD, but is also crucial in the identification of beyond the standard model phenomena that might appear at the Tevatron or the LHC. In the following sections I will present recent results from the Tevatron collider experiments on high p_T jets and photon production.

2 Dijet Azimuthal Decorrelations

The DØ collaboration has recently published [1] a study of the correlations in the azimuthal angle between the two largest transverse momentum jets ($\Delta\Phi_{\text{dijet}}$) using 150 pb^{-1} of data collected during Run II. Dijet production in hadron-hadron collisions in the absence of radiative effects results in two jets with equal transverse momenta and correlated azimuthal angles. Additional soft radiation causes small azimuthal decorrelations, but $\Delta\Phi_{\text{dijet}}$ values significantly lower than π are evidence of additional hard radiation with high p_T . Exclusive 3-jet production populates the region of $\Delta\Phi_{\text{dijet}}$ between $2\pi/3$ and π , while smaller values of $\Delta\Phi_{\text{dijet}}$ require additional radiation such as a fourth jet in the event. Distributions of $\Delta\Phi_{\text{dijet}}$ consequently provide an ideal testing ground for higher-order pQCD predictions without requiring the reconstruction of additional jets.

The analysis is based on an inclusive dijet sample in the central rapidity region ($|y| < 0.5$), and was performed in four analysis regions, defined by the requirement that the p_T of the leading jet in the event p_T^{max} be greater than 75, 100, 130, and 180 GeV, respectively. The second leading jet in the events was required to have $p_T > 40$ GeV. Jets were defined using an iterative seed-based cone algorithm (including mid-points) with radius $R_{\text{cone}} = 0.7$ [2]. The observable was defined as the differential dijet cross section in $\Delta\Phi_{\text{dijet}}$, normalized by the dijet cross section integrated over $\Delta\Phi_{\text{dijet}}$ in the same phase space $(1/\sigma_{\text{dijet}})(d\sigma_{\text{dijet}}/d\Delta\Phi_{\text{dijet}})$. The data was compared to pQCD calculations obtained using the parton-level event generator NLOJET++ [3] and CTEQ6.1M [4] PDF's. The renormalization and factorization scales were chosen to be $\mu_r = \mu_f = 0.5p_T^{\text{max}}$. It is observed that NLO pQCD provides a good description of the data. In addition, the data was compared to Monte Carlo event generators (HERWIG [3] and PYTHIA [2]), that use $2 \rightarrow 2$ LO pQCD matrix elements with phenomenological parton-shower models to simulate higher order QCD effects. HERWIG version 6.505 describes the data well over the entire range, whereas PYTHIA version 6.225 with default parameters describes the data poorly. A good agreement can be achieved between data and PYTHIA by increasing the maximum allowed virtuality by a factor of four [7]. The data can therefore benefit global efforts to tune Monte Carlo event generators.

3 b Jet Cross Sections

Measurements of the b jet cross section provide an important quantitative test of pQCD, as the mass of the b quark is considered to be large enough to justify the perturbative expansion in the strong coupling constant. Data on b quark production is therefore expected to be adequately described by NLO pQCD calculations. Both the CDF and the DØ collaborations have recently made public preliminary results on inclusive b jet cross section measurements. These results extend the upper reach of exclusive measurements using B mesons, and provide a simple observ-

^a for the CDF and DØ Collaborations

able with high sensitivity to heavy flavor production up to the highest p_T . In addition, theoretical uncertainties on fragmentation and decay are smaller in the inclusive b jet analysis than in exclusive decay studies. In the following sub-sections, I will briefly describe the methods used by CDF and $D\bar{O}$ to identify b jets, as well as present preliminary results on inclusive b jet production.

3.1 b Jet Identification

Two strategies have been developed to identify jets that originate from a b quark, referred to as b tagging: soft-lepton tagging (SLT) and secondary vertex tagging (SecVtx).

Approximately 20% of the time, a decaying b quark will yield a muon, either directly or through a sequential decay via a c quark. These muons are much softer and less isolated than the ones originating from a W boson, and when identified within the jet cone, can be used to tag that jet as originating from a b quark. Although the fraction of b quarks decaying into electrons is the same as for muons, the identification of soft electrons inside jets is quite challenging and is not being considered further in this paper.

Another method of tagging b jets profits from the relatively long lifetime of B hadrons, which allows them to travel up to several mm before decaying. The SecVtx algorithm [8] relies on the displacement of secondary vertices relative to the primary event vertex to identify B hadrons. It uses displaced tracks associated with a jet that are within a sub-cone of 0.4 in the $\eta - \phi$ space with respect to the jet axis. The algorithm looks for combinations of at least 2 tracks consistent with originating from a secondary vertex. For each secondary vertex, the distance in the transverse plane between the vertex and the primary one (L_{xy} or decay length) is calculated, and tags with positive L_{xy} are accepted as b tags.

3.2 High p_T Cross Section for μ tagged Jets

The $D\bar{O}$ collaboration has measured the inclusive jet cross section for μ tagged jets using 294 pb^{-1} of data collected during Run II. Events were recorded using single jet triggers at four different thresholds; the highest p_T threshold trigger being unrescaled. Jets were defined using an iterative seed-based cone algorithm (including mid-points) with radius $R_{\text{cone}} = 0.5$ [2], and were restricted to central rapidities of $|y| < 0.5$. Muons were detected as tracks reconstructed from hits recorded in three layers of tracking detectors and two layers of scintillators [9], both located outside the calorimeter. A 1.8 Tesla iron toroidal magnet is located outside the innermost layer of the muon detector. The p_T of the muon was required to be greater than 5 GeV, and the distance in $\eta - \phi$ space between the muon and the jet was required to be less than 0.5, which selects a sample enriched in heavy flavor jets. The data was then fully corrected for efficiencies and unsmearred to particle level. The selected sample contains contributions

from b and c quark semileptonic decays, but also from in flight decays of π and K mesons. To extract the heavy flavor component of the μ tagged jets cross section $D\bar{O}$ used a sample of QCD Monte Carlo events generated with PYTHIA and processed with a GEANT-based [10] full detector simulation. The fraction of μ tagged jets which contain at least one b or c quark as predicted by the Monte Carlo is shown in Fig. 1 (left). The overlaid fit represents the fraction used as a correction factor to the measured cross section. It ranges from about 70% at $p_T = 50$ GeV to about 45% at $p_T = 400$ GeV. The dashed lines represent the assigned systematic uncertainty on the fraction, which reflects the limited Monte Carlo statistics, will be reduced for a future update of the analysis. Fig. 1 (right) shows the comparison of the data with theoretical predictions. The result is presented as a ratio with the prediction from PYTHIA for the μ tagged jets cross section originating from b or c quarks. PYTHIA's prediction therefore is shown as a line at 1. The data is shown as dots with statistical error. The systematic error is shown as a band: the outer band corresponds to the total error, the middle band corresponds to setting the heavy-flavor fraction error to zero, and the inner band shows the exclusive contribution to the error from the jet energy scale correction. The NLO prediction was obtained from the product of the predicted inclusive jet cross section from NLOJET++ with CTEQ6M and $\mu = p_T/2$, multiplied by the fraction of jets from b or c quarks that are μ tagged, as predicted by PYTHIA. The data lays approximately between the two calculations, with errors spanning the difference. Further reduction of the experimental uncertainties is needed in order to constrain the predictions.

3.3 Inclusive b Jet Cross Section

The CDF Collaboration has measured the inclusive b jet cross section using about 300 pb^{-1} of data collected during Run II. Events were recorded using single jet triggers at five different thresholds, optimized to provide unbiased, fully efficient data selection. Jets were defined using an iterative seed-based cone algorithm (including mid-points) with radius $R_{\text{cone}} = 0.7$, and were restricted to central rapidities of $|y| < 0.7$. The SecVtx algorithm was used to tag b jets. Monte Carlo was used to derive the average correction for detector effects and p_T scale. The b tagging efficiency was measured in a Monte Carlo dijet sample, and scaled by a Data-to-Monte Carlo correction factor derived from comparing the b tagging efficiency obtained from an inclusive electron data sample and the corresponding Monte Carlo sample. To extract the heavy flavor component of the b tagged jets cross section, CDF used the shape of the SecVtx vertex mass distribution as the discriminating quantity. Templates for b , c , or light-quark jets were obtained from PYTHIA Monte Carlo in bins of jet p_T ; the templates for c and light jets were subsequently merged. The fraction of tagged jets that originate from a b quark in each jet p_T bin was obtained by fitting the data to a linear combination of the templates for b and c or light-quark jets. The obtained fraction can be seen in

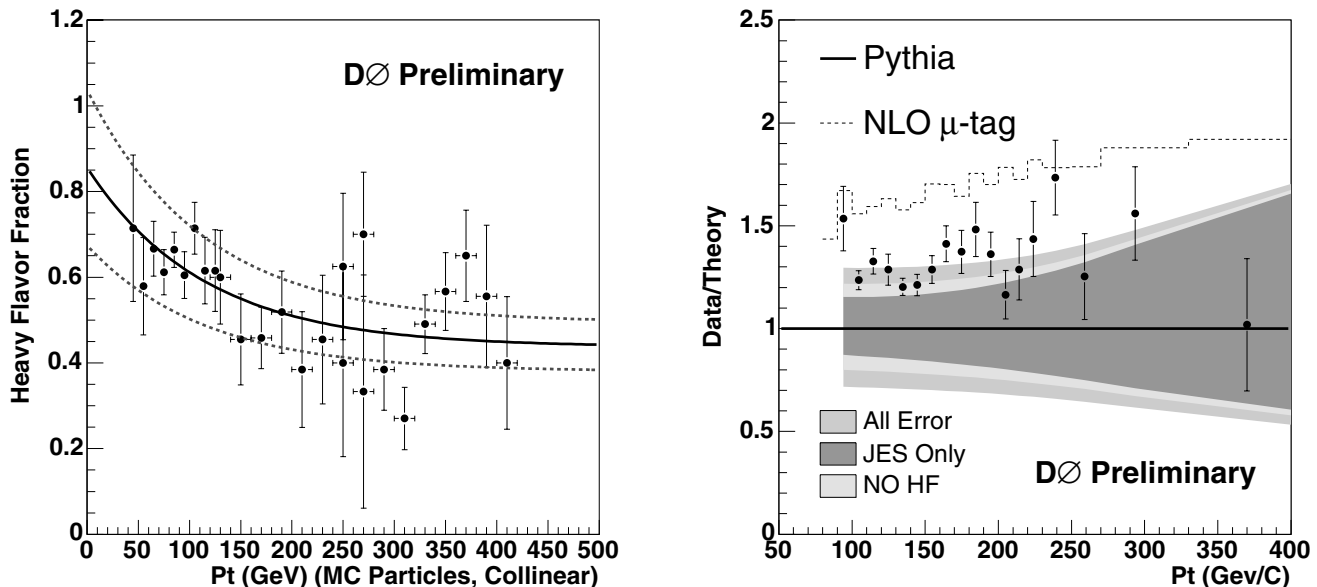


Fig. 1. Fraction of μ tagged jets coming from b or c quark semileptonic decays as predicted by PYTHIA (left). DØ measurement of the inclusive cross section for μ tagged b or c quark jets presented as a ratio with the prediction by PYTHIA, compared to the same PYTHIA prediction, and to a NLO estimate obtained as described in the text (right).

Fig. 2 (left). The measured inclusive b jet cross section is shown in Fig. 2 (right), together with the prediction from PYTHIA TUNE A, with CTEQ5L PDF. The error in the last six bins is dominated by the error on the fraction of b jets and the absolute jet energy scale. PYTHIA underestimates the data by a factor of 1.4, as expected for a LO Monte Carlo prediction. A comparison of the data with NLO QCD is in preparation.

4 Photon Studies

At the Tevatron, the dominant source for production of photons with $p_T \leq 150$ GeV is through the process $q + q \rightarrow q + \gamma$ (Compton Scattering). The production cross section is therefore sensitive to the gluon density inside the colliding hadrons. The measurement of the isolated photon cross section allows testing of NLO and resummed QCD calculations, as well as phenomenological models of gluon radiation, photon isolation, and the fragmentation process. In addition, diphoton final states serve as signature for many interesting physics processes [11], including one of the main discovery channels for the Higgs boson at the LHC [12]. Nevertheless, the QCD production rate dominates, and thus an understanding and modelling of the QCD production mechanism is needed prior to any possible discoveries.

4.1 Isolated Photon Cross Section

The DØ collaboration has measured the inclusive cross section for the production of isolated photons using 326

pb^{-1} of data collected during Run II. The preliminary result has been shown for the first time at the Hadron Collider Physics Symposium 2005 (this conference), and is presented below. Events were required to pass a combination of unprescaled EM triggers. Photons were reconstructed with a simple cone algorithm [13] with cone size $R_{\text{cone}} = 0.2$, had a minimum p_T^γ of 15 GeV, and were restricted to central rapidities of $|y| < 0.9$. Each photon candidate was required to deposit more than 95% of the detected energy in the EM section of the calorimeter, and to be isolated in an annular region between $R_{\text{cone}} = 0.2$ and 0.4 around the photon. In addition, the probability to have a track spatially matched to the EM cluster was required to be less than 0.001, and the missing transverse energy (\cancel{E}_T) had to satisfy the cut $\cancel{E}_T/p_T^\gamma < 0.7$. A set of four additional variables that are well modelled in Monte Carlo were used to build an artificial neural network (ANN) [14] optimized for pattern recognition. The network is trained in bins of p_T^γ to produce an output of unity for signal and zero for background. The normalized distribution of ANN output for data, direct photon signal Monte Carlo and a background sample of electromagnetic jets obtained directly from collider data, is shown in Fig. 3 (left) for the bin $44 < p_T^\gamma < 50$ GeV. Events that satisfy a cut in the NN output of greater than 0.5 remain in the final data sample. The purity of this sample is determined on a statistical basis by fitting the data to a linear combination of the ANN distributions for direct photon Monte Carlo (signal), and electromagnetic jets from data (background). The result is shown in Fig. 3 (right). The inclusive photon

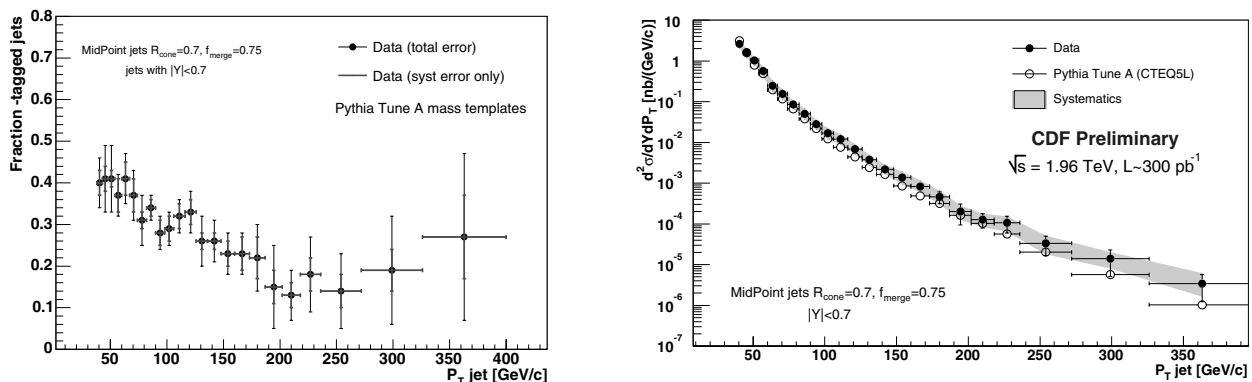


Fig. 2. Fraction of SecVtx tagged jets coming from a b quark as obtained from fits to the vertex mass distribution predicted by PYTHIA (left). CDF measurement of the inclusive b jet cross section compared with a prediction from PYTHIA TUNE A, with CTEQ5L PDF (right).

cross section was obtained by the relation

$$\frac{d^2\sigma}{dp_T^\gamma d\eta_T^\gamma} = \frac{N P f}{L \Delta p_T^\gamma \Delta \eta_T^\gamma A \varepsilon},$$

where N is the number of selected photon candidates, P is the photon purity, f is the unsmearing correction, L is the integrated luminosity, Δp_T^γ and $\Delta \eta_T^\gamma$ are the bin sizes in transverse momentum and pseudorapidity of the photon respectively, A is the acceptance, and ε is the efficiency of the selection. The ratio of the measured cross section to the NLO QCD prediction [15] is shown in Fig. 4. The prediction agrees with the data within experimental uncertainties in the whole considered range $23 < p_T^\gamma < 300$ GeV. The prediction by Gordon and Vogelsang [16], that uses a different set of fragmentation functions, is in agreement within 7%.

4.2 Diphoton Production

The CDF collaboration has recently published [17] a measurement of the production cross section for isolated prompt diphotons using 207 pb⁻¹ of data collected during Run II. The experimental result was compared to three prediction: DIPHOX [18], ResBos [19], and PYTHIA [2]. DIPHOX is a fixed-order QCD calculation that includes all subprocesses at NLO. ResBos includes subprocesses where the two photons are produced at the hard-scattering at NLO, and fragmentation contributions at LO, but re-summation is used to include the effects of initial state gluon radiation. PYTHIA is a parton shower Monte Carlo that contains the processes at LO. Several distributions were examined: the diphoton mass ($m_{\gamma\gamma}$), photon transverse momentum (p_T^γ), and the azimuthal angle between the 2 photons ($\Delta\Phi$). The predictions for the $m_{\gamma\gamma}$ distribution agree fairly well with data, except for the very low mass region, where DIPHOX predicts a higher rate. Because of high gg collision luminosity at low $m_{\gamma\gamma}$, the gg subprocess provides the greatest contribution to the cross section in that region. Low mass $\gamma\gamma$ production therefore

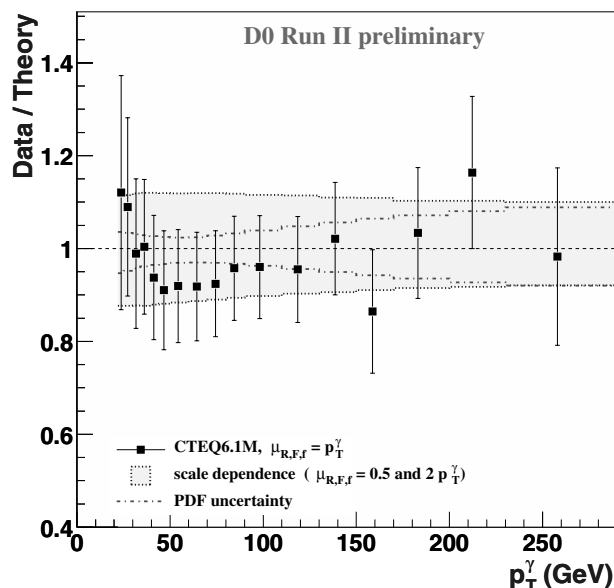


Fig. 4. Ratio of the measured isolated photon cross section to the NLO QCD [15]. Variations due to the choice of scales and PDF uncertainties are shown as blue and red lines, respectively.

serves as an interesting arena for examining production from a qq initial state in preparation for Higgs searches at the LHC. The ResBos prediction for the p_T^γ distribution provides a smooth description over the entire range, while the DIPHOX curve is unstable at low p_T^γ due to the divergence of the fixed-order QCD calculations when $p_T^\gamma \rightarrow 0$. For the $\Delta\Phi$ distribution, the ResBos curve lies above the DIPHOX prediction at values close to $\pi/2$, but lies significantly below the DIPHOX curve at small $\Delta\Phi$. Overall, the differences observed between the predictions are as expected.

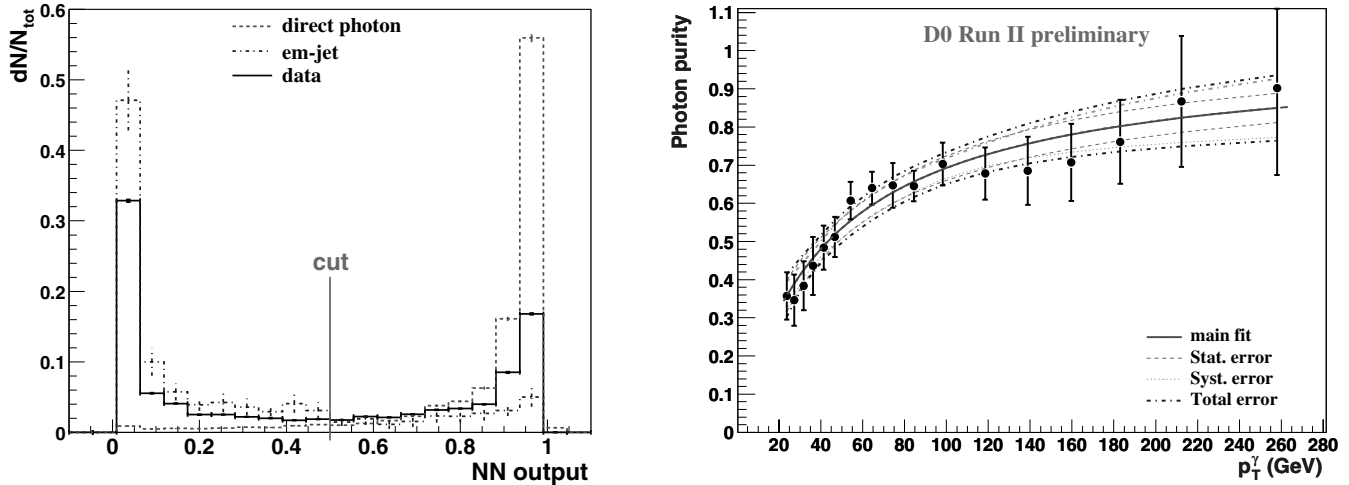


Fig. 3. Normalized distributions of ANN output for data, signal, and background events for the bin of $44 < p_T^\gamma < 50$ GeV (left). Photon purity as determined from a fit to the ANN output shown together with the chosen purity parametrization and the assigned uncertainty (right).

5 Conclusions

I presented recent measurements on dijet azimuthal decorrelations, inclusive heavy-flavor cross sections and photon studies using between 150 and 300 pb^{-1} of recent data recorded by the Tevatron hadron collider experiments. General agreement is observed between data and NLO QCD. The experimental results are approaching a precision that allows detail comparisons with different theoretical prediction and tuning of Monte Carlo event generators. Understanding QCD to the fullest extent is not only important in itself, but also crucial for many precision Standard Model measurements and searches for new physics.

6 Acknowledgments

I would like to thank my collaborators from the CDF and DØ collaborations for their help in preparing this document. I also thank the staffs at Fermilab and collaborating institutions, and acknowledge support from the National Science Foundation (USA).

References

1. V. M. Abazov *et al.*, The DØ Collaboration, Phys. Rev. Lett. **94**, (2005) 221801.
2. G. C. Blazey *et al.*, in Proceedings of the Workshop: QCD and Weak Boson Physics in Run II, edited by U. Baur, R. K. Ellis, and D. Zeppenfeld, Batavia, Illinois (2000) p. 47. See Section 3.5 for details.
3. Z. Nagy, Phys. Rev. Lett. **88**, (2002) 122003.
4. J. Pumplin *et al.*, JHEP **0207**, (2002) 12; D. Stump *et al.*, JHEP **0310**, (2003) 046.
5. G. Marchesini *et al.*, Comput. Phys. Commun. **67**, (1992) 465; G. Corcella *et al.*, JHEP **01**, (2001) 010.
6. T. Sjöstrand *et al.*, Comput. Phys. Commun. **135**, (2001) 238.
7. The PYTHIA parameter PARP(67) was increased from the default of 1.0 to 4.0.
8. T. Affolder *et al.*, Phys. Rev. D **64**, (2001) 032002.
9. V. Abazov *et al.*, Fermilab-PUB-05-034-E.
10. R. Brun and F. Carminati, CERN program library long writeup W5013 (1993).
11. B. Abbott *et al.* (The DØ Collaboration), Phys. Rev. Lett. **86**, (2001) 1156. G. F. Giudice and R. Rattazzi, Phys. Rep. **322**, (1999) 41.
12. ATLAS Collaboration, LHCC/P2 (1994), and LHCC/99-15 (1999). CMS Collaboration, LHCC/P1 (1994).
13. V. Abazov *et al.* (The DØ Collaboration), Phys. Rev. Lett. textbf87, (2001) 251805.
14. C. Peterson *et al.*, “JETNET 3.0. A versatile Artificial Neural Network Package”, Lund University Preprint LU-TP 93-29.
15. P. Aurenche *et al.*, JETPHOX package; S. Catani *et al.*, JHEP textbf0205, (2002) 028.
16. L. E. Gordon and W. Vogelsang, Phys. Rev. D textbf48, (1993) 3136 and Phys. Rev. D textbf50, (1994) 1901.
17. D. Acosta *et al.*, The CDF Collaboration, hep-ex/0412050, accepted by Phys. Rev. Lett..
18. T. Bonoath *et al.*, Eur. Phys. J. C textbf16, (2000) 311.
19. C. Balasz *et al.*, Phys. Rev. D textbf57, (1998) 6934.

Jet Measurements in ATLAS

I. Vivarelli^a

INFN Pisa and the University of Athens

Abstract. The ATLAS strategy for the jet calibration in ATLAS is reviewed here. Top mass precision measurements call for a jet scale precision within 1%. The ATLAS calibration strategy tuning is based on the tuning of the MonteCarlo simulation of the detector with TB data and on the use of the fine granularity of the detector for the identification of electromagnetic and hadronic deposits in the calorimeters.

1 Introduction

A precise knowledge of the jet energy is required for several relevant measurement of the ATLAS physics program. The most evident example is the measurement of the top quark mass in the semileptonic final state: An uncertainty of 1% in the jet scale contributes at 50% to the systematic error on the top mass in the semileptonic channel (the remaining 50% is due to the imperfect knowledge of the background, contributions from ISR and FSR, fragmentation etc.). On the contrary, if the jet scale uncertainty is 5%, its contribution to the final error δm_{top} would be the dominant one.

In the ATLAS calibration scheme, corrections for detector related issues ($e/h > 1$, non-uniformities, cracks) are decoupled from those related to physics issues such as contributions from out of cone energy, ISR, FSR, fragmentation, hadronization, underlying event. The first set of corrections should allow to measure the energy deposited by the particles traversing the detector, while the second set should allow to infer the parton energy. Detailed analysis on the detector corrections to be applied are ongoing. They include studies on the single particle response using test beam data, tuning of the detector simulation on the data, development of clusterization algorithms, calorimeter correction extraction. The corrections for physics related issues, instead, will be extracted directly from the first beam-beam interactions at the startup of the machine.

Preliminary results obtained using corrections extracted directly from jets in QCD events show that a linearity within 1% can be reached in the 20 GeV – 1 TeV jet energy range, with a resolution of $\sigma(E)/E \simeq 65\%/\sqrt{E}$ in the central region of the calorimeters, and an average resolution of $\sigma(E)/E \simeq 88\%/\sqrt{E} + 0.7\%$ in the region $|\eta| < 3.2$.

2 The ATLAS calorimeter

An overall view of the the ATLAS calorimeters [1] is shown in fig. 1. In the central region of the detector ($|\eta| < 1.7$), the ATLAS calorimeter is divided into an electromagnetic and a hadronic section. The EM calorimeter, which consists lead as absorber and Liquid Argon as active material, has three longitudinal sections plus a presampler. The total length at $\eta = 0$ is $22.3 X_0$ (where X_0 is the radiation length), and the granularity in the middle (16 X_0 long) is $\Delta\eta \times \Delta\phi = 0.025 \times 0.025$ (0.003×0.1 in the first sample, 0.05×0.025 in the third one). The hadronic calorimeter (TileCal), which is as well subdivided into three longitudinal sections, uses iron as absorber and plastic scintillator as active material. The resolution obtained exposing a section of the central calorimeter to a pion beam (in 1996 [2]) is:

$$\frac{\sigma(E)}{E} = \left(\frac{41.9\%}{\sqrt{E}} + 1.8\% \right) \oplus \frac{1.8}{E} \quad (1)$$

The End-Cap, which covers up to $|\eta| < 3.2$, uses the same LAr technology in the EM section, while the Hadronic section uses copper as absorber, LAr as active medium. The granularity, which is the same as in the central region if $|\eta| < 2.5$, becomes 0.1×0.1 if $2.5 < |\eta| < 3.2$. The calorimeter coverage is completed by a forward calorimeter, which covers up to $|\eta| < 5$.

3 Cell Clustering

The first step for the jet construction is the clusterization of the cells. At present, two different clustering algorithms are used in ATLAS. The most simple clusterization algorithm builds calorimetric towers associating cells that belong to the same $\Delta\eta \times \Delta\phi = 0.1 \times 0.1$ projective tower. Since the radial development of the shower is not taken into account, noise reduction tool have to be considered in the further steps of the jet reconstruction and calibration.

A more complex clusterization algorithm recently has been developed. It builds topological clusters associating neighbouring cells with a non negligible (compared to the

^a Partly supported by EEC RTN contract HPRN-CT-00292-2002

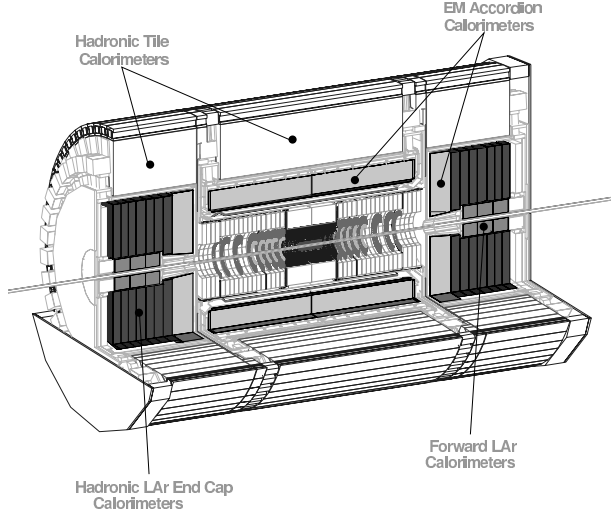


Fig. 1. Overall view of the ATLAS calorimeters.

noise) energy deposit. The clusterization algorithm proceeds with the following steps:

- All the cells with $|E_{cell}| > T_{seed}\sigma_{noise}$ are considered as seeds for the topological clusters. By default, $T_{seed} = 4$. All their neighbouring cells are checked to expand the cluster.
- If $|E_{cell}| > T_{neigh}\sigma_{noise}$, the cell is used to expand the cluster. By default, $T_{neigh} = 2$. Its neighbouring cells are checked to expand the cluster.
- If $|E_{cell}| > T_{used}\sigma_{noise}$, the cell is used to expand the cluster. By default, $T_{used} = 0$.

A split-and-merge procedure is then applied to merge or separate superimposed clusters, on the base of shared energy.

Figure 2 shows the behaviour of the clusterization algorithm for a 120 GeV pion interacting in the end-cap calorimeters (EM+HAD). The event has been recorded during the test beam done at CERN in 2002. The seed is in the middle layer of the EM calorimeter, and the shower develops toward the Hadronic End-Cap calorimeter.

Since the clusterization procedure associates neighbouring cells only when the signal is above a certain energy threshold, it also gives a good rejection against noise.

Detailed studies are undergoing to verify if it possible (using the full granularity of the EM calorimeter and the topological clustering) to separate local pure EM deposits from the rest of the energy deposit. The Monte-Carlo information (opportunistically tuned on the test beam data obtained with both the EM and the HAD calorimeters on the beam line) can then be used to locally calibrate the hadronic deposits. This local approach to the hadronic calorimeter calibration (at present under development) would allow to build jets from already calibrated clusters, thus minimizing the need for further detector corrections after the jet reconstruction.

4 Jet Reconstruction

The most used jet reconstruction algorithm in ATLAS is the seeded cone algorithm, which associates clusters (or towers) in a cone of radius R around a point in the $\eta - \phi$ space. Though expensive in terms of CPU execution time, to avoid infrared and collinear problems, a seedless cone algorithm has also been developed. This allows trial cones to be positioned anywhere in the phase space. Both the seeded and the seedless cone algorithms proceed as follows:

- A cone of radius R is built around the seed (trial seed, in the case of the seedless algorithm).
- For each cluster (tower) k , with center (η^k, ϕ^k) , the center of the cone $C_k = (\eta^{Ck} = \eta^k, \phi^{Ck} = \phi^k)$ is defined. A cluster (tower) i is included in the cone if $\sqrt{(\eta^i - \eta^{Ck})^2 + (\phi^i - \phi^{Ck})^2} \leq R$.
- Then, the E_T -weighted centroid is evaluated:

$$\begin{aligned} \bar{C}^k &= (\bar{\eta}^{Ck}, \bar{\phi}^{Ck}) \\ \bar{\eta}^{Ck} &= \frac{\sum_{i \in C^k} E_{Ti} \eta^i}{E_T^{Ck}} & \bar{\phi}^{Ck} &= \frac{\sum_{i \in C^k} E_{Ti} \phi^i}{E_T^{Ck}} \\ E_T^{Ck} &= \sum_{i \in C^k} E_{Ti} \end{aligned} \quad (2)$$

- In general the centroid \bar{C}^k is not identical to the geometric center C_k and the cone is not stable. Therefore, an iterating procedure is needed until the cone found is stable.
- The described procedure can lead to a final jet list where some of the jets overlap. A *split and merge* procedure has to be used to merge or separate jets which overlaps, in order to avoid the assignment of particles to two jets. The way to deal with this, is to merge two jets if the overlapping energy percentage is above some threshold.

The threshold for the seed in the seeded cone is $E_{Tth} = 2$ GeV, the cone size is $R = 0.7(0.4)$ for low (high) luminosity. Two jets are merged if the overlapping energy is greater than 50% of the energy of the less energetic one.

The K_T algorithm is implemented also:

1. For each cluster (tower) compute $d_i = E_{Ti}^2$. For each pair i, j define

$$d_{ij} = \min(E_{Ti}^2, E_{Tj}^2) \frac{(\eta_i - \eta_j)^2 + (\phi_i - \phi_j)^2}{D^2} \quad (3)$$

where D is a parameter (the current choice in ATLAS is $D = 1$).

2. Find $d_{min} = \min(d_i, d_{ij})$.
3. If $d_{min} = d_{ij}$ for some j , merge tower i and j to a new tower k with momentum $p_k^\mu = p_j^\mu + p_j^\mu$.
4. If $d_{min} = d_i$ then a jet is found.
5. Iterate until the list of tower is empty.

Since the K_T is an $\mathcal{O}(n^3)$ algorithm, a preclustering procedures is applied to reduce the number of input towers (clusters) to be processed.

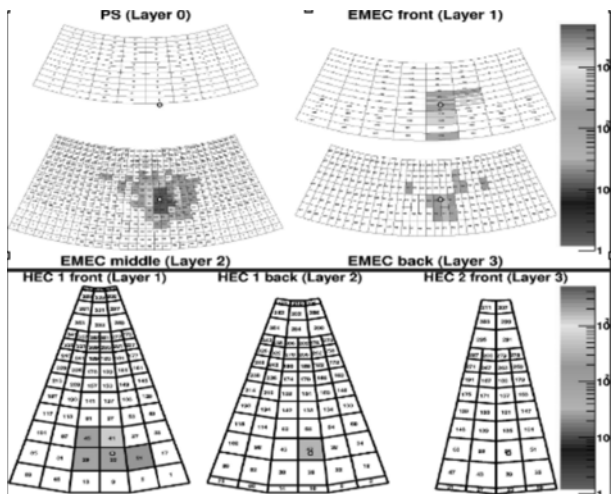


Fig. 2. Behaviour of the topological clusterization algorithm in the end-cap calorimeters for a 120 GeV pion (test beam 2002 data). The figure shows, in color code, the shape of the energy released in the preshower, in the three longitudinal sections of the EMEC and the three sections of the Hadronic End Cap calorimeter.

5 Jet Calibration

The present jet calibration in ATLAS is obtained from full simulated QCD events. Calibration coefficients depending on the cell energy density are extracted comparing the reconstructed energy of the jet with the energy of the reference jet. For the same cell energy density, a different weight is applied for different longitudinal samples and in the different sections of the ATLAS calorimeters. The reference jets are defined running on the MonteCarlo final state particles the same reconstruction algorithm used on the calorimetric clusters. Each reconstructed jet is associated with the closest (in $\Delta R = \sqrt{\Delta\eta^2 + \Delta\phi^2}$) reference jet. Once this association is done, the calibration coefficients can be extracted minimizing a χ^2 :

$$\chi^2 = \sum_e \frac{(E_e^{rec} - E_e^{ref})^2}{(E_e^{ref})^2} \quad (4)$$

The index e runs on all the jets of all the considered events and E_e^{rec} is defined as:

$$E_e^{rec} = \sum_i w_i \left(\frac{E_{ie}}{V_i} \right) E_{ie} \quad (5)$$

where i is running on all the cells belonging to the jet, E_{ie} is the energy deposit in the i -th cell for the jet e and V_i is the volume of the i -th cell.

In order to reduce the number of calibration coefficients to calculate, the dependence of w_i on the cell energy density is parametrized with a polynomial function of $i = \log(E_i/V)$:

$$w_i = a + bi + ci^2 \quad (6)$$

Figure 3 shows the ratio E^{rec}/E^{ref} after the application of the calibration coefficients in the pseudorapidity

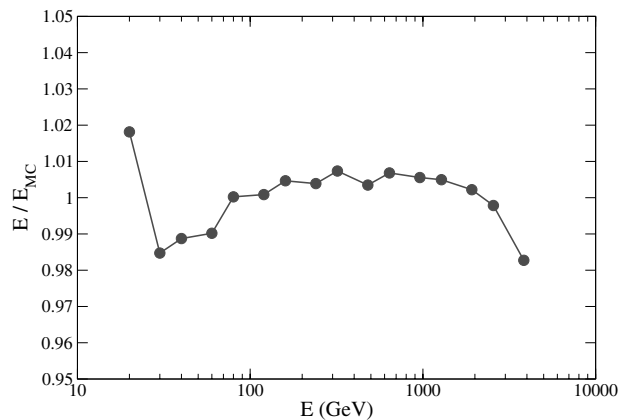


Fig. 3. The ratio E^{rec}/E^{ref} as a function of E^{ref} after the calibration.

region $|\eta| < 3.2$. The jets have been reconstructed using the cone algorithm. The simulation include the electronic noise, while it does not include the contributions from pileup. As it can be seen, the obtained linearity is almost within $\pm 1\%$ for the range $20 \text{ GeV} < E < 1 \text{ TeV}$.

Figure 4 shows instead the resolution obtained on the same pseudorapidity region. The results are fitted with:

$$\frac{\sigma(E)}{E} = \frac{a}{\sqrt{E}} + b \quad (\text{Energy in GeV}) \quad (7)$$

The obtained value for a is 88%, while the result for the constant term b is 0.7%. The resolution obtained for jets in the central calorimeter region ($|\eta| < 0.7$) has stochastic term $a \simeq 65\%$.

6 In Situ Calibration

The corrections for physics issues (contributions from out of cone energy, ISR, FSR, fragmentation, hadronization, underlying event) will be calculated *in situ* with beam-beam collisions. It has been shown ([3]) that the P_T balance in $Z + jet$ events and the constraint on the W mass for top decays can be effectively used to compute the *in situ* corrections. We will discuss here the case of the constraint on the W mass.

Let us consider a sample of $t\bar{t}$ events. For each event, the ratio R between the PDG W mass and the computed W mass can be extracted:

$$R = \frac{M_W^{PDG}}{M_W} = \sqrt{\alpha_1 \alpha_2} \quad (8)$$

where $\alpha_i = E_i^{part}/E_i^{jet}$ (E_i^{jet} is the jet energy obtained applying the corrections previously discussed). The study of the dependence of R on the jet energy allows to extract $\alpha_k = \langle \alpha_1 \alpha_2 \rangle$, whose squared root gives the correction to be applied for the jet. Figure 5 shows the ratio E^{part}/E^{jet} as a function of E^{jet} as obtained using the truth information from the MonteCarlo (theoretical curve). The dependence found using reconstructed $t\bar{t}$ events is also shown. The agreement with the theoretical curve is almost perfect.

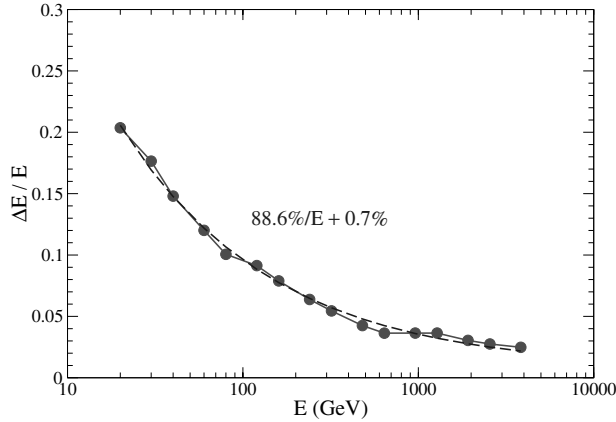


Fig. 4. The resolution $\sigma(E)/E$ as a function of E^{ref} after the calibration.

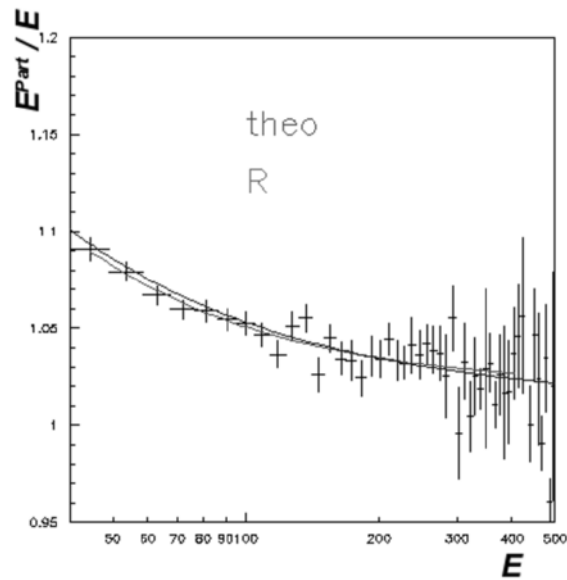


Fig. 5. Theoretical dependence of R from the jet energy. The result is obtained following the procedure described in the text is also shown.

As it is shown in fig. 6 (black error bars), once the obtained corrections are applied to the jets in top events, the linearity that is obtained in the range $50 \text{ GeV} < E < 300 \text{ GeV}$ is within $\pm 1\%$.

In fig. 6 the (preliminary) linearity obtained on $Z + jet$ events applying the corrections obtained from the constraint of the W mass in $t\bar{t}$ events is also shown. Although the linearity is worse (due to the different color structure of the final state, and, thus, to the different hadronization for the jets), it slightly exceeds $\pm 3\%$. Therefore, these preliminary results show that the corrections extracted from $t\bar{t}$ events can be used to calibrate at $\pm 3\%$ level jets in $Z + jet$ event.

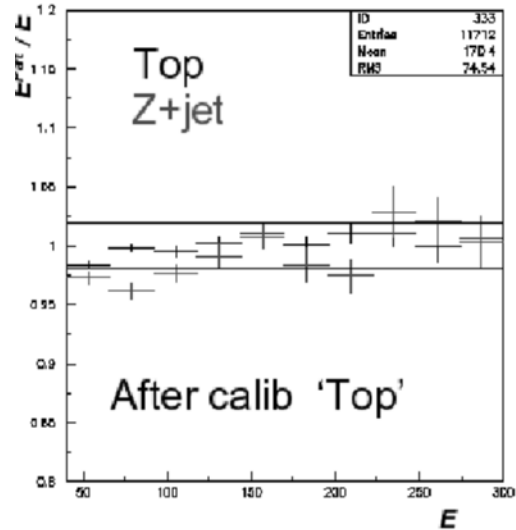


Fig. 6. Linearity obtained using the corrections extracted from the W mass constraint on top events (in black) and in $Z + jet$ events (in red).

7 Conclusions

A huge effort is ongoing in ATLAS to ensure the best hadronic calibration for jet measurement. The calibration strategy foresees to exploit the full calorimeter granularity with the use of topological clusters. They provide a powerful noise reduction tool. Studies are ongoing to develop algorithms able to recognize pure electromagnetic deposits inside the showers. This information, combined with the MonteCarlo predictions for the EM fraction inside the shower, will allow a local calibration, thus minimizing the number of detector corrections to be applied after the jet reconstruction.

At present, the jet reconstruction is implemented using both the cone (seeded and seedless) and the K_T algorithm. The calibration is done applying a cell weighting algorithm, where the weights are obtained minimizing the resolution. The linearity that can be obtained on generic QCD events for the cone algorithm is within $\pm 1\%$ on a large energy range.

In situ corrections can be calculated both from $Z + jet$ and from W decay (coming from the top quark decay) events. A linearity within 1% can be reached. Preliminary results show that the corrections calculated from $t\bar{t}$ events allow to correct at the 3% level the jets in $Z + jet$ events.

References

1. ATLAS Collaboration, CERN/LHCC/94-43, ATLAS Collaboration, (1994)
2. M.Cobal *et al.*, ATL-TILECAL-98-168, (1998).
3. R. Lefèvre and C. Santoni, ATL-PHYS-2002-026, (2002)

Jet energy measurements in CMS

Olga Kodolova¹ (CMS Collaboration)

SINP MSU, Leninsky Gory 1/2, Moscow, Russia

Abstract. The expected performance of CMS for jet energy measurements is discussed. The use of the different calibration methods allows to restore the linearity of the CMS calorimeter relative to jets and improve the jet energy resolution.

1 Introduction

Event signatures for SUSY, Higgs boson production, and other new physics processes require the reconstruction and measurement of jets coming from high-momentum quarks and gluons. The jet energy resolution and linearity are key factors in separating signal events from background and in measuring the properties of the signal.

An example of jet reconstruction in a hard interaction forming QCD dijets, with its characteristic features, is shown in Fig. 1. The parameters of the initial parton corresponding to the particle jet depends on a number of factors including final state radiation, which can lead to the splitting of the jet in the detector. Taking a large cone of $R = 1.5$ in η, ϕ , the jet reconstruction collects a large fraction of the energy of the initial parton. Such a cone is also susceptible to collecting the energy of non-isolated additional partons in the hard interaction in addition to energy from the underlying event, pile-up interactions and electronic noise.

2 CMS detector

A characteristic feature of the CMS detector is its large superconducting solenoid delivering an axial magnetic field of 4 T [2]. The hadron and electromagnetic calorimeters are located inside the coil (except the forward calorimeter) and cover the pseudorapidity range $|\eta| < 5$. The calorimeters are designed to allow jet reconstruction in the full pseudorapidity region. The calorimeter extends to $\eta = 5$, but jets can be measured if their axes lie in the range $|\eta| < 4.5$. At $\eta = 5$, half the jet will be lost. In addition, the CMS detector has a silicon tracker ($|\eta| < 2.4$) which allows track momenta to be determined with a resolution better than 1% for low- p_T tracks (p_T between 0.5 GeV and a few tens of GeV and $|\eta| < 1$).

3 Jet reconstruction

The first step in the reconstruction, before invoking the jet algorithm, is to apply noise and pile-up suppression.

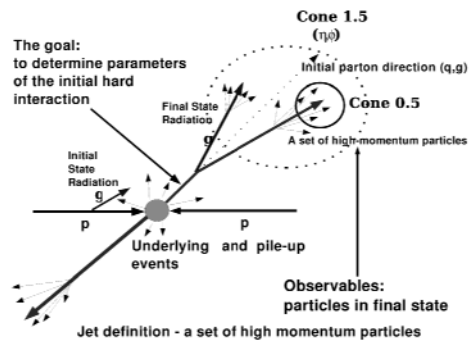


Fig. 1. Complexities in the jet definition arise from several processes include final state radiation, underlying event fragments and the detector-level collection of particle energies.

The second step is to apply one of the jet finding algorithm (iterative cone algorithm, middle point algorithm or Kt algorithm [1]- [3]) and get the jet energy and position.

The factors influencing the reconstructed jet energy can be divided into two groups. In addition to the factors, shown in Figure 1 and connected with the jet as a physical object, jets are affected by the detector performance, e.g electronic noise, magnetic field which deflects low energy charged particles out of the jet reconstruction cone, the responses of the calorimeters to electromagnetic and hadronic showers (e/h ratio), and some other sources of the energy loss. While many of the corrections for effects in the first group are channel dependent, the bulk of the detector effects are more channel independent and common correction coefficients can be provided.

At the third step the calibration methods are applied to restore a correspondence in the measured jet properties between matched reconstructed and particle-level jets.

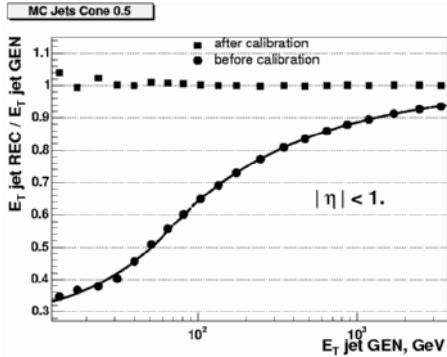


Fig. 2. The ratio of the reconstructed jet transverse energy E_T^{REC} to the generated transverse energy E_T^{MC} as a function of E_T^{MC} for jets with $|\eta_{jet}| < 1$ reconstructed by the iterative cone $R = 0.5$ algorithm before (circles) and after (squares) MC jet calibration.

4 Jet calibration

Algorithms for jet energy corrections may be classified according to the different objects that are used for the corrections.

Jet-based corrections are implemented by weighting the energies from the longitudinal calorimeter compartments.

Cluster-based coefficients are applied separately to electromagnetic and hadronic clusters, separated according to the cluster origin (electron, γ , hadron).

As for track based corrections, the tracks that are deflected from the jet region due to magnetic field can be added to the jet energy reconstructed in calorimeter. The response of charged particles within the jet area can be changed to the momentum (energy) of the tracks giving impact on the ECAL surface inside the jet region.

4.1 Monte Carlo calibration of Jet Response (jet based)

The jets are reconstructed with one of the jet finding algorithms. Particle-level jets are found by applying the same jet algorithm to stable particles (excluding neutrinos and muons). A matching criterion, based on the distance $\Delta R = \sqrt{d\eta^2 + d\phi^2} < 0.2$, is used to associate particle-level and reconstructed jets. The ratio of reconstructed jet transverse energy to the particle-level jet transverse energy as a function of the particle-level jet transverse energy is approximated by the set of functions for the different η regions.

The jet energy linearity and resolution after applying Monte-Carlo corrections are shown in Figs. 2,3 for the iterative cone algorithm.

4.2 The calibration of Jet Response with γ +jet channel (jet based)

The channels of γ/Z +jet and $W^- \rightarrow jj$ (from $t\bar{t}$ production) will give the first estimation of the absolute energy

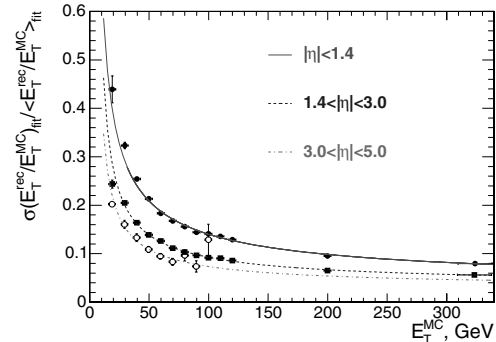


Fig. 3. The jet energy resolution as a function of generated jet energy for the different pseudorapidity intervals.

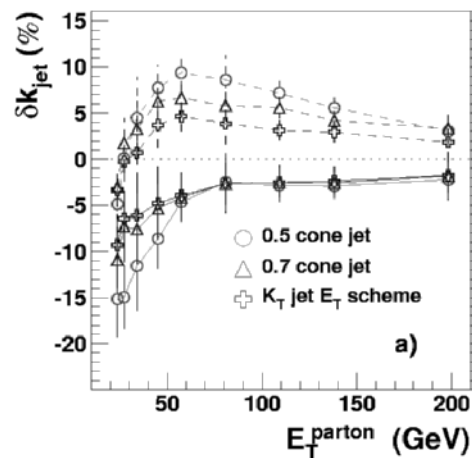


Fig. 4. Relative systematic errors $((k_{jet} - k_{jet}^{true})/k_{jet}^{true})$ on the calibration of the jets initiated by the light quarks (solid lines) and the jets from the QCD sample (including gluons, dashed lines) for the iterative cone algorithm with cone radii of $R = 0.5$ (circles) and $R = 0.7$ (triangles) and for the K_T -cluster algorithm using the E_T -scheme (crosses) for the $E_T^{tower} > 0.5$ GeV.

scale. The jet energy scale is set using the kinematics relationship of transverse momentum balancing between the direct photon and the jet. The measured observable $k_{jet} \equiv \frac{P_T^{jet}}{P_T^{parton}}$ provides an approximate value for the true parton-level calibration of the jet given by $k_{jet}^{true} \equiv \frac{P_T^{jet}}{P_T^{parton}}$. The systematic shifts introduced by the difference between gluon and quark jets are presented in Figure 4.

The correction with γ +jet channel can be applied to particle jet with the additional MC correction taking into account the difference between parton and particle jet: $E_{Tptcl}^{jet} = E_{Tjet}^{parton} \times k_{jet}^{ptcl}$.

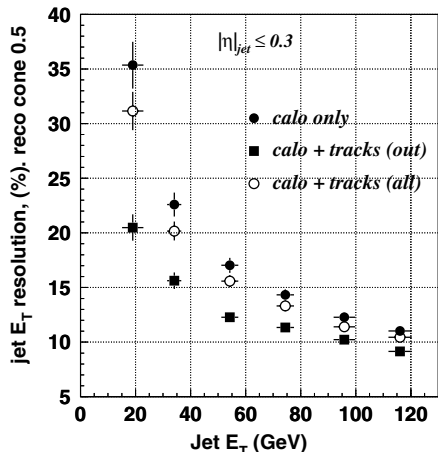


Fig. 5. The jet transverse energy resolution as a function of the original jet transverse energy in a single jet sample; reconstruction with calorimeter only (close circles), out-of-cone tracks (open circles), subtraction procedure of expected responses using library of responses (close squares).

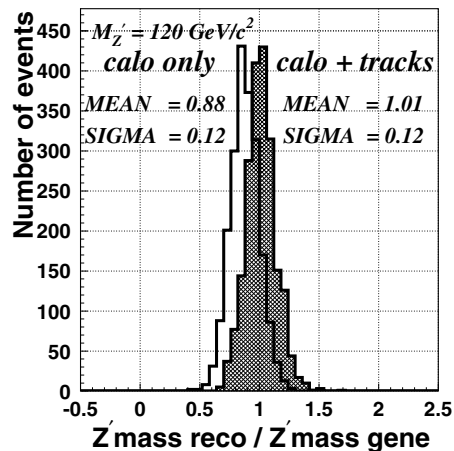


Fig. 6. Ratio of the reconstructed to the generated X mass with calorimeters only (empty histogram) and with calorimeter + tracks corrections (hatched histogram).

4.3 The calibration of Jet Response with use of tracks

A response subtraction procedure was proposed in Ref. [5]. For each track reaching the calorimeter surface within the reconstruction jet area, the expected response is subtracted from the calorimeter jet energy and the track momentum is used instead. This subtraction procedure does not require cluster separation and is therefore well suited to the case of high occupancy or coarse granularity. The momenta of the tracks that reach the calorimeter surface out of the reconstruction cone are simply added to the calorimeter jet energy.

The resolution is improved by a factor 1.7 for 20 GeV jets and by 15% for 100 GeV jets (Fig. 5). The correction

almost completely restores the mass scale and the resolution is improved by 10% (Fig. 6).

References

1. CMS TriDAS Project Data Acquisition and High-Level Trigger Technical Design Report CERN/LHCC 2002-26CMS TDR 6.2
2. CMS ECAL Technical Design Report, CERN/LHCC 97-33 (1997), CMS HCAL Technical Design Report, CERN/LHCC 97-31 (1997), CMS Technical Tracker Design Report, CERN/LHCC 98-6 (1998).
3. M.Toennesmann thesis in preparation
4. S. D. Ellis and D. E. Soper, Phys. Rev. D **48**, 3160 (1993) [arXiv:hep-ph/9305266].
5. O.Kodolova et al.,CMS NOTE-2004/015 (2004), EPJC:<http://dx.doi.org/10.1140/epjcd/s2005-02-004-2>.

Electroweak Physics at the Tevatron and LHC

Electroweak Physics at the Tevatron and LHC: Theoretical Status and Perspectives

Ulrich Baur

Physics Department, State University of New York at Buffalo, Buffalo, NY 14260, USA

Abstract. I review the status of theoretical calculations relevant for electroweak physics at the Tevatron and LHC and discuss future directions. I also give a brief overview of current electroweak data and discuss future expectations.

1 Introduction

Electroweak measurements are a very important part of the physics program of the Tevatron and the LHC. Of particular interest are the search for the Higgs boson and the determination of its properties, and the measurement of electroweak precision observables, in particular the measurement of

- the W mass, M_W , and W width, Γ_W ,
- the effective weak mixing angle, $\sin^2 \theta_{eff}$, and the forward – backward asymmetry, A_{FB} ,
- the W and Z boson cross sections, $\sigma(W)$ and $\sigma(Z)$, and their ratio, $R_{W/Z}$,
- the W forward backward charge asymmetry, $A(\eta_e)$,
- the $\ell^+ \ell^-$ ($\ell\nu$) differential cross sections above the Z (W) peak,
- and di-boson ($W\gamma$, $Z\gamma$, WW , WZ and ZZ) production.

In the following I discuss the physics interest in these measurements, give a brief overview of the current experimental status and what to expect in the future (for more details see Refs. [1] – [3]), and discuss the current status and the prospects of the relevant theoretical calculations.

2 Weak Boson Physics

2.1 Measurement of the W mass

The one-loop corrections to M_W depend quadratically on the top quark mass, m_t , and logarithmically on the Higgs boson mass, m_H . Precise measurements of M_W and m_t thus make it possible to extract information on m_H .

In Run I of the Tevatron, the W mass has been measured to $M_W = 80.456 \pm 0.059$ GeV [4]. The preliminary value of the W mass from LEP2 is $M_W = 80.392 \pm 0.039$ GeV [5]. When combined with the current world average of the top quark mass, $m_t = 172.7 \pm 2.9$ GeV [6], this yields $m_H < 219$ GeV at 95% CL [5] for a Standard Model (SM) Higgs boson.

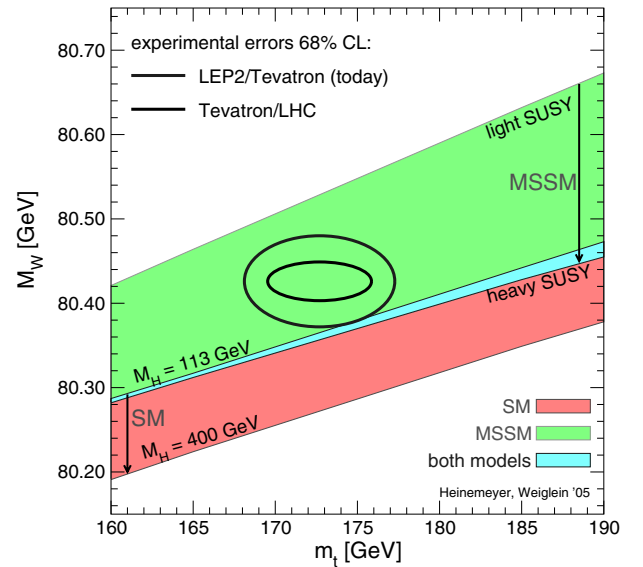


Fig. 1. Constraints on M_W and m_t from LEP2 and Tevatron data, and expectations from the LHC, compared with the predictions of the SM and the MSSM.

In Run II, one hopes to achieve a precision of $\delta M_W = 40$ MeV per lepton channel and experiment for an integrated luminosity of 2 fb^{-1} [7], while the LHC may be able to reach a precision of $\delta M_W \approx 10$ MeV using the W/Z transverse mass ratio and $W \rightarrow \mu\nu$ decays [8]. The present constraints on M_W and m_t from LEP2 and Tevatron data, and the results expected from measurements at the LHC, are compared with theoretical predictions in Fig. 1. Present data clearly favor a light SM Higgs boson, and are also in very good agreement with predictions of the minimal supersymmetric standard model (MSSM) [9].

To ensure that the M_W and m_t measurements contribute equally to the uncertainty in a χ^2 test, the precision on the top quark mass and the W mass should satisfy

the relation [10]

$$\delta M_W \approx 7 \times 10^{-3} \delta m_t. \quad (1)$$

Since one expects to measure the top quark mass with a precision of $\delta m_t = 1 - 2$ GeV at the LHC [11], one needs to determine the W mass with a precision of about $\delta M_W \approx 10$ MeV so that it does not become the dominant uncertainty in the estimate of m_H . Accurate theoretical predictions for W production are absolutely essential in order to measure the W mass with a precision of 10 MeV.

2.2 $\sin^2 \theta_{eff}$

Constraints on m_H can also be derived from the top quark mass and the effective weak mixing angle. At LEP, the effective weak mixing angle has been measured to $\sin^2 \theta_{eff} = 0.23153 \pm 0.00016$ [12]. This will be difficult to improve at the Tevatron or LHC. From a measurement of the forward – backward asymmetry, A_{FB} , at the Tevatron one expects to reach a precision of $\delta \sin^2 \theta_{eff} = 0.0006$ per lepton channel and experiment for an integrated luminosity of 10 fb^{-1} [7]. At the LHC, with 100 fb^{-1} , one hopes to achieve $\delta \sin^2 \theta_{eff} = 0.00014$ using forward electrons in a measurement of A_{FB} in $Z \rightarrow e^+e^-$ events [13].

2.3 The Weak Boson Cross Sections and the W/Z Cross Section Ratio

In the past, the measurement of the W and Z boson cross sections has provided a test of perturbative QCD. With the large data sets of Run II and the LHC, non-statistical uncertainties, in particular the luminosity error, become limiting factors. This is illustrated by the recent $D\bar{O}$ measurements of the W and Z production cross sections [14]

$$\begin{aligned} \sigma(W) \cdot B(W \rightarrow e\nu) &= 2865.2 \pm 8.3(\text{stat}) \pm 62.8(\text{sys}) \\ &\quad \pm 40.4(\text{pdf}) \pm 186.2(\text{lumi}) \text{ pb}, \\ \sigma(Z) \cdot B(Z \rightarrow e^+e^-) &= 264.9 \pm 3.9(\text{stat}) \pm 8.5(\text{sys}) \\ &\quad \pm 5.1(\text{pdf}) \pm 17.2(\text{lumi}) \text{ pb}. \end{aligned}$$

Provided that the W and Z cross sections are accurately predicted by theory, and the PDF uncertainties can be controlled, $\sigma(W)$ and $\sigma(Z)$ can be used as luminosity monitors.

The cross section ratio

$$R_{W/Z} = \frac{\sigma(p\bar{p} \rightarrow W \rightarrow \ell\nu X)}{\sigma(p\bar{p} \rightarrow Z \rightarrow \ell^+\ell^- X)}, \quad (2)$$

together with the theoretical prediction for the ratio of the total W and Z production cross sections, the LEP measurement of the branching ratio $B(Z \rightarrow \ell^+\ell^-)$, and the SM prediction for the $W \rightarrow \ell\nu$ decay width, can be used for an indirect determination of Γ_W . A recent CDF measurement, $\Gamma_W = 2079 \pm 41$ MeV [15], is in good agreement with the SM prediction $\Gamma_W^{SM} = 2092 \pm 3$ MeV [16].

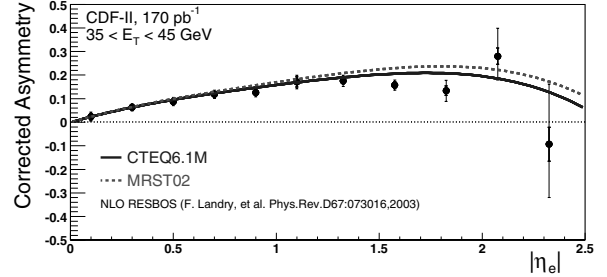


Fig. 2. The W charge asymmetry as a function of η_e for electrons with $35 \text{ GeV} < E_T < 45 \text{ GeV}$ and two different PDF parametrizations.

2.4 Direct Measurement of Γ_W

The width of the W boson can also be measured directly from the tail of the $W \rightarrow \ell\nu$ ($\ell = e, \mu$) transverse mass (M_T) distribution. Unlike the extraction of Γ_W from $R_{W/Z}$, the measurement from the tail of the M_T distribution does not depend on theoretical assumptions; however, the method is currently not as precise as the measurement using $R_{W/Z}$. This is illustrated by the recent combined Tevatron result, $\Gamma_W = 2078 \pm 62(\text{stat}) \pm 60(\text{syst})$ MeV [17]. For 2 fb^{-1} one expects the direct measurement of Γ_W to improve to $\delta\Gamma_W = 50$ MeV per lepton channel and experiment [18].

2.5 The W charge asymmetry

Another important electroweak measurement is that of the W charge asymmetry,

$$A(\eta_e) = \frac{d\sigma(e^+)/d\eta_e - d\sigma(e^-)/d\eta_e}{d\sigma(e^+)/d\eta_e + d\sigma(e^-)/d\eta_e}, \quad (3)$$

where η_e is the rapidity of the electron in $W \rightarrow e\nu$. $A(\eta_e)$ is sensitive to the u - and d -quark components of the PDFs, especially at large values of η_e and the electron transverse energy, E_T . Results from CDF for 170 pb^{-1} of Run II data [19] are shown in Fig. 2.

2.6 Search for New Physics in Drell-Yan Production

Many models of new physics predict new charged (W') or neutral (Z') gauge bosons. One can search for these particles in the high $\ell^+\ell^-$ ($\ell\nu$) invariant (transverse) mass region. Information on the couplings of a Z' boson can be obtained from the forward – backward asymmetry, A_{FB} , at large di-lepton masses. Present $D\bar{O}$ data (200 pb^{-1}) require that $m_{Z'} > 780$ GeV at 95% CL for a SM-like Z' boson [20].

At the LHC, one can discover a Z' boson with $m_{Z'} = 4 - 5$ TeV for 300 fb^{-1} and one will be able to severely constrain the couplings of the new vector boson [21].

2.7 Theory of Single Weak Boson Production

The precision foreseen for electroweak measurements in Run II and at the LHC has to be matched by precise theoretical predictions, ie. QCD and electroweak (EW) radiative corrections have to be under control.

The QCD corrections to the total W and Z boson cross sections at the next-to-next-to-leading (NNLO) level have been known for more than a decade [22]. Recently, the rapidity distribution of the Z boson has been calculated at NNLO, showing a dramatically reduced dependence of the differential cross section on the unphysical renormalization and factorization scales compared with the NLO prediction [23]. Calculations of the resummed QCD corrections to predict the transverse momentum (q_T) distributions of the W and Z bosons are also available [24]. The precise shape of the weak boson q_T distribution for small transverse momenta, however, is still uncertain, in particular at the LHC [25].

With the the uncertainty from unknown higher order QCD corrections approaching the 1% level [23], EW radiative corrections to weak boson production become important. EW corrections may also be enhanced by collinear logarithms near the W and Z resonances, and by Sudakov logarithms at large $\ell^+\ell^-$ and $\ell\nu$ invariant masses. A consistent calculation of EW radiative corrections requires parton distribution functions (PDFs) which take into account QED corrections. Such PDFs exist now [26].

There has been significant progress in the calculation of the EW radiative corrections to W and Z boson production in the past few years. Calculations of the full $\mathcal{O}(\alpha)$ EW corrections are available now [27, 28].

The main effect of the EW corrections in the vicinity of the W and Z resonances is that they shift the W and Z masses extracted from data. The magnitude of the shift is about 50 MeV (150 MeV) for $W \rightarrow e\nu$ ($W \rightarrow \mu\nu$). Since both leptons can radiate photons, the shifts are about twice as large in Z events. The shift is mostly caused by final state photon radiation which is enhanced due to collinear logarithms of the form $(\alpha/\pi) \log(M_{W,Z}^2/m_\ell^2)$, where m_ℓ is the mass of the charged lepton in $W \rightarrow \ell\nu$ or $Z \rightarrow \ell^+\ell^-$. Final state photon radiation distorts the shape of the Breit-Wigner resonance by reducing the peak cross section by 20–30%, and (significantly) enhancing the cross section below the peak. This is shown in Fig. 3 for the Z case with only QED corrections taken into account [29].

Above the W/Z peak, the purely weak corrections become increasingly important, due to Sudakov-like logarithms of the form $(\alpha/\pi) \log^2(\hat{s}/M_{W,Z}^2)$, where \hat{s} is the squared invariant mass of the $\ell^+\ell^-$ or $\ell\nu$ system. This is shown in Fig. 4 for the $e\nu$ transverse mass. The solid line shows the ratio $[d\sigma^{\mathcal{O}(\alpha^3)}/dM_T]/[d\sigma^{Born}/dM_T]$ taking into account the complete $\mathcal{O}(\alpha)$ EW corrections. The dashed line shows the ratio in the pole approximation [27, 28] where the WZ box diagrams responsible for the Sudakov logarithms are absent.

Since the logarithmic terms from the WZ box diagrams change the slope of the M_T distribution, they shift

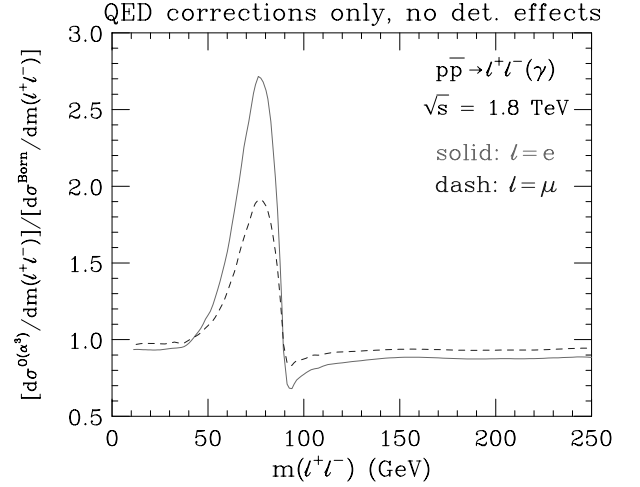


Fig. 3. Ratio of the $\mathcal{O}(\alpha^3)$ and lowest order differential cross sections as a function of the di-lepton invariant mass for $p\bar{p} \rightarrow \ell^+\ell^-(\gamma)$ at $\sqrt{s} = 1.8$ TeV.

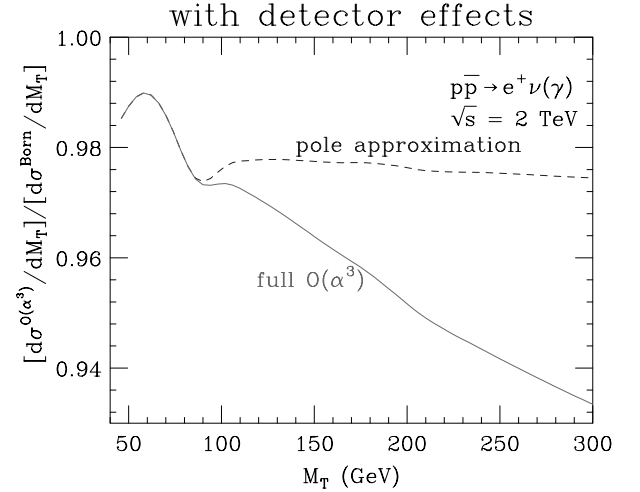


Fig. 4. The ratio $[d\sigma^{\mathcal{O}(\alpha^3)}/dM_T]/[d\sigma^{Born}/dM_T]$ as a function of the transverse mass for $p\bar{p} \rightarrow e^+\nu_e(\gamma)$ at $\sqrt{s} = 2$ TeV.

the W width extracted from the tail of the M_T distribution. This shift, $\delta\Gamma_W \approx -7$ MeV [27], while not large, cannot be neglected if the Run II goal (see Sec. 2.4) should be met.

At the LHC, it will be possible to probe di-lepton invariant and $\ell\nu$ transverse masses of several TeV. In this region, the Sudakov logarithmic terms grow so large that they have to be resummed. Although the resummation of electroweak Sudakov-like logarithms in general four fermion electroweak processes has been discussed in the literature [30, 31], a calculation of $\ell\nu$ production in hadronic collisions which includes resummation of electroweak logarithms has not been carried out yet.

Since final state photon radiation causes a significant shift in M_W and M_Z , one has to worry about multiple (final) state photon radiation in weak boson production. Two photon radiation is known to considerably change

the shape of the dilepton and $\ell\nu$ transverse mass distributions [32]. Recently, there have been several calculations of multi-photon radiation in W [33,34] and Z decays [35]. The shift in the weak boson masses caused by multiple photon radiation is found to be about 10% of the shift originating from one-photon emission [34,35]. For the muon final state, where the shift in the weak boson masses is particularly large, this is a non-negligible effect.

The experimental precision which can be achieved for M_W strongly depends on how well the transverse momentum distribution of the W is known. Knowledge of the W q_T distribution determines the missing transverse energy (E_T) resolution in W events. The E_T resolution determines how “sharp” the edge in the M_T distribution at $M_T \approx M_W$ is, which in turn determines how well M_W can be measured. To constrain the W q_T distribution, one uses data on the transverse momentum distribution of the Z boson, together with a theoretical prediction for the ratio $[d\sigma(W)/dq_T(W)]/[d\sigma(Z)/dq_T(Z)]$. For the W mass measurement one thus needs a calculation which includes both the resummed QCD corrections, the full $\mathcal{O}(\alpha)$ EW corrections, and effects from multiple photon radiation. A first step towards this lofty goal has been taken in Ref. [36], where final state photon radiation was added to a calculation of W boson production which includes resummed QCD corrections.

3 Di-boson Production

3.1 Experimental Results

Di-boson production makes it possible to probe the $WW\gamma$, WWZ , $Z\gamma\gamma$, $ZZ\gamma$ and ZZZ self-couplings (TGCs). For details on these couplings and recent TGC measurements at the Tevatron see Ref. [3]. In the following I concentrate on the $WW\gamma$ and WWZ couplings and briefly summarize recent experimental results for these couplings.

The most general WWV ($V = \gamma, Z$) vertex consistent with Lorentz invariance and electromagnetic gauge invariance has seven free parameters [37]. Assuming C and P conservation, five independent couplings, g_1^Z , κ_V and λ_V , remain. Requiring SU(2) invariance as well, $\lambda_Z = \lambda_\gamma$ and $\kappa_Z = g_1^Z - (\kappa_\gamma - 1) \tan^2 \theta_W$, where θ_W is the weak mixing angle [38], and one is left with three independent couplings. In the SM, at tree level, $g_1^Z = \kappa_V = 1$ and $\lambda_V = 0$. In order to avoid that S -matrix unitarity is violated, deviations of the TGCs from their SM values have to be momentum dependent form factors which depend on the form factor scale, Λ [39]. The form factor scale is related to the scale of the new physics which causes non-SM TGCs.

The WWV couplings can be measured in $e^+e^- \rightarrow W^+W^-$, and in $W\gamma$, WZ and WW pair production at hadron colliders. Assuming C , P and SU(2) invariance, the LEP experiments have determined the independent couplings to [40]

$$\begin{aligned} g_1^Z &= 0.984_{-0.019}^{+0.022}, \\ \kappa_\gamma &= 0.973_{-0.045}^{+0.044}, \\ \lambda_\gamma &= -0.028_{-0.021}^{+0.020}. \end{aligned}$$

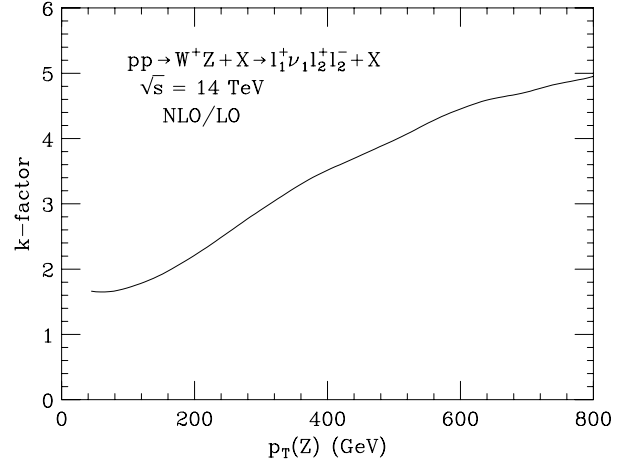


Fig. 5. The ratio of the NLO to LO cross sections as a function of $p_T(Z)$ for W^+Z production at the LHC.

W^+W^- production is sensitive to both the $WW\gamma$ and the WWZ couplings. To measure these couplings independently, one has to consider $W\gamma$ and WZ production in hadronic collisions. Measurements of the $WW\gamma$ couplings in $W\gamma$ production have been performed in Run I [41] and in Run II [3]. The DØ Collaboration recently presented the first direct measurement of the WWZ couplings from WZ production. For 0.3 fb^{-1} , and assuming $\Lambda = 1.5 \text{ TeV}$, they found that [42]

$$\begin{aligned} -0.48 < \lambda_Z < 0.48 & \quad \text{for } \kappa_Z = g_1^Z = 1, \\ 0.51 < g_1^Z < 1.66 & \quad \text{for } \lambda_Z = \kappa_Z - 1 = 0 \end{aligned}$$

at 95% CL. Note that, at hadron colliders, TGC limits depend on the form factor scale, Λ .

Bounds on TGCs from hadron collider experiments scale roughly with $(\int \mathcal{L} dt)^{1/4}$. One thus expects that the ultimate precision which can be reached for the WWV couplings at the Tevatron will be a factor 1.6 to 2.5 better than that obtained from current data, depending on the final integrated luminosity. While the TGC bounds at the Tevatron only mildly depend on the form factor scale, the dependence on Λ is much more pronounced at the LHC. In general, the WWV couplings can be measured with a precision of $\mathcal{O}(10^{-2} - 10^{-3})$ at the LHC [10].

3.2 Theory of Di-boson Production

All di-boson production processes are known to NLO in QCD [43]. At the LHC QCD corrections to di-boson production are large and increase with the p_T of the vector bosons. The ratio of the NLO to LO cross sections (k -factor) for W^+Z production at the LHC as a function of $p_T(Z)$ is shown in Fig. 5. Qualitatively similar results are obtained for the other di-boson processes. Since the QCD corrections give an effect which is qualitatively similar to that of anomalous TGCs, it will be essential to take them into account in any LHC di-boson analysis.

The EW radiative corrections to the di-boson production processes are also known [44]. As in the case of single weak boson production, they become significant at large energies, due to EW Sudakov logarithms. For invariant masses in the TeV region they reduce the cross section by typically 5 – 20%.

4 Higgs Boson Physics

The search for the SM Higgs boson is one of the main objectives of the LHC. Over the last decade, enormous progress has been made in providing accurate predictions for Higgs boson production and decays. In addition, in the last few years, many studies of how well the Higgs properties can be determined once this particle has been found have been performed.

The NLO QCD corrections to Higgs production via gluon fusion have been calculated more than 10 years ago [45]. They enhance the $gg \rightarrow H$ cross section by a factor 1.5 – 2. More recently, several groups have calculated the NNLO QCD corrections to the total $gg \rightarrow H$ cross section in the $m_t \rightarrow \infty$ limit [46], showing that the perturbative series starts to converge at this order. A fully differential NNLO calculation for $gg \rightarrow H \rightarrow \gamma\gamma$ also exists [47]. Finally, the $\mathcal{O}(\alpha)$ corrections to Higgs production via gluon fusion have been computed [48]. They change the Higgs production cross section by 5 – 8% if $m_H = 115 - 160$ GeV.

For $m_H < 200$ GeV, production via vector boson fusion (VBF), $qq' \rightarrow Hqq'$, is an important source for Higgs bosons. The QCD corrections to $qq' \rightarrow Hqq'$ have been found to be modest [49]. Associated production of Higgs bosons and top quarks, $pp \rightarrow t\bar{t}H$, is a tool for measuring the top quark Yukawa coupling. At LO, the $t\bar{t}H$ cross section strongly depends on the factorization and renormalization scales. Once NLO QCD corrections are taken into account, this dependence is greatly reduced [50].

While Higgs production is well under control theoretically, more reliable calculations are still needed for several background processes. In particular, calculations of the NLO QCD corrections are needed for $t\bar{t}j$, $t\bar{t}b\bar{b}$ and EW $WWjj$ production.

Once a Higgs candidate has been found, one would like to determine how the new particle couples to fermions, gauge bosons, and to itself. Several studies have shown that, with mild theoretical assumptions, the couplings of the new particle to fermions and gauge bosons can be measured with a precision of 10 – 30% at the LHC [51].

A measurement of the three Higgs boson self-coupling, λ , with a similar precision is considerably more difficult. In order to probe λ , one has to study Higgs pair production, $gg \rightarrow HH$. For $m_H \geq 150$ GeV, the $HH \rightarrow 4W \rightarrow \ell^\pm \ell'^\pm + 4j$ channel offers the best chances [52,53]. As shown in Fig. 6, with 300 fb^{-1} , it may be possible to rule out a vanishing of λ for $m_H = 150 - 200$ GeV, and measure the HHH coupling with up to 20% accuracy at a SuperLHC with 3 ab^{-1} . For $m_H \leq 140$ GeV, $HH \rightarrow b\bar{b}\gamma\gamma$ is the most promising final state. However, due to the tiny signal cross

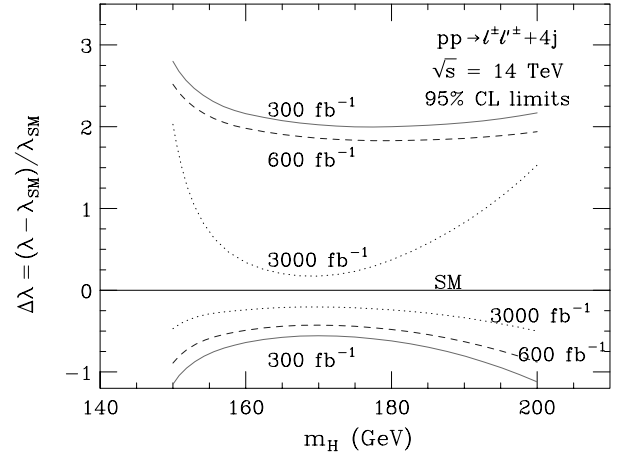


Fig. 6. Limits achievable at 95% CL for the normalized Higgs boson self-coupling, $\Delta\lambda_{HHH} = (\lambda - \lambda_{SM})/\lambda_{SM}$, at the LHC.

section in this channel, a luminosity upgrade for the LHC is needed. Even with 3 ab^{-1} one can only hope to achieve a precision of about 70% for λ [54].

While the signal to background ratio is of $\mathcal{O}(1)$ for $HH \rightarrow b\bar{b}\gamma\gamma$, it is roughly $1/5 - 1/10$ for the $\ell^\pm \ell'^\pm + 4j$ final state. The largest backgrounds contributing to $\ell^\pm \ell'^\pm + 4j$ production originate from $WWjj$, $t\bar{t}W$ and $t\bar{t}j$ production. The $t\bar{t}j$ background is particularly sensitive to the acceptance cuts imposed, and thus tricky to estimate. More realistic simulations for this background are needed. Furthermore, both signal and background cross sections show a significant scale dependence which could be reduced by full calculations of the NLO QCD corrections to $gg \rightarrow HH$ (for finite m_t), and the background reactions. None of these exist at the moment.

5 Summary

Electroweak physics at hadron colliders is precision physics. Accurate predictions are needed to fully utilize the potential of the Tevatron and LHC for electroweak measurements. The theoretical predictions for weak boson and Higgs boson production have become increasingly accurate over the past few years. However, there is still much to do. In particular a calculation which combines QCD and EW radiative corrections for W and Z is needed, as well as calculations of the NLO QCD corrections to a number of processes which contribute to the background in Higgs production.

Acknowledgments

This research was supported by the National Science Foundation under grant No. PHY-0139953.

References

1. S. Protopopescu, these proceedings.

2. M. Lancaster, these proceedings.
3. A. Goshaw, these proceedings.
4. V. M. Abazov *et al.* [CDF and DØ Collaborations], Phys. Rev. D **70** (2004) 092008.
5. M. Grünewald, talk given at the EPS2005 conference, Lisbon, Portugal, July 2005; C. Diaconu, arXiv:hep-ex/0510035.
6. The CDF and DØ Collaborations, arXiv:hep-ex/0507091.
7. R. Brock *et al.*, arXiv:hep-ex/0011009.
8. A. Schmidt, Diplomarbeit, Universität Karlsruhe, Germany, 2004; F. Gianotti, ATL-PHYS-99-001.
9. S. Heinemeyer and G. Weiglein, arXiv:hep-ph/0012364; A. Djouadi *et al.*, Phys. Rev. Lett. **78** (1997) 3626; Phys. Rev. D **57** (1998) 4179; S. Heinemeyer and G. Weiglein, JHEP **0210** (2002) 072.
10. S. Haywood *et al.*, arXiv:hep-ph/0003275.
11. M. Beneke *et al.*, arXiv:hep-ph/0003033.
12. S. Schael *et al.* [The ALEPH, DELPHI, L3, OPAL and SLD Collaborations], arXiv:hep-ex/0509008.
13. K. Sliwa, S. Riley, and U. Baur, ATL-PHYS-2000-018.
14. The DØ Collaboration, DØnote 4403-Conf (2004).
15. A. Abulencia *et al.* [CDF Collaboration], arXiv:hep-ex/0508029.
16. K. Hagiwara *et al.* [Particle Data Group], Phys. Rev. D **66** (2002) 010001.
17. B. Ashmankas *et al.* [Tevatron Electroweak Working Group], arXiv:hep-ex/0510077.
18. D. Amidei *et al.* [TeV-2000 Study Group], SLAC-REPRINT-1996-085.
19. D. Acosta *et al.* [CDF Collaboration], Phys. Rev. D **71** (2005) 051104.
20. The DØ Collaboration, DØnote 4375-CONF (2004).
21. See <http://cmsdoc.cern.ch/cms/PRS/results/susybsm/susybsm.html>.
22. W. L. van Neerven and E. B. Zijlstra, Nucl. Phys. B **382** (1992) 11 [Erratum-ibid. B **680** (2004) 513].
23. C. Anastasiou *et al.*, Phys. Rev. Lett. **91** (2003) 182002; Phys. Rev. D **69** (2004) 094008.
24. C. Balazs, J. W. Qiu and C. P. Yuan, Phys. Lett. B **355** (1995) 548.
25. S. Berge *et al.*, Phys. Rev. D **72** (2005) 033015.
26. A. D. Martin *et al.*, Eur. Phys. J. C **39** (2005) 155.
27. U. Baur *et al.*, Phys. Rev. D **65** (2002) 033007.
28. S. Dittmaier and M. Krämer, Phys. Rev. D **65** (2002) 073007; U. Baur and D. Wackerroth, Phys. Rev. D **70** (2004) 073015.
29. U. Baur, S. Keller and W. K. Sakumoto, Phys. Rev. D **57** (1998) 199.
30. P. Ciafaloni and D. Comelli, Phys. Lett. **B446** (1999) 278.
31. J. H. Kühn *et al.*, Nucl. Phys. B **616** (2001) 286 [Erratum-ibid. B **648** (2003) 455]; J. H. Kühn, A. A. Penin and V. A. Smirnov, Eur. Phys. J. C **17** (2000) 97; M. Beccaria *et al.*, Phys. Rev. D **61** (2000) 073005; J. H. Kühn and A. A. Penin, arXiv:hep-ph/9906545.
32. U. Baur and T. Stelzer, Phys. Rev. D **61** (2000) 073007.
33. W. Placzek and S. Jadach, Eur. Phys. J. C **29** (2003) 325.
34. C. M. Carloni Calame *et al.*, Eur. Phys. J. C **33** (2004) S665.
35. C. M. Carloni Calame *et al.*, JHEP **0505** (2005) 019.
36. Q. H. Cao and C. P. Yuan, Phys. Rev. Lett. **93** (2004) 042001.
37. K. Hagiwara *et al.*, Nucl. Phys. B **282** (1987) 253.
38. K. Hagiwara *et al.*, Phys. Lett. B **283** (1992) 353; Phys. Rev. D **48** (1993) 2182.
39. U. Baur and D. Zeppenfeld, Phys. Lett. B **201** (1988) 383.
40. The LEP Collaborations, LEPEWWG/TGC/2005-01.
41. See J. Ellison and J. Wudka, Ann. Rev. Nucl. Part. Sci. **48** (1998) 33 and references therein.
42. V. M. Abazov *et al.* [DØ Collaboration], Phys. Rev. Lett. **95** (2005) 141802.
43. J. Ohnemus and J. F. Owens, Phys. Rev. D **43** (1991) 3626; J. Ohnemus, Phys. Rev. D **44** (1991) 1403; Phys. Rev. D **44** (1991) 3477; Phys. Rev. D **47** (1993) 940; U. Baur, T. Han and J. Ohnemus, Phys. Rev. D **48** (1993) 5140; Phys. Rev. D **51** (1995) 3381; Phys. Rev. D **53** (1996) 1098; Phys. Rev. D **57** (1998) 2823; J. M. Campbell and R. K. Ellis, Phys. Rev. D **60** (1999) 113006; L. J. Dixon, Z. Kunszt and A. Signer, Nucl. Phys. B **531** (1998) 3; Phys. Rev. D **60** (1999) 114037; K. L. Adamson, D. de Florian and A. Signer, Phys. Rev. D **65** (2002) 094041; Phys. Rev. D **67** (2003) 034016.
44. E. Accomando, A. Denner and S. Pozzorini, Phys. Rev. D **65** (2002) 073003; E. Accomando, A. Denner and A. Kaiser, Nucl. Phys. B **706** (2005) 325; E. Accomando, A. Denner and C. Meier, arXiv:hep-ph/0509234; W. Hollik and C. Meier, Phys. Lett. B **590** (2004) 69.
45. M. Spira *et al.*, Nucl. Phys. B **453** (1995) 17.
46. R. V. Harlander and W. B. Kilgore, Phys. Rev. Lett. **88** (2002) 201801; C. Anastasiou and K. Melnikov, Nucl. Phys. B **646** (2002) 220; V. Ravindran, J. Smith and W. L. van Neerven, Nucl. Phys. B **665** (2003) 325.
47. C. Anastasiou, K. Melnikov and F. Petriello, arXiv:hep-ph/0501130.
48. U. Aglietti *et al.*, Phys. Lett. B **600** (2004) 57; G. Degrossi and F. Maltoni, Phys. Lett. B **600** (2004) 255.
49. T. Han, G. Valencia and S. Willenbrock, Phys. Rev. Lett. **69** (1992) 3274; T. Figy, C. Oleari and D. Zeppenfeld, Phys. Rev. D **68** (2003) 073005; E. L. Berger and J. Campbell, Phys. Rev. D **70** (2004) 073011.
50. W. Beenakker *et al.*, Nucl. Phys. B **653** (2003) 151; L. Reina, S. Dawson and D. Wackerroth, Phys. Rev. D **65** (2002) 053017; S. Dawson *et al.*, Phys. Rev. D **67** (2003) 071503; S. Dawson *et al.*, Phys. Rev. D **68** (2003) 034022.
51. M. Dührssen *et al.*, Phys. Rev. D **70** (2004) 113009 and references therein.
52. F. Gianotti *et al.*, Eur. Phys. J. C **39** (2005) 293.
53. U. Baur, T. Plehn and D. L. Rainwater, Phys. Rev. Lett. **89** (2002) 151801; Phys. Rev. D **67** (2003) 033003; Phys. Rev. D **68** (2003) 033001.
54. U. Baur, T. Plehn and D. L. Rainwater, Phys. Rev. D **69** (2004) 053004.

W/Z Production Cross Sections and Asymmetries at $\sqrt{s} = 1.96$ TeV

Serban Protopopescu^{1,2}

¹ for CDF and DØ collaboration

² Brookhaven National Laboratory

Abstract. We review recent measurements of W and Z boson production cross sections and asymmetries by the DØ and CDF collaborations in $p\bar{p}$ collisions at the FNAL Tevatron at $\sqrt{s} = 1.96$ TeV.

1 Introduction

The standard model (SM) makes precise predictions concerning the production of W and Z bosons in high energy $p\bar{p}$ collisions. At the present Tevatron energy and luminosity they are a copious source of high p_T leptons. Measuring their production cross sections and distributions provide not only a precision test of the standard model but also invaluable checks of the detector performance and the luminosity measurements. W events are characterized by a single high transverse momentum ($p_T > 15$ GeV) lepton and large missing transverse energy ($\cancel{E}_T > 15$ GeV), and Z events by two high p_T leptons.

CDF and DØ have recorded by the summer of 2005 close to 1 fb^{-1} of integrated luminosity ($\int L dt$). The results presented here are based on a relatively small fraction of the available data.

2 $W/Z \rightarrow \mu$'s or $\rightarrow e$'s

CDF and DØ have very similar criteria for finding W and Z bosons decaying to e 's. Events are selected with a single or double e trigger, and with additional requirements offline: (i) at least one central ($|\eta| < 1.0$) isolated e 's with $p_T > 25$ GeV (isolation criteria $E_T^{iso} < 0.1 \times E_T^e$ where E_T^{iso} is the calorimeter energy a cone $R = \sqrt{(\Delta\phi)^2 + (\Delta\eta)^2} < 0.4$ around the e and, for the W candidates, (ii) $\cancel{E}_T > 25$ GeV. Figure 1 shows the transverse mass distribution of W boson candidates for both experiments, they are very similar and the difference in number of events is due mostly to the different integrated luminosities (72 pb^{-1} for CDF and 177 pb^{-1} for DØ) of the analyzed samples. They differ in the criteria for selecting the 2nd e for Z candidates, CDF having much looser requirements ($|\eta| < 2.8$ with no track match) while DØ has almost the same requirements as for the 1st e (just slightly looser calorimeter-track matching criteria). CDF has selected 37,584 W boson and 4242 Z boson candidates, DØ 116,569 W boson and 4625 Z boson candidates. In the case of W and Z bosons decaying

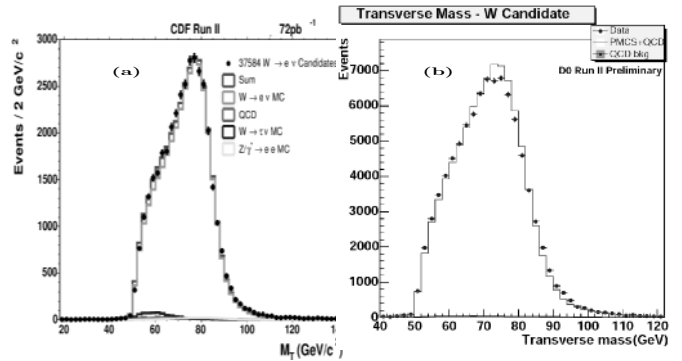


Fig. 1. Transverse mass (μ, \cancel{E}_T) from (a) CDF and (b) DØ events. Points are data, histograms Monte Carlo

to μ both experiments select events with either a single or double muon trigger and require offline $\cancel{E}_T > 20$ GeV and isolated μ 's. However, there are significant differences in the μ selection criteria. For CDF the μ 's must have $|\eta| < 1.0$, with isolation criteria $E_T^{iso} < 0.1 \times p_T^\mu$ in a cone of $R < 0.4$, at least one μ must have $p_T^\mu > 20$ GeV and a 2nd $p_T^\mu > 10$ GeV. DØ exploits the wider acceptance of their muon system by including μ 's up to $|\eta^\mu| < 2.0$ and requires $p_T^\mu > 20$ GeV for any μ . The DØ μ isolation criteria are different for W bosons and Z bosons. In the first case DØ uses an instantaneous luminosity dependent isolation ($E_T^{iso} < 1.5 \times 0.75 \times \mathcal{L}_T$), while for Z bosons it is $E_T^{iso} < 3.5$ GeV and require in addition that the $\sum p_T$ of tracks in a cone of $R < 0.4$ around the muon be < 2.5 GeV. Figure 2 shows the invariant mass of muon pairs from CDF and DØ events. The much narrower CDF peak illustrates the higher resolution of the CDF tracking system, the larger number of DØ events illustrates the higher acceptance of its muon system. CDF has selected 31,722 W boson and 1785 Z boson candidates ($\int L dt = 72 \text{ pb}^{-1}$),

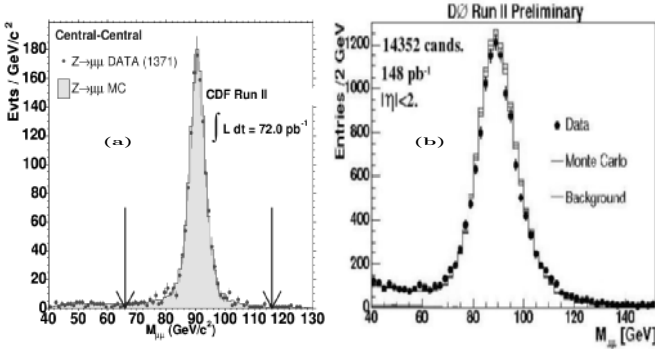


Fig. 2. Invariant mass($\mu\mu$) from (a) CDF and (b) DØ events. Points are data, histograms Monte Carlo

Table 1. $\sigma(W, Z) \times BR$

	CDF $\pm_{stat} \pm_{sys}$	DØ $\pm_{stat} \pm_{sys}$
$W \rightarrow \mu\nu_\mu$	$2768 \pm 16 \pm 64$ $\pm 166_{lum}$	$2989 \pm 15 \pm 81$ $\pm 194_{lum}$
$Z \rightarrow \mu\mu$	$248 \pm 5.9 \pm 7.6$ $\pm 15_{lum}$	$291 \pm 3.0 \pm 6.9$ $\pm 18.9_{lum}$
$W \rightarrow e\nu_e$	$2780 \pm 14 \pm 60$ $\pm 166_{lum}$	$2865 \pm 8.3 \pm 76$ $\pm 186_{lum}$
$Z \rightarrow ee$	$255.8 \pm 3.9 \pm 5.5$ $\pm 15_{lum}$	$264.9 \pm 3.9 \pm 9.9$ $\pm 17.2_{lum}$
$\sigma(W)/\sigma(Z)$	$10.92 \pm 0.15 \pm 0.14$	$10.82 \pm 0.16 \pm 0.28$
$\Rightarrow \Gamma_W$	2079 ± 41 MeV	2098 ± 74 MeV
Theory	2092.1 ± 2.5 MeV	

DØ 62,285 W boson candidates ($\int Ldt = 96 \text{ pb}^{-1}$) and 14,352 Z boson candidates ($\int Ldt = 148 \text{ pb}^{-1}$).

From these sample of events CDF and DØ calculate the W and Z production cross sections times branching ratios ($\sigma \times BR$). The results are given in table 1, the contribution to systematic uncertainties from detector effects, background and PDF are listed in table 2. In addition there is an overall 6.5% uncertainty from the luminosity determination. From the ratios $\sigma(Z) \times BR/(\sigma(W) \times BR)$ one can extract Γ_W also shown in the table 1. All measurements are in good agreement with SM expectations. The CDF results have been published [1].

With a somewhat larger sample of data ($\int Ldt = 127 \text{ pb}^{-1}$) CDF has shown that the jet multiplicity ($E_T^{jet} > 15 \text{ GeV}$, $|\eta_{det}^{jet} < 2.4$) in $W \rightarrow e\nu + n$ jets is in good agreement with theory (as calculated by Alpgen Monte Carlo [2] using a renormalization scale of $\langle p_T^2 \rangle$). A similar result is obtained by DØ for $Z/\gamma^* \rightarrow ee + n$ jets ($E_T^{jets} > 20 \text{ GeV}$, $|\eta_{det}^{jet} < 2.5$) except the normalization scale used is $M_Z^2 + \sum(p_T^{jet})^2$.

DØ has measured also the differential cross sections $\frac{d\sigma}{dY}(Z/\gamma^* \rightarrow ee)$ and $\frac{d\sigma}{dM}(Z/\gamma^* \rightarrow ee)$ using a sample of $\int Ldt = 337 \text{ pb}^{-1}$. The resulting $\frac{d\sigma}{dY}$ distribution (shown

Table 2. Systematic uncentrtainties (%)

	CDF	DØ	CDF	DØ
	$\sigma \times BR(W \rightarrow \mu\nu_\mu)$		$\sigma \times BR(Z \rightarrow \mu\mu)$	
detector	2.3	2.3	3.0	1.7
background	0.4	0.9	0.4	0.3
PDF	1.3	0.8	2.1	1.7
	$\sigma \times BR(W \rightarrow e\nu_e)$		$\sigma \times BR(Z \rightarrow ee)$	
detector	2.0	2.2	2.2	3.1
background	0.8	0.3	0.7	0.8
PDF	1.3	1.4	0.7	1.9

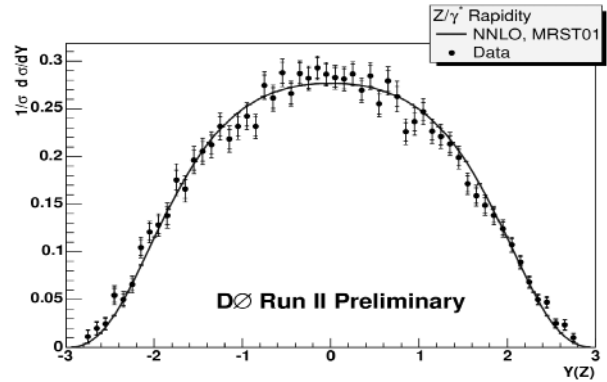


Fig. 3. $\frac{d\sigma}{dY}(Z/\gamma^* \rightarrow ee)$ vs Y . The curve is from Anastasiou et al. [3]

in Figure 3) is in good agreement with the predicted next-to-next leading order (NNLO) curve [3]. Large rapidity (Y) probes quarks with low x (~ 0.001). The $\frac{d\sigma}{dM}$ (not shown) is also in good agreement with NNLO prediction [4].

3 $W/Z \rightarrow \tau$'s

The identification of τ leptons is more difficult than that of e 's and μ 's due to the fact that τ 's have very short lifetimes and decay a short distance from the interaction point to $e(\mu)\nu_e(\nu_\mu)\nu_\tau$ or hadrons + ν_τ . Only the charged leptons or hadron remnants can be observed in the detector. The hadron remnants will appear as narrow jets and need to be separated from the far more copious jets produced by strong interaction processes. CDF and DØ have adopted somewhat different strategies for identifying τ 's. CDF defines τ candidates as narrow energy clusters in the calorimeter associated with charged tracks + π^0 's with an invariant mass smaller than the τ mass plus a requirement that no more than 80% of the cluster energy be in the electromagnetic calorimeter to remove electrons.

The CDF requirements for finding W candidates are $E_T^\tau > 25 \text{ GeV}$, $|\eta^\tau| < 1.0$ and $E_T > 25 \text{ GeV}$. These are fairly stringent requirements and only 2345 events are found in a sample with $\int Ldt = 72 \text{ pb}^{-1}$ (a factor of 20 less than in e or μ channels, see section 2) with an esti-

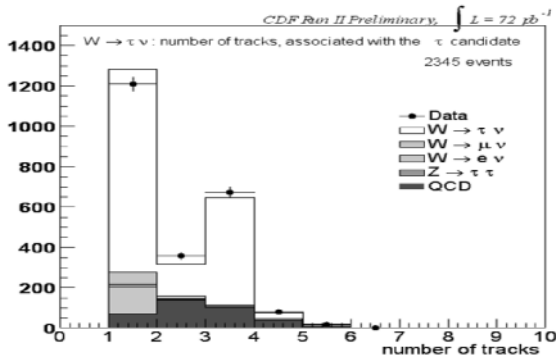


Fig. 4. $\tau \rightarrow$ hadrons track multiplicities in CDF $W \rightarrow \tau\nu$ candidates

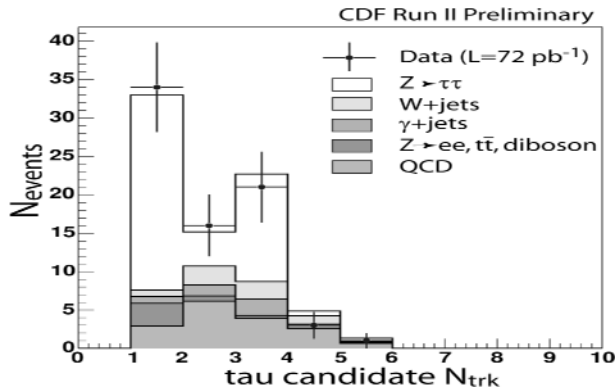


Fig. 5. $\tau \rightarrow$ hadrons track multiplicities in CDF $Z \rightarrow \tau\tau$ candidates

ated background of 26%. Figure 4 shows the track multiplicity distribution for the $\tau \rightarrow$ hadrons candidates and the expected distribution of the background. With the number of events observed the measured $\sigma \times BR(W \rightarrow \tau\nu)$ is $2670 \pm 70_{stat} \pm 210_{stat} \pm 160_{lum}$ pb. From the ratio of this cross section to $\sigma \times BR(W \rightarrow e\nu)$ one can extract the ratio of the couplings $g_\tau^W/g_e^W = 0.99 \pm 0.04$ which should be 1.0 if lepton universality holds. Combining this measurement with the run I CDF and DØ measurements (0.97 ± 0.07 and 0.98 ± 0.031 respectively [3]) gives a Tevatron average of 0.984 ± 0.025 , to be compared with the LEP average of 1.026 ± 0.014 [6].

To find Z candidates CDF uses the channel with one $\tau \rightarrow e + \nu$ and the other $\tau \rightarrow$ hadrons $+\nu$. The event selection requires $E_T^e > 10$ GeV, $|\eta^e| < 1.0$, $E_T^\tau > 15$ GeV, $|\eta^\tau| < 1.0$, $p_T(e) + p_T(\cancel{E}_T) > 25$ GeV, and $M_T(e, \cancel{E}_T) < 25$ GeV. With these requirements 72 events are left with 36% background (in $\int Ldt = 72$ pb $^{-1}$ sample). Figure 5 shows the track multiplicity distribution for the $\tau \rightarrow$ hadrons candidates and the expected distribution of the background. From this sample one obtains $\sigma \times BR(Z \rightarrow \tau\tau) = 246 \pm 48_{stat} \pm 26_{sys} \pm 15_{lum}$ pb.

DØ selects τ candidates following at first similar steps as CDF: a narrow calorimeter cluster with associated tracks and electromagnetic (EM) subclusters consistent with the τ mass. But after that the τ candidates are classified by τ -type: (1) only one track with no EM subclus-

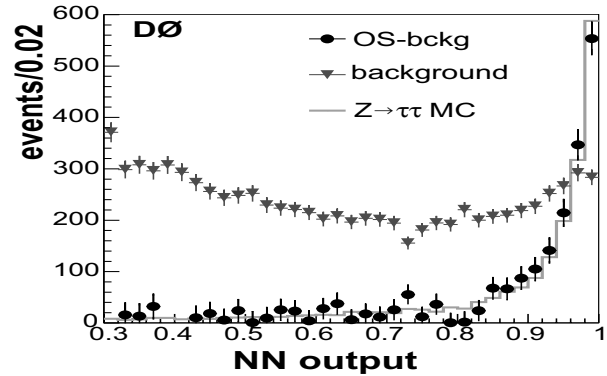


Fig. 6. $\tau \rightarrow$ hadrons NN output distributions in DØ $Z \rightarrow \tau\tau$ candidates

ters, (2) only one track with at least one EM subcluster, and (3) more than one track and any number of EM subclusters. Separate neural network (NN) for each τ -type are then trained to distinguish between τ 's and jets. The training samples are jets recoiling against non-isolated μ 's and single τ 's generated uniformly distributed in E_T and η by Monte Carlo. The NN output (NN) is 0 for jet-like and 1 for τ -like. In order to measure $\sigma \times BR(Z \rightarrow \tau\tau)$, events selected have a single isolated μ with $p_T^\mu > 12$ GeV and $|\eta^\mu| < 2.0$ (which may come from $\tau \rightarrow \mu\nu$), and a τ candidate with $NN > 0.8$, $|\eta^\tau| < 3.0$, $E_T^\tau > 10(5)$ GeV, and $\sum p_T^{tracks} > 7(5)$ GeV for τ -types 1 and 3 (2). An additional requirements is that the μ and τ be back-to-back ($|\phi_\tau - \phi_\mu| > 2.5$). Note that no attempt is made to separate τ 's from e 's as the main source of μe pairs are $\tau\tau$ pairs. The final sample of 2952 events (from $\int Ldt = 226$ pb $^{-1}$) is split into two: 944 events with same sign charge (SS) $\mu\tau$ pairs and 2008 opposite sign charge (OS) $\mu\tau$ pairs. The OS sample contains the signal and the SS sample is used to estimate part of the background. The total background in the OS sample is calculated to be 1112 events (75% from $b\bar{b}$ jets, 18% from W +jets and 7% from $Z \rightarrow \mu\mu$). Figure 6 shows the NN distribution (for $NN > 0.3$) of the calculated background, the OS - background and the predicted from $Z \rightarrow \tau\tau$. The predicted and observed distributions are in very good agreement. From these events one obtains $\sigma \times BR(Z \rightarrow \tau\tau) = 237 \pm 15_{stat} \pm 18_{sys} \pm 15_{lum}$ pb. This result has been published in [4].

4 $Z/\gamma^* \rightarrow ee$ Forward Backward Asymmetry

The e^+e^- pairs produced in $p\bar{p}$ collisions should show a large asymmetry and rapid variation near M_Z because of the interference between Z and γ^* exchanges. The interference has the form

$$d\sigma/d\cos\theta = A(1 + \cos^2\theta) + B\cos\theta$$

The forward backward asymmetry (A_{FB}) is defined as

$$A_{FB} = 3B/8A = \frac{\sigma(\theta > 0) - \sigma(\theta < 0)}{\sigma(\theta > 0) + \sigma(\theta < 0)}$$

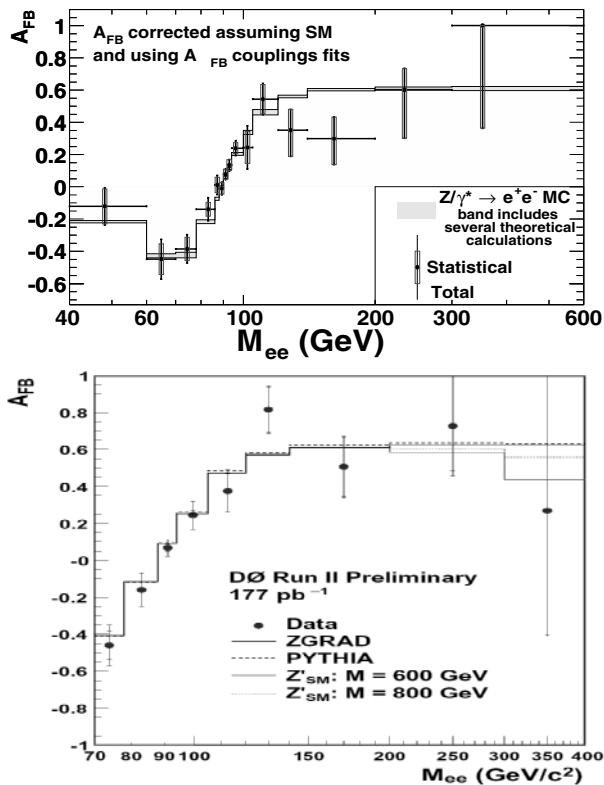


Fig. 7. $A_{FB}(Z/\gamma^* \rightarrow ee)$ as function of M_{ee} from CDF and $D\bar{O}$ events

where θ is the angle between the same sign charged incoming quark and the outgoing lepton. A_{FB} has different dependence as function of M_{ee} for u and d quarks. A new resonance could interfere with γ and Z leading to deviations from SM expectations. Both CDF and $D\bar{O}$ have measured A_{FB} using their $Z/\gamma^* \rightarrow ee$ samples and find good agreement with SM, see Figure 7.

5 $W \rightarrow e\nu$ Charge Asymmetry

Because u quarks carry a larger fraction of the p momentum the W^+ is boosted in the p direction. Equivalently the W^- is boosted in the \bar{p} direction. This leads to a charge asymmetry that varies with η and probes the u and d parton distribution functions. The charge asymmetry is defined as

$$A = \frac{d\sigma(e^+)/d\eta - d\sigma(e^-)/d\eta}{d\sigma(e^+)/d\eta + d\sigma(e^-)/d\eta} \simeq \frac{d(x)}{u(x)}$$

Wide η coverage is essential for meaningful measurements. CDF has measured A for different intervals of E_T^e with a 170 pb^{-1} sample, figure 8 shows the interval $25 < E_T^e < 35 \text{ GeV}$ which exhibits the largest effect. All intervals are in good agreement with the SM predictions as calculated by F. Landry et al. [9].

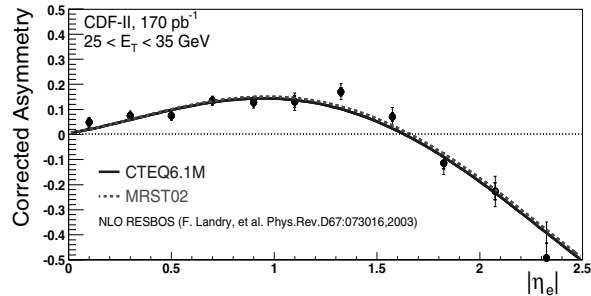


Fig. 8. $W \rightarrow e\nu$ charge asymmetry as function of $|\eta|$ for CDF events with $25 < E_T^e < 35$

6 Conclusion

Electroweak measurements with lepton channels have achieved precision of a few % at the Tevatron using only a fraction of the recorded integrated luminosity. All the results are consistent with the SM and provide detailed checks on the performance of the CDF and $D\bar{O}$ detectors. These measurements are the foundation of many important analyses and searches for physics beyond the SM.

7 Acknowledgements

The author wishes to thank the CDF and $D\bar{O}$ collaborations for providing all the results presented here.

References

1. D. Acosta et al. (CDF collaboration), Phys. Rev. Lett. **94**, (2005) 091803.
2. "ALPGEN, a generator for hard multiparton processes in hadronic collisions", Mangano et al. JHEP0307:001 (2003)
3. Anastasiou et al., Phys. Rev. **D69**, (2004) 09008
4. R. Hamberg, W. L. van Neerven, and T. Matsuura, Nucl. Phys. **B359**, 343 (1991)
5. F. Abe et al. (CDF collaboration), Phys. Rev. Lett. **68** (1992) 3398. , B. Abbot et al. ($D\bar{O}$ collaboration), Phys. Rev. Lett. **84**, (2000) 5711.
6. The LEP Electroweak Working Group: <http://lepwww.web.cern.ch/lepww/LEWWG/4f/Summer04>
7. V.M. Abazov et al. ($D\bar{O}$ collaboration), Phys. Rev. **D71**, (2005) 072004.
8. D. Acosta et al., Phys. Rev. **D71**, (2005) 051104
9. F. Landry et al., Phys. Rev. **D67**, (2003) 073016

W Mass and Properties

Mark Lancaster (on behalf of the CDF and DØ collaborations)

UCL, Department of Physics and Astronomy, Gower Street, London, UK, WC1E 6BT.

Abstract. Precise measurements of the mass and width of the W boson are sensitive to radiative corrections and can be used to place limits on new physics beyond the Standard Model and validate the consistency of the model. In particular, the W boson mass constrains the mass of the, as yet unobserved, Higgs boson and the width can be used to place limits on the existence of new particles that couple to the W. Results are presented from $p\bar{p}$ collisions recorded by the CDF and DØ experiments at the Fermilab Tevatron collider, operating at a centre of mass energy of 1.96 TeV. The uncertainty on the W mass is determined to be 76 MeV by CDF and the width, by DØ, to be 2011 ± 90 (stat.) ± 107 (syst.) MeV.

1 Introduction

The world's largest sample of W bosons is presently being analysed by the CDF and DØ collaborations. The results presented here are based on an integrated luminosity of $\sim 200\text{pb}^{-1}$, accumulated in 2002-2003; which is a factor of two larger than used in the previously published results [1]. Results on the W production cross section, angular distribution and couplings to other gauge bosons have been presented at this conference [2]. In this talk results on the W boson mass and width will be presented. The results are important in verifying the consistency of the Standard Model, placing limits on new physics, and in determining the mass of the Higgs boson.

2 CDF W Mass Measurement

At tree level, the mass of the W boson is determined by the mass of the Z boson (which has been very precisely measured at LEP [3]) and the electromagnetic and weak coupling constants. Beyond tree level, it is subject to radiative corrections which depend on the masses of all the particles the W can couple to. The largest contribution comes from the top quark and there is a weak dependence on the mass of the Higgs boson. Precision measurements of the W boson mass, in conjunction with a top quark mass measurement [4], can therefore be used to constrain the mass of the Higgs boson and other more exotic particles e.g. those predicted by super-symmetric (SUSY) models. This is shown in figure 1, which shows the predicted variation of the W and top masses for three choices of the Higgs mass and the region favoured by the minimal SUSY extension to the Standard Model (MSSM) with a light Higgs boson. In general scenarios with a light Higgs and SUSY particles tend to raise the mass of the W boson.

At hadron colliders the W mass is measured in the electron and muon decay channels since these channels can be

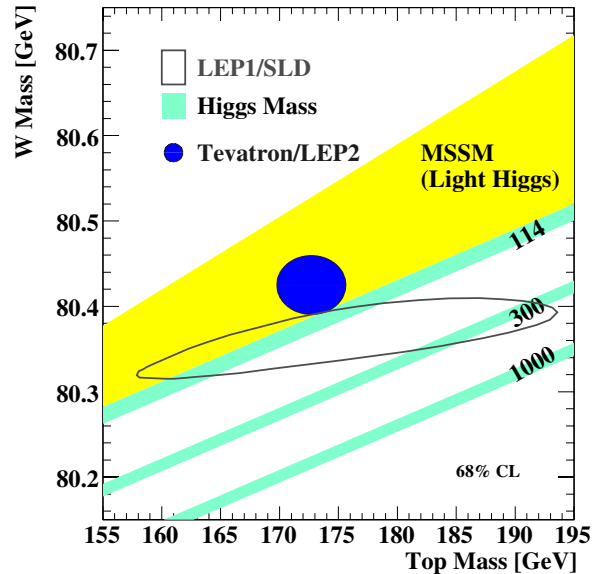


Fig. 1. The predicted W boson and top quark mass in the Standard Model for three Higgs masses (114 - the lower limit from LEP direct searches, 300 and 1000 GeV) and in the MSSM extension to the Standard Model. The present constraint from the Tevatron top and W mass and LEP2 W mass measurements are shown. The indirect constraint from precision electroweak measurements at LEP1 and SLD is also shown.

identified with high efficiency and with little background contamination. However, with these decay modes there is an accompanying neutrino whose momentum can only be inferred through momentum conservation in the transverse plane. As such the mass of the W boson has to be determined from a measurement of the mass using transverse momentum components only. It is not possible to have a simple functional form, in terms of the true W mass, for

this transverse mass owing to the effects of the varying parton-parton centre of mass energy, and the detector acceptance and resolution. Templates of the transverse mass distribution after a full simulation of the physics and the detector are therefore generated at various W mass values and the W mass is ultimately obtained from a likelihood comparison of the data with these templates. Events are generated using the NLO QCD generator RESBOS [5] and the effect of photon radiation from the decay charged leptons is taken from the WGRAD [6] calculation. This calculation only simulates the emission of a single photon and the uncertainty in the W mass arising from not including further emissions has been estimated to be 15 (20) MeV in the electron (muon) channel respectively. Owing to the similarity in the production mechanism between W and Z bosons, it is possible to predict the W transverse momentum distribution from a measurement of the Z transverse momentum distribution using the decay leptons. The uncertainty in the W transverse momentum, due to the finite statistics of the calibrating Z sample, results in a 15 MeV uncertainty in the W mass. The uncertainty in the angular distribution of the W bosons, arising from uncertainties in the parton distribution functions (PDFs) is determined using the CTEQ6 [7] and MRST [8] PDFs and is determined to be 15 MeV.

A key aspect of the measurement of the W mass is the determination of the momentum and energy scale of the charged leptons from the tracking detectors and the calorimeter. For the muons, the momentum scale is set using measurements of the J/ψ and Upsilon masses. For the electrons, the energy scale is set by requiring the energy scale to match the momentum scale (already set from the J/ψ). Both these determinations require a very detailed simulation of the photon radiation in the passive material, both in terms of simulating all possible physics processes but also in the composition and location of the material. The scale uncertainties are determined to be 70 and 25 MeV for the electron and muon channels respectively. The resolution of the energy and momentum measurements are taken from a fit to the width of the Z invariant mass distributions and the finite Z statistics result in a 15 MeV W mass uncertainty from this source for both channels.

In order to determine the neutrino momentum, through momentum conservation in the transverse plane, it is necessary to have a simulation of the underlying event, concurrent minimum bias event and the initial state QCD radiation. These components cannot be accurately modelled using a standard Monte Carlo event generator and are instead parameterised by fitting a model to real minimum bias and Z events; whose characteristics with regard to the underlying event and QCD radiation are expected to be very similar to W events. Uncertainties in this model arise from the finite statistics of the Z sample and from biases induced by the differing selection criteria and acceptance of the Z and W events e.g. Z events are selected with both leptons in the central detector region, whereas in W events there can be no such constraint on the direction of the neutrino. These uncertainties contribute a 50 MeV uncertainty in the W mass in both channels. The

Table 1. Systematic and statistical uncertainties (in MeV) for the CDF W mass analysis

Error Source	W $\rightarrow e\nu$	W $\rightarrow \mu\nu$
Statistics	45	50
Production model & decay	30	30
Charged lepton scale & resolution	70	30
Backgrounds	20	20
Recoil scale & resolution	50	50
Total	105	95

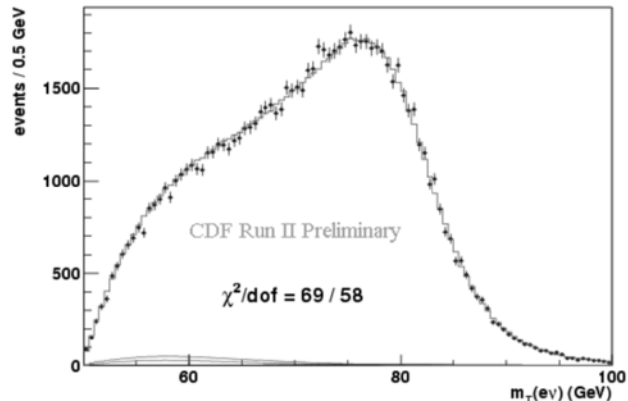


Fig. 2. The transverse mass distributions of the W $\rightarrow e\nu$ sample used to extract the W mass.

two largest sources of background : W to τ decays with subsequent τ decay to $e\nu\nu$ or $\mu\nu\nu$ and Z events where the second charged lepton escapes detection can be accurately simulated and the level of background (typically $\sim 5\%$) can be reliably estimated from the simulation. Backgrounds from QCD processes, cosmic rays and decay in flight Kaons cannot be accurately simulated and estimates of the transverse mass distributions from these sources are taken from the data by relaxing the selection cuts to provide background rich samples. Uncertainties in the level and shape of the background distributions contribute ~ 20 MeV to the W mass uncertainty. The complete list of systematic uncertainties for the CDF W mass analysis are shown in table 1. The total combined error, after taking into account correlations between the two channels, is 76 MeV. This is better than the previously published CDF W mass which had an uncertainty of 79 MeV. This systematic error analysis is a preliminary one and it is expected to be reduced before publication. The transverse mass distributions of the electron sample used to determine the W mass is shown in figure 2.

3 W Width measurement

As seen in figure 2 the W transverse mass distribution has a sharp edge close to the value of the W mass. However owing to the finite width of the W boson, it is also possible for events to be measured with transverse mass values higher

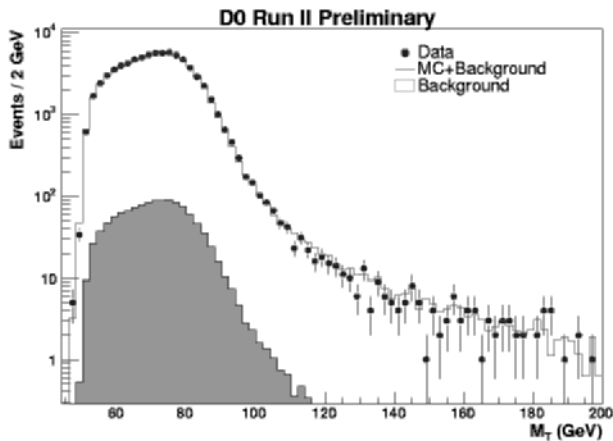


Fig. 3. The transverse mass distributions of the $W \rightarrow e\nu$ sample used to extract the W width by DØ.

than the mass of the W boson. From a likelihood fit to the transverse mass distribution in the $100 < m_T < 200$ GeV, it is therefore possible to determine the W width. However events in the high transverse mass region can also arise due to the finite resolution of the detector and so a detailed understanding and modelling of resolution effects is a vital component of this analysis and indeed dominates the systematic uncertainty for the measurement. Using 177 pb^{-1} of data, and 625 $W \rightarrow e\nu$ events in the high transverse mass region, DØ have determined the W width to be 2011 ± 93 (stat.) ± 107 (syst.) MeV; which agrees well with the Standard Model prediction of 2099 ± 3 MeV [9]. The transverse mass distribution of the $W \rightarrow e\nu$ events used by DØ to determine the W width are shown in figure 3.

4 Future measurements

The analyses presented here have been based on an integrated luminosity of $\sim 200 \text{ pb}^{-1}$. At the time of this conference the Tevatron had passed the 1 fb^{-1} milestone and the next set of W width and mass measurements are expected to be based on datasets of $1\text{-}2 \text{ fb}^{-1}$. In these analyses the limiting factor in precision will be systematic and not statistical. The systematic uncertainties arising from PDFs and QED radiative corrections are likely to be the limiting source of error in these analyses. At present these two sources contribute ~ 25 MeV to the W mass uncertainty and this is common to the two experiments. Further developments in parton fitting (additional d/u data from HERA and a more sophisticated error analysis) and the provision of a fast generator that incorporates both NLO QED (i.e $\mathcal{O}(\alpha^2)$) and NLO QCD are likely to be needed if this 25 MeV uncertainty is to be reduced. The expectations are that with a 2 fb^{-1} dataset the Tevatron experiments will produce a W mass with a combined uncertainty of 20-30 MeV and a width uncertainty of 35 MeV. These uncertainties will surpass those from LEP2; furthermore each experiment will have more precise measurements than any single LEP experiment.

5 Acknowledgements

I'd like to thank the organisers of the Hadron Collider symposium for a supremely well organised, stimulating and enjoyable conference.

References

1. T. Affolder et al, Phys. Rev. D64 052001 (2001), Phys. Rev. Lett. 85 3347 (2000); B. Abott et al, Phys. Rev. Lett. 84 222 (2000), Phys. Rev. Lett. 80 3008 (1998).
2. A. Goshaw, Diboson Physics at the Tevatron; Serban Protopopescu, W/Z production; these proceedings.
3. The ALEPH, DELPHI, L3, OPAL, SLD Collaborations and the LEP Electroweak Working Group, the SLD electroweak, heavy flavour groups; hep-ex/0509008.
4. Tomonobu Tomua, Top mass at the Tevatron, these proceedings.
5. C. Balazs, C.P. Yuan, Phys. Rev. D56 5558 (1997).
6. U. Baur, S. Keller, D. Wackerth, Phys.Rev. D59 (1999) 013002 and U. Baur, these proceedings.
7. J. Pumplin et al, J. High Energy Phys. JHEP07 (2002).
8. A.D. Martin, R.G. Roberts, W.J. Stirling, R.S. Thorne, Eur.Phys.J. C28 455 (2003).
9. P. B. Renton, Rep. Prog. Phys. 65 1271 (2002), and references therein.

Di-Boson Physics at the Tevatron

A. T. Goshaw (for the CDF and DØ Collaborations)

Duke University, Durham, NC 27708

Abstract. A summary is presented of recent measurements of di-boson production at the Tevatron. The results from the CDF and DØ experiments are based upon 130-320 pb⁻¹ of $p\bar{p}$ collisions at $\sqrt{s} = 1.96$ TeV. The $W\gamma$, $Z\gamma$, WW , and WZ production properties are compared to Standard Model predictions, and limits extracted for anomalous triple gauge couplings.

1 Introduction

A study of di-boson production at the Tevatron provides a rich source of electroweak Standard Model (SM) tests, is sensitive to new physics signatures, and opens a window into the challenges faced in searches for the Higgs boson. In this report we summarize measurements made by the CDF and DØ collaborations based upon the first significant data sets obtained from Run II of the Tevatron. The production channels are $p\bar{p} \rightarrow VV' + X$ at $\sqrt{s} = 1.96$ TeV, where the di-boson pairs are $W\gamma$, $Z\gamma$, WW , and WZ . Figure 1 shows the expected cross sections based upon SM predictions. The di-boson cross sections of interest in this review range from about 1 to 10 pb.

For these di-boson production channels, the measured cross sections and kinematic distributions are compared to leading order electroweak predictions, scaled to correct for lowest order QCD effects. Anomalous coupling parameters describing the triple gauge vertices are used as metrics for evaluating the sensitivity to new physics. These parameters determine deviations of the W and Z bosons from point particles. There are of course other sources of new physics that would appear in di-boson production, perhaps the most likely source of discoveries at the Tevatron.

Di-boson studies at the Tevatron compliment those made at LEP in several ways. Some of the triple gauge couplings (TGC's) can be better isolated using qq' collisions. For example, $qq' \rightarrow W^* \rightarrow W\gamma$ depends only on the $WW\gamma$ coupling, while $qq' \rightarrow W^* \rightarrow WZ$ depends only on the WWZ coupling. In addition the higher parton collision energy at the Tevatron explores different dynamic regions of the TGC, and opens up the possibility for the direct production of massive particles decaying into final states with di-bosons. Measurements of W/Z hadronic decays paired with a photon or a W/Z leptonic decay are useful for studies of dijet mass resolution, and provide calibration channels for searches for the Higgs boson in W/Z $H(bb)$.

2 W boson production with a photon

The reaction $p\bar{p} \rightarrow l\nu\gamma$ has contributions from W bosons produced with initial and final state photon radiation and from the direct $WW\gamma$ coupling. A study of $l\nu\gamma$ events allows extraction of the $WW\gamma$ coupling parameters, assuming that the W and photon couplings to fermions are described by the SM. Under the assumption of Lorentz and electromagnetic gauge invariance, and neglecting CP violating terms, the effective Lagrangian is [1]:

$$L_{WW\gamma} = -ie[(W_{\mu\nu}^\dagger W^\mu A^\nu - W_\mu^\dagger A_\nu W^{\mu\nu}) + \kappa_\gamma W_\mu^\dagger W_\nu F^{\mu\nu} + \lambda_\gamma/M_W^2 W_{\lambda\mu}^\dagger W_\nu^\mu F^{\nu\lambda}].$$

In the SM at tree level $\Delta\kappa_\gamma = \kappa_\gamma - 1 = 0$ and $\lambda_\gamma = 0$. Deviations of the coupling parameters from the SM values are usually parameterized with a dipole form factor to preserve tree-level unitarity at high energies: $\Delta\kappa_\gamma = \Delta\kappa_{o\gamma}/(1+s/\Lambda^2)^2$ and $\lambda_\gamma = \lambda_{o\gamma}/(1+s/\Lambda^2)^2$ where \sqrt{s} is the $W\gamma$ invariant mass and Λ sets the energy scale of new physics.

The results presented here use W decays to electrons ($E_T > 25$ GeV) and muons ($P_T > 20$ GeV/c) in association with central photons ($|\eta| < 1.0$). To suppress final state bremsstrahlung, the photon is isolated from the lepton by $\Delta R(l-\gamma) > 0.7$. The number of event candidates is 323 (273) in the CDF (DØ) experiments using integrated luminosity of 130-200 pb⁻¹. The background is dominated by W+jet events in which the jet passes the photon selection cuts. The resulting signal over background ratios vary from 0.8 to 1.9 depending on channel and experiment. For details see references [2] and [3].

Table I shows measured cross sections for $p\bar{p} \rightarrow l\nu\gamma$. These are an average of the measurements from the electron and muon decay channels, and corrected for the full W boson decay phase space. The photons have $\Delta R(l-\gamma) > 0.7$, and $E_T(\gamma)$ above the cuts indicated in the table. The photon E_T distribution from the CDF-selected $l\nu\gamma$ events is shown in Figure 2. The transverse mass spectrum of the $W\gamma$ system from DØ data is presented in Figure 3. The upper histograms are the SM predictions for $p\bar{p} \rightarrow l\nu\gamma$ plus backgrounds. All the data are consistent with SM predictions.

Table 1. Cross Sections for $p\bar{p} \rightarrow l\nu\gamma$ with $\Delta R(l-\gamma) > 0.7$

	$E_T(\gamma)$	$\sigma_{data}(l\nu\gamma)$ (pb)	$\sigma_{SM}(l\nu\gamma)$ (pb)
CDF	> 7 GeV	18.1 ± 3.1	19.3 ± 1.4
DØ	> 8 GeV	14.8 ± 2.1	16.0 ± 0.4

Anomalous $WW\gamma$ couplings would enhance the production of high E_T photons. The DØ Collaboration has used their data to set limits on $\Delta\kappa_{o\gamma}$ and $\lambda_{o\gamma}$ using a dipole form factor with $\Lambda = 2$ TeV. Holding one parameter at the SM value of zero and allowing the other to vary, the 95% CL's are: $-0.88 < \Delta\kappa_{o\gamma} < 0.96$ and $-0.20 < \lambda_{o\gamma} < 0.20$ [3].

3 W^+W^- and $W^\pm Z$ boson pair production

The production of $W^\pm Z$ pairs depends on the WWZ trilinear coupling, while W^+W^- production is sensitive to both $WW\gamma$ and WWZ couplings. In Section 1 the anomalous coupling parameters for the $WW\gamma$ vertex were introduced: $\Delta\kappa_{o\gamma}$ and $\lambda_{o\gamma}$. Under the same assumptions the WWZ vertex is described by the Lagrangian [4]:

$$L_{WWZ} = -ie \cot(\theta_W) [g_1^Z (W_{\mu\nu}^\dagger W^\mu Z^\nu - W_\mu^\dagger Z_\nu W^{\mu\nu}) + \kappa_Z W_\mu^\dagger W_\nu Z^{\mu\nu} + \lambda_Z / M_W^2 W_{\lambda\mu}^\dagger W^\mu_\nu Z^{\nu\lambda}]$$

In the SM $\Delta g_1^Z = g_1^Z - 1 = 0$, $\Delta\kappa_Z = \kappa_Z - 1 = 0$ and $\lambda_Z = 0$. As discussed previously, deviations from these SM values need to be suppressed by a form factor, usually taken of the form $\lambda_Z = \lambda_{oZ} / (1 + s/\Lambda^2)^2$, etc. Therefore a description of the $WW\gamma$ and WWZ vertices requires five parameters, $\Delta\kappa_{o\gamma}$, $\lambda_{o\gamma}$, Δg_{o1}^Z , $\Delta\kappa_{oZ}$, and λ_{oZ} , plus the scale of the new physics set by Λ .

3.1 W^+W^- measurements

The SM cross section for $p\bar{p} \rightarrow W^+W^- + X$ at $\sqrt{s} = 1.96$ TeV is (12.4 ± 0.8) pb [5]. The CDF [6] and DØ [7] collaborations have made measurements using the leptonic W^+W^- decay channels $l\nu l'\nu$ with $l, l' = e$ or μ . The branching ratio is only 4.6 % but the data have low backgrounds. The number of W^+W^- candidates is 25 (17) for DØ (CDF) using about 200 pb^{-1} of data. After all selection cuts both experiments attained a signal over background ratio of about 2.2. Correcting for decay branching ratios, the W^+W^- pair inclusive cross sections are measured to be:

$$13.8_{-3.8}^{+4.8}(\text{stat.})_{-0.9}^{+1.2}(\text{sys.}) \pm 0.9(\text{lum.}) \text{ pb (DØ)}$$

$$14.6_{-5.1}^{+5.8}(\text{stat.})_{-3.0}^{+1.8}(\text{sys.}) \pm 0.9(\text{lum.}) \text{ pb (CDF)}$$

These total W^+W^- cross sections are plotted in Figure 4, compared to the SM prediction. The lepton P_T spectrum from the W^+W^- decays measured by CDF is presented in Figure 5. All the data are in good agreement with SM expectations.

The CDF collaboration has also studied the W^+W^- channel using $W \rightarrow l\nu$ events with at least two jets having $32 \text{ GeV}/c^2 < M_{jj} < 184 \text{ GeV}/c^2$. The analysis searches for

a $W \rightarrow \text{jet-jet}$ mass peak (broadened by a small $Z \rightarrow \text{jet-jet}$ contribution) above the large di-jet QCD background. No signal is seen in 200 pb^{-1} of data. A 95% CL limit is put on the $W^+W^- + W^\pm Z$ cross section of 46 pb, compared to the SM prediction of (16 ± 1) pb. Anomalous couplings would cause an excess of events with high $W P_T$. Using a di-jet signal region $56 \text{ GeV}/c^2 < M_{jj} < 112 \text{ GeV}/c^2$, the lack of an excess of $W(l\nu)$ bosons at high P_T can be used to put limits on the $WW\gamma$ and WWZ anomalous coupling parameters. The analysis assumes that $\Delta g_{o1}^Z = 0$, $\Delta\kappa_o = \Delta\kappa_{oZ} = \Delta\kappa_{o\gamma}$ and $\lambda_o = \lambda_{oZ} = \lambda_{o\gamma}$. Setting one of the parameters zero, the 95% CL limits on the anomalous couplings are: $-0.42 < \Delta\kappa_o < 0.58$ and $-0.32 < \lambda_o < 0.35$, using a dipole form factor with $\Lambda = 1$ TeV.

3.2 $W^\pm Z$ measurements

The SM cross section for $p\bar{p} \rightarrow W^\pm Z + X$ at $\sqrt{s} = 1.96$ TeV is 3.7 ± 0.3 pb [5]. The DØ collaboration [8] has searched for $W^\pm Z$ events in the decay channels $l'\nu l^+ l^-$ using electrons and muons. With 300 pb^{-1} of data, after all selection cuts, two 3- μ and one 3- e events are isolated with a total background of 0.71 ± 0.08 events. The 95% CL upper limit on the production cross section is 13.3 pb, consistent with the SM expectations. By setting two of the three anomalous coupling parameters to their SM value of zero, a 95% CL can be set on the third. Using a scale $\Lambda = 1.5$ TeV, the results are: $-0.48 < \lambda_{oZ} < 0.48$ and $-0.49 < \Delta g_{o1}^Z < 0.66$ with no limits on $\Delta\kappa_{oZ}$.

4 Z boson production with a photon

The SM predictions for the reaction $p\bar{p} \rightarrow l^+ l^- \gamma$ include Z/γ^* production with bremsstrahlung from the initial state quarks or final state radiation from the decay $l^+ l^-$ pairs. Since the SM couplings $ZZ\gamma$ and $Z\gamma\gamma$ are zero, new physics effects would appear as deviations from bremsstrahlung predictions. Under the assumption of Lorentz and electromagnetic gauge invariance, the most general Lagrangian [9] includes 8 complex parameters of the form $h_i^V = h_{io}^V / (1 + s/\Lambda^2)^n$ where $V = Z$ or γ and $i = 1-4$. Again multipole form factors are needed to preserve unitarity at high energy.

As for the $W\gamma$ measurements, the events are triggered on high E_T central electrons or muons, and selected with charged lepton pairs and an isolated photon with $\Delta R(l-\gamma) > 0.7$. The number of event candidates are 290 (70) for the DØ (CDF) experiments using 200-320 pb^{-1} of data. Backgrounds are low, dominated entirely by Z +jet events with the jet passing the photon selection cuts. Depending on channel and experiment the signal over background ratios vary from 6 to 15. For details see references [2] and [10].

Table 2 shows measured cross sections for $p\bar{p} \rightarrow l^+ l^- \gamma$, from averages of the electron and muon decay channels and corrected for the Z/γ^* decay phase space. The photons have $\Delta R(l-\gamma) > 0.7$ and have the minimum $E_T(\gamma)$ and $M(l^+ l^-)$ shown in the table. Figure 6 shows the photon

Table 2. Cross Sections for $p\bar{p} \rightarrow l^+l^-\gamma$ with $\Delta R(l-\gamma) > 0.7$

	$E_T(\gamma)$	$M(l^+l^-)$	σ_{data} (pb)	σ_{SM} (pb)
CDF	> 7 GeV	> 40 GeV/ c^2	4.6±0.6	4.5±0.3
DØ	> 8 GeV	> 30 GeV/ c^2	4.2±0.5	3.9±0.2

E_T spectrum from the CDF data, and Figure 7 the invariant mass $M(l\bar{l}\gamma)$ from DØ measurements. The lower solid histograms are the backgrounds from Z + jet events with the jet passing photon selection cuts. The upper histograms are the sum of the background plus electroweak predictions for $p\bar{p} \rightarrow l^+l^-\gamma$ production. Both the measured total cross sections and the kinematic distributions are in good agreement with the SM.

The DØ Collaboration [10] has used their data to set limits on the anomalous coupling parameters h_{oi}^Z and h_{oi}^γ using $\Lambda = 1$ TeV. As with the other limits, all parameters but one are set to their SM values and 95% CL are determined for the remaining parameters: $|h_{10,30}^Z| < 0.23$; $|h_{20,40}^Z| < 0.020$; $|h_{10,30}^\gamma| < 0.23$; $|h_{20,40}^\gamma| < 0.019$.

5 Summary and conclusions

Using 130-320 pb^{-1} of $p\bar{p}$ collisions at $\sqrt{s} = 1.96$ TeV, the CDF and DØ Collaborations have measured di-boson production and compared the data to SM predictions. Deviations of the measured cross section from NLO SM predictions are summarized in Table 3, where the uncertainties quoted are the quadrature sum of the experimental statistical and systematic errors. All results are in good agreement with the SM.

Measurements of the P_T spectra of the bosons can be used as a more sensitive probe for new physics. Substructure of the W or Z, or massive particles decaying to di-bosons, would cause an excess of high P_T bosons. No excesses are observed in the photon, W or Z spectra. One way to quantify this is in terms of limits on anomalous TGC parameters. These are summarized in Table 4.

The diboson data described in this report represents about 5% of that expected from the Tevatron. Further increases in sensitivity will be attained by combining the CDF and DØ data, and performing joint analyses combining di-boson channels. In addition to the potential for discoveries in these di-boson data, the techniques developed will be useful for Higgs boson searches at the Tevatron and LHC.

6 Acknowledgements

I would like to thank my CDF colleagues and members of the DØ Collaboration, particularly Tom Diehl and Andrew Askew, for access to the data presented in this report. It was a pleasure to participate in the HCP05 conference, and have the opportunity to present this overview. I thank the organizing committee for giving me this opportunity.

Table 3. Cross section comparisons to Standard Model predictions

Channel ($l=e$ or μ)	$(\sigma_{data} - \sigma_{SM}) / \sigma_{SM}$
W γ [$l\nu\gamma$]	-0.06 ± 0.16 CDF -0.06 ± 0.16 DØ
Z γ [$ll\gamma$]	+0.02 ± 0.13 CDF +0.08 ± 0.13 DØ
WW [$l\nu ll$]	+0.17 ± 0.42 CDF +0.10 ± 0.32 DØ
Cross section limits	σ_{data} (95% CL)/ σ_{SM}
WZ [$l\nu ll$]	3.3 DØ
WZ + WW [$l\nu qq$]	2.4 CDF
WZ + ZZ [$ll(l\nu$ or $\nu\nu)$]	3.0 CDF [11].

Table 4. Triple gauge boson anomalous coupling limits

Coupling	limits at 95% C.L.	Energy scale Λ
WW γ	-0.88 < $\Delta\kappa_{o\gamma}$ < 0.96 -0.20 < $\lambda_{o\gamma}$ < 0.20	2 TeV
WWZ	-0.49 Δg_1^Z < 0.66 -0.48 < λ_{oZ} < 0.48	1.5 TeV
ZZ γ	$ h_{10,30}^\gamma < 0.23$ $ h_{20,40}^\gamma < 0.019$	1 TeV
ZZZ	$ h_{10,30}^Z < 0.23$ $ h_{20,40}^Z < 0.020$	1 TeV
WWZ and WW γ	-0.42 < $\Delta\kappa_o$ < 0.58 -0.32 < λ_o < 0.35	1.5 TeV

References

1. U. Baur and E. Berger, Phys. Rev. D **41**, 1476 (1990).
2. D. Acosta *et al.*, The CDF Collaboration, Phys. Rev. Lett. **94**, 040803 (2005).
3. V. Abazov *et al.*, The DØ Collaboration, Phys. Rev. D **71**, 091108 (2005).
4. Haigawara, Peccii and Zeppenfeld, Nuc. Phys. B **282**, 253 (1987).
5. J. M. Campbell and R.K. Ellis, Phys. Rev. D **62**, 114012 (2000).
6. D. Acosta *et al.*, The CDF Collaboration, Phys. Rev. Lett. **94**, 211801 (2005).
7. V. Abazov *et al.*, The DØ Collaboration, Phys. Rev. D **94**, 151801 (2005).
8. V. Abazov *et al.*, The DØ Collaboration, hep-ex/0504019 (2005).
9. J. Ellison and J. Wudka, Ann. Rev. Nucl. Part. Sci. **48**, 33-80 (1998).
10. V. Abazov *et al.*, The DØ Collaboration, Phys. Rev. Lett. **95**, 051802 (2005).
11. D. Acosta *et al.*, The CDF Collaboration, Phys. Rev. D **71**, 091105 (2005).

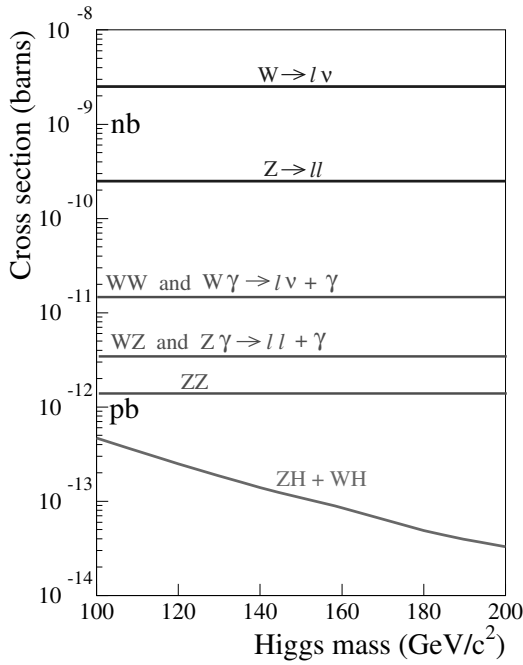


Fig. 1. Standard model predictions for boson and di-boson production cross sections. For the channels with a photon, $\Delta R(l-\gamma) > 0.7$ and $E_T(\gamma) > 10$ GeV.

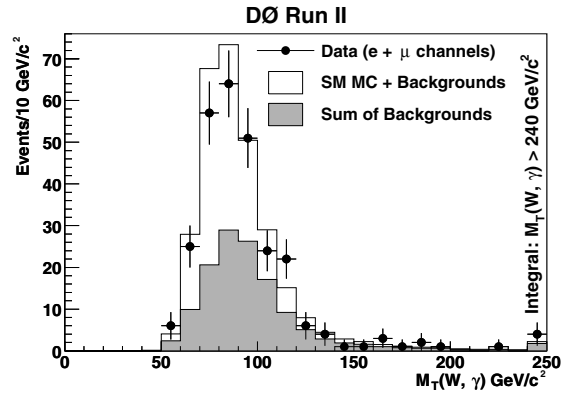


Fig. 3. Transverse mass of $W\gamma$ system from $p\bar{p} \rightarrow l\nu\gamma$ events.

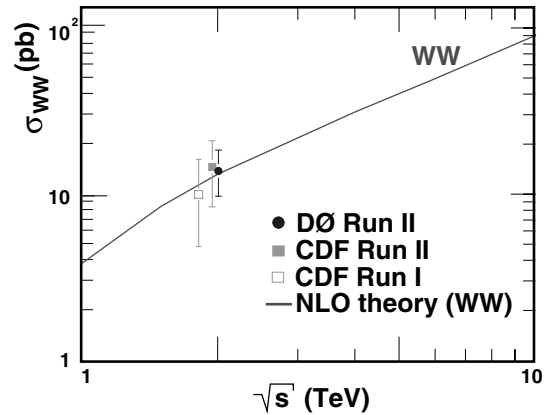


Fig. 4. Measured $p\bar{p} \rightarrow W^+W^-$ inclusive cross sections compared to the NLO SM prediction.

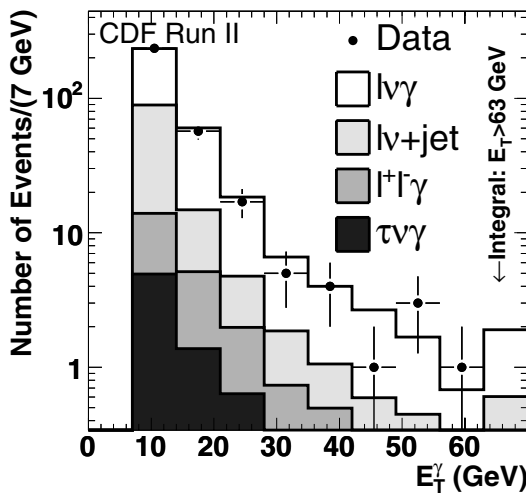


Fig. 2. Photon E_T spectrum from $p\bar{p} \rightarrow l\nu\gamma$ events.

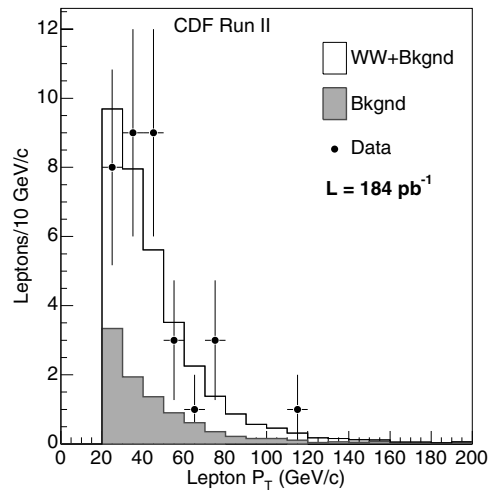


Fig. 5. Lepton P_T spectrum from $p\bar{p} \rightarrow W^+W^-$ events.

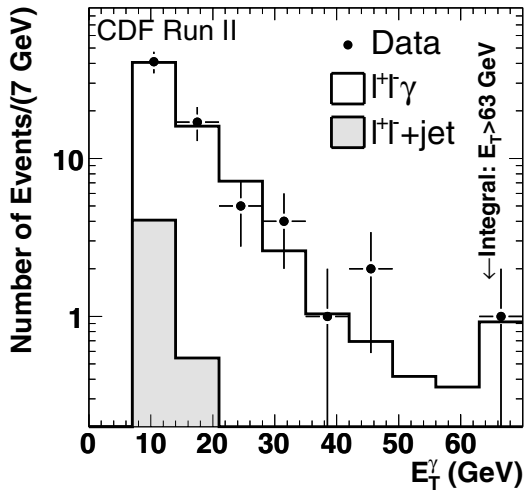


Fig. 6. Photon E_T spectrum from $p\bar{p} \rightarrow ll\gamma$ events.

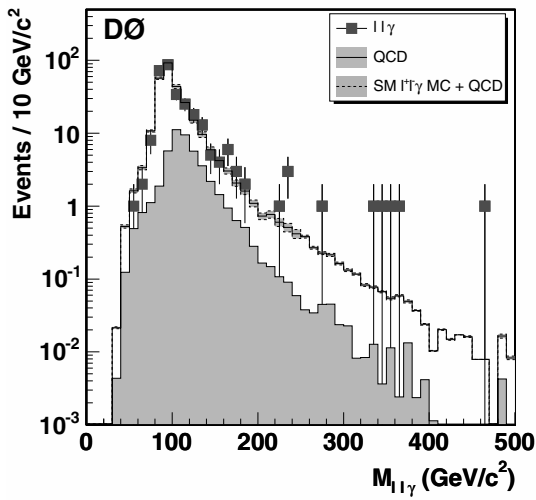


Fig. 7. Mass of $ll\gamma$ system from $p\bar{p} \rightarrow ll\gamma$ events.

Precision Electroweak Measurements at ATLAS and CMS

Nicola Amapane

CERN

Abstract. Detailed experimental knowledge of Standard Model processes will be essential to prepare for discoveries at future colliders and for their interpretation. In addition to its large discovery potential, the Large Hadron Collider will allow to perform several precision electroweak measurements, often improving the current experimental precision thanks to its large centre-of-mass energy and high luminosity. The perspective of the ATLAS and CMS experiments in selected fields of electroweak physics, including W and top physics, Drell-Yan production of lepton pairs, and Triple Gauge Boson Couplings is presented.

1 Introduction

The Large Hadron Collider (LHC) is a proton-proton collider currently under construction at CERN. In addition to its large discovery potential for the Higgs and for other new phenomena, the LHC will allow to perform a large number of precision electroweak measurements.

In this field, the main advantage of the LHC over current machines will be the available statistics. At the LHC centre-of-mass energy of 14 TeV, the cross section for several Standard Model processes is significantly higher than at the Tevatron, as shown in Fig. 1. Even at the initial luminosity of $10^{33} \text{cm}^{-2} \text{s}^{-1}$ (ten times below the design value), the production rates for W and Z bosons and for $t\bar{t}$ pairs will be 200, 50, and 1 Hz, respectively. Very large data samples are therefore expected to be collected by the two general-purpose experiments ATLAS [11] and CMS [12], so that for most measurements the statistical error will be very small. Moreover, high statistics control samples will allow a good understanding of the detector response, thus reducing the systematic errors.

2 Measurement of the W boson and top quark mass

The value of the top and Higgs masses enter in the prediction of the W boson mass through radiative corrections, with a dependence on m_t^2 and $\log m_H$. Precise measurements of m_t and m_W allow therefore to set limits on m_H and, if the Higgs is found, they will allow to perform stringent tests of the Standard Model (SM) or its extensions, like the Minimal Supersymmetric Standard Model (MSSM).

Today, the W boson mass is known with a precision of $\pm 32 \text{ MeV}/c^2$ from measurements at LEP2 and Tevatron [4]. With an expected precision on the top mass of better than $2 \text{ GeV}/c^2$ at the LHC, the W boson mass should be known with a precision of about $15 \text{ MeV}/c^2$ in

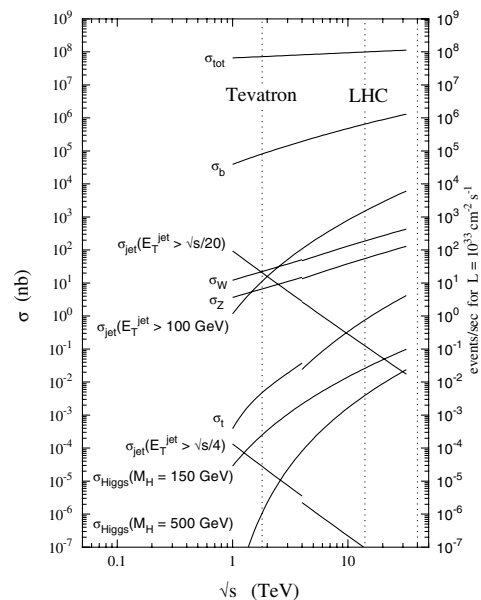


Fig. 1. Cross sections and event rates of several processes as a function of the centre-of-mass energy of proton-proton collisions [3].

order not to become the dominant error in the indirect estimation of the mass of the Higgs boson.

2.1 Measurement of the top quark mass

The most promising channel for the measurement of the top mass is $t\bar{t} \rightarrow W^+W^-b\bar{b}$ with one leptonic and one hadronic W decay, where the hadronic part is used to reconstruct the top mass and the leptonic part to select the event. Figure 2 shows the invariant mass distributions expected with ATLAS and CMS. It can be noted that the large available signal statistics allows to tune the selection criteria in order to adjust the signal to background ratio;

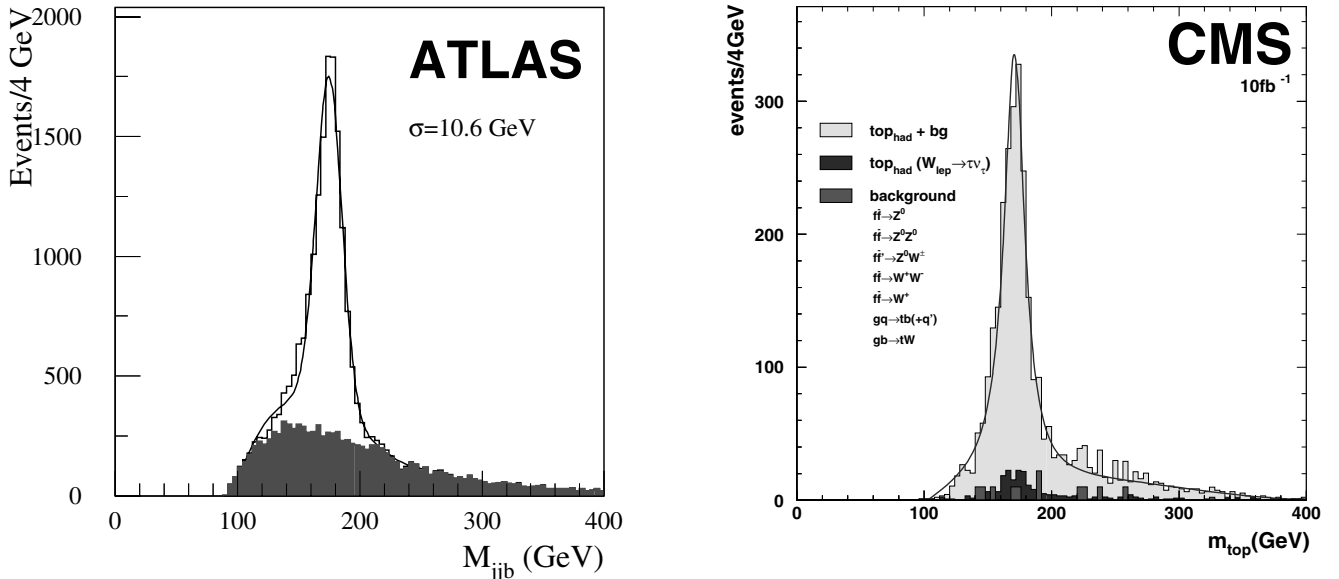


Fig. 2. Reconstructed top mass in the semileptonic channel at ATLAS [5] (left) and CMS [6] (right).

this will allow to balance the statistical and systematic errors.

The main sources of uncertainty for this measurement will be knowledge of final state radiation and of the energy scale of b-quark jets, which is affected by the knowledge of fragmentation and gluon radiation and of the response of the detectors. The same sample of $t\bar{t}$ events will provide a large number of hadronic W decays to be used for the calibration of the hadron calorimeters. A final precision of about $1.5 \text{ GeV}/c^2$ per experiment is expected [5, 6].

The measurement of the top mass will be possible in other final states as well. The fully leptonic channel is characterized by a very clean signature and low backgrounds. The presence of two neutrinos in the final state does not allow a direct measurement of the top mass, so the correlation between m_t and variables like the invariant mass of the two-lepton system has to be exploited [5].

Another very promising method is based on the selection of top decays where a J/ψ is originated by the fragmentation of the b quark and the W boson decays into a muon or electron. The J/ψ is easily identified by its two-muon decay. The invariant mass of the system $J/\psi + \ell$ is very sensitive to m_t , as shown in Fig. 3. The very small branching ratio ($< 10^{-5}$) is compensated by the very clean signature of this final state, so that it will be possible to perform this analysis at the highest LHC luminosities, where about 1000 events per year are expected. This method has the advantage to be independent from the jet energy scale, which is the main source of systematics for the semileptonic channel. The knowledge of the b fragmentation function will be the main limitation to the precision, which is expected to be about $1 \text{ GeV}/c^2$ per experiment [7].

Several other measurements will be possible in the top quark sector, including the measurement of spin correlations in $t\bar{t}$ production, of the W polarization in top decays,

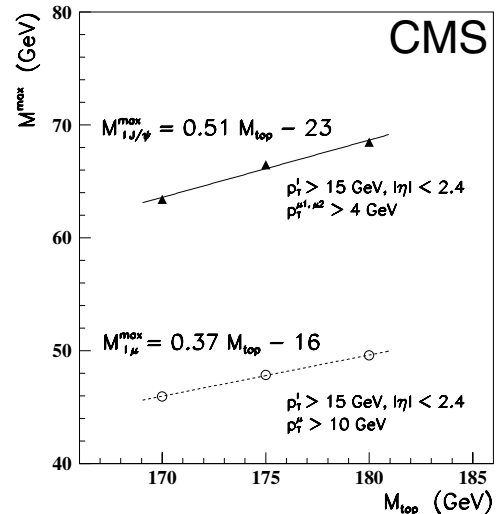


Fig. 3. Correlation between the top mass and the invariant mass of the lepton + J/ψ system (solid line), compared to the correlation with the invariant mass of the lepton plus μ -in-jet in two-lepton decays [7].

of the $t\bar{t}$ production cross section, and the observation of single top production. These are the subject of separate contributions in these proceedings [8, 9].

2.2 Measurement of the W boson mass

Since the longitudinal component of the neutrino momentum cannot be measured in hadron colliders, the W mass is obtained from a fit to the distribution of the W transverse mass. With about 3×10^7 events per year and per experiment at the initial luminosity, the statistical error for this measurement will be negligible at the LHC. How-

ever, to achieve the desired precision of about $15 \text{ MeV}/c^2$ a very good control on systematic uncertainties is required.

At the Tevatron, techniques to constrain systematic uncertainties “in situ” using real data have been developed. Similar methods will be used at the LHC, with the advantage of the availability of very large samples of $Z \rightarrow \ell\ell$ events. In particular, the reconstruction of the Z mass from the di-lepton system will allow to calibrate the lepton energy and momentum scale, which is the dominant source of uncertainty for this measurement.

The large sample of leptonic Z decays will also allow to constrain the systematic uncertainties deriving from the knowledge of the lepton energy and momentum resolution, of the p_T spectrum of the W boson, and of the detector response to the system recoiling against the W.

Other sources of systematics are the knowledge of PDFs, of the W width, and of radiative decays. According to a study from ATLAS [3], it will be possible to achieve a total uncertainty of less than $25 \text{ MeV}/c^2$ per experiment. For this purpose, the lepton energy and momentum scale must be known with a challenging precision of $\sim 0.02\%$.

3 Drell-Yan production of lepton pairs

The Drell-Yan production of lepton pairs is a process with a clean signature and low experimental backgrounds. The main interesting observables are the cross section and the forward-backward asymmetry.

The measurement of the differential cross section can provide evidence for new physics, like for example new heavy particles decaying to leptons. Figure 4 shows the expected number of dilepton events for an integrated luminosity of 100 fb^{-1} , showing a sensitivity extending up to about 1.5 TeV, well beyond the reach of Tevatron Run II. The Drell-Yan cross section is also sensitive to radiative corrections, that can be probed up to very high energies providing that the precision on the cross section is not spoiled by the knowledge of the absolute luminosity [3].

The measurement of the forward-backward asymmetry A_{FB} in Drell-Yan lepton production allows the determination of the effective electroweak mixing angle $\sin^2 \theta_{eff}^{lept}$, whose precise knowledge will constrain m_H and provide a stringent test of the SM.

Improving the current LEP+SLD accuracy on $\sin^2 \theta_{eff}^{lept}$ (1.6×10^{-4} , [4]) is a very ambitious goal. The measurement of A_{FB} requires the identification of the incoming quark and anti-quark direction, which is not possible in pp colliders. It is therefore necessary to assume that the anti-quark is the parton with the lower x value; under this assumption A_{FB} is signed according to the rapidity of the lepton pair, $y(\ell^+\ell^-)$. A large lepton acceptance is essential, since A_{FB} increases with rapidity. A study from ATLAS [10] has shown that a statistical precision of about 10^{-4} can be achieved, providing that electrons can be identified up to rapidities of $|\eta| < 4.9$ using the forward calorimeters. Systematic uncertainties arising from the knowledge of PDFs, of the lepton acceptance and of

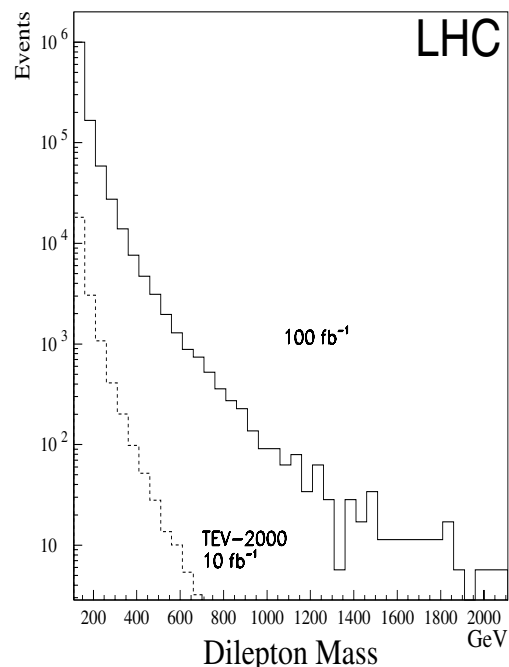


Fig. 4. Expected number of dilepton events at the Tevatron Run II and at LHC per lepton type and experiment, as a function of the dilepton invariant mass [3].

radiative corrections may however spoil the precision of this measurement.

4 Parton Distribution Functions

Accurate knowledge of PDFs is necessary for all precision measurements, since the observed processes are originated by the hard scattering of partons inside the protons. As shown in Fig. 5, the region of momentum transfer Q^2 and fractional parton momentum x accessible at the LHC extends beyond the area currently explored by fixed target experiments and by HERA. Theoretical models are therefore required to extrapolate from the current experimentally tested region to the high Q^2 region covered by LHC.

Several SM processes will offer the possibility to constrain these models directly using LHC data. For example, differential distributions as a function of pseudo-rapidity are sensitive to PDFs, since the rapidity of final state particles depends on the fractional momenta of the incoming partons.

The PDFs of the various parton species can be probed observing processes which involve different partons. In particular, Drell-Yan production of lepton pairs and production of Z and W bosons are sensitive to quark PDFs, while di-jet events ($q\bar{q} \rightarrow gg$ and $gg \rightarrow q\bar{q}$) are sensitive to both quark and gluon PDFs. The PDFs of b, c and s quarks can be probed observing the processes $gb \rightarrow b\gamma$, $gc \rightarrow c\gamma$ and $gs \rightarrow cW$, where the isolated photon or the W boson provide a signature to select the event, and the jets originated by the b and c quarks can be identified with b-tagging and with the presence of leptons [12].

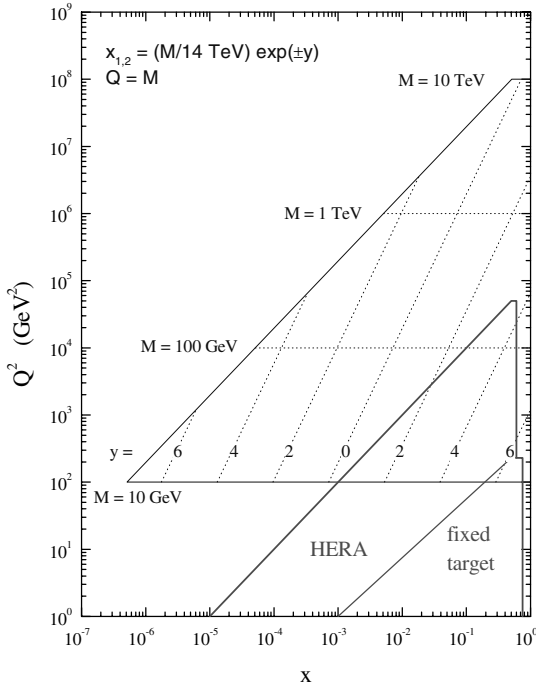


Fig. 5. Region of x vs. Q^2 accessible at LHC, compared to the region accessible at HERA and fixed target experiments.

Other observables are sensitive to PDFs as well. An example is the ratio of cross sections for W^+ to W^- bosons as a function of rapidity, which is sensitive to the ratio of PDFs for u and d quarks. The expected distributions from two sets of PDFs with small differences in the distributions of sea quarks are illustrated in Fig 6, which shows how even with small integrated luminosities it will be possible to distinguish between models.

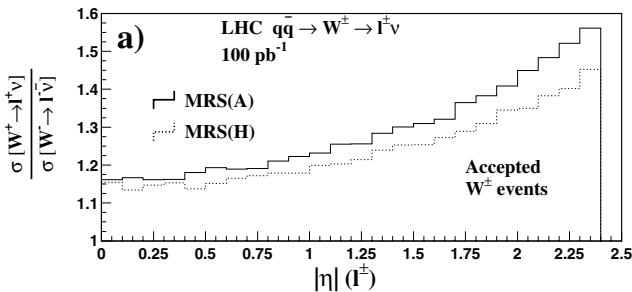


Fig. 6. Ratio of cross sections for W^+ to W^- bosons as a function of the charged lepton pseudo-rapidity for two different sets of PDFs [11].

5 Production of Vector Boson Pairs

At the lowest order, vector boson pairs are produced in $q\bar{q}$ annihilations followed by triple gauge boson vertices.

The study of these vertices is interesting since it probes directly the non-Abelian gauge symmetry of the SM. Deviations from the SM prediction can provide evidence for new physics, *e.g.* the presence of new heavy particles decaying to WW and ZZ pairs (including heavy Higgs).

In the Standard Model, only two such vertices exist, *i.e.* $WW\gamma$ and WWZ . Interesting final states are $W\gamma$ and WZ , which provide a clean signature. Deviations from the SM are described by the parameters $\lambda_{\gamma,Z}$ and $\Delta\kappa_{\gamma,Z}$ and affect both the total cross section and the shapes of distributions such as $p_T^{\gamma,Z}$. An example of how this distribution is sensible to deviations compatible with the current experimental limits is shown in Fig. 7, together with the expected limits at LHC.

The neutral vertices $ZZ\gamma$ and $Z\gamma\gamma$ are not present in the Standard Model, and anomalous couplings can be observed in $Z\gamma$ final states. An example of how two sensitive observables, the transverse momentum of the photon and the invariant mass of the $\ell\ell\gamma$ system, are affected by deviations of coupling parameters compatible with the current experimental limits is shown in Fig. 8. The LHC is expected to improve significantly these limits, since the sensitivity to anomalous couplings is strongly enhanced at high centre-of-mass energies.

6 Conclusions

Several electroweak measurements will be possible at the LHC. Thanks to the high event rates, very large signal samples will be available and the final precision will be in most cases limited by systematic uncertainties. Techniques to constrain these uncertainties “in situ” using real data will have to be developed and refined. It is expected that in many cases existing results will be improved, offering the possibility to perform precise tests of the SM and complementing the LHC discovery potential.

References

1. ATLAS Collaboration, CERN/LHCC/94-43 (1994).
2. CMS Collaboration, CERN/LHCC/94-38 (1994).
3. G. Altarelli and M. Mangano (editors), *Proceedings of the Workshop on Standard Model Physics (and more) at the LHC* (2000) CERN 2000-004.
4. The LEP Electroweak Working Group, summer results 2005 (<http://lepewwg.web.cern.ch/LEPEWWG/>).
5. I. Borjanovic *et al.*, SN-ATLAS-2004-040.
6. L. Sonnenschein, CMS NOTE 2001/001.
7. A. Kharchilava, CMS NOTE 1999/065.
8. A. Giammanco, these proceedings.
9. A. Lucotte, these proceedings.
10. K. Sliwa, S. Riley and U. Baur, SN-ATLAS-2000-018.
11. M. Dittmar, F. Pauss and D. Zürcher, *Phys. Rev.* **D56**, (1997) 7284.
12. M. Dittmar and K. Madzumar, CMS NOTE 2001/002.
13. C. Mackay and P. R. Hobson, CMS NOTE 2001/056.
14. C. Mackay and P. R. Hobson, CMS NOTE 2002/028.

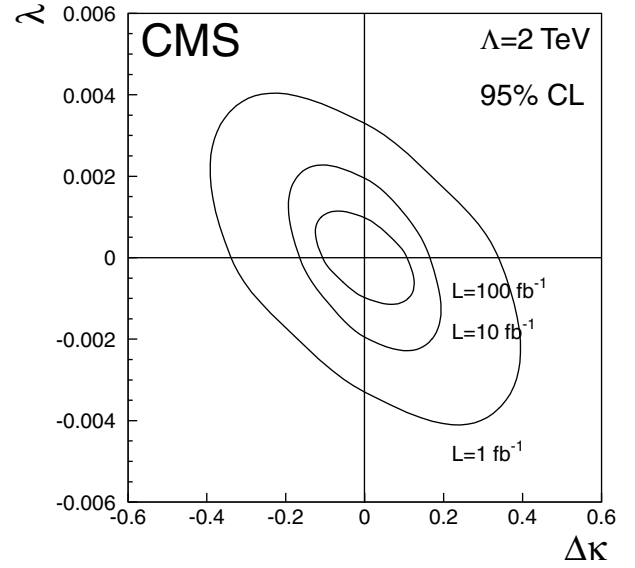
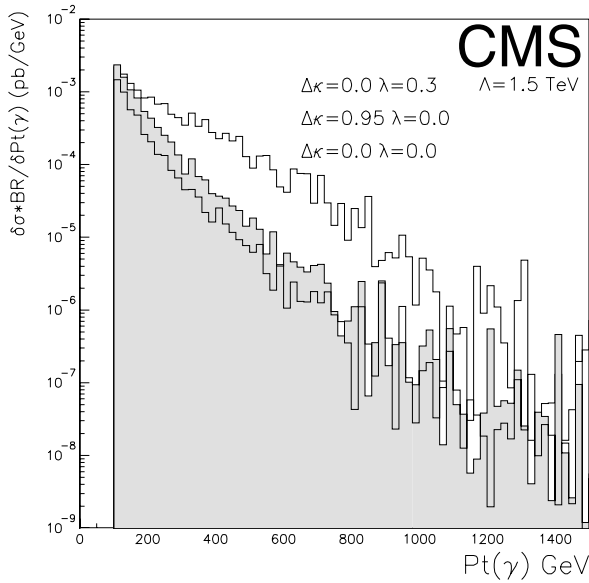


Fig. 7. Left: Transverse momentum of the photon in selected $W\gamma$ events for SM couplings, compared to the distributions obtained with λ_γ and $\Delta\kappa_\gamma$ set according to current experimental limits. Right: Expected limits on λ_γ and $\Delta\kappa_\gamma$ at LHC [13].

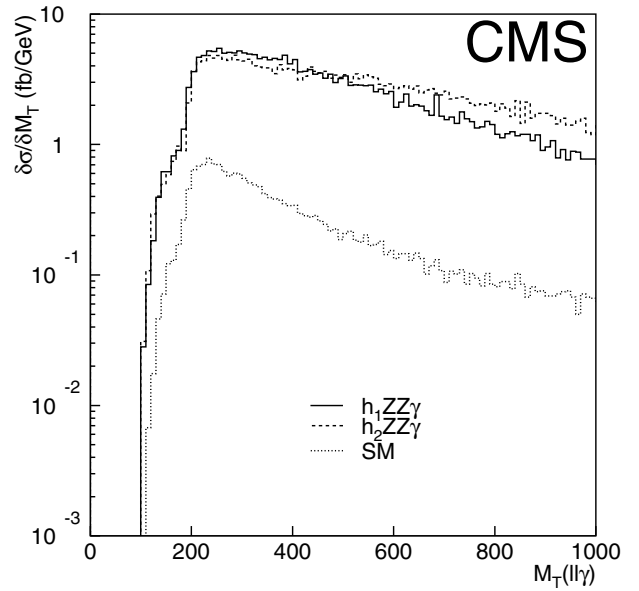
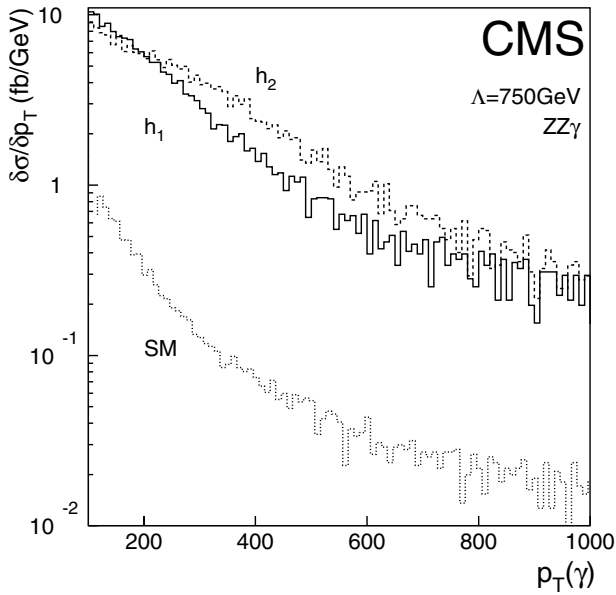


Fig. 8. Transverse momentum of the photon (left) and invariant mass of the $l\bar{l}\gamma$ system (right) for selected $Z\gamma$ events. The SM prediction is compared to the distributions obtained with anomalous coupling h_1 and h_2 set to the current limits [14].

Preparing for LHC I

Muon Identification at the Tevatron

Jeff Temple¹, for the CDF and DØ Collaborations

University of Arizona

Abstract. The muon detection and identification schemes for the CDF and DØ experiments at the Fermilab Tevatron are described. Both experiments detect muons through the use of scintillation counters and drift chambers surrounding a central tracker. Three levels of muon triggering are used to select collisions in which a muon was produced. Efficient reconstruction algorithms have been created to identify muons in these collisions.

1 Introduction

Muons produced in collisions at the Fermilab accelerator are long-lived relative to the size of the detectors, deposit minimal energy in the detector calorimeters, and produce little brems-strahlung. These properties make detecting muons at Fermilab a straightforward procedure. The utility of muons in investigating a wide range of physics processes makes muon detection not just straightforward, but desirable as well. Low- p_T muons may be used to investigate J/ψ decays or for b-jet and flavor tagging. High- p_T muons are produced in W and Z decays, and thus may be used in studying electroweak processes or top decays in which a W from a top produces a muon. High- p_T muons are also produced from Higgs decays and many processes beyond the Standard Model. Thus, muons may be used to make precision measurements of known physical processes and to explore new physics. The methods used by the CDF and DØ detectors to detect, trigger on, and reconstruct muons are described here.

2 Muon Detection

Both the CDF and DØ experiments detect muons by matching tracks found in a central tracker with hits in scintillation counters and drift chambers surrounding the detector calorimeters. The CDF central tracker consists of three individual subdetectors: a silicon vertex detector (SVX II) made up of 5 layers of double-sided silicon, an intermediate silicon detector (ISL) with 3 additional silicon layers, and an open-cell drift chamber detector (COT) containing roughly 30,000 sense wires. These three subdetectors are enclosed by a 1.4-T solenoid, and together, the detectors allow for track reconstruction of particles out to $|\eta| = 2.0$, as seen in Figure 1. The DØ central tracker also contains an inner silicon detector (SMT), which is made up of 6 barrels and 16 disks of single- or double-sided silicon. The SMT is surrounded by an 8-layer fiber tracker (CFT), with two fiber doublets per layer. These systems

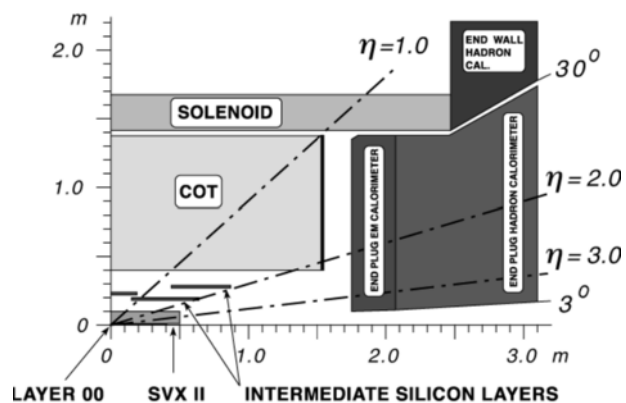


Fig. 1. The CDF central tracker

are encased in a 2-T solenoid, and the combined tracker provides coverage out to $|\eta| = 1.6$.

Dedicated muon detection systems surround the tracker and calorimeter at both experiments. At CDF, muons in the range $|\eta| < 1.0$ are detected by up to 8 planes of drift chambers and up to two layers of scintillation counters. The Central Muon Detector (CMU) and Central Muon Upgrade chambers (CMP) detect muons out to $|\eta| = 0.6$, while the Central Muon Extension chambers (CMX) detect muons in the region $0.6 < |\eta| < 1.0$. Muons outside of this range are detected by the Intermediate Muon system (IMU), which contains 2 layers of scintillators and 4 planes of drift chambers, providing continuous muon coverage out to $|\eta| = 1.5$.

At DØ, muons with $|\eta| < 1.0$ are detected by 2-3 layers of scintillators and 3 layers of drift chambers, with 3-4 chamber planes per layer. DØ's forward muon system is made up of 3 layers of scintillators and 3 layers of drift chambers, and can detect muons out to $|\eta| = 2.0$. Shielding made from a combination steel, polyethylene, and lead surrounds the section of beam pipe passing through the forward system in order to reduce backgrounds in these counters. As a consequence of this shielding, the occupancy in the forward counters has dropped by roughly a

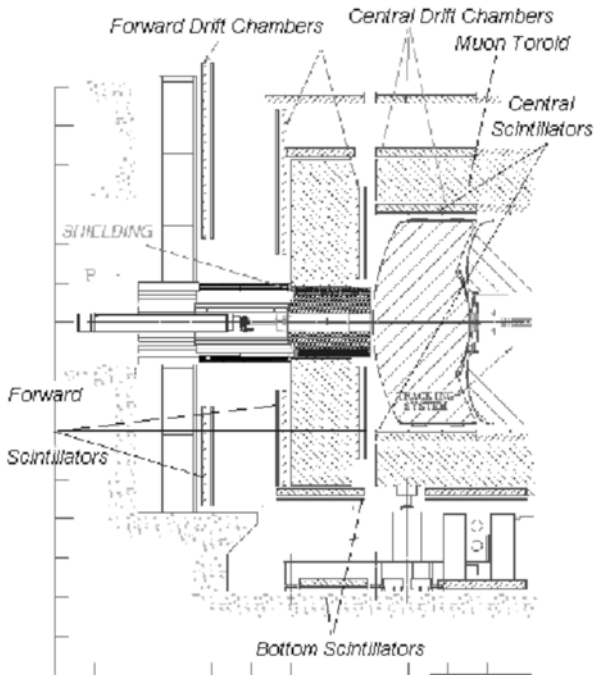


Fig. 2. The DØ central tracker and muon system

factor of 100 from what was seen in Run I. A 1.8-T toroid magnet between the first and second layer of muon detectors at DØ allows for a measurement of muon momentum independent of the central tracker. A schematic of the DØ tracker and muon system is shown in Figure 2.

3 Muon Triggering

Each detector uses three levels of triggering based on muons. At CDF, Level 1 muon triggers extrapolate tracks from COT hit information and match the extrapolated track to a muon system scintillator hit or drift chamber stub within $\Delta\phi = 2.5^\circ$ of the track. A p_T cut on the track may also be applied at this level. Dimuon triggers can require a minimum opening angle between two muons. At Level 2, there is tighter matching between the track and the muon stub as well as the opportunity to apply an additional p_T cut. Level 3 triggers are formed by first fully reconstructing the event and then using the full event information to make more precise matching and p_T requirements. These triggers are all based on muons passing through the central muon system, as high background rates in the IMU detector prevent triggering on muons in the forward region.

At DØ the Level 1 trigger can match CFT tracks to muon scintillator hits. Momentum cuts may be applied according to four p_T thresholds (1.5, 3, 5, and 10 GeV/c). Additionally, triggers may be formed independently of the CFT information. These triggers are based on hit information from the scintillators and drift chambers, and can

fire based on hits in a single detector layer or on combinations of hits between detectors inside and outside the muon toroid. The Level 2 trigger uses drift chamber timing information as well as hit information to make a more precise position measurement of the muon, allowing for further event rejection. Finally, the DØ Level 3 trigger, like its CDF counterpart, performs full event reconstruction. Events are selected based on a χ^2 fit of the muon detector hits with a reconstructed central track.

4 Muon Reconstruction

Muons reconstructed offline may be classified by region or assigned a quality according to the hits recorded by the detector. Muons at CDF are categorized according to the region in which they were detected (CMU/P, CMX, or IMU). Muons with $p_T > 20$ GeV/c are also categorized as “loose” quality if they pass track quality and isolation cuts and if they deposit minimal energy within the calorimeter. If the muon also produces a drift chamber stub within a minimal distance from the projected track position, that muon is defined as having “tight” quality. DØ muons are classified as either tight, medium, or loose. Tight muons must have scintillator and drift chamber hits both inside and outside the muon toroid, as well as a converged local χ^2 fit. Medium muons are similar to tight muons, but do not require a converged fit and allow for fewer drift chamber hits. Loose muons require only that there be scintillator and drift chamber hits in the same muon layer.

4.1 Background Rejection

Additional cuts are applied in order to remove muons produced from cosmic rays or from pion or kaon decays. CDF identifies cosmics from the track left by the muon in the COT. For each muon track found, a search is performed for a second track opposite the first, as seen in Figure 3. If a second track is found, a χ^2 fit is performed on the combination of the two tracks, and if the resulting fit is consistent with a single particle, the muon is rejected. DØ eliminates cosmics by cutting on the angle between the muon central tracks, the distance of closest approach of the muon track to the interaction point (DCA), and the recorded times of the muon hits in the scintillation counters. Both detectors’ reconstruction routines eliminate pion and kaon decays with χ^2 and DCA cuts on the muons.

4.2 ID Efficiency

The efficiency of the muon reconstruction algorithms is measured by using $Z \rightarrow \mu\mu$ decays that pass a single-muon trigger. The muon that causes the trigger to fire acts as a control for the sample, and the second track in the event is considered as a candidate for reconstruction. In order to be considered a good candidate, the second muon must pass a set of selection criteria. At CDF, the muon pair

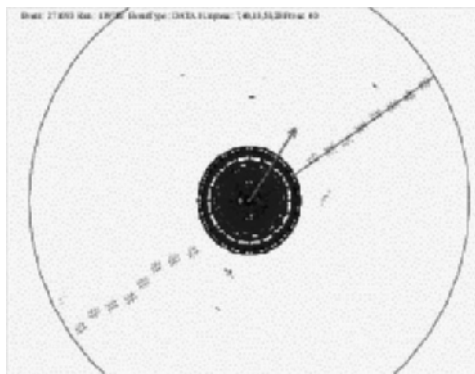


Fig. 3. DØ A cosmic ray muon passing through the CDF central tracker. The straight line indicates the reconstructed muon track.

papers from DØ and CDF made use of the respective experiments' muon systems.

must have an invariant mass between 81 and 101 GeV/c^2 , and the test muon must pass cuts on muon isolation, χ^2 , and DCA. Additionally, the muon must contain a minimum number of COT hits and the energy deposition in the calorimeter must be consistent with the signature of a minimally ionizing particle. These criteria lead to a measured reconstruction efficiency of 87% for muons in the CMU/CMP region and 93% in the CMX region.

At DØ the control muon must be matched to a medium muon with $p_T > 30 \text{ GeV}/c$, and there must be at least 2 high- p_T CFT tracks in the event. The test muon is required to pass a χ^2 cut, and must contain at least 8 CFT hits. The reconstruction efficiency for loose muons is 95%, while the efficiencies for reconstructing medium and tight muons are 82% and 78%, respectively. Much of the inefficiency comes from attempting to reconstruct muons near the boundary between the central and forward muon systems, as seen in Figure 4.

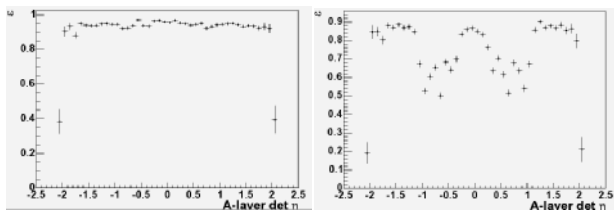


Fig. 4. DØ reconstruction efficiencies vs. η for (left) loose and (right) tight muons in $Z \rightarrow \mu\mu$ events.

5 Conclusion

Both CDF and DØ were designed to allow for detection of muons over a large rapidity range. The three-tiered trigger system used by each experiment provides flexible triggering capabilities, and the experiments' muon reconstruction routines efficiently identify muons generated in proton-antiproton collisions. These combine to form a robust muon system for use in high energy physics. At the time of this writing, roughly two-thirds of the published

Tau Identification at the Tevatron

Stephen Levy (on behalf of the CDF and D0 collaborations)

University of Chicago, Enrico Fermi Institute
Chicago, IL 60637

Abstract. Methods for reconstructing and identifying the hadronic decays of tau leptons with the CDF and D0 detectors at the Fermilab Tevatron collider in Run II are described. Precision electroweak measurements of W and Z gauge boson cross sections are presented as well as results of searches for physics beyond the Standard Model with hadronically decaying tau leptons in the final state.

1 Introduction

The ability to reconstruct and identify tau leptons at the Tevatron is useful for making precise tests of the standard model in the electroweak sector as well as for probing for phenomena beyond the Standard Model (SM) of particle physics. The heavy mass of the tau relative to electrons and muons makes it an interesting candidate to study in the context of electroweak symmetry breaking. Historically, measurements of the tau have been useful in determining the agreement of lepton universality, and the value of the QCD coupling constant at low mass. In addition, efficiently reconstructing taus leads to a larger sample of top quarks which play an important role in the Tevatron's Run II goal of constraining the Higgs boson mass.

Additional motivation for studying tau leptons comes from the minimal supersymmetric extension of the standard model (MSSM) which provides an elegant solution to the problem of fine tuning of the Higgs mass. There are three neutral and two charged Higgs bosons in this model whose couplings to the tau are enhanced in various regions of the model parameter space. Searches for anomalous tau production at the Tevatron are useful in constraining new physics models.

This paper describes the methods used by the CDF and D0 experiments to reconstruct and identify hadronic tau decays. The following sections describe the basic idea underlying the method at both experiments, the specific differences (most importantly the use of a neural net at D0), the triggers used to collect samples of tau decays, results of W and Z cross sections where the boson decays to one or more tau leptons, and results of searches for physics beyond the SM with tau leptons in the final state.

2 Hadronic Tau Reconstruction

This section describes the reconstruction of hadronic tau decays at CDF and D0. The branching fraction for hadronic tau decays is $\sim 65\%$, with the most abundant

final state consisting of exactly one charged pion and ≥ 0 π^0 s, referred to as one-prong decays. Reconstructing π^0 s is an important step in tau reconstruction since roughly three-fourths of the one-prong decays contain at least one π^0 . Reconstruction of leptonically decaying taus is accomplished via electron and muon identification and is not the subject of this proceeding.

Typically at the Tevatron identifying a lepton means identifying an isolated lepton¹ and this distinction is paramount for taus. Hadronically decaying taus are essentially a narrow jet in the detector consisting of charged track(s) pointing to hadronic calorimeter energy deposition and potentially associated electromagnetic energy from $\pi^0 \rightarrow \gamma\gamma$ decays.

The difficulty of reconstructing taus in a hadron collider environment, of course, stems from the fact that some fraction of jets and electrons are also "narrow jets". The ratio of QCD jet production to the electroweak cross section scale is order one million. Though jets may consist of the same final state of charged and neutral particles as taus, they are not an irreducible background since the final state that results from a tau decay will have an invariant mass less than the tau mass and events containing a tau will contain missing energy due to the presence of the tau neutrino. Additionally, the tau travels $\sim 100 \mu\text{m}$ before decaying which means that its decay products will have larger impact parameters (with respect to the event primary vertex) that can be measured using silicon detectors.

However, isolation provides the most powerful variable for distinguishing hadronically decaying taus from jets. Tau identification at CDF and D0 begins by requiring $\sim 5 \text{ GeV}$ of energy deposited in a narrow region of the calorimeter with a well measured track pointing at the cluster. Narrow is dictated by the segmentation of the calorimeter, which is sufficiently more granular at D0. Full

¹ Lepton isolated is defined in terms of the ratio of the transverse momenta (energy) of particles in a cone around the candidate to the lepton's transverse momentum (energy).

details of the detectors at each experiment detectors are given elsewhere [1, 2]. The specifics of the tau reconstruction diverge at this point and are described for each experiment in the following sections.

2.1 Tau Identification at CDF

Tau reconstruction begins at CDF with a well reconstructed track, termed the seed track, pointing at a narrow calorimeter cluster ($|\eta| < 1$)² which consists of ≤ 6 towers. A signal cone is defined with respect to the direction of a seed track ($p_T > 6$ GeV/c) whose opening angle is inversely proportional to the calorimeter energy of the cluster. At high calorimeter energy the angle is fixed to a minimum of 50 mrad due to resolution and at low energy to 175 mrad. An isolation region is defined as the annulus between the signal cone and 30 degrees as shown in Fig. 1. Candidates are rejected if the isolation region contains well measured tracks. The total number of well measured tracks within the single cone is commonly referred to as the number of prongs of the decay (the number of two-pronged taus is useful in understanding the number of fake candidates).

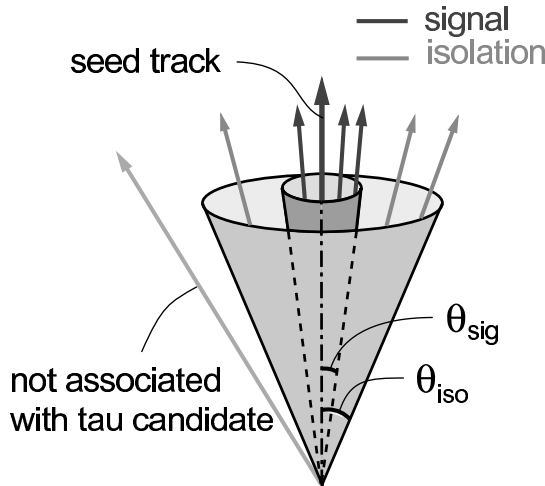


Fig. 1. Schematic illustration of the energy dependent signal and isolation region used to define a tau candidate at CDF.

The electromagnetic (EM) calorimeter at CDF has a multi-wire proportional chamber (CES) embedded at approximately six radiation lengths that is used to reconstruct π^0 candidates (as well as electrons and photons) with energy > 500 MeV. The CES provides two orthogonal measurements of the position of the π^0 candidate with spatial resolution of ~ 3 mm which are matched based on their consistency in terms of deposited energy. The energy assigned to a single π^0 candidate is the energy measured in the electromagnetic calorimeter after an average correction is made for energy deposited by charged tracks in the

² The pseudo-rapidity η is defined as $-\ln(\tan(\theta/2))$, where θ is the polar angle with respect to the proton beam direction

tower, typically of order of a few GeV. For multiple π^0 candidates, the energy in the EM calorimeter is apportioned according to the CES energy of each candidate. Additionally, a variable sized signal cone whose opening angle is inversely proportional to the candidate calorimeter energy is defined for the π^0 s and candidates are rejected if there are well measured π^0 s in the annulus between the signal and isolation cones. The tau candidate four-momentum is constructed from the sum of the four-momenta of the tracks and π^0 s in the signal region.

Tau identification normally refers to extra requirements that are applied to the reconstructed tau candidates. The specific requirements can vary based on the analysis but typical ones are summarized. Taus are required to have a mass consistent with a hadronic tau decay (< 1.8 GeV/c²). Also, to discriminate taus from electrons, the variable ξ is defined as

$$\xi = E_T^{HAD} / \sum |p_T^{trk}| \quad (1)$$

where E_T^{HAD} is the transverse component of the energy that the tau candidate deposited in the hadronic calorimeter. Requiring that $\xi > 0.2$ substantially reduces the number of electrons that are reconstructed as tau candidates. Additionally, tau candidates are required to consist of one or three prongs with the absolute value of the sum of the charge of the tau tracks equal to one. The efficiency to reconstruct and identify simulated tau decays as a function of the true energy of the hadronic system is shown in Fig. 2. The efficiency plateaus around 45% above 50 GeV. The probability for a jet to be reconstructed as a tau candidate, termed fake rate, is measured in data events triggered by jets with various energy thresholds. The fake rate is parameterized in terms of the jet cluster energy and the ratio of the jet energy and mass. Fig. 2 shows the rate of jets misidentified as taus as a function of jet energy for jets passing a 50 GeV trigger requirement. The fake rate is $\sim 0.5\%$ at 50 GeV.

2.2 Tau Identification at D0

A similar method for reconstructing hadronic tau decays is employed at D0 but the tau *identification* method differs from that used at CDF. The tau candidates are found by matching a track with $p_T > 1.5$ GeV/c to a narrow calorimeter cluster with $E_T > 5$ GeV [5]. In this case, narrowness is defined by the sum over the distance between each tower in the cluster and the cluster's center weighted by the E_T of the tower. Additional tracks within a cone $R = \sqrt{(\Delta\phi)^2 + (\Delta\eta)^2} < 0.3$ of the calorimeter cluster are added if the invariant mass of the resulting candidate calculated from the tracks is consistent with a tau. Subclusters with minimum energy 800 MeV are constructed from the cells in the EM section of the calorimeter as π^0 candidates. The tau candidates are separated into three classes based on the tracking and calorimetry information: (1) single track with no π^0 candidates, (2) single track with $\geq 1\pi^0$ candidate, or (3) more than one associated track.

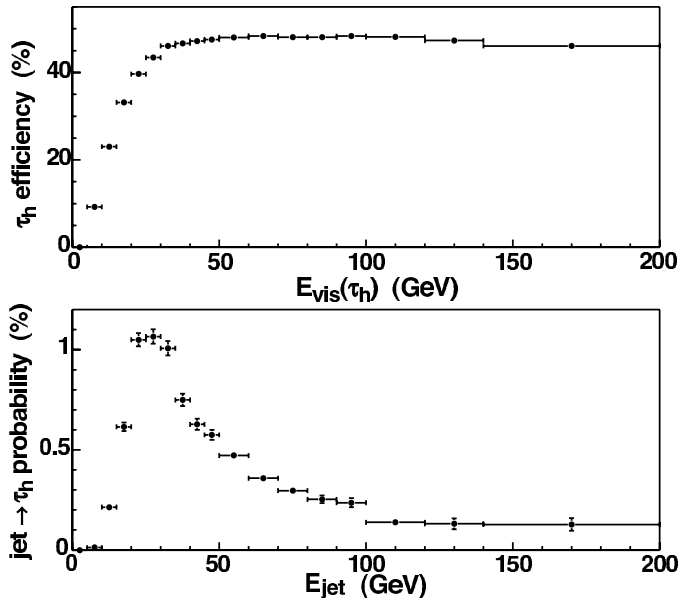


Fig. 2. Tau reconstruction and identification efficiency at CDF for simulated hadronically decaying taus as a function of visible tau energy (top). Rate of jets misidentified as taus as a function of jet energy at CDF (bottom).

A neural network (NN) is used to separate these tau candidates from the large background of jets. The neural network consists of a single input layer with several nodes, a single hidden layer, and a single output layer. Separate NN training is performed for each tau category described above using Monte Carlo simulation of single tau leptons for the signal and jets from data events for the background. The input variables of the neural net [5] are typically ratios of the tau candidate kinematic properties to minimize the dependence on the absolute energy scale of the simulation. For example, there is a powerful *profile* variable defined as $(E_{T_1} + E_{T_2})/E_T^*$ where E_{T_1} and E_{T_2} are the transverse energies of the two most energetic calorimeter towers in the tau cluster (E_T^*). This variable is used in the NN for all tau types but others are specific to the tau candidate class. It is important to note that the training is not the same for all DØ tau analyses: the training may rely on event information for the physics being investigated. The efficiency for taus selected in $Z \rightarrow \tau\tau$ Monte Carlo simulation after a cut on the output of the NN is shown in Table 1 along with the rate that QCD jets in data are identified as taus for each tau class [4]. Relative to the selection used by CDF, DØ has a larger efficiency with a correspondingly larger fake rate. There are additional restrictions that are used in tau identification that are analysis dependent: some apply an anti-muon requirement on the tau candidate or use an additional NN to separate tau from electron candidates. Performance of the NN in data will be presented in the context of a $Z \rightarrow \tau\tau$ analysis described in Sec. 4.1.

Table 1. Efficiency and fake rate for tau candidates in $Z \rightarrow \tau\tau$ simulation and QCD jets in data respectively using DØ’s neural net.

	Efficiency ($Z \rightarrow \tau\tau$)	Fake Rate (QCD)
type1	0.78 ± 0.03	0.145 ± 0.014
type2	0.75 ± 0.02	0.042 ± 0.004
type3	0.73 ± 0.02	0.039 ± 0.002

3 Tau Triggers

Before presenting the results of physics analyses relying on tau lepton reconstruction, it is necessary to briefly review the method by which both experiments collect large samples of tau decays. Both experiments have a three level trigger system which is designed to reduce the nominal crossing rate of 7.6 MHz to approximately 70 Hz which can be written to tape. The trigger consists of hardware at Levels 1 and 2 (using only axial tracking information) and a system of software algorithms executed on a computer farm at Level 3. The CDF tau triggers [3] search for a tau candidate combined with large missing transverse energy or another tau candidate, and of *lepton+track* triggers which are used to identify an electron or muon in combination with an isolated track. DØ uses their NN to identify low p_T tau candidates at Level 3. Many DØ tau analyses currently rely on the presence of a muon or electron in the event which forms the basis for the trigger. A typical rate of the *electron (muon)+track* trigger at CDF is 3.0 (1.5) Hz at Level 3 for an instantaneous luminosity of $10^{32} \text{ cm}^2 \text{ s}^{-1}$.

4 Electroweak Tau Results

Both CDF and DØ have demonstrated the ability to reconstruct large samples of hadronically decaying taus in electroweak measurements of gauge boson cross sections.

4.1 DØ Electroweak Tau Results

DØ has measured the cross section for Z production times the branching fraction to tau leptons in the channel in which one tau decays leptonically into $\mu\nu_\mu\nu_\tau$ and the other into hadrons + ν_τ [5]. The analysis is based on 226 pb^{-1} of data. The event selection primarily consists of finding an isolated muon with $p_T > 12 \text{ GeV}/c$ opposite a tau candidate. The events with a muon and tau candidate with the same charge are used to estimate the background from QCD (primarily $b\bar{b}$) and the additional background from $W \rightarrow \mu\nu + \text{jets}$ is estimated in magnitude and shape from Monte Carlo simulation. By requiring that the NN output for the tau candidate be > 0.8 the signal to background ratio is improved by a factor of ~ 1200 to roughly 1 : 1. Fig 3 compares the expected distributions for the tau E_T and muon p_T (after the NN cut) to the background from

data and to the data after the background has been subtracted. With a signal sample of ~ 900 events, DØ measures the that product of the Z cross section times the branching fraction to tau leptons is in good agreement with the NNLO prediction of 242 ± 10 pb [6].

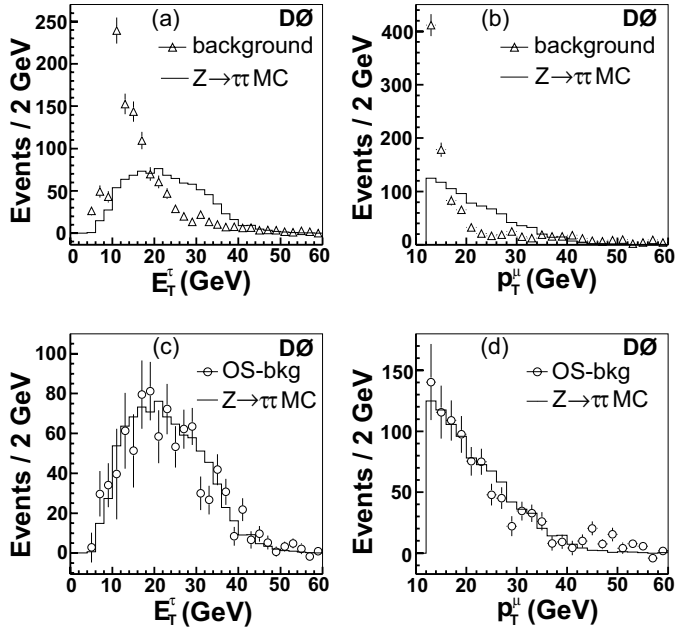


Fig. 3. DØ comparison of tau E_T and muon p_T distributions after NN cut; (a), (b) estimated background (open triangles) and predicted $Z \rightarrow \tau\tau$ signal (histogram); (c), (d) background subtracted data (open circles) and predicted $Z \rightarrow \tau\tau$ signal.

4.2 CDF Electroweak Tau Results

CDF has measured the product of the cross section for W production times the branching fraction for $W \rightarrow \tau\nu$ using 72 pb^{-1} of data [7]. The event selection requires large missing transverse energy (> 25 GeV) and a tau candidate without other significant jet activity. This selection results in an abundant pure sample of hadronic taus that are useful for understanding the differences between the tau reconstruction in data and Monte Carlo simulation. The signal to background ratio for these events is ~ 3 with a yield of $24 \text{ events pb}^{-1}$. Fig. 4 shows the distribution of the number tracks in the tau candidates along with the expected background. The analysis additionally measures the ratio of branching fractions for $W \rightarrow \tau\nu$ and $W \rightarrow e\nu$ and finds that the ratio of the tau and electron coupling constants to the W are consistent with 4% precision.

CDF has also measured the cross section for Z production times the branching fraction for $Z \rightarrow \tau\tau$ in events where one tau decays hadronically and the other decays to $e\nu_e\nu_\tau$ with 72 pb^{-1} of data [7]. The result is consistent with SM expectations.

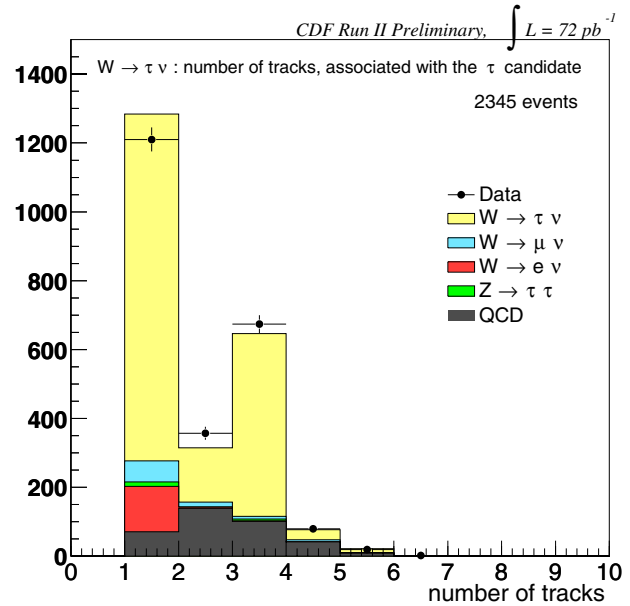


Fig. 4. CDF charged multiplicity distribution for $W \rightarrow \tau\nu$ candidates.

5 Searches for New Physics

With the tau electroweak precision measurements in hand, both experiments are focusing efforts on searches for physics beyond the SM that include taus in the final state. As this topic was the subject of other presentations at these proceedings [8], interesting results are only summarized here. DØ has a preliminary conference result involving chargino and neutralino searches in the $e\tau\ell$ final state, as well as for R-parity violated supersymmetry in the $e\tau\tau$ final state. CDF has a preliminary conference result for a search for pair production of supersymmetric top quarks decaying via R-parity violating coupling to b-quark and a tau lepton. Also, CDF has published the results of a search for anomalous resonant production of tau lepton pairs with large invariant mass [9] and submitted for publication a search for neutral MSSM Higgs boson decaying to tau pairs [10].

6 Conclusion

Though the study of final states with tau leptons is difficult in hadron environments, both CDF and DØ have demonstrated the ability to collect, reconstruct and identify large samples of tau decays. The probability for a jet to be identified as a tau is well measured using data. These samples have been used to measure electroweak gauge boson cross sections which are consistent with SM expectations. The Tevatron experiments are ramping up their searches for anomalous production of tau decays that will continue to constrain physics beyond the SM.

6.1 Acknowledgments

I would like to thank the HCP organizers for providing an excellent conference as well as the CDF and D $\bar{0}$ tau groups for their thoughtful contributions to this proceeding.

References

1. D. Acosta *et al.* (CDF Collaboration), Phys. Rev. D **71**, 032001 (2005).
2. V. Abazov *et al.* (D $\bar{0}$ Collaboration), Nucl. Instrum. Methods Phys. Rev. **A**, in preparation for submission.
3. A. Anastassov *et al.* (CDF Collaboration), Nucl. Instrum. Methods Phys. Rev. **A518**, 609 (2004).
4. A. Le Bihan *et al.* (D $\bar{0}$ Collaboration), Nucl. Phys. Proc. Suppl **144**, 333-340 (2005).
5. V. Abazov *et al.* (D $\bar{0}$ Collaboration), Phys. Rev. D **71**, 072004 (2005)
6. R. Hamberg, W. van Neerven, and T. Matsuura, Nucl. Phys. **B359**, 343 (1991).
7. A. Safonov *et al.* (CDF Collaboration), Nucl. Phys. Proc. Suppl **144**, 323-332 (2005).
8. See the proceedings at this conference from A. Goussiou, entitled "Higgs Searches at the Tevatron," and from M. Cousinou, entitled "Searches for Supersymmetry at the Tevatron."
9. D. Acosta *et al.* (CDF Collaboration), Phys. Rev. Lett. **95**, 131801 (2005).
10. A. Abulencia *et al.* (CDF Collaboration), submitted to PRL, hep-ex/0508051.

Electron and photon identification in ATLAS

Comparison between test beam data and simulation.

F. Derue¹ - For the ATLAS collaboration

LPNHE - Laboratoire de Physique Nucléaire et de Hautes Énergies. IN2P3/CNRS - Universités Paris VI et Paris VII, France

Abstract. The ATLAS experiment at the Large Hadron Collider (LHC) will face the challenge of efficiently selecting interesting candidate events in pp collisions at 14 TeV centre-of-mass energy, whilst rejecting the enormous number of background events. In this talk an overview of the current physics and system performance of the offline selection for electrons and photons is given. Test-beam data, covering a large part of the final detector, have been analysed, and measurements using various important particle identification criteria and methods are presented. The particle identification performance has also been evaluated using detailed Monte Carlo simulations. The efficiency for the signal channels as well as the background rejection capability will be highlighted.

1 Introduction

The CERN Large Hadron Collider (LHC) is a proton-proton collider with 14 TeV energy in the centre of mass and a design luminosity of $10^{34} \text{ cm}^{-2} \text{ s}^{-1}$. The ATLAS (A Toroidal LHC ApparatuS) experiment is one of the two major multi-purpose detectors currently under construction at the LHC. Its inner detector consists of tracking detectors enclosed in a solenoidal magnet with 2 T field. From the inner radius (5 cm) to the outside radius (107 cm) it consists of pixel detectors, silicon strip detectors (SCT) and transition radiation drift tubes (TRT), covering the pseudo-rapidity interval $|\eta| < 2.5$.

The inner detector is surrounded by a sampling electromagnetic calorimeter based on lead and liquid argon (LAr) technology and a hadronic calorimeter based on LAr in the end-caps and on iron/scintillator tiles in the barrel. The global detector dimensions (diameter 22 m, length 42 m) are defined by a large air-core muon spectrometer, providing precision measurements of high- p_T muons over $|\eta| < 2.5$.

The physics programme envisaged ranges from the search for the Higgs boson, which is the last missing particle within the Standard Model (SM), searches for physics beyond the SM such as supersymmetric particles, new additional W and Z bosons and also precision studies, such as measurements of the t quark and W boson masses and unexpected signals from unpredicted physics scenarios.

2 The electron and photon selection goals

Events with electrons and photons in the final state are important signatures for many physics analyses envisaged at the LHC, since electrons and photons are relatively easy

to measure precisely and to trigger on. Isolated high- p_T electrons and photons are not easy to identify at the LHC because of the very large QCD background from high- p_T jets, which result in an electron/jet ratio of about 10^{-5} at the LHC (to be compared to about 10^{-3} at the Tevatron) for isolated electrons from W/Z decays, and to a photon/jet ratio of about 10^{-4} (to be compared to about 10^{-3} at the Tevatron). Nevertheless, final states containing several electrons or photons such as $H \rightarrow 4e$ or $H \rightarrow \gamma\gamma$ decays provide convincing discovery channels [1].

Electron and photon reconstruction mainly exploits data coming from the electromagnetic calorimeter and the Inner Detector (ID) systems. As described in detail in the next sections, electromagnetic objects can be identified in the calorimeter by looking at the transverse and longitudinal shower shapes and at isolation variables. For electrons, a track is then required to match in position and energy that measured in the electromagnetic calorimeter. For photons no track is required (except in the frequent case of converted photons) but γ/π^0 separation criteria are required using some of the unique features of the electromagnetic calorimeter.

3 Beam test performance

3.1 the Transition radiation tracker

The Transition Radiation Tracker (TRT) is one of the components of the ATLAS Inner Detector. It combines electron identification capability with charged-particle track reconstruction. This is achieved by interleaving layers of xenon-filled drift tubes of small diameter (straws) with radiators. In order to test the physics performance

of the proposed detector, several small-scale TRT prototypes were built and tested in the H8 beam line at the CERN SPS accelerator over the past years. A detailed description of the test beam setup and of the measurement results can be found in [2]

Electron identification makes use of the large energy depositions due to the transition radiation (TR). Typical TR photon energy depositions in the TRT are 8–10 keV, while minimum-ionising particles, such as pions, deposit about 1–2 keV (Fig. 1, left).

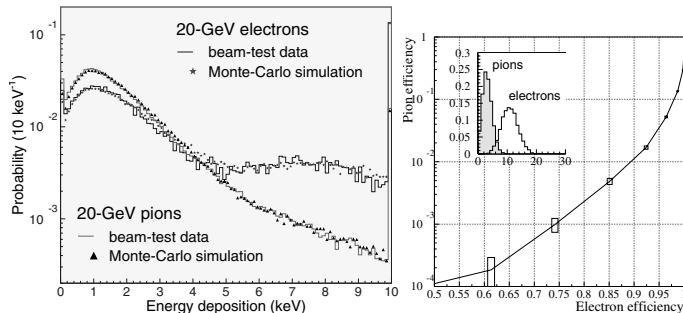


Fig. 1. Differential energy spectra from data and simulation for a single straw with radiator for 20 GeV pions (dE/dx) and electrons (dE/dx and TR) (left); resulting pion efficiency versus electron efficiency at 20 GeV (right) - see [3].

The parameter used in the electron identification is the number of local energy depositions on the track above a given threshold, which when carried provides a pion versus electron efficiency curve as shown in Fig. 1, right.

The TRT performance was evaluated using electron, pion and muon beams with energies varying from 5 to 300 GeV. The distributions of the number of energy depositions for pion and electron tracks reconstructed using a wheel sector prototype are shown for a threshold of ~ 6 keV in the top left-handed corner of Fig. 1 (right). In the same figure, the resulting pion efficiency as a function of the chosen electron efficiency is also displayed. For an electron identification efficiency of 90%, the measured pion efficiency is about 1.2%, *i.e.* a rejection factor of 75 is achieved against 20 GeV pions in a magnetic field of 0.8 T, for a geometry corresponding to that of the ATLAS Inner Detector around $|\eta| \sim 1.2$.

3.2 The electromagnetic calorimeter

A detailed description of the barrel and end-cap modules of the ATLAS electromagnetic calorimeter, and of the signal reconstruction techniques can be found in [4]- [5]. Seven production modules, four for the barrel calorimeter (three for the end-cap) were tested in the CERN H8 (H6) beam lines over several months during 2001-2002. The modules reported and in [4]- [5] were pre-production modules (“module 0”s), whereas the results presented here have been obtained with series production modules. Details on the performance obtained with these modules can

be found in [6]. The calorimeter performance was measured using secondary or tertiary electron and pion beams, with momenta ranging from 20 to 245 GeV for barrel modules and from 20 to 150 GeV for end-cap modules. The beam lines were equipped with three scintillators in front of the calorimeter for triggering purposes. Four multi-wire proportional chambers allowed to determine the beam impact point at the calorimeter with a resolution of about 250 μm in the η direction. The size of the last two scintillators, 4 \times 4 cm², defined the beam acceptance. Cryostats housing the modules were mounted on remotely controlled rails that allowed movements in η and ϕ while ensuring incident angles similar to the ones expected in ATLAS for all positions. A 3X₀ lead absorber, a pion counter, a 5 λ iron absorber and a muon counter were placed downstream of the cryostat. The readout electronics is similar to the final ATLAS electronics, since it is made of boards functionally identical to the final ones, but, however, do not yet equipped with radiation-resistant ASICs. Energy scans at fixed positions in η and ϕ were also carried out, and η -scans were done at fixed electron energy of 245 GeV for the barrel and 120 GeV for the end-cap.

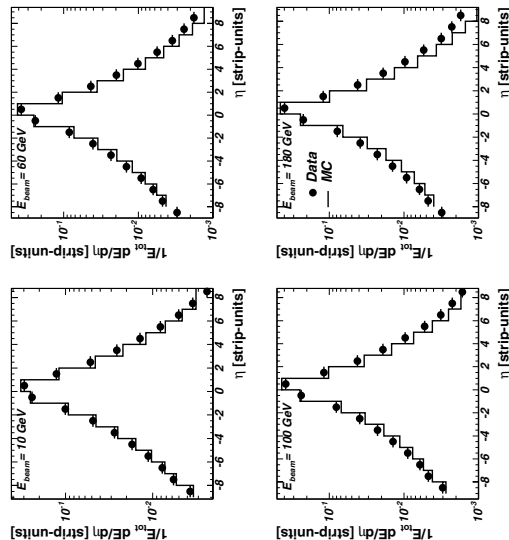


Fig. 2. Lateral shower development of electrons with energies from 10 GeV to 180 GeV in the test beam data (dots) and corresponding G4 simulation (line) - see [8].

Electromagnetic showers initiated by electrons are expected to be essentially contained in the electromagnetic calorimeter. The hadronic showers start at a larger depth of the module and there is often a substantial fraction of the total energy shower leaking into the hadronic calorimeter. However, a fraction of hadron-initiated showers may be fully contained creating a potential for particle misidentification. Therefore it is necessary to use the longitudinal and lateral segmentation of the electromagnetic calorimeter to minimise the probability to misidentify hadronic jets

as electrons while maintaining high electron identification efficiency.

The data were analysed using the standard ATLAS clustering procedure. The shape of the longitudinal shower profile was contained in the information of the energy E_i deposited in each layer of the calorimeter. Additional information was contained in the lateral shower profile, characterised by the number of hit cells in each layer, i.e. the number of cells that contain energy well above the noise level. Fig. 2 shows the lateral shower development of electrons in the test beam data and compares them to a G4 standalone simulation. The agreement between data and simulation is good over the energy range from 10 to 180 GeV.

In the search for $H \rightarrow \gamma\gamma$ decays, the calorimeter has to provide an additional rejection of about three against π^0 for a photon identification efficiency of 90%, using the fine granularity in the first sampling. This has been demonstrated using specific test-beam data [7], obtained by inserting some material in the beam line upstream of a bending magnet, to cause the incoming electron to emit hard bremsstrahlung photons. By mixing single photon events with the appropriate kinematics, it was possible to mimic a π^0 decays to two photons. The agreement between simulation and data is satisfactory, and it could be shown that the required rejection factor is reached over most of the kinematical range, as shown in Fig. 3.

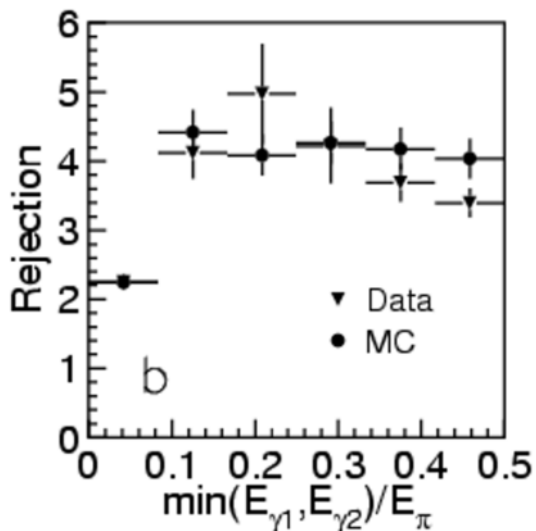


Fig. 3. π^0 rejection calculated in bins of $\min(E_{\gamma 1}, E_{\gamma 2})/E_{\pi^0}$, for data and simulation [7].

3.3 The 2004 combined test beam

In the year 2004, ATLAS has been involved in a huge combined test beam (CTB) effort in the CERN H8 beam line. A complete slice of the barrel detector and of the muon spectrometer end-caps has been tested, with the

following clear goals: pre-commission the final elements and study the combined detector performance in a realistic environment, including calibration and alignment. Thanks to this experience, a lot of experience has been acquired in terms of combined operation of all detectors, online monitoring and of data acquisition and triggering, and a considerable amount of data (4.6 TB of data, 90 million events) has been collected and is presently under analysis.

A full slice of the ATLAS experiment (Fig. 4) has been tested with beams of different particles (pions, electrons, protons, muons and photons) at different energies and polarities, ranging from 1 GeV up to 350 GeV, providing a unique opportunity to evaluate the individual sub-detector performances, but also to exploit the full power of the ATLAS detector for detailed particle identification and measurements and to understand better the detector before the commissioning phase. With the data which

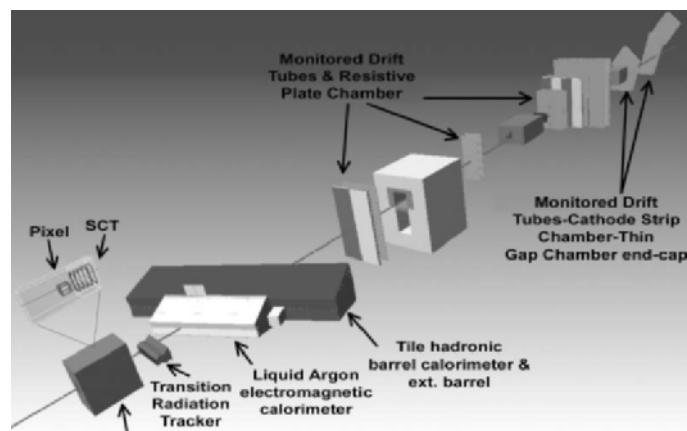


Fig. 4. Geant4 layout of the Combined Test Beam setup.

have been collected, it will be possible to study electron and pion identification and measurement under different conditions (e.g. varying the amount of material in the detector and the magnetic field). Tagged photon beams have also been used to study photon identification and measurement, including in particular photon conversions in the Inner Detector. These data will also be used for detailed G4/FLUKA validation studies and tuning.

4 Combined ID/EM calorimeter performance

This section is devoted to a brief discussion of how the combination of the Inner Detector and the EM calorimeter (and to a lesser extent, the hadronic calorimeter) can be used to identify and measure electrons and photons. During the LHC preparation phase, all experiments have substantial needs for simulated data in order to estimate the physics performance of the experiment and to prepare the software tools for data analysis. Monte Carlo data are produced during so-called Data Challenges. Most of the results presented in this section is obtained from Data Challenge 1 [9].

4.1 Photon/jet separation in ATLAS

Given the amount of material in front of the calorimeter, about 40% of the photons from e.g. $H \rightarrow \gamma\gamma$ decays convert into e^+e^- pairs before depositing their energy in the calorimeter. Since the $H \rightarrow \gamma\gamma$ signal is small, it is important to recover these conversions to maintain its efficiency as high as possible. Conversions at radii below ~ 80 cm are reconstructed in the ID. For such events and the energy deposited in the calorimeter in a 3×7 ($\eta \times \phi$) window is computed, rather than the standard 3×5 window used for unconverted photons. The larger window size collects most of the energy of the electron pair and of possible bremsstrahlung photons while preserving excellent energy resolution.

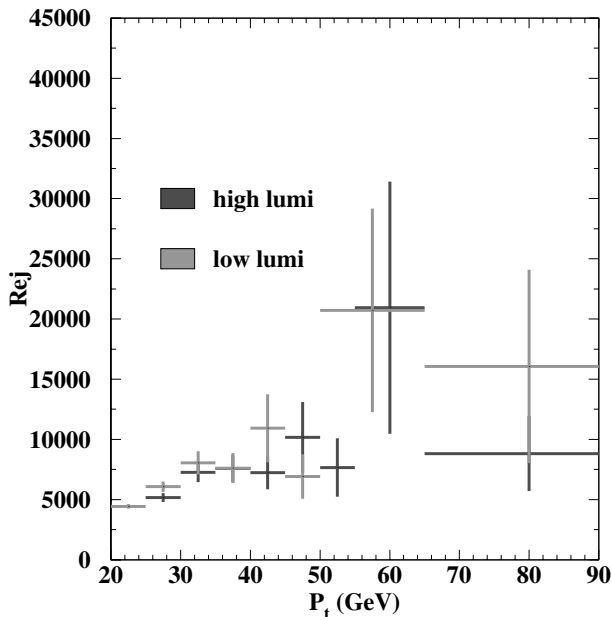


Fig. 5. For a photon identification efficiency of 80%, the jet rejection is obtained as a function of the jet E_T for events at low luminosity ($2 \times 10^{33} \text{ cm}^{-2} \text{ s}^{-1}$) and high luminosity ($10^{34} \text{ cm}^{-2} \text{ s}^{-1}$) [10].

In the more general case, the photon/jet separation relies on the search for electromagnetic objects, with cuts which include Level-1 and High Level Trigger cuts, shower shape and isolation cuts in the calorimeter, and the requirement that no track is found in the ID within a $\Delta\eta \times \Delta\phi$ region of size $\pm 0.1 \times \pm 0.1$ around the calorimeter cluster. Fig.5 shows the jet rejection after photon selection cuts as a function of the jet transverse energy E_T . A rejection of better than 7000 can be obtained for $E_T > 40$ GeV, both for low and high luminosity.

4.2 Electron/pion separation in ATLAS

The efficient tagging of low energy electrons is an important tool for B-physics, as well as a complementary method to b-tagging. Separating low energy electrons from pions by analysing the energy deposits in the calorimeter alone is not an easy task, since these electrons are within or near to jets. Instead the ID must be used to seed the calorimeter clustering. The strategy consists of several steps. First, tracks with $p_T > 2$ GeV/c are found in the ID and then one looks the EM calorimeter regions hit by the tracks. By combining various shower shape estimators, the E/p value and the information from the TRT, it is possible to get the pion rejection versus the electron identification efficiency curves of Fig. 6.

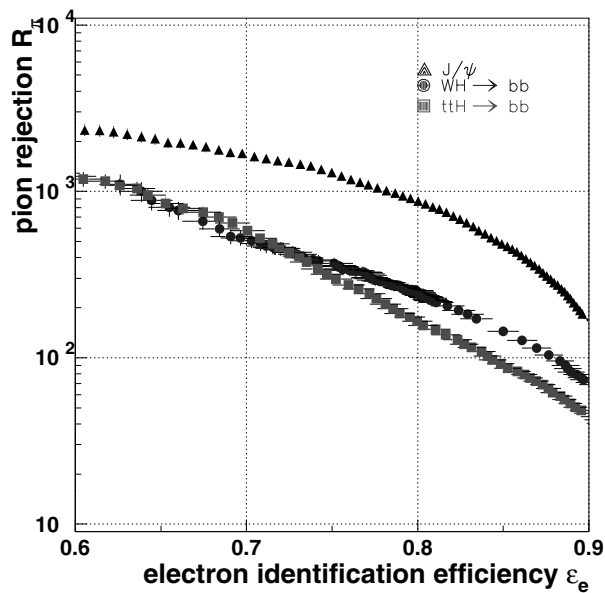


Fig. 6. Pion rejection versus electron identification efficiency for low energy electrons [12]- [13].

In the case of a J/ψ sample, a rejection factor of pion tracks 1000 is achieved for an electron identification efficiency of 80%. This allows the reconstruction of $J\psi$ events with a signal to background ratio around 2. Electrons coming from $WH \rightarrow b\bar{b}$ events are located inside jets. Thus their identification is harder. For a 80% identification efficiency, rejection of pion tracks from background sample is ~ 250 . This soft electron identification could then be used for b tagging purpose, and has been shown to be a complementary method to standard vertex-based tagging, despite the small branching ratio.

4.3 Electron/jet separation in ATLAS

The identification of isolated electrons with $p_T > 20$ GeV/c will be essential for the physics searched at the

LHC. A challenging task is to identify electrons in the presence of a huge QCD jets background, which is $\sim 10^5$ times higher, as in the case of W and top decays.

Table 1. Electron identification efficiency ε_e for single electrons with $p_T > 25$ GeV and jet rejection (with $p_T > 22$ GeV) of the offline analysis at low luminosity [11].

	ε_e (in %)	jet rejection ($\times 10^3$)
Calo	91.2 ± 0.4	1.3 ± 0.1
ID	81.3 ± 0.5	19.5 ± 2.5
ID-Calor	76.4 ± 0.6	57.0 ± 7

To separate electrons from jets, cuts were developed to maintain a reasonable electron identification efficiency even with pile-up at high luminosity, while removing a high fraction of jet events. The cuts include Level-1 and High Level Trigger cuts, shower shape and isolation cuts in the calorimeter, cuts on track in ID, cuts on ID-Calor matching in position and energy and transition radiation cuts. The effect of applying all these cuts one after the other to a single electron sample and an inclusive jet sample are shown in Tab. 1. As in the case of photon/jet separation, after calorimeter selection the dominant background consists of photons from π^0 and η decays. This is significantly reduced by requiring the presence of a high p_T track. After the ID-Calor match, charged hadron remain as the main background. The signal-to-background ratio is 2 : 1 for a QCD-jet rejection of 0.6×10^5 . The signal is equally from semileptonic decays of heavy quarks and isolated electrons from W and Z decays. The QCD-jet rejection can be improved by using the transition radiation rejection of the TRT as detailed in section 3.1. An electron identification efficiency of about 70% is obtained while a QCD-jet rejection above $\times 10^5$ is achieved. Finally, removal of photon conversions by direct reconstruction, would allow the identification of a pure electron inclusive sample with a jet rejection around 10^6 .

5 Conclusion

The ATLAS collaboration has devoted considerable effort over the past years to ever more complex test-beam data taking, culminating with the combined test-beam measurements which ended in fall 2004. The analysis of these data, focusing on complex issues such as those related to identification and measurement of electrons in magnetic field and to the reconstruction of photon conversions, will provide strong guidance to tune and validate the software tools needed for ATLAS. This thorough preparation is one of several prerequisite for the delivery of high quality physics data during the initial operation of ATLAS at the LHC. In the meantime, powerful electron and photon identification algorithms were developed and tuned over the past years on detailed Monte Carlo simulation. While maintaining high electron and photon identification

efficiency, these algorithms allow to reach very high QCD-jet rejection. These strong identification ability coupled with performance of detector themselves will be crucial for many important discovery channels.

References

1. "ATLAS detector and physics performance technical design report", ATLAS TDR 14 & 15, CERN/LHCC/99-14 & 15.
2. T. Akesson et al. (ATLAS Coll.), "ATLAS Transition Radiation Tracker test-beam results", Nucl. Instrum. Meth. **A522**, (2004) 50-55.
3. V. Mitsou et al. (ATLAS Coll.), "The ATLAS Transition Radiation Tracker", ATLAS-CONF-2003-012 (2003), proc. of ICATPP 2003
4. B. Aubert et al. (ATLAS Coll.), "Performance of the ATLAS electromagnetic calorimeter end-cap module 0", Nucl. Instrum. Meth. **A500**, (2003) 178-201.
5. B. Aubert et al. (ATLAS Coll.), "Performance of the ATLAS electromagnetic calorimeter end-cap module 0", Nucl. Instrum. Meth. **A500**, (2003) 202-231.
6. Ph. Schwemling et al. (ATLAS Coll.), "ATLAS electromagnetic calorimetry and performance of electron/photon detection", Eur. Phys. J., C 34 (2004)
7. J. Colas et al. (ATLAS EMLarg Coll.), "Position resolution and particle identification with the ATLAS EM calorimeter", Nucl. Instrum. Meth. **A550**, (2005) 96-115
8. T. Carli et al. (ATLAS EMLarg Coll.), "Energy linearity and resolution performance of the ATLAS electromagnetic barrel calorimeter in the CERN electron beam", to be submitted to NIM.
9. R. Sturrock et al. (ATLAS Coll.), "A Step Towards A Computing Grid For The LHC Experiments : ATLAS Data Challenge 1", Nucl. Instrum. Meth. **A502**, (2003) 446-449
10. M. Escalier et al., "Photon/jet separation with DC1 data", ATLAS Note ATLAS-COM-PHYS-2005-048
11. F. Derue, C. Serfon "Electron/jet separation with DC1 data", ATLAS Note ATLAS-PHYS-PUB-2005-016
12. T. Bold et al., "Pile-up studies for soft electron identification and b-tagging with DC1 data", ATLAS Note ATLAS-COM-PHYS-2005-027
13. F. Derue et al., "Reconstruction of DC1 $J/\psi \rightarrow e^+e^-$ decays and use for the low energy calibration of the ATLAS electromagnetic calorimeter", ATLAS Note ATLAS-COM-PHYS-2005-022

Muon identification at CMS, and confrontation with Monte Carlo and test beam data

Tim Cox ^a

University of California at Davis, Davis, CA 95616, USA (e-mail: Timothy.Cox@cern.ch)

Abstract. Three systems of muon detectors are currently under construction as an integral part of the Compact Muon Solenoid (CMS) experiment at the CERN Large Hadron Collider. After discussing the layout and operating principles of the detector systems, some results obtained from test beams are compared with simulation. Muon identification in CMS involves three stages: the Level 1 muon trigger, the higher-level muon trigger, and offline muon reconstruction. How these stages should work in practice is described, illustrated by results from detailed simulation.

1 Introduction

The Compact Muon Solenoid (CMS) experiment at the CERN Large Hadron Collider (LHC) is currently under construction and is expected to be ready to take data when LHC first turns on for pp collider physics at 14 TeV centre-of-mass energy in 2007. Muons will be detected and their momenta measured by three detector subsystems [1] outside the coil of the 4 T superconducting solenoid magnet, as depicted in Figs. 1 and 2. In the ‘barrel’ region, $|\eta| < 1.2$, muon tracks are detected in an array of Drift Tubes (DT), and provide a precise measurement in the bending plane. In the endcap regions $1.2 < |\eta| < 2.4$, where the solenoidal field can be non-uniform and inhomogeneous, and background charged particle hit rates can

^a Invited talk on behalf of the CMS Collaboration

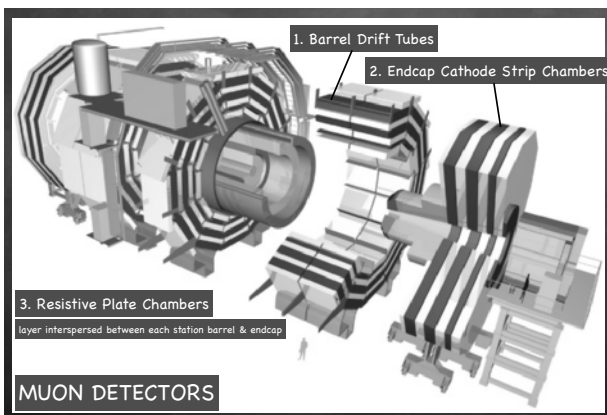


Fig. 1. Schematic expanded view of the CMS detector with the muon subsystems marked.

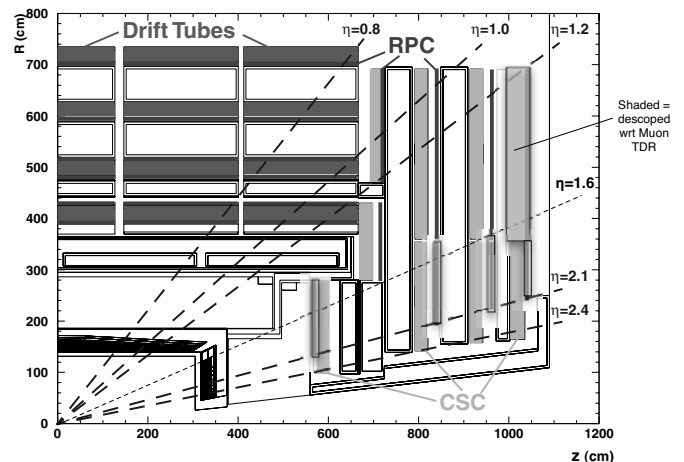


Fig. 2. The layout of the muon system in CMS showing the radial position of the detectors as a function of the position along the beam line, z . The dashed lines represent contours of constant pseudorapidity, η .

be high, a system of Cathode-readout Strip Chambers (CSC) is used. These are multi-layer detectors: in both barrel and endcap there are four ‘stations’ of detectors: at different radii, r , in the barrel, and at different positions along the beam line, z , in each endcap. A station of DTs contains 3 ‘superlayers’, measuring ϕ , θ , and ϕ again, respectively and each superlayer contains 4 layers of drift tubes. There are thus 48 drift tube layers for each of 4 stations. A station of CSCs is interspersed between each of the steel disks which return the magnetic flux of the solenoid. Each CSC is of trapezoidal shape with a maximum length 3.4 m and maximum width 1.5 m, and contains 6 planes of fan-shaped cathode strips alternating with planes of anode wires. There are chambers covering 10° and 20° sectors. A muon traversing all four stations of one endcap should (ideally) leave a total of 24 hits in

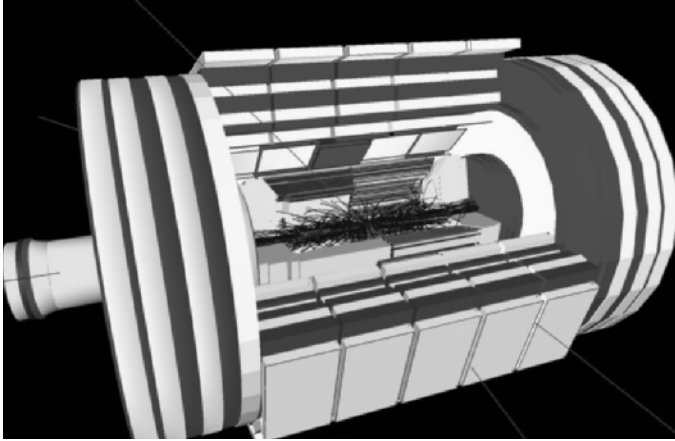


Fig. 3. Visualization of a simulated Higgs particle decaying to four muons in the CMS detector.

successive CSCs. Between the stations of DTs and CSCs there will be Resistive Plate Chambers (RPC), 6 layers in the barrel and 4 in the endcap. These have good spatial resolution and excellent time resolution: an RPC is capable of tagging the time of an ionizing interaction faster than the 25 ns separation between two successive bunch crossings of the LHC. This capability will be important in the operation of the muon trigger.

The importance of the muon detectors can be simply demonstrated by a simulated event display of an LHC event in which a Higgs particle is produced and decays ultimately into four muons, Fig. 3. Both the DT chambers and the CSCs are capable of measuring the positions of traversing muons to a precision of 250 μm or better.

2 Simulation confrontation with test beam data

Several test beams have been used for the design and development of the detectors and their electronics. CMS has a full detector simulation based on GEANT4 (in the past, GEANT3) [2] involving a detailed description of the detector geometry and materials, using a fine-grained magnetic field description based on a TOSCA simulation. The simulation of electronics and signal response is performed afterwards, and is highly CMS-specific. The trigger logic is also simulated in detail.

2.1 Cathode strip chambers

The latest 2004 test beam data involving CSCs and RPCs is still under analysis and being compared with simulation. An essential component of the CSC electronics is a Switch Capacitor Array which continuously samples pulse heights on the strips every 50 ns. When a trigger is received this is read out to ADCs, and from these values the precision position measurements in the chambers can be extracted. Figure 4 shows the pulse heights on the six layers of a CSC due to a traversing muon in a test beam [3]. The

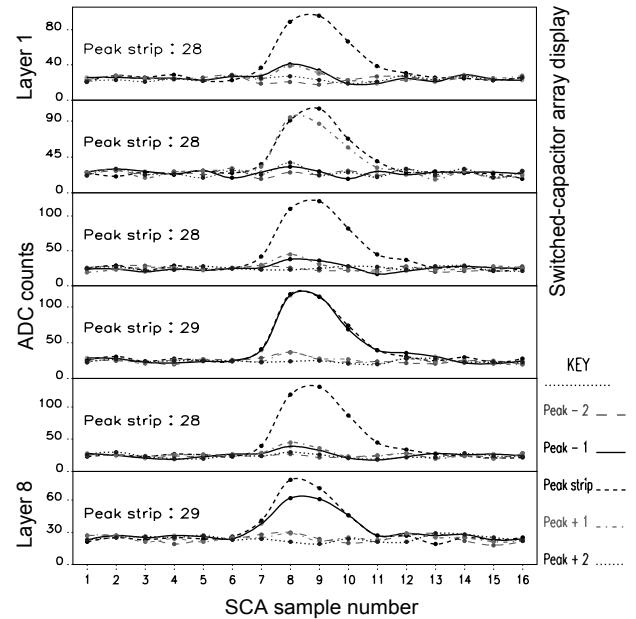


Fig. 4. Switch capacitor array pulse height distributions as a function of time in the 6 layers of an endcap cathode strip chamber. These are results from a chamber placed in a muon test beam.

simulation includes modelling of the SCA response, and preliminary results show that both shape and timing of simulation and data agree closely.

2.2 Drift tube chambers

The latest DT test beam data, also from 2004, and using two drift chamber modules, have already been compared in detail with simulation. Figure 5 compares typical drift time distributions, here for an incident muon angle of 10° , and shows very good agreement. Test beam data also validated the simulation for reconstruction within an individual chamber: Fig. 6 compares the reconstructed hit multiplicity for 300 GeV/c muons in one chamber when a clean muon track is selected in the other. The peak at 12 corresponds to a single hit in each of the 12 layers of the chamber, and the overall agreement is good. Finally, Fig. 7 compares the position resolution obtained by comparing the position of a hit in one chamber with the expected position extrapolating from a local track fit in the other chamber. The resolution of 190 μm per layer is as expected by design, and both test beam and simulation agree well.

2.3 Conclusions

There is in general good agreement between the simulated and actual behaviour of the muon detectors. Some discrepancies are still to be studied and understood, both to improve the real detector and electronics operation, and to make the simulations more realistic. We are also making

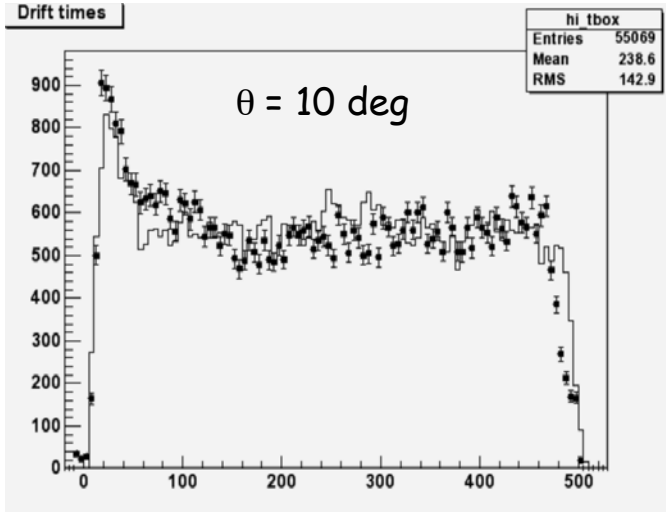


Fig. 5. Drift time distributions from a drift tube chamber in test beam data (points) and in simulated data (line).

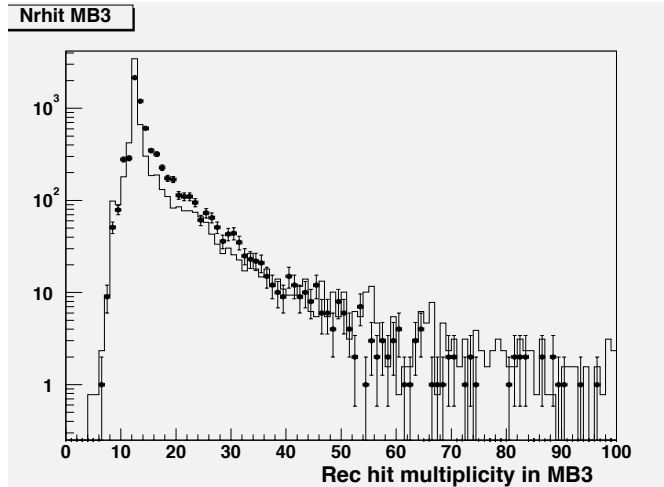


Fig. 6. Reconstructed hit multiplicity due to 300 GeV/c muons in a drift tube chamber in test beam data (points) and in simulated data (line).

an effort to simulate backgrounds in the detectors originating from low energy neutrons since these might influence the trigger.

3 Muon identification: the level 1 trigger

The level 1 (L1) muon trigger is based on detector-local reconstruction, using the multi-layer capability of each sub-detector and custom electronic logic. The DTs use shift registers to search for patterns in the DT hits, and to assign the correct originating bunch crossing. The CSCs likewise identify track segments independently in the 6 layers of strips and wires of each chamber. Hardware ‘track finders’ then find candidate tracks in the CSC and DT systems, and the RPC system uses pattern matching. The Global Muon Trigger combines candidates from all three

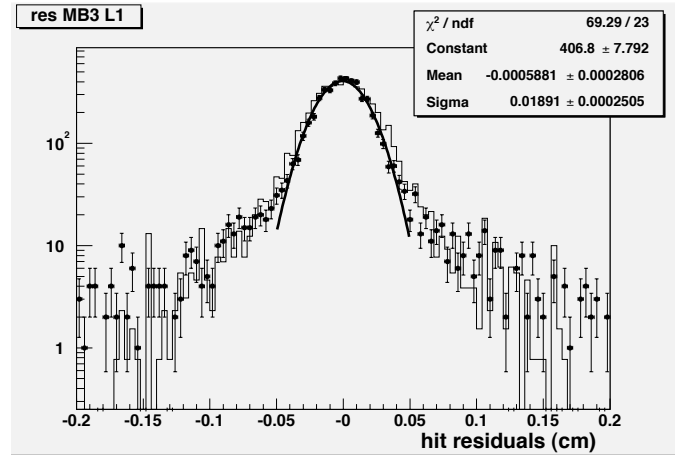


Fig. 7. Position resolution of hits in a drift tube chamber due to 300 GeV/c muons in test beam data (points) and in simulated data (line).

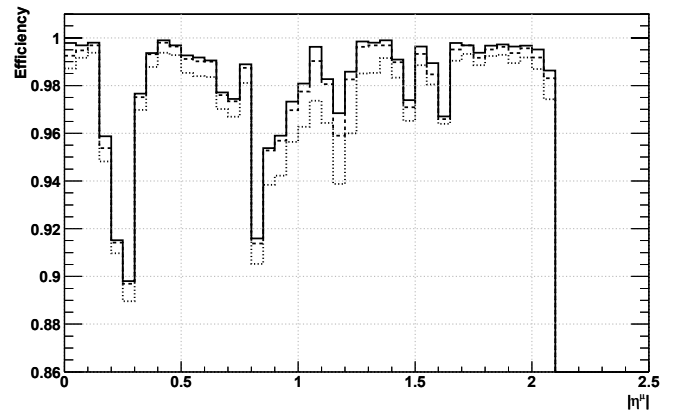


Fig. 8. The simulated efficiency of the trigger to identify a single muon candidate as a function of the muon pseudorapidity η . The solid, dashed, and dotted lines represent the level 1, level 2, and level 3 efficiencies respectively.

systems, and results in global muon candidates each with a location, quality, and an estimate of p_T . Figure 8 shows the simulated level 1 trigger efficiency as a function of the muon $|\eta|$, and Fig. 9 as a function of p_T [3].

4 Muon identification: the higher-level trigger

The Higher Level Trigger (HLT) makes use of full muon track reconstruction on a PC farm, based on the level 1 ‘seed’ candidates. CMS subdivides the HLT into level 2 (muon detectors alone) and level 3 (also including the central Tracker detector.) The tracking algorithm is based on Kalman filtering, and HLT and offline differ only in that the HLT uses level 1 candidates as seeds. Propagation through the magnet steel is performed using a subpackage of GEANT3, but a CMS-specific and optimized replacement is currently under development. The $1/p_T$ resolution

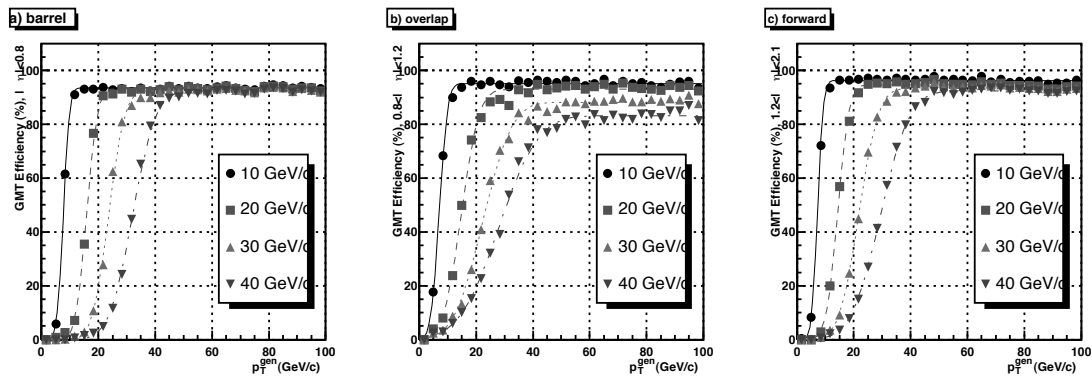


Fig. 9. The simulated level 1 muon trigger efficiency to identify a single muon above given p_T thresholds, as a function of generated p_T . The three figures correspond to three ranges of pseudorapidity η : a) $|\eta| < 0.8$, b) $0.8 < |\eta| < 1.2$, and c) $1.2 < |\eta| < 2.1$.

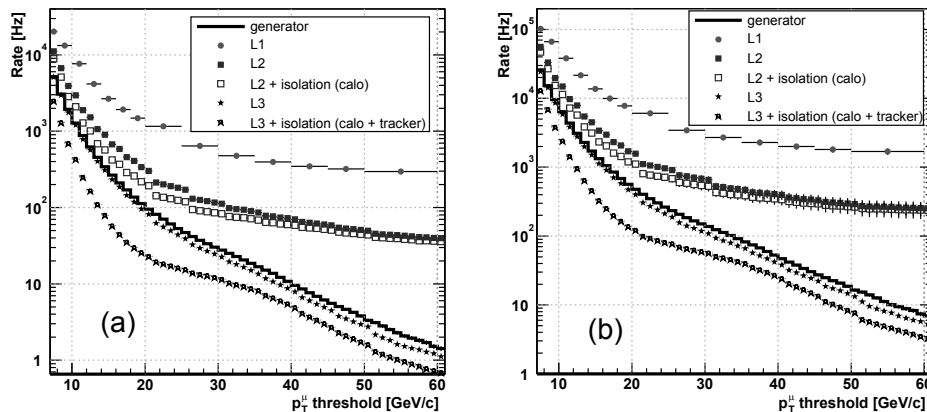


Fig. 10. The simulated single muon rates as a function of muon p_T . The different curves refer to the various stages of the trigger. The left figure represents the rates at the start-up luminosity $2 \times 10^{33} \text{ cm}^{-2} \text{ s}^{-1}$ of LHC. The right figure is at the design luminosity $10^{34} \text{ cm}^{-2} \text{ s}^{-1}$.

obtained from muon detectors alone is about 15%; including the Tracker improves this to about 1.5%. The simulated HLT efficiency is shown in Fig. 8, and the expected single muon rates as a function of p_T at L1 and HLT are shown for two luminosities in Fig. 10. Typical operating rates are expected to allow about 30 Hz for single muon triggers [3]. Since Ref. [3] the η coverage of the L1 muon trigger has been extended from 2.1 to 2.4; these plots are still restricted to $|\eta| < 2.1$.

5 Muon identification: offline reconstruction

The offline track reconstruction based on muon detectors alone uses as seeds track segments built from the hits within individual DT and CSC chambers. Hits in the RPCs are included later. The Kalman filter-based algorithm can operate in different directions through the detector system: trajectory building works from inside out,

and track fitting from outside in (towards the interaction vertex, and using it as a constraint). The global track reconstruction starts from these stand-alone muon tracks to generate seed trajectories, but also includes hits from the inner Tracker. Recent results from simulated single muons are shown in Figs. 11-14, which depict the efficiency and $1/p_T$ resolution as a function of muon η for several p_T values, both for the Muon system alone, and when the Tracker is included. The efficiency in both cases is good, although there are dips due to reduced geometrical acceptance. The major dips occur in a region through which cables and other services pass ($|\eta| \sim 0.3$), in the ‘overlap’ region in which a track passes partially through DTs and partially CSCs ($|\eta| \sim 1.2$), and at the edges of the CSCs closest to the beam line ($|\eta| > 2.2$). For $p_T \lesssim 200 \text{ GeV}/c$ the muon-only momentum resolution is dominated by multiple scattering in the material before the first muon station. With the Tracker included the

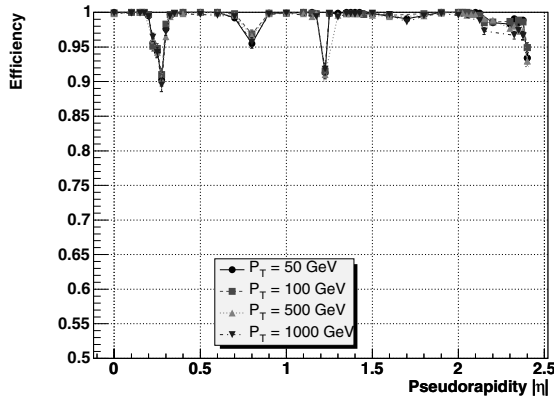


Fig. 11. The simulated single muon reconstruction efficiency as a function of the muon η , for several values of muon p_T , based on the muon detectors alone, with a vertex constraint.

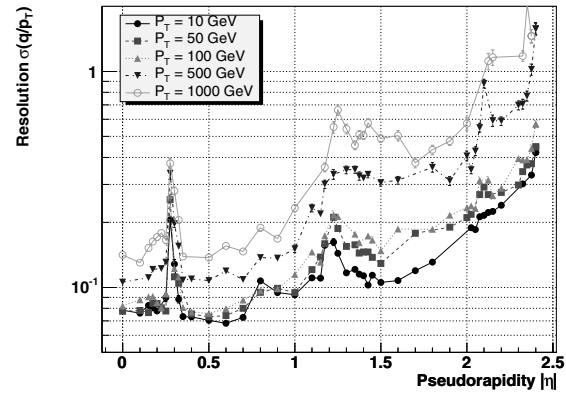


Fig. 13. The simulated single muon $1/p_T$ resolution as a function of the muon η , for several values of muon p_T , based on the muon detectors alone, with a vertex constraint.

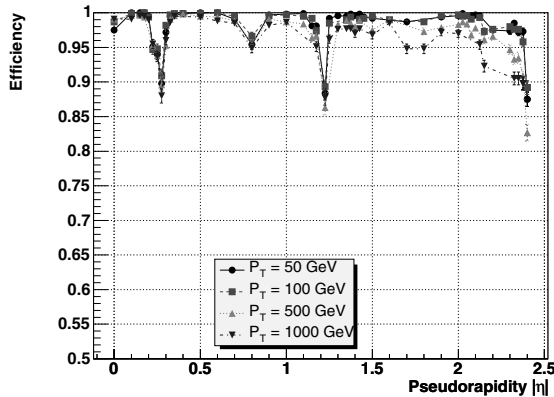


Fig. 12. The simulated single muon reconstruction efficiency as a function of the muon η , for several values of muon p_T , using both the muon and inner tracker detectors.

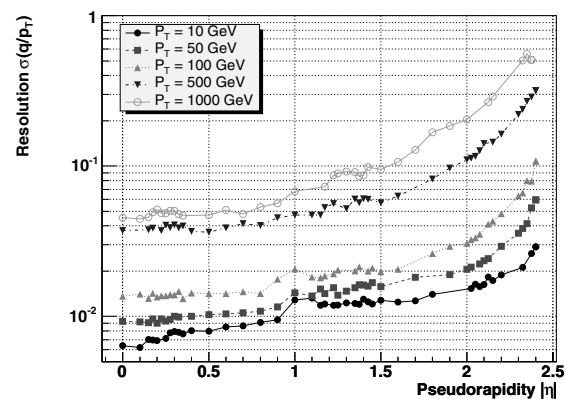


Fig. 14. The simulated single muon $1/p_T$ resolution as a function of the muon η , for several values of muon p_T , using both the muon and inner tracker detectors.

muon-only resolution is reduced by a factor of about 10: the Muon system provides robust triggering and identification capabilities and the Tracker measurements control the overall track reconstruction quality.

6 Conclusions

The muon detectors for CMS are currently being installed. Test beam data for the Drift Tube chambers show the current simulation is quite realistic and the detector-local reconstruction works. Recent test beam data for the Cathode Strip Chambers are under study. Preliminary comparisons with current simulation are very encouraging. RPC test beam data are also under study.

A first attempt at *in situ* data taking using one 60° slice of the muon system is planned for early 2006, after the first tests of the CMS solenoid magnet are complete. It is intended to instrument the slice with CSCs, DTs, RPCs, the hadron and electromagnetic calorimeters, and part of the silicon tracker. Ideally we should be able to reconstruct cosmic ray muons with the magnetic field on.

Finally, we can expect that the CMS muon system will be fully operational at the start of LHC running in 2007.

References

1. *CMS The Muon Project Technical Design Report* (CERN/LHC 97-32, 1997)
2. The GEANT4 Collaboration: S. Agostinelli *et al.*, Nucl. Instrum. Meth. **A506**, (2003) 250-303.
3. *CMS The Trigger and Data Acquisition project, Volume II: Data Acquisition and High-Level Trigger Technical Design Report* (CERN/LHC 02-26, 2002)

Muon Identification at Atlas and Comparison with Simulation and Test Beam Data

G. Avolio, on behalf of the ATLAS muon community

Università della Calabria (ITALY)

Abstract. ATLAS is one of the four detectors that will be exposed to the Large Hadron Collider (LHC) beams. Since high-momentum final-state muons are amongst the most promising and robust signatures of physics at the LHC, the ATLAS detector features a high-resolution muon spectrometer with stand-alone triggering. This paper is intended to describe the ATLAS muon system and its capability to identify and measure the muon momentum over a wide range of transverse momentum, pseudorapidity and azimuthal angle. Moreover experimental activities at CERN H8 area will be described and results about muon system performances will be given.

1 Muon System Overview

1.1 Muon System Concept

The layout of the *ATLAS* muon spectrometer [11] is shown in Figure 1. Its concept is based on the magnetic deflection of muon tracks in a system of three large superconducting air-core toroid magnets instrumented with separate-function trigger and high-precision tracking chambers. In the pseudorapidity range $|\eta| \leq 1$, magnetic bending is provided by a large barrel magnet constructed from eight coils surrounding the hadron calorimeter (peak value of the field $3.9 T$; field integral between $2 Tm$ and $6 Tm$). For $1.4 \leq |\eta| \leq 2.7$, muon tracks are bent in two smaller end-cap magnets inserted into both ends of the barrel toroid (peak value of the field $4.1 T$; field integral between $4 Tm$ and $8 Tm$). In the interval $1.0 \leq |\eta| \leq 1.4$, referred to as transition region, magnetic deflection is provided by a combination of barrel and end-cap fields. This magnet configuration provides a field that is mostly orthogonal to the muon trajectories, while minimizing the degradation of resolution due to multiple scattering.

The high level of particle fluxes has had a major impact on the choice and design of the spectrometer instrumentation. Trigger and reconstruction algorithms have been optimized to cope with the difficult background conditions resulting from penetrating primary collision products and from radiation backgrounds, mostly neutrons and photons in the $1 MeV$ range, produced from secondary interactions in the calorimeters, shielding material, beam pipe and *LHC* machine elements.

In the barrel region, tracks are measured in chambers arranged in three cylindrical layers ('stations') around the beam axis; in the transition and end-cap regions, the chambers are installed vertically, also in three stations. Over most of the pseudorapidity range, a precision measurement of the track coordinates in the principal bending

direction of the magnetic field is provided by Monitored Drift Tubes (*MDTs*, Section 2.1). At large pseudorapidities ($2.0 \leq |\eta| \leq 2.7$) and close to the interaction point, Cathode Strip Chambers (*CSCs*, Section 2.1) with higher granularity are used to sustain the demanding rate and background conditions (up to $100 Hz/cm^2$). Optical alignment systems have been designed to meet the stringent requirements on the mechanical accuracy and the survey of the precision chambers (Section 3).

The trigger system covers the pseudorapidity range $|\eta| \leq 2.4$. Resistive Plate Chambers (*RPCs*, Section 2.2) are used in the barrel and Thin Gap Chambers (*TGCs*, Section 2.2) in the end-cap regions.

The design of the muon spectrometer should allow a measurement of the muon P_t with a resolution of $\Delta P_t/P_t \approx 10\%$ at $P_t = 1 TeV$.

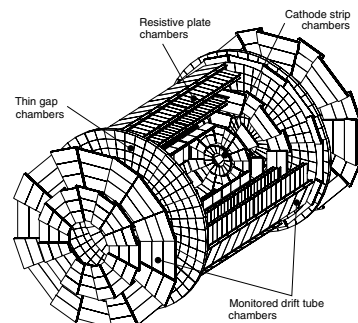


Fig. 1. Three-dimensional view of the muon spectrometer. The four different chamber technologies are indicated.

2 Muon Spectrometer Sub-Detectors

The detectors that made up the muon spectrometer can be divided into two categories: tracking detectors (*MDTs* in the barrel and in the end-caps and *CSCs* in the end-caps) and trigger detectors (*RPCs* in the barrel and *TGCs* in the end-caps).

2.1 Tracking Chambers: *MDTs* and *CSCs*

The basic detection elements of the *MDT* chambers are aluminium tubes of 30 mm diameter and 400 μm wall thickness, with a 50 μm diameter central *W - Re* wire. The tubes are operated with a non-flammable mixture of 93% *Ar* and 7% *CO₂* at 3 bar absolute pressure. The chosen working point provides for a non-linear space-time relation with a maximum drift time of ~ 700 ns, a small Lorentz angle, and excellent ageing properties. The single-wire resolution is ~ 80 μm . To improve the resolution of a chamber beyond the single-wire limit and to achieve adequate redundancy for pattern recognition, the *MDT* chambers are constructed from 2×4 monolayers of drift tubes for the inner station and 2×3 monolayers for the middle and outer stations.

The *CSCs* are multiwire proportional chambers with cathode strip readout and with a symmetric cell in which the anode-cathode spacing is equal to the anode wire pitch. The precision coordinate is obtained by measuring the charge induced on the segmented cathode by the avalanche formed on the anode wire. Good spatial resolution is achieved by segmentation of the readout cathode and by charge interpolation between neighbouring strips. The cathode strips for the precision measurement are orthogonal to the anode wires. Other important characteristics are small electron drift times (30 ns), good time resolution (7 ns), good two-track resolution, and low neutron sensitivity. The baseline *CSC* gas is a non-flammable mixture of 80% *Ar*, 20% *CO₂*. The fact that this gas contains no hydrogen, combined with the small gap width, explains the low sensitivity to neutron backgrounds.

2.2 Trigger Chambers: *RPCs* and *TGCs*

The *RPC* is a gaseous detector providing a typical space-time resolution of $1\text{ cm} \times 1\text{ ns}$ with digital readout. The basic *RPC* unit is a narrow gas gap formed by two parallel resistive bakelite plates, separated by insulating spacers. The gas is a mixture of *C₂H₂F₄* (94.7%), *C₄H₁₀* (5%) and *SF₆* (0.3%). A trigger chamber is made up of two rectangular detector layers, each one read out by two orthogonal series of pick-up strips: the ' η strips' are parallel to the *MDT* wires and provide the bending view of the trigger detector; the ' ϕ strips', orthogonal to the *MDT* wires, provide the second-coordinate measurement which is also required for the offline pattern recognition. Each chamber is made from two detector layers and four readout strip panels.

The *TGCs* are similar in design to multiwire proportional chambers, with the difference that the anode wire pitch is larger than the cathode-anode distance. Signals from the anode wires, arranged parallel to the *MDT* wires, provide the trigger information together with read-out strips arranged orthogonal to the wires. These read-out strips are also used to measure the second coordinate. The operating high voltage foreseen is 3.1 kV. The electric field configuration and the small wire distance provide for a short drift time and thus a good time resolution.

3 The Alignment System

The requirements on the momentum resolution of the spectrometer call for an accuracy of the relative positioning of chambers traversed by a muon track that matches the intrinsic resolution and the mechanical tolerances of the precision chambers. Over the large global dimensions of the spectrometer, however, it is not possible to stabilise the dimensions and positions of the chambers at the 30 μm level. Therefore, chamber deformations and positions are constantly monitored by means of optical alignment systems. All alignment systems are based on optically monitoring deviations from straight lines. Owing to geometrical constraints, different schemes are used to monitor chamber positions in the barrel, in the end-caps, and the deformations of large chambers ('in-plane alignment').

In the barrel, the chambers are arranged in projective towers. Within a projective tower, the chambers are optically connected by alignment rays which monitor the relative chamber positions. A different alignment strategy is used in the end-caps, where the positions of complete chamber planes are monitored.

4 The Muon Trigger System

The first level muon trigger is based on the measurement of muon trajectories in three different planes. Muons are deflected by the magnetic field generated by the toroids; the angle of deflection depends on their momentum and the field integral along their trajectory. Coulomb scattering in the material traversed, and for *low - P_t* triggers, the energy-loss fluctuation, are also of importance. The differences from a straight-line trajectory of an infinite-momentum track originating at the nominal interaction point are measured using three trigger stations (Figure 2). The trigger plane farthest from the interaction point in the end-cap, and nearest to the interaction point in the barrel, is called the pivot plane. The two different lever arms from the pivot to the other two trigger planes provide two different measurements of the size of the deflection due to the field. The two different lever arms allow trigger thresholds to cover a wide range of transverse momenta with reasonably good resolution: the shorter lever arm (pivot plane and station 2) covers a lower-momentum range and the longer one (pivot plane and station 1 for the end-cap, pivot plane and station 3 for the barrel), a

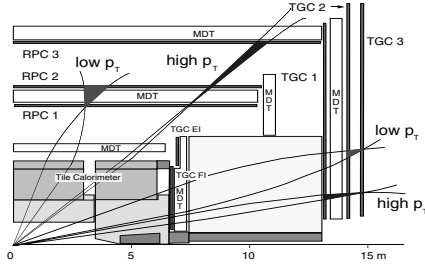


Fig. 2. The first level muon-trigger scheme. The $low - P_t$ threshold is $\sim 6 GeV$, while the $high - P_t$ threshold is $\sim 20 GeV$.

higher-momentum range. Each hit found in station *RPC1* (*TGC3*) is extrapolated to station *RPC2* (*TGC2*) along a straight line through the nominal interaction point. A coincidence window is then defined around this point, where the window size depends upon the required P_t threshold. The $low - P_t$ trigger condition is then satisfied if, for both projections, there is at least one hit within the coincidence window, and at least one of the two $low - P_t$ stations has hits in both trigger planes satisfying the three-out-of-four logic. A similar procedure is performed for the $high - P_t$ trigger, where the planes of *RPC3* (*TGC1*) together with the pivot plane are used.

5 Muon Momentum Measurement

The chambers are arranged such that particles from the interaction point traverse three stations of chambers. Each station provides a measurement along the trajectory with a resolution of $\sim 40 \mu m$. In the barrel, particles are measured near the inner and outer field boundaries, and inside the field volume, in order to determine the momentum from the sagitta of the trajectory. In the end-cap regions, for $|\eta| > 1.4$, the magnet cryostats do not allow the positioning of chambers inside the field volume. Instead, the chambers are arranged to determine the momentum with the best possible resolution from a point-angle measurement (this is also the case in the barrel region in the vicinity of the coils).

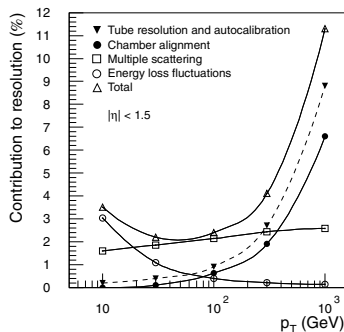


Fig. 3. Contributions of the different effects to the momentum resolution.

Figure 3 shows the contributions of the different effects to the momentum resolution: single-wire accuracy, chamber misalignment, multiple scattering, and energy-loss fluctuations. Three resolution regimes clearly emerge:

- At high momentum ($P_t > 300 GeV$), the resolution is dominated by the precision with which the magnetic deflection is measured, i.e. the intrinsic detector resolution;
- At moderate momentum ($30 < P_t < 300 GeV$), the resolution is increasingly limited by multiple scattering;
- At low momentum ($P_t < 30 GeV$) energy loss fluctuations become dominant.

6 Muon System Test at CERN H8 Area

6.1 The Experimental Setup

Extensive tests of the *ATLAS* muon spectrometer were performed at the *H8* beam line at the *CERN SPS* with the aim to validate many aspects of the system. In 2004 a full slide of *ATLAS* (inner detector, calorimeters and muon spectrometer) was installed and a complete description of the *H8* line setup can be found in the paper [2], while here we will focus mainly on the muon system.

The muon setup (Figure 4) reproduced one projective tower of the barrel and one end-cap octant. The barrel tower was made up of six *MDT* chambers (two inner – *BIL* –, two middle – *BML* – and two outer – *BOL* – large chambers) and six *RPCs*. The end-cap octant was made up of six *MTD* chambers, three *TGCs* and one *CS*. All chambers were operated at their nominal working point, fully instrumented with front end electronics (for a total of 4000 channels readout) and *MDTs* were fully equipped with the optical alignment system. An additional *MDT* chamber was present upstream the barrel sector and mounted on a rotating frame (hereafter called ‘rotating *BIL*’). Two dipole magnets were installed in order to bend the muon tracks in the horizontal plane: the first one (able to provide a maximum field integral of about $4 Tm$) between the rotating *BIL* and the barrel sector, the second one between the inner and the middle end-cap chambers.

Events with muon energies from $20 GeV$ to $350 GeV$ were collected.

6.2 MDT Calibration

An accurate knowledge of the space – time relationship (the relation between the measured drift time and the distance of the minimum approach of the particle trajectory to the wire, i.e. the drift distance) and of the t_0 value (the drift time associated to particles passing very close to the wire, i.e. the shortest drift time) is necessary to meet the muon spectrometer performance requirements. The *CALIB* [3] software was used to calibrate the *MDT*

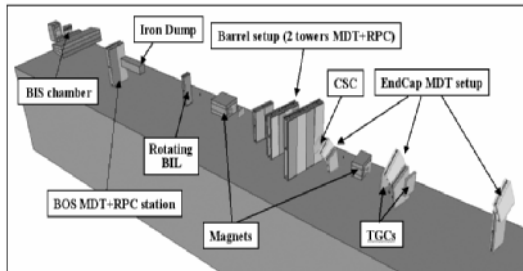


Fig. 4. Schematic view of the $H8$ beam line with muon detectors in evidence. The BOS and BIS MDT chambers where located in front of the hadronic and electromagnetic calorimeters for specific studies.

chambers. A check on calibrations was performed investigating the residual¹ distributions (Figure 5) for different chambers.

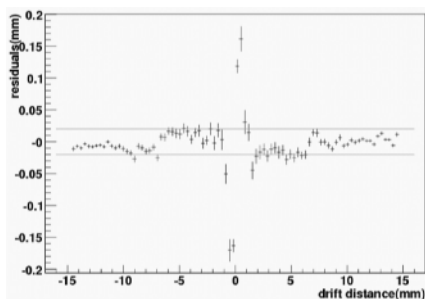


Fig. 5. Rotating BIL residuals as a function of drift distance.

6.3 Barrel Sagitta Resolution

Sagitta value of bending tracks in the Muon Spectrometer is the *key* measurement for muon momentum computation in $ATLAS$. Since the bending of a 1 TeV muon track is such that the track sagitta varies between 500 μm in the barrel and 1 mm in the end-cap, the error on the sagitta measurement must be at level of 50 μm . The $H8$ setup gave the unique possibility to measure this quantity in a realistic setup before the installation of the $ATLAS$ experiment. Since the measured sagitta resolution depends not only on the intrinsic resolution (constant term, independent from the beam momentum) but also on multiple scattering (term depending on muon momentum), a scan of the muon momentum (between 100 and 250 GeV) was used to disentangle the two contributors. The muon momentum was evaluated using the formula

$$P(GeV) = \frac{0.3BL (Tm)}{(\Delta\theta_B - \Delta\theta_0) (rad)}$$

¹ *Residual* is defined as the difference between the radius predicted by the space – time relationship and the one measured fitting track segments on a single multilayer or the whole chamber.

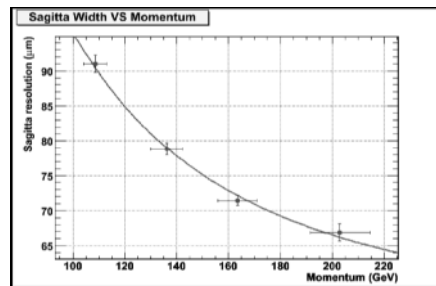


Fig. 6. Sagitta resolution as a function of the muon momentum (real data).

Table 1. Multiple scattering and intrinsic resolution terms contributing to the sagitta width. Results from real data analysis are compared with **GEANT4** simulation.

	Intrinsic Resolution (μm)	x/X_0
Real Data	53.2 ± 3.3	29.9 ± 3.6
Simulated Data	40.4 ± 2.8	33.7 ± 2.8

where BL is the magnet bending power, $\Delta\theta_B$ is the difference between the track angle (in the plane orthogonal to the MDT wires) reconstructed in the rotating BIL chamber and in the barrel region with the magnet switched on, and $\Delta\theta_0$ is the same quantity as $\Delta\theta_B$ but evaluated with the magnet switched off. This procedure allowed to avoid systematic errors due to the non perfect alignment between the rotating BIL chamber and the barrel tower. For each muon energy the sagitta resolution was calculated as the width of the distribution of the distance between the BML superpoint² and the line connecting $BIL - BOL$ superpoints.

Figure 6 shows the sagitta resolution as a function of the muon momentum. The curve was fitted using the two parameter function $\sigma = \sqrt{P_1^2 + (P_2/p)^2}$, where P_2 and P_1 are respectively the parameters estimating the contribution of multiple scattering and intrinsic chamber resolution to the sagitta width. Table 1 shows the values of the parameters (the P_2 value has been translated into radiation length units x/X_0) coming from the fit and compares them with the results of a detailed and realistic simulation using the **GEANT4** [4] package. The same reconstruction algorithm running on the real data samples has been used for the pattern recognition and track fitting performed on simulated data.

6.4 Alignment System Test

At $H8$ 1% of the full $ATLAS$ alignment system was present and two *alignment modes* were tested:

² The *superpoint* is the crossing point of the track segment at the center of the chamber.

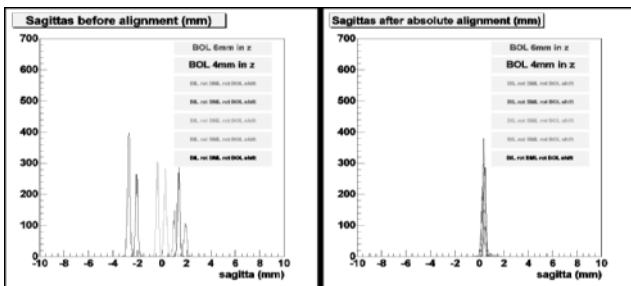


Fig. 7. *Left picture* - Sagitta values for various runs with chambers moved away from their nominal positions. The sagittas were computed without applying any alignment system correction. *Right picture* - Sagitta values after applying offline chamber position corrections.

- *Absolute alignment*: chamber positions are reconstructed using only the optical sensor responses, the knowledge of their positions and their calibrations;
- *Relative alignment*: chamber positions are assumed to be known at a given time (reference geometry) and sensor responses are used to infer the chamber movements since that time.

Some *MDT* chambers were displaced from their initial positions to test the validity of the alignment concept. Then the impact of the alignment system on the sagitta measurement was computed. Figure 7 shows how the sagitta value changed run by run when events were reconstructed with *fixed* chamber positions, and how the sagitta kept constant when the corrections foreseen by the alignment system were applied. The dispersion of the sagitta mean value distribution was of $18 \mu\text{m}$ when using the *relative alignment concept*, while the adoption of the *absolute alignment concept* gave a dispersion of $63 \mu\text{m}$ and a mean value of $\sim 350 \mu\text{m}$.

6.5 MDT Track Segment Efficiency

To compute the track segment efficiency two *MDT* stations out of three were used as reference and the third one was tested. The algorithm can be summarized into three steps:

- A reference sample was selected by asking no more than one segment of good quality in the reference stations;
- Segments were reconstructed in the reference stations in order to evaluate the most probable location of the segment in the tested station ;
- The efficiency in the tested station was computed by counting events with good tested station segment in the vicinity of the most probable location.

Table 2 shows results for all the barrel and the end-cap *MDT* chambers requiring segments with a number of hits equal or greater than the maximum number of hits available in each station.

Table 2. Track segment efficiency for barrel (*BIL*, *BML*, *BOL*) and end-cap (*EIL*, *EML*, *EOL*) chambers

N-hits	<i>BIL</i> (%)	<i>BML</i> (%)	<i>BOL</i> (%)
$\geq \text{max} - 1$	93.2 ± 0.2	94.3 ± 0.1	96.3 ± 0.2
N-hits	<i>EIL</i> (%)	<i>EML</i> (%)	<i>EOL</i> (%)
$\geq \text{max} - 1$	89.8 ± 0.2	94.9 ± 0.2	95.3 ± 0.1

7 Conclusions

The *ATLAS* muon spectrometer has been presented: it will provide powerful muon trigger and identification over the full energy range and the very good momentum resolution will ensure high quality stand alone measurements.

The system test at *CERN H8* was very useful to understand the behaviour of the spectrometer in a realistic environment:

- The *MDT* calibration procedure did not show relevant systematic uncertainties (within $20 \mu\text{m}$);
- The relative alignment concept was validated, while the absolute concept (tested at *H8* for the first time) is on the right way to meet the *ATLAS* requirements;
- Results on the sagitta resolution were in agreement with *GEANT4* simulation predictions;
- Track segment efficiency was measured to be about 95%.

8 Acknowledgements

Many thanks to Saclay Group (F. Bauer, L. Chevalier, A. Formica, P.F. Giraud, C. Guyot, S. Hassani, E. Lançon, J-F. Laporte, R. Nicolaidou, A. Ouraou, D. Pomarede, P. Schune), A. Krepouri, F. Cerutti, L. Pontecorvo, S. Ventura, E. Meoni, A. Policicchio, S. Rosati, D. Reuzzi, T. Baroncelli, D. Levin, R. Avramidou for all the help, information and plots provided for this paper.

References

1. *ATLAS Muon Spectrometer Technical Design Report*, CERN/LHCC/97-22
2. B. Di Girolamo, M. Gallas, T. Koffas, *ATLAS Barrel Combined Run in 2004*, CERN EDMS Note ATC-TT-IN-0001 - EDMS ID: 406980
3. P. Bagnaia et al, *CALIB: a Package for MDT Calibration Studies*, ATL-COM-MUON-2002-004,28-01-2002.
4. A. Agostinelli et al, *GEANT4 - a simulation toolkit*, Nucl. Inst. Meth. **A 506** (2003), 250-303.

Tau identification at ATLAS : importance, method and confrontation with Monte Carlo and test beam

F.Tarrade^a, on behalf of the ATLAS Collaboration

^a Laboratoire d'Annecy-Le-Vieux de Physique des Particules (LAPP),
9 Chemin de Bellevue, BD 110, F-74940 Annecy-Le-Vieux France
e-mail: tarrade@lapp.in2p3.fr

Abstract. Tau jets play an important role in the physics expected at the LHC. Identification of hadronic taus will be one of the keys to beyond the Standard Model searches. We discuss the hadronic tau reconstruction and identification method studied in the ATLAS experiment at CERN. A brief discussion of the tau trigger is also included.

1 Introduction

Tau leptons play an important role in the physics to be observed at LHC. They enter in electroweak measurements, studies of the top quark and are also a signature in searches for new phenomena such as Higgs, Supersymmetry and Extra Dimensions.

Tau reconstruction and identification at hadron colliders is not a simple task. The multi jet events which dominate the backgrounds have an enormous cross section. Another challenge is the hadronic tau trigger.

In this contribution, we describe two methods for τ identification and reconstruction studied in the ATLAS experiment, we discuss the hadronic τ trigger and present preliminary test beam results.

2 ATLAS detector

The ATLAS (A Toroidal LHC Apparatus) detector is illustrated in Fig.1. It measures 22 m high, 44 m long and weighs 7000 tons. We give a brief description of the detector sub-systems used for tau reconstruction. The ATLAS detector is composed of a tracker, a calorimeter system and of a large muon spectrometer. More details about the detector can be found elsewhere [1].

2.1 ATLAS tracking

The precision inner tracker is constituted of pixels and of silicon strip wafers. In addition, a continuous tracking for pattern recognition and electron identification (e/π separation) is obtained with the TRT (Transition Radiation Tracker). The inner detector is inside a 2 Tesla solenoid magnet. The expected transverse momentum resolution is

$$\sigma_{p_T}/p_T = 0.05\%P_T(GeV) + 1\%$$

and the electron/pion separation is good.

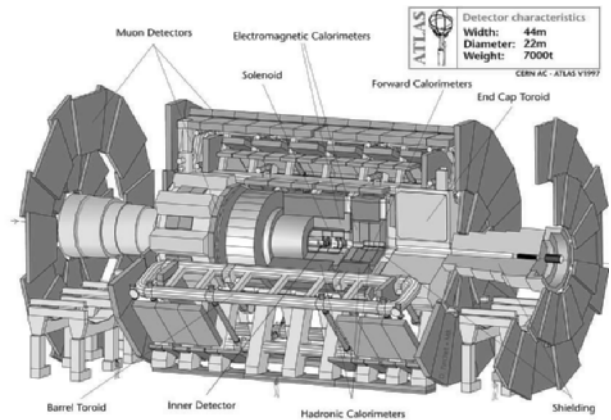


Fig. 1. A schematic view of the ATLAS detector.

2.2 ATLAS calorimetry

The barrel lead-liquid argon electromagnetic calorimeter has longitudinal segmentation (3 layers : Strips, Middle and Back) with a fine granularity in η for the first layer $\Delta\eta \times \Delta\phi = 0.003 \times 0.1$, $\Delta\eta \times \Delta\phi = 0.025 \times 0.025$ for the second layer and $\Delta\eta \times \Delta\phi = 0.05 \times 0.025$ for the last layer. The expected energy resolution is given by

$$\sigma_E/E = 10\%\sqrt{E}(GeV) \oplus 500MeV/E(GeV) \oplus 0.7\%$$

in the range $|\eta| < 3.2$.

The barrel scintillator-tile hadronic calorimeter also has 3 longitudinal samplings but with a bigger granularity ($\Delta\eta \times \Delta\phi = 0.1 \times 0.1$, for the two first layers and $\Delta\eta \times \Delta\phi = 0.2 \times 0.1$ for the last one). The expected energy resolution is given by

$$\sigma_E/E = 50\%\sqrt{E}(GeV) \oplus 3\%$$

in the range $|\eta| < 3$ The aim of the calorimeters is to measure the absolute jets energy scale to the $\approx 1\%$ level.

3 Physics processes with τ leptons and their decays

A number of benchmark processes depend on the reconstruction efficiency and identification of hadronic τ s : light Standard Model (SM) Higgs produced in Vector Boson Fusion (VBF) $qqH \rightarrow qq\tau\tau$, charged SUSY Higgs production $H \rightarrow \tau\nu$, neutral SUSY Higgs $H/A \rightarrow \tau\tau$ at large $\tan\beta$, SUSY signatures with τ s in the final state as well as Extra Dimensions. We can also use $Z \rightarrow \tau\tau$ and $W \rightarrow \tau$ events to understand and calibrate the calorimeters.

τ leptons decay to hadrons in 64.8% of the cases and to electron or muon the rest of the time. In $\approx 77\%$ of hadronic τ decays, only one charged track is produced :

$$\tau \rightarrow \nu_\tau + \pi^\pm + n\pi^0$$

and in $\approx 23\%$ we have 3 charged tracks :

$$\tau \rightarrow \nu_\tau + 3\pi^\pm + n\pi^0$$

A τ lepton decaying hadronically will generate a small jet defined as a τ jet. With hadrons and neutrinos amongst the decay products, it is difficult to reconstruct and identify efficiently a τ jet. The background misidentified as a τ is mainly QCD multi jet events, but also electrons that shower late or with strong Bremsstrahlung, or muons interacting in the calorimeter.

4 Hadronic tau reconstruction

A τ jet can be identified through the presence of a well collimated calorimeter cluster with a small number of associated charged tracks (1 or 3 tracks). Several discriminant variables used to separate real τ jets from background are defined using track and calorimeter information :

- R_{EM} : the jet radius computed using only the electromagnetic calorimeter cells within $\Delta R = 0.7$ of the jet;
- ΔE_T^{12} : the fraction of E_T in the electromagnetic and hadronic calorimeters within an isolation region of $0.1 < \Delta R < 0.2$ around the jet;
- N_{tr} : the number of charged tracks pointing to the cluster within $\Delta R = 0.3$;
- Weighted width of the energy deposition in the strips (first layer of the electromagnetic calorimeter)
- E_T/p_T : transverse energy over transverse momentum for the highest p_T track;
- Number of strips;
- Impact parameter;
- Charge : sum of charges of the tracks associated with the τ candidate.

In ATLAS, we are studying various methods of τ identification for different purposes. Here we describe two of them.

4.1 TauRec algorithm

TauRec is the official algorithm for hadronic τ reconstruction and identification in ATLAS [2] in the range $|\eta| < 2.5$. The τ jet seed consists of a calorimeter cluster, or a jet with $p_T > 15$ GeV, or isolated tracks with $p_T > 2$ GeV. For every candidate, TauRec collects all the tracks with $p_T > 2$ GeV and with $\Delta R < 0.3$ around the center of the seed. A τ candidate is defined by a deposit of energy associated to at least one track. At a hadron collider, isolation plays an important role against QCD jets backgrounds. For all candidates we build a set of variables for τ identification (see Fig.2). We see that the shape for some variables is p_T dependent and also that most τ candidates contain one to three charged tracks.

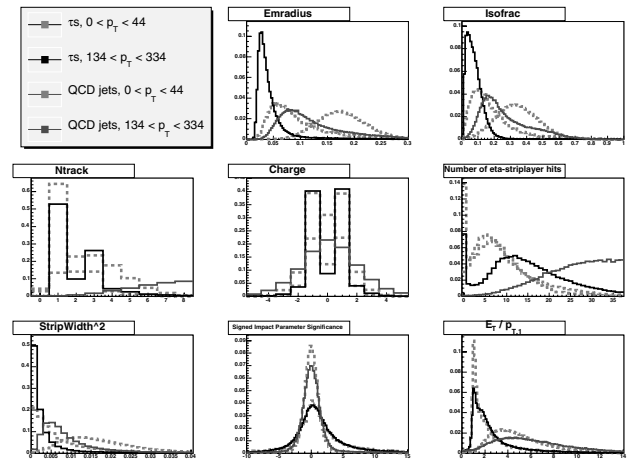


Fig. 2. Discriminant variables for τ reconstruction and identification from the TauRec algorithm for signal (true τ) : $A/H \rightarrow \tau\tau$ (red-solid line : (high p_T) and red-dashed line (low p_T)) and background : QCD jets (black-solid line : (high p_T) and black-dashed line (low p_T)).

The electromagnetic radius R_{EM} of a τ is significantly smaller than for QCD jets, which is why a fine granularity of the electromagnetic calorimeter is important for a good τ identification. Calibration of τ candidates is done using only the calorimeters using a H1-Style method with weights fitted for jets and applied directly to cell energies (depending on their E_T content, η , and layer). This weighting method gives a good jet energy resolution.

We calculate a likelihood (Fig.3) using the following variables : R_{EM} , ΔE_T^{12} , $N_{track(s)}$, strips width, N_{strips} , charge, impact parameter and E_T/p_T . To identify τ jets, we apply a cut on the likelihood which depends on the p_T .

Fig.4 shows the τ -jet identification efficiency ¹ (left) and rejection against QCD jets (right) for various seeds versus the p_T . A good level of background rejection is expected depending of the p_T . The efficiency of τ identification decreases slowly with increasing p_T , while the rejection in-

¹ The τ efficiency is defined as the ratio of true τ jets identified as a τ over the number of true τ jets in the sample

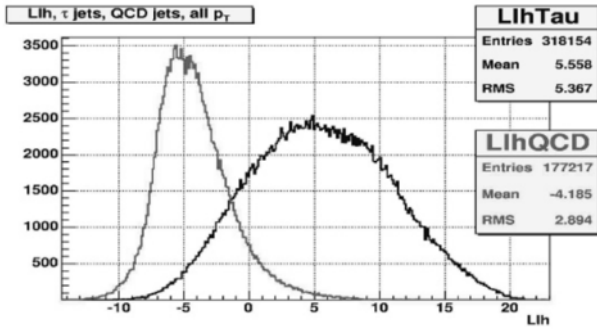


Fig. 3. Likelihood distribution from the TauRec algorithm for signal ($A/H \rightarrow \tau\tau$, reconstructed true τ in black : darkest), and for background (QCD jets in red : lightest).

creases by a factor 10. For a τ identification efficiency of 50%, a rejection between 300 and 1500 can be achieved.

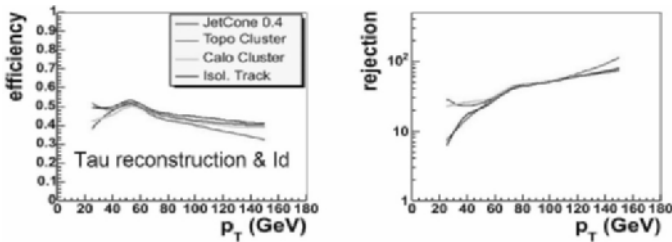


Fig. 4. Signal efficiency (left) and background rejection for an efficiency of 50% (right) obtained with TauRec using four different seeds. The sample is $t\bar{t}H \rightarrow t\bar{t}\tau\tau$.

The TauRec algorithm shows good efficiency for hadronic τ jet reconstruction and identification and a good rejection against QCD jets background. We have also a good energy resolution using H1-style.

4.2 Tau1P3P algorithm

Tau1P3P is a new and complementary algorithm aimed at soft τ reconstruction and identification [3] [4]. It is seeded by a good quality track, and an energy flow approach is used to define the energy scale. As can be seen in Fig.5, the tracker transverse momentum resolution is better than the calorimetric transverse energy resolution for $E_T < 120$ GeV. The algorithm is dedicated for τ jets with $E_T \approx 20 - 70$ GeV. It can be particularly interesting for light Higgs or for soft SUSY searches.

Tau1P3P explores exclusive features of τ leptons, where a hadronic τ does not correspond to a typical jet but rather to a single charged prong or three charged prong topology : $1 \text{ track} + \sum \pi^0$ and : $3 \text{ tracks} + \sum \pi^0$. The decay products are well collimated in space and the charged tracks direction can provide a precise estimate for the true τ direction. The algorithm starts from a "good quality" hadronic track with $p_T > 9$ GeV, then it finds nearby "good quality" tracks inside $\Delta R < 0.2$ and with

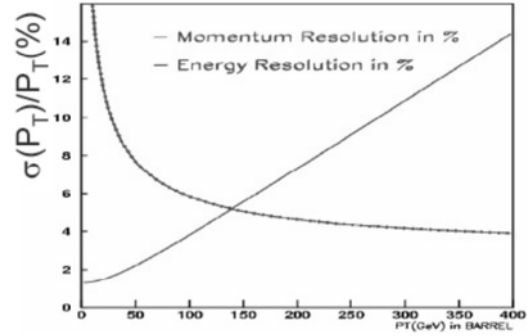


Fig. 5. Transverse momentum resolution for the tracker (red : lightest) and transverse energy resolution for the calorimeters (blue : darkest) in % versus p_T , in the barrel.

$p_T > 2$ GeV. It creates a single-prong candidate (Tau1P) if there are no nearby tracks. If there are 2 nearby tracks, it checks that the sum of the three tracks charges is consistent with a three-prong candidate (Tau3P).

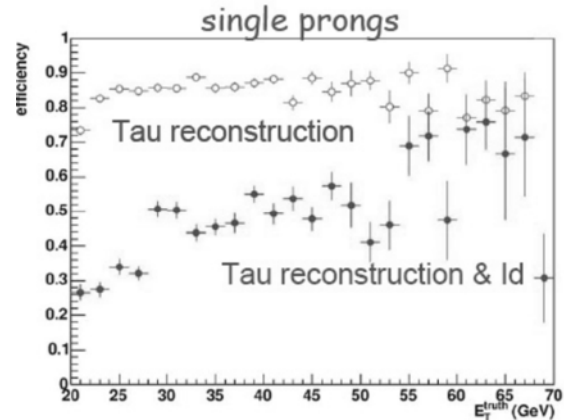


Fig. 6. Efficiency for τ reconstruction (blue circles) and for τ reconstruction and identification (red full circles) using the cut based analysis, versus the true τ transverse energy, for $Z \rightarrow \tau\tau$ events, and for $|\eta| < 1.5$.

For all candidates (Tau1P or Tau3P), the energy scale is defined using an energy flow approach [5] where tracks within a cone of $\Delta R < 0.2$ are used. This gives a good energy resolution without additional calibration.

The Tau1P3P algorithm calculates for each candidate discriminant variables [3] [4] using $\Delta R < 0.2$ as a "core" and $0.2 < \Delta R < 0.4$ only for isolation. Fig.6 shows the τ reconstruction efficiency, as well as the reconstruction and identification efficiency, using basic cuts on the tracks (i.e. p_T) for $Z \rightarrow \tau\tau$ events. The reconstruction efficiency is 82.6 % (90.3 % for single prong and 62 % for three prongs), while the reconstruction and identification efficiency, made separately for Tau1P and Tau3P using loose cuts, is 59.1 %. For QCD jets background, the efficiency of reconstruction is 2.0% for Tau1P and 4.2 % for Tau3P. For reconstructed fake candidates from QCD jets, accep-

tance for identification selection is 10-20% for TauP1 and 19-37% for Tau3P.

Table 1. The identification efficiency for the cut analysis [3] [4] and the multivariant analysis for $Z \rightarrow \tau\tau$ signal events and for QCD jets background.

	cut analysis		multivariant analysis	
	sig	bkg	sig	bkg
$\epsilon(\%)$	58.9	14.3	58.9	9.3

The Tau1P3P algorithm also uses a multivariant analysis [6] which samples the signal and background densities in a multi-dimensional phase-space using range-searching and probability density estimation. The observ-

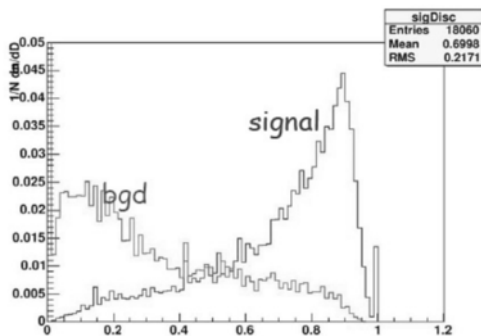


Fig. 7. Discriminant variable distribution, calculated in the Tau1P3P algorithm for $Z \rightarrow \tau\tau$ signal events (blue) and for QCD jets background (red), and for $|\eta| < 1.5$.

ables are combined into a single discriminant variable which is shown in Fig.7, for $Z \rightarrow \tau\tau$ signal events and for QCD jets background. Table 1 shows that with a multivariant analysis, the QCD jets background rejection is improved by a factor 1.5, for the same signal efficiency as the cut based analysis. As well, the energy flow approach gives a good energy resolution.

For both algorithms, TauRec and Tau1P3P, the performances still need detailed studies.

5 Tau trigger

5.1 ATLAS trigger

The ATLAS trigger system is designed to reduce the 40 MHz bunch crossing frequency to ≈ 100 Hz Fig.8. The on-line selection is based on three levels. The level 1 (L1) will reduce the initial event rate to ≈ 100 kHz. Then the High Level Trigger (HLT), which consists of the second level (L2) and of the Event Filter (EF), will reduce the rate further to ≈ 100 Hz before writing to mass storage. The

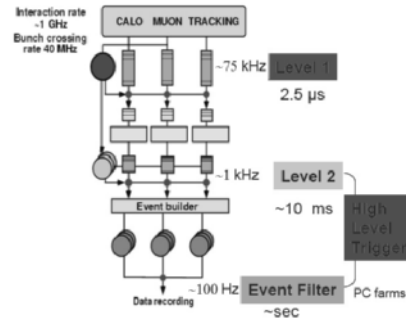


Fig. 8. A schematic view of the ATLAS trigger.

hardware based L1 Trigger decision is made with calorimeters (coarse granularity) and muon trigger chambers information, using a defined Region of Interest (RoI). The HLT is a software selection, where the L2 uses the RoI with all detectors and full granularity information. The EF refines the selection and can perform event reconstruction with latest alignment and calibration data.

5.2 Hadronic Tau trigger

The τ leptons can be selected either by the lepton trigger (electron or muon) or by the hadronic τ trigger. Here we only discuss the hadronic τ trigger (Tau Trigger). At L1 the Tau Trigger uses 2×2 towers (1 tower : $\Delta\eta \times \Delta\phi = 0.1 \times 0.1$) in the electromagnetic (EM) and hadronic calorimeters to define an RoI. For the isolation, 12×12 towers in the calorimeters (EM and hadronic) are used. The Tau Trigger at L2 uses both calorimeters and tracker information to evaluate offline variables and objects: EM radius of the cluster, width in energy deposition, isolation fraction and tracks. The Event Filter refines the selection based on the TauRec code. The trigger efficiency, rejection and rates for the hadronic τ trigger are presently being evaluated.

6 Experimental results from test beam

6.1 Introduction

In addition to using Monte Carlo data for a fully simulated detector, a great effort is made to study the response of all detectors to single particles in test beam. In 2004, a realistic slice of ATLAS was tested, with trackers, a module of the barrel electromagnetic Liquid Argon calorimeter, a Tile calorimeter module, as well as muon chambers, as show on Fig.9. 90 million events (e, μ, π) were taken. The main aim was to test the combined detector performance and to tune and validate Monte Carlo modelling of the detector response. For the hadronic τ reconstruction and identification, the effort is being put on the combined electromagnetic and hadronic energy resolution and on the e/π efficiency (TRT).

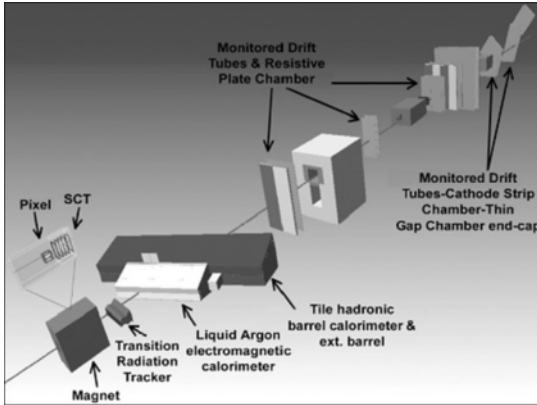


Fig. 9. Layout of the 2004 combined test beam, with a realistic slice of ATLAS.

6.2 Preliminary results

The preliminary standalone hadronic energy resolution without compensation and without correction for energy outside the hadronic calorimeter gives compatible results with previous test beam. Separation between electrons

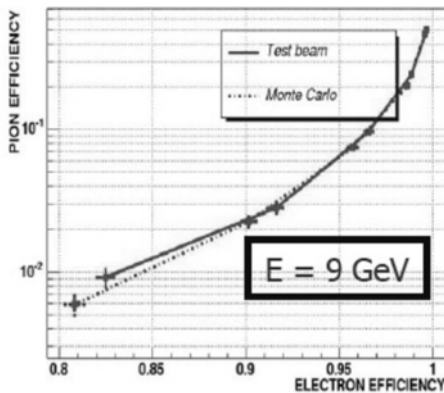


Fig. 10. Comparison between Monte Carlo and test beam data for efficiency of pions versus efficiency of electrons.

and pions is important for τ identification to reject an electron from hadronic τ candidates. The aim is to try to separate e/π by requiring a minimum number of TRT hits pers track. On Fig.10, we can see a good agreement between the data and Monte Carlo for an energy of 9 GeV and we have an efficiency of electron identification of 90 to 80% for a rejection factor for π between 50 and 250.

7 Conclusion

The identification and reconstruction of τ jets is crucial for several physics studies at LHC and challenging at a hadronic collider. In this contribution, a brief description of the method studied by ATLAS was presented. Hadronic τ decays can be efficiently reconstructed and identified

from calorimeter and inner detector tracking with two algorithms. The energy scale is also defined with two different approaches with good results. Work is ongoing towards a hadronic τ trigger. Preliminary results from the 2004 combined test beam show that a good energy resolution and a good e/π separation can be obtained.

Acknowledgement

The author would like to thank the organizers for their effort in making this conference a success. Author is also thankful P.Casado, D.Cavalli, H.Przysieznik and E.Richter-Was to for carefully reading this contribution and their useful suggestions.

References

1. "Detector and Physics Performance Technical Design Report", Volumes 1 and 2, Atlas Collaboration : CERN/LHCC/99-14, ATLAS TDR 14, 25 May 1999.
2. D.Cavalli and S.Resconi, τ jet separation in ATLAS detector, ATLAS Physics Note ATL-PHYS-98-118.
3. E.Richter-Was, H.Przysieznik and F.Tarrade, *Exploring hadronic tau identification with DC1 data samples : track based approach*, ATLAS Physics Note ATL-PHYS-2004-030.
4. E.Richter-Was and T.Szymocha, *Hadronic tau identification with track based approach : the $Z \rightarrow \tau\tau$, $W \rightarrow \tau\nu$ and di-jet events from DC1 data samples*, ATLAS Physics Note ATL-PHYS-PUB-2005-005.
5. D.Froidevaux, P.Nevski and E.Richter-Was, *Energy flow studies for hadronic τ 's with DC1 data samples*, ATLAS Physics Communication ATL-COM-PHYS-2005-024.
6. L.Janyst and E.Richter-Was, *Hadronic τ identification with track based approach : optimisation with multi-variante method*, ATLAS Physics Communication ATL-COM-PHYS-2005-028.

Tau identification in CMS

Simone Gennai¹

Scuola Normale Superiore, Pisa, Italy

Abstract. The Tau identification and reconstruction algorithms developed for the CMS experiment are described, from the first level of the trigger to the off-line reconstruction and selection.

1 Introduction

Analyses based on τ reconstruction are expected to be very helpful in the discovery of new physics at the LHC; in some part of the supersymmetric [1] (SUSY) parameter space, their use will be essential. As an example, Fig. 1 shows the discovery region in the $(m_A, \tan\beta)$ plane for the MSSM heavy Higgs bosons decaying into a $\tau\tau$ pair. While leptonic τ decays can be reconstructed with the same software used for electron and muon identification, the hadronic τ decays need a special treatment that merges jets to reconstructed tracks. The fully hadronic final state can increase the signal statistics in several searches (a couple of τ leptons decays into hadrons in the 42% of the cases) and for what regards the MSSM Higgs boson, detailed studies have demonstrated that the best mass resolution is achieved when both τ decay into hadrons [2]. This report will concentrate on the reconstruction and selection of hadronic τ decays (τ jets), based mainly on the τ jet collimation and the lepton life-time. The usage of these methods in different combinations depends on the physics channel considered, however the selection of τ jet is so fast and efficient that can be used already at trigger level.

In the following sections the trigger and off-line selections are described.

2 Tau Trigger

The CMS trigger is divided in two main stages: the Level 1 trigger (hardware) and the High Level trigger (software). The 40 MHz collision rate and the huge p-p cross section impose severe constraints on the definition of trigger logics, which need to be fast and reliable. The desired final rate for a τ trigger (single or double tag) need to go down to a few Hz. The leptonic decays are included in the lepton (e, μ) triggers.

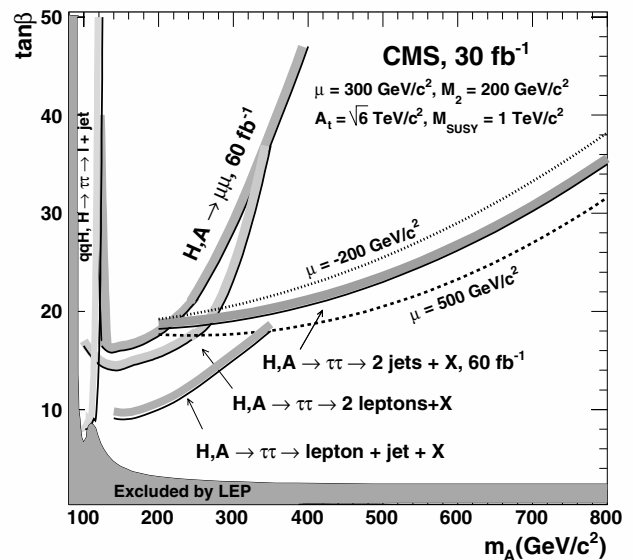


Fig. 1. The 5 sigma discovery potential for the heavy neutral MSSM Higgs bosons as a function of m_A and $\tan(\beta)$ with maximal stop mixing, for an integrated luminosity of 30 fb^{-1} .

3 Level 1 Trigger

The Level 1 τ trigger exploits a generic jet trigger based only on the calorimetric information [3]. Candidate jets are built out of groups of 12×12 ECAL and HCAL towers whose central 4×4 transverse energy (E_T) is larger than the E_T of all its 4×4 neighbours. A loose isolation criteria is applied requiring active tower patterns to be made of neighbour towers as shown in Fig.2.

The desired rate at the Level 1 is reached with a further cut on the calorimetric energy requiring a transverse energy greater than 93 GeV for one jet and 66 GeV for two jets [3]. The two leading jets represent the Level 1 Tau stream. The reconstructed jets that don't pass the isolation criteria are labeled as central jets. To evaluate the trigger performances, a benchmark channel has been cho-

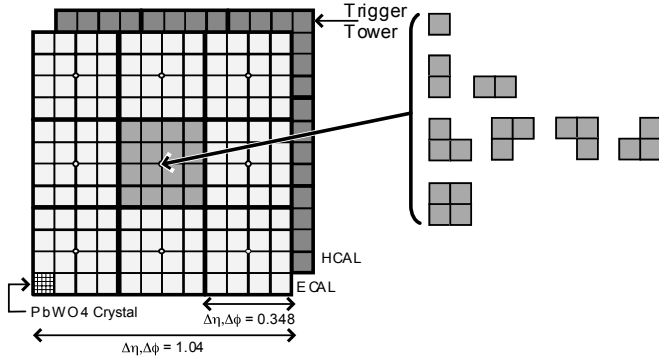


Fig. 2. Level 1 Tau trigger allowed patterns for active towers.

Table 1. Trigger thresholds and efficiency for the 200 GeV/c² Higgs boson

Lumin.	Rate	E _T 1 Tau	E _T 2 Tau	Efficiency
Low	3 kHz	93 GeV	66 GeV	0.78
Higs	8 kHz	106 GeV	72 GeV	0.62

sen:A/H → ττ → 2 τ jets; two Higgs boson mass values have been considered: 200 and 500 GeV/c². The trigger rate is saturated by QCD di-jets events, at Level 1 the rate is 3 kHz running at low luminosity and 8 kHz at high luminosity. Table 1 shows trigger efficiency for signal events for the 200 GeV/c² Higgs boson for the low and high luminosity periods [3].

In the following the report will concentrate on the triggering and tagging of events with two τ jets, in which both jets must be selected. For events with only one τ lepton, a slightly different selection is applied, briefly described later in the report.

3.1 High Level Trigger

In the HLT step the two Tau candidates are reconstructed with a better granularity and ordered in energy. The two candidates are defined as jets chosen among the two leading jets in the Tau stream and the leading jet reconstructed in the central stream, the choice is made accordingly to the jets energy and is described elsewhere [3]. The reconstruction is performed in a restricted region, obtaining performances very similar to the reconstruction used in the off line tagging, but it is much faster. This reconstruction (with the application of very low thresholds) identifies the Level-2 jets (L2 jets). An isolation algorithm is applied to these L2 jets. The isolation can be made with the electromagnetic calorimeter deposits and/or reconstructed tracks. Two different options are available:

- Level-2 calorimeter isolation, followed by a Level-2.5 pixel isolation, i.e. isolation with tracks reconstructed using only the pixel detector (faster but less efficient);
- Level-2.5 full tracker isolation, without any calorimeter isolation (slower but more efficient).

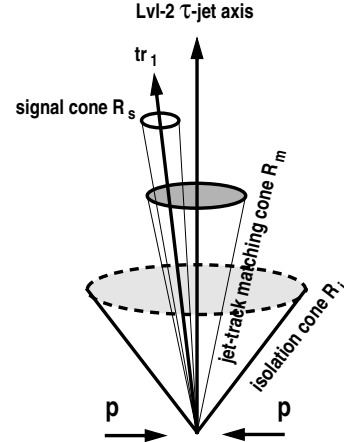


Fig. 3. Sketch of the isolation criteria.

More details on the logic of the trigger system can be found in Ref. [4], [5], [6].

3.1.1 Ecal isolation

The hadronic τ decays produce a localized energy deposit in the electromagnetic calorimeter. The electromagnetic isolation parameter P_{isol} defined as

$$P_{\text{isol}} = \sum_{\Delta R < 0.40} E_T - \sum_{\Delta R < 0.13} E_T \quad (1)$$

provides an adequate variable to discriminate between real and fake τ. The sums run over transverse energy deposits in the electromagnetic calorimeter, and ΔR is the distance in η – φ space from the τ-jet axis. Jets with $P_{\text{isol}} < P_{\text{isol}}^{\text{cut}}$ are considered as τ candidates. A background rejection of about 30% can be achieved using $P_{\text{isol}}^{\text{cut}} = 5.6$ GeV.

3.1.2 Track Isolation

In this section the isolation algorithm used in the Level-2.5 pixel trigger and Level-2.5 tracker trigger is described; more information can be found in [5], [6]. The main difference between the two options is the way in which the tracks are reconstructed. For the pixel trigger, only the 3 pixel layers are used, while the tracker trigger uses also the silicon strip layers. To speed up the reconstruction only the tracks inside the regions of interests (the jet cones) are reconstructed. Then the isolation procedure, shown in Fig. 3, is applied. To reduce the contamination from soft tracks, only tracks with $p_T > 1$ GeV/c and associated to

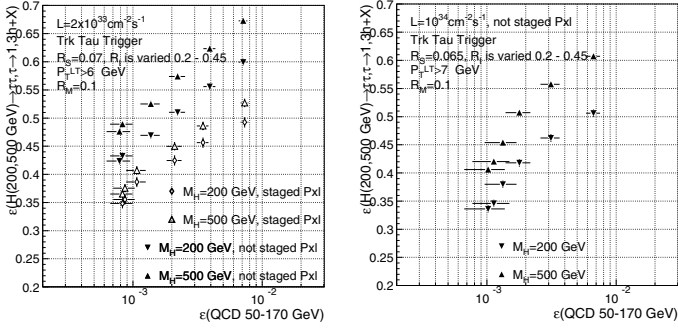


Fig. 4. Efficiency of L25 tracker isolation, with respect to Level 1 output, applied to both jets for the low (left) and high (right) luminosity. The plot represents the signal efficiency versus the QCD one. Two Higgs masses $M_H=200$ and 500 GeV/c^2 , are shown. Isolation cone is varied from 0.2 to 0.45, signal cone is 0.07, matching cone is 0.1 and the p_T of the leading track must exceed 6 GeV/c .

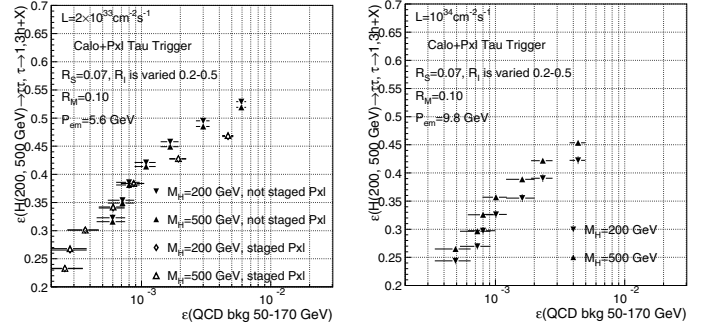


Fig. 5. Efficiency of L25 pixel isolation, with respect to Level 1 output, applied to both jets for the low (left) and high (right) luminosity. The plot represents the signal efficiency versus the QCD one. Two Higgs masses $M_H=200$ and 500 GeV/c^2 , are shown. Isolation cone is varied from 0.2 to 0.45, signal cone is 0.07, matching cone is 0.1 and the p_T of the leading track must exceed 3 GeV/c .

the signal vertex are considered, such tracks are referred to as "good tracks". The isolation-based tagging compares the number of good tracks within a "signal cone" ($R=R_S$) and within an "isolation cone" ($R=R_I > R_S$). Signal cone is defined around the direction of the leading track i.e. the highest p_T track found in the "matching cone" ($R_M=0.1$), around the jet direction. The isolation cone is defined around the jet direction for the pixel case, while it is around the leading track direction for the tracker case. The trigger selection requires zero good tracks in the ring $R_S < R < R_I$. Higher background reduction can be obtained by requiring the transverse momentum of the leading track to exceed a few GeV/c .

The usual value for the signal cone R_S is 0.07, while the "isolation" cone R_I is treated as a free parameter used to adjust the trigger rate: it is varied with a step of 0.05 from 0.2 to 0.45. The performances of the algorithm have been computed on the signal and QCD events, and are shown in Fig.4 and Fig.5 respectively for the calorimete-pixel isolation and tracker one. The plots on the left are made for the low luminosity period, the plots on the right for the high luminosity one. The different points correspond to the different sizes of the isolation cone R_I : a background efficiency of $\sim 10^{-3}$ can be easily achieved with a R_I around 0.40. A special High Level trigger selection for only one τ jet has also been studied. In this case the rejection factor of 1000 can be achieved with the isolation criteria applied on the single Tau candidate in the event (with a cut of 20 GeV/c on the p_T of the leading track) and a selection based on the transverse missing energy. This trigger has been designed and optimized for the search of a charged Higgs boson. Due to the strong cut in p_T only the L2.5 Tracker trigger can be applied; the pixel reconstruction, with its limited level arm, cannot achieve a good enough momentum resolution to allow the use of the L2.5 Pixel trigger.

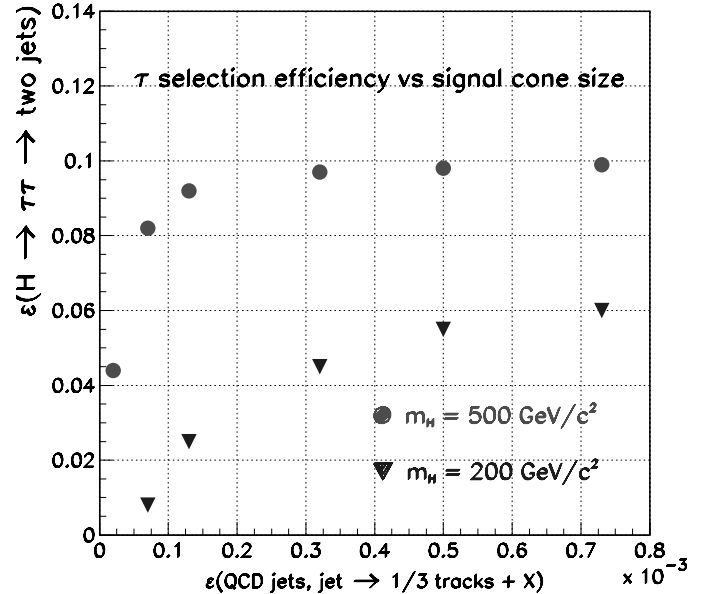


Fig. 6. Efficiency for the three prong τ selection (isolation, leading track $p_T > 40$ GeV/c , three tracks inside the signal cone), for signal vs background efficiency. Two Higgs boson mass value have been chosen: 200 and 500 GeV/c^2 , the signal cone is varied from 0.02 to 0.007.

4 Off Line Selection

While the trigger has been studied for both low and high luminosity conditions, the off-line selection have been optimized only for the low luminosity running period.

The off-line selections are based on a stronger isolation cut, with a cut on the leading track p_T up to 40 GeV/c , and a selection on the significance of the tracks impact parameter (a la b-tagging). The jets are globally reconstructed and the nearest to the flight direction of the L2 jets are selected as candidate Taus. For what regards the isolation, the signal cone is varied this time (from 0.02 up to 0.07). A further selection can be made requiring that only one or three good tracks are reconstructed inside the

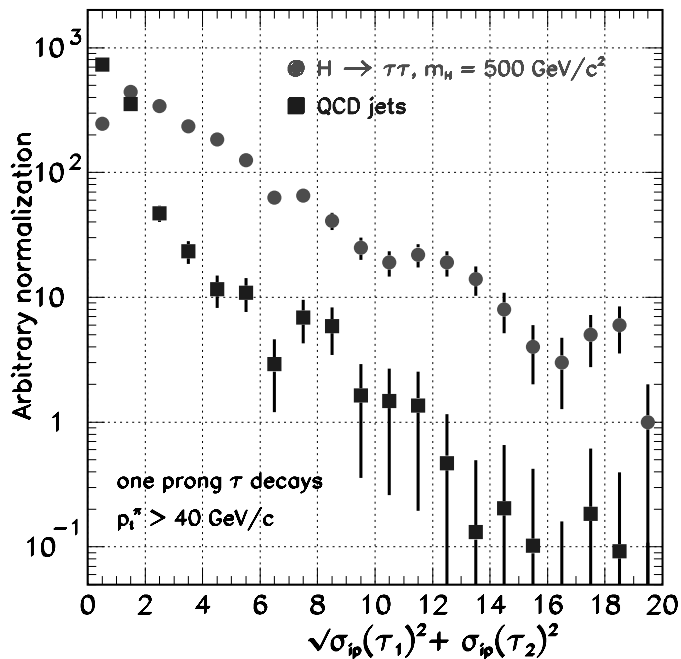


Fig. 7. Distribution for the sum of the impact parameter significance for the two Tau Candidate for 1-prong τ decay, for a Higgs boson mass of $500 \text{ GeV}/c^2$ and the QCD sample.

signal cone. Figure 6 show the performance of the off-line isolation for the two Higgs boson mass values. The background rejection can achieve the limit of 10^{-4} , with signal efficiency of few %. More details can be found in [7].

The other important criterion used is a cut on the sum of the significance of the impact parameter of the tracks inside the isolation cone of the jets:

$$\sigma_{\text{ip}} = \sqrt{\sigma_{\text{ip}}(\tau_1) + \sigma_{\text{ip}}(\tau_2)} \quad (2)$$

where $\sigma_{\text{ip}}(\tau_1, \tau_2)$ are the unsigned impact parameter significances for the leading tracks in the two τ jets. Figure 7 shows the distribution of σ_{12} for the signal ($m_H = 500 \text{ GeV}/c^2$) and the QCD di-jet events with jet $E_T > 60 \text{ GeV}$ and the leading track $p_T > 40 \text{ GeV}/c$. The minimum number of hits in the track reconstruction is set to five. Requiring more hits could improve the QCD multi-jet rejection by removing part of the accidental large impact parameters in the hadronic jets. The signal efficiencies for the cuts $\sigma_{12} > 5$ are greater than 55% (with a dependance from the jet energy), while the QCD background can be rejected by almost a factor 10.

Further improvement can include the use of a signed impact parameter instead of the unsigned one and the opposite charge of the jets. The jet charge is defined as the sum of the charge of the tracks inside the isolation cone, and for a couple of τ jets, the product of the charges must be equal to -1. Recent, preliminary, studies have shown that the reconstruction of π^0 inside the electromagnetic calorimeter can be useful to reconstruct, with the selected tracks, the τ mass and thus discriminate between QCD and real τ jets.

The τ identification is intended as the combination of all

the possible tagging criteria. Due to the very different event topology in which the τ identification can be used, there is not a unique recipe to merge all the algorithm together: the performances depends a lot on the number of jets in the event and on their energy. Detailed studies are needed to find the best combination for every considered physics channel.

5 Conclusions

The Tau identification used in the CMS experiment has been presented. The selection starts from the Level 1 trigger and go through the High Level trigger and the off-line selection. The trigger considers both the single and double τ jet case, optimized for the search of a charged and neutral MSSM Higgs boson.

Isolation and impact parameter significance are the most important criteria used. Due to the several parameters that can be introduced inside the algorithms, a detailed optimization based on the event topology, is required to get the best performance.

6 Acknowledgement

The author would thank all the collaboration, for having provided the material and for the useful discussions.

References

1. S. P. Martin, hep-ph/9709356.
2. S. Abdullin et al., CMS NOTE 2003/033.
3. CERN/LHCC/2002-26, CMS TDR 6.2, December 2002.
4. A. Nikitenko et al., CMS NOTE 2000/055.
5. A. Nikitenko et al., CMS NOTE 2001/017.
6. G. Bagliesi et al., CMS NOTE 2002/018.
7. A. Nikitenko, et al. CMS NOTE 2003/006.

Particle identification of the LHCb experiment

A. Van Lysebetten ^a

CERN, PH Division, 1211 Geneva 23, Switzerland

Abstract. One of the major challenges of the LHCb experiment is particle identification. The development and status of the different LHCb detector components associated with particle identification are presented in this article. The particle identification methods are briefly described and the overall performance is discussed for some example decay channels.

1 Introduction

The LHCb experiment [1] is dedicated to precision measurements of CP violation in the B sector and to the search of rare B decays [2]. All angles and some sides of the unitarity triangle are addressed by a multitude of B decay channels for which an efficient trigger [3] is needed. Efficient vertex identification and a high track reconstruction efficiency are other requirements set by the physics goals of the experiment. Another crucial component of the LHCb experiment is particle identification. The ability to distinguish between leptons and different hadrons in the final states of a variety of b hadron decay channels is essential for the LHCb physics program. Hadron identification is achieved using Ring Imaging Cherenkov detectors and will allow the experiment to make a distinction between signal and background processes and provide kaon identification for flavour tagging. The calorimeter and muon system provide lepton identification essential for the offline analysis and clean triggering.

In this article the particle identification systems and strategy will be described. The overall particle identification performance and its results on some of the example decay channels are also shown.

2 Hadron identification with the RICH detectors

2.1 The RICH detectors

The π /kaon separation has to be efficient in the range from ~ 1 to 100 GeV/c. The upper limit is determined by tracks from two body decays. As shown in the top plot of Fig. 1, 90% of these tracks have a momentum lower than 150 GeV/c. The lower plot of Fig. 1 shows that tagging kaons tend to have low momentum, down to 1 GeV/c, which imposes the lower momentum limit. A correlation exists between the polar angle of the track traversing the

Table 1. Characteristics of the LHCb RICH radiators.

	Aerogel	C ₄ F ₁₀	CF ₄
n	1.03	1.0014	1.0005
$\theta_c^{max}/\text{mrad}$	242	53	32
$\Delta\theta_c^{max}/\text{mrad}$	2.19	1.29	0.60
N_{pe}	7	31	23
$p_{thresh}^{pion}/\text{GeV}/c$	0.6	2.6	4.4
$p_{thresh}^{kaon}/\text{GeV}/c$	2.0	9.3	15.6

spectrometer and its momentum (see Fig. 1). In order to cover a large momentum range over a wide polar angle range a system consisting of two RICH detectors using three different radiators has been chosen.

RICH1 is installed upstream from the dipole magnet and covers track angles up to 300 mrad using aerogel [4] and gaseous C₄F₁₀ radiators, optimised for low to mid momentum tracks. RICH2 is placed further downstream, in between the tracking systems and the calorimeter system covering an acceptance up to 120 mrad. A single radiator medium (CF₄) is used and the detector is optimised for higher momentum tracks. Table 1 details the physical parameters of the three radiators.

The main optical components for both RICH detectors are similar. A track traversing the radiator media will emit Cherenkov photons which are focussed by tilted spherical mirrors. Secondary flat mirrors are used to bring the photons out of the acceptance. The spherical mirrors of RICH1 are inside acceptance, and upstream of the main tracking detectors; they are required to be as light as possible, and beryllium mirrors are the adopted solution. These requirements do not exist for the RICH2 mirrors, nor for the flat RICH1 mirrors. In these cases a glass mirror is chosen. All flat and spherical mirrors of RICH2 were installed over summer 2005 and aligned to a precision of 20 μrad and 150 μrad respectively, not degrading the particle identification performance. The design and construction of RICH1 is progressing well; the mechanical support structure, including the gas vessel with aligned mirrors, of RICH2 will be installed in the experimental area by the

^a on behalf of the LHCb collaboration

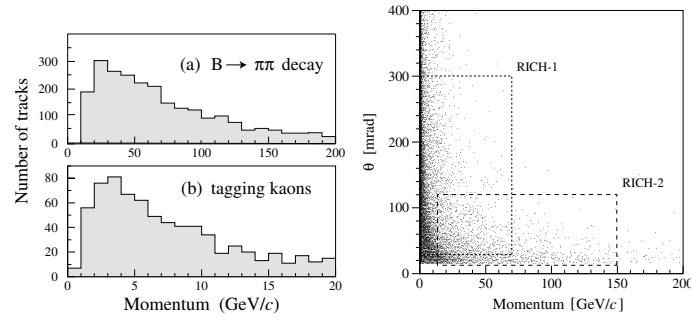


Fig. 1. Left: Momentum distributions for (a) the highest momentum pion from $B_d^0 \rightarrow \pi^+\pi^-$ decays, (b) tagging kaons. Right: Polar angle θ versus momentum for all tracks in simulated $B_d^0 \rightarrow \pi^+\pi^-$ events, the regions of interest for RICH1 and RICH2 are also indicated.

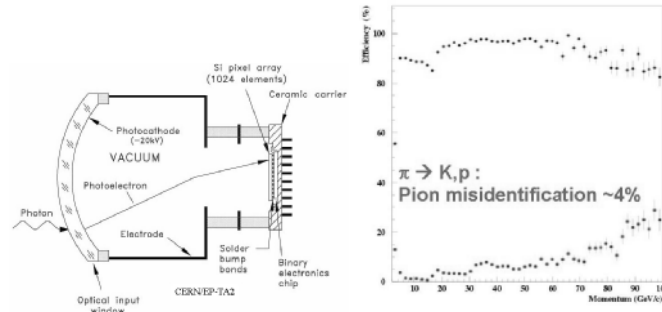


Fig. 2. Left: A schematic of the HPD. Right: Identification efficiencies for kaons (top) and misidentification efficiencies for pions (bottom) as function of momentum.

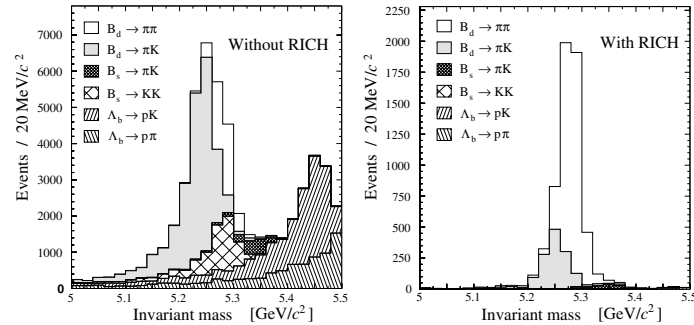


Fig. 3. Invariant mass distributions for the signal channel $B_d^0 \rightarrow \pi^+\pi^-$ and its background channels, without (left) and with (right) the RICH particle information in the analysis.

end of summer 2005.

To detect the Cherenkov photons with a high granularity ($2.5 \times 2.5 \text{ mm}^2$) over a large active area (2.8 m^2), a high efficiency position-sensitive single photon detector is needed. The adopted solution for the LHCb RICH detectors is the pixel Hybrid Photon Detector (HPD) [5]. The HPD (see Fig. 2) is a vacuum tube with a pixelated silicon detector anode assembly. The device has a quartz entrance window with a multi-alkali photocathode. Photoelectrons emitted from the photocathode are accelerated onto the anode assembly by a 20 kV cross-focussing electron op-

tics. The demagnification factor is 5. The 484 photon detectors need to operate in the fringe field of the LHCb dipole magnet. The HPD electron optics is sensitive to magnetic flux densities. Hence the HPDs are enclosed in primary magnetic shielding boxes designed to limit the field density flux to 2.5 mT and 1.0 mT in RICH1 and RICH2, respectively. In situ measurements have confirmed the simulation. The direction of the magnetic flux density at the RICH1 photon detector plane (mainly longitudinal) is different from the direction in RICH2 (mainly transverse) [6]. This is a direct consequence of the placement

and orientation of the photon detector planes within the RICH detectors. The magnetic flux density level inside the shielding boxes would still induce excessive distortions and even signal losses. Therefore, a local secondary magnetic shield of a high permeability alloy (MuMetal) is used. It has been shown that the HPDs are operational up to fields of 5.0 mT with this additional shielding. The most important distortions are expected for axial fields, but these are parameterisable and can be compensated for [7]. Calibration patterns to monitor and correct for these effects are under study.

The overall performance of the RICH system has been studied in full Geant4 simulations of LHCb events incorporating all background sources and realistic reconstruction efficiencies. Full pattern recognition in the tracking system was also included. The current particle identification approach uses an implementation of a maximum likelihood to determine the most probable mass hypothesis. In this algorithm all available reconstructed tracks through the RICH detectors, together with the knowledge of the optics of the system, are used to predict the response of the photon detectors for a given choice of particle hypotheses. By comparing these predictions to the data the most likely set of mass hypotheses for all tracks is found. This is done in the “global approach”, where all tracks are considered simultaneously in the event. This algorithm is slow but provides a complete description of the most important background contributions to a single Cherenkov ring (overlapping rings from neighbouring tracks). Alternative strategies include the “local approach”, which is faster and less dependent of the overall tracking performance as it considers the tracks individually. The last approach is the “Ring fitting” which attempts to isolate Cherenkov rings in the data without reference to reconstructed tracks.

The pion and kaon selection performance is shown in Fig. 2 against the reconstructed track momentum. The kaon identification efficiency is 88% on average and the pion misidentification 4%.

The importance of the RICH hadron identification can be clearly illustrated for the decay $B_{(s)}^0 \rightarrow h^+h^-$. A combination of the channel $B^0 \rightarrow \pi^+\pi^-$ and $B_s^0 \rightarrow K^+K^-$ allows for a precise measurement of the CP violating γ angle. With ~ 26000 $\pi^+\pi^-$ decays and ~ 37000 K^+K^- decays a precision on the angle γ of 5° is expected from one year of running (2 fb^{-1}). These channels are sensitive to new physics through the presence of penguin diagrams. With the excellent RICH hadron identification included in the analysis the purity of the selected $B_s^0 \rightarrow K^+K^-$ decays is increased from 13% to 84% whilst retaining 79% of the signal. The same effect is illustrated in Fig. 3 for $B^0 \rightarrow \pi^+\pi^-$ decays.

3 Lepton identification

Excellent lepton identification is essential for access to the CP violating angles β and ϕ_S through channels like $B \rightarrow (J/\psi \rightarrow l^+l^-) K_S/\phi$ and for rare B decays (eg. $B \rightarrow \mu\mu$). Lepton identification is also important for the trigger and flavour tagging.

3.1 Muon identification

The muon system is based on multi-wire proportional chambers and GEM detectors [8]. Muons are identified by extrapolating well reconstructed tracks with $p > 3 \text{ GeV}/c$ into the muon stations. Hits in the muon stations are then searched within a certain field of interest around the extrapolation points. The muon identification efficiency, displayed in Fig. 4, is a flat function of the momentum from 10 GeV/c onwards. The invariant mass distribution for J/ψ Reconstruction in $B \rightarrow J/\psi K_s$ decays is shown in Fig. 4. As can be seen the background is rather low. With this selection an average muon identification efficiency of 96% is obtained, while the pion misidentification rate is of the level of 2%. The pion background, mainly in the lower momentum range, can be further reduced (to the level of 0.8%) by other algorithms based on the hit-track distance, while keeping $\sim 90\%$ of the signal. These algorithms allow to provide a likelihood for the muon hypothesis and the combination of the electron, RICH and muon information for the global particle identification. These studies are under development.

3.2 Electron identification

Electrons are identified with a likelihood hypothesis approach, combining four discriminating variables from the calorimeter system [9]. The first is the χ^2 distribution resulting from matching of the track momentum with corrected charged cluster energy and matching the position of the corrected barycenter with the extrapolated track impact point. A second estimator is provided by the pre-shower detector. Electrons are expected to produce a larger signal than hadrons. A third variable is related to the matching of the Bremsstrahlung photons emitted by electrons before the magnet with the electron track extrapolation. Due to little material within the magnet the position of these neutral clusters is expected to be given well by the electron track extrapolations. Further improvement in electron identification is made by using the energy deposition in the hadron calorimeter along the extrapolated track. The resulting efficiency against momentum is shown in Fig. 5. An average electron identification efficiency of 95% is noted for tracks within the calorimeter acceptance, dropping to 81% when considering all tracks. The likelihood hypothesis built from the calorimeter system information is then combined with the RICH information. The resulting invariant mass distribution for J/ψ reconstruction in $B \rightarrow J/\psi\phi$ decays is shown in Fig. 5. The tail in the distribution is due to Bremsstrahlung. A more important background is observed for electrons than was the case for muons. Without explicit rejection criteria (a transverse momentum cut) a large combinatorial background is observed from secondary electron and ghost tracks. A cut on the transverse momentum ($p_T > 0.5 \text{ GeV}/c$) reduces the background to a manageable level ($\sim 1\%$) while keeping 78% of the signal.

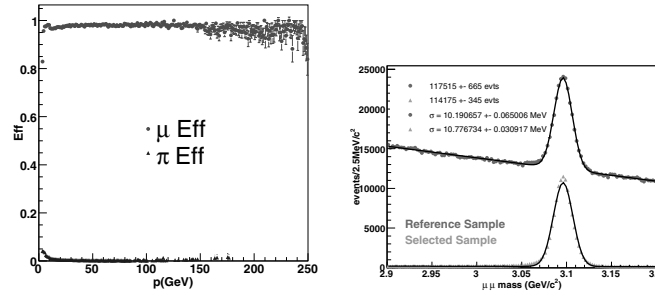


Fig. 4. Left: the muon identification efficiency versus momentum (top), pion misidentification efficiency (bottom). Right: J/ψ invariant mass distribution for $J/\psi \rightarrow \mu^+\mu^-$ reconstruction in $B_s^0 \rightarrow J/\psi K_S$ decays.

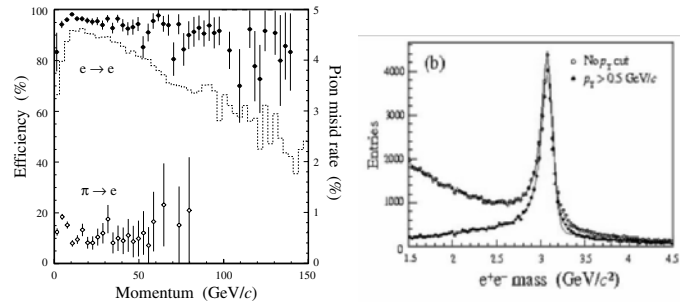


Fig. 5. Left: the electron identification efficiency versus momentum (top), pion misidentification efficiency (bottom). Right: J/ψ invariant mass distribution for $J/\psi \rightarrow e^+e^-$ reconstruction in $B_s^0 \rightarrow J/\psi\phi$ decays.

4 Conclusions

Particle identification is essential for the LHCb physics program. A three sigma pion/kaon separation in the momentum range from 1 to 100 GeV/c is provided by two RICH detectors. Efficient lepton identification (at the level of 90%) is achieved with the calorimeter and muon systems.

All particle identification systems will provide a likelihood for each hypothesis, which will be then combined for the global particle identification procedure.

The construction and installation of the detectors is well underway. The RICH2 construction is almost complete, while the construction of RICH1 is well advanced. The overall installation is expected to be ready by October 2006. A third of the total required muon chambers has been produced, and all muon filters are installed in the experimental area. The calorimeter system is currently being assembled in the experimental hall.

References

1. R. Forty: "Status of the LHCb experiment", these proceedings.
2. Y. Xie: "Event Reconstruction and physics performance of the LHCb experiment", these proceedings.
3. M. Patel: "Trigger strategy and performance of the LHCb detector", these proceedings.
4. D. Perrego: "The LHCb RICH detector", these proceedings.
5. M. Alemi et al, "First operation of a Hybrid Photon Detector prototype with electrostatic cross-focussing and integrated silicon pixel readout" Nucl. Instrum. Meth. **A449**, (2000) 48-59.
6. M. Patel, "Magnetic shielding studies of the LHCb RICH photon detectors", proceedings of RICH2004, to be published in NIMA.
7. A. Van Lysebetten, "Characterization and compensation of magnetic distortions for the pixel Hybrid Photon Detectors of the LHCb RICH ", proceedings of RICH2004, to be published in NIMA.
8. S. Amato et al, LHCb Coll.: "LHCb Muon System: Technical Design Report" CERN/LHCC/2001-010. Addendum CERN/LHCC/2003-002 and Addendum CERN/LHCC/2005-012.
9. S. Amato et al, LHCb Coll.: "LHCb Calorimeters: Technical Design Report" CERN/LHCC/2000-0036.

Beyond the Standard Model

Theoretical Developments Beyond the Standard Model

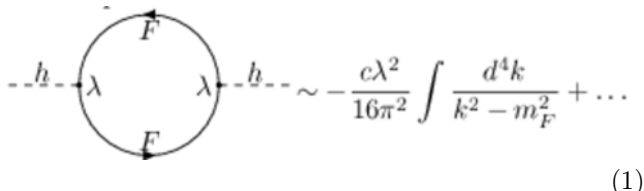
B.C. Allanach

DAMTP, CMS, University of Cambridge, Wilberforce Road, CB3 0WA, United Kingdom

Abstract. The technical hierarchy problem still remains a guiding principle for particle physics beyond the Standard Model. Low energy supersymmetry remains the only perturbatively calculable solution to the problem. It can contain a suitable dark matter candidate, which may be produced at future colliders. If enough properties of the minimal supersymmetric standard model (MSSM) are measured, a prediction of the relic density can be made, providing useful cosmological information. Universal extra dimensions (UED) is a concrete “straw man” to the MSSM, giving very similar signatures in colliders. Spin-dependent observables are necessary in order to distinguish UED from the MSSM. Some authors have questioned whether the hierarchy problem should be used as a guiding principle and have suggested split supersymmetry as an example of a model that does not solve it. There have also been suggestions which postpone the hierarchy problem to a higher energy scale, in little Higgs models for example. A T -parity symmetry helps the model to satisfy precision electroweak constraints. If one dispenses with the Higgs altogether, models with a tower of heavy W'/Z' bosons can postpone the onset of perturbative unitarity violation, with an associated relaxation in the effects of precision electroweak constraints. In the UED, MSSM and T -parity little Higgs models, a parity symmetry introduced for separate phenomenological reasons provides a stable particle which can constitute the dark matter.

1 The Technical Hierarchy Problem and Supersymmetry

The technical hierarchy problem arises with light fundamental scalars. Their self-energy graphs receive quantum corrections that are *quadratically divergent* if one admits a field theory description up to infinite energies, from graphs such as the one in Eq. 1 or graphs with scalar or vector boson loops.



$$\text{---}h\text{---}\lambda\text{---}\text{---}F\text{---}\lambda\text{---}h\text{---}\sim -\frac{c\lambda^2}{16\pi^2}\int\frac{d^4k}{k^2-m_F^2}+\dots$$

“Quadratically divergent” is defined for any diagram that is $\propto \Lambda^2$, where Λ is an ultra-violet cut-off on the loop momenta. Of course, if we take $\Lambda \rightarrow \infty$, the infinity will be absorbed by the usual renormalisation procedure, but any physical heavy energy scale Λ_n of new physics or new particles will contribute to the physical Higgs mass like

$$m_h = m_h^{\text{tree}} - \mathcal{O}(\Lambda_n/100), \quad (2)$$

where the factor of 100 comes from a loop suppression factor.

The heaviest fundamental scale of physics we know is the Planck scale $M_{Pl} \sim 10^{19}$ GeV, and substituting $\Lambda_n = M_{Pl}$ into Eq. 2, a problem emerges: the left-hand

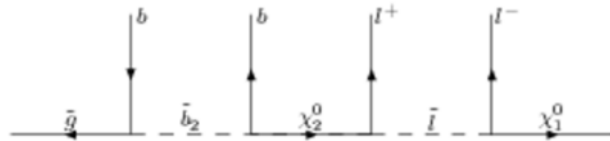


Fig. 1. An example SUSY cascade decay

side must be of order 1 TeV or less for the Higgs mechanism to provide $M_Z = 91.19$ GeV, therefore a large cancellation between the first and second terms of Eq. 2 must occur (to roughly 1 part in 10^{15}). Many find this aesthetically repugnant, since there is no symmetry to enforce such a cancellation. However, supersymmetry provides a suitable symmetry by predicting a boson for every fermion with identical coupling strengths. Supersymmetry enforces cancellation between bosonic and fermionic loops, solving the hierarchy problem. An important goal of the Tevatron and the Large Hadron Collider will be to discover and then measure the properties of supersymmetry.

One important handle upon the properties of the supersymmetric particles come from the measurements of *kinematic endpoints* of SUSY cascade decays such as the one in Fig. 1. Fig. 2 shows the simulation of such a measurement [1]. The measurement of the maximum value of the di-lepton invariant mass can be performed precisely, since it does not rely on jet measurements, and since it is

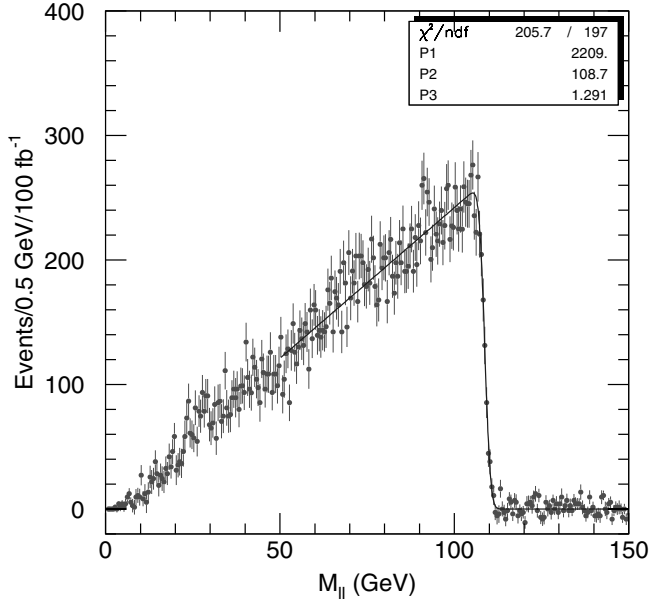


Fig. 2. Di-lepton end-point measurement for an integrated luminosity of 100 fb^{-1} .

Lorentz (and therefore boost)-invariant. In terms of SUSY particle masses, the maximum mass squared is

$$m_{ll}^2 = \frac{(m_{\chi_2^0}^2 - m_l^2)(m_l^2 - m_{\chi_1^0}^2)}{m_l^2} \quad (3)$$

and corresponds to a kinematic maximum when the leptons are back-to-back in the rest-frame of the decaying slepton. Many other invariant mass combinations can be constructed using the other 4-momenta of some of the final state particles shown in Fig. 1 in order to perform fits to the spectrum [1]. m_{ll} might be measured with per-mille precision although invariant masses involving jets often have uncertainties at the percent level. Since backgrounds are often flavour invariant, flavour subtraction is performed to reduce them. Kinematic features like the dilepton endpoint only rely weakly on the modelling of the detector and parton showers than some measurement that counts events, making them much more reliable.

1.1 Supersymmetric Dark Matter

The dark matter problem has been with us for many decades now, and is present on many different scales: on galactic scales (observed through anomalous galactic rotation velocities), on astrophysical scales (through gravitational lensing) and on cosmological scales (through a combination of the observations of the cosmic microwave background and large scale structure data). Imposing R -parity on the MSSM, we find a suitable weakly interacting dark matter candidate: the lightest neutralino χ_1^0 . The WMAP fits to cosmic microwave background temperature anisotropies and 2dFRGS large scale structure data yield [2]

$$\Omega_{DM} h^2 = 0.1126_{-0.0091}^{+0.0081}, \quad (4)$$

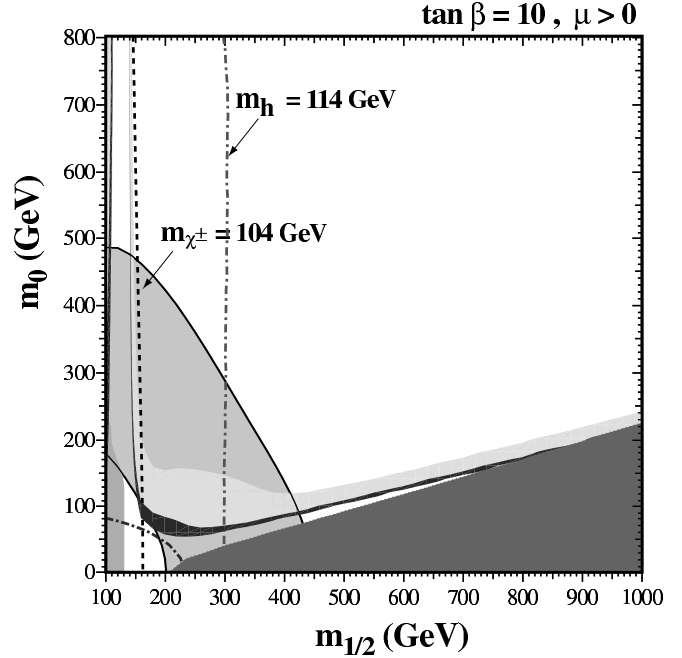


Fig. 3. Constraints upon the $m_{1/2} - m_0$ plane in mSUGRA for $\tan \beta = 10$, $A_0 = 0$, $m_t = 175 \text{ GeV}$ and central empirical values of $m_b(m_b)$ and $\alpha_s(M_Z)$. The triangular bottom right-hand dark brown region is ruled out since the lightest stable supersymmetric particle is charged there, the purple (light grey) band is favoured by the $(g-2)_\mu$ measurement and the region to the left of the red line is ruled out by LEP2 Higgs constraints. The blue (dark) strip is compatible with the WMAP constraint and the green (grey) region in the bottom left-hand corner is ruled out by the measurement of $BR[b \rightarrow s\gamma]$. The region to the left of the dashed black line is ruled out from negative chargino searches [10].

where Ω_{DM} is the relic density of dark matter and h is the Hubble parameter. Many authors have pointed out that this measurement severely constrains the MSSM, effectively reducing the available parameter space by one. Specialising to mSUGRA, where at M_{GUT} (the scale at which the electroweak gauge couplings meet) the scalar masses are all set equal to m_0 , the trilinear scalar couplings to A_0 and the gauginos to $M_{1/2}$, it appears that a special annihilation mechanism must have been present in the early universe in order to deplete the dark matter relic density. We enumerate the different mSUGRA possibilities here: 1. Stau ($\tilde{\tau}$) co-annihilation [3] at small m_0 where the lightest stau is quasi-degenerate with the lightest neutralino (χ_1^0). 2. Pseudoscalar Higgs (A^0) funnel region at large $\tan \beta > 45$ where two neutralinos annihilate through an s -channel A^0 resonance [4, 5]. 3. Light CP-even Higgs (h^0) region at low $M_{1/2}$ where two neutralinos annihilate through an s -channel h^0 resonance [4, 6]. 4. Focus point [7–9] at large m_0 where a significant Higgsino component leads to efficient neutralino annihilation into gauge boson pairs. The anomalous magnetic moment of the muon has been measured [11] to be higher than the Standard Model prediction [12, 13]. The experimental measurement is so precise that the comparison is limited

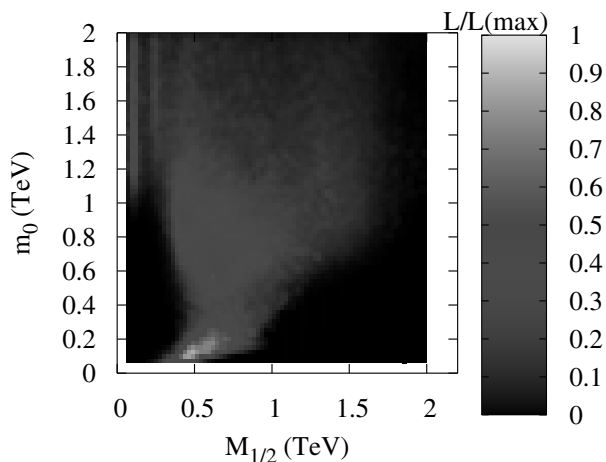


Fig. 4. Constraints upon the $m_{1/2} - m_0$ plane in mSUGRA [17]. A combined likelihood distribution from $BR[b \rightarrow s\gamma]$, $(g-2)_\mu$, $\Omega_{DM}h^2$ and the Standard Model inputs is shown marginalised down to the $M_{1/2} - m_0$ plane. The binned likelihood is shown by reference to the bar on the right, and is marginalised to the bin with maximum likelihood.

by theoretical uncertainties in the Standard Model prediction. Ref. [14], constrains any new physics contribution to

$$\Delta \frac{(g-2)_\mu}{2} = 19.0 \pm 8.4 \times 10^{-10}. \quad (5)$$

Adding theoretical errors [15] to measurement errors [4] in quadrature for the branching ratio for the decay $b \rightarrow s\gamma$, yields the empirically derived constraint

$$BR(b \rightarrow s\gamma) = 3.52 \pm 0.42. \quad (6)$$

Fig. 3 shows an example of these constraints applied to a 2d hyper-surface of the model. The WMAP constraint approximately reduces the available parameter space to a line. However, when a combined likelihood fit in the full $m_0, A_0, M_{1/2}, \tan\beta, m_t, m_b, \alpha_s(M_Z)$ parameter space is performed, the constraints upon the $m_0 - M_{1/2}$ plane are not as severe as one might think. Fig. 4 illustrates this point. The vertical sliver on the top left hand corner corresponds to light CP-even Higgs h^0 pole annihilation, the central bulk of the likelihood corresponds to CP-odd A^0 Higgs pole annihilation and at low m_0 , to stau co-annihilation.

In order to place such constraints upon the MSSM, many assumptions about the cosmology must be made. In particular, in Figs. 3,4 it has implicitly been assumed that the lightest supersymmetric particle (LSP) constitutes all of the dark matter. It has also been assumed in the prediction of $\Omega_{DM}h^2$ that radiation dominated the energy density in the post-inflation era. However, there is no clear observational evidence that between freeze-out and big-bang nucleosynthesis this was really the case. Non-standard cosmologies could also change the prediction of

$\Omega_{DM}h^2$, for example additional degrees of freedom, low reheating temperatures, extra dimensions, anisotropic cosmologies and non-thermal production of neutralinos. The literature contains examples of models with these each of these features.

If weak-scale supersymmetry (SUSY) is correct however, the LHC will turn into a dark matter factory since every SUSY particle produced will cascade decay down into the LSP. One may ask the question: can enough properties of χ_1^0 and the other particles be measured in order to get a better handle on the annihilation cross-section in the early universe, allowing a comparison between the observed WMAP relic density and the predicted one? Initial investigations [18] indicate that information from a linear collider, as well as data from the LHC, would be needed. Of course, even if SUSY is observed at a hadron collider, to be sure that the neutralino is stable on cosmological time scales and really constitutes the dark matter, confirmation from direct detection experiments would be needed.

1.2 Split supersymmetry

It has been argued [19] that the cosmological constant problem provides a much more severe fine-tuning problem than the technical hierarchy problem, being a tuning of 1 in 10^{120} in the Standard Model. Supersymmetry, although it can ameliorate the cosmological constant problem, still leaves a very severe tuning of 1 in 10^{60} . It is a logical possibility that the same mechanism that solves the cosmological constant problem also solves the technical hierarchy problem. If one abandons weak-scale supersymmetry as a solution for the technical hierarchy problem, it has been argued that gauge unification and dark matter can be provided by just the gauginos of the MSSM. One could make the scalar superpartners (and one Higgs doublet) much heavier than 1 TeV in the MSSM while keeping the gauginos and Higgsinos around the TeV scale.

At one loop, the presence of MSSM scalar superpartners does not affect the *relative* running of the Standard Model gauge couplings. The adjoint Majorana fermions, the gauginos, make a big difference however, and preserve the success of one-loop MSSM gauge unification if their mass is around the TeV scale. Also, neutralinos provide the usual SUSY dark matter at around the TeV scale, particularly if the lightest one has a significant Higgsino component, since then they annihilate sufficiently in the early universe to weak gauge boson pairs.

It is the prejudice of the author that although the initial reasoning about the technical hierarchy problem might be correct, such that it may not be a valid indicator for the form of physics beyond the Standard Model, there would then be no strong reason for any low energy supersymmetry, split or otherwise. It is not clear (for example in some string scenarios) that gauge unification is necessary, and even if it is, there are a huge number of ways of solving it without split SUSY. The assumption of a desert between the TeV scale and $M_{GUT} \sim 10^{16}$ GeV is a strong one;

there could well be intermediate particles (which can affect the running of the gauge couplings) and/or different effective gauge groups. There are also plenty of different candidates [20] for suitable weakly interactive massive particle dark matter, many of which have nothing to do with supersymmetry.

Luckily, once the Large Hadron Collider starts producing data, there will be no need to appeal to prejudice one way or the other, because there is a characteristic signature of split SUSY: quasi-stable gluinos [21, 22].

$$\Gamma \propto \frac{1}{m_{\tilde{q}}^4} \quad (7)$$

Eq. 7 shows the dominant decay mode of the gluino in split SUSY, which proceeds through an ultra-heavy virtual squark. The width is heavily mass-suppressed by the propagator and the lifetime can become quite long, e.g. $> \mathcal{O}(1)s$. Particles with lifetimes greater than $\sim 10^{-6}$ secs will not decay in the detector, and appear to be stable. The gluino will pick up quarks and gluons from the vacuum to form colour neutral R -hadrons. Much of the collider signature depends upon whether the lightest stable R -hadrons are electrically neutral or charged, but charge exchange with nuclei in the detector is expected anyway. Such particles will then appear to be slow heavy muons and should be easy to detect, provided their masses are less than 2 TeV or so [21].

1.3 Spins and Universal Extra Dimensions

So far, at the LHC, the majority of research has focused on measuring masses of supersymmetric particles through kinematics of the decay chain. However, one would wish to test supersymmetry by checking that the spins and couplings of sparticles are as is predicted in the MSSM. So far, this work has mainly been performed by assuming data from a future linear collider facility since such measurements are much easier to make there. The reasons for this are that the luminosity is much better measured and the total centre of mass energy is known.

Recently, however, a technique has been developed [23] that may allow measurement of a spin-related asymmetry at the LHC. As an example, we take a cascade like the one in the middle of Fig. 1, ie $\tilde{q}_L \rightarrow l^\pm \tilde{l}^\mp$ where the decay proceeds through an intermediate spin 1/2 Majorana neutralino. The spin of the intermediate particle shows up in the probability distribution for the invariant mass, where $m_{ql}^2 \equiv (p^\mu(q) + p^\mu(l)) \cdot (p_\mu(q) + p_\mu(l))$. $m \equiv m_{ql}/m_{ql}^{\max}$ is equal to $1/2 \sin \theta$, where θ is the angle between the lepton and quark in the rest frame of the intermediate neutralino. The probability density of m depends upon the charges of

the particles involved:

$$\frac{dP(l^+q/l^-\bar{q})}{dm} = 4m^3, \quad \frac{dP(l^-q/l^+\bar{q})}{dm} = 4m(1-m^2). \quad (8)$$

Of course the the charge of a quark can typically *not* be tagged and so the average of the quark and anti-quark combinations is measured. If the number of squarks is equal to the number of anti-squarks, this average leads to a probability distribution $\propto m$, equivalent to pure phase-space, as if the intermediate neutralino were a scalar boson. However, since the LHC is a pp collider, there is an initial state charge asymmetry, and in part of parameter space (namely where squark-gluino associated production is not much smaller than squark-squark production), more squarks than anti-squarks may be produced due to the presence of valence quarks in the proton, allowing the weighted average of the two different probability distributions in Eq. 8 to be sensitive to the neutralino spin.

We have two “straw men” to discriminate against: the first is a pure phase-space shape for the decay kinematics, but the second is somewhat more sophisticated: Universal Extra Dimensions (UED) [24]. This is a non-supersymmetric model in which a 5 dimensional space-time is compactified to 4 on a S_1/Z_2 orbifold. All of the Standard Model fields exist in the bulk and the size of the orbifold is the inverse TeV scale. Thus every Standard Model field has a tower of increasingly heavy Kaluza Klein (KK) modes with identical spin to the Standard Model partner, the first occurring at the TeV scale. 5-d momentum conservation gets broken by the orbifold to KK parity $(-1)^n$, where n is the KK level. This symmetry has the consequence that the lightest KK particle (LKP) is stable, and if it is the KK copy of the photon, is a suitable dark matter candidate. If KK modes no higher than the first level were produced at a collider, one could easily confuse the signatures physics with those of the MSSM since the LKP gives the classic missing-energy signature. Also, the KK particles will undergo cascade decays very much like they would in the MSSM. In order to distinguish UED from the MSSM it would obviously be desirable to measure the spins of the beyond the Standard Model particles, since they differ by $1/2\hbar$ in the two scenarios.

In practice, one constructs a lepton-charge asymmetry. Writing a quark/anti-quark as the generic j , we show

$$A^\pm = \frac{m_{jl^+} - m_{jl^-}}{m_{jl^+} + m_{jl^-}} \quad (9)$$

as a function of $\hat{m} \equiv m$ in Fig. 5. The power of discrimination between UED and the MSSM turns out to depend upon the mass-spectrum of KK modes/SUSY particles. If the spectrum is hierarchical, as is often the case of the MSSM, then the two models are easier to distinguish on the basis of the spin-dependent lepton-charge asymmetry. If the spectrum is rather degenerate, as is likely in UED, spin discrimination is much more difficult or impossible at the LHC. However, as Fig. 5 shows, distinguishing the MSSM from UED or phase space appears to be possible, at least for SPS 1a.

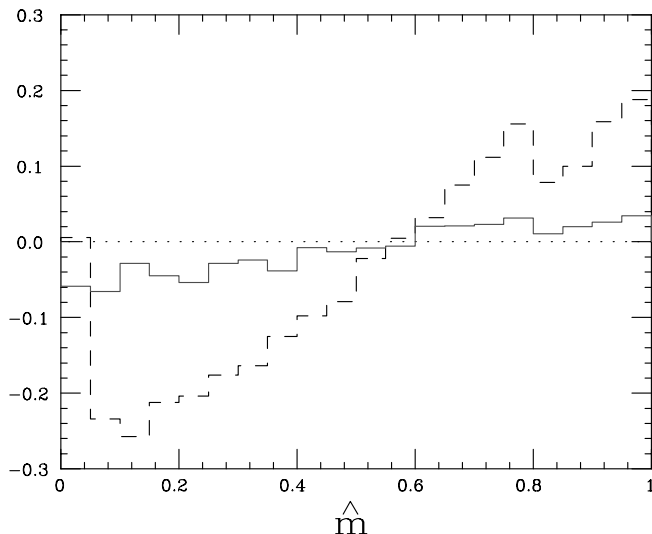


Fig. 5. Lepton charge asymmetry for SPS1a [25] mass spectrum. Dashed: MSSM. Solid/red: UED. Plot from ref. [26].

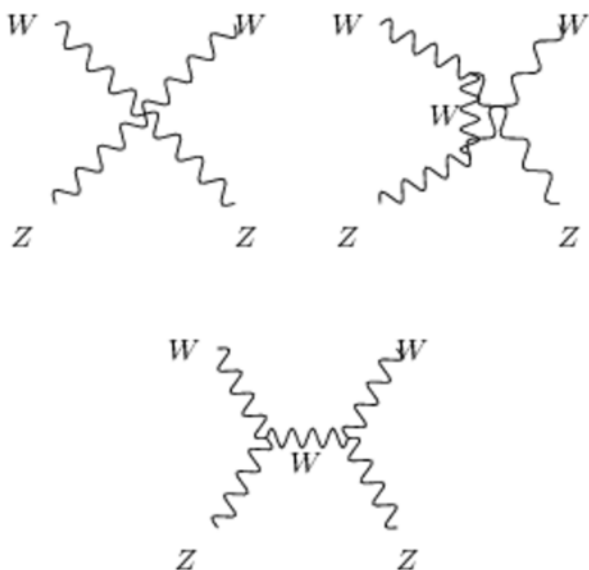


Fig. 6. Matrix element contributions to WZ scattering in the Standard Model

2 Higgsless Models

It is well known that without the Higgs boson, perturbative unitarity becomes violated in high-energy longitudinal weak boson scattering in the Standard Model. Fig. 6 shows the tree-level Standard Model contributions to WZ scattering. Writing g_4, g_3 as the quartic and trilinear couplings between gauge bosons respectively, the matrix ele-

ment M is

$$\begin{aligned}
 M \propto & (g_4 - g_3^2)[(c^2 - 6c - 3)E^4 + (c^2 - 3c - 2)M_Z^2 E^2 \\
 & - (c^2 - 9c - 4)M_W^s E^2] + g_3^2 \frac{M_Z^4 (1 - c)}{2M_W^2} E^2 \\
 & + \mathcal{O}(E^0)
 \end{aligned} \tag{10}$$

where E is the centre-of-mass energy of the colliding bosons, $M_{W,Z}$ are the masses of the W and Z bosons respectively and c is the cosine of the angle between the incoming and outgoing W 's in the centre-of-mass frame. The terms proportional to E^2 and E^4 are the ones that violate unitarity in the high E limit. When the Higgs boson is added to the Standard Model, the terms proportional $E^{2,4}$ are cancelled, restoring unitarity.

Without the Higgs, unitarity is lost in the perturbative limit, but there could be non-perturbative physics to cancel the dangerous pieces in Eq. 10. This happens at an energy scale of $\Lambda \sim 4\pi M_W/g \sim 1.8$ TeV, g being the electroweak gauge coupling. Typically, when one tries to introduce new strongly interacting physics at this scale, one runs into conflict with precision electroweak constraints. Λ may be increased by adding extra weak bosons W'_i , provided their couplings satisfy certain relations and the lightest one has a mass less than 1.8 TeV. The extra bosons will appear as propagators in M , and it can be shown [27] that two necessary conditions are

$$\begin{aligned}
 g_4 &= g_3^2 + \sum_i g'_{i3}{}^2, \\
 2(g_4 - g_3^2)(M_W^2 + M_Z^2) + g_3^2 M_Z^4 / M_W^2 &= \\
 \sum_i g'_{i3}{}^2 [3M_i'^2 - (M_Z^2 - M_W^2)^2 / M_i'^2] &
 \end{aligned} \tag{11}$$

where M'_i are the masses of the additional weak bosons and g'_{i3} are their trilinear couplings. Eq. 11 looks rather *ad hoc* at first sight, however if one puts the Higgsless Standard Model in a compactified 5-dimensional space-time, the relations hold *exactly* because of 5-d gauge symmetry. Each W'_i corresponds to a KK mode of the W and the summation in Eq. 11 must be over an infinite number of them to satisfy the conditions exactly. The 5-d theory becomes strongly interacting at some higher energy scale, thus it requires an ultra-violet cut-off and so Eq. 11 becomes only approximately satisfied. The result, however, is that perturbative unitarity survives until a higher energy scale, increasing Λ by up to a factor of 10. The advantage of a higher Λ is that non-Standard Model corrections to the precision electroweak observables become much smaller and may consequently pass the precision electroweak constraints.

Such a scenario predicts a first KK mode of the W that should have a mass considerably less than 1.8 TeV, making it ripe for discovery at the LHC. The WZ -scattering cross-section as a function of centre-of-mass energy \sqrt{s} as shown in Fig. 7 [27] and has a narrow peak corresponding to the first level KK mode. This is in contrast to the much wider peaks obtained for the strongly-interacting technicolour

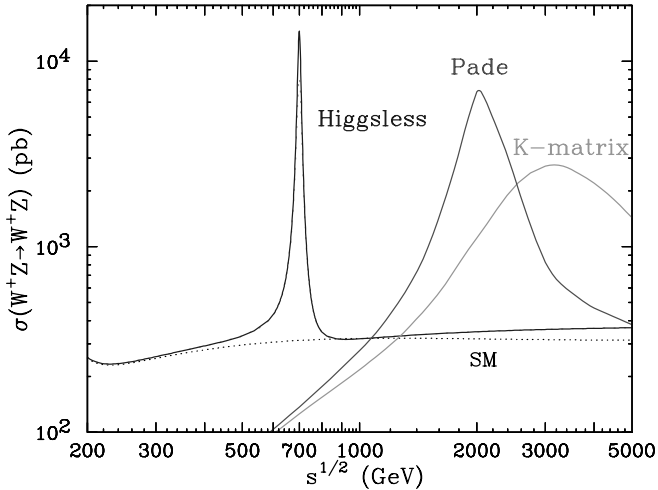


Fig. 7. Cross section for WZ scattering as a function of centre-of-mass energy for the Higgsless, Padé unitarisation and K-matrix unitarisation models.

type of models. Two examples of unitarisation parameterisations in strongly interacting scenarios are shown in Fig. 7: the Padé and K-matrix unitarisation models.

3 Little Higgs and T-Parity

Little Higgs models claim to ameliorate the hierarchy problem associated with the Standard Model Higgs mass such that the scale of new physics could be up to 100 TeV without causing a serious naturalness problem. However, GUT or Planck scale corrections could still cause fine-tuning in the Higgs mass unless new physics is added at 100 TeV in order to cancel them. For example, one might envisage breaking supersymmetry at 100 TeV down to some effective little Higgs model.

One of the simplest models, the “littlest Higgs” [29], contains a global $SU(5)$ non-linear sigma model in the electroweak sector. Part of the subgroup $[SU(2) \otimes U(1)]^2$ is gauged. It is assumed that $SU(5)$ is spontaneously broken down to $SO(5)$ by the vacuum expectation value of a $\underline{24}$ -plet, and that this breaking reduces the gauged $[SU(2) \otimes U(1)]^2$ subgroup to the $SU(2)_L \otimes U(1)_Y$ symmetry of the Standard Model. The Higgs doublet appears as a pseudo-goldstone boson of the symmetry breaking, along with¹ $\underline{1}_0 \oplus \underline{3}_0$ representations which are “eaten” by gauge bosons in the initial $[SU(2) \otimes U(1)]^2$ symmetry, leaving the Standard Model gauge bosons massless in the effective field theory. There is an additional $\underline{3}_{\pm 1}$ scalar in the spontaneously broken theory. The generators of the gauge symmetry are carefully embedded in the $SU(5)$ generators such that in the global limit of either one of the initial $SU(2) \otimes U(1)$ symmetries (by, for example, taking its gauge couplings to zero), H would be an true goldstone boson and therefore exactly massless. The result of this special embedding is then that the

¹ The representations denoted here are with respect to the electroweak symmetry $SU(2)_L \otimes U(1)_Y$.

one-loop Higgs mass squared corrections do not generate quadratic divergences, only logarithmic ones. However, at two loops, quadratic divergences are generated, so the contribution of the scale of new physics Λ_{new} to the Higgs mass is suppressed by a loop factor. Thus instead of expecting quadratic divergences to already require tuning at the TeV scale, one expects them to become relevant at the TeV-scale divided by a loop factor $\sim \mathcal{O}(1/100)$. The model also requires an additional top-like particle t' that cancels the quadratic divergences from the top and it also predicts W' and Z' particles that originate from the $[SU(2) \otimes U(1)]^2 \rightarrow SU(2)_L \otimes U(1)_Y$ spontaneous gauge symmetry breaking.

There are several phenomenological difficulties with the littlest Higgs model, however. In general, there is nothing to protect the $\underline{3}_{\pm 1}$ scalar from obtaining a vacuum expectation value and giving large corrections to the ρ parameter, which are ruled out empirically. Also, the T -parameter coming from oblique radiative corrections to W and Z propagators receives large corrections which do not agree with precision electroweak data. The predicted W' and Z' interactions with the W and Z bosons severely constrain the littlest Higgs model. It has recently been suggested to fix these problems by introducing an additional discrete symmetry called T -parity.

T -parity swaps the two initial $SU(2) \otimes U(1)$ groups and prevents the W' and Z' bosons from having tree-level interactions with the W or the Z , since they have opposite T -parity. Although they still couple at higher loops in perturbation theory, the very stringent constraints from collider W', Z' searches are ameliorated. Also, the Standard Model Higgs doublet has the opposite T -parity to the scalar triplet with the consequence that they do not mix. The lack of mixing means that the vacuum expectation value of H no longer gives a vacuum expectation value to the triplet triplet, thereby solving the problem of large corrections to the Standard Model ρ parameter prediction. Additional vector-like representations of singlet and electroweak doublet fermions are added for every Standard Model fermion in order to cancel the quartic and one-loop quadratic divergences. T -parity also greatly relieves the tuning [28] required in order to satisfy empirical bounds upon the electroweak T parameter through an additional t' with negative T -parity.

The lightest T -odd particle could potentially be a heavy copy of the hypercharge boson and would be stable because of T -parity. Such a particle satisfies the necessary conditions for a suitable dark matter candidate.

4 Conclusions

We have discussed three models which possess interesting dark matter candidates: the R -parity conserving MSSM, Universal Extra Dimensions and the littlest Higgs with T -parity. In each case, a discrete symmetry provides a suitable dark matter candidate. Although there has been a lot of study of supersymmetric dark matter in the literature, work on the other two cases is much less advanced. Each model predicts that the Large Hadron Collider could

produce a significant amount of dark matter. By studying its properties such as couplings and mass, it should be possible, by making a raft of cosmological assumptions, to predict the relic density of dark matter present in the universe today. A comparison of this prediction with cosmological observation then will provide a valuable indirect collider test of the cosmological assumptions.

27. A. Birkedal, K. Matchev, M. Perelstein, Phys. Rev. Lett. **94** (2005) 191803, [arXiv:hep-ph/0412278].
 28. H.-C. Cheng and I. Low, JHEP **0408** (2004) 061, [arXiv:hep-ph/0405243]; J. Hubisz, P. Meade, A. Noble and M. Perelstein, arXiv:hep-ph/0506042.
 29. N. Arkani-Hamed, A. G. Cohen, E. Katz and A. E. Nelson, JHEP **0207** (2002) 034.

References

1. B.C. Allanach, C.G. Lester, M.A. Parker and B.R. Webber, JHEP **0009** (2000) 004, [arXiv:hep-ph/0007009].
2. D. N. Spergel *et. al.*, Astrophys. J. Suppl. **148** (2003) 175, [arXiv:astro-ph/0302209].
3. K. Griest and D. Seckel, Phys. Rev. **D43** (1991) 3191–3203.
4. M. Drees and M. M. Nojiri, Phys. Rev. **D47** (1993) 376–408, [arXiv:hep-ph/9207234].
5. R. Arnowitt and P. Nath, Phys. Lett. **B299** (1993) 58–63, [arXiv:hep-ph/9302317].
6. A. Djouadi, M. Drees, and J.-L. Kneur, arXiv:hep-ph/0504090.
7. J. L. Feng, K. T. Matchev, and T. Moroi, Phys. Rev. Lett. **84** (2000) 2322–2325, [arXiv:hep-ph/9908309].
8. J. L. Feng, K. T. Matchev, and T. Moroi, Phys. Rev. **D61** (2000) 075005, [arXiv:hep-ph/9909334].
9. J. L. Feng, K. T. Matchev, and F. Wilczek, Phys. Lett. **B482** (2000) 388–399, [arXiv:hep-ph/0004043].
10. J. R. Ellis, K. A. Olive, Y. Santoso, and V. C. Spanos, Phys. Lett. **B565** (2003) 176–182, [arXiv:hep-ph/0303043].
11. Muon g-2 Collaboration, G. W. Bennett *et. al.*, Phys. Rev. Lett. **92** (2004) 161802, [arXiv:hep-ex/0401008].
12. M. Passera, J. Phys. **G31** (2005) R75–R94, [arXiv:hep-ph/0411168].
13. J. F. de Troconiz and F. J. Yndurain, Phys. Rev. **D71** (2005) 073008, [arXiv:hep-ph/0402285].
14. B. C. Allanach, A. Brignole, and L. E. Ibanez, JHEP **05** (2005) 030, [arXiv:hep-ph/0502151].
15. P. Gambino, U. Haisch, and M. Misiak, Phys. Rev. Lett. **94** (2005) 061803, [arXiv:hep-ph/0410155].
16. **Heavy Flavour Averaging Group.**
<http://www.slac.stanford.edu/xorg/hfag>.
17. B. C. Allanach and C. G. Lester, arXiv:hep-ph/0507283.
18. B. C. Allanach, G. Bélanger, F. Boudjema, and A. Pukhov, JHEP **0412** (2004) 020, [arXiv:hep-ph/0410091].
19. N. Arkani-Hamed and S. Dimopoulos, JHEP **0506** (2005) 073, [arXiv:hep-th/0405159]; G. F. Giudice and A. Romanino, Nucl. Phys. **B699** (2004) 65; Erratum-*ibid* **B706** (2005) 65, [arXiv:hep-ph/0406088].
20. L. Roszkowski, Pramana **62** (2004) 389, [arXiv:hep-ph/0404052].
21. W. Kilian *et al*, Eur. Phys. J. **C39** (2005) 229, [arXiv:hep-ph/0408088].
22. A. C. Kraan, J. B. Hansen and P. Nevski, ATLAS-PHYS-COM-2005-012; A. C. Kraan, [arXiv:hep-ex/0506009].
23. A. J. Barr, Phys. Lett. **B596** (2004) 205, [arXiv:hep-ph/0405052].
24. H.-C. Cheng, K. T. Matchev and M. Schmaltz, Phys. Rev. **D66** (2002) 056006, [arXiv:hep-ph/0205314].
25. B.C. Allanach *et al*, Eur. Phys. J. **C25** (2002) 113, [arXiv:hep-ph/0202233].
26. J. M. Smillie and B. R. Webber, arXiv:hep-ph/0507170.

Searches for Supersymmetry at the Tevatron

Marie-Claude Cousinou

Centre de Physique des Particules de Marseille - Université de la Méditerranée
On behalf of the DØ and CDF collaborations

Abstract. Status of the searches for supersymmetric particles performed by the CDF and DØ collaborations using samples of data from $p\bar{p}$ collisions at a center-of-mass energy of 1.96 TeV with an integrated luminosity of $\approx 300 \text{ pb}^{-1}$ (talk given at the Hadron Collider Physics symposium 2005).

1 Introduction

Supersymmetry (SUSY) postulates a symmetry between bosonic and fermionic degrees of freedom and predicts the existence of a supersymmetric partner for each Standard Model particle. A new quantum number R is introduced and the parity of R is equal to +1 for the ordinary particles, to -1 for their superpartners. In R-parity conserving modes, SUSY particles are produced in pairs and the lightest supersymmetric particle (LSP) is stable. In R-parity violating modes, a sparticle could be single produced and new coupling constants are added. One can write the R-Parity violating part of the lagrangian as follows: $\lambda_{ijk} L_i L_j E_k^c + \lambda'_{ijk} L_i Q_j D_k^c + \lambda''_{ijk} U_i^c D_j^c D_k^c$ where $L_i (Q_i)$ are the lepton (quark) SU(2) doublet superfields, $E_j (D_j, U_j)$ are the electron (down and up quark) SU(2) singlet superfield, λ , λ' and λ'' are Yukawa couplings.

The CDF [1] and DØ [2] collaborations have general purpose detectors well understood and highly efficient, with excellent calorimeters and muon chambers coverage and a precision tracking including silicon vertex detectors. Results presented here describe searches for SUSY particles, covering the 2 cases where the R-parity is conserved (RPC) or violated (RPV).

2 Searches for Charginos, Neutralinos and Sleptons.

At Tevatron the lightest chargino $\tilde{\chi}_1^\pm$ and the second-lightest neutralino $\tilde{\chi}_2^0$ could be produced in pair and are assumed to decay via sleptons (\tilde{l}) or vector boson exchange into the lightest neutralino $\tilde{\chi}_1^0$ and Standard Model (SM) fermions. The searches for charginos, in case of R-parity conservation, are described in sections 2.1 to 2.3.

In case of R-parity violation, the lightest SUSY particle, here the lightest neutralino $\tilde{\chi}_1^0$, is allowed to decay into a purely leptonic state. The events will then contain more leptons and jets and less missing transverse energy (E_T) than in the RPC case. The description of those analyses

is given in section 2.4. Searches for single production of scalar muon $\tilde{\mu}$ or scalar neutrino $\tilde{\nu}$ are described in sections 2.5 and 2.6.

2.1 Searches for the associated production of Chargino and Neutralino in final states with three leptons.

Assuming RPC, the $\tilde{\chi}_1^0$ is stable and the final state is characterized by 3 leptons and large E_T . DØ has made 6 analyses [3] looking for 2 identified leptons (e, μ , or τ), an isolated high quality track which is the third lepton, and requesting high E_T value. A third isolated track is not required for same sign muons. The numbers of observed and expected events for each of the analyses are summarized in Tab. 1 together with the integrated luminosity used.

Table 1. Number of observed events and expected SM backgrounds in the searches for charginos and neutralinos in 3 leptons (RPC).

DØ	L(pb^{-1})	channel	data	exp. SM
	320	$ee + l(\text{track})$	0	0.21 ± 0.12
	"	$e\mu + l(\text{track})$	0	0.31 ± 0.13
	"	$\mu\mu + l(\text{track})$	2	1.75 ± 0.57
	"	same sign $\mu\mu$	1	0.66 ± 0.37
	"	$e\tau + l(\text{track})$	0	0.58 ± 0.14
	"	$\mu\tau + l(\text{track})$	1	0.36 ± 0.13
CDF	L(pb^{-1})	channel	data	exp. SM
	346	$ee + l(e, \mu)$	0	0.16 ± 0.07
	224	$ee + l(\text{track})$	2	0.36 ± 0.27

On Fig 1 the observed cross-section limit, obtained from a combination of the 4 first analyses [4], is compared to three theoretical schemes. As an example, a mass below $117 \text{ GeV}/c^2$ is excluded for the $\tilde{\chi}_1^\pm$ in the "3l-max" scheme. When the two analyses with τ are included in the combination, the cross section limit improves by about 10 % for $\tan\beta = 3$ and this improvement is better at large

$\tan\beta$ values where the τ 's dominate the final state. The results of two similar analyses done by CDF [5] are summarized in Tab. 1.

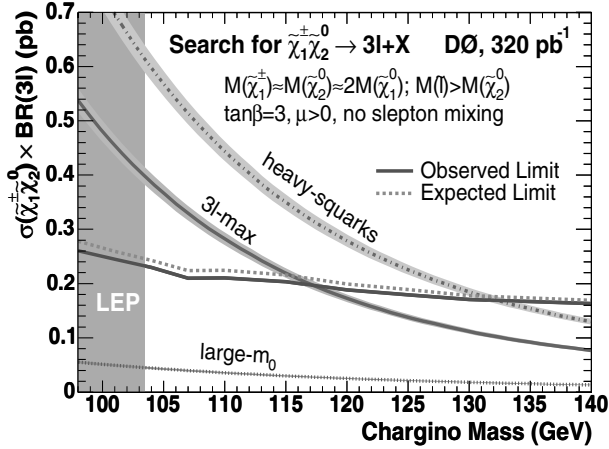


Fig. 1. Limit on $\sigma \times \text{BR}(3l)$ as a function of chargino mass, in comparison with expectation for several SUSY scenarios

2.2 Searches for the associated production of Chargino and Neutralino in final states with 2 γ and large \cancel{E}_T

Both CDF [6] and DØ [7] have reported a search for an excess of events containing two high- P_T γ and large \cancel{E}_T . The results have been interpreted in the framework of Gauge-Mediated Supersymmetry-Breaking (GMSB). In this model the $\tilde{\chi}_1^0$ is the next-to-lightest SUSY particle and decays into a gravitino and a photon. To select the candidates, CDF and DØ request two photons with E_T above 13 and 20 GeV and \cancel{E}_T above 45 and 40 GeV respectively. CDF observes no event for an expected Standard Model (SM) background equal to 0.3 ± 0.1 event and DØ 2 events when the expected background is 3.7 ± 0.6 events. On Fig. 2 the combined experimental cross section limit [8] is compared to the theoretical cross section. The mass limit for the $\tilde{\chi}_1^\pm$ is $209 \text{ GeV}/c^2$ which translates to a mass limit of $114 \text{ GeV}/c^2$ on the $\tilde{\chi}_1^0$.

2.3 Search for Charged Massive Stable Particles

A search for Charged Massive Particles having a lifetime long enough to escape the entire detector before decaying (CMSP) has been performed at DØ using 390 pb^{-1} of data [9]. Several possible models could result in a CMSP. In the Anomaly-Mediated SUSY Breaking model, when the mass difference between the $\tilde{\chi}_1^\pm$ and the $\tilde{\chi}_1^0$ is less than about 150 MeV, the $\tilde{\chi}_1^\pm$ could be a CMSP. The selection requests two isolated muons with $P_T > 15 \text{ GeV}$ and moving with a speed significantly slower than the light speed. No event has been found and the instrumental background has been determined to be 0.66 ± 0.6 event. This result could be interpreted such that a stable chargino must be

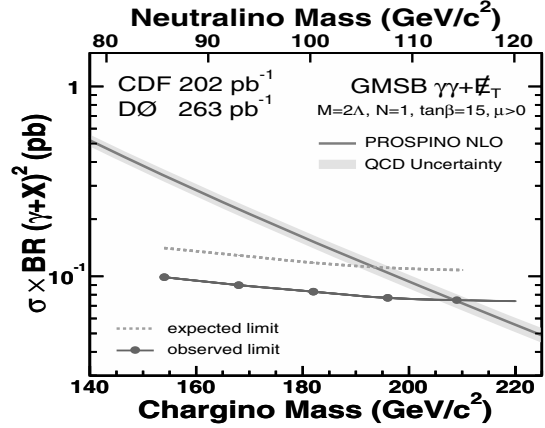


Fig. 2. The next-to-leading-order cross section and combined experimental limits as a function of chargino and neutralino mass.

heavier than $140 \text{ GeV}/c^2$ if it is higgsino-like and heavier than $174 \text{ GeV}/c^2$ if it is gaugino-like.

2.4 Searches for Charginos, Neutralinos assuming RPV.

In case of RPV, the $\tilde{\chi}_1^0$ pair produced in the $\tilde{\chi}_1^\pm$ and $\tilde{\chi}_2^0$ decays could decay itself in 4 leptons plus \cancel{E}_T . DØ has analyzed final states with at least 3 leptons corresponding to three Yukawa couplings: the final states with $eeee$, $ee\mu\mu$, or $ee\mu\mu + 2\nu$ linked to λ_{121} [10], with $\mu\mu\mu\mu$, $\mu\mu\mu e$, or $\mu\mu e e + 2\nu$ for the coupling λ_{122} [11] and the final states $\tau\tau\tau\tau$, $\tau\tau\tau e$ or $\tau\tau e e + 2\nu$ connected to the coupling λ_{133} [12]. They select events with 3 isolated leptons with a low P_T cut on the third lepton and loose \cancel{E}_T cuts. In Tab. 2 the observed and expected numbers of events for each analysis are shown together with the integrated luminosity used and the limit obtain on the $\tilde{\chi}_1^\pm$ mass in the framework of the mSUGRA model for different sets of parameters.

Table 2. Number of observed events and expected SM backgrounds in the searches for charginos and neutralinos in case of RPV.

$L(\text{pb}^{-1})$	channel	data	exp. SM	$M(\tilde{\chi}_1^\pm) > \text{GeV}$
238	$eel(l = e, \mu)$	0	0.5 ± 0.4	181
160	$\mu\mu l(l = e, \mu)$	2	0.6 ± 1.9	165
200	$ee\tau_{had}$	0	1 ± 1.4	118

The parameters set used for the 2 first analyses is $m_0=250 \text{ GeV}$ and $\tan\beta=5$. For the third analysis the values $m_0=80 \text{ GeV}$ and $\tan\beta=10$ have been used, where m_0 is the common scalar mass and $\tan\beta$ the ratio of Higgs vacuum expectation values. In both cases A_0 the trilinear coupling is taken equal to 0 and the sign of μ the Higgsino mass term positive.

2.5 Search for single production of $\tilde{\mu}$

Using 154 pb^{-1} of data, DØ has searched for $\tilde{\mu}$ which would be produced as $\bar{u}d \rightarrow \tilde{\mu}$ and decays in $\tilde{\chi}_1^0 \mu \rightarrow \mu\mu u\bar{d}$ [13]. The cross section of this process is a function of the coupling constant λ'_{211} which occurs at the production and decay levels. The events with 2 jets and 2 isolated muons (applying on the 4 objects a P_T cut $\approx 20 \text{ GeV}$) are selected. Two candidates have been found and the expected SM background is equal to 1.1 ± 0.4 events. Cross section limits or limits on the value of λ'_{211} as a function of the mass of $\tilde{\chi}_1^0$ and $\tilde{\mu}$ are given. As an example, assuming $\lambda'_{211} = 0.07$ and a $\tilde{\chi}_1^0$ mass equal to $75 \text{ GeV}/c^2$, a $\tilde{\mu}$ mass below $\approx 252 \text{ GeV}/c^2$ is excluded.

2.6 Searches for single production of $\tilde{\nu}$

CDF, using an integrated luminosity of 344 pb^{-1} , have searched for $d\bar{d} \rightarrow \tilde{\nu}_\tau$ production (via the coupling constant λ'_{311}) with a $\tilde{\nu}$ decay in an electron and a muon of opposite charges (via λ_{132}). Cuts on the P_T of the two leptons ($P_T > 20 \text{ GeV}$) and on their invariant mass ($M(e\mu) > 100 \text{ GeV}$) are applied. Five events are selected and the expected SM background is equal to 8 ± 1.1 events. On Fig 3 the experimental limit on the cross section is shown together with the theoretical NLO prediction calculated assuming $\lambda_{132} = 0.05$ and $\lambda'_{311} = 0.16$. A $\tilde{\nu}$ mass below $460 \text{ GeV}/c^2$ is excluded.

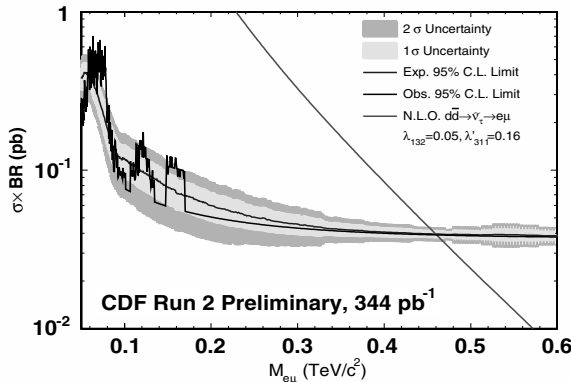


Fig. 3. Experimental $\tilde{\nu}_\tau$ cross section \times BR limit as a function of the invariant $M(e\mu)$ mass and theoretical NLO cross section.

CDF has also studied the case where the $\tilde{\nu}$ decays in e^+e^- , $\mu^+\mu^-$ or $\tau^+\tau^-$ using a sample of data corresponding to an integrated luminosity of $\approx 200 \text{ pb}^{-1}$. For the 2 first channels [14], a cut of $\approx 20 \text{ GeV}$ is applied on the P_T of the 2 leptons and the invariant mass of the 2 leptons has to be greater than $500 \text{ GeV}/c^2$. No event has been observed in the ee channel and the expected SM background is 0.5 ± 0.1 event. One candidate is selected in the $\mu\mu$ channel and the SM background is 1.2 ± 0.1 event. A

combination of these two results give a $\tilde{\nu}$ mass limit equal to $725 \text{ GeV}/c^2$. In the $\tau\tau$ analysis [15] 4 events with at least one identified hadronic tau decay and a e or a μ are selected. The expected SM background is equal to 2.8 ± 0.5 events. This analysis excludes a $\tilde{\nu}$ with a mass below $377 \text{ GeV}/c^2$. In both analyses the assumption is done that the square of the coupling constant times the branching ratio is equal to 0.01.

3 Searches for squarks and gluinos.

At hadron colliders, the most copiously produced SUSY particles should be, if sufficiently light, squarks and gluinos. The topologies of the events are a large number of jets and \cancel{E}_T and therefore the multijet background is huge. Searches made by CDF and DØ for gluinos and squarks are reported in section 3.1 and more specific searches for squarks, in which the b -tagging plays a crucial role, are described in sections 3.2 to 3.4.

3.1 Searches for squarks and gluinos.

At low m_0 the gluino is heavier than the squark and the process with the dominant cross section is the $\tilde{q}\tilde{q}$ production. As an important decay mode of the squark is $\tilde{q} \rightarrow q\tilde{\chi}$, the final topology will be acoplanar dijet event with \cancel{E}_T coming from the two neutralinos LSP. At high m_0 , the squarks are much heavier than the gluino. The process with the highest cross section is therefore $\tilde{g}\tilde{g}$. As $\tilde{g} \rightarrow q\tilde{q}\tilde{\chi}$ is an important decay mode of the gluino, their pair production will lead to a large number of jets and \cancel{E}_T . Finally for intermediate m_0 region, all squark-gluino production processes contribute to the total cross section. DØ has reported a search for squarks and gluinos [16], using 310 pb^{-1} of data, and addressing the different possibilities for the m_0 value in 3 analyses which differ by the number of jets required (see Tab.3).

Table 3. Number of observed events and expected SM backgrounds in the searches for gluinos and squarks. m_0 is the common scalar mass.

DØ (310 pb^{-1})	#jets($P_T \text{ GeV}$)	data	exp. SM
Low m_0	2 jets(60,50)	12	12.8 ± 5.4
Int. m_0	3 jets(60,40,25)	5	6.1 ± 3.1
High m_0	4 jets(60,40,30,25)	10	7.1 ± 0.9
CDF (254 pb^{-1})	#jets($P_T \text{ GeV}$)	data	exp. SM
	3 jets(125,75,25)	3	4.2 ± 1.1

Cuts on the scalar sum of the transverse energies of the jets and \cancel{E}_T are also applied. The observed number of events and the SM background expectations are summarized in Tab. 3 and are in good agreement. On Fig. 4 are shown the regions excluded at the 95% C.L. in the squark

and gluino mass plane in the mSUGRA framework. Assuming $m_0 = 25 \text{ GeV}/c^2$ the \tilde{q} must be heavier than $318 \text{ GeV}/c^2$. For a m_0 mass equal to $500 \text{ GeV}/c^2$, the \tilde{g} mass will be greater than $233 \text{ GeV}/c^2$ and finally if the masses of the \tilde{q} and the \tilde{g} are of the same order, they should be heavier than $333 \text{ GeV}/c^2$. CDF, using data corresponding to a luminosity equal to 254 pb^{-1} , selects events with at least 3 jets, a scalar sum of the transverse jet energies above 350 GeV and large \cancel{E}_T ($\cancel{E}_T > 165 \text{ GeV}$) (Tab.3). 3 candidates survived to the cuts and the SM background is equal to 4.2 ± 1.1 events.

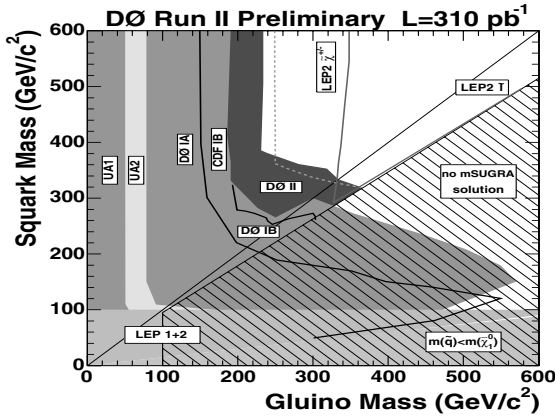


Fig. 4. In the squark and gluino mass plane, excluded regions at the 95% C.L. in the mSUGRA framework.

3.2 Searches for gluino decaying in $\tilde{b}\tilde{b}$.

CDF has searched for \tilde{b} quarks in events with b-jets and \cancel{E}_T using 156 pb^{-1} of data [17]. In a scenario where the \tilde{b} is lighter than the \tilde{g} , \tilde{b} could be produced through the decay $\tilde{g} \rightarrow \tilde{b}\tilde{b}$. The final state, then, will be 4 b-jets and \cancel{E}_T . The preselection cuts consist on requesting at least 3 jets ($P_T > 15 \text{ GeV}$), $\cancel{E}_T > 80 \text{ GeV}$, angular cuts between jets and \cancel{E}_T and no leptons. The sample is then subdivided into exclusive single and inclusive double b-tagged events. For the exclusive single tag, 21 events are selected and it is in good agreement with the SM background expectation of 16.4 ± 3.7 events. Four events are observed in the double b-tag sample and 2.6 ± 0.7 SM events are expected. The exclusion regions, as a function of the \tilde{b} and the \tilde{g} mass, are shown on Fig. 5.

At 95 % C.L. \tilde{g} with a mass smaller than $280 \text{ GeV}/c^2$ or \tilde{b} with a mass smaller than $240 \text{ GeV}/c^2$ are excluded.

3.3 Search for direct production of $\tilde{b}\tilde{b}$.

DØ has performed a search for direct pair production of sbottom \tilde{b} with 310 pb^{-1} of data [18]. The \tilde{b} decays into a b quark and a $\tilde{\chi}_1^0$. The topology of the events for this process

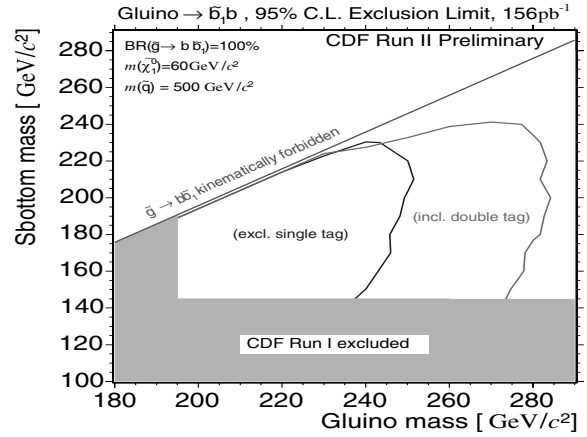


Fig. 5. 95 % C.L. exclusion contours in the \tilde{g} and \tilde{b} mass plane.

corresponds to a final state with two acoplanar b-jets and \cancel{E}_T . Different analyses cover different assumptions on the \tilde{b} mass value and the cuts are described in Tab. 4.

Table 4. Number of observed events and expected SM backgrounds in the searches for direct production of \tilde{b} .

$M(\tilde{b})$	Low val.	Med. val.	High Val.
$E_T(j_1, j_2)$ (GeV)	>(40,15)	>(40,15)	>(70,40)
\cancel{E}_T (GeV)	>60	>80	>100
Data	36	15	2
SM exp.	38.6 ± 2.8	19.6 ± 1.7	4.4 ± 0.4

Lepton veto and single b-tag are also requested. The number of observed events and expected SM backgrounds are summarized in Tab. 4. They are in good agreement and the resulting exclusion contour in the \tilde{b} and $\tilde{\chi}_1^0$ mass plane is shown in Fig. 6.

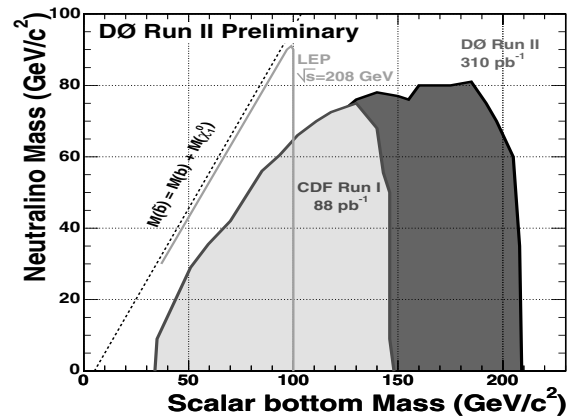


Fig. 6. 95 % C.L. exclusion contour, after all selections, including single b tagging and combining the 3 sets of cutoffs in \cancel{E}_T and jet P_T .

3.4 Search for \tilde{t} decaying in $b\tau$.

CDF has searched for pair production of scalar top \tilde{t} in a RPV scenario in 200 pb^{-1} of data [19]. Each \tilde{t} decays into a τ lepton and a b quark. The final state is either an electron or a muon from the leptonic decay of one of the τ , as well as a hadronically decaying τ , and two or more jets. P_T cuts of 10 GeV and 15 GeV are applied on the lepton and the hadronic τ respectively. To remove the W background, a cut on the transverse lepton- \cancel{E}_T mass ($M_T(l, \cancel{E}_T) < 35$ GeV) is applied. A SM background equal to 4.8 ± 0.7 events is expected and 5 candidates have been selected. Fig. 7 shows the experimental cross section limit as a function of the \tilde{t} mass together with the theoretical prediction. At 95 % C.L. the \tilde{t} should be heavier than 129 GeV/c^2 , assuming that the branching ratio of the \tilde{t} in $b\tau$ is equal to 100 %.

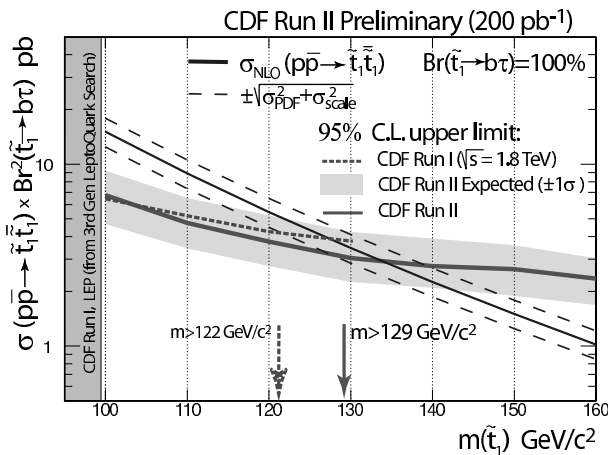


Fig. 7. Cross section exclusion limit as a function of the \tilde{t} mass.

4 Searches for $B_s^0 \rightarrow \mu^+\mu^-$ decays

In the Standard Model, the branching ratio of the decay of B_s^0 in $\mu^+\mu^-$ is very small ($\approx 3.510^{-9}$). But in many SUSY models, an enhancement of this branching ratio varying as $(\tan\beta)^6$ is expected. So, for large $\tan\beta$, this measurement is a sensitive probe of new physics. Both CDF [20] and DØ [21] has search for this decay. They select events with a μ^+ and a μ^- coming from displaced vertices and count how many events have an invariant $M(\mu\mu)$ mass in a mass window around the B_S mass. The upper limit is then normalized to the number of $B^\pm \rightarrow J/\psi K^\pm$ events and transform in an upper limit on the branching ratio. CDF uses a sample of data corresponding to a luminosity equal to 364 pb^{-1} and obtain an upper limit: $BR(B_s^0 \rightarrow \mu^+\mu^-) < 210^{-7}$ at 95% C.L. Using a sample of data of 300 pb^{-1} , DØ gives an upper limit equal to 3.710⁻⁷ at 95% C.L.

5 Conclusion

The CDF and DØ collaborations have both covered many SUSY particles searches using a sample of data corresponding to an integrated luminosity of the order of 300 pb^{-1} . In all analyses, the number of observed events is consistent with the expected number of SM background events. Hence limits have been derived. The analyses of data samples, corresponding to a luminosity of $\approx 1 fb^{-1}$, are underway and will provide either a discovery or a substantial improvement of the limits.

References

1. D. Acosta et al, Phys. Rev. D. **71**, (2005) 032001.
2. V.M Abazov et al., hep-physics/0507191, submitted to Nucl. Inst. and Methods.
3. DØ collaboration, DØ Note 4740-CONF
4. V.M Abazov et al, hep-ex/0504032.
5. CDF collaboration, CDF note 7750
6. D. Acosta et al, Phys. Rev. D. **71**, (2005) 031104.
7. V.M Abazov et al, Phys. Rev. Lett. **94**, (2005) 041801.
8. CDF and DØ collaborations, hep-ex/0504004.
9. DØ collaboration, DØ Note 4746-CONF
10. DØ collaboration, DØ Note 4522-CONF
11. DØ collaboration, DØ Note 4490-CONF
12. DØ collaboration, DØ Note 4595-CONF
13. DØ collaboration, DØ Note 4535-CONF
14. A. Abulencia et al, hep-ex/0507104.
15. D. Acosta et al, hep-ex/0506034.
16. DØ collaboration, DØ Note 4737-CONF
17. CDF collaboration, CDF note 7136
18. DØ collaboration, DØ Note 4832-CONF
19. CDF collaboration, CDF note 7398
20. A. Abulencia et al, FERMILAB-Pub-05-367-E
21. V.M Abazov et al, FERMILAB-Pub-04-215-E and DØ Note 4733-CONF.

Searches for BSM (non-SUSY) physics at the Tevatron

Heather K Gerberich¹ (for the CDF and DØ Collaborations)

University of Illinois Urbana-Champaign

Abstract. Results of searches at the Tevatron for physics (non-SUSY and non-Higgs) beyond the Standard Model using 200 pb⁻¹ to 480 pb⁻¹ of data are discussed. Searches at DØ and CDF for Z', Lepton-Quark compositeness, Randall-Sundrum Gravitons, Large Extra Dimensions, W', Leptoquarks and Excited Electrons are presented here.

1 Introduction

The discovery of anomalous behavior in data collected at high energy physics experiments could provide non-SUSY and non-Higgs explanations to questions associated with the Standard Model and provide deeper understanding to the fundamental particles and interactions in nature. Such questions include whether quarks and leptons are composite particles, the existence of extra dimensions, and the answer to the hierarchy problem in the Standard Model (SM).

Generally, a search is approached by first understanding the SM prediction for a given signal and detector backgrounds which could mimic that signal. Analyses are optimized for signal, not according to model, prior to looking in the signal region of the data. If no anomalous behavior is found, the signal acceptances of various models can be used to set limits.

2 High Mass Dilepton Searches

High mass dilepton searches are experimentally motivated by the small source of background, with the exception of the well-understood, irreducible Standard Model Z/γ* production. Search results can be used to study many theories: extended gauge theories (Z'), technicolor, lepton-quark compositeness, large extra dimensions (LED), and Randall-Sundrum gravitons.

2.1 Z'

The majority of extensions to the SM predict new gauge interactions, many of which naturally result in the prediction of neutral or singly charged bosons, such as a highly massive “Z'” particle.

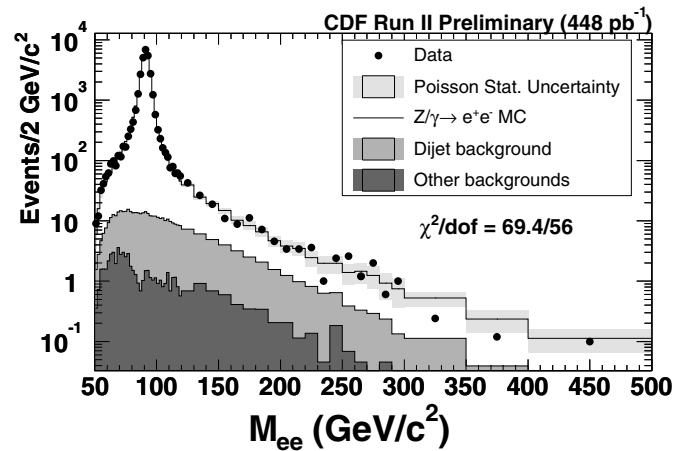


Fig. 1. Expected and observed dielectron mass distributions.

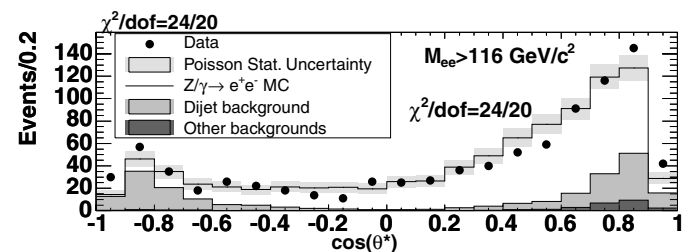


Fig. 2. Expected and observed $\cos \theta^*$ distribution for $M_{ee} > 116 \text{ GeV}/c^2$.

2.1.1 Z' Searches using M_{ee} and $\cos \theta^*$

Using 448 pb⁻¹ of data, CDF searched for Z' production by studying the distributions dielectron mass at high mass and the angular distribution $\cos \theta^*$. Figures 1 and 2 show the M_{ee} and $\cos \theta^*$ distributions, respectively.

Having observed no evidence of a signal, limits at the 95% confidence level (C.L.) are set for the sequential Z' [1] and E6 Z' models [2], as shown in Table 1. With

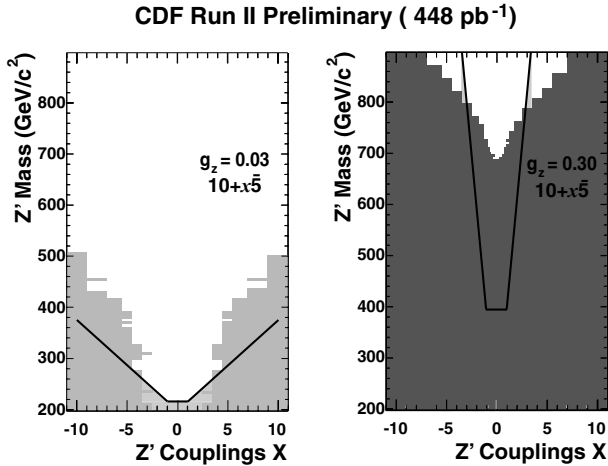


Fig. 3. Exclusion regions using a generalized formalism for Z' searches.

Table 1. Limits from CDF and DØ on the sequential Z' and E6 models using the charged lepton channels. The units used for mass limits are GeV/c^2 and for $\int \mathcal{L} \cdot dt$ are pb^{-1} .

Sequential Z'	ee	$\mu\mu$	$ee + \mu\mu$	$\tau\tau$	$\int \mathcal{L} \cdot dt$
CDF	750	735	815	394	200
CDF with $\cos\theta$	845				448
DØ	780	680			200-250

E6	Z_l	Z_X	Z_ψ	Z_η	Channel
CDF	615	675	690	720	$ee + \mu\mu$
CDF with $\cos\theta$	625	720	690	715	ee
DØ	575	640	650	680	ee

448 pb^{-1} , using the $\cos\theta^*$ information effectively increases the amount of data by $\approx 25\%$ for the sequential Z' model.

Additionally, a general formalism for Z' which uses M_{ee} and $\cos\theta^*$ [3] and allows for new models to be easily checked is studied. The formalism consists of four general model classes and are each defined by three parameters: mass ($M_{Z'}$), strength ($g_{Z'}$) and coupling parameter (x). Figure 3 shows the CDF exclusion regions for one of the model classes for two values of $g_{Z'}$. The area below the black curves represent LEP II [3] exclusion regions obtained via indirect searches for contact interactions.

2.1.2 Traditional Z' Searches

CDF and DØ both performed “traditional” Z' searches which focus on the dilepton mass distributions. All three channels - electron, muon, and tau - were studied with no evidence for a signal beyond the Standard Model expectations. Table 1 shows a summary of the limits set at the 95% C.L. for various Z' models.

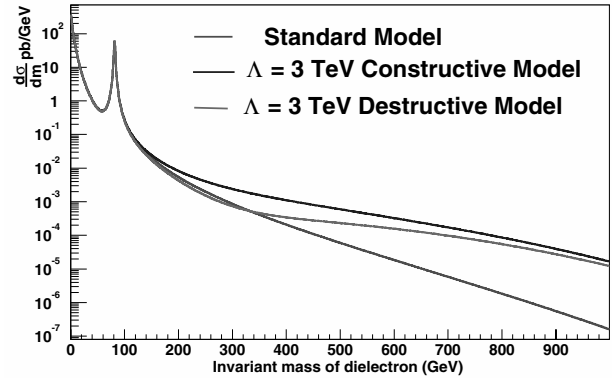


Fig. 4. M_{ee} distributions for SM dielectron production and for constructive and destructive interference due to contact interactions.

Table 2. Limits on the compositeness scale for several models.

Model	$\Lambda-$ (TeV)	$\Lambda+$ (TeV)	ee	$\mu\mu$
LL	6.2	6.9	3.6	4.2
RR	5.8	6.7	3.8	4.2
LR	4.8	5.1	4.5	5.3
RL	5.0	5.2	4.3	5.3
LL+RR	7.9	9.0	4.1	5.0
LR+RL	6.0	6.1	5.0	6.4
LL-LR	6.4	7.7	4.8	4.9
RL-RR	4.7	7.4	6.8	5.1
VV	9.1	9.8	4.9	6.9
AA	7.8	5.5	5.7	5.5

2.2 Quark-Lepton Compositeness

Contact Interaction composite models introduce hypothetical constituents of quarks and leptons called “preons” which are bound together by a characteristic energy scale known as the compositeness scale (Λ) [4]. The differential cross-section can be written as in Equation 1.

$$\frac{d\sigma_T}{dM} = \frac{d\sigma_{SM}}{dM} + \frac{I}{\Lambda^2} + \frac{C}{\Lambda^4} \quad (1)$$

For energies accessible at the Tevatron, the interference term (the second term) dominates and quark-lepton compositeness would be discovered as an excess in the tail of the dilepton distributions, an example of which is shown in Figure 4.

No evidence for signal is found in a dielectron search of 271 pb^{-1} or in a dimuon search of 400 pb^{-1} at DØ. The dimuon results are shown in Figure 5. Limits are set on Λ for several models as shown in Table 2.

2.3 Extra Dimensions

2.3.1 Large Extra Dimensions

Large Extra Dimensions (LED) provide a non-SUSY alternative solution to the “hierarchy” problem in the SM

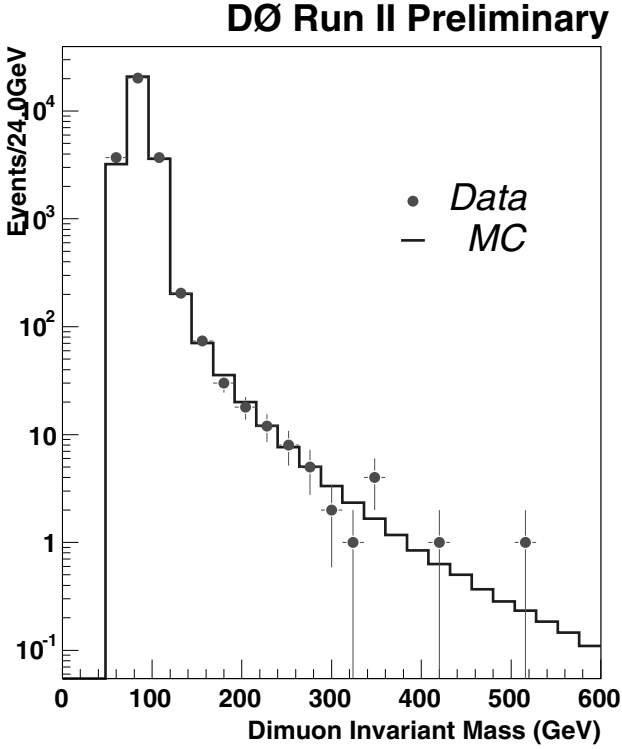


Fig. 5. $M_{\mu\mu}$ distribution for using 400 pb^{-1} of data collected at DØ.

and an explanation for the large difference between the electroweak and Planck scales ($M_{EW} \ll M_{Pl}$). The signature for LED is dilepton or diphoton production. The Large ED (ADD) model [5] predicts an increase in cross-section at high mass and depends on parameter $\eta_G = F/M_s^4$ where F is a model dependent dimensionless parameter and M_s is the UV cutoff, $M_s = M_{Pl(4+n \text{ dim})}$. An example $M_{ee} + M_{\gamma\gamma}$ distribution for $\eta_G = 0.6$ is shown in Figure 6 along with the background prediction and observed data for 200 pb^{-1} of dielectron and diphoton data at DØ. Figure 7 shows no anomaly in the $ee, \gamma\gamma \cos\theta^*$ distribution. By fitting $M_{ee}, M_{\gamma\gamma}$, and $\cos\theta^*$, DØ extracts limits on η_G at the 95% C.L. such that $\eta_G^{95\%} < 0.292 \text{ TeV}^{-4}$ for $\lambda > 0$ and $\eta_G^{95\%} > -0.432 \text{ TeV}^{-4}$ for $\lambda < 0$.

2.3.2 Warped Extra Dimensions

The Warped Extra Dimension model predicts one extra dimension that is highly curved and the production of Randall-Sundrum (RS) gravitons [6]. The model depends on k/M_{Pl} , where k is the curvature scale. CDF and DØ search for RS gravitons by studying the $M_{ee}, M_{\mu\mu}$, and $M_{\gamma\gamma}$ distributions for a resonance which would depend on k/M_{Pl} . Two-dimensional exclusion regions in the $k/M_{Pl} - M_G$ plane are established as shown in Figure 8.

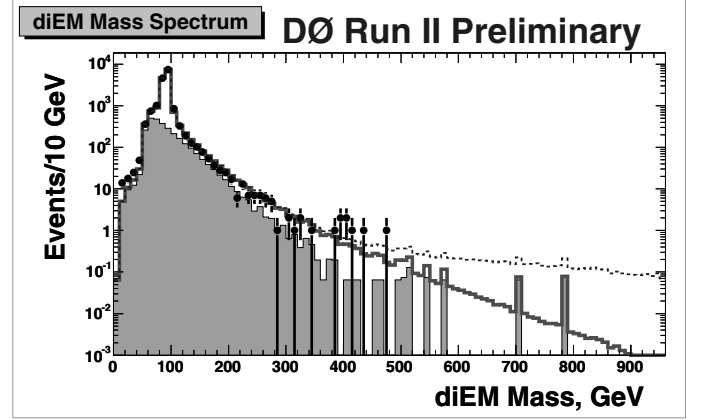


Fig. 6. Background prediction and observation of $M_{ee}, M_{\gamma\gamma}$ distributions. The dotted blue spectrum shows the LED theoretical prediction for $\eta_G = 0.6$.

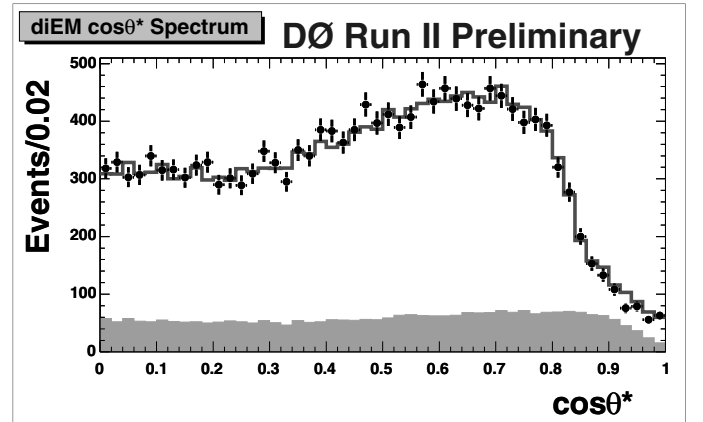


Fig. 7. $\cos\theta^*$ predicted and observed distributions for ee and $\gamma\gamma$.

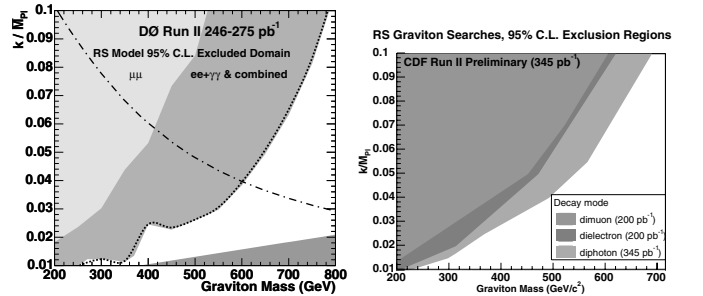


Fig. 8. Limits set on Randal Sundrum Graviton production at DØ and CDF.

3 Charged Heavy Vector Boson (W')

The production of charged heavy vector bosons, referred to as W' particles, are predicted in theories based on the extension of the gauge group [7]. The W' is modeled to decay to an electron and neutrino, where the neutrino is assumed to be SM-like: light and stable. Thus, the final state signature in the detector is a high p_T electron with high missing E_T . CDF performs a direct search for W' production and Figure 9 shows the background due to

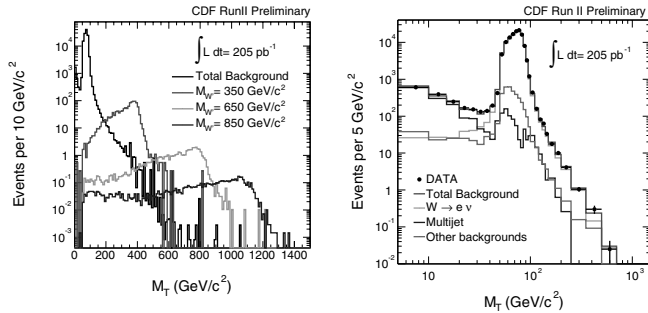


Fig. 9. The left plot has transverse mass distributions of the expected background overlaid with three W' mass choices. The right plot shows the transverse mass distributions of the irreducible SM $W \rightarrow e\nu$, multijet, and total background sources. The data is plotted and agrees well with the expectation.

SM $W \rightarrow e\nu$ production with the predicted transverse mass distributions for W' production at three different W' masses.

Figure 9 shows the expected background distributions and the observations in the data. No $e\nu$ signal above the SM expectation is observed. However, the agreement between the data and the background prediction indicate good understanding of the calorimeter energy at CDF and the detector missing energy.

Having observed no signal above the SM expectation, the limit at the 95% C.L. is set on W' production using a binned likelihood fitting method. The CDF Run II search excludes W' masses less than 842 GeV/c^2 . The CDF Run I limit was $M_{W'_{SM}} > 754 \text{ GeV}/c^2$.

4 Leptoquarks

Many extensions of the SM assume additional symmetry between lepton and quarks which requires the presence of a “new” particle, a leptoquark (LQ) [8]. Leptoquarks, which could be scalar or vector particles, carry both lepton and baryon numbers. They are assumed to couple to quarks and leptons of the same generation; thus, there are three generation of leptoquarks for which one could search.

Leptoquarks would be pair produced at the Tevatron. Their decay is controlled by parameter β , where $\beta = B.R.(LQ \rightarrow lq)$. There are three final state signatures for LQ pair production at the Tevatron: two charged leptons and two jets ($lljj$); one charged, one neutral lepton and two jets ($lvjj$); and two neutral leptons and two jets ($\nu\nu jj$). The experimental signal is a resonance in the lepton-jet invariant mass spectrum.

No evidence of LQ production is found at DØ or CDF. Figure 10 shows the two dimensional exclusion region established by DØ for the first generation with $eejj$ and $evjj$ final state signature. DØ combines 250 pb^{-1} from Run II with 120 pb^{-1} of data from Run I to obtain the exclusion region shown in Figure 10. For the case of $\beta = 1$, DØ excludes first-generation leptoquarks with masses less than

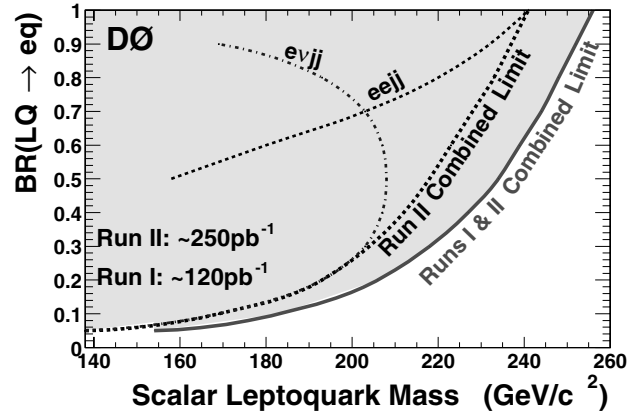


Fig. 10. Exclusion region established by DØ for first generation leptoquarks.

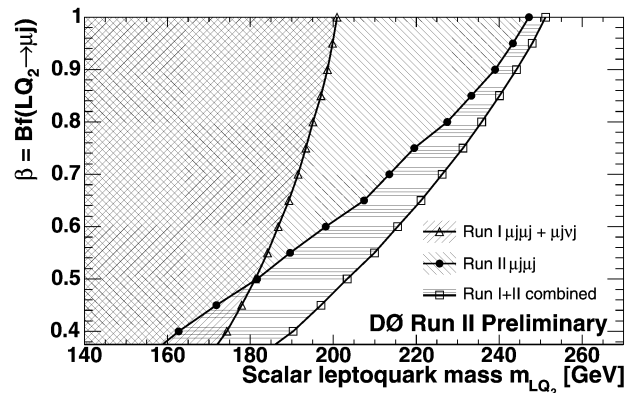


Fig. 11. Exclusion region established by DØ for second generation leptoquarks.

256 GeV/c^2 . CDF excludes masses less than 235 GeV/c^2 using 200 pb^{-1} from Run II.

Figure 11 shows the exclusion regions for generation two leptoquarks from DØ. DØ searches for $\mu\mu jj$ and $\mu\nu jj$ production; CDF searches for $\mu\mu jj$, $\mu\nu jj$, and $\nu\nu jj$ production. For $\beta = 1$, DØ Run I + II excludes LQ masses less than 251 GeV/c^2 while CDF Run II excludes mass less than 224 GeV/c^2 .

CDF has performed a search for third generation LQ production using the $\tau\tau bb$ signature. Leptoquark masses less than 129 GeV/c^2 are excluded for $\beta = 1$ using 200 pb^{-1} of data.

5 Excited Electrons

The observation of excited states of leptons or quarks would be a first indication that they are composite particles. CDF searches for singly produced excited electrons (e^*) in association with an oppositely charged electron, where the e^* decays to an electron and a photon. Thus, the final state signature is two electrons and a photon where the search signal is a resonance in the electron+photon invariant mass spectrum.

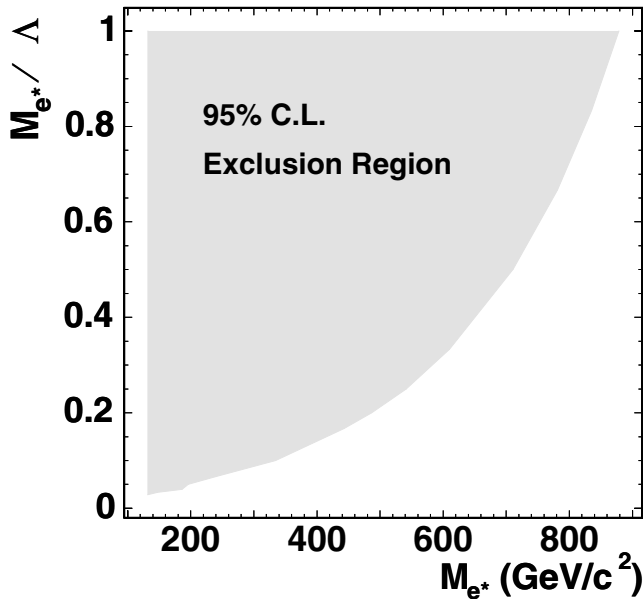


Fig. 12. Exclusion region at the 95% C.L. established by CDF for e^* production via a Contact Interaction model.

Two models are studied: a Contact Interaction (CI) model [9] and a Gauge Mediated (GM) model [10]. The CI model depends on the mass of the e^* (M_{e^*}) and the composite energy scale (Λ). In the GM model, an excited electron is produced via the decay of SM γ^*/Z . This model depends on M_{e^*} and f/Λ , where f is a phenomenological coupling constant.

In the first search for excited leptons at a hadron collider, CDF found no excess of dielectron+photon events in 200 pb^{-1} of data. Exclusion regions for each model are established. Figure 12 shows the exclusion region at the 95% C.L. in the $M_{e^*}/\Lambda - M_{e^*}$ parameter space. There are no previously published limits for e^* production using the CI model. For the GM model, it is conventional to plot the 95% C.L. exclusion region in the $f/\Lambda - M_{e^*}$ parameter space, as shown in Figure 13. CDF extends the previously published limits from $280 \text{ GeV}/c^2$ to $\approx 430 \text{ GeV}/c^2$.

6 Summary

Searches for physics beyond the Standard model using 200 pb^{-1} to 450 pb^{-1} of data collected at CDF and DØ are presented. Currently, the experiments are actively pursuing further exotic topics and analyzing up to the full 1 fb^{-1} of delivered luminosity. New and exciting results are coming out quickly. Further information regarding the analyses presented in this paper and new results can be found at [11] and [12].

References

1. J.Pati and A.Salam, Phys Rev Lett. **31**, 661 (1973); R.N.Mohapatra, Phys. Rev. **D11**, 2558 (1975); G.Sejanovic

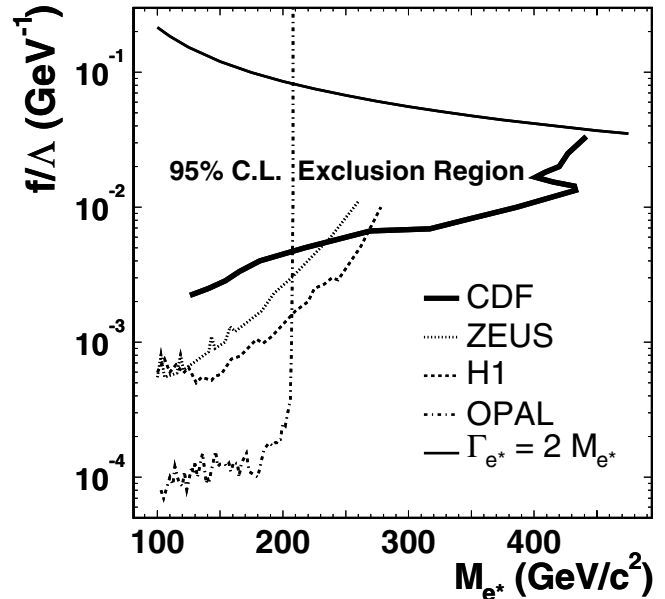


Fig. 13. Exclusion region at the 95% C.L. established by CDF for e^* production via a Gauge Mediated model.

- and R.N.Mohapatra, Phys. Rev. **D12**, 1502 (1975).
2. F.Del Aguila, M.Quiros, F.Zwirner, Nucl. Phys. **B287**, 419 (1987); D.London and J.L.Rosner, Phys. Rev. **D34**, 5, 1530 (1986).
3. M.Carena, A.Daleo, B.Dobrescu, T.Tait, Phys. Rev. **D70**, 093009 (2004).
4. E.Eichten, K.Lane and M.Peskin, Phys. Rev. Lett. **50**, 811 (1983); E.Eichten, I.Hinchliffe, K.Late and C.Quigg, Ref. Mod. Phys. **56**, 579 (1984); T.Lee, Phys.Rev. **D55**, 2591 (1997).
5. N.Arkani-Hamed, S.Dimopoulos, G.Dvali, Phys. Lett. **B429**, 263 (1998); I.Antoniadis, N.Arkani-Hamed, S.Dimopoulos, G.Dvali, Phys. Lett. **B436**, 257 (1998); N.Arkani-Hamed, S.Dimopoulos, G.Dvali, Phys. Rev. **D59**, 086004 (1999); N.Arkani-Hamed, S.Dimopoulos, J. March-Russell, SLAC-PUB-7949, e-Print Archive: hep-th/9809124.
6. L.Randall and R.Sundrum, Phys. Rev. Lett. **83**, 3370 (1999).
7. J.C.Pati and A.Salam, Phys. Rev. **D10**, 275 (1974); R.N.Mohapatra and J.C.Pati, Phys. Rev.**D11**, 566 (1975); G.Senjanovic and R.N.Mohapatra, Phys. Rev.**D12**, 1502 (1975);
8. M.Kramer, T.Plehn, M.Spira, P.M.Zerwas, Phys.Rev.Lett. **79**, 341 (1997).
9. U.Baur, M.Spira, P.M.Zerwas, Phys. Rev. **D42**,3 (1990).
10. K.Hagiwara, D.Zeppenfeld, S.Komamiya, Z. Phys. **C29**,115 (1985).
11. <http://www-cdf.fnal.gov/physics/exotic/exotic.html>
12. <http://www-d0.fnal.gov/Run2Physics/WWW/results/np.htm>

Higgs Searches at the Tevatron

Anna Goussiou

University of Notre Dame

Abstract. The latest results of the Higgs search at the Tevatron $p\bar{p}$ Collider are presented. Upper limits on cross sections times branching ratios are set for a Standard Model Higgs boson production, as well as for Higgs bosons in the Minimal Supersymmetric Standard Model.

1 Introduction

The Standard Model (SM) of particle physics explains the electroweak symmetry breaking and the generation of mass of the electroweak gauge bosons and the fermions by introducing the Higgs field. A physical manifestation of the latter is a neutral scalar particle, the Higgs boson. The SM predicts the Higgs boson properties except for its mass, M_H . Direct searches at the CERN e^+e^- Collider (LEP) have yielded a lower limit on M_H of 114 GeV (95% C.L.) [1]. At the other end, fits to electroweak precision data give an upper limit of $M_H < 280$ GeV (95% C.L.) [2]. The search for the SM Higgs is currently pursued at the Fermilab $p\bar{p}$ Collider (Tevatron). The latest results are presented in Section 2.

The Higgs sector plays also a central role in supersymmetric extensions of the Standard Model that have been postulated in order to remedy the SM shortcomings. The first results of the search for supersymmetric Higgs boson(s) at the Tevatron are presented in Section 3.

2 Standard Model Higgs

The search strategies are dictated by the Higgs production and decay modes. For a Higgs mass smaller than about 135 GeV, the preferred decay is into a pair of b -quarks (branching ratio $\sim 90\%$) and the second preferred mode is into a pair of τ -leptons (branching ratio $\sim 10\%$). For higher Higgs masses, the decay into a pair of W 's or Z 's becomes dominant.

The highest SM Higgs production cross sections at the Tevatron come from gluon-gluon fusion and, an order of magnitude smaller, from quark-antiquark interactions that produce a Higgs in association with a W or Z boson. For $M_H < 135$ GeV, where the Higgs decays predominantly into a $b\bar{b}$ pair, the gluon fusion channel is overwhelmed by QCD jet production. In this mass range, the associated Higgs production with a W/Z provides the best discovery potential, since it allows for better control of the background through the leptonic decays of the W or the Z . In the higher mass range, $M_H > 135$ GeV, both the gg and

$(W/Z)H$ production mechanisms can be explored using the $H \rightarrow WW^{(*)}$ decay mode.

2.1 $WH \rightarrow l\nu b\bar{b}$

The $D\bar{O}$ analysis proceeds in two steps: first, a search for $Wb\bar{b}$ production is performed using events that contain one electron, missing transverse energy (\cancel{E}_T), and two b -tagged jets. Then, a search for WH production is performed by applying a window cut on the $b\bar{b}$ invariant mass. The data sample corresponds to an integrated luminosity of 382 pb^{-1} .

Candidate events are selected by requiring an electron with $p_T > 20$ GeV in the central region, $\cancel{E}_T > 25$ GeV, and two jets with $E_T > 20$ GeV. Events with more than one electron, more than two jets, or a muon are excluded from the sample. Finally, the two jets are required to be tagged as b -jets using a “jet lifetime probability” algorithm. This probability is constructed from the tracks associated with the jet that have positive impact parameters in the transverse plane, and is required to be consistent with that of a b -jet.

Two types of background are considered, instrumental and physics. The instrumental background comes from multijet events in which one of the jets is misidentified as an electron, two other jets are either mistagged as b -jets or are $b\bar{b}$ pair originating from gluon splitting, and mismeasurement of the jet energies produces an apparent \cancel{E}_T . This background is estimated from data using measured probabilities of electron reconstruction and misidentification of jets as electrons.

The primary physics backgrounds to the $Wb\bar{b}$ and WH channels come from $t\bar{t} \rightarrow ll\nu\nu b\bar{b}$ ($l = e, \mu$), single top production ($t\bar{b} \rightarrow e\nu b\bar{b}$), $WZ \rightarrow e\nu b\bar{b}$, and $W+2\text{jets}$ (Wjj) production where both jets are misidentified as b -jets. The $Wb\bar{b}$ process itself is a primary irreducible background to the WH channel. The $t\bar{t}$ and WZ backgrounds, as well as the WH signal, are estimated using Monte Carlo samples generated with PYTHIA using Leading Order (LO) Parton Distribution Functions (PDF). Because PYTHIA does not

provide an adequate description of heavy-quark production and higher-order processes with larger jet multiplicities, the single top background is generated using COMPHEP and the $Wb\bar{b}$ channel is generated using ALPGEN. These events are then passed through the PYTHIA parton-shower and hadronization process. The MC events are reweighted to match the various efficiencies measured in the data. The Wjj background is estimated by subtracting the expected number of events of all other background sources that have an electron, \cancel{E}_T and 2 jets in the event from the observed number of events in the data, before requiring b -tagging.

A total of 13 events are left in the sample after all selection criteria are applied. The total background to $Wb\bar{b}$ is estimated to be 5.7 ± 1.5 . The 95% C.L. upper limit on the $Wb\bar{b}$ production cross section, obtained using a Bayesian limit calculation method, is 4.6 pb for b -jets with $p_T^b > 20$ GeV, $|\eta^b| < 2.5$ and $\Delta R_{b\bar{b}} > 0.75$.

Finally, to search for a WH signal, a sliding window cut is applied on the $b\bar{b}$ invariant mass. For example, for $M_H = 115$ GeV, a total of 4 events are observed within the mass window $85 < M_{b\bar{b}} < 135$ GeV, with 2.4 ± 0.6 events expected from background. Since no excess over the estimated background is observed for any of the Higgs mass points ($M_H = 105, 115, 125, 135$ GeV), 95% C.L. upper limits are calculated for $\sigma(p\bar{p} \rightarrow WH) \times BR(H \rightarrow b\bar{b})$; they vary from 6.9 to 7.6 pb for these mass points (see Fig. 1).

The CDF search for a WH signal uses a data sample corresponding to an integrated luminosity of 318 pb^{-1} . First, a W -candidate sample is formed by requiring an isolated electron or muon with $p_T > 20$ GeV in the central region and $\cancel{E}_T > 20$ GeV. Dilepton events are removed from the sample. The remaining events are then classified according to jet multiplicity, with jet $E_T > 15$ GeV. In the $W + 2$ jets sample, at least one jet is required to be tagged as b -jet using a ‘‘Secondary Vertex’’ algorithm. A jet is declared as tagged if it contains a secondary vertex with a transverse displacement from the primary vertex consistent with that of a b -jet.

The backgrounds considered are similar as in the $D\bar{O}$ analysis. The $W +$ heavy flavor ($Wb\bar{b}, Wc\bar{c}, Wc$) background is estimated from ALPGEN MC events calibrated using inclusive jet and $W+1$ jet data. The $t\bar{t}$ and single top contributions are estimated using HERWIG and PYTHIA calculations normalized to the NLO production cross sections. The contribution from W +jets where the jets have been misidentified as b -jets is estimated from the W +jets sample using a mistag rate parametrization measured in an inclusive jet sample. The diboson backgrounds are estimated from a combination of MC simulations and data. Finally, the instrumental background from multijet events is estimated by extrapolating the number of tagged events with an isolated lepton and low \cancel{E}_T into the signal region.

A total of 14 events are left in the $W+2$ jets sample after requiring 2 b -tags, with a total estimated background (to WH) of 15 ± 3 events. A direct search for a resonant mass peak in the reconstructed dijet invariant mass distribution is performed using a binned maximum likelihood technique. Since there is no significant

mass peak observed, a 95% C.L. upper limit is set for $\sigma(p\bar{p} \rightarrow WH) \times BR(H \rightarrow b\bar{b})$ as a function of M_H (see Fig. 1).

2.2 $ZH \rightarrow \nu\bar{\nu}b\bar{b}$

The final state for the $p\bar{p} \rightarrow ZH \rightarrow \nu\bar{\nu}b\bar{b}$ channel is characterized by \cancel{E}_T and two b -jets. The latter are boosted along the Higgs momentum direction and thus tend to be acoplanar, in contrast to typical QCD dijet production. The backgrounds are distinguished in physics and instrumental. The main physics backgrounds come from W/Z +jets production, electroweak diboson (ZZ/WZ) production, and $t\bar{t}$ production with escaping electrons or jets. The instrumental background consists of multijet events with mismeasured jet energies (which produces \cancel{E}_T) or misidentification of jets as b -jets.

The $D\bar{O}$ search for a $ZH \rightarrow \nu\bar{\nu}b\bar{b}$ signal is based on an integrated luminosity of 261 pb^{-1} . A dedicated trigger based on acoplanar jets and \cancel{E}_T was used to collect the sample. Offline, events are selected by requiring at least two jets with $E_T > 20$ GeV, no back-to-back event topology, and $\cancel{E}_T > 25$ GeV. Vetoing events with isolated tracks reduces the physics backgrounds. To further reject the $t\bar{t}$ background, the scalar sum of the jet E_T 's, H_T , is required to be less than 200 GeV. The remaining physics background is estimated from simulated samples, using PYTHIA, ALPGEN, or COMPHEP (depending on the process).

In order to reduce the instrumental background remaining after the jet acoplanarity requirement, cuts are applied on the following variables: the minimum azimuthal angle difference between the direction of \cancel{E}_T and any of the jets; the asymmetry between \cancel{E}_T and the vector sum of the jet p_T 's, \cancel{H}_T ; and the asymmetry between \cancel{E}_T and the vector sum of all tracks' p_T 's, P_T^{trk} . Finally, the residual instrumental background after the above selection is estimated from a fit to the distribution of the asymmetry between \cancel{E}_T and \cancel{H}_T within the signal region in the data.

Successive b -tagging is applied to the data using the Jet Lifetime Probability algorithm. A sliding window cut on the dijet invariant mass is then applied in the sample with two b -tagged jets. No excess is observed in the mass window for any of the Higgs mass points. Therefore, a limit is set on $\sigma(p\bar{p} \rightarrow ZH) \times BR(H \rightarrow b\bar{b})$ as a function of M_H . For example, for $M_H = 115$ GeV, a total of 3 events are observed within the mass window $80 < M_{b\bar{b}} < 130$ GeV, with 2.2 ± 0.7 events expected from background. This sets a 95% C.L. upper limit of 9.3 pb on the cross section times branching ratio for $M_H = 115$ GeV. The limits for the other Higgs mass points are shown in Fig. 1.

2.3 $H \rightarrow WW^{(*)}$

The $D\bar{O}$ search for a high-mass Higgs boson decaying into a pair of $WW^{(*)}$ is based on dilepton data with e^+e^- , $e^\pm\mu^\mp$ and $\mu^+\mu^-$ final states, corresponding to integrated luminosities of $300\text{-}325 \text{ pb}^{-1}$, depending on the final state.

The samples are selected by single or dilepton triggers. Offline, candidate events are selected by requiring two high- p_T isolated leptons, with $p_T > 15$ GeV for the leading lepton and $p_T > 10$ GeV for the trailing one, and $\cancel{E}_T > 20$ GeV, due to the neutrinos from the W decays.

The background is largely dominated by Z/γ^* production. Other physics backgrounds include diboson (WW , WZ and ZZ), W +jet/ γ , and $t\bar{t}$ production. All physics backgrounds are estimated using PYTHIA normalized to the NLO cross sections. The W +jet/ γ contribution is additionally verified using ALPGEN. Instrumental background originates from multijet production when a jet is misidentified as an electron. This is determined from the data using a sample of like-sign dilepton events with inverted lepton quality cuts (compared to the lepton quality cuts used to select the candidate events).

After the initial requirements on the lepton p_T 's and \cancel{E}_T , additional selection includes the following: an upper cut on the invariant dilepton mass, which, for leptons from the Higgs decay, is restricted to $M_H/2$ (since the charged lepton system and the neutrinos are emitted mostly back-to-back); a lower cut on the invariant dilepton mass for the $\mu^+\mu^-$ channel, to remove events from J/ψ , Y and Z/γ^* production; a cut on the sum of the lepton p_T 's and \cancel{E}_T as well as a cut on the transverse dilepton mass, to reject events from W +jet/ γ and WW production and further reduce the background from Z/γ^* production; an upper cut on H_T , to suppress the $t\bar{t}$ background; and a cut designed to remove events where the \cancel{E}_T has a large contribution from a mismeasurement of the jet energy. Finally, remaining Z boson and multijet events can be rejected with a cut on the opening angle between the two leptons, $\Delta\phi_{ll} < 2$; the backgrounds exhibit a back-to-back topology, whereas the leptons from the Higgs decay tend to point in the same direction because of the spin correlations in the decay.

After all selection criteria are applied, there is good agreement between the number of events observed in the data and the various backgrounds in all three channels. For $M_H = 160$ GeV and when combining the channels, 19 events are observed in the data with 19.7 ± 1.2 events expected from background. Limits on the production cross section times branching ratio, $\sigma(p\bar{p} \rightarrow H) \times BR(H \rightarrow WW^{(*)})$, are derived using a modified frequentist method. They are shown in Fig. 1 as a function of M_H .

2.4 $WH \rightarrow WWW^*$

The CDF search for a Higgs boson produced in association with a W boson and decaying into a pair of $WW^{(*)}$ is based on an integrated luminosity of 193.5 pb^{-1} . The analysis starts with a baseline sample by requiring two leptons of the same sign; the leading lepton with $p_T > 20$ GeV and the second lepton with $p_T > 6$ GeV. This sample is analyzed and found to be consistent with background expectations.

The largest background comes from lepton misidentification. Fake electrons are due to interactive π^\pm 's, accidental overlap of π^0 's and a track, and residual photon conversions. Fake muons are due to punch-through hadrons

and decay-in-flight muons. These backgrounds are estimated from the data by scaling the number of isolated like-sign tracks found in addition to the leading lepton in the inclusive lepton samples by the fake rate, i.e., the probability for an isolated track to pass the lepton selection cuts. Additional backgrounds include irreducible diboson (WZ and ZZ) production, and reducible Z/γ^* , WW , $t\bar{t}$ and W +heavy flavor production. The effective cross sections of the irreducible diboson backgrounds are small, whereas the Drell-Yan, WW , $t\bar{t}$ and W +jet backgrounds are strongly suppressed by the high- p_T cut, the isolation cut, and the like-sign requirement. All of these backgrounds are estimated from MC samples.

At the next level, optimized cuts are applied on the p_T of the second lepton, p_{T2} , and the vector sum of the p_T 's of the two leptons, p_{T12} , in order to determine the signal region in the plane of these two variables, i.e., enhance the signal significance. The optimization is based on the S/\sqrt{B} calculation using signal Monte Carlo and the background expectation. For $M_H < 160$ GeV (> 160 GeV), the signal region is $p_{T2} > 16$ (18) GeV and $p_{T12} > 35$ GeV. Outside of the signal region, the number of expected background events is in reasonable agreement with the number of observed events. In the signal region, no event is observed. Thus, upper limits are set on $\sigma(p\bar{p} \rightarrow WH) \times BR(H \rightarrow WW^{(*)})$. For $M_H = 110$ (160) GeV, the 95% C.L. limit is 12 (8) pb. The limits for the other Higgs mass points are shown in Fig. 1.

The $D\bar{O}$ search for $p\bar{p} \rightarrow WH \rightarrow WWW^{(*)} \rightarrow l^\pm \nu l'^\mp \nu q \bar{q}$ is based on e^+e^- , $e^\pm\mu^\mp$ and $\mu^+\mu^-$ samples of integrated luminosities 384 pb^{-1} , 368 pb^{-1} and 363 pb^{-1} , respectively. The samples are selected by requiring two isolated, like-sign leptons with $p_T > 15$ GeV, vetoing events with a third high- p_T isolated lepton, applying an additional set of track quality cuts, and requiring $\cancel{E}_T > 20$ GeV.

The main physics background originates from $WZ \rightarrow l\nu ll$ production where one of the leptons is lost. This background is estimated from the known theoretical cross section convoluted with the relevant branching ratio and the experimental efficiencies. There are two types of instrumental backgrounds. One type originates from the misreconstruction of the charge of one of the leptons. The track quality cuts mentioned above are aimed at reducing the probability of charge misreconstruction. The second type consists of like-sign lepton pairs from multijet or W +jets production. Both types of instrumental background are estimated from the data.

After all selections, there are 1, 3, and 2 events observed in the data, in the e^+e^- , $e^\pm\mu^\mp$, and $\mu^+\mu^-$ channels, respectively. The corresponding numbers of expected background events are 0.7 ± 0.1 , 4.3 ± 0.2 , and 3.7 ± 0.8 , respectively. In the absence of an excess, upper limits on $\sigma(p\bar{p} \rightarrow WH) \times BR(H \rightarrow WW^{(*)})$ are calculated using the modified frequentist approach and combining all three channels. The limits vary from 3.9 to 2.1 pb as the Higgs mass varies from 115 to 175 GeV (see Fig. 1).

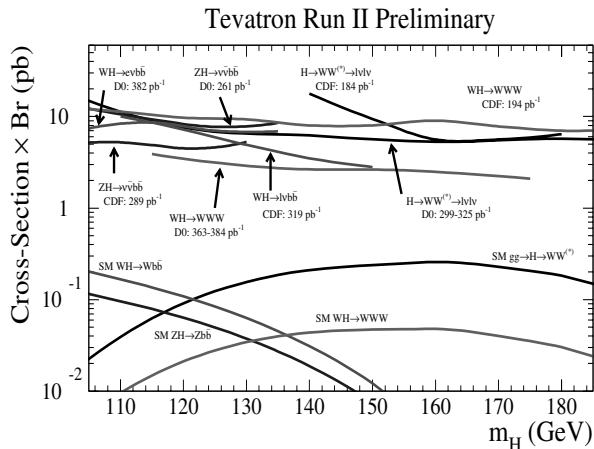


Fig. 1. Upper limits on cross section times branching ratio for a SM Higgs using various production and decay modes, from CDF and DØ. Also shown are the Standard Model expectations.

3 Higgs in the MSSM

The Higgs sector in the Minimal Supersymmetric extension of the Standard Model (MSSM) consists of five physical Higgs bosons: two neutral CP -even scalars, h and H , with $M_h < M_H$ by convention; one neutral CP -odd state, A ; and two charged bosons, H^\pm . The dominant production mechanisms of the neutral MSSM Higgs bosons at hadron colliders are gg fusion and $b\bar{b}$ fusion. The leading decay modes, for most of the MSSM parameter space, are into $b\bar{b}$ (90%) and $\tau^+\tau^-$ (10%).

At tree level, the Yukawa couplings of A to down-type fermions (such as b -quarks and τ -leptons) are enhanced by a factor of $\tan\beta$ relative to the SM. For large $\tan\beta$, one of the CP -even bosons is nearly mass-degenerate with A and has similar couplings (and therefore, enhanced couplings to down-type fermions). Thus, the production cross sections of A and either h or H , through the b -quark loop in gg fusion or through the $b\bar{b}$ fusion, are enhanced by $\tan^2\beta$. In addition, the production cross section in association with b -quarks, $p\bar{p} \rightarrow b(h/H/A)$, is also enhanced by the same factor.

Both Tevatron experiments have performed searches for an MSSM neutral Higgs boson. In the case of $p\bar{p} \rightarrow (h/H/A)$ production, the $\tau^+\tau^-$ decay mode has been used, since the $b\bar{b}$ decay channel will be overwhelmed by background. In the case of $p\bar{p} \rightarrow b(h/H/A)$ production, the presence of the extra b -quark in the final state makes it possible to use the the dominant $b\bar{b}$ decay mode.

3.1 $h/H/A \rightarrow \tau^+\tau^-$

The CDF search for neutral MSSM Higgs bosons produced through gg or $b\bar{b}$ fusion and decaying into a pair of τ 's is based on 310 pb^{-1} of data. One τ is detected in the decay to an e or μ and neutrinos, and the other in the decay to hadrons and a neutrino. The sample was selected using “lepton plus track” triggers.

The dominant background comes from $Z/\gamma^* \rightarrow \tau^+\tau^-$. It is estimated from MC with a cross section times branch-

ing ratio normalized to the experimentally measured values. The second largest background, estimated from data, comes from multijet, W +jets and γ +jets events where the jets have been misidentified as τ 's. The third group of backgrounds includes $Z/\gamma^* \rightarrow e/\mu$, diboson, and $t\bar{t}$ production; these are determined from MC samples normalized to the theoretical cross sections.

Candidate events are selected by first requiring one e or μ with $p_T > 10 \text{ GeV}$, and one hadronic τ with $p_T > 15 \text{ GeV}$ and opposite electric charge. Low-energy multijet backgrounds are suppressed by requiring that the sum of lepton p_T , hadronic τ p_T , and \cancel{E}_T is greater than 50 GeV . Backgrounds from W +jets events are suppressed by imposing a requirement on the relative directions of the visible τ decay products and \cancel{E}_T . Finally, to suppress $Z/\gamma^* \rightarrow e/\mu$ backgrounds, events with invariant mass of an e or μ and a single-track hadronic τ within 10 GeV of the Z mass are rejected.

After all selection criteria are applied, a total of 487 events are observed in the data, in agreement with $496 \pm 5(\text{stat}) \pm 28(\text{sys}) \pm 25(\text{lumi})$ events expected from backgrounds. To probe for possible Higgs signal, binned likelihood fits are performed on the visible mass of the di- τ system, defined as the invariant mass of the visible τ decay products and \cancel{E}_T . No signal evidence is observed for $M_A = 90\text{-}250 \text{ GeV}$; thus, 95% C.L. exclusion limits are set on $\sigma(p\bar{p} \rightarrow h/H/A) \times BR(h/H/A \rightarrow \tau^+\tau^-)$, shown in Fig. 2 [3]. Using the theoretical predictions for the MSSM Higgs production and decay to τ pairs, these limits can be interpreted as exclusions of parameter regions in the $\tan\beta$ vs M_A plane. Examples for two specific MSSM scenarios are shown in Figures 3 and 4.

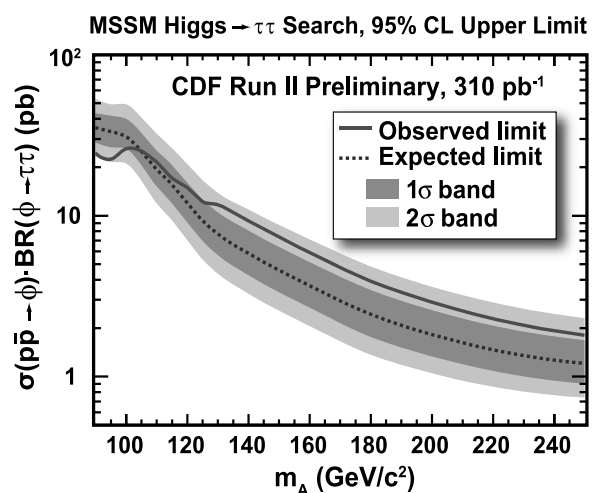


Fig. 2. Upper limits (observed at 95% C.L. and expected) on the Higgs production cross section times branching ratio to τ pairs. ($\phi = h/H/A$)

3.2 $b(h/H/A) \rightarrow b\bar{b}$

The $D\bar{O}$ search for neutral MSSM Higgs bosons produced in association with b -quarks and decaying into a pair of $b\bar{b}$ is based on 260 pb^{-1} of data. The sample was selected using a multijet trigger which required three jets with $E_T > 15 \text{ GeV}$ at the highest trigger level. Offline, candidate events are selected by requiring one jet with $E_T > 20 \text{ GeV}$ and at least two more jets with $E_T > 15 \text{ GeV}$. Jets containing b -quarks are identified using the Secondary Vertex tagging algorithm. Candidate events are required to have at least three b -tagged jets.

The main source of background is multijet production; either of genuine heavy-flavor jets, or of light-quark or gluon jets that are mistakenly tagged as b -jets, or correspond to gluons that branch into nearly collinear $b\bar{b}$ pairs. This multijet background is determined from data: the background shape is determined from doubly b -tagged data by applying a tag rate function to the non- b -tagged jets; the overall background normalization is determined by fitting the leading two jets invariant mass distribution of the estimated shape for triply b -tagged events to real triply b -tagged events, outside of the signal region. The method is cross-checked with data (by estimating the background in the doubly b -tagged sample using singly b -tagged events), as well as with simulations.

The invariant mass distribution of the leading two jets agrees well between the expected background and the data. A modified frequentist method is used to set upper limits on the production of neutral Higgs bosons in the mass range of 90 to 150 GeV [4]. The cross section limits can be interpreted in MSSM $(M_A, \tan\beta)$ parameter space. A specific example for a certain choice of MSSM parameters is shown in Fig. 3.

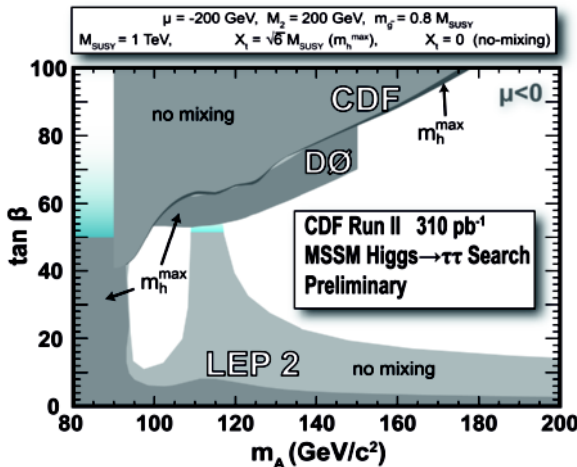


Fig. 3. Excluded regions in the $(M_A, \tan\beta)$ plane for the M_h^{max} and no-mixing scenarios with $\mu < 0$.

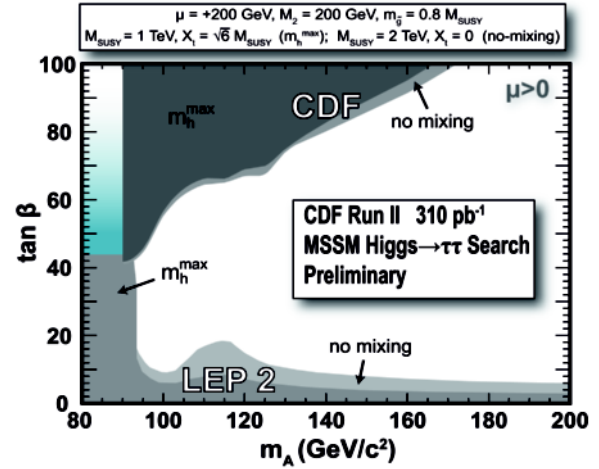


Fig. 4. Excluded regions in the $(M_A, \tan\beta)$ plane for the M_h^{max} and no-mixing scenarios with $\mu > 0$.

3.3 Conclusions

The latest results on the Higgs search from the CDF and $D\bar{O}$ experiments, based on $\sim 400 \text{ pb}^{-1}$ of Tevatron Run II $p\bar{p}$ data, have been presented. The upper limits on the cross section times branching ratio for a SM Higgs boson are currently between forty times to two orders of magnitudes higher than the SM expectations. The search for neutral MSSM Higgs bosons excludes $\tan\beta$ values as low as 50 for M_A between 100-160 GeV. Significant improvements are expected with further detector upgrades, optimization of the analysis techniques, and larger data samples.

References

1. ALEPH, DELPHI, L3 and OPAL Collaborations, Phys. Lett. **B565**, (2003) 61.
2. LEP Electroweak Group, <http://lepewwg.web.cern.ch/LEPEWWG/>.
3. A. Abulencia *et al.*, submitted to Phys. Rev. Lett.; hep-ex/0508051.
4. V. M. Abazov *et al.*, accepted by Phys. Rev. Lett.; hep-ex/0504018; Fermilab-Pub-05/058-E.

Searches for Higgs Bosons at LHC

Marco Pieri

UC San Diego California USA

Abstract. The prospects for Higgs Searches at the Large Hadron Collider with the detectors ATLAS and CMS are reviewed. Searches for the Standard Model Higgs boson and for the Higgs bosons of the Minimal Supersymmetric Model are described and the discovery potential of the detectors in the different channels are discussed.

1 Introduction

The Standard Model of electroweak interactions has been extremely successful and most of its predictions have been experimentally tested. Nevertheless one important ingredient of the theory, the Higgs sector, has not yet been verified. Until now all direct searches for the Higgs bosons gave negative results. The most stringent limits come from LEP [1] that excluded a SM higgs boson with mass less than $114.4 \text{ GeV}/c^2$ at 95% C.L. and MSSM neutral Higgs bosons h and A with masses less than 92.9 and $93.4 \text{ GeV}/c^2$ respectively. Also the existence of charged Higgs bosons has been excluded at LEP with a mass less than $89.6 \text{ GeV}/c^2$ for $\text{BR}(H^\pm \rightarrow \tau\nu=1)$ and $78.6 \text{ GeV}/c^2$ for any decay BR into $c\bar{s}$ or $\tau\nu$.

From Standard Model fits to all precision electroweak measurements it is also possible to derive indirect constraints on the mass of the SM Higgs boson. The latest results that include the new CDF top mass measurements [2] give a 95% C.L. upper limit on M_H of approximately $200 \text{ GeV}/c^2$ [3].

The Large Hadron Collider LHC is planned to start operation in 2007. The colliding proton beams will be at a centre-of-mass energy of 14 TeV. ATLAS and CMS, the two general purpose detectors that will be installed on the collider, are preparing for the searches for Higgs bosons of various models. Most of the studies presented here are still carried out with fast simulation for the background, but full simulation has been used for the signal and for the estimation of the crucial aspects of the detectors. Studies with full simulation of signal and background are in progress.

LHC is planned to operate at a luminosity of $2 \times 10^{33} \text{ cm}^{-2}\text{sec}^{-1}$ in the first years, the so-called low luminosity phase, and then to increase the luminosity up to $1 \times 10^{34} \text{ cm}^{-2}\text{sec}^{-1}$. We assume that an integrated luminosity of $\sim 30 \text{ fb}^{-1}$ per experiment at low luminosity and $\sim 300 \text{ fb}^{-1}$ per experiment at high luminosity will be collected. The main difference between the two phases from an experimental point of view is the number of random minimum bias interactions that occur in coincidence with the main

interaction. It increases from approximately 3 at low luminosity to approximately 20 at high luminosity. In the following most of the results will be shown for the first years of data taking.

2 Standard Model Higgs Boson

At LHC the SM higgs boson would be mainly produced through the gluon-gluon fusion process. Other production processes that offer additional signatures are: WW and ZZ fusion with a cross section that is about 20% of the gluon-gluon fusion at low masses and becomes approximately equal at $M_H = 1 \text{ TeV}/c^2$; the $t\bar{t}H$ process, where the Higgs boson is produced in association with a $t\bar{t}$ pair; the WH and ZH processes, where the Higgs boson is radiated by a vector boson. NLO Higgs production cross sections and branching ratios [4] are shown in figure 1 as a function of the Higgs boson mass. The Higgs boson mainly decays into $b\bar{b}$ and $\tau^+\tau^-$ for low masses, below approximately $150 \text{ GeV}/c^2$, but the backgrounds to these channels are too large and additional signatures are needed such as the production in association with a $t\bar{t}$ pair, in case of the $b\bar{b}$ decay, or WW and ZZ fusion for the $\tau^+\tau^-$ decay. For higher masses the WW and ZZ decay channels dominate and the Higgs boson can be detected in the leptonic decays of the vector bosons. In the low mass range, between 100 and $150 \text{ GeV}/c^2$, the $H \rightarrow \gamma\gamma$ decay can be exploited, it has rather small BR but a clean signature. Near the threshold for the decay into two real W bosons, around $M_H = 170 \text{ GeV}/c^2$, the $H \rightarrow WW$ has a BR that is almost 100% and is the only detectable channel.

A summary of the search channels for the different mass ranges is given in Table 1.

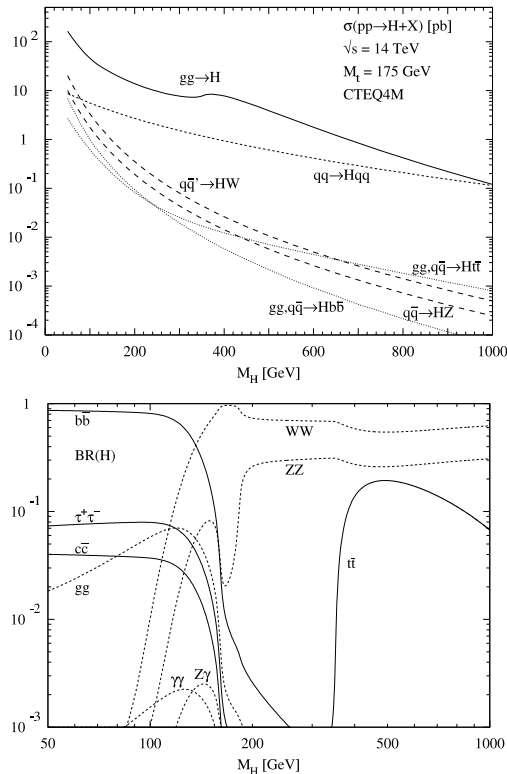
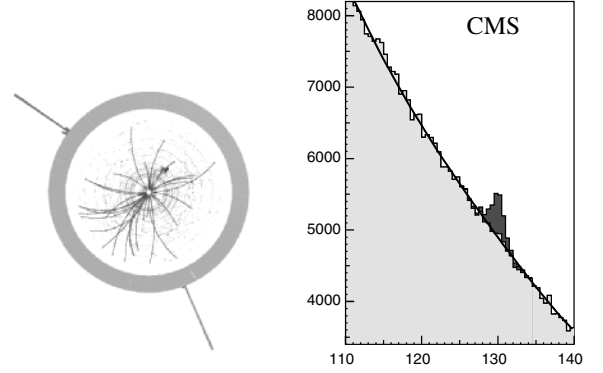
2.1 $H \rightarrow \gamma\gamma$

The branching ratio $\text{BR}(H \rightarrow \gamma\gamma)$ is small, of the order of 10^{-3} , but the distinctive features of the signal, two isolated photons with large transverse energy that give rise

Table 1. Most sensitive production and decay channels for the SM Higgs boson search

Decay	Production	Incl.	qqH	WH/ ZH	ttH
Low mass, $M_H < 200 \text{ GeV}/c^2$					
$H \rightarrow \gamma\gamma$		Yes	Yes	Yes	Yes
$H \rightarrow b\bar{b}$					Yes
$H \rightarrow \tau^+\tau^-$			Yes		
$H \rightarrow WW^* \rightarrow \ell\nu\ell\nu, \ell = e, \mu$		Yes	Yes	Yes	
$H \rightarrow ZZ^* \rightarrow 4\ell, \ell = e, \mu$		Yes			
Intermediate mass, $200 \text{ GeV}/c^2 < M_H < 700 \text{ GeV}/c^2$					
$H \rightarrow WW \rightarrow \ell\nu\ell\nu, \ell = e, \mu$		Yes			
$H \rightarrow ZZ4\ell, \ell = e, \mu$		Yes			
High mass, $M_H > 700 \text{ GeV}/c^2$					
$H \rightarrow WW \rightarrow \ell\nu q\bar{q}$			Yes		
$H \rightarrow ZZ \rightarrow \ell^+\ell^-\nu\bar{\nu}$			Yes		

to a narrow mass peak, allow to separate the signal from a large irreducible background due to two photon production from gluon-gluon fusion and quark annihilation. The reducible background coming from misidentified jets and isolated π^0 's can be reduced by applying isolation- and photon-identification requirements. For both detectors the mass measurement is extremely accurate, better than 1% for CMS and $\sim 1.5\%$ for ATLAS. Figure 2 shows a simulated event observed in the CMS detector and the Higgs mass peak above the background. Current studies show that a Higgs boson with mass between 100 and 150

**Fig. 1.** SM Higgs boson production cross section (top) and decay branching ratios (bottom)**Fig. 2.** $H \rightarrow \gamma\gamma$ simulated event reconstructed in the CMS detector (left) and mass peak from a $130 \text{ GeV}/c^2$ mass Higgs signal over the background in the CMS detector with an integrated luminosity of 30 fb^{-1} (right).

GeV/c^2 can be discovered with CMS in this channel alone with a significance of 5σ with an integrated luminosity of 30 fb^{-1} [5].

2.2 Higgs to ZZ^* to 4 leptons

The most celebrated channel for SM Higgs discovery at LHC involves the Higgs boson decay into a pair of Z bosons: $H \rightarrow ZZ^*$, with $Z \rightarrow \ell^+\ell^-$ and $\ell = e, \mu$. The only irreducible background comes from the ZZ continuum production and the main reducible backgrounds are $t\bar{t}$ and $Zb\bar{b}$. In this channel, as in the $H \rightarrow \gamma\gamma$ channel, the Higgs mass resolution is very good, of the order of 1% for both detectors and the background can be easily estimated from data by fitting the sidebands of the invariant mass distribution. Below a mass of $2M_Z$ at least one of the Z bosons is virtual and the $\sigma \times \text{BR}$ is lower. It becomes larger for higher masses, when both Z bosons are real.

2.3 Higgs to $b\bar{b}$

For very low masses ($M_H < 130 \text{ GeV}/c^2$) the Higgs boson decays into $b\bar{b}$ can be exploited at LHC. In order to cope with the formidable QCD $b\bar{b}$ background the channel $t\bar{t}H \rightarrow \ell\nu q\bar{q}b\bar{b}b\bar{b}$ is used and the signal events are triggered using the lepton from one top. The jets coming from top decays must be assigned to the right parton in order to identify the correct $b\bar{b}$ combination corresponding to the Higgs boson decay. The Higgs boson mass resolution is of the order of 10% but the presence of 4 b-quarks in the final state allows separating the signal from the background. One should keep in mind that in this channel systematic errors related to b-tagging efficiency and purity may be important and that a very detailed understanding of the detector will be needed.

2.4 Weak boson fusion

Weak boson fusion (WBF) provides additional signatures that enhance the signal over background ratio and im-

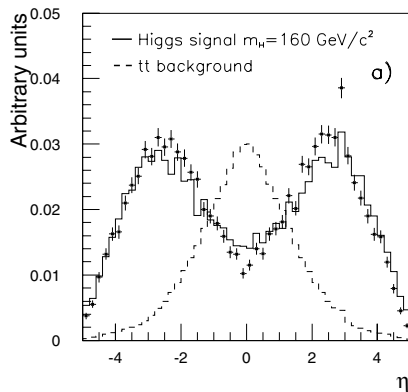


Fig. 3. Pseudo-rapidity distribution for the two tagging jets in qqH events detected in ATLAS

prove the Higgs boson discovery potential [6, 7]. In the qqH process two additional jets are produced at large rapidity and given the absence of colour flow between the two partons, the rapidity gap has low hadronic activity. These two jets can be tagged in the forward calorimeters and a jet veto can be applied in the central region. Figure 3 shows the pseudo-rapidity distribution of the two tagging jets. Thanks to this additional signature even less clean channels can become visible: in particular for low mass H the channels $qqH \rightarrow qqWW^*$ and $qqH \rightarrow qq\tau^+\tau^-$ have been studied by ATLAS [8].

ATLAS carried out the analysis for the following channels:

- $qq\tau\tau \rightarrow qq \ell\nu\nu \ell\nu\nu$
- $qq\tau\tau \rightarrow qq \ell\nu\nu \text{ had } \nu$
- $qqWW^* \rightarrow qq \ell\nu \ell\nu$
- $qqWW^* \rightarrow qq \ell\nu \text{ jet jet}$

where $\ell = e, \mu$.

The main sources of background for these channels are the processes $Z + \text{jets}$, $t\bar{t}$ and $WW + \text{jets}$.

A point worth mentioning here is the τ reconstruction. It is carried out in the following way: as the τ decay products are highly boosted one can assume that they are collinear, including the escaping neutrinos. In this hypothesis the momenta of the two neutrinos can be estimated from the modulus and direction of the missing E_t . The resulting Higgs mass resolution is approximately 10% for $M_H = 120 \text{ GeV}/c^2$.

Figure 4 shows the transverse mass distribution in the $H \rightarrow WW^* \rightarrow e\mu\nu\nu$ channel. ATLAS showed that the WBF channels provide a sensitivity that is similar to the $H \rightarrow \gamma\gamma$ and $H \rightarrow ZZ^*$ and that, in the MSSM, is less sensitive to a possible reduction of the gluon-gluon fusion cross section.

On the other hand, as we have seen, in these channels the mass resolution is not excellent and, in the case of $H \rightarrow WW^*$ decays, only the transverse mass or its approximation can be measured. As a consequence the background estimation from data will be much more difficult. In addition, due to the uncertainties on the structure of the underlying event, the background estimation, as well as the signal efficiency, will be affected by large systematic

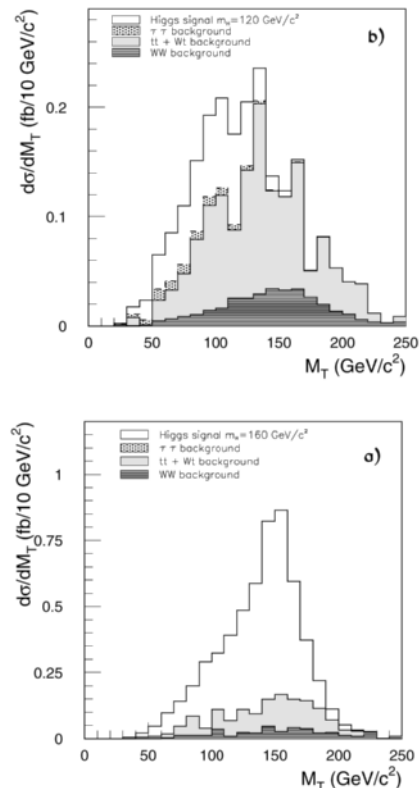


Fig. 4. Transverse mass distribution in the $H \rightarrow WW^* \rightarrow e\mu\nu\nu$ channel for a Higgs boson mass of $120 \text{ GeV}/c^2$ (top) and $160 \text{ GeV}/c^2$ (bottom).

uncertainties. All of this could make a discovery in these channels much less solid.

2.5 SM Higgs Results

Figure 5 shows the ATLAS discovery potential for a low mass SM Higgs boson. We can see that the most sensitive channels are the WBF channels and that ATLAS can discover the SM Higgs boson in the mass range from 100 to 200 GeV/c^2 with 30 fb^{-1} in more than one channel. This will also allow to measure the Higgs boson couplings. Figure 6 shows the CMS discovery potential. We can see that the full mass range is covered and that 10 fb^{-1} are sufficient to discover the SM Higgs boson with mass above the LEP lower limit. With a few fb^{-1} it would be possible to discover the Higgs boson with mass between 150 and 500 GeV/c^2 in the WW and ZZ channels.

3 MSSM Higgs searches

In the Minimal SuperSymmetric Model (MSSM) two Higgs doublets are needed, corresponding to 5 physical Higgs bosons: two neutral scalars h and H , one neutral pseudo-scalar A and two charged scalars H^\pm . At the tree level all masses and couplings in the Higgs sector are determined by two independent parameters and the mass of the lightest Higgs boson h is predicted to be below M_Z .

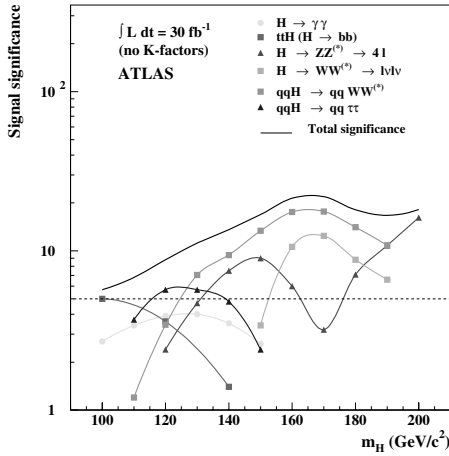


Fig. 5. ATLAS discovery potential for a low mass SM Higgs boson, no K-factors are used for the cross section calculations.

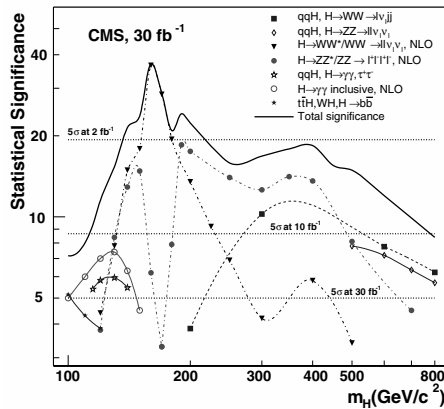


Fig. 6. CMS discovery potential for the SM Higgs boson in the whole mass range.

Radiative corrections modify the tree level predictions but the lightest Higgs boson h is still bound to be below ~ 130 GeV/c^2 for any choice of the Supersymmetric parameters. In addition for $M_A > 150$ GeV/c^2 the three heavier Higgs bosons H , A and H^\pm are approximately degenerate in mass. These features are apparent in Figure 7 that shows the value of the masses for two values of $\tan\beta$ as function of M_A . In all the following plots, once the MSSM parameters are fixed, the results are presented in the M_A - $\tan\beta$ plane, where $\tan\beta$ is the ratio of the vacuum expectation values of the two doublets and M_A is the mass of pseudo-scalar Higgs boson.

In the MSSM Higgs sector, depending on the values of the parameters, different regimes can be identified: for $M_A > 200$ GeV/c^2 we are in the so-called decoupling limit, the h boson is very similar to H_{SM} and the Standard Model Higgs boson searches directly apply to the MSSM. Given the fact that the h mass is bound to be below ~ 130 GeV/c^2 the low mass SM Higgs searches and the WBF channels are important. On the other hand, for $M_A = O(M_Z)$ and large $\tan\beta$ the H boson behaves like the SM Higgs boson and is also light. For large $\tan\beta$, in all other

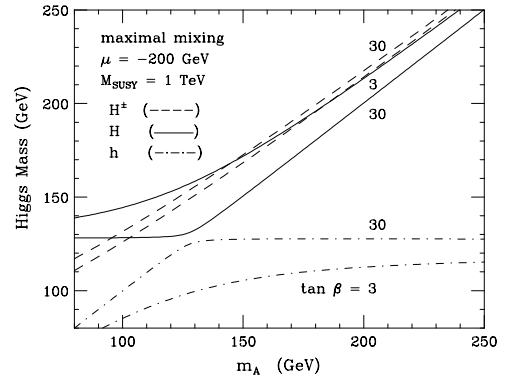


Fig. 7. Masses of h , H and H^\pm as function of M_A for two values of $\tan\beta$: 3 and 30.

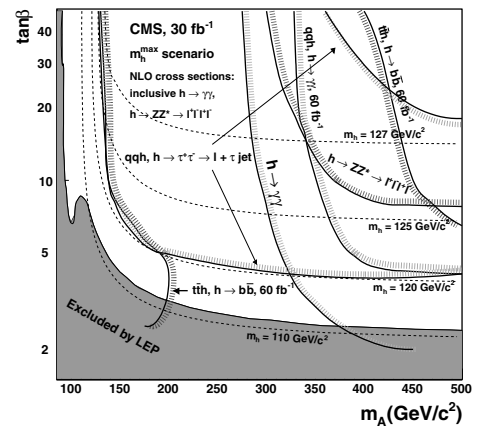


Fig. 8. CMS discovery potential at the 5σ level for the h boson in the MSSM from the SM searches.

cases, the couplings of h and H to WW and ZZ are suppressed, while $A \rightarrow WW, ZZ$ is never allowed at the tree level, and h, H and A are produced in association with a $b\bar{b}$ pair and decay with almost 100% BR into $b\bar{b}$ and $\tau^+\tau^-$. Finally for large M_A and small $\tan\beta$ H and A predominantly decay into $t\bar{t}$ but for masses around 200-300 GeV/c^2 we can also have the decays $H \rightarrow hh$ and $A \rightarrow Zh$.

Clearly, depending on their masses, supersymmetric particles may decay into Higgs bosons and viceversa.

3.1 Results from SM Higgs Searches

In a large part of the MSSM parameter space SM Higgs searches are effective to find the MSSM scalar Higgs bosons h or H . The SM discovery lines can be converted into MSSM discovery contours in the M_A - $\tan\beta$ plane. Figure 8 shows the results from CMS. In case we will discover a SM-like Higgs boson we will not be able to distinguish h from H_{SM} but in a large part of the parameter space, especially for large $\tan\beta$, it will be possible to detect also other MSSM Higgs bosons. On the other hand, in the decoupling region, it may be hard to disentangle the Standard Model from the MSSM.

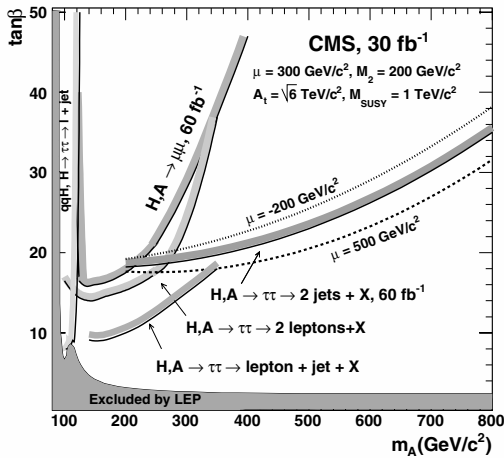


Fig. 9. CMS 5σ discovery regions for the channels $bb H, A \rightarrow bb\tau^+\tau^-$ and $bb H, A \rightarrow bb\mu^+\mu^-$.

3.2 Searches for H and A

For large $\tan\beta$ we can exploit the large cross section of Higgs boson production in association with a $b\bar{b}$ pair and search in the following channels:

- $bb H, A \rightarrow bb\tau^+\tau^-$
- $bb H, A \rightarrow bb\mu^+\mu^-$

One could also consider the $bb H, A \rightarrow bbbb$ channel but current studies show that the background is too large and that systematic errors are larger than the effect expected from the signal.

In all these channels b-tagging is the crucial issue but also τ identification and missing E_t measurement are important for the channels involving τ leptons.

In the $bb H, A \rightarrow bb\tau^+\tau^-$ channel all decay modes are used for high masses ($M_H > 400 \text{ GeV}/c^2$) while only the leptonic decays of at least one τ lepton are used for lower masses.

The channel $bb H, A \rightarrow bb\mu^+\mu^-$ has much lower rate ($\text{BR}(H \rightarrow \mu\mu) \sim 10^{-3}$) but the efficiency is higher and the Higgs boson masses are precisely measured with a resolution of about 1%.

Figure 9 shows the CMS 5σ discovery regions for these channels in the M_A - $\tan\beta$ plane.

3.3 Searches for Charged Higgs bosons

Charged Higgs boson with mass less than the mass of the top quark would be mainly produced in $t\bar{t}$ decays and within the MSSM $\text{BR}(H^\pm \rightarrow \tau\nu)$ is close to 100%. If M_{H^\pm} is larger the main production process would be $g\bar{b} \rightarrow tH^\pm$, $\text{BR}(H^\pm \rightarrow t\bar{b}) \sim 100\%$ for small $\tan\beta$ while $H^\pm \rightarrow t\bar{b}$ dominates but $\text{BR}(H^\pm \rightarrow \tau\nu)$ is still sizeable for large $\tan\beta$. The production cross section has been calculated at next to leading order [9]. ATLAS and CMS considered the cases of H^\pm mass lower and higher than $m_{t\text{top}}$; work is in progress in the mass region $M_{H^\pm} \sim m_{t\text{top}}$. The main search channel

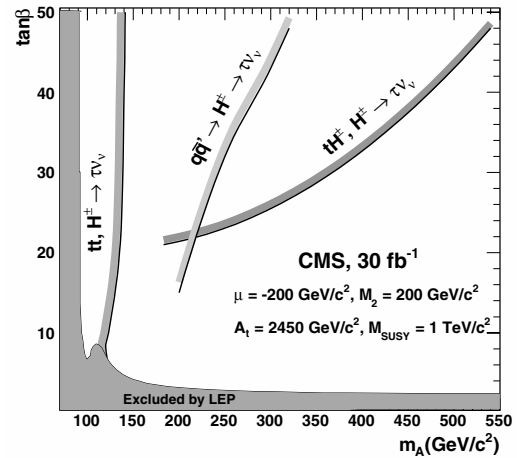


Fig. 10. CMS 5σ discovery potential for charged Higgs bosons in the $\tan\beta$ - M_A plane for maximal mixing.

is $H^\pm \rightarrow \tau\nu$, $H^\pm \rightarrow cs$ has a very large background and virtually no discovery sensitivity [10], as systematic errors are estimated to be larger than the signal contribution.

In the case of H^\pm production in top quark decays the main channel is $t\bar{t} \rightarrow bH^\pm bW \rightarrow b\tau\nu b\ell\nu$ but ATLAS also investigated $t\bar{t} \rightarrow b\tau\nu bqq$. In this case and in the case of high mass and tH^\pm final state, even if the H^\pm mass cannot be reconstructed, the transverse mass built from the τ -jet transverse energy and the missing E_t vector can be used. The background that is mainly due to W bosons has an endpoint at M_W while the signal distribution extends up to M_{H^\pm} .

Figure 10 shows CMS 5σ discovery potential for charged Higgs bosons for an integrated luminosity of 30 fb^{-1} .

3.4 MSSM scans

ATLAS studied the four CP conserving benchmarks suggested in reference [11], namely:

- M_h^{max} scenario, where the parameters are chosen in such a way that M_h is maximal ($< 133 \text{ GeV}/c^2$);
- No-mixing scenario, $M_h < 116 \text{ GeV}/c^2$;
- Gluophobic scenario, where the coupling to gluons is suppressed by means of cancellation of top-stop loops and this reduces the gluon-gluon fusion cross section;
- Small α scenario, where the coupling to bottom quarks and τ 's is suppressed for large $\tan\beta$, and $150 \text{ GeV}/c^2 < M_A < 500 \text{ GeV}/c^2$.

Figure 11 shows the 5σ discovery potential in ATLAS in the M_h^{max} scenario with an integrated luminosity of 30 fb^{-1} . We can see that the WBF channels allow the discovery of either h or H in almost all the parameter space [12]. The same result is obtained in the other three benchmark scenarios. Figure 12 shows the 5σ discovery regions for all MSSM Higgs bosons with ATLAS in the M_h^{max} scenario with an integrated luminosity of 300 fb^{-1} . We can see that all the plane is covered but there is a large area

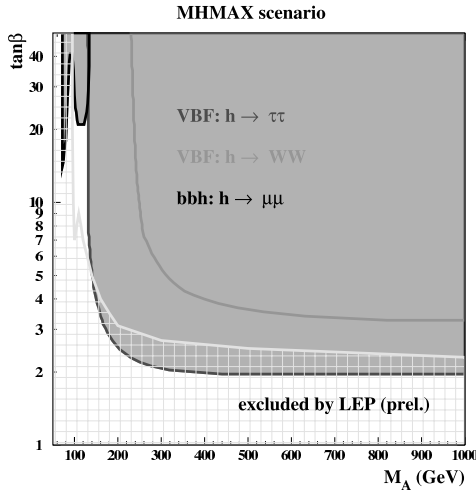


Fig. 11. ATLAS 5σ discovery potential of the WBF searches for h and H in the M_h^{\max} scenario with an integrated luminosity of 30 fb^{-1} .

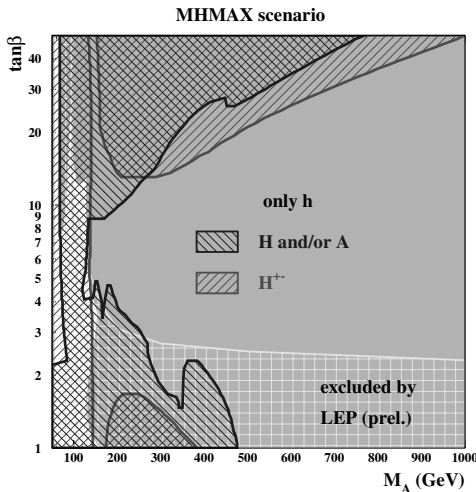


Fig. 12. ATLAS 5σ discovery potential of the WBF searches for all MSSM Higgs bosons in the M_h^{\max} scenario with an integrated luminosity of 300 fb^{-1} .

where only h can be detected. Again the results are similar in the other 3 benchmarks.

4 Measurement of Higgs bosons parameters

After discovering the Higgs bosons it will be possible to measure their parameters. Studies have been carried out by for high luminosity ($\int L dt = 300 \text{ fb}^{-1}$) and for the SM Higgs boson. The mass can be measured from direct reconstruction in the $H \rightarrow ZZ^*$, $H \rightarrow \gamma\gamma$ and Hbb channels or from a likelihood fit in the $H \rightarrow WW^*$ channel, the expected resolution from ATLAS is of the order of 1%. The width can be measured in the $H \rightarrow ZZ^*$ channel for $M_H > 200 \text{ GeV}/c^2$, when it is larger than the detector resolution. The Higgs couplings will be derived from the $\sigma \times \text{BR}$ measured in all channels where the Higgs boson will be seen [13].

5 Conclusions

ATLAS and CMS have studied in details the prospects of Higgs bosons discovery within the framework of the Standard Model and of the Minimal Supersymmetric Model. The SM Higgs boson can be discovered with 5 sigma with 10 fb^{-1} at low luminosity in the whole mass range, from $115 \text{ GeV}/c^2$ to $1 \text{ TeV}/c^2$. In the MSSM, at least one neutral Higgs boson can be found in all investigated scenarios but in some regions it would be difficult to discriminate between SM and MSSM.

Many other models have been studied by ATLAS and CMS: CP Violating MSSM, strongly interacting Higgs Sector, invisible Higgs decays and others. For details see reference [14] and the CMS physics TDR that is planned to be available before summer 2006.

We are now two years from the beginning of operation of the Large Hadron Collider. ATLAS and CMS are getting ready to perform real analyses based on data and that should make minimal use of MC information. Complete studies with full simulation of signal and of the main backgrounds are in progress.

Acknowledgments

I would like to thank F. Cerutti, A. Nikitenko and M. Schumacher for useful discussions.

References

1. LEP Higgs Working Group, Phys. Lett. **B565** (2003) 61; LEP Higgs Working Group, Searches for the Neutral Higgs Bosons of the MSSM, hep-ex/0107030; LEP Higgs Working Group, LHWG Note 2001-05.
2. Tevatron EW working group, hep-ex/0507091.
3. <http://lepewwg.web.cern.ch>.
4. A. Djouadi *et al.*, Comput. Phys. Comm. **108** 1998 56.
5. S. Abdullin *et al.*, CMS Note 2003/033.
6. Y.L. Dokshitzer *et al.*, in *Proceedings of the 6th International Conference on Physics in Collisions*, 1986.
7. D.L. Rainwater and D. Zeppenfeld, J. High Energy Phys. **12** (1997) 5. D.L. Rainwater and D. Zeppenfeld, Phys. Rev. **D60** (1999) 113004.
8. S. Asai *et al.*, Eur. Phys. J. **C32 S2** (2004) 19.
9. T. Plehn, Phys. Rev. **D67** (2003) 14.
10. S. Lowette *et al.*, CMS Note 2004/017.
11. M. Carena *et al.*, Eur. Phys. J. **C26** (2003) 601.
12. M. Schumacher, hep-ph/0410112, 2004.
13. M. Dührssen *et al.* CERN-PH-TH-2004-103.
14. ATLAS Collaboration, Physics TDR, CERN/LHCC/99-14 and CERN/LHCC/99-15.

Sensitivity to New Physics in the B-Sector

Michael Schmelling^a

MPI for Nuclear Physics, Saupfercheckweg 1, D-69117 Heidelberg

Abstract. Cosmological arguments suggest that physics beyond the Standard Model, so-called New Physics, is needed to explain the matter-antimatter asymmetry of the universe by providing extra sources of CP-violation. Precision measurements of CP-violation and rare decays in the B -sector offer a very promising way to detect such contributions. After an introduction to the basic phenomenology of CP-violation measurements, the generic signatures for New Physics are presented. Finally some of the current results from the B-factories and the prospects for LHC are discussed.

1 Introduction

Experimental evidence suggests that all hadronic matter of the universe, up to the most distant galaxies, is made of matter rather than antimatter. Neither are significant amounts of annihilation radiation observed, as would be expected from the boundary between matter- and antimatter dominated regions, nor have studies of cosmic rays found any evidence for primordial anti-Helium left over from the Big Bang. This is a very surprising result, since in the Big Bang matter and antimatter were initially created in equal amounts.

The necessary conditions to explain the matter dominance of the universe were first outlined by Sakharov [1]. He showed that the fundamental interactions require C- and CP-violation, baryon-number violation and that the universe must have passed through a phase of thermal non-equilibrium. In principle all these ingredients are realized in Standard Model (SM) based Big Bang cosmology: C- and CP-violation exist in the CKM-sector of the Standard Model, and baryon-number violation via sphalerons can occur during a first order phase transition in the early universe.

Unfortunately, quantitative calculations show that the SM-Higgs particle is too heavy to generate the required phase transition. In addition, the amount of CP-violation is too small to explain the matter dominance of the universe. The fact that extra sources of CP-violation are needed suggests to look for signs of New Physics (NP) in precision measurements of CP-violation. Here the B -sector offers the highest sensitivity.

2 CP-Violation Measurements

CP-violation is conveniently measured by a so-called CP-asymmetry, A_{CP} , which for an initial state x decaying into

a final state y is defined through

$$A_{\text{CP}} = \frac{\Gamma(x \rightarrow y) - \Gamma(\bar{x} \rightarrow \bar{y})}{\Gamma(x \rightarrow y) + \Gamma(\bar{x} \rightarrow \bar{y})}. \quad (1)$$

The quantities $\Gamma(\cdot) = |a(\cdot)|^2$ denote the partial widths, and $a(\cdot)$ the corresponding decay amplitudes. An important class are mixing-induced asymmetries of decays into a CP-eigenstate $y = \bar{y} = y_{\text{CP}}$. Here the final state can be reached in two ways: either by direct decay with amplitudes $a_D(x \rightarrow y_{\text{CP}})$ and $\bar{a}_D(\bar{x} \rightarrow y_{\text{CP}})$, or by mixing transitions with amplitudes $i a_M(x \rightarrow \bar{x})$ and $i \bar{a}_M(\bar{x} \rightarrow x)$ and subsequent decay. Introducing also the non-mixing amplitudes $a_N(x \rightarrow x)$ and $\bar{a}_N(\bar{x} \rightarrow \bar{x})$, one has

$$a(x \rightarrow y_{\text{CP}}) = a_N \cdot a_D + i a_M \cdot \bar{a}_D \quad \text{and} \\ a(\bar{x} \rightarrow y_{\text{CP}}) = \bar{a}_N \cdot \bar{a}_D + i \bar{a}_M \cdot a_D.$$

The generic forms for the contributing amplitudes are $a_N = \cos(\Delta mt/2)$, $a_M = \sin(\Delta mt/2)e^{i\phi}$ and $a_D = Ae^{i\omega}$, complex conjugation yields $\bar{a}_{N,M,D}$. The term Δm in the mixing amplitudes is the mass difference of the mass eigenstates, ϕ and ω are the mixing and decay phases, respectively. Substituting these expressions one obtains

$$A_{\text{CP}} = -\sin(\Delta mt) \sin(\phi - 2\omega). \quad (2)$$

Note that the possibility of a CP-asymmetry in mixing induced modes arises only because the factor i in front of the mixing amplitudes makes $a(\bar{x} \rightarrow y_{\text{CP}}) \neq \bar{a}(x \rightarrow y_{\text{CP}})$. This is an example of the general case that in order for a CP-asymmetry to arise, there has to be a phase which is not affected by charge conjugation. Such a phase can also come, for example, from strong interactions, which then allows to observe CP-violation also in charged B -decays.

Finally it should be mentioned that a time dependence proportional to $\sin(\Delta mt)$ in mixing-induced CP-violation is not the only possibility. In addition, there can also be contributions from direct CP-violation, which would add a term proportional to the time dependence of particle

^a *LHCb Collaboration*

propagation without mixing, $\cos(\Delta mt)$. Usually the phenomenology will therefore be much richer than the simple example discussed above, providing many observables which are sensitive to phases from the Standard Model and beyond.

3 CKM-Matrix and Unitarity Triangle

Within the Standard Model the phases ϕ and ω in eq.(2) arise only from the CKM-matrix [2] elements describing the weak charged current coupling to the different quark flavours

$$V = \begin{pmatrix} V_{ud} & V_{us} & V_{ub} \\ V_{cd} & V_{cs} & V_{cb} \\ V_{td} & V_{ts} & V_{tb} \end{pmatrix}. \quad (3)$$

The matrix V is unitary, with in general complex valued matrix elements. Since absolute phases do not affect the physics, as is illustrated by the fact that A_{CP} in eq.(2) is only a function of phase differences, there is the possibility to select a phase convention for V for which the underlying physics becomes most transparent. This is exploited by the Wolfenstein parameterization of the CKM matrix [3]

$$V = \begin{pmatrix} 1 - \lambda^2/2 & \lambda & A\lambda^3(\rho - i\eta) \\ -\lambda & 1 - \lambda^2/2 & A\lambda^2 \\ A\lambda^3(1 - \rho - i\eta) & -A\lambda^2 & 1 \end{pmatrix} + \mathcal{O}(\lambda^4). \quad (4)$$

The expansion parameter λ is the sine of the Cabibbo angle $\sin\theta_C \approx 0.22$, the parameters A, ρ and η are of order unity. The weak couplings within one generation are of $\mathcal{O}(1)$, between different generations they are of $\mathcal{O}(\lambda)$, $\mathcal{O}(\lambda^2)$ and $\mathcal{O}(\lambda^3)$, for transitions $1 \leftrightarrow 2$, $2 \leftrightarrow 3$ and $1 \leftrightarrow 3$, respectively. This hierarchy is directly related to the mass-hierarchy of the different quarks, since for a degenerate mass spectrum the CKM-matrix would reduce to the unit matrix. In other words, precision measurements in the CKM sector are complementary to the Higgs-search in addressing the problem of the origin of particle masses.

The formal criterion for V being a unitary matrix is that the scalar product of two rows or two columns satisfies $R_i \cdot R_j^* = C_i \cdot C_j^* = \delta_{ij}$. Each scalar product being a sum of three complex numbers, the case $i \neq j$ can be visualized as triangle in the complex plane. To the accuracy of eq.(4) only $C_1 \cdot C_3^*$ yields a non-degenerate triangle, the so-called Unitarity Triangle (UT). In the Wolfenstein parameterization eq.(4), the UT-angles are directly related to the phases of certain CKM-matrix elements: $\arg(V_{td}) = -\beta$, $\arg(V_{ub}) = -\gamma$. These matrix elements play a role for example in B_d -mixing (V_{td}) and in $B_d \rightarrow \pi^+\pi^-, \rho^+\rho^-$ -decays (V_{ub}). Including the next higher order term into eq.(4) one also picks up a phase in the matrix element V_{ts} which is relevant for B_s -mixing. It is given by $\arg(V_{ts}) \equiv \chi + \pi \approx \eta\lambda^2 + \pi$.

4 Probing New Physics

There are several strategies for finding New Physics in B -meson decays. One approach is to measure Standard

Model parameters, such as for example the angles of the Unitarity Triangle, both in processes which are insensitive to New Physics and in decay channels that can have NP contributions. Any discrepancy between the results would point to New Physics. Another ansatz is the study of observables which have a very small expectation value in the Standard Model. Any enhancement due to New Physics thus would be clearly noticeable. Examples for these two scenarios will be discussed below. Finally, a third possibility is the comparison of UT-angles extracted from CP-asymmetries with those from a measurement of the sides of the triangle. Incompatible results would again be indicative of physics beyond the Standard Model.

4.1 The Decay $B_d \rightarrow \phi K_s$

Figure (1) illustrates how in the Standard Model B_d -mixing is induced through second order weak transitions. From the Wolfenstein parameterization one sees that in this case the mixing phase comes from V_{td}^* , which appears twice and thus generates an overall phase of $\phi_d = 2\beta$. The dominant tree level decay into $J/\Psi K_s$ depicted in fig.(2) picks up no additional phase factor. It follows that the CP-asymmetry of the so called ‘‘golden decay’’ $B_d \rightarrow J/\Psi K_s$ measures $\sin(2\beta)$.

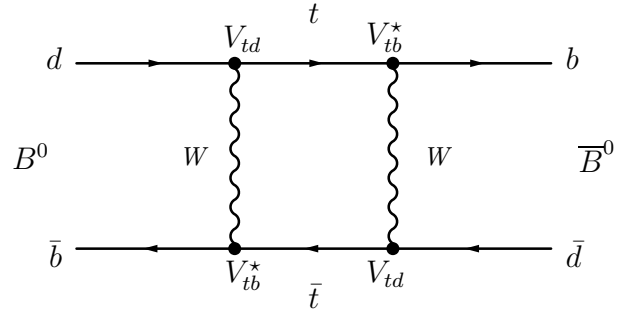


Fig. 1. Feynman-diagram describing B_d -mixing through a second order weak process

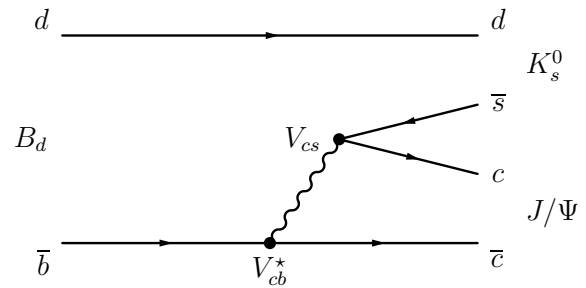


Fig. 2. Feynman diagram for the ‘‘golden decay’’ $B_d \rightarrow J/\Psi K_s$

The situation is different for the decay $B_d \rightarrow \phi K_s$ shown in fig.(3), which in the Standard Model to leading

order is mediated by a QCD penguin. Like the “golden decay”, this process does not pick up additional weak phases in the decay and its CP-asymmetry should also measure $\sin(2\beta)$.

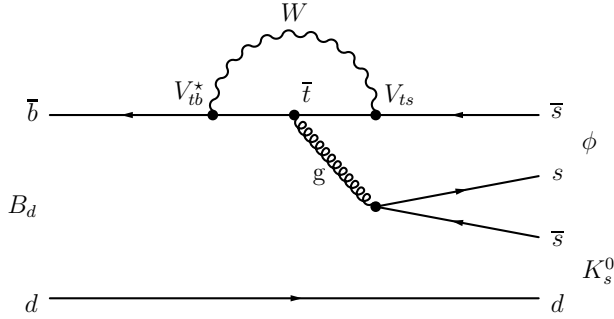


Fig. 3. Penguin decay of $B_d \rightarrow \phi K_s$

However, New Physics could contribute in many conceivable ways to the penguin loop. Several examples are sketched in fig.(4). In addition to the Standard Model W , there could be charged Higgs particles in the loop, as would be expected in the minimal supersymmetric extension of the Standard Model (MSSM). Substituting the W by a gaugino or gluino, one can even have purely supersymmetric loops. Since most of the new particles are expected to provide extra phases to the decay, a measurement of $\sin(2\beta)$ from $B_d \rightarrow \phi K_s$ could be significantly different from the result found in the “golden decay”. Early results from the B -factories showed evidence for this scenario, although the initial discrepancies were so large that most of the more plausible models for New Physics failed to reproduce the measurement. In the meantime, and with much improved statistical precision, the experiments have moved close to the Standard Model expectation.

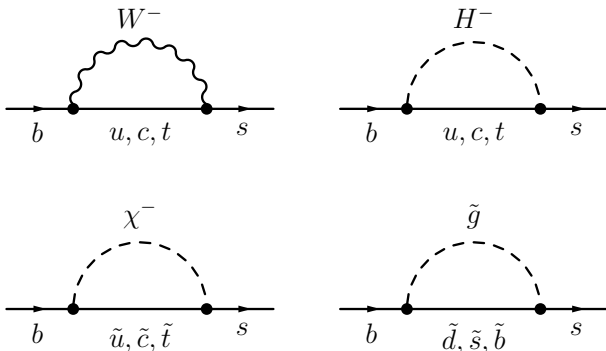


Fig. 4. Possible contribution from New Physics to a Standard Model loop (upper left) in penguin decays.

4.2 The Decay $B_s \rightarrow J/\Psi\phi$

Another interesting decay channel is the analog of the “golden decay” in the B_s system. The $J/\Psi\phi$ final state is obtained from fig.(2) by substituting the d -quark with an s -quark. In the same way as the “golden decay” measures the B_d -mixing phase, therefore $B_s \rightarrow J/\Psi\phi$ measures the B_s -mixing phase ϕ_s . It is close to zero in the Standard Model, but can adopt large values in alternative theories. For example, with supersymmetric particles in the box diagrams describing B_s -mixing, one can have values $\sin \phi_s \sim 1$ [4]. Given the existence of a new up-type quark singlet, one would naturally expect $\sin \phi_s \sim \lambda$ [5].

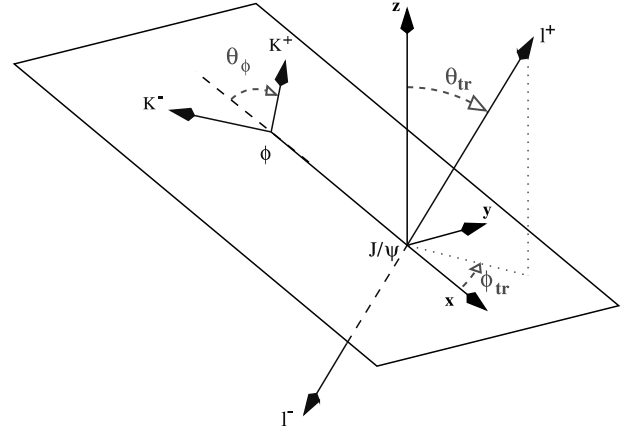


Fig. 5. Definition of decay angles in the process $B_s \rightarrow J/\Psi\phi$

In contrast to the case of the “golden decay”, the situation is complicated by the fact that the $J/\Psi\phi$ final state consists of two CP-odd vector bosons and thus is no CP-eigenstate. Still, the CP-even $A_0, A_{||}$ and the CP-odd components A_{\perp} can be disentangled by an angular analysis

$$\frac{d\Gamma}{dc} \propto [|A_0|^2 + |A_{||}|^2] \frac{3}{8}(1+c^2) + |A_{\perp}|^2 \frac{3}{4}(1-c^2)$$

with $c = \cos \Theta_{tr}$. Figure (5) illustrates how the transversity angle Θ_{tr} is defined as the angle between the direction of the leptons from the decay $J/\Psi \rightarrow \mu^+\mu^-$, measured in the J/Ψ rest frame, and the normal to the decay plane spanned by the decay products of the ϕ meson. Alternative decay channels which probe the same physics but are much more difficult to reconstruct experimentally are $B_s \rightarrow J/\Psi\eta$ and $B_s \rightarrow \eta_c\phi$. The fact that in both cases the final state is a CP-eigenstate at least simplifies the CP-analysis.

4.3 FCNC Processes and Rare Decays

In the Standard Model, Flavour Changing Neutral Current (FCNC) processes can arise only through higher order weak transitions and in addition often are GIM suppressed. As a consequence the study of FCNC processes

is a promising field to look for enhancements due to New Physics. A process that has already been observed is the decay $B \rightarrow K^* \gamma$, which to leading order proceeds through the diagram shown on the left-hand side of fig.(6) when the emitted photon is on-shell and does not convert into a lepton pair. The generic Standard Model prediction for CP-asymmetries in this type of decays is around 1 percent or below. On the other hand, New Physics with an enhanced chromomagnetic dipole operator in the effective $bs\gamma$ -vertex could cause large CP-asymmetries [6].

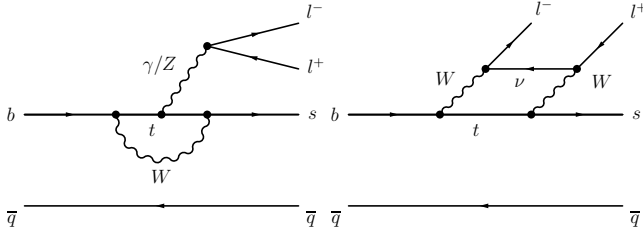


Fig. 6. Generic diagrams contributing to the FCNC decay $B \rightarrow \mu^+ \mu^- X$, where X is the hadronic final state from the $s\bar{q}$ -system.

Even more interesting are the decays $B \rightarrow \mu^+ \mu^- X$ depicted in fig.(6), with, for example, $X = K^*, \rho, \phi$. In addition to the electromagnetic penguin which mediates $B \rightarrow K^* \gamma$, one has contributions from a weak penguin and from box diagrams, which lead to a much richer phenomenology. For example, the Z -boson in the weak penguin could be replaced by an extra heavy Z' , or, like in the case of mixing diagrams, supersymmetric particles could contribute to the box graphs.

Also from the experimental point of view the study of FCNC processes of the type $B \rightarrow \mu^+ \mu^- X$ is very attractive, since the generic signature of a detached vertex with two muons is very clean. Selecting specific final states X , such as $X = K^* \rightarrow K^- \pi^+$, allows further background suppression. From the theory point of view inclusive measurements which integrate over all final states X are preferred, but also for exclusive final states the Standard Model prediction is rather reliable. This is particularly true for ratios, such as the forward-backward asymmetry A_{FB} of the final state muons with respect to their combined momentum, which is shown in fig.(7) as a function of the square of the di-muon invariant mass, s . One clearly sees the contributions from the J/Ψ and the Ψ' on top of a non resonant background. For the latter, the Standard Model predicts a zero crossing in A_{FB} at a value $s \approx 3 \text{ GeV}^2$, whereas supersymmetry naturally expects no change of sign.

Via crossing symmetry and allowing to substitute the s -quark by a d -quark, the $b \rightarrow s$ transition in the diagrams of fig.(6) also describes the rare decays $B_{d,s} \rightarrow \mu^+ \mu^-$. These decays are experimentally very clean, and in the presence of New Physics could be significantly enhanced. For example, given the ratio $\tan \beta$ of the vacuum expectation values of the two Higgs doublets in the MSSM, an enhancement proportional to $\tan^6 \beta$ is expected.

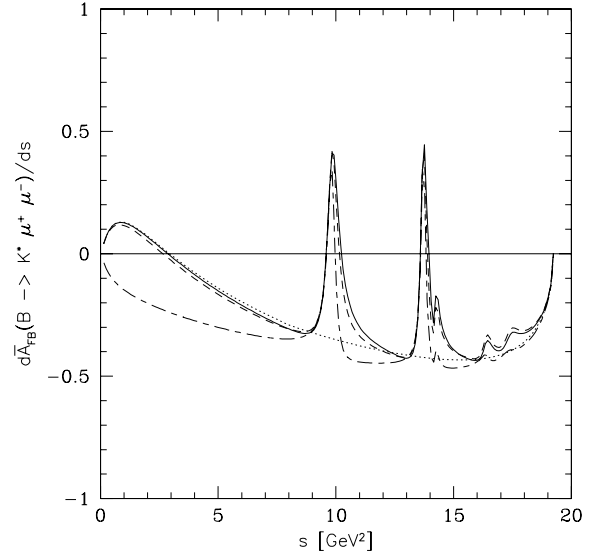


Fig. 7. Forward-Backward asymmetry in $B_d \rightarrow K^* \mu^+ \mu^-$ decays [7]. The solid line shows the Standard Model prediction, the long-dashed line is the generic expectation in supersymmetric theories.

5 Experimental Constraints on New Physics

Apart from providing a highly successful description of the fundamental interactions between all elementary particles, the Standard Model also defines the starting point in any search for New Physics. Therefore, in a phenomenological approach the generic form of a Lagrangian containing New Physics can be written as

$$\mathcal{L} = \mathcal{L}_{SM}^{\text{Higgs}} + \mathcal{L}_{SM}^{\text{gauge}} + \mathcal{L}_{SM}^{\text{Yukawa}} + \frac{1}{\Lambda} \mathcal{L}^{(5)} + \frac{1}{\Lambda^2} \mathcal{L}^{(6)} + \dots$$

The NP terms proportional to $\mathcal{L}^{(5)}$ would contribute for example to $(g-2)$ or to $b \rightarrow s \gamma$ penguin decays, terms from $\mathcal{L}^{(6)}$ could show up in FCNC processes. An analysis to extract New Physics contributions from deviations to the Standard Model could either start from a specific NP model and determine masses and coupling constants for this particular model, or be performed in a model independent way. Here the observed deviations are interpreted in terms of generic NP operators and allow to extract the scale Λ where NP starts to contribute. From precision measurements in the B -system one expects sensitivities for Λ in the range from a few-100 GeV up to a few TeV, i.e. very similar to the sensitivity of direct searches at LHC.

A first flavour of the quality of results that can be expected at LHC can already be obtained from current measurements at the B -factories. Figure (8) shows one example from the combination of two measurements, the ratio $|V_{ub}/V_{cd}|$ measured in semileptonic B -decays, and a first measurement of the UT-angle γ from tree-level dominated $B^\pm \rightarrow D^{0*} K^\pm$ decays. These two results do already significantly constrain the position of the apex of the Unitarity Triangle, giving one solution [8] for $\sin 2\beta = 0.724 \pm 0.074$, which is perfectly consistent with the world average [9]

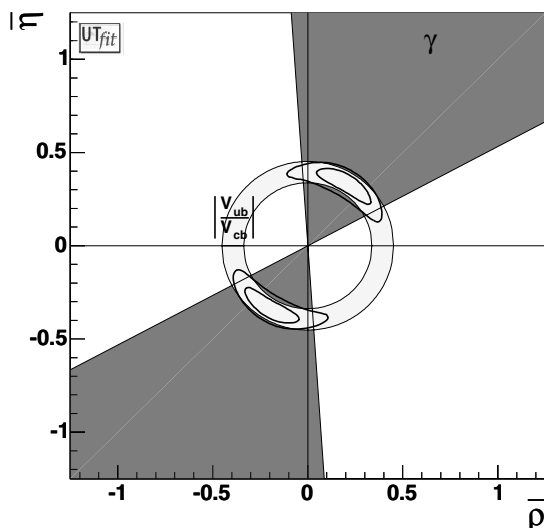


Fig. 8. Determination of the apex of the Unitarity Triangle from tree-level dominated measurements.

from the “golden decay” $\sin 2\beta = 0.69 \pm 0.03$. Assuming that the tree level processes contributing to the measurements in fig.(8) are unaffected by New Physics, then NP contributions in B_d -mixing can only be large if they have the same phase as the SM terms. Otherwise the limit is $\sim 10\%$ [10]. It follows, that New Physics is either of the type “Minimal Flavour Violation”, i.e. it does not contribute new phases w.r.t. the CKM-sector, or that new CP-violating effects are limited to the B_s -sector.

Another interesting compilation [9] is shown in fig.(9). Here results from different CP-asymmetries sensitive to $\sin 2\beta$ ($\sin 2\phi_1$ in the Belle-nomenclature) are collected and compared to the world average from $B_d \rightarrow J/\psi K_s$. Although generally compatible with each other and the global average, the results all tend to lie below the average. Since the different channels are affected differently by New Physics or higher order SM corrections, straight averaging may not be appropriate to combine these numbers into one more precise figure. On the other hand, independently of any details in the underlying physics and assuming that the true value is the same in all cases, the probability that from a total of 14 measurements at most two results fluctuate above the world average is only $p \approx 0.0065$.

6 B-Physics at LHC

At the Large Hadron Collider, LHC, B -physics will be studied with two general purpose detectors ATLAS [11] and CMS [12], and a dedicated B -physics experiment, LHCb [13]. The former two are designed for high luminosity running and provide hermetic coverage, which is essential for Higgs and SUSY discovery. The LHCb detector is a single arm forward spectrometer, optimized for the requirements of B -physics. At LHC-energies these are characterized by the fact that $b\bar{b}$ -pairs created in pp -collisions are preferentially emitted under small angles rel-

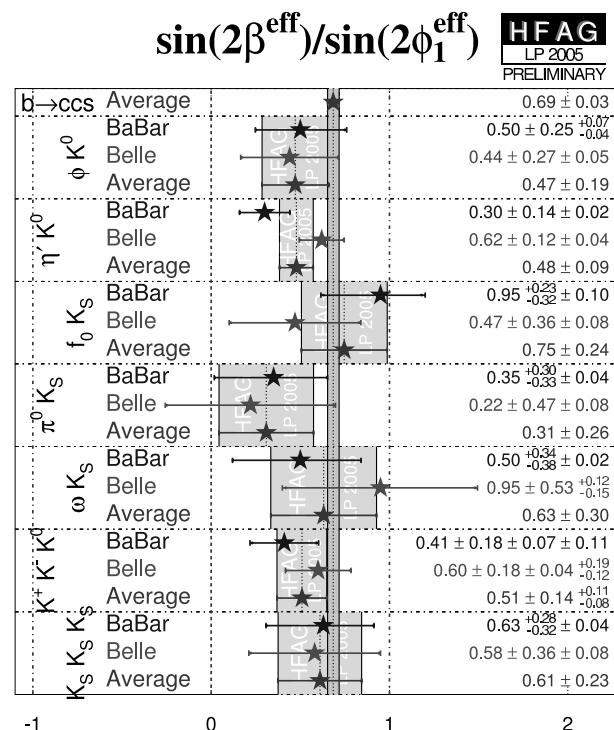


Fig. 9. CP-asymmetries $\sin 2\beta^{\text{eff}}$ from different decay channels sensitive to $\sin 2\beta$ in comparison to the world average from the “golden decay”.

ative to the beam direction. Since in most cases both quarks go into the same hemisphere, a single arm spectrometer offers a cost-effective way to cover the relevant phase space. At LHC the b -cross section is expected to be $\sigma_b = 0.5$ mb. This is around 0.5% of the total cross section, i.e. LHC is a genuine B -factory. Already at a luminosity of $\mathcal{L} = 2 \cdot 10^{32} \text{cm}^{-2} \text{s}^{-1}$, the nominal operating point of LHCb, which can be adjusted independently of the other experiments, b -events are produced at a rate of 100 kHz. This results in a total of $2 \cdot 10^{12}$ B -hadrons per nominal year of running. ATLAS and CMS are expected to operate initially at $\mathcal{L} = 10^{33} \text{cm}^{-2} \text{s}^{-1}$ before going up to the design luminosity of $\mathcal{L} = 10^{34} \text{cm}^{-2} \text{s}^{-1}$.

The phase space coverage of these experiments is shown in fig.(10). LHCb can measure down to $p_T = 2$ GeV and thereby, despite its small angular coverage $1.9 < \eta < 4.9$, has access to a visible b -cross section $\sigma_b = 230 \mu\text{b}$. In contrast, ATLAS and CMS cover the central range $|\eta| < 2.5$ but will operate at higher luminosities and thus have to raise the p_T -threshold to values around 10 GeV in order to achieve sufficient background reduction.

The trigger of LHCb is sensitive to both leptonic and hadronic B -decays, with a logging rate of 200 Hz for exclusive B -candidates, 600 Hz for high mass di-muon pairs, 300 Hz for D^* candidates and 900 Hz for an inclusive b -trigger using single high- p_T leptons. The other LHC experiments will do B -physics mainly by exploiting a high- p_T muon trigger, with an expected logging rate around 10 Hz. The large p_T -threshold and the focus on final states with muon pairs is necessary to get rid of QCD background. Typical examples for the B -physics program of

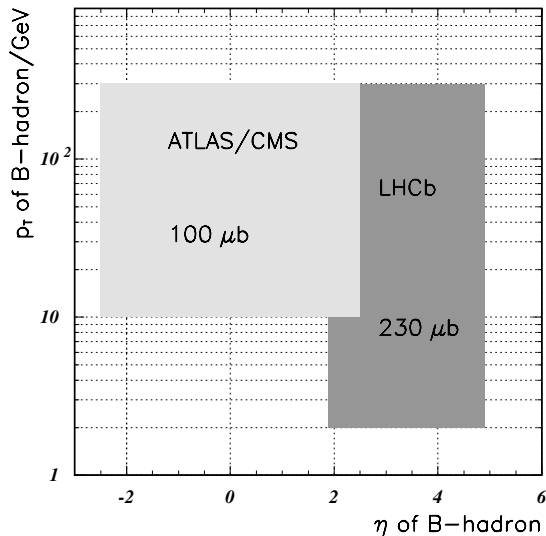


Fig. 10. Phase space coverage of the LHC experiments for B -physics

ATLAS and CMS therefore are measurements of $\sin 2\beta$ in the “golden decay” $B_d \rightarrow J/\Psi K_s$, or studies of the FCNC processes $B_d \rightarrow \mu^+\mu^-X$, with $X = K^*\rho, \phi$, and rare decays such as $B_{d,s} \rightarrow \mu^+\mu^-$. In this kind of reactions the large detectors can be expected to be competitive with LHCb.

Table (1) illustrates how many signal events are expected by the various experiments for one nominal year of running, corresponding to an integrated luminosity of 2fb^{-1} for LHCb and 100fb^{-1} for ATLAS and CMS. The numbers show how the potential advantage of being able to run at high luminosities is lost to a large extent by the requirement to fight the background.

Studies by the LHCb collaboration indicate that with two years of nominal running the zero crossing in the forward-backward asymmetry shown in fig.(7) for $B_d \rightarrow K^*\mu^+\mu^-$ can be determined with an error $\Delta s(\mu^+\mu^-) \sim 1 \text{ GeV}^2$. This would be highly significant to distinguish between the Standard Model and alternative, supersymmetric, theories.

Using the particle identification capabilities provided by the two RICH detectors, the calorimeters and the muon system, LHCb will be able to measure precisely also purely hadronic B -decays. It will thus provide precision measurements for many interesting decay channels both in the B_d - and the B_s -system, and by over-constraining the Standard Model can be expected to narrow down and hopefully find New Physics.

A measurement which illustrates the importance of precise vertexing for a B -experiment is B_s -mixing. While ATLAS and CMS have sensitivity up to $\Delta m_s \sim 30\text{ps}^{-1}$, LHCb will be able to explore oscillation rates up to $\Delta m_s \sim 68\text{ps}^{-1}$ [14]. If the Standard Model is correct, then a measurement of Δm_s should be within reach for all LHC experiments. If, however, New Physics induces much faster oscillations in the B_s -system, then only LHCb may be able to find them.

Table 1. Expected SM event yields for some FCNC processes and rare decays at LHC after one nominal year of running.

Decay channel	BR(SM)	ATLAS	CMS	LHCb
$B_d \rightarrow K^*\mu^+\mu^-$	$1.5 \cdot 10^{-6}$	6650	—	4400
$B_d \rightarrow \rho\mu^+\mu^-$	10^{-6}	740	—	—
$B_d \rightarrow \phi\mu^+\mu^-$	10^{-7}	1370	—	—
$B_d \rightarrow \mu^+\mu^-$	$1.5 \cdot 10^{-10}$	14	4	3
$B_s \rightarrow \mu^+\mu^-$	$3.5 \cdot 10^{-9}$	92	26	17

7 Summary

B -Physics is an excellent field to look for New Physics in a way which is complementary to direct searches for supersymmetric particles or other kinds of new particles at high energies. The rich phenomenology of B -decays allows to overconstrain the CKM-matrix and, by comparing tree level dominated measurements which are expected to be well described within the Standard Model to penguin- or box-dominated processes, to establish the existence of New Physics. Exploiting the fact that different processes are related at the fundamental level will then also permit to pin down the nature of these NP contributions.

The general purpose detectors ATLAS and CMS, designed to operate at high luminosities, are expected to contribute to the B -physics program at LHC by studies of rare decay processes and measurements of muonic final states. LHCb on the other hand, which is optimized for B -physics, will in addition be able to measure with high precision also purely hadronic decays. The comparatively low nominal running luminosity will enable LHCb to exploit its full physics potential essentially from day-one of LHC operations.

References

1. A.D. Sakharov, JETP Lett.**5** (1967) 24-27.
2. M. Kobayashi and K. Maskawa, Prog. Theor. Phys. **49**, (1973) 652.
3. L. Wolfenstein, Phys. Rev. Lett. **51**, (1983) 1945.
4. P. Ball et al., hep-ph/0311361.
5. J.A. Aguilar-Saavedra et al., hep-ph/0406151.
6. G. Hiller, hep-ph/0008092.
7. A. Ali et al., Phys. Rev. D **61**, (2000) 074024.
8. <http://utfit.roma1.infn.it/>;
UTfit Collaboration, hep-ph/0501199;
F.J. Botella et al., hep-ph/0502133.
9. Heavy Flavour Averaging Group,
<http://www.slac.stanford.edu/xorg/hfag/triangle/summer2005>.
10. L. Silvestrini, Lepton-Photon 2005, Uppsala.
11. ATLAS Letter of Intent, CERN/LHCC/92-4;
ATLAS Technical Proposal, CERN/LHCC/94-43;
<http://atlas.web.cern.ch/Atlas/GROUPS/PHYSICS/TDR/access.html>.
12. CMS Letter of Intent, CERN/LHCC 92-3;
CMS Technical Proposal, CERN/LHCC 94-38.
13. LHCb Letter of Intent, CERN/LHCC 95-5;
LHCb reoptimized TDR, CERN/LHCC 2003-030.
14. R. Forty, these proceedings.

Heavy Ions

Nucleus-nucleus and proton-nucleus collisions at the LHC

Urs Achim Wiedemann

¹ Department of Physics, CERN, Theory Division, CH-1211 Geneva 23

² Physics Department, University of Bielefeld, D-33501 Bielefeld, Germany

Abstract. I review shortly the perspectives for studying QCD matter at the highest density, arising with the heavy ion program at the LHC.

1 Introduction

In two years from now, the Large Hadron Collider at CERN will start operation. The study of the properties of QCD matter at the highest attainable energy densities or temperatures in nucleus-nucleus collisions is an integral part of its experimental program [1–3]. There are essentially three major motivations for studying nucleus-nucleus collisions at this high-energy frontier.

1. *For nucleus-nucleus collisions, as for proton-proton collisions, LHC is a discovery regime.*

My discussion will focus mainly on those novel phenomena in nucleus-nucleus collisions at the LHC, which follow rather directly from our understanding and extrapolation of RHIC data on Au+Au collisions up to $\sqrt{s_{NN}} = 200$ GeV. However, before narrowing the discussion to specific examples, one should recall that the search at the LHC is much wider than what can be covered in this talk: Nucleus-nucleus collisions at the LHC will be performed at a 30 times higher center of mass energy than what could be reached at RHIC. Historical experience indicates that such a big jump in energy is often accompanied by major discoveries and surprises. This in itself is a strong motivation for a broad search. For instance, the much-discussed phenomenon of perturbative saturation may result in a radical change of the properties of the produced dense QCD matter at 30 times higher incident energy. This would affect essentially all phenomena of soft and high- p_T hadron production [4–6] and could be disentangled from other dynamical origins in a dedicated proton-nucleus run. Also, many other dramatic proposals await an experimental test. For instance, it has been suggested that strong parity or CP violation, on which we have a tight experimental bound at zero temperature, may be visibly enhanced in hot and dense matter where tunneling between Θ -vacua may become easier [7, 8]. Clearly, the search is much wider than the specific avenues of exploration which I discuss now.

2. *At the LHC, a large number of precision tools will become newly available for establishing the properties of high-density QCD matter:*

Nucleus-nucleus collisions at RHIC have established that

dense QCD matter strongly modifies the distribution of particles produced in processes involving large momentum transfers [1–3, 12]. This is seen in the strong suppression of single inclusive high- p_T hadron spectra, in their centrality dependence and in their dependence on the orientation with respect to the reaction plane, as well as in back-to-back two-particle correlations and in the characterization of jet-like structures such as the hadron production associated to high- p_T trigger particles. Most generally, RHIC experiments have demonstrated that the strong sensitivity of these *hard probes* provides a wide variety of techniques for the detailed and controlled characterization of the properties of dense QCD matter [1–3, 12]. From RHIC to the LHC, the 30 times increase in center of mass energy does not only enhance the yield of essentially all hard processes (jets, heavy quark and quarkonium, high- p_T , photons, Z 's etc.) by an order of magnitude or more. It also implies that hard probes are embedded in a possibly qualitatively novel dense QCD environment and will be experimentally accessible over a much wider kinematic range in Q^2 . As discussed below, this opens many novel opportunities (for more details, see also the CERN Yellow Report on hard probes in heavy ion collisions at the LHC [1, 13–15]).

3. *Conditions for producing and studying sizeable amounts of dense QCD matter improve significantly at the LHC:*

Higher center of mass energies lead to the production of QCD matter at higher initial densities [17]. As a consequence, one either expects at the LHC a significantly longer lifetime of the produced dense matter and, due to expansion, a larger volume over which this matter is spread. Alternative model scenarios indicate that the higher initial density may drive a more explosive dynamical evolution, thereby leading to dense matter of relatively short lifetime, but exhibiting significantly stronger collective effects [18, 19]. The first data from the LHC will distinguish between such radically different scenarios. But irrespective of which dynamical scenario is realized at LHC, the conditions for studying the properties of QCD matter at the highest density are expected to be improved significantly, either because the increased strength of collective

phenomena allows us to study their dynamical origin in much more detail, or because the substantially increased lifetime of the system provides for their manifestation in experimentally more accessible and possibly qualitatively novel ways.

2 Collective phenomena at RHIC and open questions

In heavy ion collisions at all center of mass energies, one observes a pronounced asymmetry of particle production with respect to the azimuthal orientation $\varphi - \Psi_R$ to the reaction plane. The strength of this asymmetry is characterized by the coefficients v_n in the azimuthal composition of single inclusive hadron spectra

$$E \frac{d^3 N}{d^3 p} = \frac{1}{2\pi} \frac{d^2 N}{p dp dy} \left(1 + \sum_{n=1}^{\infty} 2v_n \cos[n(\varphi - \Psi_R)] \right). \quad (1)$$

The *qualitative* features of the observed asymmetries are roughly consistent with a hydrodynamic picture of the collision. At low fixed target energies ($E_{\text{beam}} = 2 - 4$ GeV), particle production is enhanced in the direction orthogonal to the reaction plane, and v_2 is negative. This is due to the effect that the spectator parts of the nuclei block the matter in the direction of the reaction plane and 'squeeze' it out in the opposite direction. At higher center of mass energies, these spectator components free the way sufficiently quickly and particle production is enhanced in the reaction plane. The result is a positive value of the elliptic flow coefficient v_2 , see Fig. 1. This phenomenon is expected in hydrodynamic scenarios in which the larger pressure gradients within the reaction plane drive a stronger expansion [20].

One of the first discoveries at RHIC is, that the observed asymmetry v_2 does not only maintain its strength but continues to grow up to the highest center of mass energies. This contradicts the naive picture inspired by asymptotic freedom, that interactions within the produced matter should be weaker at higher $\sqrt{s_{NN}}$, and should thus give rise to weaker collective motion. Rather, Fig. 1 suggests that the effective interaction between the partonic constituents of the produced matter increases with increasing $\sqrt{s_{NN}}$. This is argued to support the notion of a strongly interacting liquid [21].

However, the *quantitative* comparison of hydrodynamic simulations with experimental data raises important questions. First, at fixed target energies, simulations of the dynamical evolution based on ideal hydrodynamics overpredict the data significantly, see Fig. 1b. Second, at RHIC, the overall strength of v_2 agrees indeed for the first time with simulations based on ideal hydrodynamics and a realistic equation of state. However, attempts to base the success of such hydrodynamic simulations on a consistent microscopic model of partonic interactions have failed so far, since they require anomalously enhanced (by a factor 5 or more) partonic cross sections [22]. This is sometimes viewed as support for a strongly interacting liquid, but

it also emphasizes that we are lacking an understanding of the dynamical origin of hydrodynamic behavior. Moreover, Fig. 1b casts doubt on the validity of a hydrodynamical description of nucleus-nucleus collisions at RHIC energies. Indeed, data and simulation agrees for v_2 at the highest charged particle rapidity density, which is attained in almost central collisions. However, deviations at lower centrality are significant, and the approximately linear dependence on rapidity density may be viewed as a trend which deviates qualitatively from hydrodynamics-based expectations (see Fig. 1b). One of the very first results at the LHC will be to extend Fig. 1b to higher rapidity densities, thereby testing whether a hydrodynamics-based quantitative explanation of collective behavior can be maintained indeed at collider energies.

But there is a large set of more refined questions to be asked in this context: Are there independent tests of strong collective flow in the produced dense QCD matter, which can help us to substantiate or falsify the notion of a strongly interacting liquid? Can we access the microscopic dynamics underlying this generic flow phenomenon, or can we determine at least major aspects of it, such as the effective interaction strength seen by typical partonic constituents in the produced matter? Can we establish from this collective phenomenon general conclusions about equilibrium and non-equilibrium QCD, such as knowledge about the typical time-scales for equilibration, knowledge about the most efficient equilibration mechanism and knowledge about the generic properties of equilibrated high-density QCD matter?

Although these questions are still open, experiments at RHIC, in interplay with recent theoretical developments, have lead already to substantial progress. In particular, data for a large number of identified single inclusive hadron spectra (π , K , p , ω , Φ , Ξ , D 's, ...) establish, that at low p_T , the strength of elliptic flow v_2 changes characteristically with the mass of the identified hadron [23, 24]. This observed mass-dependence gives further support to a hydrodynamical picture in which different particle species emerge from the same single collective flow field [25–27]. Moreover, at RHIC, the measurement of strongly medium-modified high- p_T hadron spectra has provided valuable independent information on the interaction probability of partonic test particles (i.e. the hard parent partons) with the produced QCD matter (more details are given below). Another important line investigation has been opened due to first theoretical works which show that for a hydrodynamical picture to work at RHIC, one has to assume an extremely low ratio of shear viscosity to entropy. This is important since it is a statement about the absence of strong dissipative effects, which should be testable independently in a large variety of high- p_T triggered phenomena associated with parton energy loss (see below for more details). In short, experience from RHIC provides strong arguments that a dynamical understanding of collective effects can be reached by studying the propagation (and equilibration) of hard processes in the produced matter.

Low- p_T elliptic flow v_2 is a hallmark of a strong collective behavior, but it is only one of a much wider class

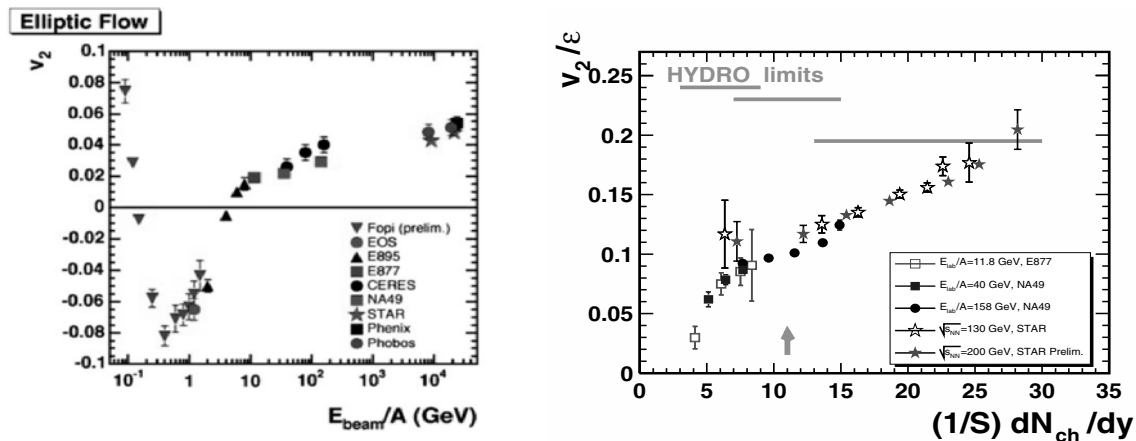


Fig. 1. Left figure from [28] shows the dependence of elliptic flow on beam energy over 6 orders of magnitude from center of mass energies close to the pion threshold up to the highest collider energies tested so far. The characteristic change of sign of v_2 agrees qualitatively with a hydrodynamic picture. Right figure from [29] shows v_2 scaled to the initial elliptic spatial anisotropy, ϵ , as a function of the charge particle density per unit transverse area. A quantitative agreement with hydrodynamic simulations is only attained at RHIC.

of intriguing low- p_T phenomena. For instance, the picture of a region of initially dense QCD matter which builds up collective phenomena during a rapid transverse collective expansion is also supported by azimuthally integrated single inclusive spectra ('radial flow') [26, 27, 30] and by the spatio-temporal characterizations of the freeze-out region via two-particle correlations. Moreover, in agreement with extrapolations from heavy ion collisions at lower center of mass energy, the hadrochemical distribution of identified hadron species in Au+Au collisions at RHIC mid-rapidity is consistent with thermal model predictions based on a grand canonical ensemble. The produced systems is hadrochemically equilibrated, and remarkably, the extracted temperature and baryochemical potential lies on the predicted QCD phase transition line [31]. However, while all these measurements are consistent with the formation of an equilibrated high-density system, it remains a challenge to clarify to what extent there is a dynamical evolution towards equilibrium and what are the microscopic mechanisms driving it. This is the major barrier for a deeper understanding of the observed phenomena. As I shall argue in the following, the abundant availability of hard processes over an unprecedented wide kinematical regime will allow to clarify this important question.

3 Probes of the produced dense matter

What happens if a hard process, such as the production of high- E_T jets, is embedded in a dense nuclear environment created e.g. in a nucleus-nucleus collision at RHIC or at the LHC? While parton-parton interactions at high virtuality $Q^2 \gg \Lambda_{QCD}^2$ occur on too short time and length scales to be affected by the typical modes in the medium, the parton showers associated to the incoming and outgoing state can interact with the medium. This is expected to result in an energy degradation of the leading parton, in a transverse momentum broadening of the parton shower,

and in an enhanced and softened multiplicity distribution of the hadronic final state [16–18, 35]. Most importantly, however, these modifications of hard processes provide a novel access to the question, how equilibration processes occur in a medium of rapidly decreasing density and how these equilibration processes are related to the fundamental properties of equilibrated dense QCD matter. To see which novel opportunities arise with the wide transverse-momentum range accessible in nucleus-nucleus collisions at collider energies one may compare e.g. hadronization and thermalization time scales [36] for a parton of high transverse energy E_T , see Fig. 2. For a parton in its own rest frame, hadronization occurs on a time scale set by its virtuality, $\sim 1/Q_{\text{hadr}}$, and owing to the Lorentz boost, the hadronization time scale in the laboratory frame is proportional to its energy $L_{\text{hadr}} \sim O(1) \frac{1}{Q_{\text{hadr}}} \frac{E_T}{Q_{\text{hadr}}}$.

What happens if the hard parton escapes into an infinitely extended quark gluon-plasma instead? Because of medium-induced gluon radiation, the initial perturbative parton splitting is even more efficient. However, the parton cannot hadronize in the dense medium. Instead, after some time, its partonic fragments can no longer be distinguished from the heat bath: the hard parton is thermalized. According to QCD-based calculations of medium-induced parton energy loss, the energy loss of the hard parton grows quadratically with the in-medium pathlength [37], and the partonic thermalization length is $L_{\text{therm}} \sim \sqrt{E_T}$.

The combination of these simple parametric estimates indicate, that for large transverse energies E_T , perturbative equilibration mechanisms can remain undisturbed by hadronization over a significant time scale, see Fig. 1. Depending on its in-medium pathlength L_{med} , the hard parton will either be absorbed ($L_{\text{therm}} < L_{\text{med}} < L_{\text{hadr}}$), or it has a sufficiently large transverse energy to suffer only the onset of equilibration processes ($L_{\text{med}} < L_{\text{therm}} < L_{\text{hadr}}$). In the latter case, the parton appears as a medium-modified jet. For lower transverse energies, there is not

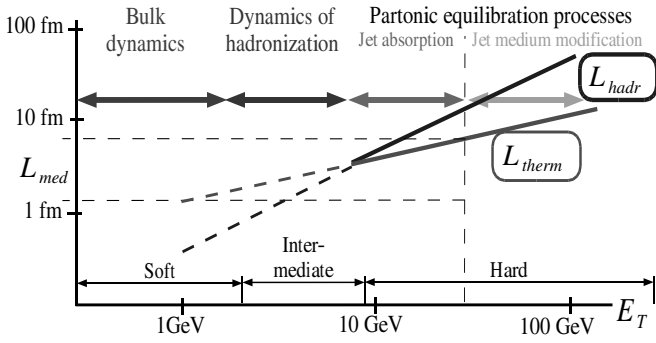


Fig. 2. Comparison of hadronization and thermalization time scales estimated for a parent quark of energy E_T , see text for more details. At sufficiently high transverse energy, partonic equilibration mechanisms can be studied unaffected by hadronization phenomena, since $L_{\text{therm}} \ll L_{\text{hadr}}$. The variation of the in-medium path length L_{med} in the range $L_{\text{med}} < L_{\text{therm}}$ provides a handle to stop the equilibration mechanism before complete thermalization. At the LHC, this gives a novel access to determining QCD equilibrium and non-equilibrium dynamics.

only a competition between the hadronization and the thermalization mechanism ($L_{\text{hadr}} \sim L_{\text{therm}}$). There is also the possibility that the medium interferes with the dynamics of the hadronization process ($L_{\text{hadr}} \sim L_{\text{med}}$). For even lower transverse momentum, the hadronization time scale is determined by the density evolution of the medium, which is not accounted for in the above estimates. Only in this kinematic “bulk” regime may formed hadrons stay in contact with the equilibrating medium for a significant duration.

3.1 Results and a Puzzle at RHIC

Experiments at RHIC have established a large body of evidence that hard partons, produced far off equilibrium, either suffer the onset of equilibration processes (i.e. jet quenching) or are even completely absorbed by the medium and indistinguishable from the thermal background, as suggested by the arguments leading to Fig. 2. One of the very first evidences, the medium-induced suppression of single inclusive hadron spectra $d^2N^{AA}/dp_T dy$ in nucleus-nucleus (AA) collisions, is commonly quantified in terms of the nuclear modification factor

$$R_{AA}(p_T, y) = \frac{d^2N^{AA}/dp_T dy}{\langle T_{AA} \rangle_c d^2\sigma^{NN}/dp_T dy}. \quad (2)$$

Here, $\langle T_{AA} \rangle_c$ is the standard nuclear overlap function, calculated as the average in the measured centrality class. In the absence of nuclear or medium effects, $R_{AA} \equiv 1$. Fig. 3 compares data from all four RHIC experiments to a calculation [19], in which the standard factorized QCD description of single inclusive spectra in terms of parton distribution functions, hard partonic matrix elements

and fragmentation functions is supplemented by medium-dependent parton energy loss of the produced partons. While nuclear modifications of incoming parton distribution functions alone (see line for $\hat{q} = 0$) cannot account for the strength of the observed suppression, final state parton energy loss can. In general, as a consequence of formation time effects, parton energy loss calculations are expected to be applicable for $p_T > 5-7$ GeV at RHIC [36], and they are in qualitative and quantitative agreement with data up to the highest transverse momentum 20 GeV tested so far.

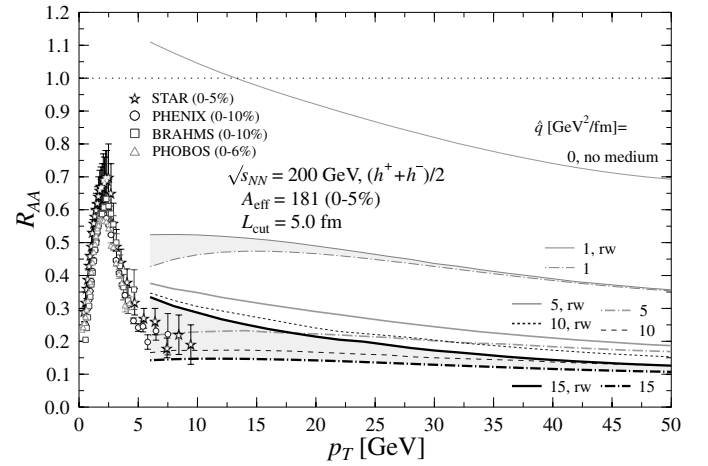


Fig. 3. The nuclear modification factor R_{AA} for charged hadrons in the 0-5 % most central Au+Au collisions at $\sqrt{s_{NN}} = 200$ GeV for different values of the time-averaged transport coefficient \hat{q} . Differences between solid and dash-dotted curves indicate uncertainties related to finite energy corrections. Figure taken from [19].

The strength of the interaction between the hard partonic projectile and the surrounding matter can be quantified by the time-averaged BDMPS transport coefficient; phenomenologically, $\hat{q} \simeq 10 \text{ GeV}^2/\text{fm}$, see Fig. 3. This quantity has a field theoretical interpretation as the short-distance coefficient of the expectation value of two light-like Wilson lines in the target average characterizing the produced medium. Physically, it simply denotes the amount of squared transverse momentum, transferred from the medium to the partonic projectile per unit path-length. On general grounds, this transport coefficient is proportional to the number density in the medium and hence

$$\hat{q} = c\epsilon^{3/4}, \quad (3)$$

where c is a medium-dependent proportionality constant. Theoretically, very little is known about how to calculate this constant. In a simplified model of the quark gluon plasma, one has found $c_{\text{QGP}}^{\text{ideal}} \approx 2$ [39], whereas an independent determination of \hat{q} and ϵ from experimental data suggests $c > 5c_{\text{QGP}}$ [19]. In short, we observe that the matter produced at RHIC is opaque even for 20 GeV partons, but

we do not understand yet the microscopic mechanism underlying this unexpectedly strong interaction between the hard parton and the medium, and the properties of the produced matter which it implies.

3.2 Opportunities at the LHC and future progress at RHIC

The above-mentioned opacity puzzle of jet quenching at RHIC is one of several important open problems which illustrate the difficulties in relating measurements in heavy ion collisions to the fundamental properties of the produced matter. I would like to emphasize now that the same problem also allows us to illustrate the opportunities of firmly establishing such relations at collider energies, and in particular at the LHC. To see this, let us consider possible solutions of the opacity puzzle in the near future: *Solution 1:* On general grounds, parton energy loss is expected to depend on the local energy momentum tensor $T^{\mu\nu} = (\epsilon + p)u^\mu u^\nu - pg^{\mu\nu}$, which reduces to the energy density ϵ entering (3) only in the in the locally comoving rest frame of matter. Model calculations indicate that if a lower energy density 'blows over' the parton trajectory with a significant flow velocity, this can have an effect similar to a large energy density [35, 41, 42]. Such a dynamical solution of the opacity puzzle can be substantiated by searching for characteristic flow-induced distortions in parton fragmentation. At the same time, it is expected to provide insight into the dynamical origin of collective flow [35, 41]. For these dynamical questions, one cannot overemphasize the importance of a logarithmically wide transverse momentum range above the background of bulk particle production, as it will be accessible for many hard probes in heavy ion collisions at the LHC, see Fig. 4. The study of the fragmentation and thermalization pattern of a hard parton may gradually become accessible with high- p_T triggered jet-like particle correlations at RHIC, but the decisive characterizations of true jet multiplicity distributions over background is only expected in heavy ion collisions at the LHC.

Solution 2: Alternatively, the model-dependent theoretical estimate for $c_{\text{QGP}}^{\text{ideal}}$ may simply be too low. For theorists, this possibility is clearly a strong motivation to develop improved calculations which start more directly from the operator definition of \hat{q} [43]. This work is at the very beginning, and involves suggestions ranging from the use of lattice QCD [44] up to AdS/CFT correspondence [45]. Also, even if \hat{q} is not accurately calculable from first principles, its energy dependence is expected to satisfy a known non-linear QCD evolution equation [43]. Also in this case, further experimental results from the LHC are crucial to substantiate our understanding of the microscopic dynamics which determines the interaction strength between hard test particles and the medium. For this purpose, two classes of measurements are now gradually coming into experimental reach [36]: First, high- p_T particle correlations [46], jet shapes and jet multiplicity

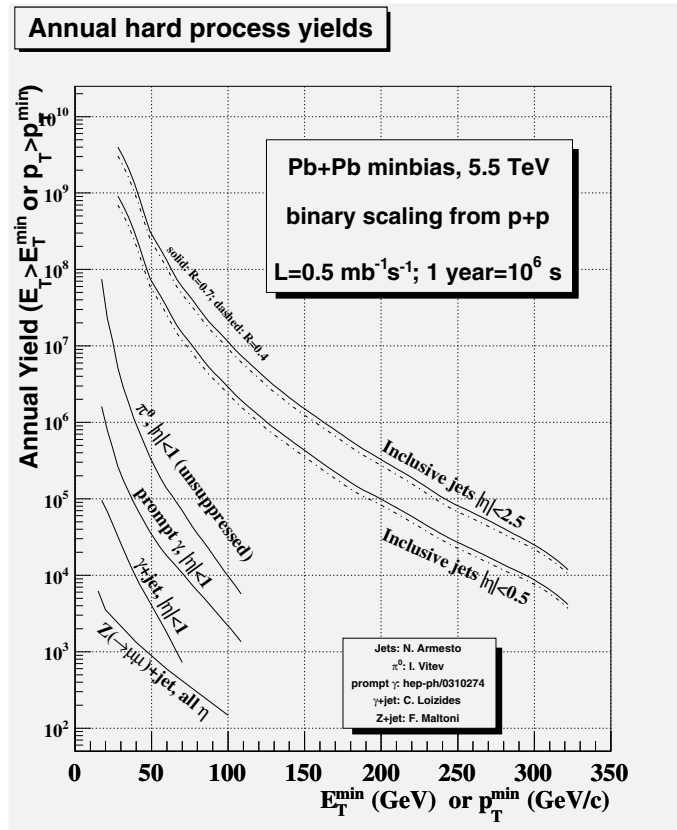


Fig. 4. The annual yield for various hard processes in nucleus-nucleus collisions at the LHC, assuming 1 month per year running at design luminosity. The wide transverse momentum range above the background of bulk particle production will allow for a detailed characterization of medium-modified jet fragmentation. As discussed in the text, this gives access to the dynamical origin of QCD equilibration mechanisms and it allows for the characterization of properties (such as density, viscosity, collective motion) of the produced matter. Figure due to P. Jacobs.

distributions [5, 48, 49] will test the predicted relation between the energy loss of the leading parton, the transverse momentum broadening of the parton shower, and the softening of its multiplicity distribution. Second, the relative yields of identified high- p_T hadrons will test the prediction that medium-induced parton energy loss depends on the identity of the parent parton, namely that hard gluons lose more energy than hard quarks due to the stronger coupling to the medium, and the energy loss of massive quarks is further reduced [50–54] due to the mass-dependent restriction of the phase space into which medium-induced gluon radiation can take place.

The opacity problem is only one of several open questions which address the relation between hard probes and properties of the produced matter. Another example is the determination of the viscosity of the produced matter. From first exploratory calculations, it is argued that the agreement of hydrodynamic simulations with bulk properties of the produced matter is indicative of an extremely

small ratio of shear viscosity to entropy. As for the opacity problem mentioned above, this is on the one hand a challenge for theory to calculate the shear viscosity of QCD matter from first principles. On the other hand, a small shear viscosity is a statement about the absence of large dissipative effects, which should have other observable consequences. In particular, the energy lost by hard partons in a viscous medium cannot dissipate but is expected to be transported in collective modes along Mach-like cones [55]. Characterizing the extent to which such structures are present or absent in the data should allow us to quantify the shear viscosity of dense QCD matter in the coming years.

In short, the field of heavy ion physics is at the beginning of understanding how a well-defined partonic test particle, embedded in a dense nuclear environment, starts to participate in QCD equilibration processes. The techniques developed to this end provide a qualitatively novel and diverse access to the fundamental problems of QCD equilibrium and non-equilibrium dynamics. This is one of several promising approaches for determining the properties of dense QCD matter at the LHC.

References

1. F. Carminati *et al.* [ALICE Collaboration], *J. Phys. G* **30** (2004) 1517.
2. G. Baur *et al.* [CMS Collaboration], CMS-Note-2000-060
3. H. Takai, [for the ATLAS Collaboration] *Eur. Phys. J. C* **34** (2004) S307.
4. L. McLerran, arXiv:hep-ph/0402137.
5. A. Kovner, arXiv:hep-ph/0508232.
6. E. Iancu and R. Venugopalan, arXiv:hep-ph/0303204.
7. D. Kharzeev and R. D. Pisarski, *Phys. Rev. D* **61** (2000) 111901.
8. D. Kharzeev, R. D. Pisarski and M. H. G. Tytgat, *Phys. Rev. Lett.* **81** (1998) 512.
9. K. Adcox *et al.* [PHENIX Collaboration], *Nucl. Phys. A* **757** (2005) 184.
10. B. B. Back *et al.*, *Nucl. Phys. A* **757** (2005) 28.
11. I. Arsene *et al.* [BRAHMS Collaboration], *Nucl. Phys. A* **757** (2005) 1.
12. J. Adams *et al.* [STAR Collaboration], *Nucl. Phys. A* **757** (2005) 102.
13. A. Accardi *et al.*, arXiv:hep-ph/0310274.
14. A. Accardi *et al.*, arXiv:hep-ph/0308248.
15. M. Bedjidian *et al.*, arXiv:hep-ph/0311048.
16. F. Arleo *et al.*, arXiv:hep-ph/0311131.
17. J. D. Bjorken, *Phys. Rev. D* **27** (1983) 140.
18. M. A. Lisa, S. Pratt, R. Soltz and U. Wiedemann, arXiv:nucl-ex/0505014.
19. K. J. Eskola, H. Honkanen, H. Niemi, P. V. Ruuskanen and S. S. Rasanen, arXiv:hep-ph/0506049.
20. P. Huovinen, P. F. Kolb, U. W. Heinz, P. V. Ruuskanen and S. A. Voloshin, *Phys. Lett. B* **503** (2001) 58.
21. E. V. Shuryak, *Nucl. Phys. A* **750** (2005) 64.
22. D. Molnar and M. Gyulassy, *Nucl. Phys. A* **697** (2002) 495 [Erratum-ibid. *A* **703** (2002) 893].
23. S. S. Adler *et al.* [PHENIX Collaboration], *Phys. Rev. Lett.* **91**, 182301 (2003).
24. J. Adams *et al.* [STAR Collaboration], *Phys. Rev. Lett.* **92** (2004) 052302.
25. M. Gyulassy and L. McLerran, *Nucl. Phys. A* **750** (2005) 30.
26. U. W. Heinz, *J. Phys. G* **31** (2005) S717.
27. F. Retiere and M. A. Lisa, *Phys. Rev. C* **70**, 044907 (2004).
28. R. Lacey, talk at Quark Matter 2005, Budapest, <http://qm2005.kfki.hu/>
29. C. Alt *et al.* [NA49 Collaboration], *Phys. Rev. C* **68**, 034903 (2003).
30. P. F. Kolb and R. Rapp, *Phys. Rev. C* **67**, 044903 (2003).
31. P. Braun-Munzinger, K. Redlich and J. Stachel, arXiv:nucl-th/0304013.
32. R. Baier, D. Schiff and B. G. Zakharov, *Ann. Rev. Nucl. Part. Sci.* **50**, 37 (2000).
33. A. Kovner and U. A. Wiedemann, arXiv:hep-ph/0304151.
34. M. Gyulassy, I. Vitev, X. N. Wang and B. W. Zhang, arXiv:nucl-th/0302077.
35. P. Jacobs and X. N. Wang, *Prog. Part. Nucl. Phys.* **54**, 443 (2005).
36. U. A. Wiedemann, *J. Phys. G* **30** (2004) S649.
37. R. Baier, Y. L. Dokshitzer, A. H. Mueller, S. Peigne and D. Schiff, *Nucl. Phys. B* **484** (1997) 265.
38. K. J. Eskola, H. Honkanen, C. A. Salgado and U. A. Wiedemann, *Nucl. Phys. A* **747** (2005) 511.
39. R. Baier, *Nucl. Phys. A* **715**, 209 (2003).
40. N. Armesto, C. A. Salgado and U. A. Wiedemann, *Phys. Rev. Lett.* **93** (2004) 242301.
41. N. Armesto, C. A. Salgado and U. A. Wiedemann, arXiv:hep-ph/0411341.
42. T. Renk and J. Ruppert, arXiv:hep-ph/0507075.
43. U. A. Wiedemann, arXiv:hep-ph/0503119.
44. B. Muller, arXiv:nucl-th/0508062.
45. S. J. Sin and I. Zahed, arXiv:hep-th/0407215.
46. A. Majumder and X. N. Wang, *Phys. Rev. D* **70** (2004) 014007.
47. C. A. Salgado and U. A. Wiedemann, *Phys. Rev. Lett.* **93** (2004) 042301.
48. S. Pal and S. Pratt, *Phys. Lett. B* **574** (2003) 21.
49. N. Borghini and U. A. Wiedemann, arXiv:hep-ph/0506218.
50. Y. L. Dokshitzer and D. E. Kharzeev, *Phys. Lett. B* **519** (2001) 199.
51. N. Armesto, C. A. Salgado and U. A. Wiedemann, *Phys. Rev. D* **69** (2004) 114003.
52. B. W. Zhang, E. Wang and X. N. Wang, *Phys. Rev. Lett.* **93** (2004) 072301.
53. M. Djordjevic and M. Gyulassy, *Nucl. Phys. A* **733**, 265 (2004).
54. N. Armesto, A. Dainese, C. A. Salgado and U. A. Wiedemann, *Phys. Rev. D* **71** (2005) 054027.
55. J. Casalderrey-Solana, E. V. Shuryak and D. Teaney, arXiv:hep-ph/0411315.

Direct Photons, Vector Mesons and Heavy Flavor Production at RHIC

K.F. Read^{1,2}

¹ Physics Division, Oak Ridge National Laboratory, Oak Ridge, TN 37831, USA, e-mail: readkf@ornl.gov

² Department of Physics and Astronomy, University of Tennessee, Knoxville, TN 37996, USA

Abstract. Recent results concerning the production of direct photons, vector mesons, charmonium, and open heavy flavor in $p+p$, $d+Au$, and $Au+Au$ collisions at $\sqrt{s_{NN}} = 200$ GeV at RHIC are discussed. The production of direct photons in $Au+Au$ collisions does not exhibit a centrality-dependent suppression at higher transverse momentum such as that observed for hadrons at RHIC. Rather, it is well-described by predictions based on NLO pQCD scaled by the number of binary nucleon-nucleon collisions. Measurements of ϕ production do exhibit a suppression in central $Au+Au$ collisions relative to scaled peripheral collisions and scaled $p+p$ collisions consistent with expectations of recombination models. Measurements of J/ψ production using dielectrons and dimuons exhibit a suppression rather than an enhancement in central $Au+Au$ collisions as predicted by some recent models. Open heavy flavor production has been measured via semileptonic decays of heavy quarks as well as direct reconstruction of charmed mesons. In $Au+Au$ collisions, although the total yield does scale by the number of binary collisions, the spectrum exhibits a strong modification relative to scaled results based on $p+p$ collisions. Measurements of the azimuthal anisotropy parameter v_2 for electrons resulting from charm meson decay in $Au+Au$ collisions are consistent with calculations in which charm quarks participate in the collective flow of the produced medium.

1 Introduction

A wealth of exciting data has been collected by the four RHIC experiments: BRAHMS [1], PHENIX [2], PHOBOS [3], and STAR [4]. Analysis of $p+p$, $d+Au$, $Cu+Cu$, and $Au+Au$ collisions at $\sqrt{s_{NN}} = 200$ GeV has yielded a broad range of important new results. In this paper we confine our attention to recent results concerning direct photons, vector mesons, and heavy flavor production.

Direct photons are an important probe in heavy ion nuclear collisions since they are relatively unaffected by the strongly interacting produced matter. Measurements of the production of direct photons can be used to discriminate whether initial or final state effects are responsible for the centrality-dependent suppression of hadron production at higher transverse momentum observed at RHIC [1–4].

The transverse momentum distribution of the nuclear modification ratio R_{CP} (defined below) of the ϕ meson production cross section in central $Au+Au$ collisions to that of scaled peripheral collisions can be used to test partonic recombination scenarios and further study the issue of hadron suppression at RHIC.

Measurements of open heavy flavor and charmonium production in $p+p$ collisions can be used to test pQCD predictions at $\sqrt{s} = 200$ GeV as well as establish a baseline for interpreting charm production in heavy ion collisions. The results of such measurements for $d+Au$ collisions are used to test predictions for modification of the gluon struc-

ture function in nuclei (shadowing). Such measurements for $Au+Au$ collisions at $\sqrt{s_{NN}} = 200$ GeV can be used to study medium modification effects such as charm quark energy loss and collective flow. They can be used to search for evidence of thermal production of charm from a possible Quark Gluon Plasma and to study predicted modifications to J/ψ production due to the produced medium.

Nucleus-nucleus collisions are classified according to *centrality*, defined to be the percentile of the total geometrical cross section (with 0% – 5% representing the most central collisions), a quantity which is related to impact parameter. At RHIC, the centrality measurement for a collision is based on a correlation of the measured charge sum in beam-beam counters (BBC) and total forward energy deposited in zero-degree calorimeters (ZDC) [5] using a Glauber Monte Carlo [6] incorporating the BBC and ZDC response. Using this model, the average number of binary nucleon-nucleon inelastic collisions, N_{coll} , can be computed for a given centrality [5]. Many of the (rare) processes investigated at RHIC and discussed below result from point-like hard scattering involving small cross sections. To the extent that $Au+Au$ collisions behave as an incoherent superposition of $p+p$ collisions, the ratio of the cross section for such hard processes in $Au+Au$ collisions compared to $p+p$ collisions at the same value of $\sqrt{s_{NN}}$ is expected to be proportional to N_{coll} for the given centrality class [2].

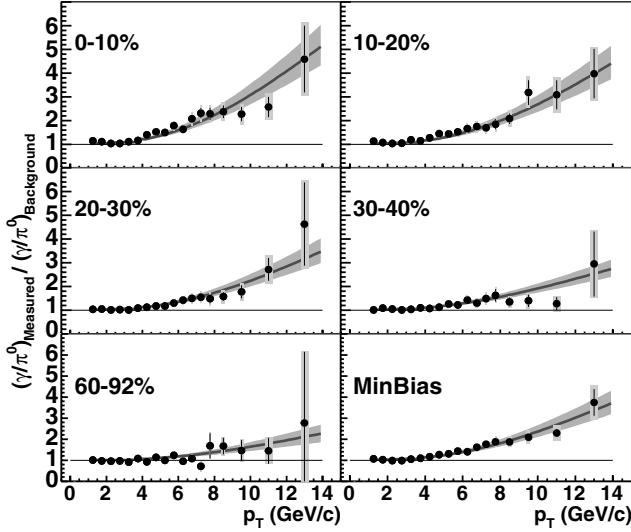


Fig. 1. Transverse momentum distribution of the ratio of the corrected inclusive photon yield compared to the background decay photon yield for different centrality bins for minimum bias $Au + Au$ collisions at $\sqrt{s_{NN}} = 200$ GeV [7]. The curves correspond to unity plus the ratio of an NLO pQCD prediction, scaled by N_{coll} , to the decay photon yield for each centrality bin.

2 Direct Photons

The following double ratio

$$\frac{\gamma_{Inclusive}/\pi^0}{\gamma_{Decay}/\pi^0} \approx \frac{\gamma_{Decay} + \gamma_{Direct}}{\gamma_{Decay}} \quad (1)$$

for minimum bias $Au + Au$ collisions at $\sqrt{s_{NN}} = 200$ GeV is displayed in Figure 1. An excess of direct photons is observed at higher transverse momentum that increases with centrality [7]. The results are consistent with NLO pQCD predictions scaled by N_{coll} .

The invariant yield of direct photons in $Au + Au$ collisions at $\sqrt{s_{NN}} = 200$ GeV is shown in Figure 2. The curves indicate the scaled NLO pQCD predictions for each centrality class. Within errors, the scaled predictions describe the photon yield well.

The centrality dependence of the nuclear modification ratio

$$R_{AA}(p_T, y; b) = \frac{d^2 N_{AA}/dydp_T}{\langle T_{AA}(b) \rangle d^2 \sigma_{pp}/dydp_T} \quad (2)$$

for transverse momenta above 6.0 GeV/c is displayed in Figure 3 [7]. For this figure, N_{part} , the average number of nucleons participating in the collision based on a Glauber Model calculation for a given centrality class, is used as a measure of centrality. The transverse momentum distribution of the nuclear modification factors for direct photons (squares) and hadrons in central $Au + Au$ collisions are displayed in Figure 4. Direct photons do not exhibit the suppression at higher transverse momentum observed for hadrons [8]. This important result provides strong evidence that the hadron suppression is due to a final state effect (such as parton energy loss).

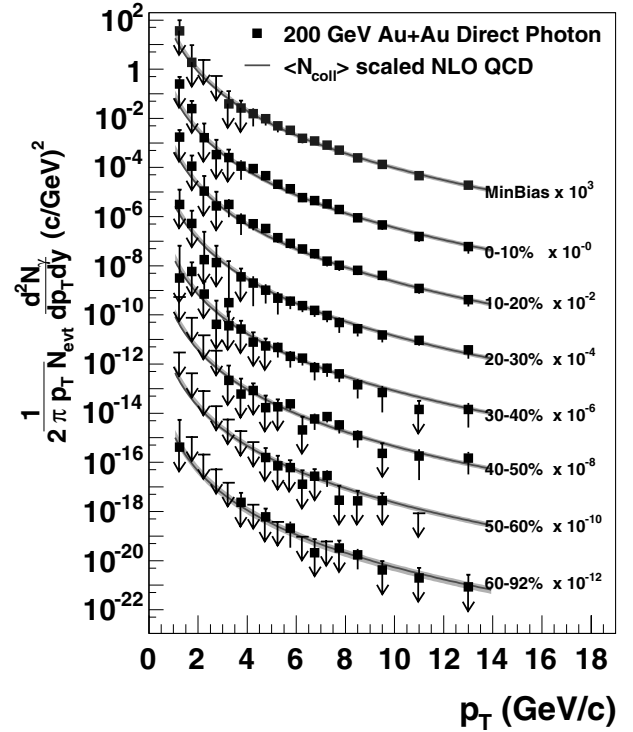


Fig. 2. Transverse momentum distribution of the invariant yield of direct photons for $Au + Au$ collisions at $\sqrt{s_{NN}} = 200$ GeV for different centrality bins, scaled by successive powers of 10 for clarity [7]. The curves indicate the corresponding scaled NLO pQCD predictions.

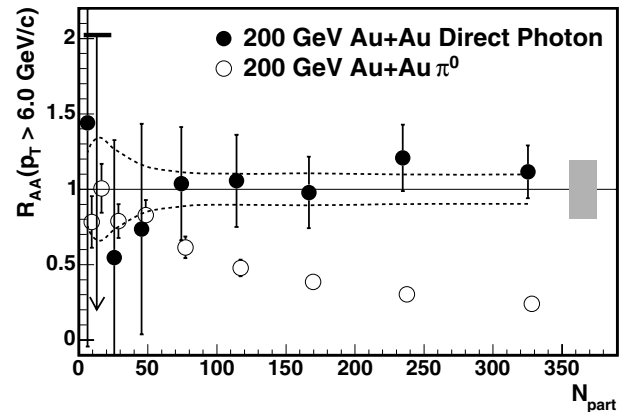


Fig. 3. Nuclear modification factor R_{AA} (defined in text) for direct photon (solid circles) and π^0 (open circles) production in $Au + Au$ collisions at $\sqrt{s_{NN}} = 200$ GeV versus the calculated number of participants for transverse momenta above 6.0 GeV/c [7].

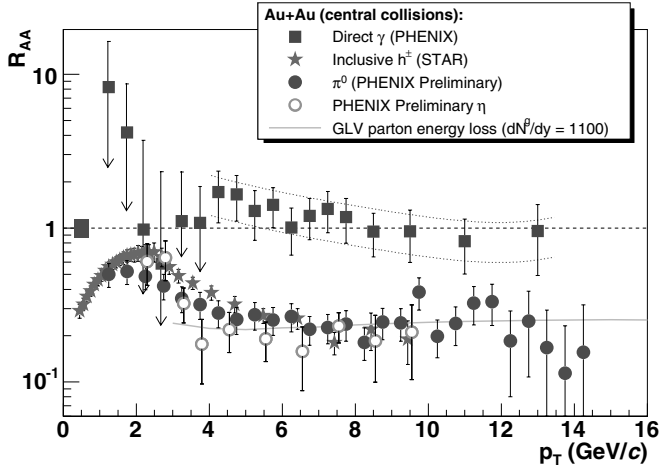


Fig. 4. Transverse momentum distribution of the nuclear modification factor R_{AA} (defined in text) for direct photon (squares) and π^0 (solid circles) production in central $Au + Au$ collisions at $\sqrt{s_{NN}} = 200$ GeV [8].

The suppression of high transverse momentum π^0 's in central $Au + Au$ collisions at RHIC greatly increases the ratio $\gamma^{Direct}/\gamma^{Decay}$, making direct photons much easier to measure. Future measurements with reduced errors will enable searches for deviations from pQCD and evidence for other contributions, e.g. thermal photons.

3 Vector Mesons

Vector meson production is a broad area of investigation at RHIC. In this section we confine the discussion to aspects of ϕ meson production.

The ratio of the ϕ meson invariant yield for central compared to peripheral $Au + Au$ collisions scaled by the relative values of N_{coll} is displayed in Figure 5a [9] and referred to as the nuclear modification factor R_{CP} . The production of ϕ mesons is suppressed in central $Au + Au$ collisions. The ratio R_{CP} for ϕ mesons is comparable to that for pions rather than protons, a pattern which is consistent with partonic recombination scenarios [9, 10].

Measurement of the ϕ meson invariant yield can be used to further test models for hadron suppression at RHIC and to study the anomalous proton to pion ratio observed in central $Au + Au$ collisions at RHIC [10].

4 Heavy Flavor Production

The J/ψ differential production cross section has been measured in $p + p$, $d + Au$, $Cu + Cu$, and $Au + Au$ collisions at RHIC. The J/ψ differential production cross section for $p + p$ collisions at $\sqrt{s} = 200$ GeV is shown in Figure 6a [11]. The measurement yields a total cross section of $\sigma_{pp}^{J/\psi} = 2.61 \pm 0.20$ (fit) ± 0.26 (abs) μb . A nuclear dependence is observed in the rapidity distribution of J/ψ production in $d + Au$ collisions compared to scaled $p + p$

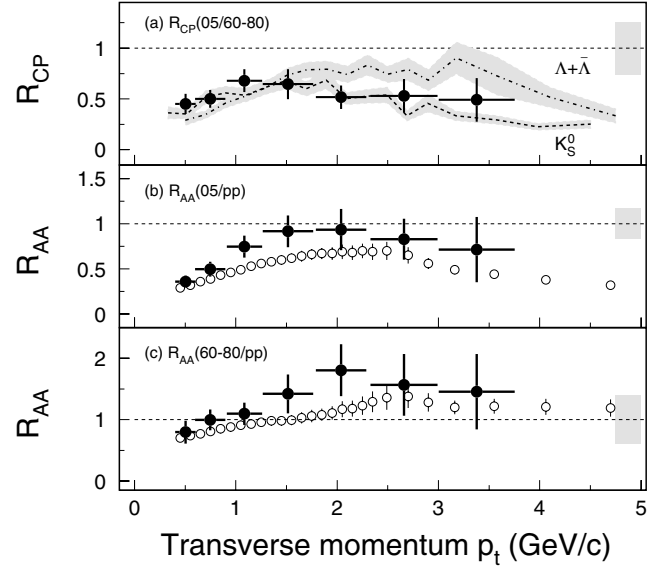


Fig. 5. STAR transverse momentum distribution of the nuclear modification ratio of the ϕ meson production cross section (solid circles) for (a) central $Au + Au$ relative to scaled peripheral $Au + Au$ results, (b) central $Au + Au$ relative to scaled $p + p$ results, and (c) peripheral $Au + Au$ relative to scaled $p + p$ results at $\sqrt{s_{NN}} = 200$ GeV [9]. The corresponding nuclear modification factors R_{AA} for charged hadrons (open circles) are shown in panels (b) and (c) for comparison.

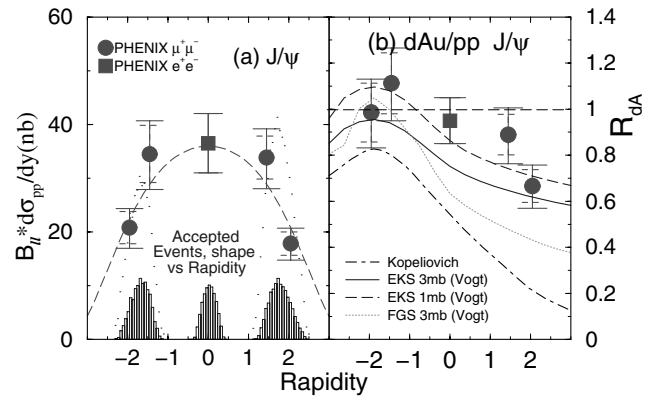


Fig. 6. (a) Rapidity distribution of branching ratio times differential J/ψ production cross section for dimuons (circles) and dielectrons (squares) for $p + p$ collisions at $\sqrt{s} = 200$ GeV. (b) Rapidity distribution of the nuclear modification ratio of the J/ψ production cross section for $d + Au$ collisions compared to $p + p$ collisions scaled by N_{coll} at $\sqrt{s_{NN}} = 200$ GeV [11].

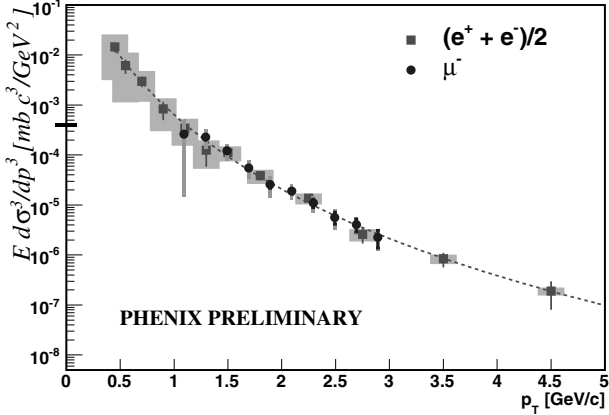


Fig. 7. Preliminary transverse momentum distribution of invariant differential production cross section for negative muons (circles) and the average of electrons and positrons (squares) from heavy flavor decay for $p + p$ collisions at $\sqrt{s} = 200$ GeV. The pseudorapidity interval is centered around $|\eta| = 1.65$ for muons and $\eta = 0$ for electrons and positrons. Systematic errors are indicated as shaded bands. The systematic error associated with the overall normalization of the muon data is separately indicated by the horizontal band on the vertical axis. The dashed curve is a power law fit to the electron data points.

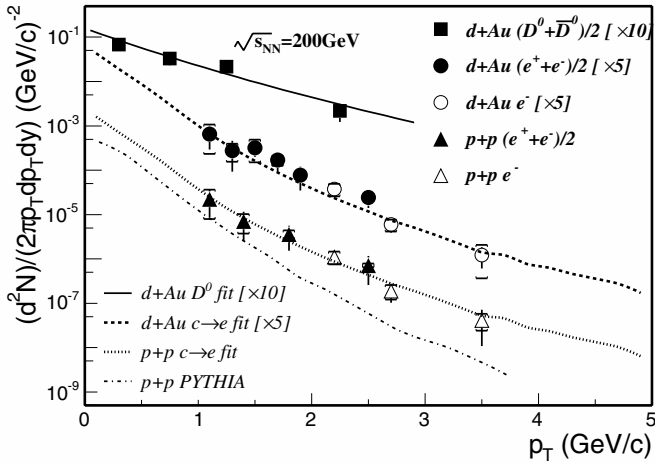


Fig. 8. STAR transverse momentum distribution of reconstructed D^0 mesons (solid squares) for $d + Au$ collisions and non-photonic electrons for $p + p$ (triangles) and $d + Au$ (circles) collisions at $\sqrt{s_{NN}} = 200$ GeV [13].

results (Fig. 6b) [11]. The ratio is near unity at backward rapidity and significantly lower at forward rapidity. Such measurements test predictions concerning modification of the gluon structure function in nuclei.

Measurements of J/ψ production in $Au + Au$ collisions [12] disfavor models with strong enhancement of production. Results based on a subsequent run with increased statistics and different colliding species ($Cu + Cu$) are in preparation.

After subtraction of physics backgrounds, measurement of single electrons and positrons (“non-photonic elec-

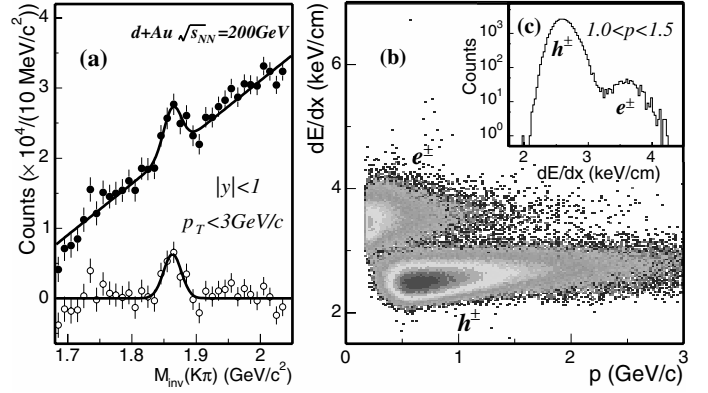


Fig. 9. (a) STAR $K\pi$ invariant mass distribution for $d + Au$ collisions at $\sqrt{s_{NN}} = 200$ GeV after mixed-event background subtraction (solid circles) and subsequent linear residual background subtraction (open circles) [13]; (b) momentum distribution of dE/dx in the STAR TPC [13].

trons”) and single muons can be used to determine the production of heavy quarks. The transverse momentum distribution of the production cross section for muons and non-photonic electrons from heavy flavor decay for $p + p$ collisions is displayed in Figure 7. The pseudorapidity interval is centered around $|\eta| = 1.65$ for muons and $\eta = 0$ for electrons and positrons. The transverse momentum distribution of non-photonic electrons for $p + p$ collisions at $\sqrt{s} = 200$ GeV is also shown in Figure 8 along with the corresponding plot for $d + Au$ collisions at $\sqrt{s_{NN}} = 200$ GeV.

Exclusive reconstruction of charmed mesons (Fig. 9) can be used to measure open charm production more directly. The D^0 meson invariant yield for $d + Au$ collisions at $\sqrt{s_{NN}} = 200$ GeV is shown in Figure 8 [13].

The transverse momentum distribution of non-photonic electrons in $Au + Au$ collisions at $\sqrt{s_{NN}} = 200$ GeV is shown in Figure 10. The data exhibit a suppression at higher transverse momentum relative to scaled $p + p$ results. The spectral shape is modified by the produced medium. The pattern is consistent with models incorporating heavy quark energy loss [14].

The initial state spatial anisotropy of the collision reaction zone leads to a final state momentum anisotropy. This results in asymmetric particle emission. The second component of a Fourier decomposition of the azimuthal distribution of particles, v_2 , indicates the degree of azimuthal anisotropy:

$$E \frac{d^3 N}{d^3 p} = \frac{d^3 N}{p_T d\phi dp_T dy} \sum_{n=0}^{\infty} 2v_n \cos(n(\phi - \Psi_{R.P.})) \quad (3)$$

where $\Psi_{R.P.}$ is the direction of the nuclear impact parameter (“reaction plane”) in a given collision.

Preliminary PHENIX and STAR measurements of the momentum distribution of the azimuthal anisotropy parameter, v_2 , are displayed in Figure 11 [15, 16]. The STAR results extend the measurement of this parameter from 1.5 to 3.0 GeV/c.

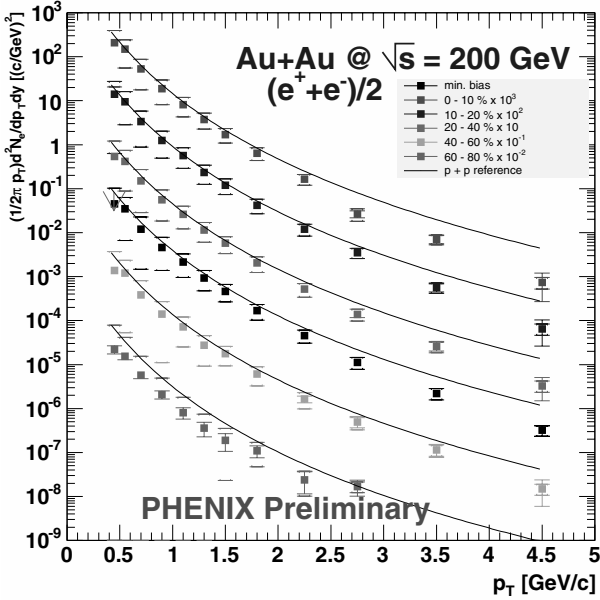


Fig. 10. Preliminary transverse momentum distribution of non-photonic electrons in $Au + Au$ collisions at $\sqrt{s_{NN}} = 200$ GeV for different centrality bins, scaled by successive powers of 10 for clarity. The curves correspond to $p + p$ collision results scaled by N_{coll} for each centrality bin.

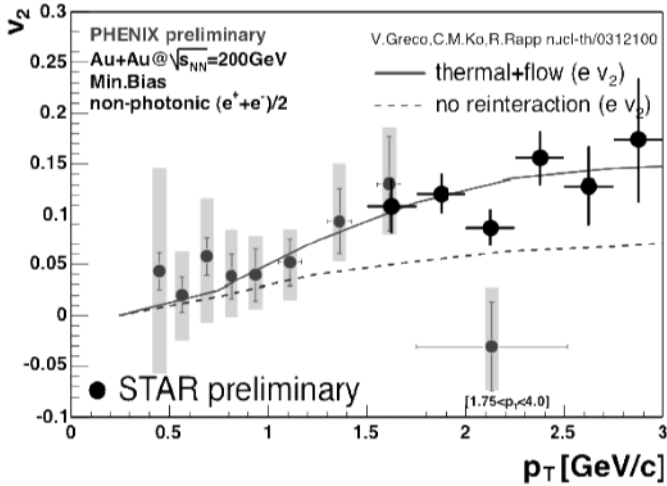


Fig. 11. PHENIX and STAR preliminary transverse momentum distributions of v_2 (defined in text) for non-photonic electrons in minimum bias $Au + Au$ collisions at $\sqrt{s_{NN}} = 200$ GeV [15, 16]. The curves indicate two different models concerning charm flow [17].

5 Summary and Conclusions

NLO pQCD predictions provide a good description of direct γ and π^0 production for $p + p$ collisions at $\sqrt{s} = 200$ GeV. Direct γ production in $Au + Au$ collisions at $\sqrt{s_{NN}} = 200$ GeV is consistent with results based on both $p + p$ data and NLO pQCD predictions scaled by N_{coll} . This supports the hypothesis that the observed hadron suppression at

higher transverse momentum in central $Au + Au$ collisions is due to a final state effect, such as parton energy loss. The suppression of the production of ϕ mesons in central $Au + Au$ collisions is consistent with partonic recombination scenarios. Heavy flavor production has been measured via semileptonic decays in $p + p$, $d + Au$, and $Au + Au$ collisions at $\sqrt{s_{NN}} = 200$ GeV. Data concerning heavy flavor production in $p + p$ and $d + Au$ collisions serve as an important baseline for interpreting heavy flavor production in $Au + Au$ collisions. Measurements of $\sigma_{c\bar{c}}$ at RHIC provide an important test of pQCD predictions. A strong modification is observed for the spectra of non-photonic electrons in $Au + Au$ collisions compared to results from $p + p$ collisions scaled by N_{coll} . Measurements of the azimuthal anisotropy parameter v_2 of non-photonic electrons in $Au + Au$ collisions are consistent with models incorporating elliptic flow of the charm quark [17].

Acknowledgements. This research was sponsored by the Division of Nuclear Physics, U.S. Department of Energy, under contract DE-AC05-00OR22725 with UT-Battelle, LLC (Oak Ridge National Laboratory) and contract DE-FG02-96ER40982 with the University of Tennessee. T. Ullrich provided information concerning recent results from the STAR Collaboration.

References

1. BRAHMS Coll., I. Arsene, et al., Nucl. Phys. A **757**, 1 (2005)
2. PHENIX Coll., K. Adcox, et al., Nucl. Phys. A **757**, 184 (2005)
3. PHOBOS Coll., B.B. Back, et al., Nucl. Phys. A **757**, 28 (2005)
4. STAR Coll., J. Adams, et al., Nucl. Phys. A **757**, 102 (2005)
5. PHENIX Coll., K. Adcox, et al., Phys. Rev. C **69**, 024909 (2004)
6. R. Glauber and J. Natthiae, Nucl. Phys. B **21**, 135 (1970)
7. PHENIX Coll., K. Adcox, et al., Phys. Rev. Lett. **94**, 232301 (2005)
8. D. d'Enterria, Eur. Phys. J. C **43**, 295 (2005)
9. STAR Coll., J. Adams, et al., Phys. Lett. B **612**, 181 (2005)
10. PHENIX Coll., S.S. Adler, et al., Phys. Rev. C **72**, 014903 (2005)
11. PHENIX Coll., S.S. Adler, et al., nucl-ex/0507032 (2005)
12. PHENIX Coll., S.S. Adler, et al., Phys. Rev. C **69**, 014901 (2004)
13. STAR Coll., J. Adams, et al., Phys. Rev. Lett. **94**, 062301 (2005)
14. Y.L. Dokshitzer and D.E. Kharzeev, Phys. Lett. B **519**, 199 (2001)
15. PHENIX Coll., S.S. Adler, et al., Phys. Rev. C **72**, 024901 (2005)
16. STAR Coll., F. Laue, et al., J. Phys. G: Nucl. Part. Phys. **31**, S27 (2005); STAR Coll., F. Laue, et al., J. Phys. G: Nucl. Part. Phys. **31**, S11211 (2005)
17. V. Greco, C.M. Ko, R. Rapp, Phys. Lett. B **595**, 202 (2004); V. Greco, C.M. Ko, R. Rapp, nucl-th/0312100 (2004)

Jet production and high p_T hadrons at RHIC

Thomas Peitzmann¹

Utrecht University, P.O. Box 80000, 3508TA Utrecht, The Netherlands

Abstract. I review the status of jet-related measurements in high-energy heavy ion collisions at a beam energy of $\sqrt{s_{NN}} = 200$ GeV, in particular results on single hadron suppression and jet-like correlations.

1 Introduction

The study of strongly interacting matter under extreme conditions has reached a new phase with the experiments at the Relativistic Heavy Ion Collider (RHIC). With the higher beam energy, partonic degrees of freedom have become more and more important. These degrees of freedom are most apparent when studying jet related observables.

A modification of jet fragmentation in high energy nuclear collisions at RHIC is now well established. The observed effects can be most easily explained by parton energy loss via medium-induced gluon radiation, also called *jet quenching*. Quantitative agreement of such calculations requires an initial density of the matter produced in these collisions of $\approx 30 - 50$ times that of cold nuclear matter. There is an abundance of results from the RHIC experiments that supports the picture of a parton dominated phase, in particular the strong elliptic flow, which appears to require early equilibration, i.e. in a partonic phase, and near-ideal hydrodynamic flow [1–4]. Some of these other results are discussed in some detail in [5], I will concentrate on the jet-related measurements at RHIC.

In high-energy nuclear collisions, jets cannot be fully reconstructed due to the high multiplicities, which provide an enormous background for jet identification. The current measurements therefore mainly rely on two more inclusive ways of obtaining information about jet production: Single hadron production at high p_T and jet-like correlations.

2 Single Hadron Suppression

Hadron production at high transverse momenta in high energy hadronic collisions is the most simple way to study jet fragmentation. Although for a given jet the average momentum fraction a hadron carries after fragmentation is $\langle z \rangle = p_{hadron}/E_{jet} \approx 0.3$, the inclusive spectrum at high p_T is dominated by those hadrons carrying a relatively large fraction of the momentum of their parent partons ($\langle z \rangle \approx 0.7$). Modifications of the parton spectrum, as e.g. from energy loss, should therefore have a direct correspondence in the hadron spectra.

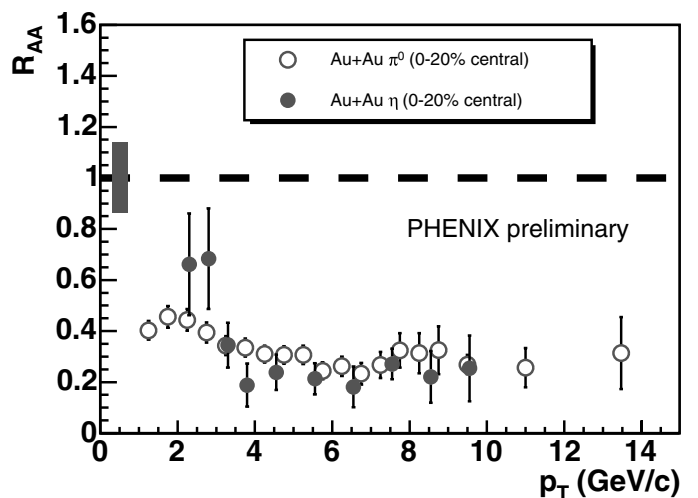


Fig. 1. Nuclear modification factor R_{AA} (see text) of π^0 and η inclusive yields as a function of p_T , for central Au+Au relative to p+p collisions [8].

The inclusive π^0 spectrum in 200 GeV p+p collisions is well represented by NLO pQCD calculations incorporating suitable fragmentation functions [6], also direct photon production in p+p is well described by pQCD [7]. Because the data for this elementary systems seem to be relatively well understood, results from p+p collisions are frequently used as a reference for judging potential modifications in A+A collisions. A common quantitative measure is the nuclear modification factor

$$R_{AA} \equiv \frac{1/p_T \cdot dN^{AA}/dp_T}{\langle N_{coll} \rangle \cdot 1/p_T \cdot dN^{pp}/dp_T}, \quad (1)$$

i.e. the ratio of the inclusive yield in nuclear collisions to the yield in p+p collisions, scaled by the number of binary collisions $\langle N_{coll} \rangle$ to remove trivial nuclear effects from the superposition of many incoherent point-like scatterings. Per definition, $R_{AA} = 1$ if there is no nuclear modification.

Figure 1 shows recent measurements of the nuclear modification factor from PHENIX [8]. The ratio shows

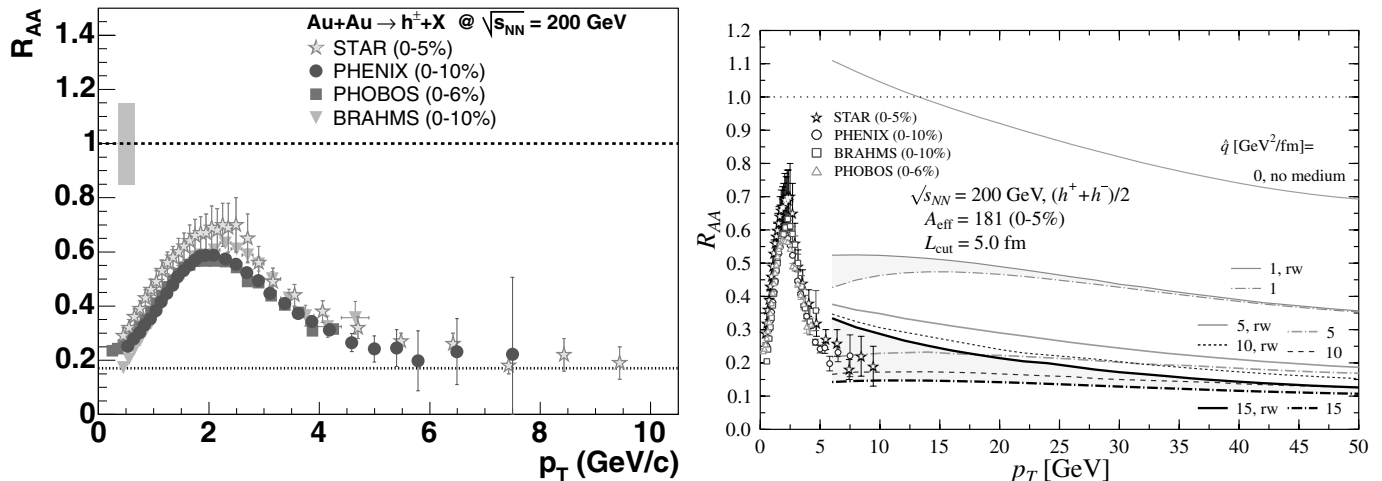


Fig. 2. Left: R_{AA} in central Au+Au collisions for charged hadrons [15]. Right: the same data compared to a BDMPS-based calculation with varying transport coefficient \hat{q} [19]. The pair of curves for each \hat{q} indicates the theoretical uncertainty due to finite energy corrections (“rw” refers to reweighting the gluon emission probability distribution so that the total radiated energy does not exceed the energy of the parent parton).

a strong suppression of a factor of ≈ 5 for neutral pions reaching out to $p_T = 14 \text{ GeV}/c$. Also shown is R_{AA} for η mesons – while those may show hints of different behaviour at $p_T \approx 2 - 3 \text{ GeV}/c$, they agree quantitatively for higher p_T . This species independence may be a hint that at high p_T the different hadrons are produced via a vacuum-like fragmentation process also in nuclear collisions. This is further supported by the suppression pattern of unidentified charged hadrons which has been measured by all RHIC experiments (see Figure 2 left side). The value of R_{AA} converges to the same numerical value as for pions regardless of the admixtures of other hadron species. There is a growth of the ratio towards lower p_T , which can be attributed to different suppression of protons at these p_T – the simple assumption of vacuum fragmentation cannot be valid in this intermediate momentum region ($p_T \approx 2 - 5 \text{ GeV}/c$).

Apparently there are significant medium-induced effects, which can be more directly seen in the ratios of protons or antiprotons to pions as shown in Figure 3 [9] and in ratios of Λ to K_S^0 [10]. In general, baryon to meson ratios are much larger (≈ 1) than values known from jet fragmentation in vacuum. While mesons at intermediate p_T are strongly suppressed, baryons seem to roughly scale as the number of binary collisions. This phenomenon appears to be more or less independent of the mass of the hadrons and points to interesting, not completely understood features of hadron production, which will be discussed below.

That the suppression mechanism is of final-state nature and relies on the strong interaction is established by the absence of suppression for hadrons in d+Au collisions [11–14] and by the absence of suppression of photons [7].

There exist quite a number of theoretical calculations of energy loss effects (for recent reviews see [16–18]). In most of these calculations medium-induced radiative en-

ergy loss has been incorporated in one of two approximations, multiple soft interactions (BDMPS) and few hard scatterings (GLV opacity expansion), and calculations applying either approach are successful in describing the inclusive hadron suppression and its systematic dependence on centrality and collision energy, though they use different mechanisms to reproduce the p_T -independence of the suppression. The right panel of Figure 2 shows a comparison of the data from the left panel to an exemplary set of calculations in the BDMPS approximation [19]. In these calculations the medium density is characterized by a transport coefficient \hat{q} . For $p_T > 5 \text{ GeV}/c$ the amount of suppression is described equally well by all choices of $\hat{q} > 5 \text{ GeV}^2/\text{fm}$. This points to an apparent opaqueness of the fireball: The energy of the hard scattered partons is completely dissipated when they originate from the core, and the observed parton fragments are biased towards outward-directed emission near the surface [19–22].

These measurements of inclusive hadron suppression are extremely valuable, but still of limited information content. Above a certain opacity of the core of the fireball there is limited sensitivity to the precise value of it, and the measured suppression may be very much influenced by the surface emission bias and e.g. by fluctuations of the surface thickness and its density. To understand the energy loss mechanisms and the modification of fragmentation in detail, and to obtain an upper limit of the opacity more exclusive measurements are needed, e.g. particle correlations.

One possibility of a more exclusive measure exploits the features of non-central collisions. When seen in the transverse plane, the fireball in such collisions is asymmetric in shape, with a smaller spatial extension in the reaction plane (spanned by the directions of the beam and the impact parameter). For a thermalized system with a corresponding pressure, this spatial anisotropy leads to an anisotropic emission of particles due to the different

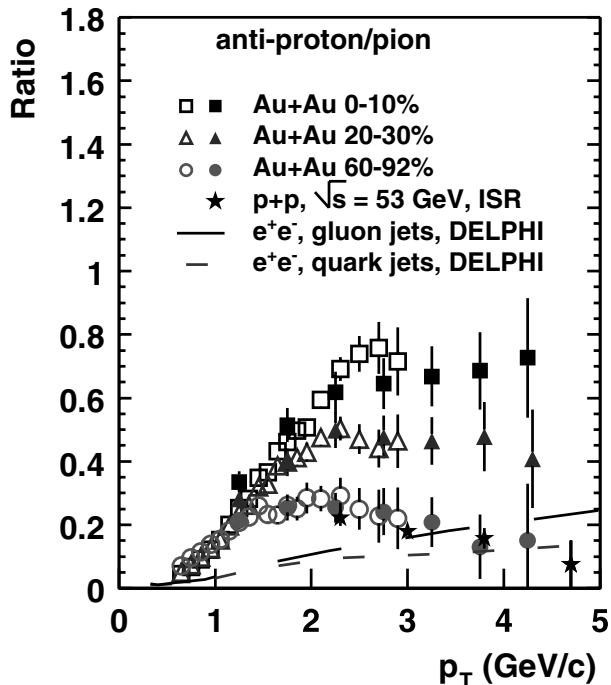


Fig. 3. Ratio of antiprotons to pions as a function of p_T , for Au+Au collisions of different centrality as measured by PHENIX. For comparison also data from p+p collisions and parameterizations from e^+e^- collisions are shown [9].

pressure gradients. This phenomenon, called *elliptic flow*, has been observed particularly for low momentum hadrons in nuclear collisions. For high momentum hadrons, which should originate from jet fragmentation, this collective motion should have little effect. However, if the single hadron suppression is due to energy loss in matter, the spatial anisotropy should lead to a similar anisotropy in suppression, and thus in particle yield, relative to the reaction plane.

The shape of the azimuthal emission pattern is usually described by a Fourier expansion, and it turns out that the second order coefficient v_2 is dominant, and characterizes the strength of the anisotropy. Figure 4 shows v_2 as a function of p_T for non-central Au+Au collisions at $\sqrt{s_{NN}}=200$ GeV [23]. The parameter v_2 has been extracted with different methods, which should be differently sensitive to other residual correlations present (e.g. from jets), as discussed in detail in [23]. v_2 rises with p_T at low momentum, the usual feature of elliptic flow originating from a collectively expanding source. As discussed above, the strength of the elliptic flow in these measurements requires early thermalization of the system. Of more relevance to our discussion here is the fact that a finite anisotropy persists out to very high momentum, which must be related to anisotropic energy loss. The quantitative interpretation of this measurement still has to be performed, but measuring the single particle yields as a function of p_T and of the angle relative to the reaction plane systematically will certainly provide important information to constrain energy loss calculations.

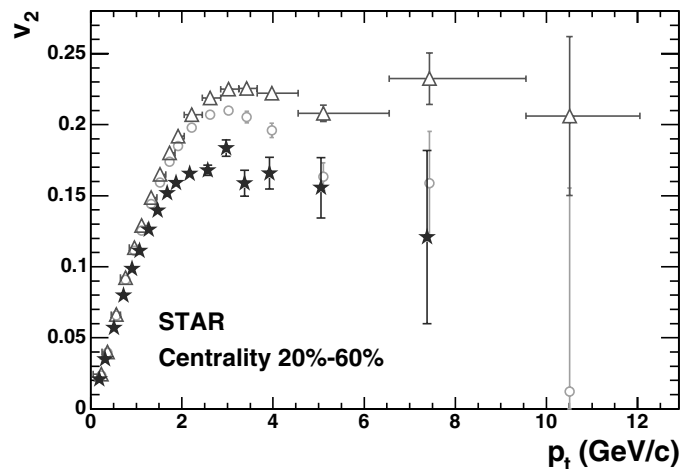


Fig. 4. Strength of the second order azimuthal anisotropy v_2 of hadron emission with respect to the reaction plane as a function of p_T in non-central Au+Au collisions at $\sqrt{s_{NN}}=200$ GeV obtained with different methods [23].

Measurements of v_2 for identified hadrons at intermediate p_T show other interesting features. The values are large, apparently exceeding the initial spatial anisotropy [23], with v_2 for baryons larger than that for mesons [24]. More quantitatively, v_2 for various meson and baryon species approximately follows a common distribution when rescaled as v_2/n vs p_T/n [24], where n is the number of constituent quarks ($n=3$ for baryons and $n=2$ for mesons). Such scaling is expected from models in which hadronization occurs via coalescence or recombination of constituent quarks [25–28]. Such a different production mechanism is also able to explain the different scaling behavior of baryons and mesons discussed above. When recombining from a system with a common thermal quark distribution, baryons will on average carry three times the quark momentum compared to two times for mesons. This populates higher momentum regions of the spectra more, and together with the exponential suppression of the underlying spectra leads naturally to a baryon enhancement relative to mesons. While these models are very promising, there are still conceptual difficulties to dynamically understand the hadronisation process including conservation laws.

3 Jet-Like Correlations

The fragmentation of the two scattered partons after the hard process, which have to approximately balance each other in transverse momentum, leads to pairs of jets of hadrons which are to first order back-to-back in azimuth. Effects of this dijet structure can be seen in correlations of high p_T hadron pairs (*dihadrons*). The left panel of Figure 5 shows the dihadron distribution as a function of relative azimuthal angle $\Delta\phi$. One hadron, the *trigger* hadron, is required to have a $p_T^{trig} > 4$ GeV/c, and the other, the associated hadron, $2 \text{ GeV}/c < p_T^{asso} < p_T^{trig}$. In

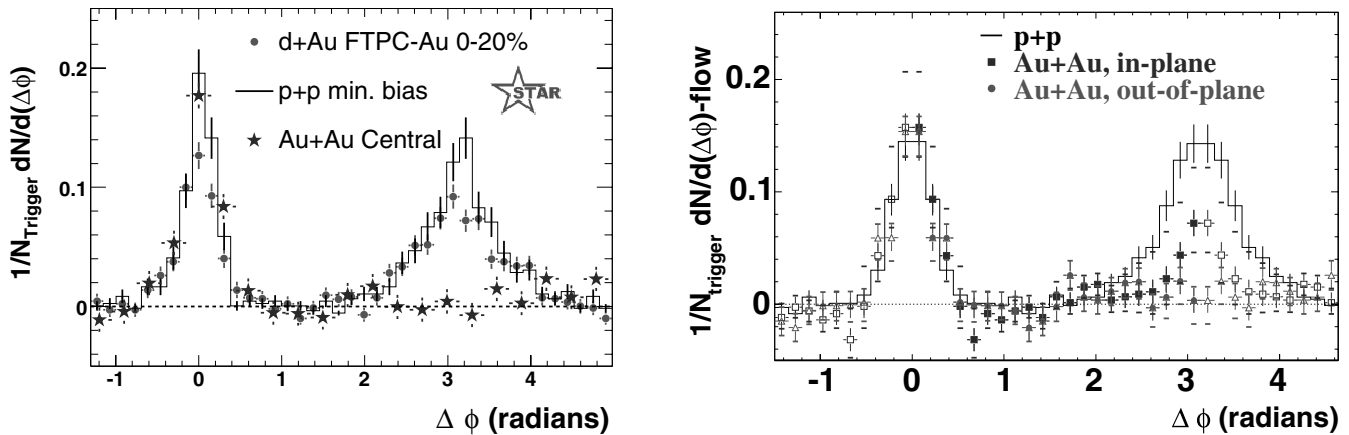


Fig. 5. Background-subtracted relative azimuthal angle distribution for high p_T dihadrons at $\sqrt{s_{\text{NN}}} = 200$ GeV. Left: p+p, d+Au and central Au+Au collisions [13]. Right: trigger particle in or out of reaction plane in non-central Au+Au collisions [23].

these distributions uncorrelated background and residual effects of elliptic flow have been subtracted.

At small relative angles, correlated dihadrons originate from the same jet. Here, a clear peak is observed, and the shape and magnitude of it appears to be very similar for p+p, d+Au, and central Au+Au collisions. This is in line with the surface bias used in the interpretation of the inclusive suppression: If the partons, which generate hadrons with p_T^{trig} , have to only traverse a very small depth of matter, the fragmentation of this jet should be very little modified by medium effects.

Correlated dihadrons at large angles ($\Delta\phi \approx \pi$) should originate from different jets of the jet pair. A clear correlation structure is again observed for p+p and d+Au collisions. In central Au+Au collisions this away-side peak is absent, which suggests a strong suppression of the higher momentum fragments of the recoiling jet, consistent with the strong medium-induced partonic energy loss derived from single hadron suppression measurements. The surface bias introduced by the trigger hadron should have the inverse effect on the away-side: partons have to traverse a longer path length and energy loss effects should be enhanced.

Also these correlation measurements can be performed more exclusively using the angle relative to the reaction plane as a control parameter. The right panel of Figure 5 shows similar high p_T dihadron distributions for non-central Au+Au collisions, with the trigger now constrained to lie within restricted azimuthal intervals centered on the reaction plane orientation or orthogonal to it [23]. Again, uncorrelated background and elliptic flow effects have been subtracted. The correlation for small relative angles is independent of the relative orientation to the reaction plane and appears again to be similar to the same correlation in p+p collisions. The large angle correlation, however, shows a striking difference between the two selections. While the correlation peak is suppressed in both cases compared to p+p collisions, there is a weaker but significant peak for the in-plane orientation, which corresponds to a short path length, and no observable

correlation for the out-of-plane selection with its longer path length. This is the clearest indication to date of the in-medium path length dependence of hadron suppression.

The uncertainties in the current measurement are large, such that a quantitative analysis will be only marginally meaningful, but for really high statistics data sets, like the RHIC Run 4, which should allow one to go to even higher p_T with correspondingly smaller background corrections, such measurements should allow a detailed investigation of the path length dependence of the suppression.

All dihadron correlation measurements shown above use relatively high transverse momentum cuts. Thus the disappearance of the far-angle correlation is not equivalent to the complete disappearance of the jet. Certainly, energy and momentum of the hard scattered parton have to be conserved. As they are no longer apparent at high p_T , the fragmentation must have been softened and the momentum should reappear at lower p_T . In [29] a dihadron correlation analysis has been performed with a lower minimum momentum of the associated hadron of $p_T^{\text{asso}} > 0.15$ GeV/c, one of the distributions obtained is shown in Figure 6. One should note that for these lower momenta the multiplicity of hadrons and with it the background to be subtracted increases drastically. Thus the measurements are extremely difficult, and a quantitative interpretation is still under discussion. Nevertheless, interesting observations can be made: the far-angle correlation appears both stronger and wider in central Au+Au collisions compared to p+p collisions. The very high yield of soft correlated particles can carry a significant fraction of the original jet momentum. The broad azimuthal distribution appears to be consistent with no dynamical correlations beyond simple momentum conservation [30]. But also on the near side, the correlation structures in p+p and central Au+Au are not as similar as was observed for higher momenta. While the peak is of similar width, the yield is strongly enhanced in Au+Au compared to p+p.

This would be in contradiction with an extreme version of the surface bias discussed above, as there is some mod-

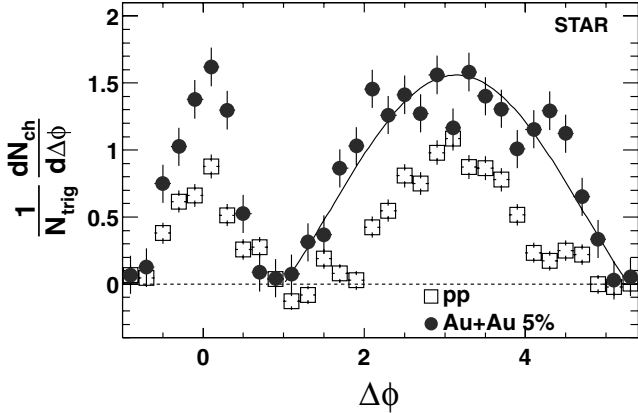


Fig. 6. Relative azimuthal angle distribution for combinations of a high p_T trigger hadron and a second softer ($p_T^{asso} > 0.15$ GeV/c) hadron in p+p and central Au+Au collisions [29] at $\sqrt{s_{NN}}=200$ GeV.

ification even of the near side fragmentation. For a given p_T^{trig} the number of associated hadrons at high p_T is similar, while there are additional soft hadrons accompanying them in Au+Au collisions, which would imply that the same high p_T^{trig} hadron would on average require a higher momentum jet to fragment. This would have lost some energy in a thin shell close to the surface, which would be transferred into soft particles. For $p_T^{asso} > 2$ GeV/c the yield per trigger particle would be unaltered, which could be related to vacuum fragmentation taking over above this threshold. This is a very naïve picture, and a clear interpretation certainly requires more precise systematic measurements. However, it is already apparent that a real interpretation of all the features of hadron suppression is much more complicated.

The strong, seemingly unaltered near-side correlation structure for a certain region of phase space is also puzzling related to baryon/meson phenomena in the scaling of yields and the elliptic flow strength. Hadrons generated from coalescence of thermal partons, in fact probably any hadrons of purely thermodynamic origin should not show jet-like correlations. Thus, if about 50% of the hadrons in this intermediate p_T region come from such a non-fragmentation source, the correlations should be considerably weakened [31]. Coalescence models have been enhanced by allowing also a recombination of thermal partons with partons from a fragmentation process (shower partons), which would lead to correlation structure between different hadrons, still one would expect significantly different correlation structures for such mixed production scenarios.

These pictures can be confronted with measurements of correlations for identified trigger particles. The PHENIX experiment has measured correlations for proton- and pion-triggers [32], which do not show significant differences in the strength. This is confirmed by measurements of the STAR experiment for Λ and K_S^0 [33]. If all the baryon excess observed in the yields would be attributed to thermal coalescence, this would certainly

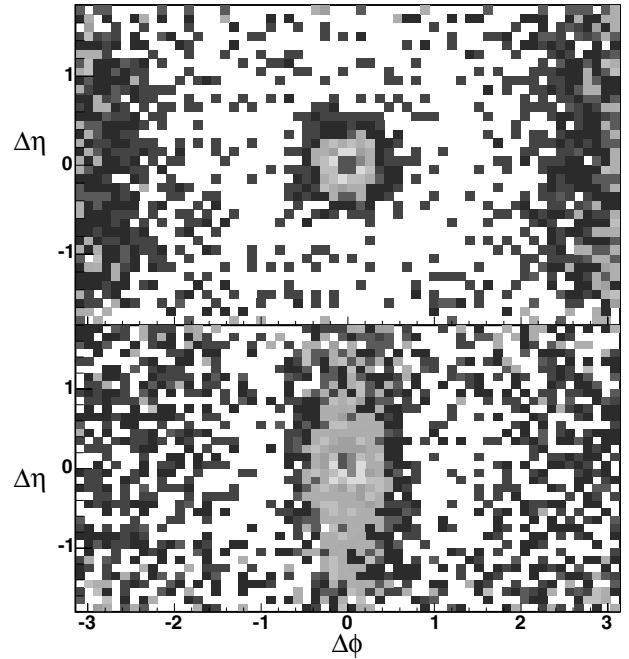


Fig. 7. Two-dimensional ($\Delta\eta \times \Delta\phi$) charged dihadron correlation functions from minimum bias p+p (upper) and central Au+Au (lower) collisions at $\sqrt{s}=200$ GeV, with $3 < p_T^{trig} < 6$ GeV/c and $2 < p_T^{asso} < p_T^{trig}$ [33].

not allow to explain the observed correlation strengths. Whether the inclusion of shower partons in coalescence models can quantitatively explain dihadron correlations remains an open question.

There are other observations which suggest a coupling of the near-side fragmentation to the medium also for higher momenta. Figure 7 shows two dimensional ($\Delta\eta \times \Delta\phi$) correlation functions for high p_T charged dihadrons from p+p (upper) and central Au+Au (lower) collisions, corrected for finite η acceptance. In p+p collisions one can see the strong small-angle correlation ($\Delta\phi \approx 0$), which is also concentrated at small relative pseudorapidity ($\Delta\eta \approx 0$), and the slightly broader correlation of the recoil jet at ($\Delta\phi \approx \pi$), which is distributed over a wider range in $\Delta\eta$ due to the possibly different values of x of the initially scattered partons. For central Au+Au collisions there are also correlations at $\Delta\phi \approx 0$ and $\approx \pi$. The latter is in this case believed to be due to elliptic flow, and not jets. The former shows also a jet-like correlation at $\Delta\eta \approx 0$, but in addition a correlation which is long-range in $\Delta\eta$ and much stronger than the one on the away side. This second component appears to be distinct from the jet-like correlation, which makes a different underlying mechanism plausible. Mechanisms involving a coupling of these associated particles to collective flow phenomena have been discussed [34, 35], but the physics underlying these observations is not at all clear yet.

4 Summary

The measurement of jet-related phenomena in heavy-ion collisions is an important tool to study dense QCD matter. At RHIC, jet quenching phenomena have been firmly established. The single inclusive hadron yield at high p_T is strongly suppressed, the amount of suppression is successfully described by models based on pQCD and incorporating partonic energy loss via gluon bremsstrahlung. An anisotropy of the yields is observed, which is most likely due to an anisotropy in energy loss. Dihadron correlations show a modification of jet fragmentation patterns: High p_T associated hadrons are suppressed on the recoil side, while there appears to be a softening of the spectra with an increased yield at low p_T . Dihadron correlations relative to the reaction plane exhibit a clear path length dependence of the suppression. While at very high p_T particles may be produced mainly from vacuum fragmentation, the intermediate p_T region shows a number of interesting phenomena following a baryon/meson classification. Some of these phenomena are naturally explained by invoking coalescence as a production mechanism, however, currently no consistent model exists, which can quantitatively explain the multitude of experimental observations. One of the keys in understanding the dynamics of the energy loss mechanisms will certainly be a detailed study of the coupling of jet related observables to the behavior of the bulk.

Many aspects of the theory behind partonic energy loss have not yet been tested. Future analysis and measurements, as e.g. the latest high luminosity RHIC data, will push the kinematical limits and provide important further advancement in the study of QCD matter.

References

1. K. Adcox *et al.* (PHENIX Collaboration), Nucl. Phys. A **757**, 184 (2005), nucl-ex/0410003.
2. B. B. Back *et al.* (PHOBOS Collaboration), Nucl. Phys. A **757**, 28 (2005), nucl-ex/0410022.
3. I. Arsene *et al.* (BRAHMS Collaboration), Nucl. Phys. A **757**, 1 (2005), nucl-ex/0410020.
4. J. Adams (STAR Collaboration), Nucl. Phys. A **757**, 102 (2005), nucl-ex/0501009.
5. K. Read, these proceedings.
6. S. S. Adler *et al.* (PHENIX Collaboration), Phys. Rev. Lett. **91**, 241803 (2003), hep-ex/0304038.
7. J. Frantz (PHENIX Collaboration), J. Phys. **G30**, S1003 (2004), nucl-ex/0404006.
8. H. Buesching (PHENIX Collaboration), proceedings of Hard Probes 2004, to be published in Eur. Phys. J. C.
9. S.S. Adler *et al.* (PHENIX Collaboration), Phys. Rev. Lett. **91**, 172301 (2003).
10. C. Adler *et al.* [STAR Collaboration], Phys. Rev. Lett. **92**, 052302 (2004).
11. B.B. Back *et al.* (PHOBOS Collaboration), Phys. Rev. Lett. **91**, 072302 (2003).
12. S.S. Adler *et al.* (PHENIX Collaboration), Phys. Rev. Lett. **91**, 072303 (2003).
13. J. Adams *et al.* (STAR Collaboration), Phys. Rev. Lett. **91**, 072304 (2003).
14. I. Arsene *et al.* (BRAHMS Collaboration), Phys. Rev. Lett. **91**, 072305 (2003).
15. D. d'Enterria, nucl-ex/0406012.
16. R. Baier, D. Schiff, and B. G. Zakharov, Ann. Rev. Nucl. Part. Sci. **50**, 37 (2000), hep-ph/0002198.
17. M. Gyulassy, I. Vitev, X.-N. Wang, and B.-W. Zhang, (2003), nucl-th/0302077.
18. A. Kovner and U. A. Wiedemann, hep-ph/0304151.
19. K. J. Eskola, H. Honkanen, C. A. Salgado, and U. A. Wiedemann, Nucl. Phys. **A747**, 511 (2005), hep-ph/0406319.
20. C. Adler *et al.* (STAR Collaboration), Phys. Rev. Lett. **90**, 082302 (2003), nucl-ex/0210033.
21. A. Drees, H. Feng, and J. Jia, Phys. Rev. C **71**, 034909 (2005), nucl-th/0310044.
22. A. Dainese, C. Loizides, and G. Paic, Eur. Phys. J. **C38**, 461 (2005), hep-ph/0406201.
23. J. Adams *et al.* (STAR Collaboration), Phys. Rev. Lett. **93**, 252301 (2004), nucl-ex/0407007.
24. J. Adams *et al.* (STAR Collaboration), Phys. Rev. Lett. **92**, 052302 (2004), nucl-ex/0306007.
25. S. A. Voloshin, Nucl. Phys. **A715**, 379 (2003), nucl-ex/0210014.
26. R. J. Fries, B. Müller, C. Nonaka and S. A. Bass, Phys. Rev. Lett. **90**, 202303 (2003).
27. V. Greco, C. M. Ko and P. Levai, Phys. Rev. Lett. **90**, 202302 (2003).
28. R. C. Hwa and C. B. Yang, Phys. Rev. **C70**, 024905 (2004), nucl-th/0401001.
29. J. Adams *et al.* (STAR Collaboration), (2005) nucl-ex/0501016.
30. N. Borghini, P. M. Dinh, and J.-Y. Ollitrault, Phys. Rev. **C62**, 034902 (2000), nucl-th/0004026.
31. T. Peitzmann, J. Phys. G **31** S443 (2005).
32. S. S. Adler *et al.* (PHENIX Collaboration), Phys. Rev. C **71**, 051902 (2005), nucl-ex/0408007.
33. D. Magestro (STAR Collaboration), proceedings of Hard Probes 2004, to be published in Eur. Phys. J. C.
34. S. A. Voloshin, nucl-th/0312065.
35. N. Armesto, C. A. Salgado, and U. A. Wiedemann, Phys. Rev. Lett. **93**, 242301 (2004), hep-ph/0405301.

Open heavy-flavour production in ALICE

A. Dainese for the ALICE Collaboration

Dipartimento di Fisica “G. Galilei”, Università degli Studi di Padova, and INFN, Italy

Abstract. After a short review of the Physics motivations for the study of open heavy flavour production in proton–proton, proton–nucleus and nucleus–nucleus collisions at the LHC, we present results on the expected performance of the ALICE experiment for charm and beauty production measurements.

1 Introduction

The ALICE experiment [1] will study nucleus–nucleus (AA) collisions at the LHC, with a centre-of-mass energy $\sqrt{s_{NN}} = 5.5$ TeV per nucleon–nucleon (NN) collision for the Pb–Pb system, in order to investigate the properties of QCD matter at energy densities of up to several hundred times the density of atomic nuclei. Under these conditions a deconfined state of quarks and gluons is expected to be formed.

The measurement of open charm and open beauty production allows to investigate the mechanisms of heavy-quark production, propagation and hadronization in the hot and dense medium formed in high-energy nucleus–nucleus collisions. The open charm and open beauty cross sections are also needed as a reference to measure the effect of the transition to a deconfined phase on the production of quarkonia. Heavy-quark production measurements in proton–proton and proton–nucleus collisions at the LHC, besides providing the necessary baseline for the study of medium effects in nucleus–nucleus collisions, are interesting *per se*, as a test of QCD in a new energy domain.

2 Heavy-flavour production from pp to AA

Heavy-quark pairs ($Q\bar{Q}$) are expected to be produced in primary partonic scatterings with large virtuality $Q^2 > (2m_Q)^2$ and, thus, on small temporal and spatial scales, $\Delta t \sim \Delta r \sim 1/Q \lesssim 0.1$ fm (for $m_c = 1.2$ GeV). In nucleus–nucleus reactions, this implies that the initial production process is not affected by the presence of the dense medium formed in the collision. Given the large virtualities, the baseline production cross sections in NN collisions can be calculated in the framework of collinear factorization and perturbative QCD (pQCD) [2]. For the estimate of baseline production yields in nuclear collisions (to be used for performance studies and preparation of the analysis strategies), a scaling of the yields with the average number $\langle N_{\text{coll}} \rangle$ of inelastic NN collisions (binary

scaling) is usually assumed:

$$d^2 N_{AA(\text{pA})}^Q / dp_t dy = \langle N_{\text{coll}} \rangle \times d^2 N_{pp}^Q / dp_t dy. \quad (1)$$

The expected $c\bar{c}$ and $b\bar{b}$ production yields for different collision systems at the LHC are reported in the first line of Table 1 [3]. These numbers, assumed as the ALICE baseline, are obtained from pQCD calculations at NLO [2], including the nuclear modification of the parton distribution functions (PDFs) [4] in the Pb nucleus (details on the choice of pQCD parameter values and PDF sets can be found in [3]). Note that the predicted yields have large uncertainties, of about a factor 2, estimated by varying the values of the calculation parameters. An illustration of the theoretical uncertainty band for the D meson cross section as a function of p_t will be shown in section 3, along with the expected sensitivity of the ALICE experiment.

Several effects can determine the breakdown of binary scaling in pA and AA collisions. They are usually divided in two classes, that we discuss in the following.

Initial-state effects, such as nuclear shadowing, the modification of the parton distribution functions in the nucleus due to gluon recombination at small momentum fraction x . Initial-state effects can, at least in principle, be studied by comparing proton–proton and proton–nucleus collisions. It has recently been argued that, indeed, at LHC energy, gluon recombination may occur even in pp collisions and affect the charm production cross section [5].

Final-state effects in AA collisions, due to the interaction of the produced partons with the medium. Partonic

Table 1. Expected $Q\bar{Q}$ yields per event at the LHC, from NLO pQCD calculations [3]. For p–Pb and Pb–Pb, PDF nuclear modification is included and N_{coll} scaling is assumed.

colliding system	pp	p–Pb	Pb–Pb
$\sqrt{s_{NN}}$	14 TeV	8.8 TeV	5.5 TeV
centrality	–	min. bias	0–5% σ^{inel}
$c\bar{c}$ pairs	0.16	0.78	115
$b\bar{b}$ pairs	0.0072	0.029	4.6

energy loss in the medium is the main example of such an effect. Believed to be at the origin of the jet quenching phenomena observed in Au–Au collisions at RHIC [6], energy loss is expected to depend on the properties of the medium (gluon density and volume) and on the properties of the ‘probe’ parton (colour charge and mass). Due to the large values of their masses, charm and beauty quarks are qualitatively different probes with respect to light partons, since, on QCD grounds, the in-medium energy loss of massive partons is expected to be reduced relative to that of ‘massless’ partons (light quarks and gluons) [7–9]. In addition to that, since at LHC energy most of the measured light-flavour hadrons will originate from a gluon parent, heavy-flavour particles, such as D mesons, will provide a tool to tag a quark parent. As pointed out in [10], the comparison of the high- p_t suppression for D mesons and for light-flavour hadrons should test the colour-charge dependence (quark parent vs. gluon parent) of parton energy loss, while the comparison for B mesons and for light-flavour hadrons should test its mass dependence (massive parent vs. massless parent) — in section 4 and 5 we show some predictions from [10] and compare them to the expected ALICE sensitivity for these quenching studies.

3 Heavy-flavour detection in ALICE

The ALICE experimental setup [1, 11] was designed in order to allow the detection of D and B mesons in the high-multiplicity environment of central Pb–Pb collisions at LHC energy, where up to several thousand charged particles might be produced per unit of rapidity. The heavy-flavour capability of the ALICE detector is provided by:

- Tracking system; the Inner Tracking System (ITS), the Time Projection Chamber (TPC) and the Transition Radiation Detector (TRD), embedded in a magnetic field of 0.5 T, allow track reconstruction in the pseudo-rapidity range $-0.9 < \eta < 0.9$ with a momentum resolution better than 2% for $p_t < 20$ GeV/c and a transverse impact parameter¹ resolution better than 60 μm for $p_t > 1$ GeV/c (the two innermost layers of the ITS are equipped with silicon pixel detectors)².
- Particle identification system; charged hadrons are separated via dE/dx in the TPC and in the ITS and via time-of-flight measurement in the Time Of Flight (TOF) detector; electrons are separated from charged pions in the dedicated Transition Radiation Detector (TRD) [12], and in the TPC; muons are identified in the forward muon spectrometer covering in acceptance the range $-4 < \eta < -2.5$.

¹ The transverse impact parameter, d_0 , is defined as the distance of closest approach of the track to the interaction vertex, in the plane transverse to the beam direction.

² Note that, for pp collisions, the impact parameter resolution maybe slightly worse, due to the larger transverse size of the beam at the ALICE interaction point. This is taken into account in the studies presented in the following.

Detailed analyses [13], based on a full simulation of the detector and of the background sources, have shown that ALICE has a good potential to carry out a rich heavy-flavour Physics programme. In section 4 we describe the expected performance for the exclusive reconstruction of $D^0 \rightarrow K^- \pi^+$ decays in pp, p–Pb and Pb–Pb collisions, and the estimated sensitivity for the study of charm energy loss in Pb–Pb collisions. In sections 5 and 6 we present the perspectives for the measurement of beauty production in central Pb–Pb collisions in the semi-electronic and semi-muonic decay channels.

For all studies a multiplicity of $dN_{\text{ch}}/dy = 6000$ was assumed for central Pb–Pb collisions³. We report the results corresponding to the expected statistics collected by ALICE per LHC year: 10^7 central (0–5% σ^{inel}) Pb–Pb events at $\mathcal{L}_{\text{Pb–Pb}} = 10^{27} \text{ cm}^{-2}\text{s}^{-1}$ and 10^9 pp events at $\mathcal{L}_{\text{pp}}^{\text{ALICE}} = 5 \times 10^{30} \text{ cm}^{-2}\text{s}^{-1}$, in the barrel detectors; the forward muon arm will collect about 40 times larger samples (i.e. 4×10^8 central Pb–Pb events).

4 Measurement of charm production and in-medium quenching

One of the most promising channels for open charm detection is the $D^0 \rightarrow K^- \pi^+$ decay (and its charge conjugate) which has a branching ratio (BR) of about 3.8%. The expected production yields (BR \times dN/dy at $y = 0$) for D^0 (and \bar{D}^0) mesons decaying in a $K^\mp \pi^\pm$ pair in central Pb–Pb (0–5% σ^{inel}) at $\sqrt{s_{\text{NN}}} = 5.5$ TeV, in minimum-bias p–Pb collisions at $\sqrt{s_{\text{NN}}} = 8.8$ TeV and in pp collisions at $\sqrt{s} = 14$ TeV are, in the order, 5.3×10^{-1} , 3.7×10^{-3} and 7.5×10^{-4} per event.

Figure 1 (left) shows a sketch of the decay: the main feature of this topology is the presence of two tracks with impact parameters $d_0 \sim 100 \mu\text{m}$. The detection strategy [14] to cope with the large combinatorial background from the underlying event is based on:

³ This value of the multiplicity can be taken as a conservative assumption, since extrapolations based on RHIC data predict $dN_{\text{ch}}/dy = 2000\text{--}3000$.

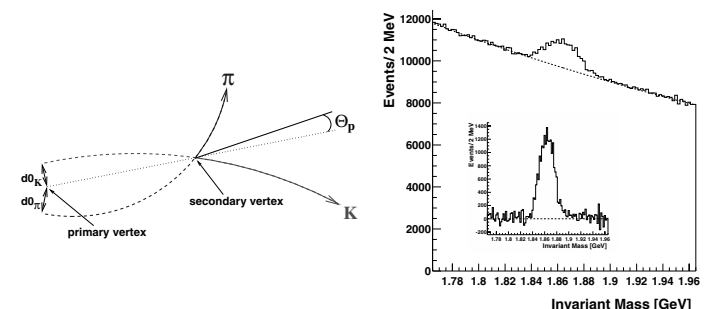


Fig. 1. Schematic representation of the $D^0 \rightarrow K^- \pi^+$ decay (left). $K\pi$ invariant-mass distribution corresponding to 10^7 central Pb–Pb events (right); the background-subtracted distribution is shown in the insert.

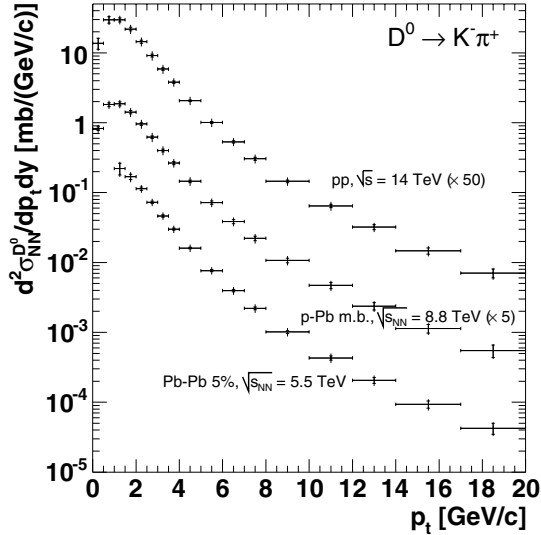


Fig. 2. p_t -differential cross section per NN collision for D^0 production, as expected to be measured with 10^7 central Pb–Pb events 10^8 minimum-bias p–Pb events, and 10^9 pp minimum-bias events. Statistical (inner bars) and quadratic sum of statistical and p_t -dependent systematic errors (outer bars) are shown. A normalization error of 9% for Pb–Pb, 9% for p–Pb and 5% for pp is not shown.

1. selection of displaced-vertex topologies, i.e. two tracks with large impact parameters and small pointing angle Θ_p between the D^0 momentum and flight-line (see sketch in Fig. 1);
2. identification of the K track in the TOF detector;
3. invariant-mass analysis (see p_t -integrated distribution in Pb–Pb after selections in Fig. 1).

This strategy was optimized separately for pp, p–Pb and Pb–Pb collisions, as a function of the D^0 transverse momentum [13,15]. As shown in Fig. 2, the accessible p_t range is 1–20 GeV/c for Pb–Pb and 0.5–20 GeV/c for pp and p–Pb, with a statistical error better than 15–20% and a systematic error (acceptance and efficiency corrections, centrality selection for Pb–Pb) better than 20%. More details are given in Ref. [13,15].

For the case of pp collisions, the experimental errors on the p_t -differential cross section are expected to be significantly smaller than the current theoretical uncertainty band from NLO pQCD calculations (estimated by varying the values of the charm quark mass and of the factorization and renormalization scales). The resulting ‘data/theory’ plot in Fig. 3 shows that this will allow us to perform a sensitive test of the pQCD predictions for charm production at LHC energy.

We studied [16] the sensitivity for a comparison of the energy loss of charm quarks and of massless partons by considering:

- the *nuclear modification factor* of D mesons as a function of p_t

$$R_{AA}^D(p_t) \equiv \frac{1}{\langle N_{\text{coll}} \rangle} \times \frac{dN_{AA}^D/dp_t}{dN_{pp}^D/dp_t}, \quad (2)$$

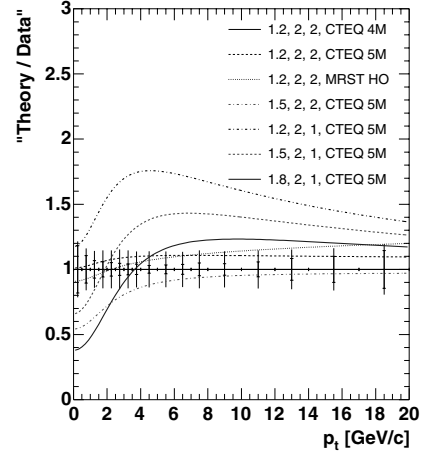


Fig. 3. Sensitivity on $d^2\sigma^{D^0}/dp_t dy$, in pp at 14 TeV, compared to pQCD predictions obtained with different sets of input parameters: m_c [GeV], the factorization and renormalization scales, in units of $m_{t,c}$, and the PDF set. The comparison is shown as a ‘data/theory’ plot. Error bars are defined as in Fig. 2.

which is used to characterize the medium-induced high- p_t suppression — in central Au–Au collisions at RHIC, R_{AA} is found to be $\simeq 0.2$ for both π^0 and charged hadrons for $p_t > 4$ GeV/c [6];

- the *heavy-to-light ratio* of the nuclear modification factors of D mesons and of charged hadrons:

$$R_{D/h}(p_t) \equiv R_{AA}^D(p_t) / R_{AA}^h(p_t). \quad (3)$$

In Fig. 4 we compare our estimated sensitivity on R_{AA}^D and $R_{D/h}$ to theoretical calculation results [10] that implement radiative parton energy loss with medium density described by transport coefficient values in the range, $\hat{q} = 25\text{--}100$ GeV²/fm, expected for central Pb–Pb collisions at $\sqrt{s_{NN}} = 5.5$ TeV on the basis of quenching measurements at RHIC. The experimental uncertainties, reported in Fig. 4 for the case $\hat{q} = 50$ GeV²/fm and $m_c = 1.2$ GeV, are discussed in detail in Refs. [15,16]. The effect of nuclear shadowing, introduced via the EKS98 parameterization [4], is clearly visible in the R_{AA} without energy loss for $p_t \lesssim 7$ GeV/c. Above this region, only parton energy loss is expected to affect the nuclear modification factor of D mesons. The small difference between the theoretical R_{AA} predictions for $m_c = 0$ and 1.2 GeV indicates that the charm quark behaves similarly to a light quark, as far as energy loss is concerned. Therefore, the enhancement of the heavy-to-light ratio $R_{D/h}$ is a sensitive measurement, free of mass effects, to study the colour-charge dependence of parton energy. As shown by the error bars in the figure, $R_{D/h}$ can be measured with good accuracy (as it is a double ratio (AA/pp) / (AA/pp), some common systematic uncertainties cancel out).

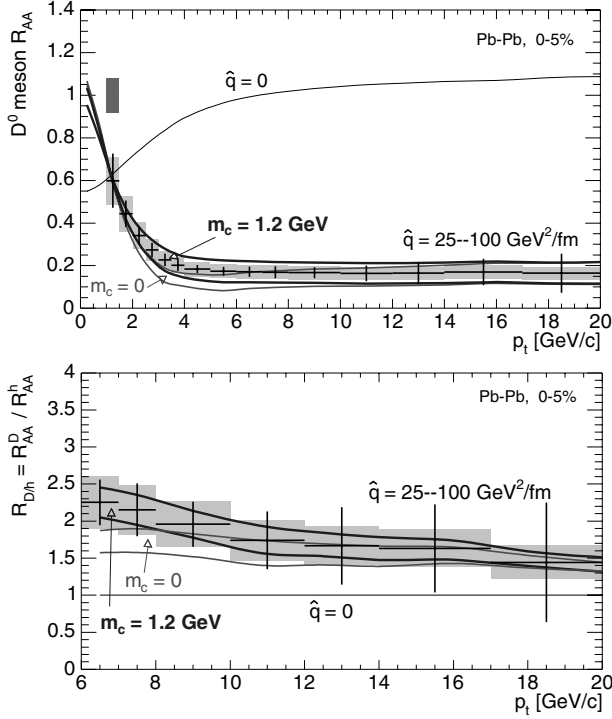


Fig. 4. Nuclear modification factor for D^0 mesons (top) and heavy-to-light ratio of the nuclear modification factors for D^0 mesons and for charged hadrons (bottom). Predictions [10] with and without the effect of the charm mass are shown for the medium density range $\hat{q} = 25\text{--}100 \text{ GeV}^2/\text{fm}$. Errors corresponding to the case ‘ $\hat{q} = 50 \text{ GeV}^2/\text{fm}$ and $m_c = 1.2 \text{ GeV}$ ’ are reported: bars = statistical, shaded area = systematic.

5 Measurement of beauty production in the semi-electronic decay channel

The production of open beauty can be studied by detecting the semi-electronic decays of beauty hadrons, mostly B mesons. Such decays have a branching ratio of $\simeq 10\%$ (plus 10% from cascade decays $b \rightarrow c \rightarrow e$, that only populate the low- p_t region in the electron spectrum). The expected yields ($\text{BR} \times dN/dy$ at $y = 0$) for $b \rightarrow e + X$ plus $b \rightarrow c(\rightarrow e + X) + X'$ in central Pb–Pb(0–5% σ^{inel}) at $\sqrt{s_{\text{NN}}} = 5.5 \text{ TeV}$ and in pp collisions at $\sqrt{s} = 14 \text{ TeV}$ are 1.8×10^{-1} and 2.8×10^{-4} per event, respectively.

The main sources of background electrons are: (a) decays of D mesons; (b) neutral pion Dalitz decays $\pi^0 \rightarrow \gamma e^+ e^-$ and decays of light mesons (e.g. ρ and ω); (c) conversions of photons in the beam pipe or in the inner detector layers and (d) pions misidentified as electrons. Given that electrons from beauty have average impact parameter $d_0 \simeq 500 \mu\text{m}$ and a hard momentum spectrum, it is possible to obtain a high-purity sample with a strategy that relies on:

1. electron identification with a combined dE/dx (TPC) and transition radiation selection, which is expected to reduce the pion contamination by a factor 10^4 ;

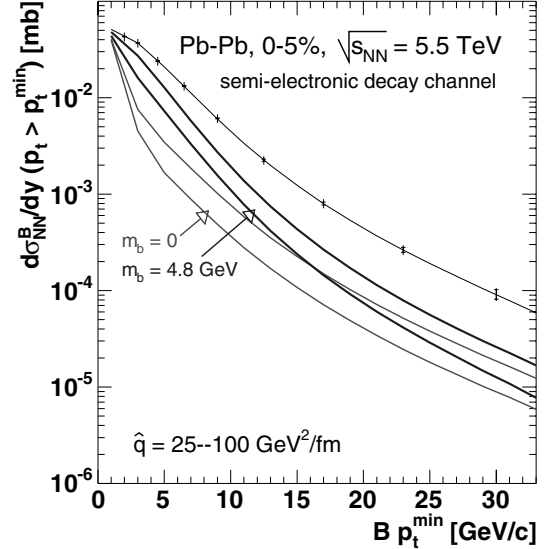


Fig. 5. Minimum- p_t -differential production cross section per NN collision for B mesons at $y = 0$, as expected to be measured from semi-electronic decays with 10^7 central Pb–Pb events. Statistical errors (inner bars) and quadratic sum of statistical and p_t -dependent systematic errors (outer bars) are shown. A normalization error of 9% is not shown. Suppression predictions [10] with and without the effect of the beauty mass are shown for the medium density range $\hat{q} = 25\text{--}100 \text{ GeV}^2/\text{fm}$.

2. impact parameter cut to reject misidentified π^\pm and e^\pm from Dalitz decays and γ conversions (the latter have small impact parameter for $p_t \gtrsim 1 \text{ GeV}/c$);
3. p_t cut to reject electrons from charm decays.

As an example, with $d_0 > 200 \mu\text{m}$ and $p_t > 2 \text{ GeV}/c$, the expected statistics of electrons from b decays is 8×10^4 for 10^7 central Pb–Pb events, allowing the measurement of electron-level p_t -differential cross section in the range $2 < p_t < 18 \text{ GeV}/c$. The residual contamination of about 10%, accumulated in the low- p_t region, of electrons from prompt charm decays, from misidentified charged pions and γ -conversion electrons can be evaluated and subtracted using a Monte Carlo simulation tuned to reproduce the measured cross sections for pions and D^0 mesons. A Monte-Carlo-based procedure can then be used to compute, from the electron-level cross section, the B-level cross section $d\sigma^B(p_t > p_t^{\min})/dy$ [13]. In Fig. 5 we show this cross section for central Pb–Pb collisions with the estimated statistical and systematic uncertainties. The covered range is $2 < p_t^{\min} < 30 \text{ GeV}/c$.

The predicted suppression of the B meson p_t^{\min} -differential cross section due to b quark energy loss is also plotted in Fig. 5. The transport coefficient range $25\text{--}100 \text{ GeV}^2/\text{fm}$ is considered and the two bands represent the results for $m_b = 0$ and 4.8 GeV ; the two bands are well separated up to $p_t^{\min} \simeq 15 \text{ GeV}/c$. The quenching predictions are shown only for illustration, since the study of the B meson suppression will have to be performed by using as a reference the cross section measured in pp collisions. The sensitivity of this study is currently being investigated.

6 Measurement of beauty production in the semi-muonic decay channel

Beauty production can be measured also in the ALICE forward muon spectrometer, $-4 < \eta < -2.5$, analyzing the single-muon p_t distribution and the opposite-sign dimuons invariant mass distribution [13, 17].

The main backgrounds to the ‘beauty muon’ signal are π^\pm , K^\pm and charm decays. The cut $p_t > 1.5$ GeV/c is applied to all reconstructed muons in order to increase the signal-to-background ratio. For the opposite-sign di-muons, the residual combinatorial background is subtracted using the technique of event-mixing and the resulting distribution is subdivided into two samples: the low-mass region, $M_{\mu^+\mu^-} < 5$ GeV, dominated by dimuons originating from a single b quark decay through $b \rightarrow c(\rightarrow \mu^+)\mu^-$ (BD_{same}), and the high-mass region, $5 < M_{\mu^+\mu^-} < 20$ GeV, dominated by $b\bar{b} \rightarrow \mu^-\mu^+$, with each muon coming from a different quark in the pair (BB_{diff}). Both samples have a background from $c\bar{c} \rightarrow \mu^+\mu^-$ and a fit is performed to extract the charm- and beauty-component yields. The single-muon p_t distribution has three components with different slopes: K and π , charm, and beauty decays. The first component is subtracted on the basis of the identified hadron spectra measured in the central barrel. Then, a fit technique allows to extract a p_t distribution of muons from beauty decays. A Monte Carlo procedure, similar to that used for semi-electronic decays, allows to extract B-level cross sections for the data sets (low-mass $\mu^+\mu^-$, high-mass $\mu^+\mu^-$, and p_t -binned single-muon distribution), each set covering a different B-meson $p_t > p_t^{\text{min}}$ region. The results using only the single muons are shown in Fig. 6. Since only minimal cuts are applied, the reported statistical errors (inner bars) are very small and the high- p_t reach is excellent. The main sources of systematic errors (outer bars) are: corrections for acceptance and efficiency, subtraction of the background muons from charged pion and kaon decays, and fit procedure to separate the beauty and charm components.

7 Conclusions

Heavy quarks, abundantly produced at LHC energies, will allow to address several physics issues, in pp, pA and AA collisions. In particular, they provide tools to: probe, via parton energy loss and its predicted colour-charge and mass dependences, the dense medium formed in Pb–Pb collisions; probe, in pp collisions, the pQCD calculations parameters space; probe the small- x regime of the PDFs, where saturation effects are expected to be important.

The excellent tracking, vertexing and particle identification performance of ALICE will allow to fully explore this rich phenomenology, as we have shown with some specific examples on D and B meson measurements.

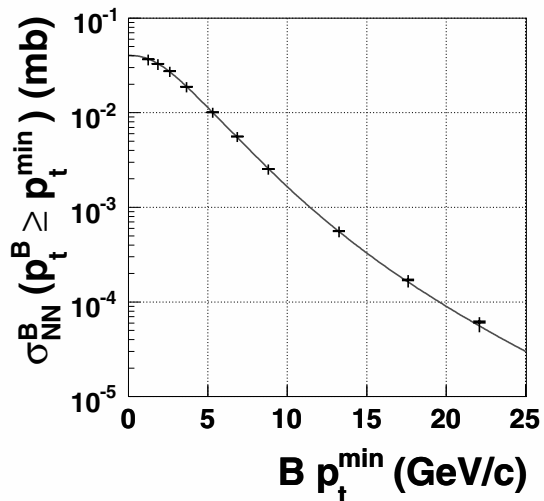


Fig. 6. Minimum- p_t -differential production cross section per NN collision for B mesons with $-4 < y < -2.5$ in central Pb–Pb collisions, as expected to be measured from the single-muon data set. Statistical errors (inner bars) corresponding to 4×10^8 events and p_t -dependent systematic errors (outer bars) are shown. A normalization error of 10% is not shown.

References

- ALICE Collaboration, Physics Performance Report Vol. I, J. Phys. G **30**, 1517 (2003) (CERN/LHCC 2003-049).
- M. Mangano, P. Nason and G. Ridolfi, Nucl. Phys. B **373**, 295 (1992).
- N. Carrer and A. Dainese, ALICE Internal Note, ALICE-INT-2003-019 (2003), arXiv:hep-ph/0311225.
- K.J. Eskola, V.J. Kolhinen, C.A. Salgado, Eur. Phys. J. C **9**, 61 (1999).
- A. Dainese, R. Vogt, M. Bondila, K.J. Eskola and V.J. Kolhinen, J. Phys. G **30**, 1787 (2004).
- T. Peitzmann, these proceedings.
- Yu.L. Dokshitzer and D.E. Kharzeev, Phys. Lett. B **519**, 199 (2001).
- N. Armesto, C.A. Salgado and U.A. Wiedemann, Phys. Rev. D **69**, 114003 (2004).
- M. Djordjevic and M. Gyulassy, Phys. Lett. B **560**, 37 (2003); Nucl. Phys. A **733**, 265 (2004).
- N. Armesto, A. Dainese, C.A. Salgado and U.A. Wiedemann, Phys. Rev. D **71**, 054027 (2005).
- H.-A. Gustafsson, these proceedings.
- C. Adler, these proceedings.
- ALICE Collaboration, Physics Performance Report Vol. II, in preparation.
- N. Carrer, A. Dainese and R. Turrisi, J. Phys. G **29**, 575 (2003).
- A. Dainese, Ph.D. Thesis (2003), arXiv:nucl-ex/0311004.
- A. Dainese, Eur. Phys. J. C **33**, 495 (2004).
- R. Guernane *et al.*, ALICE Internal Note, ALICE-INT-2005-018 (2005).

Identification of high energy direct photons and photon-jet events at LHC with ALICE

G. Conesa^{1,2}, H. Delagrangé², J. Díaz¹, Y.V. Kharlov³, and Y. Schutz^{2,4}

¹ IFIC (Centro Mixto Universidad de Valencia-CSIC), Valencia, Spain

² SUBATECH UMR6457 (Ecole des Mines-CNRS-Université de Nantes), Nantes, France

³ Institute for High-Energy Physics, Protvino, Russia

⁴ CERN, Genève, Switzerland

Abstract. Prompt photons and light neutral-mesons will be detected and identified in the ALICE experiment at LHC with the PHOS detector and, if finally funded, with the EMCAL detector. Charged particles will be detected and identified by the central tracking system. The possibility to tag jets with photons is examined. Methods to identify prompt photons and prompt photon-jet events and to distinguish them against the background of decay photons are discussed.

1 Introduction

The experimental study of hadron jets at LHC is expected to provide decisive data for understanding the properties of the quark gluon plasma (QGP) formed in ultra-relativistic nucleus-nucleus collisions [1]. Hadron jets are generated by the hadronization of final-state partons with high transverse momentum (p_T) scattered in primary collisions. Bjorken suggested more than 20 years ago that partons propagating through a nuclear medium suffer an energy loss which is strongly dependent on the color charge density of the medium [2]. Medium modification manifests as a modification of the energy spectrum of jet hadrons, which is known as the jet quenching effect. This effect has indeed been observed in central Au-Au collisions at $\sqrt{s_{NN}} = 130$ and 200 GeV in measurements of high p_T charged and neutral hadrons ($p_T \sim 2-15$ GeV/ c) by various RHIC experiments [3,4] in which the yields of inclusive charged hadrons and π^0 mesons are suppressed by as much as a factor 5, independent of their p_T value, compared to the properly scaled pp , d -Au and peripheral Au-Au yields.

The ALICE experiment will extend these studies to much higher \sqrt{s} . Due to the larger cross sections of hard processes at LHC compared to RHIC, jets will be abundantly produced at LHC (10^5 jets with $p_T > 100$ GeV/ c per year are expected) allowing inclusive and exclusive jet measurements. In particular, jet characteristics (jet shape, jet *heating*, fragmentation function. . .) could be measured in order to study the energy distribution of jets [5]. To carry out these studies, the identification of jets and the accurate measurement of the jet energy before and after quenching is required. A very attractive method to perform these measurements is to tag jets with prompt photons emitted opposite to the jet direction. The dominant elementary processes which produce such events are $g + q \rightarrow \gamma + q$ (Compton) and $q + \bar{q} \rightarrow \gamma + g$ (anni-

hilation), although recent theoretical studies show that high order bremsstrahlung processes also contribute significantly to the photon yield below 50 GeV/ c [6]. Photons emerge almost unaltered from a dense medium and provide a measurement of the original energy and direction of the parton emitted in the opposite direction. Medium effects could be identified from the behavior of the fragmentation function, i.e., the distribution of the jet energy among the jet constituents, rather than from the total jet energy.

In ALICE, photons will be detected by the PHOTON Spectrometer (PHOS) which enables to measure with high precision their 4-momentum, although, only in a limited acceptance [7]. The identification power of prompt photons is limited by the background created by decay photons (mainly from π^0 decay). The identification of photon-jet events in ALICE is optimal for photons with energy larger than 20 GeV. Below this value, decay and prompt photons cannot be efficiently separated on an event by event basis. In the present article, we discuss the feasibility of identifying prompt photons in pp and heavy-ion collisions by analysis of topological characteristics of the shower and isolation criteria. In addition, we discuss an algorithm for identifying photon-jet events and for reconstructing hadron jet features. A detailed description of the work discussed here can be found in Ref. [8].

2 Event simulation and main reconstruction features

Acceptances and energy and position resolutions for all the detectors involved in this study (PHOS and EMCAL¹

¹ ElectroMagnetic CALorimeter still under discussion.

Detector	$ \eta $	ϕ_{min}	ϕ_{max}	$\sigma_E/E(\%)$	σ_{pos}
PHOS	0.12	220°	320°	1 – 1.5	0.8 – 2.5 cm
TPC	0.7	0°	360°	2	1.1°
EMCal	0.7	60°	180°		

Table 1. TPC, EMCal and PHOS detector acceptances, and energy and position resolutions. The real TPC η acceptance is larger ($|\eta| < 0.9$), but we selected this lower value to ensure good track matching. The EMCal performance is still under investigation. Azimuthal angles are given in the ALICE global reference system.

for photons and TPC² for charged particles) are reported in Tab. 1. A full description of the ALICE detector is given in Ref. [9].

We assume that prompt photon production arises from γ -jet events in the leading order of the Standard Model, comprising Compton and annihilation processes. These processes were simulated with the event generator PYTHIA 6.203 [10] for pp collisions at $\sqrt{s} = 5.5$ TeV. The default parton distribution function, GRV 94L [11], was used. Events were generated in the energy range $20 < p_T < 100$ GeV/ c . In order to enrich the sample with events within the PHOS acceptance, we restricted the prompt photon pseudorapidity range to $|\eta_\gamma| < 0.2$ and the azimuthal aperture to $200^\circ < \phi_\gamma < 340^\circ$ in the event generation.

Events with two jets in the final state, called jet-jet events, are a significant source of background. They were simulated by hard QCD $2 \rightarrow 2$ processes in the leading pQCD order. These processes contribute to the background through hard π^0 -mesons which decay photons may be detected in PHOS as single electromagnetic showers and which may mimic prompt photons. To simulate a continuous p_T -spectrum of π^0 -mesons from 20 to 100 GeV/ c , we generated hard QCD processes in the p_T range from 30 to 300 GeV/ c . The generation of hard QCD processes was restricted to $|y_{parton}| < 0.2$ and to $|\eta_{jet}| < 0.15$, without any azimuthal angle limitation. This more severe restriction in rapidity compared to the γ -jet case was imposed to enrich the fraction of events with detectable π^0 -mesons.

Pb-Pb collisions were simulated by merging pp collisions generated by PYTHIA with heavy-ion events produced by the HIJING 1.36 [12] event generator for Pb-Pb collisions at $\sqrt{s_{NN}} = 5.5A$ TeV and impact parameter $b < 2$ fm.

In this study, a full-fledged Monte Carlo simulation of the transport of particles in PHOS was carried out. To reduce computing time, we applied a fast reconstruction method for particles detected in the TPC and EMCal [8]. The response of EMCal was assumed, as a first approximation, identical to that of PHOS.

Collision	\mathcal{L} (cm ⁻² s ⁻¹)	t (s)
pp	10^{30}	10^7
Pb-Pb	5×10^{26}	10^6

Table 2. Beam luminosity and running time for the ALICE experiment during a standard year of running at LHC.

Centrality (%)	f_C	$\langle T_{AA} \rangle_C$ (mb ⁻¹)
5	0.05	26.0
10	0.10	23.2
minimum bias	1.00	5.58

Table 3. Centrality factor and values of the nuclear overlap function for Pb-Pb collisions, given for different collision centralities. Values of the nuclear overlap function are taken from Appendix I of [13].

2.1 Expected experimental rates

The p_T distributions, $N(p_T)$, obtained from simulations were normalized to the number of events expected in a standard LHC running year by,

$$N(p_T) = \sigma_{AA}(p_T) \cdot \mathcal{L} \cdot t \quad (1)$$

where \mathcal{L} and t are the luminosity and the experiment running time reported in Tab. 2. The cross section for pp collisions, σ_{pp} , was obtained from PYTHIA and the cross section for Pb-Pb collisions, σ_{AA} , was calculated by scaling σ_{pp} with the “binary scaling” equation,

$$\left(\frac{d^2\sigma_{AA}}{dp_T dy} \right)_C = \langle T_{AA} \rangle_C \cdot \sigma_{AA}^{geo} \cdot f_C \cdot \frac{d^2\sigma_{pp}}{dp_T dy} \quad (2)$$

where $\langle T_{AA} \rangle_C$ is the mean nuclear overlap function for the corresponding centrality class C , f_C the centrality factor and $\sigma_{AA}^{geo} = 7745$ mb the geometrical cross section given by Eq. (133) of [13]. The parameter values needed are listed in Tab. 3. The resulting spectra for Pb-Pb collisions at 5.5A TeV, for minimum bias conditions, are shown in Fig. 1.

3 Prompt photon identification: Isolation Cut Method

Two different procedures to select prompt photons from inclusive photons, which include bremsstrahlung and decay photons from jet-jet events, were applied: the Shower Shape Analysis (SSA) [7], and the Isolation Cut Method (ICM). In the former method, photons were identified by analyzing the shape of the shower in PHOS, and in the latter method, photons were tagged and identified as prompt if they appear isolated, i.e., without charged particles in their vicinity.

Photon spectra from γ -jet and jet-jet events were identified with the PHOS SSA analysis. The shower generated in the PHOS calorimeter by a particle can be characterized by several parameters which define the shower

² Time Projection Chamber.

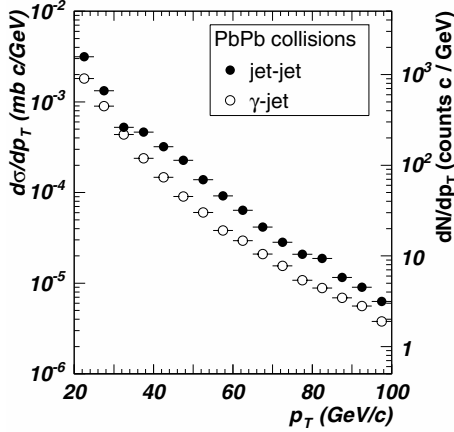


Fig. 1. Spectra of prompt photons (γ -jet events, \circ) and γ -like (single and overlapped photons from jet-jet events, \bullet) detected in PHOS, for minimum bias Pb-Pb collisions at $\sqrt{s_{NN}} = 5.5A$ TeV. Differential cross sections are given on the left y -axis of the plots and the expected number of particles on the right y -axis. Both quantities are determined for a standard LHC running year.

shape. Usually, they are taken as the length of the principal axes of the shower surface, λ_0 and λ_1 , the shower lateral dispersion, the core energy, the sphericity defined as $(\lambda_0 - \lambda_1)/(\lambda_0 + \lambda_1)$, the maximal energy fraction deposited in one single crystal and the shower multiplicity. These parameters are found to be correlated to a large extent. To select a smaller number of parameters conveying the maximal information about the shower shape, we uncorrelated the above parameters through a principal component analysis in which these seven parameters are transformed into new seven uncorrelated parameters given by the eigenvectors of the covariance matrix. We found that a good description of the shower shape is obtained when only the two most significant parameters, corresponding to the largest eigenvalues, are kept. These two principal components are found to be distributed in a Gaussian way for large samples of photon showers. We defined low, medium and high purity photons as those within three, two and one standard deviations, respectively, of the mean of their Gaussian distributions. For medium purity level, the prompt photon identification efficiency is about 85 % for pp collisions and about 75 % for Pb-Pb collisions. The misidentification probability of background events as prompt photons ranges, as a function of p_T , from 0 to 40 % for one-cluster neutral pions³ and medium purity identification, and from 0 to 15 % for hadrons. The remaining π^0 background has a contribution similar to the prompt photon signal. Requiring higher purity photons, improved the background rejection at the cost of an important reduction of the identification efficiency. To keep the identification efficiency to an acceptable value while achieving a good

³ An energetic π^0 , $E > 30$ GeV, decays into two photons with a too small opening angle to be separated in PHOS, generating in this way a single cluster.

background rejection, additional identification procedures are required.

Since prompt photons are produced in parton collisions in which the final state photon and parton are emitted in opposite directions, no hadron belonging to the parton jet fly in the same direction as the photon⁴. However, the underlying event generated by the heavy-ion collision may perturb this ideal geometrical scheme. We have developed two isolation algorithms, both based on the search for hadrons inside a cone centered around the direction (η_0, ϕ_0) of high- p_T photon candidates ($p_T > 20$ GeV/ c) identified by the SSA. The cone size is given by

$$R = \sqrt{(\phi_0 - \phi)^2 + (\eta_0 - \eta)^2}. \quad (3)$$

For γ -jet events in pp collisions, there is almost no particle inside the cone, independently of the energy of the prompt photon but for jet-jet events a clear dependence of the particle multiplicity inside the cone on the jet energy is found. Thus, the p_T distribution of particles inside a cone around a photon candidate can be used to distinguish between γ -jet and jet-jet events. Following this idea, we have developed two different selection criteria to decide if a photon candidate is isolated and can be accepted as a prompt photon:

1. There is no hadron with p_T above a given threshold in the cone.
2. The sum of the transverse momentum of all hadrons inside the cone, Σ_{p_T} , must be smaller than a given threshold.

After an exhaustive analysis we found the following optimal parameters for prompt photon identification:

- In the case of pp collisions, a γ -jet identification probability of 100 % and a jet-jet misidentification probability of 3 % was obtained with $R = 0.2$ and $\Sigma_{p_T} < 0.7$ GeV/ c .
- In the case of Pb-Pb collisions, a γ -jet identification probability of 50 % and a jet-jet misidentification probability of 7 % was obtained with $R = 0.2$ and $p_T^{th} = 2$ GeV/ c . The resultant prompt photon spectra (Fig. 2) indicate that a sufficient background reduction was attained.

We conclude that a sufficient background rejection is achieved by the ICM for pp and Pb-Pb collisions. In the case that a quenching factor of 5, as reported by RHIC [14], exists at LHC energies, the signal to background ratio would increase from 4 to 20.

3.1 Final prompt photon spectrum

We have constructed the prompt photon spectrum with the corresponding statistical and systematic errors expected to be measured during one LHC running period.

⁴ This is not true for next to leading order processes like bremsstrahlung. However, PYTHIA predicts that such processes are suppressed compared to π^0 production. This statement might have to be revised according to recent studies [6], which suggest that at high p_T the bremsstrahlung could be a dominant process ($p_T < 50$ GeV/ c).

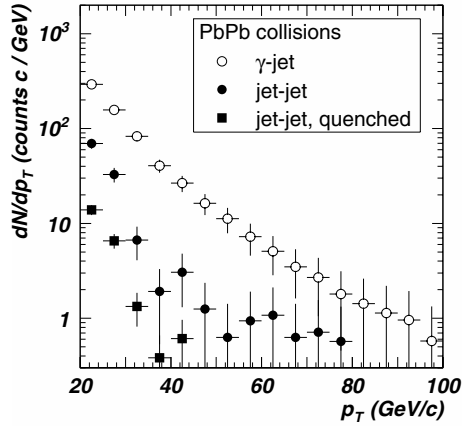


Fig. 2. Spectra with statistical errors of events identified as prompt photons in ALICE during a LHC running year by medium purity SSA and ICM ($R = 0.2$, $p_T^{th} = 2$ GeV/c) methods, due to jet-jet (\bullet) and γ -jet events (\circ), for Pb-Pb collisions at 5.5A TeV. The spectrum obtained with a quenching factor of 5 for jet-jet events is also shown (\blacksquare).

We obtained the total identified prompt photon spectrum N_γ^{id} , as the addition of the identified prompt photon spectrum from γ -jet events to the background spectrum due to jet-jet events. From the known identification probabilities, we can reconstruct the original prompt photon spectrum as follows: let N_γ be the original prompt photon spectrum, N_{π^0} the original π^0 spectrum, N_h the original hadron spectrum, ε_i^{id} the identification probability of particle i as a photon by SSA and ε_i^{ic} the identification probability of particle i as prompt photon by ICM, where i can be a photon, a one-cluster π^0 or any other hadron. We can write

$$N_\gamma^{id} = N_\gamma \varepsilon_\gamma^{id} \varepsilon_\gamma^{ic} + N_{\pi^0} \varepsilon_{\pi^0}^{id} \varepsilon_{\pi^0}^{ic} + N_h \varepsilon_h^{id} \varepsilon_h^{ic} = \zeta N_\gamma. \quad (4)$$

As discussed in the previous sections, we deduced each of the factors needed above (the ICM misidentification probabilities for π^0 and hadrons are almost identical) and calculated the correction factor ζ for the various sets of identification criteria (purity levels, cone sizes and p_T thresholds). The systematic error of the particle identification methods (PID) was calculated as the dispersion of the corrected spectra obtained by the different identification criteria. This systematic error was added quadratically to the average background spectra in order to obtain the total systematic error. The statistical error was calculated from the photon statistics as $\sqrt{N_\gamma^{id}}$. The final spectrum of identified photons and its comparison with the original spectra are shown in Fig. 3. If the assumption that hadrons are quenched by a factor 5 is made, the systematic error is significantly reduced.

4 Photon-tagged jets identification

We developed an algorithm to tag jets by prompt photons. Two different experimental configurations were con-

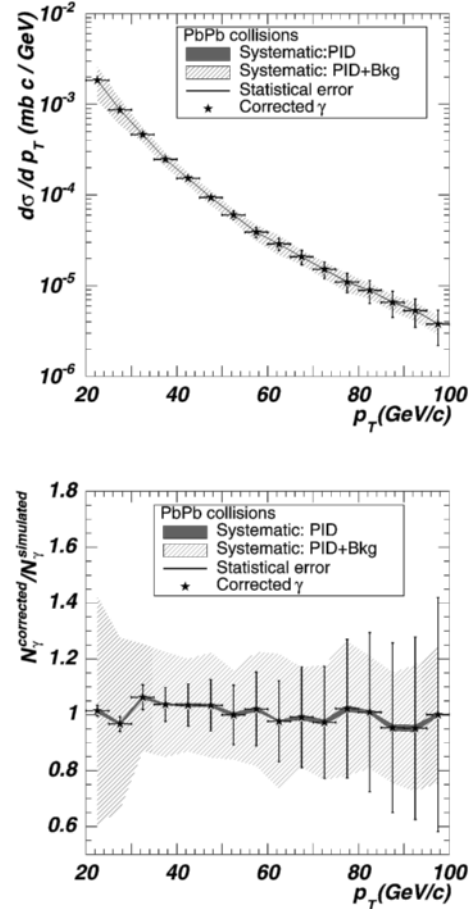


Fig. 3. Upper frame: Simulated final prompt photon spectrum measured in ALICE during a LHC running year with statistical and systematic errors. Lower frame: Ratio of the corrected prompt photon spectrum to the original simulated spectrum.

sidered : i) Charged particles are detected in the central tracking system (TPC) and neutral particles in EMCal; this configuration is labeled as TPC+EMCal; ii) Only the central tracking system is available and consequently only charged particles can be detected; this configuration is labeled as TPC. The steps of the algorithm are:

1. Search in each event for the most energetic prompt photon identified by PHOS.
2. Search for the jet leading particle⁵ (the charged hadron or neutral pion with the highest p_T value), detected by the central tracking system or EMCal, and emitted almost opposite to the photon in azimuthal angle, i.e., with $\Delta\phi$ close to 180° , $0.9\pi < \Delta\phi < 1.1\pi$. An additional condition to be satisfied by the leading particle is that its p_T value must be at least the 10 % of the photon energy.
3. Reconstruct the jet as the ensemble of all particles contained inside a cone with axis aligned along the leading particle direction defined by Eq. (3). We have

⁵ A significant proportion of the jet energy (in average 40%) is always carried by a few particles.

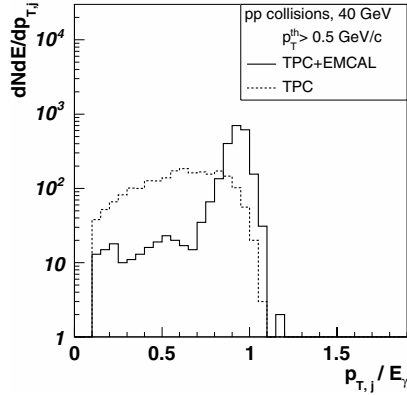


Fig. 4. Simulated jet distribution as a function of the ratio $p_{T,j}/E_{\gamma}$ for 40 GeV γ -jet events in the case of pp collisions. A jet cone of $R = 0.3$ and a jet particle threshold of $p_T > 0.5$ GeV/ c were assumed. Results for the setups without EMCAL (dashed line) and with EMCAL (solid line) are given.

taken here $R = 0.3$, and the particle p_T threshold as 0.5 GeV/ c .

4. Finally, the event is identified as a photon-jet pair if the ratio of the reconstructed energies of the jet and the prompt photon differs less than a given value. In the case of pp collisions, a photon-jet event observed in the setup including EMCAL was well identified if the ratio $p_{T,j}/E_{\gamma}$ is close to one, as displayed in Fig. 4 for 40 GeV jets. In the case of Pb-Pb collisions, the background is very important and the $p_{T,j}/E_{\gamma}$ distributions are wide and peak at values larger than one. We required in this case a higher particle momentum threshold, $p_T > 2$ GeV/ c , to calculate the energy of the jet. We took two different values for the lower $p_{T,j}/E_{\gamma}$ limit depending on the experimental setup: 0.3 for the configuration without EMCAL and 0.8 for the configuration with EMCAL.

The jet reconstruction algorithm failed for jets with $p_T < 10$ GeV/ c because the ratio $p_{T,j}/E_{\gamma}$ suffers from large fluctuations in this case. Therefore, we excluded these jets from our investigation.

We studied the jet selection efficiency, defined as the ratio of the number of identified γ -tagged jets to the number of prompt photons found in PHOS. The efficiency of the configuration without EMCAL is 40-50 % which is larger than the efficiency for the configuration with EMCAL (30 %) due to the following points: i) the wider selection angular range for the configuration without EMCAL (which is also associated to a lower identification quality); and ii) the requirement that jets measured in the configuration with EMCAL fall completely into the EMCAL acceptance which is smaller than that of the central tracking system. We applied also the γ -jet algorithm to jet-jet events in order to estimate the contamination due to these events. If no prompt photon identification is performed in PHOS, only about 10 % of the events were accepted in the setup with EMCAL but the value raises to 40-50 % in the absence

of EMCAL. Similar results were obtained for both pp and Pb-Pb collisions.

4.1 Fragmentation functions

A satisfactory observable for studying quantitatively the interaction of jets with the medium is the phase space distribution of jet hadrons [5], which is called the jet fragmentation function. The experimental fragmentation function is the distribution of charged hadrons within jets as a function of the variable z , defined for hard processes with a γ -jet pair in the final state as $z = p_T/E_{\gamma}$. Simulations of jet fragmentation functions expected to be measured in a standard year of LHC running for both pp and Pb-Pb collisions, were carried out. Identified γ -jet events in the energy range from 20 to 100 GeV were considered. The fragmentation functions obtained for jet-jet events misidentified as γ -jet events were also studied. Figure 5 shows the fragmentation function for Pb-Pb collisions. The following conclusions are drawn:

- For pp collisions, a signal (γ -jet) to background (jet-jet) ratio of about 20 in the configuration without EMCAL and almost a 100 % background rejection for the setup with EMCAL was obtained. Prompt photon identification reduces the statistics of γ -jet by a 15 %.
- In the case of Pb-Pb collisions, the contribution from the heavy-ion collision (HIC) underlying event has been eliminated statistically in the final distributions by subtracting a pseudo-fragmentation function calculated outside the cone of the leading particle. The final signal to background ratio obtained is about 4 in the case without EMCAL and rises to about 10 with EMCAL. Prompt photon identification reduces the statistics of γ -jet events by a 60 %.

To evaluate the sensitivity of photon-tagged jet fragmentation functions to nuclear medium modifications, we have calculated the nuclear modification factor R_{FF} which is defined as the ratio of the fragmentation function measured in AA collisions to the fragmentation function measured in pp collisions, scaled by the number of binary NN collisions. This factor should be equal to one in the absence of nuclear effects. We indeed obtain a value close to one over the entire z range as shown in Fig. 6 since no medium modification effect was included in our simulations. The statistical and systematic errors indicate that in the range $0.1 < z < 0.5$ variations of R_{FF} larger than 5 % could be measured in both setups. We have also considered the case in which hadrons from jet events are quenched by a factor 5 as observed at RHIC. In this case, the systematic error is under 5 % for both setups. However, the measurement of the nuclear modification factor with an accuracy better than 5 % is prevented by the expected statistics.

We still may consider another measurement approach in which EMCAL is employed for prompt photon detection and jets are detected by the central tracking system⁶. In

⁶ It is not well-advised to use PHOS as a detector of jet neutral particles due to its reduced acceptance.

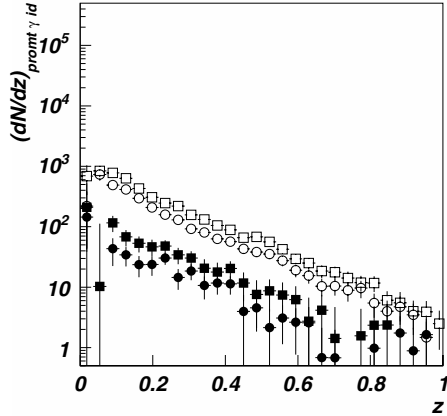


Fig. 5. Fragmentation function for γ -jet and jet-jet events with energy larger than 20 GeV for Pb-Pb collisions, for a LHC running year. Prompt photons in coincidence with jets were identified in PHOS by medium purity SSA and ICM. The HIC background has been statistically subtracted. Statistical errors are shown in the figure.

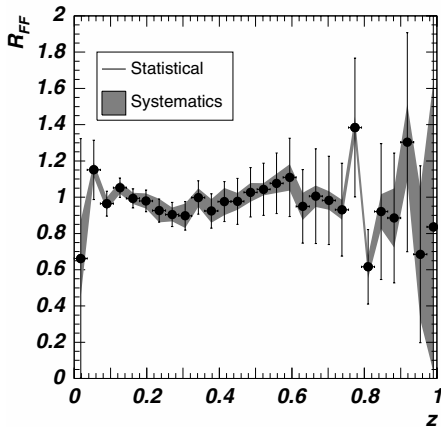


Fig. 6. Ratio of the fragmentation functions of γ -tagged jets with energy larger than 20 GeV for Pb-Pb collisions scaled by Eq. (2) to pp collisions detected in the central tracking system and EMCal. The shaded region represents the systematic error due to the contamination from jet-jet events. A similar ratio and systematics is obtained without EMCal.

this setup, if similar prompt photon identification features of PHOS and EMCal are assumed, the prompt photon statistics is enhanced by a factor seven and consequently the statistical errors are reduced by a factor 2.6.

5 Conclusions

We developed an algorithm to identify prompt photons and γ -jet events generated in pp and Pb-Pb collisions in ALICE. Prompt photons are identified efficiently in PHOS with the help of a shower shape analysis, which is capable of rejecting hadrons, and the isolation cut criterion

to reject π^0 mesons. We estimated the spectrum of the identified prompt photons for the statistics of the ALICE integrated luminosity in a standard year of running at LHC. Photon-jet events were identified by selecting a prompt photon in PHOS and searching for a leading particle in the opposite direction inside the ALICE central tracking system. Jets were reconstructed by an algorithm which takes all particles within a cone around the leading particle found which has to fulfill the requirement of being correlated with the photon. As jet-jet events have a larger cross section than photon-jet events, they originate a considerable background due to π^0 decay photons misidentified in PHOS as direct photons. In the configuration with EMCal, these events are effectively rejected and their contribution reduced to a negligible level of contamination by shower shape and isolation cut analysis. Fragmentation functions can be accurately calculated and used to obtain the nuclear modification factor, R_{FF} . We found that nuclear modifications can be measured if they produce variations of R_{FF} larger than 5 % in the region $0.1 < z < 0.5$.

References

1. Accardi, A. et al, hep-ph/0310274 (2004)
2. Bjorken, J. D., FERMILAB-PUB-82-059-THY (1982)
3. Adler, C. et al., Phys. Rev. Lett. **89**, 0202301 (2002)
4. Adler, S. et al., Phys. Rev. Lett. **91**, 072301 (2003)
5. Salgado, C. A. and Wiedemann, U. A., Phys. Rev. Lett. **93**, 42301 (2004)
6. Arleo, F. et al., JHEP **11**, 009 (2004)
7. G. Conesa et al., Nucl. Instr. and Meth. A **537**, 363-367 (2005)
8. G. Conesa et al., ALICE-INT-2005-014, (2005)
9. ALICE Collaboration, J. Phys. G: Nucl. Part. Phys. **30**, 1517-1763 (2004)
10. Sjostrand, T. et al., hep-ph/0108264, (2001)
11. Gluck, M. et al., Z. Phys. C **67**, 433-448 (1995)
12. Gyulassy, M. and Wang, X.N., Comput. Phys. Commun. **83**, 307-331 (1994)
13. Arleo, F. et al., hep-ph/0311131 (2003)
14. Adcox, K. et al., Nucl. Phys A **757**, 184 (2005)

Electron Identification with the ALICE TRD

Clemens Adler (for the ALICE TRD Collaboration)

Physikalisches Institut der Universität Heidelberg, Philosophenweg 12, 69120 Heidelberg

Abstract. In this talk an overview of the ALICE TRD detector status is presented. The TRD provides identification of electrons with a momentum of $p > 1$ GeV/c. Its main objective is the measurement of heavy quarkonia in heavy ion collisions. The final detector will consist of 540 individual drift chambers with 1.2 million read out channels. Fast on-detector reconstruction of the data enables the TRD to deliver its information already on the trigger level. Results concerning position and angle resolution and electron identification as well as measurements of transition radiation spectra from a recent test beam are shown and discussed. Three different methods of electron identification are explained and their performance is discussed.

1 Introduction

The ALICE Transition Radiation Detector (TRD) will be one of the large detector systems of the ALICE experiment at the LHC collider. An important part of the ALICE physics program is to study Υ and J/ψ production in heavy ion collisions. Compared to existing heavy ion accelerators the LHC opens up new opportunities for measurements, e.g.:

- Due to the much higher energy of the collisions a high initial production rate of charm and bottom quarks is expected which facilitates the usage of the two flavors as a probe of the matter created in the collisions.
- It is expected that all the primary J/ψ at LHC will be suppressed due to hard gluon induced breakup [1].
- A strong secondary production of J/ψ by means of statistical hadronization is predicted [2]. This model also predicts a strong centrality dependence of the J/ψ yield.
- The expected temperature of the Quark-Gluon-Plasma at LHC should be high enough to observe the onset of Υ suppression [3].

The TRD can contribute to the measurement of those observables by the identification of electrons with a momentum of $p > 1$ GeV/c. Together with the other central barrel detectors of ALICE, the Time Projection Chamber (TPC) and the Inner Tracking System (ITS) [4] the TRD will make the following measurements accessible: In the di-electron channel the production of J/ψ , Υ and the continuum can be measured. This is complementary to the muon arm measurement with the additional possibility to reconstruct displaced vertices with the ITS and therefore identify J/ψ from B decays [5]. In the single electron channel semi-leptonic decays of open charm and beauty as a handle on charm and beauty production cross section can be measured [6].

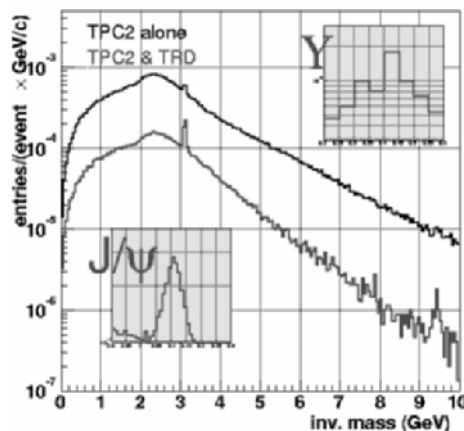


Fig. 1. Fast simulation of the ALICE Central Barrel detector performance [7]. The black line shows the background and J/ψ and Υ signals when only the TPC is used for electron identification, the red spectrum shows the performance including TRD.

The use of the TRD in those measurements can be seen in Fig. 1, where the invariant mass spectra with and without the TRD contribution to electron identification is shown.

Since the TRD can deliver a signal already 6 μ s after a collision its information can be used in the level-1 trigger. The applications are trigger on high- p_t particles with a momentum above 3 GeV/c and electron identification which will be used to enrich the Υ data sample. The TRD can also provide a Jet trigger to study jet quenching.

2 The ALICE TRD

The operation principle of the ALICE TRD is illustrated in Fig. 2. A wire chamber with a 3 cm drift region is

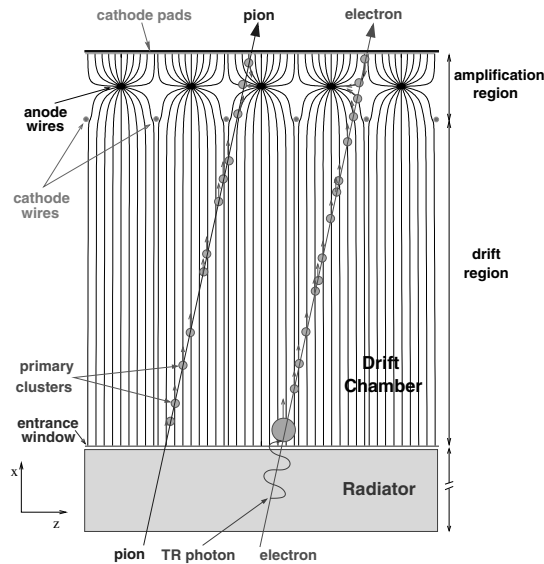


Fig. 2. Operation principle of the ALICE TRD

equipped with a Radiator consisting of a carbon reinforced Rohacell foam structure filled with polypropylene fiber mats. Any charged particle will produce a signal in the drift chamber, while only electrons with a momentum of $p > 1$ GeV/c produce transition radiation in the radiator. This radiation is absorbed in the gas (85% Xe, 15% CO₂) and an additional signal is produced which together with the higher ionization of an electron will therefore produce on average a larger signal than a pion. The signals are read out by cathode pads of sizes between 5.15 and 9.65 mm in ϕ and 75 to 85 mm in z -direction. Typically a signal is distributed over 2-3 pads in ϕ -direction enabling reconstruction of the position of a cluster to a few hundred μm .

The ALICE TRD consists of 540 individual drift chambers in 12 different sizes between 1 and 1.7 m² and a thickness of 11 cm. They are arranged azimuthally in 18 super modules, each carrying 30 chambers, arranged in 6 radial layers and 5 longitudinal stacks. The detector will cover a pseudo rapidity range of $-0.9 < \eta < 0.9$ and the full ϕ range.

Due to the large number of drift chambers the production is distributed over five production sites in Germany (Inst. für Kernphysik Universität Frankfurt, GSI Darmstadt, Physikalisches Institut Universität Heidelberg), Romania (NIPNE, Bukarest) and Russia (JINR, Dubna). For quality assurance a central procurement of all materials was adopted and a common well defined set of procedures for construction as well as for quality control was defined. The first super module will be assembled early 2006, while the production of read out chambers for the full detector is expected to last until early 2008.

The signals are read out into 1.2 million electronics channels, resulting in an on-detector bandwidth of 15 TB/s which requires a preprocessing of the data on the detector. In our case the reconstruction of tracklets is already done in the front end electronics and only if an event is stored the raw data will be shipped to the DAQ-

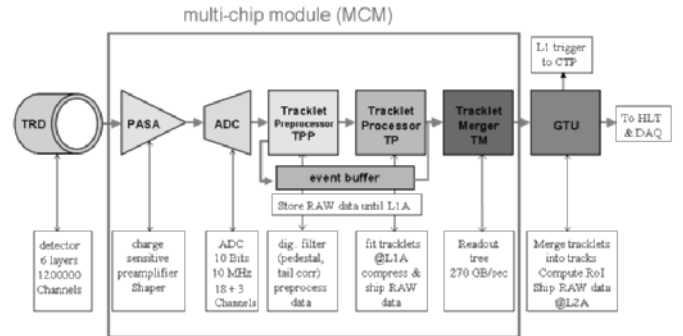


Fig. 3. Schematic view of the electronics read out chain.

system. The most part of the functionality is contained in a multi chip module (MCM) integrating an analog preamplifier-shaper (PASA) and a mixed analog-digital chip called tracklet processor (TRAP). The latter incorporates an ADC and four CPUs for filtering, tracklet reconstruction and local event building (Fig. 3) [8]. One MCM reads out the signals of 18 read out pads resulting in 65664 MCMs being active during read out. The data from the MCMs is collected in the global tracking unit (GTU), where tracks are reconstructed from the individual tracklets in the chambers. Based on this information trigger decisions can be issued to the central trigger processor (CTP) and in case of a read out, data is formatted and sent to the DAQ-system.

The design and evaluation of the PASA and TRAP chips is finished, production of the MCM chips and read out boards is currently ongoing.

3 Electron Identification

Figure 4 shows the distribution of the integrated charge deposited by electrons and pions in one TRD chamber. These distributions give the probability that a certain energy was deposited by either a pion $P(E|\pi)$ or an electron $P(E|e)$. With those probabilities the likelihood that a certain deposited energy was produced by an electron or a pion can be calculated, resulting in a distribution similar to the one shown in Fig. 6. This method of extracting the PID information is called L_Q -method.

Due to the large absorption cross-section in the Xe-based gas mixture, the transition radiation photons are absorbed predominantly close to the drift cathode. This is shown in Fig. 5 where an increased probability for absorption at later drift times for electrons can be seen, while there is no position dependence of the production of the maximum cluster in case of pions. Together with the total charge information a two-dimensional likelihood (Fig. 6) can be calculated. This method is called L_{QX} -method

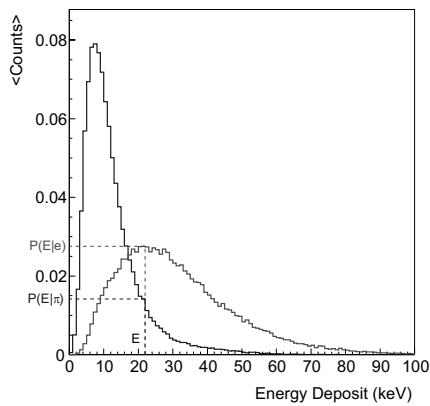


Fig. 4. Total charge spectrum in one drift chamber. Electrons in red, pions in blue.

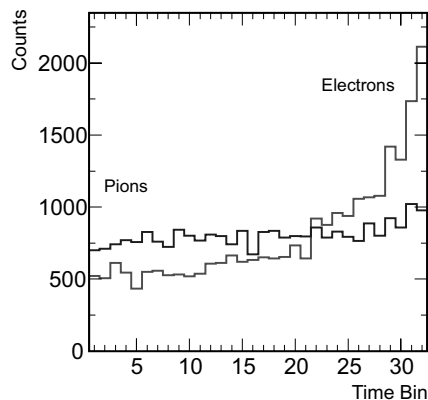


Fig. 5. Time bin position of the cluster with maximum charge.

and displays a 30% improved performance compared to the L_Q -method (see Fig. 7).

As a third method for extracting the PID information from the TRD signals an approach using neural networks was evaluated [9]. Since at the time of this analysis only test beam data of 4 small size prototype chambers was available the analysis was done for 4 chambers and extrapolated to six chambers. Figure 7 shows the pion efficiency at different momenta for the 3 different methods to calculate the particle identification. The neural network approach shows a significantly better performance than the L_{QX} method. Based on this result, ongoing efforts are devoted to improve the pion rejection using more sophisticated likelihood methods.

4 Recent Test Beam Results

In October 2004 a test beam at the CERN PS was used to do measurements with the first 6 production TRD chambers. Those chambers were for the first time equipped with the final electronics. In addition precision measurements of transition radiation spectra were done with 4 small size prototype chambers. The large chambers were mounted in a stack of 6 chambers close to the geometry of one stack in a super module.

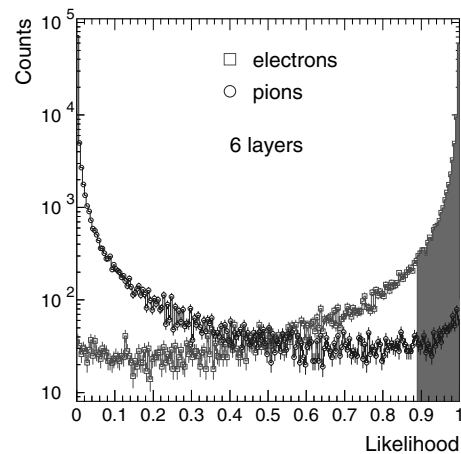


Fig. 6. Likelihood distribution for electrons and pions of a stack of 6 chambers. The pink area includes 90% of the electrons.

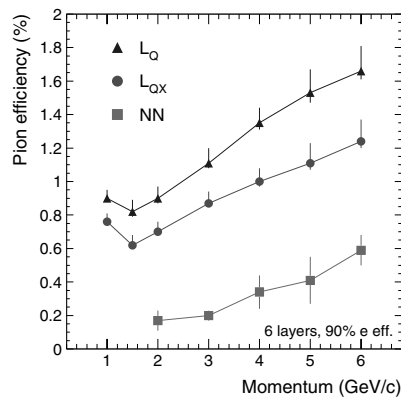


Fig. 7. Pion efficiency for the 3 different methods of electron identification. These results are based on test beam data from 2002.

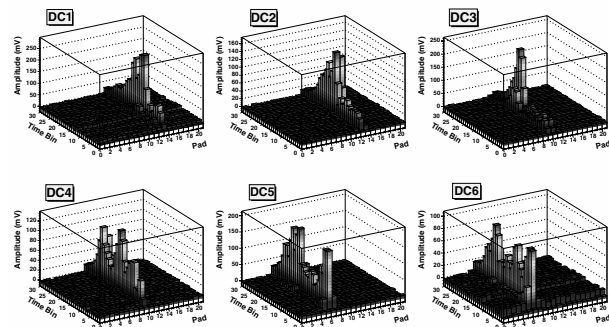


Fig. 8. One event in the 6 real size chambers in an online event display. Collected charge in all time bins and pads of one MCM module is shown.

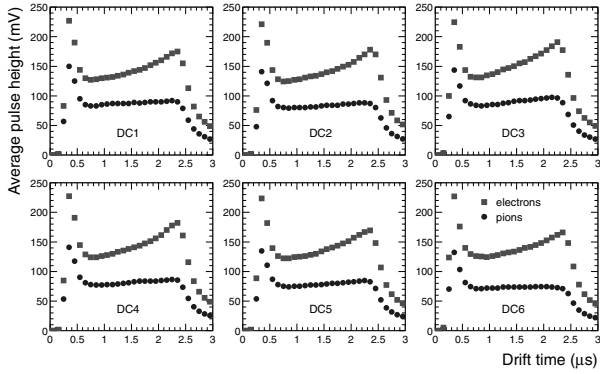


Fig. 9. Average pulse height of electrons and pions with 4 GeV/c momentum versus drift time in the 6 real size drift chambers.

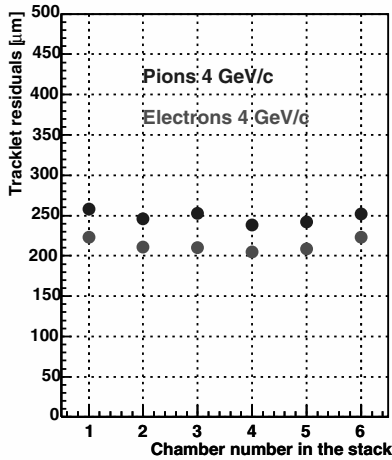


Fig. 10. Residuals of reconstructed tracklets for electrons and pions at 4 GeV/c.

Figure 8 shows an online event display of a particle traversing all 6 chambers. Summing those signals up over many events gives the picture in Fig. 9 where the different signals of electrons and pions can be seen.

One goal of the test beam was to verify with the final detector chambers that the expected performance in terms of position resolution, angle resolution and pion efficiency can be reached. The position resolution represented by the residuals of reconstructed tracklets is shown in Fig. 10. The real size chambers show a position resolution of 200-300 μm . A good angle resolution is needed in case of the TRD to give a good momentum resolution. The goal was to achieve an angle resolution of $\sigma_\alpha \leq 0.5^\circ$. Figure 11 shows that this value is achieved.

The preliminary result for pion efficiency shown in Fig. 12 is a bit worse than the pion efficiency achieved in the 2002 test beam (cf. Fig. 7). The reasons for this difference are still under evaluation.

With the small prototype chambers precision measurements of transition radiation spectra at different momenta

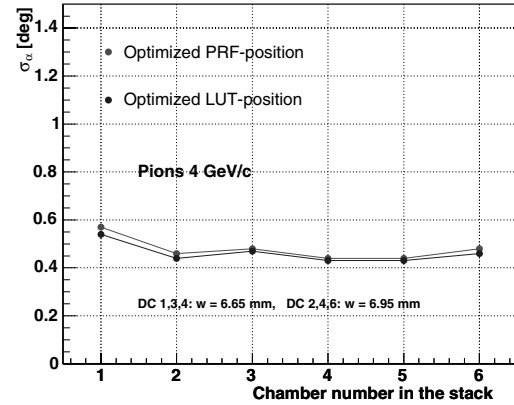


Fig. 11. Angle resolution of 4 GeV/c pions in the real size chambers in the 2004 test beam.

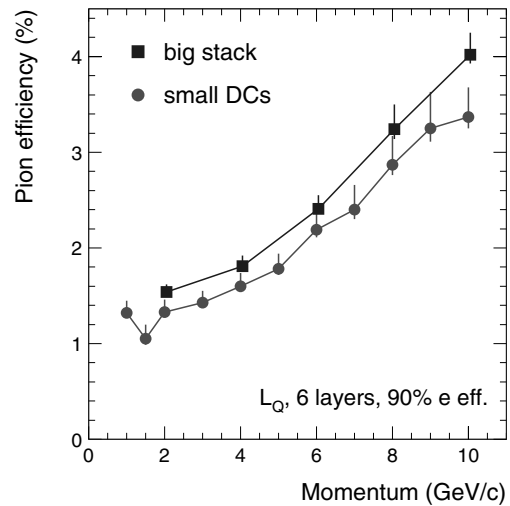


Fig. 12. Pion efficiency of the real size chambers (blue) and the small prototype chambers (red) in the 2004 test beam.

were done to verify our simulation of the detector. An Example is shown in Fig. 13. It should be noted that there is no normalization on the yield of transition radiation showing a very good absolute agreement of simulation with data [10].

Since the trigger efficiency is dependent on the quality of the online reconstruction on the front end electronics, a comparison was made to quantify deviations of the reconstructed angle on the chips compared to the reconstructed angle with the offline analysis software based on raw data. The result is shown in Fig. 14. The left part shows the relative deviation of angles of tracklets reconstructed online resp. offline. This is with 2.5% well in the acceptable range. The right panel shows the correlation between online and offline reconstruction where very few events can be seen where the online reconstructed angle does not agree with

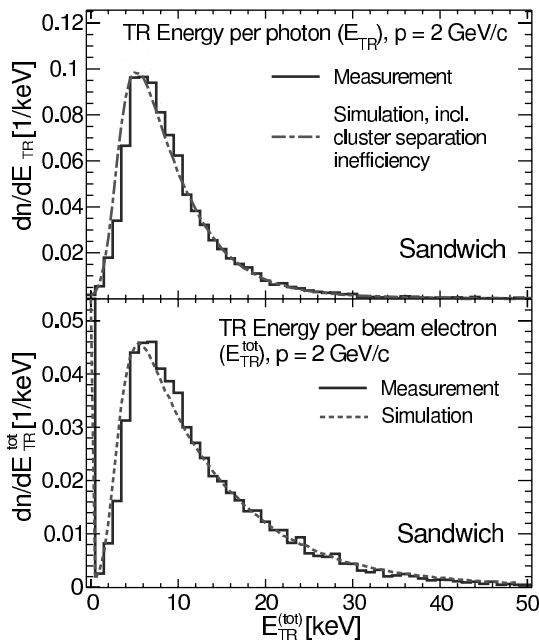


Fig. 13. Transition radiation energy spectrum from simulation and data. Top: energy per transition radiation photon. Bottom: total energy of transition radiation produced by an electron crossing one layer.

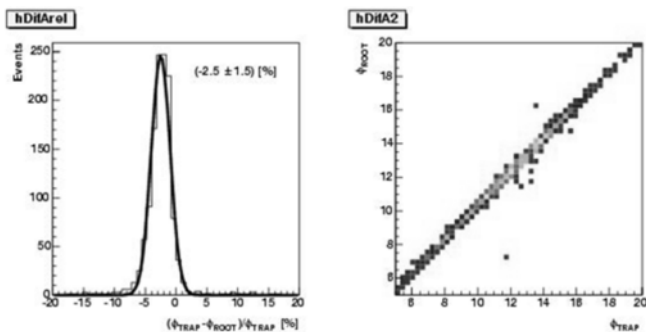


Fig. 14. Comparison of online (in the MCM) and offline reconstructed tracklet angle. Left: relative differences between reconstructed angle. Right: offline reconstructed angle (ϕ_{Root}) versus online reconstructed angle (ϕ_{TRAP}).

the offline reconstructed angle. This was evaluated and the cause of this rare deviation (per mille level) can be found in the different calculation precision. While offline analysis calculates with 32 bit numbers, the online calculation is done with 12 bit numbers.

5 Conclusions

The ALICE TRD can complement the TPC and the ITS with electron identification sufficient to measure heavy quarkonia in heavy ion collisions at the LHC and thereby give access to new physics. The detector is currently under construction with the goal to assemble a first super module early 2006. The performance of the detector was

evaluated in several test beams. For the latest one in October 2004 a stack of six final chambers was equipped for the first time with a full electronics chain with the final chips. The results of this test beam show that the TRD meets all requirements. The approach to use neural networks for the electron identification shows that there is still room for improvement of the electron identification. Currently work is done to better understand what additional information is used by the neural network and incorporate this into a likelihood approach. Precision measurements of transition radiation spectra and comparison to simulation show the level of precision achieved in modeling our detector. Finally the evaluation of the online tracking algorithm shows the high performance of the TRD electronics in reconstructing tracklets online and providing a qualified trigger decision on high- p_t electrons and jets.

References

1. M. Bedjidian *et al.*, hep-ph/0311048.
2. A. Andronic *et al.*, Phys. Lett. B **571**, (2003) 36.
3. S. Digal, P. Petreczky, H. Satz, Phys. Rev. D **64** (2001) 094015.
4. S. Arcelli, these proceedings.
5. ALICE TRD Technical Proposal, CERN/LHCC 99-13.
6. A. Dainese, these proceedings.
7. T. Mahmoud, Phd thesis, Heidelberg 2004.
8. ALICE TRD Technical Design Report, CERN/LHCC 2001-021.
9. C. Adler *et al.* (ALICE TRD Coll.), accepted in NIM A (physics/0506202).
10. R. Bailhache, TRD 2005 Bari, proceedings to appear in NIM A.

Heavy Ions in ATLAS

L. Rosselet¹ for the ATLAS Collaboration

¹ University of Geneva, CH-1211 Geneva 4

Abstract. The ATLAS experiment is designed to study proton–proton collisions at the LHC. This paper reports on an evaluation of the ATLAS potential for heavy–ion physics. Most of the detectors retain nearly their full capability even in the presence of high–multiplicity soft background from nucleus–nucleus collisions. These studies show that, in addition to "day–one" measurements such as global observables and elliptic flow, heavy–quarkonia suppression and jet quenching, which are crucial probes to study the formation of a quark–gluon plasma, are accessible in ATLAS.

1 Introduction

The main motivation to collide ultra–relativistic heavy–ions is the study of nuclear matter under extreme conditions of density and temperature. Pb beams are foreseen to be run in the LHC, one month per year starting from 2008, at $\sqrt{s} = 5.5$ TeV per colliding nucleon pair. At these energies, central collisions will produce an enormous number of virtual partons, mainly gluons, which will be deconfined and should form a new phase of QCD matter, often referred to as the quark–gluon plasma (QGP). According to lattice QCD simulations, this phase transition is expected to coincide with a partial restoration of chiral symmetry. One advantage of LHC over RHIC or SPS is the higher initial energy and partonic density leading to the creation of a larger volume of deconfined state which will last longer, making easier the study of the QGP and the exploration of the phase diagram of strongly interacting matter. Moreover, the phase transition should occur at a lower baryo–chemical potential, closer to the conditions which prevailed in the early universe, a few μs after the Big–Bang.

The study of the capabilities of the ATLAS detector for heavy–ion physics [1] was initially focused on high p_T signatures, which are better matched to the original ATLAS design concept than soft final states. This includes a variety of phenomena, ranging from jet quenching to heavy–quarkonia suppression, which are essential probes to study the QGP. Then, the global event characterization through the measurements of charged particle multiplicity and transverse energy flow, as well as proton–nucleus and ultra–peripheral collisions have been investigated. The basic idea is to take full advantage of the excellent calorimeter and muon systems of ATLAS, which are suitable not only for pp but also for heavy–ion physics.

2 Simulations

The ATLAS detector contains an inner detector with silicon pixels, silicon strips and a transition radiation tracker (TRT) inside a solenoid. Surrounding it, there are electromagnetic and hadronic calorimeters, and, outermost, a stand–alone muon–spectrometer in a toroidal field [1]. Some features of the detector relevant for heavy-ion studies are: the hermetic coverage of the calorimeters ($|\eta| < 4.9$), their fine granularity and longitudinal segmentation with 6 layers (3 both in the electromagnetic and hadronic part), the excellent jet reconstruction, and the large acceptance of the inner detector ($|\eta| < 2.5$) as well as of the muon–spectrometer ($|\eta| < 2.7$).

Although it is foreseen to run a variety of ion beams, we first studied the worst–case scenario of Pb–Pb central collisions with an impact parameter smaller than 1 fm. The simulation was done with HIJING 1.38 and GEANT3. The maximum charged particle pseudorapidity density $dN_{ch}/d\eta$ is about 3200. This number is rather pessimistic when compared to the multiplicity of 1200 expected from extrapolation of RHIC data [3] or to the 2000 charged particles predicted by the saturation model [4]. Most of produced particles have a low p_T and are stopped in the first longitudinal layer of 4 radiation lengths of the electromagnetic calorimeter. If one considers energy deposition only beyond this first layer, detector response for central Pb–Pb events is not very different from that expected for high–luminosity pp collisions at LHC. If there are some limitations when switching from p to Pb beams, these limitations concern the inner detector, and more specifically the TRT, which cannot be fully exploited due to the high occupancy expected in central Pb–Pb collisions. The TRT has therefore not been considered in the present study, although its partial usage is the subject of ongoing studies. On the other hand, the occupancy of the silicon pixel detector, below 2%, and of the strip detector, below 20% (10%) in the innermost (outermost) layer, allows track reconstruction with an efficiency of about 70% for p_T in

the range 1–10 GeV and with a fake rate of the order of 5%, as shown in Fig. 1. These results were obtained with the standard *xKalman* reconstruction algorithm [1] using only the pixel and strip silicon detectors (no TRT), and requiring at least 10 hits per track out of 11 available (13 when end-cap regions are also included) and at most one hit shared with other tracks. Typically 2000 tracks are reconstructed per central Pb-Pb event ($b < 1$ fm) with $p_T > 1$ GeV and $|\eta| < 2.5$. The p_T resolution ranges from about 4% in the end-cap region to 2% at $\eta = 0$ for $p_T > 1$ GeV and is limited by multiple scattering. The fake rate at high p_T can be reduced by matching tracks with the calorimeter clusters and the TRT hits, which is currently under investigation.

3 Global observables

The first measurements will concern global variables, such as charged particle and transverse energy distributions (N_{ch} , $dN_{ch}/d\eta$, E_T , $dE_T/d\eta$), elliptic flow and azimuthal distributions. These fundamental observables reflect all physics processes happening during the collision and give access to basic event properties. For several of these global variables, the track reconstruction in the inner detector is not needed. This is the case for the charged particle multiplicity which can be inferred from the total number of hits recorded in the silicon pixel and strip detectors. The distribution of the true versus estimated charged particle multiplicity can be seen in Fig. 2. The agreement is very good. Similarly, the charged particle pseudorapidity density $dN_{ch}/d\eta$ can be obtained on an event-by-event basis with an accuracy of about 5% for central collisions using an algorithm based on merging neighboring pixels into clusters. The impact parameter of the collision, b , can also be deduced with an accuracy of the order of 1 fm from the monotonic relation between the number of hits in silicon detectors or the energy deposited in the calorimeters and the centrality of the collision. Using the forward calorimeters to reconstruct the reaction plane, also the strength of elliptic flow can be measured from the angular distribution of hits and hit clusters in pixel detectors. For this purpose, peripheral HIJING events were generated with an elliptic flow $v_2 = 0.05$, constant in η and N_{ch} . Fig. 3 shows the reconstructed flow which is found close to the input value, and flat against η and N_{ch} . The observed 10% difference is attributed to dilution by secondary particle production in the detector material, and will be accounted for by Monte-Carlo corrections. Note that the measurement of the elliptic flow and its comparison with predictions of the hydrodynamical model has revealed that the matter observed at RHIC has unexpected fluid-like properties [5]. It is therefore of utmost importance to repeat this measurement at the LHC, and the accessibility of this global variable in ATLAS without a full reconstruction of the event is very promising.

4 Heavy-quarkonia suppression

The long-range confining potential of QCD can be studied through the dissociation of heavy-flavour bosons, when the color screening length in a hot dense deconfined medium becomes shorter than the size of the quarkonia and prevents their formation [6]. As each resonance is characterized by a different dissociation temperature, the systematic measurement of the suppression of these quarkonia provides some sort of thermometer for the early stage of the system evolution. The possibility of observing Υ and J/ψ productions via their decay into μ 's, and, hence, their expected suppression in a partonic medium, has been studied. The stand-alone muon-spectrometer gives insufficient mass resolution to separate the different states inside the Υ and J/ψ families. Thus two algorithms have been developed to match μ candidates with tracks in the inner detector. The first algorithm associates tracks fully traversing the muon-spectrometer with inner detector tracks through a global fit. The second algorithm uses a tagging method which selects inner detector tracks whose extrapolation coincides with a track segment of the muon-spectrometer. The advantage of the first technique is to reduce the contamination and to improve slightly the momentum resolution, whereas the second method reconstructs μ 's with a lower momentum threshold which increases the acceptance for the J/ψ (Υ) typically by a factor of 3.5 (1.5). For this study, di-muons are used with at least one μ reconstructed by the first method. The large μ -background coming from π and K in-flight decays is suppressed both by a minimum p_T cut and a set of χ^2 and geometry cuts in the matching algorithms. At the Υ peak, the mass resolution ranges from 120 MeV to 160 MeV depending on the pseudo-rapidity η of the decay μ 's. A compromise has to be found to clearly separate Υ states with maximum statistics. Typically, limiting the acceptance to $|\eta| < 2$ would provide a resolution of 145 MeV, sufficient to separate Υ and Υ' states, with a combined acceptance and efficiency of 12.5% and a signal to background ratio of 0.2. The number of $\Upsilon \rightarrow \mu^+\mu^-$ events accumulated in one month of Pb-Pb running is expected to be 1.5×10^4 , which should allow the study of the Υ production as a function of p_T for different centrality values of the collision. This result is estimated for a Pb-Pb luminosity of $4 \times 10^{26} \text{ cm}^{-2}\text{s}^{-1}$ and assuming 10^6 s of effective data taking time per month of running. A di-muon trigger using a μ - p_T cut in the 3–4 GeV range is being investigated.

In the J/ψ region, the mass resolution is 68 MeV, which is sufficient to separate clearly the ψ states (Fig. 4). Due to the low mass of the J/ψ , the acceptance is mainly for $|\eta| > 1.5$, and the low p_T range is not accessible for a μ - p_T cut at 3 GeV as considered for the Υ 's. On the contrary, with a μ - p_T cut at 1.5 GeV, the J/ψ can be measured from $p_T = 0$, with the acceptance and efficiency (0.53%) 10 times larger as compared to 3 GeV cut, and signal to background ratio close to 0.2. The corresponding number of $J/\psi \rightarrow \mu^+\mu^-$ events expected in one month of Pb-Pb running is 10^5 . A study of a trigger based on a low μ - p_T cut for $|\eta| > 1.5$ is under way. A solution currently

under investigation is to reduce the toroidal field of the muon-spectrometer for heavy-ion runs.

5 Jet quenching

Jet quenching is due to the energy loss by gluon radiation of the hard-scattered partons while traversing the dense partonic medium produced in heavy-ion collisions [7, 8]. This induced gluon radiation results in a rearrangement of the energy inside the jets and, consequently, in the modification of jet properties like a broader angular distribution and a suppression of high- z ($z = p^{had}/p^{jet}$) hadrons from the jet fragmentation, correlated with an increase in the number of low-momentum hadrons inside the jet. Jet quenching should manifest itself as an increase in the jet width or as an apparent reduction of the jet cross section when measured for a fixed cone size at high- p_T . Recent measurements at RHIC reveal a reduction of high- p_T particles in single-hadron spectra [9, 10] and a suppression of the back-to-back correlation between high- p_T hadrons in the most central Au-Au collisions [10], which can be related to jet quenching. The theoretical understanding of quenching at the LHC is still rather limited, and whether quenching mechanisms are best measured via back-to-back correlation, jet cross section, jet profiles or otherwise is still debated. From the experimental point of view, it is most important to demonstrate the ability to measure in the ATLAS detector as many jet properties as possible.

Without quenching, the expected jet rate per month ranges from 30×10^6 events with a jet p_T larger than 50 GeV down to 4.4×10^4 for a jet $p_T > 200$ GeV. It should be noted that because of the good hermeticity of the calorimeters, every accepted jet event is a jet-jet event. Jet studies were made by embedding PYTHIA di-jets into Pb-Pb HIJING central events. The first attempt of reconstruction was done using the standard ATLAS sliding window algorithm with $\Delta\phi \times \Delta\eta = 0.4 \times 0.4$ with a splitting/merging procedure and a two-step background subtraction [1]. The efficiency of the reconstruction procedure was evaluated by counting reconstructed jets matching the generated PYTHIA jets within a cone of size $\Delta R=0.2$. Fig. 5 (top panel) shows the jet reconstruction efficiency and the rate of fake jets as a function of E_T for $|\eta| < 3.2$. At 40 GeV, the efficiency is already 82%, the fake rate 18%, and above 75 GeV, the efficiency and fake rate are respectively above 95% and below 5%. The jet energy resolution is displayed in Fig. 5 (bottom panel) as a function of E_T . Above 150 GeV the jet resolution energy is comparable to what is expected in pp collisions. The reconstruction procedure is not yet fully optimized for Pb-Pb events and different algorithms are under evaluation, e.g. ones with the calorimeter front layers not included in the jet finding procedure. In particular, a new study going on attempts to fit both a jet profile and a background around the jet axis determined with the sliding window algorithm. This technique improves the energy resolution of jets and minimizes the fake jet rate.

Direct measurements of jet profiles, although more challenging than jet cross-section comparisons, are more

straightforward to observe any change induced by the dense partonic medium. For that purpose, in addition to jet profile fitting in the calorimeters, we plan to measure the fragmentation function, dN/dz , $z = p_T^{track}/E_T^{jet}$, obtained for charged particle tracks associated to the jet. The z -distribution is shown in Fig. 6 for tracks with $p_T > 3$ GeV within a cone of radius $R=0.4$ for jets with $E_T = 100$ GeV. The distributions of generated and reconstructed tracks from jets in HIJING Pb-Pb events are in agreement and are similar to the distribution in pp events, which will be used as reference sample. The agreement between pp and Pb-Pb events indicates that the fragmentation function can be measured in the dense heavy-ion environment, and that the not quenched partons look similar in pp and Pb-Pb reactions. With these different techniques, it seems feasible to achieve a sensitivity of the order of 10% for the fractional energy loss for 100 GeV jets in Pb-Pb collisions.

The radiative energy loss in a dense deconfined medium is expected to be different for light and heavy quarks [11] because the finite velocity of heavy quarks reduces the energy loss, suppressing the production of collinear gluons (dead cone effect). An analysis of the jets initiated by a b-quark (b-jets) provides an additional tool to understand jet quenching. The b-tagging performances were evaluated by looking at $pp \rightarrow WH \rightarrow l\nu b\bar{b}$ and $lvu\bar{u}$ events with $m_H = 400$ GeV and by searching for displaced vertices [1]. The rejection factors against u-jets for pp events as well as for events embedded in central Pb-Pb HIJING events were estimated as a function of the b-tagging efficiency. For a rejection factor of 50, the b-tagging efficiency is 40% in central Pb-Pb reactions whereas it is 60% in pp collisions. These preliminary results were based exclusively on vertex impact parameter cuts. The results should improve with an algorithm optimized for the heavy-ion environment and when combined with a μ -tagging in the muon-spectrometer.

6 Proton-nucleus physics

The study of collisions between a proton and a nucleus is essential to get the baseline for heavy-ion measurements, providing a link between pp and nucleus-nucleus physics. In addition, proton-nucleus reactions are interesting in their own right, giving access to very low- x (10^{-5} - 10^{-4}) parton distributions in the nuclear wave-function, where gluon saturation may occur [12], and probing pQCD in nuclear environment. The conditions for these studies are very favorable in ATLAS, because the soft background and the occupancy in p-Pb collisions are lower than expected in pp events in high-luminosity runs. The full capability of the ATLAS detector will then be available for such studies. Moreover, the large rapidity coverage of the experimental setup is good for the study of asymmetric collisions, with a mean rapidity shift of 0.5 in the extreme case of p-Pb events.

7 Conclusion

The ATLAS detector performs well in the dense heavy-ion environment, with the exception of the TRT. Even without the TRT, efficient tracking is possible using the precision layers of the silicon inner detector. Global observables (including the elliptic flow) can be measured accurately, even without track reconstruction in the inner detector. Despite the additional soft background, jet reconstruction is possible with a good efficiency even at relatively low jet E_T . Above 150 GeV, jet energy resolution is comparable to what is expected in pp collisions. These results were obtained with standard reconstruction programs developed for pp analysis and there is a substantial potential for improvement by tailoring these algorithms to heavy-ion events. Heavy-quarkonia physics is very promising. Υ and Υ' states can be separated. The J/ψ can also be measured using a specially developed tagging method with the background from π and K decays reduced to an acceptable level. Consequently, heavy-quarkonia suppression and jet quenching, which are good probes to study the QGP, are well accessible in ATLAS. This offers a substantial addition to the physics potential of the experiment and can provide a significant contribution to the LHC heavy-ion physics programme.

References

1. *ATLAS Collaboration, Heavy Ion Physics with the ATLAS Detector*, Letter of Intent, CERN/LHCC 2004-009; L. Rosselet for the ATLAS Collaboration, proceeding of the conference Physics at LHC, Vienna, July 2004, in press.
2. *ATLAS Collaboration, ATLAS Detector and Physics Performance*, Technical Design Report, CERN/LHCC 99-14.
3. B.B. Back et al., Phys. Rev. Lett. **88** (2002) 022302, and references therein.
4. D. Kharzeev, E. Levin, and M. Nardi, hep-ph/0111315.
5. K.H. Ackermann et al., Phys. Rev. Lett. **86** (2001) 402; M. Gyulassy and L. McLerran, Nucl. Phys. **A750** (2005) 30.
6. T. Matsui and H. Satz, Phys. Lett. **B178** (1986) 416.
7. I. Vitev and M. Gyulassy, Phys. Rev. Lett. **89** (2002) 252301.
8. U. Wiedemann, Nucl. Phys. **A690** (2001) 731; N. Armesto, C.A. Salgado, and U. Wiedemann, Phys. Rev. Lett. **93** (2004) 242301.
9. B.B. Back et al., Phys. Rev. Lett. **91** (2003) 072302; S.S. Adler et al., Phys. Rev. Lett. **91** (2003) 072303; I. Arsene et al., Phys. Rev. Lett. **91** (2003) 072305.
10. J. Adams et al., Phys. Rev. Lett. **91** (2003) 072304; *STAR Collaboration*, nucl-ex/0501016.
11. Y.L. Dokshitzer and D.E. Kharzeev, Phys. Lett. **B519** (2001) 199.
12. Z. Huang, H.J. Lu, and I. Sarcevic, Nucl. Phys. **A637** (1998) 79.

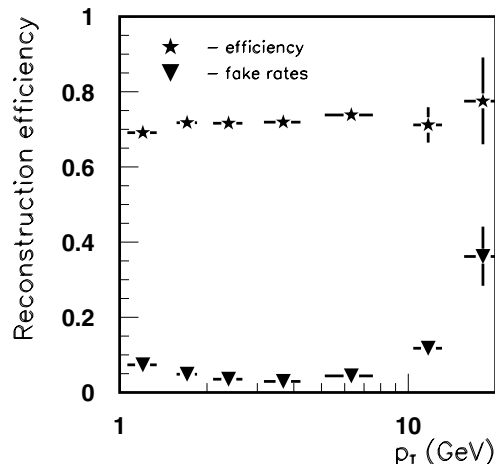


Fig. 1. Reconstruction efficiency and percentage of fake tracks as a function of the reconstructed particle p_T , for tracks with $|\eta| < 2.5$ in central Pb-Pb collisions.

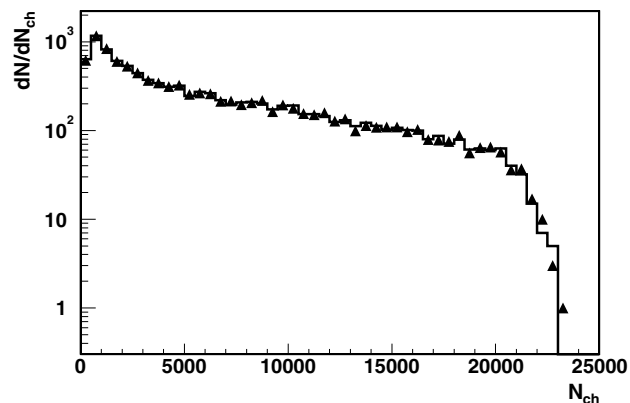


Fig. 2. Comparison between the event charged multiplicity estimated from pixel information (triangles) and the generated multiplicity (histogram).

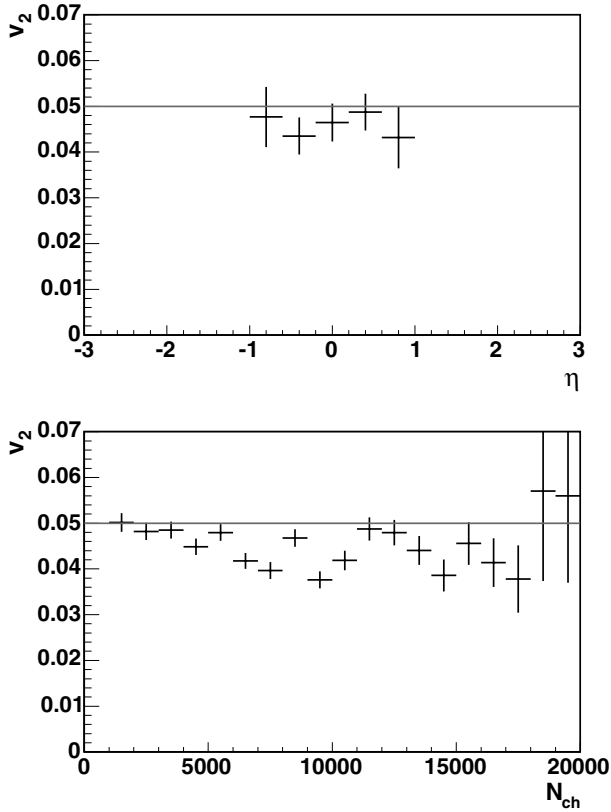


Fig. 3. Reconstructed anisotropy parameter v_2 as a function of pseudo-rapidity η (top panel) and number of charged particles N_{ch} (bottom panel). The lines correspond to generated values.

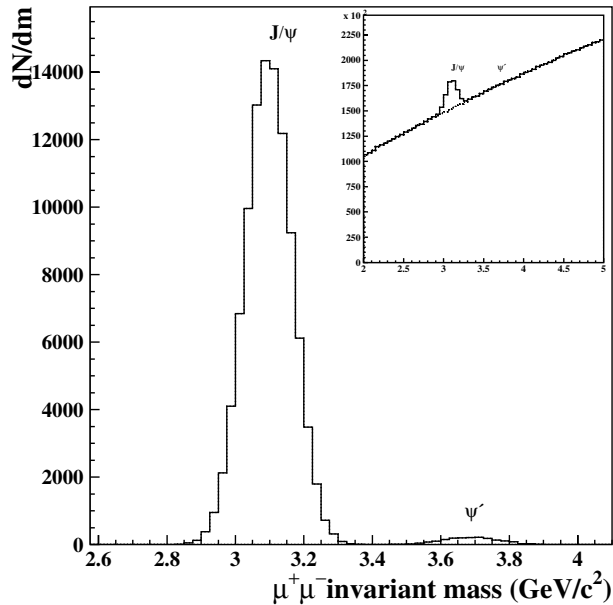


Fig. 4. Reconstructed $\mu^+\mu^-$ invariant mass distribution in the J/ψ region without background, and with background in the inset.

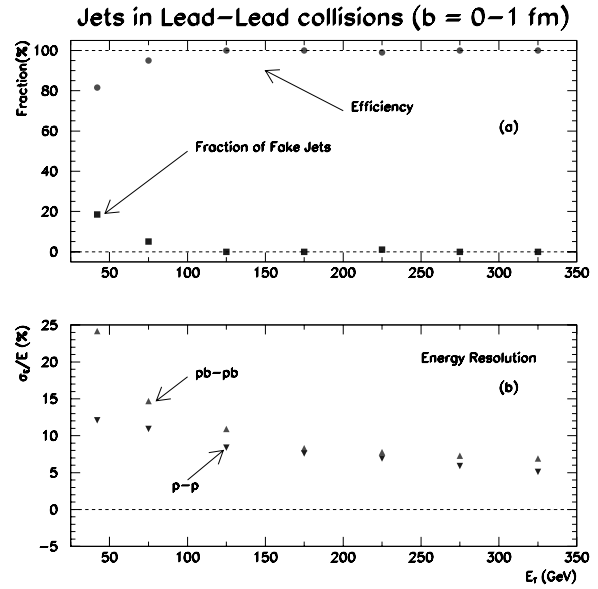


Fig. 5. Jet reconstruction efficiency and fraction of fake jets (top panel), energy resolution (bottom panel) in pp and central Pb-Pb collisions.

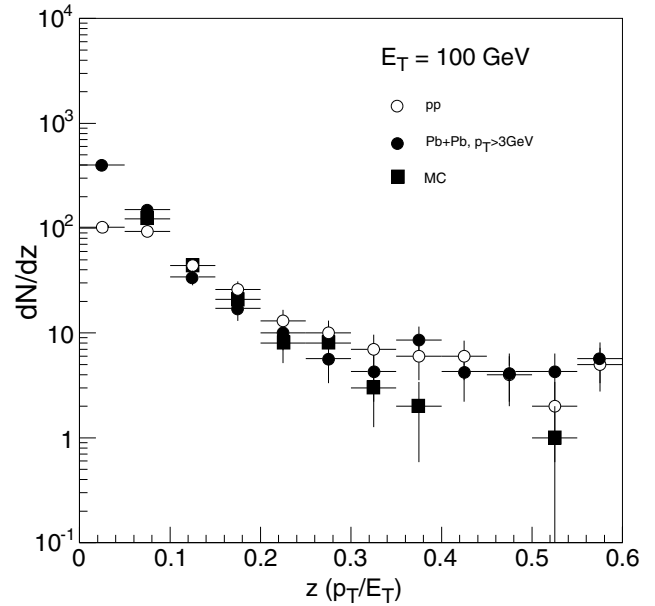


Fig. 6. Measured fragmentation function for charged hadrons inside jets with $E_T = 100$ GeV in pp and central Pb-Pb collisions.

Heavy Quark Physics

Beauty Physics: Theoretical Status and Future Perspectives

Luca Silvestrini^{1,2}

¹ Physik-Department T31, Technische Universität München, D-85748 Garching, Germany

² Dip. di Fisica, Univ. di Roma “La Sapienza” and INFN, Sez. di Roma, P.le A. Moro, 2, I-00185 Roma, Italy

Abstract. We review the status of B physics in the Standard Model and beyond. We analyze the determination of the unitarity triangle and the model-independent constraints on new physics that can be derived from this analysis. We find stringent bounds on new contributions to $B_d - \bar{B}_d$ mixing, pointing either to models of minimal flavour violation or to models with new sources of flavour and CP violation in $b \rightarrow s$ transitions. We discuss the status of the universal unitarity triangle in minimal flavour violation, and study rare decays in this class of models. We then turn to supersymmetric models with nontrivial mixing between second and third generation squarks, discuss the present constraints on this mixing and analyze the possible effects on CP violation in $b \rightarrow s$ nonleptonic decays and on $B_s - \bar{B}_s$ mixing. We conclude presenting future prospects for this field.

1 Introduction

The physics of Beauty hadrons has witnessed impressive developments in the last few years, both from the theoretical and from the experimental point of view. The large amount of data coming from the B factories allows us to test the Standard Model (SM) and its extensions with an unprecedented accuracy. A very useful tool to summarize our knowledge of the SM flavour sector is given by the Unitarity Triangle (UT). In the last two years, measurements of angles of the UT other than the “classic” $\sin 2\beta$ have become available, leading to a strong overconstraining of the UT fit and to the possibility of putting stringent constraints on New Physics (NP). Additionally, rare decays have been thoroughly studied, and they constitute a complementary tool to the UT analysis to test the SM and look for NP. In this talk, I will review the impact of B physics in the UT analysis, the constraints on NP that can be obtained from B decays and the future opportunities to look for NP in the B system.

2 The SM UT analysis

The values and errors of the relevant quantities used in the standard analysis of the CKM parameters are summarized in Table 1. Additional inputs corresponding to the measurements of the angles γ and α can be found in ref. [1], while ref. [2] describes the procedure followed to extract these constraints from experimental data.

The main novelty in the last two years in the UT analysis is the measurement of the angles of the UT at the B factories. While $\sin 2\beta$ is by now part of the “classic” fit, it is only recently that the measurements of the CP asymmetry in $B \rightarrow J/\psi K^*$ (of $B \rightarrow D^0 h^0$ decays) have

Table 1. Values of the relevant quantities used in the UT fit.

Parameter	Value	Gaussian	Uniform
λ	0.2258	0.0014	-
$ V_{cb} (\text{excl.})$	$41.4 \cdot 10^{-3}$	$2.1 \cdot 10^{-3}$	-
$ V_{cb} (\text{incl.})$	$41.6 \cdot 10^{-3}$	$0.7 \cdot 10^{-3}$	$0.6 \cdot 10^{-3}$
$ V_{ub} (\text{excl.})$	$38.0 \cdot 10^{-4}$	$2.7 \cdot 10^{-4}$	$4.7 \cdot 10^{-4}$
$ V_{ub} (\text{incl.})$	$43.9 \cdot 10^{-4}$	$2.0 \cdot 10^{-4}$	$2.7 \cdot 10^{-4}$
Δm_d	0.502 ps^{-1}	0.006 ps^{-1}	-
Δm_s	$> 14.5 \text{ ps}^{-1}$	@ 95% C.L.	-
$f_{B_s} \sqrt{\hat{B}_{B_s}}$	276 MeV	38 MeV	-
ξ	1.24	0.04	0.06
\hat{B}_K	0.79	0.04	0.09
ε_K	$2.28 \cdot 10^{-3}$	$1.3 \cdot 10^{-5}$	-
f_K	159 MeV	fixed	-
$\sin 2\beta$	0.687	0.032	-
\bar{m}_t	165.0 GeV	3.9 GeV	-
\bar{m}_b	4.21 GeV	0.08 GeV	-
\bar{m}_c	1.3 GeV	0.1 GeV	-
$\alpha_s(M_Z)$	0.119	0.003	-

provided a determination of $\cos 2\beta$ (β). These additional measurements can suppress one of the two bands determined by $\sin 2\beta$. The angle γ can be determined studying the interference of $b \rightarrow u$ and $b \rightarrow c$ transitions in $B \rightarrow D^{(*)}K^{(*)}$ decays, using the GLW, ADS or Dalitz methods. Studying $B^0 \rightarrow D^{(*)}\pi(\rho)$ decays, it is possible to extract $\sin(2\beta + \gamma)$ from the time-dependent CP asymmetries. However, present data are insufficient to allow this determination, so that additional input is needed. This can come from SU(3)-related $B \rightarrow D_s$ channels, if one neglects annihilation contributions. The total theoretical error in this procedure can be estimated around 100%. The angle α can be extracted from the time-dependent CP asymmetry in $B \rightarrow \pi\pi, \rho\pi, \rho\rho$ decays, with the uncertainty

related to penguin pollution. Given the presently unclear experimental situation and the large penguin pollution, we do not consider here $B \rightarrow \pi\pi$ decays.

Using the angle measurements described above, it is possible to obtain a determination of the UT with an accuracy comparable to the determination obtained using all the other measurements (see Fig. 1). The UT fit is therefore now strongly overconstrained, and it tests in a highly nontrivial way the CKM picture of flavour and CP violation.

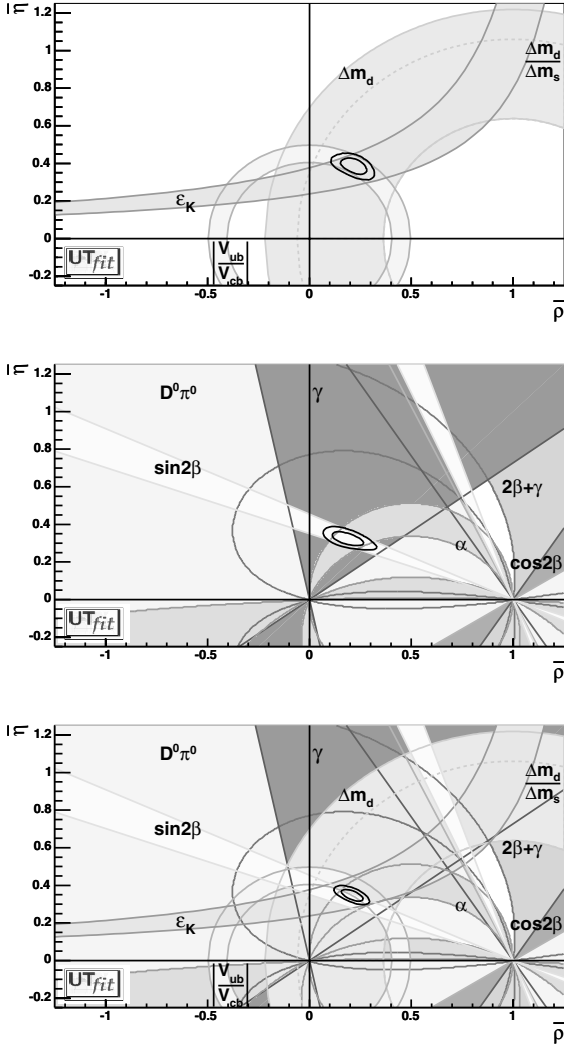


Fig. 1. Determinations of the UT without using angle measurements (top), using only angles (middle) and using all information (bottom).

Combining all available information, we obtain the “state of the art” determination in Fig. 1, and the results for UT parameters reported in Table 2. Comparing the results of the fit with the input values, there is a small ($< 2\sigma$) discrepancy in the values of $\sin 2\beta$ and $|V_{ub}|$ from inclusive decays.

Table 2. Values and probability ranges for the UT parameters obtained from the UT fit using all constraints.

	68%	95%
$\bar{\rho}$	0.208 ± 0.036	[0.135, 0.277]
$\bar{\eta}$	0.347 ± 0.021	[0.306, 0.388]
$\alpha[^\circ]$	97.1 ± 5.6	[86.0, 107.7]
$\beta[^\circ]$	23.8 ± 1.4	[21.3, 26.2]
$\gamma[^\circ]$	58.9 ± 5.4	[48.7, 69.9]
$\sin 2\beta$	0.736 ± 0.023	[0.690, 0.781]
$ V_{ub} [10^{-4}]$	38.5 ± 1.4	[35.7, 41.4]

3 The UT analysis beyond the SM

As it can be seen from Fig. 1 it has become possible to add NP contributions to all quantities entering the UT analysis and to perform a combined fit of NP contributions and SM parameters. In general, NP models introduce a large number of new parameters: flavour changing couplings, short distance coefficients and matrix elements of new local operators. The specific list and the actual values of these parameters can only be determined within a given model. Nevertheless, each of the meson-antimeson mixing processes is described by a single amplitude and can be parameterized, without loss of generality, in terms of two parameters, which quantify the difference between the full amplitude and the SM one [3]. Thus, for instance, in the case of $B_q^0 - \bar{B}_q^0$ mixing we define

$$C_{B_q} e^{2i\phi_{B_q}} = \frac{\langle B_q^0 | H_{\text{eff}}^{\text{full}} | \bar{B}_q^0 \rangle}{\langle B_q^0 | H_{\text{eff}}^{\text{SM}} | \bar{B}_q^0 \rangle}, \quad (q = d, s) \quad (1)$$

where $H_{\text{eff}}^{\text{SM}}$ includes only the SM box diagrams, while $H_{\text{eff}}^{\text{full}}$ includes also the NP contributions. As far as the $K^0 - \bar{K}^0$ mixing is concerned, we find it convenient to introduce a single parameter which relates the imaginary part of the amplitude to the SM one:

$$C_{\epsilon_K} = \frac{\text{Im}[\langle K^0 | H_{\text{eff}}^{\text{full}} | \bar{K}^0 \rangle]}{\text{Im}[\langle K^0 | H_{\text{eff}}^{\text{SM}} | \bar{K}^0 \rangle]}. \quad (2)$$

Therefore, all NP effects in $\Delta F = 2$ transitions are parameterized in terms of three real quantities, C_{B_d} , ϕ_{B_d} and C_{ϵ_K} . NP in the B_s sector is not considered, due to the lack of experimental information, since both Δm_s and $A_{\text{CP}}(B_s \rightarrow J/\psi\phi)$ are not yet measured.

NP effects in $\Delta B = 1$ transitions can also affect some of the measurements entering the UT analysis, in particular the measurements of α and A_{SL} [4]. However, under the hypothesis that NP contributions are mainly $\Delta I = 1/2$, their effect can be taken into account in the fit of the $B \rightarrow \pi\pi, \rho\pi, \rho\rho$ decay amplitudes. Concerning A_{SL} , penguins only enter at the Next-to-Leading order and therefore NP in $\Delta B = 1$ transitions produces subdominant effects with respect to the leading $\Delta B = 2$ contribution.

The results obtained in a global fit for C_{B_d} , C_{ϵ_K} , ϕ_{B_d} vs. ϕ_{B_d} , and γ vs. ϕ_{B_d} are shown in Fig. 2, together with the corresponding regions in the $\bar{\rho}-\bar{\eta}$ plane [4].

To illustrate the impact of the various constraints on the analysis, in Fig. 3 we show the selected regions in the

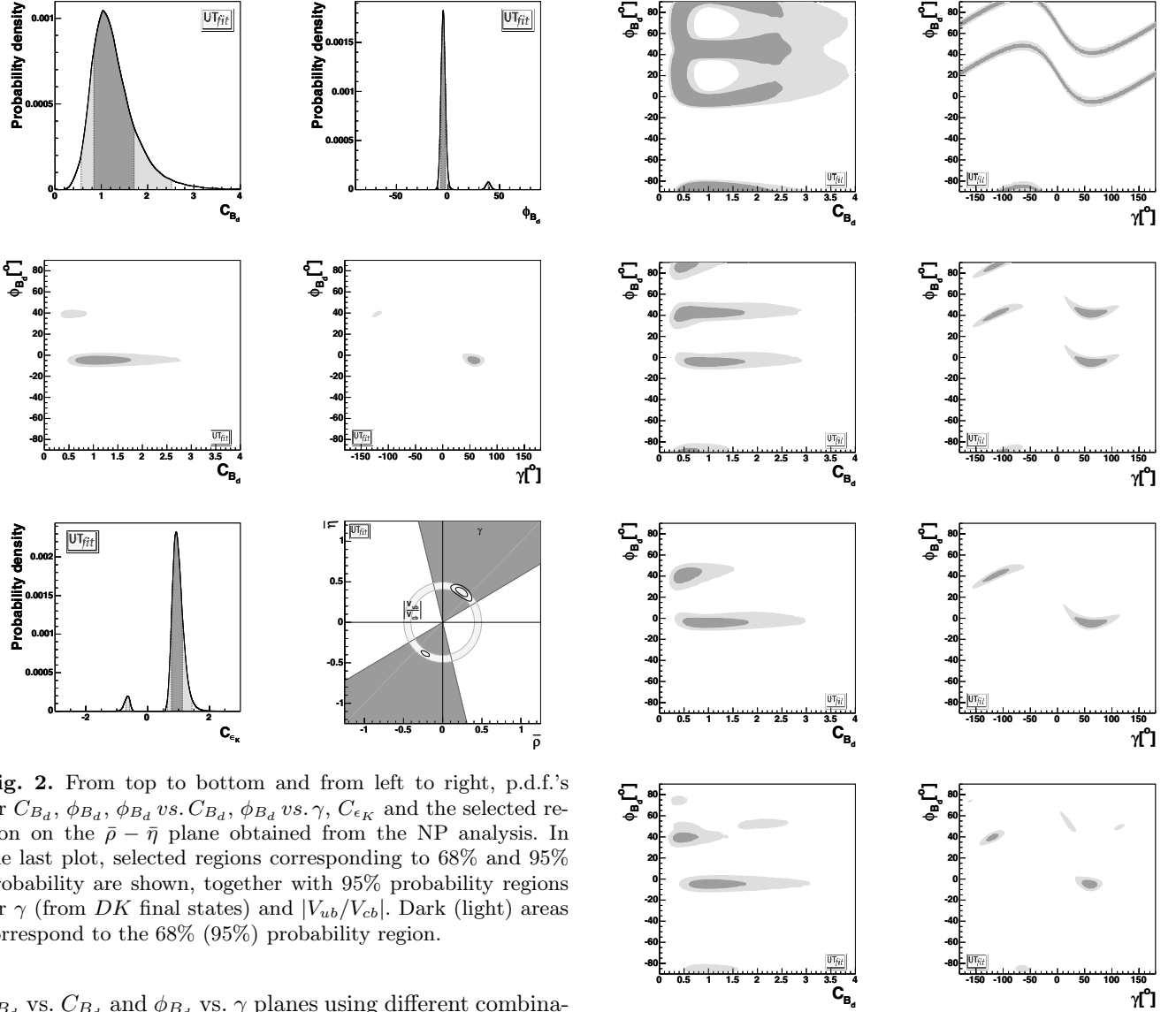


Fig. 2. From top to bottom and from left to right, p.d.f.'s for C_{B_d} , ϕ_{B_d} , ϕ_{B_d} vs. C_{B_d} , ϕ_{B_d} vs. γ , C_{ϵ_K} and the selected region on the $\bar{\rho} - \bar{\eta}$ plane obtained from the NP analysis. In the last plot, selected regions corresponding to 68% and 95% probability are shown, together with 95% probability regions for γ (from DK final states) and $|V_{ub}/V_{cb}|$. Dark (light) areas correspond to the 68% (95%) probability region.

ϕ_{B_d} vs. C_{B_d} and ϕ_{B_d} vs. γ planes using different combinations of constraints. The first row represents the pre-2004 situation, when only $|V_{ub}/V_{cb}|$, Δm_d , ϵ_K and $\sin 2\beta$ were available, selecting a continuous band for ϕ_{B_d} as a function of γ and a broad region for C_{B_d} . Adding the determination of γ (second row), only four regions in the ϕ_{B_d} vs. γ plane survive, two of which overlap in the ϕ_{B_d} vs. C_{B_d} plane. Two of these solutions have values of $\cos 2(\beta + \phi_{B_d})$ and $\alpha - \phi_{B_d}$ different from the SM predictions, and are therefore disfavoured by $(\cos 2\beta)^{\text{exp}}$ and by the measurement of $(2\beta)^{\text{exp}}$ from $B \rightarrow Dh^0$ decays, and by α^{exp} (third and fourth row respectively). On the other hand, the remaining solution has a very large value for A_{SL} and is therefore disfavoured by $A_{\text{SL}}^{\text{exp}}$, leading to the final results already presented in Fig. 2. The numerical results of the analysis can be found in ref. [4] (see ref. [5,6] for previous analyses).

Before concluding this section, let us analyze more in detail the results in Fig. 2. Writing

$$C_{B_d} e^{2i\phi_{B_d}} = \frac{A_{\text{SM}} e^{2i\beta} + A_{\text{NP}} e^{2i(\beta + \phi_{\text{NP}})}}{A_{\text{SM}} e^{2i\beta}}, \quad (3)$$

Fig. 3. From top to bottom: distributions of ϕ_{B_d} vs. C_{B_d} (left) and ϕ_{B_d} vs. γ (right) using the following constraints: i) $|V_{ub}/V_{cb}|$, Δm_d , ϵ_K and $\sin 2\beta$; ii) the constraints in i) plus γ ; iii) the constraints in ii) plus $\cos 2\beta$ from $B_d \rightarrow J/\psi K^*$ and β from $B \rightarrow Dh^0$; iv) the constraints in ii) plus α .

and given the p.d.f. for C_{B_d} and ϕ_{B_d} , we can derive the p.d.f. in the $(A_{\text{NP}}/A_{\text{SM}})$ vs. ϕ_{NP} plane. The result is reported in Fig. 4. We see that the NP contribution can be substantial if its phase is close to the SM phase, while for arbitrary phases its magnitude has to be much smaller than the SM one. Notice that, with the latest data, the SM ($\phi_{B_d} = 0$) is disfavoured at 68% probability due to a slight disagreement between $\sin 2\beta$ and $|V_{ub}/V_{cb}|$. This requires $A_{\text{NP}} \neq 0$ and $\phi_{\text{NP}} \neq 0$. For the same reason, $\phi_{\text{NP}} > 90^\circ$ at 68% probability and the plot is not symmetric around $\phi_{\text{NP}} = 90^\circ$.

Assuming that the small but non-vanishing value for ϕ_{B_d} we obtained is just due to a statistical fluctuation, the

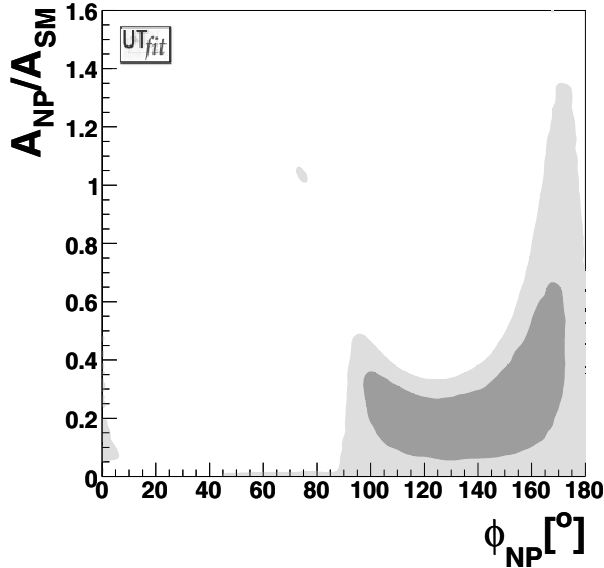


Fig. 4. P.d.f. in the (A_{NP}/A_{SM}) vs. ϕ_{NP} plane for NP in the $|\Delta B| = 2$ sector (see Eq. (3)).

result of our analysis points either towards models with no new source of flavour and CP violation beyond the ones present in the SM (Minimal Flavour Violation, MFV), or towards models in which new sources of flavour and CP violation are only present in $b \rightarrow s$ transitions. In the rest of this talk we will consider these two possibilities, starting from the former.

4 MFV models

We now specialize to the case of MFV. Making the basic assumption that the only source of flavour and CP violation is in the Yukawa couplings [7], it can be shown that the phase of $|\Delta B| = 2$ amplitudes is unaffected by NP, and so is the ratio $\Delta m_s/\Delta m_d$. This allows the determination of the Universal Unitarity Triangle independent on NP effects, based on $|V_{ub}/V_{cb}|$, γ , $A_{CP}(B \rightarrow J/\Psi K^{(*)})$, β from $B \rightarrow D^0 h^0$, α , and $\Delta m_s/\Delta m_d$ [8]. We present here the determination of the UUT, which is independent of NP contributions in the context of MFV models. The details of the analysis and the upper bounds on NP contributions that can be derived from it can be found in ref. [4].

In Fig. 5 we show the allowed region in the $\bar{\rho} - \bar{\eta}$ plane for the UUT. The corresponding values and ranges are reported in Tab. 3. The most important differences with respect to the general case are that i) the lower bound on Δm_s forbids the solution in the third quadrant, and ii) the constraint from $\sin 2\beta$ is now effective, so that we are left with a region very similar to the SM one.

Starting from the determination of the UUT, one can study rare decays in MFV models [9]. In general, a model-independent analysis of rare decays is complicated by the large number of higher dimensional operators that can contribute beyond the SM [10]. The situation drastically

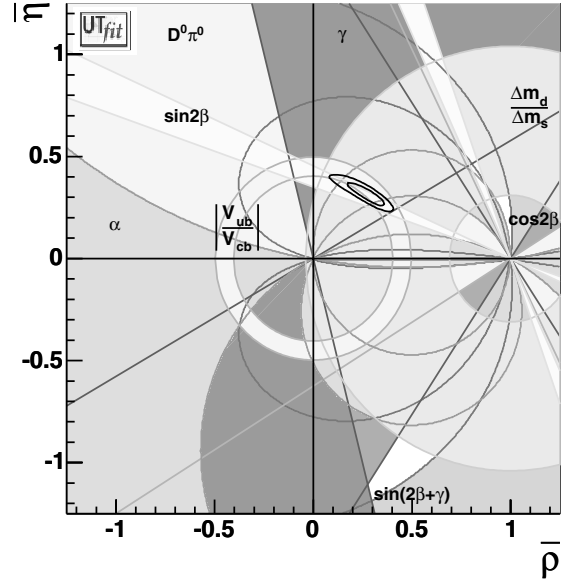


Fig. 5. The selected region on $\bar{\rho}-\bar{\eta}$ plane obtained from the determination of the UUT.

Table 3. Results of the UUT analysis.

	UUT (68%)	UUT (95%)
$\bar{\rho}$	0.259 ± 0.068	$[0.107, 0.376]$
$\bar{\eta}$	0.320 ± 0.042	$[0.241, 0.399]$
$\sin 2\beta$	0.728 ± 0.031	$[0.668, 0.778]$
$\alpha [^\circ]$	105 ± 11	$[81, 124]$
$\gamma [^\circ]$	51 ± 10	$[33, 75]$
$[2\beta + \gamma] [^\circ]$	98 ± 12	$[77, 123]$
$\Delta m_s [\text{ps}^{-1}]$	20.6 ± 5.6	$[10.6, 32.6]$

simplifies in MFV models, where (excluding large $\tan \beta$ scenarios) no new operators arise beyond those generated by W exchange. Since the mass scale of NP must be higher than M_W , we can further restrict our attention to operators up to dimension five, since higher dimensional operators will suffer a stronger suppression by the scale of NP. In this way, we are left with NP contributions to two operators only: the FCNC Z and magnetic vertices.¹ NP contributions can be reabsorbed in a redefinition of the SM coefficients of these operators: $C = C_{SM} + \Delta C$ for the Z vertex and $C_7^{\text{eff}} = C_{7SM}^{\text{eff}} + \Delta C_7^{\text{eff}}$ for the magnetic operator.²

The analysis goes as follows: using the CKM parameters as determined by the UUT analysis, one can use $\text{BR}(B \rightarrow X_s \gamma)$, $\text{BR}(B \rightarrow X_s l^+ l^-)$ and $\text{BR}(K^+ \rightarrow \pi^+ \nu \bar{\nu})$ to constrain ΔC and ΔC_7^{eff} . Then, predictions can be obtained for all other K and B rare decays. Fig. 6 shows the constraints on the NP contributions. Three possibilities emerge: i) the SM-like solution with NP corrections

¹ The chromomagnetic vertex should also be considered, but this is not necessary for the analysis presented here [9].

² We find it convenient to redefine the C function at the electroweak scale, and the C_7^{eff} function at the hadronic scale.

close to zero; ii) the “opposite C ” solution with the sign of C flipped by NP and C_7^{eff} close to the SM value; iii) the “opposite C_7 ” solution with the sign of C_7^{eff} flipped, which however requires a sizable deviation from the SM also in C .

The corresponding 95% probability upper bounds on rare decays are summarized in Tab. 4, together with the SM predictions obtained starting from the UUT analysis. It is clear that, given present constraints, rare decays can be only marginally enhanced with respect to the SM, while strong suppressions are still possible. Future improvements in the measurements of $\text{BR}(B \rightarrow X_s \gamma)$, $\text{BR}(B \rightarrow X_s l^+ l^-)$ and $\text{BR}(K^+ \rightarrow \pi^+ \nu \bar{\nu})$ will help us to reduce the allowed region for NP contributions. Another very interesting observable is the Forward-Backward asymmetry in $B \rightarrow X_s l^+ l^-$ [11]. Indeed, the two solutions for ΔC_7^{eff} and the corresponding possible values of ΔC give rise to different profiles of the normalized A_{FB} (see eq. (3.10) of ref. [9], where more details can be found).

5 New Physics in $b \rightarrow s$ transitions

We concluded sec. 3 pointing out two possible NP scenarios favoured by the UT analysis: the first one, MFV, was discussed in the previous section, now we turn to the second one, *i.e.* models with new sources of flavour and CP violation in $b \rightarrow s$ transitions. Indeed, most NP models fall in this class. Since the SM flavour $SU(3)$ symmetry is strongly broken by the top (and bottom) Yukawa couplings, flavour models are not very effective in constraining NP contributions to $b \rightarrow s$ transitions [13]. The same happens in models of gauge-Higgs unification or composite Higgs models, due to the large coupling between the third generation and the EW symmetry breaking sector [14]. Last but not least, the large atmospheric neutrino mixing angle suggests the possibility of large NP contributions to $b \rightarrow s$ processes in SUSY-GUTs [15].

This well-motivated scenario is becoming more and more interesting since B factories are probing NP effects in $b \rightarrow s$ penguin transitions, and the Tevatron and LHCb will probe NP effects in $B_s - \bar{B}_s$ mixing in the near future. For the latter process, there is a solid SM prediction which states that $\Delta m_s > 28$ (30) ps^{-1} implies NP at 2σ (3σ). For $b \rightarrow s$ penguin transitions, $B \rightarrow X_s \gamma$ and $B \rightarrow X_s l^+ l^-$ decays strongly constrain the FCNC Z and magnetic effective vertices, as already discussed in the previous section in the simplified case of MFV. On the other hand, NP contributions to the chromomagnetic $b \rightarrow s$ vertex and to dimension six operators are only mildly constrained by radiative and semileptonic decays, so that they can contribute substantially to $b \rightarrow s$ hadronic decays, although in any given model all these NP contributions are in general correlated and thus more constrained.

B -factories are now probing NP in $b \rightarrow s$ transitions by measuring the coefficient \mathcal{S} of the $\sin \Delta m_d t$ term in time-dependent CP asymmetries for $b \rightarrow s$ nonleptonic decays. Neglecting the doubly Cabibbo suppressed $b \rightarrow u$ contributions, one should have $\mathcal{S} = \sin 2\beta$ for all $b \rightarrow s$ channels within the SM, so that deviations from this equality would

signal NP in the decay amplitude [16]. However, $b \rightarrow u$ terms may also cause deviations $\Delta \mathcal{S}$ from the equality above, so that the estimate of $\Delta \mathcal{S}$ becomes of crucial importance in looking for NP. While a detailed analysis of $\Delta \mathcal{S}$ goes beyond the scope of this talk [17], the reader should be warned that $\Delta \mathcal{S}$ might be quite large for channels that are not pure penguins, and in particular for final states containing η' mesons.³ In this respect, it is of fundamental importance to improve the measurement of pure penguin channels, such as ϕK_S , as well as to enlarge the sample of available $b \rightarrow s$ and $b \rightarrow d$ channels, in order to be able to use flavour symmetries to constrain $\Delta \mathcal{S}$.

The problem of computing $\Delta \mathcal{S}$ in any given NP model is even tougher: as is well known, in the presence of two contributions to the amplitude with different weak phases, CP asymmetries depend on hadronic matrix elements, which at present cannot be computed in a model-independent way. One has then to resort to models of hadronic dynamics to estimate $\Delta \mathcal{S}$, with the large theoretical uncertainties associated to this procedure.

With the above *caveat* in mind, let us now focus on SUSY and discuss the phenomenological effects of the new sources of flavour and CP violation in $b \rightarrow s$ processes that arise in the squark sector [19]. In general, in the MSSM squark masses are neither flavour-universal, nor are they aligned to quark masses, so that they are not flavour diagonal in the super-CKM basis, in which quark masses are diagonal and all neutral current (SUSY) vertices are flavour diagonal. The ratios of off-diagonal squark mass terms to the average squark mass define four new sources of flavour violation in the $b \rightarrow s$ sector: the mass insertions $(\delta_{23}^d)_{AB}$, with $A, B = L, R$ referring to the helicity of the corresponding quarks. These δ 's are in general complex, so that they also violate CP. One can think of them as additional CKM-type mixings arising from the SUSY sector. Assuming that the dominant SUSY contribution comes from the strong interaction sector, *i.e.* from gluino exchange, all FCNC processes can be computed in terms of the SM parameters plus the four δ 's plus the relevant SUSY masses: the gluino mass $m_{\tilde{g}}$, the average squark mass $m_{\tilde{q}}$ and, in general, $\tan \beta$ and the μ parameter.⁴ Barring accidental cancellations, one can consider one single δ parameter, fix the SUSY masses and study the phenomenology. The constraints on δ 's come at present from BR's and CP asymmetries in $B \rightarrow X_s \gamma$, $B \rightarrow X_s l^+ l^-$ and from the lower bound on Δm_s . Since gluino exchange does not generate a sizable ΔC in the notation of the previous section, the combined constraints from radiative and semileptonic decays are particularly stringent.

Fixing as an example $m_{\tilde{g}} = m_{\tilde{q}} = -\mu = 350$ GeV and $\tan \beta = 10$, one obtains the constraints on δ 's reported in Fig. 7. Several comments are in order at this point: i) only $(\delta_{23}^d)_{\text{LL,LR}}$ generate amplitudes that interfere with the SM one in rare decays. Therefore, the constraints from

³ Theoretical uncertainties might be larger than what expected even in the golden mode $B \rightarrow J/\psi K_S$, although they can be reduced with the aid of other decay modes [18].

⁴ The last two parameters are irrelevant as long as $\tan \beta$ is of $\mathcal{O}(1)$.

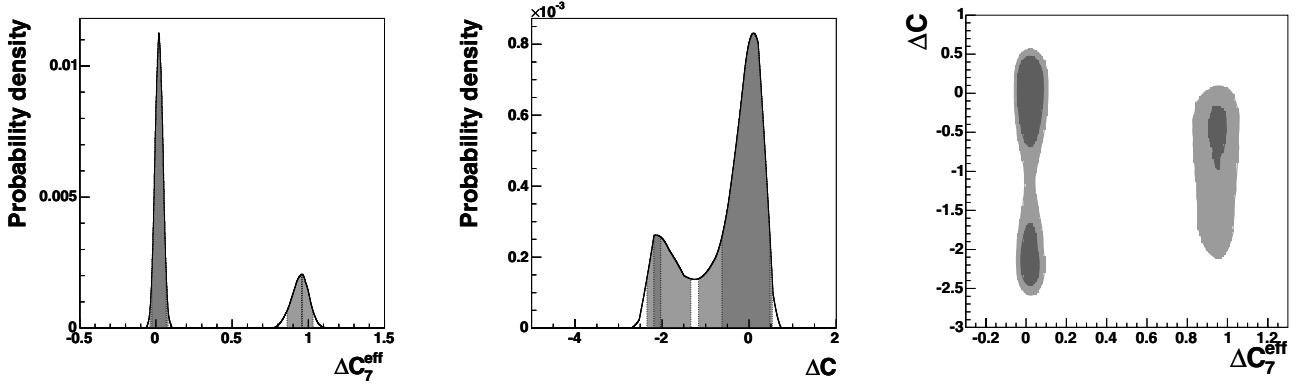


Fig. 6. P.d.f.'s for ΔC_7^{eff} (left), ΔC (middle) and ΔC vs. ΔC_7^{eff} (right).

Table 4. Upper bounds for rare decays in MFV models at 95% probability, the corresponding values in the SM (using inputs from the UUT analysis) and the available experimental information.

Branching Ratios	MFV (95%)	SM (68%)	SM (95%)	exp [12]
$Br(K^+ \rightarrow \pi^+ \nu \bar{\nu}) \times 10^{11}$	< 11.9	8.3 ± 1.2	(6.1, 10.9)	$(14.7^{+13.0}_{-8.9})$
$Br(K_L \rightarrow \pi^0 \nu \bar{\nu}) \times 10^{11}$	< 4.59	3.08 ± 0.56	(2.03, 4.26)	$< 5.9 \cdot 10^4$
$Br(K_L \rightarrow \mu \bar{\mu})_{\text{SD}} \times 10^9$	< 1.36	0.87 ± 0.13	(0.63, 1.15)	-
$Br(B \rightarrow X_s \nu \bar{\nu}) \times 10^5$	< 5.17	3.66 ± 0.21	(3.25, 4.09)	< 64
$Br(B \rightarrow X_d \nu \bar{\nu}) \times 10^6$	< 2.17	1.50 ± 0.19	(1.12, 1.91)	$< 2.2 \cdot 10^2$
$Br(B_s \rightarrow \mu^+ \mu^-) \times 10^9$	< 7.42	3.67 ± 1.01	(1.91, 5.91)	$< 1.5 \cdot 10^2$
$Br(B_d \rightarrow \mu^+ \mu^-) \times 10^{10}$	< 2.20	1.04 ± 0.34	(0.47, 1.81)	$< 3.9 \cdot 10^2$

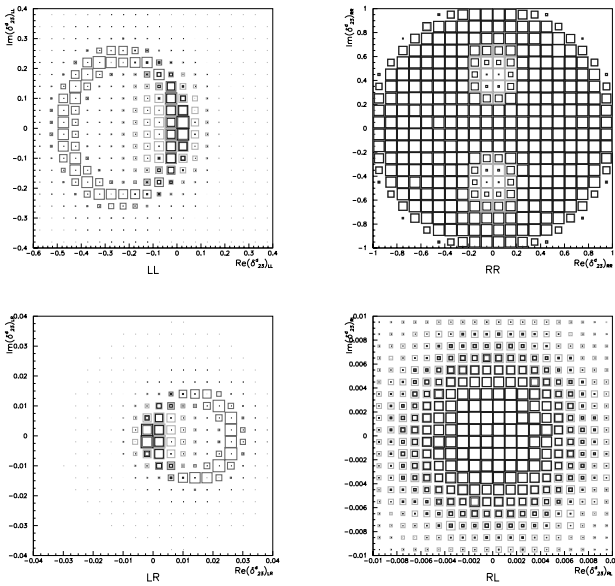


Fig. 7. P.d.f.'s in the $\text{Re}(\delta_{23}^d)_{AB} - \text{Im}(\delta_{23}^d)_{AB}$ plane for $A, B = L, R$, as determined by $B \rightarrow X_s \gamma$ (violet), $B \rightarrow X_s l^+ l^-$ (light blue) and all constraints (dark blue).

rare decays for $(\delta_{23}^d)_{\text{RL,RR}}$ are symmetric around zero, while the interference with the SM produces the circular shape of the $B \rightarrow X_s \gamma$ constraint on $(\delta_{23}^d)_{\text{LL,LR}}$. ii) We recall that LR and RL mass insertions generate much larger contributions to the (chromo)magnetic operators,

since the necessary chirality flip can be performed on the gluino line ($\propto m_{\tilde{g}}$) rather than on the quark line ($\propto m_{\tilde{b}}$). Therefore, the $B \rightarrow X_s \gamma$ constraint is much more effective on these insertions. iii) The $\mu \tan \beta$ flavour-conserving LR squark mass term generates, together with a flavour changing LL mass insertion, an effective $(\delta_{23}^d)_{\text{LR}}^{\text{eff}}$ that contributes to $B \rightarrow X_s \gamma$. Having chosen a negative μ , we have $(\delta_{23}^d)_{\text{LR}}^{\text{eff}} \propto -(\delta_{23}^d)_{\text{LL}}$ and therefore the circle determined by $B \rightarrow X_s \gamma$ in the LL and LR cases lies on opposite sides of the origin (see Fig. 7). iv) For LL and LR cases, $B \rightarrow X_s \gamma$ and $B \rightarrow X_s l^+ l^-$ produce bounds with different shapes on the $\text{Re} \delta - \text{Im} \delta$ plane (violet and light blue regions in Fig. 7), so that applying them simultaneously only a much smaller region around the origin survives (dark blue regions in Fig. 7). This shows the key role played by rare decays in constraining new sources of flavour and CP violation in the squark sector. v) For the RR case, the constraints from rare decays are very weak, so that almost all δ 's with $|(\delta_{23}^d)_{\text{RR}}| < 1$ are allowed, except for two small forbidden regions where Δm_s goes below the experimental lower bound.

Having determined the p.d.f.'s for the four δ 's, we now turn to the evaluation of \mathcal{S} as defined at the beginning of this section. We use the approach defined in ref. [20] to evaluate the relevant hadronic matrix elements, warning the reader about the large uncontrolled theoretical uncertainties that affect this evaluation. Let us focus for concreteness on the effects of $(\delta_{23}^d)_{\text{RL}}$. Imposing that the BR 's are correctly reproduced, we obtain the estimates of \mathcal{S} for the ϕK_s , $\eta' K_s$, ωK_s and $\pi^0 K_s$ final states reported in

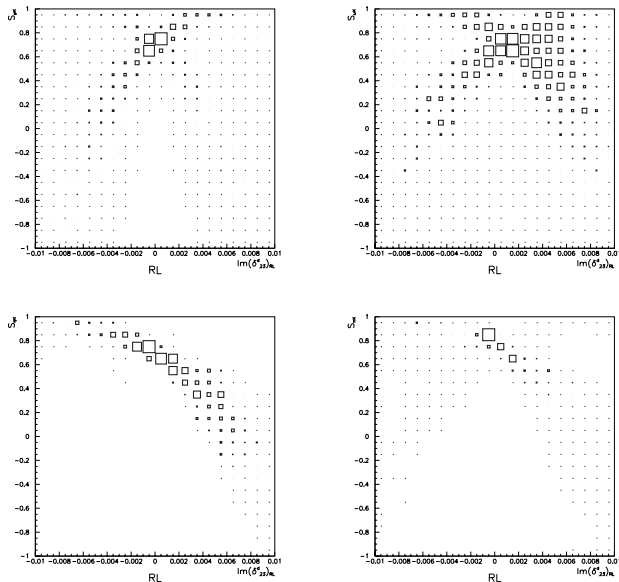


Fig. 8. From top to bottom and from left to right, p.d.f.'s for S for B decays to ϕK_S , ωK_S , $\eta' K_S$ and πK_S as a function of $\text{Im}(\delta_{23}^d)_{\text{RL}}$.

Fig. 8. One can see that $(\delta_{23}^d)_{\text{RL}}$ insertions can produce sizable deviations from the SM expectations for S in the $\eta' K_s$ and ωK_s channels. Similar results hold for the other δ 's.

Another place where δ_{23}^d mass insertions can produce large deviations from the SM is Δm_s . In this case, hadronic uncertainties are under control, thanks to the Lattice QCD computation of the relevant matrix elements [21], and the whole computation is at the same level of accuracy as the SM one [22]. Considering for example the contribution of $(\delta_{23}^d)_{\text{RR}}$ mass insertions, starting from the constraints in Fig. 7, one sees that values of Δm_s much larger than in the SM are possible in the SUSY case, generally accompanied by large values of the CP asymmetry in $B_s \rightarrow J/\psi\phi$: both would be a clear signal of NP to be revealed at hadron colliders.

6 Outlook

We are bound to witness further improvements in the experimental and theoretical inputs to the above analysis in the near future. In the next few years, the UUT analysis might well become the standard analysis, NP contributions to $\Delta F = 2$ transitions will be either revealed or strongly constrained, and rare decays will provide stringent bounds on NP in $\Delta F = 1$ processes or, hopefully, show some deviation from the SM expectation. In Fig. 9 I show a pessimistic view of what we might see at HCP 2010, in the dull scenario in which everything remains consistent with the SM [4]. Also in this case, however, flavour physics will remain a crucial source of information on the structure of NP. This information is complementary to the direct signals of NP that we expect to see at the LHC.

References

1. The Heavy Flavour Averaging Group, summer 2005 averages.
2. M. Bona *et al.* [UTfit Collaboration], *JHEP* **0507** (2005) 028; www.utfit.org.
3. J. M. Soares and L. Wolfenstein, *Phys. Rev. D* **47**, 1021 (1993); N. G. Deshpande *et al.*, *Phys. Rev. Lett.* **77**, 4499 (1996); J. P. Silva and L. Wolfenstein, *Phys. Rev. D* **55**, 5331 (1997); A. G. Cohen *et al.*, *Phys. Rev. Lett.* **78**, 2300 (1997); Y. Grossman *et al.*, *Phys. Lett. B* **407**, 307 (1997).
4. M. Bona *et al.* [UTfit Collaboration], arXiv:hep-ph/0509219.
5. J. Charles *et al.* [CKMfitter Group], *Eur. Phys. J. C* **41**, 1 (2005).
6. S. Laplace *et al.*, *Phys. Rev. D* **65**, 094040 (2002); M. Ciuchini *et al.*, eConf **C0304052**, WG306 (2003); Z. Ligeti, *Int. J. Mod. Phys. A* **20**, 5105 (2005); F. J. Botella *et al.*, *Nucl. Phys. B* **725**, 155 (2005); K. Agashe *et al.*, arXiv:hep-ph/0509117.
7. G. D'Ambrosio *et al.*, *Nucl. Phys. B* **645**, 155 (2002).
8. A. J. Buras *et al.*, *Phys. Lett. B* **500**, 161 (2001).
9. C. Bobeth *et al.*, *Nucl. Phys. B* **726**, 252 (2005).
10. A. Ali *et al.*, *Phys. Rev. D* **66**, 034002 (2002); G. Hiller and F. Kruger, *Phys. Rev. D* **69**, 074020 (2004); G. Buchalla *et al.*, *JHEP* **0509**, 074 (2005);
11. G. Burdman, *Phys. Rev. D* **57**, 4254 (1998).
12. V. V. Anisimovsky *et al.* [E949 Collaboration], *Phys. Rev. Lett.* **93** 031801 (2004); A. Alavi-Harati *et al.* [The E799-II/KTeV Collaboration], *Phys. Rev. D* **61** 072006 (2000); R. Barate *et al.* [ALEPH Collaboration], *Eur. Phys. J. C* **19** 213 (2001); B. Aubert *et al.* [BABAR Collaboration], *Phys. Rev. Lett.* **93** 091802 (2004); A. Abulencia *et al.* [CDF Collaboration], arXiv:hep-ex/0508036.
13. A. Masiero *et al.*, *Phys. Rev. D* **64**, 075005 (2001).
14. K. Agashe *et al.*, *Nucl. Phys. B* **719**, 165 (2005); G. Martinelli *et al.*, *JHEP* **0510**, 037 (2005).
15. T. Moroi, *Phys. Lett. B* **493**, 366 (2000); D. Chang *et al.*, *Phys. Rev. D* **67**, 075013 (2003); R. Harnik *et al.*, *Phys. Rev. D* **69**, 094024 (2004).
16. Y. Grossman and M. P. Worah, *Phys. Lett. B* **395**, 241 (1997); M. Ciuchini *et al.*, *Phys. Rev. Lett.* **79**, 978 (1997); D. London and A. Soni, *Phys. Lett. B* **407**, 61 (1997); Y. Grossman *et al.*, *Phys. Rev. D* **58**, 057504 (1998); M. Ciuchini *et al.*, arXiv:hep-ph/0407073.
17. See the session of WG4 on this topic at the CKM 2005 workshop.
18. M. Ciuchini *et al.*, arXiv:hep-ph/0507290.
19. F. Gabbiani *et al.*, *Nucl. Phys. B* **477**, 321 (1996); R. Barbieri and A. Strumia, *Nucl. Phys. B* **508**, 3 (1997); A. L. Kagan and M. Neubert, *Phys. Rev. D* **58**, 094012 (1998); S. A. Abel *et al.*, *Phys. Rev. D* **58**, 073006 (1998); A. Kagan, arXiv:hep-ph/9806266; R. Fleischer and T. Mannel, *Phys. Lett. B* **511**, 240 (2001); T. Besmer *et al.*, *Nucl. Phys. B* **609**, 359 (2001); E. Lunghi and D. Wyler, *Phys. Lett. B* **521**, 320 (2001); M. B. Causse, arXiv:hep-ph/0207070; G. Hiller, *Phys. Rev. D* **66**, 071502 (2002); S. Khalil and E. Kou, *Phys. Rev. D* **67**, 055009 (2003); *Phys. Rev. Lett.* **91**, 241602 (2003); eConf **C0304052**, WG305 (2003); *Phys. Rev. D* **71**, 114016 (2005); G. L. Kane *et al.*, *Phys. Rev. D* **70**, 035015 (2004); S. Baek, *Phys. Rev. D* **67**, 096004 (2003); K. Agashe and C. D. Carone, *Phys. Rev. D* **68**, 035017 (2003); J. F. Cheng *et al.*, *Phys. Lett. B* **585**, 287 (2004); D. Chakraverty *et al.*,

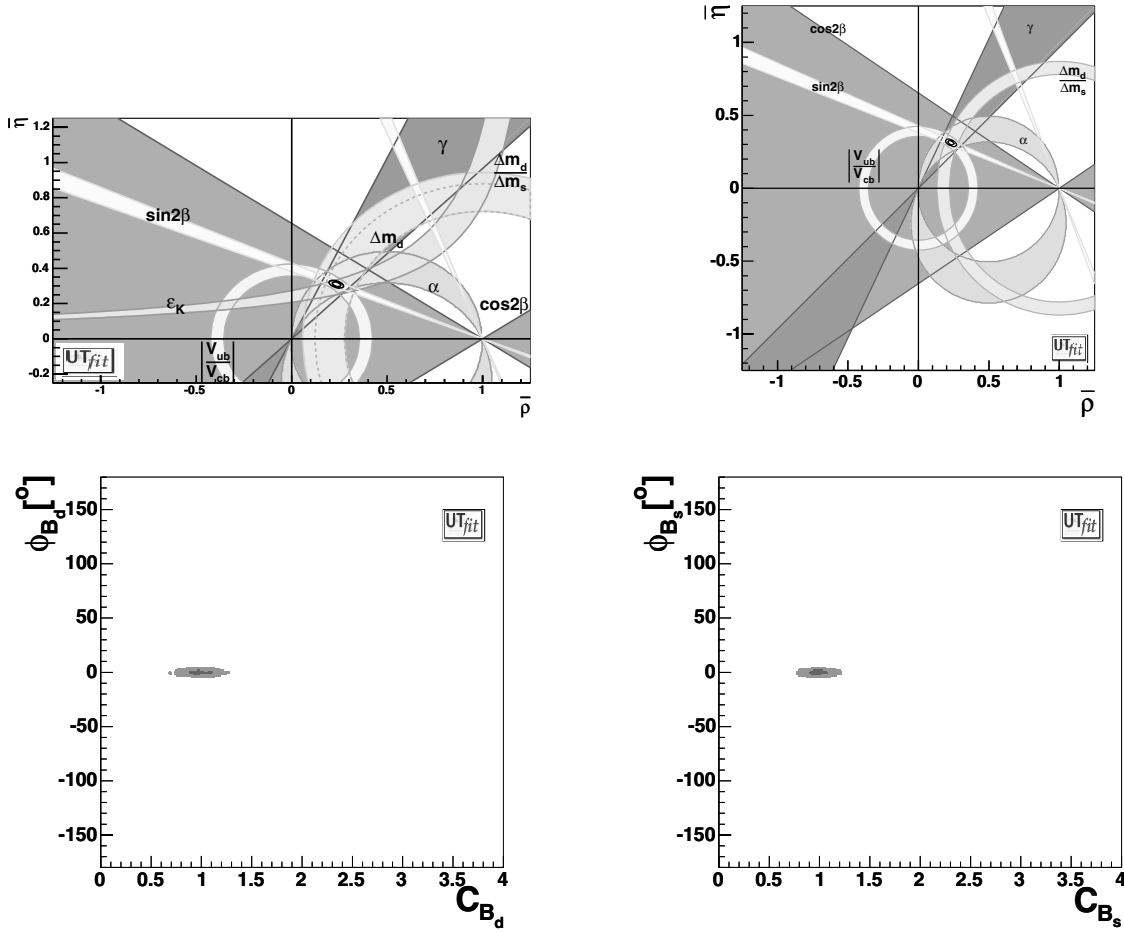


Fig. 9. Outlook for Lepton-Photon 2009: the SM UT (top left), the UUT (top right), the ϕ_{B_d} vs. C_{B_d} plane (bottom left) and the ϕ_{B_s} vs. C_{B_s} plane (bottom right). See the text for details.

Phys. Rev. D **68**, 095004 (2003); J. F. Cheng *et al.*, *Nucl. Phys. B* **701**, 54 (2004); E. Gabrielli *et al.*, *Nucl. Phys. B* **710**, 139 (2005); S. Khalil, *Mod. Phys. Lett. A* **19**, 2745 (2004); *Phys. Rev. D* **72**, 035007 (2005).

20. M. Ciuchini *et al.*, *Phys. Rev. D* **67**, 075016 (2003) [Erratum-ibid. *D* **68**, 079901 (2003)].

21. D. Becirevic *et al.*, *JHEP* **0204**, 025 (2002).

22. M. Ciuchini *et al.*, *Nucl. Phys. B* **523**, 501 (1998); A. J. Buras *et al.*, *Nucl. Phys. B* **586**, 397 (2000).

Results from Belle and BaBar

Paoti Chang

National Taiwan University

Abstract. We report results of B decays using large data samples collected with the Belle and BaBar detectors at the $\Upsilon(4S)$ resonance in the e^+e^- asymmetric energy collider. The updated world average of the CP violating parameter, $\sin 2\phi_1(\sin 2\beta)$, obtained from the $b \rightarrow c\bar{c}s$ transition is 0.687 ± 0.032 , where $\cos 2\phi_1$ is consistent with 0. Results of the ϕ_1 determination from other processes are shown and the average of $\sin 2\phi_1^{\text{eff}}$ in $b \rightarrow s$ penguin transition is 2.6σ away from $\sin 2\phi_1$. Measurements of the other two angles of unitarity triangle will be discussed and measurements of various rare B decays will be presented.

1 Introduction

After start taking data in 1999, both Belle and BaBar have accumulated lots of data and produced many important results. The main physics goal, observation of mixing induced CP violation in $b \rightarrow c\bar{c}s$ transition, was achieved in 2001 [1], [2]. Three years later, direct CP violation was observed in $B \rightarrow K^\pm\pi^\mp$ decays [3]. The focus of B factory is shifted to precisely measure the Standard Model (SM) parameters and to search for new physics. One of the highlights in 2004 is the 3.8σ deviation [4] between the average effective $\sin 2\phi_1(\sin 2\beta)$ measurements from various $b \rightarrow s\bar{q}q$ decay modes and that in the $b \rightarrow c\bar{c}s$ process. Although in principle each decay mode may not yield the same $\sin 2\phi_1$, theoretically the difference should be within 15%. If a sizeable deviation is indeed confirmed especially for the $\eta'K^0$ and ϕK^0 modes, which are dominated by the $b \rightarrow s\bar{s}s$ transition, it may suggest an existence of particles beyond the SM in the penguin loop [5]. Hence, precision measurement for these $b \rightarrow s$ penguin modes becomes one of the most important tasks in B factory now.

Recently a lot of progress has been made theoretically and experimentally to extract the other two angles of unitarity triangle, $\phi_2(\alpha)$ and $\phi_3(\gamma)$. Although they were regarded as difficult subjects when B factory was proposed, physicists are able to develop a good strategy for each angle. Moreover, large accumulated data enable searches for rare B meson decays, which not only help understand the B decay mechanism but also probe physics beyond the SM. In this article we report the measurements of the three angles of the unitarity triangle and rare B meson decays using data samples upto 227 million $B\bar{B}$ pairs for BaBar and 386 million for Belle. Both BaBar and Belle detectors are large-solid-angle magnetic spectrometers, The detectors are described in detail elsewhere [6].

2 ϕ_1/β Extraction

In the decay chain $\Upsilon(4S) \rightarrow B^0\bar{B}^0 \rightarrow f_{CP}f_{\text{tag}}$, where one of B mesons decays at time t_{CP} into a CP eigenstate f_{CP} and the other B meson decays at time t_{tag} to a state f_{tag} , the decay rare has a dependence given by

$$\mathcal{P}(\Delta t) = \frac{e^{-t/\tau}}{4\tau} \times \{1 + q[S_f \sin(\Delta m_d \Delta t) + A_f \cos(\Delta m_d \Delta t)]\}. \quad (1)$$

Here, S_f and $A_f(-C_f)$ are the CP violating parameters, τ is the B^0 lifetime, Δm_d is the mass difference between the two B^0 mass eigenstates, $\Delta t = t_{CP} - t_{\text{tag}}$ and the B flavor charge $q = +1(-1)$ when the tagging B^0 meson is a $B^0(\bar{B}^0)$. To a good approximation, the SM predicts $S_f = -\xi_f \sin 2\phi_1$, where $\xi_f = +1(-1)$ corresponds to CP -even (-odd) final state, and $A_f = 0$ for both $b \rightarrow c\bar{c}s$ and $b \rightarrow s\bar{q}q$ transitions.

In summer 2005, the Belle collaboration has updated the $\sin 2\phi_1$ measurement in $B^0 \rightarrow J/\psi K^0$ [7]. With 386 million $B\bar{B}$ pairs, $5264 \pm 73B^0 \rightarrow J/\psi K_S^0$ and $4792 \pm 105B^0 \rightarrow J/\psi K_L^0$ signals are reconstructed. And the measured S_f and A_f are given in Table 1. Clear separations between B^0 and \bar{B}^0 events are seen in the Δt distributions (see Fig. 1) and the corresponding raw asymmetries reveal a sine wave behavior, indicating that CP violation is large. The updated $\sin 2\phi_1$ is measured to be $+0.652 \pm 0.039 \pm 0.020$ while A_f is $+0.010 \pm 0.026 \pm 0.036$, consistent with no asymmetry. Including this updated result, the new world average of $\sin 2\phi_1$ is $+0.687 \pm 0.032$, where the last error includes both statistical and systematic errors.

Although $\sin 2\phi_1$ is precisely measured, there exists four-fold ambiguity for ϕ_1 . Both Belle and BaBar have tried to reduce the ambiguity to two by extracting $\cos 2\phi_1$ from time-dependent angular analysis of $B^0 \rightarrow J/\psi K^{*0}$, $K^{*0} \rightarrow K_S^0\pi^0$. BaBar resolves the sign ambiguity due to

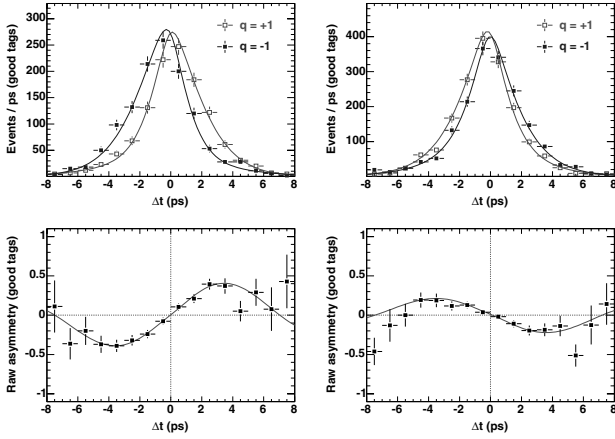


Fig. 1. Δt distributions and raw asymmetries in (left) $B^0 \rightarrow J/\psi K_S^0$ and (right) $B^0 \rightarrow J/\psi K_L^0$ for events with good flavor tags.

the choice of the strong phase by examining the s wave and p wave interference near K^{*0} (892) [8] while Belle assumes s-quark helicity conservation [9]. The obtained $\cos 2\phi_1$ is $+2.72^{+0.50}_{-0.79} \pm 0.27$ for BaBar and $+0.87 \pm 0.74 \pm 0.12$ for Belle.

The first ϕ_1 extraction without any ambiguity is provided by Belle in 2005 [10]. The strategy to extract $2\phi_1$ is to perform a time dependent Dalitz analysis on the $\bar{B}^0 \rightarrow D^0(K_S^0\pi^+\pi^-)h^0$ events (h^0 could be π^0, η or ω). The $B \rightarrow Dh$ decay is dominated by the CKM favored $b \rightarrow \bar{c}d$ diagram, while the contribution from the Cabibbo suppressed $b \rightarrow u\bar{c}d$ diagram is only 2% and, therefore, can be ignored. Since the D^0 meson is identified via its $K_S^0\pi^+\pi^-$ decay, the final state of B meson decay is a CP eigenstate. Consequently, the time dependent $K_S^0\pi^+\pi^-$ distributions in the Dalitz plot are different for B^0 and \bar{B}^0 . If the amplitude of $\bar{D}^0 \rightarrow K_S^0\pi^+\pi^-$ is described by $f(m_+^2, m_-^2)$, where the m_+ and m_- are respectively the invariant masses of $K_S^0\pi^+$ and $K_S^0\pi^-$, the amplitude of the corresponding D^0 decays is given by $f(m_-^2, m_+^2)$, assuming no CP violation in D^0 meson. The decay amplitudes of B^0 and \bar{B}^0 at time Δt can be described as,

$$M_{B^0}(\Delta t) = f(m_+^2, m_-^2) \cos\left(\frac{\Delta m \Delta t}{2}\right) - ie^{+2\phi_1} \quad (2)$$

$$\xi_{h^0} (-1)^l f(m_-^2, m_+^2) \sin\left(\frac{\Delta m \Delta t}{2}\right), \text{ and}$$

$$M_{\bar{B}^0}(\Delta t) = f(m_-^2, m_+^2) \cos\left(\frac{\Delta m \Delta t}{2}\right) - ie^{-2\phi_1} \quad (3)$$

$$\xi_{h^0} (-1)^l f(m_+^2, m_-^2) \sin\left(\frac{\Delta m \Delta t}{2}\right),$$

where ξ_{h^0} denotes the CP eigenvalue of h^0 and l is the orbital angular momentum of the Dh^0 system. We use the inclusive $D^{*+} \rightarrow \bar{D}^0 p i^+$ sample to determine $f(m_+^2, m_-^2)$, which is expressed as the sum of 18 resonant and one non-resonant amplitudes. The left plot of Figure 2 shows the time integrated Dalitz plot for the $D^0 h^0$ candidates in

Table 1. Results of Δt fits. The first error is statistical and the second systematic.

Mode	SM expt. for S_f	S_f	A_f
ϕK^0	$+\sin 2\phi_1$	$+0.44 \pm 0.27 \pm 0.05$	$+0.14 \pm 0.17 \pm 0.07$
ϕK_S^0	$+\sin 2\phi_1$	$+0.19 \pm 0.32$	$+0.12 \pm 0.20$
ϕK_L^0	$-\sin 2\phi_1$	-1.54 ± 0.59	$+0.38 \pm 0.36$
$\eta' K^0$	$+\sin 2\phi_1$	$+0.62 \pm 0.12 \pm 0.04$	$-0.04 \pm 0.08 \pm 0.06$
$\eta' K_S^0$	$+\sin 2\phi_1$	$+0.60 \pm 0.14$	-0.04 ± 0.09
$\eta' K_L^0$	$-\sin 2\phi_1$	-0.73 ± 0.29	-0.02 ± 0.18
$K_S^0 K_S^0 K_S^0$	$-\sin 2\phi_1$	$-0.58 \pm 0.36 \pm 0.08$	$+0.50 \pm 0.23 \pm 0.06$
$K_S^0 \pi^0 K_S^0$	$+\sin e\phi_1$	$+0.22 \pm 0.47 \pm 0.08$	$+0.11 \pm 0.18 \pm 0.08$
$f_0 K_S^0$	$-\sin 2\phi_1$	$-0.47 \pm 0.36 \pm 0.08$	$-0.23 \pm 0.23 \pm 0.13$
ωK_S^0	$+\sin 2\phi_1$	$+0.95 \pm 0.53^{+0.12}_{-0.15}$	$+0.19 \pm 0.39 \pm 0.13$
$K^+ K^- K_S^0$	$-(2f_{\pm} - 1)$	$-0.52 \pm 0.16 \pm 0.03$	$-0.06 \pm 0.11 \pm 0.07$
$\sin 2\phi_1$			
$J/\psi K^0$	$+\sin 2\phi_1$	$+0.652 \pm 0.039 \pm 0.020$	$-0.010 \pm 0.026 \pm 0.036$
$J/\psi K_S^0$	$+\sin 2\phi_1$	$+0.668 \pm 0.047$	-0.021 ± 0.034
$J/\psi K_L^0$	$-\sin 2\phi_1$	-0.619 ± 0.069	$+0.049 \pm 0.039$

the B signal region. With $309 \pm 31 D^0 h^0$ events, a time-dependent Dalitz analysis is performed to obtain $\phi_1 = (16 \pm 21 \pm 12)^\circ$. The corresponding 95% confidence interval is $-30^\circ < \phi_1 < 62^\circ$, equivalent to exclude the solution of $\phi_1 = 67^\circ$ at $95 \frac{N(\bar{B}) - N(B)}{N(\bar{B}) + N(B)}$, is shown in the right plot of Fig. 2.

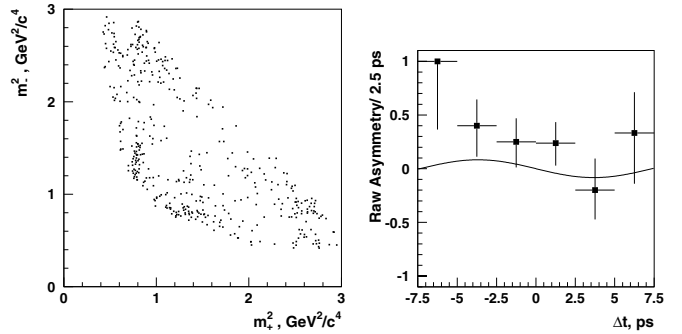


Fig. 2. Left: Time integrated Dalitz plot for $D^0 h^0$ candidates in the B signal region. Right: Raw asymmetry distribution superimposed with the curve resulting from the time dependent Dalitz fit.

3 CP violation in $b \rightarrow s\bar{q}q$

As described in the introduction paragraph, time dependent CP analysis on $b \rightarrow s$ penguin modes is one of the most important channel to search for new physics. The Belle collaboration has updated their measurements not only with more data but also making improvements on event selection and background suppression [7]. The $b \rightarrow s$ penguin modes include the decays of $B^0 \rightarrow \phi K^0, \eta' K^0, K^+ K^- K_S^0, f_0 K_S^0, \omega K_S^0, K_S^0 K_S^0 K_S^0$ and $K_S^0 \pi^0$. Table 1 summarizes the Belle new updates with 386 million $B\bar{B}$ pairs. No significant difference in S_f is found between each $b \rightarrow s$ penguin mode and $B \rightarrow J/\psi K^0$; the A_f values are all consistent with zero.

Figure 3 summarizes the world average of effective $\sin(2\phi_1)$ for each decay mode. Although the central values of all the $b \rightarrow s$ modes except $B^0 \rightarrow f_0 K_S^0$ are smaller than $\sin(2\phi_1)$, the deviations are all within 1.5σ . If we naively average all the s penguin results and neglect their intrinsic differences, the average is 0.50 ± 0.06 , which is 2.6σ away from the obtained $\sin(2\phi_1) = 0.69 \pm 0.03$. More data are needed to distinguish the deviation of S_f between $b \rightarrow s\bar{q}q$ and $b \rightarrow c\bar{c}s$.

Among all the decay modes, $B^0 \rightarrow \phi K^0$ and $B^0 \rightarrow \eta' K^0$ are the two best channels to search for new physics because they are predominantly through $b \rightarrow s$ penguin transition. It's interesting to notice that the new update from the Belle collaboration, $S_f = 0.62 \pm 0.12 \pm 0.04$ for $B^0 \rightarrow \eta' K^0$, is more than 4σ away from zero. Besides B to charmonium decays, this is the second channel to reveal mixing induced CP violation in the B sector. However, the BaBar collaboration gave somewhat lower central value with similar statistical uncertainty in summer 2004 [11]. Within one or two years, this small discrepancy can be resolved and it will provide the best probe for new physics.

many methods proposed to constrain the other two angles, they were considered to be difficult in the B factory era. After B factory starts taking data, new ideas come out and a lot of progress has been made experimentally and theoretically. Now we are able to perform precision measurements for the three angles of the unitarity triangle in B decays.

Three channels have been used to measure the angle ϕ_2 . The first method was suggested by A. Snyder and H. Quinn [12], who proposed to extract ϕ_2 without ambiguity using a time dependent Dalitz analysis of $B \rightarrow \pi^+\pi^-\pi^0$ decays. The BaBar collaboration has performed the Dalitz analysis with 16 parameters in Summer 2004 [13]. The obtained ϕ_2 and the strong phase are $\phi_2 = 113^{+27}_{-17} \pm 6^\circ$ and $\delta_{+-} = -67^{+28}_{-31} \pm 7$. Since there are many parameters in the fit, we need much more statistics to reduce the statistical errors.

The second and the third channels for extracting ϕ_2 have the similar strategy, measuring ϕ_2 through a time dependent CP fit and an isospin analysis. If there are only box and tree diagrams that contribute to $B^0 \rightarrow \pi^+\pi^-$ and $B^0 \rightarrow \rho^+\rho^-$ decays, A_f in Eq. 1 will be zero and S_f will equal to $\sin 2\phi_2$. However, possible penguin contribution will interfere the other two diagrams, which causes A_f to be proportional to sine of the phase angle difference between the strong phases of the penguin and tree diagrams. And the S_f term is modified to be $S_f = \sqrt{1 - A_f^2} \sin 2\phi_{2\text{eff}}$. Theoretically, $\phi_{2\text{eff}}$ can be converted into ϕ_2 based on an isospin symmetry of the decays $B \rightarrow hh$ (h is π or ρ) [14]. The decay amplitudes of $B^0 \rightarrow h^+h^-$, $B^0 \rightarrow h^0h^0$ and $B^+ \rightarrow h^+h^0$ (denoted as A^{+-} , A^{00} and A^{+0} , respectively) can be expressed as a complex triangle as illustrated in Fig. 4. The difference of ϕ_2 and $\phi_{2\text{eff}}$ is thus determined using the the branching fractions and partial rate asymmetries.

Experimentally, physicists tried to measure ϕ_2 firstly in $B \rightarrow \pi\pi$ but it turned out that this may not be a good channel. Both Belle and BaBar have observed unexpectedly large branching fraction for the decay $B^0 \rightarrow \pi^0\pi^0$ [15]. However, the branching fraction is not large enough to provide good statistics to measure the partial rate asymmetry. Consequently, the two triangles in Fig. 4 cannot be well separated and, thus, the error of ϕ_2 is large. Moreover, the Belle collaboration has observed both large S_f and A_f in $B^0 \rightarrow \pi^+\pi^-$ while the BaBar results are all consistent with zero [16]. We need larger statistics and more efforts to understand this experimental discrepancy.

The first ϕ_2 extraction in $B \rightarrow \rho\rho$ was performed by the BaBar collaboration [17] and it becomes the best way to measure ϕ_2 . Later on, Belle also reported her measurements with slightly more data [18]. Since $B \rightarrow \rho\rho$ is a vector-vector (VV) mode, one has to determine the helicity states before performing the time dependent CP analysis. Table 2 shows the results of $B \rightarrow \rho\rho$. Four reasons facilitate the ϕ_2 extraction in the $\rho\rho$ mode. First of all, the branching fractions of $B^0 \rightarrow \rho^+\rho^-$ and $B^+ \rightarrow \rho^+\rho^0$ are relatively large, which provide good statistics to measure $\phi_{2\text{eff}}$. Secondly if there are both longitudinally and

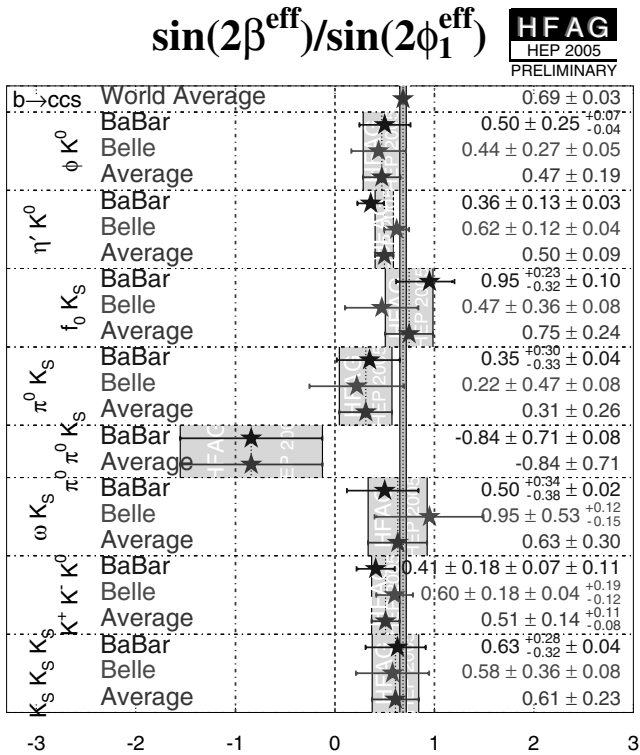


Fig. 3. Average effective $\sin(2\beta)/\sin(2\phi_1)$ for $b \rightarrow c\bar{c}s$ and $b \rightarrow s$ penguin modes.

4 $\phi_2(\alpha)$ and $\phi_3(\gamma)$

When B factory was proposed, only ϕ_1 extraction could be surely done with good accuracy. Although there were

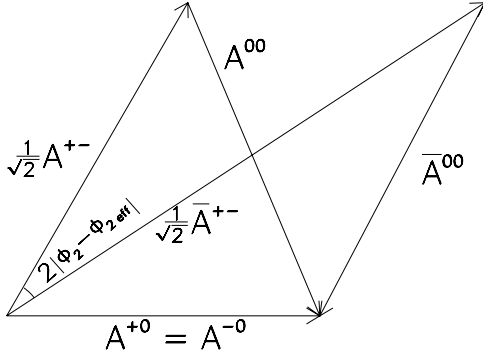


Fig. 4. Complex triangles of $B \rightarrow \pi\pi$ and $B \rightarrow \rho\rho$ decays. Since both $B^+ \rightarrow \pi^+\pi^0$ and $B^+ \rightarrow \rho^+\rho^0$ have pure tree contributions, the decay amplitudes are the same for B^+ and B^- .

Table 2. Summary of the $B \rightarrow \rho\rho$ measurements. The first row is the longitudinal polarized fraction and the last three are the branching fractions. The second and third rows are the S_f and A_f in $B^0 \rightarrow \rho^+\rho^-$ decays.

Item	BaBar	Belle
f_L	$0.978 \pm 0.014^{+0.021}_{-0.029}$	$0.951^{+0.033+0.029}_{-0.039-0.031}$
S_f	$-0.33 \pm 0.24^{+0.08}_{-0.14}$	$0.09 \pm 0.42 \pm 0.08$
A_f	$0.03 \pm 0.18 \pm 0.09$	$0.00 \pm 0.30^{+0.10}_{-0.09}$
$\mathcal{B}_{\rho^+\rho^-}$	$(30 \pm 4 \pm 5) \times 10^{-6}$	$(24.4 \pm 2.2^{+3.8}_{-4.1}) \times 10^{-6}$
$\mathcal{B}_{\rho^+\rho^0}$	$(22.5^{+5.7}_{-5.4} \pm 5.8) \times 10^{-6}$	$(31.7 \pm 7.1^{+3.8}_{-6.7}) \times 10^{-6}$
$\mathcal{B}_{\rho^0\rho^0}$	$< 1.1 \times 10^{-6}$	—

transversely polarized fractions in a $B \rightarrow VV$ decay, the presence of CP even and CP odd contribution will dilute the measurement of mixing induced CP violation. Fortunately the $\rho\rho$ mode is predominantly longitudinally polarized. Thirdly, non-resonant $B \rightarrow 4\pi$ and $B \rightarrow \rho\pi\pi$ backgrounds are small. Since the ρ width is relatively wide, one has to consider the possible background contribution from other states, which will also dilute the CP measurement. It turns out that the possible background is small. Lastly, the branching fraction of $B^0 \rightarrow \rho^0\rho^0$, unlike $B^0 \rightarrow \pi^0\pi^0$, is small. Therefore, the B^0 triangle in Fig. 4 almost coincides with the \bar{B}^0 triangle, resulting in $\phi_{2\text{eff}} \sim \phi_2$. With the above four reasons, $B \rightarrow \rho\rho$ provides the best ϕ_2 measurement, which is $\phi_2 = (96 \pm 13)^\circ$ when combining the Belle and BaBar results in Table 2.

Figure 5 shows the combined ϕ_2 result based on all the experimental measurements of $B \rightarrow \pi\pi, \rho\rho$ and $\rho\pi$. The obtained value is $\phi_2 = (99^{+12}_{-9})^\circ$, which is consistent with the result of the global CKM fit without using the angle measurements, $\phi_2 = (96^{+11}_{-12})^\circ$.

Several methods have been proposed and tried to measure the third angle of unitarity triangle [19]. The most promising way is to extract ϕ_3 from the interference between $B^- \rightarrow D^{(*)0}K^{(*)-}$ and $B^+ \rightarrow D^{(*)0}K^{(*)+}$, where

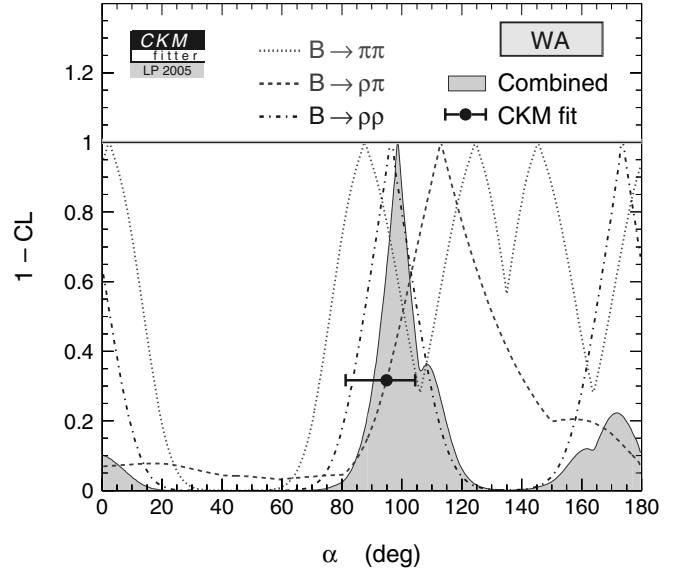


Fig. 5. Averaging confidence level curves for the $\pi\pi$ and $\rho\rho$ isospin analysis and $\rho\pi$ Dalitz plot analysis.

where D^0 meson decays to $K_S^0\pi^+\pi^-$ [20]. A $K_S^0\pi^+\pi^-$ Dalitz plot analysis enables us to extract ϕ_3 , the strong phase difference δ_B and the ratio of amplitudes r_B . Both Belle and BaBar have performed the Dalitz plot analysis before the summer 2005 /citephi3rest. The obtained results in the $D^{(*)}K$ modes are $\phi_3 = (68^{+14}_{-15} \pm 13 \pm 11)^\circ$ and $\phi_3 = (67 \pm 28 \pm 12 \pm 11)^\circ$ for Belle and BaBar, respectively. It is $\phi_3 = (112 \pm 35 \pm 9 \pm 11 \pm 8)^\circ$ for the Belle DK^* analysis. The third errors of the measurements are the modelling errors of $D^0 \rightarrow K_S^0\pi^+\pi^-$ decays and can be reduced using large inclusive D^0 data in the future. The fourth error for the DK^* mode comes from the possible contribution of non-resonant or other $K\pi$ state underneath the K^* resonance. This K^* background contribution will be examined using events outside the K^* resonance region and the corresponding systematic error will be reduced. We expect to have 1 ab^{-1} data in two years in both B factories and it's possible to measure ϕ_3 within 10° uncertainty.

Figure 6 shows the constraints in the $\rho - \eta$ plane including all experimental measurements in the global CKM fit [22]. All experimental results are consistent with the hypothesis of the KM mechanism.

5 Rare Decays with Leptons or Photons

Rare B decays often proceeds with $b \rightarrow s$ penguin or $b \rightarrow u$ transitions. New gauge bosons or SUSY particles may appear in the penguin loop or the tree diagram to either enhance/reduce the decay branching fractions or change the event topology predicted by the SM. Therefore, rare B decays provide a good robe for new physics. The decay $B \rightarrow \tau\nu$ is one of these decays and also provides direct access of the Cabibbo-Kobayashi-Maskawa (CKM) matrix

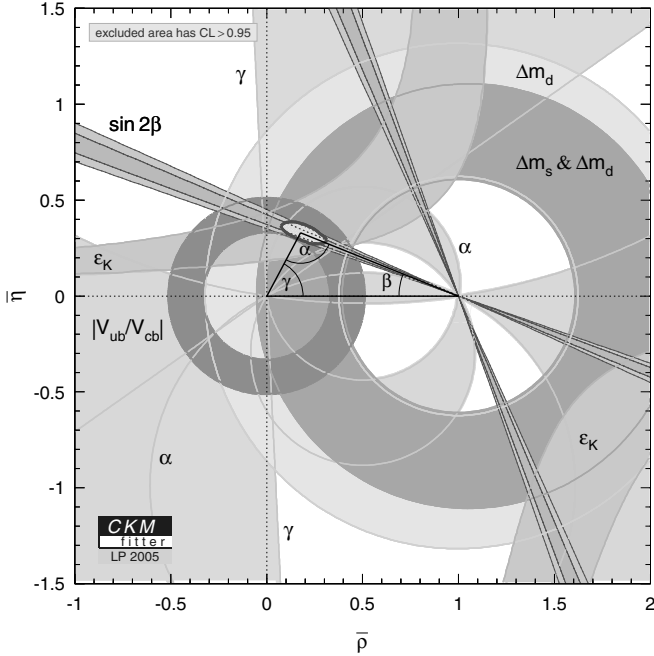


Fig. 6. Constraints of unitarity triangle with all experimental measurements.

element V_{ub} and the B meson decay constant f_B . Experimentally $B \rightarrow \tau\nu$ is searched by identifying the accompanying B_s through either the hadronic or semi-leptonic decays and comparing properties of the remaining particles in the event. The Belle and BaBar collaborations have reported their search results with 275 million and 232 million $B\bar{B}$ pairs, respectively [23]. Although no clear signals have been seen, the corresponding upper limits as shown in Table 3 are not far from the SM prediction, $\text{cal}B(B \rightarrow \tau\nu) = (8.1 \pm 2.5) \times 10^{-5}$. Both B factory experiments will be able to examine the SM prediction in two years. Although only upper limits are provided, they can set a good constraint on the charged Higgs mass. Figure 7 shows the exclusion boundaries in the $[M_{H^+}, \tan\beta]$ plane based on the measured upper limits.

The decays $B \rightarrow K^{(*)}l^+l^-$ (l is a lepton), result from $b \rightarrow s$ flavor-changing neutral current, in which new physics may significantly modify the decay rates and kinematics. The search for $B^+ \rightarrow K^+\nu\bar{\nu}$ was reported by the Belle collaboration in summer 2005 using the same technique in the $\tau\nu$ analysis on 275 million $B\bar{B}$ pairs. Although the obtained upper limit is lower than the previous BaBar measurement [24] with 89 million $B\bar{B}$ pairs, it is still an order of magnitude away from the theoretical expectation. Although we will not reach the SM prediction with 1 ab^{-1} of data, stringent limit can still rule out some exotic models, which suggest heavy non-SM particles in the penguin loop.

Observations of $B \rightarrow K^{(*)}e^+e^-$ and $B \rightarrow K^{(*)}\mu^+\mu^-$ were established at B factories and the accumulated data already allowed studies for event kinematics. For instance, the Belle collaboration has first shown the forward-backward asymmetry of K^*ll in ICHEP2004 [citekl],

Table 3. Branching fractions of charmless B decays. Branching fractions are in units of 10^{-6} and upper limits are obtained at 90% confidence level.

Mode	BaBar	Belle
$\tau^+\nu$	< 260	< 180
$K^+\nu\bar{\nu}$	< 52	< 36
$\pi^+\nu\bar{\nu}$	< 100	—
Kll	$0.34 \pm 0.07 \pm 0.03$	$0.550^{+0.075}_{-0.070} \pm 0.027$
K^*ll	$0.78^{+0.19}_{-0.17} \pm 0.12$	$1.6 \pm 0.23 \pm 0.10$
$\gamma\gamma$	< 1.7	< 0.54
$\rho^+\gamma$	< 1.8	$0.55^{+0.43+0.12}_{-0.37-0.11}$
$\rho^0\gamma$	< 0.4	$1.17^{+0.35+0.09}_{-0.31-0.08}$
$\omega\gamma$	< 1.0	$0.58^{+0.35+0.07}_{-0.34-0.11}$
$\rho/\omega\gamma$	< 1.2	$1.34^{+0.27+0.11}_{-0.31-0.10}$
K^+K^-	< 0.6	< 0.37
K^0K^+	$1.45^{+0.53}_{-0.46} \pm 0.11$	$1.0 \pm 0.4 \pm 0.1$
K^0K^0	$1.19^{+0.40}_{-0.35} \pm 0.13$	$0.8 \pm 0.3 \pm 0.1$

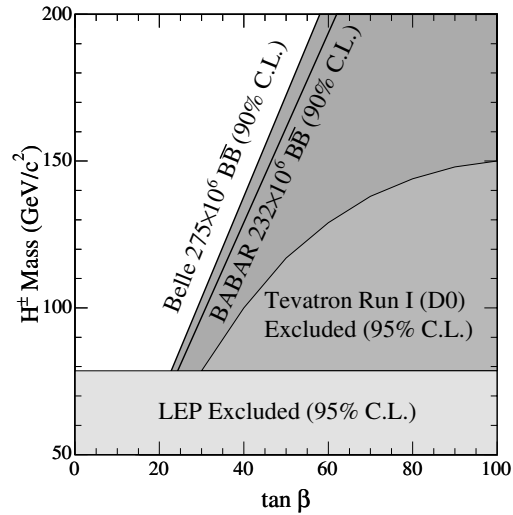


Fig. 7. The 90% confidence level exclusion boundaries in the $[M_{H^+}, \tan\beta]$ plane based on the obtained upper limits on $\mathcal{B}(B \rightarrow \tau\nu)$.

which is a good test for SUSY signals. The BaBar collaboration has updated the branching fraction measurements, as listed in Table 3, with 227 million $B\bar{B}$ pairs in summer 2005 [26]. Although the experimental results have small discrepancies ($< 3\sigma$) between the two B factories, they are consistent with the theoretical expectations. And no direct CP violating asymmetry is observed.

Another interesting measurement was reported. The upper limit of $\mathcal{B}(B^0 \rightarrow \gamma\gamma)$ is reduced from $< 1.7 \times 10^{-6}$ to $< 5.4 \times 10^{-7}$ with 110 million $B\bar{B}$ pairs [27]. Three years later we will reach the SM prediction, around 3×10^{-8} , with the Belle and BaBar data combined.

6 Other CPV Results and More Observations

Study of time dependent CP violation in $b \rightarrow s\gamma$ processes is another good place to search for new physics. In the SM, the photon emitted from $B^0(\bar{B}^0)$ mesons is predominantly left-handed (right-handed). Therefore, the decay of B^0 meson is almost flavor specific, resulting small mixing-induced CP violation. Any deviation from a small CP asymmetry indicates new physics. Both Belle and BaBar have reported their CP violation searches on $B \rightarrow K_S^0\pi^0\gamma$ [28] with 386 million and 232 million $B\bar{B}$ pairs, respectively. Events in two kinematic regions have been used: the invariant mass of $K^0\pi^0$ between 0.8 and 1.0 GeV/c^2 ($K^*(892)$ resonance) and events outside the $K^*(892)$ resonance. All experimental results are consistent with no asymmetry.

One of the highlights in 2004 is the observation of direct CP violation in the decay $B^0 \rightarrow K^+\pi^-$ [3]. One year later, the Belle collaboration has updated the CP violating asymmetry with ~ 100 million more $B\bar{B}$ pairs [29]. The obtained asymmetry is $A_{CP} = -0.113 \pm 0.022 \pm 0.088$, confirming previous Belle and BaBar results. Furthermore, direct CP asymmetries of the $K^+\pi^0$ and $\pi^+\pi^0$ modes are also updated and results are consistent with 0. The world averages of the asymmetries are $A_{CP}(K^+\pi^-) = -0.115 \pm 0.018$ and $A_{CP}(K^+\pi^0) = +0.04 \pm 0.04$, which has 3.9σ deviation from each other. Theoretically, several explanations have been given to explain this A_{CP} difference either from the SM or new physics point of view. More precise measurements and results from other decay modes, such as the asymmetry of the $K^0\pi^0$ mode, will provide us information to understand the dynamics of B decays and, thus, help examine the new physics. The CP asymmetry measurements of the $K\pi$ modes become one of the most important topics in the B factory.

The highlight of the B factories in the summer of 2005 is the observation of $b \rightarrow d$ penguin. The exclusive modes, $B \rightarrow (\rho, \omega)\gamma$ and B meson decays to two kaons, are easiest modes to search for the $b \rightarrow d$ transition. For the former modes, both Belle and BaBar have previously reported their upper limits. Table 3 shows the BaBar results using 211 million $B\bar{B}$ pairs and the combined upper limit is $\mathcal{B}(B \rightarrow (\rho, \omega)\gamma) < 1.2 \times 10^{-6}$ [30]. With more data, the Belle collaboration has observed the decays this year, see 3 and Fig. 8, and the combined branching fraction is $\mathcal{B}(B \rightarrow (\rho, \omega)\gamma) = (1.34^{+0.34+0.14}_{-0.31-0.10}) \times 10^{-6}$ [31]. Furthermore, Belle also reported the ratio of the two CKM elements V_{td} and V_{ts} based on the ratio of branching fractions ($\mathcal{B}(B \rightarrow (\rho, \omega)\gamma)/\mathcal{B}(B \rightarrow K^*\gamma)$) and the prescription in [32]:

$$|V_{td}/V_{ts}| = 0.200^{+0.026}_{-0.025}(\text{exp.})^{+0.038}_{-0.020}(\text{theo}), \quad (4)$$

where the first error is a quadric sum of statistical and systematic errors, and the second error is the theoretical error, which comes from the the uncertainties of the form factor ratio and the $SU(3)$ -breaking correction.

Although there is a small experimental discrepancy on the exclusive decays of $b \rightarrow d\gamma$, Belle and BaBar observed

the evidence of the $b \rightarrow d$ penguin in B decays into two kaons. Clear signals appear in the decays $B^0 \rightarrow K_S^0 K_S^0$ and $B^+ \rightarrow K^+ K_S^0$ with branching fractions around 1×10^{-6} , while no $B^0 \rightarrow K^+ K^-$ signal is found [33]. Experimental results are consistent with each other (see Table 3) and agree with some theoretical predictions [34].

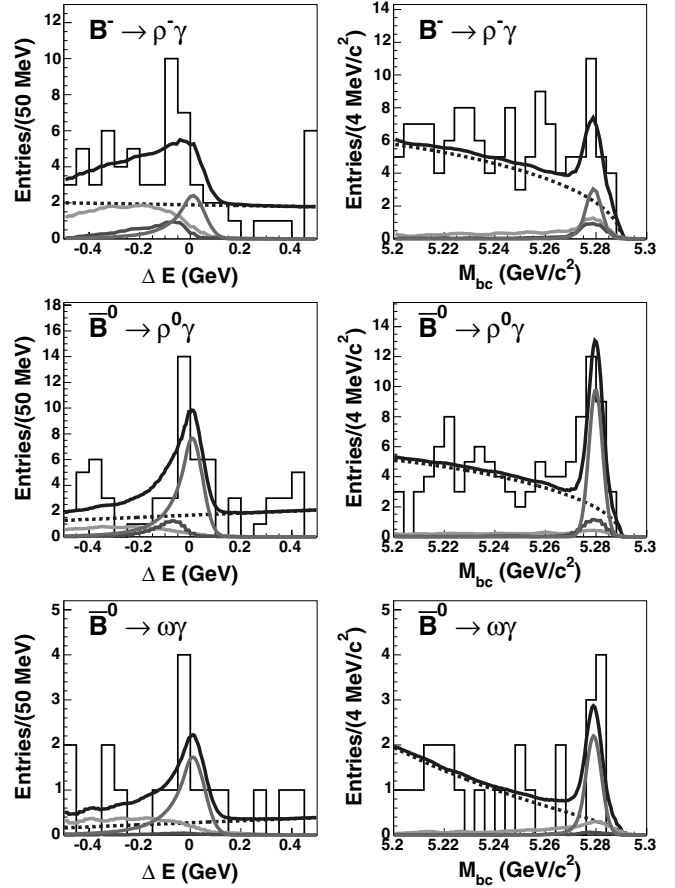


Fig. 8. Projections of the fit results to M_{bc} and ΔE for the individual modes. Lines represent the signal (magenta), continuum (blue-dashed), $B \rightarrow K^*\gamma$ (red), other B decay background (green) components, and the total fit result (blue solid).

Another important aspect of physics at B factory is the discovery of new physics states. There have been 7 particle states discovered by the Belle collaboration before 2005 and all of them are in the charm sector. This year, another state with heavy mass is observed by the BaBar collaboration. In a study of initial-state radiation events, $e^+e^- \rightarrow \gamma_{\text{ISR}}\pi^+\pi^-J/\psi$, a resonance near 4.2 GeV/c^2 at the invariant mass of $\pi^+\pi^-J/\psi$ is observed [35]. With an excess of 125 ± 23 events, a fit with a single resonance hypothesis gives a width of $\Gamma = 88 \pm 23 \text{ MeV}/c^2$, as shown in Fig. 9. However, the current statistics is limited to exclude or establish a multi-resonance hypothesis.

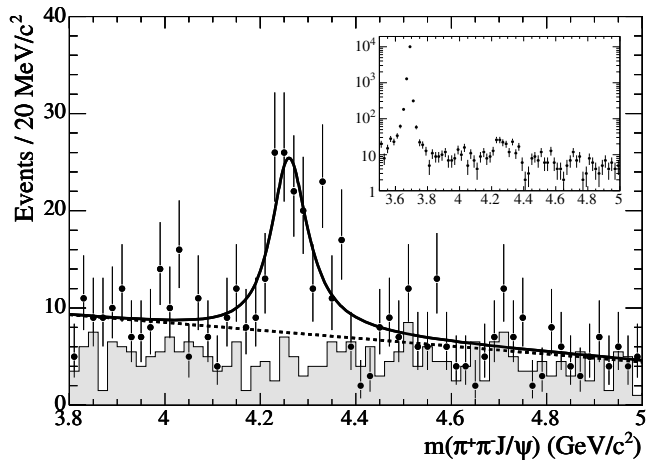


Fig. 9. The $\pi^+\pi^-J/\psi$ invariant mass spectrum in the range 3.8–5.0 GeV/c^2 and (inset) over a wider range that includes the $\psi(2S)$. The points with error bars represent the selected data and the shaded histogram represents the scaled data from neighboring e^+e^- and $\mu^+\mu^-$ mass regions (see text). The solid curve shows the result of the single-resonance fit described in the text; the dashed curve represents the background component.

7 Summary

We have reported the new or updated results of B factory experiments. The new world average of $\sin 2\phi_1$ measured from the $b \rightarrow c\bar{c}s$ transition is $\sin 2\phi_1 = 0.687 \pm 0.032$. It becomes a calibration mode for all other time dependent CP analysis. A lot of efforts have been made for the other two angles, ϕ_2 and ϕ_3 . With current statistics, the angle ϕ_2 is determined with ~ 10 degree accuracy. Although more data is needed to measure the third angle, the $D^{(*)}K^{(*)}$ Dalitz method looks very promising to extract ϕ_3 . The effective $\sin 2\phi_1$ obtained in the $b \rightarrow s\bar{q}q$ process is updated with the value less deviated from the SM expectation. However, this CP analysis provides the most sensitive probe for new physics; therefore, further frequent update is forseen. Many new or updated measurements for charmless B decays are shown with improved measurements. Both Belle and BaBar are expected to accumulate 1 ab^{-1} of data in two to three years. Not only will more properties of B mesons be observed, but also testing the SM can be performed with better sensitivity.

References

1. Belle Collaboration, K. Abe *et al.*, Phys. Rev. Lett. 87, (2001) 091802.
2. BaBar Collaboration, B. Aubert *et al.*, Phys. Rev. Lett. 87, (2001) 091801.
3. Belle Collaboration, Y. Chao *et al.*, Phys. Rev. Lett. 93, (2004) 191802; BaBar Collaboration, B. Aubert *et al.*, Phys. Rev. Lett. 93, (2004) 131801.
4. The combined averages of b -hadron properties are provided by the heavy flavor averaging group. All results shown in and before Summer 2004 are documented in hep-ex/0412073.

5. A. K. Akeroyd *et al.*, hep-ex/0406071.
6. Belle Collaboration, A. Abashina *et al.*, Nucl. Instrum. Methods Phys. Res., Sec. A.479, (2002) 117; BaBar Collaboration, B. Aubert *et al.*, Nucl. Instrum. Methods Phys. Res., Sec. A.479, (2002) 1.
7. Belle Collaboration, K. Abe *et al.*, hep-ex/0507037.
8. BaBar Collaboration, B. Aubert *et al.*, Phys. Rev. D 71, (2005) 032005.
9. Belle Collaboration, R. Ito *et al.*, Phys. Rev. Lett. 95, (2005) 091601.
10. Belle Collaboration, K. Abe *et al.*, hep-ex/0507065.
11. BaBar Collaboration, B. Aubert *et al.*, hep-ex/0507087.
12. A.E. Snyder and H. R. Quinn, Phys. Rev. D. 48, (1993) 2139.
13. BaBar Collaboration, B. Aubert *et al.*, hep-ex/0408099.
14. M. Gronau and D. London, Phys. Rev. Lett. 65, (1990) 3381.
15. Belle Collaboration, Y. Chao *et al.*, Phys. Rev. Lett. 94, (2005) 181803; BaBar Collaboration, B. Aubert *et al.*, Phys. Rev. Lett. 94, (2005) 181802.
16. Belle Collaboration, H. Ishino *et al.*, Phys. Rev. Lett. 95, (2005) 101801; BaBar Collaboration, B. Aubert *et al.*, Phys. Rev. Lett. 95, (2005) 151803.
17. BaBar Collaboration, B. Aubert *et al.*, Phys. Rev. Lett. 95, (2005) 041805.
18. Belle Collaboration, K. Abe *et al.*, hep-ex/0507039.
19. M. Gronau and D. Wyler, Phys. Lett. B265, (1991) 172; M. Gronau and D. London, Phys. Lett. B253, (1991) 483; D. Atwood, I. Dunietz and A. Soni, Phys. Rev. Lett. 78, (1997) 3257.
20. A. Giri *et al.*, Phys. Rev. D68, (2003) 054018; Belle Collaboration, A. Poluektov *et al.*, Phys. Rev. D70, (2004) 072003.
21. Belle Collaboration, K. Abe *et al.*, hep-ex/0411049 and hep-ex/0504013; BaBar Collaboration, B. Aubert *et al.*, Phys. Rev. Lett. 95, (2005) 121802.
22. CKMfitter group, J. Charles *et al.*, Eur. Phys. J. C41, (2005) 1.
23. Belle Collaboration, K. Abe *et al.*, hep-ex/0507034, BaBar Collaboration, B. Aubert *et al.*, hep-ex/0407038.
24. BaBar Collaboration, B. Aubert *et al.*, Phys. Rev. Lett. 94, (2005) 101801.
25. Belle Collaboration, K. Abe *et al.*, hep-ex/0410006.
26. BaBar Collaboration, B. Aubert *et al.*, hep-ex/0507005.
27. Belle Collaboration, K. Abe *et al.*, hep-ex/0507036 ; BaBar Collaboration, B. Aubert *et al.*, Phys. Rev. Lett. 87, (2001) 241803.
28. Belle Collaboration, K. Abe *et al.*, hep-ex/0507059; BaBar Collaboration, B. Aubert *et al.*, Phys. Rev. D72, (2005) 051103.
29. Belle Collaboration, K. Abe *et al.*, hep-ex/0507045.
30. BaBar Collaboration, B. Aubert *et al.*, hep-ex/0408034.
31. Belle Collaboration, K. Abe *et al.*, hep-ex/0506079.
32. A. Ali, E. Lunghi and A. Parkhomenko, Phys. Lett. B595, (2004) 323.
33. Belle Collaboration, K. Abe *et al.*, hep-ex/0506080; BaBar Collaboration, B. Aubert *et al.*, hep-ex/0507023.
34. J.D. Bjorken, Nucl. Phys. (Proc. Suppl.) B11, (1989) 325; H-n. Li and B. Tseng, Phys. Rev. D57, (1998) 443; C.-H. Chen and H.-n. Li, Phys. Rev. D63, (2001) 014003; Y.-Y. Keum and A. I. Sanda, Phys. Rev. D67, (2003) 054009; R. Fleischer and S. Recksiegel, Eur. Phys. J C 38, (2004) 251.
35. BaBar Collaboration, B. Aubert *et al.*, hep-ex/0506081.

B_s Properties at the Tevatron

Guillermo Gómez-Ceballos^a

Instituto De Física de Cantabria, Avda. de los Castros s/n, 39002 Santander, Cantabria, Spain

Abstract. The Tevatron collider at Fermilab provides a very rich environment for the study B_s mesons. In this paper we will show a few selected topics from the CDF and DØ collaborations, giving special attention to the B_s Mixing analyses.

1 Introduction

The Tevatron collider at Fermilab, operating at $\sqrt{s}=1.96$ TeV, has a huge b production rate which is 3 orders of magnitude higher than the production rate at e^+e^- colliders running on the $\Upsilon(4S)$ resonance. Among the produced B particles there are as well heavy and excited states which are currently uniquely accessible at the Tevatron, such as for example B_s , B_c , Λ_b , θ_b , B^{**} or B_s^{**} . Dedicated triggers are able to pick 1 B event out of 1000 QCD events by selecting leptons and/or events with displaced vertices already on hardware level.

The aim of the B Physics program of the Tevatron experiments CDF and DØ is to provide constraint to the CKM matrix which takes advantage of the unique features of a hadron collider. Several topics related to B_s mesons were discussed by other speakers in the conference, therefore we will focus this paper in three flaship analyses: $B_s \rightarrow h^+h'^-$, $\Delta\Gamma_s/\Gamma_s$ and Δm_s [1,2].

Both the CDF and the DØ detector are symmetric multi-purpose detectors having both silicon vertex detectors, high resolution tracking in a magnetic field and lepton identification [1,2]. CDF is for the first time in an hadronic environment able to trigger on hardware level on large track impact parameters which indicates displaced vertices. Thus it is very powerful in fully hadronic B modes.

2 $B_{s(d)} \rightarrow h^+h'^-$ Decays

Using the new trigger on displaced tracks, CDF has collected several hundred events of charmless B_d and B_s decays in two tracks. The invariant mass spectrum of the $B_{s(d)} \rightarrow h^+h'^-$ candidates with pion mass assignment for both tracks is shown in Fig. 1. A clear peak is seen, but with a width much larger than the intrinsic CDF resolution due to the overlap of four different channels under the peak: $B_d \rightarrow K^+\pi^-$, $B_s \rightarrow K^+K^-$, $B_d \rightarrow \pi^+\pi^-$ and $B_s \rightarrow \pi^+K^-$. One of the goals of CDF is to measure

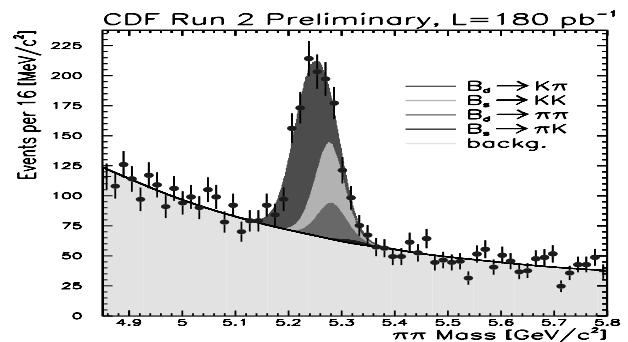


Fig. 1. $\pi\pi$ invariant mass distribution of $B_{s(d)} \rightarrow h^+h'^-$ candidates.

time-dependent decay CP asymmetries in flavor-tagged sample of $B_s \rightarrow K^+K^-$ and $B_d \rightarrow \pi^+\pi^-$ decays. The first step has been to disentangle the different contributions. To do that a couple of variables has been combined in an unbinned maximum likelihood fit in addition to the reconstructed mass. The first variable is the dE/dX information, which has a separation power between kaons and pions of about 1.4σ . The other variable is the kinematic charge correlation between the invariant mass $M_{\pi\pi}$ and the signed momentum imbalance between the two tracks, $\alpha = (1 - \frac{p_1}{p_2}) * q_1$, where p_1 (p_2) is the scalar momentum of the track with the smaller (larger) momentum and q_1 is the charge of the track with smaller momentum. The distribution from Monte Carlo simulation of $M_{\pi\pi}$ versus α is shown in Fig. 2.

With this, we obtain the first observation of $B_s \rightarrow K^+K^-$:

$$\frac{f_s}{f_d} \frac{R(B_s \rightarrow K^+K^-)}{BR(B_d \rightarrow K\pi)} = 0.46 \pm 0.08(stat.) \pm 0.07(syst.),$$

and a big improvement in the limit on $B_s \rightarrow K^+\pi^-$:

$$BR(B_s \rightarrow K\pi) < 0.08 * BR(B_d \rightarrow K\pi) * (f_s/f_d) @90\% C.L.$$

In the B_d sector we obtain:

^a e-mail: ceballos@fnal.gov

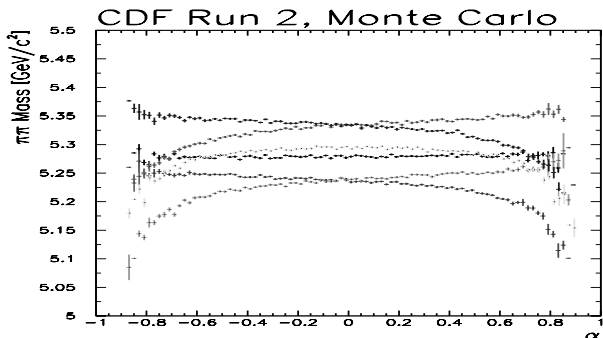


Fig. 2. Monte Carlo distribution of $M_{\pi\pi}$ versus $(1 - \frac{p_1}{p_2}) * q_1$ for different $B_{s(d)} \rightarrow h^+ h'^-$ channels.

$$A_{CP}(B_d \rightarrow K\pi) = \frac{N(B_d \rightarrow K^+ \pi^-) - N(\bar{B}_d \rightarrow K^- \pi^+)}{N(B_d \rightarrow K^+ \pi^-) + N(\bar{B}_d \rightarrow K^- \pi^+)} = -0.022 \pm 0.078(stat.) \pm 0.012(syst.),$$

being this result perfectly compatible with B factories. It is important to notice that A_{CP} systematics are at the level of Babar and Belle experiments, and we expect to reach Y(4S) precision on the statistical uncertainty with the current sample on tape as well.

3 $\Delta\Gamma_s/\Gamma_s$ Measurement in $B_s \rightarrow J/\Psi\phi$ Decays

In order to measure the decay width difference $\Delta\Gamma_s$ we need to disentangle the heavy and light B_s mass eigenstates and measure their lifetimes separately. In the B_s system CP violation is supposed to be small ($\delta\phi_s \approx 0$). Thus the heavy and light B_s mass eigenstates directly correspond to the CP even and CP odd eigenstates. So the separation of the B_s mass eigenstates can be done by identifying the CP even and CP odd contributions.

Generally final states are mixtures of CP even and odd states, but for pseudoscalar particles where the B_s decays into two vector particles such as the J/Ψ and the ϕ it is possible to disentangle the CP even and CP odd eigenstates by an angular analysis. The decay amplitude decomposes into 3 linear polarization states with the amplitudes A_0, A_{\parallel} and A_{\perp} with

$$|A_0|^2 + |A_{\parallel}|^2 + |A_{\perp}|^2 = 1. \quad (1)$$

A_0 and A_{\parallel} correspond to the S and D wave and are therefore the CP even contribution, while A_{\perp} corresponds to the P wave and thus to the CP odd component.

It is possible to measure the lifetimes of the heavy and light B_s mass eigenstate, by fitting at the same time for the angular distributions and for the lifetimes.

A similar angular analysis has been already performed by the BABAR and BELLE experiments in the $B_d \rightarrow J/\Psi K^{*0}$ mode. This mode has as well been studied at the Tevatron as a cross check for the $B_s \rightarrow J/\Psi\phi$ analysis.

In order to perform this analysis first of all a $B_s \rightarrow J/\Psi\phi$ signal has to be established. Both experiments have

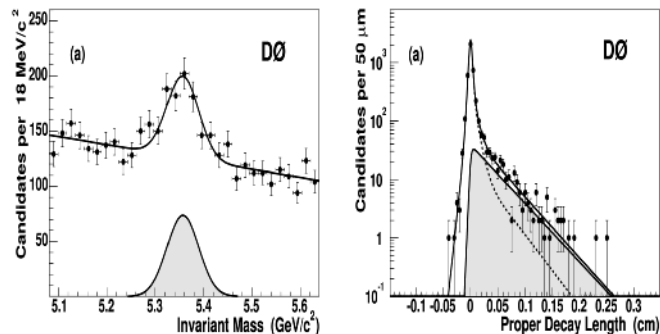


Fig. 3. Mass (left) and average lifetime (right) distributions of $B_s \rightarrow J/\Psi\phi$ candidates from $D\phi$.

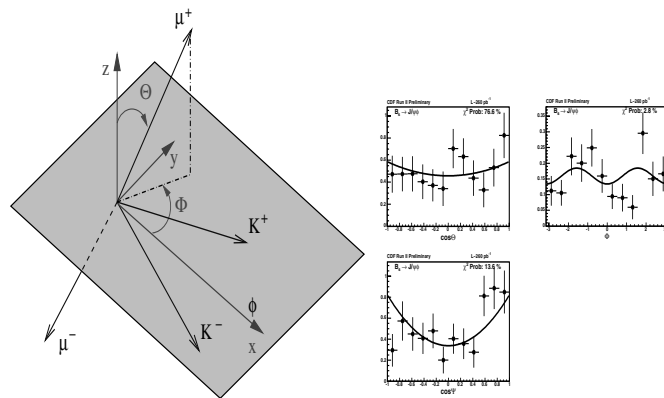


Fig. 4. Definition of the transversity frame and the transversity angles (left) and fit projections of the common fit of both lifetime and angular distributions from the CDF analysis (right).

Table 1. $\Delta\Gamma_s/\Gamma_s$ results from CDF and $D\phi$.

Experiment	$\Delta\Gamma_s/\Gamma_s$	$\langle \tau \rangle$ (ps)	τ_L (ps)	τ_H (ps)
CDF	$0.65^{+0.25}_{-0.33}$	$1.40^{+0.15}_{-0.13}$	$1.05^{+0.16}_{-0.13}$	$2.07^{+0.58}_{-0.46}$
$D\phi$	$0.21^{+0.33}_{-0.45}$	$1.39^{+0.13}_{-0.16}$	$1.23^{+0.16}_{-0.13}$	$1.52^{+0.39}_{-0.43}$

measured the B_s mass and lifetime, as shown in Fig. 3 for the $D\phi$ analysis, where the lifetime τ_s is measured with respect to τ_d from the topological similar decay $B_d \rightarrow J/\Psi K^{*0}$.

The angular analysis has been performed in the transversity basis in the J/Ψ rest-frame which is introduced in Fig. 4. The fit projections of the common fit of the both lifetimes and the angular distributions for the CDF analysis and for the $D\phi$ analysis are shown in Fig. 4.

The results of both experiments are summarized in Tab. 1 and Fig. 5. The combined result slightly favors high values of Δm_s , but is currently statistically limited. The systematic uncertainties are very small, thus this is a precise measurement ones more data is available.

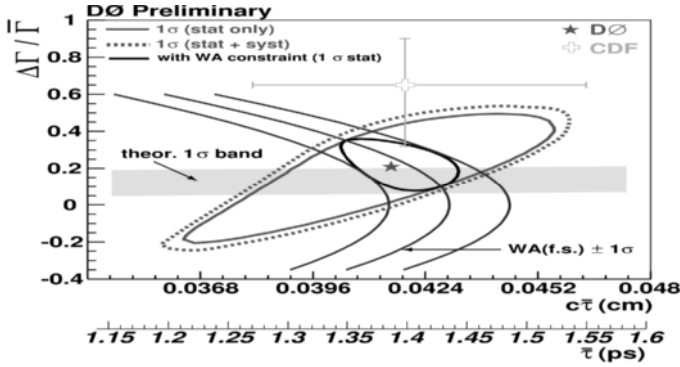


Fig. 5. $\Delta\Gamma_s/\Gamma_s$ versus $c\langle\tau\rangle$ results from CDF and DØ.

4 B_s Mixing

The probability that a B meson decays at proper time t and has or has not already mixed to the \bar{B} state is given by:

$$P_{unmix}(t) \approx \frac{1}{2}(1 + \cos \Delta mt), \quad (2)$$

$$P_{mix}(t) \approx \frac{1}{2}(1 - \cos \Delta mt). \quad (3)$$

The canonical B mixing analysis, in which oscillations are observed and the mixing frequency, Δm , is measured, proceeds as follows. The B meson flavor at the time of its decay is determined by exclusive reconstruction of the final state. The proper time, $t = m_B L / pc$, at which the decay occurred is determined by measuring the decay length, L , and the B momentum, p . Finally the production flavor must be tagged in order to classify the decay as being mixed or unmixed at the time of its decay.

Oscillation manifests itself in a time dependence of, for example, the mixed asymmetry:

$$\mathcal{A}_{mix}(t) = \frac{N_{mixed}(t) - N_{unmixed}(t)}{N_{mixed}(t) + N_{unmixed}(t)} = -\cos \Delta mt \quad (4)$$

In practice, the production flavor will be correctly tagged with a probability P_{tag} , which is significantly smaller than one, but larger than one half (which corresponds to a random tag). The measured mixing asymmetry in terms of dilution, \mathcal{D} , is

$$\mathcal{A}_{mix}^{meas}(t) = \mathcal{D}\mathcal{A}_{mix} = -\mathcal{D}\cos \Delta mt \quad (5)$$

where $\mathcal{D} = 2P_{tag} - 1$.

First of all a good proper decay time resolution, which is specially important in order to resolve high Δm_s mixing frequency.

The second important ingredient for a mixing analysis is the flavor tagging. As the examined decays are flavor specific modes the decay flavor can be determined via the decay products. But for the production flavor additional information from the event has to be evaluated in order to tag the event. A good and well measured tagging performance is needed to set a limit on Δm_s .

The last component are the B_s candidates. Sufficient statistic is need to be sensitive to high mixing frequencies.

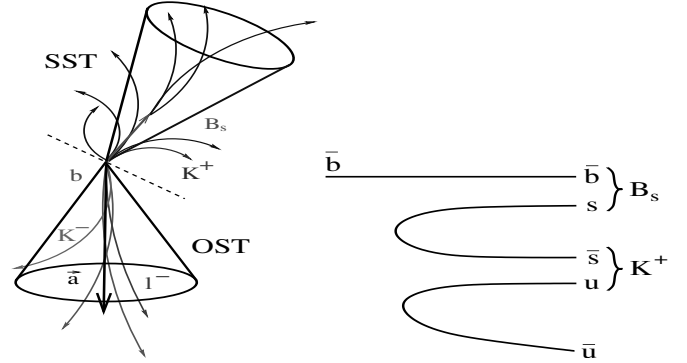


Fig. 6. Left: Sketch of different tagging algorithms; Right: Same-side kaon tagging.

4.1 Flavor Tagging

There are two different kinds of flavor tagging algorithms, opposite side tagging (OST) and same side tagging (SST), which are illustrated in Fig. 6. OST algorithms use the fact that b quarks are mostly produced in $b\bar{b}$ pairs, therefore the flavor of the second (opposite side) b can be used to determine the flavor of the b quark on the signal side.

4.1.1 Jet-Charge Tagging

The average charge of an opposite side b -jet is weakly correlated to the charge of the opposite b quark and can thus be used to determine the opposite side b flavor. The main challenge of this tagger is to select the b -jet. Information of a displaced vertex or displaced tracks in the jet help to identify b -jets. This tagging algorithm has a very high tagging efficiency, but the dilution is relatively low. By separating sets of tagged events of different qualities e.g. how b like the jet is, it is possible to increase the overall tagging performance.

4.1.2 Soft-Lepton-Tagging

In 20 % of cases the opposite semileptonic b decays either into an electron or a muon ($b \rightarrow l^- X$). The charge of the lepton is correlated to the charge of the decaying B meson. Depending on the type of the B meson there is a certain probability of oscillation between production and decay (0 % for B^\pm , 17.5 % for B_d and 50 % for B_s). Therefore this tagging algorithm already contains an intrinsic dilution. Another potential source of miss-tag is the transition of the b quark into a c quark, which then forms a D meson and subsequently decays semileptonically ($\bar{b} \rightarrow \bar{c} \rightarrow l^- X$). Due to the different decay length and momentum distribution of B and D meson decays this source of miss-tag can mostly be eliminated.

4.1.3 Same-Side-Tagging

During fragmentation and the formation of the $B_{s/d}$ meson there is a left over \bar{s}/\bar{d} quark which is likely to form

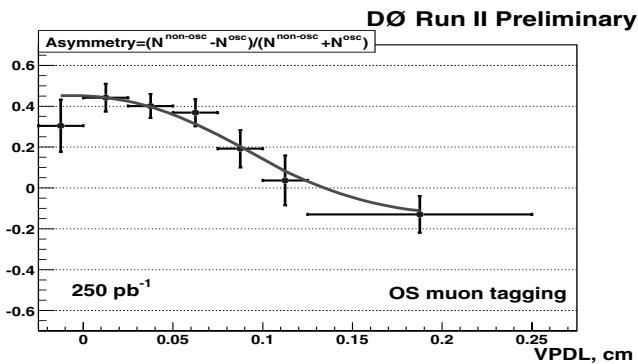


Fig. 7. Asymmetry fit projection for Δm_d using opposite side muon tagger in semileptonic decays from D^0 .

a K^+/π^+ (Fig. 6). So if there is a near by charged particle, which is additionally identified as a kaon/pion, it is quite likely that it is the leading fragmentation track and its charge is then correlated to the flavor of the $B_{s/d}$ meson. While the performance of the opposite side tagger does not depend on the flavor of the B on the signal side the SST performance depends on the signal fragmentation processes. Therefore the opposite side performance can be measured in B_d mixing and can then be used for setting a limit on the B_s mixing frequency. But for using the SST for a limit on Δm_s we have to heavily rely on Monte Carlo simulation. The SST potentially has the best tagger performance, but before using it for a limit, fragmentation processes have to be carefully understood.

4.2 Δm_d Measurement and Calibration of Taggers

For setting a limit on Δm_s the knowledge of the tagger performance is crucial. Therefore it has to be measured in kinematically similar B_d and B^+ samples.

The Δm_s and Δm_d analysis is a complex fit with up to 500 parameters which combine several B flavor and several decay modes, various different taggers and deals with complex templates for mass and lifetime fits for various sources of background. Therefore the measurement of Δm_d is beside the calibration of the opposite side taggers very important to test and trust the fitter framework, although the actual Δm_d result at the Tevatron is not competitive with the B factories.

Both CDF and D^0 have demonstrated that the whole machinery is working, being Δm_d measurements compatible with the PDG average value of $0.510 \pm 0.004 \text{ ps}^{-1}$ [5]. The combined tagging performance of the opposite-side taggers is about 1.5-2%.

An example of the fitted asymmetry using the opposite side muon tagger on the semileptonic decay modes from D^0 is displayed in Fig. 7.

4.3 Amplitude Scan

An alternative method for studying neutral B meson oscillations is the so called ‘‘amplitude scan’’, which is explained

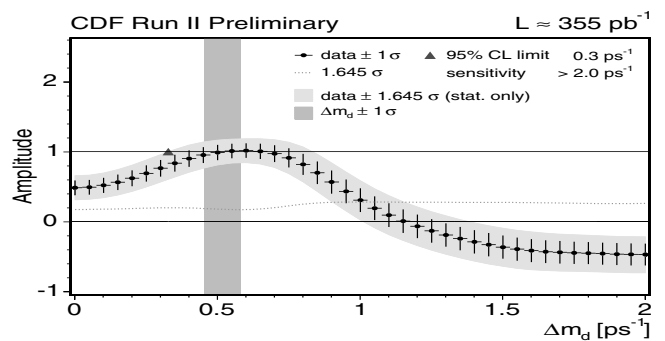


Fig. 8. Amplitude scan for Δm_d in hadronic decay modes (CDF). The scan is compatible with 1 around the result of the actual Δm_d fit.

in detail in Reference [6]. The likelihood term describing the tagged proper decay time of a neutral B meson is modified by including an additional parameter multiplying the cosine, the so-called amplitude A .

The signal oscillation term in the likelihood of the Δm thus becomes

$$\mathcal{L} \propto \frac{1 \pm AD \cos(\Delta mt)}{2} \quad (6)$$

The parameter A is left free in the fit while \mathcal{D} is supposed to be known and fixed in the scan. The method involves performing one such A -fit for each value of the parameter Δm , which is fixed at each step; in the case of infinite statistics, optimal resolution and perfect tagger parameterization and calibration, one would expect A to be unit for the true oscillation frequency and zero for the remaining of the probed spectrum. In practice, the output of the procedure is accordingly a list of fitted values (A, σ_A) for each Δm hypothesis. Such a Δm hypothesis is excluded to a 95% confidence level in case the following relation is observed, $A + 1.645 \cdot \sigma_A < 1$.

The sensitivity of a mixing measurement is defined as the lowest Δm value for which $1.645 \cdot \sigma_A = 1$.

The amplitude method will be employed in the ensuing B_s mixing analysis. One of its main advantages is the fact that it allows easy combination among different measurements and experiments.

The plot shown in Figure 8 is obtained when the method is applied to the hadronic B_d samples of the CDF experiment, using the exclusively combined opposite side tagging algorithms.

The expected compatibility of the measured amplitude with unit in the vicinity of the true frequency, $\Delta m_d = 0.5 \text{ ps}^{-1}$, is confirmed.

However, we observe the expected increase in the amplitude uncertainty for higher oscillation frequency hypotheses. This is equivalent to saying that the significance is reduced with increasing frequency.

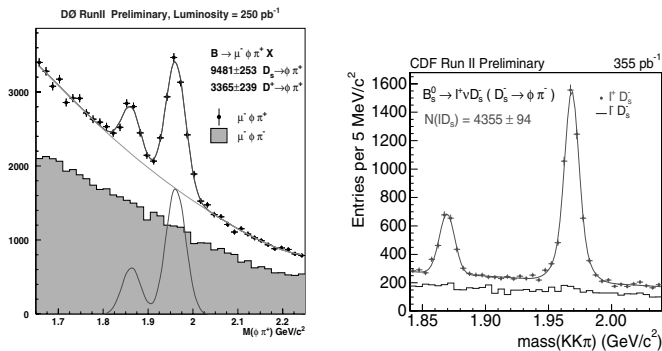


Fig. 9. Reconstructed semileptonic $B_s \rightarrow lXD_s$, ($D_s \rightarrow \phi\pi$) candidates from DØ (left) and CDF (right).

4.4 Reconstructed B_s Decays

DØ exploits the high statistics muon trigger to study semileptonic B_s decays. Several thousands candidates have been reconstructed in the $B_s \rightarrow \mu XD_s$, ($D_s \rightarrow \phi\pi$) mode. Additionally DØ is also working on reconstructing $B_s \rightarrow \mu XD_s$, ($D_s \rightarrow K^*0K$) candidates and on reconstructing fully hadronic B_s decays on the non trigger side in this sample.

CDF performs the B_s mixing analysis using both fully reconstructed B_s decays ($B_s \rightarrow D_s\pi$) obtained by the two track trigger and semileptonic decays ($B_s \rightarrow lXD_s$) collected in the lepton+displaced track trigger. In both cases the D_s is reconstructed in the $D_s \rightarrow \phi\pi$, $D_s \rightarrow K^*0K$ and $D_s \rightarrow \pi\pi\pi$ modes.

Fig. 9 shows the reconstructed semileptonic $B_s \rightarrow lXD_s$, ($D_s \rightarrow \phi\pi$) candidates from DØ and CDF.

4.5 First Δm_s Limits in Run II

Finally, an amplitude scan, repeating the Likelihood fit for the amplitude A for different values of Δm_s , was performed in both DØ and CDF. The results of the amplitude scans are shown in Fig. 10 and 11. The amplitude scan yields a Δm_s sensitivity of $8.4(4.6) ps^{-1}$ and a lower exclusion limit of $7.9(5.0) ps^{-1}$ is set on the value of Δm_s at a 95% confidence level in CDF (DØ).

Those results are good enough for the first round of the analysis, but there is still a huge room for improvements in the near future.

5 Conclusions

The large amount of data collected by the CDF and DØ experiments are improving our knowledge about B_s mesons. A few selected topics have been discussed in this paper. The measurement of the decay width difference $\Delta\Gamma_s$ of the heavy and light B_s mass eigenstate is especially sensitive to high Δm_s values. The B_s mixing analysis is sensitive to lower values. Together they have the potential to cover the hole range of possible Δm_s values in the Standard Model and as well beyond.

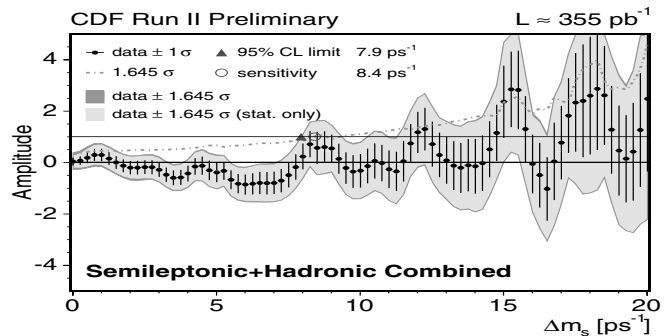


Fig. 10. Combined amplitude scan from CDF. The black dots represent the fitted amplitude with their respective statistical errors for each value of Δm_s . The yellow region indicates 1.645σ using statistical errors only while the green band includes combined statistical and systematic errors. The measurement is dominated by statistical uncertainties. Note, neighboring points are statistically correlated.

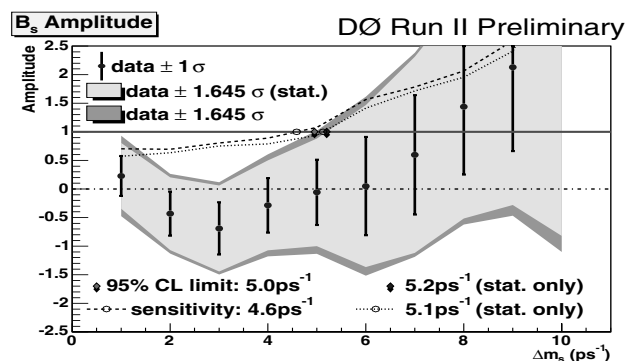


Fig. 11. Combined amplitude scan from DØ.

References

1. The CDF Collaboration, <http://www-cdf.fnal.gov/physics/new/bottom/bottom.html>.
2. The DØ Collaboration, <http://www-d0.fnal.gov/Run2Physics/WWW/results/b.htm>.
3. R. Blair *et al.*, *The CDF-II detector: Technical Design report*, FERMILAB-PUB-96-390-E (1996).
4. A. Abachi *et al.*, *The DØ upgrade: The detector and its physics*, FERMILAB-PUB-96-357-E (1996).
5. S. Eidelman *et al.* [Particle Data Group], <http://pdg.web.cern.ch/pdg>.
6. H.G. Moser, A. Roussrie, *Mathematical methods for $B^0\bar{B}^0$ oscillation analysis*, NIM A384 (1997), 491-505.

Searches for Rare B meson decay at Tevatron

Shashikant R. Dugad¹

Tata Institute of Fundamental Research,
Homi Bhabha Road, Colaba, Mumbai, India-400 070
For D0/CDF Collaboration

Abstract. Purely leptonic decay modes of B mesons is a Flavor Changing Neutral Current (FCNC) process and it is forbidden in Standard Model. However such decay mode can proceed through higher level diagrams with much smaller branching fractions. We have analysed $p\bar{p}$ collision data, ($\sqrt{s} = 1.96$ TeV) from CDF and D0 experiments at Tevatron to search for several rare decay modes of B meson such as, $B_{s/d} \rightarrow \mu^- \mu^+$ and $B_s \rightarrow \mu^- \mu^+ \phi$. Data with total integrated luminosity of 300 pb^{-1} and 364 pb^{-1} has been used for present analysis from D0 and CDF detectors respectively. In the absence of signal events due to any of these decay modes, upper limits on the branching fraction of each of these decay modes are obtained. Using data recorded by D0 experiment, we obtain upper limit at 95% C.L. on the branching fraction of $B_s \rightarrow \mu^- \mu^+$ and $B_s \rightarrow \mu^- \mu^+ \phi$ decay modes to $\leq 3.7 \times 10^{-7}$ and $\leq 4.1 \times 10^{-6}$ respectively. Similarly, from CDF experiment we obtain upper limit at 95% C.L. on the branching fraction of $B_s \rightarrow \mu^- \mu^+$ and $B_d \rightarrow \mu^- \mu^+$ decay modes to be $\leq 2.0 \times 10^{-7}$ and $\leq 4.9 \times 10^{-8}$ respectively. Work on obtaining combined limits on the $B_s \rightarrow \mu^- \mu^+$ decay mode, using data from both the experiments, is under progress.

1 Introduction

Flavor Changing Neutral Current processes are forbidden in Standard Model. Pure leptonic decay modes of B mesons which are of this type provides quite clean topology that can be easily detected in the data. Though these decay modes (*ex.* $B_{s/d} \rightarrow \mu^- \mu^+$) are forbidden under the Standard Model at tree level, there are higher level diagrams (Fig. 1) through which such decay can take place with very low branching fractions. Search for $B_s \rightarrow \mu^- \mu^+$, $B_d \rightarrow \mu^- \mu^+$ and $B_s \rightarrow \mu^- \mu^+ \phi$ has been carried out at Tevatron experiment; SM branching fraction is estimated to be $3.4 \pm 0.4 \cdot 10^{-9}$, $1.5 \pm 0.9 \cdot 10^{-10}$ and $1.6 \pm 0.5 \cdot 10^{-6}$ respectively for these channels. Decay rate of B_d w.r.t. B_s , is highly suppressed due to presence of $|V_{td}/V_{ts}|^2$ term. In addition to the SM processes, decay amplitudes of these decay modes of B meson can be significantly enhanced in some extensions of SM. For example, in the type-II, two Higgs Doublet Model (2HDM), the decay amplitude enhances significantly with the mass of charged Higgs and $\tan^4 \beta$. In Minimal Supersymmetric Standard Model, the decay amplitude increases as $\tan^6 \beta$. There are several other models beyond SM which predicts branching fraction of pure leptonic decay modes much higher than that predicted by SM. Therefore, it is important to search for these decay modes in the data.

Inclusive cross section for b-quark production at Tevatron is quite high ($\approx 100 \mu\text{b}$), leading to copious production of all flavors of B mesons. Due to fine tracking system placed in high magnetic field, both the detectors possess ex-

cellent capabilities to reconstruct leptonic decay modes of B meson. In D0 data, we have searched for two different rare decay modes, *viz.* $B_s \rightarrow \mu^- \mu^+$ and $B_s \rightarrow \mu^- \mu^+ \phi$. Due to limited mass resolution of D0 detector, it cannot resolve between mass distribution of B_s and B_d mesons and hence D0 data is not sensitive to the $B_d \rightarrow \mu^- \mu^+$ signal decay mode. In CDF data, search has been carried out for both, $B_s \rightarrow \mu^- \mu^+$ as well as $B_d \rightarrow \mu^- \mu^+$ decay modes. It is to be noted that the CDF detector is capable of resolving between B_s and B_d mass peaks.

2 Methodology

General methodology to obtain the branching fraction (or the upper limit) is quite similar in both the detectors. First events with mass around signal mass region are identified in the data. Then, we search for known decay mode of B-meson (normalisation channel) in the data which has topology very similar to signal decay mode. Using events with known decay mode, the ratio of acceptance, trigger and reconstruction efficiency of the detector for signal and normalisation channel is obtained. Then using the observed number of events in the normalisation channel, its branching fraction and relative efficiency the, upper limit on the branching fraction of signal channel can be obtained as shown in Eq.(1). Use of proper normalisation channel substantially reduces systematic effects in determining acceptance and various efficiencies associated with detector response, reconstruction, simulation *etc.*

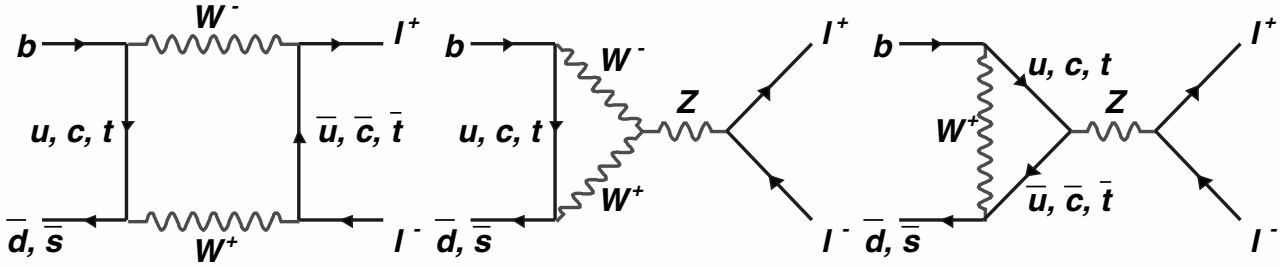


Fig. 1. Higher level Feynman Diagrams for $B_{s/d} \rightarrow \mu^- \mu^+$ decay

$$\mathcal{B}(B_s) \leq \frac{N_{ul}}{N_{B^\pm}} \cdot \frac{\epsilon_{\mu\mu K}^{B^\pm}}{\epsilon_{\mu\mu}^{B_s}} \cdot \frac{\mathcal{B}_1(B^\pm) \cdot \mathcal{B}_2(J/\psi)}{\frac{f_{b \rightarrow B_s}}{f_{b \rightarrow B_{u,d}}} + R \cdot \frac{\epsilon_{\mu\mu}^{B_d}}{\epsilon_{\mu\mu}^{B_s}}} \quad (1)$$

where, N_{ul} is the upper limit on the number of signal events. N_{B^\pm} is the number of events observed in normalisation channel. For $B_{s/d} \rightarrow \mu^- \mu^+$ search, we used $B^\pm \rightarrow \mu^- \mu^+ K$ as normalisation channel and for $B_s \rightarrow \mu^- \mu^+ \phi$ search we have used $B_s \rightarrow J/\psi + \phi$ as the normalisation channel. $\epsilon_{\mu\mu K}^{B^\pm}$ and $\epsilon_{\mu\mu}^{B_s}$ are overall efficiencies of the normalisation and signal channel, obtained from MC simulation of each of the detector. $f_{b \rightarrow B_s} / f_{b \rightarrow B_{u,d}} = 0.270 \pm 0.034$ is the fragmentation ratio of a b (\bar{b}) quark producing a B_s and a B^\pm or B_d . $\mathcal{B}_1 \cdot \mathcal{B}_2$ is the branching fraction of the normalisation channel.

In D0 data, due to limited mass resolution, contributions from B_d decaying to dimuons cannot be separated from B_s decaying to the same. Last term at denominator shown in Eq.(1) is due to this. R is the branching fraction ratio of B_d and B_s decaying into dimuons and $\epsilon_{\mu\mu}^{B_d} / \epsilon_{\mu\mu}^{B_s}$ is the ratio of efficiency of respective decay modes. Since decay of B_d is highly suppressed due to $|V_{td}/V_{ts}|^2$ term, R is assumed to be 0 in D0 data analysis. This assumption will give more conservative estimate of the branching fraction. For CDF data analysis this term does not arise since B_d and B_s mass distribution are well separated.

3 Data Processing

The main detection element relevant for this analysis are central tracking system immersed in high solenoidal magnetic field and muon system providing good muon identification with reasonable tracking. Excellent position and momentum resolution in both the detectors enables efficient identification of signal channel in the data. In both the detectors, data triggered by different dimuon trigger are used for analysis. From this data set, first events are preselected with preliminary selection criteria such as good primary and secondary vertex, good muon tracks and mass of secondary vertex to be around around signal mass *etc.*. This eliminates majority of background events without loss of signal events. For final selection, surviving candidate events are further subjected to additional selection criteria that are more sensitive to the signal selection

with efficient background rejection. B meson lives sufficiently longer to have significant displacement from primary vertex. Significance of displacement ($L/\delta L$) of secondary vertex w.r.t. primary vertex is used to reject random combinatoric background arising from fake muons. The fragmentation characteristic of b-quark are such that most of its momentum is carried out by B hadron. Thus, number of tracks in the vicinity of B candidate are expected to be low. Second discriminant is therefore, (referred as an isolation variable of the muon pair) defined as:

$$I = \frac{|\vec{p}(B_s)|}{|\vec{p}(B_s)| + \sum_{\text{other tracks } i} p_i(\Delta\mathcal{R} < 1)} \quad (2)$$

Isolation variable basically represents fractional momentum carried out by B candidate in cone of $\Delta\mathcal{R} < 1$ where, $\Delta\mathcal{R} = \sqrt{\Delta\eta^2 + \Delta\phi^2}$. The final discriminating variable is the pointing angle α , defined as the angle between momentum vector of B candidate and the vector between primary and secondary vertex. The pointing angle is expected to be small for real candidate. These three variable have the most effective discriminating power to reject background events without losing signal events. Cuts on these variables to optimize signal to background (S/B) ratio have been obtained somewhat differently in CDF and D0 experiments.

In D0 experiment, a Random Grid Search and an optimisation procedure suggested by Punzi [1] were used to find the optimal cut values of discriminating variables by maximising parameter $P = \epsilon / (a/2 + \sqrt{N_{Back}})$, where, ϵ is the reconstruction efficiency of signal events (after pre-selection). The efficiency is obtained using MC sample of signal events. N_{Back} is number of background events obtained by extrapolation from sidebands into the signal region. Parameter a, represents the number of sigmas corresponding to the confidence level at which signal hypothesis is to be tested. This parameter is set to 2 corresponding to a C.L. of 95%. Distributions of discriminating variables for signal MC ($B_s \rightarrow \mu^- \mu^+$) and data events (dominated by background) after pre-selection are shown in Fig. 2

In CDF experiment a *Multi Variate Relative Likelihood Discriminant* is used to distinguish between signal and background. The relative likelihood is defined as,

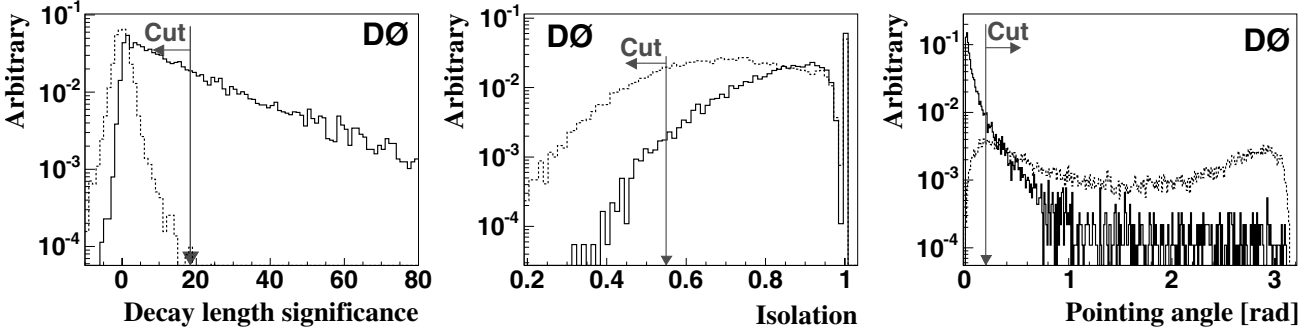


Fig. 2. Distribution for discriminating variables for MC and data events from sidebands (selected after pre-selection cuts). Arrow indicates cut value obtained from optimisation scheme

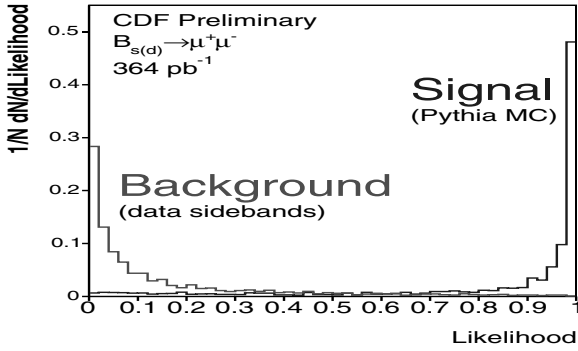


Fig. 3. Distribution of relative likelihood for Signal and Background events in CDF experiment

$$\text{LH} = \frac{\prod_i P_s(x_i)}{\prod_i P_s(x_i) + \prod_j P_b(x_j)} \quad (3)$$

where, i and j represents 3 discriminating variables described above that are used to construct the likelihood. $\prod_i P_{s(b)}(x_i)$ is a composite probability of a given event due to signal (or background). By construction, LH varies between 0 to 1. Large value of LH implies that event is more likely due to signal. Distribution of likelihood variable (LH) distribution for signal MC ($B_s \rightarrow \mu^- \mu^+$) and background event (after pre-selection) are quite well separated as shown in Fig. 3.

4 Analysis of D0 Data

300 pb^{-1} of $p\bar{p}$ collision data has been used for analysis to search for $B_s \rightarrow \mu^- \mu^+$ and $B_s \rightarrow \mu^- \mu^+ \phi$ decay modes. Detailed analysis of these decay modes are described in [3, 4]. First, we describe analysis for $B_s \rightarrow \mu^- \mu^+$ decay mode. Final cuts on discriminating variables obtained as described in Section 3 ($\alpha < 0.18$ rad, $L/\delta L > 18.5$ and $I > 0.6$) yields an efficiency of $38.6 \pm 0.7\%$ to retain the signal events in the data sample. 28 events are observed in the entire mass region of 4.5-7.0 GeV. Dimuon mass resolution of the D0 detector is about, $\sigma = 90$ MeV. Extrapolation of sideband region into the signal region ($M \pm 2\sigma$) yields a background of 4.3 ± 1.2

where as, 4 events are observed in the signal region, consistent with an estimated background, hence no excess of events are seen due to the signal. Mass distribution of signal and normalisation channel events are shown in Fig. 4 (top). Ratio of trigger/reconstruction efficiency for signal and normalisation channel is obtained from MC simulation of each of these decay mode. The ratio, $\epsilon_{\mu\mu K}^{B^\pm} / \epsilon_{\mu\mu}^{B_s}$ is estimated to be $0.229 \pm 0.008 \pm 0.014$. Using these numbers and overall background uncertainty (30%) arising from each of the term shown in Eq.1, the upper limit on the branching fraction is estimated to be $3.7(3.0) \cdot 10^{-7}$ at 95% (90%) C.L. using Fedlman and Cousins approach [2].

Search for $B_s \rightarrow \mu^- \mu^+ \phi$ decay mode is carried using the same data sample of 300 pb^{-1} . $B_s \rightarrow J/\psi(\rightarrow \mu^- \mu^+) + \phi$ is used as normalisation channel. Cut values on discriminating variables obtained using the same optimisation procedure are, $\alpha < 0.1$ rad, $L/\delta L > 10.3$ and $I > 0.72$. These cuts yields a signal efficiency of $54 \pm 3\%$ to retain the signal events in the data sample. In the entire mass region of 4.5-6.1 GeV, 8 candidate events are observed. Due to ϕ mass constraint, mass resolution of this channel ($\sigma = 75$ MeV) is better than previous channel (90 MeV). Expected number of background events in the signal region, obtained by extrapolation of sideband region into the signal region ($M \pm 2\sigma$), are 1.6 ± 0.4 . No events are observed in this region which is consistent with the estimated background. Since error on branching fraction of normalisation channel is quite high (36%), the upper limit on ratio of branching fraction of signal and normalisation channels is obtained using the same procedure followed for other channel described above. Mass distribution of signal and normalisation channel events are shown in Fig. 4 (middle). Ratio of combined efficiency of trigger, reconstruction *etc.* for signal and normalisation channel ($\epsilon_{J/\psi\phi}^{B_s} / \epsilon_{\mu\mu\phi}^{B_s}$) is estimated to be 2.80 ± 0.21 from MC simulation of each of these decay modes. The ratio of fragmentation factor in Eq.1 will be unity since signal and normalisation channels are of same flavor. Using observed and estimated values for each of the corresponding numbers in Eq.1 with overall background uncertainty of 25% arising from those terms, we obtain an upper limit on the ratio of branching fraction ($\mathcal{B}(B_s \rightarrow \mu^+ \mu^- \phi) / \mathcal{B}(B_s \rightarrow J/\psi \phi)$) to be $4.4(3.5) \cdot 10^{-3}$ at

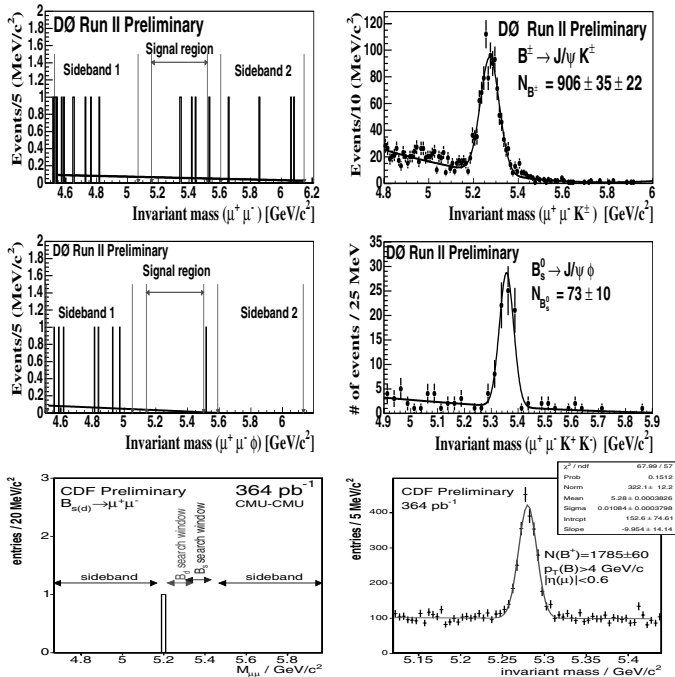


Fig. 4. Mass distribution for signal (left) and normalisation channel (right). Top: $B_s \rightarrow \mu^+ \mu^-$ decay mode in D0, Middle: $B_s \rightarrow \mu^+ \mu^- \phi$ in D0 and Bottom: $B_{s/d} \rightarrow \mu^+ \mu^-$ in CDF detector

95% (90%) C.L. using Fieldman Cousine approach. Using the central value of $\mathcal{B}(B_s \rightarrow J/\psi \phi)$ ($9.3 \pm 3.3 \cdot 10^{-3}$), the limit on $\mathcal{B}(B_s \rightarrow \mu^+ \mu^- \phi)$ corresponds to $4.1(3.2) \cdot 10^{-6}$ at 95% (90%) C.L.

5 Analysis of CDF Data

In CDF detector data is separated as per detection of muons. Dataset corresponding to detection of both the muon in the central muon detector (CMU-CMU, $|\eta| < 0.6$) has a integrated luminosity of 364 pb^{-1} where as, with one of the muon detected in forward muon detector (CMU-CMX) has a integrated luminosity of 336 pb^{-1} . CMX has a rapidity coverage of $0.6 < |\eta| < 1.0$. CDF detector has an excellent dimuon mass resolution of 25 MeV. Due to this, the data has been used for search for B_s as well as B_d decaying to dimuons. Detailed analysis of this decay mode is described in [1]. Normalisation channel used is same ($B^\pm \rightarrow \mu^- \mu^+ K$) for both of these decay modes. Only those events passing through selected dimuon triggers are used for this analysis. In each of the dataset, the data was first filtered through baseline cuts such as trigger match, track and muon quality, vertex constraints with additional coarser cuts on isolation and pointing angle variable. This ensures significant rejection of background without much loss of signal events. Relative likelihood (LH) cut (see Section 3) was optimised to get best limits on branching fraction. LH cut value of > 0.99 was applied on the data. This corresponds to signal efficiency of 38% (obtained from MC of signal) with a

background rejection of more than 99%. With these cuts 0 events are observed in the signal region for both (CMU-CMU, CMU-CMX) the datasets with a background of 0.81 ± 0.12 and 0.66 ± 0.13 in each of these datasets. For normalisation channel, only baseline cuts were used with an additional requirement of dimuon mass around J/ψ mass as well as primary and secondary vertex quality cuts. LH cut was not applied for this purpose. Mass distribution of signal and normalisation channel events are shown in Fig. 4 (bottom) for CMU-CMU region. Ratio of overall efficiency of trigger, reconstruction *etc.* for signal and normalisation channel ($\epsilon_{\mu\mu K}^{B^\pm} / \epsilon_{\mu\mu}^{B_s}$) is obtained from MC simulation and it is 0.274 ± 0.021 for CMU-CMU region 0.174 ± 0.014 for CMU-CMX region. Using these values and error on background uncertainty (15%-20%), we obtain an upper limit on the branching fraction of $B_s \rightarrow \mu^+ \mu^-$ to be $2.0(1.5) \cdot 10^{-7}$ at 95% (90%) using Eq.1,

Analysis carried out for $B_d \rightarrow \mu^- \mu^+$ decay mode is quite similar to that of $B_s \rightarrow \mu^- \mu^+$. All the cuts applied on the data are same. Limit on branching fractions of this decay mode is measured to be $4.9(3.8) \cdot 10^{-7}$ at 95% (90%)

6 Results

CDF and D0 have analysed 364 pb^{-1} and 300 pb^{-1} data respectively. Both experiments at Tevatron have demonstrated excellent sensitivity to search for FCNC decay modes of B-mesons. Limits on branching fractions (B.F.) obtained by CDF and D0 detector are best among existing limits measured by other experiments. Limit on B.F. of $B_s \rightarrow \mu^- \mu^+$ decay mode are measured to be $2.0 \cdot 10^{-7}$ and $3.7 \cdot 10^{-7}$ by CDF and D0 experiment respectively at 95% C.L. Combined analysis CDF and D0 results is under progress and it will further improve limits on these decay modes. CDF has obtained a limit of $4.9 \cdot 10^{-8}$ on B.F. of $B_d \rightarrow \mu^- \mu^+$ decay mode at 95% C.L. $B_s \rightarrow \mu^- \mu^+ \phi$ decay mode has been studied by D0 experiment and the limit on B.F. of this decay mode is measured to be $4.1 \cdot 10^{-6}$ at 95% C.L. This limit is obtained without including error on branching fraction normalisation channel.

References

1. G. Punzi, **physics/0308063**, (2003)
2. G. J. Feldman and R.D. Cousins, Phys Rev. D. **57**, (1998), p3873
3. D0-Collaboration, D0 Note, **4733-conf**, (2005)
4. D0-Collaboration, D0Note **4862-conf**, (2005)
5. CDF-Collaboration, CDF Note, **7670**, (2005)

Trigger Strategy and Performance of the LHCb Detector

Mitesh Patel^a

CERN, Geneva

Abstract. The strategy and performance of the three level trigger system that will be used in the LHCb experiment is described. Emphasis is given to the advantages of using RICH information for fast hadron identification within the final level of the trigger.

1 Introduction

The LHCb experiment [1] will make high precision studies of CP violation and other rare phenomena in B meson decays [2]. The experiment will run at the LHC at a nominal luminosity of $2.0 \times 10^{32} \text{ cm}^{-2}\text{s}^{-1}$ with proton-proton bunch-crossings at a rate of 40 MHz. The $b\bar{b}$ cross-section at the LHC energy is expected to be $\sim 500 \mu\text{b}$, this is $\sim 0.5\%$ of the total cross-section and a powerful trigger system is therefore required to select the small number of interesting signal events from the combinatoric background. This paper reports the trigger strategy employed to access the interesting $b\bar{b}$ events and reviews the trigger performance. Particular emphasis is given to the use of RICH data for fast hadron identification within the final level of the trigger.

2 Trigger Strategy

To meet LHCb's physics goals the trigger must be able to select not only the multitude of signal channels that will allow the experiment to over-constrain the unitarity triangle, but also the channels required for calibration, alignment and systematic studies. In addition, decay modes that allow the purity of the tagging of B flavour to be evaluated must be selected, as well as a set of unbiased control channels. Moreover, the system must be simple, robust and flexible.

In the lower levels of the trigger, LHCb's open geometry and excellent tracking capabilities allow B candidates to be selected with good efficiency using the high transverse momentum (p_T) and impact parameter (IP) characteristic of B decays. In the higher levels of the trigger the strategy employed is to select both 'hot' physics channels such as $B_s \rightarrow D_s h$, where h represents a hadron, by mimicing the offline selection in exclusive triggers; and also by selecting inclusive streams which look for signatures that generically indicate a B meson decay. In total 2 kHz of events will be written to storage. This rela-

Rate	Event type
200 Hz	Exclusive B candidates
600 Hz	Inclusive high mass di-muons
300 Hz	D^* candidates
900 Hz	Inclusive single-muon

Table 1. Composition of the output rate from the Trigger.

tively high rate can be afforded since the event size is relatively small ($\sim 25 \text{ kB}$). The exclusively selected streams will comprise 200 Hz of this with the remainder divided among a number of inclusive streams (Table 2).

As well as selecting directly important physics channels, the exclusive triggers will also provide 'self-tagging' data samples where the flavour of the B meson is known. By running the flavour tagging algorithms on such samples the purity of the tagging will be determined from the data.

Among the inclusive streams, the single muon stream will allow events to be selected in an unbiased way. By triggering events on a high p_T , high IP muon from one B decay, the decay of the other B produced in the proton-proton interaction is automatically recovered. This will allow trigger efficiencies to be determined. By selecting $B \rightarrow J/\Psi(\mu\mu)X$ decays the di-muon stream gives a sample with a sharp mass peak that is useful for checking the alignment and momentum scale calibration. This sample can be selected without lifetime bias, enabling the lifetime resolution to be computed from prompt J/Ψ events. The D^* stream will provide a sample where kaons and pions from $D^{*+} \rightarrow D(K^-\pi^+)\pi^+$ decays can be unambiguously separated. This will allow the particle identification to be calibrated with data. All of the inclusive streams will provide samples which can be 'mined' for B decays.

^a On behalf of the LHCb Collaboration

3 The three levels of the LHCb trigger

The 40 MHz bunch-crossing rate of the LHC will give visible interactions in LHCb at a rate of 10 MHz. This will be reduced to the 2 kHz that will be stored in three steps:

3.1 The Level-0 Trigger

A fully synchronous and pipe-lined first level trigger (Level-0) will be used to reduce the rate from 10 MHz to 1 MHz [3]. The Level-0 trigger is implemented in custom hardware and has a latency of $4\mu s$. It uses calorimeter and muon detector information to select events characteristic of B meson decays. The decision is based on the so-called ‘local’ variables : the two highest p_T muons in the muon chambers (reconstructed with a momentum resolution $\Delta p/p \sim 20\%$) and the highest transverse energy (E_T) γ , e , π^0 and hadron candidates; and the ‘global’ variables: the total E_T , vertex position, the number of tracks in the first and second vertex candidates and the charged multiplicity.

The variation of the rate with the muon p_T threshold is shown for the $B_s \rightarrow J/\Psi(\mu\mu)\phi(KK)$ signal channel and for minimum bias background events in Fig 1.

The Level-0 trigger efficiency is $\sim 50\%$ for hadronic channels, $\sim 90\%$ for muonic channels and $\sim 70\%$ for radiative channels. All efficiencies are cited for events selected by the final ‘offline’ selections for a given channel. The performance is shown for a number of signal channels in Fig 2(a). The Level-0 trigger enhances the $b\bar{b}$ content of the data from $\sim 1\%$ to $\sim 3\%$.

3.2 The Level-1 Trigger

The second and third levels of the LHCb trigger are software-triggers running on a farm of about 1600 CPU nodes [4]. The first level software trigger (Level-1) [3] uses information from the Silicon tracker located around the interaction point, the VERtEx LOCator (VELO) [5], part

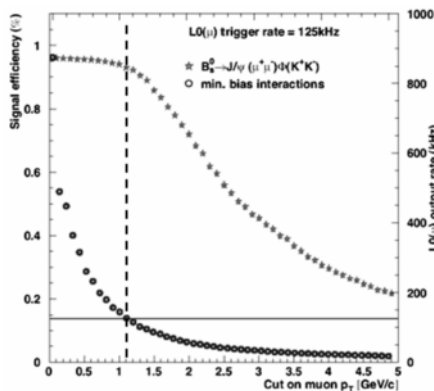


Fig. 1. The Level-0 $B_s \rightarrow J/\Psi(\mu\mu)\phi(KK)$ signal efficiency and minimum bias rate as a function of the cut on the muon p_T . The nominal cut used is indicated.

of the downstream silicon tracking detector and a summary from the preceding trigger level. The Level-1 trigger has an average latency of ~ 1 ms and outputs events at a rate of 40 kHz.

The LHCb VELO provides tracking information around the proton-proton interaction point. It consists of a series of radius, r , and azimuthal angle, ϕ , measuring silicon detector stations with retractable semi-circular sensors (Fig 3). The separation of r and ϕ sensors in this geometry is essential to the Level-1 trigger.

The Level-1 trigger reconstructs primary vertices and the impact parameters of tracks with respect to these vertices using information from the VELO. This is done first in two dimensions (r - z), using information from the radius measuring stations of the VELO detector, giving ~ 70 tracks. For the ~ 10 tracks which have $0.15\text{ mm} < \text{IP} < 3\text{ mm}$ or are matched to a Level-0 muon, the ϕ station information from the VELO is added, allowing full three dimensional track reconstruction.

In order to reject low momentum tracks that happen to have a high IP, a momentum estimate is obtained from the first Silicon tracking station downstream of the interaction region, the Trigger Tracker (TT) [6]. The TT allows the momentum to be reconstructed with a precision $\Delta p/p \sim 20 - 40\%$. For muons a momentum resolution of

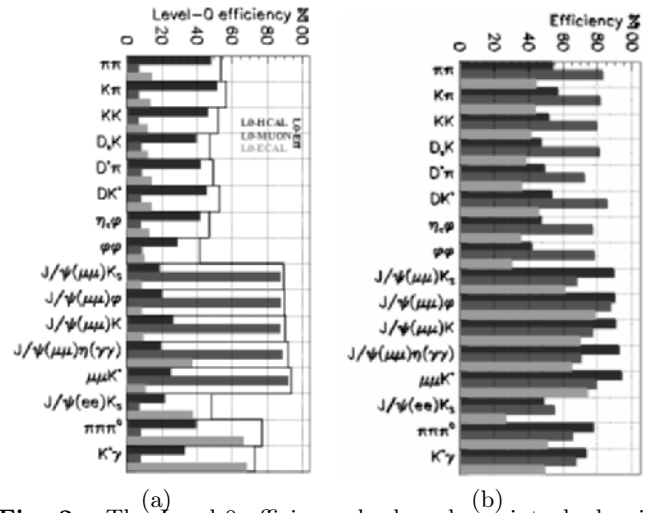


Fig. 2. The Level-0 efficiency broken down into hadronic, muonic and electromagnetic components (a). The Level-0, Level-1 and combined Level-0xLevel-1 trigger efficiencies (b).

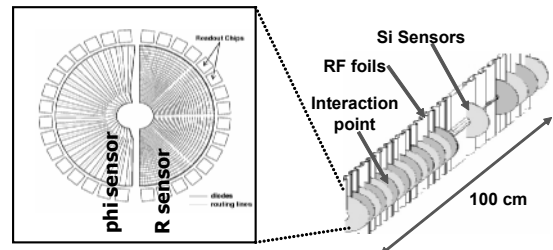


Fig. 3. Schematic of the Silicon sensors in the LHCb VELO detector.

$\Delta p/p \sim 5\%$ is achieved using the VELO and muon detector information.

Events are selected through any of a number of streams:

The generic line looks at the variable $\log(p_{T1}) + \log(p_{T2})$ where $p_{T1,2}$ are the transverse momenta of the two highest p_T tracks. The distribution of this quantity is shown for two signal channels and for the minimum bias background in Fig 4. The generic line gives good efficiency for a large number of signal channels and takes $\sim 75\%$ of the 40 kHz Level-1 output bandwidth.

A number of muon lines are used to select signal events. The single muon line searches for muons with $p_T > 2.3$ GeV and $IP > 0.15$ mm while the di-muon line selects events around the J/ψ invariant mass or with $m_{\mu\mu} > 0.5$ GeV and $IP > 0.05$ mm or with $m_{\mu\mu} > 2.5$ GeV. Together the muon lines take $\sim 6\%$ of the Level-1 bandwidth.

The remaining bandwidth is used for electron and photon lines that are used to select radiative events. These use a relaxed cut on the generic variable, as well as making a requirement on the calorimeter energy $E_{CAL} > 3.1$ GeV.

The Level-1 trigger takes the OR of these lines. The combined Level-0 and Level-1 trigger efficiencies are then $\sim 30\%$ for hadronic channels, $\sim 70\%$ for muonic channels and $\sim 40\%$ for radiative channels. The performance is shown for a number of signal channels in Fig 2(b). The $b\bar{b}$ content is enhanced from the $\sim 3\%$ output by the Level-0 trigger to $\sim 16\%$ after the Level-1 trigger.

3.3 The High Level Trigger

When an event is accepted by the Level-1 trigger the complete detector data are read out and fed into the second level software trigger called the ‘‘High Level Trigger’’ (HLT). This final trigger level has an average latency of ~ 10 ms and reduces the rate to the 2 kHz that is stored. The HLT uses the complete tracking information, allowing an improved version of the Level-1 algorithm to be run. This Level-1 confirmation takes 4 ms and reduces the accepted rate of events from 40 kHz to 10 kHz, thereby leaving 24 ms for further decisions to be made.

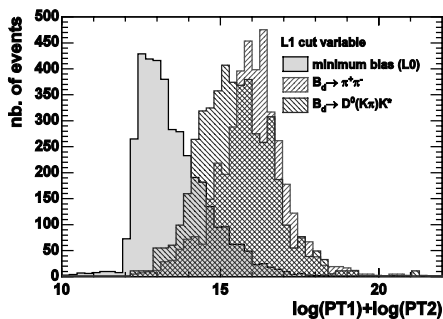


Fig. 4. The distribution of the Level-1 trigger generic stream variable $\log(p_{T1}) + \log(p_{T2})$ for signal and minimum bias events.

The inclusive streams outlined in section 2, single and di-muon and D^* decays, are selected with few additional requirements. Further events are selected by searching for complete decays exclusively and applying cuts mimicking the offline selection to control the minimum bias background. At the present time the exclusive HLT trigger is being tuned on ~ 10 channels that are representative of the LHCb physics programme. This will eventually be extended to include other channels. At present efficiencies of between 60 and 90% are achieved for ~ 15 Hz of minimum bias background per channel. In the HLT, mass resolutions are within a factor two of those obtained from the full offline reconstruction e.g. for the B_s and D_s masses in $B_s \rightarrow D_s h$ events, resolutions of 30 and 9 MeV respectively are obtained. To allow the background to be examined in mass sidebands, windows around the nominal B mass of > 500 MeV are used when selecting B candidates.

The $B_s \rightarrow \phi\phi$ channel, where both the ϕ 's decay into K^+K^- , has an HLT exclusive efficiency of $\sim 70\%$. While the selection cuts required to reject the minimum bias background keep 97% of the signal, efficiency is lost by requiring that all four tracks be found online. The difference between on- and off-line tracking, motivated by the need to be fast in the trigger, results in a small on-line tracking ‘inefficiency’ for the tracks used in the HLT, even when the tracks are reconstructed by the offline algorithm. This inefficiency can be recovered by triggering on these decays searching for only three of the four tracks i.e. searching for ‘‘ $B_s \rightarrow \phi(KK)K$ ’’. In order to cope with the substantial increase in the background that this creates, it is necessary to use particle identification information from LHCb’s Ring Imaging Cherenkov (RICH) detectors.

4 Using RICH information in the trigger

A system of mirrors is used in LHCb’s RICH detectors to get Cherenkov photons out of the experiments acceptance and focussed onto the Hybrid Photon Detectors (HPDs) used to detect the Cherenkov light [7]. In order to reconstruct a given photons Cherenkov angle, a quartic equation describing the optics must be solved [8]. The computation time required to do this is such that RICH particle identification information is not available in the HLT. In order to overcome this, a fast particle identification algorithm has been developed that parameterises the optical distortions [9]. This algorithm performs the RICH reconstruction fast enough such that pion/kaon separation can be made available in the HLT.

The $\phi\phi$ mass distribution is shown for $B_s \rightarrow \phi\phi$ candidates from both signal and minimum bias events in Fig 5. The ϕK mass distribution is shown in Fig 6. The omission of one of the kaons results in a broader distribution from the signal events which is not centred at the nominal B_s mass. The minimum bias events are shown with other selection cuts relaxed in order to improve the statistics. It can be seen that the RICH particle identification information allows the background to be reduced by an order of magnitude. Applying other selection requirements, this allows control of the minimum bias rate while making a

ϕK selection. The effect is to increase the efficiency from $0.97(\text{selection cuts}) \times 0.73(\text{online tracking}) = 0.71$ in the $\phi\phi$ case, to $0.93(\text{selection cuts}) \times 0.94(\text{online tracking}) = 0.87$ in the ϕK case.

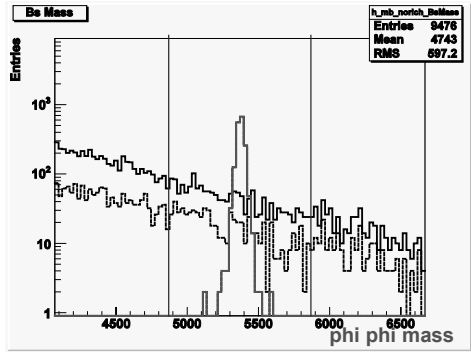


Fig. 5. The $\phi\phi$ invariant mass distribution for candidates from signal (red) and minimum bias (black) events in the HLT. The lower black line shows the minimum bias after RICH information is used to flag kaons.

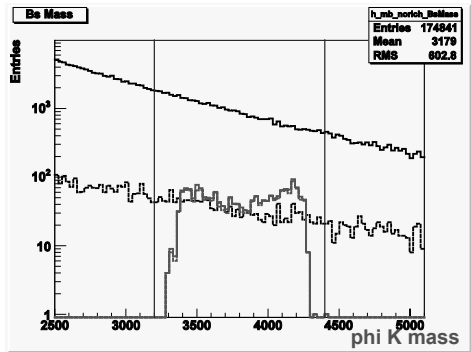


Fig. 6. The ϕK invariant mass distribution for candidates from signal (red) and minimum bias (black) events in the HLT. The lower black line shows the minimum bias after RICH information is used to flag kaons.

While there are four kaons in the final state in this example and hence the RICH information is used maximally, there are a number of other channels where substantial gains in the HLT trigger efficiency can be achieved. For example, in the exclusive selections, the efficiency for the channel $B_s \rightarrow D_s h$ can be increased from 60 to 70%. In addition, RICH information also allows an inclusive hadronic ϕ selection to be made in the HLT : this can be used to select a number of channels, including $B_s \rightarrow D_s(\phi\pi)h$ and $B_s \rightarrow \phi\phi$ with very good efficiency. This inclusive ϕ stream also allows the selection of channels such as $B_d \rightarrow \phi K_s$. The flight of the K_s makes online selection of its decay products in the large downstream tracking stations of LHCb problematic in the regular exclusive trigger. The full implications of the use of RICH information in the HLT are still being investigated, however, it is clear that

the availability of online particle identification gives significant additional discriminatory power. By using RICH information rather than harder cuts on less discriminating variables - such as p_T - significant gains in trigger performance can be realised.

5 Conclusion

LHCb will use a powerful three-level trigger system to select the rare CP-violating decays of B hadrons that will occur at the LHC. The trigger outputs data streams that include exclusively selected B decay modes but, in addition, inclusive modes that are rich in B decays. As well as being a significant source of physics data the latter will also provide samples for alignment and control channels to allow the trigger efficiencies to be determined.

The Level-0 trigger is hardware-based and searches for high p_T particles in the calorimeter and muon systems. It has a latency of $4 \mu\text{s}$ and an output rate of 1 MHz. The remaining two trigger levels are implemented in software and will be run on a large CPU farm. The Level-1 trigger uses VELO information to search for tracks with large impact parameter and also finds high p_T particles using the correlation with the Level-0 results or TT information. The Level-1 trigger has an average latency of about 1 ms and an output rate of 40 kHz. The final level of the trigger, the HLT, performs a full reconstruction of the event, allowing events of interest to be selected in a similar fashion to the offline selection. The HLT has an average latency of about 10 ms and will output the 2 kHz of events that will be stored. The use of a parameterisation of the optical distortions allows the RICH reconstruction to be made fast enough to make pion/kaon separation available in the HLT. This gives a powerful constraint to reject the minimum bias background and therefore allows other selection cuts to be relaxed. More inclusive selections are then possible, allowing significant gains in trigger efficiencies.

References

1. LHCb collaboration, LHCb technical proposal, no. 1998-004 in CERN/LHCC, CERN, Geneva, Switzerland, 1998.
2. LHCb collaboration, Reoptimized Detector Design and Performance, no. 2003-030 in CERN/LHCC, CERN, Geneva, Switzerland, 2003.
3. LHCb collaboration, Trigger System Technical Design Report, no. 2003-031 in CERN/LHCC, CERN, Geneva, Switzerland, 2003.
4. LHCb collaboration, Online System Technical Design Report, no. 2001-040 in CERN/LHCC, CERN, Geneva, Switzerland, 2001.
5. LHCb collaboration, Vertex Locator Technical Design Report, no. 2001-011 in CERN/LHCC, CERN, Geneva, Switzerland, 2001.
6. LHCb collaboration, Inner Tracker Technical Design Report, no. 2002-039 in CERN/LHCC, CERN, Geneva, Switzerland, 2002.

7. M.Moritz *et al.*, *Performance Study of New Pixel HPD Prototypes for the LHCb RICH*, Nucl.Instrum.Meth.A442,164-170,2000
8. R. Forty, O. Schneider, RICH Pattern Recognition, Tech. Rep. LHCb-98-040, CERN (1998).
9. R. Forty, C. Jones and M. Patel RICH RICH Particle Identification for the High Level Trigger, LHCb-2005-052, CERN (2005).

Event reconstruction and physics performance of the LHCb experiment

Yuehong Xie (on behalf of the LHCb Collaboration)

University of Edinburgh, JCMB, the King's Buildings, Mayfield Road, Edinburgh EH9 3JZ

Abstract. The LHCb detector and software performance for event reconstruction is summarised. Physics sensitivity in typical channels for study of B_s mixing, CP violation and rare B decays is presented.

1 Introduction

At the LHCb interaction point 10^{12} B hadron events per 10^7 seconds (a nominal year) will be produced in pp collisions with a luminosity of $2 \times 10^{32} \text{ cm}^{-2} \text{ s}^{-1}$. This provides a great opportunity to look for new physics in neutral B meson mixing, CP violation and rare B decays. Study of both, B meson mixing and time-dependant CP violation, needs three key elements in the event reconstruction: the exclusive signal reconstruction, the proper time-determination and the flavour tagging of the B meson. Exclusive B meson reconstruction requires good mass resolution, which needs precise momentum resolution for momenta up to $100 \text{ GeV}/c$. In order to resolve the B_s oscillation, which is at least 30 times faster than B_d oscillation, an excellent proper time resolution of about 40 fs is required. therefore a very precise vertex reconstruction is needed. Efficient particle identification capability in the momentum range 2-100 GeV/c is required for flavour tagging of events containing B hadrons and for background rejection.

The LHCb detector is optimized to achieve its physics goals [1]. Section 2 describes the performance of tracking, vertexing, particle identification and flavour tagging obtained from a full simulation. Section 3 illustrates the expected sensitivities in B_s mixing, in measurements of the unitary angles and in studies of rare B meson decays. Most results are extracted from reference [1].

2 Event reconstruction performance

The LHCb spectrometer comprises a beam pipe, a Vertex Locator (VELO), a tracking system with a dipole magnet, two Ring Imaging Cherenkov detectors (RICH1 and RICH2), an electromagnetic and a hadronic calorimeter and a muon system (Fig. 1). For a detailed description of each detector, see the corresponding Technical Design Report, respectively [1] [2] [3] [4] [5] [6] [7] [8].

2.1 Tracking

The following detectors are used in measuring charged tracks: VELO, Trigger Tracker, Inner and Outer Tracker. A dipole magnet analyses the track momenta. The aim is to reconstruct all types of tracks that leave sufficient detector hits. The most important tracks for physics analyses are the long tracks, which traverse the full tracking setup. In Fig. 2 we show the performance of the long track finding reconstruction. For tracks with a momentum higher than $10 \text{ GeV}/c$ the average efficiency is 94%. The effective ghost rate for tracks with a transverse momentum $p_T > 0.5 \text{ GeV}/c$ is approximately 3%. In Fig. 3 (a), we show that the track momentum resolution degrades from $\delta p/p = 0.35\%$ at low momentum to $\delta p/p = 0.55\%$ at $140 \text{ GeV}/c$. In Fig. 3 (b) the track impact parameter resolution is plotted as a function of $1/p_T$. The linear dependence can be parameterized as $\sigma_{\text{IP}} = 14 \mu\text{m} + 35 \mu\text{m}/p_T$ where p_T is in GeV/c . In Fig. 4 we show the reconstructed B_s mass distribution for $B_s \rightarrow D_s K$ events. The mass resolution is approximately $14 \text{ MeV}/c^2$.

2.2 Vertexing and proper time resolution

The proper time of a B hadron decay is determined from the distance between its production and decay vertex and from its momentum. In LHCb, the primary vertex precision is much better than that of the decay vertex. Using a double Gaussian fit to the residual z-vertex distribution the core z-resolution on a primary vertex is measured to be $44 \mu\text{m}$, with 25% events in the second Gaussian, which is 2 to 3 times wider. A resolution of $168 \mu\text{m}$ is obtained for the $B_s \rightarrow D_s K$ decay vertex using a single Gaussian fit. Therefore, the proper time resolution is dominated by the resolution on the B decay vertex. The proper time resolution for $B_s \rightarrow D_s K$ signal events is shown in Fig. 5. Using a double Gaussian fit the core resolution is measured to be 33 fs. The second Gaussian accounting for 31% of the events has a width of 67 fs.

Table 1. Tagging power

Tag	B_d	B_s
μ	1.2%	1.4%
e	0.6%	0.6%
K opposite-side	2.1%	2.4%
Jet/Vertex charge	0.7%	0.8%
K/π same-side	0.7%(π)	3.1%(K)
Combined	4.4%	7.5%

2.3 Particle identification

The RICH detectors provide excellent K/π separation. The average kaon identification efficiency for momenta between 2 and 100 GeV/ c is 88% with a $\pi \rightarrow K$ misidentification rate of 3%. A display of detected photoelectrons for a typical event in RICH1 is shown in Fig. 6.

Electron and muon identification are mainly provided by the electromagnetic calorimeter and the muon system, respectively. The RICH detectors also add some separation between leptons and hadrons. Using the technique of a combined likelihood, an average efficiency of about 94% is achieved for both muons and electrons above a few GeV/ c with a 1% pion misidentification rate. More details about the current status of the particle identification can be found in reference [9].

2.4 Flavour tagging

The identification of the initial b -quark charge - the flavour - of a reconstructed B hadron decay is performed using opposite-side and same-side tagging algorithms. Opposite-side tagging uses the charge of leptons from a semileptonic decay or a kaon from a $b \rightarrow c \rightarrow s$ decay or the charge of all particles in a jet or at a vertex to determine the flavour of the accompanying B. Same-side tagging uses the charge of fragmentation particles which are correlated in phase space with the signal B meson to determine its flavour.

Table 1 lists the tagging power of each tagging category and the combined tagging power for B_d and B_s mesons. Within errors, the opposite-side tagging performance for a B_d meson is consistent with that of a B_s meson.

3 Physics sensitivity

3.1 Physics program

A main physics goal of the LHCb experiment is to search for new physics in the flavour sector. The huge statistics of B events, particularly of B_s events, provides a unique opportunity for LHCb to make indirect searches for new physics in three aspects: new particles contributing to B_s mixing, new CP violating phases in B_s mixing and other B meson decays and new particle contributions to very rare processes in the Standard Model. In Section 3.2, 3.3 and 3.4 selected channels are used to demonstrate the

sensitivity of the LHCb experiment to B_s mixing measurements, unitary angle measurements and rare B decay measurements.

3.2 B_s mixing

B_s mixing is a probe of new physics. New physics contributions to the box diagrams could significantly increase Δm_s from its Standard Model prediction of $\Delta m_s = (14.3 - 26.0) ps^{-1}$ [10]. The mixing phase ϕ_s , which is predicted to be ~ -0.04 in the Standard Model, is also sensitive to new weak phases in box diagrams.

The decay $B_s \rightarrow D_s \pi$ is the gold-plated channel to measure Δm_s . Annually, LHCb is expected to reconstruct 80k $B_s \rightarrow D_s \pi$ events. The estimated background to signal ratio (B/S) in a 100 MeV/ c^2 window is around 0.32. The proper time resolution for this mode is about 40 fs. The amplitude fit method is employed to assess the sensitivity to Δm_s . The performance is shown in Fig. 8. With LHCb we will be able to observe B_s oscillation in one year with 5σ statistical significance for Δm_s values up to 68 ps^{-1} . This extends well above the current Standard Model prediction. Once oscillation is observed, Δm_s can be measured to a precision of $\sigma(\Delta m_s) = 0.01 ps^{-1}$.

The decay $B_s \rightarrow J/\psi \phi$ is the gold-plated channel to measure the B_s mixing phase ϕ_s [11] and the B decay width difference $\Delta \Gamma_s$. In one year, LHCb will reconstruct 120k $B_s \rightarrow J/\psi \phi$ events with $B/S < 1$. The proper time resolution in this mode is about 35 fs. Using a maximum likelihood method to fit the proper time and the transversity angle distributions, the one-year sensitivity is measured to be $\sigma(\phi_s) = 0.06$ and $\sigma(\Delta \Gamma_s/\Gamma_s) = 0.018$. A similar sensitivity for $\sigma(\Delta \Gamma_s/\Gamma_s)$ can be achieved using untagged events. The CP eigenstate decay modes $B_s \rightarrow J/\psi \eta$ and $B_s \rightarrow \eta_c \phi$ are also studied and a comparable performance is obtained.

3.3 Unitary angles

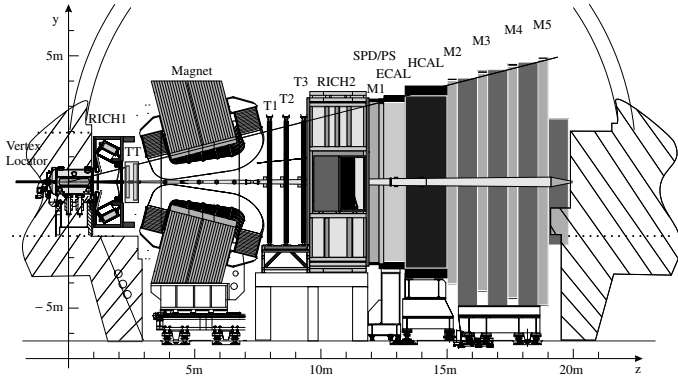
In order to over-constrain the Unitary Triangle, LHCb will measure the unitary angles γ, α, β in different processes which may be affected differently by new physics.

Three methods to measure the angle γ have been studied: using the gold-plated decay mode $B_s \rightarrow D_s K$ [12]; using the decay modes $B_s \rightarrow K^+ K^-$ and $B_d \rightarrow \pi^+ \pi^-$ [13]; and using $B_d \rightarrow \bar{D}^0(D^0) K^{*0}$ [14]. In one year, 5.4k $B_s \rightarrow D_s K$ events will be reconstructed by LHCb with a $B/S < 1$. The angle $\gamma + \phi_s$ will be measured using the four time-dependent tree level decays of the B_s and \bar{B}_s meson into the $D_s^+ K^-$ and $D_s^- K^+$ final states. The mixing phase ϕ_s is taken from $B_s \rightarrow J/\psi \phi$. Therefore the measured γ is not affected by new physics in mixing. The one-year sensitivity is summarised in Table 2.

In one year, 26k $B_d \rightarrow \pi^+ \pi^-$ events and 37k $B_s \rightarrow K^+ K^-$ events will be reconstructed with $B/S < 0.7$ and $B/S = 0.3$, respectively. Using U-spin symmetry, the CP angle γ can be determined from the time-dependent asymmetries in the two decay processes. A statistical precision

Table 2. one-year γ sensitivity with $B_s \rightarrow D_s K$.

Δm_s	$20ps^{-1}$	$25ps^{-1}$	$30ps^{-1}$
$\sigma(\gamma)$	14.2°	16.2°	18.3°

**Fig. 1.** LHCb detector layout.

of about 5° can be obtained. Fig. 7 shows the expected confidence regions in the (d, γ) plane using one year of data, where d is a hadronic parameter describing the ratio of penguin to tree contribution in these two decay modes. Using U-spin symmetry d is assumed to be the same in the two processes. Despite the systematic uncertainty from U-spin symmetry breaking, this measurement is sensitive to new physics contributions to penguin diagrams.

About 3400 $B_d \rightarrow \bar{D}^0(K^-\pi^+)K^{*0}$ events, 500 $B_d \rightarrow D^0(K^+\pi^-)K^{*0}$ event, 600 $B_d \rightarrow D_{CP}^0(K^-K^+)K^{*0}$ events will be reconstructed per year, all with $B/S < 2$. Using the six time-integrated tree-level rates the angle γ can be measured to a statistical precision of about 8° .

The sensitivity for an α measurement using the decay $B_d \rightarrow \rho\pi$ has been studied. 14k events will be reconstructed per year with $B/S = 0.80$. Using a time-dependent Dalitz fit method [15], the angle α can be determined to a precision of better than 10° using one year of data. Further work on the α determination from $B \rightarrow \rho\rho$ is ongoing.

3.4 Rare B decays

Flavour changing neutral current transitions, $b \rightarrow s$ and $b \rightarrow d$, occur with a very low probability in the Standard Model, but can be significantly enhanced in new physics models like SUSY [16]. This provides a probe of new particles virtually participating in rare decays. Several rare decays have been studied in LHCb. For the channel $B_s \rightarrow \mu^+\mu^-$, 17 events per year are expected assuming the Standard Model branching ratio $Br(B_s \rightarrow \mu^+\mu^-) = (3.5 \pm 1.0) \times 10^{-9}$. The present limit on background level estimated from B hadrons decaying semileptonically is $B/S < 5.7$ at 90% confidence level. The LHCb experiment will be able to observe clear signals of rare B decays and study possible new physics effects.

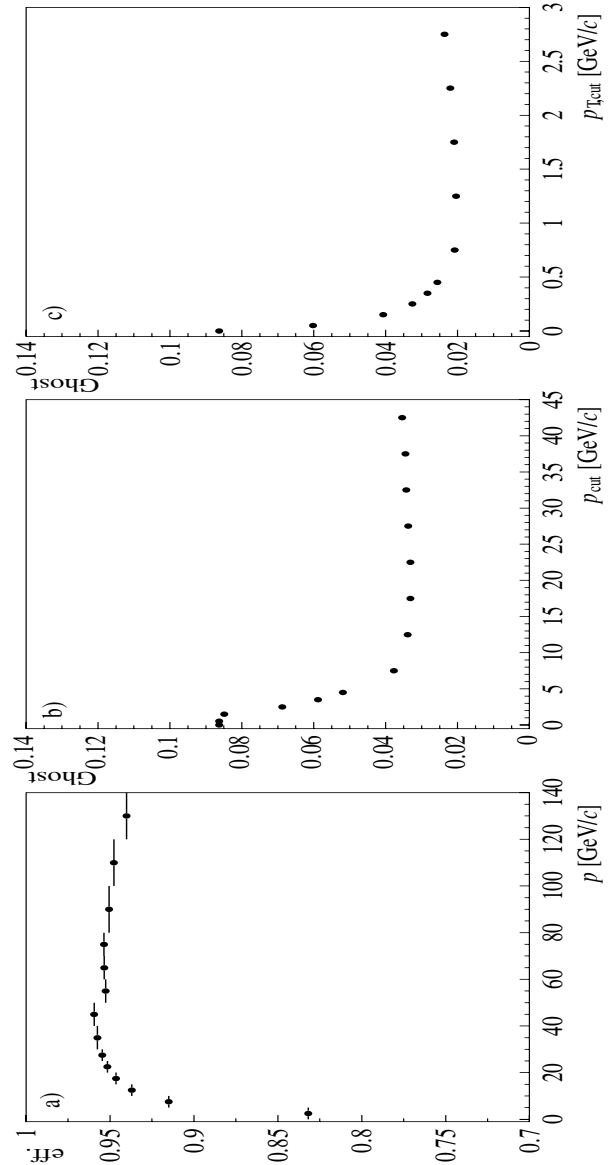


Fig. 2. Performance of the long track finding reconstruction: (a) efficiency as a function of the momentum of the generated particle; (b) ghost rate, for tracks with reconstructed momentum greater than p_{cut} ; (c) ghost rate, for tracks with reconstructed transverse momentum greater than $p_{T,\text{cut}}$.

4 Conclusion

Based on a large simulation of the LHCb detector, we conclude that the LHCb experiment and software can efficiently reconstruct many different B decay modes with a very good performance in proper time resolution, particle identification, mass resolution and flavour tagging. This will enable the LHCb experiment to fully explore B_s mixing, to extract CKM parameters using various methods with high precision and to perform studies of rare B decays. The LHCb experiment will have a great opportunity to make precision tests of the Standard Model in the flavour sector in order to find new physics or push possi-

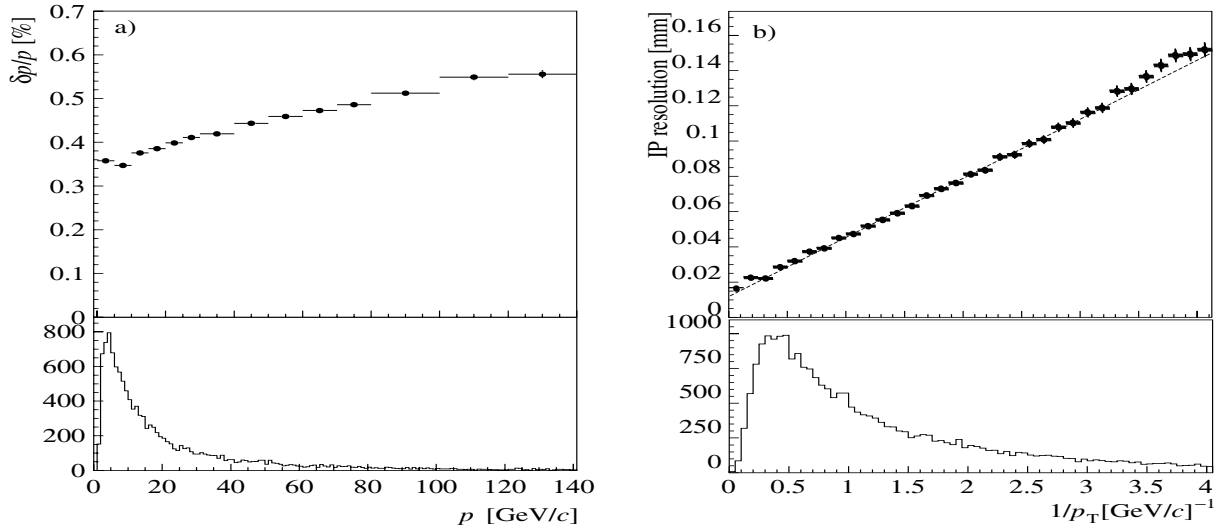


Fig. 3. Track parameter resolution at production vertex: (a) momentum resolution as a function of track momentum; (b) impact parameter resolution as function of $1/p_T$.

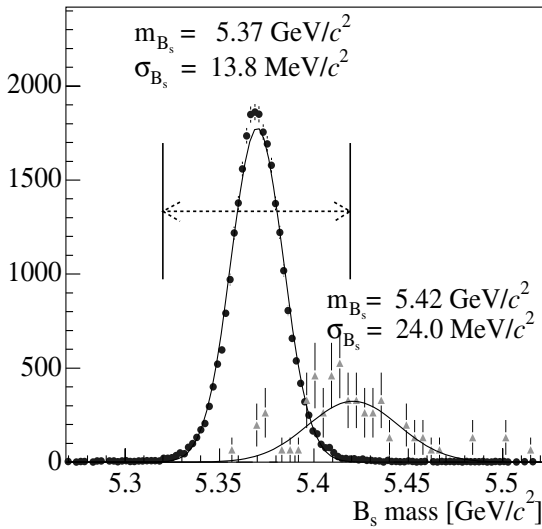


Fig. 4. Mass distribution for $B_s \rightarrow D_s K$ events (filled circles). Misidentified $B_s \rightarrow D_s \pi$ events normalized to their branching ratios are shown as triangles.

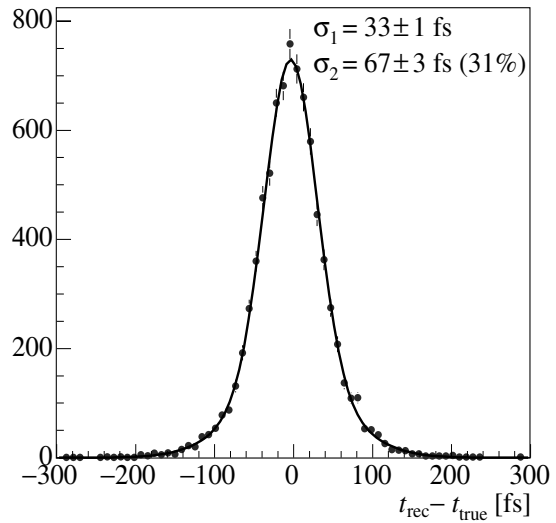


Fig. 5. Proper time resolution for the decay $B_s \rightarrow D_s K$.

ble new physics to a higher mass scale. LHCb needs to be ready on the first day of data taking.

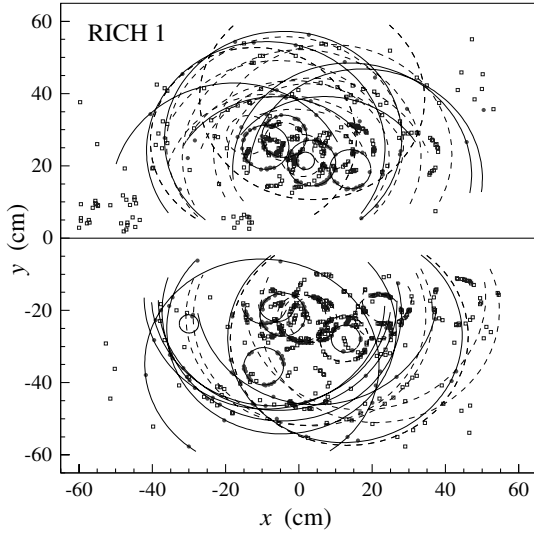


Fig. 6. Display of the detected photoelectrons for a typical event in RICH1. Fitted rings are superimposed, indicated by solid lines for rings from long tracks and dashed lines for other tracks.

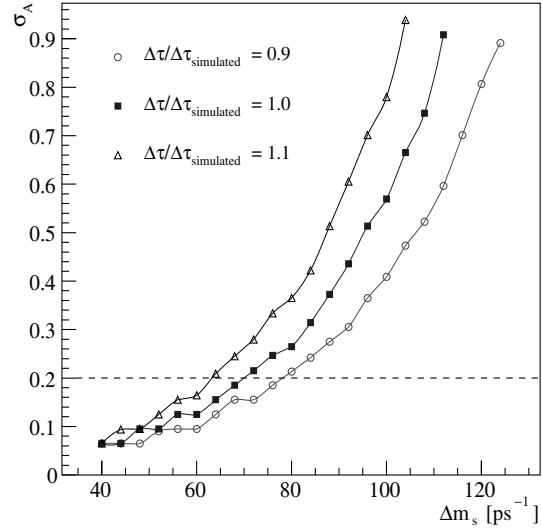


Fig. 8. Statistical uncertainty on the B_s oscillation amplitude A as a function of Δm_s using one year of $B_s \rightarrow D_s \pi$ data. Also shown are σ_A when the decay time resolution is varied by $\pm 10\%$. The dashed line at $\sigma_A = 1/5$ corresponds to an observation of B_s oscillation with a 5σ statistical significance.

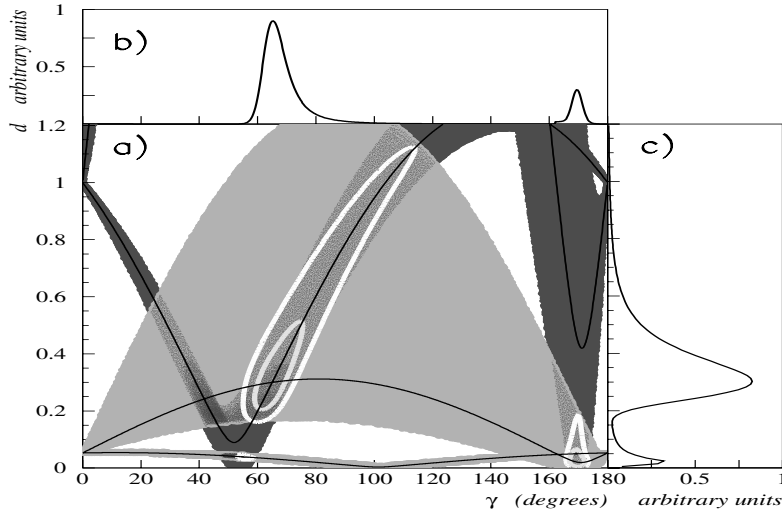


Fig. 7. Confidence regions in the (d, γ) plane for one year of $B_s \rightarrow K^+ K^-$ and $B_d \rightarrow \pi^+ \pi^-$ data: The light (dark) shaded areas are the 95% confidence regions for $B_s \rightarrow K^+ K^-$ ($B_d \rightarrow \pi^+ \pi^-$) and the white lines enclose the 90% and 95% overlap regions. Projections onto the d and γ axes are also shown.

References

1. LHCb Collaboration, *LHCb Reoptimized Detector Design and Performance* (CERN-LHCC-2003-030)
2. LHCb Collaboration, *LHCb Velo Technical Design Report* (CERN-LHCC-2001-011)
3. LHCb Collaboration, *LHCb Magnet Technical Design Report* (CERN-LHCC-2000-007)
4. LHCb Collaboration, *LHCb Inner Tracker Technical Design Report* (CERN-LHCC-2002-029)
5. LHCb Collaboration, *LHCb Outer Tracker Technical Design Report* (CERN-LHCC-2001-024)
6. LHCb Collaboration, *LHCb RICH Technical Design Report* (CERN-LHCC-2000-037)
7. LHCb Collaboration, *LHCb Calorimeters Technical Design Report* (CERN-LHCC-2000-036)
8. LHCb Collaboration, *LHCb Muon Technical Design Report* (CERN-LHCC-2001-010)
9. Ann Van Lysebetten, these proceedings.
10. P. Ball *et al.*, *B decays at the LHC*, (CERN 2000-4), arXiv: hep-ph/0003238
11. A. S. Dighe, I. Dunietz and R. Fleischer, *Eur. Phys. J.* **C6**, (1999), 647
12. R. Aleksan, I. Dunietz and B. Kayser, *Z. Phys.* **C54**, (1992) 653.
13. R. Fleischer, *Phys.Lett.* **B459**, (1999) 306.
14. M. Gronau and D. Wyler, *Phys.Lett.* **B265**, (1991) 172.
15. A. Snyder and H.R. Quinn, *Phys.Rev.* **D48**, (1993) 2139.
16. R. Arnowitt *et al.*, *Phys Lett.* **B538** (2002) 121.

B-Physics expectations at ATLAS and CMS

On behalf of the ATLAS and CMS Collaborations

Petridou Chariclia¹

Aristotle University of Thessaloniki

Abstract. The capabilities of the two general purpose experiments ATLAS and CMS to exploit the copious production of $b\bar{b}$ pairs at the Large Hadron Collider at CERN is presented. The strategy that the two experiments will follow in order to fully tackle b-physics issues, especially questions concerning b-trigger and b-tagging techniques is given. Finally b-physics topics where the two experiments can be competitive and in some cases complementary LHC-b as well as their sensitivity to New Physics is described.

1 Introduction

The decays of b-flavoured hadrons offer a very fertile testing ground of the Standard Model description of the electroweak interactions. Although a remarkable progress has been made at the B-factories in measuring the parameters of the unitarity triangle [1], the study of the b-hadron decays at the Large Hadron Collider (LHC), provides a window to look for New Physics (NP). The large $b\bar{b}$ production cross section at LHC, makes B-Physics an appealing topic for the two general purpose experiments, ATLAS and CMS. At the design luminosity of $10^{34} \text{ cm}^{-2} \text{ sec}^{-1}$, about 10^6 $b\bar{b}$ pairs/s are produced at 14TeV center-of-mass energy in pp collisions at LHC. Already at startup of LHC, B-Physics studies can be carried by both experiments.

ATLAS and CMS can detect B-hadrons, with transverse momentum $p_T > 6\text{GeV}$, which are produced centrally in a pseudorapidity region between -2 and 2, contrary to the LHCb, which is a forward detector and covers a pseudorapidity region between 2 and 4 and can detect B-hadrons with $p_T > 2\text{GeV}$. Although the geometrical acceptance of ATLAS and CMS results in a reduction of about a factor of 2 in measured cross section compared to LHCb, their complementarity in the searches of exclusive B-decays through leptonic and semileptonic channels, even at high luminosities is unquestionable.

In the present paper we concentrate on measurements of the B_s mixing parameters and exclusive rare B-hadron decays. In section 2 the general strategy and approach to B-physics of the two experiments are given, in section 3 the detector performance on impact parameter and meson/baryon mass reconstruction. In section 4 the expectations on the measurement of the B_s mixing parameters and possible indications for NP, in section 5 the ATLAS and CMS sensitivity to rare B-hadron decays and in section 6 the summary are presented.

2 The strategy of ATLAS and CMS on B-Physics

ATLAS [2] and CMS [3] order to maintain a low trigger rate (a total rate of $< 100\text{Hz}$ has to be maintained), do not foresee any dedicated b-trigger. Both experiments have chosen to use only the multileptonic and photon decay channels of the B-hadrons and keep the contribution to the trigger rate from b-physics events to about 10Hz . Such channels are sensitive to NP. To reduce trigger rates, preference is given to exclusive channels and the reconstruction of the b-hadron mass and its decay length is done online. b-tagging techniques are used for flavor identification in order to perform $B-\bar{B}$ mixing measurements and $b\bar{b}$ correlations.

2.1 B-Physics trigger in ATLAS and CMS

ATLAS and CMS have as primary goal to explore the high p_T region. At LHC most of the QCD produced b quarks have small transverse momentum (p_T). The trigger concept in both experiments comprises of combinations of electron (e), muon (μ), photon (γ), jet and missing transverse energy 'objects' above a p_T threshold. Events resulting from the decay of B-hadrons may have either or all of the e, γ , μ and jet 'objects'. The trigger systems differ in the two experiments. ATLAS has three levels in decision making [4] while CMS has a first level and a High Level trigger (HLT) [6]. At the first level a decision is taken on the bases of the coarse information of the calorimeters and the muon detector for the existence of e, γ , μ or jet objects. In ATLAS at this point the Region of Interest (RoI) is built -the η, ϕ location of the 'object' and transmitted at the Level-2. Level-2 uses the RoI seeds to selectively access data with full granularity and does a fast processing or rejection of the event. The decision time is a few msecs. The third level -Event Filter (EF) refines the selection

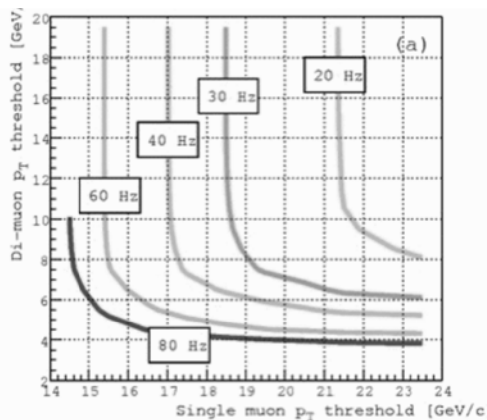


Fig. 1. CMS detector: Cumulative muon trigger rates in Hz at the HLT as a function of single muon and di-muon thresholds in p_T

'seeded' by the level-2 RoI's and accepts the event after analysis with offline-like algorithms and using calibration and alignment data. Level-2 and EF consist the HLT for ATLAS.

In CMS level-2 and level-3 are merged into the HLT. the full information of the events that are accepted at Level-1 -approximate rate 100 kHz- are distributed to a farm of processors to be analyzed with offline like algorithms and to be reduced, in about 1sec, to the desirable rate of 100Hz. Because of the large background, the rate at the Level-1 trigger is dominated by 'electron/photon-objects'. Therefore b-hadron inclusive decays to electrons are swamped by background, while b-quark to muons are not. As an example single muon rates with $p_T > 6\text{GeV}$ is about 20 kHz at level-1 trigger. In Figure 1 are presented the necessary thresholds, for the CMS experiment, for single muon and di-muon events, at the High Level Trigger (HLT), in order to maintain the desired trigger rate. From the figure becomes evident that in order to maintain efficient selection of B-hadrons it is necessary to concentrate on exclusive b-decays. The events should then be selected, at the HLT on the basis of the reconstructed mass and the decay distance. Quite often it will be sufficient to reconstruct at HLT the mass of a J/ψ from its decay to two muons into an η, ϕ region of the detector, declared as Region of Interest (RoI). For this it is necessary to have at the level-1 trigger a single muon with $p_T > 6\text{GeV}$, while at HLT it is required a second muon with the mass constraint of the J/ψ (see Sect. 2).

2.2 B-hadron tagging

In order to measure $B^0-\bar{B}^0$ mixing, algorithms for the tagging of the b-quark flavor have to be used. To this end the charge of the same or opposite side muon or electron it is used, or the charge of the same or opposite side jet. For the method used the tagging efficiency and the dilution factor have to be estimated each time using monte

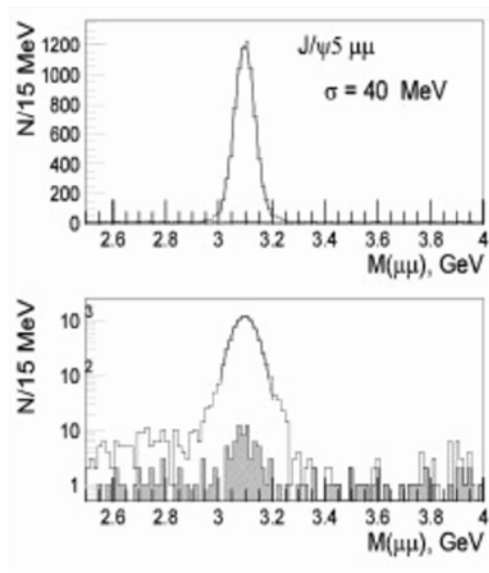


Fig. 2. Offline $J/\psi \rightarrow \mu\mu$ mass reconstruction for ATLAS, in linear and logarithmic scales (upper and lower plots respectively). For the muon reconstruction both the muon precision chambers and the inner detector were used.

carlo data. The dilution factor D_{Tag} because of the tagging method used is: $D_{Tag} = 1 - 2w$ where w is the rate of the wrong tags. If ϵ_{Tag} is the tagging efficiency of the method, the overall tag quality factor is: $\epsilon_{Tag} D_{Tag}$. For example in the case of $B_d \rightarrow J/\psi K_s$ the tag efficiency using same side jet charge is $\epsilon_{Tag} = 0.64$ and the wrong tag probability $w = 0.42$, while using opposite side electron or muon $\epsilon_{Tag(electron)} = 0.012$, $w_{Tag(electron)} = 0.27$ and $\epsilon_{Tag(muon)} = 0.025$, $w_{Tag(muon)} = 0.24$ respectively.

3 Detector performance

Since there is no dedicated B-trigger, the selection of B-hadron candidates, for both experiments, rely heavily on the performance of the detector in the key parameters on which the B-triggers are based. Such parameters are invariant masses of either B-mesons and B-baryons, like B_s or B_d and Λ_b exclusive decays, or their decay products like J/ψ mass reconstruction. Figure 2 shows the $J/\psi \rightarrow \mu\mu$ mass reconstruction for ATLAS, using the offline algorithm, in linear and logarithmic scales (upper and lower plots respectively). For the muon reconstruction both the muon precision chambers and the inner detector were used. Another parameter is the proper time reconstruction of the decay by measuring the impact parameter of the B-hadron candidate. The proper time resolution for the latest (final) layout of ATLAS is 100 fsec for some representative B-decays: $B_s \rightarrow D_s \pi$, $B_s \rightarrow J/\psi(\mu\mu)\phi$, $B \rightarrow \mu\mu$. The worsening of the proper time resolution will mainly affect B-hadrons with p_T below 7GeV. One of the main source of backgrounds in identifying b-events which inclusively decay to one electron and a

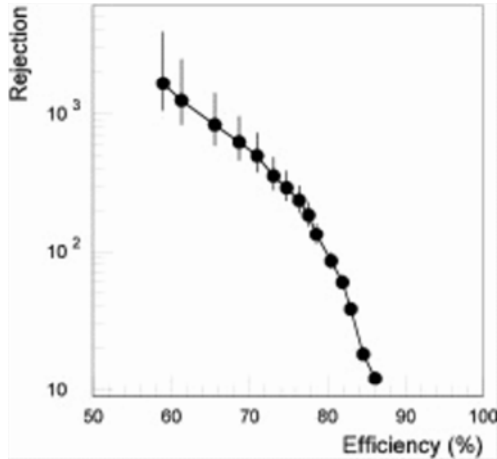


Fig. 3. Rejection factor of the $b\bar{b} \rightarrow \mu(> 6\text{GeV})X$ events without electron as a function of the efficiency to select $b\bar{b} \rightarrow \mu(> 6\text{GeV})e(> 5\text{GeV})$ events in ATLAS, using the combined information of the electromagnetic calorimeter and the TRT for the identification of the electron.

muon : $b\bar{b} \rightarrow \mu(> 6\text{GeV})e(> 5\text{GeV})$ is hadrons misidentified as electrons from decays $b\bar{b} \rightarrow \mu(> 6\text{GeV})X$. To reject them the combined information of the electromagnetic calorimeter and the Transition Radiation Tracker (TRT) is used in ATLAS. Figure 3 gives the rejection of $b\bar{b} \rightarrow \mu(> 6\text{GeV})X$ as a function of the efficiency to identify $b\bar{b} \rightarrow \mu(> 6\text{GeV})e(> 5\text{GeV})$ decays. A rejection factor of over 500 is achieved for an efficiency of 0.70

4 Measurement of the B_s mixing parameters

The mixing of the B_s and \bar{B}_s mesons in the Standard Model (SM) of the electroweak interaction take place via box diagrams. The mass difference ΔM_s and their difference in the decay rates $\Delta\Gamma_s$ of the two physical eigenstates can be both calculated in the SM and measured experimentally. The oscillation frequency χ_s is then given by : $\chi_s = \Delta M_s/\Gamma_s$. The mixing phase ϕ_s arises from the interference of mixing and decaying amplitudes can also be determined experimentally. The latter, expressed in terms of the Wolfenstein parameters λ, η is: $\phi_s = -2\lambda^2\eta$. This parameter is small in the SM and is highly sensitive to SUSY contributions.

4.1 CP Violation in the $B_s \rightarrow J/\psi\phi$ and New Physics

The $B_s \rightarrow J/\psi\phi$ decay leads to three final state helicity configurations and their linear combinations are CP eigenstates [7]. This decay has the advantage that the helicity amplitudes can be separated. The experimental observables are the three independent angles of the decay products and the B_s proper time of the decay :

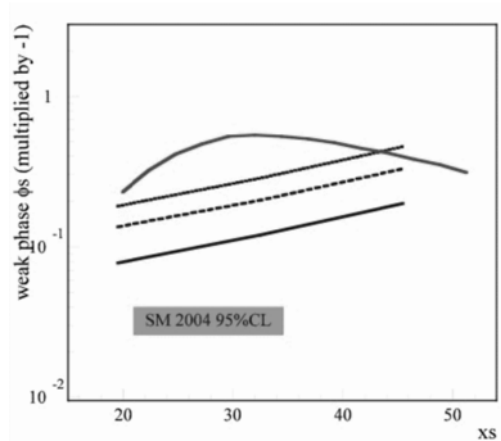


Fig. 4. Figure 4. Sensitivity of ATLAS and CMS to the weak mixing phase ϕ_s as a function of χ_s , for 5, 10 and 30 fb^{-1} , upper, middle and lower curves respectively. In red the prediction of the SUSY model by Ball and Khalil.

$B_s \rightarrow J/\psi\phi \rightarrow \mu^+\mu^-K^+K^-$. From the parametrization of the decay the three transversity amplitudes the three B_s mixing parameters : $\Gamma_s, \Delta\Gamma_s$ and ΔM_s , as well as the weak mixing phase ϕ_s can be extracted from the data. The differences in the decay rates, $\Delta\Gamma_s, \Gamma_s$, and ϕ_s along with the two helicity amplitudes and their strong phases were simultaneously determined. In Figure 4 the sensitivity for ATLAS and CMS in the measurement of the weak phase ϕ_s is shown as a function of the oscillation frequency χ_s for three different integrated luminosities : 5 (upper), 10 (middle) and 30 (lower) fb^{-1} . The red curve represents prediction of a SUSY model [8]. Note that the SM value is lower than the experimental sensitivity at 30 fb^{-1} .

4.2 Measurement of ΔM_s in the $B_s\bar{B}_s$ system

From the decay $B_s \rightarrow D_s\pi$ the probability that an initially pure B_s sample will be observed as \bar{B}_s and the one that the sample will remain as B_s are described in terms of $\Gamma_s, \Delta\Gamma_s$ and ΔM_s . From the ratio of the two probabilities ΔM_s can be derived. The ATLAS performance parameters for the $B_s \rightarrow D_s\pi$ process and the background were determined by detector simulations and the corresponding parameters were used as input to a fit in repeated Monte Carlo experiments. Already with 10 fb^{-1} integrated luminosity the ATLAS and CMS sensitivity will reach the SM upper bound which is 25 ps^{-1} .

5 Rare Decays, prospects for ATLAS and CMS

Flavor changing neutral current decays involving $b \rightarrow s$ and $b \rightarrow d$ transitions occur only at loop level in the SM. The branching ratios for these decays are therefore small,

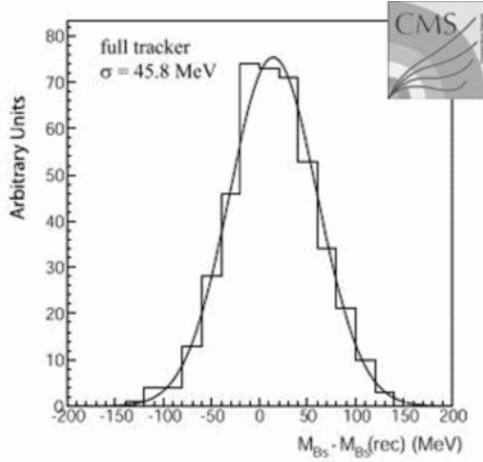


Fig. 5. Figure 5 Difference of the generated and reconstructed invariant mass of the $B_s \rightarrow \mu^+\mu^-$ for CMS using the full tracker reconstruction for the muons.

$Br < O(10^{-5})$ and thus they provide an excellent probe for new physics effects. In the SM these decays are sensitive to the CKM matrix elements $|V_{ts}|$, $|V_{td}|$. The B factories and the Tevatron can access some of these decays like $B \rightarrow K^*\gamma$ which can be accurately measured by the time LHC starts. Also the decay $B \rightarrow K^*\mu^+\mu^-$ can be seen, however the mass and angular distribution of the decay can only be studied at LHC. The current experimental limits on purely muonic decays from CDF and BELLE are two and three orders of magnitude below the SM predictions [9]. The following exclusive decays can be accessed at LHC by ATLAS and CMS :

Very rare and purely muonic decays : $B_s \rightarrow \mu^+\mu^-$, $B_d \rightarrow \mu^+\mu^-$

Di-muonic decays : $B_d \rightarrow K^*\mu^+\mu^-$, $B_s \rightarrow \phi\mu^+\mu^-$, $\Lambda_b \rightarrow \Lambda\mu^+\mu^-$

Radiative decays : $B_s \rightarrow \phi\gamma$, $B_d \rightarrow K^*\gamma$

Figure 5 shows the accuracy in the invariant mass reconstruction of $B_s \rightarrow \mu^+\mu^-$ for CMS using the full tracker information. Already at HLT level, with more than 6 hits per track required, the deviation from the B_s mass is $\sigma = 74\text{MeV}$ to be compared with $\sigma = 48.5$ with full reconstruction. After one year of running at $1 \times 10^{34} \text{cm}^{-2} \text{sec}^{-1}$ CMS expects 26 $B_s \rightarrow \mu^+\mu^-$ events and 4 $B_d \rightarrow \mu^+\mu^-$ events over 6 events background. ATLAS on the other hand predicts for the same integrated luminosity 21 events $B_s \rightarrow \mu^+\mu^-$ and 60 background, their sensitivity to $B_d \rightarrow \mu^+\mu^-$ at 95% CL is 3×10^{-10} . Dedicated studies of the background with more statistics are under way.

In ATLAS and CMS purely muonic and semi-muonic decays are using the di-muon trigger. Selective cuts on vertex and invariant mass are performed at the HLT or event filter (EF) level. These channels can be studied even at high luminosity ($2 \times 10^{34} \text{cm}^{-2} \text{sec}^{-1}$) by using harder cuts on the di-muon trigger at level 1.

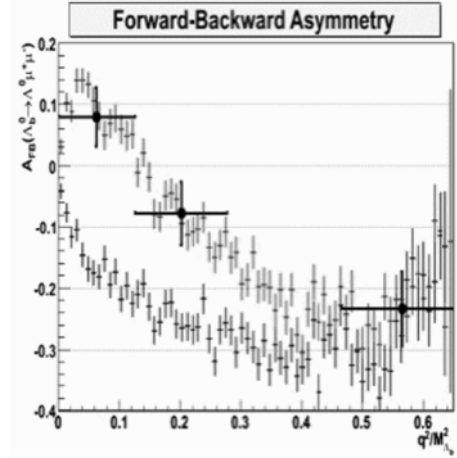


Fig. 6. The sensitivity of ATLAS for 10fb^{-1} in the forward-backward asymmetry for the decay $\Lambda_b \rightarrow \Lambda\mu^+\mu^-$ for three different values of the di-muon invariant mass. The red points are the simulated events with SM and the blue with MSSM and positive Wilson coefficient c_{eff}^7

For the radiative decays, in order to trigger at luminosity $10^{33} \text{cm}^{-2} \text{sec}^{-1}$, an electromagnetic cluster with $E_T > 5 \text{GeV}$ and a muon with $p_T > 6 \text{GeV}$ are required at level 1 trigger while mass and vertex constrain cuts are applied at the HLT or EF trigger levels.

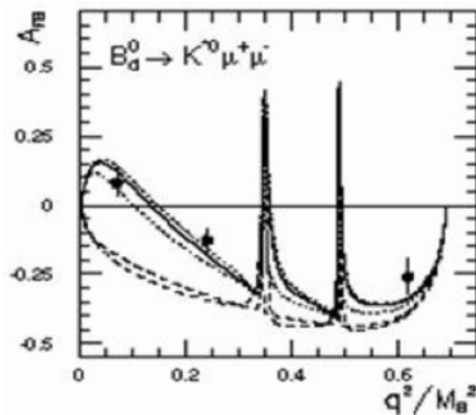
The semi-muonic decays are easier to select compared to the radiative ones which are difficult to trigger and where the background is higher. The decays $B_d \rightarrow K^*\mu^+\mu^-$, $\Lambda_b \rightarrow \Lambda\mu^+\mu^-$ are of interest to ATLAS and CMS. ATLAS studied the prospects of measuring the forward backward asymmetry A_{FB} by measuring the angle between the di-muon system and the B meson or baryon in the center of mass of the muon pair.

The A_{FB} and its precision in ATLAS for an integrated luminosity of 10fb^{-1} was estimated in three regions of di-muon invariant mass. In figure 6 the results for the $\Lambda_b \rightarrow \Lambda\mu^+\mu^-$ is given and in figure 7 for the $B_d \rightarrow K^*\mu^+\mu^-$ together with the asymmetry values for the SM and MSSM with different Wilson coefficients: $c_{eff}^7 > 0$ and < 0 [10]

6 Conclusions

B-Physics measurements at LHC provide a window to look for New Physics, despite the remarkable progress at the B-factories. The strategy of ATLAS and CMS experiments is to focus on exclusive B-channels which can also be accessed at high luminosity and do not require a dedicated b-trigger at level 1.

Measurements of the mixing weak angle ϕ_s in the channel: $B_s \rightarrow J/\psi\phi$ and the B_s mixing parameters: Γ_s , $\Delta\Gamma_s$ can be done with 30fb^{-1} integrated luminosity, while ΔM_s can be constrained from the decay $B_s \rightarrow D_s\pi$



10. P.Ball *et al*, Phys. Lett. **B475**, (2000), 111

Fig. 7. The sensitivity of ATLAS for $10fb^{-1}$ in the forward-backward asymmetry for the decay $B_d \rightarrow K^* \mu^+ \mu^-$ for three different values of the di-muon invariant mass. The solid line is the prediction of SM and the dashed lines the MSSM predictions for Wilson coefficients $c_{eff}^7 > 0$ and < 0

A large number of reconstructed data after only one year of running will allow to measure precisely parameters sensitive to New Physics like the forward backward asymmetry in the semi-muonic decay channels $\Lambda_b \rightarrow \Lambda \mu^+ \mu^-$ and $B_d \rightarrow K^* \mu^+ \mu^-$. Finally the very rare purely muonic decays are accessible by both experiments even at nominal luminosity, confirming thus the complementarity of ATLAS and CMS to the LHCb experiment.

7 Acknowledgments

Thanks to the ATLAS and CMS collaborations and especially to Maria Smizanska for her help in the preparation of the work presented in this conference.

References

1. J.Charles *et al*, The European Physical Journal C **41**, (2005) 1.
2. The ATLAS Collaboration, *ATLAS Technical Proposal*, CERN/LHCC 94-43, (1994)
3. The CMS Collaboration, *CMS Technical Proposal*, CERN/LHCC 94-38, (1994)
4. The ATLAS Collaboration, *ATLAS first level trigger TDR*,CERN/LHCC 1998-14,(1998) and *ATLAS High level trigger TDR*,CERN/LHCC 2000-17, (2000)
5. The CMS Collaboration, *The trigger and DAQ project*,CERN/LHCC 2000-38 **V1**, (2000), and CERN/LHCC 2002-26 **V2**, (2002),
6. Author, Journal **Volume**, (year) page numbers.
7. The ATLAS Collaboration, *Detector and physics performance TDR*, CERN/LHCC 1999-15, **V1**, **V2**, (1999)
8. P.Ball *et al*, hep-hp/0311361 **V1**, (2003)
9. The CDF Collaboration,Phys. Rev. Letters **93**, (2004) 032001 and The D0 Collaboration, Phys. Rev. Letters, **94**, (2005) 071802

Preparing for LHC II

b-tagging at DØ

K. Hanagaki¹ for the DØ Collaboration

Fermi National Accelerator Laboratory, P.O. Box 500, Batavia, Illinois 60510

Abstract. Many high p_T physics analyses at the Tevatron contain a b -quark and hence a b -jet in the final states. We report on the b -jet identification methods in DØ and their performance. For 0.5% of light jet tagging rate, 40 or 45% of b -jet tagging efficiency is achieved for jets with $35 < E_T < 55$ GeV and $|\eta| < 1.2$.

1 Introduction

In many high p_T physics analyses in the Tevatron, such as low mass Higgs searches, $t\bar{t}$ production, and so on, the final state involves b -quarks or actually b -jets. The cross sections of these interesting processes are much smaller than the dominant QCD production cross sections where many light quark jets (u , d , s , or gluon origin) are created. For example, $t\bar{t}$ cross section is ~ 7 pb, while the total cross section of $p\bar{p}$ collision at the Tevatron is ~ 80 mb. Therefore, the identification of b -jets (or b -tagging) is one of the most important factors in these high p_T physics analyses.

There are two ideas to discriminate b -jets from light quark jets. The first is to make use of the lifetime difference between b -hadrons and the other light hadrons. The b -hadrons have typically 400 or 500 μm of lifetime in $c\tau$. Because of the lorentz boost, they tend to travel a few mm before they decay. On the other hand, the hadrons originated from light quarks decay immediately by the strong force, cascading into hadrons with much longer lifetime, such as pions or kaons. As a result, b -hadrons have a decay vertex displaced from the original $p\bar{p}$ interaction point (primary vertex), while light hadrons do not. The displaced vertex or charged particles which do not originate from the primary vertex is the signature to identify b -jets.

The other widely used idea is to find a lepton (either electron or muon) near the jet. The branching ratio of semileptonic decay of b -hadrons is about 11% (there is also $b \rightarrow c \rightarrow \mu X$ cascade decays), while the chance to have leptons from light hadron decays is much smaller because of their long lifetime and the lorentz boost. Therefore, existence of associated lepton is a signature of b -jets.

In this report, we discuss the b -tagging methods using the first idea in DØ, as well as their performance. We also make some remarks for b -tagging in both general and specific in hadron collider.

2 The DØ Detector

The detailed description of DØ detector can be found in [1]. Here we describe only the charged particle tracking system which consists of a silicon microstrip tracker (SMT) and a central fiber tracker (CFT), both located within a 2 T superconducting solenoidal magnet. The design is optimized for tracking and vertexing capabilities at pseudorapidities $|\eta| < 3$, where $\eta = -\ln(\tan(\theta/2))$ and θ is the polar angle with respect to the proton beam direction (z).

The SMT is composed of six barrels, 12 central disks, and four forward disks. The barrels and central disks cover the ~ 25 cm RMS long luminous region or $|\eta|$ up to 1.5. The forward disks provides coverage for $|\eta| < 3$. Each barrel is 12 cm long and consists of 72 ladders arranged in 8 layers with pairs of layers forming four super-layers, occupying the radial space from 2.7 cm to 10.5 cm. The strip pitch varies depending on the detector type, and is typically 50 μm .

The CFT consists of eight super-layers of scintillating fibers, occupying the radial space between 20 and 52 cm. Each super-layer is composed of one doublet fibers aligned along z and another doublet with a stereo angle. The two inner (six outer) layers are 1.66 m (2.52 m) long. The outer layers provides coverage for $|\eta| < 1.7$. The fiber's diameter is 835 μm , leading to doublet layer resolution of about 100 μm .

3 Methods

In DØ we have three methods for b -tagging, two based on the impact parameter of charged tracks (d_0), and the other based on reconstruction of the secondary vertex [2]. The charged tracks are reconstructed using stereo information, and hence d_0 and secondary vertex are 3D quantities. The projection of d_0 or the decay length from the primary to secondary vertex in the plane perpendicular to z is used as discriminant.

The primary vertices are reconstructed in two passes using tracks having at least two SMT hits and $p_T >$

0.5 GeV/c. In the first pass, $S(d_0)$ of track is calculated with respect to the coordinate origin. The seed vertices are formed from tracks with $S(d_0) < 100$. Tracks that contribute to a $\chi^2/\text{d.o.f.}$ greater than a certain threshold are iteratively removed one by one, and new vertices are formed until a stable set of seeds is obtained. In the second pass, vertex fit is performed using tracks with $S(d_0)$ less than a certain threshold with respect to each seed vertex. This improves the position resolution on the vertex, because the fit is less affected by poorly reconstructed tracks. In order to select hard scatter vertex, the p_T distribution of the associated tracks is used. Comparing the p_T of the associated tracks with the distribution obtained from minimum bias events, the probability for the vertex to be consistent with that of soft interaction is computed. The vertex that has the smallest probability is selected as the primary interaction vertex.

With the primary vertex calculated, d_0 can be determined. The sign of d_0 is given by using jet momentum vector, \vec{p}_T^{jet} , and another vector, \vec{v}_{ip} , whose direction is defined as primary vertex to the closest approach of the track under consideration. The d_0 's sign is the same as $\vec{p}_T^{\text{jet}} \times \vec{v}_{ip}$. Figure 1 shows d_0 divided by its measurement

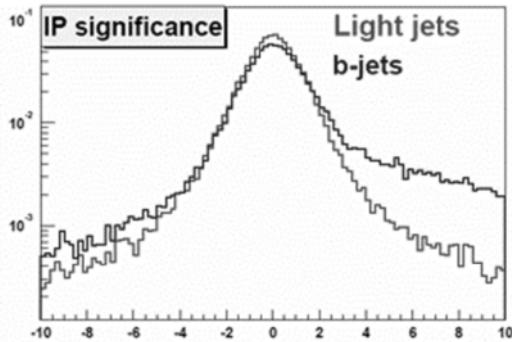


Fig. 1. Impact parameter (d_0) significance in Monte Carlo simulation for b -jets and light jets.

error, $S(d_0) \equiv d_0/\sigma(d_0)$, referred to as signed significance, in Monte Carlo simulation (MC). The symmetric distribution in the light jets is caused by the resolution of the tracking system, while the asymmetry in the b -jets is due to the b -hadron's lifetime as explained in Introduction.

In all the three b -tagging methods, K_S^0 , A , and photon conversion are explicitly removed by checking the invariant mass of any two oppositely charged tracks with the $S(d_0) > 3$.

3.1 Counting Signed Impact Parameter (CSIP)

In the first method, named CSIP, tracks near a jet within a cone of $\Delta R = \sqrt{\phi^2 + \eta^2} < 0.5$, where ϕ is azimuthal angle, are required to have $p_T > 0.5$ GeV/c and $|d_0| < 0.2$ (0.4) cm in the plane transverse to (along) z . At least

two hits in the SMT are also required. In addition, the tracks with $\Delta\Psi > 0.02$, where $\Delta\Psi$ is the opening angle between the track and jet axis, are accepted only if d_0 is positive¹. A jet is assumed to be b -jet if it contains at least two tracks with $S(d_0) > 3$, or at least three tracks with $S(d_0) > 2$. The operating point, i.e. tightness of the selection criteria, is varied by changing the threshold of the p_T cut on the tracks.

3.2 Jet Lifetime Probability (JLIP)

In the second method, named JLIP, the same criteria as CSIP are used for the track selection, except for the $\Delta\Psi$ requirement. Each track was categorized by three quantities; $p(\sin\theta)^{3/2}$ where p is the particle momentum, hit configuration to SMT and CFT, and the number of tracks associated to the reconstructed primary vertex. In each category, a resolution function of $S(d_0)$ was formed using only the negative part of the d_0 . Based on this resolution function, a probability for the track to originate from the primary vertex (P_{trk}) can be calculated. Then all N_{trk}^+ (N_{trk}^-) tracks associated with the jet with a positive (negative) $S(d_0)$ can be used to compute a jet lifetime probability P_{jet}^+ (P_{jet}^-);

$$P_{jet}^\pm = P^\pm \times \sum_{j=0}^{N_{trk}^\pm - 1} \frac{(-\log P^\pm)^j}{j!},$$

where $P^\pm = \prod_{i=1}^{N_{trk}^\pm} P_{trk}$. P_{jet}^\pm for light jets are uniform by construction, while P_{jet}^+ for b -jets has a peak near zero. A jet is considered to be a b -jet if P_{jet}^+ is smaller than a threshold.

3.3 Secondary Vertex Tagger (SVT)

The third method named SVT reconstructs a secondary vertex. Tracks are selected in the same manner as JLIP with one tighter requirement, $|d_0| < 0.15$ cm in the plane transverse to z , and formed into track-jets using fixed-cone jet algorithm of $\Delta R = 0.5$. A seed for secondary vertex is built from pairs of tracks, which are used to form the track-jet, with $S(d_0) > 3$. Additional tracks pointing to the seed according to the χ^2 contribution by the vertex fit are attached iteratively. A jet is regarded as b -tagged when it has at least one secondary vertex, whose direction is within a cone of $\Delta R < 0.5$ relative to the jet axis, with a decay length (L_{xy}) divided by its uncertainty L_{xy}/σ_{xy} greater than a threshold.

4 Performance & Issues

4.1 b -tagging Efficiency and Light Jet Tagging Rate

The b -tagging efficiency is measured using two sets of data. The first one contains muons associated with a jet

¹ Tracks with $d_0 < 0$ are accepted to count so-called negative tagging rate which is explained in Section 4.

($\mu\text{on}+\text{jet}$). The second dataset is required to have another jet which is b -tagged as well as the requirement for the first sample (awaytag). Since the awaytag sample is inclusive of the $\mu\text{on}+\text{jet}$ sample, we assume the relative fraction of c - to light jets are similar in the two samples. For the jets in the sample we apply two tagging algorithms. The first is the one we are trying to measure the efficiency, and second a simple muon-tagging², leading to 8 equations in total, i.e. no b -tagged sample, sample tagged by the method under testing, muon b -tagged sample, and sample tagged by both; and we have $\mu\text{on}+\text{jet}$ and awaytag sample each. There are 8 unknowns; four are the number of b -jets and the number of backgrounds (sum of c -jets and light jets) in each $\mu\text{on}+\text{jet}$ and awaytag samples, the other four are the b -tagging efficiency and the tagging rate to the backgrounds by each two methods. Solving the 8 equations with 8 unknowns gives the b -tagging efficiency without relying on much MC information.

One of the major source of systematic uncertainty in the efficiency measurement is the factorization of b -tagging efficiency, i.e. it is assumed that the efficiencies are the same before and after applying muon tagging. The other major source of systematic uncertainty is the assumption that the efficiencies are the same for $\mu\text{on}+\text{jet}$ and awaytag samples. Combining these two and other minor contributions, the relative systematic error in the b -tagging efficiency measurement is about 3-4% in the relevant E_T range. In Fig. 2, for example, the absolute systematic uncertainty in CSIP is shown as a function of E_T . The sta-

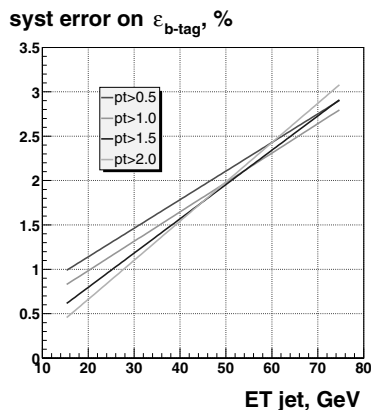


Fig. 2. The absolute systematic uncertainty of b -tagging efficiency measurement in CSIP as a function of jet E_T .

tistical error is much smaller (less than 1% in relative).

In principle, light jets are mis-tagged due to the effects of inefficiency and resolution in tracking and vertexing. Therefore, the light jet tagging rate can be estimated by using the tagging rate computed from negative $S(d_0)$ or L_{xy}/σ_{xy} (referred to as negative tagging rate). In reality, however, there are two contributions we have to take into account; the asymmetric distribution of $S(d_0)$ or L_{xy}/σ_{xy}

² In the tagging by muon, p_T of muon with respect to the jet axis is required to be above a certain threshold.

in light jets which can be mainly caused by decays of π^\pm and K^\pm , and the fraction of non-light jets. These two effects in the negative tagging rate are corrected by MC, resulting in the light jet tagging rate.

In order to eliminate the effect of fake jet, such as caused by calorimeter noise, or poor coverage of tracking system, the b -tagging efficiency below is defined relative to a so-called taggable jet in which existence of charged tracks in the jet cone is ensured. The taggability is typically 85 or 90% in data. The primary vertex position is also restricted to be $|z| < 60$ cm.

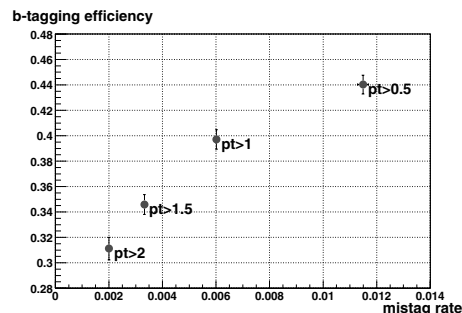


Fig. 3. b -jet tagging efficiency vs light jet tagging rate in CSIP with various p_T cuts on tracks which satisfy the $S(d_0)$ requirements.

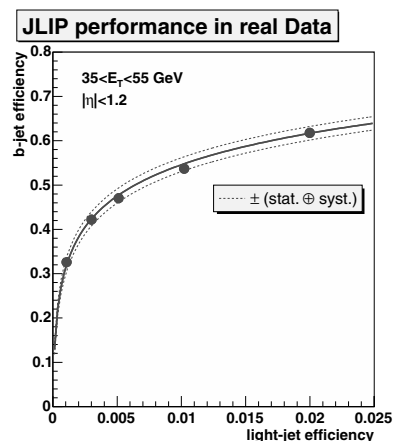


Fig. 4. b -jet tagging efficiency vs light jet tagging rate in JLIP with various cuts on P_{jet}^+ .

Figure 3, 4, and 5 show the b -tagging efficiency vs light jet tagging rate measured in data for the three different methods. The central region ($|\eta| < 1.2$) and moderate E_T range ($35 < E_T < 55$ GeV) of jets are considered here. With 0.5% of the light jet tagging rate, for example, the b -tagging efficiencies are about 40 or 45% depending on the method.

In Fig. 6, b -tagging efficiency in JLIP is shown as a function of E_T and $|\eta|$ of jets. The efficiency goes up until

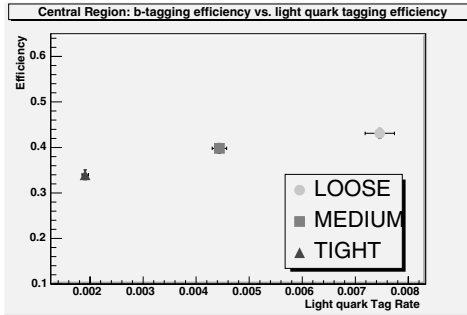


Fig. 5. b -jet tagging efficiency vs light jet tagging rate in SVT with various cuts on L_{xy}/σ_{xy} .

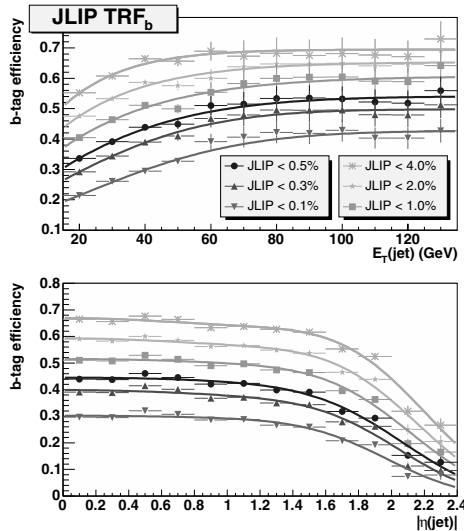


Fig. 6. b -jet tagging efficiency in JLIP as a function of E_T (top) and $|\eta|$ (bottom) of jets.

60 GeV as the E_T increases, and then reaches the plateau. Thanks to the excellent acceptance coverage by the tracking system, the efficiency is almost flat up to $|\eta|$ of 1.5 or so. Even at $|\eta| = 2$, the efficiency relative to the central region is still 50% or higher.

Among the three methods, the correlation are found to be around 70% in b -tagging efficiency, and about 20% in the negative tagging rate. This implies the possibility of improvement by combining the three methods. The development of such combination is in progress where neural network is employed for the combination.

4.2 Issues

One of the difficulties in the analyses is the fact that the performance in MC does not reproduce reality. If the discrepancy were uniform in jet E_T and η , or jet E_T and η distributions are identical to the data sample used to measure the efficiency, the analyses would not be so complicated. Analyzer could use simply one scale factor to

correct the efficiency in MC. However, the real world is not that simple. We therefore measure the b -tagging efficiency and the light jet tagging rate in bins of jet E_T and η , and parametrized them in the 2D space. This parametrization must be used in any analyses in DØ which needs b -jet tagging.

The second issue is the lack of calibration source. There is no process giving pure b -jets in the hadron collider. DØ has developed the novel technique described above to measure the efficiency relying minimally on MC. Still there exists some sources of systematic uncertainty. There is a future possibility to use b -quarks in top decays, but it is not realistic given the current statistics in the Tevatron. Another nasty feature in the hadron collider is that b -jet can be created by gluon splitting, where two b -quarks exist within a jet cone. The b -tagging efficiency should be different, but has not been measured independently in data yet.

The third issue is the performance in high luminosity environment, which will be very crucial in the LHC experiments. The number of interactions per bunch crossing is about three in the highest luminosity operation so far. Even with this luminosity, we already see some minor degradation of performance, which is under current study.

5 Conclusions

To conclude, we have described the methods of identification of b -jets in DØ, how to measure the b -tagging efficiency and tagging rate to light jets, and the results. Typically between 40 and 45% of efficiency was achieved with a fake rate of 0.5%. Some issues both in general and specific in the hadron collider environment were also discussed.

Acknowledgment

I thank the members of b -tagging working group. My special thanks go to those who work hard for designing, constructing, operating and calibrating the detectors.

References

1. V. Abazov *et al.* (DØ collaboration), “The Upgraded DØ Detector” submitted to Nucl. Instrum. Methods Phys. Res. A. physics/0507191.
2. V. Abazov *et al.* (DØ collaboration), Phys. Rev. Lett. **94**, 161801 (2005).

B tagging at CDF

Experience, performance, lessons for LHC

Daniel Jeans for the CDF collaboration

INFN CNAF, Bologna, Italy & INFN Roma1, Roma, Italy

Abstract. We describe the algorithms used to identify b jets in CDF, and discuss various methods used to measure their performance.

1 Introduction

The identification of b jets is fundamental in the study of many interesting physics processes at high energy hadron colliders. Examples are the measurement of the top quark properties, the search for Higgs bosons, and precision tests of QCD.

b jets (jets whose originating parton is a b quark) can be identified in several ways, making use of the distinguishing characteristics of B hadrons with respect to hadrons containing only lighter quarks: their long lifetime ($\sim 1.5ps$), large mass ($\sim 5GeV/c^2$), and large decay fraction into leptons ($\sim 20\%$).

2 Tevatron and CDF

The Tevatron produces $p\bar{p}$ collisions at a centre-of-mass energy of 1.96 TeV, which take place at the centre of the experiments D0 and CDF. The luminous region is large: it is approximately Gaussian, with widths of around $30cm$ along the beam direction, and $26 \rightarrow 32\mu m$ in the plane transverse to the beam, varying along the z (beam) axis.

Bunch crossings occur every 396 ns, and at typical luminosities of $10^{32}cm^{-2}s^{-1}$, the mean number of interactions per bunch crossing is around three.

CDF [1] is a general purpose detector consisting of a high precision charged particle tracking system inside a uniform solenoidal magnetic field of 1.4 Tesla, electronic and hadronic calorimeters, and muon detectors. Some of its components are sketched in figure 1.

The Central Outer Tracker (COT) is a large wire chamber, which covers the region with pseudorapidity $|\eta| < 1$. It measures up to 96 points per track; half the wires are at a small stereo angle to the beam direction, allowing full three dimensional track reconstruction.

Inside the COT are the various components of the silicon tracker. Layer00 is mounted directly on the beam pipe, and is a single sided silicon detector, designed to be radiation hard. Outside L00 lie the five double sided silicon layers of the SVXII, followed by 1 or 2 layers of

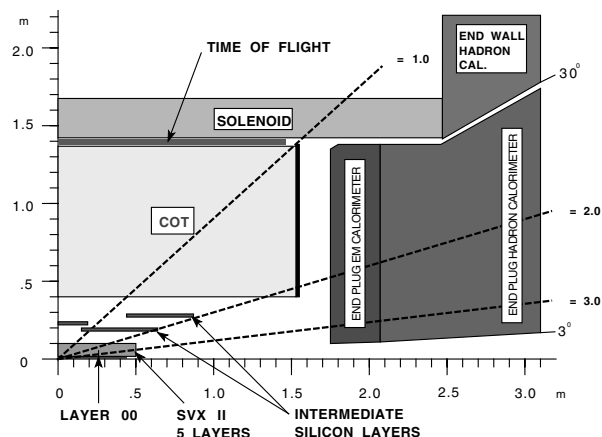


Fig. 1. Schematic of a quarter of the CDF detector

the Intermediate Silicon Layers (ISL). These layers contain strips parallel to, and at a small stereo angle to, the beam axis, giving full three dimensional information. The silicon tracker covers the region $|\eta| < 2$.

3 Tracking and Primary Vertex finding

Tracks are first reconstructed in the COT. These COT tracks are then extrapolated into the silicon detector, and matching silicon hits are attached to the track. The remaining unassociated silicon hits are then used to search for additional tracks, which are then extrapolated into the COT, and any matching COT hits are added to the track.

Typical impact parameter resolution in the plane transverse to the beam for tracks with COT and silicon information is around $40 \mu m$, including a contribution of around $30 \mu m$ from the width of the beam, as shown in figure 2.

Since the luminous region where the collisions take place is large, and the track reconstruction precision is

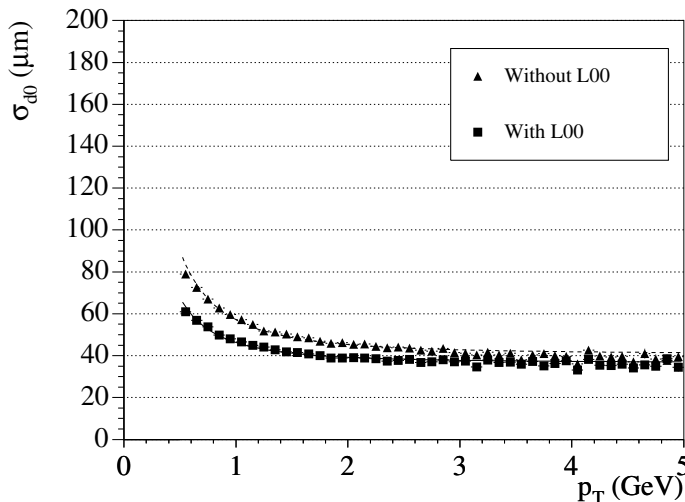


Fig. 2. Impact parameter resolution as a function of track p_T

good, improved information on the position of the interaction can be obtained by reconstructing the event primary vertex. First a seed position in z is identified by looking where an event’s tracks approach closest to the beamline. Tracks displaced from this vertex by less than 1 cm in z , and with a two-dimensional impact parameter significance with respect to the beam position of less than three are used to fit a vertex constrained to lie inside the beamline. Tracks giving a large contribution to the vertex χ^2 are excluded from the vertex. Typical resolution on the primary vertex position is in the range $10 \rightarrow 32\mu\text{m}$ in the plane transverse to the beam direction, depending mostly on the number of tracks used in the fit. This resolution is significantly smaller than the width of the beam.

4 Lifetime tagging algorithms

4.1 SecVtx

The SecVtx algorithm searches for track vertices inside a jet displaced from the primary vertex position, making use of the long lifetime of B hadrons.

Tracks lying inside the jet cone are considered; they are required to have both COT and silicon hits associated to them, and to satisfy various quality requirements. Tracks are required to lie within 2 cm of the primary vertex in z (to remove tracks from possible multiple interactions), and to have an impact parameter significance of at least 2.5 (to remove tracks produced at the primary vertex). In order to reduce the effects of particle interactions in the detector material, tracks with an impact parameter greater than 0.15 cm are rejected. Tracks identified as coming from K_S, Λ decays, or from photon conversions, are also rejected.

The remaining tracks are then used to search for a vertex: in a first pass a vertex made of at least three tracks is required; if such a vertex is not found, vertices with only two tracks (with more stringent track quality requirements) are accepted. The resolution on the separation of

the primary and secondary vertices is typically $190\mu\text{m}$. To identify a jet as a b jet, the significance of the separation between the primary and secondary vertices is required to be significant, and the χ^2 of the vertex fit reasonable; the vertex is required to lie on the “correct” side of the primary vertex with respect to the jet axis. Two track vertices reconstructed inside the detector material are rejected.

Two versions of this algorithm are in use, one optimised for higher efficiency (“loose”), the other for higher purity (“tight”); the precise requirements on track quality, vertex separation, and vertex χ^2 are different in the two versions.

More details can be found in [2];

4.2 JetProbability

The JetProbability algorithm also makes use of the long lifetime of the B hadron to tag b jets, by identifying jets whose tracks are unlikely all to have been produced at the primary vertex.

The impact parameter of tracks is signed with respect to the jet direction in such a way that tracks from long-lived particle decays are more likely to have positive impact parameters, while tracks from the primary vertex have equal positive and negative contributions.

The method is calibrated in generic jet data. Tracks are classified according to various quality criteria. In each track class, the negative side of the signed impact parameter significance distribution (dominated by tracks produced at the primary vertex) is parameterized.

To tag a jet, only tracks with a positive impact parameter are used. For a given track, the appropriate parameterization is used to calculate the probability that a track from the primary vertex would have a larger impact parameter significance. Using all tracks in the jet (after removal of identified K_S, Λ and conversion tracks), the per-track probabilities are combined to produce a per-jet probability. This is constructed in such a way that light-flavour jets have a flat probability distribution between 0 and 1, while jets containing long-lived particles tend to have a small probability.

b jets are typically tagged by requiring that the Jet-Probability is less than 1 or 5 %, depending on the efficiency & purity required by the analysis.

4.3 Data/simulation scale factor

The various processes to which b tagging is applied to have different distributions of b jets in energy and pseudorapidity. To understand the efficiency for correctly tagging an event, MonteCarlo simulation is used to take account of these differences.

To account of imperfections in the simulation (arising from, for example, imperfect description of silicon detector efficiency, tracking efficiency and resolution, or of the B hadron decay), the efficiencies measured in the simulation must be corrected by a “scale factor” to apply them to real data. This scale factor is measured in a large, independent

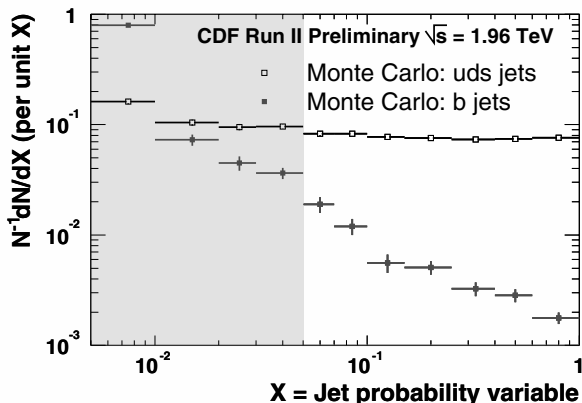


Fig. 3. JetProbability distribution

dataset, and then applied to the simulation of the physics channel of interest.

First the efficiency of the btagging algorithm being considered is measured: the basic idea is to find a sample of jets with a high b content, and measure how many of the b jets are tagged by the algorithm.

To do this, events with a jet containing an identified lepton are selected; these jets have an enhanced heavy flavour content with respect to generic jets. To further enhance the HF fraction, the jet is required to be balanced by a second jet, which is required to be tagged as a heavy flavour jet.

The heavy flavour fraction in the jet containing the lepton (the “lepton jet”) is estimated using several techniques: a fit to the distribution of the muon p_t relative to the jet axis (which is different for heavy and light quark jets), as illustrated in figure 4; the number of jets with both an identified electron and muon of opposite sign (one coming from the primary B hadron decay, the second from the decay of a charmed hadron from the B decay); or the number of lepton jets which contain an identified D^0 meson in addition to the charged lepton.

By using these techniques to estimate the number of heavy flavour jets in the lepton jet sample before and after applying the b tagging algorithm, the efficiency of the algorithm can be measured.

A sample of MonteCarlo data is then produced to simulate the lepton jet sample, and the same technique is used to measure the b-tagging efficiency in this sample. The comparison of the efficiencies measured in data and simulation gives the scale factor. It is typically in the range $82 \rightarrow 93 \pm 6\%$, depending on the tagger being considered.

Figure 5 shows the efficiency of the JetProbability algorithm in $t\bar{t}$ MonteCarlo as a function of jet pseudorapidity. The efficiency has been corrected by the scale factor.

4.4 Mistagging probability

As well as understanding the efficiency of a tagging algorithm, it is also important to understand the mistagging

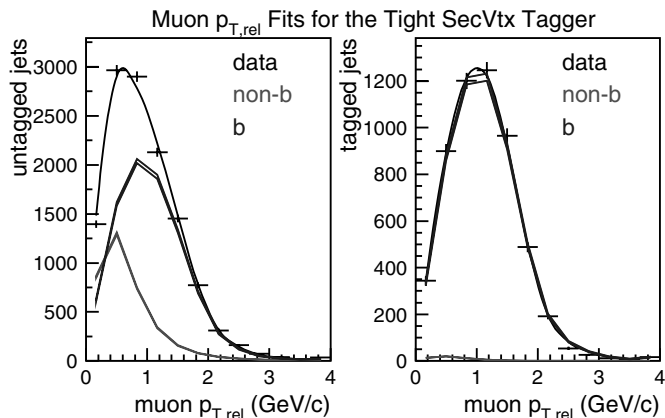


Fig. 4. Fits to μ relative p_T distributions

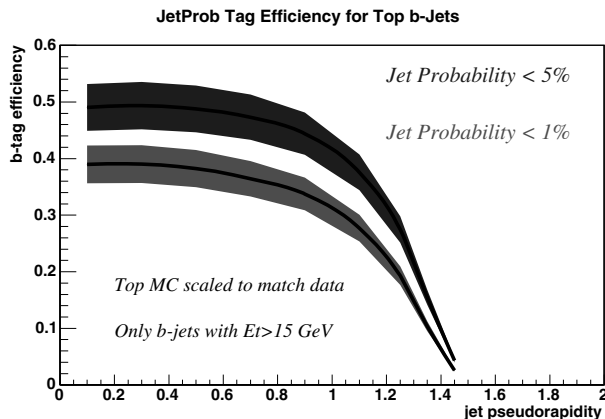


Fig. 5. JetProbability efficiency as a function of η

probability: the fraction of light-flavoured jets which are incorrectly tagged as being b jets.

A first-order approximation of the mistagging rate is given by the negative tag rate. In the case of SecVtx, a negative tag is defined as when the identified vertex is well separated from the primary vertex, but lies on the “wrong” side of the primary vertex with respect to the jet direction. Such vertices are usually due to finite tracking resolution (or incorrect hit assignments), and are therefore assumed to be symmetrical positive-negative.

In the case of JetProbability, the “negative JetProbability” is the probability measured using only tracks with a negative signed impact parameter (with respect to the jet direction).

The fraction of jets with a negative tag is measured in jet data, as a function of the jet transverse energy, azimuthal angle and pseudorapidity, the number of tracks inside the jet, and the sum of the transverse energies of all jets in the event. To estimate the mistagging rate, the negative tag rate is corrected for effects due to interactions in the detector material, unidentified long-lived strange hadrons (mostly K_S and Λ), and the b content of negative tags in the jet data.

Figure 6 shows the mistag rate for the SecVtx algorithm as a function of the jet transverse energy.

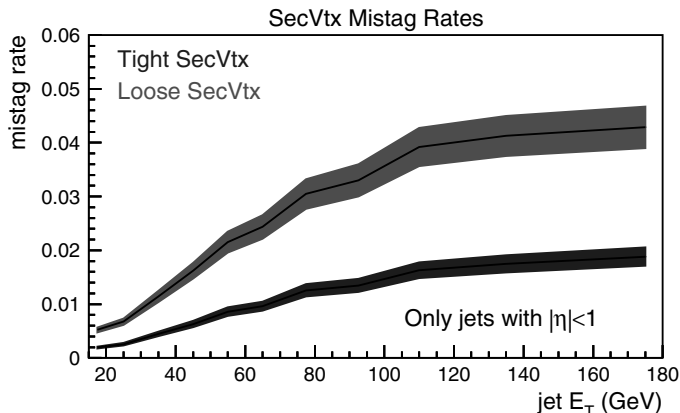


Fig. 6. SecVtx mistag rate as a function of jet E_T

5 Soft Muon tagger

In total, around 20 % of B hadrons decay into muons, 11 % directly, and the remainder via a charmed hadron. These muons are non-isolated, and have a relatively soft p_T distribution. These properties preclude the use of the calorimeter for muon identification, and induce significant multiple scattering to the muon as it passes through the detector material. A dedicated muon identification algorithm has been developed to identify these muons, based on the matching of tracks to muon chamber track segments.

After muons identified as decay products of the J/ψ , γ or Z bosons have been rejected, a jet is regarded as tagged if it contains an identified muon.

The efficiency of this algorithm is measured directly in data, by looking at “second legs” of J/ψ and Z events; it is measured to be between 70 and 90%, depending in the p_T of the muon. Since the muon tracks in these samples tend to be more isolated than those found in b jets, the efficiency measurement is cross-checked in $b\bar{b}$ events. The measured identification efficiency for muons in the central region is shown in figure 7.

The fake rate due to the positive identification of non-muon tracks is measured in generic jet data, which, after the removal of tracks due to J/ψ , γ and Z decays, have a rather small true muon content. The fraction of remaining tracks identified as a muon is parameterised as a function of track p_T , azimuthal angle and pseudorapidity. Values of the mistagging rate are typically in the range $0.6 \rightarrow 0.9\%$. More details can be found in [3].

6 Conclusions and plans for improvements

At CDF, a number of stable and well understood tools are used for the identification of b jets. The performance of the algorithms is measured in data, and correction factors to be applied to simulation are calculated.

At present, various new tagging techniques are being studied, including the identification of electrons inside jets, and more sophisticated tagging algorithms, based on

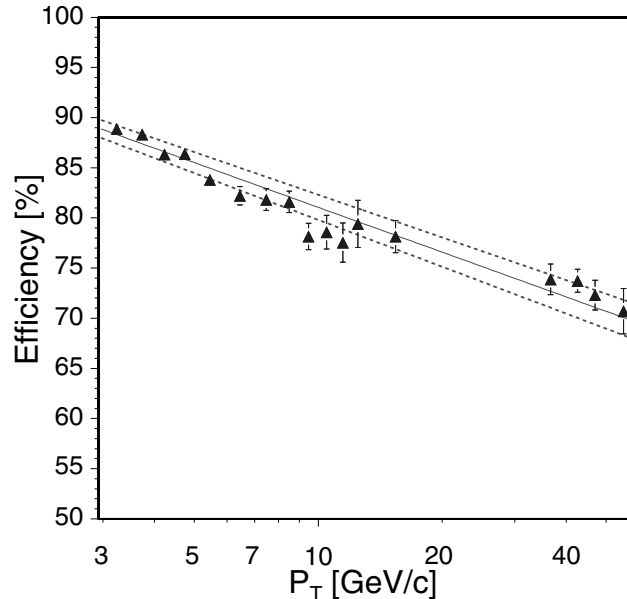


Fig. 7. μ ID efficiency as a function of μp_T

Neural Networks, which make use of more information contained inside the jet.

References

1. D. Acosta et al., Phys. Rev. **D71**, (2005) 032001
2. D. Acosta et al., Phys. Rev. **D71**, (2005) 052003
3. D. Acosta et al., Phys. Rev. **D72**, (2005) 032002

Pixel detector in BTeV

Tracking and vertexing at first level trigger

Mauro Dinardo¹ for the BTeV collaboration

Istituto Nazionale di Fisica Nucleare and Università degli Studi di Milano, e-mail: Mauro.Dinardo@mi.infn.it

Abstract. A pixel detector, to perform tracking and vertexing at first level trigger, has been developed in the R&D context of the BTeV experiment. The BTeV trigger inspects every beam crossing of the Fermilab Tevatron, running at a luminosity of $2 \times 10^{32} \text{ cm}^{-2} \text{ s}^{-1}$, and selects events that have “detached vertices” from B decays occurring downstream of the main interaction. The system uses a massively parallel system of FPGAs and microprocessors to produce a trigger decision on average every 396 ns. The trigger calculations are facilitated by the 23 million channel pixel detector that provides the input to the trigger. Front end electronics sparsifies the remainder of event data and sends it to large, Tbyte, memory buffers that store it until the trigger decision can be made.

1 Introduction

BTeV was supposed to study CP violation and mixing in the decays of particles containing bottom and charm quarks, at the Tevatron hadron collider [1] (Tab. 1 shows the Tevatron main features). Hadron colliders, in fact, have huge potentials for heavy flavour physics studies. They have a bigger b production cross-section ($100 \mu\text{b}$ at Tevatron) compared to b -factories (typically 1 nb), moreover all species of b -hadrons are produced (B_d , B_u , B_s as well as b -baryons of all kind). On the other hand hadron at colliders one has to face several experimental challenges like: isolate the signal in a nasty environment ($S/N \simeq 1/500$ at Tevatron); high data rate; radiation damage. The BTeV innovative feature, that made it unique, was to bring tracking and vertexing at lower level in trigger and archive only fully reconstructed data. The core of the spectrometer that would allow to meet this challenge was the Silicon pixel vertex detector.

Feature	Value
Luminosity	2×10^{32}
Interactions / s	15×10^6
$B\bar{B} / 10^7 \text{ s}$	2×10^{11}
B events per background	1 / 500 (only 1/500000 are “interesting” B decays)
Bunch spacing	396 ns (originally 132 ns)
Luminous region length	$Z = 30 \text{ cm}$
Luminous region radius	$\sigma_x \simeq \sigma_y \simeq 30 \mu\text{m}$
Interactions / beam crossing	$< 6 >$

Table 1. Tevatron main features.

2 The physics basis of the trigger

To form a trigger, we must exploit properties of events with B -hadrons that differentiate them from the much larger number of ordinary, or “minimum bias”, events. Fig. 1 illustrates the key characteristic that distinguishes B -events. The B 's produced in the interaction travel a short distance, between a few tenths of a mm and a few mm from the point of the interaction and then decay into two or more (typically 5) particles. The presence of these “detached vertices” or “secondary vertices” is the signature of a B event. However, this requires the trigger to reconstruct tracks and assemble them into vertices to find those with evidence of detached vertices. This task must be done in quasi-real time so that a decision can be made on average every 396 ns. This represents a formidable challenge that has not been achieved yet in particle physics. Conventional high energy physics triggers are usually based on a three level hierarchy. The lowest level, which we will refer to as Level 1, uses fairly simple signals to form triggers, usually within a fixed amount of time, typically a few microseconds. They choose events within this limited time budget based on relatively simple criteria, such as various sums of calorimeter pulse heights or muon signature. This reduces the data rate so that Level 2 has more time to spend on each remaining event. Level 2 usually is a mixture of dedicated trigger hardware and computing elements. The Level 2 trigger further reduces the rate providing a relatively small sample of events to the Level 3 trigger that now has enough time to process them. This is performed by a massively parallel farm of microprocessors using algorithms that are quite similar to those of a full offline analysis to make the final decision to discard the event or write it to archival storage for offline physics studies. BTeV also has a three level trigger hierarchy [2].

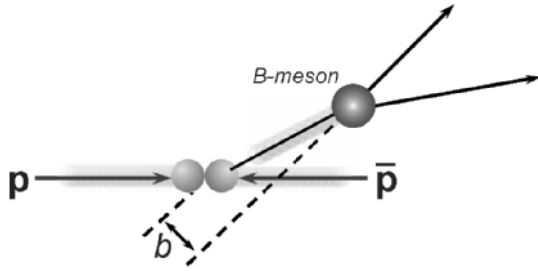


Fig. 1. Events containing a B -hadron showing a detached vertex from a B -meson that eventually decays into two particles. Secondary B -decay vertex significantly detached from the primary vertex.

The main difference, with a conventional approach, is that massive computing is applied at Level 1. The challenge for the BTeV trigger and data acquisition system is to reconstruct particle tracks and interaction vertices for every interaction that occurs in the detector and to select preferably interactions with B decays. The trigger performs this task using 3 stages, referred to as Levels 1, 2 and 3:

- L1: looks at every interaction, and rejects at least 98% of background based on full track and vertex reconstruction using a Silicon pixel detector described below;
- L2: uses L1 results and performs more refined analyses for data selection;
- L3: performs a complete analysis using all of the data for an interaction. The total effect of the trigger is to reject $> 99.8\%$ of background and keep $> 50\%$ of B events.

The Data Acquisition System (DAQ) [3] saves all of the detector data in memory for as long as is necessary for Level 1 to analyse each interaction (0.5 ms on average for L1) and moves data to L2/3 processing units and archival storage for selected interactions. The key ingredients that make it possible to meet this challenge are:

- BTeV pixel detector [4] with its exceptional pattern recognition capabilities;
- rapid development in technology and lower costs for FPGAs, microprocessor CPUs and memory.

The most important features related to the trigger are:

- A precision vertex detector of planar pixel arrays located right near the Interaction Region (IR). This provides sufficient track resolution to separate the various vertices. The pixel detector position resolution is of order $6 \mu\text{m}$.
- The pixel detector is located in the middle of a large dipole magnet (1.6 T), also centred on the IR. It produces measurements that enables the trigger to determine the momentum of charged tracks that traverse the detector. This is essential because it allows the trigger to eliminate from its calculations very low momentum tracks that can be badly scattered and appear to be detached from the primary vertex. These tend to result in “fake” triggers. The decay products of B events are generally high momentum particles.

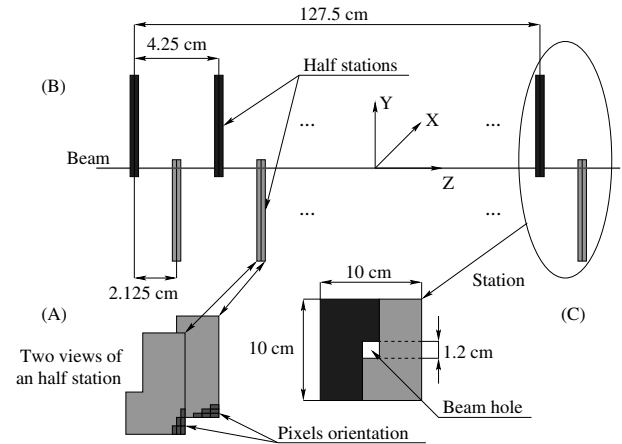


Fig. 2. Schematic of BTeV pixel detector. (A) shows the crossed rectangular pixels in a single station. Each station provides a high precision and lower (but still very good) precision measurement of both X and Y ; (B) shows the layout along the beam (in Z); and (C) shows the layout transverse to the beam. The detector is only $10 \text{ cm} \times 10 \text{ cm}$ in cross section, occupies $\sim 1.3 \text{ m}$ along the beam, and has 23 million pixels. It has a $12 \text{ mm} \times 12 \text{ mm}$ hole in the center that the beams pass through. The whole system is under vacuum.

- A vertex reconstruction at the lowest level of the trigger system that can select events based on evidence for detached vertices.
- A very high speed, high capacity data acquisition system that is capable of recording every B event that is selected by the trigger without exercising further judgment as to the exact topology or “physics value” of the B decay.

3 Pixel detector

In order to carry out tracking and vertex calculations at very high rates with an affordable amount of hardware, one needs to provide the trigger system with the best possible tracking information in a form that eases the task of pattern recognition. BTeV has chosen to develop a high speed, high rate precision tracker based on Silicon pixel detectors. The detector, shown schematically in Fig. 2, has 30 stations of pixels distributed along the IR. The pixels sensors are made of Silicon doped $n + /n/p+$ type, with pixel dimensions of $50 \mu\text{m} \times 400 \mu\text{m}$. Each station consists of two views, one measuring X with high precision and Y with lower precision and the second measuring Y with high precision and X with lower precision. This technology is chosen because:

- gives essentially 3-dimensional space points;
- has excellent spatial resolution of $5 \div 10$ microns depending on the angle of the track as it traverses the plane of the pixel detector;
- has a very low occupancy of 10^{-4} ;
- has a very fast signal that ends well before the next beam crossing;

Property	Value
Total station radiation length (incl. RF shielding)	3%
Total pixels	$\sim 2.3 \times 10^7$
Read out	digital (3 bits, i.e. 8 thresholds)
Trigger	on-the-fly sparsified (signals are used in Level 1)
Rate requirements	time between beam crossings: 396 ns, 132 ns BCO also fully supported
Noise requirement	desired: $< 10^{-6}$ per chn/crossing required: $< 10^{-5}$ per chn/crossing
Resolution	better than $9 \mu\text{m}$
Angular resolution	better than 0.1 mrad
Radiation tolerance	$> 6 \times 10^{14}$ particles/cm ² (10 years of BTeV operation)
Power per pixel	$\sim 60 \mu\text{W}$
Occupancy	$\sim 10^{-4}$ (at 396 ns BCO)
Vertex separation resolution	$138 \mu\text{m}$ (from simulations)
Proper time resolution	46 fs (from simulations)

Table 2. Pixel vertex detector properties.

- is radiation hard, this enables the detector elements to be placed very close to the beam (in vacuum, separated from the beam only by a few thin strips for RF shielding), minimizing track extrapolation errors, a necessary condition for excellent vertex resolution.

During beam refill, the half stations of the detector will be placed away to $\sim \pm 2$ cm from the beam using a system of actuators and motion sensors. When the beam is stable, the detectors will then be moved close to the beam for data taking with a reproducibility better than 1 micron. In order to reduce the noise and increase the sensors lifetime the pixel detector will operate at -5°C . Moreover the high spatial resolution needed, requires to place the detector close to the beam, inside the beam pipe; therefore an RF shield is needed. That will be the only separation between the 10^{-8} torr of the pixel vacuum vessel and the 4×10^{-10} torr of the Tevatron beam pipe. The other vertex detector properties are reported in Tab. 2.

While pixel detectors of comparable complexity are being developed for other detectors, including CMS and ATLAS at the LHC, the BTeV pixel detector is unique in that it is used directly in the lowest level of the trigger and that each of the 23 million pixels has its own 3 bit flash ADC. This allows us to exploit charge sharing to improve the spatial resolution. Excellent spatial resolution helps the pixel detector measure the curvature of tracks so that the momentum can be calculated at the trigger level. The whole system is digitised, sparsified and read out into the trigger system at the beam-crossing rate. The near-3D space points returned by the pixel detector make pattern recognition very simple and reduce the amount of

computing time needed to carry out tracking and vertex calculations two orders of magnitude relative to a Silicon strip detector. The high quality inputs make the trigger calculations possible with a reasonable number of processors.

4 The BTeV front end electronics and data acquisition system

The trigger system actually deals with “beam crossings”, treating each crossing as a separate computing problem and trying to determine whether any of the interactions are B events. Since the crossings have a variable number of interactions and the individual interactions have varying complexity, the time it takes to compute for an individual crossing is highly variable. In order to keep all processing elements busy, BTeV’s trigger and DAQ have:

- no fixed latency at any level. Decisions are made in variable amounts of time and transmitted as soon as they are known;
- no requirement of time ordering. It is common for system to be carrying out computations on a crossing while it has already completed several later ones.

This in turn requires massive amounts of buffering throughout the system. To limit the amount of data that needs to be buffered, on-the-fly sparsification (zero suppression) in the front ends is implemented. By sparsifying the data and shipping it out every 396 ns, the front ends keep the data volume from the very large number of channels from the pixel detector and all the other BTeV detectors manageable. The DAQ must store the sparsified data from all the detectors for as long as it takes to make the Level 1 trigger decision. Once the Level 1 trigger makes a decision, the 98÷99% of the crossings that fail the trigger are erased from the buffers, freeing the memory for other events. The 1÷2% that pass are moved to other buffers for Level 2/3 processing. Since the amount of data is vastly reduced, it is possible to store crossings that have passed Level 1 for very long amounts of time while the Level 2/3 calculations are being performed.

Each pixel sensor is bump bonded to the Fermilab PIXEL read out chip (FPIX), made in $0.25 \mu\text{m}$ CMOS technology. FPIX performs on-the-fly sparsified read out and provides the following information:

- channel up threshold (row-column coordinate);
- BCO counter over 8 bit (the time-stamp);
- digitalised charge over 3 bits.

Data is transported from the front ends by the Data Combiner Board (DCB) that serializes the data and sends it to the Control Room over fibre optic links. The data are stored in the Level 1 Buffer System (L1B) while the trigger is making its decision.

5 First level trigger implementation

The first level trigger is based on the pixel detector. Fig. 3 is a schematic of the first portion of the electronics. The

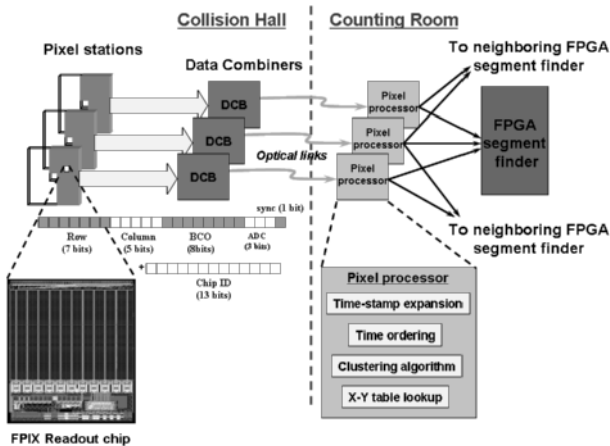


Fig. 3. Pixel trigger electronics showing the pixel detector halfstations, the pixel read out chip, the DCBs, the optical fibres to the counting room and the pixel processor.

pixel processor collects hits from the same crossing (time ordering), applies a clustering algorithm, and produces a coordinate for each cluster. It passes the list of coordinates to the segment finder that executes the first part of the tracking algorithm. The trigger algorithm has two major stages:

1. segment finding
2. track and vertex finding

5.1 Segment finding

Pixel hits from three neighboring stations are used to find the beginning and ending segments of tracks. These three station segments are called triplets. An “inner triplet” is associated with a track as it enters the pixel detector from the interaction region and represents the start of the track. Since nearly all tracks entering the pixel detector this way and that will enter the forward spectrometer have a hit in the first centimetre of the pixel detector, only that limited region is used to “seed” or initiate searches for triplets. This greatly reduces the number of calculations that have to be performed. Similarly, an “outer triplet” is associated with a track as it leaves the pixel detector, either through the side or the front or rear faces. An “outer triplet” represents the end of the track in the pixel detector. Again, nearly all outer triplets start very close to the detector boundary so only a limited region is used to seed the search for outer triplets. The segment finding algorithm is very standard and works as follows:

1. starting with a seed hit in the “inner region” of plane $N - 1$, one projects a cone onto plane N that corresponds to a range of legitimate and interesting tracks that would fall within the pixel detector acceptance;
2. for each hit, “ I_N ”, within this range, one projects from this hit and the seed back to the Z position of plane $N - 2$. If the projection falls within pixel plane $N - 2$, then the seed is not the first point on an inner segment with hit I_N . One advances to the next hit in plane N ;

3. if the projection falls inside the beam hole in the pixels at station $N - 2$ instead, then one projects the seed and hit I_N into pixel plane $N + 1$; if a confirming hit “ J ” is found, this seed, I_N , and J_{N+1} are an “inner segment”.

Outer segment finding is done in the same way and in parallel. In the bend view, both inner and outer segments are found (research for straight tracks over three stations in the bend view guarantees a momentum cut of $p > 3$ GeV/c). These will eventually be matched and the difference in directions between an inner segment and its outer matching segment will give a measurement of the momentum. In the non-bend view, segment finding is done in parallel with the bend view, but only inner segments are searched, since they provide enough information to measure the track horizontal position and angle to extrapolate it back to the interaction vertex. The segment finding algorithm is implemented with a system of 480 FPGAs. This number is based on a prototype implementation of the algorithm for an Altera [5] EPC20K1000 FPGA. Our work shows that the current design will fit comfortably in various devices offered by Altera and that similar devices from Xilinx [6] can be used with minor changes to the code. Segment finding FPGAs do their tasks whenever hit data are available. Segments for several different crossings are being generated all at one.

5.2 Track and vertex finding

The next stage involves delivering all the segments associated with a single beam crossing to one CPU in the track/vertex finding processor farm. The processor then does segment matching to form tracks and applies an algorithm to find “primary interaction vertices”. Vertex finding constitutes projecting found tracks back into the interaction region and clustering them. Since tracks from B decays tend to have somewhat higher transverse momentum relative to the beam direction than tracks from the main interaction vertex, a requirement is placed on the tracks used in the clustering that they be below a certain transverse momentum. Typically several interaction vertices are found in each crossing, but they are usually quite well separated due to the length of the Tevatron luminous region. Each track not falling into these clusters and whose transverse momentum is above some value (typically 300 MeV/c) is extrapolated back to the nearest interaction vertex and its impact parameter b , relative to that vertex and its associated uncertainty σ_b , are calculated. The quantity b/σ_b is used to evaluate detachment. A value of $b/\sigma_b > 3$ is currently taken as the requirement to call a track “detached”. The primary Level 1 trigger currently requires two tracks detached with respect to the same primary vertex to meet the criteria for a “Level 1 accept”.

6 Level 1 trigger performances

Fig. 4 and 5 show an example of simulated Level 1 trigger background rejection and efficiency, respectively. To avoid

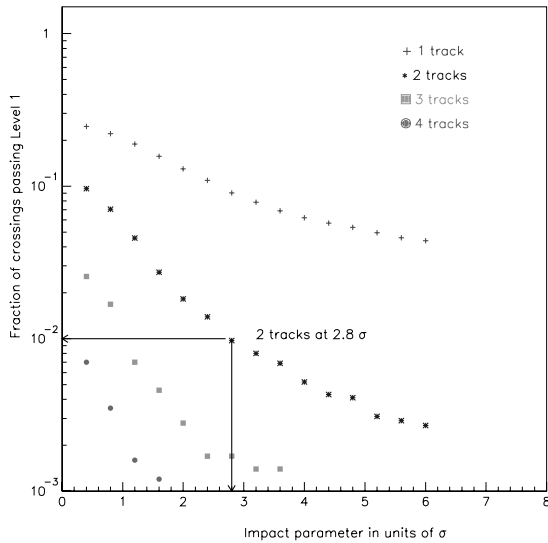


Fig. 4. Level 1 trigger background rejection. Trigger response for minimum bias events for a crossing time of 132 ns and an average of 2 interactions per bunch crossing.

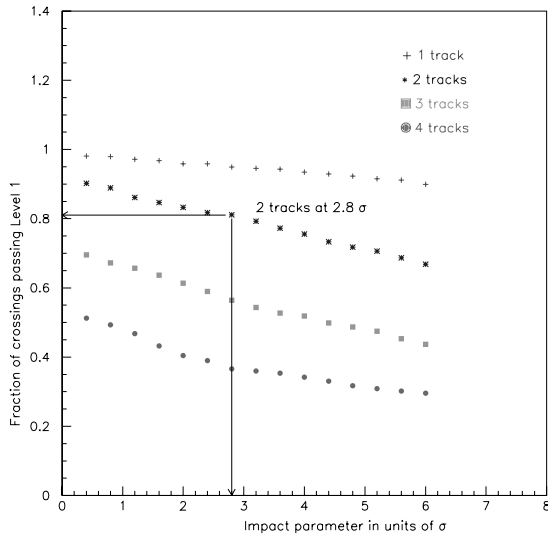


Fig. 5. Level 1 trigger efficiency. Trigger efficiency for $B_s \rightarrow D_s^+ K^-$ events with a crossing time of 132 ns and an average of 2 interactions per bunch crossing.

trigger saturation, less than 1% of crossings should pass the trigger; this is attained with the condition to have 2 detached tracks with $b/\sigma > 2.8$. With this condition and for the process¹ $B_s \rightarrow D_s^+ K^-$ we get 80% of efficiency (efficiency here means the fraction of the off-line reconstructable events that pass the trigger). Tab. 3 reports

Cuts	Values
Momentum p	> 3 GeV/c (implicit in the reconstruction)
Transverse momentum p_t	< 1.2 GeV/c (for track making the primaries) > 0.5 GeV/c (for candidate heavy flavour daughter tracks)
Impact parameter b	< 2 mm
b/σ_b	> 2.8
Primary multiplicity	> 3 tracks
Detached tracks	≥ 2

Table 3. Level 1 trigger cuts.

Process	Efficiency
Minimum bias	1%
$B_s \rightarrow D_s^+ K^-$	80%
$B^0 \rightarrow J/\psi K_s$	65%
$B^0 \rightarrow \phi K_s$	74%
$B^0 \rightarrow 2$ -body modes ($\pi^+ \pi^-$, $K^+ \pi^-$, $K^+ K^-$)	80%

Table 4. Level 1 trigger efficiencies for (first entry) crossings containing only minimum bias events and (remaining entries) crossings also containing B decays.

the Level 1 trigger cuts, used to compute the efficiencies reported in Tab. 4, for a crossing time of 132 ns and an average of 2 interactions per bunch crossing.

7 Conclusions

The BTeV main features of tracking and vertexing at Level 1 trigger, have been implemented with Silicon pixel detectors, for which custom chips (FPIX) has been developed and successfully tested. The simulation results indicate a very promising background rejection and a very high efficiency on all the B -decay modes.

References

1. Fermilab web site: <http://www.fnal.gov>.
2. BTeV Technical Design Report, Chapter 11, The BTeV Trigger (contact erik@fnal.gov).
3. BTeV Technical Design Report, Chapter 12, Event Read out and Control System (contact votava@fnal.gov).
4. BTeV Technical Design Report, Chapter 4, The Pixel Vertex Detector (contact swalk@fnal.gov).
5. Altera web site: <http://www.altera.com/products/devices/devindex.jsp>
6. Xilinx web site: <http://www.xilinx.com>

¹ $D_s^+ \rightarrow \phi \pi^+$, $K^{*0} K^+$.

Track and Vertex Reconstruction in CMS for Key Physics Processes

P. Vanlaer, for the CMS collaboration

Interuniversity Institute for High Energies, Université Libre de Bruxelles

Abstract. Track and vertex finding in LHC experiments are challenging tasks: combinatorial pattern recognition algorithms have to be made fast enough to allow the use of tracks and vertices at trigger level, in spite of the high charged particle multiplicity expected. In addition, precise estimation of track and vertex parameters is rendered difficult by the large background of soft tracks, noise hits, and non-Gaussian tails of the hit resolutions and of multiple scattering. In this paper, we describe track and vertex finding in the CMS experiment, with an emphasis on their application at High-Level Trigger. We also describe the application of robust fitting techniques to track and vertex reconstruction in CMS, in order to reduce the effect of noise and non-Gaussian tails.

1 Introduction

The CMS Tracker is a cylindric detector of 5.5 m in length, 1.1 m in radius. It is equipped with silicon pixel detectors for the innermost part ($R < 14$ cm, $|z| < 50$ cm) and silicon strip detectors for the outer layers ($R < 110$ cm, $|z| < 275$ cm). The pixel detectors provide 2 to 3 three-dimensional hits with a precision of about $10 \mu\text{m}$ in $R\phi$ and $15 \mu\text{m}$ in z . The strip detectors measure 8 to 14 hits with a precision ranging from $10 \mu\text{m}$ to $60 \mu\text{m}$ in $R\phi$, 5 hits being doubled by an additional measurement in a tilted projection. The tracker acceptance extends up to $|\eta| = 2.4$ [1]. A longitudinal section of one quarter of the CMS tracker is shown in Figure 1

To cope with the rate of background events at the LHC, a large fraction of the detector data will be analysed online for event selection. The CMS trigger system consists of a hardware Level-1 trigger, provided by the calorimeters and the muon system, and a software High-Level Trigger (HLT) running on a farm of a few thousand commercial processors. The data from the tracker become available right after the Level-1 trigger. This allows the use of the tracker at early trigger stages, provided that reconstruction algorithms can be made fast enough. The use of standard processors in the HLT farm makes it possible to use offline-quality code online, providing a high flexibility for the trigger, and avoiding code duplication.

In this paper, we describe track and vertex reconstruction in the CMS experiment, for both offline and online applications. In section 2 the CMS track finding is described, with an emphasis on the techniques that have been developed to reduce computation time. At extremely high particle densities like in Heavy Ion collisions, the default track finding has to be further adapted. The modifications are also described in section 2. In section 3 the Gaussian-Sum technique introduced to account for non-Gaussian tails in

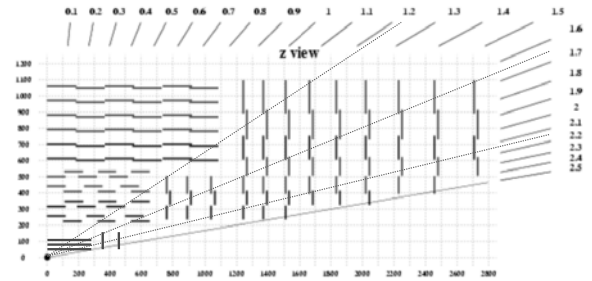


Fig. 1. Longitudinal section of one quarter of the CMS tracker. Pixel detectors are located at $R < 140$ mm, $|z| < 500$ mm, double silicon strip modules equip two barrel layers and two endcap rings at $200 \text{ mm} < R < 400$ mm, as well as two barrel layers and one endcap ring at $600 \text{ mm} < R < 700$ mm, and single silicon strip modules equip the remaining layers and rings.

track fitting is explained. Results for low momentum electrons are shown. In section 4 vertex finding in CMS is presented, with an emphasis on online primary vertex finding. Robust vertex fitting techniques, introduced in order to reduce the influence of mis-measured and mis-associated tracks on the vertex precision, are discussed in section 5.

2 Track reconstruction

2.1 Offline track reconstruction

Offline track reconstruction in CMS proceeds as follows:

- initial track segments (seeds) are searched for by combining 2 hits in the pixel layers, compatible with a helix originating from the beam spot area within some tolerance;
- each track seed is grown into a track using a Kalman filter [2] algorithm. Successive steps of extrapolation into the next detection layer, and improvement of the track parameters by including compatible hits, are performed. Track building proceeds until the outermost tracker layer is reached, or until no hits are found in two successive layers. The latter condition traduces the fact that, with efficient and hermetic detection layers, particles cannot cross two successive layers without leaving a hit. Hence, efficient and hermetic detection layers are of great help in reducing the amount of track candidates to be grown;
- duplicated tracks are removed on the basis of the number of hits shared;
- a final track smoothing [2] is performed, providing optimal precision of the track parameters all along the particle trajectory, in particular at the interaction region and at the entry point into the electromagnetic calorimeter.

This procedure is called the combinatorial Kalman filter.

The efficiency to reconstruct tracks with the combinatorial Kalman filter is $\sim 98\%$ for single muons with $1\text{GeV}/c < p_T < 100\text{GeV}/c$ and $|\eta| < 2$. In the range $2 < |\eta| < 2.4$ the efficiency drops progressively, due to the reduction of acceptance. The efficiency for single pions is lower, about 85%, due to nuclear interaction with the tracker material.

The transverse momentum (p_T) and transverse impact parameter (d_0) resolutions as a function of $|\eta|$ are shown in Figures 2 and 3, for single muons with different p_T values. At high p_T , the transverse momentum resolution is determined by the spatial resolution of the pixel and strip detectors. The p_T resolution degrades at $|\eta| > 1.7$, for particles exiting the tracker at $R < 1.1$ m. In the range $p_T \leq 10$ GeV/ c , the p_T resolution is dominated by multiple scattering in the tracker material. The d_0 resolution also is determined by detector resolutions at high p_T , and by multiple scattering for $p_T \leq 10$ GeV/ c .

2.2 Track reconstruction at High Level Trigger

To allow fast track reconstruction at the High Level Trigger, the offline combinatorial Kalman filter must be combined with other techniques:

- **regional reconstruction.** Conical regions of interest are defined around calorimeter clusters or muon candidates reconstructed at Level-1 trigger, with the primary vertex of the hard $p-p$ collision as the origin of

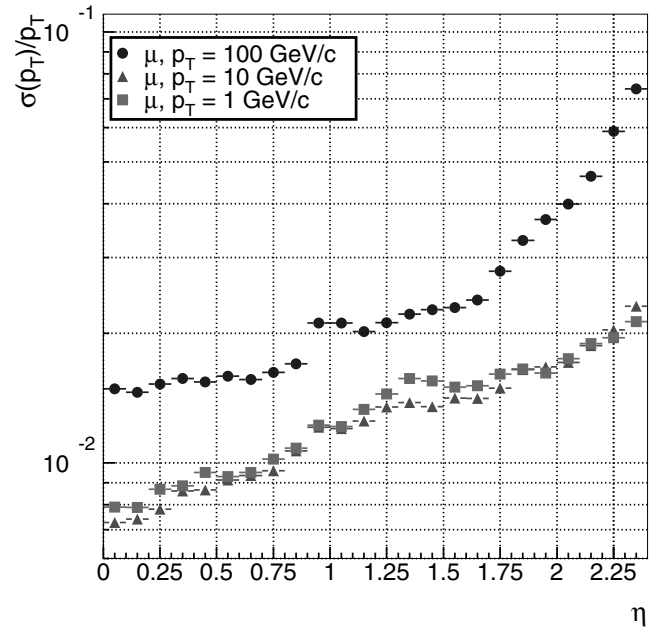


Fig. 2. Relative transverse momentum resolution for single muons with different p_T values as a function of the pseudorapidity $|\eta|$ [3].

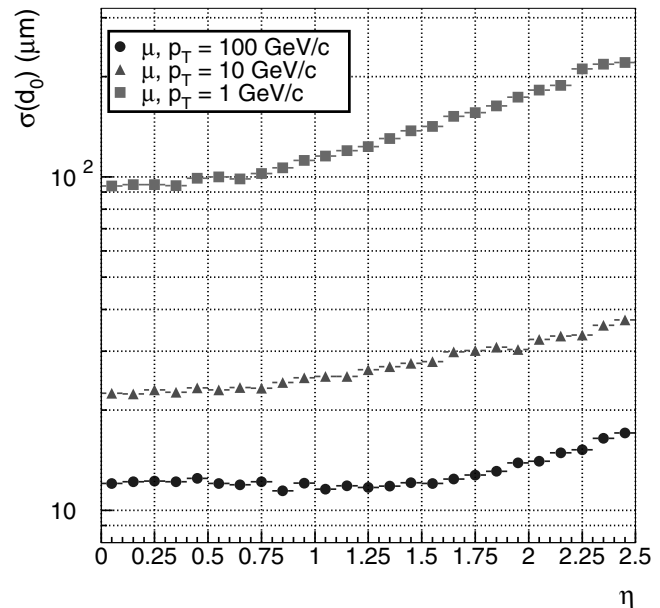


Fig. 3. Transverse impact parameter resolution for single muons with different p_T values as a function of the pseudorapidity $|\eta|$ [3].

the cone. Since the LHC beam spot has a large RMS of 5.3 cm in z , a fast reconstruction of the primary vertex must be performed to better define the cone origin. This reconstruction is described in section 4.

- **partial reconstruction.** Track reconstruction stops as soon as the precision of the track parameters is sufficient for event selection. Figure 4 shows the transverse impact parameter resolution of tracks in b -jets as a function of the number of hits for tracks with

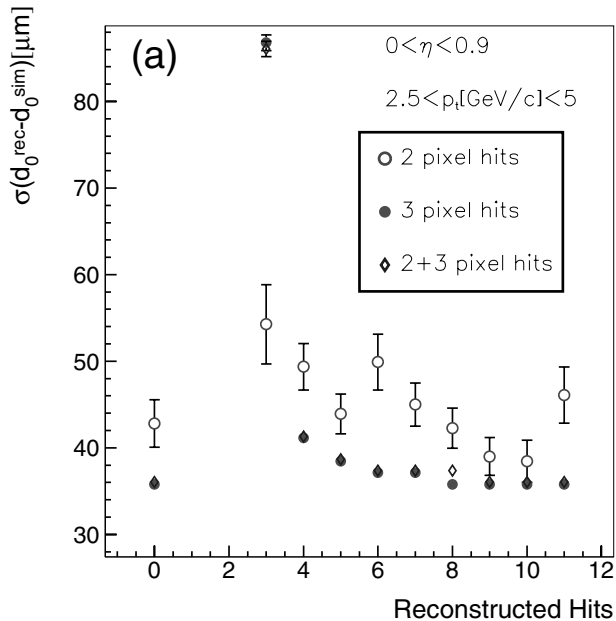


Fig. 4. Transverse impact parameter resolution as a function of the number of hits used to reconstruct tracks in b -jets, 0 hits denoting complete tracking [3].

$2.5\text{GeV}/c < p_T < 5\text{GeV}/c$. Tracks with 5-6 hits are reconstructed with a precision comparable to the offline reconstruction, while the processing time is reduced by a factor around 1.4 [3].

2.3 Track reconstruction in Heavy Ion collisions

In heavy ion collisions the extremely high particle density of up to 3000 charged particles per unit rapidity in central events leads to a very high detector occupancy in the silicon strip detectors. To cope with the resulting combinatorial problem the default track reconstruction procedure needs to be modified as follows:

- The seeding of the track reconstruction relies on triple-hit combinations in the pixel detectors to achieve more precise initial estimates of the track parameters.
- Merged hits are recognised in the silicon strip detectors by comparing the found cluster width with the width expected from the angle of the trajectory to the detector surface. An error proportional to the cluster width is assigned to merged hits.
- In the final smoothing step, hits in the double silicon strip layers are split and treated as separate hits.

To protect against fake tracks the final track sample can be selected based on the quality of the reconstructed tracks. The reconstruction quality can be addressed by the number of reconstructed hits on the track, the χ^2 -probability of the track fit and the compatibility of the track with the event vertex.

With these modifications a high algorithmic reconstruction efficiency can be achieved in central heavy ion

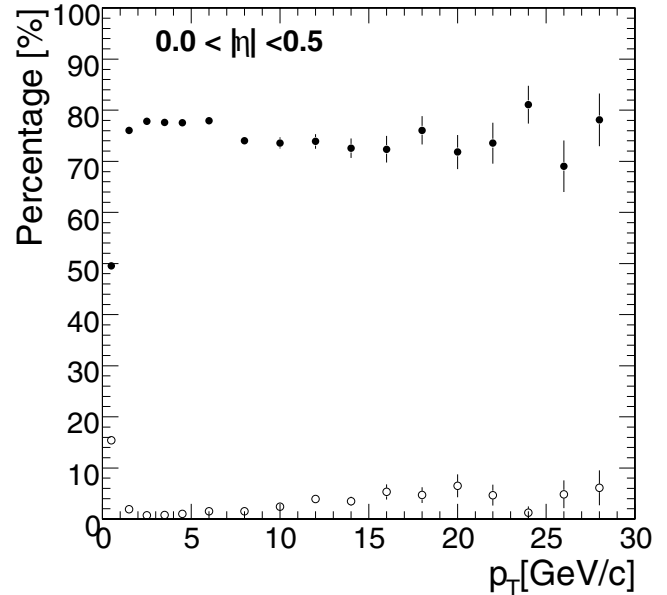


Fig. 5. Reconstruction efficiency (closed symbols) and rate of fake tracks (open symbols) as function of transverse momentum in the barrel region of the tracker for central Pb+Pb collisions with a charged particle density of $dN/dy \approx 3000$.

collisions while retaining a very low fake rate. Figure 5 shows the track reconstruction efficiency and rate of fake tracks as function of transverse momentum in the barrel region of the tracker for a track sample selected by requiring 12 hits on track (counting stereo hits as 2 hits), a χ^2 probability bigger than 1% and a 3 sigma compatibility cut with the event vertex. The momentum and impact parameter resolution achieved in heavy ion collisions is comparable to the resolution in low occupancy $p-p$ events [4].

3 Gaussian-Sum track reconstruction for electrons

Several advanced track fitting techniques have been introduced in CMS: the Deterministic Annealing Filter [5], aiming at reducing the effect of noise hits by attributing them a low weight in the track fit, the Multi-Track Fit [5], a simultaneous fit of several tracks suited to very dense jets, and the Gaussian-Sum Filter (GSF). The Gaussian-Sum Filter is an algorithm which is suitable when the energy loss is non-Gaussian, like in the case of bremsstrahlung from electron tracks, and when measurement errors are not Gaussian. It will be described further below. The application of the Deterministic Annealing Filter and the Multi-Track Fit to track fitting will not be described here, but similar techniques applied to vertex fitting will be discussed further in the text.

The CMS tracker contains a significant amount of material due to the silicon detectors and to services (from 0.4 up to 1.4 radiation lengths depending on η). The bremsstrahlung energy loss distribution of electrons propagating

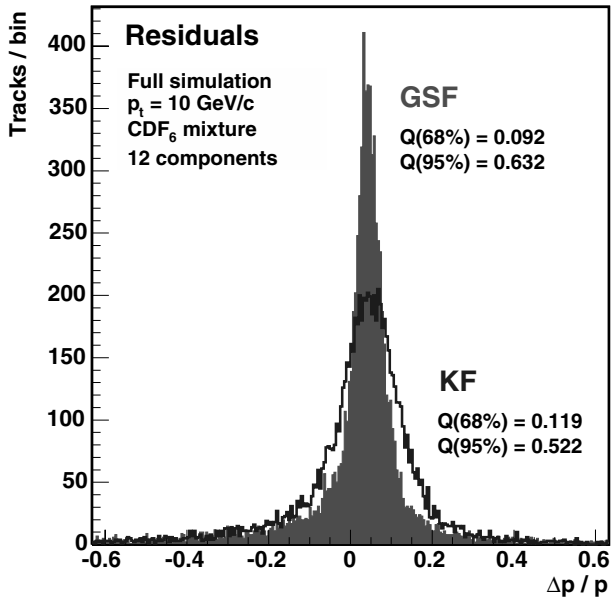


Fig. 6. Residual distribution of the momentum for the Gaussian-Sum Filter (solid histogram) and the Kalman filter (open histogram) for electrons with a p_T of 10 GeV/ c . A six-component mixture has been used to approximate the energy loss, while the track parameters are described by a twelve-component mixture.

in matter is described by the Bethe-Heitler model and it is highly non-Gaussian. With the Gaussian-Sum Filter, the energy loss distribution is modeled by a mixture of Gaussian components. The track parameters also become distributed like a Gaussian mixture. The GSF is implemented as a number of Kalman filters running in parallel, where each Kalman filter corresponds to the combination of one component of the energy loss distribution with one component of the track parameter distribution. The combination of each component of the track parameters with each component of the energy loss at each detection layer leads to an exponential explosion of the number of components. In order to limit this number, components are merged together according to a given distance definition and replaced by a single Gaussian [6]. This merging is done at each detection layer.

Figure 6 shows the distribution of the momentum residuals, for electrons with $p_T = 10$ GeV/ c reconstructed with the Kalman filter and the GSF. The improvement of the GSF with respect to the Kalman filter is significant on the core of the residuals distribution, while tails are slightly reduced. The irreducible tails in the momentum residuals are due to the fact that the radiation in the innermost layer of the Tracker can not be detected. This effect can be partially compensated by including a vertex constraint. In addition, an improvement is expected if also the measured positions are modeled by a mixture of Gaussians.

Since the GSF accounts for track kinks due to bremsstrahlung, the selection of the electron track hits can be refined. Figure 7 shows a comparison of the distributions

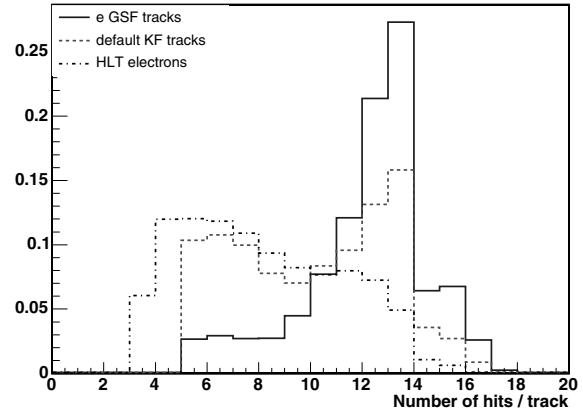


Fig. 7. Distributions of the number of hits in a reconstructed electron track, for offline electron track reconstruction based on the GSF (e-GSF), for standard offline track reconstruction (default KF), and for High-Level Trigger electron reconstruction (HLT electrons).

of the number of hits, for offline electron track reconstruction based on the GSF (e-GSF), for standard offline track reconstruction (default KF), and for High-Level Trigger electron reconstruction (HLT electrons). GSF-based tracking selects most electron hits, i.e. up to the outer tracker layer. A precise estimate of the electron momentum is provided at each tracker layer. The difference in momentum at the primary vertex and at the electromagnetic calorimeter surface shows, when using GSF-based tracking, a strong correlation with the simulated bremsstrahlung photon energy. This correlation could thus be used in order to detect electrons which have radiated a significant fraction of their energy [7].

4 Vertex Finding

Vertex reconstruction typically involves two steps: *vertex finding*, where clusters of tracks originating from the same vertex are grouped together as vertex candidates, and *vertex fitting*, where, from a set of tracks, the most compatible vertex position is computed and used to constrain track parameters at the vertex. The reconstruction of primary vertices can be performed at an early stage, using the Pixel detector alone. The first estimation of the primary vertex of the hard event is used to constrain track reconstruction (regional reconstruction).

4.1 Online vertex finding with the Pixel detector

The first estimation of the z -coordinate of the primary vertex is obtained with the only Pixel detector response. A fast tracking is performed in order to find sets of three hits compatible with a track (tracklets), to be used as inputs to the vertex finding. Two algorithms have been implemented in CMS [8]:

- the *Histogramming method* which clusterizes tracklets on the basis of their longitudinal impact parameter;
- the *Divisive method* which iteratively discards tracklets incompatible with the vertex estimate and recover discarded tracklets to make a new vertex.

Several vertices are reconstructed. The vertex from the hard event is then identified from the p_T of the tracklets associated to it. The efficiency ε to find a primary vertex within $\pm 500 \mu\text{m}$ from the simulated primary vertex, as well as the efficiency ε_{tag} to find and identify it, are given in table 1. The numbers are close to 100% for most event topologies. In the $H(115\text{GeV}/c^2) \rightarrow \gamma\gamma$ and $B_s^0 \rightarrow J/\psi\phi \rightarrow \mu^+\mu^-K^+K^-$ channels the identification of the hard vertex is more difficult and several primary vertex candidates have to be considered in the analysis.

Table 1. Efficiencies of primary vertex finding for the Histogramming and Divisive Pixel primary vertex finding algorithms (see text for definitions of ε and ε_{tag}).

	Histogram		Divisive	
	ε	ε_{tag}	ε	ε_{tag}
u -jets; $E_T = 100\text{GeV}$	0.99	0.98	1.00	0.99
u -jets; $50 < E_T < 100\text{GeV}$	0.97	0.90	0.99	0.94
b -jets; $E_T = 100\text{GeV}$	0.98	0.96	0.99	0.99
b -jets; $30 < E_T < 50\text{GeV}$	0.97	0.89	1.00	0.96
$H(115\text{GeV}/c^2) \rightarrow \gamma\gamma$,	0.89	0.75	0.94	0.80
g -fusion				
$H(150\text{GeV}/c^2) \rightarrow ZZ \rightarrow 2e2\mu$	0.97	0.96	1.00	1.00
$B_s^0 \rightarrow J/\psi\phi$	0.81	0.61	0.97	0.68
$t\bar{t}$	0.99	0.98	1.00	1.00
$t\bar{t}H, H(120\text{GeV}/c^2) \rightarrow b\bar{b}$	1.00	0.99	1.00	1.00

4.2 Offline vertex finding

The offline vertex finding process is accomplished in two steps: first of all, primary vertices are reconstructed, identifying the one which triggered the event. Then, in b -jet candidates, the reconstruction of displaced vertices is performed.

The main algorithm to search for primary and secondary vertex implemented in CMS adopts a divisive approach. Tracks with less than 5% compatibility to the vertex candidates are discarded and the search for secondary vertices follows among the discarded tracks. The efficiency to find the trigger primary vertex in $b\bar{b}$ with b -jet $p_T = 100 \text{ GeV}/c$ events is 95% with no pile-up and decreases to 92% at low luminosity.

In Figure 8 the efficiency to find secondary vertices in b -jets with a p_T of 100 GeV/ c and $|\eta| < 0.9$ is shown as a function of the transverse impact parameter significance of the track with the second largest significance, and for two different requirements on the track association purity of the reconstructed secondary vertices. With a purity above 50%, the efficiency to find a secondary vertex in a b -jet is around 48%, that allows an efficiency to identify b -jets of about 50% with a mistagging rate below 1% [3].

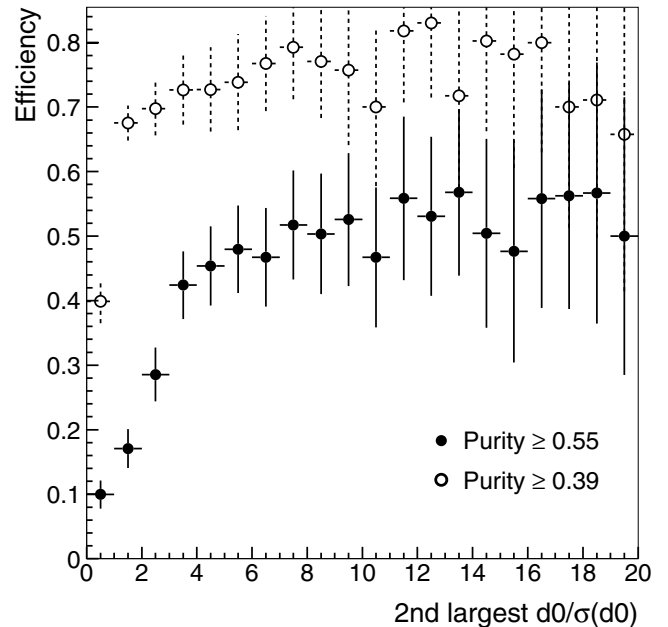


Fig. 8. Secondary vertex finding efficiency in b -jets of $p_T = 100 \text{ GeV}/c$ and $|\eta| < 0.9$, as a function of the transverse impact parameter significance of the track with the second largest significance in the vertex, for two different requirements on the track association purity of the reconstructed secondary vertices [3].

5 Vertex Fitting

Vertex fitting usually consists in a least-squares fit formulated as a Kalman filter. This method can be shown to be optimal when the measurement uncertainties are Gaussian and the vertex candidate is not contaminated by mis-measured or mis-associated tracks (*outliers*). Since none of these conditions will hold for the real data at the LHC, robust statistical methods have been envisaged for vertex fitting in CMS, as the *Trimmed* and the *Adaptive Vertex Fitters* [9, 10].

The Trimmed Vertex Fitter iteratively discards tracks on the basis of their compatibility to the vertex, starting from the worst, until no incompatible track is found. The Adaptive Fitter is a re-weighted least-squares fit, where tracks are down-weighted by a factor which is a sigmoidal function of the reduced track-vertex distance $\chi_{track} = (x_{track} - x_{vertex})/\sigma_{track}$. The weights are fractional (soft assignment) and are adapted in the course of iteration.

In order to have a better treatment of non-Gaussian tails of measurement errors, a Gaussian-Sum Vertex Fitter has also been developed and implemented. The performance of the Gaussian-Sum Vertex Fitter for simplified Monte-Carlo events is detailed in [11] and will not be discussed here.

The resolution, tails (95% coverage) and width of the pulls obtained with the least-squares, adaptive and trimmed fitters are listed in table 2 for different types of vertices. The adaptive and trimmed fitters are consistently more precise than the least-squares method. Tails in the

Table 2. Resolutions, tails (95% coverage) and width of the pulls for the Kalman, Adaptive and Trimmed Vertex Fitters, for the primary vertex of the $t\bar{t}H$ and $B_s^0 \rightarrow J/\psi \phi$ channels, as well as the secondary vertex of the $B_s^0 \rightarrow J/\psi \phi$ channel. The effect of track misassociations is not accounted for.

Filter	x -coordinate			z -coordinate		
	σ [μm]	Tails [μm]	Pull	σ [μm]	Tails [μm]	Pull
$t\bar{t}H$						
Kalman	16.7	102	1.41	20.1	117	1.31
Adaptive	12.2	28.0	0.97	16.2	41.8	0.97
Trimmed	12.4	28.8	0.98	16.6	43.0	1.00
$B_s^0 \rightarrow J/\psi \phi$ - primary vertex						
Kalman	44.1	176	1.11	54.3	224	1.07
Adaptive	38.4	94.9	0.94	48.7	140	0.94
Trimmed	39.4	98.7	0.97	49.5	144	0.95
$B_s^0 \rightarrow J/\psi \phi$ - secondary vertex						
Kalman	54.8	164	1.08	73.8	471	1.08
Adaptive	53.6	155	1.02	73.0	440	1.02
Trimmed	54.0	174	1.04	75.0	502	1.05

vertex position residuals are largely reduced. The improvement is more pronounced in vertices with larger track multiplicity [10]. It has however to be noted that the tracks included in the vertex are selected using Monte-Carlo generator information. The effect of track misassociations is thus not yet included.

6 Conclusions

Simulation studies show that the CMS experiment has a robust and versatile central tracker, able to operate in the challenging environment of the LHC. The combinatorial Kalman filter algorithm developed for track reconstruction in CMS yields high track reconstruction efficiency, 98% for isolated muons within acceptance. The pixel detector located nearest to the beam is a key element: it is able to provide high-quality track seeds even at High-Level Trigger. This in turn allows primary vertex finding to be performed at High-Level Trigger. The identification of the primary vertex of the hard $p-p$ collision is useful in order to restrict tracking to particles originating from that vertex. Such techniques make track reconstruction fast enough to be used at High-Level Trigger, which will be an important asset for background rejection at the LHC. It has also been shown that the standard track finding can be adapted to perform track finding in Heavy Ion events, yielding a track finding efficiency of about 75%.

Powerful statistical techniques have also been introduced in order to robustify track and vertex fitting. The Gaussian-Sum track fit is well-suited to treat the Bethe-Heitler energy loss distribution of bremsstrahlung in electron reconstruction. In vertex reconstruction, Trimming and Adaptive methods are shown to improve the vertex position resolution and reduce resolution tails.

Track and vertex reconstruction software in CMS is well-advanced. Benchmark analyses, meant to ensure the readiness of the CMS reconstruction and analysis software

before LHC startup, will test this software further and ensure that the required functionality is available.

References

1. The CMS Collaboration, *The Tracker Project Technical Design Report*, CERN/LHCC 98-6.
CMS Collaboration, *Addendum to the Tracker TDR*, CERN/LHCC 2000-016.
2. R. Frühwirth, *Nucl. Instrum. Methods A* **262** 444 (1987).
3. The CMS Collaboration, *The Trigger and Data Acquisition Project*, CERN/LHCC 2002-26.
4. Ch. Roland, *Track Reconstruction in Heavy Ion Events using the CMS Tracker*, CMS Analysis Note 2005-023.
Ch. Roland, *Status of the Track Reconstruction Package for Heavy Ion Events in the CMS Tracker*, CMS Rapid Note 2003/003.
5. M. Winkler, PhD. Thesis, CMS Thesis 2002-015, Vienna University of Technology and CERN, 2002.
6. W. Adam, R. Frühwirth, A. Strandle and T. Todorov, CMS NOTE 2005/001.
7. C. Charlot, C. Rovelli, Y. Sirois, *Reconstruction of Electrons at Low PT Using Gaussian Sum Filter Tracks*, CMS Note in preparation.
8. S. Cucciarelli, M. Konecki, D. Kotlinski, T. Todorov, CMS NOTE 2003/026.
9. R. Frühwirth, J. D'Hont, P. Vanlaer, W. Waltenberger, CMS NOTE 2004/002.
10. T. Speer, K. Prokofiev, R. Frühwirth, W. Waltenberger, P. Vanlaer, *Vertex Fitting in the CMS Tracker*, CMS Note in preparation.
11. R. Frühwirth, T. Speer, CMS NOTE 2005/005.

CDF computing and event data models

F.D. Snider¹ for the CDF Collaboration

Fermi National Accelerator Laboratory, Batavia, IL 60510, USA

Abstract. We discuss the computing systems, usage patterns and event data models used to analyze Run II data from the CDF-II experiment at the Tevatron collider. A critical analysis of the current implementation and design reveals some of the stronger and weaker elements of the system, which serve as lessons for future experiments. We highlight a need to maintain simplicity for users in the face of an increasingly complex computing environment.

1 Introduction¹

High performance computing is an essential component of most modern high energy physics experiments. In general terms, the computing resources required to produce physics results scales linearly either the total number of events, the total data volume or the average event logging rate. For many experiments such as CDF [1], the resulting demand for computing increases dramatically over the life of the experiment. The maximum data logging rate, for instance, will increase by a factor of three between 2004 and 2006; the volume of archived data during the final four years of operation will more than quadruple the volume of data from the first three. In short, the computing problem becomes more difficult with time and requires increasingly sophisticated and robust solutions to ensure that the systems scale stably. At the same time, users must be provided tools that hide the underlying complexity and make computing on increasingly large scales appear “simple”.

The general computing strategy revolves around three basic principles. First, centralize and automate control of common and repetitive computing tasks, such as full event reconstruction, Monte Carlo (MC) production and major dataset stripping. Second, distribute computing hardware as needed to perform user analysis and MC production since no single facility can host the required computing. Finally, provide users with stable, simple interfaces to the broad range of resources deployed, thereby allowing them to focus on what they are computing rather than on the mechanics of how to do it.

In this talk, we describe the major elements of the CDF computing model, the current migration toward grid-based distributed computing to meet the increasing computing demands of the experiment and the mechanisms by which users access this computing power. We will then discuss some details of the Event Data Model (EDM), the principal interface between users and the data, the de-

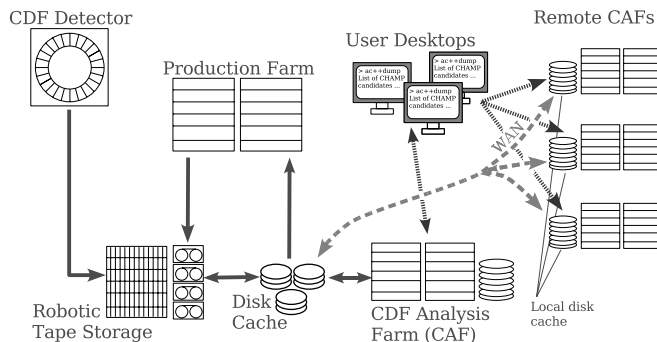


Fig. 1. CDF computing systems and data flow

iciencies of the EDM and several general ways to increase productivity through a better approach to the EDM. Finally, we review some of the strengths of the current computing model.

2 Computing model and data flow

The central CDF computing systems consist of five major hardware components, as shown in Fig. 1: robotic data archive and disk cache; the “production farm”; local and remote CDF Analysis Farms (CAF) [2]; and interactive systems both at Fermilab and at remote institutions. Various collaborating institutions host the remote CAFs.

The arrows in Fig.1 represent the data flow, which proceeds as follows. Raw data from the detector is first logged in the tape archive. It is then read into a disk cache, served to the production farm where full event reconstruction takes place and written back into the tape library. The production output is copied into another disk cache where it is served to the CAF or distributed to remote CAFs for further reduction and analysis. Users submit analysis jobs from interactive computers (primarily desktops and laptops) located anywhere to any of the CAFs. Results

¹ Work supported by the U.S. Department of Energy under contract No. DE-AC02-76CH03000.

from the CAFs are written to the disk cache, into the tape archive or returned directly to the user.

A Data Handling (DH) system automates the cataloging and movement data between various elements of the computing system as well as delivery to analysis jobs. All data stored in the tape archive are under control of the DH system; a significant fraction of data in the disk cache is not.

3 Computing systems

In this section, we briefly describe salient details of the major computing systems.

3.1 Data archive and storage systems

Data from the experiment is archived in a robotic tape library with a total capacity of 2.2 PBytes using the existing tape technology. The total will grow to about 6 PBytes through the life of the experiment. A bank of 18 tape drives, each with a bandwidth of about 30 MBytes/sec, provides I/O to the contents of the library. A disk cache of approximately 370 TBytes stages data from the archive and from analysis jobs.

3.2 Data handling system

The Data Handling system is perhaps the most important and technically demanding of the various computing systems and consumes by far the largest development effort. Since all interactions with data involve the DH system, performance, robustness and scalability through the duration of the experiment are the paramount concerns.

The DH system fills several important roles. First, it archives the data and provides a metadata catalog by which the data can be managed. Upon request, the system provides high bandwidth channels to individual data files, moving data as needed to deliver a file or achieve high throughput, and organizing access to multiple files in an efficient manner. Throughout these operations, the DH system ensures the integrity of all delivered data. Details of these transactions are transparent to the user. The two major components providing these services are "SAM" (Sequential Access via Metadata [3]) and "dCache" [4].

The dCache system distributes data across an arbitrary number of local file-servers and mediates tape transactions. Clients specify files using fixed, location-independent identifiers. The system associates these identifiers to the physical locations and returns a direct I/O channel to the client. Each day, upward of 100k such file transactions are processed, routinely delivering up to 75 TBytes. More typical volumes are in the range of 10–25 TBytes per day, of which 5–10 TBytes are restored from tape.

SAM expands upon the capabilities of dCache by providing support for highly distributed data. SAM also includes features designed to aid handling of large datasets,

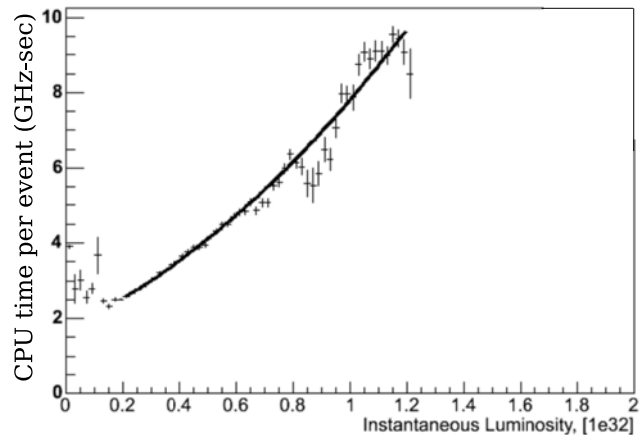


Fig. 2. Reconstruction CPU time per event. The time is approximately linear to luminosities of $2 \times 10^{32} \text{ cm}^{-2}\text{s}^{-1}$.

such as a simple mechanism to create datasets based upon metadata queries, storage of file tracking information to facilitate data processing and tools to automate certain processing tasks. The production farm uses SAM to automate most tasks. At the time of writing, SAM is in the final stages of deployment to general users.

3.3 Production farm

The objective of the production farm is to reconstruct all raw data from the experiment as soon as possible after data taking. As the most predictable of the computing problems, all production tasks can be fully automated. The required computing is easily calculated from the event logging rate (130 Hz in FY2005 and 220 Hz for FY2006 and beyond), the average instantaneous luminosity (upward of $10^{32} \text{ cm}^{-2}\text{s}^{-1}$ in FY2006 and beyond) and the required CPU time per event (Fig. 2).

The processing strategy for the production farm has three steps. In the first, a fraction of the data is processed within three days of data taking to provide data quality monitoring. The accumulated monitoring data from the previous month is analyzed in the second step to produce final calibration constants. Finally, all the data from that month is processed using final calibrations, typically within four to eight weeks after data taking. Using this scheme, the data from a given year is processed about 1.3 times with no later re-processing required.

With 150 dual processor PC's providing the equivalent of about 1.2 THz of PIII CPU's or 48k SpecInt2k's, the current farm can process about 18 million events per day. Processing can expand into the CAF as needed in order to provide short term increases in throughput.

3.4 CDF Analysis Farm

The CAF [2] is the primary analysis platform for the experiment and contains the bulk of the available computing capacity. Activities on the CAF fall into three major

categories. The first is user analysis, consisting of ntuple creation and analysis, and all other CPU-intensive calculations. Semi-coordinated activities run by the physics groups represent the second major set of tasks, and include secondary and tertiary dataset production and experiment-wide ntuple production. The final category includes production of large-scale MC datasets. Monte Carlo production and experiment-wide ntuple creation present reasonably predictable loads on the system, some of which scale with the rate of data taking. User analysis is less predictable and typically scales with the full dataset size.

CAF installations at nine remote institutions² contain approximately 40% of the 5.6 THz (PIII equivalents) of analysis computing at CDF. All installations exhibit near 100% utilization. The CAF at Fermilab typically processes in excess of 10k jobs per day for about 100 users.

3.4.1 CAF usage

Over the first 10 months of 2005, about 50% of the load on the CAF at Fermilab was in analysis of production output data, 20% in analysis of ntuple, 20% in MC generation and the balance in unidentified activities (see Fig. 3). At remote CAFs, the load fractions were about 40% in MC generation and 50% in either production data or ntuple analysis. Among organized analysis activities, the B-physics group consumed the majority of CPU cycles (Fig. 4).

Analysis jobs on production data required an average of 0.75 seconds of CPU per event (Fig. 5). About 20% of these jobs consumed more than one second per event and represented about 40% of the total CPU used in production data analysis. For comparison, event input and unpacking requires about 60 msec per event.

The long tail in Fig. 5 results from track re-fitting and vertex finding. These tasks are integral parts of a typical B-physics analyses and others that exploit the precision tracking available at CDF. Both of these tasks require the full analysis framework and must therefore occur in jobs that process production data rather than ntuple.

3.4.2 CAF user-level features

Simple graphical and command-line interfaces provide access to the resources within the CAF. Users specify a file to execute, the number of parallel segments that should be run and the site at which the jobs should be executed. The system creates a tarball from the input directory, ships it to the appropriate nodes and executes the specified file. Output can be directed to any location to which the user has write access. A number of quasi-interactive features are also available, such as the ability to look at log files or

² The institutions hosting remote CAFs are CNAF, Bologna, Italy; KNU, Korea; Academia Sinica, Taiwan; University of California at San Diego; Rutgers University; University of Toronto; Tsukuba, Japan; Cantabria, Spain; and Massachusetts Institute of Technology.

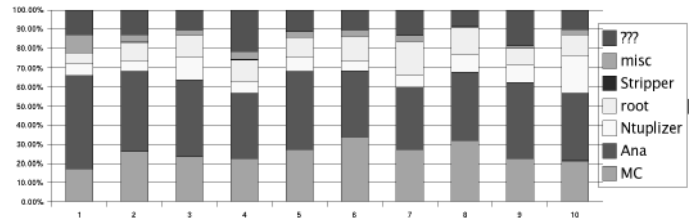


Fig. 3. CAF usage by task for the first 10 months of 2005. The task classifications include: Monte Carlo generation (“MC”); three categories of production output analysis (“Ana”, “Ntuplizer”, “Stripper”); analysis of ntuple using root (“root”); various small categories (“misc”); and unknown (“???”).

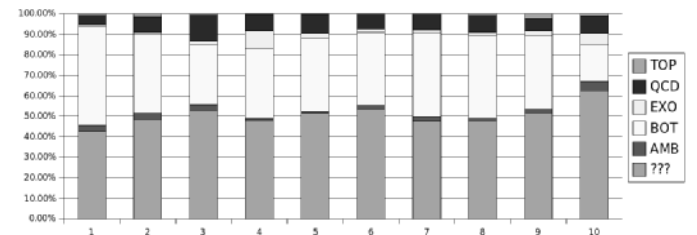


Fig. 4. CAF usage by physics group for the first 10 months of 2005. The group classifications correspond to top physics, QCD, searches for exotic particles, and bottom quark physics. The physics group affiliation could not be determined for jobs in the “???” category.

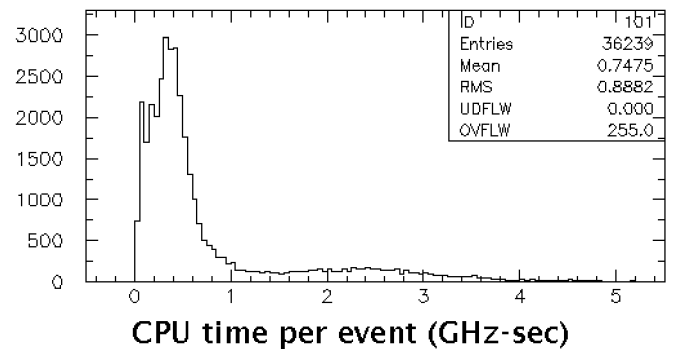


Fig. 5. CPU time per event for randomly selected analysis jobs that read production output files.

a directory listing on a specific worker node, or to connect a debugger to a running process on a worker node. Monitoring of CPU, memory and status for individual processes is also available.

4 Grid migration plans

As collaborating institutions invest in large common pools of computing for the LHC, they will become increasingly reluctant to expand pools of computers dedicated to CDF. Indeed, some institutions will require that CDF computers be consolidated into shared, grid-based pools just to maintain access to existing computing capacity. In order to meet the increasing demand for off-site CPU, CDF must

therefore adopt the grid-based technologies and infrastructure that will enable utilization of computing in these shared pools. Grid technologies will also allow opportunistic use of more general Open Science Grid [5] (OSG) and LHC Computing Grid [6] (LCG) resources, which could deliver significant computing to CDF until LHC data taking begins.

The basic approach toward achieving interoperability with both OSG and LCG will be to adopt incremental changes, deploying functionality in stages and, if necessary, using partial solutions in the short term until more complete deployments are possible. Throughout this migration, the existing user interfaces will remain unchanged.

Recently, CDF has utilized the Condor “glide-in” [7] technique to gain access to computers within OSG and LCG shared pools. In this scheme, a small job submitted via the grid gatekeeper of the remote pool installs client software for a batch system on one or more worker nodes within the pool. This software contacts a locally maintained CAF headnode and registers the worker node as a worker in an associated virtual CAF. Jobs submitted to the headnode can then be routed to registered workers as if they belonged to a dedicated CAF. Upon termination of a job segment, the worker node can be returned to the common pool. Using a glide-in CAF effectively reduces the remote dedicated resources from a pool of computers to a single headnode.

At present, CDF operates glide-in CAFs at the LCG tier-1 center at CNAF in Italy and at OSG-based farms at Fermilab. Future worker node procurements for CDF at Fermilab will be added to the common OSG pool. Negotiations are now under way to deploy glide-in CAFs at several other sites.

The use of glide-in CAFs will suffice to meet our needs for at least the next year. In the mean time, efforts are under way to re-implement the CAF functionality using native grid tools under both LCG and OSG. When successful, no dedicated computing resources will be required at the remote site beyond local disk, which at the present time is needed in all grid implementations.

5 Event data model

The Event Data Model is the set of structures for raw and reconstructed data, typically stored within some larger shared data structure, and the associated user interfaces and utilities needed to locate, manipulate and store the data. Since the EDM provides the lowest-level contact with the data for all users, a well-designed interface and feature set is essential.

A simple example of an EDM is an ntuple. CDF physics groups maintain several standardized nuples, which are often created in some organized fashion. The CDF offline framework, however, uses a more complex EDM designed to address certain analysis issues and support specific features of the data from the experiment. A few of the basic features of the EDM are summarized below:

- EDM objects consist of fully-featured C++ objects with the following common attributes: a unique ID number, two independent description strings, a print method, an equivalence operator and a serialization function used to store (and restore) the object within a file.
- Once entered into the event record, data objects can no longer be modified, thereby preserving the processing history of the event.
- The EDM provides a number of standard containers so that arrays of objects or references to objects can be stored in the event record.
- Search utilities allow objects to be located based upon any combination of criteria, including the common attributes or internal data.

Several design features help prevent some of the most common programming errors encountered in earlier generations of the experiment. Making objects in the event read-only, for instance, prevents unrequested and unexpected modification of existing data within the event. Many of these features are disliked by a large fraction of the users, despite the benefits offered from a programming perspective.

5.1 Deficiencies of the EDM and advice for future EDM designers

In the opinion of the author, the EDM at CDF suffers from two significant problems.

1. There is far too much functionality built into data objects. As new C++ developers and novices in object-oriented design, many code authors created data objects that provided a number of complex features. An important example is the track object (of which the present company was a co-author), which includes a topological fitting interface and a rich class hierarchy. While both could in principle be useful, neither are used as intended. The class hierarchy, in fact, is rendered largely inaccessible due to the technical requirements of EDM-based containers. In both cases, however, all the associated code must be carried along even if the only quantities of interest are the track parameters or the number of hits within the tracking chamber.

Conclusion: All data objects should be very simple structures. Any extra functionality, such as that noted above for tracks, should be placed within auxiliary or helper classes that use the data objects as input. This design pattern adds flexibility and clarity, yet makes it no more difficult to use the more complex features.
2. The EDM is effectively tied to the offline analysis framework due in large measure to the integration of the serialization methods within the low-level objects. Since the reconstruction algorithms are written to use EDM objects, the entire body of primary reconstruction code, along with many useful tools and utilities, are held hostage to that same analysis

framework, despite the fact that neither the data nor the reconstruction algorithms have any intrinsic connection to the offline analysis framework.

Conclusion: The serialization methods should be separated from the EDM. A separation of the serialization methods would allow the EDM to be highly portable. An entirely root-based representation, for instance, could be rather trivially achieved. Then, by taking care to write reconstruction algorithms with respect to the low-level data structures alone, the entire reconstruction framework becomes portable as well. All the tools and utilities that are useful for analysis become liberated for use within an arbitrary ntuple environment, for instance. Such a scheme provides vastly more flexibility while retaining user-level simplicity.

6 Successes

Among the better aspects of the CDF computing model, the author notes the following.

- Development of the CAF and simple submission and monitoring tools, all of which have made using large computing resources “easy”.
- Adopted a computer language that supports highly structured data representations.
- Established and maintained a good physical design for offline software.
- Defined many sensibly defined datasets that are produced as output from the production farm. This step has greatly simplified many processing steps.
- Wrote a fast reconstruction program.

7 Summary

CDF has deployed over 5.6 THz of CPU deployed around the world. A simple job submission interface has led to very high utilization of these resources by a large number of collaborators. The C++ based EDM has facilitated the development of structured data representations, although many times at the cost of unnecessary complication stemming from a lack of discipline in low-level design. Finally, the continued need to increase the computing resources available to the experiment will drive the adoption of grid technologies.

The most important issue facing the future development of computing at CDF is the increasing complexity that accompanies growth in the scale of the computing problem. Maintaining robust and scalable data handling systems throughout this growth, for instance, is difficult. The need for other new technologies potentially further complicates this picture. Given these realities, it is imperative that we develop the tools and automation that make it simple for the user to marshal the resources needed to analyze data. Users should be well insulated from the underlying complexities and system details that have little

value to them. User interfaces must remain simple and stable. Ideally, the EDM, reconstruction and analysis tools should be context independent. In short, users should be able to focus on the physics rather than the computing problem. Success in this goal will require a determined effort, particularly by those physicists with a computing specialization.

8 Acknowledgments

The author thanks Mircea Coca, Ashutosh Kotwal, Elliot Lipeles, Pasha Murat, Liz Sexton-Kennedy and Igor Sfiligoi for valuable input during the preparation of this report.

References

1. A description of the CDF-II experiment can be found in D. Acosta, *et al.*, Phys. Rev. **D71**, (2005) 032001.
2. T.H. Kim *et al.*, IEEE Trans. Nucl. Sci. **51**, (2004) 892.
3. A. Baranovski *et al.*, FERMILAB-TM-2175 (2002); D. Bonham *et al.*, eConf **C0303241**, (2003) TUAT004.
4. See <http://www.dcache.org/>.
5. A. Pordes, FERMILAB-CONF-04-466-CD; the home page for the organization is at <http://opensciencegrid.org/>.
6. A. Pfeiffer *et al.*, Nucl. Instrum. Meth. A **534**, (2004) 106; the home page for the organization is at <http://lcg.web.cern.ch/LCG/>.
7. Details on Condor glide-in can be found at <http://www.cs.wisc.edu/condor/>.

Preparation for Analysis at CMS

Christian Weiser

Institut für Experimentelle Kernphysik
Universität Karlsruhe

Abstract. The Large Hadron Collider will start operation in 2007. This article describes the status of the tools needed to analyse the data once they are available.

1 Introduction

The CMS detector [1] is a general purpose detector currently being under construction to take data at the Large Hadron Collider (LHC), starting operation in 2007. Apart from the construction of the detector, big efforts are made to be prepared for the analysis of the data.

CMS is currently in the process of writing the Physics Technical Design Report (Physics TDR). One of the purposes of this document is to demonstrate the readiness of the software, the reconstruction and analysis tools and also the people's skills to get to real physics results from the data taken by the detector. The Physics TDR will come in two volumes. Vol. I will cover the detector performance and operations, the physics reconstruction tools and software and data issues. First-run plans (with about $1fb^{-1}$ of integrated luminosity) and the physics reach for different integrated luminosities will be discussed in Vol. II. Some full analyses, which have to be studied in all detail, including e.g. effects of a not perfectly aligned detector, will also be contained in Vol. II. These benchmark channels for the full analyses have been selected by the four PRS (Physics Reconstruction and Selection) detector groups in CMS in order to be adequate to test the reconstruction and analysis tools developed by that corresponding group. Figure 1 shows a summary.

Since reconstruction tools like e.g. muon, electron, jet, track and vertex reconstruction have been covered in other talks at this conference (see the corresponding contributions to these proceedings), this article focuses on how the existing tools are put together to perform an analysis in CMS.

2 Tools for Analysis

2.1 From Generator to Analysis

A large number of Monte Carlo generators are available in CMS, general purpose generators as well as dedicated generators for special processes. After the event generation,

ECAL-e/γ:	- $H \rightarrow \gamma\gamma$ - $H \rightarrow ZZ^{(*)} \rightarrow 4e$	γ id., ECAL resolution electron reconstruction
Muon:	- $H \rightarrow ZZ^{(*)} \rightarrow 4\mu$ - $H \rightarrow WW^{(*)} \rightarrow 2\mu$ - $Z' \rightarrow \mu\mu$	μ reconstruction and identification high stat. di-muons, jet veto high p_t muons
Tracker-b/τ:	- ttH ($H \rightarrow bb$) - $A/H \tau\tau$ - $B_s \rightarrow J/\psi \Phi$	b-tagging, top reconstruction τ tagging, trigger vertex reconstruction, low p_t tracking
HCAL-JetMET:	- SUSY (0.5 TeV) - qqH - $Z' \rightarrow \text{jet jet}$	jets, missing E_t , forward jets, trigger high p_t jets, di-jet mass resolution

Fig. 1. The benchmark channels of the PRS detector groups in CMS selected for the full analyses together with their main experimental challenges.

a full detector simulation is performed. CMS has successfully made the transition to a GEANT4 based object oriented framework (OSCAR [2]). However, a large number of events simulated with the old GEANT3 based detector simulation is also available. It follows the digitisation of the detector signals depending on the luminosity assumed. The final step is the DST (Data Summary Tape; see 2.2 for details) production where reconstructed physics objects are stored persistently. The DST is the data format used for the physics analyses. The steps described above are typically performed using GRID computing resources and tools [3]. The end user jobs analysing the DST can also be performed on the GRID. A dedicated job submission tool (CRAB = CMS Remote Analysis Builder) exists that takes care to find out where the requested data is located and to 'send the job to the data'.

2.2 Reconstruction Programs and DST

ORCA (Object-oriented Reconstruction for CMS Analysis) [4] is the program that contains the reconstruction algorithms to be used both offline and in the High Level Trigger (HLT). It also has tools for the simulation of the trigger system (both L1 and HLT) and some analysis tools.

It follows the concept of 'Reconstruction on demand', a reconstruction algorithm is only executed if its products (reconstructed objects like e.g. tracks, jets, vertices) are requested. It also allows to perform regional and partial reconstruction, particularly important for the application in the HLT where events cannot be fully reconstructed because of time constraints.

For simulation studies, not all samples needed can be fully simulated and reconstructed because of CPU constraints. A simulation program allowing to perform both fast simulation and fast reconstruction is thus desirable. The FAMOS (FAst MONte Carlo Simulation) [5] program fulfills these requirements. The time budget is about one second per event (depending on the event topology). Most of the reconstructed physics objects (e.g. tracks, jets, muons, electrons, b and τ tagging) are available and can be accessed in a very similar way as in the full reconstruction framework. This allows to run the same analysis code in both frameworks with only minor modifications. A large fraction of the algorithms from the full reconstruction is re-used, the only difference being that they are fed with input from the fast reconstruction. The fast reconstruction goes far beyond simple parametrisations, e.g. for the track reconstruction, individual smeared hits (according to the resolution of the corresponding detector component) are fit in the same way as in the full reconstruction.

As already mentioned, the DST is the data format used for physics analysis¹. The DST contains physics objects from reconstruction algorithms (tracks, jets, muons, electrons, trigger output etc.) to avoid CPU expensive reconstruction. However, higher level reconstruction is still possible with the information stored on the DST, e.g. jet reconstruction from calorimeter towers, vertex reconstruction from tracks or track refitting from the stored hits associated to the tracks. The typical size of an event in the DST format is about 250 KB (depending on the topology of the event). Currently, more than 100 million events are available for analyses.

CMS is currently in the process of redesigning its software framework. In the future, more levels of analysis will be provided, allowing e.g. to analyse directly in a ROOT [6] session the physics objects as written to the persistent store by the reconstruction programs.

3 Conditions

In our detector simulation, we model an almost perfect detector. It is perfectly aligned, no detector components are missing, there are no dead modules and different detector modules of the same kind give uniform response. However, we know that this is not the real situation when facing real data. The alignment is known only with limited precision before data taking and even after a data based alignment the precision that can be reached may still be in the order of or even exceed the spatial resolutions for some detector components. CMS will very likely not start

¹ In the future, there will be another, more compact format, called AOD [3].

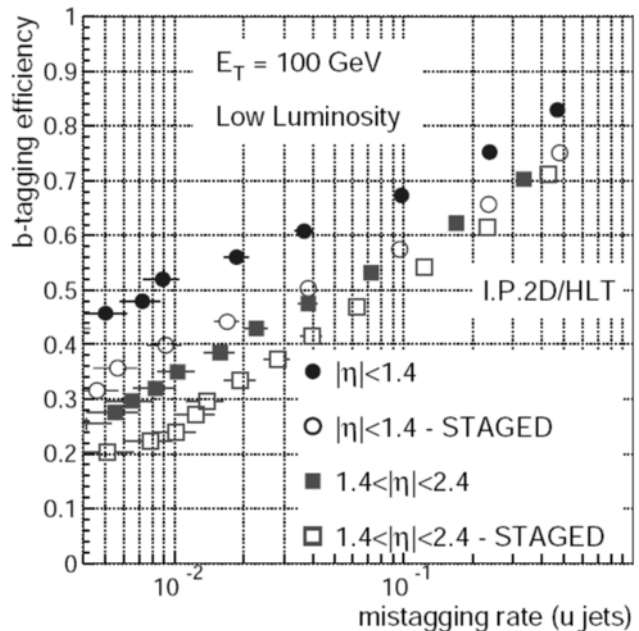


Fig. 2. The degradation of the b-tagging performance for a scenario with one missing layer of pixel detectors (open symbols) compared to a fully equipped detector (closed symbols) (from [7]).

with a complete detector in 2007, e.g. the electromagnetic calorimeter in the endcaps of the detector will be installed for the 2008 physics run, as well as the pixel detectors. Furthermore, an accurate description of the detector material in the simulation is difficult and might differ significantly from the one in the real detector.

To be prepared for data taking and get the best possible performance from the reconstruction algorithms, these issues have to be addressed well in advance. The full analysis studies mentioned before will study these effects in view of the individual analyses.

3.1 Staged Scenario

The current standard track reconstruction algorithm relies on the pixel detector to create the track seeds needed for an initial trajectory². Obviously, this does not work if no pixel detectors are available. Furthermore, the current approach is not very efficient to reconstruct charged particle tracks stemming from the decay of very long lived particles, e.g. V^0 decays. Therefore, alternative track reconstruction algorithms not relying on the pixel detectors are under development. Scenarios, where only one pixel layer is missing also have to be studied. Figure 2 shows the degradation of the b-tagging performance in case of a missing layer of pixel detectors compared to the fully

² Other seeding algorithms starting in external detectors like the electromagnetic calorimeter or the muon chambers exist for dedicated tasks, like e.g. the reconstruction of converted photons.

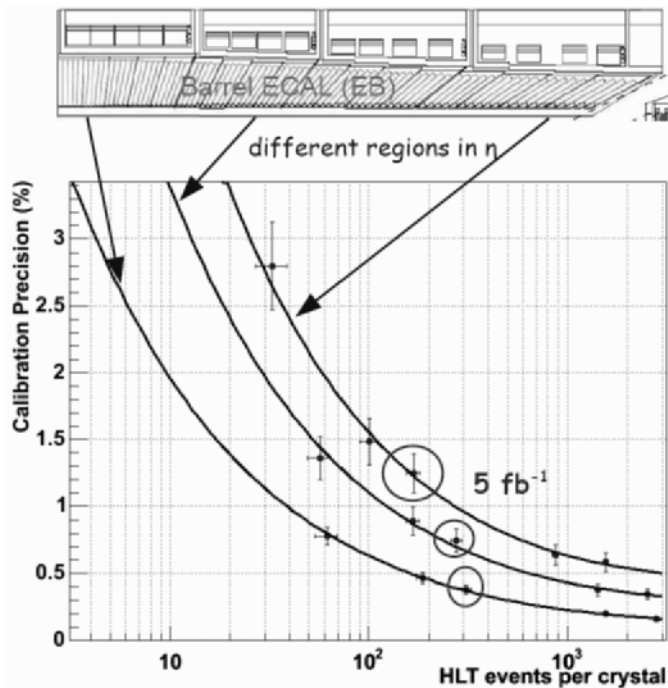


Fig. 3. The achievable precision for the inter-calibration of the ECAL crystals in dependence on the number of $W \rightarrow e\nu_e$ events passing the High Level Trigger selection. The three curves correspond to different regions of the barrel ECAL as indicated by the arrows. The points corresponding to an expected integrated luminosity of 5fb^{-1} are marked by circles.

equipped detector [7]. These studies will be redone for the Physics TDR.

3.2 Detector Calibration

For a discovery of a low-mass Higgs boson in the decay channel $H \rightarrow \gamma\gamma$, the resolution of the electromagnetic calorimeter (ECAL) has to be at the level of a percent. Thus, the ECAL crystals have to be inter-calibrated with a precision at the same level. Before applying calibration algorithms using real data from physics events, measurements in the laboratory, test beam studies and cosmic muons allow an inter-calibration with an accuracy of about 3-4%. Isolated electrons from physics events ($W \rightarrow e\nu_e$ in the study described here) can then be used for an in-situ calibration, based on the ratio E/p , where E is the energy measured in the ECAL crystals and p the momentum measured in the tracking detector. To select electrons which have not undergone significant Bremsstrahlung, information from the tracking detector, e.g. the number of hits associated to the electron track and the electromagnetic calorimeter itself, e.g. the ratio of the energies contained in 3×3 and 5×5 crystals. Figure 3 shows the expected precision in dependence on the number of events per crystal. Other information can also be used for the inter-calibration, e.g. the symmetry in the azimuth angle Φ or decays like $\pi^0, \eta \rightarrow \gamma\gamma$.

3.3 Alignment

To fully exploit the spatial resolutions of the different detector components, these detectors have to be aligned with a precision at least comparable to the spatial resolution. One of the biggest challenges is the alignment of the tracking detector. Aligning about 20000 modules means that one has to deal with a number of alignment parameters which is in the order of 100.000. Since the pixel and silicon strip detectors are extremely precise devices with spatial resolutions of about $10\mu\text{m}$ for the inner layers, the ultimate goal is to be able to get an alignment accuracy at that level. The alignment of the tracker is performed in several steps, the knowledge on the position of the modules improving after each step. After the mechanical mounting, typical expected accuracies are e.g. about $10\text{-}30\mu\text{m}$ for the sensors on the modules and about $50\text{-}500\mu\text{m}$ for the modules on the layers. In the second step, the laser alignment system is used to align mainly global support structures and monitor relative movements. Because of the way the laser beams are injected into the detector, the endcap disks benefit most from this method. The final step is the alignment using reconstructed charged particle tracks, e.g. isolated muon tracks from W or Z decays (the latter ones could be useful to connect different regions of the detector by applying a mass constraint), giving the final precision that can be achieved. Currently, several alignment algorithms using reconstructed tracks are under study. They have been proven to work for simpler geometries (e.g. a cosmic beam test setup or a model detector with a significantly reduced number of elements). However, aligning the fully equipped tracking detector is a task of enormous complexity, e.g. depending on the algorithm huge matrix inversions have to be performed, and is still a field heavily worked on.

To be able to study the effects of a not perfectly aligned detector, misalignment tools have been developed. They allow shifts and rotations of individual components as well as of larger structures by amounts as defined by the user. Charged particle tracks or muons can then be refit using the displaced hits as input (this can be done even from the information stored on the DST; if all hits are available, pattern recognition can be completely redone).

Two mis-alignment scenarios have been defined, “*first data taking*” (accuracy as expected from mounting precision, the laser system and some track based alignment for the pixel detectors as expected after an integrated luminosity of less than 1fb^{-1}) and “*long term*” (ultimate precision as expected from the track based alignment after a period of data taking with sufficient integrated luminosity, about 10fb^{-1}). The assumed accuracy for the *long term* is typically about a factor 10 better than for the *first data taking*, apart for the pixel detectors where alignment precisions of about $10\mu\text{m}$ are assumed for both scenarios. The alignment errors are added in quadrature to the nominal hit errors. Figure 4 shows the transverse impact parameter resolutions for the different scenarios.

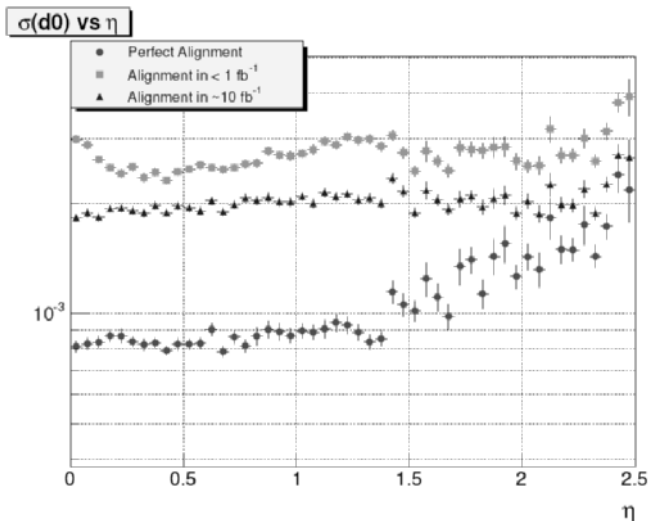


Fig. 4. The transverse impact parameter resolution for muons with $p_t = 100 \text{ GeV}/c$ versus pseudo-rapidity for perfect alignment (circles), the *long term* (stars) and *first data taking* (squares) scenarios.

4 Algorithm Calibration in Data

Because of the complexity of the detector and its description, the Monte Carlo and detector simulations can not be expected to match perfectly the real data delivered by the detector. This is particularly true for the first periods of data taking. Therefore, methods have to be developed to calibrate not only the detector components, but also the performance of the reconstruction algorithms using the data themselves. To be able to perform these tasks, the analysis of Standard Model processes (e.g. events involving W or Z bosons, top quarks) is indispensable. As an example, the calibration of the b-tagging algorithms is given. The algorithms to tag b-quark jets are high-level algorithms relying on many other reconstruction algorithms like e.g. track and vertex reconstruction. A study is going on analysing semi-leptonic and fully leptonic $t\bar{t}$ events. Because of $BR(t \rightarrow Wb) \approx 1$, these events can provide samples enriched and depleted in b-quark jets. Due to the large $t\bar{t}$ cross section ($\sigma_{t\bar{t}} \approx 800 \text{ pb}$), a measurement of the b-quark tagging efficiency with an accuracy not dominated by the statistics after some months of data taking seems feasible.

5 Example Analysis: Associated Higgs Boson Production

The channel of associated Higgs boson production, $t\bar{t}H$, with the Higgs boson decaying into a pair of b-quarks, $H \rightarrow b\bar{b}$, is one of the benchmark channels selected for the Physics TDR (see Figure 1). The dominating diagrams for this production process and the cross sections for different Higgs boson production processes are shown in Figure 5. This channel allows a search in decay mode $H \rightarrow b\bar{b}$, that is the dominating one for low Higgs boson masses

($m_H \lesssim 135 \text{ GeV}/c^2$). It is complementary to the channel $H \rightarrow \gamma\gamma$, where the Higgs boson is produced in the dominating production processes (mainly gluon-gluon fusion). It also offers the possibility to measure the top-Higgs Yukawa coupling. The main background channels are expected to be $t\bar{t}$ events with additional jets, $t\bar{t}jj$ (irreducible in case of additional b jets). Another motivation to choose this channel as benchmark channel for the full analysis is, that it is experimentally very challenging because of its complex event topology and makes highest demands on the reconstruction algorithms for several physics objects. The event topology for the semi-leptonic channel is also shown in Figure 5. One expects at least six jets, four b jets from the top quark and Higgs boson decays and two non-b jets from the hadronic W boson decay. Additional jets from the signal vertex might come from initial and final state radiation, increasing further the number of jets in the event. From the leptonically decaying W boson one gets a high energetic lepton (an electron or muon which is isolated in a large fraction of the events) and missing transverse energy from the undetectable neutrino. The isolated lepton is important to efficiently trigger these events (however, other trigger streams might also contribute). Due to the large jet multiplicity in the final state, the task of finding the b-jets from the Higgs boson decay is difficult because of the enormous number of possible combinations within the event. To resolve the combinatorics ambiguities, an attempt is made to benefit from the distinct signature the additional top quarks are giving by fully reconstructing the $t\bar{t}$ system.

The focus in this article is not to present the full analysis with final results but to show the interaction between analysis and reconstruction groups that has been triggered by this complex channel.

To identify the lepton (e or μ) from the W boson decay, a Likelihood ratio method has been developed to reject leptons from other sources (because of four b jets in the final state, a large fraction of reconstructed leptons are real leptons in b jets). The most important variables entering in the Likelihood ratio are kinematical properties of the lepton, isolation criteria and the track impact parameter significance.

Performant jet reconstruction in a dense hadronic environment is required in this channel. In order not to lose too much efficiency, good efficiency and resolution are crucial also for jets with low transverse momenta. Several jet algorithms are available in CMS (iterative cone algorithm, k_t algorithm etc.). An activity has been started to compare these algorithms in terms of how well the reconstructed jets reproduce the initial parton directions and energies and how efficiently all signal jets of the event are found. Parameters of the algorithms are scanned in order to find the optimal configuration. This is done for different topologies with a different number of jets expected in the final state (e.g. semi-leptonic $t\bar{t}$ and $t\bar{t}H$, fully hadronic $t\bar{t}H$). Since there are four b jets expected in the final state, dedicated jet energy corrections are developed to account for the missing neutrino in case of semi-leptonic b hadron decays, tagged by the presence of an identified lepton in

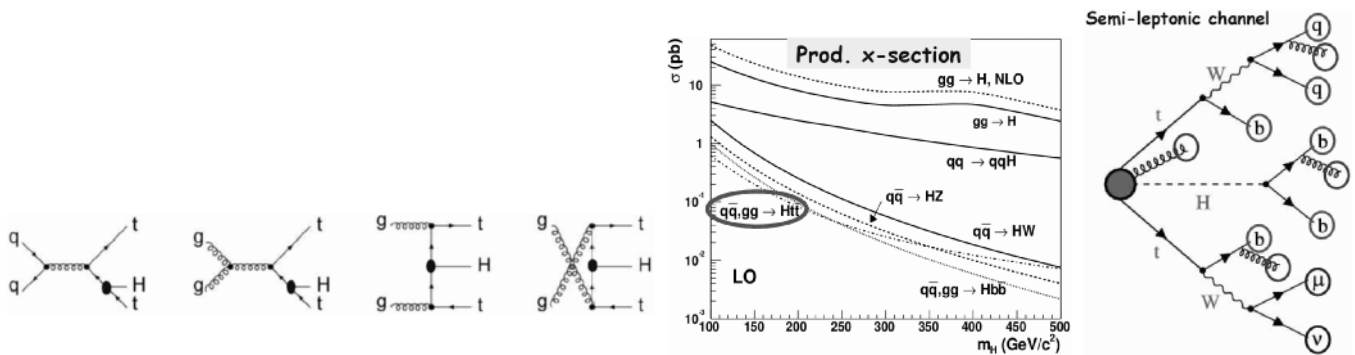


Fig. 5. The diagrams for Higgs boson production in association with a $t\bar{t}$ pair (left), the Higgs boson production cross sections for several processes (middle) and the event topology of the semi-leptonic $t\bar{t}H$ final state (right).

a jet. A precise determination of the missing transverse energy is needed for the computation of the longitudinal momentum of the neutrino from the leptonic W boson decay.

Another crucial ingredient for this analysis is the tagging of b jets. A performant b -tagging algorithm is needed to find the correct configuration within the event and to suppress the $t\bar{t}jj$ background. Since four b jets are present in the final state, the global reconstruction efficiency is sensitive to small variations of the b -tagging efficiency. The most performant b -tagging algorithm available in CMS is an algorithm combining kinematic and topological variables from an inclusive vertex reconstruction and track impact parameter significances. Even in the dense hadronic environment of this channel, a b -tagging efficiency of about 60% with rejection factors of about 10 and 100 for c jets and light quark jets (including gluon jets), respectively, seems feasible.

The analysis is then carried out according to the following steps for the events having passed the High Level Trigger. The leptonically decaying W boson is reconstructed from the isolated lepton and missing E_t and the hadronically decaying W boson from two jets which have not been tagged as b jets. The top quarks are then reconstructed from the W bosons and tagged b jets. The Higgs boson is reconstructed from the remaining two b jets. However, because of the large jet multiplicity in the event, many possible combinations exist. To select the most probable event configuration, a χ^2 or Likelihood method is used, where e.g. masses of intermediate resonances and other kinematical variables enter. In about 30-35% of the signal events, the correct b jets from the decay of the Higgs boson can be found.

An important topic to be studied is how the background can be estimated from the data, not to rely fully on Monte Carlo simulations for the background subtraction.

6 Summary

The preparation of the Physics TDR serves as a test of the ability to get physics results out of the data that will

be recorded by the CMS detector. It is a test of the software, the computing environment, reconstruction tools, calibration and alignment tools and analysis tools. Most of these tools are either already available or currently under development. The use of some of these tools has been demonstrated in the $t\bar{t}H$ example analysis.

References

1. CMS Collaboration, CMS Technical Proposal, CERN/LHCC 94-38.
2. M. Stavrianakou et al., “An Object-Oriented Simulation Program for CMS”, Proceedings of the CHEP’04 Conference, Interlaken, Switzerland, 2004, published on InDiCo.
3. CMS Collaboration, The Computing Project, Technical Design Report, CERN/LHCC 2005-023.
4. S. Wynhoff, “Using the Reconstruction Software, ORCA, in the CMS Data Challenge”, Proceedings of the CHEP’04 Conference, Interlaken, Switzerland, 2004, published on InDiCo.
5. F. Beaudette, “FAMOS, a FAst Monte-Carlo Simulation for CMS”, Proceedings of the CHEP’04 Conference, Interlaken, Switzerland, 2004, published on InDiCo.
6. R. Brun et al., “ROOT, An Object-Oriented Data Analysis Framework”, <http://root.cern.ch>.
7. CMS Collaboration, “The Trigger and Data Acquisition Project, Volume II: Data Acquisition and High-Level Trigger Technical Design Report”, CERN/LHCC 2002-26.

Top Quark Physics

Top Mass at the Tevatron

Tomonobu Tomura for the CDF and DØ Collaborations

University of Tsukuba, Tsukuba, Ibaraki 305-8571, Japan

Abstract. We present the recent analyses of top quark mass by the CDF and DØ experiments at Run II of the Tevatron. The current most accurate single measurement by the CDF template method for the lepton + jets channel gives $173.5^{+2.7}_{-2.6} \pm 2.5 \pm 1.7$ GeV/ c^2 , where the errors are statistical, jet energy scale systematic, and other systematic uncertainties, respectively. A preliminary average of the top mass measurement at Tevatron is $174.3 \pm 2.0 \pm 2.8$ GeV/ c^2 , where the errors are statistical and systematic, respectively.

1 Introduction

The top quark mass is a fundamental parameter of the Standard Model (SM), and plays an important role in the precise prediction of electroweak observables like the Higgs boson mass. Indeed, the radiative corrections of many electroweak observables are dominated by the large top quark mass. Thus, a precise measurement of the top quark mass provides a crucial test of the consistency of the SM and could help constraining physics beyond the SM.

2 Measurements of Top Mass

At the Tevatron, the top quark is mostly pair produced through quark-antiquark annihilation and gluon-gluon fusion. The SM top quark decays almost exclusively to a W boson and a b quark. Depending on the W decays, we categorize the $t\bar{t}$ events as: lepton + jets channel, where one W decays hadronically and the other W leptonically (electron or muon), accounts for 30% of $t\bar{t}$ events; dilepton channel, where both W s decay leptonically, takes 5% of $t\bar{t}$; all hadronic channel, where both W s decay hadronically, amounts to 44%; the rest is the τ channel. In this report, we show the top mass measurements using lepton + jets and dilepton channels.

There are two kinds of method for the top mass measurements. One is the “Template” method, which reconstructs the invariant mass of the top quark for each event and compares its distribution with the Monte Carlo (MC) to extract the top quark mass. The other is the “Matrix Element (ME)” method, which uses the matrix element to calculate the probability density function for each event and performs maximum likelihood fit to determine the top quark mass.

2.1 Lepton + Jets Channel

The lepton + jets events consist of one high transverse momentum (p_T) lepton (electron or muon) and large trans-

verse missing energy \cancel{E}_T due to the neutrino from the W decay and at least four jets including 2 b -jets in the final state.

2.1.1 CDF Template Method

In this method, an invariant mass of the top quark is reconstructed from the top decay products (lepton candidate, four highest transverse energy (E_T) jets, and \cancel{E}_T) using a χ^2 kinematic fit for each event. The χ^2 expression to be minimized is defined as

$$\chi^2 = \sum_{i=\ell, 4\text{jets}} \frac{(\hat{p}_T^i - p_T^i)^2}{\sigma_i^2} + \sum_{j=x,y} \frac{(\hat{p}_j^{\text{UE}} - p_j^{\text{UE}})^2}{\sigma_j^2} + \frac{(m_{jj} - m_W)^2}{\Gamma_W^2} + \frac{(m_{\ell\nu} - m_W)^2}{\Gamma_W^2} + \frac{(m_{bjj} - m_t^{\text{reco}})^2}{\Gamma_t^2} + \frac{(m_{b\ell\nu} - m_t^{\text{reco}})^2}{\Gamma_t^2}, \quad (1)$$

where σ_ℓ and σ_{jet} correspond to the resolutions of the lepton and jets, and $p_{x,y}^{\text{UE}}$ and $\sigma_{x,y}$ are the x and y composition of the unclustered energy and resolution, respectively. Since we do not know from which parton a given jet comes, we try all 12 possible jet-parton assignments, but if one or more jets are b -tagged, the b -tagged jets are assigned to a b -quark in the fitter. There is an additional combination due to the two solutions for the p_z of the neutrino arising from solving a quadratic equation. After minimizing the χ^2 expression, the m_t^{reco} corresponding to the combination that yields the lowest χ^2 is considered the reconstructed top quark mass for that event.

The dijet mass from hadronic W decay, m_{jj} , is sensitive to the jet energy scale (JES), but relatively insensitive to the top quark mass. It can thus be used to determine fully *in situ* the JES with little uncertainty on top mass. In this analysis, the JES is determined using both the m_{jj} templates and the *a priori* determination of JES by CDF. The combination of both estimates provides an optimal

constraint on this parameter. m_{jj} is simply reconstructed from the measured three-momenta of jets and no χ^2 fitter is used. The combinatoric problem is dealt with by considering all jet-parton assignments made of the four highest E_T jets that are not b -tagged.

The distributions of m_t^{reco} and m_{jj} are constructed from MC for various M_{top} and JES values. Smooth probability density functions are obtained by fitting the mass distributions as a function of M_{top} and JES using an analytic function whose parameters depend linearly on each of these two parameters. We divide the sample into 4 categories according to the number of b -tags and jet E_T . We use different template for each subsample.

The reconstructed mass distributions from data are compared to the signal and background templates using an unbinned maximum likelihood fit. For each subsample, the likelihood is given by

$$L_{\text{sample}} = L_{\text{shape}}^{m_t^{\text{reco}}} \times L_{\text{shape}}^{m_{jj}} \times L_{\text{nev}} \times L_{\text{bg}}, \quad (2)$$

where the first two terms represents the probabilities of obtaining m_t^{reco} and m_{jj} given the signal and background templates and the expected numbers of signal and background events. L_{nev} expresses the likelihood associated with observing r^w and r^t events in the two samples given the expected number of events and efficiencies. The background normalizations are constrained for b -tagged samples by L_{bg} . The *a priori* constraint on the JES [$L_{JES} = \exp(-JES^2/2)$] is used in the likelihood. The total likelihood is given by the product of the likelihoods of four subsamples and the JES constraint.

The likelihood procedure is applied to 138 candidate events obtained from the data sample of 318 pb^{-1} and the result is a top quark mass of $173.5_{-3.6}^{+3.7}(\text{stat.}+JES) \pm 1.7(\text{syst.}) \text{ GeV}/c^2$. The dominant sources of systematic uncertainty are background shape ($1.1 \text{ GeV}/c^2$), b -jet energy ($0.6 \text{ GeV}/c^2$), and final state radiation ($0.6 \text{ GeV}/c^2$). Figure 1 shows the consistency of the reconstructed top quark mass distribution in each subsample with the combined fit results.

2.1.2 DØ Template Method

This “template” method is a technique very similar to that used for the first top quark mass measurement by DØ [1]. We present results from the analysis of two samples of events selected using criteria designed to preferentially select $t\bar{t}$ events over background processes. One sample requires one or more b -tagged jets in an event (“ b -tagged analysis”). The other strategy is to exploit the unique topology of $t\bar{t}$ events due to the large mass of the top quark in the event selection (“topological analysis”). In order to get discrimination between signal and background for this analysis, we derive a discriminant (Low Bias Discriminant, LB) constructed from the topology of the events. The discriminant is designed to be uncorrelated with the top quark mass. We developed this discriminant by closely following the work described in Ref. [1].

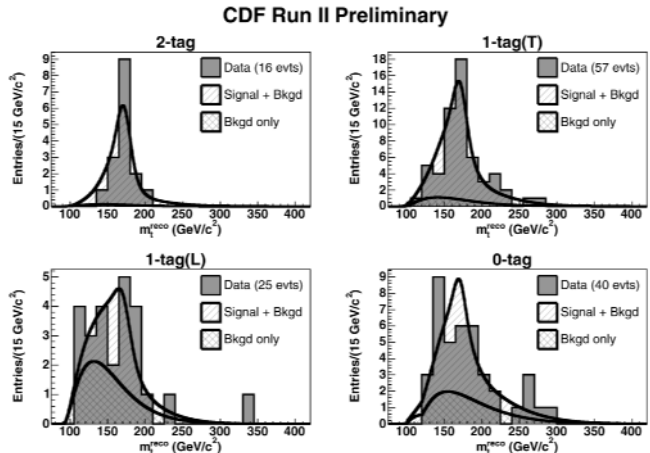


Fig. 1. The reconstructed top quark mass distribution for each subsample is shown overlaid with the expected distribution using the top mass, jet energy scale, signal normalization, and background normalization from the combined fit.

We use a constrained kinematic fit to extract mass information from the events. The fit technique is the same as used in the Run I template analysis [1]. The object resolutions used in the fit were updated to reflect those of the Run II DØ detector.

We use the fitted top quark mass from the permutation with the smallest χ^2 as the mass estimator for each event. In order to extract the top quark mass, we use a binned maximum likelihood fit. We write the probability density function for the mass estimator in terms of the number of signal events n_s and the number of background events n_b in the sample. We constrain the fraction of background events to the expected number using a Poisson probability term. For each hypothesized top quark mass, the likelihood is maximized as a function of the number of signal and background events. The mass with the largest likelihood, or equivalently the smallest negative log likelihood ($-\ln L$) is identified and a parabola is fit to the values of $-\ln L$ for all hypothesized top quark masses within a small range around the mass with the largest likelihood.

Using 229 pb^{-1} of the data sample, we find 94 data events in the topological analysis sample. The fit mass distribution of the event is shown in Fig. 2 (left). The fit for the top quark mass is shown in Fig. 2 (right). We fit a top quark mass of $169.9 \pm 5.8(\text{stat.})_{-7.1}^{+7.8}(\text{syst.}) \text{ GeV}/c^2$. The dominant sources of the systematic uncertainty are jet energy scale ($_{-6.5}^{+6.8} \text{ GeV}/c^2$), gluon radiation ($\pm 2.6 \text{ GeV}/c^2$), and signal model ($+2.3 \text{ GeV}/c^2$).

There are 69 events in the b -tagged events sample. Figure 3 shows the fit mass distribution for MC and data (left) and the fit to the $-\ln L$ versus the assumed top quark mass (right). The result of the likelihood fit leads to a measurement of the top quark mass of $170.6 \pm 4.2(\text{stat.}) \pm 6.0(\text{syst.}) \text{ GeV}/c^2$. The dominant sources of the systematic uncertainty are jet energy scale ($_{-5.3}^{+4.7} \text{ GeV}/c^2$), gluon radiation ($\pm 2.4 \text{ GeV}/c^2$), and signal model ($+2.3 \text{ GeV}/c^2$).

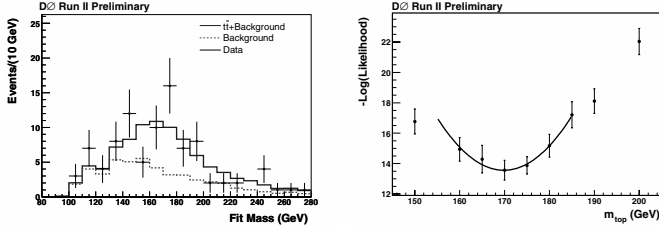


Fig. 2. The distribution of fit masses of the topologically selected events (left) and the negative log likelihood distribution as a function of the fit top quark mass to these events (right) are shown. The red curve is the expectation from background only events (normalized to the fraction preferred by the fit) while the blue curve is the sum of the expectation from signal and background for the mass point closest to the fit result.

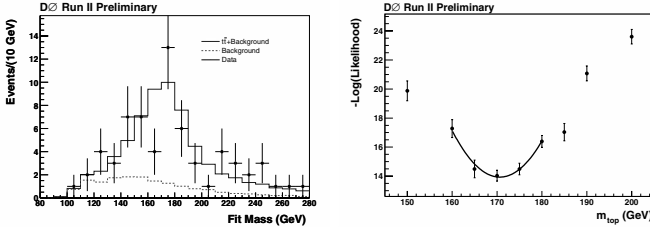


Fig. 3. The distribution of fit masses of the b -tagged events (left) and the negative log likelihood distribution as a function of the fit top quark mass to these events (right) are shown. The red curve is the expectation from background only events (normalized to the fraction preferred by the fit) while the blue curve is the sum of the expectation from signal and background for the mass point closest to the fit result.

2.1.3 CDF Dynamical Likelihood Method

The Dynamical Likelihood Method (DLM) [2] is the maximum likelihood method where the likelihood function is calculated from the matrix elements of $t\bar{t}$ production and their decay processes.

The likelihood of the i -th event is defined as

$$L^i(M_{\text{top}}) = \sum_{I_t} \sum_{I_s} \int \frac{2\pi^4}{\text{Flux}} F(z_a, z_b; p_T) |M|^2 w(\mathbf{x}, \mathbf{y}) d\mathbf{x}, \quad (3)$$

where F is the parton distribution function for (z_a, z_b) and p_T of $t\bar{t}$ system, M is the matrix element of $t\bar{t}$ process, and w is the transfer function that describes the probability density function for parton variable set \mathbf{x} when a set of observables \mathbf{y} is given. The sums are taken over all the jet-parton assignments (I_t) and all the solutions for p_z of ν (I_s).

Using 318 pb^{-1} of data, we have 63 $t\bar{t}$ candidates events passing the event selection criteria. The joint negative log likelihood of these events is shown in Fig. 4 (left) and fitted with a second order polynomial. From the fit, we obtain $171.8^{+2.18}_{-2.02} \text{ GeV}/c^2$, assuming there is no background. We apply the mapping function to remove the mass-pulling effect of the background, and the final result is $173.8^{+2.7}_{-2.5}(\text{stat.}) \pm 3.3(\text{syst.}) \text{ GeV}/c^2$. The dominant sources of systematic uncertainty are jet energy

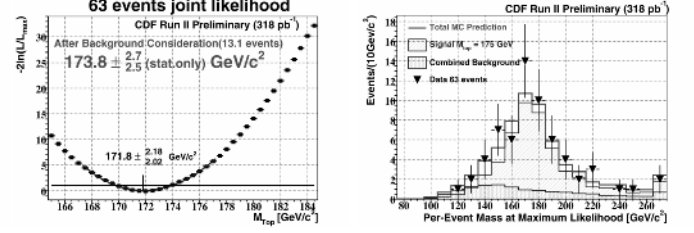


Fig. 4. The joint negative log likelihood distribution of the 63 events (left) and the maximum likelihood mass distributions in data and MC (right) are shown.

scale ($3.0 \text{ GeV}/c^2$), background fraction ($0.6 \text{ GeV}/c^2$), background modeling ($0.6 \text{ GeV}/c^2$), and b -jet modeling ($0.6 \text{ GeV}/c^2$). The maximum likelihood mass in each event is shown in Fig. 4 (right) for both data and MC.

2.2 Dilepton Channel

The dilepton events consist of 2 high- p_T leptons, 2 b -jets, and large \cancel{E}_T due to the 2 neutrinos from the W decays.

2.2.1 CDF Neutrino Weighting Algorithm

The Neutrino Weighting Algorithm (NWA) was the method used in Run I to obtain the final published results by CDF [3] in this channel.

In this method, we assume we know the top mass, the W mass, the η 's of the two neutrinos, and the lepton-jet pair which originated from the top quark decay. Then, we apply energy-momentum conservation on the t side and obtain up to two possible solutions for the 4-vector of the neutrino. We repeat on the \bar{t} -side, and end up with up to four possible pairs of neutrino-antineutrino solutions. Each of the four solutions is assigned a probability w_i that of the observed missing E_x and E_y within their uncertainties. We add up the four weights. We scan the neutrino η distributions and each pair of neutrino η 's is assigned a probability of occurrence $P(\eta_\nu, \eta_{\bar{\nu}})$ derived from MC. Then, the event weight is calculated by summing up the product of the weight and $P(\eta_\nu, \eta_{\bar{\nu}})$ for each neutrino η pair. Finally, the two resulting weights for the lepton-jet pairings are added up. Thus the final weight is only a function of the top mass. For simplicity, we pick one indicative top mass from each event: we use the top mass which best explains the event as a $t\bar{t}$ dilepton decay.

We build the “template” distributions of the top masses reconstructed as explained above using the fully simulated MC. Parametrizing these templates, we construct probability density functions for signal and background events to be used in the likelihood. The parameters of signal template are constrained to be linearly dependent on the top mass.

We have 46 events satisfying the selection in 358.6 pb^{-1} of data, with 45 events resulting in NWA solutions. From the maximum likelihood fit, we obtain $170.6^{+7.1}_{-6.6}(\text{stat.}) \pm 4.4(\text{syst.}) \text{ GeV}/c^2$, where the dominant

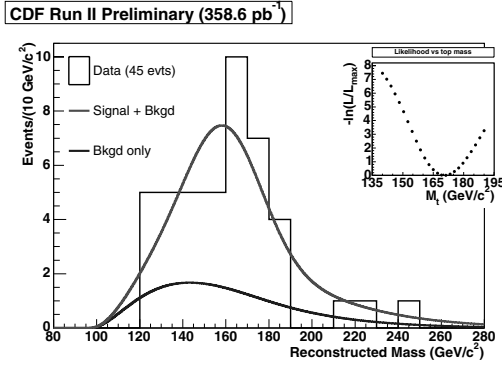


Fig. 5. Reconstructed top mass for 19 data events (histogram). The normalized shapes of the background and signal plus background probability density functions are shown as hatched curves. The shape of the negative log likelihood function is shown in the inset.

sources of the systematic uncertainty are background shape ($3.0 \text{ GeV}/c^2$) and jet energy scale ($2.6 \text{ GeV}/c^2$). Figure 5 shows the reconstructed top masses in data, normalized background shape, the normalized sum of the signal and background shapes, and the variation of $-\ln L$ as a function of the top mass in the inset.

2.2.2 DØ Template Method

The method used here is similar to that used by DØ Collaboration to measure the top quark mass in the dilepton channel using Run I data [4]. We follow the ideas proposed by Dalitz and Goldstein [5] to reconstruct events from decays of top-antitop quark pairs. We assign the two highest p_T jets to the b and \bar{b} quarks, then assign a likelihood to hypothesized value of the top quark mass. We find the pairs of t and \bar{t} momenta that are consistent with the observed lepton and jet momenta and missing p_T . We call this pair a solution. We assign a weight to each solution, given by

$$w = f(x)f(\bar{x})p(E_\ell^*|m_t)p(E_{\bar{\ell}}^*|m_t), \quad (4)$$

where $f(x)$ ($f(\bar{x})$) is the parton distribution function for the parton for the momentum fraction x carried by the initial quark (antiquark), $p(E_\ell^*|m_t)$ is the probability for the hypothesized top quark mass m_t that the lepton ℓ has the observed energy in the top quark rest frame. The likelihood for each value of the top quark mass m_t is given by the sum of the weights over all the possible jet assignments and solutions. We account for the effect of the detector resolution by repeating the weight calculation with input values for the particle momenta that are drawn from normal distributions centered on the measured value with widths equal to the resolution of the momentum measurements. We take the average of these weight calculations.

For each event, we use the value of hypothesized top quark mass at which the weight calculated above reaches its maximum. We call this mass value the peak mass. We then compare the peak mass distribution of the observed

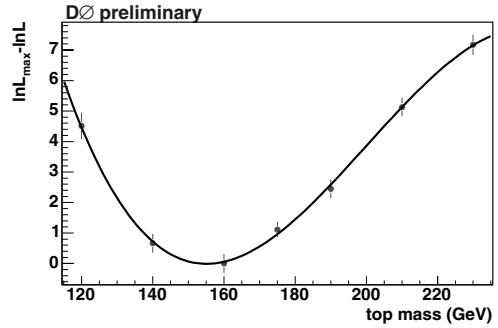


Fig. 6. Negative log likelihood curve for the 13 data events.

events to the templates generated from MC using a binned maximum likelihood fit.

Using 230 pb^{-1} of data, we found 13 $t\bar{t}$ candidate events. From the binned maximum likelihood fit, we obtain $155_{-13}^{+14}(\text{stat.}) \pm 7(\text{syst.}) \text{ GeV}/c^2$. Figure 6 shows the joint negative log likelihood curve for the 13 data events. The dominant sources of the systematic uncertainty are jet energy scale ($5.6 \text{ GeV}/c^2$) and event generation ($3.0 \text{ GeV}/c^2$).

2.2.3 CDF Matrix Element Method

The information contained in an event regarding the top mass can be expressed as the conditional probability $P(\mathbf{x}|M_t)$, where M_t is the top pole mass and \mathbf{x} is a vector of measured event quantities. We calculate the posterior probability using the theoretical description of the $t\bar{t}$ production process expressed with respect to the measured event quantities:

$$P(\mathbf{x}|M_t) = \frac{1}{\sigma(M_t)} \frac{d\sigma(M_t)}{d\mathbf{x}}, \quad (5)$$

where $d\sigma/d\mathbf{x}$ is the per-event differential cross-section.

To evaluate the probability, we integrate over quantities which are unknown, such as neutrino energies. Quark energies are not directly measured, but are estimated from the observed energies of corresponding jets. We parametrize this uncertainty using a transfer function $f(p, j)$ that gives the probability of measuring jet energy j given parton energy p . The total expression for the probability of a given pole mass for a specific event can be written as

$$P(\mathbf{x}|M_t) = \frac{1}{N} \int d\Phi_6 |\mathcal{M}_{t\bar{t}}(p; M_t)|^2 \prod_{\text{jets}} f(p_i, j_i) f_{\text{PDF}}(q_1) f_{\text{PDF}}(q_2), \quad (6)$$

where the integral is over the entire six-particle phase space, q is the vector of incoming parton-level quantities, p is the vector of resulting parton-level quantities, and $|\mathcal{M}_{t\bar{t}}(p; M_t)|$ is the $t\bar{t}$ production matrix element as defined in Ref. [6]. The constant term N in front of the

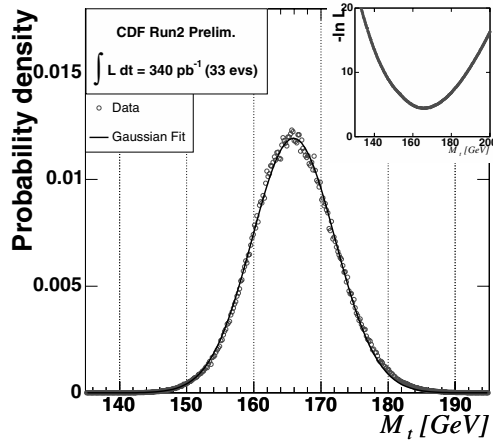


Fig. 7. Final posterior probability density as a function of the top mass for the 33 candidate events in data. The negative log likelihood curve is shown in the inset.

integral ensures that the normalization condition for the probability is satisfied.

We apply the above procedure to the 33 candidate events observed in the 340 pb⁻¹ of data. From these events, we obtain $165.3 \pm 6.3(\text{stat.}) \pm 3.6(\text{syst.})$ GeV/ c^2 . The dominant sources of the systematic uncertainty are jet energy scale (2.6 GeV/ c^2) and background MC (1.5 GeV/ c^2). The final posterior probability density for the events in the data can be seen in Fig. 7.

3 Summary

In this report, we presented the latest top quark mass measurements by the CDF and DØ collaborations. The results are summarized in Figs. 8 and 9. CDF template method is the most precise measurement from a single experiment. The preliminary Tevatron average of the top quark mass is $174.3 \pm 2.0(\text{stat.}) \pm 2.8(\text{syst.})$ GeV/ c^2 as shown in Fig. 8.

The Tevatron is performing well and large datasets are becoming available. We will reach the goal of measuring the top quark mass with an uncertainty of 2 GeV/ c^2 in Run II using a single analysis and by combining the different measurements, more improvement is expected.

References

1. DØ Collaboration, S. Abachi *et al.*, Phys. Rev. Lett. **79**, (1997) 1197; DØ Collaboration, B. Abbott *et al.*, Phys. Rev. D **58**, (1998) 052001.
2. K. Kondo, J. Phys. Soc. Jpn. **57**, (1988) 4126; **60**, (1991) 836; K. Kondo, T. Chikamatsu, and S. H. Kim, *ibid.* **62**, (1993) 1177; K.Kondo, RISE Technical Report 05-01 (2005) Waseda University.
3. CDF Collaboration, F. Abe *et al.*, Phys. Rev. Lett. **82**, (1999) 271.

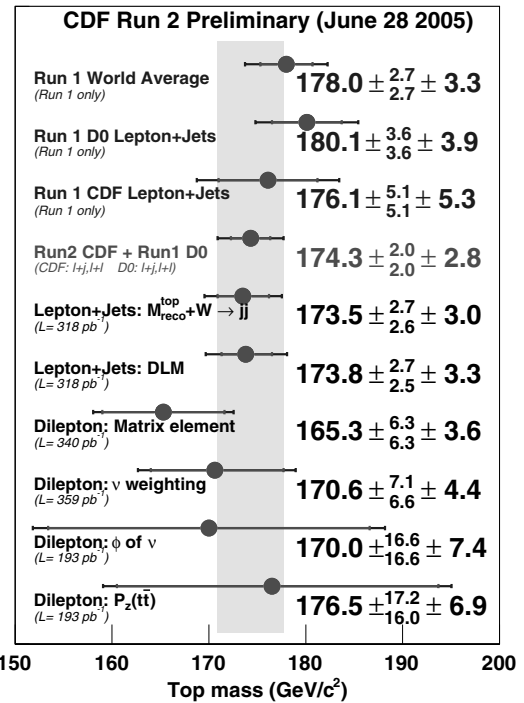


Fig. 8. Comparison of the results of top mass measurements among CDF.

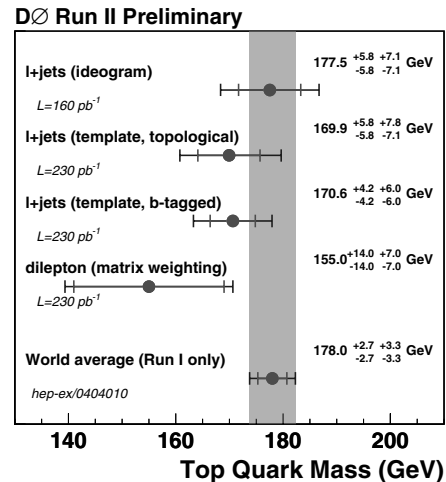


Fig. 9. Comparison of the results of top mass measurements among DØ.

4. DØ Collaboration, B. Abbott *et al.*, Phys. Rev. Lett. **80**, (1998) 2063; Phys. Rev. D **60**, (1999) 052001.
5. R. H. Dalitz and G. R. Goldstein, Phys. Rev. D **45**, (1992) 1531.
6. G. Mahlon and S. Parke, Phys. Lett. **B411**, (1997) 173; Phys. Rev. D **55**, (1996) 7249.

$t\bar{t}$ cross section at the Tevatron

Emmanuel Busato

LPNHE, Universités Paris VI and VII, IN2P3-CNRS, Paris, France

Abstract. Preliminary results obtained by the CDF and DØ collaborations on the top quark pair production cross section in $p\bar{p}$ collisions at a center of mass energy of $\sqrt{s} = 1.96$ TeV are presented. The measurements are obtained using various final states and are based on data collected during years 2002-2004 at the Tevatron Run II.

1 Introduction

The top quark, whose mass approaches the electroweak symmetry breaking scale, is by far the heaviest known elementary particle. New physics is therefore expected to have its most important effect in the top sector. The Tevatron is, currently, the only collider able to produce the top quark. Among all possible production processes in the Standard Model (SM), the $t\bar{t}$ pair production via strong interaction, first observed in 1995, is the one with the largest cross section.

Full NLO computations predict a $t\bar{t}$ pair production cross section of $6.7^{+0.7}_{-0.9}$ pb for $\sqrt{s} = 1.96$ TeV and $M_{top} = 175$ GeV [1], which represents a 30% increase with respect to the cross section at $\sqrt{s} = 1.8$ TeV.

In the SM, the top quark decays almost 100% of the time to a W boson and a b -quark. The final state is therefore determined by the W decay. This paper covers the recent top quark cross section measurements performed by the CDF and DØ collaborations in the di-lepton channels, where both W decay leptonically into an electron or a muon (ee , $e\mu$, $\mu\mu$), in the lepton+jets channels, where one of the W decays leptonically and the other hadronically (e +jets, μ +jets), and in the all-jets final state where both W decay hadronically. In each channel, many measurements have been done using different analysis strategies. Not all of them are described in this paper but only the most precise/recent ones. The complete list is given on CDF's and DØ's public web pages [2].

2 Di-lepton channels

The di-lepton final state is characterized by the presence of two oppositely charged and isolated high p_T leptons, large \cancel{E}_T and at least two high p_T jets. In spite of a small statistics (it represents only 5% of the full $t\bar{t}$ sample), it is very interesting to study because the backgrounds are rather small compared to the other channels. The potential physics backgrounds to such a signature come from $W^+W^- \rightarrow l^+l^-$ and $Z/\gamma^* \rightarrow \tau^+\tau^-$ events. Each of these

can be produced with ≥ 2 associated jets and constitute significant backgrounds. Instrumental backgrounds arise from mismeasured \cancel{E}_T in $Z/\gamma^* \rightarrow l^+l^-$ production and from fake lepton in W +jets events.

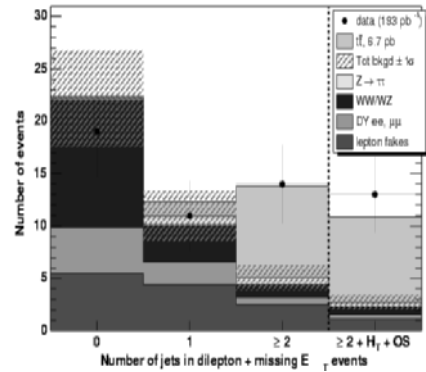


Fig. 1. Jet multiplicity in CDF di-lepton events with 193 pb^{-1} . The dots denote the observed number of events in data. The filled histograms represent the backgrounds and the $t\bar{t}$ expectation from the SM.

CDF has used $\sim 200 \text{ pb}^{-1}$ of data to select $t\bar{t} \rightarrow ll + \cancel{E}_T + \geq 2$ jets candidates in two complementary analysis. In one of the analysis both leptons are explicitly identified as either electron or muon. Events are selected applying basic kinematic cuts : $p_T^{\text{leptons}} > 20$ GeV, $\cancel{E}_T > 25$ GeV, $E_T^{j1, j2} > 20$ GeV and total transverse energy of event $H_T > 200$ GeV. Figure 1 shows the jet multiplicity distribution. The expected number of events with ≥ 2 jets is (including the SM $t\bar{t}$) 10.9 ± 1.4 , while 13 candidates are observed in data. In an other analysis, no explicit identification is required for one of the lepton. Instead, an isolated track is considered as a lepton candidate. Although this leads to a higher background contamination, it also gives higher signal acceptance. Furthermore, the selection is efficient for $t\bar{t}$ events with $W \rightarrow \tau\nu$, $\tau \rightarrow 1 - \text{prong}$ decay. The combination of the two analysis yields¹ [3] :

¹ CDF's systematic uncertainty includes the uncertainty on the integrated luminosity measurement.

$$\text{CDF} : \sigma(t\bar{t}) = 7.0_{-2.1}^{+2.4}(\text{stat})_{-1.2}^{+1.7}(\text{syst}) \text{ pb}$$

DØ has analyzed 370 pb^{-1} of data to select di-electron, electron-muon and di-muon events with $p_T^{\text{leptons}} > 15 \text{ GeV}$, $\cancel{E}_T > 25 \text{ GeV}$ and ≥ 2 jets with $p_T > 20 \text{ GeV}$. A total of 28 events have been observed while $24.1_{-2.4}^{+2.9}$ events are expected. The combined $\sigma(t\bar{t})$ measurement for the three channels is :

$$\text{DØ} : \sigma(t\bar{t}) = 8.6_{-2.0}^{+2.3}(\text{stat})_{-1.0}^{+1.2}(\text{syst}) \pm 0.6(\text{lumi}) \text{ pb}$$

Both measurements are in good agreement with the SM prediction.

3 Lepton+jets channels

The signature of the lepton + jets channel consists of one isolated high p_T lepton, large \cancel{E}_T and at least four high p_T jets (two of them are b -jets). The statistics is 6 times higher than in the di-lepton channel but the backgrounds are also much more important. The dominant background processes are W +jets and QCD multijet production where one of the jets fakes an isolated lepton. Two approaches are used to discriminate the signal from the backgrounds. The first approach makes use of the distinct topology between $t\bar{t}$ events and background events and relies on kinematic selection criteria only. The second approach makes use of the differences in flavor content between the signal and the backgrounds. The signal indeed contains at least two b -jets in the final state coming from the decay of the top and anti-top quarks whereas the backgrounds are made essentially of light quark jets. Requiring one or two b -jets therefore allows to extract $t\bar{t}$ events. In both approaches, at the first stage of the analysis (so called preselection) a data sample enriched in W +jets and $t\bar{t}$ events is defined. The remaining QCD multijet background originates primarily from π^0 's and γ 's misidentified as jets (e +jets channel) or from heavy flavor decays (μ +jets channel), and is evaluated directly from data.

3.1 Topological analysis

In 347 pb^{-1} of data CDF has selected 936 events with $p_T^{\text{lepton}} > 20 \text{ GeV}$, $\cancel{E}_T > 20 \text{ GeV}$ and ≥ 3 jets with $p_T > 15 \text{ GeV}$. In order to separate the signal from the backgrounds, various kinematic variables have been combined into a Neural Network (NN) discriminant. Its distribution for the selected data events has been fitted with signal and background templates (cf figure 2). The variables entering the NN have been chosen so that the discriminating power is maximal and the jet energy scale dependence minimal (since this is the dominant source of uncertainty). The extracted cross section is :

$$\text{CDF} : \sigma(t\bar{t}) = 6.0 \pm 0.8(\text{stat}) \pm 1.0(\text{syst}) \text{ pb}$$

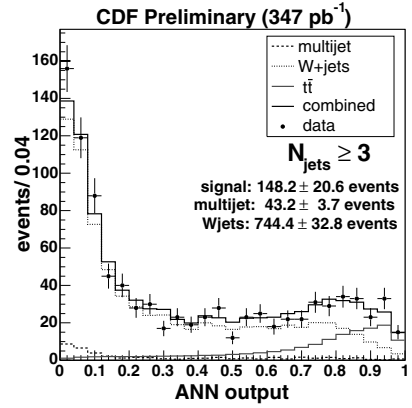


Fig. 2. Neural Network output distribution for lepton + \cancel{E}_T + ≥ 3 jets events obtained by CDF with 347 pb^{-1} .

In a similar manner, DØ has combined topological variables into an event likelihood discriminant (D). The preselection is essentially the same as the one done by CDF except that only events with ≥ 4 jets are considered. The likelihood discriminant distributions in the e +jets and μ +jets analysis, both using $\sim 230 \text{ pb}^{-1}$ of data, are shown in figure 3-a and 3-b respectively. The agreement is good in the background dominated region ($D \rightarrow 0$) and the excess for high values of D is due to the $t\bar{t}$ signal. The $t\bar{t}$ production cross section is obtained by fitting the data with background and signal templates and is found to be [4] :

$$\text{DØ} : \sigma(t\bar{t}) = 6.7_{-1.3}^{+1.4}(\text{stat})_{-1.1}^{+1.6}(\text{syst}) \pm 0.4(\text{lumi}) \text{ pb}$$

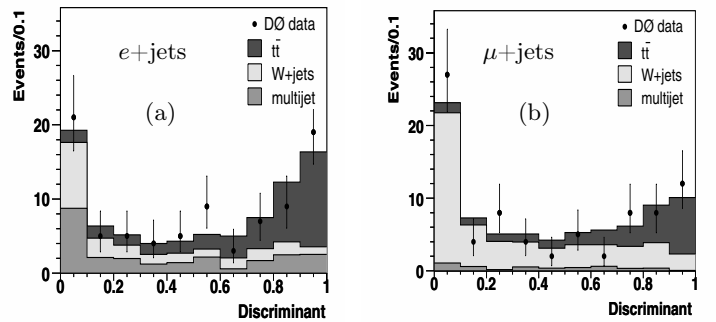


Fig. 3. Likelihood discriminant distribution for the e +jets analysis (a) and the μ +jets analysis (b) obtained by DØ with 230 pb^{-1} .

3.2 Lifetime tag analysis

The final state in lepton+jets events contains at least two b quarks coming from the decays of the top and anti-top

quarks. These quarks hadronize into B hadrons which are identifiable experimentally. Indeed, B hadrons are long lived particles which, when coming from top decays, travel few hundreds of μm in the transverse plane before decaying. This distance can effectively be resolved thanks to new Silicon Microvertex sub-detectors in both CDF and $D\bar{O}$ experiments. Both collaborations use similar b -tagging algorithms which consist in reconstructing explicitly secondary vertices with a large decay length significance with respect to the primary vertex. Applying b -tagging requirement in the preselected samples substantially reduces contamination from W +jets and QCD multijet processes.

In 318 pb^{-1} of data CDF has observed 138 events with at least one tagged jet and 33 events with at least two tagged jets. The jet multiplicity distributions are shown in figures 4-a and 4-b. The excesses of events give :

$$\text{CDF } (\geq 1 \text{ } b\text{-tag}) : \sigma(t\bar{t}) = 7.9 \pm 0.9(\text{stat}) \pm 0.9(\text{syst}) \text{ pb}$$

$$\text{CDF } (\geq 2 \text{ } b\text{-tag}) : \sigma(t\bar{t}) = 8.7 \pm 1.7(\text{stat}) \pm 1.5(\text{syst}) \text{ pb}$$

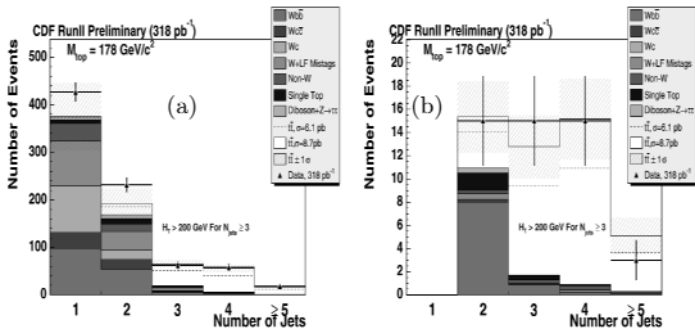


Fig. 4. Jet multiplicity for events with ≥ 1 tagged jet (a) and ≥ 2 tagged jets (b) obtained by CDF with 318 pb^{-1} .

CDF has done another measurement using a different approach and a reduced data sample of 162 pb^{-1} . Rather than extracting $\sigma(t\bar{t})$ from a counting experiment, a fit to the leading jet p_T distribution with templates for the background and the signal is performed (cf figure 5). The measured cross section is [5] :

$$\text{CDF} : \sigma(t\bar{t}) = 6.0 \pm 1.6(\text{stat}) \pm 1.2(\text{syst}) \text{ pb}$$

$D\bar{O}$ has performed a b -tagged analysis by combining not only the electron and muon channels but also the 3 jets and ≥ 4 jets events and the 1-tagged jet and ≥ 2 tagged jets events. An integrated luminosity of 230 pb^{-1} is used in this measurement. The jet multiplicity distributions for single tagged and ≥ 2 tagged jets events are shown in figure 6-a and 6-b. The resulting cross section is [6] :

$$D\bar{O} : \sigma(t\bar{t}) = 8.6^{+1.6}_{-1.5}(\text{stat} + \text{syst}) \pm 0.6(\text{lumi}) \text{ pb}$$

All lepton+jets channel measurements are in good agreement with the SM prediction.

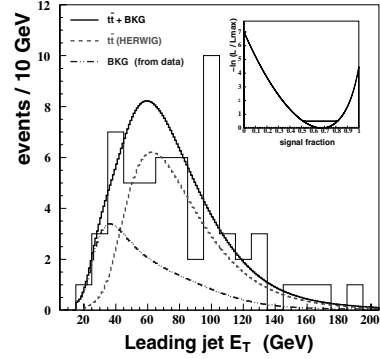


Fig. 5. Distribution of the leading jet p_T for lepton + ≥ 3 jets events where at least one jet is identified as a b jet obtained by CDF with 162 pb^{-1} .

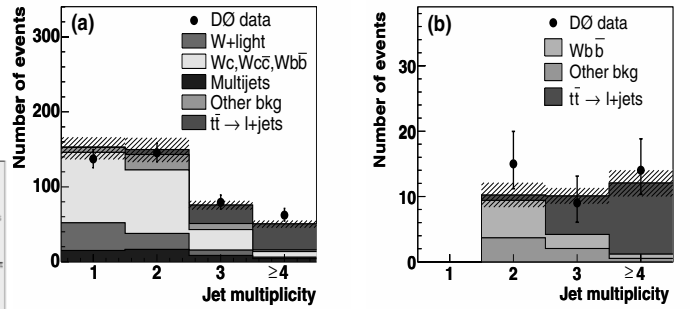


Fig. 6. Jet multiplicity for events with 1 tagged jet (a) and ≥ 2 tagged jets (b) obtained by $D\bar{O}$ with 230 pb^{-1} .

4 All-jets channel

The most challenging of the three considered signatures from $t\bar{t}$ events is the one arising when both W decay into hadrons, and thus leading to events with ≥ 6 jets. Indeed, this signal is overwhelmed by a very large QCD multijet background. The only efficient way to suppress this background is to apply both a strong topological selection and b -tagging.

CDF has used 165 pb^{-1} of data to extract the $t\bar{t}$ production cross section. Events are required to have between 6 and 8 jets with $p_T > 20 \text{ GeV}$ and to pass a certain number of topological criteria. In addition, one of the jets has to be identified as a b jet. The observed excess of events after such a selection gives :

$$\text{CDF} : \sigma(t\bar{t}) = 7.8^{+2.5}_{-2.5}(\text{stat})^{+4.7}_{-2.3}(\text{syst}) \text{ pb}$$

$D\bar{O}$'s strategy is slightly different. Events with more than 8 jets are included in the measurement and instead of cutting on individual topological variables, a chain of three Neural Network is built to separate the signal from the QCD multijet background. The variables included in the NN describe the event energy, the event shape, the rapidity distributions and the top properties. Figure 7 shows the output of the third NN (so called NN2) obtained on 162 pb^{-1} of data. Only events with $\text{NN2} > 0.75$ are retained in the measurement. 220 events are observed in

data while $186 \pm 5(stat)$ are expected to come from the background, yielding a cross section of :

$$D\emptyset : \sigma(t\bar{t}) = 7.7^{+3.4}_{-3.3}(stat)^{+4.7}_{-3.8}(syst) \pm 0.5(lumi) \text{ pb}$$

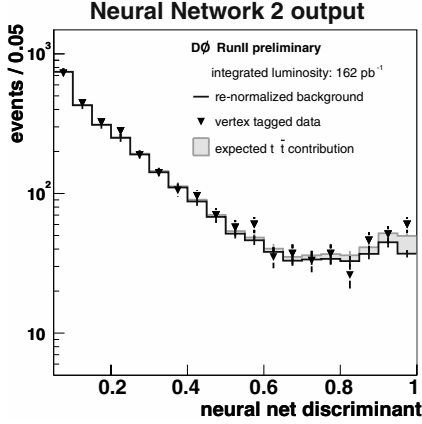


Fig. 7. Neural Network output distribution in $t\bar{t} \rightarrow all - jets$ events selected by $D\emptyset$ with 162 pb^{-1} .

Both measurements are in good agreement with the SM prediction.

5 Summary

The top pair production cross section has been measured by both CDF and $D\emptyset$ collaborations in a variety of final states using Tevatron Run II data. The compilation of the results is given in figure 8 for CDF² and figure 9 for $D\emptyset$ along with the theoretical prediction [1]. All measurements are in good agreement with the theoretical prediction.

References

1. R. Bonciani, S. Catani, M.L. Mangano and P. Nason, Nucl. Phys. B **529**, (1998) 424, updated in arXiv:hep-ph/0303085.
2. CDF results : <http://www-cdf.fnal.gov/physics/new/top/top.html>
 $D\emptyset$ results : <http://www-d0.fnal.gov/Run2Physics/top/public/public.html>
3. CDF Collaboration, D. Acosta *et al.*, Phys. Rev. Lett. **93**, (2004) 142001.
4. $D\emptyset$ Collaboration, V.M.Abazov *et al.*, arXiv:hep-ex/0504043.
5. CDF Collaboration, D. Acosta *et al.*, Phys. Rev. **D71**, (2004) 072005.
6. $D\emptyset$ Collaboration, V.M.Abazov *et al.*, arXiv:hep-ex/0504058.

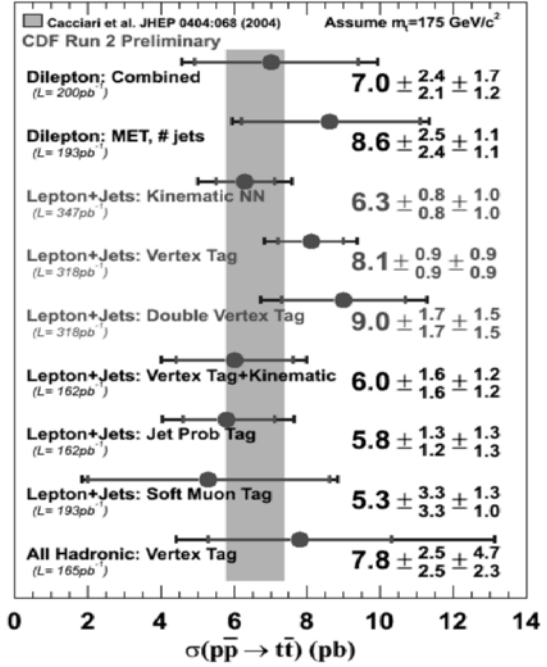


Fig. 8. Cross section measurements for the top pair production at the Tevatron Run II by CDF in a variety of final states. The band represents the theoretical prediction with its uncertainty.

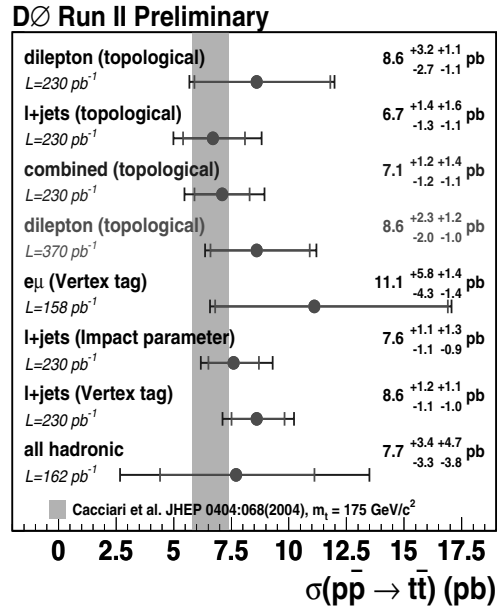


Fig. 9. Cross section measurements for the top pair production at the Tevatron Run II by $D\emptyset$ in a variety of final states. The band represents the theoretical prediction with its uncertainty.

² It has to be pointed out that for the recent measurements from CDF ($\mathcal{L} > 300 \text{ pb}^{-1}$), the $t\bar{t}$ cross sections are larger in figure 8 than in the text. This is due to different top quark mass assumptions ($M_{top} = 175 \text{ GeV}$ in the figure and $M_{top} = 178 \text{ GeV}$ in the text).

Single Top At The Tevatron

Anyes Taffard (on behalf of the CDF & DØ collaborations)

University of Illinois
Urbana-Champaign, IL 61801

Abstract. We review the status of the search for the electroweak production of single top quarks by the CDF and DØ collaborations at the Fermilab Tevatron proton-antiproton collider using Run II data. With a dataset of approximately 160 pb^{-1} for CDF and 230 pb^{-1} for DØ, neither experiment finds evidence for single top production and sets 95% C.L. upper limits on the production cross-sections. The CDF limits are 10.1 pb for the t channel, 13.6 pb for the s channel and 17.8 pb for the combined production cross-sections of s and t channel. The DØ limits are 5.0 pb for the t channel, 6.4 pb for the s – channel production cross-sections. Both experiments investigate the prospect for a 3σ evidence and a 5σ discovery.

1 Introduction

In $p\bar{p}$ collisions at a center of mass of 1.96 GeV, top quarks are predominantly produced in pairs via strong interactions processes. Within the standard model (SM), top quarks can also be produced singly in electroweak interactions involving a Wtb vertex [1]. At the Tevatron, the two relevant production modes are the t and the s channel exchange of a virtual W boson. This production mechanism allows for a direct measurement of the CKM mixing angle $|V_{tb}|$. It is also sensitive to physics beyond the standard model which predicts anomalously altered single-top production rates [2]. The most recent next-to-leading order (NLO) calculations, assuming $|V_{tb}| = 1$, predict cross-sections of $1.98 \pm 0.25 \text{ pb}$ for the t channel and $0.88 \pm 0.11 \text{ pb}$ for the s channel at $\sqrt{s} = 1.96 \text{ TeV}$ with $m_t = 175 \text{ GeV}$ [3].

The final state for the s channel consists of the decay products from the W and a b -quark jet both originating from the top decay and a b -quark jet produced with the top quark. The final state for the t channel consists of the decay products from the W and a b -quark jet both originating from the top decay and a light quark jet produced with the top quark. High-order corrections can result in additional jets in both the s channel and t channel. In particular in the t channel, where an additional b -quark jet originates from the splitting of an initial state gluon in a $b\bar{b}$ pair. The experimental searches for single top production focus on the decay of the W to an electron or a muon since the all-hadronic channel has overwhelming background from QCD multi-jet events.

This document describes the searches for electroweak production of single top quark by the CDF [5] and the DØ [6] collaborations using a data sample from the Tevatron Run II. Results of searches performed at $\sqrt{s} = 1.8 \text{ TeV}$ (Run I) can be found in Refs. [4].

2 CDF Search For Single Top Quark Production

The CDF strategy consists of a combined search for the sum of the s and t channel single top signals aiming to optimize the discovery potential and a separate search where the rates for the two single top processes are measured in order to increase sensitivity to new physics. The data sample corresponds to an integrated luminosity of $162 \pm 10 \text{ pb}^{-1}$. The common event selection for both analyses accepts events with the evidence of a leptonic W decay: one isolated electron(muon) with $E_T > 20 \text{ GeV}$ ($P_T > 20 \text{ GeV}/c$) and $|\eta| < 1.0$, missing transverse energy from the neutrino, $\cancel{E}_T > 20 \text{ GeV}$ and requires exactly two jets with $E_T > 15 \text{ GeV}$ and $|\eta_{det}| < 2.8$. At least one of the jets must be identified as originating from a b quark with a secondary vertex algorithm (b -tagging) [7]. The effective coverage of the b -tagging ranges up to $|\eta_{det}| \leq 1.4$ with an efficiency per b jet averaging $\sim 40\%$ and a “mistags” rate, defined as the probability of erroneously identified a light-quark jet, ranging from 0.5% to 1%. The sensitivity is then increase by requiring that the invariant mass of the lepton, the neutrino and the b -tagged jet satisfies $140 \text{ GeV}/c^2 \leq M_{l\nu b} \leq 210 \text{ GeV}/c^2$. For the separate search, the sample is subdividing into events with exactly one b -tagged jet (t channel) and events with exactly two b -tagged jets (s channel). For the singly-tagged sample, the leading jet is required to have $E_T > 30 \text{ GeV}$.

The event detection efficiency, ϵ_{evt} , estimated with signal events generated by the matrix element event generator MadEvent [8], followed by parton showering with PYTHIA [9] and the full CDF II detector simulation [10]. MadEvent features the correct spin polarization of the top quark and its decay products. For the t channel, two samples are generated, one $b + q \rightarrow t + q'$ and the other $g + q \rightarrow t + \bar{b} + q'$, which are then merged to reproduce

the P_T spectrum of the \bar{b} expected from NLO differential cross-section calculations [3]. The event detection efficiency is $1.06 \pm 0.08\%$ for the s channel and $0.89 \pm 0.07\%$ for the t channel and includes the kinematic and fiducial acceptance, branching ratios, lepton and b -jet identification as well as trigger efficiencies.

Two background components are considered: $t\bar{t}$ and non-top background. The $t\bar{t}$ background is estimated from events generated with PYTHIA, normalized to the theoretical cross-section $\sigma_{t\bar{t}} = 6.7^{+0.7}_{-0.9}$ pb for $m_t = 175$ GeV [11]. The primary source of non-top background is W +heavy flavor processes, where the rates are extracted from ALPGEN [12] Monte Carlo (MC) events and normalized to the data before b -tagging correcting for the presence of QCD multi-jets and $t\bar{t}$ [7]. Additional background from W +light-flavor jets and QCD multi-jet events, such as $b\bar{b}$ production, are determined from Run II data. Diboson production are estimated from PYTHIA MC events normalized to theory predictions [13].

Good agreement is found between observation and expectation, with a total of 42, 33 and 6 events observed versus 38.1 ± 5.9 , 30.3 ± 4.7 and 3.53 ± 0.72 expected for the combined, t channel and s channel respectively.

In order to test for the signal content in the data, a maximum likelihood fit to a discriminant variable in data is performed, using a sum of templates determined from Monte Carlo events. In the case of the combined search, the variable H_T , defined as the sum of the lepton P_T , \cancel{E}_T and jets E_T , is chosen since it shows a similar distribution for both the s and t channel processes but is different for the background processes (see Figure 1). For the t channel, the $Q \times \eta$ distribution (see Figure 1), where Q is the charge of the lepton and η is the pseudorapidity of the untagged jet, is very asymmetric and peaked in the forward direction for t -channel signal events while it is symmetric and centrally distributed for the backgrounds. This distribution is used in the case of the separate search in a join likelihood with the number of events with two b -tagged jets, to obtain separately the contribution from s and t channel events. In the fits, the backgrounds are allowed to float but are constrained to their SM expectation with a Gaussian prior. The systematic uncertainties on the shapes of the distributions are included in the likelihood. The actual fit parameters are the deviations with respect to the SM cross-sections, *i.e.* $\beta_i = \sigma_i / \sigma_i^{SM}$, with the index i denoting single top s or t channel, $t\bar{t}$ and non-top. The fitted signal content in data are found to be compatible with zero in both searches: $\beta = 0.0^{+2.4}_{-0.0}$ for the t channel, $\beta = 5.2^{+4.3}_{-4.3}$ for the s channel and $\beta = 2.7^{+1.8}_{-1.7}$ for the combined $s + t$ channel. An upper limit on the single top cross-section is determined from a Bayesian approach using the likelihood and a flat prior on β . The single top cross-section limits at 95% C.L. observed in the data are $\sigma_s < 13.6$ pb for the s channel, $\sigma_t < 10.1$ pb for the t channel and $\sigma_{s+t} < 17.8$ pb for the combined $s + t$ channel.

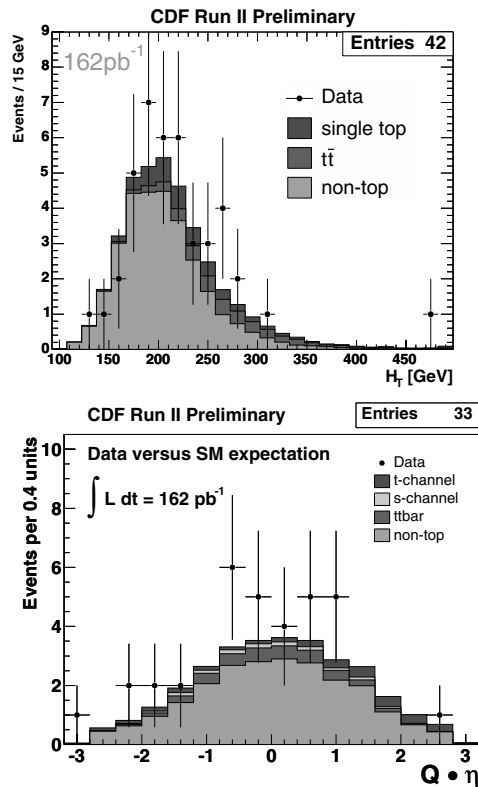


Fig. 1. H_T (top) and $Q \times \eta$ (bottom) distributions for data in the combined and t -channel searches respectively compared to the MC predictions for signal and background.

3 DØ Search for Single Top Quark Production

The DØ strategy for the single top search consists of a very loose event selection designed to select events containing a W and at least two jets while keeping a high acceptance for single top events. The analysis is performed separately for the electron and muon channels, using a data sample corresponding to an integrated luminosity of $\sim 230 \pm 15$ pb $^{-1}$. The event selection consists of identifying exactly one isolated electron (muon) with $P_T > 15$ GeV and $|\eta_{det}| < 1.1$ ($|\eta_{det}| < 2.0$), $\cancel{E}_T > 15$ GeV and between two to four jets where the leading jet must have $P_T > 25$ GeV and $|\eta_{det}| < 2.5$ and all the other jets must satisfy $P_T > 15$ GeV and $|\eta_{det}| < 3.4$. At least one of the jets must be identified as originating from a b quark with a secondary vertex algorithm [14]. The DØ b -tagger performance is similar to that of the CDF one. For both the s channel and t -channel searches, the data sample is separated into independent analysis sets based on the lepton flavor and the number of b -tagged jets: exactly 1-tag and ≥ 2 tags. For the t -channel search, it is required that one of the jets is not b -tagged.

The kinematic and geometrical acceptances for the s channel and t channel are estimated with signal events generated by the matrix element event generator COM-PHEP [15]. The overall acceptances, including trigger and

selection efficiencies, for events with at least one b -tagged jet are $2.7 \pm 0.2\%$ for the s channel and $1.9 \pm 0.2\%$ for the t channel. For the s -channel search, the t channel is considered as background and vice versa.

The W +jets and diboson backgrounds are estimated using events generated with ALPGEN [12]. The W +jets yield is normalized to the yield in the data before b -tagging, corrected for the presence of QCD multi-jets, $t\bar{t}$ and dibosons. The fraction of heavy flavor events ($Wb\bar{b}$) is obtained from the ratio of the NLO cross-sections for $Wb\bar{b}$ and W +jets [16]. The $t\bar{t}$ background is estimated using events generated with ALPGEN and normalized to the cross-section of $\sigma_{t\bar{t}} = 6.7^{+0.7}_{-0.9}$ pb for $m_t = 175$ GeV [11]. The parton-level samples are then processed with PYTHIA [9] and the full GEANT-based simulation of the DØ detector [17]. Additional background from QCD multi-jet events is determined from data.

Good agreement is found between observation and expectation, with a total of 283 and 271 events observed versus 287.4 ± 31.4 and 275.8 ± 31.5 expected for the s channel and t channel, respectively.

In order to discriminate between signal and background events, 25 variables are combined in neural networks using eleven variables each. The set of variables can be categories as object kinematics (*e.g.* P_T^1 of the leading b -tagged jet, jet_{1b}), global event kinematics (*e.g.* $M_{W,jet_{1b}}$) and angular correlations (*e.g.* $\cos(\text{lepton}, jet_{1b})$). Eight different neural networks are trained separately for electron and muon (to account for the different η coverage) and the four pair combinations of signals (s or t channel) and backgrounds ($t\bar{t}$ or $Wb\bar{b}$). Figure 2 shows an example of the neural net output for the s channel trained for $t\bar{t}$ (top) and $Wb\bar{b}$ (bottom), combining the electron and muon channels, and requiring at least one b -tagged jet. The $Wb\bar{b}$ neural networks separate less efficiently the signal from the background than the $t\bar{t}$ one because the event kinematics are similar between the signal and background.

The observed data are consistent with the background predictions for all eight neural networks analyses. Upper limits on the single top quark production cross-section separately for the s -channel and t -channel searches are set using a Bayesian approach [18]. In each search, two-dimensional histograms are constructed from the $t\bar{t}$ and $Wb\bar{b}$ neural-network outputs. A likelihood is built from these histograms for signal, background and data as a product of all channels (electron, muon, single and double b tagged events) and bins. For the observed number of events in each bin, a Poisson distribution is assumed and a flat prior probability is used for the signal cross-section. The prior for the background yield and the combined signal acceptance is a multivariate Gaussian with uncertainties and correlations described by a covariance matrix. The single top cross-section limits at 95% C.L. are $\sigma_s < 6.4$ pb for the s channel, $\sigma_t < 5.0$ pb for the t channel for expected upper limits of $\sigma_s < 4.5$ pb and $\sigma_s < 5.8$ pb respectively.

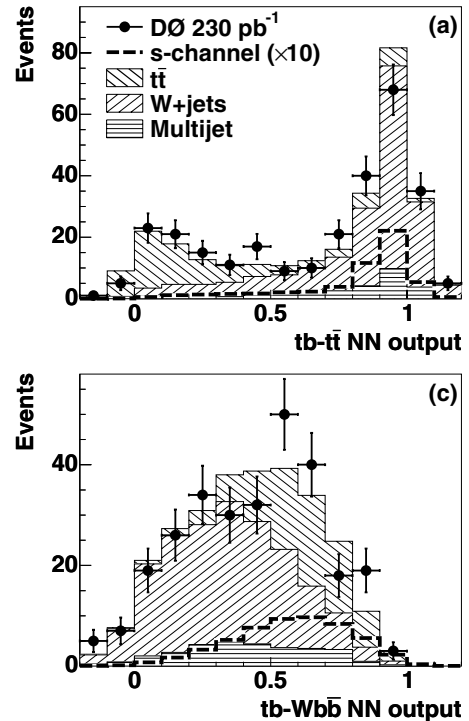


Fig. 2. Comparison of s -channel signal, background and data for the neural networks outputs, trained with $t\bar{t}$ (a) and $Wb\bar{b}$ (c) for the electron and muon channels combined, requiring at least one b -tagged jet.

4 Conclusions And Projections

The Tevatron collider experiments, CDF and DØ, are in a unique position to search for new physics in the top quark sector. Both experiments have searched for single top production in the s channel and t channel using a data sample of 160 pb^{-1} for CDF and 230 pb^{-1} for DØ. They find good agreement between the expected backgrounds and the observed data and set 95% C.L. upper limits on the single top production cross-section.

Currently, each experiment is taking an aggressive approach in developing advance analysis technique, optimizing event selections and improving the systematic uncertainties. Both experiments have looked into the projection for a 3σ evidence and a 5σ discovery, and find that, although the task is challenging, advanced analysis techniques can significantly improve the sensitivity. CDF projects to reach a 3σ evidence¹ with 1.5 fb^{-1} . With the Tevatron performing on design and expected to deliver 8 fb^{-1} by 2009 and the already 0.8 to 1 fb^{-1} that is being analysed for the Winter conferences of 2006, the next few years of the Tevatron could turn out to be quite exciting.

¹ This projection does not take into account the systematic uncertainties

4.1 Acknowledgments

I would like to thank the HCP organizers for providing an excellent conference that was very enjoyable despite the poor weather. I also would like to thank my colleagues from CDF and DØ top groups whose works went in to the results presented here in those proceedings.

References

1. T. Stelzer, Z. Sullivan, S.S. Willenbrock, Phys. Rev D**56**, (1997) 5919; M.C. Smith and S.S Willenbrock, Phys. Rev D**54**, (1996) 6696; S. Mrenna and C.-P. Yuan, Phys. Lett. B**416**, (1998) 200.
2. T. Tait and C.-P. Yuan, Phys. Rev. D**63**, (2001) 014018.
3. B.W. Harris, E.Laenen, L. Phaf, Z. Sullivan and S. Weinzierl, Phys. Rev. D**66**, (2002) 054024.
4. CDF Collaboration, D. Acosta *et al.*, Phys. Rev. D**65**, (2002) 091102; DØ Collaboration, B. Abbott *et al.*, Phys. Rev. D**63**, (2001) 031101; DØ Collaboration, V. M. Abazov *et al.*, Phys. Lett. B**517**, (2001) 282.
5. CDF Collaboration, D. Acosta *et al.*, Phys. Rev. D**71**, (2005) 012005.
6. DØ Collaboration, V. M. Abazov *et al.*, Phys. Lett. B**622** (2005) 265.
7. CDF Collaboration, D. Acosta *et al.*, Phys. Rev. D**71**, (2005) 052003.
8. T. Stelzer and W.F. Long, Comput. Phys. Commun, **81**, (1994) 337; F. Maltoni and T. Stelzer, J. High Energy Phys. **02**, (2003) 027.
9. T. Sjöstrand *et al.*, Comput. Phys. Commun. **135**, (2001) 238.
10. E. Gerchtein and M. Paulini, ECONF **C0303241**, TUMT005 (2003), arXiv:physics/0306031.
11. R. Bonciani *et al.*, Nucl. Phys. B**529**, (1998) 424; M. Cacciari *et al.*, J. High. Energy Phys. **04** (2004) 068.
12. F. Caravaglios *et al.*, Nucl. Phys. B**539**, (1999) 215; M. Mangano *et al.*, Nucl. Phys. B**632**, (2002) 343; M. Mangano *et al.*, J. High Energy Phys. **07**, (2003) 001.
13. S. R. Slabospitsky and L. Sonnenschein, Comput. Phys. Commu. **148**, (2002) 87.
14. DØ Collaboration, V. M. Abazov *et al.*, hep-ex**0504058**, submitted to Phys. Rev. Lett.
15. CompHEP Collaboration, E.Boos *et al.*, Nucl. Instrum. Meth A**534**, (2004) 250.
16. DØ Collaboration, V. M. Abazov *et al.*, Phys. Rev. Lett**93**, (2004) 141801 .
17. R. Brun *et al.* CERN Program Library Long Writeup **W5013**, (1994).
18. I. Bertram *et al.*, FERMILAB-TM2104 (2000).

Top Properties and Rare Decays from the Tevatron

Arnulf Quadt^{1,2}

¹ Physikalisches Institut, Universität Bonn, Nußallee 12, D-53115 Bonn, Germany

² University of Rochester, New York, c/o Fermilab - P.O. Box 500, 60510, IL, USA

Abstract. The top quark is the most recently discovered quark. Relatively little is known about its properties so far. Due to its very large mass of about $175 \text{ GeV}/c^2$, the top quark behaves differently from all other quarks and provides a unique environment for tests of the Standard Model. Furthermore, it is believed to yield sensitivity to physics beyond the Standard Model. This report discusses the latest measurements and studies of top quark properties and rare decays from the Tevatron in Run II.

1 Introduction

The top quark discovery in 1995 by the experiments CDF and $D\bar{O}$ [1] defines the start of the exciting era of top quark physics at the Tevatron. After very successful upgrades of the $p\bar{p}$ collider Tevatron for higher beam energy and luminosity and of both experiments for faster readout and trigger electronics, better tracking and muon detection, data taking in Run II started in the year 2001. Since then, the Tevatron provided more than 1 fb^{-1} of $p\bar{p}$ collision data at $\sqrt{s} = 1.96 \text{ TeV}$ to each experiment. At present, up to 370 pb^{-1} have been analyzed in top quark studies.

Top quark physics at the Tevatron can be divided into the following categories: 1) top quark production, 2) fundamental properties of the top quark, 3) top quark interactions to gauge bosons, 4) anomalous top quark production, 5) anomalous top quark decays, and 6) new physics in events with $t\bar{t}$ topology.

The first category, the top quark production, is studied via the measurements of the strong $t\bar{t}$ production cross section and the search for the electroweak single-top production, in the Standard Model (SM) expected to be around 7 pb and $\approx 3 \text{ pb}$, respectively. Measurements of the $t\bar{t}$ production cross section have been performed in many different top quark decay modes. The results are found to be consistent between the two experiments, all channels and with the Standard Model (SM) expectation within a combined precision of $\approx 14\%$ [2]. The corresponding data sets, quantitatively understood in terms of selection efficiency and signal and background contribution form the basis of all studies of properties and rare decays of the top quark. Single-top production is expected to be observed with $1 - 2 \text{ fb}^{-1}$ of data [3].

The other categories are discussed in turn in this document in Sections 2 to 6. All limits are quoted at the 95% CL unless noted otherwise.

In the SM, assuming unitarity of the three-generation CKM matrix, the matrix element $|V_{tb}|$ is found to be essentially unity. Therefore, the top quark is expected to

decay to a W -boson and a b -quark nearly 100% of the time. The W -boson subsequently decays either to a pair of quarks or a lepton-neutrino pair. Depending on the lepton or hadronic decay of the two W -bosons, the resulting event topologies of $t\bar{t}$ decays are classified as all-jets channel (46.2%), lepton+jets (ℓ +jets) channel (43.5%), and dilepton ($\ell\ell$) channel (10.3%). Each decay topology contains at least two b -jets. While ℓ in the above classification refers to e , μ , or τ , most of the results to date rely on the e and μ channels. Therefore, in what follows, ℓ will be used to refer to e or μ , unless noted otherwise.

2 Top Quark Interactions to Gauge Bosons

2.1 Spin Correlation

$D\bar{O}$ has searched for evidence of spin correlation of $t\bar{t}$ pairs [5]. The t and \bar{t} are expected to be unpolarized but to be correlated in their spins. Since top quarks decay before hadronizing, their spins at production are transmitted to their decay daughter particles. Spin correlation is studied by analyzing the joint decay angular distribution of one t daughter and one \bar{t} daughter. The sensitivity to top spin is greatest when the daughters are down-type fermions (charged leptons or d -type quarks), in which case, the joint distribution is

$$\frac{1}{\sigma} \frac{d^2\sigma}{d(\cos\theta_+)d(\cos\theta_-)} = \frac{1 + \kappa \cdot \cos\theta_+ \cdot \cos\theta_-}{4}, \quad (1)$$

where θ_+ and θ_- are the angles of the daughters in the top rest frames with respect to a particular spin quantization axis, the optimal choice being the off-diagonal basis. In this basis, the SM predicts maximum correlation with $\kappa = 0.88$ at the Tevatron. In Run I, $D\bar{O}$ analyzed six dilepton events and obtained a likelihood as a function of κ , which weakly favored the SM ($\kappa = 0.88$) over no correlation ($\kappa = 0$) or anti-correlation ($\kappa = -1$, as would be

Table 1. Measurements and lower limits of $R = B(t \rightarrow Wb)/B(t \rightarrow Wq)$ and $|V_{tb}|$ from CDF and DØ.

R or $ V_{tb} $	Source	$\int \mathcal{L} dt$ (pb $^{-1}$)
$R = 1.12^{+0.27}_{-0.23}$	CDF Run II [6]	160
$R > 0.61$	CDF Run II [6]	160
$R = 1.03^{+0.19}_{-0.17}$	DØ Run II [7]	230
$R > 0.64$	DØ Run II [7]	230
$ V_{tb} > 0.78$	CDF Run II [6]	160
$ V_{tb} > 0.80$	DØ Run II [7]	230

expected for $t\bar{t}$ produced via an intermediate scalar). DØ quotes a limit $\kappa > -0.25$ at 68% CL. With improved statistics in the ongoing Run II analyses, an observation of $t\bar{t}$ spin correlation would support that the top quark decays before hadronization and allow further test of the QCD production mechanism.

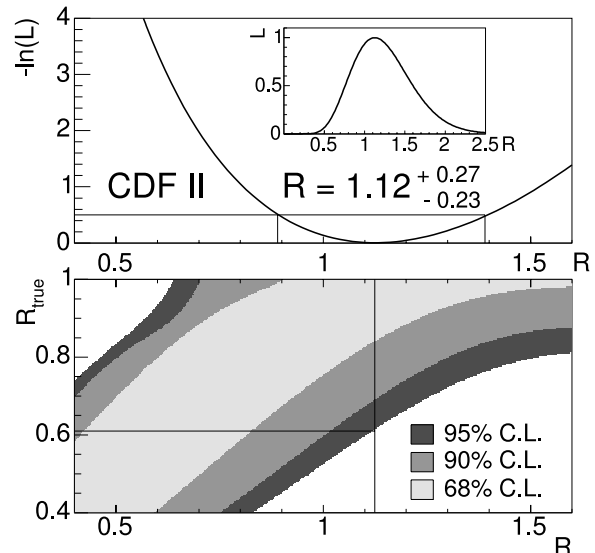
2.2 Measurement of $B(t \rightarrow Wb)/B(t \rightarrow Wq)$

CDF and DØ report direct measurements of the $t \rightarrow Wb$ branching ratio [6, 7]. Comparing the number of events with 0, 1 and 2 tagged b jets in the lepton+jets channel, and for CDF also in the dilepton channel, and using the known b -tagging efficiency, the ratio $R = B(t \rightarrow Wb)/\sum_{q=d,s,b} B(t \rightarrow Wq)$ can be extracted (Figure 1). DØ performs a simultaneous fit for the production cross section $\sigma_{t\bar{t}}$ and the ratio R . A deviation of R from unity would imply either non-SM top decay, a non-SM background to $t\bar{t}$ production, or a fourth generation of quarks. Assuming that all top decays have a W boson in the final state, that only three generations of fermions exist, and that the CKM matrix is unitary, CDF and DØ also extract the CKM matrix-element $|V_{tb}|$. The results of these measurements are summarized in Table 1. The top quark decay to Wb is indeed found to be dominant, although these studies are presently limited by statistics and will profit from the upcoming larger data sets.

A more direct measurement of the Wtb coupling constant will be possible when enough data are accumulated to detect the s -channel and t -channel single-top production processes [3]. The cross sections for these processes are proportional to $|V_{tb}|^2$, and no assumption is needed on the number of families or on the unitarity of the CKM matrix in extracting $|V_{tb}|$.

2.3 Study of $B(t \rightarrow \tau\nu q)$

The SM's heavy third generation particles, the top and bottom quarks, the tau and the tau neutrino are intriguing. The high energies required to produce the third generation particles, particularly in the case of the top quark, have resulted in the particles being the least studied in the SM. Current measurements leave room for new physics in the interactions and decays of these particles. The high masses of the particles give rise to the hope that studying


Fig. 1. Top: CDF likelihood as a function of R (inset) and its negative logarithm. Bottom: Confidence level bands for R_{true} as a function of R . The measurements of $R = 1.12$ (vertical line) implies $R > 0.61$ (horizontal line).

them could help shed light on the origin of fermion masses. CDF measures the rate of top-antitop events with a semi-leptonically decaying tau in $t\bar{t} \rightarrow e\tau bb\nu\nu$ and $t\bar{t} \rightarrow \mu\tau bb\nu\nu$ events in 200 pb $^{-1}$ of Run II data [8]. Semi-leptonic tau decays account for 64% of all tau decays. This analysis does not include taus decaying to electrons or muons because their leptonic tau decays are difficult to differentiate from prompt leptons. CDF compares the observed with the predicted rate as a test of the SM. Many extensions to the SM predict identical final states which could lead to an anomalous rate. For example the charged Higgs decay from $t\bar{t}$, $t\bar{t} \rightarrow H^\pm Wb\bar{b}$, $H^\pm \rightarrow \tau^\pm\nu_\tau$. This analysis is a search for any such anomalous processes that could show up in the final state as an enhanced (or suppressed) rate for tau leptons in top decays. The ratio $r_\tau \equiv B(t \rightarrow b\tau\nu)/B_{SM}(t \rightarrow b\tau\nu)$ is found to be $r_\tau < 5.0$ and therefore consistent with the SM.

2.4 Measurement of the Helicity of the W -Boson in Top Quark Decays

Studies of decay angular distributions provide a direct check of the $V-A$ nature of the Wtb coupling and information on the relative coupling of longitudinal and transverse W bosons to the top quark. In the SM, the fraction of decays to longitudinally polarized W bosons is expected to be $\mathcal{F}_0^{\text{SM}} = x/(1+x)$, $x = m_t^2/2M_W^2$ ($\mathcal{F}_0^{\text{SM}} \sim 70\%$ for $m_t = 175$ GeV/ c^2). Fractions of left- or right-handed W bosons are denoted as \mathcal{F}_- and \mathcal{F}_+ , respectively. In the SM, \mathcal{F}_- is expected to be $\approx 30\%$ and $\mathcal{F}_+ \approx 0\%$. CDF and DØ use various techniques to measure the helicity of the W boson in top quark decays in lepton+jets events. The first method uses a kinematic fit, similar to that used in the lepton+jets mass analyses [4], but with the top

Table 2. Measurement and upper limits of the W helicity in top quark decays from CDF and $D\bar{O}$. The integrated luminosity $\int \mathcal{L}dt$ is given in units of (pb^{-1}) .

W helicity	Source	$\int \mathcal{L}dt$	Method
$\mathcal{F}_0 = 0.91 \pm 0.39$	CDF Run I [9]	106	p_T^ℓ
$\mathcal{F}_0 = 0.56 \pm 0.32$	$D\bar{O}$ Run I [10]	125	ME
$\mathcal{F}_0 = 0.74^{+0.22}_{-0.34}$	CDF Run II [11]	200	$M_{\ell b}^2 + p_T^\ell$
$\mathcal{F}_+ < 0.18$	CDF Run I [12]	110	$M_{\ell b}^2 + p_T^\ell$
$\mathcal{F}_+ < 0.27$	CDF Run II [11]	200	$M_{\ell b}^2 + p_T^\ell$
$\mathcal{F}_+ < 0.25$	$D\bar{O}$ Run II [13]	230-370	$\cos\theta^* + p_T^\ell$

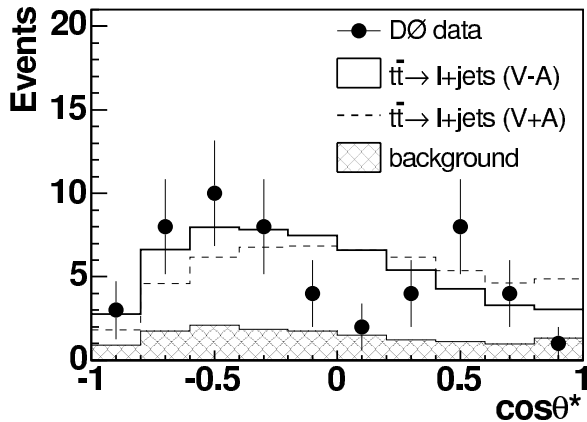


Fig. 2. $\cos\theta^*$ distribution observed in the $D\bar{O}$ data along with the SM prediction (solid line) and a model with a pure $V+A$ interaction (dashed line) for the b -tagged lepton+jets sample.

quark mass constrained to $175 \text{ GeV}/c^2$, to improve the reconstruction of final state observables and choose the assignment to quarks and leptons as that with the lowest χ^2 . The distribution of the helicity angle ($\cos\theta^*$) between the lepton and the b quark in the W rest frame, provides the most direct measure of the W helicity (Figure 2). The second method (p_T^ℓ) uses the different lepton p_T spectra from longitudinally or transversely polarized W -decays to determine the relative contributions. This method is also used by both experiments in the dilepton channel. A third method uses the invariant mass of the lepton and the b -quark in top decays ($M_{\ell b}^2$) as an observable, which is directly related to $\cos\theta^*$. Finally, the Matrix Element method (ME), initially developed for the top quark mass measurement, has also been used, forming a 2-dimensional likelihood $\mathcal{L}(m_{top}, \mathcal{F}_0)$, where the mass-dependence is integrated out so that only the sensitivity to the W -helicity in the top quark decay is exploited. The results of all CDF and $D\bar{O}$ analyses, summarized in Table 2, are in agreement with the SM expectation, but within large statistical uncertainties.

2.5 Search for Top Quark Decay via FCNC Couplings

Physics beyond the SM can manifest itself by altering the expected rate of flavor-changing neutral-current (FCNC)

interactions. FCNC decays of the top quark are of particular interest. The large mass of the top quark suggests a strong connection with the electroweak symmetry breaking sector. Evidence for unusual decays of the top quark might provide insights into that mechanism. For the top quark, the FCNC decays $t \rightarrow qZ$ and $t \rightarrow q\gamma$ (where q denotes either a c - or a u -quark) are expected to be exceedingly rare (branching fractions of 10^{-10} or smaller), since they are suppressed by the GIM mechanism and any observation of these decays in the available data sample would indicate new physics. In general, FCNC interactions are present in models which contain an extended Higgs sector, Supersymmetry, dynamical breaking of the electroweak symmetry, or an additional symmetry.

CDF reported a search for flavor changing neutral current (FCNC) decays of the top quark $t \rightarrow q\gamma$ and $t \rightarrow qZ$ in the Run I data [14]. CDF assumes that one top decays via FCNC while the other decays via Wb . For the $t \rightarrow q\gamma$ search, two signatures are examined, depending on whether the W decays leptonically or hadronically. For leptonic W decay, the signature is $\gamma\ell$ and missing E_T and two or more jets, while for hadronic W decay, it is $\gamma + \geq 4$ jets. In either case, one of the jets must have a secondary vertex b tag. One event is observed ($\mu\gamma$) with an expected background of less than half an event, giving an upper limit on the top branching ratio of $B(t \rightarrow q\gamma) < 3.2\%$. In the search for $t \rightarrow qZ$, CDF considers $Z \rightarrow \mu\mu$ or ee and $W \rightarrow qq'$, giving a $Z + \text{four jets}$ signature. One $\mu\mu$ event is observed with an expected background of 1.2 events, giving an upper limit on the top branching ratio of $B(t \rightarrow qZ) < 0.33$. These limits on top quark decay branching ratios can be translated into limits on the flavor-changing neutral current couplings $\kappa_\gamma < 0.42$ and $\kappa_Z < 0.73$. With 2 fb^{-1} , CDF and $D\bar{O}$ are expected to improve their sensitivity to κ_γ and to κ_Z significantly with the increased Run II data set.

3 Fundamental Properties of the Top Quark

3.1 Top Quark Mass

The Tevatron Electroweak Working Group has recently combined all available direct measurements of the top quark mass yielding a new world average of $m_{top} = 172.7 \pm 2.9 \text{ GeV}/c^2$ [4, 15]. The ultimate precision from the Tevatron on the top mass measurement is expected to be better than $2.0 \text{ GeV}/c^2$ per experiment.

3.2 Electric Charge of the Top Quark

The top quark is the only quark whose electric charge has not been measured through a production threshold in e^+e^- collisions. Since the CDF and $D\bar{O}$ analyses on top quark production do not associate the b , \bar{b} and W^\pm uniquely to the top or antitop, decays such as $t \rightarrow W^+\bar{b}$, $\bar{t} \rightarrow W^-b$ are certainly conceivable. A charge $4/3$ quark of this kind would be consistent with current electroweak precision data. The $Z \rightarrow \ell^+\ell^-$ and $Z \rightarrow b\bar{b}$ data can

be fitted with a top quark of mass $m_t = 270 \text{ GeV}/c^2$, provided that the right-handed b quark mixes with the isospin $+1/2$ component of an exotic doublet of charge $-1/3$ and $-4/3$ quarks, $(Q_1, Q_4)_R$. CDF and $D\bar{O}$ study the top quark charge in double-tagged lepton+jets events. Assuming the top and antitop quarks have equal but opposite electric charge, then reconstructing the charge of the b -quark through jet charge discrimination techniques, the $|Q_{top}| = 4/3$ and $|Q_{top}| = 2/3$ scenarios can be differentiated. CDF and $D\bar{O}$ both have already collected sufficient data to obtain sensitivity to the $|Q_{top}| = 4/3$ case. The analyses are ongoing, results are expected to be made public soon.

4 Anomalous Top Quark Production

4.1 Cross Section Ratio $\sigma_{\ell\ell}/\sigma_{\ell+jets}$

It is a priori not obvious, that the ‘top quark’, observed in the dilepton decay mode is identical to the ‘top quark’ in the lepton+jets decay mode. If both decay modes result exclusively from the decay of the SM top quark, they should have the same production cross section. If the production or the decay of the top quarks had non-SM contributions, one mode might be enhanced with respect to the other.

CDF has measured the cross section ratio $R_\sigma = \sigma_{\ell\ell}/\sigma_{\ell+jets}$ of the $t\bar{t}$ production cross section in the dilepton and the lepton+jets channels in 125 pb^{-1} of Run II data. CDF finds $R_\sigma = 1.45^{+0.83}_{-0.55}$ and $R_\sigma > 0.46$ (< 4.45), consistent with the SM. This result is also translated into generic top decay branching ratio limits. The considered cases are a fully hadronic decay $t \rightarrow Xb$, where $Br(X \rightarrow qq) = 100\%$ or a fully leptonic decay, i.e. $t \rightarrow Yb$, where $Br(Y \rightarrow qq) = 100\%$. The limits on R_σ translate into limits on the fully hadronic or the fully leptonic decay of the top quark as $Br(t \rightarrow Xb) < 0.46$ and $Br(t \rightarrow Yb) < 0.47$.

4.2 Anomalous Kinematics in $t\bar{t}$ Events

CDF reports a search for anomalous kinematics of $t\bar{t}$ dilepton events in 193 pb^{-1} [17]. A new *a priori* technique has been developed, designed to isolate the subset of events in a data sample which reveals the largest deviation from SM expectation and to quantify the significance of this departure. Four variables are considered: the missing transverse energy, \cancel{E}_T , the transverse momentum of the leading lepton p_T^ℓ , the angle $\phi_{\ell m}$ between the leading lepton and the direction of \cancel{E}_T in the plane transverse to the beam, and a variable T , representing how well the kinematics of an event satisfy the $t\bar{t}$ decay hypothesis based on the expected and observed \cancel{E}_T vector. This method is especially sensitive to data subsets that preferentially populate regions where new high- p_T physics can be expected. No such subset is found. Although the lepton p_T distribution exhibits a mild excess at low p_T , CDF determines the level of consistency of the $t\bar{t}$ dilepton sample with the SM expectation

and finds a p -value of $1.0 - 4.5\%$, showing good agreement with the SM.

This type of search for anomalous kinematics is presently statistics limited and will improve with larger data sets.

4.3 Top Production via Intermediate Resonances

Motivated by the large mass of the top quark, several models suggest that the top quark plays a role in the dynamics of electroweak symmetry breaking. One example is topcolor, where a large top quark mass can be generated through the formation of a dynamic $t\bar{t}$ condensate, X , which is formed by a new strong gauge force coupling preferentially to the third generation. Another example is topcolor-assisted technicolor, predicting a heavy Z' boson that couples preferentially to the third generation of quarks with cross sections expected to be visible at the Tevatron. CDF and $D\bar{O}$ have searched for $t\bar{t}$ production via intermediate, narrow-width, heavy vector bosons X in the lepton+jets channels. The t and \bar{t} final states are identified through a kinematic fit. The possible $t\bar{t}$ production via an intermediate resonance X is sought for as a peak in the spectrum of the invariant $t\bar{t}$ mass. CDF and $D\bar{O}$ exclude narrow width heavy vector bosons X [18] with mass $M_X < 480 \text{ GeV}/c^2$ and $M_X < 560 \text{ GeV}/c^2$, respectively, in Run I [19], and $M_X < 680 \text{ GeV}/c^2$ in $D\bar{O}$ Run II [20].

5 Anomalous Top Quark Decays

5.1 Search for Charged Higgs Boson in $t\bar{t}$ Decays

Both CDF and $D\bar{O}$ have searched for non-SM top decays, particularly those expected in supersymmetric models, such as $t \rightarrow H^+b$, followed by $H^+ \rightarrow \tau^+\bar{\nu}$ or $c\bar{s}$. The $t \rightarrow H^+b$ branching ratio has a minimum at $\tan\beta = \sqrt{m_t/m_b} \simeq 6$, and is large in the region of either $\tan\beta \ll 6$ or $\tan\beta \gg 6$. In the former range, $H^+ \rightarrow c\bar{s}$ is dominant, while $H^+ \rightarrow \tau^+\bar{\nu}$ dominates in the latter range. These studies are based either on direct searches for these final states, or on top ‘disappearance’. In the standard lepton+jets or dilepton cross section analyses, any charged Higgs decays are not detected as efficiently as $t \rightarrow W^\pm b$, primarily because the selection criteria are optimized for the standard decays, and because of the absence of energetic isolated leptons in Higgs decays. A significant $t \rightarrow H^+b$ contribution would give rise to measured $t\bar{t}$ cross sections lower than the SM prediction (assuming that non-SM contributions to $t\bar{t}$ production are negligible).

In Run II, CDF has searched for charged Higgs production in dilepton, lepton+jets and lepton+hadronic tau final states, considering possible H^+ decays to $c\bar{s}$, $\tau\bar{\nu}$, t^*b or W^+h^0 in addition to the SM decay $t \rightarrow W^+b$ [21]. Depending on the top and Higgs decay branching ratios, which are scanned in a particular 2-Higgs Doublet benchmark Model, the number of expected events in these decay channels can show an excess or deficit when

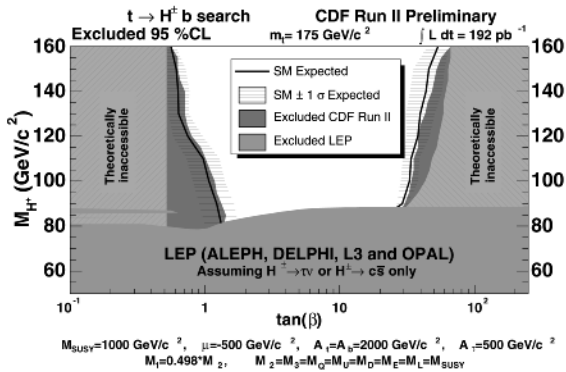


Fig. 3. CDF exclusion region (red solid region) along with the expected exclusion limits (black solid line) and the 1-sigma confidence band around it in the $(M_{H^\pm}, \tan \beta)$ plane.

compared to SM expectations. A model-independent interpretation, yields a limit of $B(t \rightarrow H^\pm b) < 0.91$ for $80 \text{ GeV} < m_{H^\pm} < 160 \text{ GeV}$. Stronger limits are set assuming specific H^\pm decay scenarios (see Figure 3).

6 New Physics in Events with $t\bar{t}$ Topology

6.1 Search for a Fourth Generation t' Quark

Recent theoretical developments, such as Little Higgs Models, 2-Higgs Doublet scenarios, $N = 2$ SUSY models, or the “beautiful mirror” model [16], hypothesize the existence of a heavy t' . Assuming that such a new heavy t' quark is pair-produced strongly, has mass greater than the top quark, and decays promptly to Wq final states, the final state event topology is very similar to that of $t\bar{t}$ events, except that the distribution of the total transverse energy H_T would tend to larger values.

CDF has performed a search for such a heavy t' quark in the lepton+jets channel using 200 pb^{-1} of Run II data [22]. The observed H_T distribution is compared to a combination of SM background and $t\bar{t}$ signal, the latter with floating normalization, plus a possible $t'\bar{t}'$ signal using a maximum likelihood fit, allowing to set upper cross section limits for t' production as a function of the t' mass. In comparison to the expected QCD $t'\bar{t}'$ production cross section, these results are translated into t' mass limits, ruling out a t' with mass greater than about $175 \text{ GeV}/c^2$, if the true top mass is about the same value. For a smaller top mass the excluded t' mass is lower, and vice versa for higher masses. The CDF limit on the t' production will steadily improve with more data in Run II.

7 Summary

After the top quark discovery in Run I and the re-establishment of the top quark signal with the upgraded detectors and improved analysis techniques in the early Run II, top quark physics at the Tevatron has now entered the stage of detailed studies of the top quark properties. A

wealth of results on top quark properties in the SM as well as searches for new top quark couplings and decays are becoming available. This development is expected to even accelerate with $\geq 1 \text{ fb}^{-1}$ of data being available to both, CDF and DØ, very soon.

Acknowledgment

I thank to organizers of HCP2005 for a stimulating conference and acknowledge the support by the Alexander von Humboldt Foundation and the University of Rochester.

References

1. Abe, F. et al., The CDF Collaboration, Phys. Rev. Lett. **74**, (1995) 2626; Abachi, S. et al., The DØ Collaboration, Phys. Rev. Lett. **74**, (1995) 2632.
2. E. Busato, $t\bar{t}$ Cross Section Measurements at the Tevatron, these proceedings, (2005).
3. A. Taffard, Single Top at the Tevatron, these proceedings, (2005).
4. T. Tomura, Measurement of the Top Quark Mass at the Tevatron, these proceedings, (2005).
5. B. Abbott et al., The DØ Collaboration, Phys. Rev. Lett. **85**, (2000) 256.
6. D. Acosta et al., The CDF Collaboration, to be published in Phys. Rev. Lett., hep-ex/0505091, (2005).
7. V.M. Abazov et al., The DØ Collaboration, DØ-conference note 4833, (2005).
8. D. Acosta et al., The CDF Collaboration, CDF conference note 7179, (2004).
9. T. Affolder et al., The CDF Collaboration, Phys. Rev. Lett. **84**, (2000) 216.
10. V.M. Abazov et al., The DØ Collaboration, Phys. Lett. B **617**, (2005) 1.
11. A. Abulencia et al., The CDF Collaboration, To be submitted to Phys. Rev. Lett., CDF conference note 7804, (2005).
12. D. Acosta et al., The CDF Collaboration, Phys. Rev. D **71**, (2005) 031101.
13. V.M. Abazov et al., The DØ Collaboration, Phys. Rev. D **72**, (2005) 011104; V.M. Abazov et al., The DØ Collaboration, DØ conference note 4839, (2005).
14. F. Abe et al., The CDF Collaboration, Phys. Rev. Lett. **80**, (1998) 1998.
15. Tevatron Elektroweak Working Group, hep-ex/0507091, (2005).
16. D. Choudhury et al., Phys. Rev. D **65**, (2002) 053002.
17. A. Abulencia et al., The CDF Collaboration, Phys. Rev. Lett. **95**, (2005) 022001.
18. R.M. Harris et al., Fermilab-FN-687, hep-ph/9911288, (1995).
19. T. Affolder et al., The CDF Collaboration, Phys. Rev. Lett. **85**, (2000) 2062; V.M. Abazov et al., The DØ Collaboration, Phys. Rev. Lett. **92**, (2004) 221801.
20. V.M. Abazov et al., The DØ Collaboration, DØ conference note 4880, (2005).
21. A. Abulencia et al., The CDF Collaboration, CDF conference note 7712, (2005).
22. D. Acosta et al., The CDF Collaboration, CDF conference note 7113, (2004).

Top physics prospects in ATLAS

From early data to precision measurements

Arnaud Lucotte¹

LPSC-IN2P3 - 53, Av. des martyrs, 38000 Grenoble, France

Abstract. Top Physics aspects are reviewed. A particular emphasis is put on the precision measurements of the top mass, top polarization and on the single-top cross-section measurements during the low luminosity period of the LHC data taking.

1 Introduction

The discovery of the Top quark at Fermilab's collider in 1995 by the CDF and DØ collaborations suggested a confirmation of the three generation quark family as predicted by the Standard Model of particle physics. Since then, determinations of top quark properties, its mass, spin, charge and couplings to fermions or bosons have been investigated. But the precision for most of these measurements is still statistically limited and will most presumably still be at the end of a 2 fb^{-1} TeVatron run.

With more than 8 millions of top pair and more than 2 millions of single top events produced every year at low luminosity, the LHC era will open a new opportunity for top quark physics. One of the first goals will be a determination of the top quark mass at the 1% level. This determination constitutes a crucial test of the electro-weak sector and put stringent constraints onto its symmetry breaking mechanism, either in the Standard Model (SM) or in a supersymmetric framework (MSSM). The top quark spin properties, through W polarization and top spin correlation measurements at a precision better than 5% level, will also lead to a deep insight of the nature of the top quark couplings to fermions and to the mechanisms (SM or not) responsible for its production. Finally, a precise determination of the (electro-weak) single-top production cross-sections at a few percent precision level also constitutes a stringent test of the SM. These measurements offer a direct access to V_{tb} at the few percent level, as well as stringent tests of any departure to SM physics with a sensitivity to anomalous couplings. Single-top analyses can also be a direct way of evidence for an extra charged Higgs bosons.

2 Top quark mass measurement

Fig. 1 displays the present experimental values taken by the top and W boson masses compared to their predictions in the SM or in an unconstrained SUSY models [1].

In the SM, the indirect precision measurements of the electro-weak sector (Z resonance, etc..) tend to favour the presence of a light neutral Higgs below $295 \text{ GeV}/c^2$ at 95% CL [2].

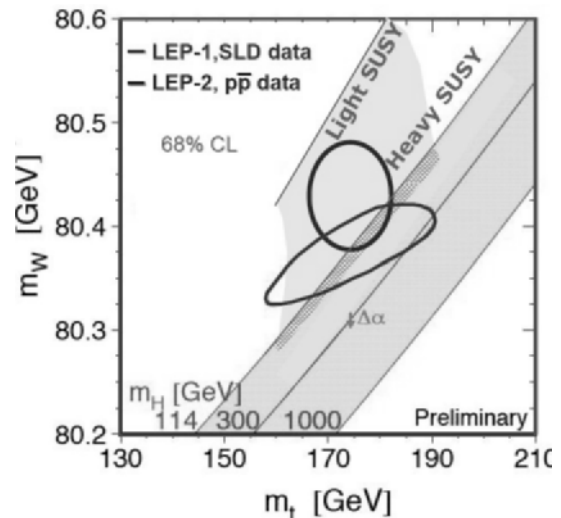


Fig. 1. Constraints from precise determination of m_W and m_t on the electro-weak sector of the SM (yellow band) and MSSM framework (blue band)

In the MSSM, the mass of lightest Higgs is predicted and must lie below $135 \text{ GeV}/c^2$. In both cases, given the level of the present precision in Δm_t and Δm_W , no particular framework appears yet as the preferred one. The main source of uncertainty in the global fitted Higgs mass actually is the precision of m_t with $\Delta m_W \simeq 0.7\% \Delta m_t$, making a $\Delta m_t = 1 \text{ GeV}/c^2$ the target for the LHC.

At the LHC, only top pair events have been used so far for the determination of the top mass. Originating from gluon fusion (90%) and quark annihilation (10%), the corresponding cross-section has been computed up to the

Next To Leading Order (NLO) of corrections resulting in $\sigma_{t\bar{t}} = 835 \text{ pb}$ [3] for $m_t = 175 \text{ GeV}/c^2$ with a 10% uncertainty. Within the SM, the top decays almost exclusively into a W boson and a b quark. Signatures of top pair events thus depend exclusively upon the W boson decays, and are splitted into three samples: a 'lepton+jets' sample, where one W decays hadronically while the other decays into a charged lepton and a neutrino, with a branching ratio (BR) of about 30%; a 'dilepton' sample, where both W's decay into a lepton and a neutrino with a branching ratio of 5% and a 'full hadronic' channel where all W bosons decay into hadrons, which occurs in about 44% of the time.

2.1 Top mass in the 'lepton+jets' channel

A detailed report of this analysis may be found in Ref. [4]. The preselection of such events requires an isolated high p_T lepton, a high missing energy due to the undetected neutrino and at least four jets with p_T above $15 \text{ GeV}/c$. Among those four jets, one jet at least must be tagged as a b jet. The signal efficiency is about 4.5% resulting in about 87,000 events for $\mathcal{L} = 10 \text{ fb}^{-1}$, while physics backgrounds, formed by the QCD $b\bar{b}$, W/Z+jets and di-boson productions add up to a total below 2,000 events. The main background to the mass determination is thus composed by the jet-pairing combinatorial of top pair events themselves. Selected events are then separated into two classes according to the number of b-tagged jets, a single b-tag and a 2 b-tag samples.

The mass determination makes use of the top quark decaying hadronically $t \rightarrow Wb \rightarrow jjb$ by reconstructing the three jet invariant mass M_{jjb} . The W boson is first reconstructed using the invariant mass formed by all two-jet combinations among non b-tagged jets, keeping the solution with the closest value to the W mass. This approach leads to an overall W purity of 66% (55%) in the '2-btag' ('1-btag') sample for a right combination contained in the $|m_{jj} - m_W| < 20 \text{ GeV}/c^2$ window, and corresponds to an overall efficiency of 3.2%. A b-jet must then be associated to the reconstructed W. In the '1-btag' sample, the association is performed if the b jet is closer to the W than to the isolated lepton. For '2-btag' events, the b-jet leading to the highest top transverse momentum is chosen (Fig. 2). An overall efficiency of 1.2% (2.5%) is achieved for a corresponding purity of 69% (65%) for events such that $|m_{1\nu b} - m_t| < 35 \text{ GeV}/c^2$. The event yields are about 30K expected events for a $12 \text{ GeV}/c^2$ resolution, resulting to a statistical uncertainty below $0.1 \text{ GeV}/c^2$ [4].

A mismeasurement of 1% of jet energy induces a top mass shift of $1.6 \text{ GeV}/c^2$. Similarly, a mismeasurement of 1% in the cosine of the opening angle for W jets or between the b-jet and the W direction results in a mass shift of $1.2 \text{ GeV}/c^2$. An in situ calibration of direction and energy of light jet is then performed using a purified sample of $W \rightarrow jj$ events, by keeping only jets with $|m_{jj} - m_W| \leq 15 \text{ GeV}/c^2$. This sample is used to correct for the energy scale bias as well as for mis-estimate of the jet direction. The proper use of this technique could

result in a determination of the absolute energy scale at the 1% level [4]. This determination will be checked with an external calibration based on the use of Z+jets events, that is shown to systematically underestimate the energy sharing of $W \rightarrow jj$ jets.

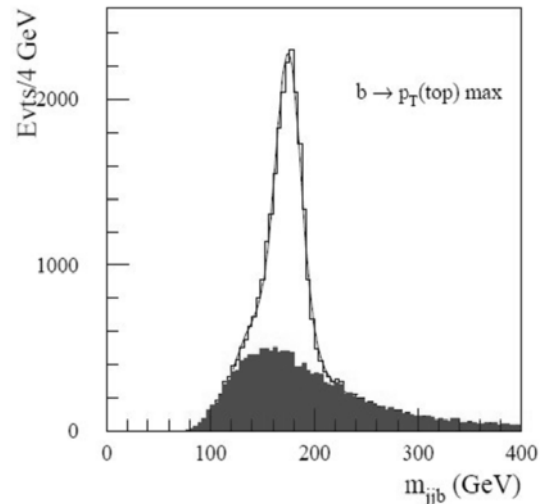


Fig. 2. Invariant mass reconstructed in the "2-btag" sample [1]

The main challenge to the top mass determination is the control of the systematic biases. The dominant source of uncertainty comes from the knowledge of the jet energy scale. For b-jet, a 1% mismeasurement results in a shift of $0.7 \text{ GeV}/c^2$ in the top mass, that grows linearly with the miscalibration factor. Regarding light jets, a 1% mismeasurement induces a $0.2 \text{ GeV}/c^2$ mass shift. In this case, the use of the in situ calibration will be a determinant factor. Initial state radiation directly influences the number of reconstructed jets in the event, thus leading to inefficiencies in the light jet association to the W. Final state radiations affect the jet reconstruction through gluon radiations which lead generally to an underestimated jet energy. This effect can result in a mis-estimate of the selection efficiency due to jets cut by the preselection threshold. Such effects also show a dependence to the jet reconstruction algorithm parameters, depending crucially on the cone size. The corresponding quoted systematics represents 20% of the mass shift due to the addition of the ISR or FSR in the Monte Carlo, which is conservative with respect to the uncertainty in the strong coupling constant α_s . A way to reduce the systematics is to use the leptonic decay of the other top quark as a constraint. A kinematic fit is applied to the entire $t\bar{t}$ event by reconstructing both the leptonic and hadronic W bosons and by requiring the leptonic top mass to be equal to the hadronic one. It is shown that the formed χ^2 can be used to reduce the contribution from badly reconstructed jets due to FSR effects. This method thus directly shows up in the systematics associated to the FSR effects, by limiting the effect below $0.5 \text{ GeV}/c^2$. Providing a miscalibration factor of 1% in

Table 1. Sources of uncertainty and size of the effects on the top mass determination. Numbers into parenthesis correspond to the leptonic kinematic fit constraint [4]

Sources of uncertainty	δm_t in GeV/c^2		
	'lepton+jets'	'dilepton'	'full hadron'
jet energy scale	0.2	–	0.8
b-jet energy scale	$0.7 \times \Delta\%$	$0.7 \times \Delta\%$	$0.7 \times \Delta\%$
ISR	0.1	0.6	2.8
FSR	1.0 (0.5)	0.6	2.8
b-quark frag.	0.1	0.7	0.3
combinatorial	0.1	—	0.4
Pdf's	–	1.2	–

the b-jet and light jet energy scales, a total systematic uncertainty around $1 \text{ GeV}/c^2$ seems achievable.

2.2 Top mass in the 'dilepton' and 'full-hadronic' channels

The 'dilepton' analysis is presented in details in Ref. [4] [5]. Trigger and selection are based upon the detection of two isolated high p_T leptons of opposite signs, a high transverse missing energy due to the presence of two neutrinos in the final state, and at least two high p_T jets, among which one or two at least has to be b-tagged. About 80 K events are expected to be selected in 10 fb^{-1} with a ratio $S/B \approx 10$. Each $t\bar{t}$ event is then fully reconstructed by solving a system of 6 equations and 6 unknowns (3 components of neutrino momenta) based upon the conservation of the overall transverse momentum of the $t\bar{t}$ system, the mass constraint on the lepton+neutrino coming from the W, as well as top mass constraints on to the lepton, neutrino and b jet. The complete kinematic reconstruction can be performed with an efficiency above 97% and with the right solutions in 73% events.

For the top mass determination, the reconstruction algorithm is fed with different top mass inputs. For each solution a weight is then attributed according to the fit comparing the event topology and kinematics with the MC expectations. The top mass is then defined as the preferred value on an event by event basis. The final top mass is obtained using the full sample by fitting the distribution of all event weights. A mass resolution of $13 \text{ GeV}/c^2$ seems achievable with a statistical error below $0.3 \text{ GeV}/c^2$.

Main systematics comes from the miscalibration effect of b-jets, which accounts for $0.6 \text{ GeV}/c^2$ in the mass, as well as ISR/FSR modelling. Variation of b-quark fragmentation parameters result to an error of $0.6 \text{ GeV}/c^2$. The new source of uncertainty comes from the high dependence to the MC simulation used to attribute the weight. This shows up in the parton distribution function contribution. An overall systematics of $1.6 \text{ GeV}/c^2$ seems achievable.

The full hadronic channel is most challenging given the high level of jet background. Based on the selection of at least 6 central high p_T jets with 2-btagged jets, the analysis makes use of kinematical, topological and event shape

variables to discriminate the signal from the backgrounds. A constrained kinematic fit to both W bosons and to top mass distributions is performed using only events with high p_T reconstructed top candidates. A mass resolution of $13 \text{ GeV}/c^2$ is achieved for about 3,300 events remaining with a ratio S/B approx 18/1. Systematics are completely dominated by the FSR modelling, b-jet and light jet energy scale. An overall uncertainty of $3.1 \text{ GeV}/c^2$ seems achievable.

For all the present analyses, the main source of systematics comes from the b-jet energy scale. This result lead to the developpment of an alternative analysis. This approach is based on the identification of the $J\Psi$ originating from the b-quark decay and uses the linear correlation in m_t of the reconstructed invariant mass $M(1, J/\Psi)$ [6]. While this approach is not affected by the b-jet energy scale uncertainty, it however is characterized by a small $BR \approx 5 \times 10^{-5}$ and requires 100 fb^{-1} at high luminosity to achieve a precision around $1 \text{ GeV}/c^2$.

3 W and top quark polarization in $t\bar{t}$ events

Because of its high mass, the top quark decays before it hadronizes or its spin flips, thus leaving an imprint of its spin on its angular decay distributions [7]. This feature constitutes a unique opportunity to measure quark spin properties. The measurements of the W boson and top polarization constitute a test of both the top production and W decay with the same initial sample.

A detailed report of the analyses conducted in ATLAS may be found in Ref. [8]. Top pairs are selected similarly as they are in the top mass analyses, ending up with 85,000 signal events in the 'lepton+jets' sample and 21,000 events in the 'di-lepton' sample [9]. To enhance the spin correlation effects, selected events are required to have a reconstructed invariant mass $M_{t\bar{t}}$ below $550 \text{ GeV}/c^2$.

3.1 W polarization measurement

W bosons decay of top quarks are produced with a longitudinal, left-handed or a right-handed polarization. In $t\bar{t}$ events, W bosons are mainly produced longitudinally with the corresponding probabilities $F_0 = 0.695$, $F_L = 0.304$ and $F_R = 0.001$ for a W^+ [10]. Thus, any deviation of F_0 from the SM value would pinpoint an inconsistency in the Higgs mechanism, responsible for the longitudinal degree of freedom of the massive bosons. Any deviation seen in F_L or F_R would be a sign of additional (V+A) admixture as predicted in the $SU(2)_L \times SU(2)_R \times U(1)$ extensions of the SM [11].

3.1.1 Method

The W-polarisation is measured from the angular distribution of its decay products : the charged lepton from a left-handed (right-handed) W^+ tend to be emitted in the opposite (same) W^+ direction, leading to a softer (harder)

p_T spectrum than the lepton from a longitudinal W. As the knowledge of the isospin of the produced fermion is necessary to assess the helicity of the initial decaying W, charged leptons are the best candidates or 'spin analyzer'.

Both 'di-leptonic' and 'lepton+jets' samples have been used. The polarization is assessed via the measurement of Ψ defined as the angle between the lepton direction in the W rest frame and the W direction in the top quark rest frame:

$$\frac{1}{N} \frac{dN}{d\cos\Psi} = \frac{3}{2} \left[F_0 \left(\frac{\sin\Psi}{\sqrt{2}} \right)^2 + F_L \left(\frac{1 - \cos\Psi}{2} \right)^2 + F_R \left(\frac{1 + \cos\Psi}{2} \right)^2 \right]$$

As both rest frames are used in the analysis, the event topology has to be fully reconstructed, which makes the 'lepton+jets' sample the best choice for such analysis. In the 'di-lepton' sample, because of the presence of two neutrinos, the Ψ angle is reconstructed using the following relation [12]:

$$\cos\Psi \approx \frac{2M_{lb}^2}{m_t^2 - m_W^2} - 1$$

where m_t and m_W are set to 175 GeV/ c^2 and 80.41 GeV/ c^2 .

The selection requirements affect both the reconstructed p_T and the angular distributions of the physics objects. A procedure has been defined to recover the original shape of the $\cos\Psi$ via the use of a weighting function applied on an event by event basis. This correction function results from the fitted ratio of the normalized $\cos\Psi$ distributions at the reconstructed level over the generated level. It is computed on an independent data sample and then applied event by event on the analysis sample.

The search for non-SM contributions lead to the development of a (quasi-) independent correction function that is formed iteratively, by starting from the SM function and re-injecting the non-zero fitted value of F_R as input to the new function. It is shown that a few iterations are enough to reach convergence.

3.1.2 Results and sensitivity to new physics

Table 2 reports the performance expected in the SM framework for an integrated luminosity of 10 fb⁻¹. Combining 'lepton+jets' and 'di-lepton' analyses, F_L and F_R are determined at a few percent precision level. The results are 3 to 5 times better than the statistical sensitivity expected at the TeVatron with 2 fb⁻¹ [13].

Measurements are largely dominated by the systematic uncertainties. At the generation level, the main systematics originate from the scale used for the parton generation, the uncertainty in the generated top mass and the choice of the pdf's. Biases due to the event simulation and reconstruction come from the effects of ISR/FSR on the angles and energy reconstruction, the uncertainty on the top mass knowledge as well as the b-jet energy scale that directly affects the determination of $\cos\Psi$. Uncertainty in

Table 2. W polarization results with 10 fb⁻¹ at 10³³ cm⁻²s⁻¹. Central values are those predicted by the Standard Model at LO

	LHC (10 fb ⁻¹)	TeVatron (2 fb ⁻¹)
F_L	$0.303 \pm 0.003_{\text{stat}} \pm 0.024_{\text{syst}}$	
F_0	$0.697 \pm 0.004_{\text{stat}} \pm 0.015_{\text{syst}}$	$\pm 0.09_{\text{stat}}$
F_R	$0.000 \pm 0.003_{\text{stat}} \pm 0.012_{\text{syst}}$	$\pm 0.03_{\text{stat}}$

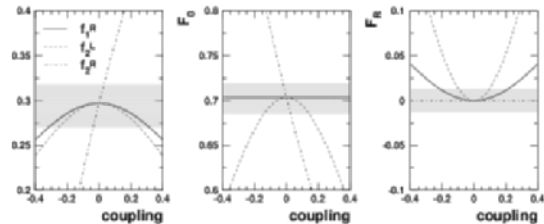


Fig. 3. Sensitivity to anomalous couplings via the measurement of F_L , F_0 and F_R with 10 fb⁻¹. Grey bands correspond to 1 σ uncertainty

the determination of the background and pile-up effects have also been taken into account.

In a more general effective CP-conserving lagrangian, the Wtb interaction can be parametrized using f_1^L , f_1^R as vector-like couplings and f_2^L , f_2^R as tensor-like couplings. In the SM $f_1^L = V_{tb}$ while $f_1^R = f_2^L = f_2^R = 0$. The sensitivity to those quantities are shown on Fig. 3 together with the expected precision on F_L , F_0 and F_R .

3.2 top quark polarization measurement

In the top pair production, top quarks are not polarized. However, the top and anti-top spins are correlated due to their production mechanism: the $q\bar{q}$ annihilation generates a ³S₁ state resulting in aligned top and anti-top spins directions, while the gluon fusion produces a ¹S₀ final state leading to opposite direction spins. In the helicity basis, the following observable is used :

$$\mathcal{A} = \frac{\sigma(t_L \bar{t}_L) + \sigma(t_R \bar{t}_R) - \sigma(t_L \bar{t}_R) - \sigma(t_R \bar{t}_L)}{\sigma(t_L \bar{t}_L) + \sigma(t_R \bar{t}_R) + \sigma(t_L \bar{t}_R) + \sigma(t_R \bar{t}_L)}$$

\mathcal{A} can be written as function of the measured angular distributions of θ_1 and θ_2 , where θ_1 (θ_2) of the t (\bar{t}) spin analyzer in the t (\bar{t}) rest frame and the t (\bar{t}) direction in the $t\bar{t}$ center of mass of the system, are used to estimate the $t\bar{t}$ correlation. Another observable \mathcal{A}_D defined in [8] can be used as well to describe $t\bar{t}$ correlation.

3.2.1 Results

A weighting function is defined iteratively following the procedure used for the W polarization measurements. The correction function is computed this time by fitting the $\cos\theta_1 \cos\theta_2$ distributions on an independent sample. The

sensitivity in the 'lepton+jets' channel is, again, driven by the systematic uncertainties. This is no longer true in the 'di-lepton' analysis where statistical error is similar to the systematic one. The sources of systematics are similar to the one listed in the previous section.

A precision of 6.5% in \mathcal{A} and below 5% in $\mathcal{A}_{\mathcal{D}}$ can be achieved in the SM framework. These results can be compared with the TeVatron 40% precision (stat.) expected with a luminosity of 2 fb^{-1} . Any deviation from the SM predictions can sign the presence of new heavy resonances in the $t\bar{t}$ production of spin-0 particle ($H \rightarrow t\bar{t}$) or spin-2 particle (Kaluza-Klein gravitons). It can also probe presence of technicolor or topcolor theories.

4 Single-top cross-section measurement

Although non-dominant, the single-top production represents a third of the total top quark pair production. If a 5σ -evidence of single-top events at the Fermilab $p\bar{p}$ collider seems to be achievable with $2\text{-}4 \text{ fb}^{-1}$, precise measurements will only be possible at the LHC. The measurement of all three contributions to the total cross-section will provide a valuable test of the electro-weak top production, which in turn, will allow the first direct determination of V_{tb} at the 1% level of precision. They also constitute a powerful probe for new physics, being sensitive to additional contributions from an extra charged Higgs boson as predicted by 2HDM models.

4.1 Event selection

In the SM the electroweak single-top production is due to three different mechanisms: the W-boson gluon fusion mode Wg or t-channel contribution (Wg); the associated production of a top quark and a W ($W+t$); and the s-channel coming from the exchange of an off-shell mass W^* . For leptonic W decays, the dominant contribution is the t-channel accounting for about $\sigma \times \text{BR} = 53.5 \text{ pb}$, followed by the Wt events for 18.0 pb [15] and by the W^* channel for 2.2 pb [14]. The corresponding cross-sections have been computed at NLO, but the present analyses make use the LO TopRex generator, normalized to NLO predictions.

The present analyses make use only of the leptonic decays (e, μ) of the W boson, leading to a common pre-selection based on the presence of one high- p_T lepton above $25 \text{ GeV}/c$, a large transverse missing energy, at least two high- p_T jets above $30 \text{ GeV}/c$, among them at least one must be tagged as a b-jet. A secondary high- p_T lepton veto is applied to reduce di-lepton events and a jet invariant mass cuts above the Z mass is used to reduce di-boson contamination.

Contrary to the top mass analysis, single-top measurements are affected by a significant level of background contamination. Top pair production constitutes the dominant source with a cross-section about 3 times as large as the total single-top, with 'lepton+jets' and 'di-lepton' channels, followed by the tau decays involving one or two top

quarks. $Wb, b\bar{b}$ and $Wc, c\bar{c}$ events also represent a significant background. Corresponding cross-sections are based on specific calculations imposing "realistic" constraints to final state partons, and lead to 300 pb [16] for a lepton and at least 2 b-jets above $15 \text{ GeV}/c$.

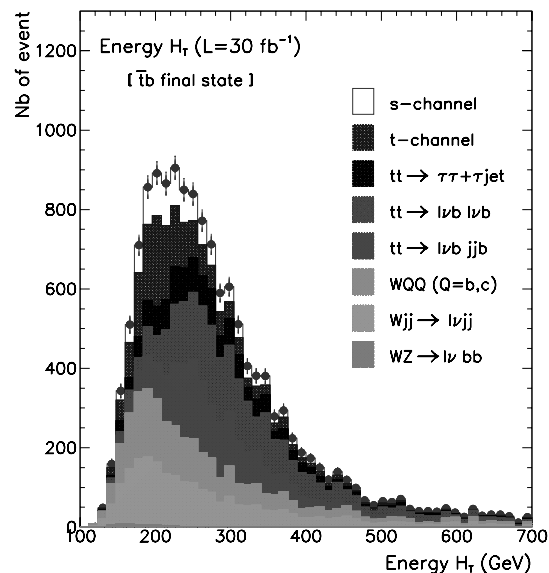


Fig. 4. Total energy H_T in the s-channel analysis for the $t\bar{b}$ final state and main backgrounds for 30 fb^{-1}

W +light jets events constitute a major source of background because of a cross-section several orders of magnitude above the signal's one. This processus can mimic the signal in the case where one or two light jets are (wrongly) tagged as a b-jet(s). Total cross-sections may be found in Ref. [16] for $W+j$, $W+jj$ and $W+jjj$ events with realistic thresholds put on the lepton and jets acceptance and p_T . For these analyses, the Herwig generator has been used and the results normalized to NLO cross-sections when available. Di-boson events constitute a background to our signal. The dominant contribution comes from the $WZ \rightarrow l\nu b\bar{b}$ events with a cross-section of $\sigma \times \text{BR} = 440 \text{ fb}$.

4.2 Wg cross-section

The selection of t-channel is largely based upon topological variables. Events with exactly two high- p_T jets are selected to reduce the top pair events contamination. Among them, exactly one jet is required to be b-tagged, the second b-jet being expected at high rapidity region outside the vertex tracker acceptance. The non-b tagged jet must point toward the forward rapidity region with $|\eta| > 2.5$. A window is applied upon the reconstructed leptonic top mass $M_{l\nu b}$ to help reduce non-top events. Other requirements are applied on the total energy H_T defined as the scalar sum of physics objects transverse momentum, to reduce further W +jets and top pair event contamination.

About 7,000 signal events are expected for 30 fb^{-1} with a ratio S/B of 3. The corresponding statistical sensitivity $\sqrt{S+B}/S$ is shown to stay below 1.5%. This analysis will be dominated by systematic uncertainties, originating from the precision of the luminosity determination, and the (b)-jet energy scale.

4.3 $W+t$ cross-section

The event selection requires that exactly three high p_T jets are detected, in order to reduce top pair and W +jet contamination. Among those jets, exactly one jet must be b-tagged. The reconstructed leptonic top mass, as well as H_T and the total mass of the events are used to improve background rejection. The reconstructed hadronic W boson mass is used as an additional constraint to further reduce non-top background.

Typical efficiencies at the 1% level are found for a ratio $S/B \approx 15\%$. For $\mathcal{L} = 30 \text{ fb}^{-1}$ this results in a statistical sensitivity of about 4%.

4.4 W^* cross-section

The selection of the s-channel events requires exactly two high p_T b-tagged jets with a veto of an extra light jet above $15 \text{ GeV}/c$. This criterium allows to reduce significantly top pair contamination as well as W +light jets events. Extra requirements based on cuts on the reconstructed top mass $M(l\nu b)$ and H_T are used to further purify the sample. As for the other channels, the analysis can be performed separately for the $t\bar{b}$ and $\bar{t}b$ final states in order to help reduce charge-symmetric backgrounds like top pairs, as shown in Fig. 4. About 1,200 (800) signal events are expected in the $t\bar{b}$ ($\bar{t}b$) final state, for ratio a S/B ranging between 10-15%. A statistical sensitivity of 7-8% seems achievable for 30 fb^{-1} . Main systematics will be the effect of the ISR/FSR and the uncertainty on the background normalization (W +heavy quarks, W +jets and top pair).

4.5 Sensitivity to new physics

In 2HDM, two higgs fields are assumed to generate the electro-weak symmetry breaking. This results into five physical states associated each to a higgs boson : three neutral (h , H and A) and two charged bosons (H^+ , H^-). In SUSY, Higgs mass spectrum is determined and depends upon one mass, usually m_A , and the $\tan\beta$ parameter, defined as the ratio of the two vacuum expectation values (vev) for the higgs fields.

In those models, the contribution to the W^* channel is expected to be enhanced due to the addition of a graph involving the H^\pm with $H^+ \rightarrow t\bar{b}$, resulting in a deviation from the SM expectations. The result of the analysis is shown in Fig. 5 in the $(m_H, \tan\beta)$ plane. A 5σ discovery seems achievable for high $\tan\beta$ and higgs mass above $250 \text{ GeV}/c^2$. This result should be improved by using

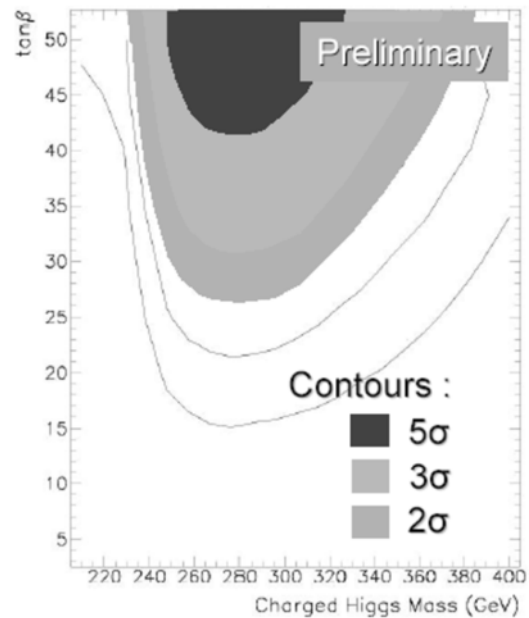


Fig. 5. Discovery contours for a charged higgs in the $(m_H, \tan\beta)$ plane, using only the s-channel cross-section measurement

a selection based on the specific properties of the scalar H^\pm , and should also benefit from the combination with the $W+t$ channel analysis.

5 Conclusion

The LHC opens a new era of precision measurements in the top quark physics that will lead to a thorough determination of the top quark property, as its mass, width, couplings and polarization. But besides stringent tests of the SM, those measurements also constitute powerful probes in the search for new physics and could lead to new discoveries in the first three years of the LHC low luminosity data taking period.

References

1. S. Heinemeyer, G. Weiglin, hep-ph/0307177 (2003)
2. LEP EWWG page / Summer 2005
3. R. Bonciani et al., Nucl. Phys. B 528 (1998) 424
4. I. Borjanovic et al., hep-ex/0403021
5. V. Simak et al., ATL-COM-PHYS-99-073
6. C.S. Hill et al., hep-ex/0501043
7. D. Chakraborty et al., hep-ph/0303092
8. F. Hubaut et al. SN-ATLAS-2005-052
9. V. Simael et al., ATL-PHYS-2001-018
10. H.S. Do et al., Phys. Rev. D67(2003) 091501
11. M. Beg et al., Phys. Rev. Lett. 38(1977) 1252
12. G.L. Kane et al., Phys. Rev. D45(1992)124
13. D. Chakraborty, hep-ex/0212027
14. J. Campbell et al., hep-ph/0408158
15. F. Maltoni, HCP 2005 proceedings
16. J. Campbell et al., hep-ph/0308195

Top quark studies and perspectives with CMS

Andrea Giammanco

SNS & INFN Pisa

Abstract. The LHC (Large Hadron Collider) at CERN will be a "top factory" given the high top quark production cross section. This paper reports on the perspectives for top-physics measurements that will be possible with the CMS detector.

1 Introduction

The top quark discovery [1, 2] and mass measurement [3] highlighted the uncommon nature of the heavier quark. Top decays proceed through the channel $t \rightarrow Wb$ with a BR of 0.99, yielding energetic b-jets. The fact that the electroweak decay is faster than the hadronization time scale implies that the top quark exists only as a free quark, so that the effects from new physics should show up very clearly by comparing measurements with the precise Standard Model predictions. Some SUSY particles and heavy resonances have the top quark as decay product: as a consequence the Standard Model production of the top quark is the background to many new physics channels.

The top pair production at LHC has been computed at the NLO order [4] to be $(833^{+52}_{-39})pb$ ($\pm 3.5\%$ PDF error), about 100 times higher than the one at Tevatron. At low luminosity LHC will then produce $8 \cdot 10^6$ $t\bar{t}/y$ (almost one top pair per second).

2 Top quark mass measurement at LHC

The top mass enters into the prediction of the W mass via loop corrections containing virtual top quarks, giving rise to terms proportional to m_t^2/m_Z^2 . Similarly, loops involving the Higgs boson give contributions of the form $\log m_H/m_Z$. Combining the existing measurements of the W and the top masses thus gives an indirect prediction of the Higgs mass, as shown in Fig. 1 [5].

2.1 Top mass measurement from the production cross section

At LHC, an indirect measurement with negligible statistical error will come from the $t\bar{t}$ cross section, due to the strong dependence of the cross section on the top mass (shown in Fig. 2).

With a luminosity of $2 \times 10^{33} \text{ cm}^{-2}\text{s}^{-1}$ and selecting semileptonic events (even without making use of b-tagging), a week of data taking will provide approximately

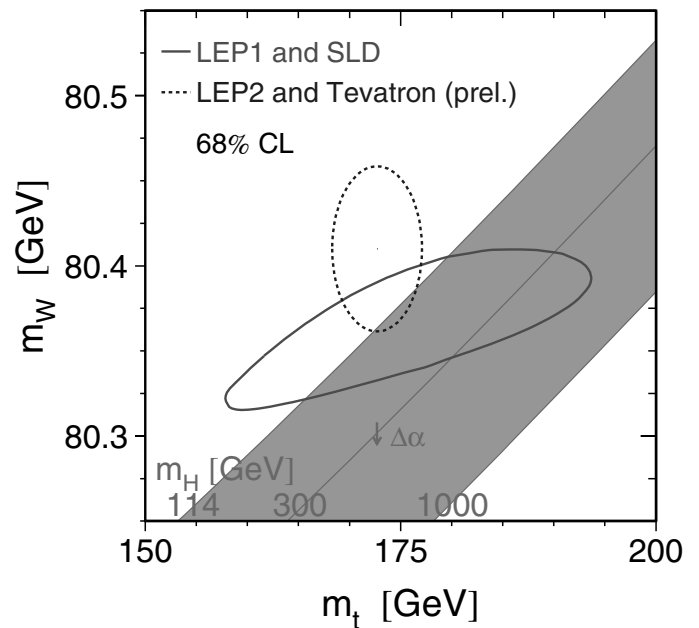


Fig. 1. Direct and indirect measurements of the W-boson and top-quark masses compared to lines of constant Higgs-boson mass in the Standard Model [5].

2×10^3 signal events, corresponding to a relative statistical error $\Delta\sigma_{tt}/\sigma_{tt} = 2.5\%$. Very soon statistics will not be an issue, and the limitation will come from systematic and theoretical errors, most notably the uncertainty on the luminosity and the sensitivity to the PDFs (Parton Distribution Functions) and on the renormalization and factorization scales. A 5% uncertainty is achievable on the luminosity. Since $\Delta\sigma_{tt}/\sigma_{tt} \approx 5\Delta M_t/M_t$, this means a 2 GeV error on top mass. The uncertainty on the PDFs is about 10% (meaning $\Delta M_t \approx 4$ GeV).

On the other hand, combining the cross section measurement with a precise determination of the top mass from direct measurements (like the ones described in the following) will provide a test of QCD.

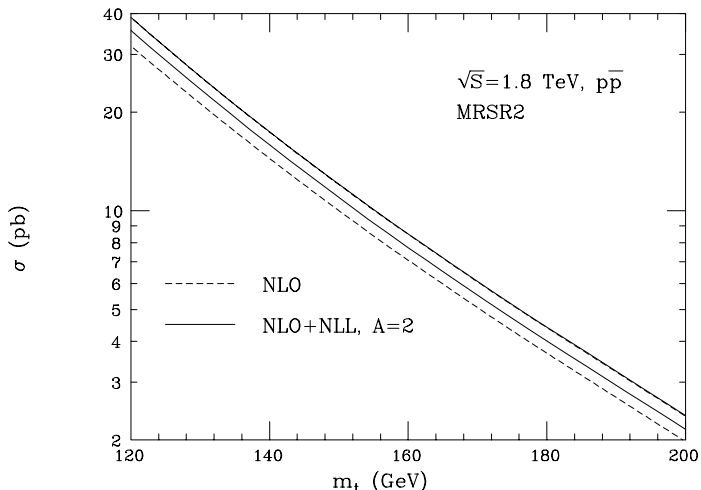


Fig. 2. Production cross section for $t\bar{t}$ events as a function of the top mass in pp collisions at $\sqrt{s} = 1.8$ TeV [4].

2.2 Semi-leptonic channel

The lepton + jets channel is the golden channel for the measurement of top mass since it is easily triggered and has a BR of 29.6%, that is $2.5 \cdot 10^6$ events for a luminosity of $10fb^{-1}$. The hadronically decaying top can be fully reconstructed by combining the two light quark jets into a W candidate (rescaled to the nominal W mass) and then adding one of the b -tagged jets. The leptonic decaying top can be partially reconstructed by imposing $E_T(\nu) = E_T(\text{missing})$ and $M_{l\nu} = M_W$. The main background to this process arises from W +jets production and $t\bar{t} \rightarrow \tau + X$. The top mass peak is shown in Fig.3 for the CMS [6] experiment with $10fb^{-1}$. The expected mass resolution is $1 \div 2GeV$, where the main contributions to the overall uncertainty come from the b -jet energy scale and from the theoretical uncertainty on the FSR (Final State Radiation).

2.3 J/ψ channel

Another interesting analysis is based on the search for a J/ψ in the final state, which is easily reconstructed in the dimuon decay. The top mass depends on the invariant mass of the system lepton+ J/ψ (Fig.4). This analysis is unrealistic at low luminosity, while it becomes promising at full luminosity with an expected sample of about 1000 events/y. The interesting feature of this analysis is that it's free from jet energy scale systematic uncertainty. The main limitation comes instead from the theoretical uncertainties on the b fragmentation, limiting the expected precision to $1 GeV/c^2$.

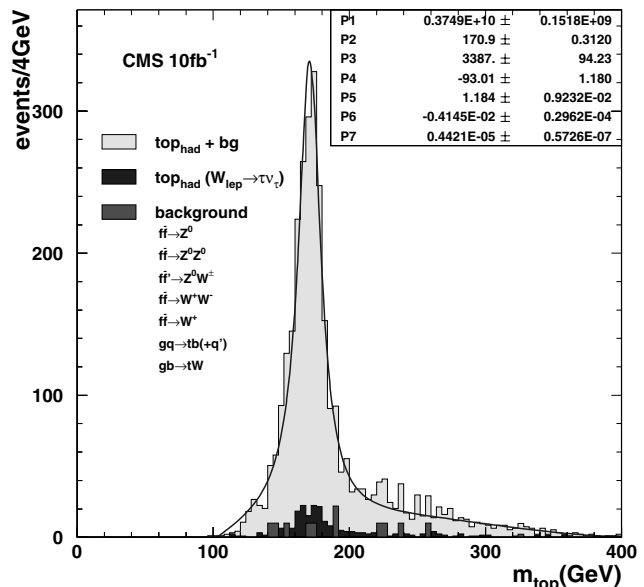


Fig. 3. The mass of the reconstructed top in the semileptonic channel after all cuts including the contribution of background processes at CMS [6].

3 Spin correlations

As top quarks decay faster than the hadronization time scale their decay products (e.g. the leptons from subsequent W decay) retain informations on the top quark spin.

In fully leptonic $t\bar{t}$ decays the angles $\theta_{l\pm}^*$ between the leptons in the top rest frames and the direction of the top in the $t\bar{t}$ system are distributed as in Fig. 5 according to

$$\frac{1}{N} \frac{d^2 N}{d \cos \theta_{l+}^* d \cos \theta_{l-}^*} = \frac{1}{4} (1 - A \cos \theta_{l+}^* \cos \theta_{l-}^*), \quad (1)$$

where

$$A \equiv \frac{N(t_L \bar{t}_L + t_R \bar{t}_R) - N(t_L \bar{t}_R + t_R \bar{t}_L)}{N(t_L \bar{t}_L + t_R \bar{t}_R) + N(t_L \bar{t}_R + t_R \bar{t}_L)} \quad (2)$$

is the asymmetry of finding top and anti top in the same or different polarization state.

This asymmetry may be extracted by fitting eq. 1 to data. The Standard Model predicts $A = 0.31$ at LHC, as a result of the $q\bar{q} \rightarrow t\bar{t}$ and $gg \rightarrow t\bar{t}$ production processes, having respectively $A = -0.469$ and $A = +0.431$. After $30 fb^{-1}$ a measurement is expected in CMS with 0.035 statistical and 0.028 systematic uncertainty [8].

4 W polarization in top decay

The angular distribution of the lepton from W decay is related to its polarization. The Standard Model predicts 70% of the W 's from top decay to be in the longitudinal polarization state, with the rest being left-handed.

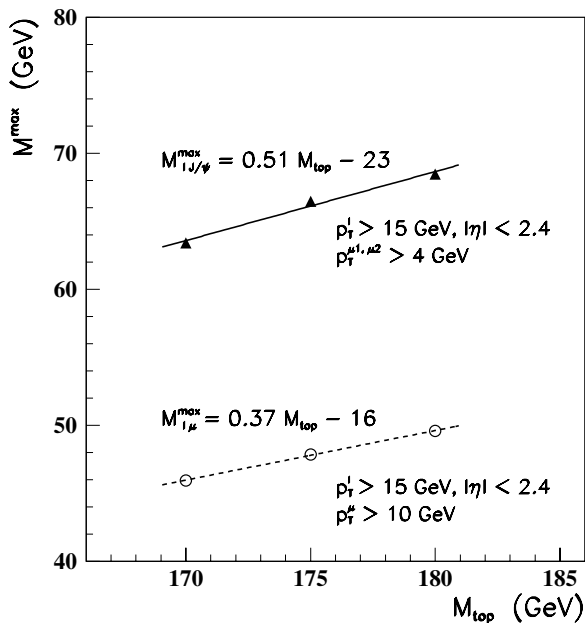


Fig. 4. Dependence on top quark mass of the lepton- J/ψ invariant mass (solid line) and of the isolated-lepton plus μ -in-jet (dashed line) [7].

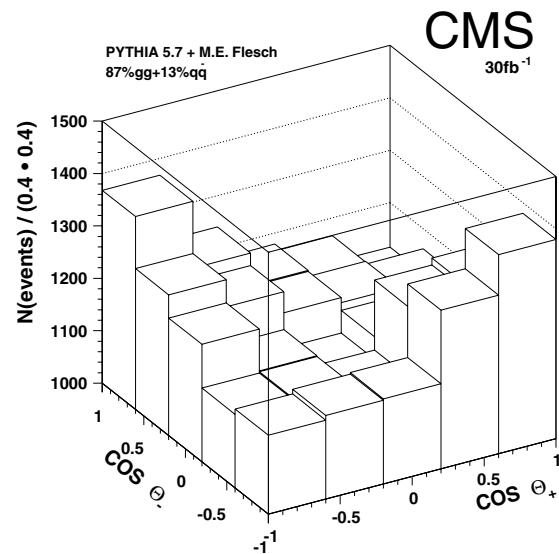


Fig. 5. Double differential distribution of $\cos \theta_{i\pm}^*$ for 30 fb^{-1} . [8].

Fig. 6 shows the distribution of $\cos \theta_i^*$ (where θ_i^* is the angle between the lepton in the W rest frame and the direction of the W in the top rest frame) at parton level for left and longitudinal polarization and for the Standard Model expectation. Semileptonic $t\bar{t}$ events are used.

With 10 fb^{-1} integrated luminosity, the fraction of longitudinally polarized W bosons is expected to be measured by CMS with 0.023 statistical and 0.022 systematic uncertainty [8].

5 Single top production

The electroweak single top production provides a direct measurement of the V_{tb} CKM element and is particularly sensitive to new physics beyond the Standard Model, entering the $W - t - b$ vertex.

This process has never been observed so far; published Tevatron analyses only give cross section upper limits [9–11].

Single top quarks can be produced at hadron colliders via the three processes shown in Fig. 7: t-channel (or W -gluon fusion) is the main production mechanism with $\sigma \approx 250 \text{ pb}$ expected at LHC [12], Wt associated production follows with $\sigma \approx 60 \text{ pb}$ [13], and s-channel (or W^*) process has only $\sigma \approx 10 \text{ pb}$ [12]. It is interesting to study the three processes separately, since they are differently sensitive to new physics: the existence of a new massive vector boson W' would increase the s-channel signal, while a $FCNC$ process $gu \rightarrow t$ would signal itself in the t-channel process, and in a light SUSY scenario [14] the Wt production would have to be separated from a significant $H^\pm t$ production.

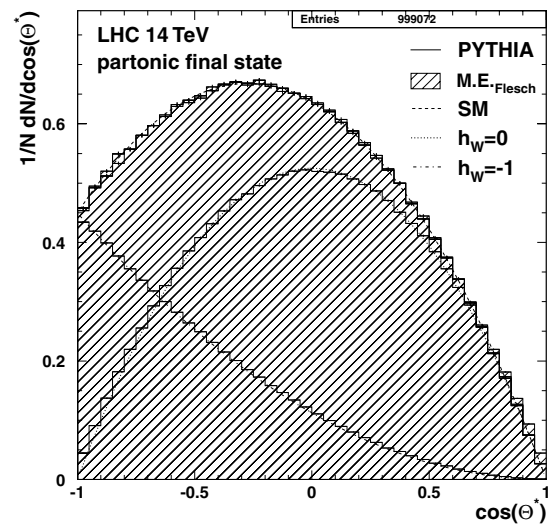


Fig. 6. Distribution of $\cos \theta_i^*$ at parton level for different W polarization states. [8].

Furthermore, the three processes have different backgrounds and their systematic errors are different (see Table 1). The s-channel has the lowest rate, but is the best theoretically understood mechanism of electroweak top production.

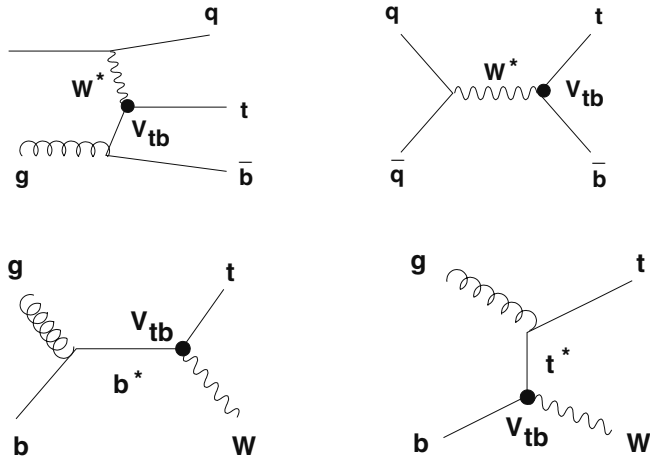


Fig. 7. Single top diagrams: t -channel (top left), s -channel (top right) and associate production (bottom).

	$d\sigma/\sigma$ (%)	$d\sigma/\sigma$ (%)	$d\sigma/\sigma$ (%)
Source of error	s-channel	t-channel	Wt
PDF	4	10	-
μ (scale)	4	5	-
$\delta m_t = 2$ GeV	5	2	-
Total theory error	7.5	11	50

Table 1. Relative errors in the cross section for the three single top production processes.

The main backgrounds, due to final states similar to the processes under study, are $t\bar{t}$ ($\sigma \approx 830$ pb) and $Wb\bar{b}$ ($\sigma > 300$ pb). To reduce the enormous QCD multi-jets background, all the proposed analyses require a high p_T lepton in order to select $t \rightarrow l\nu b$ decays.

The most characteristic feature of the t -channel final state is the presence of a forward light jet from the “spectator” quark, i.e. the one recoiling against the W (see Fig. 7). Furthermore, the \bar{b} (b) quark associated to the t (\bar{t}) quark tends to be produced at very small angle, resulting outside of the detector acceptance in most cases (see Fig. 8). So, the typical selection requires exactly two jets with only one tagged as b -jet. As an example [15], requiring a jet in the forward calorimeter ($2.5 < |\eta| < 4.0$) and another jet in the central region ($|\eta| < 2.5$), selects 6600 signal events and 1900 background events ($S/B=3.5$) in a window around the nominal top mass with 10 fb^{-1} integrated luminosity, yielding a 1.5% relative statistical uncertainty on the cross section.

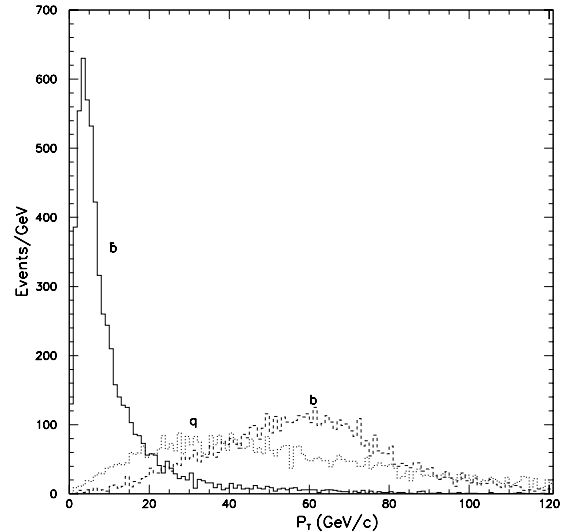


Fig. 8. Transverse momentum spectra for the final state partons in the t -channel production of single top quarks [15].

6 Conclusions

Top quarks will be produced with very high cross section at the LHC, allowing for a very broad physics program, with many interesting results being achievable with the first 10 fb^{-1} . The analyses summarised in this paper give examples of how studies in the top sector will improve our knowledge of the Standard Model.

References

1. CDF Collaboration, Phys.Rev.Lett. **74**, (1995) 2626.
2. D0 Collaboration, Phys.Rev.Lett. **74**, (1995) 2632.
3. CDF and D0 Collaborations and Tevatron Electroweak Working Group (P. Azzi et al.), hep-ex/0404010.
4. R. Bonciani, S. Catani, M. Mangano and P. Nason, Nucl.Phys. B **529**, (1998) 424.
5. The LEP Electroweak Working Group, Summer results 2005 (<http://lepewwg.web.cern.ch/LEPEWWG/>)
6. L.Sonnenschein, CMS NOTE 2001/001
7. A. Kharchilava, CMS NOTE 1999/065
8. L.Sonnenschein, PhD Thesis, 2001
9. CDF Collaboration, Phys.Rev. D **69**, 052003 (2004)
10. CDF Collaboration, hep-ex/0410058
11. D0 Collaboration, Phys.Lett. B **517**, 282 (2001)
12. B.W.Harris, Phys.Rev. D **66**, 054024 (2002)
13. T.Tait, Phys.Rev. D **61**, 034001 (2000)
14. M.Beccaria, F.M.Renard, C.Verzegnassi, Phys.Rev. D **71**, 033005 (2005)
15. D.Green, K.Maeshima, R.Vidal, J.Womersley, W.Wu, CMS NOTE 1999/048

Conclusion

Experimental Summary and Perspectives

John Womersley

CCLRC Rutherford Appleton Laboratory, Chilton, Didcot, OX11 0QX, UK

Abstract. I attempt to summarise, and place in context, the results presented at the Hadron Collider Physics Symposium 2005.

1 Outline

Had I attempted in my concluding talk to actually summarise all of the experimental presentations given at this workshop, I could have devoted approximately 40 seconds to each one. My sense was that this would not be terribly enjoyable or informative for the audience (or indeed for the speaker). Instead, I used the organisers' invitation to talk about "perspectives" as a licence to step back, look at the big picture, and try to set the week's themes in context. I therefore focused only on a subset of the results shown, chosen as examples. My apologies to those whose work I omitted—it is not intended as any reflection of relative importance.

2 What is the universe made of?

This is a very old question, and one that has been approached in many ways. We have found that the only reliable way to answer this question is by directly enquiring of nature, through experiments. We live in a cold and empty universe: only the stable relics and leftovers of the big bang remain. All unstable particles have decayed away with time, and the symmetries have been broken as the universe has cooled. Nonetheless, every kind of particle that ever existed is still there, in the quantum fluctuations of the vacuum. The vacuum "knows" about all the degrees of freedom and all the symmetries. We use colliders to pump sufficient energy into the vacuum to re-create the particles and uncover the symmetries that existed in the earliest universe. Accelerators, which were invented to study the structure of matter, are therefore also tools to study the structure of the vacuum—the space-time fabric of the universe itself.

In his opening talk, Georg Weiglein—perhaps emulating another famous German who worked in Britain—made a persuasive case that the collapse of the present order is inevitable and imminent. The standard model makes precise and accurate predictions and provides an understanding of what nucleons, atoms, stars, you and me are made of; but, just as Karl Marx claimed of capitalism, it

contains the seeds of its own destruction. Its spectacular success in describing phenomena at energy scales below 1 TeV is based on at least one unobserved ingredient—the SM Higgs—whose mass is unstable to loop corrections. Something like supersymmetry is required to fix this, and even then, the Higgs field has an energy density 10^{60} times too great to exist in the universe we live in. The way forward is through experiment (and only experiment). This is tantalising, since we know the answers are accessible, and frustrating, as we have known this for over 20 years. Indeed, some of us went to Waxahachie, Texas in pursuit of this goal (without success, alas).

Meanwhile our view of the universe has radically changed. If one asked "what shapes the cosmos?" the old answer was the mass it contains, through gravity. But we now know there is much more mass than we'd expect from the stars we see, or from the amount of helium formed in the early universe. There is a huge amount of dark matter. Even stranger, the velocity of distant galaxies shows that there is some kind of energy driving the expansion of the universe (as well as the mass slowing it down): we call this dark energy. We are faced with the rather shocking conclusion that we do not know what 96% of the universe is made of.

There are rather general arguments suggesting that dark matter particles should have masses and cross sections typical of the electroweak scale. It is intriguing that these two questions, the breakdown of the standard model and the dark content of the universe, seem to come together at the same energy scale. In exploring this scale, our accelerators are looking at what the universe contained about one picosecond after the Big Bang.

How are these accelerators doing? We heard about continued progress with both the Tevatron [1] and LHC [2]. At Fermilab, luminosities are substantially increased over 2004 and are routinely in the $10^{32} \text{ cm}^{-2}\text{s}^{-1}$ range. Electron cooling, the last major component of the Run II accelerator upgrades, appears to be working. The two experiments have each received about 1 fb^{-1} of integrated luminosity so far and the complex is on track to deliver 8.5 fb^{-1} by the end of FY2009. At CERN, half of the LHC

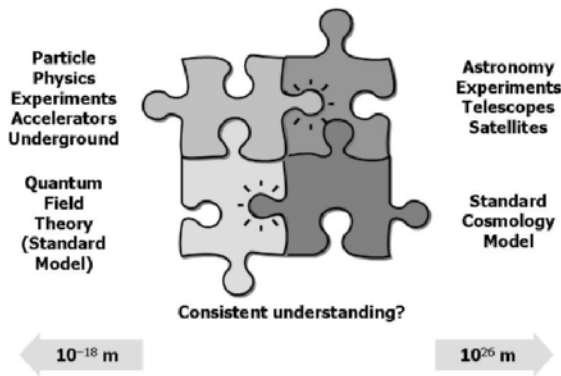


Fig. 1. Two approaches to describing the universe

dipoles are now completed, and dipole installation in the tunnel has begun. The schedule shows beam in 2007, with the first physics data probably in 2008.

We also heard about progress on the LHC detectors [3]; all four can point to impressive progress now being made on installation, and indeed the first cosmic rays have been seen in the ATLAS detector in its cavern. We also heard a large number of presentations on physics object reconstruction and algorithms. A vast amount of work has been carried out at the Tevatron to understand and model $\bar{p}p$ collisions, to develop reliable and trusted techniques for electron, photon, muon, tau, and jet ID, and to characterise their performance. This work is ramping up at the LHC, hopefully embodying all this experience. While there is far too much for me to describe in detail, the third generation deserves some mention. The physics of the electroweak scale appears to couple to mass, so the ability to select b -jets and taus is not just important for specific models (such as SUSY at large $\tan\beta$) but is a good investment in general. This has already proved to be the case at the Tevatron and will surely be true at the LHC.

3 Describing the Universe

How then do we apply these tools to learn about the universe we live in? As shown in Fig. 1, our knowledge of the basic laws of the cosmos comes from two directions. On the left, we have particle physics experiments, looking at the behaviour of matter at distance scales of order 10^{-18} m, and a theoretical synthesis called the standard model. On the right, we have astronomy, looking at distance scales of order 10^{26} m, and a theoretical synthesis in the form of a standard cosmological model. It should be obvious that these seek to describe the same universe, and one test of whether our knowledge makes sense (or is complete) is whether the left hand and right hand sides of the figure fit together to form a consistent view of the universe. We can apply the logic of Fig. 1 to a series of physics questions.

3.1 Supersymmetry

As a first example, consider dark matter. Dark matter in the universe is an observation on the right hand side (‘astronomy’) side of the picture. On the left hand side, dark matter is being directly sought in underground experiments. We also have candidates for extending the standard model description of particles and forces in ways that include plausible dark matter candidates—supersymmetry, in which the lightest neutralino fills this role, is perhaps the most popular such extension. The challenge for hadron colliders is then to search for supersymmetry, or other extensions of the standard model, on the left hand side, and to see if things are consistent with dark matter on the right.

As we heard here [4], supersymmetry is very actively being sought at the Tevatron. There are two classic search modes: jet(s) + E_T^{miss} signatures for strongly produced squarks and gluinos, and multilepton signatures for electroweakly produced charginos and neutralinos. These search strategies are now probing the mass range beyond LEP and there is real potential for discovery. The rather general searches are complemented by more targeted analyses, among them searches for $\tilde{g} \rightarrow \tilde{b} + b$, sbottom pair production, stop pair production, gauge mediated SUSY with $\gamma + E_T^{miss}$ signatures, R -parity violation in various channels probing different R violating couplings: multileptons, jets + muons, $\tilde{\chi}^0 \rightarrow e\mu, ee, \mu\mu, \tau\tau$, and stop pairs $\rightarrow b\tau b\tau$, and charged massive (quasi-)stable particles such as staus or charginos.

At the LHC [5], production of electroweak scale superpartners is copious and discovery will likely be relatively straightforward. The question is, how much can be learned about the spectrum and the quantum numbers of these new particles? If nature is kind with decay chains, one can learn quite a bit, though extraction may be model dependent. A key issue is whether the spins of the superpartners can be determined—without such a determination, the identification of the new particles as being signatures of supersymmetry can only be tentative.

3.2 Higgs

Referring again to Fig. 1, on the right hand side cosmology tells us that the universe is filled with some kind of dark energy field. On the left, our standard model field theory also posits an energy field filling the universe—the Higgs field. So far so good. Unfortunately, the energy density of the Higgs field seems to be at least 10^{60} times greater than what is expected for dark energy. There is a gross inconsistency between the two views of the universe. Our goals for hadron colliders must be to pin down as much as we can about the Higgs field, both from direct searches and indirectly through precision studies, especially of the top quark.

3.2.1 Direct Higgs Searches

A number of Tevatron Higgs searches were presented here. The limits obtained [6] with roughly 300 pb^{-1} are 20–100 times higher than the standard model cross section. The experiments have quantified the improvements in sensitivity needed to reach their projected reach: these include EM coverage, EM efficiency, dijet mass resolution, and b -tagging efficiency. A lot of work is underway, and the collaborations remain committed to this search—it was always understood to be a challenge. The Tevatron is starting to see some of the rare SM processes that will be important backgrounds, such as WZ production [7].

At the LHC [8], the whole Higgs mass range is accessible with 30 fb^{-1} . With even a few inverse femtobarns it will be possible to discover the Higgs in the WW and ZZ channels, if its mass is between about 150 and 500 GeV. The LHC can also measure ratios of the couplings of the Higgs at the 10–30% level.

It is worth noting that the vector boson fusion process, which requires forward jet tagging, adds a lot of significance to the Higgs searches at low mass. I am not completely convinced that forward jet tagging (or central jet vetoing) will be straightforward to implement: at the Tevatron, we are used to seeing a lot of energy in the forward region and forward jet identification is not simple.

In minimal supersymmetric extensions to the standard model, the Higgs sector is more complex, but cross sections can be higher. Searches at the Tevatron have focused on $H/h/A \rightarrow \tau\tau$ and $\bar{b}b$ which cover complementary regions at large $\tan\beta$ and $\mu \ll 0$. These searches are already sensitive to $\tan\beta \sim 60$ and have the potential to reach significantly lower values.

At the LHC, at least one MSSM Higgs can always be found, but there is a significant region of parameter space where only the lightest scalar h can be seen, and it cannot always be distinguished from the standard model H .

3.2.2 The Top Quark and Precision Measurements

The Tevatron Collider is currently the world's only source of top quarks. Top couples strongly to the Higgs field and thus offers a potential window on the mechanism of fermion mass generation. We need to measure its properties with greatly increased statistics, especially the top mass which constrains the Higgs sector, and search for any surprises and anomalies.

The top-antitop production cross section at the Tevatron has been measured [9] in many decay modes by both experiments. All channels are consistent with each other and with QCD. The experiments have also searched for anomalous production through $\tilde{t} \rightarrow t + X$.

At this meeting, the CDF collaboration reported [10] a new measurement of the top quark mass $m_t^{CDF} = 173.5 \pm 4.1 \text{ GeV}$. This implies a new world average $m_t^{ave} = 174.3 \pm 3.4 \text{ GeV}$, which in turn shifts the best fit to the Higgs mass (from electroweak precision fits) to $m_H = 98_{-36}^{+52} \text{ GeV}$ and $m_H < 208 \text{ GeV}$ (95% C.L.). A precision of $\Delta m_t < 2 \text{ GeV}$

in Run II should be attainable. [A new $D\bar{O}$ top mass result also became available soon after this meeting.]

The next question is how does top decay [11]? In the standard model, top decays almost exclusively to a W and a b -quark, but in principle it could decay to other down-type quarks too. This can be tested by measuring $R = B(t \rightarrow b)/B(t \rightarrow q)$ by comparing the number of double b -tagged to single b -tagged events. Both experiments find results consistent with $R = 1$ *i.e.* 100% of top decaying to b , as in the Standard Model. CDF has also searched for $t \rightarrow \tau\nu$ and $t \rightarrow H^\pm$. There should soon be enough data to determine the electric charge of top, at least at the level of excluding the exotic possibility of its having a $4/3$ electric charge.

Both experiments have also studied spin in top decays. Because its mass is so large, the top quark is expected to decay very rapidly (in of order 10^{-24} seconds) and has no time to form a top meson. The $t \rightarrow Wb$ decay then preserves the spin information, which is reflected in decay angle and momentum of lepton in the W rest frame. $D\bar{O}$ finds the fraction of right handed W s to be $F_+ < 0.25$ (95% C.L.) while CDF finds the fraction of longitudinal W s to be $F_0 = 0.27_{-0.24}^{+0.35}$ (from a fit to the lepton p_T) and $F_0 = 0.89_{-0.38}^{+0.34}$ (from a fit to $\cos\theta^*$). In the SM, we expect $F_+ \approx 0$ and $F_0 \sim 0.7$, so everything is consistent with the standard model.

Single Top production has not yet been observed. This process probes the EW properties of top and is a good place to look for new physics connected with top. It is desirable to separate the s and t -channel production modes since they have different sensitivities to new physics. The best current limits [12] are around 6 pb from $D\bar{O}$. While they are not yet sensitive to the standard model cross section (~ 1 pb in the s channel and 2 pb in the t -channel), they are starting to reach the cross sections predicted by some models of new physics. The current $D\bar{O}$ analysis would require $\sim 2.5 \text{ fb}^{-1}$ for a 3σ signal in the t -channel. We can thus be fairly sure that single top will be discovered in Run II, but improvements in the sensitivity are still desirable.

The other dominant ingredient in precision fits is the W mass. Improved top mass precision yields diminishing returns without corresponding progress on the W mass. The Tevatron goal is to improve on LEP2. The CDF collaboration [13] showed a status report with $\sim 200 \text{ pb}^{-1}$ of $W \rightarrow e\nu$ data, yielding an uncertainty of $\Delta m_W = 76 \text{ MeV}$, but the central value is still blinded.

At LHC, both top and W will benefit from truly enormous statistics [14]. The top cross section is ~ 150 times larger than at the Tevatron, giving a roughly 1 Hz rate of $t\bar{t}$ production. It should be possible to measure the mass to the 1 GeV level (the dominant systematic is the b -jet energy scale) and make precise measurements of such quantities as spin correlations and angular distributions. High statistics measurements of single top should be possible, as well as tests of the production mechanism (e.g. through top polarisation). The LHC will also have sufficient statistics to permit the W mass to be measured at the 15 MeV level, but to reach this precision will be a challenging,

multi-year project. It is not yet clear whether there will be a physics need for this level of accuracy, though there are scenarios [15] where it is desirable, for example to make precision tests of SUSY.

3.3 B physics at hadron colliders

Turning again to Fig. 1, we know that in the universe as a whole (the right hand side of the figure) matter dominates over antimatter. On the left, however, particle physics is almost exactly matter-antimatter symmetric, except for small CP violation. Are these consistent? Not really—while CP violation in the early universe can account in principle for the absence of antimatter today, the observed level of CP violation in the quark sector is insufficient for this to work out in practice. The goal for hadron colliders is then to complement the e^+e^- B -factories in exploring CP violation, to search for new sources, and to use the B sector as a probe of new physics.

If quark mixing is described by a unitary 3×3 matrix, we can parameterise the phases and magnitudes by a triangle. Hadron colliders confront this unitarity triangle in ways that complement measurements at the B -factories, e.g. through the B_S^0 system. B_S^0 mixing is a good way to see indirect effects of new physics that would not be detectable at a B -factory. Indeed, there is a teasing hint [16] of a 2.6σ discrepancy in the B -factory data, between the CP β angle extracted from charmonium modes and strange quark penguin modes which might point to some new physics in loops containing b and s quarks.

The flagship B -physics analysis at the Tevatron is the search for B_S^0 oscillations. We heard [17] that the CDF collaboration is reporting a limit on oscillation frequency $\Delta m_S > 7.9 \text{ ps}^{-1}$. With $3\text{--}4 \text{ fb}^{-1}$ of data, CDF and $D\bar{O}$ should be able to observe a 5σ signal at the favoured SM value of $\sim 18 \text{ ps}^{-1}$. The oscillation frequency measures the mass difference; a complementary measurement is the width difference. The width difference $\Delta\Gamma_S/\Gamma$ from CDF is larger than expected, and the central value would imply a large Δm_S (and new physics). However, the errors are large, the $D\bar{O}$ result is smaller, and the combined CDF and $D\bar{O}$ result is consistent with the SM.

Rare decays of B -mesons are another important way to search for indirect signals of new physics. For example, the rare decay $B_S^0 \rightarrow \mu^+\mu^-$ has a standard model branching ratio of $3.4 \pm 0.4 \times 10^{-9}$. In the minimal supersymmetric standard model, this can be increased to as much as a few times 10^{-7} depending on the model parameters. CDF and $D\bar{O}$ reported [18] 95% C.L. limits in this mode of 2.0 and 3.7×10^{-7} respectively, which is starting to constrain SUSY models. Other rare decays where interesting limits are being set are $B_d^0 \rightarrow \mu^+\mu^-$, $< 4.9 \times 10^{-8}$ (CDF) and $B_S^0 \rightarrow \mu^+\mu^-\phi$, $< 4.1 \times 10^{-6}$ ($D\bar{O}$).

At the LHC [19], B -Physics will be an important part of the toolkit to look for new physics. Firstly, there are many ways to overconstrain the CKM matrix by comparing tree-level dominated processes, penguins and box diagrams. Discrepancies can reveal new (CP violating)

physics and could in fact be the only window on CP violation in any new physics. Secondly, rare decays can reveal new physics up to $O(\text{TeV})$. Both of these complement direct searches for new physics and the results can be beaten against each other. LHCb is a dedicated B -physics experiment with good particle identification (and with a guaranteed bread-and-butter CKM physics program). It is complemented by ATLAS and CMS, which have no particle ID, but do have the ability to run at high luminosities. This is particularly powerful for rare decays where these experiments will even be capable of seeing the tiny SM rates.

3.4 Measuring the shape of space-time

Let's take one last look at Fig. 1. In the previous examples, we have aimed for a consistent understanding of phenomena on the left and right hand sides. But there is a candidate for such an overarching theory of everything: string theory. What does it predict for hadron colliders? Certainly it predicts the existence of supersymmetry, but beyond this, string theory ideas hint that the universe may have more than three plus one dimensions of space-time. The Tevatron experiments are searching for physics signatures of such a possibility [20]. There are many possible phenomenologies, such as virtual graviton exchange (e.g. in the Arkani-Hamed, Dimopoulos and Dvali framework) which would lead to an enhancement of photon and electron pair production at large invariant masses; and Kaluza-Klein excitations (e.g. of the graviton in the Randall-Sundrum framework) which would appear as a massive resonance decaying to e^+e^- . No deviation from three plus one dimensions is seen, but interesting limits can be set on the size and properties of extra dimensions. The fact that collider experiments are capable of measuring the shape of space-time is certainly unexpected and exciting.

3.5 QCD

Quantum chromodynamics underlies everything we do with hadron colliders. It also contains its own puzzles. Pretty much everyone believes that QCD is the correct theory of the strong interaction—but this is not the same as having detailed predictions of the behavior of quarks and gluons under all conditions.

As the Tevatron presentations showed [21], at high momentum transfers things pretty much do what we expect; but perturbative calculations must continue to confront data if we are to improve our understanding of signals and backgrounds. We were shown [22] a detailed list of new perturbative calculations that would be desirable; it would be interesting to know what (if anything) the experiments should measure, over and above their existing physics programs, to help this process (one example I have been asked about is the six-jet inclusive cross section, which has been studied as a background to top but never published in its own right).

What can HERA do for us? We heard [23] of two ways that HERA data help to confront QCD: first by determining parton distributions, where there are still significant uncertainties (the Tevatron and LHC can help too). At this meeting, the first experimental determination of the b -quark distribution was presented; this is needed for (*e.g.*) single top at the Tevatron/LHC and was never directly determined until now. Secondly, HERA can deliberately push to lower momentum transfers where QCD enters the ‘non-intuitive’ regime and the question is often what is the right way to think/calculate (*e.g.* DGLAP vs. BFKL)?

A clear case of ‘non-intuitive’ behavior is hard diffraction [24]. Why does it happen so often (apparently ten percent of the time at HERA)? How can it happen at all? What is/are the exchanged particle(s)? Is it some kind of collective behaviour, like colour transparency? In the particular case of diffractive Higgs production, much of the controversy has calmed down, and the predictions are converging. The calculations are roughly in line with the observed rate for $\bar{p}p \rightarrow \bar{p}(\text{gap})\chi_C(\text{gap})p$ at CDF. One expects ~ 10 Higgs events per year after cuts in the TOTEM experiment at LHC.

It now seems clear [25] that some new kind of opaque quark-gluon phase is being formed in heavy ion collisions at RHIC. This phase blocks jets, leading to clear suppression of opposite-side high- p_T particles, and enhancement and broadening at low p_T . In my personal view, something interesting is going on in the RHIC data for sure, but I don’t feel that we have quite figured out how to grasp it. Many of the variables and the probes seem non-intuitive, at least to me (my apologies if this offends those more familiar with this field). It feels reminiscent of the situation 20–25 years ago, when we were trying to convince ourselves we were seeing jets in fixed target experiments. Hence I suspect that things will get clearer at higher collision energies and with a more focused approach (just as we only really understood QCD in $\bar{p}p$ interactions when we could go to high energies where jets became clear). The implied lessons from this are that we want high p_T probes, which means jets, and which for me requires calorimetry; and that we want a higher \sqrt{s} . I am therefore looking forward with interest to the results from heavy ion collisions at the LHC.

4 A Few Closing Comments

Big collaborations are founded on mutual trust and understanding, with a shared sense of purpose and a common experience base. The size and geographic dispersion of the LHC collaborations brings new challenges. For both ATLAS and CMS, ‘preparing for physics’ is also an exercise in community building. We heard [26] about one example of this in the case of the ATLAS Rome physics meeting. It’s also good to see that the successful series of LHC Symposia is now unified with the Hadron Collider Physics conference series. We should see ourselves as one community; we address one set of physics goals.

Before I conclude, I would like to thank the scientific program committee, Allan Clark and the local organising committee, the conference secretariat, the hotel staff, the Swiss Institute of Particle Physics and CERN, for all making this such a well-organised and high-quality meeting. And of course, thanks to all of the speakers and the poster presenters!

5 Conclusions

The physics program discussed here this week is (in my opinion) hard to match in breadth and importance. It is based on the detailed understanding of Standard Model particles and forces, including QCD, that we have obtained over the last few decades. With that basis we can address some very big questions about the universe, for example: *What is the cosmic dark matter? Is it Supersymmetry? Or something else? Is the universe filled with a Higgs Field? How does this relate to dark energy? What is the structure of spacetime? Are there extra dimensions?* The ability of hadron colliders to do this is both beautiful and surprising. We are now sailing into unexplored territory — who knows what we will find?

References

1. D. McGinnis, these proceedings.
2. L. Evans, *ibid.*
3. H.-A. Gustafsson, S. Stapnes, T. Virdee, R. Forty, *ibid.*
4. M.-C. Cousinou, *ibid.*
5. C. Lester, *ibid.*
6. A. Goussiou, *ibid.*
7. A. Goshaw, *ibid.*
8. M. Pieri, *ibid.*
9. E. Busato, *ibid.*
10. T. Tomura, *ibid.*
11. A. Quadt, *ibid.*
12. A. Taffard, *ibid.*
13. M. Lancaster, *ibid.*
14. N. Amapane, A. Giammanco, *ibid.*
15. A. Lucotte, *ibid.*
16. P. Chang, *ibid.*
17. G. Gomez-Ceballos, *ibid.*
18. S. Dugad, *ibid.*
19. M. Schmelling, C. Petridou, *ibid.*
20. H. Gerberich, *ibid.*
21. C. Gerber, *ibid.*
22. K. Ellis, *ibid.*
23. M. Klein, *ibid.*
24. M. Deile, *ibid.*
25. T. Peitzmann, *ibid.*
26. A. dell’Aqua, *ibid.*

Einstein's Contributions to Quantum Theory

Norbert Straumann

Institute for Theoretical Physics
University of Zürich, Switzerland

Abstract. Einstein's revolutionary light quantum hypothesis of 1905 and his further contributions to quantum theory are reviewed.

1 Introduction

During this *World Year of Physics* physicists celebrate all over the world the astounding sequence of papers that Einstein wrote in rapid succession during the year 1905. But already before this *annus mirabilis* Einstein had published remarkable papers in the *Annalen der Physik*, the journal to which he submitted most of his early work. Of crucial importance for his further research were three papers on the foundations of statistical mechanics, in which he tried to fill what he considered to be a gap in the mechanical foundations of thermodynamics. At the time when Einstein wrote his three papers he was not familiar with the work of Gibbs and only partially with that of Boltzmann. Einstein's papers form a bridge, parallel to the *Elementary Principles of Statistical Mechanics* by Gibbs in 1902, between Boltzmann's work and the modern approach to statistical mechanics. In particular, Einstein independently formulated the distinction between the microcanonical and canonical ensembles and derived the equilibrium distribution for the canonical ensemble from the microcanonical distribution. Of special importance for his later research was the derivation of the energy-fluctuation formula for the canonical ensemble.

Einstein's profound insight into the nature and size of fluctuations played a decisive role for his most revolutionary contribution to physics: the light-quantum hypothesis. Indeed, Einstein extracted the light-quantum postulate from a statistical-mechanical analogy between radiation in the Wien regime¹ and a classical ideal gas of material particles. In this consideration Boltzmann's principle, relating entropy and probability of macroscopic states, played a key role. Later Einstein extended these considerations to an analysis of energy and momentum fluctuations of the radiation field. For the latter he was also drawing on ideas and methods he had developed in the course of his work on Brownian motion, another beautiful application of fluctuation theory. This definitely established the re-

ality of atoms and molecules, and, more generally, gave strong support for the molecular-kinetic theory of thermodynamics.

Fluctuations also played a prominent role in Einstein's beautiful work on critical opalescence. Many years later he applied this magic wand once more to gases of identical particles, satisfying the Bose-Einstein statistics. With this work in 1924 he extended the particle-wave duality for photons to massive particles. It is well-known that Schrödinger was much stimulated by this profound insight. As an application, Einstein also discovered what is known as Bose-Einstein condensation, that has become a very topical research field.

2 Einstein's first paper from 1905

The generations of physicists that learned quantum theory after the great breakthrough in 1925-26 rarely know about the pioneering role of Einstein in the development of this field during the previous twenty years. With his work on quantum theory alone he would already belong to the central figures of twentieth century physics. In the first of his 1905 papers he introduced the hypothesis of light quanta, a step that he considered himself as his only revolutionary one. The course of physics would presumably have been quite different without this rather bold suggestion. Indeed, Einstein was the first who clearly realized that the empirical energy distribution of the black-body radiation was in dramatic conflict with classical physics, and thus a radically different conception of radiation was required. Most physicists reduce the content of Einstein's paper "On a heuristic point of view concerning the production and transformation of light" to what he wrote about the photoelectric effect. This was, however, just an important application of a much more profound analysis, that he soon supplemented in various ways.

We begin by briefly reviewing the line of thought of the March paper (CPAE Vol. 2, Doc. 14) "whose significance and originality can hardly be overestimated" (Res Jost). In a first section Einstein emphasizes that classical

¹ The 'Wien regime' corresponds to high frequency and/or low temperature, such that $h\nu \gg kT$, where h and k are Planck's and Boltzmann's constants respectively.

physics inevitably leads to a nonsensical energy distribution for black-body radiation, but that the spectral distribution, $\rho(T, \nu)$, must approximately be correct for large wavelengths and radiation densities (classical regime).² Applying the equipartition theorem for a system of resonators (harmonic oscillators) in thermal equilibrium, he found independently what is now known as the Rayleigh-Jeans law³: $\rho(\nu, T) = (8\pi\nu^2/c^3)kT$. Einstein stresses that this law “not only fails to agree with experience (...), but is out of question” because it implies a diverging total energy density (ultraviolet catastrophe). In a second section he then states that the Planck formula “which has been sufficient to account for all observations made so far” agrees with the classically derived formula in the mentioned limiting domain for the following value of the Avogadro number

$$N_A = 6.17 \times 10^{23}. \quad (1)$$

This value was already found by Planck, though not using a correspondence argument, but rather relying on the strict validity of his formula and the assumptions that led to its derivation. Einstein's correspondence argument now showed “that Planck's determination of the elementary quanta is to some extent independent of his theory of black-body radiation.” Indeed, Einstein understood from first principles exactly what he did. A similar correspondence argument was used by him more than ten years later in his famous derivation of Planck's formula (more about this later). Einstein concludes these considerations with the following words:

“The greater the energy density and the wavelength of the radiation, the more useful the theoretical principles we have been using prove to be; however, these principles fail completely in the case of small wavelengths and small radiation densities.”

Einstein now begins to analyze what can be learned about the structure of radiation from the empirical behavior in the Wien regime, i.e., from Wien's radiation formula for the spectral energy-density

$$\rho(T, \nu) = \frac{8\pi\nu^2}{c^3} h\nu e^{-h\nu/kT}. \quad (2)$$

Let $E_V(T, \nu)$ be the energy of radiation contained in the volume V and within the frequency interval $[\nu, \nu + \Delta\nu]$ ($\Delta\nu$ small), that is,

$$E_V(T, \nu) = \rho(T, \nu) V \Delta\nu. \quad (3)$$

and, correspondingly, $S_V(T, \nu) = \sigma(T, \nu) V \Delta\nu$ for the entropy. Thermodynamics now implies

$$\frac{\partial \sigma}{\partial \rho} = \frac{1}{T}. \quad (4)$$

² This is, to our knowledge, the first proposal of a ‘correspondence argument’, which is of great heuristic power, as we will see.

³ Einstein uses the following relation between $\rho(T, \nu)$ and the mean oscillator energy $\bar{E}(T, \nu)$ at temperature T , found by Planck: $\rho(T, \nu) = \frac{8\pi\nu^2}{c^3} \bar{E}(T, \nu)$.

Solving (2) for $1/T$ and inserting this into (4) gives

$$\frac{\partial \sigma}{\partial \rho} = -\frac{k}{h\nu} \ln \left[\frac{\rho}{8\pi h\nu^3/c^3} \right]. \quad (5)$$

Integration yields

$$S_V = -k \frac{E_V}{h\nu} \left\{ \ln \left[\frac{E_V}{V \Delta\nu 8\pi h\nu^3/c^3} \right] - 1 \right\}. \quad (6)$$

In his first paper on this subject, Einstein focused attention to the volume dependence of radiation entropy, as displayed by this expression. Fixing the amount of energy, $E = E_V$, one obtains

$$S_V - S_{V_0} = k \frac{E}{h\nu} \ln \left(\frac{V}{V_0} \right) = k \ln \left(\frac{V}{V_0} \right)^{E/h\nu}. \quad (7)$$

So far only thermodynamics has been used. Now Einstein brings into the game what he called Boltzmann's principle, which was already of central importance in his papers on statistical mechanics. According to Boltzmann, the entropy S of a system is connected with the number of possibilities W , by which a macroscopic state can microscopically be realized, through the relation

$$S = k \ln W. \quad (8)$$

In a separate section Einstein recalls this fundamental relation between entropy and “statistical probability” (Einstein's terminology), before applying it to an ideal gas of N particles in volumes V and V_0 , respectively. For the relative probability of the two situations one has

$$W = \left(\frac{V}{V_0} \right)^N, \quad (9)$$

and hence for the entropies

$$S(V, T) - S(V_0, T) = kN \ln \left(\frac{V}{V_0} \right). \quad (10)$$

For the relative entropies (7) of the radiation field, Boltzmann's principle (8) now gives

$$W = \left(\frac{V}{V_0} \right)^{E/h\nu}. \quad (11)$$

>From the striking similarity of (9) to (11) Einstein finally concludes:

“Monochromatic radiation of low density (within the range of Wien's radiation formula) behaves thermodynamically as if it consisted of mutually independent energy quanta of magnitude $h\nu$.”

So far no revolutionary statement has been made. The famous sentences just quoted express the result of a statistical mechanical analysis.

Light quantum hypothesis

Einstein's bold step consists in a statement about the quantum properties of the free electromagnetic field, that was not accepted for a long time by anybody else. He formulates his heuristic principle as follows:

"If, with regard to the dependence of its entropy on volume, a monochromatic radiation (of sufficient low density) behaves like a discontinuous medium consisting of energy quanta of magnitude $h\nu$, then it seems reasonable to investigate whether the laws of generation and conversion of light are so constituted as if light consisted of such energy quanta."

In the final two sections, Einstein applies this hypothesis first to an explanation of Stokes' rule for photoluminescence and then turns to the photoelectric effect. One should be aware that in those days only some qualitative properties of this phenomenon were known. Therefore, Einstein's well-known linear relation between the maximum kinetic energy of the photoelectrons (E_{\max}) and the frequency of the incident radiation,

$$E_{\max} = h\nu - P, \quad (12)$$

was a true prediction. Here P is the work-function of the metal emitting the electrons, which depends on the material in question but not on the frequency of the incident light.

It should be stressed that Einstein's bold light quantum hypothesis was very far from Planck's conception. Planck neither envisaged a quantization of the free radiation field, nor did he, as it is often stated, quantize the energy of a material oscillator per se. What he was actually doing in his decisive calculation of the entropy of a harmonic oscillator was to assume that the *total* energy of a large number of oscillators is made up of *finite* energy elements of equal magnitude $h\nu$. He did not propose that the energies of single material oscillators are physically quantized.⁴ Rather, the energy elements $h\nu$ were introduced as a formal counting device that could at the end of the calculation not be set to zero, for, otherwise, the entropy would diverge. It was Einstein in 1906 who interpreted Planck's result as follows (CPAE, Vol. 2, Doc. 34):

"Hence, we must view the following proposition as the basis underlying Planck's theory of radiation: The energy of an elementary resonator can only

⁴ In 1911 Planck even formulated a 'new radiation hypothesis', in which quantization only applies to the process of light emission but not to that of light absorption (Planck 1911). Planck's explicitly stated motivation for this was to avoid an effective quantization of oscillator energies as a *result* of quantization of all interaction energies. It is amusing to note that this new hypothesis led Planck to a modification of his radiation law, which consisted in the addition of the temperature-independent term $h\nu/2$ to the energy of each oscillator, thus corresponding to the oscillator's energy at zero temperature. This seems to be the first appearance of what soon became known as 'zero-point energy'.

assume values that are integral multiples of $h\nu$; by emission and absorption, the energy of a resonator changes by jumps of integral multiples of $h\nu$."

3 Energy and momentum fluctuations of the radiation field

In his paper "On the present status of the radiation problem" of 1909 (CPAE, Vol. 2, Doc. 56), Einstein returned to the considerations discussed above, but extended his statistical analysis to the entire Planck distribution. First, he considers the energy fluctuations, and re-derives the general fluctuation formula he had already found in the third of his statistical mechanics articles. This implies for the variance of E_V in (3):

$$\langle (E_V - \langle E_V \rangle)^2 \rangle = kT^2 \frac{\partial \langle E_V \rangle}{\partial T} = kT^2 V \Delta\nu \frac{\partial \rho}{\partial T}. \quad (13)$$

For the Planck distribution this gives

$$\langle (E_V - \langle E_V \rangle)^2 \rangle = \left(h\nu\rho + \frac{c^3}{8\pi\nu^2} \rho^2 \right) V \Delta\nu. \quad (14)$$

Einstein shows that the second term in this most remarkable formula, which dominates in the Rayleigh-Jeans regime, can be understood with the help of the classical wave theory as due to the interferences between the partial waves. The first term, dominating in the Wien regime, is thus in obvious contradiction with classical electrodynamics. It can, however, be interpreted by analogy to the fluctuations of the number of molecules in ideal gases, and thus represents a particle aspect of the radiation in the quantum domain.

Einstein confirms this particle-wave duality, at this time a genuine theoretical conundrum, by considering also the momentum fluctuations. For this he considers the Brownian motion of a mirror which perfectly reflects radiation in a small frequency interval, but transmits for all other frequencies. The final result he commented as follows:

"The close connection between this relation and the one derived in the last section for the energy fluctuation is immediately obvious, and exactly analogous considerations can be applied to it. Again, according to the current theory, the expression would be reduced to the second term (fluctuations due to interference). If the first term alone were present, the fluctuations of the radiation pressure could be completely explained by the assumption that the radiation consists of independently moving, not too extended complexes of energy $h\nu$."

Einstein discussed these issues also in his famous Salzburg lecture (CPAE Vol. 2, Doc. 60) at the 81st Meeting of German Scientists and Physicians in 1909. Pauli (1949) once said that this report can be regarded as a turning point in the development of theoretical physics.

In this Einstein treated the theory of relativity and quantum theory and pointed out important interconnections between his work on the quantum hypothesis, on relativity, on Brownian motion, and statistical mechanics. Already in the introductory section he says prophetically:

“It is therefore my opinion that the next stage in the development of theoretical physics will bring us a theory of light that can be understood as a kind of fusion of the wave and emission theories of light.”

We now know that it took almost twenty years until this was achieved by Dirac in his quantum theory of radiation.

4 Reactions

We already stressed that Einstein's bold light quantum hypothesis was very far from Planck's conception. This becomes particularly evident from the following judgement of Planck.

When Planck, Nernst, Rubens, and Warburg proposed Einstein in 1913 for membership in the Prussian Academy their recommendation concludes as follows:

“In sum, one can say that there is hardly one among the great problems in which modern physics is so rich to which Einstein has not made a remarkable contribution. That he may sometimes have missed the target in his speculations, as, for example, in his hypothesis of light-quanta, cannot really be held to much against him, for it is not possible to introduce really new ideas even in the most exact sciences without sometimes taking a risk.”

It took almost ten years until Einstein's application of the light quantum hypothesis to the photoelectric effect was experimentally confirmed by Millikan, who then used it to give a first precision measurement of h (slope of the straight line given by (12) in the ν - E_{\max} plane) at the 0.5 percent level (Millikan 1916). Strange though understandable, not even he, who spent 10 years on the brilliant experimental verification of its consequence (12), could believe in the fundamental correctness of Einstein's hypothesis. In his comprehensive paper (Millikan 1916) on the determination of h , Millikan first commented on the light-quantum hypothesis:

“This hypothesis may well be called reckless, first because an electromagnetic disturbance which remains localized in space seems a violation of the very conception of an electromagnetic disturbance, and second because it flies in the face of the thoroughly established facts of interference.”

And after reporting on his successful experimental verification of Einstein's equation (12) and the associated determination of h , Millikan concludes:

“Despite the apparently complete success of the Einstein equation, the physical theory of which it was designed to be the symbolic expression is found so untenable that Einstein himself, I believe, no longer holds to it.”

Most of the leading scientists (Sommerfeld, von Laue, Bohr, etc) strongly opposed Einstein's idea of the light-quantum, or at least openly stated disbelief.

5 Derivation of the Planck distribution

A peak in Einstein's endeavor to extract as much as possible about the nature of radiation from the Planck distribution is his paper “On the Quantum Theory of Radiation” of 1916 (CPAE, Vol. 6, Doc. 38). In the first part he gives a derivation of Planck's formula which has become part of many textbooks on quantum theory. Einstein was very pleased by this derivation, about which he wrote on August 11th 1916 to Besso: “An amazingly simple derivation of Planck's formula, I should like to say *the* derivation”. For it he introduced the hitherto unknown process of induced emission⁵, next to the familiar ones of spontaneous emission and induced absorption. For each pair of energy levels he described the statistical laws for these processes by three coefficients (the famous A - and B -coefficients) and established two relations amongst these coefficients on the basis of his earlier correspondence argument in the classical Rayleigh-Jeans limit and Wien's displacement law. In addition, the latter also implies that the energy difference $\varepsilon_n - \varepsilon_m$ between two internal energy states of the atoms in equilibrium with thermal radiation has to satisfy Bohr's frequency condition: $\varepsilon_n - \varepsilon_m = h\nu_{nm}$. In Dirac's 1927 radiation theory these results follow —without any correspondence arguments—from first principles.

In the second part of his fundamental paper, Einstein discusses the exchange of momentum between the atoms and the radiation by making use of the theory of Brownian motion. Using a truly beautiful argument he shows that in every elementary process of radiation, and in particular in spontaneous emission, an amount $h\nu/c$ of momentum is emitted in a random direction and that the atomic system suffers a corresponding recoil in the opposite direction. This recoil was first experimentally confirmed in 1933 by showing that a long and narrow beam of excited sodium atoms widens up after spontaneous emissions have taken place (R. Frisch 1933). Einstein's paper ends with the following remarkable statement concerning the role of “chance” in his description of the radiation processes by statistical laws, to which Pauli (1948) drew particular attention:

“The weakness of the theory lies, on the one hand, in the fact that it does not bring us any closer to a merger with the undulatory theory, and, on the other hand, in the fact that it leaves the time and direction of elementary processes to ‘chance’; in spite of this I harbor full confidence in the trustworthiness of the path entered upon.”

⁵ Einstein's derivation shows that without assuming a non-zero probability for induced emission one would necessarily arrive at Wien's instead of Planck's radiation law.

6 Bose-Einstein statistics for degenerate material gases

The last major contributions of Einstein to quantum theory were stimulated by de Broglie's suggestion that material particles have also a wave aspect, and Bose's derivation of Planck's formula that made only use of the corpuscular picture of light, though based upon statistical rules using their indistinguishability. Einstein applied Bose's statistics for photons to degenerate gases of identical massive particles. With this 'Bose-Einstein statistics', he obtained a new law, to become known as the Bose-Einstein distribution. As for radiation, Einstein considered again fluctuations of these gases and found both, particle-like and wave-like aspects. But this time the wave property was the novel feature, that was recognized by Einstein to be necessary.

In the course of this work on quantum gases, Einstein discovered the condensation of such gases at low temperatures. (Although Bose made no contributions to this, one nowadays speaks of Bose-Einstein condensation.) Needless to say that this subject has become enormously topical in recent years.

Schrödinger acknowledged in his papers on wave mechanics the influence of Einstein's gas theory, which from today's perspective appear to be his last great contribution to physics. In the article in which Schrödinger (1926) establishes the connection of matrix and wave mechanics, he remarks in a footnote: "My theory was inspired by L. de Broglie and by brief but infinitely far-seeing remarks of A. Einstein (*Berl. Ber.* 1925, p. 9ff)".

It is well-known that Einstein considered the 'new' quantum mechanics less than satisfactory until the end of his life. In his autobiographical notes he says, for example,

I believe, however, that this theory offers no useful point of departure for future developments. This is the point at which my expectation departs widely from that of contemporary physicists."

7 Einstein and the interpretation of quantum mechanics

The new generation of young physicists that participated in the tumultuous three-year period from January 1925 to January 1928 deplored Einstein's negative judgement of quantum mechanics. In his previously cited article on Einstein's contributions to quantum mechanics, Pauli (1949) expressed this with the following words:

"The writer belongs to those physicists who believe that the new epistemological situation underlying quantum mechanics is satisfactory, both from the standpoint of physics and from the broader knowledge in general. He regrets that Einstein seems to have a different opinion on this situation (...)."

When the Einstein-Podolski-Rosen (EPR) paper (Einstein *et al.* 1935) appeared, Pauli's immediate reaction (see

Pauli 1985-99, Vol. 2) in a letter to Heisenberg of June 15th was quite furious:

"Einstein once again has expressed himself publicly on quantum mechanics, namely in the issue of Physical Review of May 15th (in cooperation with Podolsky and Rosen – not a good company, by the way). As is well known, this is a catastrophe each time when it happens."

From a greater distance in time this judgement seems exaggerated, but it shows the attitude of the 'younger generation' towards Einstein's concerns. In fact, Pauli understood (though not approved) Einstein's point much better than many others, as his intervention in the Born-Einstein debate on Quantum Mechanics shows (Born 2005, letter by Pauli to Born of March 31st 1954). Whatever one's attitude on this issue is, it is certainly true that the EPR argumentation has engendered an uninterrupted discussion up to this day. The most influential of John Bell's papers on the foundations of quantum mechanics has the title "On the Einstein-Podolsky-Rosen paradox" (Bell 1964). In this publication Bell presents what has come to be called "Bell's Theorem", which (roughly) asserts that *no hidden-variable theory that satisfies a certain locality condition can produce all predictions of quantum mechanics*. This signals the importance of EPR's paper in focusing on a pair of well-separated particles that have been properly prepared to ensure strict correlations between certain of their observable quantities. Bell's analysis and later refinements (1987) showed clearly that the behavior of entangled states is only explainable in the language of quantum mechanics.

This point has also been the subject of the very interesting, but much less known work of S. Kochen and E.P. Specker (1967), with the title "The Problem of Hidden Variables in Quantum Mechanics". Loosely speaking, Kochen and Specker show that quantum mechanics *cannot* be embedded into a classical stochastic theory, provided two very desirable conditions are assumed to be satisfied. The first condition (KS1) is that the quantum mechanical distributions are reproduced by the embedding of the quantum description into a classical stochastic theory. (The precise definition of this concept is given in the cited paper.) The authors first show that hidden variables in this sense can always be introduced if there are no other requirements. (This fact is not difficult to prove.) The second condition (KS2) imposed by Kochen and Specker states that a function $u(A)$ of a quantum mechanical observable A (self-adjoint operator) has to be represented in the classical description by the very same function u of the image f_A of A , where f is the embedding that maps the operator A to the classical observable f_A on 'phase space'. Formally, (KS2) states that for all A

$$f_{u(A)} = u(f_A). \quad (15)$$

The main result of Kochen and Specker states that if the dimension of the Hilbert space of quantum mechanical states is larger than 2, an embedding satisfying (KS1) and (KS2) is 'in general' *not possible*.

There are many highly relevant examples—even of low dimensions with only a finite number of states and observables—where this impossibility holds.

The original proof of Kochen and Specker is very ingenious, but quite difficult. In the meantime several authors have given much simpler proofs; e.g. Straumann (2002).

We find the result of Kochen and Specker entirely satisfactory in the sense that it clearly demonstrates that there is no way back to classical reality. Einstein's view that quantum mechanics is a kind of glorified statistical mechanics, that ignores some hidden microscopic degrees of freedom, can thus not be maintained without giving up locality or (KS2). It would be interesting to know his reaction to these developments that have been triggered by the EPR paper.

Entanglement is not limited to questions of principle. It has already been employed in quantum communication systems, and entanglement underlies all proposals of quantum computation.

Acknowledgements

I sincerely thank Domenico Giulini for a fruitful collaboration on an extensive paper devoted to "Einstein's Impact on the Physics of the Twentieth Century", to appear in "Studies in History and Philosophy of Modern Physics". Many thanks go to Frank Lehner for all his technical support, and to Allen Clark for his kind hospitality.

References

1. Bell, J.S. (1964). On the Einstein-Podolsky-Rosen Paradox. *Physics*, 1, 195-200.
2. Bell, J.S. (1987). *Speakable and Unsayable in Quantum Mechanics* (Cambridge Univ. Press, Cambridge).
3. Born, M. (2005). *The Born-Einstein Letters 1916-1955* (Macmillan).
4. CPAE, *The Collected Papers of Albert Einstein*, Vols. 1-9 (Princeton University Press, 1987). See also: [<http://www.einstein.caltech.edu/>].
5. Einstein, A., Podolsky, B., and Rosen, N. (1935). Can quantum-mechanical description of physical reality be considered complete? *Phys. Rev.*, 47, 777-780.
6. Frisch, R. (1933) Experimenteller Nachweis des Einsteinschen Strahlungsrückstoßes. *Zeitschrift für Physik*, 86, 42-48.
7. Kochen, S. and Specker, E. (1967). The Problem of Hidden Variables in Quantum Mechanics. *Journal of Mathematics and Mechanics*, 17, 59-88.
8. Millikan, R.A. (1916). A direct photoelectric determination of Planck's 'h'. *Phys. Rev.*, 7, 355-388.
9. Pauli, W. (1949). Einstein's Contributions to Quantum Theory. In *Albert Einstein: Philosopher-Scientist*, edited by P. A. Schilpp (Illinois: The Library of Living Philosophers), p. 149.
10. Pauli, W. (1985-99). *Wissenschaftlicher Briefwechsel mit Bohr, Einstein, Heisenberg u.a.* Vol. 1-4, edited by K. von Meyenn (Springer-Verlag, New York).
11. Schrödinger, E. (1926). Über das Verhältnis der Heisenberg-Born-Jordan'schen Quantenmechanik zu der meinen. *Ann. Phys. (Leipzig)*, 79, 734-756.
12. Straumann, N. (2002). *Quantenmechanik* (Springer Verlag, Berlin), Epilog, pp. 371.

Posters

The construction of the ALICE hmpid rich detector

B.Belin* on behalf of the ALICE-HMPID group ^a

Bari-INFN and Politecnico, CERN, Moscow-INFN, *Istanbul-TUBITAK, Istanbul Technical University

Abstract. The ALICE-HMPID (High Momentum Particle Identification) detector consists of seven RICH (Ring Imaging Cherenkov) proximity focusing counters devoted to the identification of charged pions and kaons in the range $1 < p < 3$ GeV/c and protons and kaons in the range $2 < p < 5$ GeV/c. The total CsI photocathode area is 11m^2 . The production and the performance of the detector in test beam will be discussed.

1 Introduction

ALICE (A Large Ion Collider Experiment) is a heavy ion experiment designed to study especially Pb-Pb collisions at the CERN-LHC collider at a center of mass energy per nucleon pair of $\sqrt{s_{NN}}=5.5$ TeV and at a maximum luminosity of $10^{27}\text{ cm}^{-2}\text{s}^{-1}$ [1]. ALICE will detect and study both hadronic and leptonic signals over more than 3 orders of magnitude in momentum, from less than 100 MeV/c to 100 GeV/c. The HMPID detector consists of seven RICH counters $1.5\text{ m} \times 1.5\text{ m}$ each, located at a radial distance of 4.7 m from the interaction point and covering 5 % of the ALICE barrel acceptance. Each module contains six CsI photocathodes of size $0.64\text{ m} \times 0.4\text{ m}$, for a total active area of 11 m^2 . The HMPID identifies pions and kaons in the range $1 < p < 3$ GeV/c and protons and kaons in the range $2 < p < 5$ GeV/c [2].

2 Detector

Each RICH counter has a 15 mm thick C_6F_{14} (perfluorohexane) liquid radiator circulated in vessels having 5 mm fused silica windows nearly transparent to the Cherenkov radiation. The C_6F_{14} refractive index n is 1.2989 at a wavelength of 175 nm. Each module has a total volume of 200 L and can be flushed up to 100 L/h with Ar or CH_4 during stand by or operation, respectively.

The readout of the HMPID modules is based on 2 chips, GASSIPLEX and DILOGIC. The GASSIPLEX chip is a 16 channel charge sensitive pre-amplifier and shaper while the DILOGIC chip is a digital processor. Detailed description of the ALICE HMPID RICH can be found in [3] - [4]. Each module is equipped with three radiator vessels of $1330\text{ mm} \times 413\text{ mm} \times 24\text{ mm}$ made of NEO-CERAM, a transparent ceramic having thermal coefficient very close to the fused silica plates used as UV-transparent

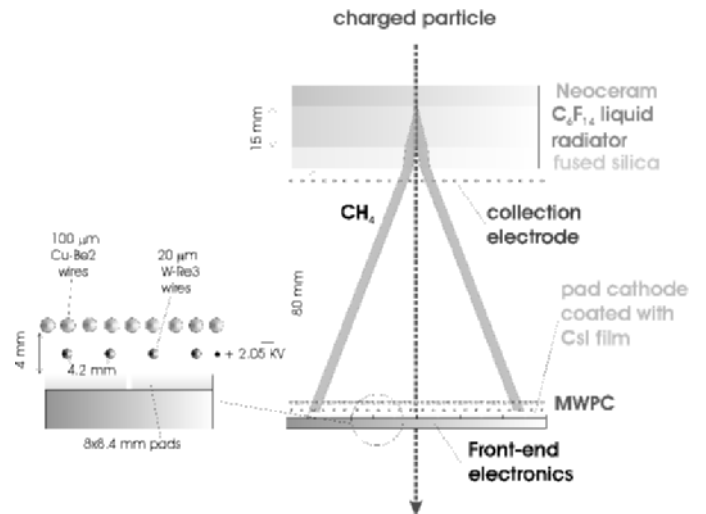


Fig. 1. Schematic cross-section of the HMPID RICH detector.

windows (Fig.1). The photodetector is a Multi Wire Proportional Chamber (MWPC) consisting of a stack of four Al frames of $1.5\text{ m} \times 1.5\text{ m}$ each, holding the different wire planes. It is closed on one side by the radiator panel support and on the other side by the CsI PCs. Viton O-rings are inserted between the frames to make a gas-tight vessel still dismountable. The gap between the anode wires, of $20\text{ }\mu\text{m}$ diameter, gold plated W-Re 3%, and the PC is 2 mm. They are tensioned at 47 g, about 70 % of the elastic limit, and soldered manually on the anode printed circuit boards with a pitch of 4.2 mm, using positioning marks resulting in a $50\text{ }\mu\text{m}$ accuracy. The second cathode plane is located at 2.45 mm from the anode plane and obtained by stretching $100\text{ }\mu\text{m}$ gold plated Cu-Be wires, with a pitch of 2.1 mm, at a tension of 210 g. The cathode wire plane is with the pre-deformation system and a detail of the comb structure used to hold the crimping pins in order to obtain minimum deviation among the wires. The final deformation, produced by the total wire tension of 140 g, has been estimated and is applied to the frame

^a Present address: CERN-ALICE Geneva 23 1211 CH - Switzerland

prior to wire fixation to ensure the uniformity of the wire tension. Finally, the collection electrode located next to the radiator consists of 100 μm gold plated Cu-Be wires stretched at a tension of 55 g with a pitch of 5 mm.

3 Quality Control

During the assembly process a full set of quality control checks are performed, including metrology, wire tension measurements, leak rate measurements, HV tests under CO_2 and gain mapping with a Sr^{90} source under CH_4 .

Tension measurements of cathode wires were performed measuring the wire frequency f which is related to the tension T , wire length L and mass per unit length σ according to the following relationship [5].

$$T = 4L^2 f^2 \sigma \quad (1)$$

Tension measurements of anode wires were performed using the C.A.E.N. Mod. SY502 Wire Stretch Meter. Acoustic excitation of the wire vibration and resonance detection method were used for the measurements of cathode wires (Fig.2).

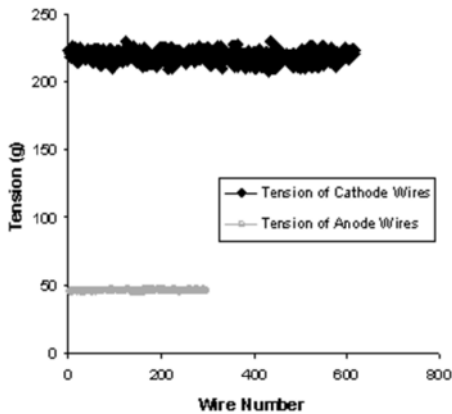


Fig. 2. Tension graph of anode and cathode wires.

The detector has been tested for gas tightness by monitoring the pressure drop inside the modules kept stagnant, i.e. after stopping the gas flow. The measurement was carried out in a room with temperature control after stabilization of the temperature of the module under test. The atmospheric pressure was also monitored and recorded. The leak rate measurements of the modules was found to be 0.6 cc/min, fully complying with the safety regulation (Fig.3).

4 CsI Photocathode

The CsI QE is affected by the choice of the substrate and its surface quality at microscopic level, as well as by the

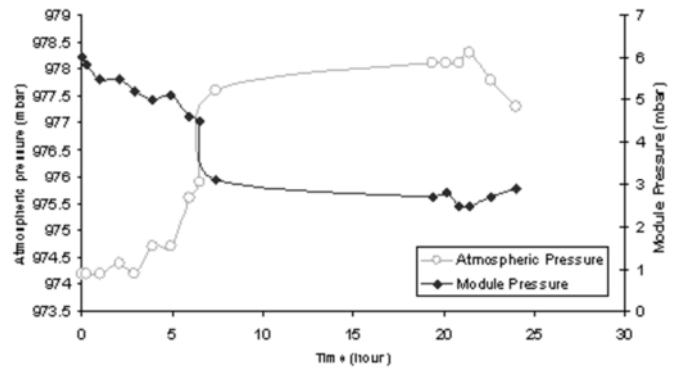


Fig. 3. Pressure changing in Module 5 during gas leak rate measurement

CsI deposition. The final PC processing, improved by several new tests on substrate types, preparation, heat conditioning, and use of a transfer system designed to avoid exposure to air, is in use since 2000, when the first pre-series photo-cathode was produced.

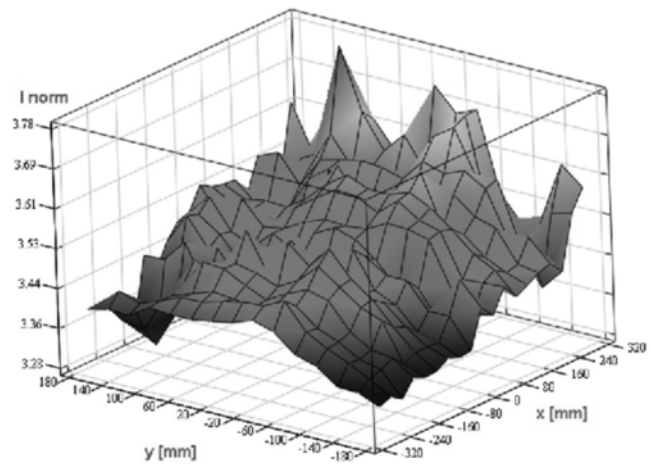


Fig. 4. The normalized photocurrent response mapping of PC45 characterized by an average of 3.5 over the full sensitive area.

Double layer printed circuit boards (PCBs) with blind holes have been adopted to provide leak-tight connections of the cathode pads to the FEE connectors on the back of the PC. The PCBs are specially prepared to act as substrate for the CsI layer. The Cu pads, accurately polished by chemical and mechanical treatments are covered with a 7 μm layer of Ni and a 0.5 μm of Au. The first layer acts as a barrier preventing the reaction of CsI with Cu, the second was found to be suitable for CsI coating. A pad cathode panel composed of two such PCBs is glued onto a stiff Al frame (4 cm thick) using a vacuum table to achieve planarity better than 50 μm .

In order to characterize the PCs during the mass production a VUV scanner system has been built and installed in a large vessel attached to the evaporation plant. After CsI deposition a PC is transferred under vacuum

to the VUV scanner system, where the photocurrent induced by a collimated light beam from a deuterium lamp with MgF_2 window is recorded over the full photosensitive area. Fig. 4 shows the photocurrent mapping for PC45, normalized to the photocurrent of a reference PMT with a semi-transparent CsI photocathode. The average ratio is 3.5, corresponding to more than 20 photons detected for $\beta=1$ particles. The spread is 10% over the full area as required.

5 Test Beam

Module 1 has been equipped with pre-series CsI PCs and tested in 2003. Module 2,3 and 4 have been tested during the summer of 2004 in CERN/SPS-X5 area with 120 GeV π^- beam at different intensities. A Cherenkov event is characterised by the so called resolved clusters, representing the best estimation of the detected Cherenkov photons. The signal corresponding to a single photoelectron

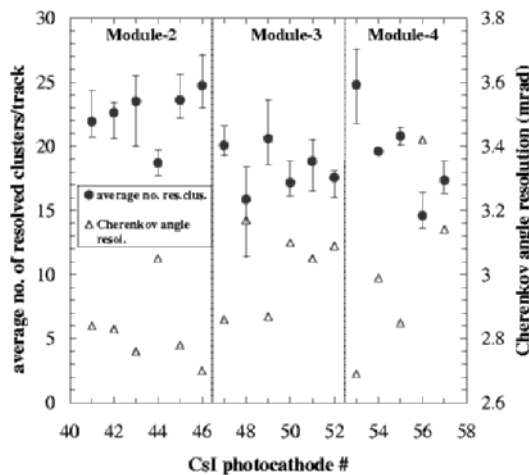


Fig. 5. The average number of resolved clusters and the corresponding Cherenkov angle resolution for each PC produced so far @ 2050V.

can be induced on one pad only or spread on a cluster of adjacent pads. Raw pad clusters can be generated by more than one photon due to generated overlapping. Therefore the raw clusters have to be split into smaller resolved clusters to measure correctly the amount and position of the detected Cherenkov photons [6].

The beam was applied in nine different positions of each photocathode. Fig.5. shows the summary of the PC performance. The error bars represent the maximum and minimum number of resolved clusters. Gain variations are about 5 % and PC response variations are about 10 % over the full area.

6 Conclusion

All the seven detector modules (MWPC + radiator vessels) have been completed and commissioned in laboratory and/or with test beam.

The mass production of the 42 photo-cathodes started in May 04 and 21 photo-cathodes have already been coated with CsI. All chips needed for the FEE, 10080 GASSI-PLEX and 3360 DILOGIC chips have been mounted on cards and tested. Two modules will be tested with cosmic rays before the installation in the ALICE cavern in April 2006.

References

1. ALICE Collaboration, *Physics Performance Report 1*, CERN/LHCC 2003-049.
2. ALICE Collaboration, *HMPID TDR*, CERN/LHCC 98-19.
3. F. Puiz et al, Nucl.Instr. and Meth.**A433**,(1999)222.
4. F. Puiz et al, Nucl.Instr. and Meth.**A433**,(1999)178.
5. Y. Bonushkin, CMS TN (1996).
6. A. Di Mauro et al, IEEE Transactions on Nuclear Science **Vol.52**,No.4,(2005)972-979.

CDF spectroscopy results

Mario Campanelli¹

Univeristy of Geneva, Switzerland

Abstract. We present results for measurements of mass and widths of hadrons containing heavy flavours, possible with the new CDF hadronic trigger

1 Introduction

For Tevatron Run II, the CDF detector received several upgrades. The most relevant to heavy flavour physics is the development of a system, the Silicon Vertex Tracker (SVT) [1] allowing the determination of track quantities at trigger level. The five track helix parameters are available at level 2, including the impact parameter, with a resolution of about 50 μm , of which about 30 are due to the beam spread. This allows building trigger paths requiring the presence of one or more tracks with a large impact parameter, largely enhancing the heavy flavor content of the samples collected this way. We'll present results on several channels collected from SVT samples.

2 $D_s^+ D^+$ mass difference

The first CDF II paper used only 11.6pb^{-1} of data to get a precision measurement of the mass difference between the D_s and the D^+ , both decaying into $\Phi\pi^+$, followed by the decay $\Phi^- \rightarrow K^+ K^-$. This measurement was possible thanks to a precision calibration of the tracker material used to refit tracks, made possible checking the stability of the mass of known resonances as a function of p_T . The final result is $m(D_s) - m(D^+) = 99.41 \pm 0.38 \pm 0.21 \text{ MeV}/c^2$ [2].

3 Masses of B hadrons

Large dataset collected with SVT-based and μ -based triggers allowed world-class measurements for light and heavy states. Some examples are the masses of B^0 and B^+ , measured in the $J/\Psi K^0$ and $J/\Psi K^+$ decay modes to be $5279.63 \pm 0.53 \pm 0.33$ and $5279.10 \pm 0.41 \pm 0.36 \text{ MeV}^2$, respectively, with precision similar or better than that of CLEO [3]. CDF is of course dominating the world average for the masses of the heavy states. B_s and A_b are measured respectively in the $J/\Psi \psi$ and $J/\Psi \Lambda$ decay modes and yield a mass of $m(B_s) = 5366 \pm 0.73 \pm 0.33 \text{ MeV}/c^2$ and $m(A_b) = 5619.7 \pm 1.2 \pm 1.2 \text{ MeV}/c^2$.

4 Mass and width of orbitally-excited charm states

$L=1$ states of the D^0 are mass degenerate in the heavy quark limit, but a calculable hyperfine splitting occurs between the four possible combinations of total and spin momentum. If we consider the heavy quark to be at rest, the total (angular plus spin) angular momentum of the light quark can be $1/2$ or $3/2$; the $j_q=3/2$ states can only decay via P-wave, so they have longer lifetime and a width comparable to this hyperfine splitting. We reconstructed the two narrow states D_1 and D_2 in the decay mode $D^{*+}\pi^-$, followed by $D^{*+} \rightarrow \pi + D^0$, $D^0 \rightarrow K\pi$, and only the D_2 state in the channel $D_2^* \rightarrow D^+\pi^-$, $D^+ \rightarrow K^-\pi^+\pi^+$, where the D_1 cannot decay due to parity conservation. The observed spectra in the two channels are shown in figures 1 and 2, and are fitted with a combination of narrow state, combinatorial background and possible contribution from the larger broad state. The measured values for masses and widths are $m(D_1) = 2421.7 \pm 0.7 \pm 0.6 \text{ MeV}/c^2$, $\Gamma(D_1) = 20.0 \pm 1.7 \pm 1.2 \text{ MeV}/c^2$, $m(D_2) = 2463.3 \pm 0.6 \pm 0.8 \text{ MeV}/c^2$, $\Gamma(D_2) = 49.2 \pm 2.3 \pm 1.3 \text{ MeV}/c^2$. This is the best world measurement for these quantities.

5 Observation of the X(3872)

The observation by Belle of a new state with invariant mass of $3872 \text{ MeV}/c^2$ in the channel $J/\Psi\pi^+\pi^-$ pushed CDF to look for the first confirmation of this state. The first paper [4] found 730 candidates, for a mass of $m(X) = 3871.3 \pm 0.7 \pm 0.4 \text{ MeV}/c^2$. It was also found that requiring an invariant mass of the dips larger than $500 \text{ MeV}/c^2$ was reducing the background leaving the signal almost unchanged. The two main hypotheses on this state is that it can be a 3D_2 charmonium state or a $D^0 - D^{0*}$ molecule. To distinguish the two cases, the lifetime of this state has been studied, using a likelihood as well as a background subtraction method. The two methods give compatible results, and the likelihood lifetime is $\lambda(X) = 431 \pm 109 \mu\text{m}$; also the fraction of X coming from B decays is measured,

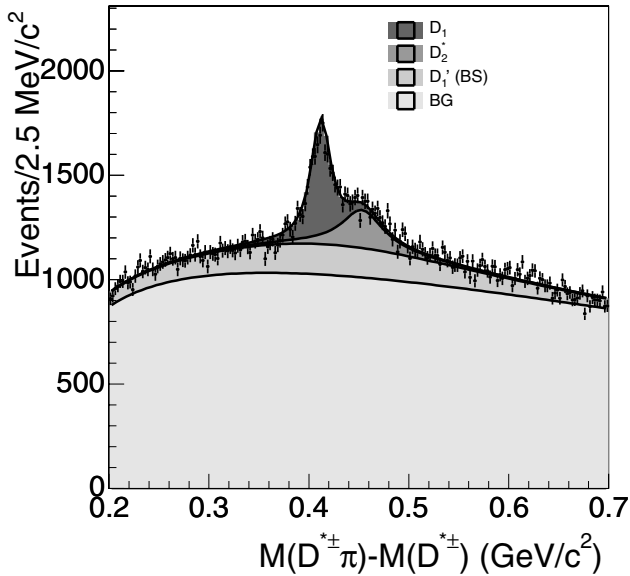


Fig. 1. Invariant mass of the $D^{*+}\pi^-$ final state

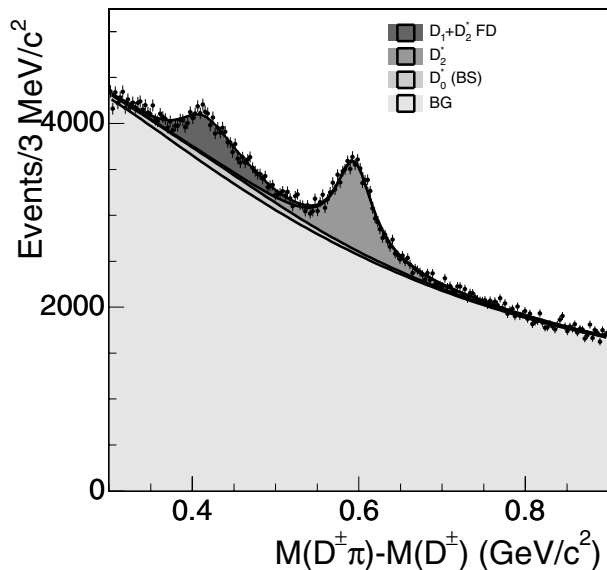


Fig. 2. Invariant mass of the $D^+\pi^-$ final state

and it turned out to be $16.1 \pm 4.9 \pm 2.0\%$, similar to that of the $\Psi(2S)$ state. At this stage both interpretations are still possible.

6 Study of the helicity of the X(3872)

To help giving hints to the nature of this state, the mass spectrum of the $\pi\pi$ system is studied, and compared with spin models for the various charmonium states. In practice, the $J/\Psi\pi\pi$ spectrum is fitted for various windows of the $\pi^+\pi^-$ mass, and the X production as a function of

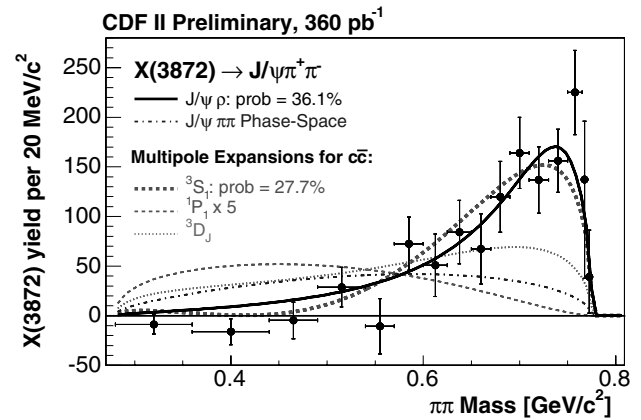


Fig. 3. Dipion mass spectrum for X(3872)

$M_{\pi\pi}$ is measured (figure 3). We see that most of the models, including the 3D_2 , fail to describe the data, that seem to support the hypothesis of a decay proceeding through $X \rightarrow J/\Psi\rho^0$, even if other mechanisms like virtual couplings to $D^0 - D^{*0}$ for charmonium are still possible.

7 Conclusions

We presented a review of some spectroscopic measurements performed with the upgraded CDF detector. These measurements have been performed with 200 pb^{-1} or less, so there is large room for improvement with the data already collected by CDF.

References

1. W.Ashmanskas *et al.* Nucl. Instrum. Meth., **A 447** 218 (2000).
2. D. Acosta *et al.*, The CDF Collaboration, Phys. Rev. D **68**, 072004 (2003)
3. D. Acosta *et al.*, The CDF Collaboration, submitted to PRL, hep-ex/0508022
4. D. Acosta *et al.*, The CDF Collaboration, Phys. Rev. Lett. **93**, 072001 (2004)

Effective K-factors: a method to include higher order QCD corrections in parton shower Monte Carlos: the example of $H \rightarrow WW^* \rightarrow 2\ell 2\nu$

Giovanna Davatz

Institute for Particle Physics, ETH Zurich, Switzerland

Abstract.

In the last years, a large effort has gone into accurate higher order (HO) calculations of the Higgs production and various background cross sections. Many reactions are now known to next-to-leading order (NLO) accuracy. For the dominant Higgs production mechanism, the gluon-gluon fusion $gg \rightarrow H$, even the next-to-next-to leading order (NNLO) calculations have been performed [1]. In this production channel, higher order QCD corrections were found to increase the leading order (LO) cross section by a factor of more than 2. Most simulations for the LHC are based on LO parton shower Monte Carlos (e.g. PYTHIA [2], HERWIG [3]), which do not include these higher order QCD corrections. In order to get more accurate simulations, it is important to take such contributions into account. A simple and effective method to include most up-to-date higher order QCD corrections in parton shower Monte Carlos is presented here. More details can be obtained from Ref. [6].

The simplest method to include HO QCD corrections is to scale the LO results with the so-called inclusive K-factor, which is defined as the ratio of $\sigma(\text{higher order})/\sigma(\text{leading order})$. If a signature is not sensitive to jet activities, this should lead to reasonable results (e.g. in the decay $H \rightarrow ZZ \rightarrow 4\ell$ [4]). However, if event kinematics have to be exploited in order to separate signal from the background, this approach is not sufficient.

A typical example is the Higgs search in the mass range between 155 and 180 GeV, where $H \rightarrow WW \rightarrow 2\ell$ is expected to be the main discovery channel at LHC [5]. For this channel, a jet veto is required in order to remove $t\bar{t}$ background¹. The Higgs is balanced by the jets, therefore, if a jet veto is applied, only the events with low p_T Higgs remain.

If one compares the p_T Higgs spectrum from PYTHIA and NNLO+NNLL resummed calculation obtained from M.Grazzini et al [7], one can see that PYTHIA is much softer than the HO spectrum and differs from the perturbative

calculation over the whole p_T Higgs range (Figure 1). The ratio of the two is defined as the p_T -dependent K-factor

$$K(p_T) = \left(\frac{d\sigma_{\text{NNLO}}(p_T)}{dp_T} \right) / \left(\frac{d\sigma_{\text{PYTHIA-LO}}(p_T)}{dp_T} \right). \quad (1)$$

PYTHIA as a LO parton shower MC cannot produce the hard spectrum correctly, thus the p_T -dependent K-factors are very large at very high p_T . However, as the signal selection in the $H \rightarrow WW \rightarrow 2\ell 2\nu$ channel rejects those high p_T events, such high K-factors have not to be taken into account. Therefore, it is not accurate to apply an inclusive K-factor. So far, no rapidity spectrum for the Higgs in NNLO has been available, therefore, the effective K-factor was only calculated as a function of the transverse momentum of the Higgs. However, as the kinematic cuts favours a central Higgs, where the rapidity distribution is flat, this approach should lead to a reasonable result.

In Figure 1, also the case is shown where PYTHIA is reweighted with an inclusive K-factor. The shapes are clearly different.

The efficiency after all signal selection cuts are applied and for different jet veto cuts is shown in Figure 2 as a function of the p_T of the Higgs. Signal events with large p_T Higgs are almost always rejected with the proposed criteria, and the efficiency drops quickly as p_T Higgs reaches the value of the jet veto.

The effective p_T -dependent K-factors, which take the cuts in account, are defined in the following way:

$$K_{eff}(p_T) = \left(\frac{d\sigma_{\text{NNLO}}(p_T) \times d\epsilon(p_T)}{d^2p_T} \right) / \left(\frac{d\sigma_{\text{PYTHIA-LO}}(p_T) \times d\epsilon(p_T)}{d^2p_T} \right). \quad (2)$$

Each PYTHIA event has to be reweighted with its corresponding effective K-factor, depending on its p_T Higgs. A similar procedure was applied for the main background, the continuum production of WW pairs $q\bar{q} \rightarrow WW$. Here, the p_T Higgs spectrum in NLO+NLL is used to reweight

¹ In addition, the other cuts exploit the spin correlation between the W bosons and the resulting transverse momentum (p_T) spectra of the charged leptons.

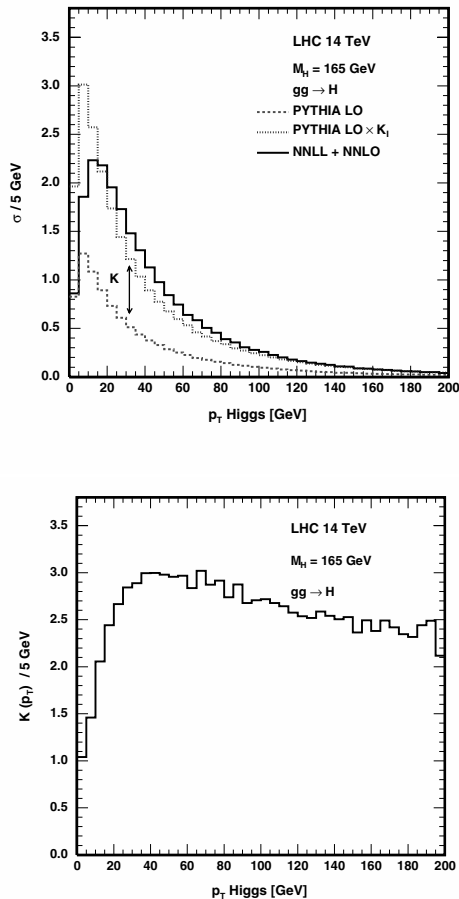


Fig. 1. Cross section for PYTHIA and NNLO+NNLL as a function of p_T Higgs. Also PYTHIA multiplied with an inclusive K-factor is shown for comparison. On the right, the ratio of the PYTHIA and NNLO+NNLL cross sections is shown, which is the p_T -dependent K-factor.

the leading order spectrum. To take the dependence of the mass of the WW system into account, three different mass regions were investigated: $M_{WW} = 170 \pm 5$ GeV, 200 ± 5 GeV and 250 ± 5 GeV. As most of the relevant continuous background comes from events with an invariant mass around threshold and relatively low p_T , we take as an approximate weighting factor for the WW events the one obtained for the mass range of 170 ± 5 GeV, which will slightly overestimate this background.

The total effective experimental K-factor can be computed from the sum of the ratios of the accepted HO cross sections over LO cross sections over all p_T bins. For a Higgs mass of 165 GeV, the inclusive K-factor without any selection cuts is found to be 2.37. The total effective K-factor is 2.04, which is about 15 % smaller than the inclusive K-factor.

Similar numbers are obtained for other Higgs masses (140 and 180 GeV). The estimated effective K-factor of the WW background, integrated over the whole WW mass spectrum, is found to be 1.36. For a Higgs mass of 165

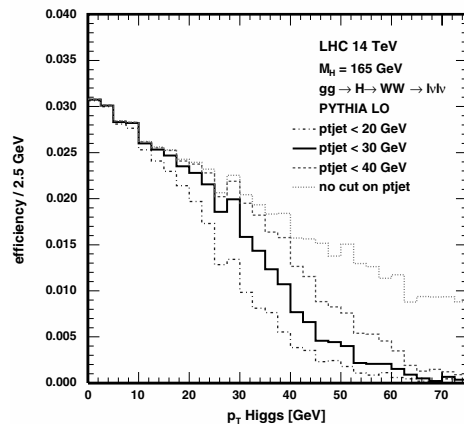


Fig. 2. Signal selection efficiency as a function of the Higgs transverse momentum, for a Higgs mass of 165 GeV and three different jet veto cuts. For completeness, the efficiency curve for all cuts, excluding the jet veto, is also shown.

GeV, a signal to background ratio of almost 2 can be achieved. The Higgs discovery potential for the channel $gg \rightarrow H \rightarrow WW \rightarrow 2\ell$ is found to be significantly increased by including higher order QCD corrections. Signals with a statistical significance of five standard deviations should be observable for a SM Higgs boson with masses between 140 and 180 GeV after the first few fb^{-1} of integrated luminosity. This reweighting technique can be applied to other final states and the results should be particularly accurate for hard scattering processes with little additional jet activity.

References

1. S. Catani, D. de Florian and M. Grazzini, JHEP **0105** (2001) 025; R. V. Harlander and W. B. Kilgore, Phys. Rev. D **64** (2001) 013015; Phys. Rev. Lett. **88** (2002) 201801; C. Anastasiou and K. Melnikov, Nucl. Phys. B **646** (2002) 220; Phys. Rev. Lett. **93** (2004) 262002; V. Ravindran, J. Smith and W. L. van Neerven, Nucl. Phys. B **665** (2003) 325.
2. T. Sjostrand, L. Lonnblad, S. Mrenna and P. Skands, “PYTHIA 6.3: Physics and manual”, [arXiv:hep-ph/0308153].
3. G. Corcella *et al.*, “HERWIG 6.5 release note”, [arXiv:hep-ph/0210213].
4. K. Cranmer, B. Mellado, W. Quayle and S. L. Wu, arXiv:hep-ph/0307242.
5. M. Dittmar and H. K. Dreiner, Phys. Rev. D **55** (1997) 167 [arXiv:hep-ph/9608317] and CMS NOTE-1997/083.
6. G. Davatz, G. Dissertori, M. Dittmar, M. Grazzini and F. Pauss, “Effective K-factors for $g g \rightarrow H \rightarrow W W \rightarrow l \nu l \nu$ at the LHC”, JHEP **0405** (2004) 009 [arXiv:hep-ph/0402218].
7. G. Bozzi, S. Catani, D. de Florian and M. Grazzini, Phys. Lett. B **569** (2003) 65.

Construction and Performance of the ATLAS Semi-Conductor Tracker Barrels

Bilge M. Demirköz ^a

Oxford University, e-mail: demirkoz@physics.ox.ac.uk

Abstract. ATLAS is a multi-purpose particle detector for the LHC and will detect proton collisions with a center of mass energy of 14TeV. Part of the central inner detector, the Semi-Conductor Tracker (SCT) is assembled and tested. The barrel SCT is composed of 4 layers of silicon strip modules with two sensor layers with $80\mu\text{m}$ pitch. The high granularity and low noise occupancy ($< 5 \times 10^{-4}$) of the silicon detectors will enable ATLAS to have good tracking and vertex resolution and so a high physics reach.

1 Introduction

The semiconductor tracker (SCT) is of vital importance to ATLAS since it provides good tracking and momentum resolution up to a pseudo-rapidity η of 2.5 extending from a radius of 0.3m to 0.52m. The SCT has a central barrel system and two end-cap systems on each side. The modules have been mounted on the carbon fibre support structures, called barrels, at Oxford University. The end-caps are being assembled at Liverpool University and at NIKHEF and consist of 9 disks each. In total, there are 4088 silicon detector modules in the SCT, with 6 million channels, each providing a 1-bit binary signal at each bunch-crossing every 25 nanoseconds.

2 SCT modules and readout

An SCT module comprises of four single-sided p-on-n silicon detectors. Each silicon detector is $6.36 \times 6.40\text{cm}^2$ and has 768 readout strips, each of $80\mu\text{m}$ pitch. For each side of an SCT module, two of these silicon detectors are wire-bonded together to give an active strip length of approximately 12cm, [1]. The two sides of a module are glued together with a small (40mrad) stereo angle to provide positional information in two dimensions. Information about module production and performance tests performed during module production and reception testing can be found in [2,3]. The spatial resolution in the bending direction is $16\mu\text{m}$ and in the non-bending direction is $180\mu\text{m}$.

The readout electronics of the module is mounted on a copper-kapton hybrid above the detectors. There are 12 ABCD3TA ASICs [4] which provide the binary readout of 128 detector channels each. The readout chain consists of a front-end amplifier and shaper and then a programmable threshold discriminator, followed by a binary pipeline. There is a programmable 8-bit DAC for the

threshold adjustments across each chip and a 4-bit DAC for inter-chip variations in response. The pipeline is 132 cells deep, corresponding to the time it takes for a Level-1 trigger to arrive. If there was a trigger, the pipeline output is transferred to a de-randomizing buffer of 8 events deep for readout. The chips readout serially through the master chip, the VDC(The VCSEL Driver Chip) [5] and the VCSEL (Vertical Cavity Surface Emitting Laser).

The off detector readout components are housed in what is known as a ROD crate. In this crate, there are ROD (Readout Drivers) and BOC (Back of Crate) cards which are responsible for the control and the readout of the modules as well as a TIM (Timing Interface Module), responsible for relaying timing and trigger information to the sub-system. The clock (at 40.08 MHz) and command signals from a BOC are sent to a module encoded in the bi-phase of one optical signal from the DORIC chip, [6]. In return, the BOC receives one optical data stream from each side of the module.

3 SCT Barrel Construction and testing

The four SCT barrels are numbered from 3 to 6, since the zeroth, first and second layers of the tracker are pixel barrels. All barrels have been tested at Oxford and have been shipped to CERN. The completed Barrel 6 is shown in Fig. 1.

There are 12 modules on each row, also called LMT since each row is serviced by a LMT (Low Mass Tape) from each end. To ensure hermetic coverage in $r\phi$ and z , the modules are staggered in upper and lower positions and provide overlap. The modules are placed on the barrel by a purpose built robot [7] in a clean room. Testing of the modules generally takes place after a whole cooling loop worth of modules has been placed on a barrel, which is 4 rows. The testing is performed using an online software developed by the SCT which has the tasks of configuring, calibrating and controlling the modules and analyzing the

^a for the ATLAS SCT Collaboration

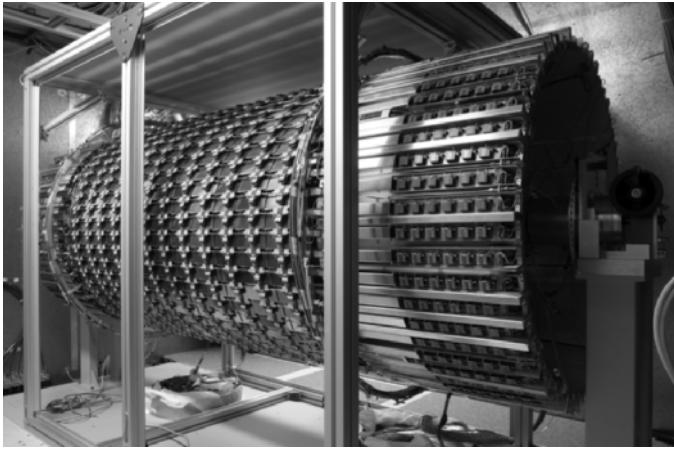


Fig. 1. Barrel 6 completed and ready to be sent to CERN.

data. This online software, known as SctRodDaq runs in a very distributed environment, [8].

A long testing sequence is employed to ensure that the modules perform according to specifications during assembly testing and final cold testing. Here is a brief list of some of the digital and analog tests and their purpose.

Counter Error Test: The ASIC, ABCD3T chip has 4 bits of Level1 trigger counter and 8 bits of Bunch Crossing Counter. The purpose of this test is to check that these bits in the data headers read from the master chips on a module are correct. If there is a counter error, it will not be possible to verify the synchronization with the rest of the detector and therefore the module is replaced. The test sends 64 consecutive triggers to the module and reads them back. Only the first 64 bits of the reply are plotted. The analysis checks that the counters are non-zero and compares the counters from the two links of a module. It identifies and reports the erroneous header bit if there is a defect.

Three Point Gain Test: For each point or injected charge, the occupancy is measured as the threshold is scanned. The test is performed at 0.5, 1 and 1.5fC. In each case, a complementary error function is fitted to the data. For each injected charge, the threshold at which occupancy is 50% corresponds to the median of the injected charge distribution. The variance is a measure of the output noise (in mV). The gain of each channels is calculated from a linear fit to the three scan points. The output noise at 1fC is divided by the gain to determine the input noise (in fC or ENC). Also, the uniformity of trimming is checked by looking at variances in gain and offset.

Noise Occupancy Test: The purpose of this test is to measure the noise occupancy at different thresholds. A linear fit to a plot of $\log(\text{noise occupancy})$ vs threshold^2 , allows for the estimation of Gaussian noise of each module. A deviation from this linear behavior, particularly at high thresholds is indicative of non-Gaussian behavior such as presence of common mode noise. The occupancy at a nominal 1fC threshold as determined for $> 99\%$ efficiency from testbeam [9] is typically $< 10^{-4}$.

Double Trigger Noise Test: The purpose of this test is to identify problematic electrical and optical pickup during the readout of the module. The VCSELS operate at 850nm and silicon has a good quantum efficiency at this wavelength. The VCSELS operate synchronously with the readout by definition. Also they output 1mW of optical power and even a small percentage of leakage is detectable. The Level1 buffer depth on an ABCD chip is 132 deep so that the readout of an event on the module always happens 132 bunch-crossings after the event was taken. The test is performed in the following sequence: sending one trigger, waiting for “n” bunch-crossings, sending another trigger. The number “n” is chosen to be close to the Level1 buffer depth as to identify pick-up from the readout of the first trigger, in the readout by the second trigger. In this test, “n” is varied between 120 and 160 and a defect is reported if the peak occupancy is 5 sigma away from the baseline or if the peak occupancy is higher than 1×10^{-4} . Two modules on Barrel 3 were discovered to show lightleak related problems. A careful visual inspection of the other barrels before assembly showed that there were some optopackages which were not fully covered. These optopackages are now fully sealed. On other barrels no significant light leaks were found, however there are a few minor electrical pickup candidates.

4 Conclusions

All four SCT barrels have been assembled and tested. 99.7% of the 3.2×10^6 channels in the barrel system are working. The noise occupancy of at the nominal 1fC threshold is typically $< 10^{-4}$ and has not changed significantly since testing at SCT module assembly sites. We acknowledge financial help from all the funding agencies contributing to the SCT.

References

1. T. Kondo et al., NIM A 485:27-42, 2002
2. D. Robinson et al., NIM A 485:84-88, 2002
3. P. W. Phillips, System performance of ATLAS SCT detector modules, 8th Workshop on Electronics for LHC Experiments, France, 9-13 Sep 2002
4. Design and Performance of the ABCD3T ASIC for the readout of silicon strip detectors in the ATLAS semiconductor tracker, in preparation
5. D. J. White et al., NIM A 457:369, 2001
6. M. L. Chu et al., NIM A 530:293-310, 2004
7. S. Terada et al., NIM A 541:144-149, 2005
8. A. Barr, Calibrating the ATLAS Semiconductor Tracker Front End Electronics, Proceedings of IEEE NSS, 2004
9. F. Campabadal et al., NIM A 538:384-407, 2005

Charmless B decays at CDF

Mauro Donegà for the CDF collaboration^a

Département de Physique Nucléaire et Corpusculaire, Université de Genève.
Quai E. Ansermet 24 CH-1211 Genève 4.

Abstract. We report on the charmless B decays measurements performed on 180 pb⁻¹ of data collected with the CDF II detector at the Fermilab TeVatron collider. This paper will describe: the first observation of the decay mode $B_s \rightarrow K^+K^-$ and the measurement of the direct CP asymmetry in the $(\bar{B}_d) \rightarrow K^\pm\pi^\mp$ decay; the first evidence of the decay mode $B_s \rightarrow \phi\phi$ and the branching ratio and CP asymmetry for the $B^\pm \rightarrow \phi K^\pm$ decay.

1 Introduction

The Fermilab TeVatron collider is currently the only machine able to produce all species of b hadrons: both the B_d and the B_s mesons and all the b-baryons. The CDF II detector [1], thanks to its Silicon Vertex Trigger (SVT) is the only detector able to trigger on vertexes with two displaced tracks. This unique combination makes it possible to study several B decays and opens new windows in the understanding of the flavor dynamics of the SM. The principal characteristics of the detector used in the presented analysis, are related to the tracking and trigger systems. The tracks are reconstructed using the silicon detector and the central drift chamber. For the muons is also required the identification in the muons chambers. The online resolution of 35 μm on the impact parameter and the fast readout electronics are the key factors to allow the online pattern recognition of the SVT. The particle identification of the CDF II detector is based, for tracks with momenta above 2 GeV/c as required for the SVT, on the specific ionization (dE/dx) measured in the volume of the drift chamber.

2 $B_{d/s}^0 \rightarrow h^\pm h^\mp$

The long term goal of this analysis is to measure the time-dependent CP asymmetries in the flavor tagged samples $B_d \rightarrow \pi^+\pi^-$ and $B_s \rightarrow K^+K^-$. A strategy to measure the angles β and γ , based on these decays has been proposed by Fleisher [2].

The invariant mass spectrum of the two tracks sample is shown in Fig. 1. The clear peak in the distribution corresponds to the following decays: $B_d \rightarrow K^+\pi^-$, $B_s \rightarrow K^+K^-$, $B_d \rightarrow \pi^+\pi^-$, $B_s \rightarrow K^-\pi^+$.

The first steps performed on this sample are to disentangle the four signal contributions, to get to the relative

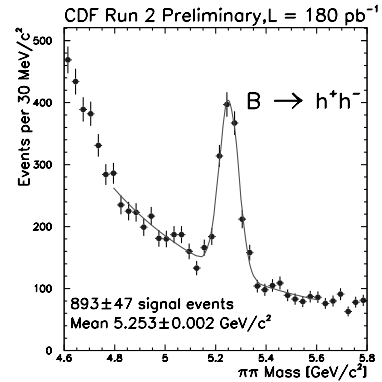


Fig. 1. Invariant mass for the $B_{d/s}^0 \rightarrow h^\pm h^\mp$ candidates.

branching ratios and then to measure the CP asymmetry for the $(\bar{B}_d) \rightarrow K^\pm\pi^\mp$. An analysis of the signals lifetime is ongoing and further in the future the flavor tagging will be added to tackle the time-dependent CP asymmetries. To separate the four channels it is possible to take advantage of their (little) difference in the kinematics and use the particle identification on the tracks couples to separate kaons from pions. Since none of the two is powerful enough to allow an event by event separation, the signals are analyzed through a maximum likelihood fit. The $B_{d/s}^0 \rightarrow h^\pm h^\mp$ modes are two body decays of the (spin 0) B meson. Kinematically the channels differ only for the B_d/B_s and kaon / pion mass difference. This tiny difference translates into an unbalance in the momenta of the boosted decay products. The tracks in CDF II are all reconstructed in the π mass hypothesis. Thus, to fully exploit this kinematics difference a new variable α has been defined as $(1-p_1/p_2) \cdot q_1$, where $p_1(p_2)$ is the modulus of the lower(higher) momentum of the track. In this way the $B_d \rightarrow \pi^+\pi^-$ will not show any dependence on α while the other channels, where one or both tracks have been re-

^a md@fnal.gov

constructed with the wrong mass assignment, will exhibit a distinctive dependence [3]. This allows to separate the $B_d \rightarrow K^+\pi^-$ and $B_s \rightarrow K^-\pi^+$ decays from the others, but not the $B_d \rightarrow \pi^+\pi^-$ and $B_s \rightarrow K^+K^-$ decays that have an identical α dependence. To distinguish the latter the dE/dx information has been included in the fit. With the actual data set it is possible for the first time to measure the $B_s \rightarrow K^+K^-$ branching ratio relative to $B_d \rightarrow K^+\pi^-$:

$$\frac{f_d BR(B_s \rightarrow K^+K^-)}{f_s BR(B_d \rightarrow K^+\pi^-)} = 0.50 \pm 0.08(stat.) \pm 0.07(syst.)$$

where f_s , f_d are the world averaged fragmentation fractions. Moreover it is possible to measure the direct CP asymmetry in the $(\bar{B}_d) \rightarrow K^\pm\pi^\mp$ decay:

$$\begin{aligned} A_{CP} &= \frac{N(\bar{B}_d \rightarrow K^-\pi^+) - N(B_d \rightarrow K^+\pi^-)}{N(\bar{B}_d \rightarrow K^-\pi^+) + N(B_d \rightarrow K^+\pi^-)} = \\ &= -0.04 \pm 0.08(stat.) \pm 0.01(syst.) \end{aligned}$$

3 $B_s \rightarrow VV$ decays

The peculiarity of $B_s \rightarrow VV$ decays resides in the presence of both CP-even and CP-odd components in the decay amplitudes, possibly leading to both the observation of CP violation and the measurement of the $\Delta\Gamma_s$. Recent measurements on decays mediated by $b \rightarrow s\bar{s}s$ amplitude show discrepancies with respect to the SM predictions [4], placing in the spotlight the presented decays: $B_s \rightarrow \phi\phi$ and $B^\pm \rightarrow \phi K^\pm$ ($\phi \rightarrow K^\pm K^\mp$) [5].

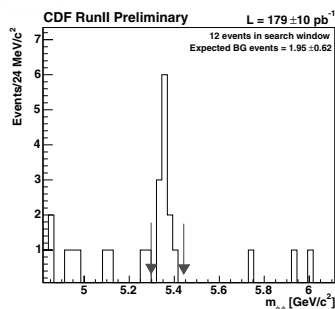


Fig. 2. Invariant mass for the $\phi\phi$ candidates

3.1 $B_s \rightarrow \phi\phi$

A blind analysis has been performed for the search of the $B_s \rightarrow \phi\phi$ decay. The selection cuts are optimized for pairs of tracks whose invariant mass is in a window around the ϕ mass. The two main sources of background are expected to be the combinatorial, studied on data using the sidebands, and the cross-feed of the $B_d \rightarrow \phi K^{0*}$ where the pion from the K^{0*} decay is misreconstructed as a kaon,

studied with MC. As shown in Fig. 2 after the cuts optimization 12 events have been found in the signal region with an expected background of 1.95 ± 0.63 , corresponding to a 4.8σ significance.

A sample of $B_s \rightarrow J/\psi\phi$ is then used as normalization to extract the relative branching ratio as reported in table 1.

3.2 $B^\pm \rightarrow \phi K^\pm$

The analysis of the signal yield and CP asymmetry defined as

$$A_{CP} = \frac{N(B^- \rightarrow \phi K^-) - N(B^+ \rightarrow \phi K^+)}{N(B^- \rightarrow \phi K^-) + N(B^+ \rightarrow \phi K^+)}$$

on the $B^\pm \rightarrow \phi K^\pm$ ($\phi \rightarrow K^+K^-$) sample have been performed through an extended maximum likelihood fit in the following variables: the three kaons invariant mass, the invariant mass of the ϕ candidate, the ϕ helicity and the kaon dE/dx . A combination of MC and sideband data have been used to model the signal and the different background components. A sample of $B^+ \rightarrow J/\psi K^+$ is then used as normalization to extract the relative branching ratio. The results of the analysis are reported in table 1.

4 Conclusion

All the presented analysis are already being updated with a better tracking and better dE/dx calibrations. At the time of the conference already twice the integrated luminosity is available for analysis, leading to more precise measurement and bringing to the CDF II reach new B_s decay modes such as $B_s \rightarrow K^{0*}\bar{K}^{0*}$ and $B_s \rightarrow \phi\rho$.

Table 1. Preliminary CDF II results for $B^+ \rightarrow \phi K^+ B_s \rightarrow \phi\phi$

	$B^+ \rightarrow \phi K^+$	$B_s \rightarrow \phi\phi$
Yield	$47.0 \pm 8.4 \pm 1.4$	$7.3 \pm 2.8 \pm 0.4$
BR $\cdot 10^5$	$0.76 \pm 0.13 \pm 0.06$	$1.4 \pm 0.6 \pm 0.6$
A_{CP}	-0.07 ± 0.17	$^{+0.03}_{-0.02}$

References

1. CDF Collaboration, FERMILAB-PUB-96/390-E(1996)
2. R. Fleisher, Phys. Lett. **B 459**, (1999) 306.
3. G. Punzi *Beijing 2004*, ICHEP 2004, vol. 2*, 925-929
4. Z. Ligeti, *Beijing 2004*, ICHEP 2004, vol. 1*, 49-62
5. D. Acosta *et al*, Phys.Rev.Lett. **95**, (2005) 031801

Standard Model Higgs Searches at ATLAS

Luis Roberto Flores Castillo, on behalf of the Higgs Working Group of the ATLAS collaboration
University of Wisconsin-Madison

Abstract. Some channels under study for the search of the Standard Model Higgs boson are briefly described. The combination of channels can provide ATLAS a 5σ significance with $30fb^{-1}$ of data.

e-mail: luis.flores.castillo@cern.ch

1 Introduction

The search for the Higgs boson is one of the main experimental goals at the LHC. In ATLAS, the existence of a Standard Model Higgs boson can be established for the full mass range of interest, from the LEP limit ($114.1 \text{ GeV}/c^2$) up to about 1 TeV, with over 5σ significance in $30fb^{-1}$ of data, as shown in figure 1.

At a center of mass energy of 14 TeV, the production cross-section for a SM Higgs boson is dominated by gluon-gluon fusion, followed by vector boson fusion (VBF). Searches can be performed regardless of production mechanism (as in $H \rightarrow \gamma\gamma$ or $H \rightarrow 4l$), or exploiting properties of the VBF topology ($H \rightarrow WW$, $H \rightarrow \tau\tau$). A brief description of both kinds of searches follows.

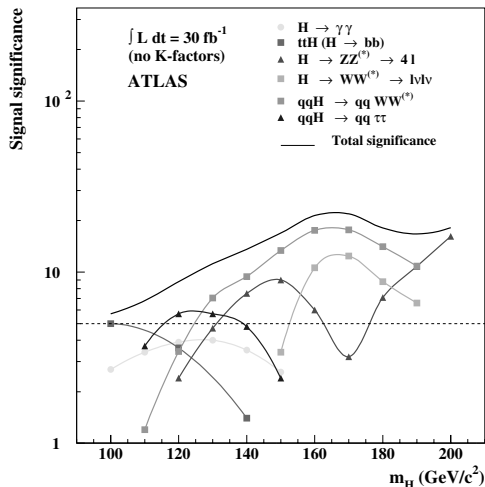


Fig. 1. Expected significance in ATLAS after $30fb^{-1}$, as a function of Higgs mass, for various channels.

2 Inclusive final states

2.1 $H \rightarrow \gamma\gamma$

Although only observable over a limited range of Higgs boson masses, this is a promising channel for $100 \text{ GeV} < m_H < 150 \text{ GeV}$. It requires an excellent performance of the EM calorimeter, since the mass resolution has to be of $O(1\%)$, if the signal is to be observed above the irreducible $\gamma\gamma$ continuum.

2.2 $H \rightarrow ZZ^{(*)} \rightarrow 4l$

This channel provides a clean signature for $m_H > 120 \text{ GeV}$. Its branching ratio, larger than that of the $\gamma\gamma$ channel, increases with m_H up to $m_H \sim 150 \text{ GeV}$ and has a dip at $150 \text{ GeV} < m_H < 180 \text{ GeV}$ due to the opening of the $H \rightarrow WW$ channel, but for higher masses ($m_H > 2m_Z$), the “golden channel,” with the Higgs decaying into two real Z bosons, opens up.

Signal reconstruction Three distinct final states can be reconstructed for this channel: $4e$, 2μ and $2e2\mu$. The mass resolution is expected to be around 1.5 GeV in all of them.

Reducible backgrounds Besides the irreducible QCD ZZ background, the main backgrounds for this channel are $t\bar{t}$ and $Zb\bar{b}$ production, which can be strongly reduced using lepton isolation and impact parameter cuts. Efficiency and rejection of reducible backgrounds have been studied for low and high luminosity conditions. Fig. 2 shows the rejection of $t\bar{t}$ (left) and $Zb\bar{b}$ (right) for $m_h = 130 \text{ GeV}$.

3 Vector Boson Fusion

The relative contribution of VBF with respect to the total production cross section depends on m_H ; it represents about 20% for $m_H < 2m_Z$ and becomes a higher fraction with increasing mass. However, some features of VBF can be used to suppress the large backgrounds.

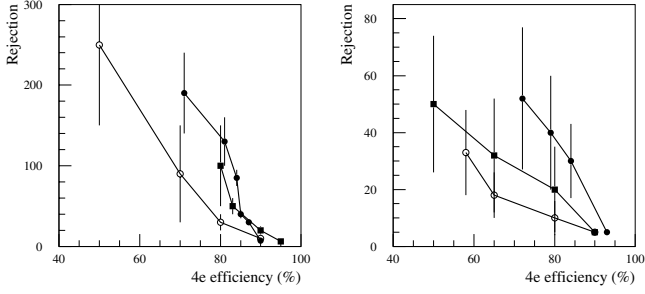


Fig. 2. Black circles: track isolation, low luminosity. Black squares: Calorimeter isolation, low luminosity. Open circles: Calorimeter isolation, high luminosity.

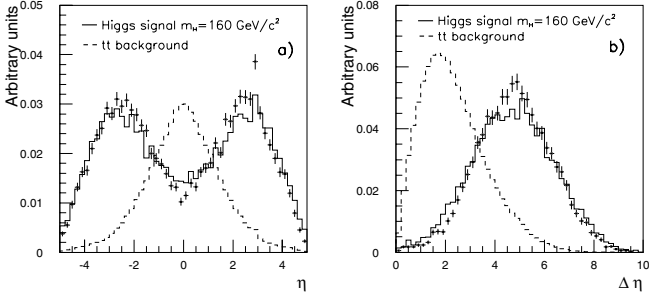


Fig. 3. Left: Pseudorapidity distribution of the tag jets for signal and for $t\bar{t}$ background with $m_H = 160$ GeV. Histograms: signal, parton level; dots: reconstructed signal. Dashed: background. Right: η separation between tag jets.

3.0.1 Signal selection

From the topology of the VBF production process, it is expected that the two tag jets are reconstructed with a sizeable P_T in opposite hemispheres and have a large separation in pseudorapidity. Consequently, events are rejected if at least one jet with a transverse momentum above 20 GeV/ c is found in the η range between the tag jets, or if $|\Delta\eta|$ between the tag jets is too small.

3.1 $H \rightarrow WW$

Daughter W bosons of the scalar H have opposite spins. The resulting lepton and antilepton tend to be emitted in the same direction, so their angular separation $\Delta\phi_{ll}$ can help distinguish signal from backgrounds. Also, in the Higgs' rest frame, the neutrino system is emitted opposite to the dilepton system; as a result, the invariant mass of the visible leptons, M_{ll} , can be required to be below $\sim m_H/2$. The distributions for both $\Delta\phi_{ll}$ and M_{ll} are shown in fig. 4.

After all cuts have been applied, most background events lie in the same region of transverse mass as the signal. An estimation of the $t\bar{t}$ background should be possible from $t\bar{t}$ events. Also, varying the selection cuts, as shown in fig. 5, can allow the background to extend to higher M_T values. This high- M_T region can be used to estimate the background below the signal peak.

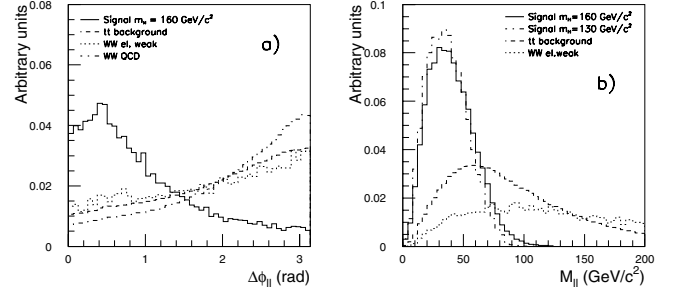


Fig. 4. M_T distribution.

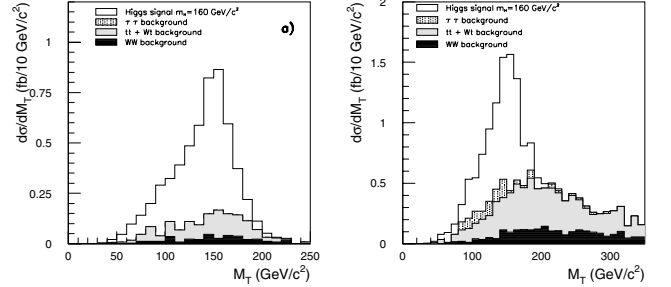


Fig. 5. M_T distribution.

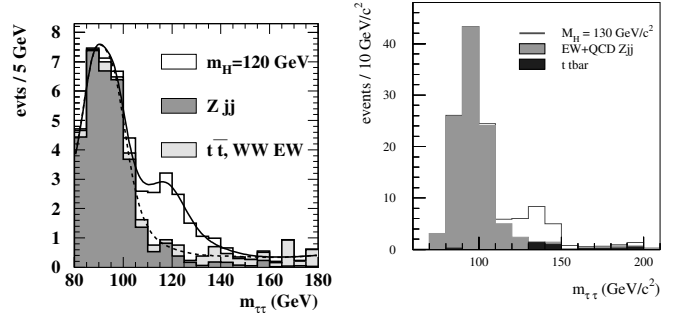


Fig. 6. $H \rightarrow \tau\tau$ reconstruction.

3.2 $H \rightarrow \tau\tau$

Due to the high p_T of H and Z bosons, the τ decay products are nearly collinear in the laboratory frame. Assuming collinearity, the fractions $x_{\tau 1}$, $x_{\tau 2}$ of the tau energy carried by each lepton or hadronic tau system can be found using the missing transverse momentum vector; from them, the Higgs mass can be reconstructed. Fig. 6 shows the reconstructed Higgs mass in the $e\mu$ channel (left plot) and in the lepton-hadron channel (right plot).

4 References

All the material presented can be found in

1. The ATLAS Collaboration, *Detector and Physics Performance Technical Design Report*, CERN/LHC/99-14 (1999),
2. Asai, S. *et.al.* ATL-PHYS-2003-005 (2003)

And references therein.

The LHCb trigger and readout

Federica Legger and Thomas Schietinger

Laboratoire de Physique des Hautes Energies (LPHE), Ecole Polytechnique Fédérale de Lausanne (EPFL)

Abstract. We give a brief overview of the LHCb readout scheme and trigger strategy. The latter is based on three levels designed to reduce the event rate from 40 MHz to 2 kHz.

1 Introduction

The LHCb detector is a single arm spectrometer designed to exploit the large $b\bar{b}$ cross section at the LHC, in order to make precision measurements of CP violation and rare decays in the B sector. The LHCb experiment plans to operate at an average luminosity of $2 \times 10^{32} \text{ cm}^{-2}\text{s}^{-1}$, while the LHC bunch crossing rate is 40 MHz [1]. The low luminosity and the LHC bunch structure will provide about 10 MHz of interactions visible to the LHCb detector, which will contain a rate of $b\bar{b}$ pairs of the order of 100 kHz. However, only 15% of these events contain at least one B -meson with all its decay products in the acceptance. Furthermore, the final states useful to study CP violation have typical branching fractions below 10^{-3} . Hence the task of the trigger system consists in reducing the initial 10 MHz rate to a few kHz, at which rate the events can be written to permanent storage, while maintaining the highest possible efficiency for the decay channels of interest for CP violation studies [2]. This reduction is achieved in three trigger levels: the L0 trigger, which is implemented in custom electronics, will reduce the acquisition rate from the initial 40 MHz down to 1 MHz; the L1 trigger will accept events at a rate of 40 kHz, while the HLT will further reduce the rate down to 2 kHz in the present implementation. Both the L1 and HLT algorithms will be executed on a dedicated PC farm (about 1600 CPUs).

In the next Section we present the current implementation of the readout system, while in Section 3 we briefly discuss the trigger strategies.

2 Readout system and trigger architecture

The LHCb spectrometer and all its subsystems are fully described in [3], and major updates and modifications are reported in [1]. A detailed scheme of the Data Acquisition (DAQ) system is shown in Fig. 1; for a complete description of the readout scheme we refer to [2]. The architecture of each trigger level is straight-forward: it consists of some data processing (preamplification, digitization, zero-suppression), a buffer to store raw data (the size of which

is defined by the trigger latency), an output buffer to de-randomize the data transmission to the next trigger level, and an interface to receive the trigger decision.

The LHC environment will be quite harsh in terms of radiation exposure, requiring the use of full custom electronics in the proximity of the detectors. To cope with the high event rate and data bandwidth, however, most of the data processing will be done with standard electronics in the counting house behind a shielding wall. Thus synchronization and timing are essential issues for a correct readout. LHCb will have both a fast Timing and Trigger Control (TTC) system to distribute the LHC clock, resets and triggers [4], and a slow Experiment Control System (ECS), responsible for configuration, control and monitoring of all online components [5]. Synchronization and scheduling of trigger decisions are accomplished by the Readout Supervisor (RS) [6].

The L0 electronics, i.e. the DAQ components before the L0 decision, will be located in the LHCb cavern, and its implementation is specific to each subdetector. The L0 decision unit, which receives data from the various L0 trigger processors and delivers the L0 decision to the RS, is located in the counting house. The L0 is a fully synchronous and pipelined hardware trigger with a fixed latency of $4 \mu\text{s}$, which gives a buffer depth of 160 events. The front-end is required to readout events in 900 ns, hence the maximal L0 accept rate is 1.11 MHz.

The L1 electronics, i.e. what comes before the L1 decision, is implemented with standard electronics, since it is entirely situated in the counting house, where data are sent to over long (50–100 m) analog or digital links from the L0 electronics. The L1 is a variable latency trigger with a buffer size of 58524 events, which combined with the minimal events spacing of 900 ns and the requirement to deliver the decisions chronologically allows a latency up to 52.4 ms. All LHCb subdetectors but the RICH have chosen the TELL1 board [7] as a common solution for the L1 readout. The TELL1 is an FPGA based board designed to take as input L0 accepted data and, after some processing specific to each subdetector, to output them

to the L1 and HLT readout network, which is based on standard GigaBit Ethernet.

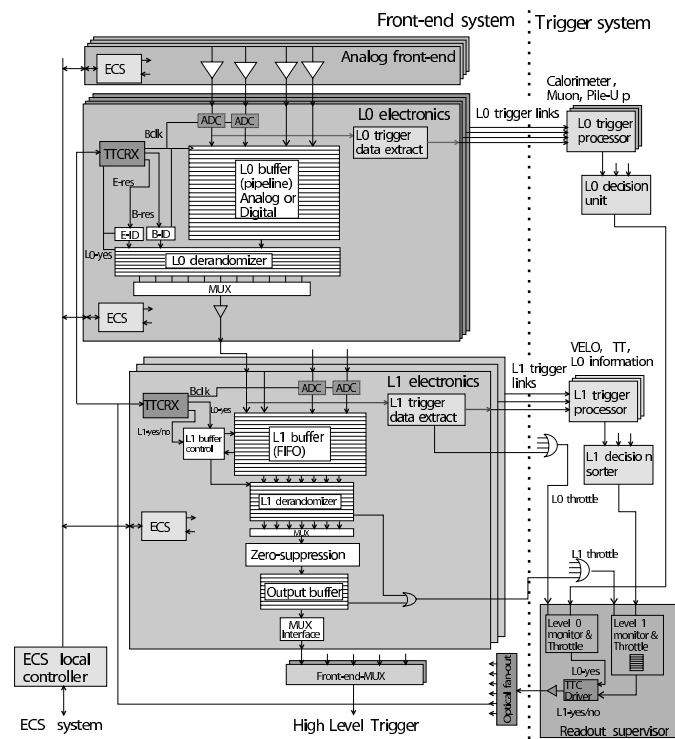


Fig. 1. The LHCb front-end trigger architecture.

3 The trigger strategies

The LHCb trigger system is fully described in [2]. Here we give a short summary of the various trigger algorithms and an update on their performances. In Table 1, the b and c content in generated events after each trigger level is shown.

The objective of the $L0$ trigger is to reduce the acquisition rate so that all sub-detectors data can be digitized and stored in the L1 buffer. $L0$ exploits the large mass of b hadrons, looking for events with large transverse energy deposition in the calorimeters and in the muon chambers. It also features a Pile-Up system to reject events with multiple interactions. The achieved efficiencies vary from as high as 90% for channels with dimuons in the final states to about 50% for hadronic channels.

The $L1$ trigger consists of a set of parallel algorithms, whose individual decisions provide the input to a logical OR giving the final decision. A generic trigger line enhances the b content by selecting events containing tracks with both high transverse momentum and large impact parameter, whereas some specific lines select final states with electrons, photons and muons. The inclusive muon line is particularly important in order to have an unbiased sample to use for life times sensitivity studies. The efficiencies are around 80% for purely hadronic channels, and about 90% for channels with dimuons.

The *High Level trigger* algorithms can be divided in two parts. In the first, generic part, the L1 decision is reconfirmed, and a fast muon identification is performed. In the second, specific part, an inclusive stream of muons and D^* events is formed, which covers about 1.8 kHz of the available bandwidth, while the remaining 200 Hz are reserved to the exclusive selection of some core channels of the LHCb physics programme. Preliminary results show efficiencies of the order of 95% for dimuon channels, and around 90% for channels with two hadrons in the final state.

Table 1. Rates of crossings with at least one bottom ($b\bar{b}$), and if no bottom at least one charm ($c\bar{c}$), in generated minimum-bias events after each trigger level.

	$b\bar{b}$ (kHz)	$c\bar{c}$ (kHz)
Generated	165	840
After L0	30	106
After L1	6.4	7.2
After HLT generic	3.8	2.7

4 Conclusions

We have presented an overview of the present implementation of the LHCb trigger and readout scheme. Most of the electronics components are being delivered and tested in these months. The $L0$ trigger performance is quite stable, while $L1$ and HLT algorithms are still being optimized. A dedicated “Real Time Trigger Challenge” has been successfully setup and run in July 2005 to test the online environment under realistic data taking conditions, such as full-speed data path (from simulated detector output to storage) and long term operation (hours).

References

1. Antunes Nobrega, R. et al. (LHCb Collab.), *LHCb Reoptimized Detector Design and Performance Technical Design Report*, CERN/LHCC 2003-030.
2. Antunes Nobrega, R. et al. (LHCb Collab.), *LHCb Trigger System Technical Design Report*, CERN/LHCC 2003-031.
3. Amato, S. et al. (LHCb Collab.), *LHCb Technical Proposal*, CERN/LHCC 1998-004.
4. Timing, Trigger and Control (TTC) Systems for the LHC, <http://ttc.web.cern.ch/TTC/intro.html>.
5. Gaspar, C. et al., *An integrated experiment control system, architecture, and benefits: the LHCb approach*, IEEE Trans. Nucl. Sci. **51** 513–520, 2004.
6. Jacobsson R., Jost, B., and Guzik, Z., *Readout supervisor design specifications*, LHCb public note 2001-012.
7. Legger, F. et al., *TELL1: Development of a common readout board for LHCb*, Nucl. Instrum. Meth. A **535** 497–499, 2004.

Anomalous single top production with ATLAS

Orhan Çakır

Ankara University, Faculty of Sciences, Department of Physics, 06100, Tandogan, Ankara, Turkey.

Abstract. The top quark may play a unique role for probing new physics beyond the SM due to the large mass close to the electroweak symmetry breaking scale. Anomalous top production via $u(c)g \rightarrow t$ and decay $t \rightarrow W+b$ are studied for the ATLAS experiment. The sensitivity to anomalous coupling κ/Λ down to 0.02 TeV^{-1} can be achieved.

1 Introduction

The top quark being heavy and having poorly measured couplings, could have different dynamics than other quarks. Although higher dimensional operators can be included in the standard model (SM) through higher order loops, their effects are too small to be observable. Any observed signal indicating these types of couplings will be the direct evidence for physics beyond the SM. The anomalous couplings can lead to different signatures than those of SM processes of single top production, including potentially interesting polarization and charge observables. However, top quark flavour changing interactions (tqV , where $q = u, c$ and $V = g, \gamma, Z$) can be parametrized in a model independent way by the effective lagrangians with dimension 4 and dimension 5 couplings

$$\begin{aligned}
 L = & \frac{\kappa_q^g}{\Lambda} g_s \bar{q} \sigma_{\mu\nu} (A_q^g + B_q^g \gamma_5) T^a t G_a^{\mu\nu} \\
 & + \frac{\kappa_q^\gamma}{\Lambda} g_e Q_q \bar{q} \sigma_{\mu\nu} (A_q^\gamma + B_q^\gamma \gamma_5) t F^{\mu\nu} \\
 & + \frac{\kappa_q^Z}{\Lambda} \frac{g}{2 \cos \theta_W} \bar{q} \sigma_{\mu\nu} (A_q^Z + B_q^Z \gamma_5) t Z^{\mu\nu} \\
 & + \frac{g}{2 \cos \theta_W} \bar{q} \gamma_\mu (C_q^Z - D_q^Z \gamma_5) t Z^\mu + H.c. \quad (1)
 \end{aligned}$$

In the Lagrangian L , Λ is the new physics scale; κ_q^V define the strength of anomalous couplings; $V^{\mu\nu}$ is the gauge field tensor of the vector bosons; g_e and g_s is the electromagnetic and strong coupling constant, respectively; T^a are Gell-Mann matrices; A_q^V and B_q^V both determine the strength of anomalous interaction and relative contribution of γ_5 term, and they are assumed to satisfy the constraint $|A_q^V|^2 + |B_q^V|^2 = 1$. In the Lagrangian above C_q^Z and D_q^Z are non-diagonal Z couplings. Using the above Lagrangian we calculate the anomalous decay width of top

Table 1. Predicted branching ratios for $t \rightarrow qV$ decay in different models.

	$\text{BR}(t \rightarrow qg)$	$\text{BR}(t \rightarrow q\gamma)$	$\text{BR}(t \rightarrow qZ)$
SM	10^{-10}	10^{-12}	10^{-13}
2HDM	10^{-5}	10^{-7}	10^{-6}
SUSY	10^{-5}	10^{-6}	10^{-6}
EXQ	10^{-3}	10^{-5}	10^{-2}

quark as

$$\Gamma(t \rightarrow qg) = \left(\frac{\kappa_q^g}{\Lambda} \right)^2 \frac{2\alpha_s}{3} m_t^3 \quad (2)$$

$$\Gamma(t \rightarrow q\gamma) = \left(\frac{\kappa_q^\gamma}{\Lambda} \right)^2 Q_q^2 \frac{\alpha}{2} m_t^3 \quad (3)$$

$$\begin{aligned}
 \Gamma_{D5}(t \rightarrow qZ) = & \left(\frac{\kappa_q^Z}{\Lambda} \right)^2 \frac{\alpha m_t^3}{4 \sin^2 2\theta_W} \\
 & \times \left(1 - \frac{m_Z^2}{m_t^2} \right)^2 \left(2 + \frac{m_Z^2}{m_t^2} \right) \quad (4)
 \end{aligned}$$

$$\begin{aligned}
 \Gamma_{D4}(t \rightarrow qZ) = & \frac{(|C_q^Z|^2 + |D_q^Z|^2) \alpha m_t^3}{16 m_Z^2 \sin^2 2\theta_W} \\
 & \times \left(1 - \frac{m_Z^2}{m_t^2} \right)^2 \left(1 + 2 \frac{m_Z^2}{m_t^2} \right) \quad (5)
 \end{aligned}$$

The anomalous couplings may be significant in many extensions to the standard model (SM), such as two Higgs doublet model (2HDM), supersymmetry (SUSY) and exotic quarks (EXQ) as shown in Table 1 [1]. The experimental limits (Fig.1) by the CDF collaboration for the FCNC decays of top quarks are $\text{BR}(t \rightarrow q\gamma) < 0.032$ and $\text{BR}(t \rightarrow qZ) < 0.33$ [2]. The OPAL results [3] improve the limits on the anomalous coupling for tqZ as $\text{BR}(t \rightarrow qZ) < 0.137$ and the H1 results [4] put an upper limit of 0.28 on the $tq\gamma$ couplings. The FCNC decays were considered in ATLAS TDR [5] and the reach for $t \rightarrow qV$ are given as $\text{BR}(t \rightarrow qZ) \simeq \text{BR}(t \rightarrow q\gamma) = 10^{-4}$ at 5σ level and $\text{BR}(t \rightarrow qg) = 7.4 \times 10^{-3}$ at 95% C.L.

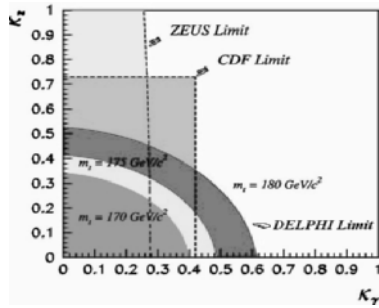


Fig. 1. LEP, Tevatron and HERA limits on anomalous couplings in the $\kappa_\gamma - \kappa_Z$ plane at % 95 C.L.[6].

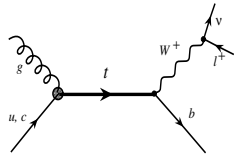


Fig. 2. Anomalous top production at hadron colliders

2 Anomalous Production

We study single top quark production in the resonance channel through the anomalous production subprocess $qg \rightarrow t \rightarrow Wb$ as shown in Fig. 2. The anomalous top quark production and relevant backgrounds are simulated taking into account the experimental conditions prevailing at LHC for the ATLAS detector, the TOPREX event generator [7] and ATLFAST [8] detector fast simulation packages were used. TOPREX takes into account top polarization, and sums LO+NLO processes for t-channel single top production.

Since we still expect the dominant decay mode for top quark as $t \rightarrow Wb$ and the leptonic decay mode of W gives a clear signal, we search for a signal in the detector through the presence of a b -tagged jet, an isolated lepton and missing transverse momentum. The applied transverse momentum cuts are: $p_T^e > 25$ GeV, $p_T^b > 20$ GeV, $p_T^{\text{miss}} > 50$ GeV. Top quark mass is reconstructed from $b\nu$ system [9].

The most important backgrounds to the signal are (after cuts and b-tagging):

- W +jet (2.86 pb)
- Single production of top quarks (0.64 pb)
- Wbb events (0.09 pb)
- Pair production of top quarks (0.04 pb)
- ZW / WW processes (0.007 pb).

The reconstructed signal+background is given in Fig. 3 for $\kappa/\Lambda=0.4$ TeV^{-1} . The resulting S/\sqrt{B} values in the mass window of top quark are given in Table 2. From Table 2, one can conclude that discovery at 95% C.L. is possible if $\kappa/\Lambda=0.02$ TeV^{-1} . We can translate this value to the branching ratio $\text{BR}(t \rightarrow ug)=5 \times 10^{-3}$. This value of the branching can be compared to the values given in Table 1 to predict the model origin of the FCNC.

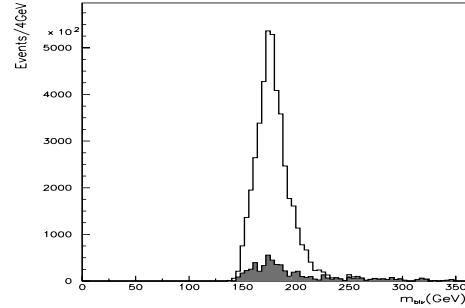


Fig. 3. The signal+background events for $\kappa/\Lambda=0.4$ TeV^{-1} .

Table 2. statistical significance for the anomalous top production at the CERN LHC for $L_{int}=100$ fb^{-1} .

κ/Λ (TeV^{-1})	0.4	0.2	0.1	0.01	0.001
S	3.4×10^6	8.6×10^5	2.5×10^5	2.3×10^3	2.3×10^1
S/\sqrt{B}	5.6×10^3	1.4×10^3	4.1×10^2	3.9×10^0	4.0×10^{-2}

3 Conclusion

We have calculated the discovery limits on the anomalous couplings $u(c)gt$ at the LHC. Taking into account an uncertainty of 10% in the single top quark production the sensitivity to anomalous coupling κ/Λ can be achieved down to 0.02 TeV^{-1} . In this case the expected number of anomalous top events is 15400.

This work has been performed within the ATLAS Collaboration with the help of the simulation framework and tools which are the result of the collaboration-wide efforts.

References

1. A. Ahmadov et al., Proceedings of the workshop on the Standard Model physics (and more) at the LHC, Ed. G. Altarelli and M.L. Mangano (Geneva), CERN 2000-004, p. 484.
2. F. Abe et al., (CDF Collaboration), Phys. Rev. Lett. 80, 2525 (1998).
3. G. Abbiendi et al., (OPAL Collaboration), Phys. Lett. B 521, 181 (2001).
4. A. Aktas et al., (H1 Collaboration), hep-ex/0310032 (2003).
5. ATLAS Collaboration, ATLAS TDR 14/15, CERN/LHCC 99-14/15 Vol. I/II.
6. S. Dusi, Nucl. Phys. B (Proc. Suppl.) 109, 262 (2002).
7. S. R. Slabospitsky and L. Sonnenschein, Comput. Phys. Commun. 148, 87 (2002); hep-ph/0201292 (2002).
8. E. Richter-Was, D. Froidevaux, L. Poggioli, ATLFAST program manual, ATLAS Internal Note ATL-PHYS-98-131, (1998).
9. O. Cakir and S. A. Cetin, SN-ATLAS-2004-046; J. Phys. G: Nucl. Part. Phys. 31, N1-N5 (2005).

LHCb RICH Detectors

D. L. Perego¹ on behalf of the LHCb RICH Collaboration

Università degli Studi di Milano Bicocca e INFN, Piazza della Scienza 3, 20126 Milano, Italia

Abstract. The LHCb experiment will perform high precision studies of CP violation and other rare phenomena in the B meson sector. Particle identification will be essential to enhance the signal to background ratio in the selection of B -decay channels and to provide an efficient kaon tag. LHCb will use two RICH detectors, one covering the charged particle momentum range 1 – 65 GeV/c using solid silica aerogel and gaseous C_4F_{10} radiators, and the other covering up to 100 GeV/c using gaseous CF_4 . Hybrid Photon Detectors (HPDs) have been developed to detect Cherenkov light in the wavelength range 200 – 600 nm. The engineering design of the upstream RICH-1 detector is very well advanced and the assembly of the downstream RICH-2 is almost complete.

1 LHCb RICH Detectors

LHCb is the dedicated experiment for precise measurements of CP violation and rare decays at the Large Hadron Collider, LHC. Based on the expected topology of $b\bar{b}$ pair production at the LHC, its design consists of a single-arm spectrometer with a forward coverage from 10 mrad to 300 (250) mrad in the bending (non-bending) plane [1].

Particle identification, essential to enhance the signal to background ratio in the selection of B -decay channels and to provide an efficient kaon tag, will be achieved using Ring Imaging Cherenkov (RICH) detectors. Due to the strong correlation between the polar angle and the momentum of the particles, shown in Fig. 1, two detectors are designed (RICH-1 and RICH-2). To cover the wide momentum range 1 – 100 GeV/c, three radiators are required. The first, solid silica aerogel ($n = 1.03$), is suitable for the lowest momentum particles up to ~ 10 GeV/c. Gaseous C_4F_{10} ($n = 1.0014$) and CF_4 ($n = 1.0005$) then provide particle identification of the intermediate and the

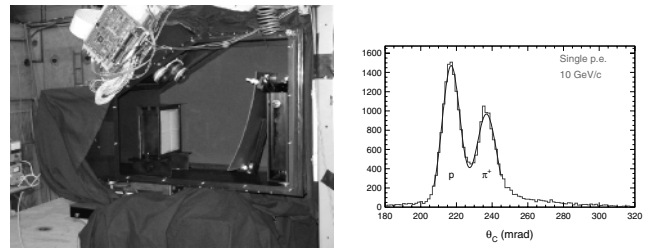


Fig. 2. Left: photograph of the Cherenkov vessel used to study the resolution and performance of aerogel blocks and Hybrid Photon Detectors. Right: reconstructed Cherenkov angle θ_C for a mixed beam of π^+ and p .

highest momentum particles up to approximately 65 GeV/c and 100 GeV/c, respectively. The Cherenkov angle for the three radiators as a function of momentum is shown in Fig. 1 for the π , K and p hypotheses [2,3].

2 Silica Aerogel

Silica aerogel is a solid material made of SiO_2 with a very low density. It consists of a linked network of particles of 2 – 5 nm in diameter, and pores whose average radius is about 20 nm. The density is calibrated during production and it is typically between 0.003 and 0.35 g/cm³. It is transparent and its refractive index can be tuned within the wide range of 1.008 – 1.08. Depending on the manufacturing procedure, silica aerogel can be hygroscopic or hydrophobic.

Photon scattering within the aerogel is the factor limiting the performance of this material as a Cherenkov radiator. The dominant contribution is from the Rayleigh scattering mechanism with a cross section proportional to λ^{-4} , where λ is the wavelength of the photon.

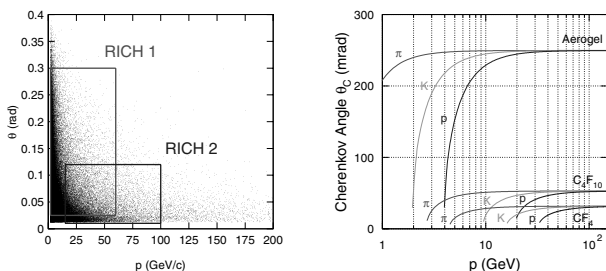


Fig. 1. Left: polar angle vs momentum for all the tracks in simulated $B_s^0 \rightarrow D_s^- \pi^+$ events; the regions of interest for RICH-1 and RICH-2 are drawn. Right: Cherenkov angle vs momentum for different particle hypotheses for the three radiators.

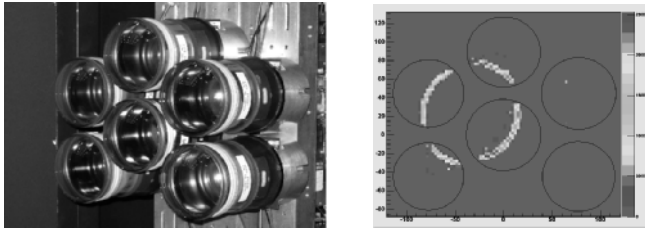


Fig. 3. Left: photograph of six pre-production HPDs successfully operated in a beam test. Right: the ring due to Cherenkov photons produced in C_4F_{10} .

The LHCb RICH-1 detector will be equipped with $200 \times 200 \times 50 \text{ mm}^3$ tiles of hygroscopic silica aerogel produced by the Boreskov Institute of Catalysis in Novosibirsk (Russia). These tiles have the largest size ever fabricated. Several tests have been done to check the optical properties required by the experiment. Possible ageing effects due to intense irradiation and to humidity absorption have been studied: no evidence of permanent degradation of the optical properties has been detected [4]. The index of refraction homogeneity complies with the specifications $\sigma(n-1)/(n-1) < 1\%$. From a beam test an excellent p/π^+ separation has been achieved up to $10 \text{ GeV}/c$, as shown in Fig. 2.

3 Hybrid Photon Detectors

Cherenkov photons will be detected by a total of 484 Hybrid Photon Detectors (HPDs). The photon detector planes of both RICH detectors cover a total area of about 2.8 m^2 , with an active over total ratio greater than 70%.

Pixel HPDs consist of a cylindrical vacuum tube of diameter 83 mm. On the inner surface of the 7 mm thick quartz spherical entrance window, a multialkali photocathode is deposited. The base of the tube houses a silicon sensor equipped with 1024 pixels of size $0.5 \times 0.5 \text{ mm}^2$ which, due to an electrostatic image demagnification factor of five, corresponds to a $2.5 \times 2.5 \text{ mm}^2$ granularity at the HPD photocathode. The HPD is sensitive in the wavelength range between 200 nm and 600 nm.

Photoelectrons created at the photocathode are accelerated and cross-focused onto the silicon sensor by a 20 kV potential difference. An overall iron shield and individual Mumetal tubes allow the HPDs to operate safely in the residual magnetic field of up to 25 gauss.

Recently the full readout chain has been successfully tested in a $10 \text{ GeV}/c$ π^- and e^- beam test. Cherenkov photons produced in a C_4F_{10} radiator have been detected by six pre-production HPDs integrated with *Low Voltage* (LV) and *High Voltage* (HV) boards. A photograph of the HPDs and a detected pion ring integrated over many events are shown in Fig. 3.

4 RICH Particle ID Performance

The task of particle identification (PID) is to assign a particle type to each reconstructed track [6]. Fig. 4 shows

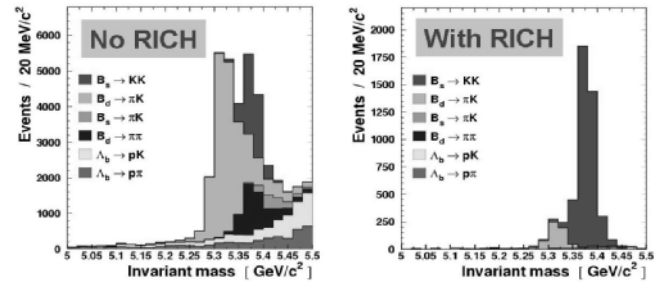


Fig. 4. Left: invariant mass spectrum of $B_s^0 \rightarrow K^+K^-$ candidates before any particle identification is applied. Right: the same as before, but with particle identification applied.

the mass spectrum of candidate $B_s^0 \rightarrow K^+K^-$ events before and after PID is applied. The powerful PID allows rejection of almost all the backgrounds during the offline analysis.

Two approaches have been developed for ring reconstruction: a “local” method which treats each track separately and a “global” one which optimizes the assignment of particle types for all the tracks in RICH-1 and RICH-2 simultaneously. In both methods a likelihood function is maximized varying the mass hypothesis. Typical values of PID performances are 95% for K identification and 5–7% π misidentification between 20–60 GeV/c . Varying the cut on the difference of log-likelihood functions used to separate kaons from pions, the misidentification rate of pions can be reduced (improving the purity of the selected sample) at the cost of reducing the kaon identification efficiency.

Pion-kaon separation is achieved at about 3σ over most of the momentum range of interest 2–100 GeV/c .

5 Status RICH Detectors

The status of RICH detectors is on schedule for LHC turn-on [6]. The design of RICH-1 is very well advanced and the magnetic shielding boxes have been installed in the pit. The construction of RICH-2 is finished, and it is ready to be installed in its final position. The production of the silica aerogel and the HPDs is underway.

References

1. The LHCb Coll., *LHCb Technical Proposal*, CERN/LHCC/98-4 (1998)
2. The LHCb Coll., *LHCb RICH Technical Design Report*, CERN/LHCC/2000-037 (2000)
3. The LHCb Coll., *LHCb Reoptimized Detector Design and Performance*, CERN/LHCC/2003-030 (2003)
4. T. Bellunato et al., *Nucl. Instr. and Meth. A* **527**, (2004) 319–328
5. A. Van Lysebetten, *these conference proceedings*
6. R. Forty, *these conference proceedings*

Production and test of the LHCb Muon Wire Chambers

D. Pinci¹ and A. Sarti²

on behalf of the LHCb collaboration

¹ Università di Roma “La Sapienza” and INFN sezione di Roma, Italy

² INFN-Laboratori Nazionali di Frascati (LNF), Italy

Abstract. The LHCb Muon Detector is composed of five tracking stations. The performance demanded for the Level-0 trigger of LHCb imposes very stringent requirements on the quality of the muon chambers. This paper describes the tests that chambers must overcome before being mounted in the experimental setup. Up to June 2005, about 500 chambers have been built and the end of the whole production phase is foreseen in April 2007.

1 Introduction

The LHCb experiment is dedicated to study the decays of beauty hadrons. The Level-0 trigger of the experiment calls for fast measurement of the muon transverse momentum and a high capability of bunch-crossing identification. The muon detector must therefore have a high detection efficiency and a good spatial and time resolution. The LHCb muon detector [1] [2] is composed of five tracking stations (M1–M5) which comprise 1368 MultiWire Proportional Chambers (MWPC) now under construction in different sites: CERN (CH), LNF-Frascati (ITA), Ferrara (ITA), Firenze (ITA) and PNPI-San Petersburg (RU).

The gas gap is filled with an Ar/CO₂/CF₄ (40/55/5) gas mixture. The anode plane is composed of 30 μm diameter gold-plated tungsten wires with a pitch of 2 mm. While chambers in station M1 will be composed of two single gaps the ones of stations M2–M5 are composed of two double gaps in which the corresponding pads are ganged in pairs. The front-end electronics performs a further logical OR between the two signals of the single (double) gaps.

In order to meet the performance required for triggering and for physics analysis, each single (double) gap must satisfy the following conditions:

1. double-gap efficiency $\geq 95\%$, within a 20 ns time window;
2. low cross-talk between pads giving an average pad-cluster size ≤ 1.1 ;
3. good ageing properties, allowing 10 years of operation at an average luminosity of $2 \times 10^{32} \text{ cm}^{-2} \text{ s}^{-1}$ with a chamber gain of about 10^5 .

Several prototypes were tested at CERN on a minimum ionizing particle beam [3]. The results obtained (see Fig. 1) allowed to define a 170 V wide HV working region (WR) of the chambers. Since the gas gain (G) doubles for a HV increase of about 110 V, the HV working region corresponds to a gain interval:

$$1/1.7 \leq G/G_0 \leq 1.7 \quad (1)$$

where G_0 is the nominal gas gain at the centre of the WR. This requirement on the chamber gain fixes the mechanical precision to be achieved during production, particu-

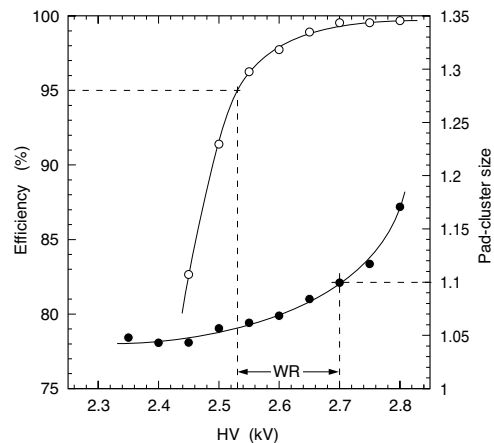


Fig. 1. Efficiency (left scale and open circles) and pad-cluster size (right scale and solid circles) of a double-gap MWPC as functions of the high-voltage (HV). The working region (WR) is shown. Curves are drawn to guide the eye.

larly regarding the position and the tension of the wire and the size of the gap. These constraints were evaluated by a numerical simulation [4] of the operation of a chamber. In order to check that the produced chambers fulfill these constraints a series of quality tests was organized.

2 Quality tests

Five tests have been developed to monitor the chambers quality during their production. The following subsections describe these tests and their results.

2.1 Wire pitch

The precision required on the wire pitch (WP) is:

$$\text{WP} = 2.00 \pm 0.05 \text{ mm} \quad (2)$$

The position of the wire is precisely determined by the combs of the wiring machine, however it is important to check that no wire pitch is out of the acceptance. The WP is measured using an automatic device: two cameras placed at both ends of wires scan the wire plane and photograph three contiguous wires at the same time. Each picture is acquired and analysed by a software that can evaluate the distance between the wires. Two consecutive wire pitches are then measured in each picture with a precision of 20 μm .

2.2 Wire mechanical tension

In the LHCb muon detector the MWPC wires are vertical, so that no gravitational sagitta is present. Nevertheless to avoid mechanical instabilities due to electrostatic repulsion, the mechanical tension of the wires, τ , must be greater than 300 mN. The upper limit of τ is set by the elastic limit of the wire which is about 1200 mN. A safe condition is thus:

$$500 \text{ mN} \leq \tau \leq 900 \text{ mN} \quad (3)$$

Two automated different systems were been developed by the collaboration ([5], [6]) which deduces the mechanical tension of the wire by measuring its mechanical resonance frequency ν_0 . In a first method the wire is forced to oscillate by means of a periodical electric field and the amplitude of the oscillations are deduced from the variation of the capacitance between the wire under measurement and a sense wire.

In the second method mechanical sollicitations on the panel make the wire oscillate and the amplitude of oscillations is monitored with an optical device. A resolution of about 10 mN is achieved in both cases.

2.3 Chamber tightness

The gas-tightness of a chamber is verified by filling it with nitrogen to an overpressure of about 5 mbar with respect to the atmospheric pressure. The chamber is then closed and the difference in pressure (Δp) between the chamber and the atmosphere is recorded during about one hour. If a gas leakage is present, Δp will decrease during the observation time.

To reduce the fluctuations due to variations in the temperature and pressure of the environment during the measurement process, the same procedure is applied to a reference chamber known to be leakage-free. The difference, $\Delta p - \Delta p_{\text{ref}}$, reported in Fig. 2 shows that this quantity is practically independent of the environmental conditions. This method permits better evaluation of the rate of leakage with an accuracy of about 0.1 mbar/hour. The maximum leakage rate allowed for each chamber is 2 mbar/hour.

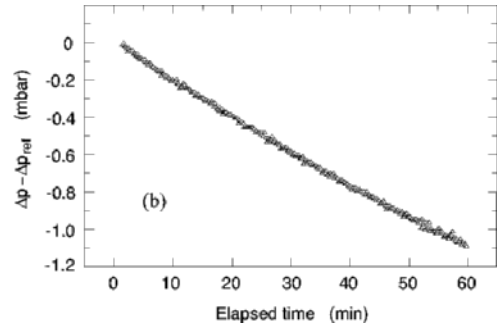


Fig. 2. Time dependence of the overpressure applied to the chamber under test after subtraction of the overpressure of the reference chamber.

2.4 Gain uniformity

The uniformity of the gas gain inside each gap is tested with a 40 mCi ^{137}Cs source which is moved by means of mechanical arms over the whole surface of the test table. During this test the HV is set to 2750 V and currents drawn by the four gaps are recorded for each position of the source. The chamber surface ($\sim 130 \times 27 \text{ cm}^2$) is scanned in 3×54 positions of the source.

This test is repeated on every chamber produced. Each double-gap is classified, according to the uniformity of its current (I), in one of the following two categories:

$$\text{Category A :} \quad 1/1.5 \leq I/I_0 \leq 1.5 \quad (4)$$

$$\text{Category B :} \quad 1/1.7 \leq I/I_0 \leq 1.7 \quad (5)$$

where $I_0 = 470 \text{ nA}$ is the current drawn by a double-gap at the nominal gain G_0 . Fig. 3 shows the distribution of the values of I/I_0 for the chambers produced. Only few double gaps don't belong to Category A and all the double gaps produced belong to Category B.

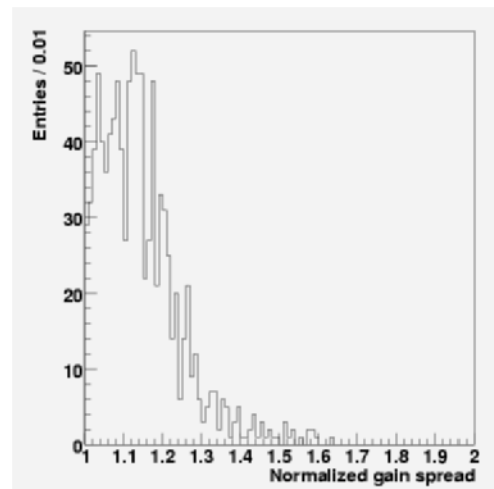


Fig. 3. Average current measured in each double-gap, normalized to I_0 (see text). The vertical bars represent the gain spread found for each double-gap.

2.5 Cosmic ray test

The last test on the chambers is performed using cosmic rays. Up to six chambers, fully equipped with the CARIOCA read-out electronics [7] can be tested simultaneously. In Fig. 4 the time resolution of 3 different types of chambers as a function of the high voltage applied is shown. No significant differences have been found and all type of

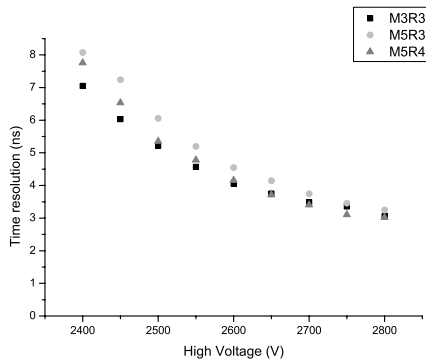


Fig. 4. Time resolution as a function of the high voltage applied to the wires for 3 different types of chamber.

chambers reach time resolution of about 4 ns at a high voltage value of about 2600 V.

3 Production status

Up to June 2005 production sites have produced about 500 chambers. In Fig. 5 the number of chambers produced in each site and the total are shown and compared with the scheduled values. The current production rate is equal

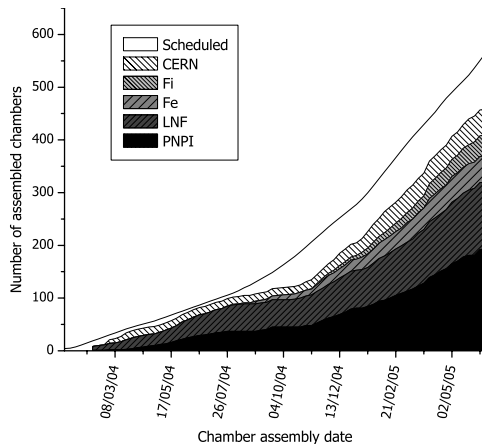


Fig. 5. Number of produced chambers in the LHCb muon production sites and total compared with the scheduled one.

to the expected one. The end of the production phase is foreseen in April 2007.

4 Conclusion

A series of tests was organised to permit online control of the muon chambers produced. The measurements of the pitch and mechanical tension of the wires enabled us to check the quality of the wire winding with the necessary accuracy, before assembling the chamber. Possible gas leakage can be measured with the required sensitivity. The study of the gas gain uniformity inside each gap gives a rapid indication of the quality of the chamber, enabling improvements to be made to the assembly procedure, where necessary. The test with cosmic rays makes it possible to study the time performance of the chambers. About 500 MWPC have already been produced and all of them satisfy the requirements on detection performance.

References

1. LHCb Collaboration, “LHCb Muon System Technical Design Report”, CERN/LHCC 2001-010 (2001).
2. LHCb Collaboration, “Addendum to the Muon System Technical Design Report”, CERN/LHCC 2003-002 (2003).
3. M. Anelli *et al.*, “Test of MWPC Prototypes for Region 3 of Station 3 of the LHCb Muon System”; LHCb-Muon 2004-074 (2004).
4. W. Riegler, “Chamber requirements and specifications”; Talk given for the MWPC Engineering Design Report, CERN, Available: <http://agenda.cern.ch/fullAgenda.php?ida=a03841>
5. P. Ciambro *et al.*, “Automated wire tension measurement system for LHCb muon chambers”, *Nucl. Instrum. Methods A* vol. 545 pp. 156-163, 2005.
6. S. Germani *et al.*, “Status of Ferrara production” talk given at the Muon Meeting, Available: <http://agenda.cern.ch/fullAgenda.php?ida=a041446>
7. W. Bonivento *et al.*, “Development of the CARIOCA front-end chip for the LHCb muon detector”, *Nucl. Instrum. Methods A* vol. 491 pp. 233-243, 2002.

Techniques for B_s mixing at CDF

Giuseppe Salamanna *on behalf of the CDF Collaboration*

University of Rome *La Sapienza* and INFN Roma 1 P.le A.Moro, 2 - 00185 Rome (Italy) - salaman@fnal.gov

Abstract. The techniques used to perform a measurement of the mixing frequency of the B_s meson (ΔM_s) with the CDF detector at the TeVatron collider are described. Particular stress is put on CDF techniques for flavour tagging, which is possibly the major issue for mixing measurements at a hadron collider. Also CDF performances on lifetime and final state reconstruction are described. The final amplitude scanning result presented at 2005 Winter Conferences is shown.

1 Introduction

The measurement of the mixing frequency of the B_s meson (ΔM_s) is a key point for the determination of the CKM matrix. Knowledge of this parameter, together with the measurement of ΔM_d from the B-Factories, would constrain the Unitarity Triangle in the Standard Model by measuring one of its sides with an overall uncertainty $\approx 5\%$ (from theory). Furthermore, this is wide room for New Physics, as several non-SM particles are expected to contribute in the mixing *box* diagram. At present, the B_s meson can only be produced in incoherent *parton-parton* collisions at the $p - \bar{p}$ TeVatron collider ($E_{CM} = 1.96$ TeV). This renders the observation of the flavour oscillations in the B_s a major point in the B-physics program of both the TeVatron experiments, *CDFII* and *D0*; although its determination represents a big experimental challenge, in particular as far as the time resolution is concerned ($\Delta M_s \approx 30 \times \Delta M_d$). In order to observe the oscillations, the following steps are needed: a) determination of the flavour of the mixing B meson at creation; b) measurement of the length the meson traveled from production point to decay; c) knowledge of its flavour at decay.

2 Flavour Tagging

To infer the flavour of the mixing candidate at production, CDF has considered both Same Side (*SST*) and Opposite Side (*OST*) taggers: all of them exploit the correlation between the b -flavour and the electric charge of a track (or a weighted combination of tracks into a jet) topologically linked to the B. While *SST* looks at fragmentation particles close to the B meson, *OST* aim to tag the accompanying b -hadron's flavour by looking at specific decay products (leptons, kaons or jets). In practice, a vast number of fragmentation tracks is produced in the primary interactions at hadron colliders, so that a tagger's prediction is highly diluted by their random flavour-charge correlation. For comparison, while at the B-factories the tagging figure

of merit is $\varepsilon D^2 \approx 30\%$ ([1]) CDF has around 1.5% (*current OST only*).¹ So far, only 2 of these taggers were used at CDF for mixing analyses, both from Opposite Side.

2.1 Soft Lepton Taggers

These taggers exploit the fact that, in semileptonic decays of the OS b -hadron, $b \rightarrow l^-$ ($l = \mu, e$), while $\bar{b} \rightarrow l^+$. CDF implemented a likelihood based algorithm to select the lepton using our muon chamber system and calorimeter information. The main background for these taggers is given by sequential decays of the kind $\bar{B} \rightarrow DX \rightarrow l^+Y$, which returns a wrong sign in charge. To suppress this contribution, the dilution D is calculated on an *event-by-event* basis, weighting it for the lepton likelihood value and the p_t^{rel} of the tagging lepton with respect to the axis of the opposite B jet. The greater this is, the more likely the lepton is to come straight from the b .

2.2 Jet Charge Tagger

One can also look at the overall charge of the OS b -jet, weighting each track in a given cone around the jet axis (CDF: $\Delta R = 0.7$ ²) for their p_t ; three different types of jets are considered: a) look for Secondary Vertexes in the cone; b) if not any explicitly found, evaluate probability that tracks within cone are displaced (*JetProb*); c) use Jet with highest p_t .

2.3 OST calibration

The taggers' performances (shown in table 1) were evaluated using a high statistics *semileptonic* sample, by comparing the tagger's response to that of the lepton; mixing on both sides and (mainly *charm*) background on trigger side have been accounted for by correcting raw dilution for a calibration factor. Removal of the overlap among the various OST taggers, $\varepsilon D^2 = -0.2\%$, was performed. Finally, the taggers have been tuned for combined use in mixing (reweighting e.g. for different p_t spectra w.r.t. the sample used in development) applying tagging in a measurement

¹ $\varepsilon = \frac{N_{events\ when\ decision\ possible}}{N\ triggered\ events}$ and $D = 1 - 2W$, with W the mis-tag rate

² $\Delta R = \sqrt{(\Delta\eta)^2 + (\Delta\phi)^2}$

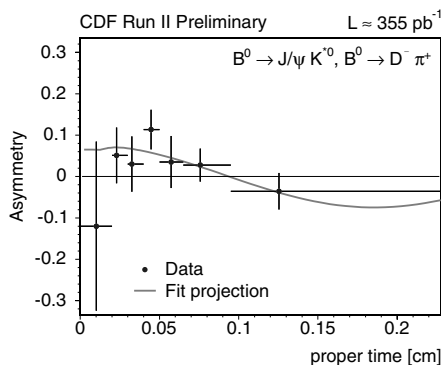
Tag type	εD^2 (%)
Muon	(0.70 ± 0.04)
Electron	(0.37 ± 0.03)
SecVtx	(0.36 ± 0.02)
JetProb	(0.21 ± 0.02)
Highest P_t	(0.15 ± 0.01)
Total	$\approx 1.8\%$

Table 1. Performance of OST's

of the known quantity ΔM_d to return the effective dilution:

$$\varepsilon D^2 = 1.1(\text{hadronic}) - 1.4(\text{semilept}) \%$$

$$\Delta M_d = 0.503 \pm 0.063(\text{stat}) \pm 0.015(\text{syst}) \text{ ps}^{-1}$$

**Fig. 1.** B_d mixing asymmetry from fully reconstructed decays using OST

2.4 Possible improvements

Flavour tagging is the largest room for improvement of our sensitivity. CDF has undergone a major study and implementation of Same Side Kaon Tagging. The comprehension of the production and fragmentation processes is the main point to control sources of dilution, so that Monte Carlo tuning for TeVatron environment is the main effort at this point. At the same time, CDF is also evaluating the feasibility of an Opposite Side Kaon Tagger, following the same principles of SLT. MC shows this should be doable and needs to be studied on data. Both of them use the CDF Particle ID system (Time of Flight + dE/dx from ionization in the COT chamber), whose informations are combined using a ratio of likelihoods.

3 Decay length

The amplitude of mixing asymmetry is diluted by an exponential factor $D_{\sigma_{ct}} = \exp\left(-\frac{(\Delta m \times \sigma_{ct})^2}{2}\right)$, where the reso-

lution on mixing meson's proper time is

$$\sigma_t = \sqrt{(\sigma_{ct}^0)^2 + (ct \times \frac{\sigma_{p_t}}{p_t})^2}$$

where σ_{ct}^0 is the resolution on Primary Vertex. In the case of fully hadronic final states, the kinematics is completely reconstructed, so that only the vertexing counts: we achieve a $\langle \sigma_{ct}^0 \rangle \approx 30 \mu\text{m}$, while $\frac{\sigma_{p_t}}{p_t} \leq 1\%$. CDF has so far used the average beamline position to find the PV: recently, though, an event-by-event vertex finder has been developed, which is expected to improve time resolution in the hadronic case of 10 to 20%. In the semileptonic case, the missing neutrino accounts for a significant part of the B momentum, so that $\frac{\sigma_{p_t}}{p_t} \approx 15\%$: CDF corrects this effect using a so called K factor extracted from MC.

4 Final state reconstruction

CDF performed a mixing amplitude scanning both for the semileptonic and the hadronic sample, thanks to the Two (displaced) Track Trigger, new for RunII. Up to now only the $B_s \rightarrow D_s \pi$ (or $D_s l \nu$), with $D_s \rightarrow \phi \pi, K^* \pi, 3\pi$ have been considered. At present CDF is also trying to include the $B_s \rightarrow D_s 3\pi$ modes and a further semileptonic sample triggered with the TTT, to increase our statistics. The yields we find out of 355 pb^{-1} are: ≈ 7700 (semileptonic), ≈ 900 (hadronic). It has to be noticed that 20% of the semileptonic yield is background from prompt $c\bar{c}$ and $B \rightarrow DDX$ decays (*with one D decaying semileptonically*), which cannot be fully suppressed due to missing kinematics.

5 Significance and results

Given the above numbers, the final CDF combined limit on ΔM_s is [2]:

$$\Delta M_s \geq 7.9 \text{ ps}^{-1}, \text{ sensitivity} = 8.4 \text{ ps}^{-1}$$

With the above improvements, if a gain of +2% in εD^2 , and a -20% in σ_t are achieved, we expect to enhance our sensitivity up to $\approx 35 \text{ ps}^{-1}$ at the end of Run II ($\int \mathcal{L} = 8 \text{ fb}^{-1}$) [3].

References

1. H.Kakuno *et al.*, NIM **A533**, (2004) 516-531.
2. F.Bedeschi *for the CDF Collab.*, Presentation at the XXXX *Rencontres de Moriond* (2005)
3. The CDF Collab., CDF Public Note 7671 (2005)

Heavy flavour production at CDF

Mario Campanelli¹ Monica D'Onofrio¹ Sofia Vallecorsa¹ and Anant Gajjar² A. Metha² Tara Shears²

¹ Univeristy of Geneva, Switzerland

² University of Liverpool, UK

Abstract. We present results for some measurement including b-production recently performed by the CDF collaboration: the inclusive b-jet cross section, the $b\bar{b}$ cross section and the $\gamma +$ heavy flavour production cross section

1 Introduction

At the Tevatron beauty production measurements benefit from relatively high cross section $\sigma(b\bar{b})$ $50\mu b$ (at 1.96 TeV), that with the high luminosity of the collider result in a high event rate (a few kHz).

Past measurements published in RunI by both CDF and D0 indicated a possible excess with respect to QCD predictions. Recently, though, developments of theoretical calculation behind NLO and a different experimental approach (mainly the use of physical observables as b-hadrons or b-jets) resulted in a better agreement between data and theory [1].

2 Heavy flavour jets identification at CDF

Jets produced by heavy flavour fragmentation are identified (i.e. tagged) reconstructing a "b decay" (secondary) vertex, and the invariant mass of the particles coming from this secondary vertex. Even though it is impossible to fully reconstruct the quark mass from the masses of the tracks produced in the fragmentation and decay process, still the shape of its distribution is different in the case of a heavy flavour or a light jet. Fig. 2 shows the efficiency of finding a secondary vertex on data as function of the transverse momentum of the jet.

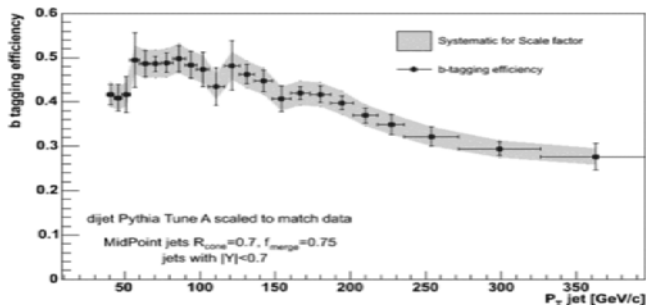


Fig. 1. b tagging efficiency as a function of Pt

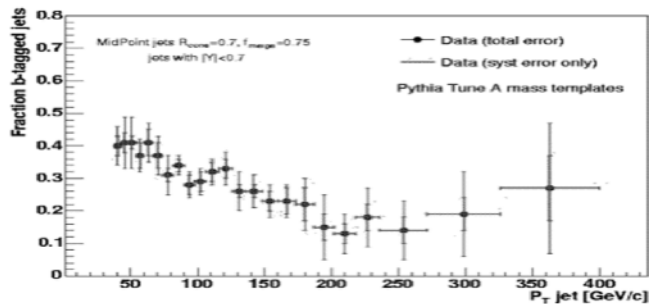


Fig. 2. Fraction of b-tagged jets:total errors and systematic uncertainties are superimposed

The fraction of b-tagged jets is estimated by fitting the secondary vertex invariant mass to templates (for b, c and lights) obtained by MC simulation (PYTHIA tune A) . The result is shown in fig. 2, as calculated directly from data.

3 Inclusive b -jet production cross section

The inclusive b-jet cross section measurement in Run II relies on $300 pb^{-1}$ of data, collected using calorimetric triggers with different thresholds. Using jet allows in fact a wider pt range (38-400 GeV/c compared to a b-hadron measurement < 25 GeV) and reduces theoretical uncertainties due to fragmentation. A cone-based iterative algorithm (Midpoint) is used for jet reconstruction in the $Y-\phi$ space, with a cone of radius 0.7. Only jets in the central region ($|\eta| < 0.7$) are reconstructed and the jet energy scale is corrected for detector effects (calorimeter energy losses) using a MC simulation.

Fig. 3 shows the inclusive b-jet cross section. Statistical and systematics uncertainty are dominated by the error on b-jet fraction and on the jet energy scale (5%). Fig. 3 also shows a comparison to leading order Pythia Tune A prediction (CTEQ5L), results are in reasonable agreement with expectations, and the factor 1.4 of average ratio in

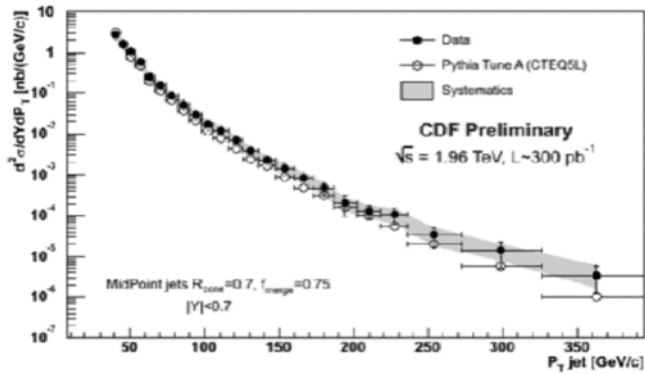


Fig. 3. Up: b-jet cross section as a function of corrected jet Pt superimposed to Pythia MonteCarlo LO (CTEQ5L) prediction. Down: Ratio Data/Pythia as a function of corrected Pt

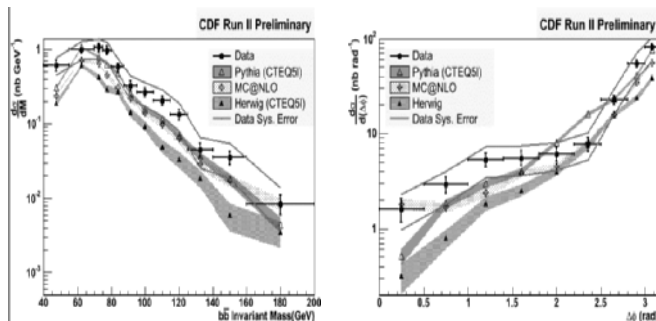


Fig. 4. Left: $b\bar{b}$ cross section. Right: $b\bar{b}$ $\Delta\phi$ distribution

the cross section can probably be explained by the fact that the hard scattering is only computed at LO.

4 $b\bar{b}$

A preliminary $b\bar{b}$ cross section measurement has been performed on 64 pb^{-1} of data collected using a calorimetric trigger with a transverse energy cut at 20 GeV. Two tagged jets in the central region are required and an asymmetric cut on their transverse energy is applied. The jets are corrected for the energy scale to the hadron level. A value of $34.5 \pm 0.18 \pm 10.5 \text{ nb}$ is found for the total cross section and the resulting differential cross section as a function of the $b\bar{b}$ invariant mass is shown in Fig. 4

Main sources of systematics are the b-fraction estimate and the jet-energy scale. Fig. 4 also shows the $b\bar{b}$ $\Delta\phi$ dis-

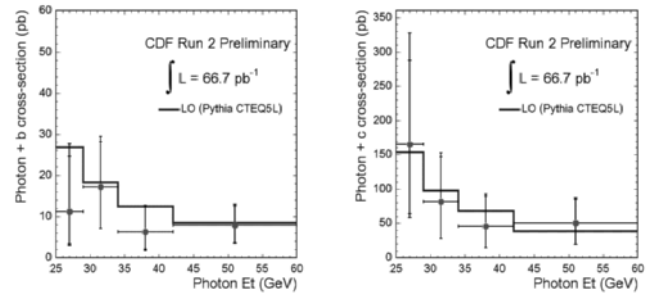


Fig. 5. Left: $\gamma + b$ cross section. Right: $\gamma + c$ production cross section

tribution between the two jets. Both curves are compared to LO as well as NLO MonteCarlo.

5 Photon + heavy flavour

A photon triggered dataset corresponding to an integrated luminosity of 64 pb^{-1} is used to measure $\gamma + b$ and $\gamma + c$ cross sections. A photon candidate with $E_t > 25 \text{ GeV}$ and a tagged jet are required. Photons are identified using the Central Electromagnetic Calorimeter (CEM) and two wire chambers: Central PreRadiation detector (CPR) just in front of the CEM and Central Shower Maximum (CSM) embedded inside the CEM at 6 radiation lengths, to remove the large π^0 background. Photon candidates are required to have an isolated e.m. shower with no tracks associated to them, the energy deposited in the hadronic calorimeter is required to be very small compared to the e.m. energy. To estimate the background the number of hits in the CPR is used: since the probability for a conversion to take place is much higher in the case of multiple photon than in the case of single photons, multiple photons are more likely to generate a hit in the CPR detector.

Fig. 5 shows the resulting cross section for $\gamma + b$ and $\gamma + c$ production. Both cases show good agreement with LO pythia predictions but show a large statistical uncertainty.

6 Conclusions

We have presented the b-jet production cross section at 1.96 TeV. It is in reasonable agreement with the expectations, and a comparison to NLO calculations is ongoing.

The $b\bar{b}$ and photon + heavy flavour analyses show a good agreement with expectation, but they are both statistically limited. Work is in progress to add more data to both measurements

References

1. M. Cacciari, S. Frixione, M. Mangano, P. Nason, J. High En. Phys. **07**, (2004) 033.

SPRINGER PROCEEDINGS IN PHYSICS

- 60 **The Physics and Chemistry of Oxide Superconductors**
Editors: Y. Iye and H. Yasuoka
- 61 **Surface X-Ray and Neutron Scattering**
Editors: H. Zabel and I.K. Robinson
- 62 **Surface Science**
Lectures on Basic Concepts and Applications
Editors: F.A. Ponce and M. Cardona
- 63 **Coherent Raman Spectroscopy**
Recent Advances
Editors: G. Marowsky and V.V. Smirnov
- 64 **Superconducting Devices and Their Applications**
Editors: H. Koch and H. Lübbling
- 65 **Present and Future of High-Energy Physics**
Editors: K.-I. Aoki and M. Kobayashi
- 66 **The Structure and Conformation of Amphiphilic Membranes**
Editors: R. Lipowsky, D. Richter, and K. Kremer
- 67 **Nonlinearity with Disorder**
Editors: F. Abdullaev, A.R. Bishop, and S. Pnevmatikos
- 68 **Time-Resolved Vibrational Spectroscopy V**
Editor: H. Takahashi
- 69 **Evolution of Dynamical Structures in Complex Systems**
Editors: R. Friedrich and A. Wunderlin
- 70 **Computational Approaches in Condensed-Matter Physics**
Editors: S. Miyashita, M. Imada, and H. Takayama
- 71 **Amorphous and Crystalline Silicon Carbide IV**
Editors: C.Y. Yang, M.M. Rahman, and G.L. Harris
- 72 **Computer Simulation Studies in Condensed-Matter Physics IV**
Editors: D.P. Landau, K.K. Mon, and H.-B. Schüttler
- 73 **Surface Science**
Principles and Applications
Editors: R.F. Howe, R.N. Lamb, and K. Wandelt
- 74 **Time-Resolved Vibrational Spectroscopy VI**
Editors: A. Lau, F. Siebert, and W. Werncke
- 75 **Computer Simulation Studies in Condensed-Matter Physics V**
Editors: D.P. Landau, K.K. Mon, and H.-B. Schüttler
- 76 **Computer Simulation Studies in Condensed-Matter Physics VI**
Editors: D.P. Landau, K.K. Mon, and H.-B. Schüttler
- 77 **Quantum Optics VI**
Editors: D.F. Walls and J.D. Harvey
- 78 **Computer Simulation Studies in Condensed-Matter Physics VII**
Editors: D.P. Landau, K.K. Mon, and H.-B. Schüttler
- 79 **Nonlinear Dynamics and Pattern Formation in Semiconductors and Devices**
Editor: F.-J. Niedernostheide
- 80 **Computer Simulation Studies in Condensed-Matter Physics VIII**
Editors: D.P. Landau, K.K. Mon, and H.-B. Schüttler
- 81 **Materials and Measurements in Molecular Electronics**
Editors: K. Kajimura and S. Kuroda
- 82 **Computer Simulation Studies in Condensed-Matter Physics IX**
Editors: D.P. Landau, K.K. Mon, and H.-B. Schüttler
- 83 **Computer Simulation Studies in Condensed-Matter Physics X**
Editors: D.P. Landau, K.K. Mon, and H.-B. Schüttler
- 84 **Computer Simulation Studies in Condensed-Matter Physics XI**
Editors: D.P. Landau and H.-B. Schüttler
- 85 **Computer Simulation Studies in Condensed-Matter Physics XII**
Editors: D.P. Landau, S.P. Lewis, and H.-B. Schüttler
- 86 **Computer Simulation Studies in Condensed-Matter Physics XIII**
Editors: D.P. Landau, S.P. Lewis, and H.-B. Schüttler
-